FACULTY OF MECHANICAL AND CIVIL ENGINEERING
IN KRALJEVO
UNIVERSITY OF KRAGUJEVAC

XI TRIENNIAL
INTERNATIONAL CONFERENCE

HEAVY MACHINERY HM 2023

Proceedings

VRNJAČKA BANJA, SERBIA
June 21– June 24, 2023

FACULTY OF MECHANICAL AND CIVIL ENGINEERING IN KRALJEVO
UNIVERSITY OF KRAGUJEVAC
KRALJEVO – SERBIA

THE ELEVENTH TRIENNIAL INTERNATIONAL CONFERENCE

HEAVY MACHINERY
HM 2023

PROCEEDINGS

ORGANIZATION SUPPORTED BY:

Ministry of Science, Technological Development and Innovation, Republic of Serbia

Vrnjačka Banja, June 21–24, 2023

FACULTY OF MECHANICAL AND CIVIL ENGINEERING IN KRALJEVO
UNIVERSITY OF KRAGUJEVAC
KRALJEVO – SERBIA

PUBLISHER:

Faculty of Mechanical and Civil Engineering in Kraljevo

YEAR:

2023

EDITOR:

Prof. dr Mile Savković

PRINTOUT:

SATCIP DOO VRNJAČKA BANJA

No. of copies: 60

ISBN-978-86-82434-01-6

REVIEWS:

All papers have been reviewed by members of scientific committee

CONFERENCE CHAIRMAN

Prof. dr Mile Savković, FMCE Kraljevo, Serbia

INTERNATIONAL SCIENTIFIC PROGRAM COMMITTEE

CHAIRMAN

Prof. dr Radovan Bulatović, FMCE Kraljevo, Serbia

VICE-CHAIRMAN

Prof. dr Milan Bižić, FMCE Kraljevo, Serbia

MEMBERS

Prof. dr M. Alamoreanu, TU Bucharest, Romania
Prof. dr D. Atmadzhova, VTU "Todor Kableshkov", Sofia, Bulgaria
Prof. dr M. Banić, FME Niš, Serbia
Prof. dr M. Berg, Royal Institute of Technology-KTH, Sweden
Prof. dr G. Bogdanović, Faculty of Engineering Kragujevac, Serbia
Prof. dr H. Bogdevicius, Technical University, Vilnus, Lithuania
Prof. dr N. Bogojević, FMCE Kraljevo, Serbia
Prof. dr I. Božić, FME Belgrade, Serbia
Prof. dr S. Bikić, Faculty of Technical Sciences, Novi Sad, Serbia
Prof. dr M. Bjelić, FMCE Kraljevo, Serbia
Prof. dr M. Blagojević, Faculty of Engineering Kragujevac, Serbia
Prof. dr S. Bošnjak, FME Belgrade, Serbia
Prof. dr A. Bruja, TU Bucharest, Romania
Prof. dr S. Ćirić-Kostić, FMCE Kraljevo, Serbia
Prof. dr I. Despotović, FMCE Kraljevo, Serbia
Prof. dr M. V. Dragoi, Transilvania University of Brasov, Romania
Prof. dr B. Dragović, Faculty of Maritime Studies Kotor, Montenegro
Prof. dr Lj. Dubonjić, FMCE Kraljevo, Serbia
Prof. dr R. Durković, FME Podgorica, Montenegro
Prof. dr Z. Đinović, ACMIT, Wiener Neustadt, Austria
Prof. dr R. Đokić, Faculty of Technical Sciences, Novi Sad, Serbia
Prof. dr K. Ehmann, Northwestern University, Chicago, USA
Prof. dr I. Emeljanova, HGTUSA Harkov, Ukraine
Prof. dr O. Erić Cekić, FMCE Kraljevo, Serbia
Prof. dr V. Gašić, FME Belgrade, Serbia
Prof. dr D. Golubović, FME East Sarajevo, Bosnia and Herzegovina
Prof. dr P. Gvero, FME Banja Luka, Bosnia and Herzegovina
Prof. dr B. Jerman, FME Ljubljana, Slovenia
Prof. dr R. Karamarković, FMCE Kraljevo, Serbia
Prof. dr M. Karasahin, Demirel University, Istanbul, Turkey
Prof. dr I. Kiričenko, HNADU Kiev, Ukraine
Prof. dr K. Kocman, Technical University of Brno, Czech Republic
Prof. dr S. Kolaković, Faculty of Technical Sciences, Novi Sad, Serbia
Prof. dr M. Kolarević, FMCE Kraljevo, Serbia
Prof. dr M. Kostić, Northern Illinois University, DeKalb, USA
Prof. dr M. Krajišnik, FME East Sarajevo, Bosnia and Herzegovina
Prof. dr M. Králik, FME Bratislava, Slovakia
Prof. dr E. Kudrjavcev, MGSU, Moscow, Russia
Prof. dr Đ. Lađinović, Faculty of Technical Sciences, Novi Sad, Serbia
Prof. dr D. Marinković, TU Berlin, Germany
Prof. dr G. Marković, FMCE Kraljevo, Serbia
Prof. dr A. Milašinović, FME Banja Luka, Bosnia and Herzegovina
Prof. dr I. Milićević, Technical Faculty Čačak, Serbia
Prof. dr V. Milićević, FMCE Kraljevo, Serbia
Prof. dr Z. Miljković, FME Belgrade, Serbia

Prof. dr D. Milković, FME Belgrade, Serbia
Prof. dr B. Milošević, FMCE Kraljevo, Serbia
Prof. dr V. Milovanović, Faculty of Engineering Kragujevac, Serbia
Prof. dr G. Minak, University of Bologna, Italy
Prof. dr D. Minić, FME Kosovska Mitrovica, Serbia
Prof. dr V. Nikolić, FME Niš, Serbia
Prof. dr E. Nikolov, Technical University, Sofia, Bulgaria
Prof. dr V. Nikolov, VTU "Todor Kableshkov", Sofia, Bulgaria
Prof. dr M. Ognjanović, FME Belgrade, Serbia
Prof. dr J. Peterka, FMS&T, Trnava, Slovakia
Prof. dr D. Petrović, FMCE Kraljevo, Serbia
Prof. dr M. Popović, Technical Faculty Čačak, Serbia
Prof. dr J. Polajnar, BC University, Prince George, Canada
Prof. dr D. Pršić, FMCE Kraljevo, Serbia
Prof. dr N. Radić, FME East Sarajevo, Bosnia and Herzegovina
Prof. dr B. Radičević, FMCE Kraljevo, Serbia
Prof. dr V. Radonjanin, Faculty of Technical Sciences, Novi Sad, Serbia
Prof. dr D. Sever, Maribor, Civil Engineering, Slovenia
Prof. dr V. Stojanović, FMCE Kraljevo, Serbia
Prof. dr I. S. Surovcev, VGSU, Voronezh, Russia
Prof. dr S. Šalinić, FMCE Kraljevo, Serbia
Prof. dr J. Tanasković, FME Belgrade, Serbia
Prof. dr LJ. Tanović, FME Belgrade, Serbia
Prof. dr D. Todorova, VTU "Todor Kableshkov", Sofia, Bulgaria
Prof. dr R. Vujadinovic, FME Podgorica, Montenegro
Prof. dr K. Weinert, University of Dortmund, Germany
Prof. dr N. Zdravković, FMCE Kraljevo, Serbia
Prof. dr N. Zrnić, FME Belgrade, Serbia
Prof. dr D. Živanić, Faculty of Technical Sciences, Novi Sad, Serbia

ORGANIZING COMMITTEE

CHAIRMAN:

Prof. dr Goran Marković, FMCE Kraljevo

VICE-CHAIRMAN:

Doc. dr Miljan Marašević, FMCE Kraljevo, Serbia

MEMBERS:

Doc. dr M. Bošković, FMCE Kraljevo, Serbia
Doc. dr V. Grković, FMCE Kraljevo, Serbia
Doc. dr V. Mandić, FMCE Kraljevo, Serbia
Doc. dr A. Nikolić, FMCE Kraljevo, Serbia
Doc. dr M. Nikolić, FMCE Kraljevo, Serbia
Doc. dr A. Petrović, FMCE Kraljevo, Serbia
Doc. dr B. Sredojević, FMCE Kraljevo, Serbia
Dr N. Pavlović, FMCE Kraljevo, Serbia
Doc. dr N. Stojić, FMCE Kraljevo, Serbia

PREFACE

Ladies and gentlemen, dear colleagues,

Welcome to Vrnjačka Banja, to the International Scientific Conference Heavy Machinery. The first conference was held in 1993, so this is the thirtieth anniversary of the Heavy Machinery conference.

This year the Eleventh International Conference Heavy Machinery is held by the Faculty of Mechanical and Civil Engineering in Kraljevo, University of Kragujevac, from 21 to 24 June 2023.

The conference has gained a unique recognizable form of exchange of information, ideas and new scientific research. It is held in the year when the Faculty of Mechanical and Civil Engineering in Kraljevo celebrates 63 years of university teaching.

During several decades of its existence, the Faculty has acquired a specific and recognizable form in domestic and foreign scientific circles thanks to its scientific and research results.

The goal of the Conference is to make the research in the fields covered at the Faculty of Mechanical and Civil Engineering in Kraljevo available and applicable within both domestic and foreign frames. Also, our scientists will have the opportunity to learn about the results of research done by their colleagues from abroad in the fields of transport design in industry, energy control, production technologies, and civil engineering through the following thematic sessions:

- Earth-moving and transportation machinery,
- Railway engineering,
- Production technologies,
- Automatic control and fluid technique,
- Applied mechanics,
- Thermal technique and environment protection,
- Civil engineering.

The high scientific reputation of domestic and foreign participants as well as the number of papers provide guarantees that the Conference will be very successful. The papers reflect the state-of-the-art and deal with a wide spectrum of important topics of current interest in heavy machinery.

I would especially like to thank the Ministry of Science, Technological Development and Innovation of the Republic of Serbia for its support to the organization of the Conference and our efforts to promote science and technology in the areas of mechanical and civil engineering in Serbia. Also, I would like to express our gratitude to other sponsors of the Conference: Serbian Chamber of Engineers, TeamCAD d.o.o. Zemun-Belgrade, Banim reklame d.o.o. Kraljevo, Radijator Inženjering d.o.o. Kraljevo and Messer Tehnogas AD Belgrade.

My sincere thanks also go to all members of the scientific, organizing and technical committees, the reviewers, and all the participants including the invited speakers for their participation in the Conference and presentation of their papers.

Thank you and see you at the next conference in three years.

Kraljevo – Vrnjačka Banja, June 2023

Conference Chairman,

Prof. dr Mile Savković

PLENARY SESSION

SESSION A: EARTH-MOVING AND TRANSPORTATION MACHINERY

SESSION B: RAILWAY ENGINEERING

SESSION C: PRODUCTION TECHNOLOGIES

SESSION D: AUTOMATIC CONTROL AND FLUID TECHNIQUE

SESSION E: APPLIED MECHANICS

SESSION F: THERMAL TECHNIQUE AND ENVIRONMENT PROTECTION

SESSION G: CIVIL ENGINEERING

PLENNARY SESSION

Warehousing 4.0

Boris Jerman[1*], Jurij Hladnik[1]
[1]Faculty of Mechanical Engineering, University of Ljubljana, Ljubljana (Slovenia)

The article presents research on robotic warehouse order-picking systems that can also be used as feeding systems in production processes. In the first part, robotic grippers of different types (vacuum grippers, servo-electric two-finger grippers, pneumatic two-finger grippers, gecko grippers, etc.) are studied in terms of gripping quality as a function of the characteristics of the objects to be gripped. For this investigation, a suitable test method was selected from the known methods and a suitable object set was chosen that is comparable to those used in other similar investigations. The object set used consists of various tools, cloths, chains, fruits, boxes, balls, etc. In the second part, the design and testing of our own pneumatic two-finger robotic soft gripper is presented. Its fingers were 3D printed from Flexible 80A and TPU 90A plastics using stereolithography and selective laser sintering, respectively. The developed gripper was tested for functionality and its gripping force was measured for different pneumatic pressures and for different gripping points. The last part of the article presents the modelling of the gripping with the two-finger robotic gripper in Adams software.

Keywords: Order-picking Systems, Robot Grippers, Gripping Quality, Flexible Grippers, Grasping Forces, Multibody Dynamics

1. INTRODUCTION

The development of automated warehousing is in full swing. Automated warehouses shorten picking time, enable better utilization of space, reduce the need for the number of employees and, above all, increase the reliability of product storage and commissioning. A big problem in warehouse automatization is still the order-picking of individual pieces according to the order list [1]. Order-picking is usually only partially automated, although most of the movements are repetitive. The problem presents bin-picking due to the wide assortment of pieces of different dimensions, shapes, masses and materials, which makes it difficult for robots to compete with humans in terms of speed, adaptability, and dexterity [2].

Full automation of bin-picking tasks is challenging because it involves 3D object recognition, pose estimation, grasp planning, path planning, and collision avoidance [3]. Each of these problems presents a vast area of research and is usually treated separately. E.g., in [4] and [5] new object recognition and grasping algorithms were studied, in [6] the positioning and orientation of the objects within a stock keeping unit was studied and in [7] the usage of different grasping devices was analysed.

The ability to grasp never-before-seen objects is something that humans develop in their first year of life [8] and is a major challenge for robots. One way to improve grip is by developing better robotic vision and detecting poor grips. The disadvantage of such systems is sensitivity to brightness, to light-reflective and transparent surfaces, and to darkened parts of objects [8].

Grasping is inherently related to forces that cannot be perceived by sight. Therefore, touch sensors are used to improve robot grasping, which must be connected with intelligent algorithms. For example, in [9], a better grip location was estimated using the measured force vector at the contact location.

Another research area deals with the assessment of the grasping performance of the robot arms [10, 11]. Its aim is to develop objective and reproducible tests to obtain comparable results between different grippers. Falco [12, 13] divides the grasp performance measures into quantitative and qualitative. While qualitative measures are easily found in the literature, quantitative measures to evaluate the grasp performance are rarer [14 to 17]. He presented [12] multiple quantitative assessments of the robotic hand grasp performance: e.g. touch sensitivity (measures the smallest force that the hand perceives), finger strength (measurement of the maximum force of the fingers), grip strength (measurement of the maximum force caused by the hand on two cylinders of different diameters), sliding resistance (measurement of the force at which a halved cylinder, which is pulled along the axis, slides out of the grip), etc., where all these assessments were performed by an external measurement system.

2. STRUCTURE OF A PAPER

The article presents research on robotic warehouse order-picking systems. In the first part, robot grippers of different types are examined for their gripping quality. In the second part, the design and testing of a custom robot soft gripper is presented. In the last part of the article, the modelling of gripping with the two-finger robot gripper in Adams software is presented, and at the end the conclusions are given with ideas for further work.

3. THE ROBOT GRIPPER EVALUATION

The evaluation of the quality and efficiency of gripping different types of objects with different types of robotic grippers is carried out by real experiments. The procedure and results are briefly presented in this section. For more details, see the literature [1].

3.1. The grippers considered and objects to gripped

In this study, the following types of robotic grippers were tested: electric two-finger gripper (2F gripper), vacuum gripper with one vacuum end unit (vacuum gripper), a robotic gripper with a sticky surface (gecko gripper), and a soft two-finger gripper (soft gripper).

We used the modified YCB test object set, which consisted of 45 objects divided into 8 groups based on the

*Corresponding author: Faculty of Mechanical Engineering, Aškerčeva 6, SI-1235 Ljubljana, Slovenia; boris.jerman@fs.uni-lj.si

characteristics that affect their handling, such as shape, size, stiffness, etc.:

1. Packaging: boxes, cans and bottles, wooden logs and sponges for cleaning. Characterized by simple shapes in which no dimension stands out and of even mass distribution.
2. (Plastic) fruits. Characterized by various specific shapes.
3. Tools: workshop, office, and kitchen tools. Characterized by complex shapes, in which one dimension often stands out, and of uneven mass distribution.
4. Spherical objects: different diameters, stiffness, and surface structures.
5. Cutlery: flat and shell-shaped objects with openings and handles (e.g. spoon, fork, knife).
6. Small objects: of simple shapes, at least one dimension of which is distinctly small.
7. Deformable objects: objects whose shape changes during their manipulation.
8. Task objects: objects for performance of tasks (e.g. wooden blocks, LEGO bricks, Rubik's cube, magazine).

3.2. The testing method

The UR5e collaborative robot was used to perform the tests, and its motions are described in the coordinate system with horizontal X-axis positioned radially to the first vertical axis of rotation of the robot in the direction of the robot arm, Z-direction aligned with the first vertical axis of rotation of the robot, and horizontal Y-axis perpendicular to the X- and Z-axes.

Each object is positioned in front of the robot at four different locations: the initial location determined to be the optimal location for gripping, and three additional locations that differ by 10 mm from the first. Exceptions are flat objects, for which only three positions are used, and deformable objects, for which only the optimal position is used.

After that, the following steps follow:

1. The object is grasped by the gripper.
2. The object is raised for 150 mm and held for 3 seconds.
3. The object is rotated 90° around the X-axis and held for 3 seconds.
4. The object is rotated 90° around the Y-axis and held for 3 seconds (this step is additional to YCB testing procedure).
5. The object is returned to its starting position.

If the optimal position of the object causes the object to fall, the test with that object is completed. If the object falls in the second or third start position, the test continues.

For each completed test, the following evaluation is performed. If the object is not released in the 2nd step and no free movement of the object within the gripper is detected, 2 points are awarded. If free movement of the object is detected, only 1 point is awarded. If the object is not released in the 3rd and 4th steps and free movement of the object is not detected, another 2 points are awarded. If free movement of the object is detected, only 1 point is awarded. This procedure is repeated for all 4 start positions.

The test procedure for deformable objects is different. The object is raised 150 mm, held for 3 s, and returned. This is repeated twenty times.

For deformable objects, any grasp in which no part of the object touches the ground after the second step is considered successful and 0.5 points are awarded.

3.3. The results of the testing

Figure 1 shows the results for the overall efficiency of the robot grippers. The most efficient, and thus the most universal, are the 2F and soft grippers with 72% and 71% efficiency, respectively.

Figure 2 shows the results for gripping efficiency by categories of test objects. It is clear that 2F and soft grippers are the most efficient with 94% and 95% efficiency for the packaging and spherical object categories, respectively.

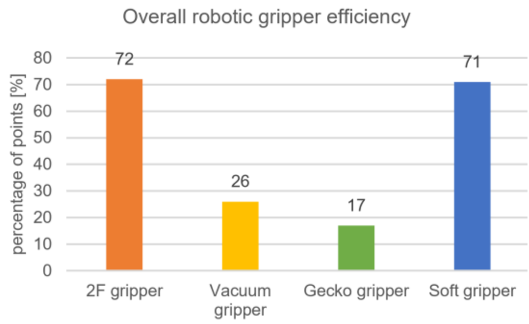

Figure 1: New soft finger design

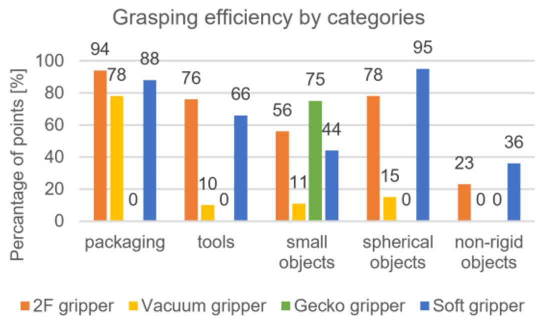

Figure 2: New soft finger design

4. THE DEVELOPEMENT OF OWN TWO-FINGER PNEUMATIC SOFT GRIPPER

4.1. The design of the pneumatic finger

The next objective of the study was to investigate the mechanism of soft grippers functioning. We studied designs of soft grippers currently available on the market and found that none of them were suitable for our research purposes. Therefore, we developed a new design of the soft finger of the gripper (Figure 3), where the effect of the pneumatic force can be described analytically more accurately and easily.

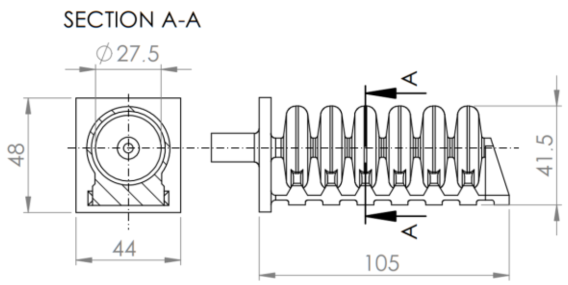

Figure 3: New soft finger design

The soft fingers of the grippers were printed using the 3D printing technology of stereolithography and selective laser sintering from Flexible 80A (Figure 4) and TPU 90A (Figure 5) filaments, which ensures the flexibility and airtightness of the fingers.

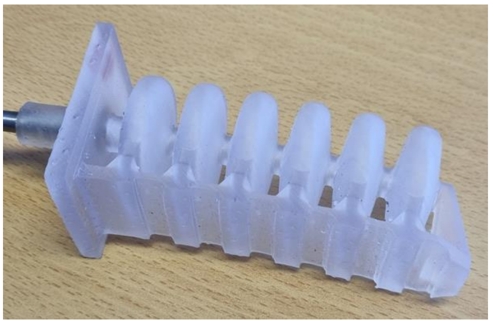

Figure 4: Photo of new soft finger made of Flexible 80A plastics

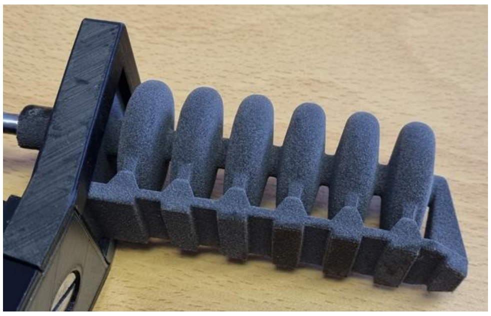

Figure 5: Photo of new soft finger made of TPU 90A Powder

The pairs of gripper fingers were integrated into the modular gripper base to form a soft robotic gripper (Figures 6 and 7).

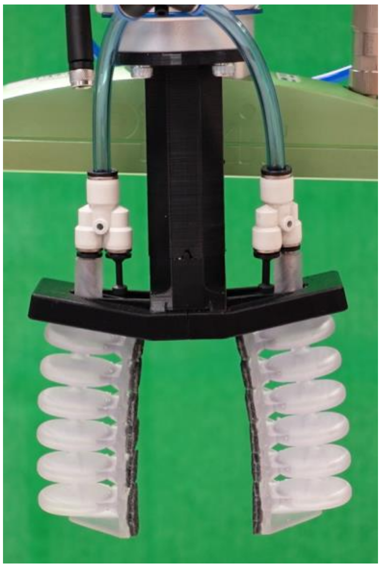

Figure 6: Soft gripper with fingers made of Flexible 80A plastics with additional rubber pads

Figure 7: Soft gripper with fingers made of TPU 90A Powder

4.2. The configuration of measurements

A special force sensor consisting of two lamellae was made to measure the gripping force. The figure 8 - left shows the 3D model of the force sensor with black spacer, grey lamellae and blue hemispheres, which provides the exact point of contact with the fingers of the gripper. Figure 8 - centre shows the photo of the sensor with white spacer, black metallic lamellas and white hemispheres. Figure 8 - right shows the photo of the force sensor lamella equipped with four 350 ± 1.0 Ω strain gauges (type FLAB -3-350-11-LJB-F, Tokyo Measuring instruments Lab., Japan, gauge factor k = 2.07) connected in a full bridge configuration (Type I) on a bended beam [18]. The full bridge was connected via a coaxial cable to a data acquisition system (SCXI 1520, National Instruments Corporation), which supplied the strain gauges with a DC voltage of 10 V, and to a measurement station (NI PXIw-1062Q, National Instruments Corporation), where the output signal was acquired and processed (LabView 16.0, National Instruments Corporation). The strain gauges were protected with a silicone coating and plastic shields. The measuring lamella was calibrated by clamping it to a table and loading it with known loads (weights) at the point where the lamella was supposed to be loaded (Figure 9). Excellent linearity, accuracy and repeatability of the force sensor were demonstrated and a suitable scale factor was determined.

Figure 8: The 3D model and photo of the gripping force sensor and the modified sensor lamella with four strain gauges (two visible and two hidden on the other side)

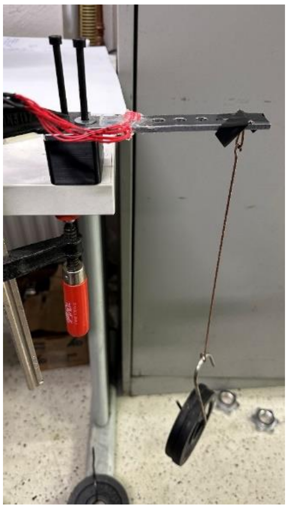

Figure 9: Calibration of force sensor by applying known weights on the loading point

Figure10 shows the current configuration of the gripping force measurement. The force sensor is located on the left side. It has black spacers, black/metallic modified lamellas and black contact half-cylinders instead of contact hemispheres. The soft two-finger gripper is on the right side, with transparent fingers, black/white/red gripper base and blue pneumatic tubes. The sensor and gripper are both attached to the table with clamps so that the contact point between the fingers and the sensor can be precisely determined.

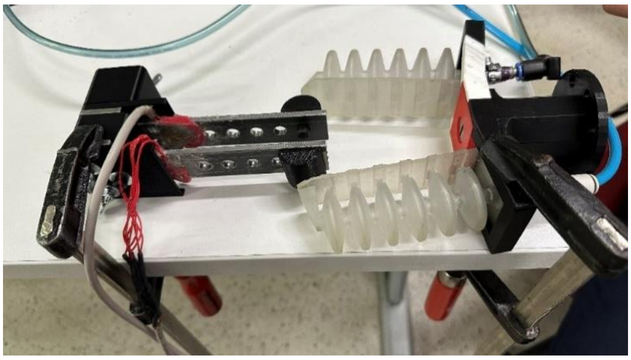

Figure10: The gripping force measurements configuration

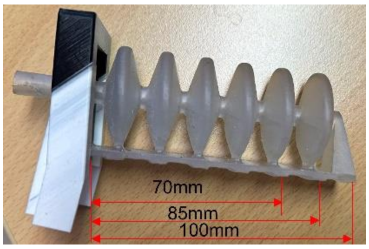

Figure11: The positions of the grasping force measurements points (contact points) on the finger, cantilever mounted into the gripper base

The selected contact points are shown in Figure11, which indicates that the gripping force generated by the gripper is generated at distances (R) 70 mm (3), 85 mm (2), and 100 mm (1) from the fingers cantilever-mounted in the gripper base.

Pressures (P) of 0.5 bar to 1.5 bar were used for both the (i) Flexible 80A and (ii) TPU 90A fingers.

The measurements were repeated three times under the same conditions.

4.3. The results of grasping force measurements

Selected results of the gripping force measurements (for position (1), R=100 mm) are shown in diagrams in figures 12 to 17. All results are summarized in figure 18.

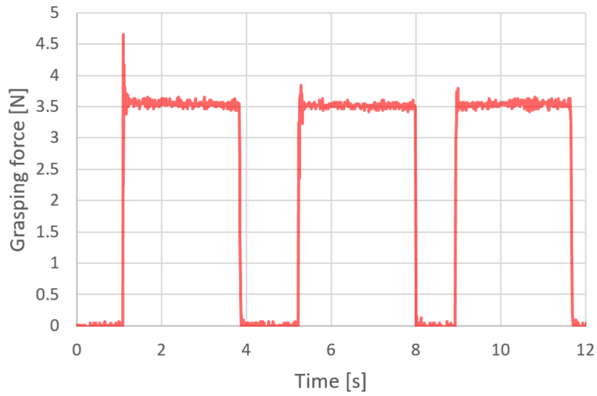

Figure 12: The grasper force for the gripper (i) at position (1) and pressure 0.5 bar

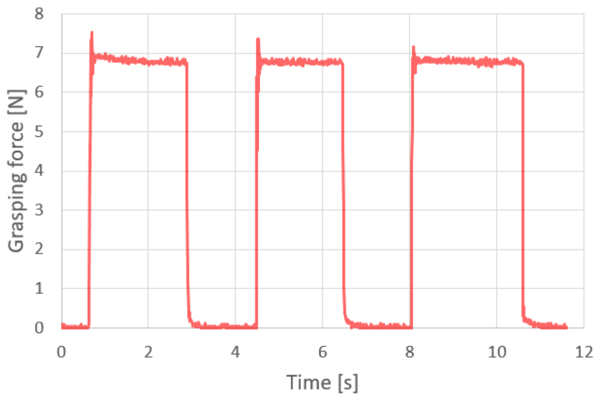

Figure13: The grasper force for the gripper (i) at position (1) and pressure 1.0 bar

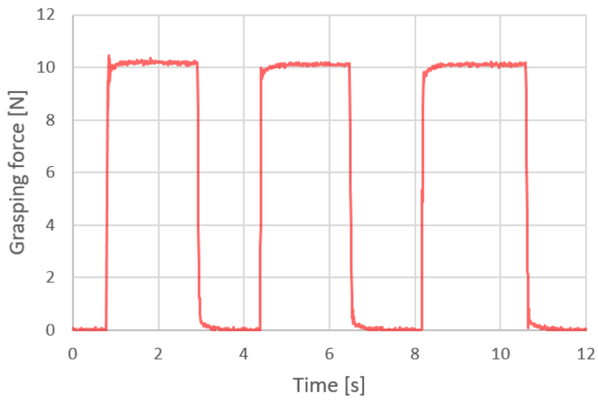

Figure 14: The grasper force for the gripper (i) at position (1) and pressure 1.5 bar

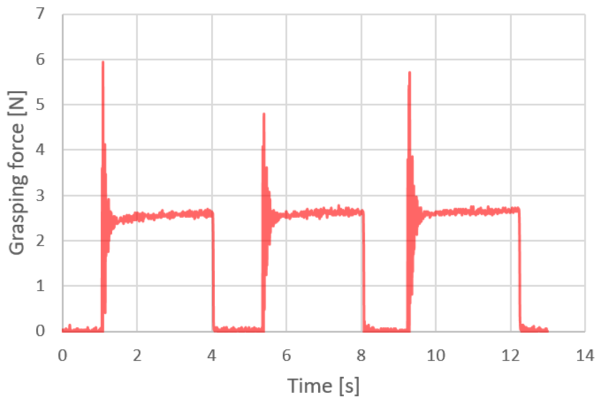

Figure 15: The grasper force for the gripper (ii) at position (1) and pressure 0.5 bar

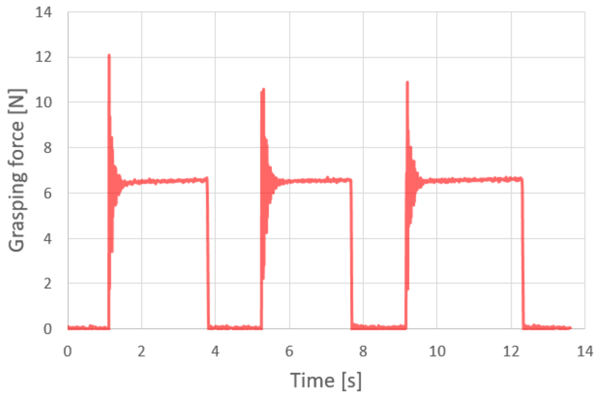

Figure 16: The grasper force for the gripper (ii) at position (1) and pressure 1.0 bar

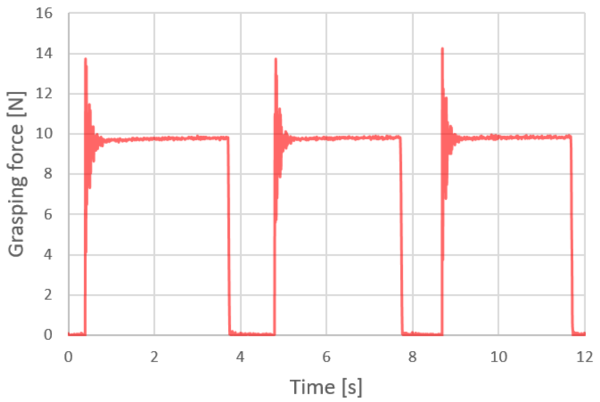

Figure 17: The grasper force for the gripper (ii) at position (1) and pressure 1.5 bar

From the diagrams in figures 12 to 14 for finger (i), it is evident that at the time of contact between the gripper and the object to be gripped, a relatively small contact force peak occurs, followed by force fluctuations that fade out in a tenth of a second. After that a steady gripping force is observed.

On the other hand, the graphs in Figures 15 to 15 for finger (ii) show much larger force peaks at the time of contact, followed by force fluctuations that fade out in a few tenths of a second. After that a uniform gripping force can be observed.

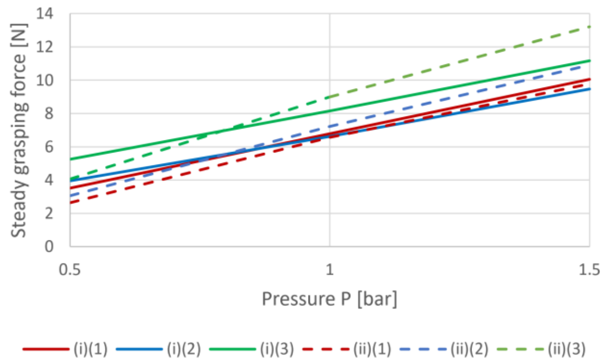

Figure 18: Steady grasping force with regard to input pressure P (0.5 bar, 1.0 bar, 1.5 bar), grasping point R ((1), (2) or (3)) and type of flexible fingers ((i) or (ii))

From figure 18 it is evident that the increase in constant gripping force is linear with the increase in pressure applied to the flexible fingers. It is also clear that the gripping force is significantly greater at the lowest pressure for finger type (i), which is made of a more elastic (less rigid) material, since less of the input pressure is spent on elastic deformation of the finger and therefore more of it is available for gripping. The next observation is that at higher pressure, the gripping force of finger type (ii) becomes larger than that of finger type (i), except at the gripping point (1), where it remains somewhat smaller.

5. THE NUMERICAL MODELLING OF THE GRASPING OF AN OBJECT

5.1. The numerical model

Gripping of an object with a classical two-finger (2F) gripper was numerically modelled in Adams software to numerically test the gripping performance of the 2F gripper in gripping differently oriented rigid objects of different shapes and sizes gripped at different gripping points and with differently oriented grippers.

The main challenge was to allow arbitrary orientation of the object. This problem was solved using an auxiliary object - the base box - into which the object was thrown from above at the beginning of the simulation (Figure 19). Since the base box is in an inclined position, the object slides into the lowest corner and thus its position and orientation are known.

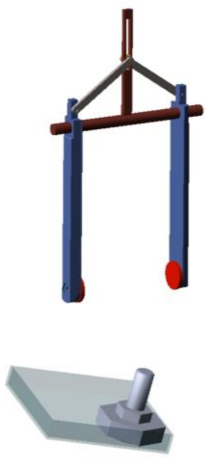

Figure 19: The object (bolt), thrown into the inclined base box, slides into base box's lowest corner

In the next step, the base box can be rotated around all axes to get its arbitrary orientation (Figure 20 - right). Since the gripper can also be rotated around all axes and moved along them (Figure 20 - left), it can reach the arbitrary orientation and gripping point.

Since the contacts are modelled only between the object and the base box and, of course, between the object and the gripper fingers, the base box doesn't hinder the gripping of an object.

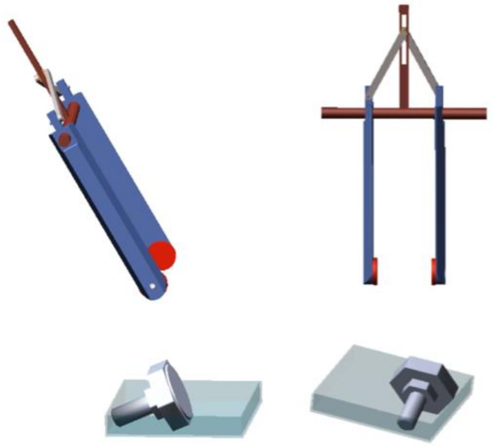

Figure 20: With appropriate input parameters the position and orientation of the gripper and of the object in the base box can be controlled

After successfully incorporating this solution into Adams' numerical model, this model will be prepared for extensive numerical testing in MATLAB Simulink, automating the modification of input parameters and the recording of results.

6. CONCLUSIONS

The research project on robot commissioning is presented in the paper.

In the physical testing of the efficiency of the robot grippers, it was found that the 2F gripper has the best overall gripping efficiency (72%) and that the soft gripper has almost the same overall efficiency (71%). In addition, it was found that the vacuum and gecko grippers are only good for certain applications,

The most efficient gripper within individual category is the soft gripper for spherical objects (95%), followed by the 2F gripper (with 78% efficiency).

The experiments show that non-rigid objects are the most problematic for the grippers included in the study (the efficiency is 36% or less).

Through the development and testing of the numerical model in Adams, it was found that the Adams software is suitable for the simulation of the gripping process, where the model of the gripper can be largely simplified to allow efficient simulations, while the objects must have a realistic shape, but a 3D model should be used rather than scanned geometry.

To ensure the accurate position and orientation of the object, the rotating base box can be included in the Adams model.

In the future, it is planned to test the gripping efficiency of the newly developed soft gripper and compare the results with those presented in this paper. The operation of the new soft robot gripper and its finger will also be described analytically and numerically, and the results will be compared with those measured. It is planned to publish the results of the comparison in a scientific article. The numerical model of the gripping process developed in Adams will be integrated into MATHLAB Simulink software to enable extensive simulations of the gripping efficiency of the gripper in question.

ACKNOWLEDGEMENTS

This article is the result of the joint work of members of the Laboratory of Cognitive Systems in Logistics at the University of Maribor, Faculty of Logistics, and the Laboratory of Material Handling and Machine Structures LASOK at the University of Ljubljana, Faculty of Mechanical Engineering. We thank Kristjan Uhan, Rok Jelovčan and the Laboratory of Fluid Power and Controls LFT at the University of Ljubljana, Faculty of Mechanical Engineering, for their help in performing the measurements. We also thank the company IB-CADDY d.o.o., Dunajska cesta 106, Si-1000 Ljubljana, Slovenia, for 3D printing the flexible pneumatic fingers of the robot gripper from various flexible filaments. The research was supported by the Slovenian Research Agency (ARRS) under the applied research project entitled "Warehousing 4.0-Integration model of robotics and warehouse order-picking systems"; grant number: L5-2626.

REFERENCES

[1] T. Lerher, P. Benčak, L. Bizjak, D. Hercog, B. Jerman, “Robotic bin-picking: Benchmarking robotic grippers with modified YCB object and model set”, Proceedings of International Material Handling Research Colloquium IMHRC 2023”, Dresden (Germany), 19-23 June 2023, (2023)

[2] S. Morgan *et al.*, "Benchmarking Cluttered Robot Pick-and-Place Manipulation With the Box and Blocks Test," *IEEE Robotics and Automation Letters,* Article vol. 5, no. 2, pp. 454-461, 2020, Art no. 8936856, doi: 10.1109/lra.2019.2961053

[3] Boschetti, G.; Sinico, T.; Trevisani, A. Improving Robotic Bin-Picking Performances through Human–Robot Collaboration. Appl. Sci. 2023, 13, 5429. https://doi.org/10.3390/app13095429

[4] N. Correll et al., "Analysis and Observations From the First Amazon Picking Challenge," IEEE Transactions on Automation Science and Engineering, vol. 15, no. 1, pp. 172-188, 2018, doi: 10.1109/TASE.2016.2600527

[5] J. Mahler et al., "Learning ambidextrous robot grasping policies," Sci Robot, Article vol. 4, no. 26, Jan 16 2019, Art no. eaau4984, doi: 10.1126/scirobotics.aau4984

[6] X. Li et al., "A Sim-to-Real Object Recognition and Localization Framework for Industrial Robotic Bin Picking," IEEE Robotics and Automation Letters, Article vol. 7, no. 2, pp. 3961-3968, 2022, doi: 10.1109/LRA.2022.3149026

[7] S. Hasegawa, K. Wada, Y. Niitani, K. Okada, and M. Inaba, "A three-fingered hand with a suction gripping system for picking various objects in cluttered narrow space," in IEEE International Conference on Intelligent

Robots and Systems, 2017, vol. 2017-September, pp. 1164-1171, doi: 10.1109/IROS.2017.8202288

[8] COCKBURN, D., ROBERGE, J. P., LE, T. H. L., MASLYCZYK, A. & DUCHAINE, V. 2017. Grasp Stability Assessment through Unsupervised Feature Learning of Tactile Images. IEEE International Conference on Robotics and Automation (ICRA). Singapore

[9] Dang H, Weisz J, Allen PK. Blind Grasping: Stable Robotic Grasping Using Tactile Feedback and Hand Kinematics. *Ieee Int Conf Robot.* 2011

[10] B. Calli, A. Walsman, A. Singh, S. Srinivasa, P. Abbeel, and A. M. Dollar, "Benchmarking in Manipulation Research: Using the Yale-CMU-Berkeley Object and Model Set," *IEEE Robotics & Automation Magazine*, Article vol. 22, no. 3, pp. 36-52, 2015, Art no. 7254318, doi: 10.1109/mra.2015.2448951

[11] ROA, M. A. & SUAREZ, R. 2015. Grasp quality measures: review and performance. Autonomous Robots, 38, 65-88

[12] FALCO, J., VAN WYK, K., LIU, S. & CARPIN, S. 2015. Grasping the Performance Facilitating Replicable Performance Measures via Benchmarking and Standardized Methodologies. Ieee Robotics & Automation Magazine, 22, 125-136

[13] J. Falco et al., "Benchmarking Protocols for Evaluating Grasp Strength, Grasp Cycle Time, Finger Strength, and Finger Repeatability of Robot End-Effectors," in IEEE Robotics and Automation Letters, vol. 5, no. 2, pp. 644-651, April 2020, doi: 10.1109/LRA.2020.2964164

[14] A. M. Dollar, L. P. Jentoft, J. H. Gao, and R. D. Howe, "Contact sensing and grasping performance of compliant hands," Auton. Robot., vol. 28, no. 1, pp. 65–75, 2010

[15] G. A. Kragten, C. Meijneke, and J. L. Herder, "A proposal for benchmark tests for underactuated or compliant hands," Mech. Sci., vol. 1, no. 1, pp. 13–18, 2010

[16] C. Meijneke, G. A. Kragten, and M. Wisse, "Design and performance assessment of an underactuated hand for industrial applications," Mech. Sci., vol. 2, no. 1, pp. 9–15, 2011

[17] V. Wright, "Prosthetic outcome measures for use with upper limb amputees: A systematic review of peer-reviewed literature," J. Prosthet. Orthot., vol. 21, no. 4, pp. 3–63, 2009

[18] K. Hoffmann, "Applying the Wheatstone Bridge Circuit," In: HBM, (2001)

Development of a Domestic 4-axis SCARA Robot

Zoran Miljković[1*], Nikola Slavković[1], Bogdan Momčilović[1], Đorđe Milićević[2]
[1]Faculty of Mechanical Engineering, Department for Production Engineering, University of Belgrade, Belgrade (Serbia)
[2] Smurfit Kappa Paper Factory Belgrade LLC, Belgrade (Serbia)

The global manufacturing industry has been demanding a steady increase in active industrial robots worldwide for years. The fields and technological tasks in which industrial robots are applied are rapidly expanding with a constant demand for improvement of their functions, technical characteristics as well as control and programming systems. One of the goals of the current research in the Laboratory for Robotics & AI is development of a domestic industrial robot with the possibility of automated programming based on information obtained from the camera. The paper presents the first part of the research developing a 4-axis SCARA industrial robot with the control system integrated camera. Professor Hiroshi Makino from Yamanashi University designed SCARA (Selective Compliance Assembly Robot Arm), and this robot is the most famous robot configuration originated at the universities. This part of the research includes the design of the mechanical structure, preliminary CAD/CAM testing, development of control and programming systems, virtual robot simulation, and robot production that were parts of two Master theses done in 2022. The realization of the robot control system starts from a well-known SCARA robot kinematic model. The open architecture control system realized in the LinuxCNC software allows the possibility of further development and full camera integration. The control system includes the integrated virtual robot model configured using several predefined Python classes and OpenGL as a digital shadow of the developed SCARA robot. Several successfully done examples of technological tasks of laser engraving have shown the verification of the complete robotic system.

Keywords: Industrial robot, Control and programming, Virtual robot

1. INTRODUCTION

One of the outcomes of Industry 4.0 is highly powerful, safe, and cost-effective intelligent factories developed with advanced robotics, cloud computing, the Internet of Things, and other advanced technological developments. Industrial robotics is an essential technology of Industry 4.0, which provides extensive capabilities in the field of manufacturing [1]. Industrial robots have a crucial role in modern factories with tasks such as picking and placing, inspection, assembly, machining, additive manufacturing, etc. Robot arms are complex enough to perform these tasks. However, the fields and technological demands in which industrial robots are applied are rapidly expanding with the constant requirement to improve their functions, technical characteristics as well as control and programming systems. This results in the robot arm being constantly modified with additional subsystems that result in advanced capabilities of its functionality. In other words, many industrial robots operating in intelligent factories use artificial intelligence to perform the high-level tasks. Today, they can also decide and learn from the experience in various ongoing situations [1].

Robot off-line programming and simulation through differently realized digital models are crucially important for some complex manufacturing tasks. As it is known, one of the essential Industry 4.0 technologies is a digital twin technology. The digital twin presents a virtual representation of the process, system or other physical entity using virtual and augmented reality, 3D visualization, and data modelling. Off-line programming can be generally categorized into computer-aided design-based (CAD-based) and vision-based approaches. These two off-line programming approaches, as a hybrid approach, have been widely applied in robotic systems to realize many manufacturing tasks [2].

The complexity of industrial robot programming in the manufacturing tasks such as cutting, laser engraving, 3D printing, etc., lies in the fact that there is no unique robot native language [3, 4]. Unlike robots, standard ISO 6983 (G-code) is used to program the machine tools. For this reason, it is difficult to involve widely available machine tools' CAD/CAM systems for programming machining robots. One way to solve this problem is by using the appropriate specialized CAM systems for robot programming or the developed translators to convert toolpaths for machining tasks into the corresponding robotic languages [4]. Robots' CAM systems or translators are not cost-effective and could be developed. Another way presents the open architecture control system development that allows programming in G-code [3].

One of the main goals of the current research in the Laboratory for Robotics & AI, Department of the Production Engineering at the Faculty of Mechanical Engineering within the University of Belgrade, is development of a domestic industrial robot and its digital twin with the possibility of automated programming based on the information obtained from the camera and AI techniques.

The selected robot for this research is SCARA (Selective Compliance Assembly Robot Arm) most famous robot configuration that originated at universities. The report [5] recounts mainly the first stage of the development of the SCARA. As stated in [5], the SCARA was invented by Professor Hiroshi Makino of the University of Yamanashi, Japan, the author of the report [5], and developed by him in collaboration with his colleagues and industrial partners. The SCARA is an industrial robot typical for those widely used in assembly processes. The prototype of the SCARA robot was built in 1978. Fundamental studies were done on the characteristics and

*Corresponding author: Kraljice Marije 16, 11120 Belgrade 35, Serbia, zmiljkovic@mas.bg.ac.rs

usability of this prototype, and the second was built in 1980. In 1981, some industrial partners began to market their versions of the SCARA. These models were called SCARA-type robots.

2. OUTLINE OF THE CONCEPT

The development of a domestic 4-axis SCARA industrial robot with programming in G-code and its digital twin with the possibility of a hybrid approach for automated programming based on information obtained from the camera and AI techniques consists of two parts.

The first part of the research includes the design of the mechanical structure, preliminary CAD/CAM testing, development of control and programming systems, virtual robot simulation, and robot production that were parts of two Master theses done in 2022 [6, 7]. This part is presented in the paper. The realization of the robot control system starts from a well-known SCARA robot kinematic model. The open architecture control system realized in the LinuxCNC software, which enables programming in G-code, allows further development and full camera integration. The control system includes the integrated virtual robot model configured by using the several predefined Python classes and OpenGL as a digital shadow of the developed SCARA robot. Several successfully done examples of technological tasks of laser engraving have shown the verification of the complete robotic system.

The highlights of the further research (the second part) will include: (1) the development of analytical and machine learning methods based on artificial neural networks to realize the accurate robot position based on camera information, (2) the applying artificial intelligence techniques and information obtained from the camera to generate the path of the robot end-effector for a selected class of tasks in a technological environment, and (3) the development of the experimental environment to achieve the software-hardware integration of the control system and visual detection based on the camera for automatic hybrid robot programming.

3. KINEMATIC MODELLING AND DESIGN

The kinematic modelling necessary for development of the control and programming system starts from well-known kinematic equations of the SCARA robots [8, 9]. The kinematic modelling of the robot includes: solutions for inverse and direct kinematic problems and analysis of the workspace.

3.1. Kinematic modelling of the 4-axis SCARA robot

The direct kinematic problem of serial manipulators can be easily solved by using Denavit-Hartenberg parameters and homogenous transformation.

The geometric model of the SCARA robot, its planar part including the first two links, is presented in Figure 1a. The world coordinate vector, Figure 1a and Figure 2a, is defined as:

$$\boldsymbol{x} = [p_x \quad p_y \quad p_z \quad \phi]^T \tag{1}$$

In the same manner, the joint coordinate vector is derived as:

$$\boldsymbol{\theta} = [\theta_1 \quad \theta_2 \quad d_3 \quad \theta_4]^T \tag{2}$$

From Figure 1a, it could be derived equation (3) as follows:

$$p_x{}^2 + p_y{}^2 = a_1{}^2 + a_2{}^2 + 2a_1a_2c\theta_2 \tag{3}$$

By expressing in terms of the unknown variable θ_2 the equation (4) is derived as:

$$c\theta_2 = \frac{p_x{}^2+p_y{}^2-a_1{}^2-a_2{}^2}{2a_1a_2} \tag{4}$$

Now using the expression $s\theta_2 = \pm\sqrt{1-(c\theta_2)^2}$ the joint coordinate θ_2 can be determined as:

$$\theta_2 = Atan2(s\theta_2, c\theta_2) \tag{5}$$

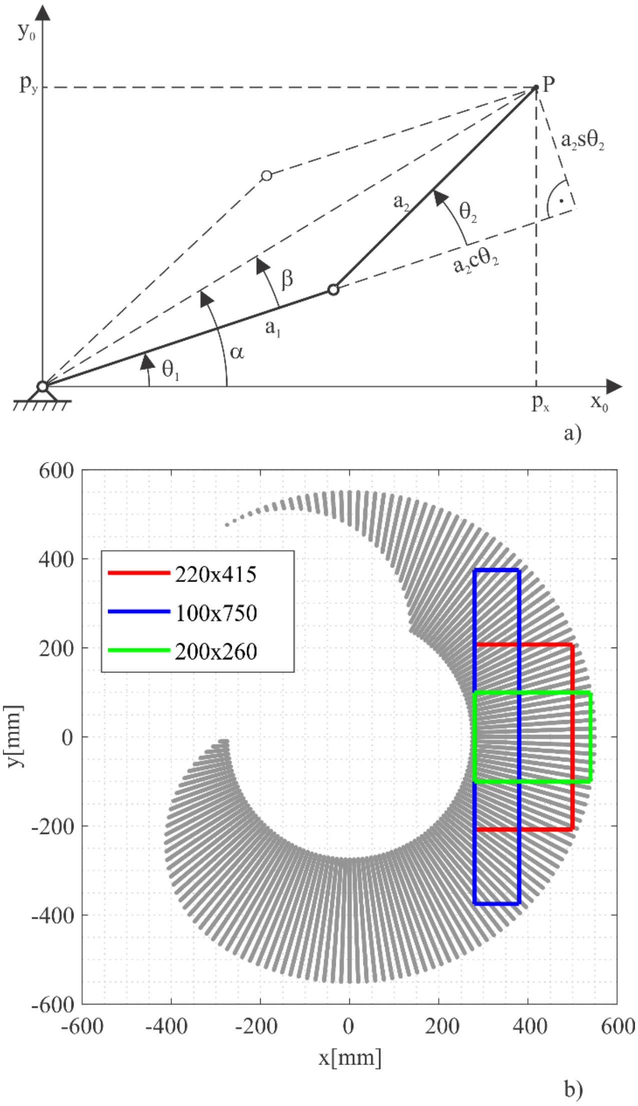

Figure 1: Kinematic model of SCARA robot

Joint coordinate θ_1 can be derived according to the value of angles α and β as:

$$\theta_1 = \alpha - \beta \tag{6}$$

$$\theta_1 = Atan2(p_y, p_x) - Atan2(a_2s\theta_2, a_1 + a_2c\theta_2) \tag{7}$$

Based on Figure 2a, the remaining two joint coordinates can be calculated simply as:

$$d_3 = d_1 - p_z \tag{8}$$

$$\theta_4 = \phi - \theta_1 - \theta_2 \tag{9}$$

Another characteristic of the robot structure for developing the virtual model and the physical prototype is the robot workspace. The method used to determine workspace considers whether the point defined in Cartesian space is reachable, according to the limits in the joints, based on solutions of the inverse kinematic problem. Designing a new prototype implies that the working space analysis is an iterative procedure. It involves the mechanism parameters being changed and, in the end, adopted based on the satisfactory dimensions of the workspace [10]. The robot parameters are $a_1 = a_2 = 275\,mm$, and joint coordinates θ_1 and θ_2 have limits $\pm 120°$. Figure 1b presents the shape and dimension of the workspace of the considered SCARA 4-axis robot in the xy plane. The third dimension of the workspace depends on joint coordinate d_3, Figure 2a. According to the robot structure, it is evident that the shape and dimensions of the workspace in the xy plane are the same along the z axis direction. The operators could use all portions of the workspace with irregular shape or reduced workspace to appropriate parallelepiped according to the task.

3.2. Designing the considered SCARA robot

Figure 2 shows the project of the SCARA robot, which is created within the CAD/CAM system PTC Creo, with its elements and gear ratios of the actuated axes. As it is said, the robot has four degrees of freedom. As with any robot of the SCARA configuration, the end-effector position in the horizontal plane is ensured by the coupled movement of the two segments by two rotary joints. The kinematic pair of a screw spindle and nut enables the position in the vertical plane. The fourth actuated rotary axis achieves orientation of the end-effector around its axis.

All axes are actuated by a stepper motor, which ensures the precise positioning of the moving elements of the robot. The first two rotating axes use NEMA 23, 57x112, 3.0A, 2.8Nm stepper motors, while the remaining two axes use, NEMA 23, 57x56, 2.8A, 1.17Nm. The torque transmission from the motor to the shafts of the actuated axis is achieved by using a toothed belt pair, HTD-5M/15. As we can see in Figure 2b, the gear ratio of the first actuated axis is $i_1 = 18/34$, the second $i_2 = 32/34$, the third $i_3 = 12/12$, and the fourth $i_4 = 30/30$. Since stepper motors are used while no encoders measure the joint position, the robot has four inductive sensors (one for each axis). These sensors are used in the initialization step when the physically determined zero-position of the robot has to be found.

The CAD/CAM environment in which the robot is configured can also be used as a system for programming and simulating the machining task of the industrial robots. To include the virtual prototype of the robot in the simulation of the programmed path, the robot must be configured with appropriate kinematic links, which was previously done by applying the rotary joints (Pin) and translatory joints (Slider). It is necessary to define the local coordinate systems of the robot and end-effector. The robot (machine) coordinate system is defined in the boundaries of the workspace as MACH_ZERO and on the workpiece. The coordinate system of the end-effector is defined as the TOOL_POINT. This coordinate system is automatically generated on the tool when it's selected. By matching these coordinate systems on a virtual model prototype, it is possible to start the robot simulation along the given toolpath.

During this research, the CAD model of the robot is also statically analysed by using the primary functions of the FEM method available in the CAD environment. One of the results of this analysis is the deformation of the robot in the most unfavourable configuration when the robot is in the most extended position loaded only by the gravity force.

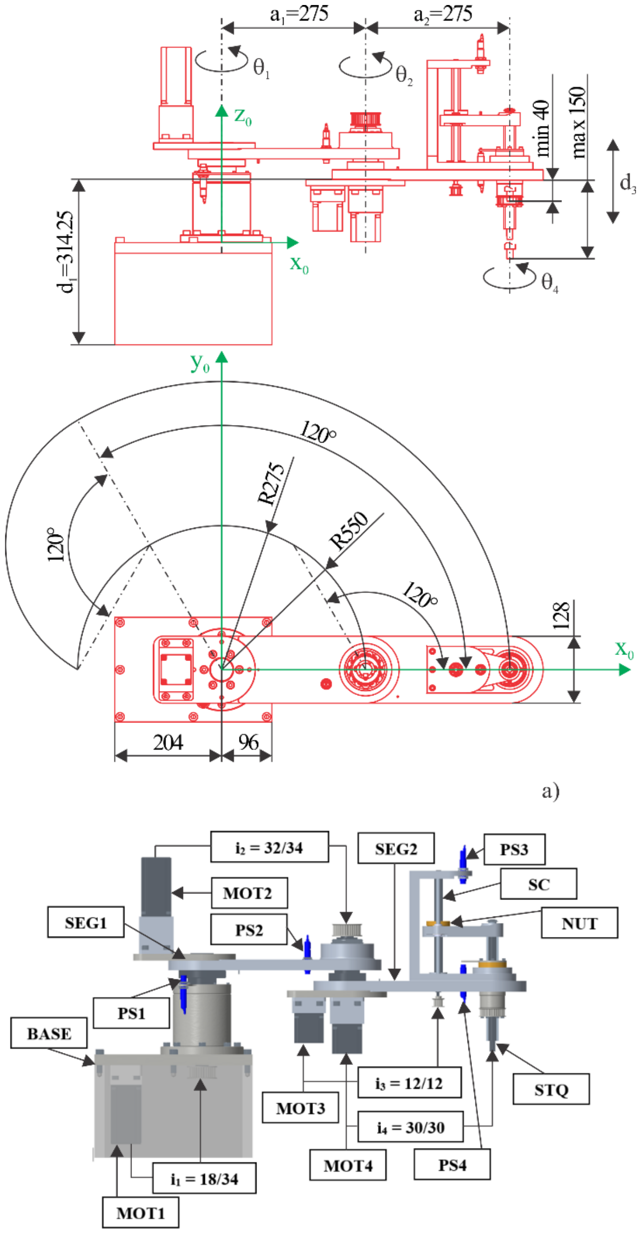

SEG1 – *first segment*

SEG2 – *second segment*

SC – *screw*

STQ – *shaft for torque transmission and achieving desired orientation of the end-effector*

MOT(1-4) – *motors of the first, second, third an fourth axis, respectively*

PS(1-4) – *proximity sensors for initialization of the first, second, third and fourth axis, respectively*

$i_{(1-4)}$ – *gear ratios of the first, second, third and fourth axis, respectively*

b)

Figure 2: CAD model of SCARA robot

The deformation is 0.07mm, which is acceptable for the robot laser engraving tasks. The analysis also includes the deformation analysis for different masses considered deformation of the robot model for the manipulation tasks.

4. DEVELOPMENT OF CONTROL AND PROGRAMMING SYSTEM

One of the features of this research is that the robot is applied directly by CNC machine tool programmers using the existing CAD/CAM systems and programming in G-code. The open architecture control system could enable this approach. Such control system can allow correctly implemented applications in it to work smoothly on different platforms of different suppliers and provide those applications cooperation with other system applications enabling the same communication with the user.

4.1. Open architecture control system software analysis

Various open architecture control systems are available today, which can be applied as a control system for the realized SCARA robot.

GRBL represents an open architecture control system with a built-in G-code interpreter (according to the RS274D standard) and a high-performance CNC (Computer Numerical Control) controller written in the optimized C programming language. Such control system can run on a microcontroller development environment called Arduino. The Atmega328p used on the Arduino platform provides the real-time positioning and asynchronous operations. Also, it can be used with various modifications to control milling machines, 3D printers, lathes, and SCARA configuration robots. However, the limitation refers to the control of three-axis only, so for the consideration of the SCARA robot, this control system can only be used when three axes are needed to perform the task. Figure 3a shows the position of GRBL in an open architecture CNC control system. GRBL can be seen as a firmware, which needs to be implemented in the Arduino to control the stepper motors. It is important to note that this system provides the control of machines that use stepper motors. The system uses low-cost stepper motor drivers current up to 2A. However, it can control high-current stepper motors where the current is provided by directly connecting the driver to the Arduino development environment (without Arduino CNC Shield). One of the advantages of such system is the low price of the hardware for the implementation of satisfactory control performance, as well as the fact that there is no need for the computer to have a Parallel Port, so a laptop computer is usually used. Figure 3b shows the connection diagram of the hardware components needed to realize the control of the SCARA robot with only two rotary axes, which ensure positioning in the horizontal plane. This example refers to the technical task of two-axis laser engraving, which the robot needs to perform. The micro switches are used to set the axes in the reference position, but the inductive sensors can be used identically with interface relays. With such a system, communication with the user can be achieved using different graphical user interfaces (GUI - Graphical User Interface). Such interfaces allow the user to send commands to the machine related to start the program, sending commands in manual mode, sending all axes to the reference position, etc. The frequently used GUI is the so-called UGS – Universal G-code Sender. It is possible to read each axis position at any time, as well as the programmed feed rate and spindle speed, which in the case of laser engraving would represent a percentage of the power of the laser beam.

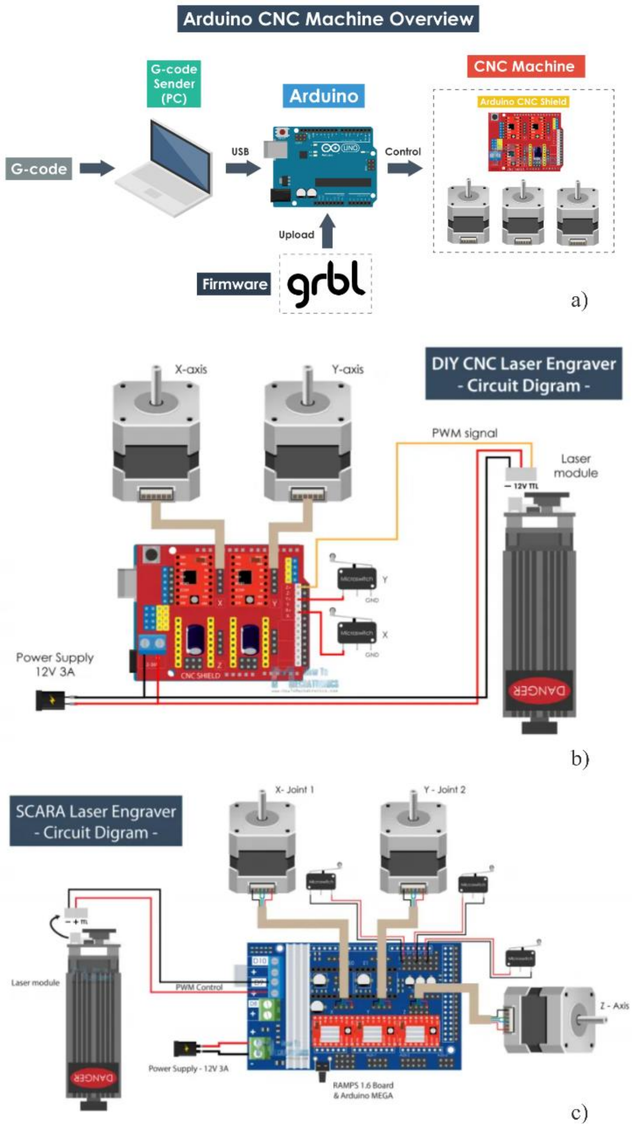

Figure 3: Open architecture control systems [11]

Marlin Firmware is an open architecture control system most commonly used for 3D printer control purposes. The firmware can also control CNC machines and laser engraving machines, Figure 3c. The firmware is used on a microcontroller development environment called Arduino Mega2560 and a board called RAMPS 1.6. Its main feature is reconfigurability and adaptability with different configurations, and accordingly, it supports Cartesian, DELTA, or SCARA kinematics. The firmware enables the execution of all machine activities in real-time, including the 3D printer heaters control, stepper motors, sensors, LCD screens, and everything else needed. Similar to the previously described GRBL, this firmware is implemented on the microcontroller, which should ensure the operation of the machine. For communication with machine users, there are several options in this case. The graphical user interface called Repetier-Host is popular in 3D printing. This interface is suitable when the SCARA robot is used as a 3D printer or a laser engraving machine.

The developed open architecture control system is based on the LinuxCNC software system. It is a real-time control system for machine tools and robots where code can be freely used, modified, and distribute [3]. Software LinuxCNC enables machine tools and robot programming according to the RS-274 or ISO 6983 standard. Configuring the control system includes configuring both hardware and software.

4.2. Development of control system based on LinuxCNC

The LinuxCNC software structure is shown in Figure 4. It consists of four basic modules: motion controller (EMCMOT), discrete I/O controller (EMCIO), task coordinating module (EMCTSK), and graphical user interface (GUI).

The GUI (Graphical User Interface) is an external program that communicates with the EMC by sending commands such as: turning on the machine, switching to automatic mode, starting the program, switching on, etc. The user interfaces can also send commands initiated by the operator, such as moving the machine axes into the manual mode or sending all axes to the reference position. The AXIS interface is often used because it looks like several numerically controlled machine tools. It is expanded to the specific application needs of the proposed robotic machining system [3, 12].

EMCIO (Discrete I/O Controller) is a module that performs all communications not related to motion control. This module has child modules for the main spindle, tool change, coolant and lubricant, auxiliary functions all stop, lubrication, etc.

EMCTSK (Task Coordinating Module - process controller) is a module that distributes commands on the machine. Performs program interpretation in G-code, according to the RS 274 NGC standard.

Of the four modules, only EMCMOT is a real-time module. EMCMOT module performs trajectory planning, direct and inverse kinematics calculations, and computation of desired outputs to motor drivers.

The HAL (Hardware Abstraction Layer) is designed as a flexible interface between the motion controller on the one hand and everything needed to interface with the user and the machine on the other. It represents a method for activating or switching on all the necessary modules so a numerical control system is completed which can be used adequately in industrial robots to perform certain groups of tasks.

LinuxCNC enables the control of machines and robots with complex (non-trivial) kinematics. Such system is controlled based on the solved inverse and direct kinematic problems, which are programmed in the C language and implemented instead of the existing trivial kinematics. As the SCARA configuration represents a machine with serial but non-trivial kinematics, the inverse and direct kinematics were translated into the C programming language format and incorporated into the machine kinematics file. The kinematics file of the machine must then be compiled so that when starting, the robot works according to the defined kinematics.

When configuring the hardware for the robot control system, it is necessary to determine the electronic components needed to perform the task, Figure 5.

As said, the robot uses stepper motors. The stepper motor drivers, DM542, 20-50VDC, Max 4.2A, and TB6600, 9-40VDC, Max 4.5A are used. Both types of drivers (DM542 and TB6600) have current and micro-stepping adjustments via DIP micro-switches, according to the motors and the application for which they are used.

For the initialization step, PNP NO (normally open) inductive sensors with an operating voltage of 24VDC are used. These sensors are connected via an interface relay to the control panel.

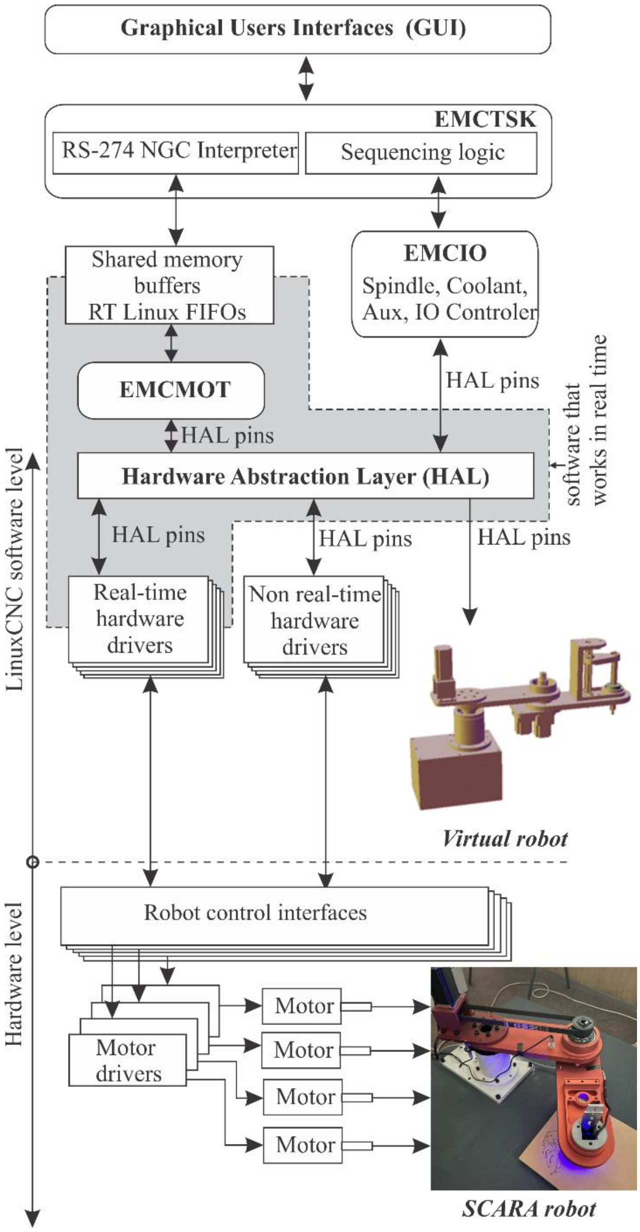

Figure 4: Developed robot control system

The laser module is necessary to perform the technological task of laser engraving, which emits a laser beam with sufficient optical power for engraving on wood. A laser module with an output optical power of 15W is used with a suitable driver that regulates the output optical power and fan speed, as well as a power supply whose input is alternating current with voltage 220VAC, while the output is direct current with voltage 12VDC and 5A current (module input power is 60W). The driver of the laser module can control the PWM signal.

As LinuxCNC communicates with the peripherals of the PC through the parallel port, the Mach3 CNC Controller board is used to connect with the necessary components. This board can control up to five axes, which are actuated by stepper motors.

Only the crucial electronic components are listed here. All selected electronic components are arranged and circuited according to an electrical diagram, Figure 5.

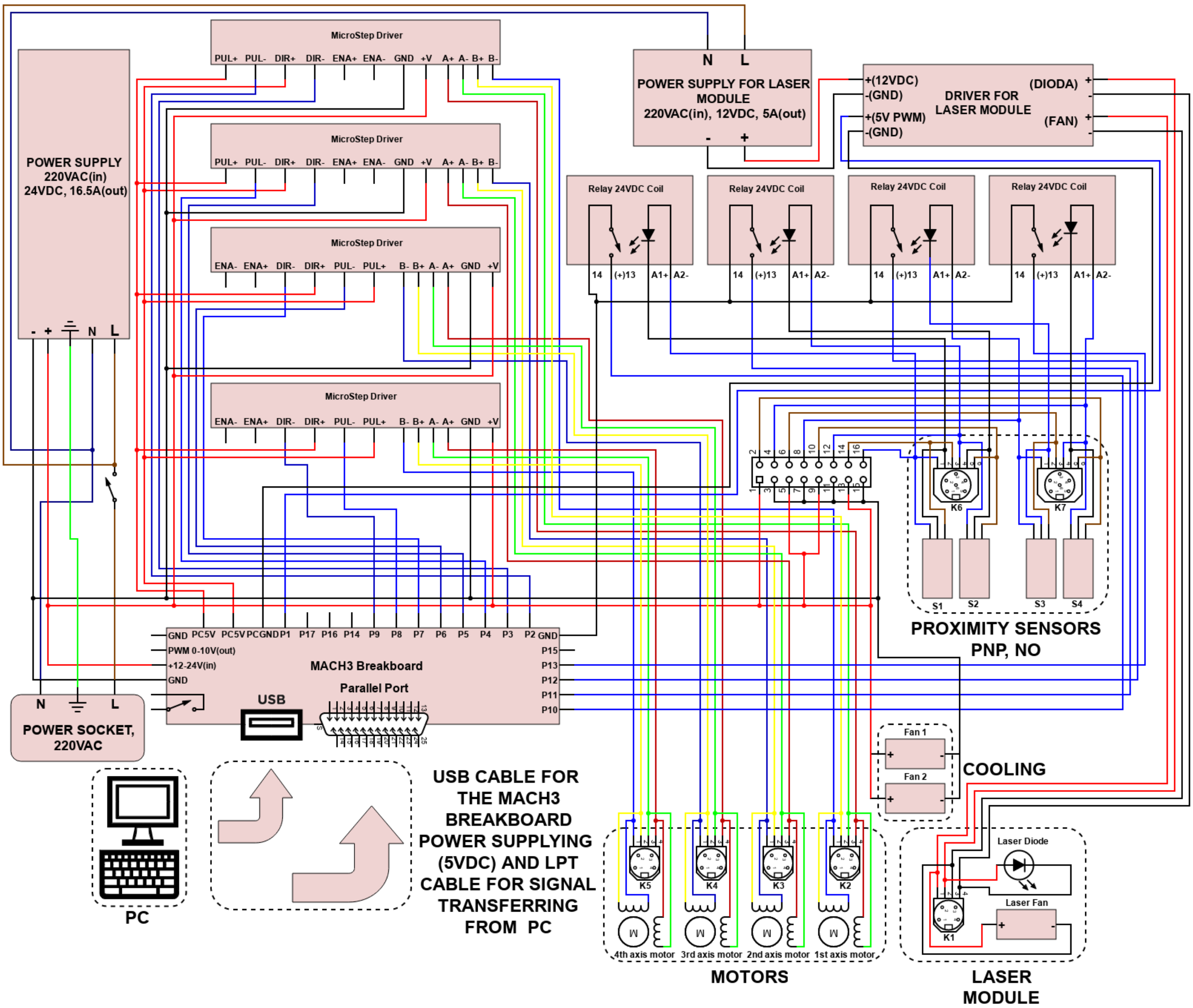

Figure 5: The electrical circuit of electronic components

4.3. Virtual robot configuring

The virtual robot is configured in the Python 3D environment. Python is a programming language that can be used to program graphical user interfaces allowing the programming and connecting of geometric primitives and their integration with the LinuxCNC AXIS GUI environment.

Python functions can create and animate machine tools or robot models. The machine or robot model is displayed in a 3D environment with the robot moving parts virtually actuated and moved with changes in the corresponding signal values received via the HAL pin connection.

The basic flow of activities in configuring virtual robots in the Python 3D environment is [12]:

- create HAL connections that control movement and actuated moving axes,
- create components that make up the robot structure. It can be programmed in the Python environment itself and grouped into collections, or it can be loaded as finished components,
- creation of moving robotic elements,
- creation of animated robot components, and
- assembling the robot model by loading and positioning the components in the appropriate place.

Configuring virtual robots directly in Python is practically programming the coordinates of the geometric primitives that define the virtual robot models. It is easier to model a simplified machine model in a CAD system, where the required coordinates can be obtained. Then the programming of the virtual robot components is approached in the Python programming language, Figure 6. The virtual robot components can be significantly simplified and described by an elementary geometric primitive (box, cylinder, sphere, ...). The position of the primitive is programmed relative to a given reference coordinate system. Primitives, which form a whole, are grouped into collections. Moving elements are connected by using the appropriate rotary or translatory connections. The virtual robot parameters are set correctly, as on the real robot, and the axis directions are set according to the defined kinematic model. During programming, errors are immediately detected and corrected. Then the next component is defined.

The second way allows obtaining more realistic copies of real robots in the virtual world and consists of loading robot subassemblies prepared in a CAD/CAM environment. Components are in ASCII STL or ASCII OBJ format, which Python can load directly into the reference coordinate system, and then it must be positioned and oriented appropriately.

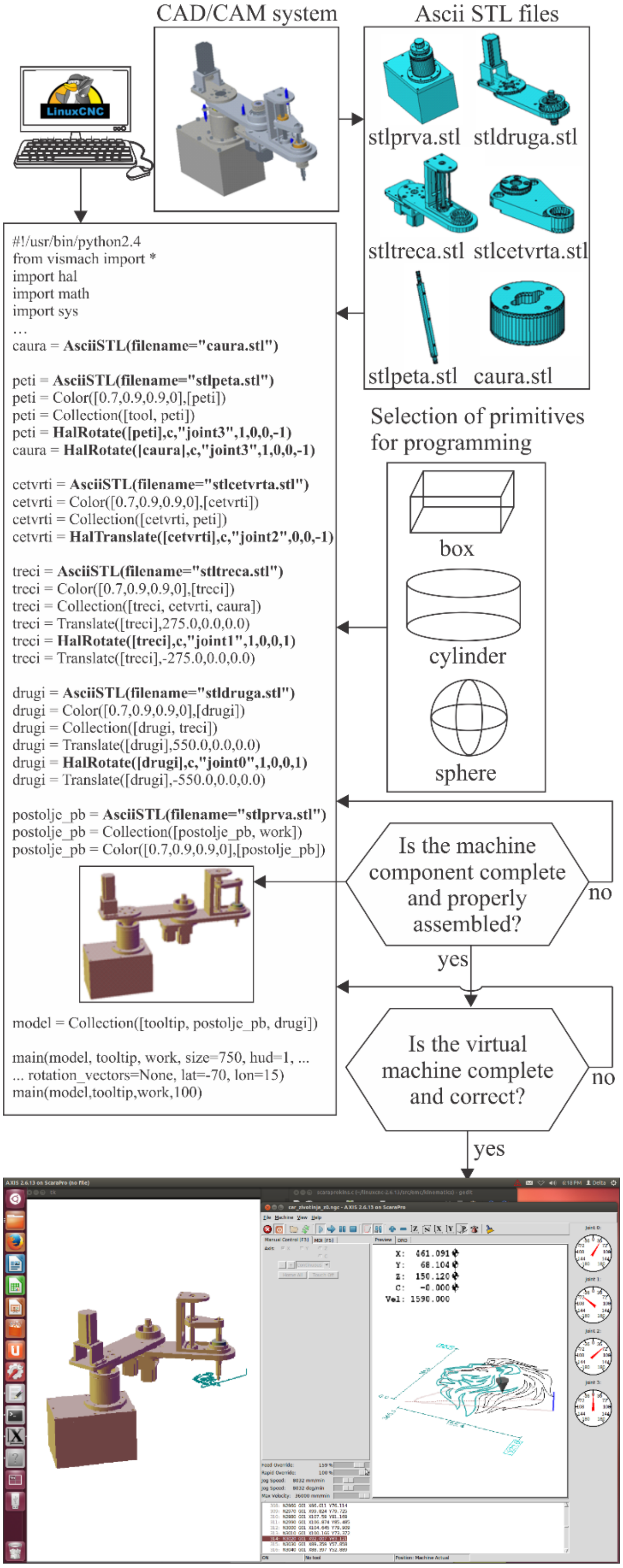

Figure 6: Virtual robot configuring in LinuxCNC

The result of any described procedure is a virtual robot or machine in the Python 3D environment integrated with the AXIS graphical interface. The virtual robot runs in the Python 3D environment and allows the robot axis movement through the toolpath simulation. The simulation is generated as a result of executing the G-code in real-time, in the same way as if a real machine were being controlled. In this way, it is possible to complete and verify the control system before the completion of the actual robots. According to the second described procedure, a virtual SCARA robot is generated and integrated with the developed open architecture control system, Figure 6.

5. EXPERIMENTAL VERIFICATION

The programming method is conventional and starts from the CAD/CAM environment. After verifying the toolpath (CL file), the procedure follows post-processing and obtaining the G-code. Thus the robot program in G-code is loaded into the control software and then verified on a virtual robot in real-time, Figure 6. Then the control signals can safely be directed to a real robot, Figure 7a.

When starting the control and programming system, a choice is made between controlling a virtual or a real robot. Usually, the virtual robot starts, initializes, and sets it up first. Then testing the program in two ways is realized. First, loading the G-code into the AXIS interface of the LinuxCNC software on the screen shows the programmed toolpath, and second, the final program verification on a virtual robot.

This is important for checking the toolpath, as well as for checking the placement of the workpiece within the limits of the working space and the correctness of determining the zero point.

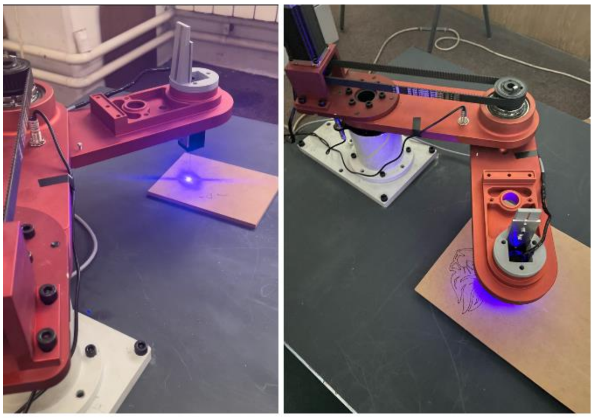

a)

b)

Figure 7: Robot laser engraving

Several successfully done examples of technological tasks of laser engraving have shown the verification of the complete robotic system. Figure 7b shows some realized examples of robot laser engraving of contours on a wood plate. The examples shown are laser engraving of the silhouette of the lion's head and its complete figure.

For both examples, G-codes were generated in the CAD/CAM environment based on the DXF file.

After switching on the robot, the robot's physical position is unknown to the control system due to the stepper motor uses without an encoder. Before starting the robot task, an initialization sequence must be performed to LinuxCNC calculates the reference position for counting motor pulses. The prepared program is generated concerning the zero point of the workpiece, marked with the G55 function, the workspace position has to be determined in the robot workspace and forwarded to the control system.

After the program is generated and loaded, the initialization is done. Another step describes the procedure for testing on a virtual robot. Then, the laser engraving tasks for selected examples are done, Figure 7.

6. CONCLUSION

Industrial robot applications are rapidly expanding with a permanent improvement of their functions, technical characteristics as well as control and programming systems. The presented research includes the development of a domestic 4-axis SCARA industrial robot with the possibility of automated programming based on information obtained from the camera and AI techniques. The first part of this research covered the production of the selected robot. This part includes the design of the mechanical structure, preliminary CAD/CAM testing, development of control and programming systems, and virtual robot simulation.

Among several open architecture control software, the LinuxCNC system is selected. Software LinuxCNC enables machine tools and robot programming according to the RS-274 or ISO 6983 standard. It is a real-time control system for machine tools and robots whose code can be freely used, modified, and distributed. This system enables the use of widely available machine tools' CAD/CAM systems for programming machining robots. The control system includes the integrated virtual robot model configured using several predefined Python classes and OpenGL. The virtual robot prototype is configured based on the developed complete kinematic model of the robot and the robot CAD model. This virtual model is a digital shadow of the developed SCARA robot.

Further advanced research will include applying the artificial intelligence techniques and information obtained from the fully integrated camera to extract the toolpath of the robot for automatic hybrid robot programming.

ACKNOWLEDGEMENTS

This work has been financially supported by the Ministry of Science, Technological Development and Innovation of the Serbian Government through the project Integrated research in macro, micro, and nano mechanical engineering (contract No. 451-03-47/2023-01/200105).

REFERENCES

[1] M. Javaid, A. Haleem, R.P. Singh and R. Suman, “Substantial capabilities of robotics in enhancing industry 4.0 implementation”, Cognitive Robotics, Vol. 1, pp. 58-75, (2021)

[2] C. Zheng, Y. An, Z. Wang, H. Wu, X. Qin, B. Eynard and Y. Zhang, “Hybrid offline programming method for robotic welding systems”, Robotics and Computer-Integrated Manufacturing, Vol. 73, 102238, (2022)

[3] D. Milutinovic, M. Glavonjic, N. Slavkovic, Z. Dimic, S. Zivanovic, B. Kokotovic and Lj. Tanovic, “Reconfigurable robotic machining system controlled and programmed in a machine tool manner”, International Journal of Advanced Manufacturing Technology, Vol. 53(9-12), pp. 1217-1229, (2011)

[4] N. Slavkovic, S. Zivanovic and D. Milutinovic, “An indirect method of industrial robot programming for machining tasks based on STEP-NC”, International Journal of Computer Integrated Manufacturing, Vol. 32(1), pp. 43–57, (2019)

[5] H. Makino, “Development of the SCARA”, Journal of Robotics and Mechatronics, Vol. 26(1), pp. 5-8, (2014)

[6] B. Momcilovic, “Development of the control system of the 4-axis SCARA robot”, M.Sc. Thesis, University of Belgrade, Faculty of Mechanical Engineering (Serbia), 2022

[7] Dj. Milicevic, “Designing the prototype of the 4-axis SCARA industrial robot”, M.Sc. Thesis, University of Belgrade, Faculty of Mechanical Engineering (Serbia), 2022

[8] J. Fang and W. Li, “Four degrees of freedom SCARA robot kinematics modeling and simulation analysis”, International Journal of Computer, Consumer and Control, Vol. 2(4), pp. 20-27, (2013)

[9] N.R. Slavković, S.T. Živanović and N.M. Vorkapić, “Configuring a virtual prototype of a BiSCARA robot”, Tehnika, Vol. 76(3), pp. 311-317, (2021)

[10] N. Slavkovic, S. Zivanovic, N. Vorkapic and Z. Dimic, “Development of the Programming and Simulation System of 4-axis Robot with Hybrid Kinematic”, FME Transactions, Vol. 50(3), pp. 403-411, (2022)

[11] https://howtomechatronics.com/category/projects/

[12] N. Slavković, N. Vorkapić, S. Živanović, Z. Dimić and B. Kokotović, “Virtual BiSCARA robot integrated with open-architecture control system”, Proceedings of 14th International Scientific Conference “Flexible Technologies MMA 2021”, Novi Sad (Serbia), 23-25 September 2021, pp. 63-66, (2021)

30 Years of the International Scientific Conference Heavy Machinery

Mile Savković[1*], Goran Marković[1], Milan Bižić[1], Nataša Pavlović[1]
[1]Faculty of Mechanical and Civil Engineering in Kraljevo, University of Kragujevac, Serbia

The first conference "Heavy Machinery" was held in Kruševac and Vrnjačka Banja (Serbia) from 8 to 10 October 1993. The conference is triennial so that the eleventh one is in 2023. At the beginning, the main thematic fields were: Design and calculations, Production technologies, Testing and control. New scientific knowledge, fast technological development, lifting sanctions on our country and the globalisation of the world market caused significant changes in science and research. Accordingly, the thematic fields of the conferences have been adjusted. Their number has increased so that the papers from the last conference were classified into seven scientific fields: Earth-moving and Mining machines and Transportation systems, Railway vehicles, Production technologies, Automatic control, robotics and fluid technique, Applied mechanics, Thermal technique and environment protection and Civil engineering and materials.

This year's conference covers similar fields. Thirty years of tradition are also an opportunity to sum up the results from the previous conferences as well as to establish the directions of further research, the place and the role of the conference "Heavy Machinery", regarding both the development of the faculty and the influence on a wider scientific community.

Keywords: heavy machinery, mechanical engineering, civil engineering, history

1. INTRODUCTION

The name "Heavy Machinery" imposed itself as a term used in studying machines, systems and components of large dimensions, masses and complexity. It covers civil and mining machines, transportation machines, machine tools for deforming and cutting, railway and road transportation systems, power plants, etc.

The name of the conference "Heavy Machinery" is greatly connected with the development of the Faculty of Mechanical Engineering in Kraljevo. At the end of December 1981, the Department in Kraljevo grew into the Basic Organization of Associated Labour for Heavy Machinery within the Faculty of Mechanical Engineering in Belgrade, which provided the conditions for establishing a specific programme for education of mechanical engineers for the Heavy Machinery field. The year 1987 marked the beginning of the procedure of separating the Basic Organization of Associated Labour for Heavy Machinery from the structure of the Faculty of Mechanical Engineering of the University of Belgrade and thus the Faculty of Mechanical Engineering in Kraljevo was formed.

After its foundation, the Faculty of Mechanical Engineering in Kraljevo oriented itself towards research in heavy machinery and tried, in cooperation with the surrounding factories whose production programmes were based on heavy machinery, to contribute to the identification of complex problems and their solutions as well as to enable such research that would involve new production programmes and revitalization of the existing ones [1].

Having in mind the above mentioned, in 1993 the management of the Faculty launched an initiative for the organization of the first international scientific conference. The goal of the conference was to contribute to a more complete and more comprehensive definition of the current state and, particularly, the future development of heavy machinery.

2. OVERVIEW OF THE "HEAVY MACHINERY" CONFERENCES HELD SO FAR

2.1. First conference "Heavy Machinery - HM 1993"

The first conference "Heavy Machinery – HM 1993" was held in Kruševac and Vrnjačka Banja in the period from 8 to 10 October 1993 [1]. Prof. Dr Ranko Rakanović, Prof. Dr Vučko Mečanin, Dr Milomir Gašić – Docent, Dr Vladan Karamarković – Docent and Dr Svetislav Radović – Docent were appointed members of the Editorial Committee of the first conference "Heavy Machinery". The Editorial Committee was appointed on 08.07.1993 – Figure 1. Prof. Dr Mihajlo Milojević was added to the Editorial Committee by a subsequent decision.

The organization of the conference drew considerable attention of enterprises so that the conference had 50 sponsors. Apart from the enterprises from the surroundings, three enterprises from Montenegro and one from Bosnia and Herzegovina participated as sponsors.

The papers were classified into four sections: plenary papers, Design and Calculations, Production Technologies, Materials – Testing and Control. In 1993, sanctions were imposed on Serbia so that the teachers and associates as well as the researchers were not allowed to travel to other countries. Taking that into account, it is no wonder that an extremely large number of papers were registered for the conference – a total of 228.

There were 5 plenary papers, 93 papers in the session Design and Calculations, 97 in the session Production Technologies and 33 papers in the session Testing and Control. The structure of papers is presented in Table 1.

It should be emphasized that in the first year of the organization of the conference the relevant Ministry did not clearly define what requirements should be fulfilled by a conference so that it could be recognized as international. The authors were required to write the title and the abstract in English, and the official languages of the conference were: Serbian, English and Russian. The papers of the

*Corresponding author: Dositejeva 19, 36000 Kraljevo, Serbia, savkovic.m@mfkv.kg.ac.rs

authors coming from Montenegro were treated as domestic papers. The Chairman of the Editorial Committee was Prof. Dr Ranko Rakanović.

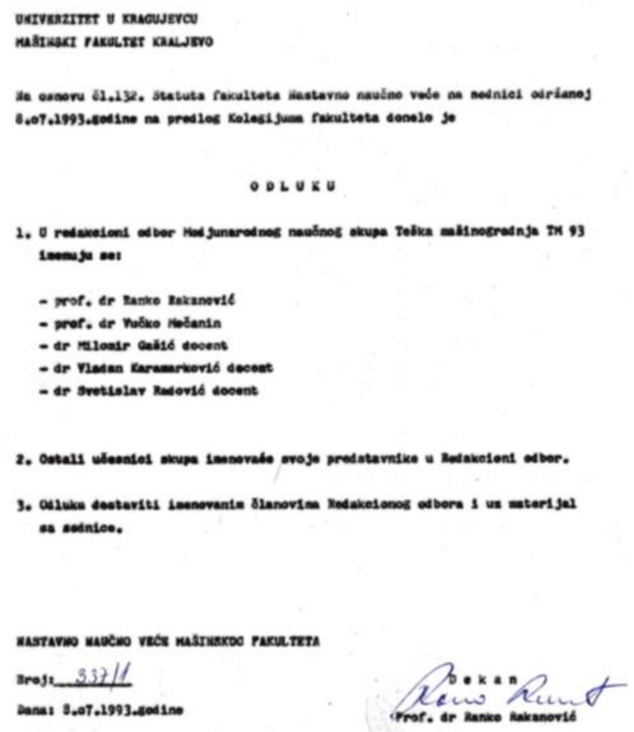
UNIVERZITET U KRAGUJEVCU
MAŠINSKI FAKULTET KRALJEVO

Na osnovu čl.132. Statuta fakulteta Nastavno naučno veće na sednici održanoj 8.07.1993.godine na predlog Kolegijuma fakulteta donelo je

O D L U K U

1. U redakcioni odbor Medjunarodnog naučnog skupa Teška mašinogradnja TM 93 imenuju se:

- prof. dr Ranko Rakanović
- prof. dr Vučko Mečanin
- dr Milomir Gašić docent
- dr Vladan Karamarković docent
- dr Svetislav Radović docent

2. Ostali učesnici skupa imenovaće svoje predstavnike u Redakcioni odbor.

3. Odluku dostaviti imenovanim članovima Redakcionog odbora i uz materijal sa sednice.

NASTAVNO NAUČNO VEĆE MAŠINSKOG FAKULTETA

Broj: 337/1

Dana: 8.07.1993.godine

Dekan
Prof. dr Ranko Rakanović

Figure 1: Decision of the Scientific-Teaching Council of the Faculty of Mechanical Engineering Kraljevo on appointing the Editorial Committee of the conference

Table 1: The structure of papers at the first conference "Heavy Machinery - HM 1993"

Session	Number of papers		
	Domestic	Foreign	Total
Plenary	5	0	5
Design and Calculations	83	10	93
Production Technologies	88	9	97
Testing and Control	30	3	33
Σ	206	22	228

2.2. Second conference "Heavy Machinery - HM 1996"

The second conference "Heavy Machinery - HM 1996" had ten members of the Programme Committee, four of them from abroad. It was held in Kraljevo-Mataruška Banja in the period from 28 to 30 June, 1996 (Figure 2) [2].

The conference was organized under the auspices of the Ministry of Science and Technology of the Republic of Serbia. This conference also attracted a lot of attention among enterprises so that the conference had 25 sponsors.

The Chairman of the Programme Committee was Prof. Dr Ranko Rakanović.

The total number of published papers was 130. The papers were classified into eight sections, and the structure of papers is shown in Table 2.

Figure 2: Presiding (from the left to the right): Prof. Dr Milisav Kalajdžić, Faculty of Mechanical Engineering in Belgrade, Prof. dr Mircea Alamoreanu, Technical University of Civil Engineering of Bucharest, Romania, Prof. Dr Ranko Rakanović, Faculty of Mechanical Engineering in Kraljevo, Igor Pavlovich Filonov, Belarusian State Polytechnic Academy, Belarus, Dmitry Pavlovich Volkov, Moscow State University of Civil Engineering, Russia, behind the lectern Prof. Dr Vučko Mečanin, Faculty of Mechanical Engineering in Kraljevo

Table 2: The structure of papers at the first conference "Heavy Machinery - HM 1996"

Session	Number of papers		
	Domestic	Foreign	Total
Plenary	3	0	3
Railway engineering	8	3	11
Civil and mining machines	14	3	17
Production engineering	43	7	50
Control systems and components	14	2	16
Transportation systems	16	1	17
Thermal power plants	7	0	7
General joint session	8	1	9
Σ	113	17	130

2.3. Third conference "Heavy Machinery - HM 1999"

The third conference "Heavy Machinery – HM 1999" was organized in difficult conditions, in the year when our country was bombed and devastated by the NATO alliance.

However, even in such conditions, but with enormous efforts, the conference was held. It should be mentioned that, unlike the previous conferences, the Ministry of Science and Technology of the Republic of Serbia defined more precise conditions for recognizing the conference as the international one. The third conference had the International Programme Committee – even 9 members, out of 18, were from abroad. The language of the conference was English, and the papers were published in Russian, too. The conference was held under the auspices of the Ministry of Science and Technology of the Republic of Serbia, but 23 domestic companies were sponsors as well. The conference was held in Kraljevo-Mataruška Banja in the period from 28 to 30 October 1999 [3]. The Chairman of the Conference was Prof. Dr Vučko Mečanin, and the editors were Prof. Dr Vučko Mečanin and Prof. Dr Novak Nedić.

The total number of published papers was 84. The papers were classified into seven sections, and the structure of papers is shown in Table 3.

Table 3: The structure of papers at the first conference "Heavy Machinery - HM 1999"

Session	Number of papers		
	Domestic	Foreign	Total
Plenary	2	1	3
Mining and earth-moving machines	5	6	11
Production technology	21	8	29
Automatic control and fluid power technology	9	1	10
Railway machines	10	1	11
Transportation systems	7	3	10
Applied mechanics and structure strength	7	3	10
Σ	61	23	84

2.4. Fourth conference "Heavy Machinery - HM 2002"

The fourth conference "Heavy Machinery - HM 2002" was held in Mataruška Banja in the period from 28 to 30 June 2002 [4].

Having the previous conference as its model, the fourth conference also had the International Programme Committee – out of its 35 members, 12 was from abroad. The Ministry of Science, Technology and Development of the Republic of Serbia, the Federal Secretariat for Development and Science as well as Magnohrom Kraljevo supported the conference. The Chairman of the Conference was Prof. Dr Milomir Gašić, the Chairman of the International Programme Committee was Prof. Dr Milomir Gašić, and the Vice-Chairman of the international Programme Committee was Prof. Dr Miroslav Vesković.

The total number of published papers was 114. The papers were classified into seven sections, and the structure of papers is presented in Table 4.

Table 4: The structure of papers at the fourth conference "Heavy Machinery - HM 2002"

Session	Number of papers		
	Domestic	Foreign	Total
Plenary	1	2	3
Earth-moving and mining machines and transportation systems	18	8	26
Thermal power plants	7	0	7
Railway vehicles	10	6	16
Production technology of the heavy machinery	28	6	34
Automatic control and fluid technique	6	6	12
Applied mechanics and basic machine structures	12	4	16
Σ	82	32	114

2.5. Mini Jubilee – Fifth Conference "Heavy Machinery - HM 2005"

The fifth conference "Heavy Machinery - HM 2005" was held in Kraljevo-Mataruška Banja in the period from 28 June to 3 July 2005 (Figure 3) [5]. From the fifth conference, the last day of the conference was traditionally closed by participation in the rafting down the Ibar river within the manifestation "Jolly Regatta". The faculty, as the organizer of the conference, provided the boats as well as an experienced guide for all participants who wanted to participate in this manifestation.

Figure 3: Presiding (sitting – from the left to the right): Prof. Dr Ljubomir Lukić, Faculty of Mechanical Engineering in Kraljevo, Prof. Dr Milomir Gašić, Faculty of Mechanical Engineering in Kraljevo, Prof. Dr Igor Stepanovich Surovtsev, Voronezh State University of Architecture and Civil Engineering, Rector, Russia, Prof. Dr Pavel Ivanovich Nikulin, Voronezh State University of Architecture and Civil Engineering, Russia, behind the lectern Prof. Dr Miloš Đuran, Rector of the University of Kragujevac

The International Programme Committee consisted of 50 members, and 17 of them were from abroad. The Ministry of Science and Environmental Protection of the Republic of Serbia supported the conference. The Chairman of the Conference was Prof. Dr Milomir Gašić, the Chairman of the International Programme Committee was Prof. Dr Milomir Gašić, and the Vice-Chairman of the International Programme Committee was Prof. Dr Milan Dedić.

The total number of published papers was 114. The papers were classified into seven sections, and the structure of papers is shown in Table 5.

Table 5: The structure of papers at the fifth conference "Heavy Machinery - HM 2005"

Session	Number of papers		
	Domestic	Foreign	Total
Plenary	1	0	1
Earth-moving and mining machines and transportation systems	14	9	23
Automatic control and fluid technique	12	1	13
Construction and machines	12	4	16
Railway vehicles	12	8	20
Production technology	26	10	36
Urban engineering	7	2	9
Σ	83	34	117

2.6. Sixth conference “Heavy Machinery - HM 2008”

The sixth conference “Heavy Machinery - HM 2008” was held in Kraljevo-Mataruška Banja in the period from 24 - 29 June 2008 [6].

The International Programme Committee consisted of 49 members, and 21 were from abroad. The Ministry of Science and Environmental Protection of the Republic of Serbia supported the conference. The Chairman of the Conference was Prof. Dr Novak Nedić, and the chairman of the Programme Committee was Prof. Dr Milomir Gašić.

The total number of published papers was 108. The papers were classified into nine sections, and the structure of papers is shown in Table 6.

Table 6: The structure of papers at the sixth conference “Heavy Machinery - HM 2008”

Session	Number of papers		
	Domestic	Foreign	Total
Plenary	2	2	4
Automatic control and fluid technique	9	4	13
Earth-moving and mining machines and transportation systems	9	13	22
Railway vehicles	4	8	12
Thermal technique, environment protection and urban engineering	10	0	10
Machine design and mechanics	10	6	16
Production technologies, material application and entrepreneurial engineering and management	5	9	14
Computer-integrated processes and design of machining processes	8	0	8
Urban engineering	7	2	9
Σ	64	44	108

2.7. Seventh conference “Heavy Machinery - HM 2011”

The seventh conference “Heavy Machinery - HM 2011” was held in Vrnjačka Banja in the period from 29 June to 2 July 2011 (Figures 4 and 5) [7].

The International Programme Committee had 61 members, and 31 of them were from abroad. The Ministry of Science and Environmental Protection of the Republic of Serbia supported the conference. The Chairman of the Conference was Prof. Dr Novak Nedić, the Chairman of the International Scientific Programme Committee was Prof. Dr Milomir Gašić, and the Vice-Chairman was Prof. Dr Mile Savković.

The total number of published papers was 109. The papers were classified into nine sections, and the structure of papers is presented in Table 7.

The first student conference SRMA 2011, at which the papers of students from Serbia and abroad were presented, was held together with the conference “Heavy Machinery HM 2011”.

Table 7: The structure of papers at the seventh conference “Heavy Machinery - HM 2008”

Session	Number of papers		
	Domestic	Foreign	Total
Plenary	2	2	4
Railway vehicles	3	9	12
Earth-moving and mining machines and transportation systems	13	10	23
Automatic control and fluid technique	9	3	12
Design and mechanics	12	5	17
Production technologies	16	1	17
Urban engineering	9	4	13
Structures and materials in civil engineering	9	2	11
Σ	73	36	109

Figure 4: Presiding at the conference “Heavy Machinery - HM 2011” (sitting – from the left to the right): Prof. Dr Ljubomir Lukić, Prof. Dr Novak Nedić, Dragana Sladoje –student, Milica Panović – MC, all from the Faculty of Mechanical Engineering in Kraljevo

Figure 5: Participants in the plenary session of the conference “Heavy Machinery - HM 2011”

2.8 Eighth conference “Heavy Machinery - HM 2014”

The eighth conference “Heavy Machinery HM 2014” was held at Zlatibor in the period from 25 to 28 June 2014 (Figures 6-9) [8].

The International Programme Committee consisted of 63 members, and 32 of them were from abroad. The Ministry of Science and Environmental Protection of the

Republic of Serbia supported the conference. The Chairman of the Conference was Prof. Dr Milomir Gašić, the Chairman of the International Scientific Programme Committee was Prof. Dr Mile Savković, and the Vice-Chairman was Prof. Dr Milan Kolarević

The total number of published papers was 110. The papers were classified into eight sections, and the structure of papers is presented in Table 8.

Table 8: The structure of papers at the eight conference "Heavy Machinery - HM 2014"

Session	Number of papers		
	Domestic	Foreign	Total
Plenary	0	4	4
Earth-moving and mining machines and transportation systems	12	18	30
Production technologies	8	5	13
Civil engineering and materials	6	3	9
Automatic control, robotics and fluid technique	7	9	16
Mechanical design and mechanics	11	1	12
Railway vehicles	5	9	14
Urban engineering, thermal technique and environment protection	10	2	12
Σ	59	51	110

The second student conference SRMA 2014, at which the papers of students from Serbia and abroad were presented, was held together with the conference "Heavy Machinery HM 2014".

Figure 6: Presiding at the conference "Heavy Machinery HM 2014" (sitting – from the left to the right): Prof. Dr Ivan Ivanovich Nazarenko, Kyiv National University of Construction and Architecture, Ukraine, Prof. Dr Mircea Alamoreanu, Technical University of Civil Engineering Bucharest, Romania, Prof. Dr Milomir Gašić, Faculty of Mechanical and Civil Engineering in Kraljevo, Prof. Dr Nenad Filipović, Vice-Rector of the University of Kragujevac, behind the lectern Prof. Dr Desimir Jeftić, at the back Milica Panović – MC

Figure 7: Plenary session of the conference "Heavy Machinery - HM 2014"

Figure 8: Closing of the working part of the conference, socializing at the gala dinner

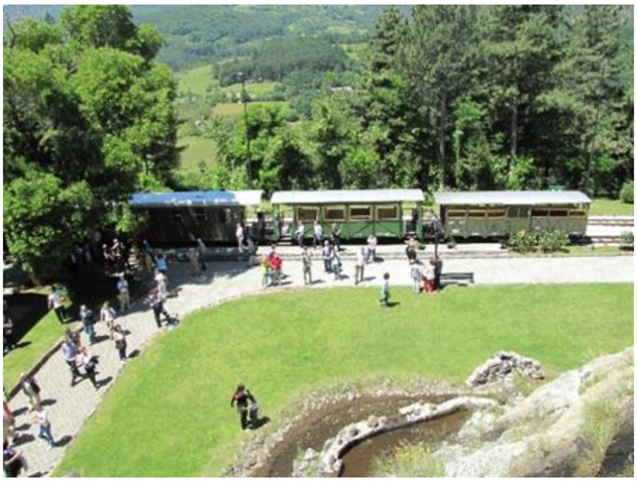

Figure 9: Social programme – visit to the "Šargan Eight"

2.9. Ninth conference "Heavy Machinery - HM 2017"

The ninth conference "Heavy Machinery - HM 2017" was held at Zlatibor in the period from 28 June to 1 July 2017 (Figures 10-13) [9].

The International Programme Committee consisted of 66 members, and 30 of them were from abroad. The Ministry of Science and Environmental Protection of the Republic of Serbia supported the conference. The Chairman of the Conference was Prof. Dr Milomir Gašić, the Chairman of the International Scientific Programme Committee was Prof. Dr Mile Savković, and the Vice-Chairman was Prof. Dr Milan Kolarević.

The total number of published papers was 94. The papers were classified into eight sections, and the structure of papers is presented in Table 9.

Table 9: The structure of papers at the ninth conference “Heavy Machinery - HM 2017”

Session	Number of papers		
	Domestic	Foreign	Total
Plenary	1	4	5
Earth-moving and mining machines and transportation systems	11	10	20
Production technologies	10	9	19
Automatic control, robotics and fluid technique	9	1	10
Mechanical design and mechanics	5	5	10
Railway vehicles	5	6	11
Thermal technique and environment protection	7	4	11
Civil engineering and materials	6	1	7
Σ	54	40	94

The third student conference SRMA 2017, at which the papers of students from Serbia and abroad were presented, was held together with the conference “Heavy Machinery - HM 2017”.

Figure 10: Presiding at the conference “Heavy Machinery HM 2017” (sitting – from the left to the right): Prof. Dr Dario Croccolo, Department of Industrial Engineering, University of Bologna, Italy, Prof. Dr Dobrinka Atmadzhova, Department of Transport Equipment, University of Transport, Sofia, Bulgaria, Prof. Dr Mile Savković, Faculty of Mechanical and Civil Engineering in Kraljevo, Prof. Dr Milomir Gašić, Faculty of Mechanical and Civil Engineering in Kraljevo, Prof. Dr Anatoly Dotsenko, National Research Moscow State University of Civil Engineering, Russia, behind the lectern Jelena Tomić – MC

Figure 11: Plenary session of the conference “Heavy Machinery - HM 2017”

Figure 12: Closing of the working part of the conference, socializing at the gala dinner

Figure 13: Social programme – visit to the national park “Uvac“

2.10. Tenth conference “Heavy Machinery - HM 2021”

The tenth jubilee conference “Heavy Machinery - HM 2021” was held in Vrnjačka Banja in the period from 23 to 25 June 2021 (Figures 14 and 15) [10]. This conference was not held three years after the previous one due to the prohibition on group gathering caused by the COVID 19 pandemic – it was postponed for one year.

The International Programme Committee consisted of 72 members, and 30 of them were from abroad. The Ministry of Science and Environmental Protection of the

Republic of Serbia supported the conference. The Chairman of the Conference was Prof. Dr Mile Savković, the Chairman of the International Scientific Programme Committee was Prof. Dr Milan Kolarević, and the Vice-Chairman was Prof. Dr Milan Bižić.

The total number of published papers was 110. The papers were classified into eight sections, and the structure of papers is presented in Table 10.

Table 10: The structure of papers at the tenth conference “Heavy Machinery - HM 2021”

Session	Number of papers		
	Domestic	Foreign	Total
Plenary	1	2	3
Earth-moving and mining machines and transportation systems	11	2	13
Production technologies	10	1	11
Automatic control, robotics and fluid technique	7	5	12
Applied mechanics	7	1	8
Railway vehicles	6	5	11
Thermal technique and environment protection	8	1	9
Civil engineering and materials	5	1	6
Σ	55	18	73

Figure 14: Behind the lectern Dr Nataša Pavlović – MC, presiding at the conference “Heavy Machinery HM 2021” (sitting – from the left to the right): Prof. Dr Mile Savković, Faculty of Mechanical and Civil Engineering in Kraljevo, Prof. Dr Nenad Filipović, Rector of the University in Kragujevac, Prof. Dr Milan Kolarević, Faculty of Mechanical and Civil Engineering in Kraljevo

Figure 15: Plenary session of the conference “Heavy Machinery - HM 2021”

The opening of the conference was followed by a signing ceremony at which the agreements on cooperation between the University of Kragujevac and the companies from Kraljevo and its surroundings with which the Faculty of Mechanical and Civil Engineering has a long successful cooperation were signed (Figure 16). The agreements were signed with the following companies: Leoni, Amiga, Radijator Inženjering, FMO Ekonom, Elektromontaža, Unipromet, Eurotermik, Evrotehna, Pekom Inženjering, CIP and Odžačar Kotloremont.

Figure 16: Rector of the University of Kragujevac Prof. Dr Nenad Filipović signing agreements on business and technical cooperation with companies from the territory of Kraljevo

3. COMPARATIVE OVERVIEW OF THE NUMBER OF PAPERS PUBLISHED AT THE PREVIOUS TEN “HEAVY MACHINERY“ CONFERENCES

The structure of papers at the previous ten conference can be seen in the diagram in Figure 17.

From the diagrams in Figures 17 and 18 it can be seen that a very large number of papers were published at the first two conferences. The main reason lies in the fact that the sanctions were imposed on our country during the mentioned period and, hence, publishing papers at conferences abroad was rather difficult.

What should be taken into account is that the reviews were not too “demanding”, the papers were published in Serbian or in the authors’ mother tongues. Also, there was a significant support in the form of sponsorship by enterprises so that the conference fee was small.

When the Ministry of Science and Technology of the Republic of Serbia defined more precise conditions for recognition of the conference as international (conference language, number of pages per paper, proofs of reviewing, conference duration, international programme committee,…), both the number of registered papers and the number of published papers were reduced – Figure 18.

The modifications of the Law on Higher Education of 2008 and 2010 and the corresponding Rules for Promotion into Academic Ranks as well as the changes regarding the accreditation conditions significantly diminished the importance of conferences. This relates to international and, especially, national conferences. These facts have become more pronounced in the course of time, and the same can be stated for national journals. The number of papers published in SCI-indexed journals has been imposed as the main condition for promotion of teachers and researchers, which has demotivated authors to participate in international and, particularly, national conferences. This can be clearly seen from the diagrams in Figures 19 and 20.

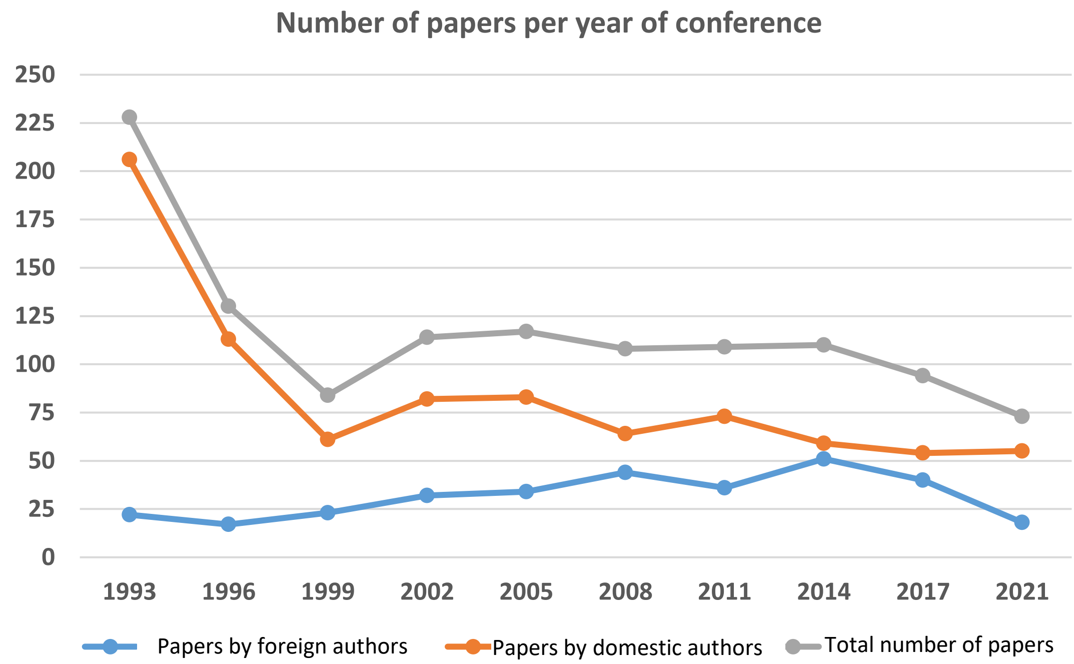

Figure 17: Structure of papers at the previous ten conferences

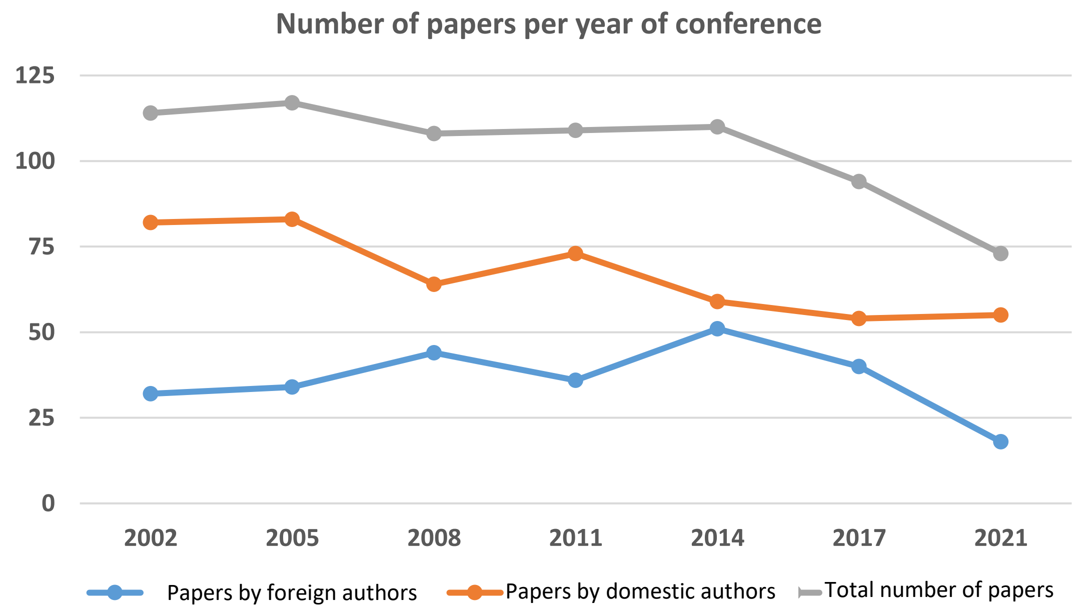

Figure 18: Structure of papers at the previous seven conferences

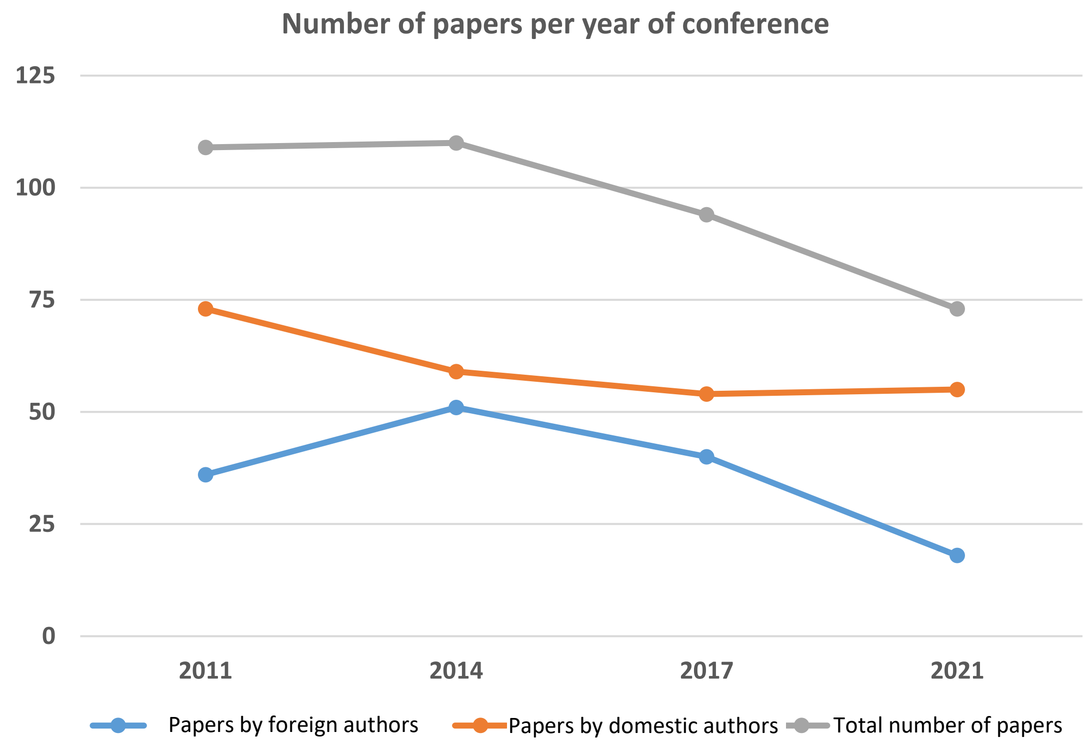

Figure 19: Total number of papers at the previous four conferences

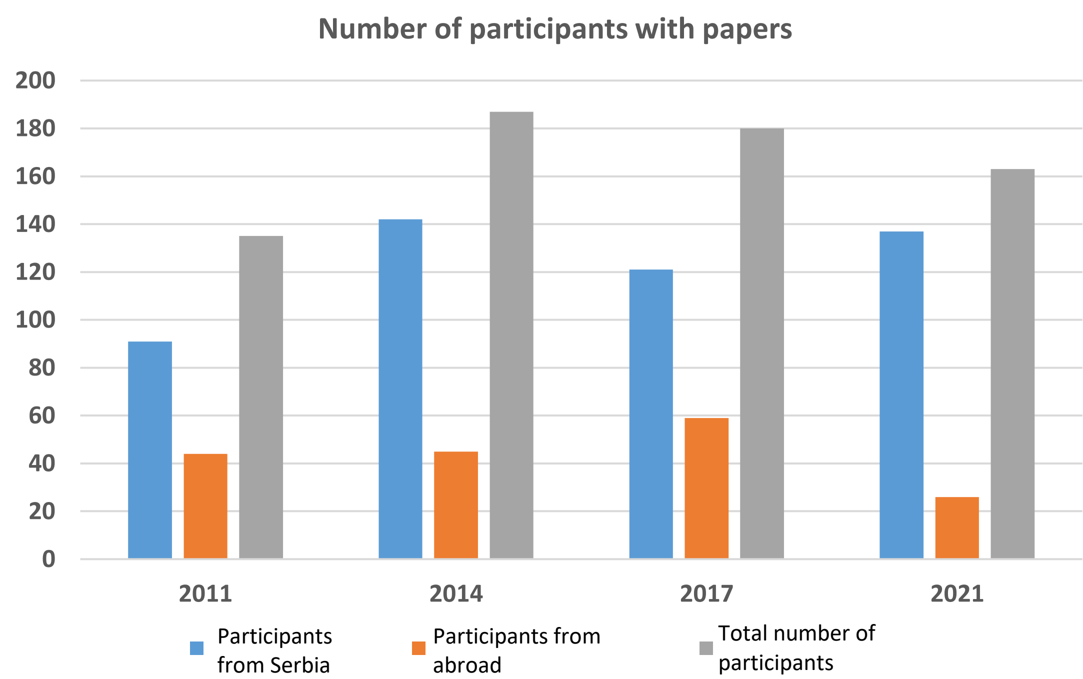

Figure 20: Total number of participants with papers at the previous four conferences

4. CONCLUDING REMARKS

Despite numerous challenges, the conference "Heavy Machinery - HM" has been successfully realized and its tradition has been kept for 30 years.

The scientific conference "Heavy Machinery" contributes to spreading international scientific-technical cooperation among universities, especially spreading scientific-technical and educational cooperation with universities from the Balkan countries as well as cooperation with the EU countries, Russia and ex-Soviet Union countries.

The last ten years have shown a noticeable decreasing trend in the number of papers and the number of participants at the conference if compared to the conferences held in the nineties of the twentieth century.

This problem is also present at the other conferences organized by our universities, and especially national conferences. Papers published at conferences have a lesser or no value for the promotion to academic and research ranks or for applying to national and international projects, which considerably decreases motivation for publishing papers.

The mentioned conditions have already been applied in the EU countries for a considerable period of time. This has affected the motivation of authors to appear at conferences which require additional costs: accommodation, travel, translation of papers, fees, etc.

Regardless all difficulties, the conference "Heavy Machinery HM" has been accomplishing its main goal successfully – to gather scientists and experts in this field, from our country and the region.

The conference also offers a possibility to young researchers to present their results to a wider scientific community.

The participation of scientists and professionals from thematic fields, from our country and abroad, with the presentation of their own results of research represents a significant support to the successful work of educational and scientific organizations in our country. The participants of the conference show that, in spite of currently difficult conditions for work, there are potentials which could contribute to the development of science and economy.

The conferences that have so far provided the presentation of results of research in the fields that are of current interest can significantly contribute to the education of experts in these fields as well as to the application of the results in the companies of our country. Therefore, the organizer of the "Heavy Machinery HM" conference should certainly make further efforts to keep its successful realization in the period to come.

ACKNOWLEDGEMENTS

The authors are grateful to the Ministry of Science, Technological Development and Innovation of the Republic of Serbia for support (contract no. 451-03-47/2023-01/200108).

REFERENCES

[1] International Conference Heavy Machinery - HM 1993, Kruševac-Vrnjačka Banja, 1993, Proceedings, Kraljevo, 8-10 October 1993.

[2] International Conference Heavy Machinery - HM 1996, Kraljevo, 1996, Proceedings, Kraljevo-Mataruška Banja, 28-30 June 1996.

[3] The Third Triennial International Conference Heavy Machinery - HM 1999, Kraljevo, 1999, Proceedings, Kraljevo-Mataruška Banja, 28-30 October 1999.

[4] The Fourth Triennial International Conference Heavy Machinery - HM 2002, Kraljevo, 2002, Proceedings, ISBN 86-82631-55-6, Kraljevo-Mataruška Banja, 28-30 June 2002.

[5] The Fifth Triennial International Conference Heavy Machinery - HM 2005, Kraljevo, 2005, Proceedings, ISBN 978-86-82631-45-3, Kraljevo-Mataruška Banja, 28 June- 03 July 2005.

[6] The Sixth Triennial International Conference Heavy Machinery - HM 2008, Kraljevo, 2008, Proceedings, ISBN 978-86-82631-45-3, Kraljevo-Mataruška Banja, 24-29 June 2008.

[7] The Seventh Triennial International Conference Heavy Machinery - HM 2011, Kraljevo, 2011, Proceedings, ISBN 978-86-82631-45-3, Vrnjačka Banja, 29 June-02 July 2011.

[8] The Eighth Triennial International Conference Heavy Machinery - HM 2014, Kraljevo, 2014, Proceedings, ISBN 978-86-82631-74-3, Zlatibor, 25-28 June 2014.

[9] The Ninth Triennial International Conference Heavy Machinery - HM 2017, Kraljevo, 2017, Proceedings, ISBN 978-86-82631-89-7, Zlatibor, 28 June-01 July 2017.

[10] The Tenth Triennial International Conference Heavy Machinery - HM 2021, Kraljevo, 2021, Proceedings, ISBN 978-86-81412-09-1, Vrnjačka Banja, 23-25 June 2021.

SESSION A

EARTH-MOVING AND TRANSPORTATION MACHINERY

Strength of Fillet-welded Joint Connections: Comments on Correlation Between Classical and Particular Finite Element Approach

Vlada Gašić*, Aleksandra Arsić, Nenad Zrnić
Faculty of Mechanical Engineering, University of Belgrade, Belgrade (Serbia)

The paper deals with strength of load-carrying fillet welds with application of two different approaches. First one is calculation by classical/scholar approach while second one is devoted to finite element analysis. The classical approach is concerned with national and European engineering practice. The finite element approach includes the application of particular tool which preserves main recommendations from modern postulations in design of joints. The object of interest is welded beam-to-column joint with different structural elements and the stresses are obtained for two models. It is investigated correlation of results of weld stresses from both the approaches. Direct matching of results was neither expected nor found but basic correlation is revealed within the joint behaviour under loadings. Considering finite element approach as prevailing, its advantage is clearly shown throughout inclusion of local effects of plates. However, classical approach is essential for proper understanding of joint behaviour and should be always the first step in structural analysis. The usage of at least two different approaches is one way of improving safety checks in engineering and stands for purpose of validation or verification of design.

Keywords: Joint, Fillet weld, Stress, Classical approach, FEA

1. INTRODUCTION

Welding is the joining method that creates one-piece member out of several components. The earliest form of welding has traces back to ancient times but the welding as we recognize it today was developed in the last decades of the 19th century. One may say that modern welding brought the revolution and freedom in design of large-scale structures.

The transfer of load and stiffness, by welded connections, can be introduced in a gradual continuous manner, instead of in step changes through bolted connections. Welded connections can be considered as very important for safety and durability of steel structure. However, ensuring weld quality and performance require perfect correlation between the design and fabrication. First step is dedicated to designer who are responsible for the selection of joint type, weld size, weld properties and calculation of design resistance. Fabrication is very important because it depends of parameters such as right choice of welding process, skills and experience of welders, working conditions, etc [1]. The final step in welding process is inspection which is dedicated to approval of welds with respect to the level of flaws.

Basic categories of welds are fillet and butt. The design resistance of a butt weld (full penetration) should be taken as equal to the design resistance of the weaker of the parts connected, provided that weld characteristics are not less than those specified for the parent metal. Butt welds are often subjection to inspection which gives the best insight in quality of fabrication process.

Hence, this paper deals with calculation of fillet weld connections due to the fact that they are widely present in structures and sometimes considered as the weakest link in structural strength. Also, they are essential for the corner joints (sometimes referred as T-configuration) at framed structures in mechanical engineering and are rarely subjected to inspection. Since their production is much cost effective then butt welds, the comprehensive design of fillet welds should be the cost to pay to ensure safety of the structure.

It is known that weldable structural steels should be preferred within this topic. Any other postulation is in relation to experimental investigations/tests [2]. Also, the problem of residual stress and deformation caused by welding are present in researches [3,4].

The aim of this paper is to check the correlation between the results of calculation of design resistance of fillet weld connections by two completely different approaches. The emphasis in this paper is given only on the strength of load-carrying welds. First approach is conventional way of calculation which implies application of knowledge from the theory of strength of materials and steel structures. Theoretical background may have deviations for welded or bolted connections and structural analysis in such locations requires special attention. Therefore, this approach will be based mostly on national engineering practice. It presents long-lasting tradition in engineering and even today is in everyday usage. It is accompanied with set of guidances due to issues of small sizes of welds when compared with sizes of beams which are usually subjected for joining by welding process.

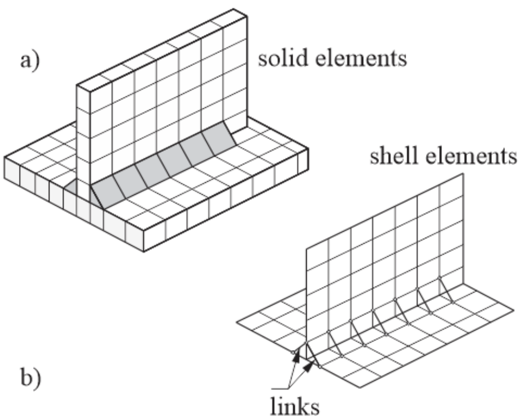

Figure 1:Modelling ways of welds with FEA

*Corresponding author: Kraljice Marije 16, Belgrade, Serbia, vgasic@mas.bg.ac.rs

Regarding classical approach one also have to consider requirements from Eurocode. Within the title topic, especially is important Eurocode 3: Design of steel structures-Part 1-8: Design of joints (EC 3-1-8) which introduced the concept of joint as a system of interconnected items, i.e. component method (CM), [5].

Second approach is numerical simulation of weld stresses which is often performed by the finite element analysis (FEA). Here, FEA belongs to the typical static analysis while other type like thermal analysis can be used for simulation of the welding process [6].

There are two characteristic ways of modelling by FEA. One is usage of solid elements (standard technique in engineering) where is preferred to model welds as separate bodies (Fig. 1.a). Sometimes, it requires the volume modelling of welds and is often challenging task because of weld shape to be analyzed which makes a crucial influence on the results. The second way is modelling with 2D elements and is common and allowed by most of the standards. For the cases where results are affected by local influences, the welds may be included by inclined elements having appropriate stiffness or by links to couple node displacements (Fig. 2.a). Along with big advantages with FEA, significant drawback comes from the fact that is necessary to find stresses and reorient them into the weld direction to perform the checks.

Here, the FEA will be concerned with the usage of shell elements for modelling of joint. In order to narrow down the field of FEA, it will be used software which preserves main recommendations from EC 3-1-8 (which traced the component based methods in calculation of joints). This software can be concerned as modern and particular tool for calculation of joints.

The experimental approach within this field is highly appreciated but expensive and reserved to simple cases of welded joints [7,8,9]. It had valuable importance in 20th century but now is common opinion that finite element approach can be used with confidence to predict failure loads of joint under various loadings [10].

2. DESIGN RESISTANCE OF THE FILLET WELD

When design resistance of the fillet weld is considered, an uniform distribution of stress is assumed on the throat section of the weld, leading to the normal stress and shear stresses shown in Fig. 2, as follows: $\sigma_\perp$ - the normal stress perpendicular to the throat, $\tau_\perp$ - the shear stress perpendicular to the length of the weld, $\tau_\parallel$ - the shear stress parallel to the length of the weld.

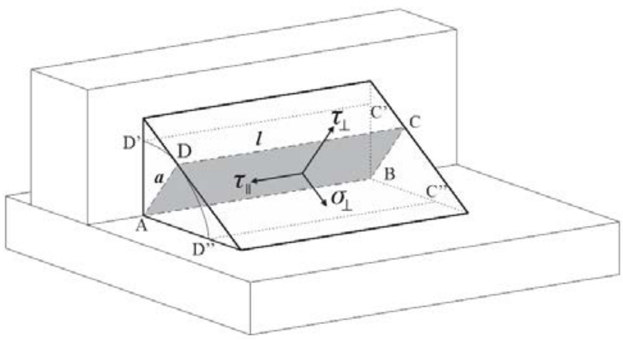

Figure 2: Stresses on the throat section of a fillet weld

2.1. Requirements of the EC3 standard

According to the EN 1993-1-8, the design resistance of the fillet weld should satisfy following expressions:

$$\sqrt{\sigma_\perp^2 + 3\left(\tau_\perp^2 + \tau_\parallel^2\right)} \leq \frac{f_u}{\beta_w \gamma_{M2}} \tag{1}$$

$$\text{and } \sigma_\perp \leq 0,9\frac{f_u}{\gamma_{M2}} \tag{2}$$

where: f_u - the nominal ultimate tensile strength of the weaker part joint; β_w - appropriate correlation factor (0,8 for S235 and 0,9 for S355); γ_{M2} - partial safety factor for joints (recommended 1,25).

It is common to understand the (1) in the following form:

$$\sigma_{w,eq} \leq \sigma_{w,Rd} \tag{3}$$

where $\sigma_{w,eq}$ represents the weld equivalent stress (can be considered as von Mises stress and in further text denoted as σ_{eq}) while $\sigma_{w,Rd}$ represents design (permissible) stress. For the sake of clarity, the right side of (2) will be denoted as $\sigma_{w,Rd,1}$ which presents the limit value for normal stress.

In order to use previous relations, the objects of calculation should be made of weldable structural steels (e.g. yield strengths in the range 185-460 MPa). Also, required quality level of weld should be C (according to EN ISO 2518) if not otherwise specified.

2.2. Requirements of the national standard

Due to position (slope) of the throat section, determination of the stresses in throat section can be fairly complicated. According to Serbian engineering practice, the long-lasting usage of regulations of the Serbian standard JUS U.E7.150 (probably based on DIN) allows the calculation of stresses in horizontal/vertical neighbouring plane which share root line with the throat section (Fig.2). Obviously, this can be considered as needed but represents the initial approximation in calculation. This can simplify the process of calculation for the designer. In further text, this will be marked as classical (sometimes called conventional) approach.

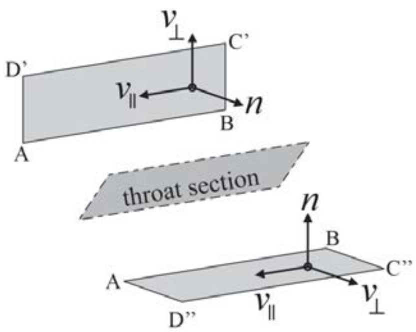

Figure 3: Stresses in neighboring planes

Hence, the calculation of stresses can be done in section ABC'D' or ABC''D'', according to the perspective of the designer (Fig.2). The design resistance is governed by following expression:

$$\sqrt{n^2 + v_\perp^2 + v_\parallel^2} \leq 0.5\frac{f_u}{v} \tag{4}$$

where: n - normal stress, $v_{\perp}$ - shear stress perpendicular to the length, $v_{\|}$ - shear stress parallel to the length, ν - safety factor (usually 1.5 for standard load cases).

This can be presented in form:

$$\sigma_u \leq \sigma_{w,dop} \tag{5}$$

where σ_u represents the vector sum of the three components while $\sigma_{w,dop}$ represents the permissible stress in weld.

Obviously, the classic approach have different designation of stress components in the weld from the designation of stresses in throat section. This is proper hypothesis which provides valuable results when adequate governing condition is used (4).

In order to find mathematical correlation between the stresses from two different equations (1,4), one may use for 90º-fillet weld following:

$$\sigma_{\perp} = \frac{n + v_{\perp}}{\sqrt{2}} \tag{6}$$

$$\tau_{\perp} = \frac{n - v_{\perp}}{\sqrt{2}} \tag{7}$$

$$\tau_{\|} = v_{\|} \tag{8}$$

These relations are valid for the vertical plane, i.e. section ABC'D', but can be similarly derived for horizontal plane [11].

3. MODEL DEFINITION

The object for two different approaches is the same and represents the corner beam-to-column joint which is widely present at structures in mechanical engineering. In order to expand the level of comparison between the classical and FEA approach, the results are obtained for two models of corner joint: Model 1 and Model 2. For both models, it is assumed that all the steel members are made of structural steel S235 with ultimate tensile strength of f_u=360 MPa and designed for normal working conditions. Hence, one may calculate permissible stresses by EC3 or by national requirements, as given in Table 1.

Table 1: Limit values of stresses [MPa]

JUS	EC3	
$\sigma_{w,dop}$	$\sigma_{w,Rd}$	$\sigma_{w,Rd,1}$
120	360	259

Model 1 includes a beam with rectangular hollow section (EN 10210) 200x100x8 mm and a column of HEA 300 (Euronorm 53-62). The joint is designed to be welded with the 90º-fillet weld with the throat size of 5 mm (a). Welds on the flanges of hollow section has length of 60 mm (l_1) while welds on the webs has length of 160 mm (l_2). With intention to find as much characteristic informations as possible, the arrangement of welds excludes the all-round fillet weld for rectangular section. The used lengths of welds can be considered as effective (load-carrying) lengths.

Model 2 includes a beam with circular tube section (EN 10210-2) 219,1x8 mm and a column with rectangular hollow section (EN 10210) 300x300x10 mm. The joint is welded all-round with the throat size of 5 mm (a). The idea behind this model is to check the effects of circular meshing in FEA.

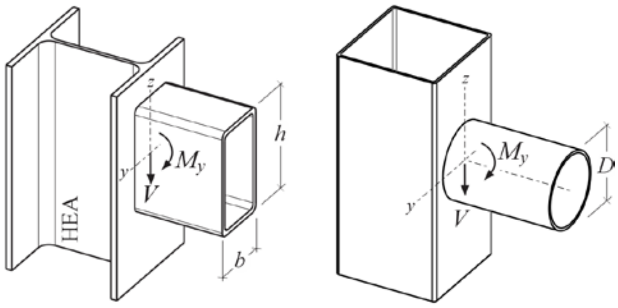

Figure 4: Beam-to-column joint: Model 1, Model 2, respectively

It is used the most common case of loading at frame structures which includes the presence of vertical force (V) and moment (M_y, in further text denoted only as M), i.e. loadings in vertical plane. In order to compare the stresses between the two approaches the influence of loadings will be considered individually and then combined. For the sake of clarity, the load cases are denoted as follows:

Case 1: vertical force-V
Case 2: moment –M
Case 3: combination, V+M

3.1 Classical approach

The postulation of statical model in chapter 3 is fairly simple according to classical approach. For Model 1, the known stress distributions from the influence of loadings are depicted in Fig. 5 where is assumed that section of vertical welds is carrying the vertical force. There are distinguished three characteristic points for calculation of stresses.

Normal stresses can be conducted upon following:

$$n = \frac{M_y}{I_{y,w}} z \tag{9}$$

where $I_{w,y}$ is second order moment of area of the weld section related to the y-axis.

Shear stresses can calculated by

$$v_{\|} = \tau = \frac{V}{2a \cdot l_1} \tag{10}$$

or with parabolic distribution, exceptionally for the point 3 and for Case 1, as

$$v_{\|} = 1{,}5\tau \tag{11}$$

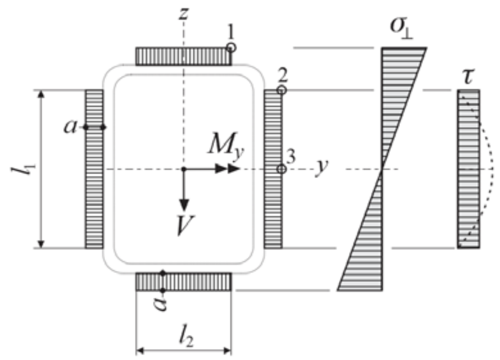

Figure 5: Model 1-Stress distribution

For Model 2, the stress distribution is presented in Fig. 6. The normal stresses can be conducted with (9) while shear stresses have to be obtained by

$$v_{\parallel} = \tau = \frac{V \cdot S_{w,y}}{I_{w,y} \cdot 2a} \tag{12}$$

where $S_{w,y}$ is first order moment of area of the weld section related to the y-axis.

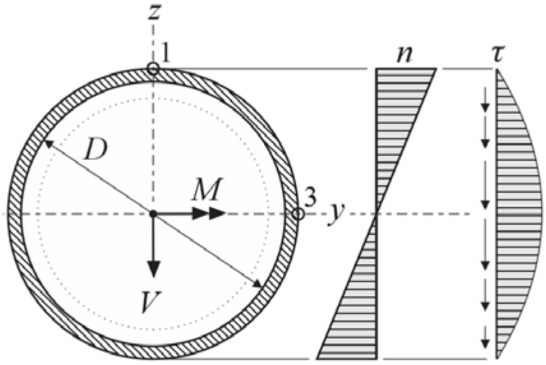

Figure 6: Model 2-Stress distribution

There are distinguished two characteristic points for calculation of stresses (denoted as 1 and 3) to correspond to points from Model 1.

The geometrical properties of weld section, for each model, belong to the class of calculation for simple shapes which can be found in literature [12].

For both models, the external loadings are taken as V=100 kN and M=1000 kNcm (10 kNm). It will be shown in further text that these values are assumed in order to get „high“ values of stresses which are close to the permissible stresses.

3.2 FEA approach

As mentioned in introduction chapter, the FEA approach is here oriented towards particular tool for design of steel structural joints. It is used software IDEA StatiCa which introduced Component Based Finite Element Model (CBFEM) as extension of classical FEM with main parts of CM [13]. Hence, the behaviour of components such as column web in shear and in compression, beam flange and web in compression and column flange in bending are incorporated in software. According to the authors, this software is: comprehensive enough to provide: good informations about joint behaviour, stress, strain and about overall safety and reliability; fast enough in daily practice to provide results in a time comparable to other FE tools.

Regarding postulated object of interest, both the flanges and webs of connected members are modelled with shell elements with 4-nodes at its corners having six degrees of freedom. The welds are treated as multi-point constraints (MPC) and relates the finite element nodes of one plate edge to another. The constraint allows modelling the midline surface of the connected plates with the offset, which respect the real weld configuration and throat thickness. The load distribution in the welds is derived from the MPC, so the stresses are calculated in the throat section. This is important due to postulation given in chapter 2.1.

The basic representation of FEA models is given at figure 7, according to postulation in chapter 3. The external loadings are acting on the joints for both models and presented by software on the “free” beam ends due to visibility.

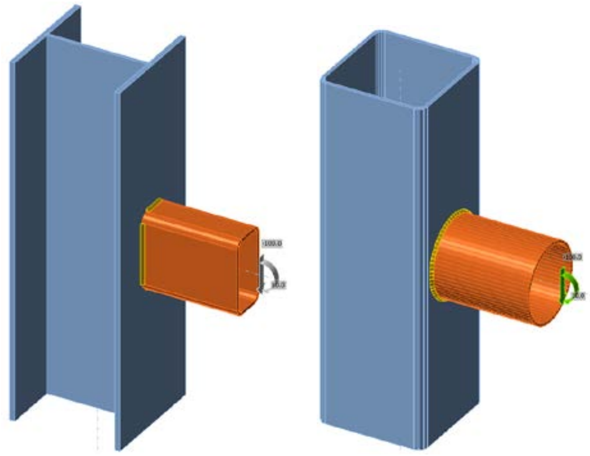

Figure 7: FE models- Model 1and Model 2, respectively

4. RESULTS AND DISCUSSION

Before consideration of stresses for characteristic models, one have to perceive the limit values of stresses (permissible stresses) obtained from two different standards (Table 1). It is obvious that values are significantly different. For used material (S235), the governing criterion for permissible stress by EC3 gives value which is three times bigger than obtained by JUS. This cannot serve for direct comparison due to the fact that permissible stresses by these standards correspond to the working stresses which are not observed in the same sections. EC3 uses von Mises criterion for calculation of nominal stress in weld while JUS uses direct sum of vectors for same purpose. Even for 90^{o}-fillet weld, where is known relations between the vectors from throat section and the neighbouring plane, one may find a gap between the limit values of stresses. It can be concluded that limit values of stresses by JUS (probably based on DIN) can be considered as conservative and very strict. The EC3, as relatively new standard, has to be considered as governing due to 30-years usage in European engineering practice. Regarding the design resistance of weld, it cannot be considered as so strict due to fact that limit values of stresses in weld are higher than for structural elements. One may assume that this point comes from the research and knowledge from development of calculation models in structural analysis. Due to postulation which concerns the behaviour of various components in joints, the EC3 can be considered as exceptionally comprehensive.

4.1 Model 1

Upon the model definition in chapter 3, one may find geometrical properties of the weld section and consequently the values of stresses. Table 1 presents review of calculated results obtained with (5,9,10,11). Furthermore, it is performed mathematical transformation with (6,7) to obtained corresponding equivalent stress.

The corresponding analysis is performed with CBFEM software and main results for stresses in welds are shown in Table 3. The results are shown for horizontal welds (length of 60 mm) and for vertical welds (length of 160 mm), for the purpose of distinction.

Table 2: Obtained stresses-classical approach [MPa]

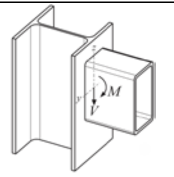	Load	Case 1 (*V*)				Case 2 (*M*)				Case 3 (*V* + *M*)			
	Point	n	$v_{\|\|}$	σ_u	σ_{eq}	n	$v_{\|\|}$	σ_u	σ_{eq}	n	$v_{\|\|}$	σ_u	σ_{eq}
	1	0	0	0	0	109	0	109	154	109	0	109	154
	2	0	62.5	62.5	108	85	0	85	120	85	62.5	105	161
	3	0	93.7	93.7	162	0	0	0	0	0	62.5	62.5	108

Table 3: Obtained stresses-FEA approach [MPa]

	Case 1				Case 2				Case 3			
	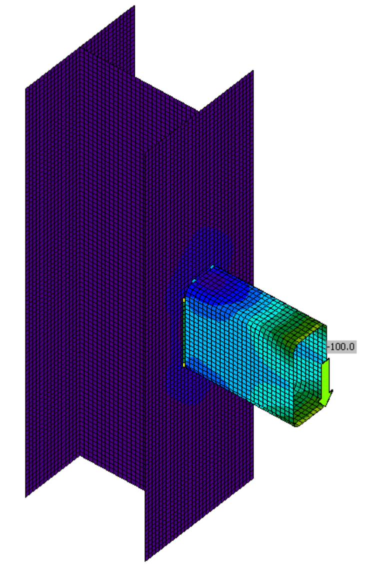				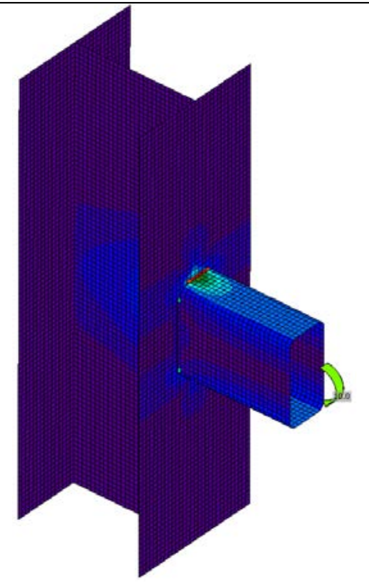				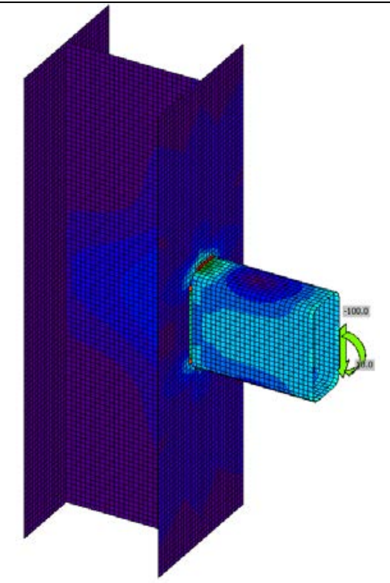			
Weld	$\sigma_\perp$	$\tau_{\|\|}$	$\tau_\perp$	σ_{eq}	$\sigma_\perp$	$\tau_{\|\|}$	$\tau_\perp$	σ_{eq}	$\sigma_\perp$	$\tau_{\|\|}$	$\tau_\perp$	σ_{eq}
Horiz.	±26.2	-34.2	±9.2	66.6	±128	64.7	130	283	±128	73.3	±130.9	289.9
Vertic.	-13.8	±77	-1.1	134	-33.9	±29.9	31.3	82	20	±107	-32.5	194.7

The first comparison can be done with following observations of corresponding equivalent stresses (σ_{eq}) from different approaches (Table 2 vs. Table 3): there is not direct matching of results; the values from FEA are up to twice higher than from classical approach. Many reasons can be found to explain previous statement because this FEA includes: elastoplastic behaviour in equivalent weld; behaviour of plates (webs and flanges of connecting elements) under loadings. However, this cannot be considered as ending point for evaluation between these approaches.

In the second phase of comparison the values from FEA (Table 2) should be looked separately. The choice of load Case 1 and Case 2 can serve as background for analysis. One may notice following: for Case 1, the biggest value of the shear stress parallel to the length of the weld ($\tau_{||}$=77 MPa) is reserved for vertical welds; for Case 2, the biggest values are reserved for $\sigma_\perp$ and $\tau_\perp$ (128 MPa and 130 MPa), which mutually contribute to the stress oriented normal to the vertical plane; for Case 3, the previous observations are also preserved as their combination. Hence, it can be said that joint behaviour sustains known effects of vertical force and bending moment. Apart from main tabular data, software provides graphical distribution of equivalent stresses for welds. This option will be sketched in Figure 8 and is used for final phase of comparison. Due to symmetrical weld section, the presentation at this figure is given for both the characteristic cases (1 and 2).

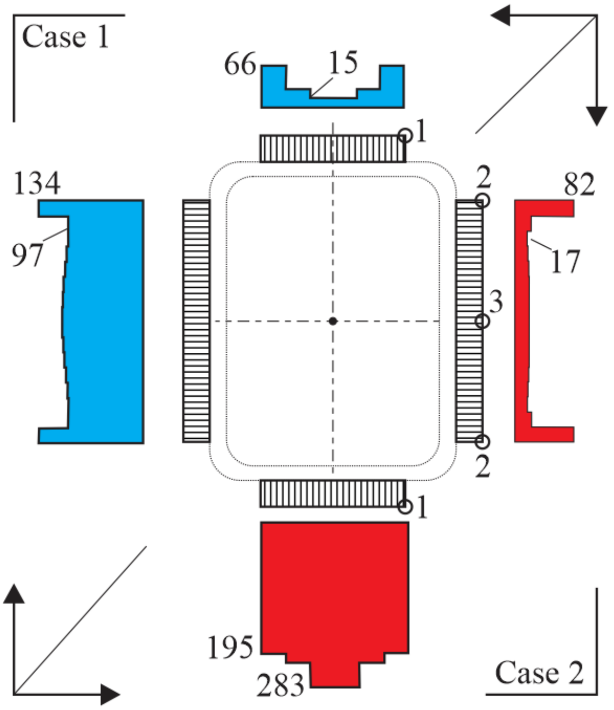

Figure 8: FE models, sketched stress distribution

It is obvious from Fig.8 that stress distribution is different than from classical approach (Fig. 5). It was expected because, as stated in software manual, IDEA StatiCA gives plastic stress redistribution in welds. The given stress distribution provides the highest and the lowest value of stress. The highest level can be named as stress peaks and can be an issue of discussion. Moreover, these stress peaks are only given in main tabular data (Table 3) and used directly for checks of the weld. It may be on the safe side of design resistance but certainly requires more explanations and instructions in manual. Disregarding the stress peaks in distribution for vertical welds, for Case 1, one may found relatively uniform distribution over length. This can be questioning point for the usage of the (11) in classical approach which is common approximation to preserve safe side of check.

Considering the current model, the main questionable point can be stress distribution for vertical welds in Case 2. In order to test this specific situation, the additional model is done with stronger column (HEM300) which have stiffeners, with the idea to prevent the local effects as much as possible (Fig. 9). The sketched distribution is given in figure 9 and has the shape which resemble the known stress distribution due to bending moment. This step of modelling can be considered as creating highly rigid column but one may found this as very useful possibility of the software for the review of results by the engineer with respect to hand calculations.

The classical approach relies only on geometrical properties of weld sections. It implies the knowledge and experience in engineering regarding the design of connections in terms of member thickness and need for stiffeners. However, it can be said that is related to the zone of rigid connections which can be considered as basic drawback.

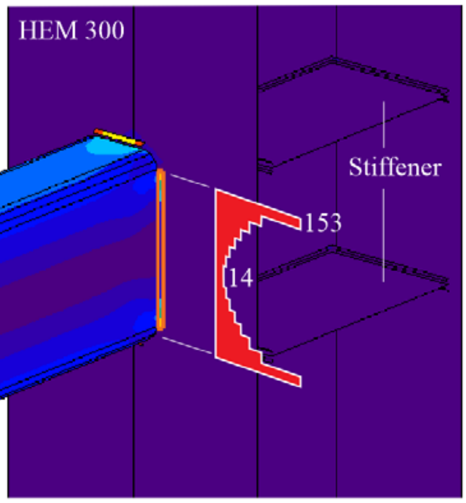

Figure 9: Sketched stress distribution (rigid joint)

4.2 Model 2

The corresponding procedure from previous chapter is performed for Model 2. The results by classical approach are given in Table 4, upon the usage of (9) and (12) and consequently the (6) and (7) for determination of equivalent stress. The results from CBFEM are given in Table 5, based on maximal stresses found by software.

Table 4: Model 2-Obtained stresses-classical approach [MPa]

Load	Case 1 (*V*)				Case 2 (*M*)				Case 3 (*V* + *M*)			
Point	n	$v_{\parallel}$	σ_u	σ_{eq}	n	$v_{\parallel}$	σ_u	σ_{eq}	n	$v_{\parallel}$	σ_u	σ_{eq}
1	0	0	0	0	48	0	48	67	48	0	48	67
3	0	55	55	95	0	0	0	0	0	55	55	95

Table 5: Model 2-Obtained stresses-FEA approach [MPa]

Case 1				Case 2				Case 3			
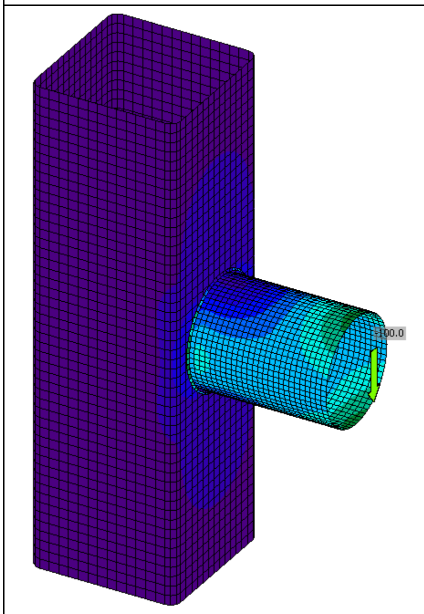				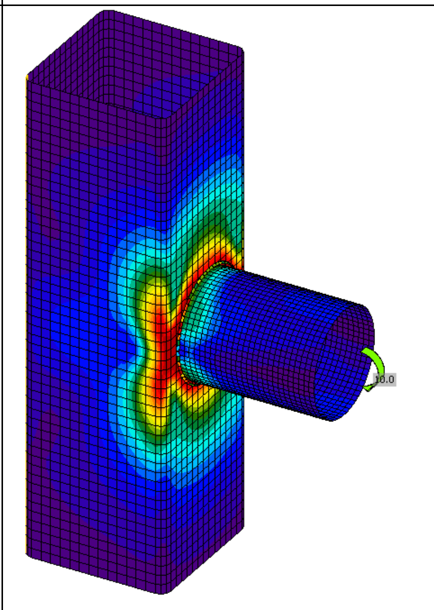				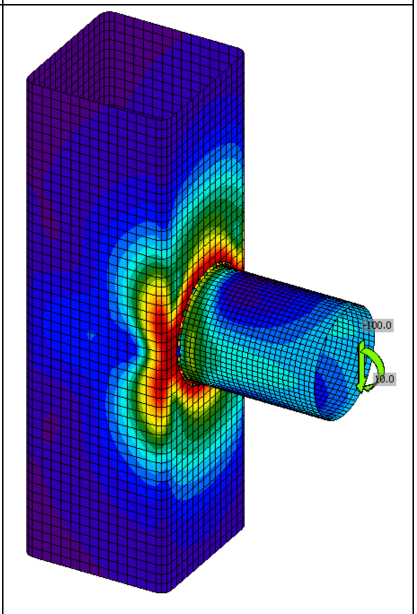			
$\sigma_{\perp}$	$\tau_{\parallel}$	$\tau_{\perp}$	σ_{eq}	$\sigma_{\perp}$	$\tau_{\parallel}$	$\tau_{\perp}$	σ_{eq}	$\sigma_{\perp}$	$\tau_{\parallel}$	$\tau_{\perp}$	σ_{eq}
5	-58	-2.2	100.6	63.8	132.5	-33.1	245	-123	112	92.3	280

For this model, one may also cannot find direct matching of results for corresponding equivalent stresses (σ_{eq}). This is not related to the Case 1 where is obtained good correlation which cannot serve as conclusion due to *low* importance of shear stresses in structural analysis.

The difference in results is especially noticeable for Case 2 and consequently for Case 3. The reason is shown in graphical presentation of stresses for these cases (by software) where it is obvious that local effects of the connecting plates have high influence on the stress level. The gap between the results could be smaller if one assumes that shear stress has uniform distribution in the vertical direction of the weld. This could be one point of view for increase of safety zone in weld calculation by scholar approach.

This kind of joint does not have much possibility for placing stiffeners at the column and modification towards increase of joint rigidity can be done only with bigger thickness of the box tube. It is not given here because of detailed comparison for Model 1 which can be used as general explanation for current model. The graphical distribution of equivalent stresses for welds, as capability of software, is not readable as for Model 1. It can be assumed that this problem arises from the circular shape of welds which certainly invokes the problem of presentation. Hence, the comparison with the stress distributions on the Fig. 6 cannot be performed.

5. CONCLUSION

Two different approaches are concerned here regarding the strength of fillet-welded joint connections. First one is calculation with classical (scholar) approach while second one is devoted to finite element analysis by particular software. The object for calculations represents the corner beam-to-column joint which is widely present at structures in mechanical engineering. The weldable structural steel is default material within this topic. The strength analysis is related to load-carrying welds which are often subjected to safety checks.

Within the classical approach, the design resistance of the fillet weld is considered with two different expressions. Basic one is requirement from national standard (JUS, most likely based on DIN) which has long-lasting tradition and fairly simplifies the process of calculation. This one can be named as scholar approach. The second one is requirement from EC3 which deals with stresses on the throat section of a weld. In order to perform calculations in classical way, one have to start with scholar approach and use mathematical transformations for vectors in corresponding planes. Hence, these two requirements are different and cannot be easily compared. One may say that requirements from EC3 invokes the finite element approach for determination of stresses.

The usage of FEA is performed with particular, comprehensive and modern software which includes the component method in joint design. The results are presented in tabular form, along with many informations about joint behaviour. The graphical presentation of stress state is extremely valuable, along with deformed shape which provides useful comprehension of joint behaviour under loadings.

The aim of this paper was not to compare the incomparable but to find some point of correlation with classical and FEA approach. It is shown that basic nature of weld resistance under loadings is preserved with both the approaches, without direct matching of numerical values. As presented in chapter 4, previous conclusion is not so obvious even considered as expected. According to presented procedures and current trends in engineering, many points go in favour of the usage of FEA. The main advantage is surely the implementation of local influence of plates in connected members. The software used in this research is especially valuable and one may found many possibilities for the design of joints. Regarding weld stresses only point of discussion can be the occurrence of stress peaks because of lack of informations for this in instructions which should be accompanied with mathematical postulations of MPC. The sort of recommendation is to give stress distribution oriented to the position of the weld which will improve the perception of the results. Previous statement is especially noticeable for round welds in Model 2. Some reference points in welds should be predefined in order to allow engineers to perform easier comparison with classical approach. The previous does not diminish the benefits of the presented software but only serve as a point of improvement for readability of results.

According to the authors, some level of validation or verification should be present in structural analysis. Even with FEA as dominant trend in engineering, the classical approach should be concerned in some form. The time spent for reading and understanding the results from software should be the cost for better qualifications of an structural engineer.

ACKNOWLEDGEMENTS

This work is a result of research supported by the Ministry of Science, Technological Development and Innovation of the Republic of Serbia by Contract 451-03-47/2023-01/ 200105, 03.02.2023.

REFERENCES

[1] M. Tavodarova, N. Naprstkova, M. Hnilicova, P.Beno, “Quality Evaluation of Welding Joints by Different Methods”, FME Transactions, 48 (4), pp.816-824, (2020)

[2] M. Arsić, N. Zdravković, V. Grabulov, S. Bulatović, M. Mladenović, “Strength of the Welded Joint with Improved Mechanical Properties of Weld Metal and Heat Affected Zone”, Proc. of the X Int.Conf. “Heavy Machinery-HM 2021”, Vrnjačka Banja (Serbia), 23-25 June 2021, pp. 43-46, (2021)

[3] M. Perić, Z. Tonković, K. Maksimović, D. Stamenković, „ Numerical Analysis of Residual Stresses in a T-joint Fillet Weld Using a Submodeling Technique“, FME Transactions 47, pp. 183-189, (2019)

[4] M. Arsić, S. Bošnjak, N. Zrnić, A. Sedmak, N. Gnjatović, „Bucket wheel failure caused by residual stresses in welded joints“, Engineering Failure Analysis 18, pp. 700-712, (2011)

[5] CEN (European Committee for Standardization), Design of Steel Structures, Part 1.8: Design of Joints, EN 19993:1-8, Brussels, 2005.

[6] R.N. Mhetre, S.G. Jadhva, “Finite element analysis of welded Joints“, International Journal of Instrumentation Control and Automation, Vol. 2 (1), (2012)

[7] H. Lu, P. Dong, S. Boppudi,“Strength analysis of fillet welds under longitudinal and transverse shear conditions“, Marine Structures, Vol. 42, pp. 87-106, (2015)

[8] D. Deng, W. Liang, H. Murakawa, „Determination of welding deformation in fillet-welded joint by means of numerical simulation and comparison with experimental measurements“, Journal of Materials Processing Technology, Vol. 183 (2), pp. 219-225, (2007)

[9] M. Krejsa, J. Brozovsky, D. Mikolasek, P. Parenica, J. Flodr, A. Materna, R. Halama, J. Kozak, „Numerical modeling of steel fillet welded joint“, Advances in Engineering Software, Vol. 117, pp.59-69, (2018)

[10] B.G. Mellor, R.C.T. Rainey, N.E. Kirk, „ The static strenght of end and T fillet weld connections“, Materials&Design, Vol. 20 (1), pp. 193-205, (1999)

[11] W. Fricke, M. Mertens, C. Weqissenborn, „Finite Element Calculation and Assessment of Static Stresses in Load-Carrying Fillet Welds“, Conference: Annual Assembly of International Institute of Welding, Vol. IIW-Doc.XV-1151-03, (2003)

[12] D. Ružić, R. Čukić, M. Dunjić, M. Milovančević, N. Anđelić, V. Milošević-Mitić, „Otpornost materijala-tablice“, Mašinski fakultet, Beograd (Srbija), (2015).

[13] https://www.ideastatica.com/.

Continuously Variable Transmission for Construction Machines to increase efficiency and productivity

Jasna Glišović[1*], Vanja Šušteršič[1], Jovanka Lukić[1], SašaVasiljević[2]

[1]Faculty of Engineering/Department for Motor Vehicles and Motors, University of Kragujevac, Kragujevac (Serbia)
[2]High Technical School of Professional Studies, Kragujevac (Serbia)

According to estimates, by 2050 two-thirds of the world’s population will live in large cities. This trend also comes with disadvantages: fuel emissions, fine dust and noise impact the environment and residents. Ideally, the construction site of the future should not only be environmental neutral, but it should also operate safely and efficiently. Mobile machines used in construction, mining, forestry and agriculture are engineered to withstand extreme working environments while allowing operators to control equipment safely, comfortably and efficiently. Power transmissions make it possible to move extremely heavy loads by applying a multiple increase in torque. However, transmissions must also allow vehicles to move with loads at speeds appropriate to the situation. Careful selection of transmissions can provide an optimal solution: towing or pushing loads at low speeds and operating at higher speeds when needed. Very few mobile construction machines made today are equipped with purely manual transmissions; instead, they are more likely to be equipped with variable-speed transmissions or other automated transmission types. Continuous variable transmission is characterized by: an infinite number of ratios improving vehicle performance and engine optimization, and increasing work efficiency; automatic shifting with smooth forward/reverse shuttling, increasing productivity and drive comfort; maximize fuel savings versus current technologies, allowing cost savings. An objective comparative analysis of various design solutions of continuously variable transmission for modern construction machines and assessment of the most likely trend of the future development of this class of heavy machines was carried out in the paper.

Keywords: CVT, Construction Machines, performance, productivity, design ring

1. INTRODUCTION

Mobile machines used in construction, mining, forestry and agriculture are engineered to withstand extreme working environments, while allowing operators to control equipment safely, comfortably and efficiently. These machines must also be productive and efficient when moving materials. The two main powertrain components used on off-road vehicles that can meet these basic requirements are forward/reverse transmissions and powershift transmissions.

Power transmissions make it possible to move extremely heavy loads by applying a multiple increase in torque. However, transmissions must also allow vehicles to move with loads at speeds appropriate to the situation. Careful selection of the gearbox and its gear ratios can provide an optimal solution: towing or pushing the load at low speeds and working at higher speeds when necessary. Transmissions are designed according to the purpose and tasks of the machine in which they are installed to achieve these goals. Very few mobile construction machines made today are equipped with purely manual transmissions; instead, they are more likely to be equipped with variable-speed transmissions or other automated transmission types. There have been radical changes in the operation and control of hydraulic systems; the use of hybrid drive systems (Figure 1) and great energy savings are some new technological trends in the field of construction machinery [1,2].

The construction industry is faced with massive changes, caused by volatile markets, economic uncertainties, and governmental regulations, demanding high flexibility and fast development cycles. Until recently, hydrostatic-mechanical power split CVT (Continuously Variable Transmission) drivelines have not found a place in construction machinery. The majority of these vehicles still use hydrodynamic powershift transmissions, full-hydrostatic transmissions or mechanical direct-shift transmissions. Hydrostatic drive lines are widely used in construction machinery possessing lower engine power. The upper power range is dominated by hydrodynamic powershift transmissions.

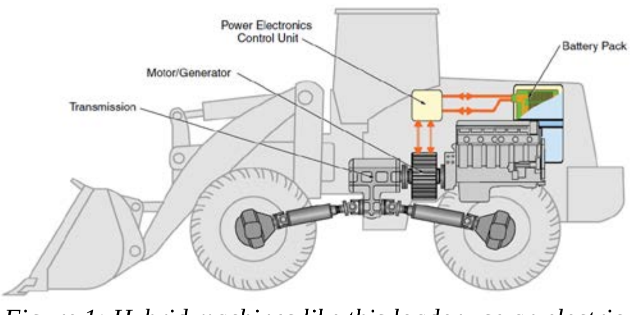

Figure 1: Hybrid machines like this loader use an electric motor between the engine and the transmission, which reduces the fuel consumption and emissions of construction machinery. [3]

2. DEVELOPMENT TREND OF CONSTRUCTION MACHINERY TRANSMISSIONS

In some machines, such as dozers and wheel loaders, it is useful to have the same number of forward and reverse gears. These types of machines usually repeat the same task throughout their workday, such as digging a pile of soil, then carrying it to a dump truck and dumping the load, and then returning to the pile again. To accommodate this cyclical workload, manufacturers typically use an auxiliary gearbox either before the main standard gearbox, or integral with it. The auxiliary transmission uses two multi-plate couplings. Figure 2 shows a forward/reverse gearbox.

The auxiliary gearbox for forward/reverse movement (reverser) is a set of two hydraulic multi-plate couplings, the first of which, when activated, rotates the gears of the gearbox in the direction of forward movement (clockwise), and when the second is activated, the transmission is achieved in the reverse direction (counter-clockwise). This arrangement can increase the cycle speed of the machine by allowing quick changes between forward and reverse without the need to change the mechanical gear ratio. Although these changes can be made while moving, it is still recommended to stop the vehicle before making the change of direction. In these types of transmissions, the input power is usually delivered to the auxiliary transmission via a torque converter that can mitigate the rapid changes in direction and shock loads on the other power transmission elements of the machine.

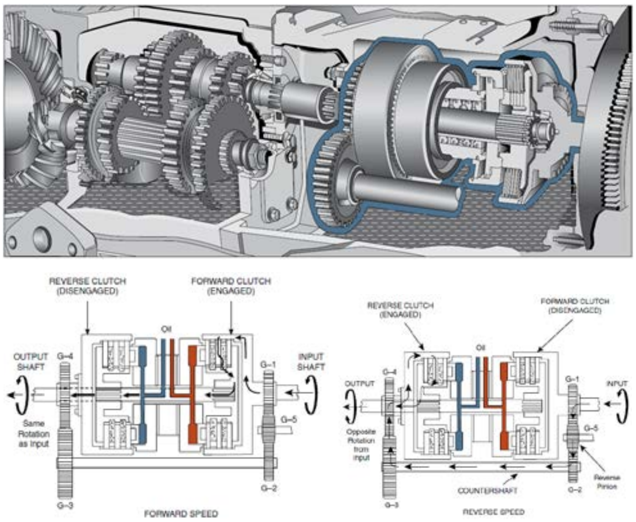

Figure 2: Forward/reverse auxiliary gearbox with two multi-plate couplings [3]

Automated manual transmissions (AMTs) are quickly becoming a presence in the heavy-duty truck market for a number of reasons, primarily fuel economy. These gearboxes are able to optimize the gear change points, resulting in savings of around 5-7% in fuel consumption. This increases the thermal efficiency of the vehicle's engine, meaning that more of the fuel is used to do useful work. By saving fuel, they also reduce the production of carbon dioxide, which contributes to the greenhouse gas effect and thus global warming. These gearboxes, however, also offer other benefits: they reduce driver fatigue, as they no longer have to constantly change a gear, which in turn allows the driver to pay more attention to the road and his surroundings, improving traffic safety. The simplicity of driving vehicles equipped with these transmissions also solves another problem in the trucking industry: the availability of trained drivers to operate construction machines and trucks.

The add-on AMT transmission with dual countershafts uses an auxiliary part to multiply the available gear ratios. The auxiliary is essentially a second gear box bolted to the rear of the main gearbox, so the output of the main gearbox becomes the input for the auxiliary. The auxiliary part can achieve two, three or even four different gear ratios that are used to multiply the available gear ratios of the five-speed main gearbox, resulting in transmissions that have 9, 10, 13, 15 and 18 gear ratios. The auxiliary part can deliver very high torque (high gear ratios) for off-road work, or it can achieve close values of gear ratios to achieve high fuel economy when driving on the highway. Figure 3 shows the power flow for a 10-speed auxiliary transmission.

The range change gear is a large gear on the countershaft auxiliary, and power from the main transmission can be transmitted directly through the range gear (low range), or it can be directly transmitted to the mainshaft auxiliary (high range or direct). In low range, the range synchronizer is moved rearward by a shift fork powered by an air piston. The synchronizer slip clutch engages the range gear engagement teeth, locking them to the mainshaft auxiliary. The output from the main shaft of the main gearbox is connected to the auxiliary part of the drive gear. Power flows from the auxiliary part of the drive gear to the countershaft and back to the range change gear, as shown in Figure 3a.

In high range, the range synchronizer moves forward and locks the auxiliary drive gear directly to the auxiliary main shaft, and power flows straight through the auxiliary, as shown in Figure 3b. The range change system allows the main gear torque to be multiplied by two.

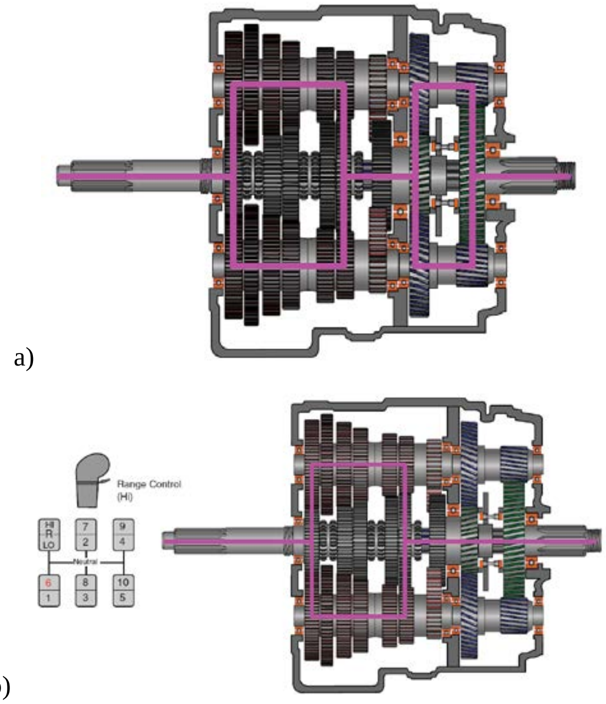

Figure 3: a) Auxiliary gearbox in low range. b) In the high range, the power flows straight through the auxiliary section unchanged [3]

Several off-road vehicles manufacturers are developing or have developed dual clutch transmissions. Figure 4 shows a dual clutch transmission for mid-range trucks. Dual-clutch transmissions save fuel by shifting gears without interrupting torque transmission and shifting much faster than a conventional automatic transmission. Changeover speeds are reduced from 100 to 200 milliseconds to as little as 6 to 12 milliseconds. Because dual clutch transmissions have two separate power input paths, a solid input shaft and a hollow input shaft, the transmission control unit can select the next gear while still in the previous gear. To change ranges, the transmission simply switches the input clutch to drive a different input shaft, making it much faster.

With the primary input shaft connected to the output shaft, the transmission can achieve sixth gear by shifting to the secondary input clutch and driving the primary input shaft through the secondary input shaft and intermediate shaft. All those transmission ratios go through a planetary gear set. This achieves six forward transmission ratios in the low range with a planetary gear system. The same six ratios are repeated in high range when the planetary gear system allows the power flow to pass through the transmission unchanged. This makes a total of 12 forward gear ratios.

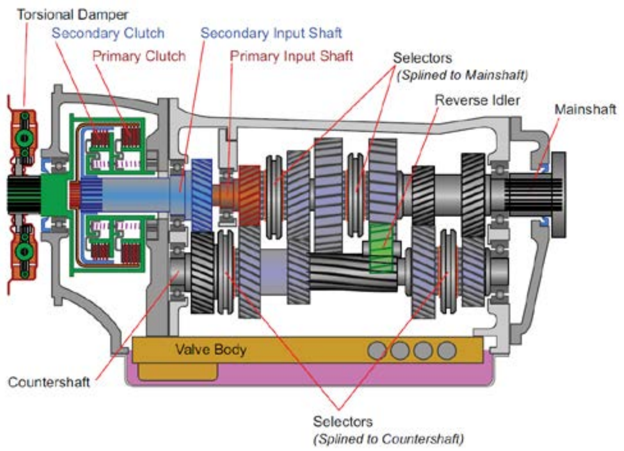

Figure 4: Double clutch transmission with synchro mesh on the main shaft and intermediate shaft [3]

Powershift is a type of transmission developed to allow the operator to shift gears up or down and change direction in motion and under load without loss of acceleration or torque and without using the clutch foot control. More specifically, a powershift transmission transfers torque from the engine's flywheel or torque converter and changes speed, torque and direction of rotation through various gear ratios. Then those changes are transmitted to the rest of the power train, which may include a differential, a set of drive shafts, etc. (Figure 5).

The ability of powershift transmissions to change gears without interrupting the power flow is achieved by means of hydraulic multi-plate clutches that engage and disengage series of gears and are operated by a hydraulic system.

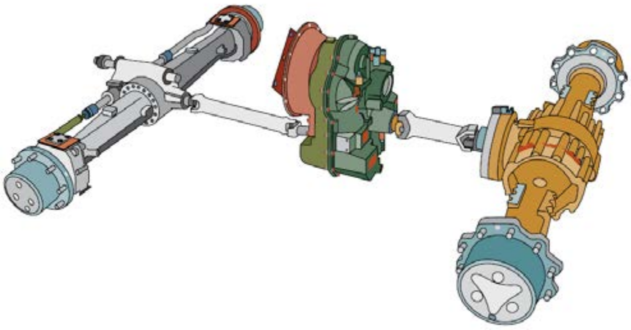

Figure 5: Typical example of a power transmission with a powershift gearbox [3]

There are two main types of powershift transmissions: intermediate shaft and planetary. These names refer to the type of gear arrangement used to transmit torque through the transmission. Both types have permanently toothed gears, meaning that each of the gears inside the transmission is always meshed with another gear. When one or more gears are hydraulically coupled to the shaft, torque is transmitted through the gearbox. In a countershaft transmission, the hydraulic couplings operate counter-rotating shafts by meshing gears. This type of power transmission is commonly found in small to medium wheel loaders, graders, trucks and other machines that have a range of 75-300 kW.

In a planetary power transmission, hydraulic couplings actuate sets of planetary gears to transmit power. Planetary powershift transmissions can be found in any type or size of machine, from less than 75 kW to 750 kW or more.

The powershift intermediate shaft transmission used in the John Deere 872D grader serves as a good example of how this type of transmission is incorporated into the machine's power transmission (Figure 6).

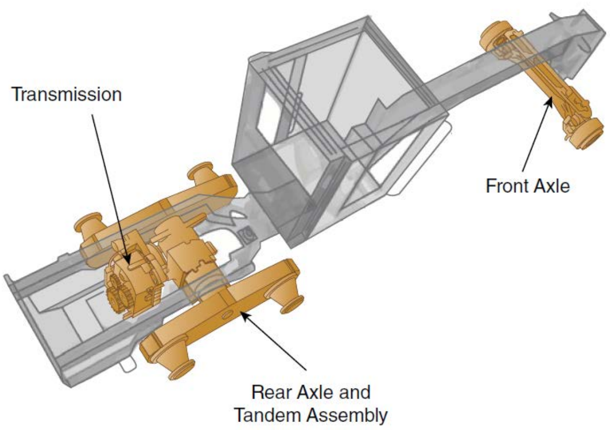

Figure 6: Layout of the elements of the powershift transmission with an intermediate shaft in the grader transmission [3]

Several construction machinery manufacturers offer continuously variable transmissions (CVTs) as standard or optional equipment. A CVT is a transmission in which the transmission ratios are continuously and almost infinitely variable. This type of transmission provides several advantages to the operator. The biggest advantage is that the engine can run at the best rpm in terms of fuel economy and engine efficiency.

Construction machines using a hydrostatic transmission are highly efficient under lower working speed condition, but less capable at higher transport velocities. To increase overall efficiency, the powertrain design can combine a hydrostatic transmission with a dual-clutch transmission (DCT). Unlike other mechanical gearboxes, the DCT avoids the interruption of torque transmission in the process of shifting without sacrificing more transmission efficiency. However, there are some problems of unstable torque transmission during the shifting process, and an excessive torque drop occurring at the end of the gear shift, which result in a poor drive comfort. A novel structure that combines the HST with a dual-clutch transmission is presented in Figure 7. [4]

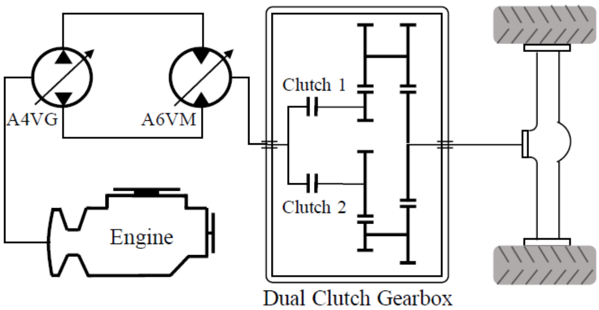

Figure 7: HST+DCT drivetrain [4]

3. IMPROVEMENT OF FUEL EFFICIENCY AND PRODUCTIVITY OF CONSTRUCTION MACHINES

Fuel economy has also been a growing trend over the past decade. However, the additional cost of more complex technologies must be compensated by the savings in fuel cost over a time period of 2-3 years. The transmission’s efficiency highly contributes to the vehicle’s fuel consumption. [5]

Despite the development of emission-free construction machinery, diesel vehicles will continue to dominate the global market for a long time to come. But they too must meet requirements for lower fuel consumption and CO_2 emissions. This is where most manufacturers come in with its solutions for reducing emissions and saving energy that also work to increase efficiency and productivity. Today’s technology is not advanced enough to operate large construction machinery by purely electric means. To meet the demands of tomorrow's construction sites, modern working machines must reduce fuel consumption and give off minimal emissions, while also remaining efficient, convenient, productive, and easy to use.

The proven and tested fully automatic powershift transmission system (Figure 8) has today been optimized for different off-highway machinery types and offers the innovative feature of six instead of four or five gears. The noise-optimized transmission allows even more comfortable and easier handling, high shifting quality and flexibility. Moreover, the operating costs can be further reduced due to various features like converter lock-up, engine de-rating, operating mode selection and much more. For example, the ZF-ERGOPOWER provides additional possibilities for connecting an electronic driveline management, thus enabling vehicle-specific controls (Figure 9). Easy shifting and shift quality by the electronic device is a derivate from the passenger car application with automatic transmissions. Efficiency and safety features are our main targets for the improvement of these transmission ranges.

Whether its wheel loaders, dumpers, graders, forest applications or material handling - in its customized EFFICIENCY PACKAGE (Figure 9), ZF unites its expertise in transmission, axle and software development to offer more than the sum of the advantages of individual applications. System components such as ZF axles and transmissions are optimized for compatibility and enable greater efficiency and easy handling. In light of calls for sustainability, fuel savings of up to 15% are already possible with hydrodynamic technology.

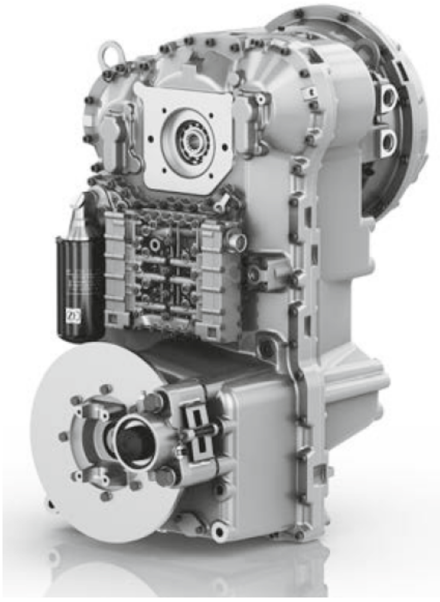

Figure 8: ZF fully automated or manual powershift transmission

Figure 9: ZF ERGOPOWER with efficiency package

CVTs have found applications in machinery that operates at relatively low power, but their applications in the automotive industry have gone through many setbacks and it is only in recent decades that the CVT vehicle market share has become significant. The status of CVT technologies today is the result of intensive research and development by researchers and engineers both in the academic community and in the automotive and construction equipment industry. [6]

An increasing number of machinery manufacturers follow a rising demand for continuously variable transmissions in the construction and agricultural machinery market [8]. Hydrostatic technology is more and more displacing hydrodynamic (torque converter) transmissions especially in construction machinery systems. A trend towards lower engine speeds and the demand for engine stabilization by a constant speed concept are the future challenges. The continuously variable meets both requirements.

Movement sequences flow easier using continuously variable transmissions. Therefore, construction machines can be controlled more precisely. With gear shifting, the drop in power associated with the change of gear does not occur. This ensures more constant engine speeds. The driver profits from the continuously variable technology as well, since manual gear shifting is no longer needed and he can completely concentrate on his work.

Figure 10: ZF cPOWER CVT Technology [7,10,11]

To meet the increasing demands for reductions in fuel consumption and higher productivity with regard to sustainability, ZF has equipped its work machinery with fully power-split CVT technology. The new ZF cPOWER (Figure 10) offers full power-split and perfectly combines hydrostatical and mechanical advantages throughout the whole range. It benefits from the high degree of hydrostatical efficiency at low speeds and at the same time from the great mechanical efficiency at high speeds. Reduced fuel consumption of more than 25% and an increase of productivity of more than 20% are possible. The high tech CVT is 100% assembly-compatible with ZF-ERGOPOWER transmissions. The application of an elaborate hydraulic transmission-control unit and transmission-integrated on-board electronic unit optimally completes driving functions.

But not only in wheel loaders does ZF’s cPOWER transmission help reduce fuel and increase productivity. In the Diesel-engine-powered lift truck market, a trend towards lower engine speeds and the demand for engine stabilization by a constant speed concept are the future challenges. The continuously variable cPOWER meets both requirements.

As for forestry equipment, ZF is already supplying the cPOWER transmission design for the Skidder application. In addition, this transmission system is also the ideal driveline solution for the forwarder application. The installation of the cPOWER in these vehicles guarantees a maximum in traction, excellent driving comfort and easy handling.

The entire driving range, forwards and backwards, uses cPOWER stepless control. Regardless of driving speed, lower engine speeds provide greater efficiency and optimum comfort. The result is fuel savings of up to 25% compared to standard ERGOPOWER drives. If cPOWER is combined with the ZF EFFICIENCY PACKAGE, the fuel savings increase by a further 5%. The newly developed EFFICIENCY PACKAGE and the cPOWER CVT technology enable ZF to tailor its solutions to customer needs and market demand. The developers have succeeded in reducing emissions and fuel consumption while increasing efficiency and productivity, without compromising on comfort. (Figure 11).

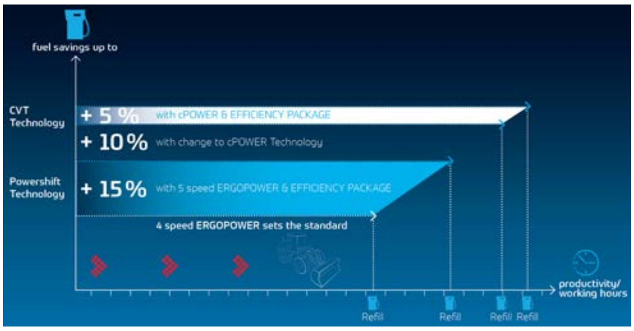

Figure 11: Efficiency package-less fuel and higher productivity [10]

Figure 12 shows the efficiency curves for a two-range CVT in comparison to a 4-speed torque converter power shift transmission. Because CVT is fully power split in the 1st and 2nd range, the efficiency remains stable through the entire vehicle speed range. The hydrostatic module transmits a higher percentage of power at lower vehicle speeds. At these low speeds, where high torque is needed, the power losses of CVT are much lower than a torque converter transmission. At higher speeds, power is transmitted mechanically, allowing the CVT efficiency to remain high while a hydrostatic transmission would lose efficiency rapidly. The first range of CVT covers vehicle speeds of up to 10 km/h allowing highest possible efficiency during productive work. The high and constant efficiency allows more flexibility for OEMs to optimize their power packaging and working hydraulics according to their own operation strategies.

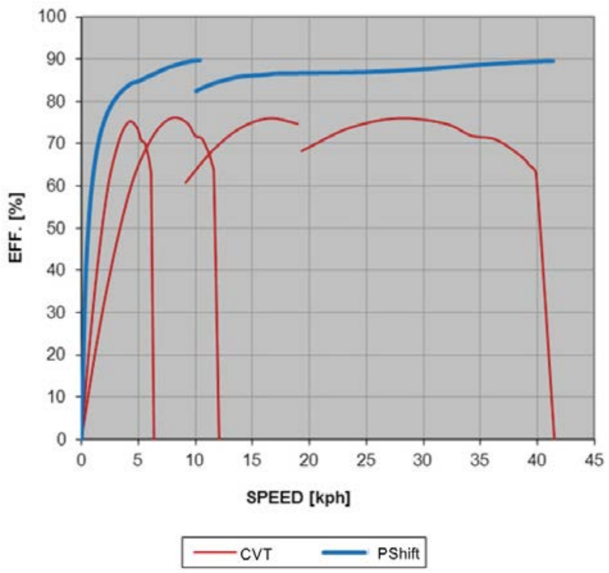

Figure 12: Comparison of Efficiency of CVT and Torque Convertor Power Transmission [4]

CVTCORP, the world leader in the design and development of mechanical continuously variable transmissions (mCVTs) for high-powered off-highway vehicles and his partner Bonfiglioli, a worldwide designer, manufacturer and distributor of a complete range of geared motors, drive systems, planetary gearboxes and inverters, presented a ECGenius line of products. ECGenius is a high-power, efficient and cost-effective CVT dedicated to telehandler vehicles but also suitable for other equipment. The patented technology at the core of this product is the result of over 15 years of development and enables OEM's downsize engine while providing unmatched operational ease, and overall vehicle performance improvements in the 20-30% range. Torque and power are transferred seamlessly through 6 actuated rollers, thanks to the elastohydrodynamic lubrication which prevents metal to metal contact while ensuring the correct torque transfer without slippage (Figure 13). Traction drive toroidal architecture offers smooth, seamless shifting with no steps through an infinite number of effective forward speeds. The innovative transmission design with advanced control and clutch reduces the number of mechanical components, therefore reducing mechanical and viscous losses. Seamless shifting allows the engine to operate at its optimal operating point. [9]

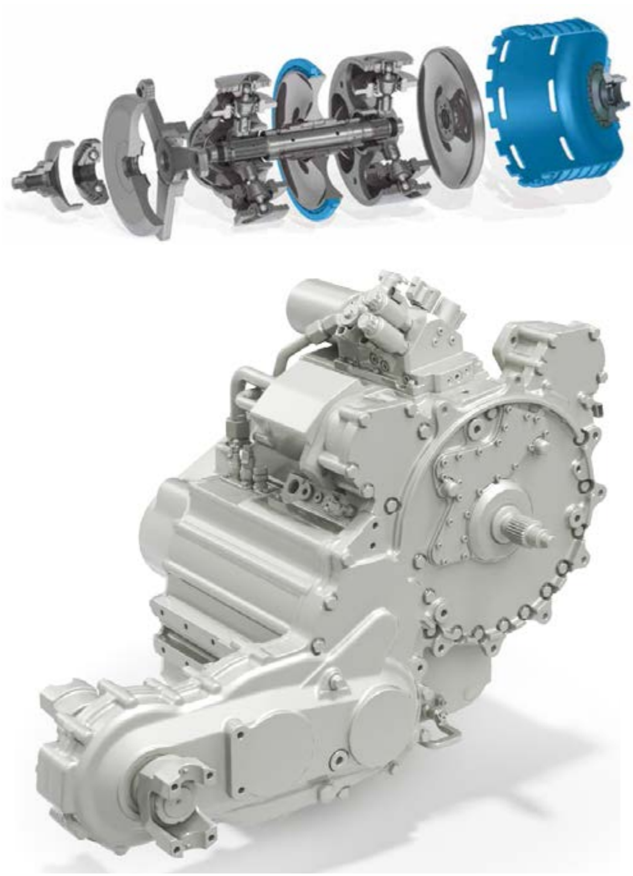

Figure 13: Bonfiglioli Continuously Variable Transmission [9]

4. ELECTRIC POWER TRANSMISSION

The trend towards electromobility is not confined to passenger cars. Electric power transmissions in the field of motor vehicles have found a wider application in special heavy-duty vehicles (so-called dumpers) used for transporting loose loads (ore and tailings) in day mines. The main advantages of the electric power transmission on motor vehicles consist in the fact that it is possible to continuously change the power parameters without its interruption from the source to the drive wheels, simple transmission of power over longer distances with simple electrical conductors, less driver fatigue and the possibility of using the transmission for efficient braking. However, the main disadvantage of this type of power transmission is the heavy weight of its basic components. On vehicles equipped with electric transmissions, the mechanical energy given off by the internal combustion engine is converted into electrical energy in the generator, and this energy is converted into mechanical energy in the electric motors.

Until now, two basic systems of electric power transmission on motor vehicles have been developed: with direct current and with alternating current. In a DC system, the mechanical energy of the internal combustion engine is converted into electrical energy (in a DC generator), and electrical into mechanical energy (in DC motors). In an alternating current system, the mechanical energy of the internal combustion engine is converted into electricity in an alternating current generator. A rectifier is installed between this generator and the direct current electric motors, in which the alternating current is rectified into direct current. As seen in the system, DC electric motors are used, which can be regulated very easily in a wide range of angular speed and torque.

Manufacturers use a wide variety of configurations for AC electric drive systems to drive machinery. In most systems, the flywheel of the diesel engine directly drives the generator, but one machine uses a gearbox located between the flywheel and the generator. The output shaft of the gearbox transmits the torque to the input shaft of the generator. Figure 14 shows the gear drive of the generator. For this machine, the engine speed is tripled to increase the generator speed to 5,400 rpm when the engine is running at 1,800 rpm. The gearbox also drives the machine's hydraulic pump.

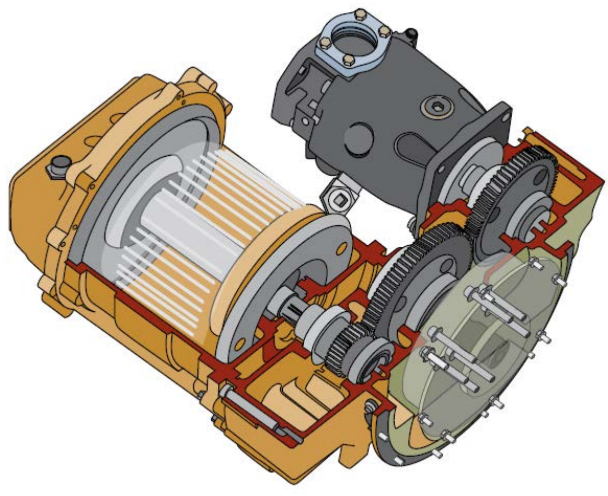

Figure 14: Generator-electric motor gearbox type [3]

The main differences between the systems are the type and number of generators, as well as the type and number of drive motors and how they are controlled. Almost all machines use one generator to power one or more electric motors. There are, however, machines that use two generators.

Electronic controls can precisely control the inverter output to the AC motors to match the operator's speed and direction requirements, while the motor-driven generator rotates at a constant number of revolutions (Figure 15).

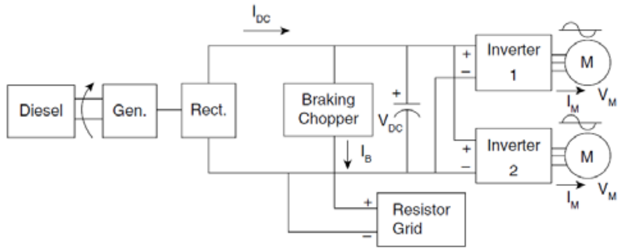

Figure 15: Block diagram of the electrical power transmission system [3].

E-mobility solutions for compact vehicles such as loaders, site dumpers or telehandlers are the first to enter the construction equipment market, especially in urban or emission-regulated areas. ZF starts volume production of new electrified driveline for compact wheel loader (Figure 16). The 48V system is the basis of a modular platform which can be scaled up to 650V and can cover compact vehicle loaders from 4 to 8 tones. Electric motor enables hybrid drive as well as purely electric driving, boost function, and zero-emission operation of equipment. Electric motor acts as retarder or recuperator, which reduces brake wear and thus maintenance costs.

Figure 16: Generator-electric motor gearbox type [10]

5. CONCLUSION

The industry of construction machinery and construction site vehicles is more and more focused on topics like reduced fuel consumption, driver comfort or environmental compatibility. Less fuel consumption, reduced wear and emission, increased efficiency, extended service intervals, easier and better handling, and more automation are all topics in the focus of engineers in this field.

By advancing the CVT powersplit technology known from agricultural machinery, the construction machines transmission provides significant consumption benefits and productivity increases with a level of efficiency previously inconceivable.

Leading manufacturers are also committed to the advancement of alternative drives – not only on the road, but also for off-road applications, so the first hybrid drive for construction machinery is already developed. An electric motor supports the conventional drive and prevents high power peaks. This significantly lowers fuel consumption and reduces the load on the drive. By integrating a hybrid module with the proven powershift transmission, the logical step toward the future was undertaken.

Ideally, the future of construction should not only be climate neutral, but it should also operate safely and efficiently. To ensure this, leading manufacturers are already developing future-oriented system solutions for smart construction sites. Based on all the activities in the passenger car and commercial vehicle segment, a broad portfolio of Know-How and products can be re-used for Off-Highway vehicle applications. Radar-based environment perception is just one example to ensure safe vehicle operation.

ACKNOWLEDGEMENTS

The Ministry for education, science and technological development of the Government of the Republic of Serbia supported the research presented in the article (grant number TR35041).

REFERENCES

[1] D. Janošević, "Projektovanje mobilnih mašina", Univerzitet u Nišu, Mašinski fakultet, Niš, (2006)

[2] A.F. Andreev, V.I. Kabanau, V.V. Vantsevich, "Driveline Systems of Ground Vehicles. Theory and Design", CRC Press, Taylor & Francis Group, Boca Raton, US, (2010)

[3] O.C. Duffy, S.A. Heard, G. Wright, "Fundamentals of Mobile Heavy Equipment", Jones & Bartlett Learning, Burlington, USA, (2019)

[4] Y. Xiang, R. Li, C. Brach, X. Liu and M. Geimer, "A Novel Algorithm for Hydrostatic-Mechanical Mobile Machines with a Dual-Clutch Transmission", Energies, Vol. 15, 2095, (2022)

[5] J. Legner, W. Rebholz, R. Morrison, "ZF cPower – Hydrostatic-Mechanical Powersplit Transmission for Construction and Forest Machinery", 10th International Fluid Power Conference (10. IFK) March 8 - 10, Vol. 3, pp. 45-5, (2016)

[6] Y. Zhang and C. Mi, "Automotive Power Transmission Systems", John Wiley & Sons Ltd, Hoboken, USA, (2018)

[7] HL975A CVT Wheel Loader - Hyundai Construction Equipment, Product Catalog, https://www.hyundai-ce.eu/en/products/loaders/wheel-loaders/hl975a-cvt

[8] The New Cat 966K XE Wheel Loader with advanced powertrain, Product Catalog, https://www.cat.com/en_IN/news/machine-press-releases/the-new-cat-sup-174sup966kxeefficientcomfortablesustainable.html

[9] Bonfiglioli Continuously Variable Transmissions, Product Catalog, https://www.dropbox.com/home/HM2023?preview=Bonfiglioli_LateralVertical.pdf

[10] ZF Construction Machinery Systems, From Less to Zero, Product Catalog, https://www.zf.com/products/media/industrial/construction/downloads_1/new/Construction_Machinery_Systems.pdf

[11] Doosan DL420CVT-5 Wheel Loader, Product Catalog, https://www.lloyd.ltd.uk/wp-content/uploads/2021/03/EN_DL420CVT-5_Brochure_D4600130_01-2019_LowRes.pdf

Artificial intelligence (AI) and the future of the machine elements design

Marko Popović[1*], Nedeljko Dučić[1], Vojislav Vujičić[1], Milan Marjanović[1], Goran Marković[2]
[1]Faculty of Technical Science, University of Kragujevac, Čačak (Serbia)
[2] Faculty of Mechanical and Civil Engineering in Kraljevo, University of Kragujevac, Kraljevo (Serbia)

The document also contains defined quick-styles that may be used for fast formatting of the submitted papers. Artificial intelligence (AI), is becoming an important tool in the fields of mechanical engineering. AI have potential power, to give fast predict of the dimensions and shapes of the machine elements, trought optimisation process in initial and the final design stage. This paper give the review of the potential use of the AI in the field of the machine element design.

Keywords: Machine Design, Machine Elements, Artificial Intelligence (AI)

1. INTRODUCTION

Artificial intelligence (AI) technology is becoming increasingly important in people's lives as it becomes more widely used in people's daily lives, such as the widespread use of smart dishwashers and smart sweepers, which are the products of the fusion of AI and the mechanical manufacturing industry [1]. Indeed, AI has been widely utilized in the mechanical manufacturing business, which not only ensures production precision, but also enhances job productivity and workplace safety. The rise of AI has caused significant changes in the manufacturing industry as a whole.

With the continuous progress of science and technology, mechanical engineering is also constantly evolving and changing, from the traditional mechanical engineering to the state-of-the art mechanical engineering [2]. And its level of automation and intellectualization has a continuous improvement, it went into a new stage of development, thus, the combination of AI and mechanical engineering has become a hotspot. AI is applied under the premise of the development of computer technology, which improved the computer technology through the analysis of it to achieve the realization of intelligent technology.

The applications of AI in mechanical engineering is not only the use of computer technology, but also combined with information technology, psychology, linguistics and other knowledge. The AI is in fact the simulation of the process of data interaction of human thinking, hoping to understand the essence of human intelligence and then produce a smart machine, this intelligent machine can be the same as human thinking to respond and deal with the problem [2].

2. DESIGN OF MACHINE ELEMENTS

The design process of machine elements can be observed through processes of the analysis and synthesis of different informations and data. Objective of analysis, is to examine machines and/or machine elements for which sizes, shapes, and materials have already been proposed or selected, so that loading severity parameters (e.g., stresses) may be calculated and compared with critical capacities (e.g., strengths corresponding to governing failure modes) at each critical point [3]. Adjunct analyses might also be undertaken to calculate and compare such attributes as cost, life, weight, noise level, safety risks, or other pertinent performance parameters. The objective of the synthesis, is to examine performance requirements associated with a particular design mission, then select the best possible material and determine the best possible shape, size, and arrangement, within specified constraints of life, cost, weight, safety, reliability, or other performance parameters.

Design process is the first step in the process of conceptualising a machine components [4]. The design process involves analyzing a function and performance requirements, determining its materials and manufacturing methods, and then creating detailed drawings and specifications that can be used to manufacture the component [5]. The main phases in process of the design of the machine components, machine elements and machines are:

- *Conceptual Design.* The design process typically starts with conceptual design, where the basic requirements and constraints of the component are defined.
- *Detailed Design.* Conceptual design is followed by detailed design, where the component is designed to meet the requirements and constraints, considering factors such as materials, manufacturing methods, and cost.
- *Analysis and Optimization*. The design then goes through an analysis and optimization stage. Analysis and optimization rely on computer-aided design (CAD) and 3D mechanical engineering simulation (CAE) tools to ensure they will function as intended and meet performance requirements.
- *Multi-Objective Optimization.* Optimizing of the parts, assembly and machines means considering several objectives (sometimes contrasting) and constraints coming from targets on weight, cost, size etc. This is called multi-objective optimization.

Machine elements design is a very time consuming and responsible task. It is the first phase of the manufacturing process, and its aim is to anticipate the impact of external factors on the designed component [6]. Therefore designers must be able to correctly combine knowledge of many fields.

When the engineers designs the machine elements or the complete machines, they have to consider several important factors:

1. Functionality, high output and efficiency

*Corresponding author: Svetog Save 65, Čačak, marko.popovic@ftn.kg.ac.rs

2. Strength, stiffness and rigidity
3. The cost
4. Operational safety
5. Easy of assembly, and disassembly
6. Light weight and minimum dimension
7. Reliability
8. Durability
9. Accessibility
10. Compliance with state standards
11. Ergonomics and industrial design

3. ARTIFICIAL INTELLIGENCE AND EXPERT SYSTEMS

In smart applications, the terms AI, machine learning, and deep learning are frequently used interchangeably [1]. However, there are distinctions between them. A part of machine learning is called deep learning. All machine learning applications are considered to be examples of AI since machine learning is a subset of AI that may operate intelligent applications (Fig.1).

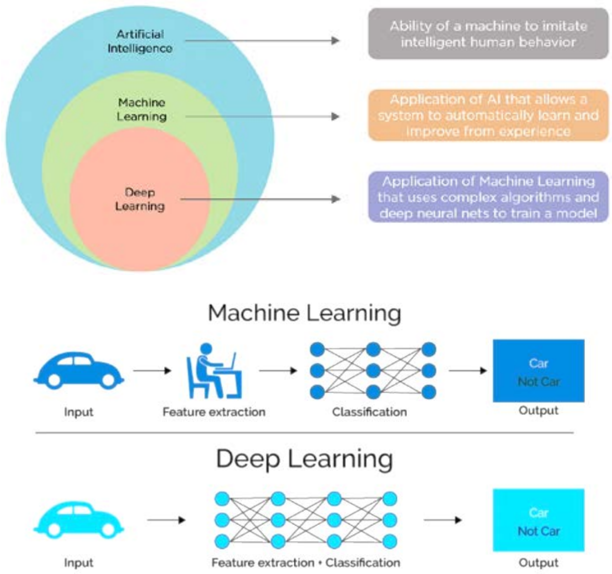

Figure 1: Fundamental differences between AI, machine learning, and deep learning [8], [9]

Generaly an entity that possesses the following properties is considered to be intelligent:

- *Generalized learning.* An adequate reaction of the machine to a new or changing external environment
- *Decision-making.* Decision-making based on given criteria and the current environment
- *Problem Solving.* Finding a solution based on the current environment and given input parameters

AI technologies often refer to methodologies like expert systems, genetic algorithms, fuzzy logic, artificial neural networks etc. [7], [1]. The expert system can be seen as a kind of specialized knowledge of computer intelligent program system, it can use expertise and experience provided by experts in specific areas and the use of reasoning techniques in AI to solve and simulate complex problems that can often be solved by experts [2].

Expert Systems (ES) give the possibility of solving specialized problems which require professional expertise, which means that they can replace an expert in a given field, often without a need of expert’s support during program operation. A characteristic feature of this system is a division of knowledge gained from an expert, called knowledge base, and the rest of the system containing, among others, mechanisms of reasoning on the basis of knowledge resources from a given domain. Expert Systems can be generally divided into three categories:

1. *advisory* – systems presenting the user certain solutions, which are evaluated in order to choose the most adequate one, or to ask for another solution,
2. *taking decisions without human control (dictatorial)* – systems, which do not consult end results with the user,
3. *criticizing* – are characterized by taking input values related to the given problem and possible solution.

Expert Systems are able to: gather complete knowledge from a given domain and update it constantly, copy the way of thinking of an expert, which results in offering decisions and providing their variants, explain the way of thinking of the user to the adopted solutions, communicate in a language comfortable for the user.

4. AI AND DESIGN OF MACHINE ELEMENTS

There are various areas where AI finds applications in mechanical engineering. It comprises of data handling and automation, to perform the work with minimum of human intervention [4]. The fourth industrial revolution involves integrating the internet, big data, cloud computing, the internet of things, and AI into the mechanical manufacturing industry as of the beginning of the twenty-first century [1].

This big data inflow, is base start point for the AI application in mechanical engineering, especially in the fields such as machine design, manufacturing, crash simulation, predictive maintenance, robotics, industry 4.0 applications etc.

In his book [10], T.H.Davenport proposed the following advice on making AI technologies practical:

- Use AI to improve processes or products by automating the repetitive or structured aspects of design
- Look for “low-hanging fruit” opportunities to improve efficiency
- Create smart products that “work alongside smart people”

In according with previous, there are several ways AI may be used in mechanical engineering. The design and optimization of mechanical systems and parts, such as engines, gears, and bearings, may be automated using AI, for instance [12]. The performance of mechanical systems may also be simulated and analyzed using AI in order to forecast behavior, spot future issues, and suggest changes. AI may also be used to track and manage mechanical systems in real-time, improving their dependability and efficiency. Overall, applying AI to mechanical engineering may assist to increase the effectiveness, dependability, and performance of mechanical systems as well as promote the creation of novel and cutting-edge technologies.

Can engineers apply AI in the process of the machine element design? AI can be applied in the process of the machine elements design, because this process is characterized by the properties (*in terms of its structure and* *method of implementation*), which are fully compatible with the AI technology:

- This design process have a structure and process algorithm
- It is a repeatable process
- It is an iterative process
- Machine elements are well structured and standardized
- The process requires adaptation to certain criteria (*typification, unification*)
- Great importance of the engineer's experience
- Good practice are often used in design process
- Machine elements information can be storage in the database
- Design of the machine elements, contains process of the optimization

In which stage of machine and machine elements design, engineers can use AI? AI can be use from early stage of design – conceptual design, through detail design with analysis and optimisation process, to the final stage, with generating of the detail technical documentation. *In the conceptual design,* the initial form of machine structure will affect both performance and cost of the machine [11]. In this context, the search for shapes becomes one of the key steps in the conceptual design phase, as its results are inputs for the next steps in the design process, in the subsequent construction phase, and throughout the life cycle of the machines. In the proces of the *simulation,* AI can improve the design proces, by combining different parallel analyses of physics, solid mechanics, fluid mechanics etc. It is possible to learn AI to distinguish between parts and different assemblies, which can be used in the future for designing a wide range of components and machines. Different *optimization methods* have matured in recent years due to extensive research conducted by applied mathematicians and engineers. In this context, the utilization and principles of AI, may be prevalent for using in the optimization process.

How engineers may use AI? There are several ways that AI may be used in the machine elements design, starting from conceptual, to the final design. In according, authors give the list of possible use of AI in the machine element design process:

1. Design assistent – *best shape, cost etc. application*
2. Generation of the state-of the-art collaborative framework
3. CAD/CAE integration – based on the proven designs and analysis
4. AI interactive CAD System
5. Big data and proven CAD models for optimization process
6. AI automated parts and assembly adoption – *date from databases (from local to the world database)*
7. Advance virtual prototypes
8. Shape and behavior prediction
9. AI evaluation of the design
10. Topology, shape and dimension optimisation – *AI fine tuning*
11. Reverse engineering – *automated generating 3D model from point cloud*
12. Virtual reality optimisation design
13. FEM model development
14. Alternative FEM models
15. Automated cost analysis – *started from the conceptual design*
16. Optimization from the aspect of the position and orientation of the parts – *the influence of the other parts in assembly to the considered part design*)
17. Generative design – *advance multi object optimisation*

Below are given several examples of the application of AI in the machine elements design process, which are currently in the different development stages.

At this moment, the most important field for implementation of AI for machine elements design is a CAD/CAE technology. As already appoinment in the paper [1], CAD uses AI that typically operates on knowledge-based systems. In CAD, design artifacts, rules, and issues are archived for subsequent use by CAD designers. AI and CAD are combined using model-based reasoning. Building a predictive model of machine element, machine and equipment, requires all the physics and components found in CAD and CAE models. Running simulations on the engineering model can then generate a dataset that an AI algorithm can use for processing [12].

When speaking about AI interactive CAD System, the main thing to point out is that drawing still takes too much of a designer's thought processing. In complex design tasks liberating the designer from the necessity of manually using slow interfaces will allow engineers to focus on the other important steps, that require much higher knowledge and responsibility. The research which is presented in the [6], involves the development of intelligent interactive automated systems for designing machine elements and assemblies, using descriptions of structural elements' features in a natural language. This new concept proposed a novel approach to these systems, with particular emphasis on their ability to be truly flexible, adaptive, human error-tolerant, and supportive both of design engineers and data processing systems. The foundation of interactivity is bi-directional communication between the data processing system and the user. Results of evaluation, performed with AI, of the designed solutions are used at as early as the design stage. This system can analyses of design engineer's messages, analyses of constructions, encoding and assessments of constructions, CAD system controlling and visualizations. It also presents the developed methodology for similarity analysis between structural features of designed machine elements and corresponding antipatterns allowing normalization of parameters of the analysed structural solutions.

An example of the used AI in the proces of the machine elements design - shaft design, is given on the following figure. At this figure are given a two stages of the interation process of the shaft design. Upper picture showen the first iteration proces of generation of the shaft shape, and on the below picture, is given design with AI suggestion for the shaft details. Suggestins are given in according with the shaft production technology and assembly process for gears and bearings.

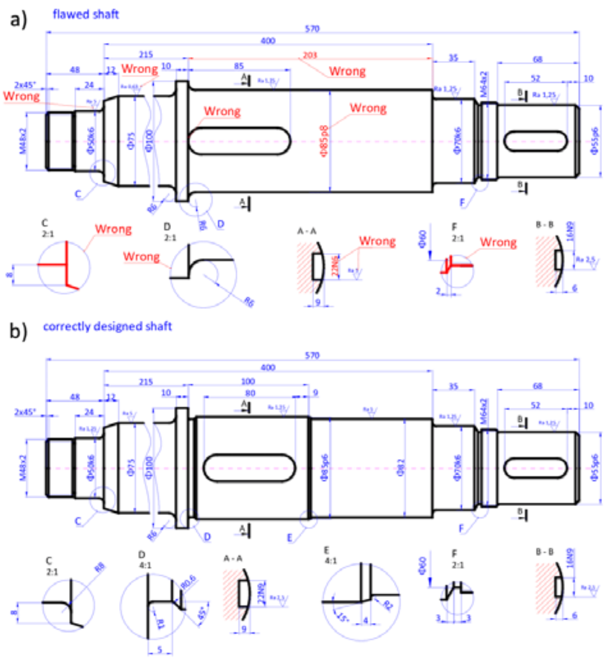

Figure 2: A machine shaft with highlighted errors: a) an antipattern, b) correct design [6]

When we consider AI automated parts and assembly adoption (date from different databases), in the study [13] examined a comprehensive, annotated benchmark of mechanical components for classification and retrieval operations. This dataset enables the data-driven study of machine component symptoms and enables data-driven feature learning for mechanical components. Examining the form description of machine elements is vital for all automatic processing from computer vision through the different industrial applications. The dataset enables data-driven feature learning for mechanical components.

Obtaining 3D models is difficult because annotating machine elements requires technical expertise. The primary contributions of this study are the establishment of a large reference collection of annotated machine elements, the definition of a hierarchical taxonomy for machine elements, and a comparison of the performances of deep learning classifiers for shape analysis applied to machine elements.

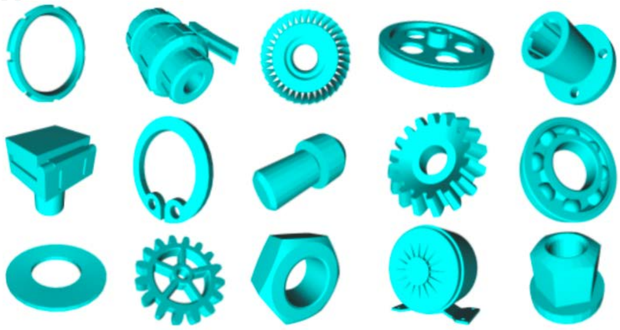

Figure 3: 3D machine elements objects for deep learning classifiers [13]

Generally, in the process of the machine design, cost analysis is one of the most important economic criteria for design adoption. Because of that, it is very important for engineers to track the cost from conceptual, to the final stage of machine design. In the paper [7], are given solution for the use of the AI in the process of the real time cost calculation through the whole design process.

The basic tool here is a dedicated expert system. A very significant stage of database design is determining the way of knowledge representation. On the basis of the conducted analysis, knowledge representation was accepted in form of frames and rules. Paper present methodology that delivers the particulars about real costs of products, realized processes and connected activities which constitute the basis for decision-making in the production process management.

In the presented methodology, production cost of a product covers the ensemble of activity cost, as a consequence of which a finished product of a given value is created from raw material or materials. The complexity of manufacturing is determined by the level of difficulty and constructional and manufacture connections taking place between different levels of a product (sets, subsets, elements).

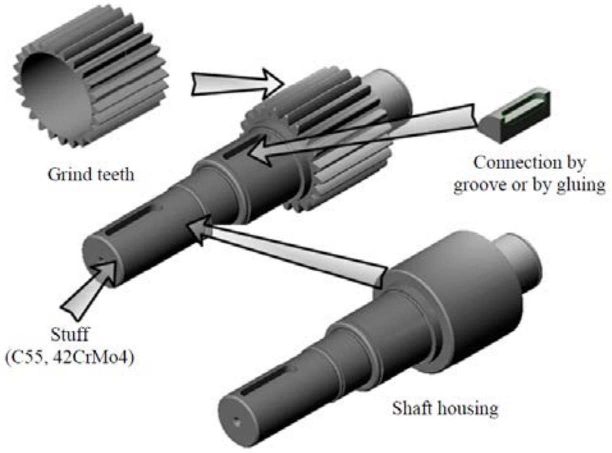

Figure 4: The main features of a sample designed element, for the cost calculation [7]

Generative design or multi objective optimisation, with rapid prototyping, represent the state of the art in the mechanical engineering, which may have a full potential of the using AI technology. Generative design leverages AI to turn engineering design processes into a sophisticated and natural interaction between computer and engineer [14]. The main part of the topology optimization and simulation is automatically conducted by the computing unit. Next-generation algorithms can be trained to not only optimize a design for specific engineering parameters, such as weight or durability, but also for commercial parameters, like production costs or even aesthetic requirements.

Generative design works best in conjunction with other technologies, like rapid prototyping. The 3D printing makes it possible to quickly prototype and test new designs without committing to a costly and time-consuming custom manufacturing run. On the other hand, 3D printing can produce extremely complex structures that traditional methods, such as milling and boring, are unable to manufacture.

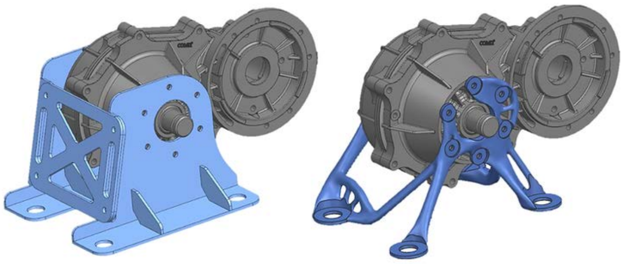

Figure 5: Generative design approach in design of the gearbox carrier [15]

5. CONCLUSION

Works aiming to develop basics of automation of processes in designing machine elements and assemblies with the use of AI in uncertainty and unrepeatability of processes have been started [6]. In machine element design process, based on the AI, where we can use a natural-language description of structural features and an intelligent interface of natural speech and hand-drawn sketches, application of design antipatterns, state of the art simulation, generative design etc., can have a great influence to the effectiveness and development of whole machine design process.

The design and optimization process of machine elements and parts, such as shafts, gears, bearings etc., may be automated using AI. On the other hand, the performance of machines may also be simulated and analyzed using AI in order to forecast behavior, spot future issues, and suggest changes.The majority of mechanical engineers at this moment can employ AI as a component of a CAD/CAM tool and FEA softwares, or to as assist data analysis and decision-making.

A workflow for combining AI and machine elements design, can be organised by three key following components:

1. Wellorganized dataset collected from the differnt sources (literature, existing databases, previous experiments and simulations, etc.)
2. AI model development, that is capable to learn and parse the representation for certain tasks
3. Well-defined research design problem that has not been addressed by conventional methods, or has been solved but can be outperformed by AI-based approaches.

Implementation of AI in the process of the design of machine elements aims at increasing efficiency and comfort of designers and speeding up creation of designs. The main benefits of AI used in the field of machine elements design will be:

- Reducing the human error rate
- Continuous operation 24/7 working hours
- Automation of repetitive tasks
- Digital use and assistants
- Faster decision-making
- Easy integration with current CAD/CAE tools
- Optimal final design (technical and economic criterias)

The evolution of engineering through history, shows that the "machine's desire" for autonomy, compensated by the machine's symbiosis with the human [16]. Therefore, AI machines will not replace people, and in the future that relationship will go towards a closer connection and the establishment of a new human-AI relationship. Such developments will certainly lead to the full application of AI in the process of machine design, which will achieve a complete symbiosis of human and AI. Advances in AI offer the perfect opportunity to integrate this technology into the an engineering design team, as a full member.

ACKNOWLEDGEMENTS

This study was supported by the Ministry of Education, Science and Technological Development of the Republic of Serbia, Grant No. 451-03-68/2022-14/200132 with University of Kragujevac - Faculty of Technical Sciences Čačak.

REFERENCES

[1] F. Artkin, "Applications of Artificial Intelligence in Mechanical Engineering", European Journal of Science and Technology, Special Issue 45, pp. 159-163, (2022)

[2] Q. Huang, "Application of Artificial Intelligence in Mechanical Engineering", Advances in Computer Science Research, Vol. 74, pp.855-860, (2017)

[3] J. A. Collins, H. R. Busby, G. H. Staab, "Mechanical Design of Machine elements and machines - A Failure Prevention Perspective", John Wiley & Sons, ISBN-13 978-0-470-41303-6, (2010)

[4] H. Mishra, V. Verma, M. A. Murtaza, "Artificial Intelligence and Applications in Mechanical Engineering", International Journal of Innovative Research in Science, Engineering and Technology (IJIRSET), Volume 9, Issue 6, pp.4237-4243, (2020)

[5] https://www.neuralconcept.com/post/how-is-ai-used-in-mechanical-engineering

[6] W. Kacalak, M. Majewski, K. D. Stuart, Z. Budniak, "Interactive systems for designing machine elements and assemblies", Management and Production Engineering Review, Vol. 6, No.3, pp. 21–34, (2015)

[7] D. Więcek, "Implementation of artificial intelligence in estimating prime costs of producing machine elements", Advances in manufacturing science and technology, Vol. 37, No. 1, (2013)

[8] https://www.simplilearn.com/tutorials/artificial-intelligence-tutorial/ai-vs-machine-learning-vs-deep-learning

[9] https://www.turing.com/kb/ultimate-battle-between-deep-learning-and-machine-learning

[10] T. H. Davenport,"The AI advantage - How to Put the Artificial Intelligence Revolution to Work", The MIT Press Cambridge, Massachusetts, (2018)

[11] J. Jenis, J. Ondriga, S. Hrcek, F. Brumercik, M. Cuchor, E. Sadovsky, "Engineering Applications of Artificial Intelligence in Mechanical Design and Optimization", Machines 2023, 11, 577, https://doi.org/10.3390/machines11060577, (2023)

[12] https://www.digitalengineering247.com/article/artificial-intelligence-beyond-the-hype/generative-design

[13] K. Sangpil, C. Hyung-gun,H. Xiao, H. Qixing, R.Karthik, “Large-scale Annotated Mechanical Components Benchmark for Classi_cation and Retrieval Tasks with Deep Neural Networks”, Purdue University, West Lafayette, USA, pp.1-17, (2019)

[14] F.Wunner, T. Krüger, B. Gierse, “How AI-driven generative design disrupts traditional value chains”, Industry X magazine (on-line), www.accenture.com, May 28, (2020)

[15] https://www.caexperts.com.br/

[16] G. Chapouthier, F. Kaplan, “L'Homme, L'Animal et la Machine”, CNRS Editions, ISBN 978-86-1002976-5, Paris, (2011)

[17] K. Guo, Z. Yang, C-H. Yu, M, J. Buehler, “Artificial intelligence and machine learning in design of mechanical materials”, The Royal Society of Chemistry, Mater. Horiz., 2021, 8, pp.1153–1172, (2021)

A Study of Emerging Technologies Scheduling at Container Terminals using Conceptual Mapping

Branislav Dragović[1*], Nenad Zrnić[2], Andro Dragović[2]
[1]Maritime Faculty of the University of Montenegro, Kotor (Montenegro)
[2]University of Belgrade, Faculty of Mechanical Engineering, Belgrade (Serbia)

The main long-term objectives in container terminal (CT) development are Automation, Electrification and Digitalization (AED). The paper studied the integrated scheduling trends of the CTs emerging technologies. The recent achievements of these trends are reviewed and relevant research topics in the CTs. Thus, a study how these trends would facilitate the CTs to achieve their strategic objectives is conducted. Multiple Correspondence Analysis-based Conceptual Mapping of the CTs towards AED is employed. The paper aims to fill the gap in the literature resulting from the need to enumerate and evaluate these relevant elements that must be taken into account on AED change at the CTs. The results indicate that despite the common interest in long-term plans, there are still gaps between theory approach and real practice at the CTs. Some research directions are highlighted for AED objectives in the coming years.

Keywords: Emerging Technologies Scheduling, CT, Conceptual Mapping, Multiple Correspondence Analysis

1. INTRODUCTION

Container terminals (CTs) go to many transition challenges due to emerging trends such as automation, digitalization and electrification (AED). Really, these innovations in CTs are very complex and complicated for many reasons. That way, they were not recognized as common technologies which applied predominantly. It still says in the literature how many CTs are automated (ACTs) and semi-automated (SACTs) in ports over the world. It implies which CT activities were automated or which additional activities could be automated. Therefore, a simple question arises: Is there a fully automated CT (FACT) in any port? Although CT operators would like to realize some automation projects inside CT main links, FACT does not yet exist. Many reports and studies indicate there are more than 50 ACTs and SACTs which are automated to a certain degree related to CTs main links (see e.g. [1], [2] and [3]). To conclude, the limited scope of automation is used inside CTs ([1] and [4]). As operation technologies at the CTs are changing through standard ones, ACTs, ACTs up to FACTs, the present paper conducted an integrative analysis of a framework that incorporates automation, electrification and digitalization of CTs to support automated systems for CT handling operations. In contrast to common studies, the present paper underlines the CT itself is generally a cooperative system and coordination among AED subsystems is much needed to understand the integrated scheduling trends of the CTs emerging technologies.

In order to map the structure of AED subsystems related to emerging technologies scheduling at the CTs, the present paper recorded all the collected papers through keywords. In that way, according to [5]-[7], concept mapping (CM) is a structured process, focused on a topic or construct of interest, involving input from multiple subjects, that produces an interpretable pictorial view of their ideas and concepts and how these are interrelated. Then, the multiple correspondence analysis (MCA) to examine the relationship between keywords papers, i.e. the conceptual structure of the AED is conducted, [8] and [9].

The following section details the CT operations and handling equipment. This is followed by methodology used to obtain the bibliometric data. Next section provides results and analyses. The last session outlines concluding remarks.

2. CONTAINER TERMINAL OPERATINS AND HANDLING EQUIPMENT

A CT represents a complex system consisting of principally the same subsystems as shown in Fig. 1 ([10] and [11]). The CT process can be divided into the following principal links with the specification of CT operations, summarized in Fig. 1: ship-berth link (seaside link) with the loading/unloading stage of ships, an internal transport link for moving containers from apron area to storage area and vice versa, container storage inside container yard (CY) and receiving/ delivery operations from/to external vehicles (EVs) (landside link). The CT operations modeling by operation research (OR) techniques are developed at these links either separately or complementary to each other. The most explored area of modeled operations refers to the ship-berth link [10].

The handling processes at a CT includes: ship operations, receiving/delivery operations from/to EVs and container handling and storage operations on the CY. Loaded and unloaded containers are temporarily stored awaiting a new journey. Inbound containers arrive by ship and quay cranes (QC) transfer containers to a yard truck or automated guided vehicle (AGV) [or buffer space for straddle carriers (SC), shuttle carriers and automated lifting vehicles (ALV)]. The transfer equipment then delivers the inbound container to a yard crane (YC) which picks it off the yard truck or AGV (or from CY buffer space) and stacks it into the respective storage location, which moves back to the quay crane to receive the next unloaded container. The storage location is given by row, bay and tier within the block and is assigned in real time upon arrival of the container in the terminal. Inbound as well as outbound containers are stocked in a CY which is divided into a number of blocks. Each block consists of the container stacks which are reserved for reefer

*Corresponding author: Dobrota/P I BB, 36, 85330 KOTOR, Montenegro, branod1809@gmail.com

containers or to store hazardous goods among others. For the loading operation, the process is reversed. This is an indirect transfer system in which container handling equipment delivers a container between the apron area and the CY. Rubber-tired or rail-mounted gantry cranes store the containers at yard stacks in CY. In direct transfer system (DTS), no YCs are needed because SC is used to pick up (put down) containers from (into) the CY, deliver it to (from) the apron, and transfer it to (from) a quay crane. European CTs are based upon the DTS in which transport of containers from ship to stack and vice versa and stacking (retrieval) of containers into (from) the slots assigned in the CY are performed by SCs. It is pure SC systems or SC terminals. Direct transfer system requires the larger area due to dedicated lanes required for SCs to access slot position, while the indirect transfer system minimizes yard area requirements [10].

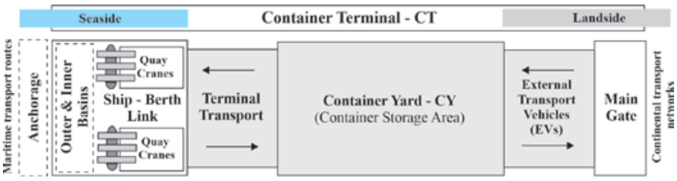

Figure 1. CT system with main subsystems ([10] and [11])

CTs are greatly differing by the type of transfer and handling equipment used. Improving CTs operations and attaining handling processes excellence to gain competitive advantage has attracted a lot of attention in the last few years. Although there are no automated container QCs, a few CTs have remote crane operators (from a separate operations centre) [1]. Many CT operations and many of the technological advances in port like Decision Support Systems, AGVs, ALVs, Automated Stacking Cranes, Global Positioning Systems (GPS), differential GPS, Radio Frequency Identification, Real-time Location System, Information Technologies, QC double cycling, indented container berth, dual-hoist tandem QC, dual-hoist triple tandem QC and automated CT admit modelling via OR techniques [10]. Then, according to [4] Internet of Things (IoT) and sensing solutions, cybersecurity, horizontal and vertical system integration, cloud computing, 3D printing and additive manufacturing, big data and business analytics, autonomous robots, augmented reality and simulation and modeling are the main features of Industry 4.0 or smart port or smart CT concept. In this paper, the literature available on the application of AED at the CTs is assessed, in order to identify integrated scheduling trends of the CTs emerging technologies.

3. METHODOLOGY

The Scopus database has been searched to identify only one part of research papers regarding AED, as well as smart CT concept. The following search terms were used: “CT and automation”, “Port AND Electrification”, “CT and digitalisation”, “CT and smart port”, respectively (as well as some the truncated combinations of a few groups of search strings). Some very rigorous exclusion criteria were used during the filtering process. According to this, the dataset is therefore composed of 76 research papers as follows (24 [12]-[35], 25 [36]-[60], 11 [61]-[71] and 16 [72]-[87] papers related to AED, as well as smart CT concept, respectively). Various bibliometric methods have been applied for the analysis of collected papers [12]-[87].

By following a bibliometric approach, the keywords analysis is conducted. The keywords were extracted using the Bibliometrix R package ([8] and [9]) and then they have been refined to ensure consistency. Further, the MCA (an exploratory data analysis without any restrictive assumption, [8] and [9]) is conducted to investigate the relationship between keywords papers, i.e. the conceptual structure of the AED including smart CT concept [9]. Bibliometrix tool [8] was used to perform MCA-based CM. Also, some keywords were reformulated to provide greater clarity of the final map.

4. RESULTS AND ANALYSES

The results provide information on the relationship between the keywords AED and smart CT concept. As known very-well in the research papers are very often insert multiple keywords. In that way, it is possible to determine the investigation trend, features and drawbacks in the discussion of emerging technologies introduced at the CTs. It simply identifies this emerging research area. Therefore, the combination of main keywords, representing AED and smart CT concept is shown in Fig. 2 (prepared by authors using Biblioshiny).

Figure 2. Word TreeMap

A word cloud of keywords included in AED and smart CT concept research papers is given in Fig. 3 (prepared by authors using Biblioshiny) where are shown the general trends such as AGVs, scheduling, cold ironing, smart grid, port electrification, digital transformation, cloud computing, smart port emission among others. On the other side, apart from these general terms, some of the highlighted keywords are ACT, IoT, intelligent system, blockchain, information technology, digital twin and so on. AGV, cloud computing, smart grid and power management via the cloud depict high potential in AED and smart CT and would mark an increment in the amount of these emerging technologies in the near future.

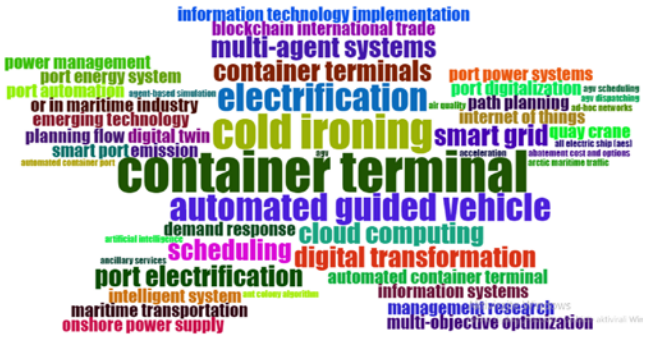

Figure 3. Word cloud of AED and smart CT concept keywords

The countries whose researchers and universities adopt AED and smart CT concept are shown in Fig. 4 (e.g. China is the most focused on the investigated subject, followed by South Korea, France and the Netherlands among others). Some countries have more interest to adopt automation and digitalisation, while some others have more concern to specific parts of emerging technologies.

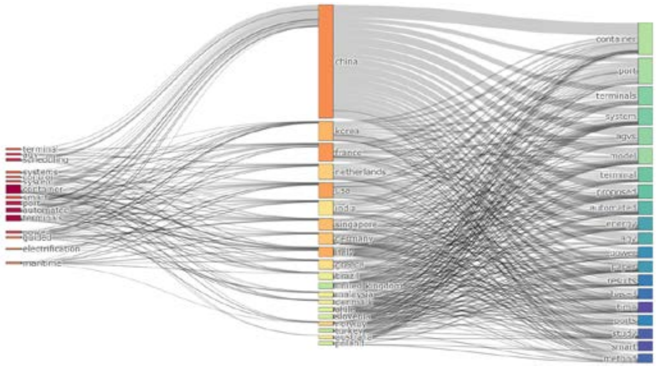

Figure 4. Multi-fields plot between countries (in the middle), title's keywords (left side) and abstract's keywords (right side) - (prepared by authors using Biblioshiny)

The results of the conceptual thematic map (CTM) analysis are given in Fig. 5 via the motor themes, the basic themes, the emerging or declining themes, and the niche themes by Callon centrality and density, [8] and [9]. Motor themes are highly relevant and well developed in AED and smart CT concept with high levels of centrality and density. There are two motor themes. In the first cluster flows keywords such as cloud computing, digital transformation and smart grid, while the second cluster is represented by CT, port electrification and digital twin.

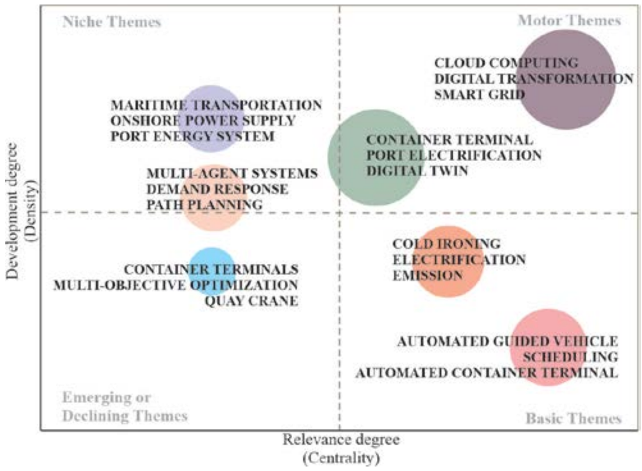

Figure 5. CTM of *of AED and smart CT concept using authors' keywords (prepared by authors using Biblioshiny)*

The niche themes belong to the second quadrant. They are highly developed but not very relevant for research. In Fig. 5 there are two niche themes where the first one faces the energy system and second ones to multi-agent systems among others. The emerging or declining themes are represented in the third quadrant where clusters are based on less important and poorly developed themes. Apart from CTs appears multi-objective optimization which is still emerging and continuously improved by new solving techniques (e.g. meta-heuristics and hybrid-heuristics). The fourth quadrant represents basic themes which are low developed but very relevant themes for the research subject. Low levels of density and high levels of centrality are characteristics for these clusters. ACT, AGV and scheduling very well express the first cluster, while the second one concerns cold ironing (shore power) and electrification which directly implies significant reduction of ship emissions on the berth inside CTs.

The CTM analysis of AED and smart CT concept is useful to highlight which the themes are contributing mostly in research area development. The relationship between them is also important to understand development of emerging technologies trends and level of their application at the CTs.

To construct a conceptual structure map (CSM), MCA on the keywords plus is conducted which identifies relationships between variables in AED and smart CT concept. CSM is presented in Fig. 6. Two clusters are distinct compositions which have been interpreted by red and blue colours.

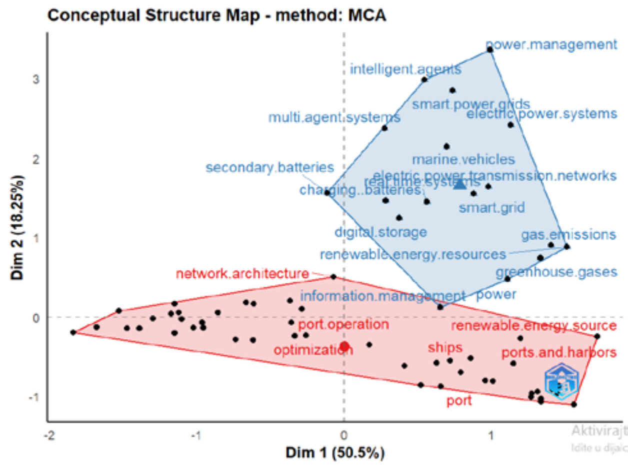

Figure 6. Conceptual structure map (prepared by authors using Biblioshiny)

Words and phrases such as renewable energy source, emission, emission control, cold ironing, environmental impact, electrification, sustainable development, numerical model, electrification, automated stacking crane, discrete event simulation, AGVs, vehicles, mobile robots, automation, ACTs, network architecture, scheduling, integer programming, decision making, optimization, operations among all others, represent the red cluster. It seems a good relationship between automation and digitalisation is reached by this cluster which represents the real situation at the CTs. Some elements of smart concept are also included

The blue cluster consists of the following words and phrases: power management, smart power grids, intelligent agents, electric power system, multi agent system, marine vehicles, power transmission network, smart grid, secondary batteries, digital storage, information management, power, greenhouse gases, gas emission and renewable energy resources. This cluster is focused on electrification which is also connected with smart approaches related to energy management.

The AED and smart CT concept field remains integrative and instead of separate investigation could benefit from a series of greater multi-objective research with emerging approaches in port systems such as real practice at the CTs over the world. This emphasises that future research could look into the impact of close relationships between them.

5. CONCLUSIONS

With continuous application of AED technologies which rapidly changed inside CTs, the ports'/CTs' throughput of containers were growing in the past decades. This dynamic regulation was substantially improved related to the AED and smart CT concept.

In order to realize a unique approach, i.e. MCA-based Conceptual Mapping of the CTs towards AED is presented in this paper. This approach includes the relationship between AED subsystems and smart CTs concept (simultaneously has explored the fronts of research/studies and each subsystem separately). The trend faces homogeneous key information that can be easily drawn from obtained results. It implies a leading role in CTs developing with application AED and smart techniques.

The employed methodology makes the results reproducible and verifiable. Mutual analysis of the AED subsystems enables one to understand their role within the whole CTs system based on their role which indicates further research directions. Of course, there have been limited investigations into this relationship up to now, but using keywords to analyse the CTs allow new scientific insights.

As the present paper shows, the optimization of application of AED involves many interrelated and interactive aspects between each subsystem. Therefore, future research directions may be based on some additional studies. All together should highlight and reveal frameworks on how to reach more central and important investigation, as well as to point out emerging themes and their application via AED on the CTs.

In the same manner, the inquiries on how to achieve mutual representation by CTM and MCA-based Conceptual Mapping of AED inside the CTs by scientific approach, really should arise in the investigation concept. Which systems or subsystems are also closely incorporated and analyzed via CTM in the CT system by integration with each other, may be an additional research question for further research directions.

ACKNOWLEDGEMENT

This paper is the result of research supported by the Ministry of Science of the Republic of Serbia by contract 451-03-47/2023-1/200105, 03.02.2023.

REFERENCES

[1] ITF '21, “Container port automation: Impacts and implications,” International Transport Forum (ITF) Policy Papers, No. 96, OECD Publishing, Paris, (2021)

[2] T. Notteboom, A. Pallis and J-P. Rodrigue, “Port economics, management and policy,” New York: Routledge, 690 pages, (2022)

[3] K.X. Li, M. Li, Y. Zhu, K.F. Yuen, H. Tong, H. Zhou, “Smart port: A bibliometric review and future research directions,” Transportation Research Part E, Vol. 174, 103098, pp. 1–15, (2023)

[4] I. de la Pena Zarzuelo, M.J. Freire Soeane, B. Lopez Bermudez, “Industry 4.0 in the port and maritime industry: A literature review,” Journal of Industrial Information Integration, Vol. 20, 100173, pp. 1–18, (2020)

[5] W.M. Trochim, “Introduction to concept mapping for planning and evaluation,” Evaluation and Program Planning, Vol. 12, pp. 1–16, (1989)

[6] W.M. Trochim, “Introduction to a special issue on concept mapping,” Evaluation and Program Planning, Vol. 60, pp. 166–175, (2017)

[7] W.M. Trochim, “Hindsight is 20/20: Reflections on the evolution of concept mapping,” Evaluation and Program Planning, Vol. 60, pp. 176–185, (2017)

[8] M. Aria and C. Cuccurullo, “bibliometrix: An R-tool for comprehensive science mapping analysis,” Journal of Informetrics, Vol. 11(4), pp. 959–975, (2017)

[9] C. Cuccurullo, M. Aria, F. Sarto, “Foundations and trends in performance management: A twenty-five years bibliometric analysis in business and public administration domains,” Scientometrics, Vol. 108, pp. 595–611, (2016)

[10] B. Dragovic, E. Tzannatos and N.K. Park, “Simulation modelling in ports and container terminals: literature overview and analysis by research field, application area and tool,” Flexible Service and Manufacturing Journal, Vol. 29, pp. 4–34, (2017)

[11] B. Dragović, N. Zrnić, E. Tzannatos, N. Kosanić and A. Dragović, “A bibliometric analysis and assessment of container terminal operations research,” Maritime Business Review, Vol. ahead-of-print, No. ahead-of-print, pp. 1–25, (2023) https://doi.org/10.1108/MABR-07-2022-0035

[12] N. Pourmohammad-Zia, F. Schulte, R.G. González-Ramírez, Voß S., R.R. Negenborn, “A robust optimization approach for platooning of automated ground vehicles in port hinterland corridors,” Computers and Industrial Engineering, Vol. 177, pp. 1–16, (2023)

[13] Z. Zhong, Y. Guo, J. Zhang, S. Yang, “Energy-aware integrated scheduling for container terminals with conflict-free AGVs,” Journal of Systems Science and Systems Engineering, (2023) https://doi.org/10.1007/s11518-023-5563-y

[14] Z. Xing, H. Liu, T. Wang, E.P. Chew, L.H. Lee, K.C. Tan, “Integrated automated guided vehicle dispatching and equipment scheduling with speed optimization,” Transportation Research Part E: Logistics and Transportation Review, Vol. 169, pp. 1-18, (2023)

[15] H. Zhang, L. Qi, W. Luan, H. Ma, “Double-Cycling AGV scheduling considering uncertain crane operational time at container terminals,” Applied Sciences (Switzerland), Vol. 12, pp. 1–18, (2022)

[16] S.H. Park, J. Hwang, S. Yun, S. Kim, “Automatic Guided Vehicles introduction impacts to Roll-On/Roll-Off Terminals: simulation and cost model analysis,” Journal of Advanced Transportation, 6062840, pp. 1–14, (2022)

[17] R. Liu, “Improved ant colony algorithm-based automated guided vehicle path planning research for sensor-aware obstacle avoidance,” Sensors and Materials, Vol. 33, pp. 2679–2691, (2021)

[18] Q. Zhang, W. Hu, J. Duan, J. Qin, “Cooperative scheduling of AGV and ASC in Automation Container Terminal relay operation mode,” Mathematical Problems in Engineering, 5764012, pp. 1–18, (2021)

[19] P. Zhou, L. Lin, K.H. Kim, “Anisotropic Q-learning and waiting estimation based real-time routing for automated guided vehicles at container terminals,” Journal of Heuristics, (2021) DOI: 10.1007/s10732-020-09463-9

[20] N. Ma, C. Zhou, A. Stephen, “Simulation model and performance evaluation of battery-powered AGV systems in automated container terminals,” Simulation Modelling Practice and Theory, Vol. 106, pp. 1–21, (2021)

[21] G.L. Kumawat, D. Roy, “AGV or Lift-AGV? Performance trade-offs and design insights for container terminals with robotized transport vehicle technology,” IISE Transactions, Vol. 53, pp. 751–769. (2021)

[22] K. Guo, J. Zhu, L. Shen, “An improved acceleration method based on multi-agent system for AGVs conflict-free path planning in automated terminals,” IEEE Access, Vol. 9, pp. 3326–3338, (2020)

[23] Y. Xu, L. Qi, W. Luan, X. Guo, H. Ma, “Load-In-Load-Out AGV route planning in automatic container terminal,” IEEE Access, Vol. 8, pp. 157081–157088, (2020)

[24] X. Ma, Y. Bian, F. Gao, “An improved shuffled frog leaping algorithm for multiload AGV dispatching in automated container terminals,” Mathematical Problems in Engineering, 1260196, pp. 1-12, (2020)

[25] H. Lu, S. Wang, “A study on multi-ASC scheduling method of automated container terminals based on graph theory,” Computers and Industrial Engineering, Vol. 129, pp. 404–416, (2019)

[26] D. Liu, Y.-E. Ge, “Modeling assignment of quay cranes using queueing theory for minimizing CO_2 emission at a container terminal,” Transportation Research Part D: Transport and Environment, Vol. 61, pp. 140–151, (2018)

[27] J.-J. Li, B.-W. Xu, O. Postolache, Y.-S. Yang, H.-F. Wu, “Impact analysis of travel time uncertainty on AGV catch-up conflict and the associated dynamic adjustment,” Mathematical Problems in Engineering, 4037695, pp. 1–11, (2018)

[28] D. Pjevcevic, M. Nikolic, N. Vidic, K. Vukadinovic, “Data envelopment analysis of AGV fleet sizing at a port container terminal,” International Journal of Production Research, Vol. 55, pp. 4021–4034, (2017)

[29] S.-Y. Zhang, Y.-S. Yang, C.-J. Liang, B.-W. Xu, J.-J. Li, “Optimal control of multiple AGV path conflict in automated terminals,” Jiaotong Yunshu Xitong Gongcheng Yu Xinxi/Journal of Transportation Systems Engineering and Information Technology, Vol. 17, pp. 83–89. (2017)

[30] K.-G. Huo, Y.-Q. Zhang, Z.-H. Hu, “Research on scheduling problem of multi-load AGV at automated container terminal,” Dalian Ligong Daxue Xuebao/Journal of Dalian University of Technology, Vol. 56, pp. 244–251. (2016)

[31] Q. Li, A. Pogromsky, T. Adriaansen, J.T. Udding, “A control of collision and deadlock avoidance for automated guided vehicles with a fault-tolerance capability,” International Journal of Advanced Robotic Systems, Vol. 13, pp. 1-24, (2016)

[32] F. Corman, J. Xin, R.R. Negenborn, A. D'Ariano, M. Samà, A. Toli, G. Lodewijks, “Optimal scheduling and routing of free-range AGVs at large scale automated container terminals,” Periodica Polytechnica Transportation Engineering, Vol. 44, pp. 145–154, (2016)

[33] H. Fazlollahtabar, M. Saidi-Mehrabad, “Methodologies to optimize Automated Guided Vehicle scheduling and routing problems: A review study,” Journal of Intelligent and Robotic Systems: Theory and Applications, Vol. 77, pp. 525–545, (2015)

[34] S. Gelareh, R. Merzouki, K. McGinley, R. Murray, “Scheduling of intelligent and autonomous vehicles under pairing/unpairing collaboration strategy in container terminals,” Transportation Research Part C: Emerging Technologies, Vol. 33, pp. 1–21, (2013)

[35] H. Dkhil, A. Yassine, H. Chabchoub, “Optimization of container handling systems in automated maritime terminal,” Studies in Computational Intelligence, Vol. 457, pp. 301–312, (2013)

[36] Z. Chen, F. Fan, N. Tai, C. Li, Zhang X., “Multi-objective voltage/VAR control for integrated port energy system considering multi-network integration,” International Journal of Electrical Power and Energy Systems, Vol. 150, pp. 1–13, (2023)

[37] N.N. Abu Bakar, N. Bazmohammadi, J.C. Vasquez, J.M. Guerrero, “Electrification of onshore power systems in maritime transportation towards decarbonization of ports: A review of the cold ironing technology,” Renewable and Sustainable Energy Reviews, Vol. 178, pp. 1–16, (2023)

[38] H. Mahdi, B. Hoff, T. Ostrem, “A Review of power converters for ships electrification,” IEEE Transactions on Power Electronics, Vol. 38, pp. 4680–4697, (2023)

[39] D. Bosich, M. Chiandone, M.D. Feste, Sulligoi G., Cold “Ironing integration in city port distribution grids: Sustainable electrification of port infrastructures between technical and economic constraints,” IEEE Electrification Magazine, Vol. 11, pp. 4680–4697, (2023)

[40] J. Prousalidis, F. D'Agostino, “Looking toward the energy-sustainable smart port: A resilient energy hub in the electric grids [Viewpoint],” IEEE Electrification Magazine, Vol. 11, pp. 52–60, (2023)

[41] S. Chen, Q. Zeng, Y. Li, “Integrated operations planning in highly electrified container terminals considering time-of-use tariffs,” Transportation Research Part E: Logistics and Transportation Review, Vol. 171, pp. 90–92, (2023)

[42] P. Kovalishin, N. Nikitakos, B. Svilicic, J. Zhang, A. Nikishin, D. Dalaklis, M. Kharitonov, A.-A. Stefanakou, “Using Artificial Intelligence (AI) methods for effectively responding to climate change at marine ports,” Journal of International Maritime Safety, Environmental Affairs, and Shipping, Vol. 7, pp. 1–12, (2023)

[43] N.N.A. Bakar, N. Bazmohammadi, H. Çimen, T. Uyanik, J.C. Vasquez, J.M. Guerrero, “Data-driven ship berthing forecasting for cold ironing in maritime transportation,” Applied Energy, Vol. 326, pp. 1–12, (2022)

[44] C. Zhou, S. Zhu, M.G.H. Bell, L.H. Lee, E.P. Chew, “Emerging technology and management research in the container terminals: Trends and the COVID-19 pandemic impacts,” Ocean and Coastal Management, Vol. 230, pp. 1–14, (2022)

[45] T.Z. Oo, Y. Ren, A.W.-K. Kong, Y. Wang, X. Liu, “Power System Design Optimization for a Ferry Using Hybrid-Shaft Generators,” IEEE Transactions on Power Systems, Vol. 37, pp. 2869–2880, (2022)

[46] Y. Zhang, C. Liang, J. Shi, G. Lim, Y. Wu, “Optimal port microgrid scheduling incorporating onshore power supply and berth allocation under uncertainty,” Applied Energy, Vol. 313, pp. 1–10, (2022)

[47] S. Zhu, M.M. Kinnon, J. Soukup, A. Paradise, D. Dabdub, S. Samuelsen, “Assessment of the greenhouse gas, Episodic air quality and public health benefits of fuel cell electrification of a major port complex,” Atmospheric Environment, Vol. 275, pp. 1–14, (2022)

[48] Mao, T. Yu, Z. Ding, S. Fang, J. Guo, Q. Sheng, “Optimal scheduling for seaport integrated energy system considering flexible berth allocation,” Applied Energy, Vol. 308, pp. 1–9, (2022)

[49] Y. Zhang, L. Sun, F. Ma, Y. Wu, W. Jiang, L. Fu, “Collaborative optimization of the battery capacity and sailing speed considering multiple operation factors for a battery-powered ship,” World Electric Vehicle Journal, Vol. 13, pp. 1–24, (2022)

[50] E. Kurtulu, “Optimizing inland container logistics and dry port location-allocation from an environmental perspective,” Research in Transportation Business and Management, 100839, pp. 1–16, (2022)

[51] M.U. Mutarraf, Y. Terriche, M. Nasir, Y. Guan, C.-L. Su, J.C. Vasquez, J.M. Guerrero, “A communication-less multimode control approach for adaptive power sharing in ship-based seaport microgrid,” IEEE Transactions on Transportation Electrification, Vol. 7, pp. 3070–3082, (2021)

[52] L. Wang, C. Liang, J. Shi, A. Molavi, G. Lim, Y. Zhang, “A bilevel hybrid economic approach for optimal deployment of onshore power supply in maritime ports,” Applied Energy, Vol. 292, pp. 1–10, (2021)

[53] K.T. Gillingham, P. Huang, “Long-run environmental and economic impacts of electrifying waterborne shipping in the United States,” Environmental Science and Technology, Vol. 54, pp. 9824–9833, (2020)

[54] C. Savard, A. Nikulina, C. Mécemmène, E. Mokhova, “The electrification of ships using the Northern Sea Route: An approach,” Journal of Open Innovation: Technology, Market, and Complexity, Vol. 6, pp. 1–16, (2020)

[55] F.D. Kanellos, E.-S.M. Volanis, N.D. Hatziargyriou, “Power management method for large ports with multi-agent systems,” IEEE Transactions on Smart Grid, Vol. 10, pp. 1252–1268, (2019)

[56] Y.C.E. Jonathan, S.B.A. Kader, “Prospect of emission reduction standard for sustainable port equipment electrification,” International Journal of Engineering, Transactions B: Applications, Vol. 31, pp. 1347–1355, (2018)

[57] F. Esposito, E. Mancinelli, M. Morichetti, G. Passerini, U. Rizza, “A cogeneration power plant to integrate cold ironing and district heating and cooling,” International Journal of Energy Production and Management, Vol. 3, pp. 214–225, (2018)

[58] R. Itiki, S.G. Di Santo, E.C.M. Costa, R.M. Monaro, “Methodology for mapping operational zones of VSC-HVDC transmission system on offshore ports,” International Journal of Electrical Power and Energy Systems, Vol. 93, pp. 266–275, (2017)

[59] F.D. Kanellos, “Real-Time control based on multi-agent systems for the operation of large ports as Prosumer Microgrids,” IEEE Access, Vol. 5, pp. 9439–9452, (2017)

[60] H. Lindstad, G.S. Eskeland, H. Psaraftis, I.Sandaas, A.H. Strømman, “Maritime shipping and emissions: A three-layered, damage-based approach,” Ocean Engineering, Vol. 110, pp. 94–101, (2015)

[61] P. Ricardianto, E. Christy, Y. Pahala, E. Abdurachman, A. Soekirman, O.R. Purba, S.T. Prasetiawan, E.S. Wiguna, A.B. Wibawanti, E. Endri, “Digitalization and logistics service quality: Evidence from Indonesia national shipping companies,” International Journal of Data and Network Science, Vol. 7, pp. 781–790, (2023)

[62] J. Seo, B.K. Lee, Y. Jeon, “Digitalization strategies and evaluation of maritime container supply chains,” Business Process Management Journal, Vol. 29, pp. 1–21, (2023)

[63] J. Li, C. Gu, Y. Xiang, F. Li, “Edge-cloud computing systems for smart grid: State-of-the-art, architecture, and applications,” Journal of Modern Power Systems and Clean Energy, Vol. 10, pp. 805–817, (2022)

[64] S. Nguyen, P. Shu-Ling Chen, Y. Du, “Risk assessment of maritime container shipping blockchain-integrated systems: An analysis of multi-event scenarios,” Transportation Research Part E: Logistics and Transportation Review, Vol. 163, pp. 1-23, (2022)

[65] M. Kassou, S. Bourekkadi, O. El Imrani, A. Boulaksili, S. Aharouay, A. Ourdi, H. Chikri, S. Khoulji, “Digital transformation in flow planning: The case of container terminals at a smart port,” Journal of Theoretical and Applied Information Technology, Vol. 99, pp. 1966–1976, (2021)

[66] K.C. Iyer, V.P.S.N. Nanyam, “Concentration analysis of container terminals in India,” Maritime Transport Research, Vol. 2, pp. 1–15, (2021)

[67] W. Guo, B. Atasoy, W.B. van Blokland, R.R. Negenborn, “A dynamic shipment matching problem in hinterland synchromodal transportation,” Decision Support Systems, Vol. 134, pp. 1–13, (2020)

[68] O. Baccelli, P. Morino, “The role of port authorities in the promotion of logistics integration between ports and the railway system: The Italian experience,” Research in Transportation Business and Management, Vol. 35, pp. 1–14, (2020)

[69] C. Senarak, “Shipping-collaboration model for the new generation of container port in innovation district: A case of Eastern Economic Corridor,” Asian Journal of Shipping and Logistics, Vol. 36, 65–77, (2020)

[70] L.Yu. Andreeva, A.V. Fedorov, E.S. Prokopenko, R.A. Sichev, “Financial engineering of infrastructure projects: The concessional mechanism,” International Journal of Economics and Business Administration, Vol. 7, pp. 61–73, (2019)

[71] L. Heilig, E. Lalla-Ruiz, S. Voß, “Multi-objective inter-terminal truck routing,” Transportation Research Part E: Logistics and Transportation Review, Vol. 106, pp. 178–202, (2017)

[72] Y. Feng, D.-P. Song, D. Li, “Smart stacking for import containers using customer information at automated container terminals,” European Journal of Operational Research, Vol. 301, pp. 502–522, (2022)

[73] Y. Zhang, C. Yang, K. Tang, J. Dai, “Study on distributed consistent cooperative control of multi-art in automated container terminals,” IEEE Access, Vol. 10, pp. 122965–122980, (2022)

[74] J.O. Eom, J.Y. Kim, S.H. Lee, J.H. Yoon, S.W. Kim, “Digital Twin development for berthing planning of ships,” Journal of Institute of Control, Robotics and Systems, Vol. 28, pp. 724–732, (2022)

[75] Y. Triska, E.M. Frazzon, V.M.D. Silva, L. Heilig, “Smart port terminals: conceptual framework, maturity modeling and research agenda,” Maritime Policy and Management, (2022) https://doi.org/10.1080/03088839.2022.2116752

[76] N.M. Ochara, F.N. Kutame, A. Kadyamatimba, “Adoption of cloud computing in business continuity management for container terminal operations in South Africa,” International Journal of Business Continuity and Risk Management, Vol. 12, pp. 91–115, (2022)

[77] A. Kaliszewski, A. Kozowski, J. Dobrowski, H. Klimek, “LinkedIn survey reveals competitiveness factors of container terminals: Forwarders’ view,” Transport Policy, Vol. 106, pp. 131–140, (2021)

[78] T.Y. Lin, G. Shi, C. Yang, Y. Zhang, J. Wang, Z. Jia, L. Guo, Y. Xiao, Z. Wei, S. Lan, “Efficient container virtualization-based digital twin simulation of smart industrial systems,” Journal of Cleaner Production, Vol. 281, pp. 1–19, (2021)

[79] S. Jakovlev, T. Eglynas, M. Voznak, “Application of neural network predictive control methods to solve the shipping container sway control problem in quay cranes,” IEEE Access, Vol. 9, pp. 78253–78265, (2021)

[80] M. Kolenc, N. Ihle, C. Gutschi, P. Nemek, T. Breitkreuz, K. Gödderz, N. Suljanovic, M. Zajc, Thanh Nguyen, “Virtual power plant architecture using OpenADR 2.0b for dynamic charging of automated guided vehicles,” International Journal of Electrical Power and Energy Systems, Vol.104, pp. 370–382, (2019)

[81] V.O. Gekara, V.-X. “New technologies and the transformation of work and skills: a study of computerisation and automation of Australian container terminals,” New Technology, Work and Employment, Vol. 33, pp. 219–233, (2018)

[82] L. Heilig, E. Lalla-Ruiz, S. Voß, “port-IO: an integrative mobile cloud platform for real-time inter-terminal truck routing optimization,” Flexible Services and Manufacturing Journal, Vol. 29, pp. 504–534, (2017)

[83] M.G.C.A. Cimino, F. Palumbo, G. Vaglini, E. Ferro, N. Celandroni, D. La Rosa, “Evaluating the impact of smart technologies on harbor’s logistics via BPMN modeling and simulation,” Information Technology and Management, Vol. 18, 223–239, (2017)

[84] S. Kang, S. Lee, Y.-Y. Choo, “Development of a remote operation system for a quay crane simulator,” Journal of Institute of Control, Robotics and Systems, Vol. 21, pp. 385–390, (2015)

[85] L. Kai-liang, Y. Wei, Y. Hao, B. Yan, L. Xiang-rui, “Structural and running safety assessment of the handling and distributing system in automated container terminal considering container vehicle-truss bridge coupled vibration,” International Journal of Security and its Applications, Vol. 7, pp. 417–432, (2013)

[86] R., Katulski, J. Sadowski, J. Stefaski, S. Ambroziak, B. Miszewska, “Self-organizing wireless monitoring system for cargo containers,” Polish Maritime Research, Vol. 16, pp. 45–50, (2009)

[87] Y.H.V. Lun, C.W.Y. Wong, K.-H. Lai, T.C.E. Cheng, “Institutional perspective on the adoption of technology for the security enhancement of container transport,” Transport Reviews, Vol. 8, pp. 21–33, (2008)

FEM Recommendation for Shuttle Racking Tolerances and Clearances

Rodoljub Vujanac[1*], Nenad Miloradovic[1], Snezana Vulovic[2]
[1]Faculty of Engineering / Mechanical Construction and Mechanization, University of Kragujevac, Kragujevac (Serbia)
[2]Institute of Information Technologies, University of Kragujevac, Kragujevac (Serbia)

Compared to conventional drive-in and drive-through accumulation racking systems, more efficient for the great amounts of the same storage units are shuttle racking systems. These systems operated by shuttles, conventional fork lift trucks, storage and retrieval machines or aisle carriers provide further increase in productivity, reduced damages, improved safety and ergonomics. This paper provides basic information on the requirements, design and use of shuttle pallet racking system in accordance with state-of-the-art regulations and standards with special emphasis on minimal required clearances and tolerances for safety operation.

Keywords: Pallet Racking, Shuttle, Tolerance, Clearance

1. INTRODUCTION

Selective adjustable pallet racking as the most represented racking system enable rational use, economical and clear storage of different, usually palletized, but also non-palletized unit loads as shown in figure 1. Direct access to each unit load is possible from the working or operational aisle, where the unit load is usually placed only on a pair of horizontal beams between the vertical frames of the rack. Therefore, the unit load is placed and taken from the same racking place. Various variants of selective racks with lot of different accessories and applicable material handling equipment are possible [1].

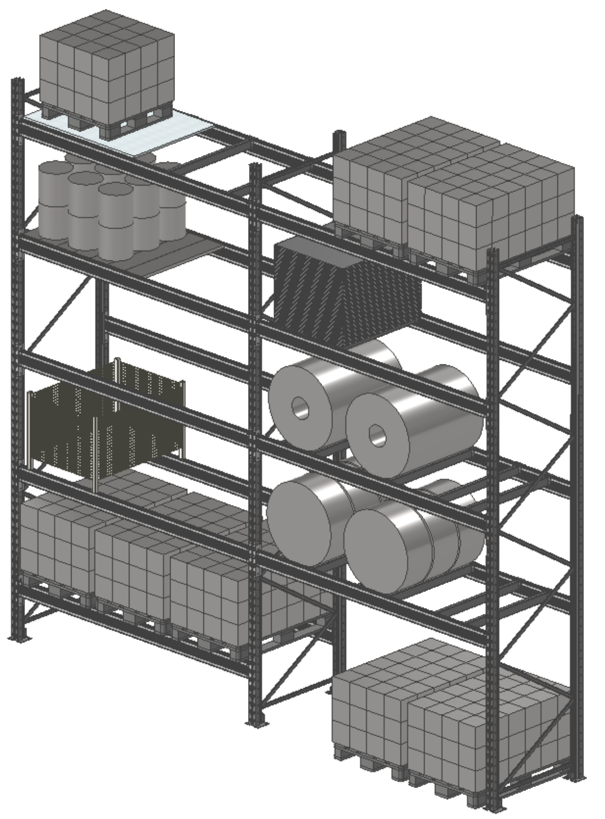

Figure 1: Selective adjustable pallet rack [1]

Various static and dynamic racking systems are widely used in practice for the storage of palletized goods in a small assortment but in a large quantity. The most widespread static system of rack tunnels connected in one block is drive-in or drive-through rack. Two ways of performing this rack system are possible, figure 2. The first one, known as the Drive-In Rack (DIR) type, functions according to the First-In Last-Out (FILO) principle, i.e. the input and output of the unit load is on the same side of the system, or the second type, Drive-Through Rack (DTR), where the forklift can freely pass through the tunnel when there is no pallet in it, which corresponds to the so-called FIFO principle (First-In First-Out, where the first pallet that enters the rack leaves rack as the first).

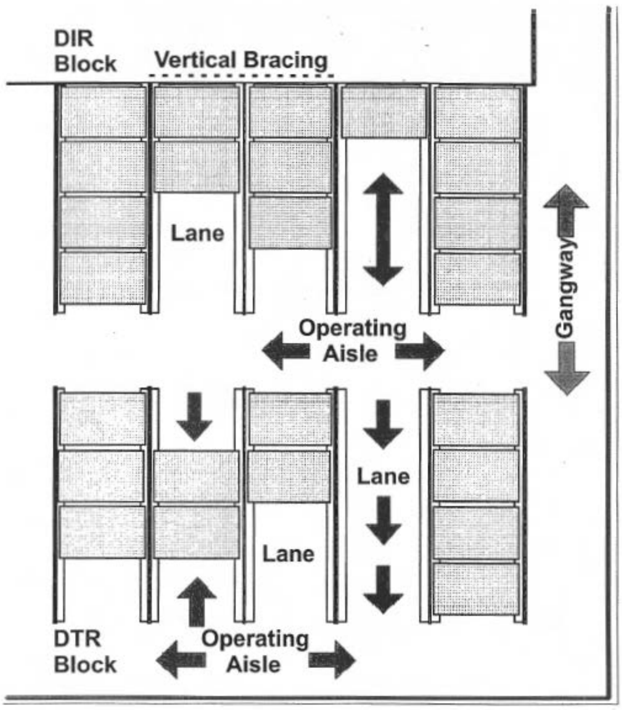

Figure 2: Layout of a Drive-In Rack and a Drive-Through Rack [2]

The principle of operation of the dynamic racking system of flow racks is that the unit load moves along the rack corridors (rack tunnels), i.e. changes its position in relation to the place of placement. The movement of the pallet can be achieved in two basic ways: by gravity force

*Corresponding author: Sestre Janjic 6, 34000 Kragujevac, vujanac@kg.ac.rs

(there is an incline of the "rack tunnel", and the movement of the pallet is carried out on roller tracks), or by excitation force ("tunnel" is not necessary to be inclined, and the force is achieved by pneumatic, hydraulic or electric drive) [3]. The tracking of goods (very important for perishable goods) is simple, because the goods that first enter a certain racking corridor are the first to go out according to the FIFO principle shown in figure 3, so that such systems have primarily found their purpose in the food, chemical and pharmaceutical industries.

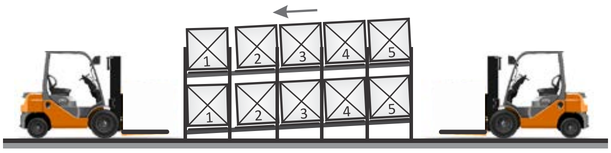

Figure 3: Dynamic FIFO pallet rack [1]

Based on the FILO working principle where the first pallet that enters is the last to leave the rack tunnel, figure 4, it is possible well-known push back execution of these dynamic racks, which is characterized by the storage of usually two, three or four, and at most eight pallets per depth of the racking tunnel. Helped by a forklift, pallets are loaded and taken from the same place, i.e. entrance/exit of the racking tunnel. Palletized goods are placed or picked up usually from a roller track, or rarely from a cart that are telescopically "stretched" along the track over each other. This type of rack with trolleys is often called a telescopic rack.

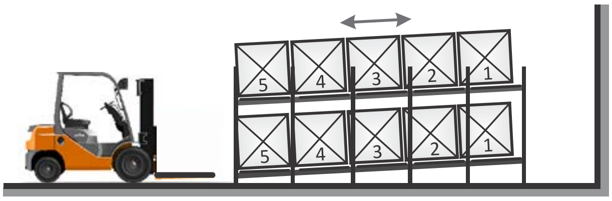

Figure 4: Dynamic FILO pallet rack [1]

The use of mobile racks as a special type of dynamic warehouses achieves optimal use of storage space, with maximum use of the storage area, figure 5. The racking structure is mounted on a mobile base - a cart, which moves along rails placed in the floor. With this type of pallet racking, there is only one operating isle for handling pallets. By automatically opening the aisle, the place intended for serving is available. Pallet racks are moved individually or in a block to allow access to each pallet. Movable racks are used in cases of need for large capacity, when the speed of flow of stored goods is not primary.

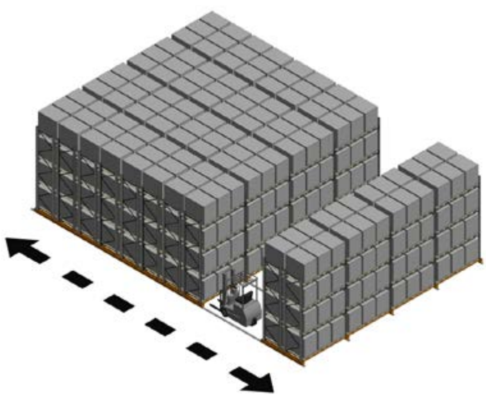

Figure 5: Mobile pallet racks [1]

The functionality of drive-in or drive-through racks can be improved by automating the material handling process, whereby appropriate material handling systems can achieve better results instead of traditional forklifts. Initially as a standard equipment a special self-propelled cart, named as pallet runner or satellite - "shuttle" [4] was introduced. Further improvement was with the also mobile carriers of those shuttles named "mother shuttle" [5], which together with elevators - "lifters" [6], leads to the complete automation of this system shown with basic elements in figure 6. In addition to faster handling, these systems enable a further increase in productivity, reduction of damage, improved safety and ergonomics, but on the other hand, they also require significant investments.

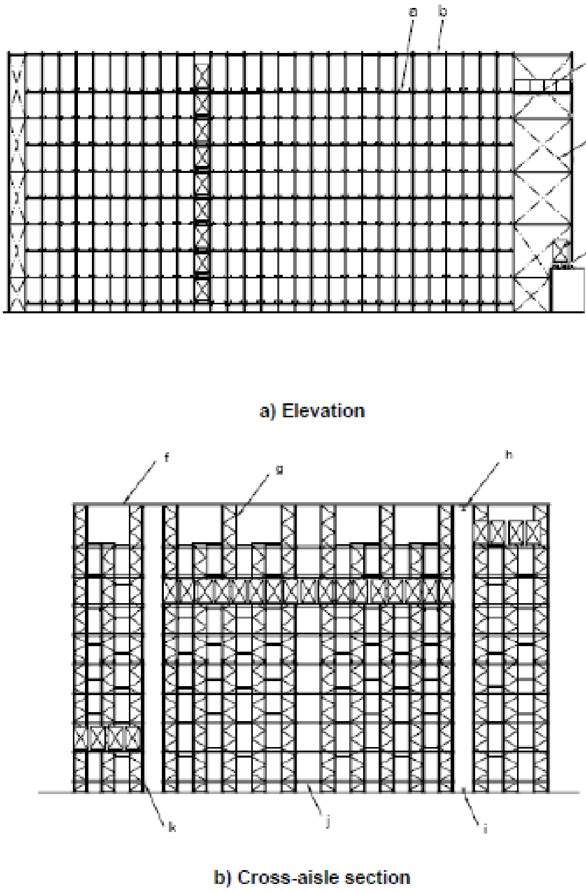

Figure 6: Shuttle racking system: a) beam, b) tie beam, c) spine bracing, d) conveyor, e) maintenace area, f) top plan bracing, g) frame, h) upper guied rail, i) bottom rail, j) shuttle rail, k) shuttle entry guide [7]

FEM 10.2.07 code [2] defines the supplementary design procedure for specific requirements of Drive-In Racks and Drive-Through Racks since they are pallet storage systems differing from adjustable pallet racking in terms of their structural elements, structural behaviour and method of operation. Additionally, a document FEM 10.2.19, "The Design of Shuttle Racking" [8], provides a methodology for the design of steel pallet racking storage systems for shuttle systems. FEM 10.2.19 is based on the safety and design concept of the European Standards series "Steel Static Storage Systems" and provides supplementary design rules to suit the peculiarities of racking systems. This document is not independent and is intended to be used in conjunction with FEM 10.2.03 [9] and FEM 10.2.04 [10].

2. MAIN FEATURES OF SHUTTLE RACKING

2.1. Shuttle racking configuration

Shuttle is machine shown in figure 7, feed by an innovative lithium battery easy to recharge, that loads, carries, conveys good on pallets in and out of deep storage drive-in tunnels, allowing in an economical way the maximum use of warehouse volume, the easy movement of the goods, the working quickness.

Figure 7: Shuttle [11]

Main dimensions of the deep shuttle racking tunnels created by the installation of double rails at various elevations in a high-density racking system, with parallel carrier rails for the shuttle located just underneath pallet storage rails are shown in figure 8 as following:

A - Space between uprights;
B - Free dimension between rails;
C - Minimum height of the first level;
D - Minimum clearance between pallets.

The shuttle is placed into the appropriate lane and the fork lift operator then loads a pallet onto the pallet rail above, and presses the button on the hand-held remote control, which sends a radio frequency signal to the shuttle. The shuttle lifts the pallet, and then carries it to the next available storage position. Then the shuttle returns to pick up the next pallet.

To pick pallets, the operator places the pallet runner into the lane and pushes the button on the remote control, sending the shuttle into the lane to pick up the next available pallet, and return it to the pick face. While the operator moves the pallet to the loading dock, the pallet runner retrieves the next pallet.

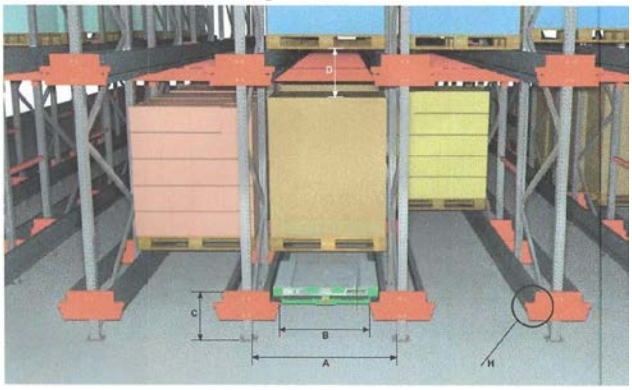

Figure 8: Dimensions in racking tunnel [11]

2.2. Types of Shuttle Racking

Shuttle racking system classification depending on used material handling equipment:

- Shuttle racking operated by industrial trucks.
- Shuttle racking operated by Storage/Retrieval Machines.
- Shuttle racking operated by aisle carrier.
- Shuttle racking operated by omnidirectional shuttle.

3. INSTALLATION TOLERANCES OF SHUTTLE RACKING

Tolerances are dimensional variations from the ideal arising from manufacture, assembly and erection of handling and storage equipment and other aspects of their environment that may affect the system such as building, and the unit load, and the concrete floor. The tolerances given in table 1 and table 2 are believed to represent a reasonable compromise between practicality of construction and wear and tear to the shuttle device; different tolerances may be specific cases [8].

Table 1: Shuttle systems – tolerances [8]

Shuttle operated system	Tolerance
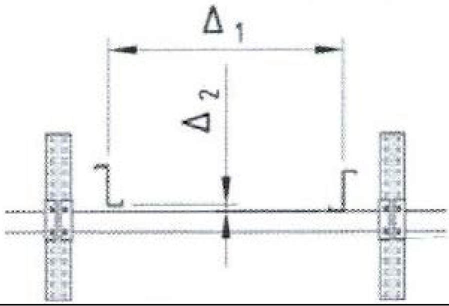	
Δ_1 tolerance between guide faces of the lane rail. Δ_2 tolerance on difference in lane rail height across the line.	Δ_1=±2,0 mm Δ_2=±2,0 mm
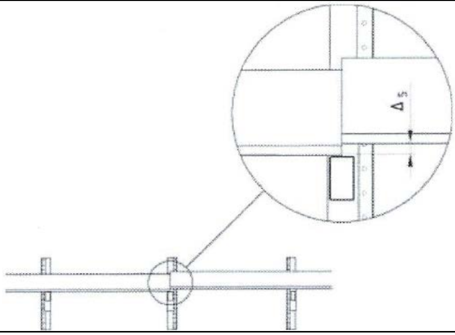	
Δ_5 vertical step in lane rail.	Δ_5=±1,0 mm
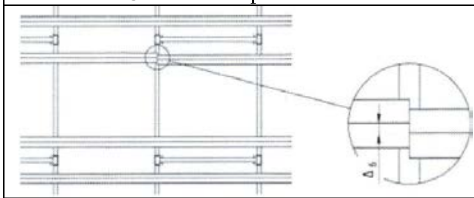	
Δ_6 horizontal step in lane rail.	Δ_6=±1,0 mm
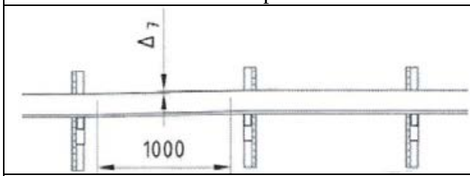	
Δ_7 tolerance on slope of lane rail	Δ_7=3,0 % Maximum 15 mm over the length of the rail

Table 2: Aisle carrier system – tolerances [8]

Aisle carrier operated system	Tolerance
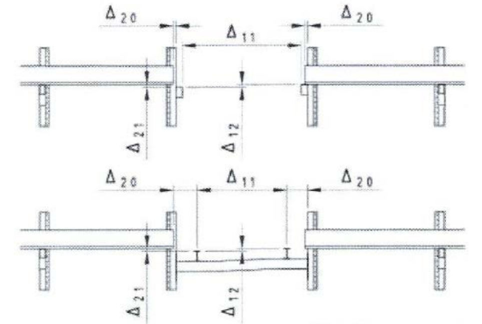	
Δ_{11} tolerance between running faces of the aisle rail. Δ_{12} tolerance on difference in aisle rail height across the aisle. Δ_{20} position tolerance for and of lane rail to aisle rail. Δ_{21} tolerance of lane rail to aisle rail running surface.	Δ_{11}=±3,0 mm Δ_{12}=±5,0 mm Δ_{20}=±5,0 mm Δ_{21}=+0 -4 mm
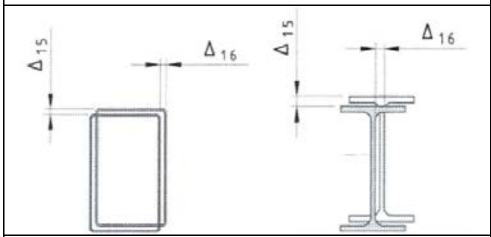	
Δ_{15} vertical step in aisle rail.[a] Δ_{16} horizontal step in aisle rail.[a]	Δ_{15}=±1,0 mm[a] Δ_{16}=±1,0 mm[a]
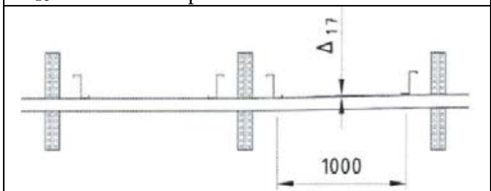	
Δ_{17} horizontal slope in aisle rail.	Δ_{17}=3,0 % Maximum 15 mm over the length of the rail
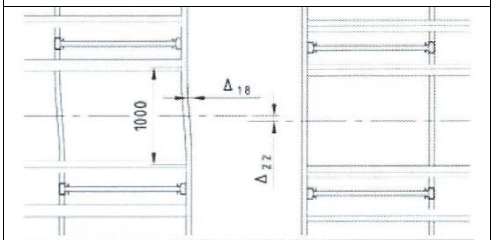	
Δ_{18} tolerance on the alignment of aisle rail. Δ_{22} tolerance on the alignment of lane centreline.	Δ_{18}= refer to FEM 9.831-1 Δ_{22}= refer to FEM 9.831-1

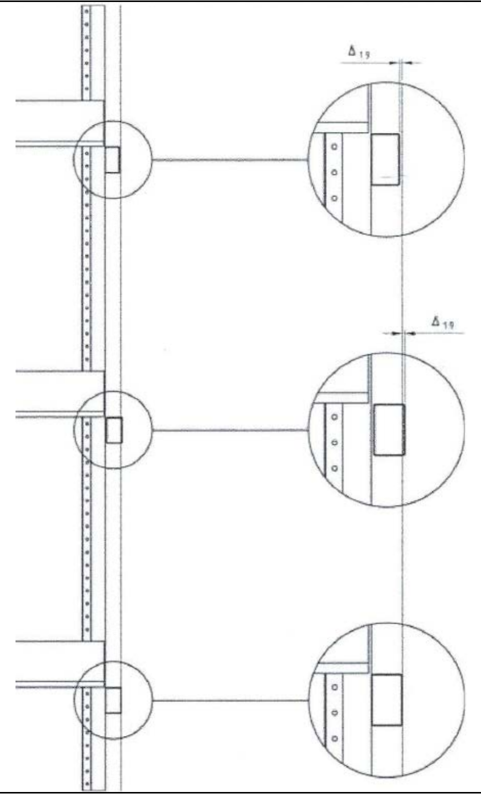	
Δ_{19} tolerance on vertical alignment of aisle rail.[b]	Δ_{19}=±2,0 mm[b]
[a] In the “as-rolled” condition some hot-rolled profiles may not be able to achieve the tolerance Δ_{15} and may need grinding - refer to FEM 9.831-clause 4.5 and 4.6	
[b] Δ_{19} is only relevant at the elevator position for aisle carriers that change level	

4. CLEARANCES AND DIMENSIONAL LIMITS OF SHUTTLE RACKING

Clearances are the required nominal dimensions between moving and fixed parts of the system that, allowing for the worst-case summation of all pertinent tolerances and deformations, prevent collisions.

4.1. Lane clearances

In addition to the provisions of FEM 10.3.01 [12], the following clearances shall be considered. Clearances shall be considered in relation to the overall dimensions of the unit load including any overhang. Unless specified otherwise, table 3 indicates the recommended values for:

x_1-horizontal clearance between lane rails that need to satisfy the clearances required by the shuttle, provide support for pallets on the lane rail and provide support for shuttles on the lane rail, figure 9;

x_2-horizontal clearance between the unit load and the upright, figure 9;

x_3-horizontal clearance between the load make up accessories and the upright, figure 9;

x_4-horizontal clearance between unit loads, figure 10;

x_5-horizontal clearance between load make up accessories, figure 10;

y_1-vertical clearance when the unit load is placed on the lane rail between the top of the unit load and the bottom part of the arm, the beam, the lane rail, the sprinkler systems or any other device whichever is the lowest, figure 9;

y_2-vertical clearance when the unit load is lifted on the shuttle between the top of the unit load and the bottom part of the arm, the beam or the lane rail whichever is the lowest, figures 9 and 10;

y_3-the lifting stroke of the shuttle inside the lane, figures 9 and 10;

d_1-vertical dimension between the running surface and the bottom bolt, figure 11;

d_2-vertical dimension between rails, figure 11;

d_3-free contact surface for guidance wheel, figure 11;

d_4-screw head protrusion, figure 11;

z_1-horizontal clearance between unit loads in cross - isle direction, figure 12;

z_2-horizontal clearance between load make up accessories figure 12;

z_3-horizontal clearance between the edge of the lane rail and the unit load placed closest to the aisle, figure 12.

Table 3: Recommended lane clearances [8]

Clearance	Industrial truck operated systems	S/R machine operated systems	Aisle carrier operated systems
x_1	To be defined by shuttle supplier	To be defined by shuttle supplier	To be defined by shuttle supplier
x_2, x_3	≥ 75 mm [a] ≥ 100 mm [b]	≥ 75 mm	≥ 75 mm
x_4, x_5	≥ 100 mm [a] ≥ 125 mm [b]	≥ 100 mm	≥ 100 mm
y_1	≥ 100 mm [c] ≥ 125 mm [a] ≥ 150 mm [d]	≥ 100 mm	≥ 100 mm
y_2	$= y_1 - y_3$	$= y_1 - y_3$	$= y_1 - y_3$
y_3	25 mm	25 mm	25 mm
z_1, z_2	50 mm	50 mm	50 mm
z_3	50 mm	50 mm	50 mm
d_1, d_2, d_3, d_4	To be defined by shuttle supplier	To be defined by shuttle supplier	To be defined by shuttle supplier

[a] for top storage level up to 9 m,

[b] for top storage level higher than 9 m,

[c] for top storage level up to 6 m,

[d] for any storage level up to 13 m.

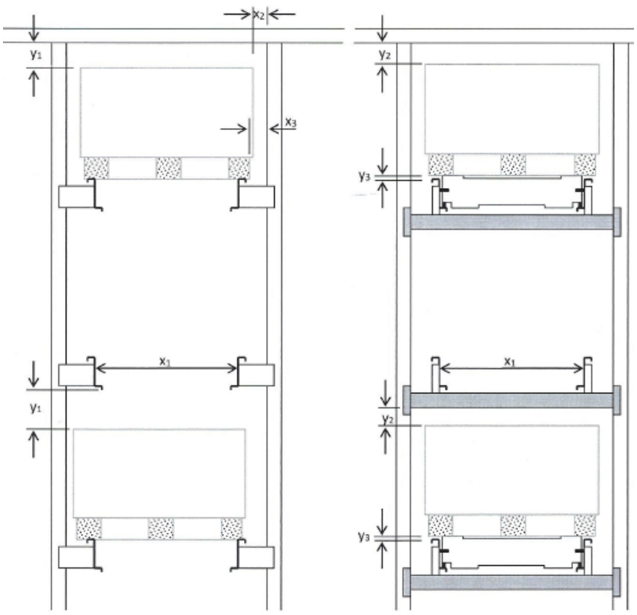

Figure 9: Vertical and horizontal clearances in down-aisle direction X and vertical direction Y for one loaded tunnel [8]

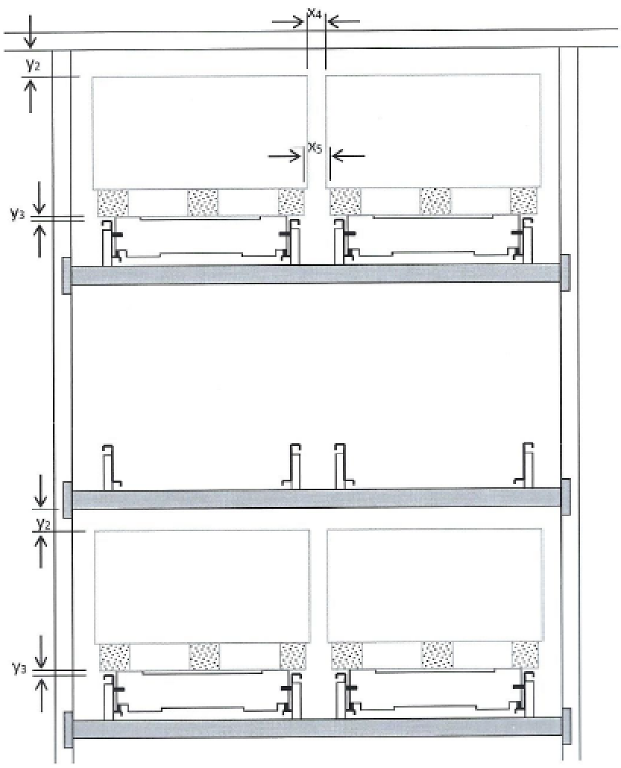

Figure 10: Vertical and horizontal clearances in down-aisle direction X and vertical direction Y for two loaded tunnel [8]

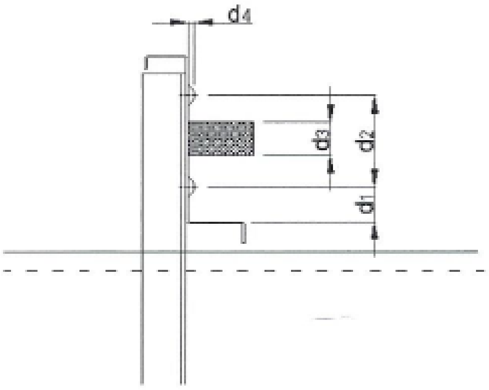

Figure 11: Vertical dimensions clearances in down – isle direction X and vertical direction Y [8]

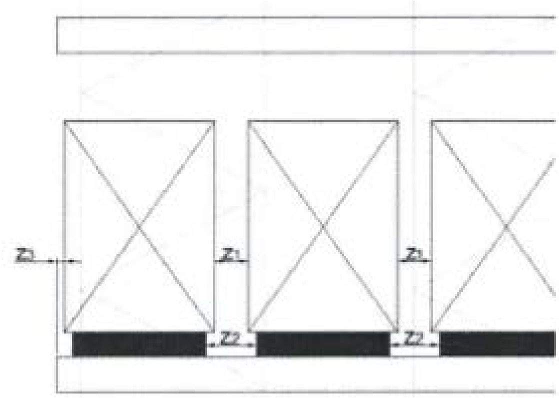

Figure 12: Horizontal clearances clearances in cross - isle direction Z [8]

4.2. Aisle clearances for S/R machine and aisle carrier operated systems

In addition to the provisions of FEM 9.831 [13], the following clearances shall be considered:

z_4 – horizontal clearance between rails shall satisfy the clearances required by the aisle carrier and provide support for the shuttles on the lane rail, figure 13;

z_5 – horizontal clearance between the lane rail and the aisle rail, figure 13.

Both dimensions z_4 and z_5 must be defined by shuttle supplier in case of S/R machine operated system or aisle carrier operated systems.

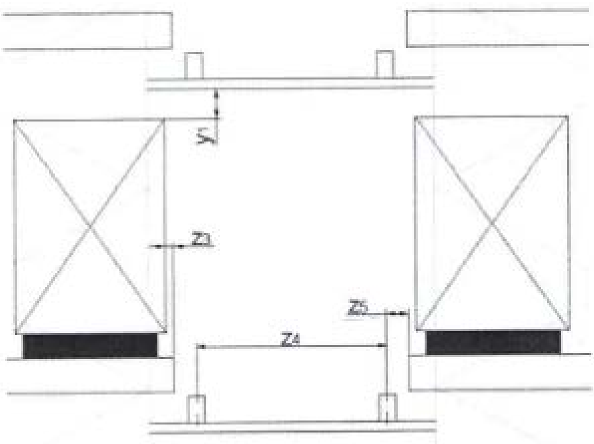

Figure 13: Aisle clearances for aisle carrier operated systems [8]

5. CONCLUSIONS

Drive-In and Drive-Through racking system is strongly represented high density storage solution especially in refrigerated chambers, food warehouses, water and drink manufacturers and distribution centers. As its name implies, racking requires a forklift truck to enter the system to deliver and retrieve pallets. The density of this systems was additionally improved with automatization of handling process. Placing shuttle in own appropriate working pallets buffering channel, it is able to pick, place, reorganize pallets with good accuracy and efficiency. Shuttle is easy moved from one channel to another by various material handling equipment with different level of automatization. Instead of the lift truck driving in to the rack like in the drive - in or drive - through systems, the shuttle delivers pallet loads in and out of the rack. But even in this improved system in order to ensure safe operation, it is necessary to follow recommended operating clearances as well as manufacturing, assembly and erection tolerance limitations defined in state-of the art standards and regulations.

REFERENCES

[1] R. Vujanac, N. Miloradovic, “Basics of Storage and Material Handling Systems”, Faculty of Engineering University of Kragujevac, Kragujevac, (2023)

[2] FEM 10.2.07, “The Design of Drive-In and Drive-Through Racking”, European Materials Handling Federation. Hitchin (England), (2012)

[3] R. Vujanac, N. Miloradovic and S. Vulovic, “Dynamic Storage Systems”, Annals of Faculty Engineering Hunedoara – International Journal of Engineering, Vol. XIV, pp. 79-82, (2016)

[4] R. Vujanac, N. Miloradovic and R. Slavkovic, “Radio Shuttle Racking – New Generation of High-Density Storage System”, Proceedings of the 7th International Scientific Conference “Research and Development of Mechanical Elements and Systems IRMES 2011”, Zlatibor (Serbia), 27 April-28 April 2011, pp. 205-208, (2011)

[5] R. Vujanac, R. Slavkovic, M. Blagojevic, “Autosatmover - New Solution for Automatic Multi-Depth Pallet Storage System”, Proceedings of 7th International Symposium About Machine and Industrial Design in Mechanical Engineering KOD 2012”, Balatonfured (Hungary), 24 May-25 May, pp. 139-142, (2012)

[6] R. Vujanac, R. Slavkovic, N. Miloradovic and M. Blagojevic, “Vertical Reciprocating Conveyor as a Part of Fully Automated Multi Depth Pallet Rack Storage System”, Proceedings of XI International Conference on Accomplishments in Electrical and Mechanical Engineering and Information Technology DEMI 2013” , Banja Luka (BiH), 30 May – 1 June 2013, pp. 1105-1112, (2013)

[7] EN 15878:2011, “Steel Static Storage Systems - Terms and Definitions”, European Committee for Standardization, Brussels (Belgium), (2010)

[8] FEM 10.2.19, “The Design of Shuttle Racking”, European Materials Handling Federation. Hitchin (England), (2021)

[9] FEM 10.2.03, “Guidelines for Specifiers of Static Steel Racking and Shelving”. European Materials Handling Federation. Hitchin (England), (2000)

[10] FEM 10.2.04, “Guidelines for the Safe Use of Static Steel Racking and Shelving”, European Materials Handling Federation. Hitchin (England), (2000)

[11] https://automha.com/products-industrial-handling-system/

[12] FEM 10.3.01, “Adjustable Beam Pallet Racking – Tolerances, Deformations & Clearances”, Federation Europeene De La Manutention, Section X. Birmingham, (England), (1997)

[13] FEM 9.831, “Calculation Principles of Storage and Retrieval Machines-Tolerances, Deformation and Clearances in the High-bay Warehouse”, Federation Europeene De La Manutention, Section X. Birmingham, (England), (1995)

Comparative analysis of a large span gantry crane structure subjected to skewing force calculated using JUS and Eurocode 1 standards

Marko Todorović[1*], Goran Marković[1], Nebojša Zdravković[1], Mile Savković[1], Goran Pavlović[2]
[1]Faculty of mechanical and civil engineering in Kraljevo, University of Kragujevac, Kraljevo, Serbia
[2]Faculty of electronic engineering, University of Niš, Niš, Serbia

The way the skewing effect is being calculated differs between the JUS and Eurocode 1 standards. As a part of internal logistic systems many industries heavily rely on gantry cranes for their robustness and reliability which depend largely on the structure of the crane. Wire model of a truss structure of a gantry crane with approximately 60 m span used in timber industry was created and subjected to the loads in vertical plane and the skewing force in order to perform structural analysis using the finite element method for the skewing force calculated using both standards. The results of the conducted structural analysis were displayed in this paper.

Keywords: Large span gantry crane, finite element method, truss structure, structural analysis

1. INTRODUCTION

Every internal logistic system of an industrial facility or a warehouse as inseparable part of the larger scale logistic system is consisted of many different material handling devices. Cranes of all forms heavily participate in day-to-day operations as the only, or the most efficient way to transport the material from one place to another. Gantry cranes are especially important in timber industry where moving large and heavy logs is the central part of the operation.

Considering the high intensity loads gantry cranes are subjected to during their operation, their structure needs to be thoroughly analysed.

Many authors analysed causes and consequences of gantry crane breakdowns. In the [1] it was shown that a trivial design error such as use of passive rail clamps with half the required capacity can lead to derailment and failure of a gantry crane. Improper choice of the members of the gantry crane structure can lead to premature failure as it is shown in the paper [2] where improper thermic treatment of the crane wheels lead to derailment of the crane. The broken tooth phenomena in slewing bearing’s large gear rings was studied in [3] as it has a great impact on the production efficiency of Chinese ports which causes huge economic losses. As gantry cranes are used in many different environments where people interact with the devices, the cranes have a part in the occupational accident risk analysis [4].

Since the failure of gantry cranes can cause great material damage and they have negative impact on the occupational safety of the workers, it is imperative to design the cranes that can withstand the loads they are being loaded with during their operation. In order to accomplish this, many methods and procedures for structural and dynamic analysis of the crane structures and components had been developed, where the numerical methods took the lead. Dynamics analysis of the cranes attracted a lot of interest from the researches. The authors of the [5] studied the dynamic behaviour of a nonlinear gantry crane system using the dynamic model that was derived using Lagrange equations. Transverse and longitudinal vibrations of a gantry crane system where the moving body was considered as a moving oscillator obtained using a numerical, combined finite element method and analytical method was studied in [6].

In structural analysis the effects of dynamic behaviour of the structure are usually taken into account by introducing the dynamic coefficients which are applied on the static loads [7]. These coefficients are usually built into standards that regulate loads the structure of the crane has to withstand, such as [8]–[10].

Numerical methods such as finite element methods were largely used for structural analysis singled out components of the cranes observing how common mechanical phenomena effect their structure. In the paper [11] such analysis was done on a main grinder of a single grinder portable gantry crane. Finite element analysis was also used in order to determine the effect of the main grinder cross section on the levels of generated stress [12]. In the paper [13] the strength analysis of the overhead traveling crane was conducted using the finite element methods with Abaqus, finite element analysis software.

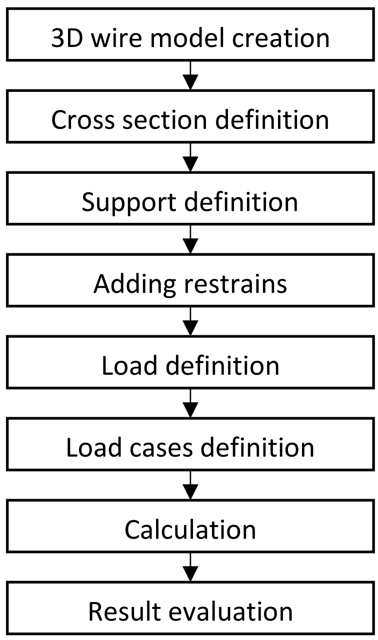

Figure 1: Structural analysis flow chart

*Corresponding author: Dositejeva 19, 36000 Kraljevo, Serbia, todorovic.m@mfkv.kg.ac.rs

However, there are not many papers focused on structural analysis of the whole gantry crane structure, which is the gap this paper is set to fill. The structural analysis will be completed using Autodesk Robot Structural Analysis software on a large span gantry crane structure. The structure of the paper follows the steps shown in Figure 1.

2. THE MODEL CREATION

The observed gantry crane, displayed in Figure 2, consists of two legs, one rigid and one elastic, connected with the main grinder with the span of 60.95 m. On each side there is an overhang. If the rigid leg is considered to be on the left side, and the elastic leg on the right side of the crane, the overhang on the left side is 15.9 m long, while the length of the overhang on the right side is 10.6 m. Total lifting capacity of the crane is set to be 50 kN. The lifting hight 7.6 m while the main grinder is on the 12.58 m distant from the ground plane.

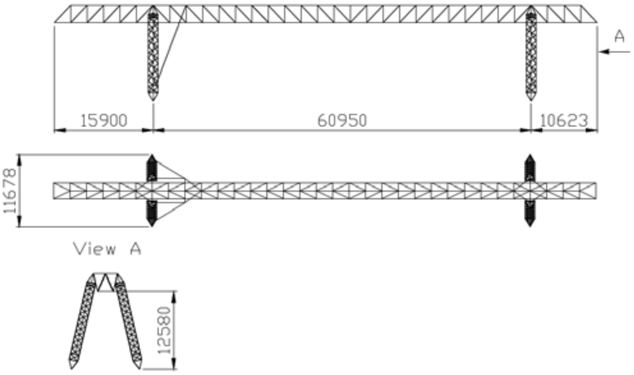

Figure 2: Large span gantry crane

The crane is used for moving logs in timber industrial facility. The hoist is equipped with grabbing device for lifting the logs. The weight of the grabbing device is 15 kN, while the weight of the hoist with the cabin for the operator combined equals 25 kN.

2.1. Three-dimensional wire model of the crane

The three-dimensional model of the crane was created from the available documentation and it is consisted of lines drawn in three-dimensional space where each line represents a member of the truss structure of the gantry crane. For creating the three-dimensional wire model, displayed in Figure 3, a CAD software was used, and the drawing was exported to .dxf format.

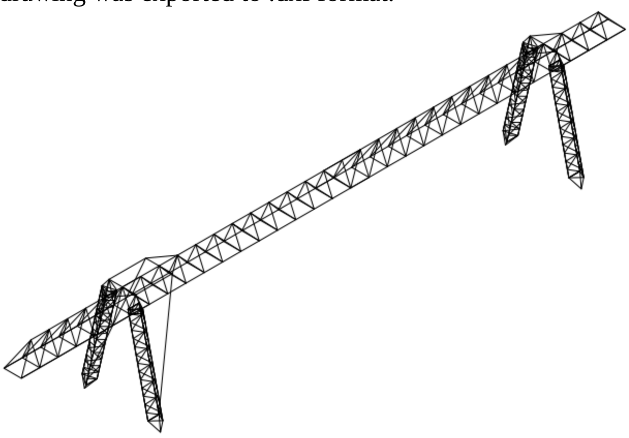

Figure 3: Isometric view of the three dimensional wire model of the gantry crane

2.2. Cross section definition

After the creation of the three-dimensional wire model of the gantry crane, and after it was exported to the .dxf format, as such it can be imported into the software for structural analysis and simulation using the finite element method, which can be seen in figure 4. In this software the lines that make the wire model are given physical properties: geometrical properties of the cross section as well as the properties of the material from which they are consisted.

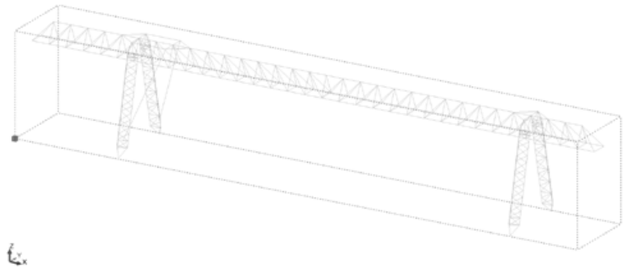

Figure 4: Three dimensional wire model imported into Autodesk Robot Structural Analysis

Each line of the wire model represents the one-dimensional finite element – the beam. In Figure 5 the model with assigned cross sections and materials is displayed.

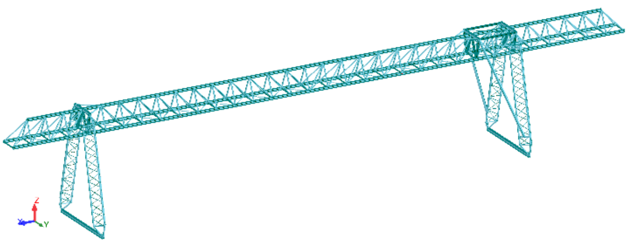

Figure 5: Three dimensional wire model with cross sections assigned to finite elements

Geometrical properties of the cross sections assigned to the members of the structure, surface areas and axial moments of inertia for all three local axes, are given in tables 1 and 2.

Table 1: List of used standard profiles and their surface areas

Profile	*AX [cm²]*	*AY [cm²]*	*AZ [cm²]*
2 CAE100x10	38.31	20	20
2 UPE360	155.8	74.8	86.4
2 UPN350	151.67	63.21	94.09
HE200A	53.83	38.68	13.28
IPN360	96.91	55.46	45.66
ROND50	19.63	16.57	16.57
ROND90	63.62	53.68	53.68
TREC100x50x5	13.88	6.17	6.17
TRON139x4	17.05	8.53	8.53
TRON168x4.5	23.16	11.58	11.58
TRON 323x5.6	56	28	28

Table 2: List of used standard profiles and their axial moments of inertia

Profile	*IX [cm⁴]*	*IY [cm⁴]*	*IZ [cm⁴]*
2 CAE100x10	12.67	353.4	6168.03
2 UPE360	24939.43	29650	11734.12
2 UPN350	111.9	25680	9379.22
HE200A	18.6	3692.15	1335.51
IPN360	118	19566	817.56
ROND50	61.36	30.68	30.68
ROND90	644.13	322.06	322.06
TREC100x50x5	134.6	169.9	55.06
TRON139x4	785.72	392.86	392.86
TRON168x4.5	1554.43	777.22	777.22
TRON 323x5.6	14188	7094.01	7094.01

All finite elements were assigned the same material property. Structural steel S355 was used for the whole structure. This material was modelled in the software using the data displayed in Table 3.

Table 3: Material properties

Material	E [MPa]	G [MPa]	ν	ρ [kN/m³]	Re [MPa]
S 355	210000	81000	0.3	77.01	355

…where E denotes the modulus of elasticity, G denotes the shear modulus, ν is Poisson's ratio, ρ is material density, and Re is yield strength.

2.3. Structure supports

Various load combinations that are defined by different standards require different ways of supporting the structure. However, for the most of the needed load combinations according to [9] and [14], the supports are defined as displayed in figure 6 and 7 where the two supports in nodes 1 and 260 are set to be fixed in all three directions, and the nodes 159 and 209 are fixed in the vertical (z) and traverse (x) direction while the movement in the y direction, direction in which the crane moves, is allowed.

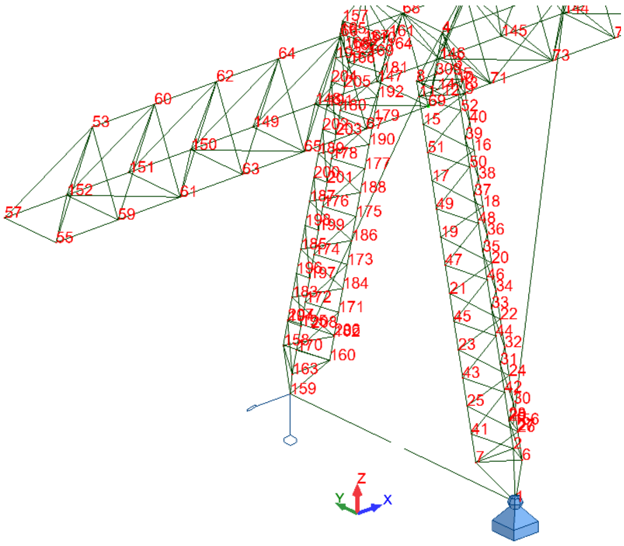

Figure 6: Supports in nodes 1 and 159

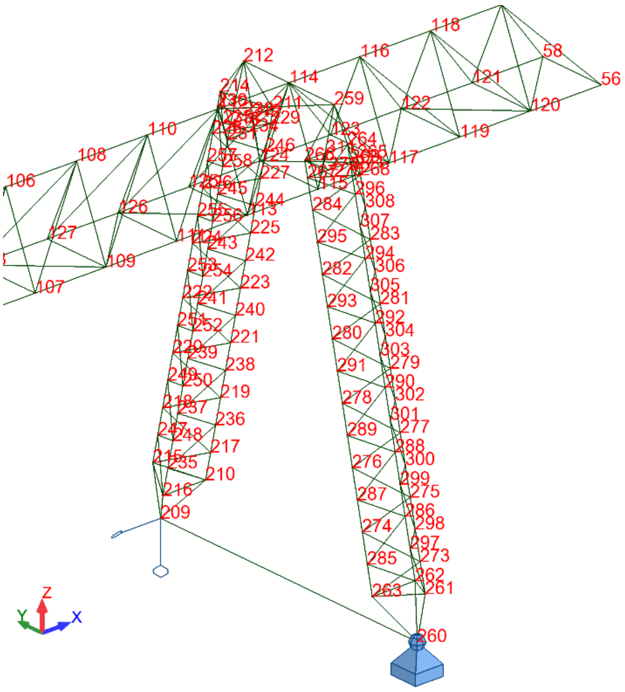

Figure 7: Supports in nodes 209 and 260

2.4. Releases

Based on the available documentation and photographs of the crane structure, it was concluded that the main grinder was connected to the crane legs with a pin in the global x direction which means that the momentum around the global x axis is not carried onto the crane legs. In the Figure 8 the releases in joints which form the described connection are shown.

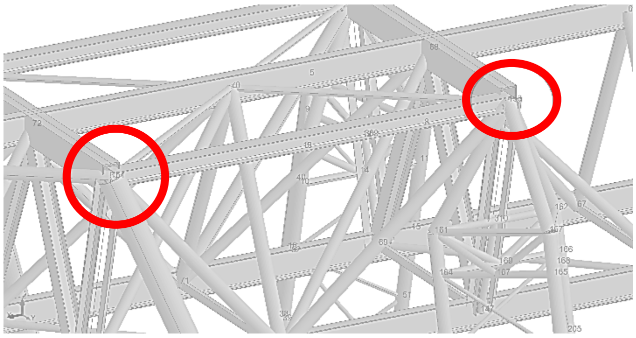

a) Releases for the riggid leg

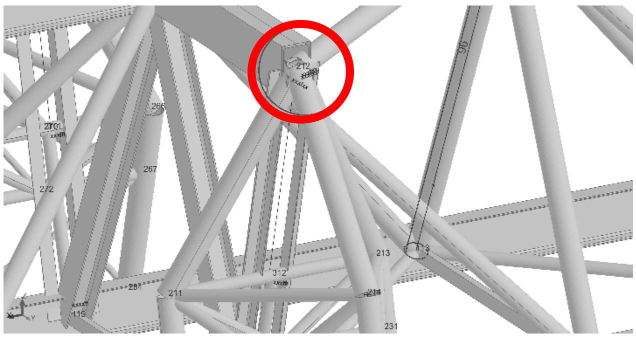

b) Releasess for the elastic leg

Figure 8: Releases in the connection between legs and the main grinder

The legs are also connected to the grinder via the pipe that is pinned on both sides, which is displayed in the Figure 9. Pinned connections assumes that moments around any of the global axis do not get transferred with that connection. The connection between the beam that stiffens the rigid leg and the top of the lower part of the leg is in the form of a pin. This release is shown in the Figure 10.

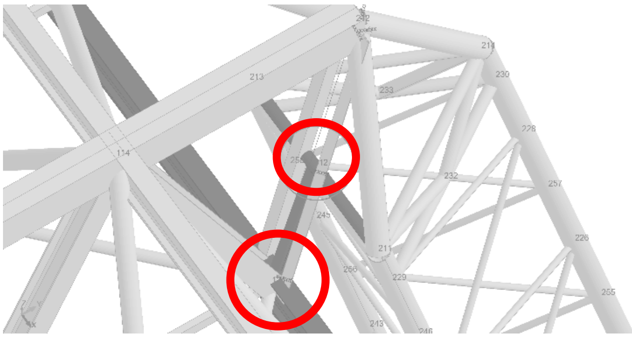

Figure 9: Releases for the bar pinned on both ends

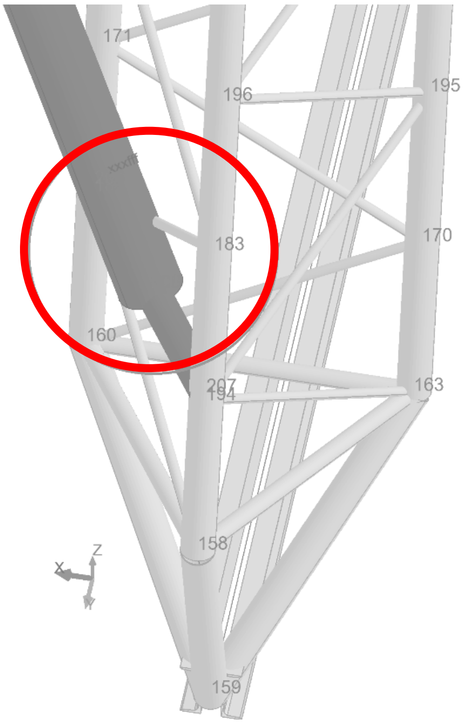

Figure 10: Releases between the crane leg and the stiffner

3. LOAD DEFINITION

The loads can be divided into two groups of loads, depending on the plane in which their vectors lay, to vertical and horizontal loads [9].

The vertical loads come from the weight of the crane structure, the weight of hoist, and the weight of the lifted load. Since the crane has a large span, the cabin for the operator is mounted to the hoist. It is considered that the resultant of the weight of the hoist and the cabin is located in the centre of the hoist, and that the weights of the hoist, cabin and lifted load is equally distributed on the wheels of the hoist, as it is show in the Figure 11, where R_1, R_2, R_3 and R_4 are the reactions, and the Q_t is the sum of the weight of the hoist Q_h, the cabin Q_c, the grabbing device Q_g and the lifted load Q_l:

$$Q_t = Q_h + Q_c + Q_g + Q_l \quad (1)$$

$$R_1 = R_2 = R_3 = R_4 = \frac{Q_t}{4} \quad (2)$$

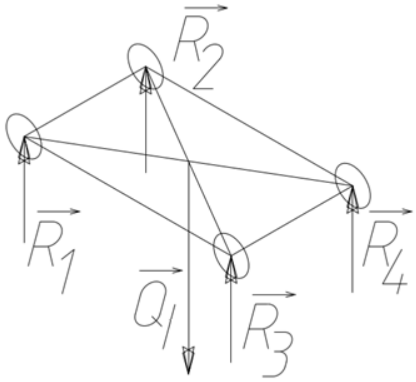

Figure 11: Reactions in the wheels of the loaded hoist

The values of the weights, as well as the intensities of the reactions on the wheels of the hoist are given in the table 4. When the hoist is empty, meaning it does not carry any useful load, as shown in the Figure 12, the values of the reactions on the hoist wheels are presented in Table 5.

Table 4: Table of weights and reactions

Denotation	Value [kN]	Description
Q_{cr}	530.02	Weight of the crane
Q_h	25	Weight of the hoist
Q_c		Weight of the cabin
Q_g	15	Weight of the grabbing device
Q_l	50	Weight of the load
R_1, R_2, R_3, R_4	22.5	Reactions

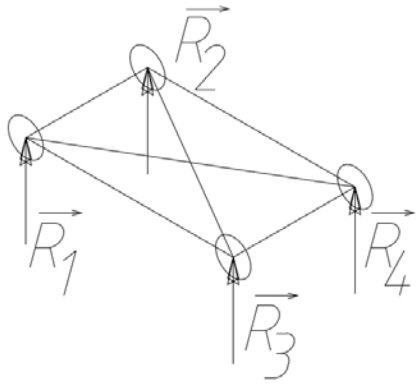

Figure 12: Reactions in the wheels of the empty hoist

Table 5: Table of weights and reactions in the wheels of the hoist

Denotation	Value [kN]	Description
Q_{cr}	530.02	Weight of the crane
Q_h	25	Weight of the hoist
Q_c		Weight of the cabin
Q_g	15	Weight of the grabbing device
Q_l	0	Weight of the load
R_1, R_2, R_3, R_4	10	Reactions

When it comes to the load in the horizontal plane, for the sake of comparison of the two standards, the focus of will be on the skewing forces. The skewing forces are defined differently in JUS and Eurocode 1 standards as the JUS standard defines the skewing load which acts on the structure of the crane above the elastic leg while the Eurocode 1 standard defines the skewing forces for the wheels of the crane.

In the Figure 13, the horizontal and vertical loads

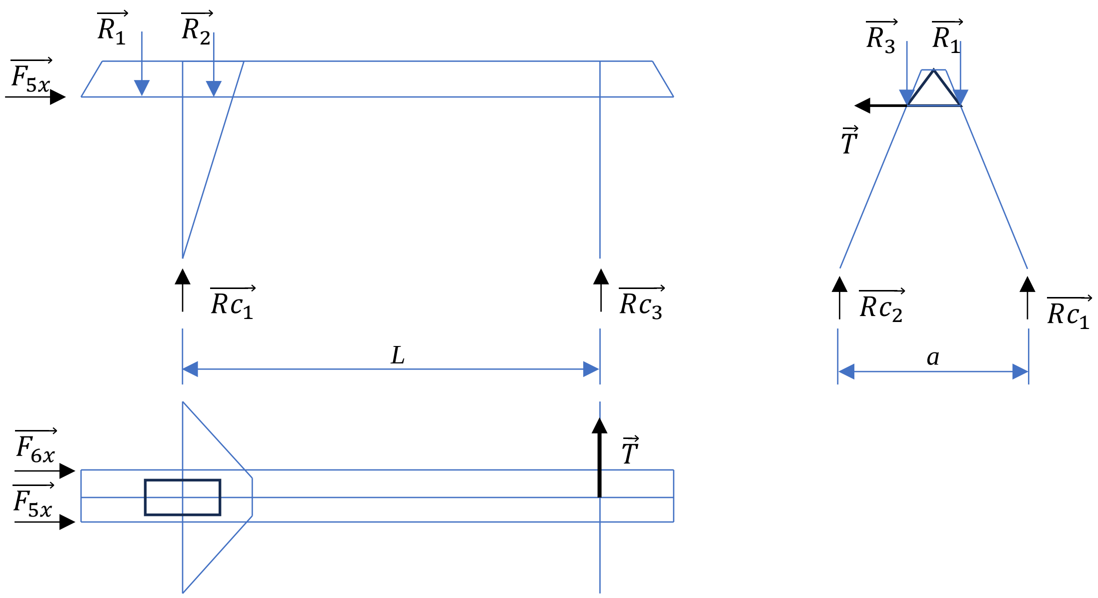

Figure 13: Crane with horizontal forces needed for calculating skewing load according to JUS standard

needed for calculating the intensity of the skewing force $\vec{T}$ are shown. According to the JUS standards [14], the intensity can be calculated using the following equation:

$$T = \frac{F_{H,max} \cdot a}{L} \tag{3}$$

$$F_{H,max} = \max(R_{C1}, R_{C2}, R_{C3}, R_{C4}) \cdot \lambda \tag{4}$$

For the case when the loaded hoist is located above the rigid leg, the values of the reactions of the crane wheels are given in the table 6. The parameter λ is the function of the ratio of traverse and longitudinal distance between the crane wheels, and in this case, according to [14] equals 0.1305. The intensity of the skewing force is given in the table 6.

Table 6: Reactions in crane wheels for the case when the loaded hoist is located above the rigid leg and the intensity of the skewing force

R_{C1} [kN]	R_{C2}[kN]	R_{C3}[kN]	R_{C4}[kN]	T [kN]
211.56	211.52	129.49	129.45	5.291

The forces F_{5x} and F_{6x} are forces that are taking into account the slipping of the wheels of the rigid leg [14], and they can be calculated as follows:

$$F_{5x} = 0{,}1 \cdot R_{C1}; F_{6x} = 0.1 \cdot R_{C2} \tag{5}$$

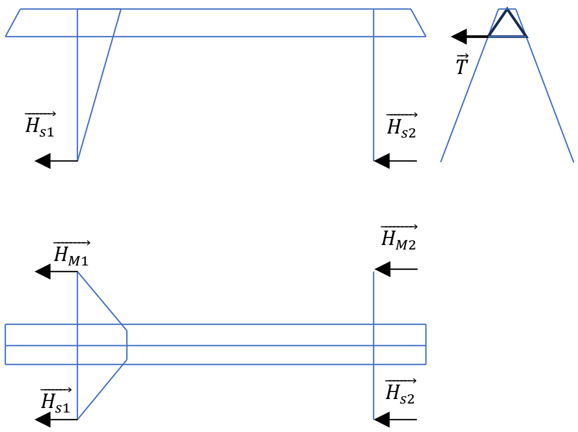

Figure 14: Skewing force displaced on the structure of the crane

The Eurocode 1 standard defines the skewing forces for each of the crane wheels individually. However, considering that the crane wheels in this case are modelled as supports for the structure within the software for finite element structural analysis, the forces in horizontal plane defined by the standard have to be displaced to the structure itself in order to be properly taken into account. As a step in this process, the forces from the individual wheels of the crane can be replaced with the appropriate forces for the group of the wheels H_{S1} and H_{S2}, as presented in the Figure 14. The momentum from displacing the forces can be replaced with the coupling of forces H_{M1} and H_{M2}. The intensity of the skewing force can finally be expressed as following:

$$T = \frac{a \cdot (HS - HM)}{2L} \tag{6}$$

$$HS = H_{S1} + H_{S2} \tag{7}$$

$$HM = H_{M1} + H_{M2} \tag{8}$$

The intensity of the skewing force T calculated using equations (6)-(8) for the specific case equals 4.922 kN.

The skewing force $\vec{T}$ is placed on the structure, as displayed in figure 13 and 14, above the elastic leg of the crane for both, JUS standard and Eurocode 1 cases.

After the forces are calculated, the loading cases are to be defined. The loads that are being taken into account for each load case with the proper dynamic coefficients are displayed in table 7. The loads are multiplied by coefficients and as such are used for the calculation. For this load case it is considered that the loaded hoist is located above the rigid leg as displayed in the Figure 13. The force of the wind is neglected, as well as the horizontal forces from the acceleration and deceleration of the crane.

Table 7: Load case definition

Load case: Skewing	
Load name	Coefficient value
Self-weight of the crane	1,1
Self-weight of the hoist	1,1
Self-weight of the load	1,1
Skewing load	1,0

4. RESULTS

After the model creation and after the calculation was finished the minimal and maximum stress distribution for both JUS and Eurocode 1 cases stayed similar, and it is displayed in figure 15.

The global maximum of the stress in both cases is in the member 353. One node of the member is the joint between the elastic leg of the crane and the main grinder, and the member itself is a part of the elastic leg. The load and stress distribution in the local coordinate system of the member 353 is displayed in the Figure 16 for the both observed cases. In the table 8 the values of the stresses were compared between the cases for the member 353. The same diagrams are given for the main grinder beam with the highest stress value in the Figure 17. The numerical values of the calculation results for the beam are displayed in the table 9.

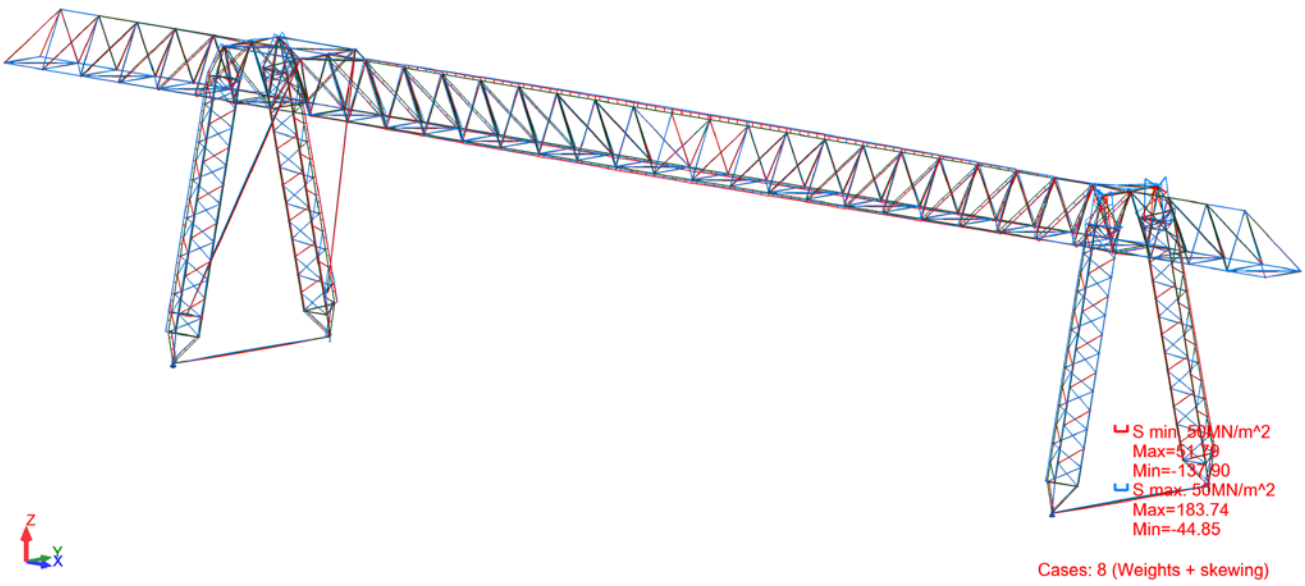

Figure 15: Stress distribution for the case with the skewing force calculated using JUS standard

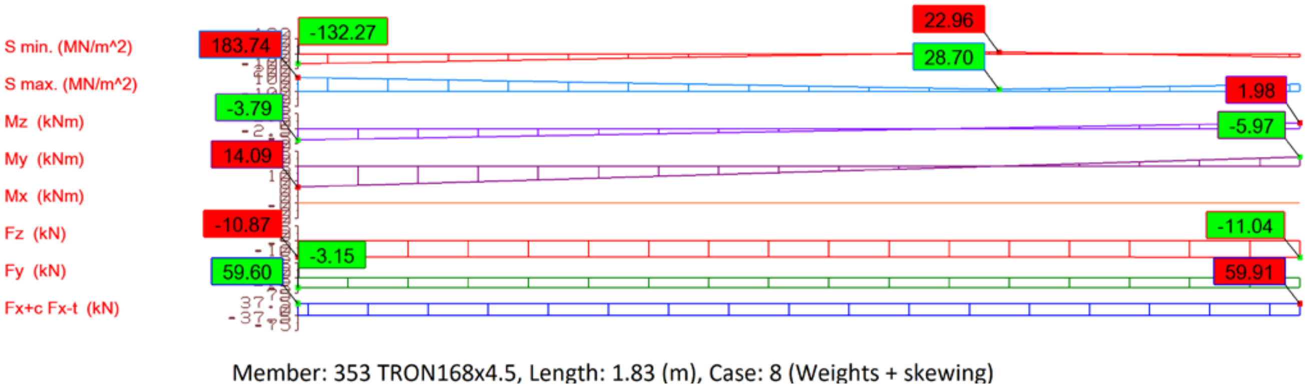

a) Eurocode 1

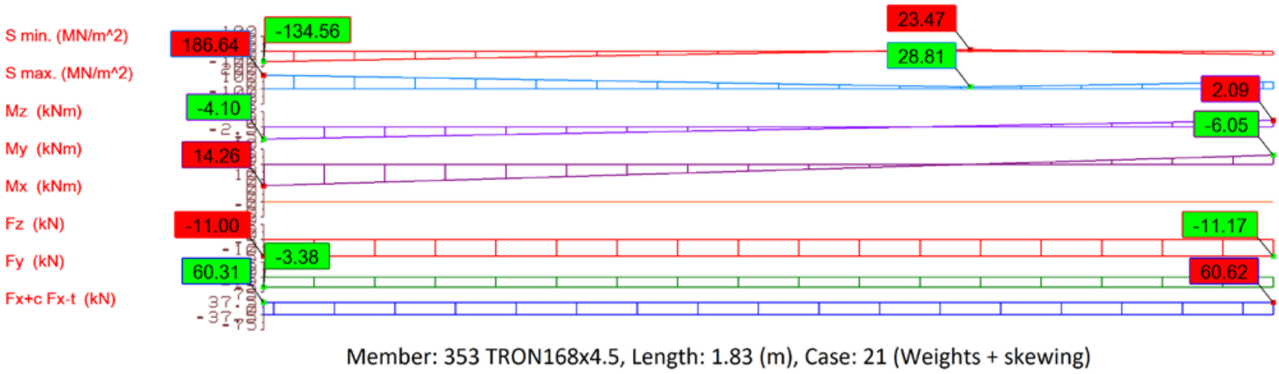

b) JUS

Figure 16: Stress distribution, moemntum, shear and axial diagrams for member 353

Table 8: The stress comparison for the critical member 353

Eurocode 1				JUS				Δ (MPa)			δ [%]		
	S max (MPa)	S min (MPa)	Fx/Ax (MPa)		S max (MPa)	S min (MPa)	Fx/Ax (MPa)	S max	S min	Fx/Ax	S max	S min	Fx/Ax
MAX	183.74	45.31	51.97	MAX	186.64	45.34	51.98	-2.9	-0.03	-0.01	1.553793	0.066167	0.019238
Member	353	7	283	Member	353	7	283						
Node	212	6	159	Node	212	6	159						
	S max (MPa)	S min (MPa)	Fx/Ax (MPa)		S max (MPa)	S min (MPa)	Fx/Ax (MPa)	S max	S min	Fx/Ax	S max	S min	Fx/Ax
MIN	-39.1	-137.9	-46.55	MIN	-39.19	-140.27	-46.66	0.09	2.37	0.11	0.22965	1.689599	0.235748
Member	211	421	211	Member	211	354	211						
Node	112	259	112	Node	112	212	112						

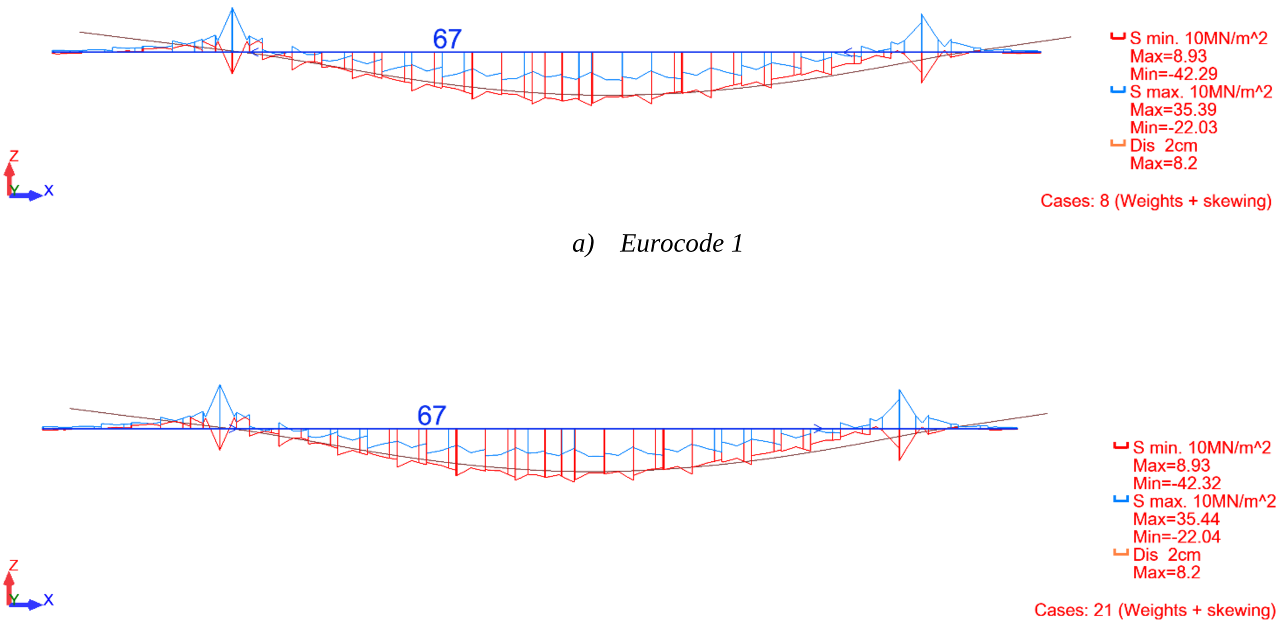

a) Eurocode 1

b) JUS standard

Figure 17: Stress distribution and deflection diagrams for the member 67

Table 9: Results comparison of the structural analysis for the member 67

Eurocode 1				JUS				Δ		δ	
	S max (MPa)	S min (MPa)	Deformation (cm)		S max (MPa)	S min (MPa)	Deformation (cm)	S max (MPa)	S min (MPa)	S max (%)	S min (%)
MAX	35.39	8.93	8.2	MAX	35.44	8.93	8.2	0.05	0	0.14108	0
Member	67	67	67	Member	67	67	67				
Point	x = 0.182	x = 0.208	x = 0.541	Point	x = 0.1818	x = 0.2082	x = 0.5411				
MIN	-22.03	-42.29	0	MIN	-22.04	-42.32	0	-0.01	-0.03	0.0453	0.071
Member	67	67	67	Member	67	67	67				
Point	x = 0.576	x = 0.545	x = 0.532	Point	x = 0.5758	x = 0.5455	x = 0.5323				

5. DISCUSSION AND CONCLUSIONS

The results of the analysis show that the skewing of the large span gantry crane plays an important part in the analysis of the structure. The figure 15 shows that the most critical part of the structure of the crane when skewing happens are the members that make up the elastic leg of the crane.

Even though the JUS and Eurocode 1 standards define skewing forces in different places within the structure, diagrams shown in figures 16 and 17 show that the stress distribution is similar in both cases. The intensities of the skewing forces calculated in JUS and Eurocode 1, in case of this large span gantry crane differ by 7,01 % in favour of JUS standard. However, the maximum stress value in the structure, in the member 353 according to the table 8 is only 1,56 % higher when the skewing force was calculated using JUS standard, which implies that the forces in vertical plane have dominance over the skewing force.

The difference in the intensity of the skewing force did not show any change in the deflection of the main grinder, and for both cases, according to the table 9 and figure 17, it stayed unchanged.

ACKNOWLEDGEMENTS

This work has been supported by the Ministry of Science, Technological Development and Innovation of the Republic of Serbia, through the Contracts for the scientific research financing in 2023, 451-03-47/2023-01/200102 and 451-03-47/2023-01/200108.

REFERENCES

[1] F. Frendo, “Gantry crane derailment and collapse induced by wind load”, Engineering Failure Analysis, Vol. 66, pp. 479-488, (2016), doi: 10.1016/j.engfailanal.2016.05.008

[2] E. E. Vernon, M. E. Stevenson and J. L. McDougall, “Premature failure of steel gantry crane wheels”, Journal of Failure Analysis and Prevention, Vol. 4, pp. 16-18, (2004), doi: 10.1361/15477020420783

[3] J. Xiao, Y. Wu, X. Long and C. Xu, “Failure Analysis of Gantry Crane Slewing Bearing Based on Gear Position Accuracy Error”, Applied Sciences, Vol. 12(23), p. 11907, (2022), doi: 10.3390/app122311907

[4] M. Erosy, “A Proposal on Occupational Accident Risk Analysis: A Case Study of a Marble Factory”, Human and Ecological Risk Assessment: An International Journal, Vol. 21(8), pp. 2099-2125, (2015), doi: 10.1080/10807039.2015.1017878

[5] H. I. Jaafar, Z. Mohamed, J. J. Jamian, A. F. Z. Abidin, A. M. Kassim, and Z. A. Ghani, “Dynamic Behaviour of a Nonlinear Gantry Crane System”, Procedia Technology, Vol. 11, pp. 419–425, (2013), doi: 10.1016/j.protcy.2013.12.211

[6] N. Đ. Zrnić, V. M. Gašić, and S. M. Bošnjak, “Dynamic responses of a gantry crane system due to a moving body considered as moving oscillator”, Archiv.Civ.Mech.Eng, Vol. 15(1), pp. 243–250, (2015), doi: 10.1016/j.acme.2014.02.002

[7] I. Gerdemeli and S. Kurt, “Design and Finite Element Analysis of Gantry Crane”, Key Engineering Materials, Vol. 572, pp. 517–520, (2014), doi: 10.4028/www.scientific.net/KEM.572.517

[8] ASME B30.2-2005: Overhead and Gantry Cranes

[9] Eurocode 1. Actions on structures. Actions induced by cranes and machines. London: British Standards Institution, 2006.

[10] “Rules for the design of cranes”, British Standards Institution

[11] L. Sowa, Z. Saternus and M. Kubiak, “Numerical Modelling of Mechanical Phenomena in the Gantry Crane Beam”, Procedia Engineering, Vol. 177, pp. 225-232, (2017), doi: 10.1016/j.proeng.2017.02.193

[12] L. Sowa, T. Skrzypczak and P. Kwiatoń, “The effect of the gantry crane beam cross section on the level of generated stresses”, MATEC Web Conf., Machine Modelling and Simulations 2017 (MMS 2017), Vol. 157, (2018), doi: 10.1051/matecconf/201815702047

[13] T. Haniszewski, “Strength analysis of overhead traveling crane with use of finite element method”, Transport Problems, Vol. 9(1), pp. 19–26, (2014)

[14] D. Ostrić, “Dizalice”, Mašinski fakultet Beograd, (1992), ISBN 86 – 7083 – 199 – 6

The optimization of the loading ramp mechanism of a heavy-weight trailer

Predrag Z. Mladenović[1*], Radovan R. Bulatović[1] , Nebojša B. Zdravković[1], Mile M. Savković[1], Goran Đ. Marković[1], Goran V. Pavlović[2]

[1]Faculty of Mechanical and Civil Engineering in Kraljevo, University of Kragujevac, Serbia
[2]Faculty of Electronic Engineering, University of Niš, Niš, Serbia

This research optimized the loading ramp mechanism of the trailer for transporting heavy construction machinery to minimize the force in the hydro-cylinder. Firstly, a mathematical model for the mechanism transition between the loading and unloading position was established. Then, it was used to optimize the lengths of the mechanism members using the metaheuristic method to achieve the operational function of the ramp. Besides the lengths of the members, the positions of the lever, which transfers the action of the hydro-cylinder to the ramp and the hydro-cylinder, were also considered during the optimization process. Finally, the optimized positions were determined by their coordinates in the vertical plane.

Keywords: Optimization, trailer, loading ramp, mechanism, hydro-cylinder, special vehicle

1. INTRODUCTION

The increase in infrastructure projects demands various construction machines whose characteristics prevent their independent transport from one place to another. In addition to their characteristics, which primarily concern their speed and powertrains, a big problem with their transport is their overall dimensions. Thus, special truck trailers have been developed to transport such machines. The construction of such trailers is quite simple and can be seen in Figure 1.

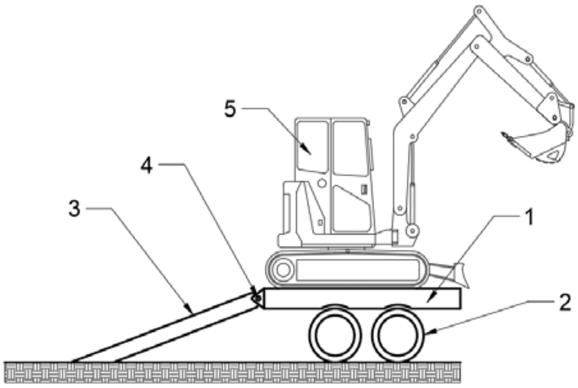

Figure 1: Illustration of a trailer for the transport of heavy machinery

Figure 1 shows: the carrying platform (1), pneumatics (2), loading ramp (3), loading ramp support (4), and the vehicle being transported (5). The part of the trailer used when loading and unloading the vehicles being transported is the subject of the study of this paper. The platform at the very end of the trailer must be lowered onto the ground, thus enabling the construction machine to place onto the trailer with its drive train. After loading the machine, the ramp returns to its original position, meeting the conditions for transporting it to the desired location. Several different solutions are used as a drive for ramp manipulation. The first and the most primitive solution is to move the ramp manually, with the help of human power or with the help of a machine's working device. However, this method is only possible in the case of smaller trailers that transport machines with smaller weights or trailers that transport excavators that enable the ramp to be moved with the excavator's arm. A solution that can also be used is described in paper [1] and involves springs that facilitate the start of the ramp during its manipulation. The described system is shown in Figure 2.

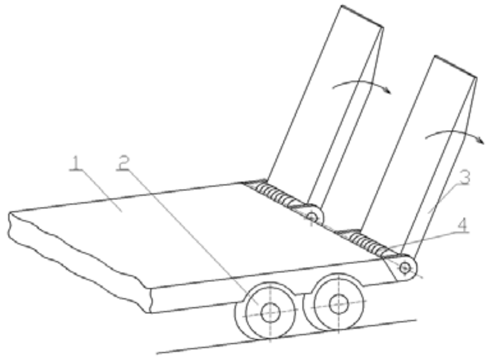

Figure 2: Illustration of the solution with the swathe springs [1]

The parts of the solution that are shown in Figure 2 are the carrying platform (1), pneumatics (2), slipway device, and swathe springs (4).

In transporting heavy machines with large mass, the loading ramps must be more massive and designed to withstand the heavy load when the machine passes over it. In that case, the ramps also have a greater mass, so a mechanism or device is needed for manipulation. Existing solutions involve the use of hydraulic cylinders located near the ramp construction. It is possible to create a mechanism for manipulating the ramp, which will enable the reduction of the force required for the manipulation of the ramp, which will also reduce the force required in the hydraulic cylinder. The lower the force in the hydraulic cylinder, the more it will be possible to install a cylinder with a smaller diameter rod, which will simultaneously require a smaller unit and other hydraulic components. The mentioned mechanism will consist of a system of rods and a lever of a complex shape, which will be supported by a pin on the vehicle's chassis. A mechanism similar to the one described can be found in the article[2]. The drive

*Corresponding author: Dositejeva 19, 36000 Kraljevo, mladenovic.p@mfkv.kg.ac.rs

for manipulating the ramp comes from a hydraulic cylinder, in which one end, i.e. the support, is located on the vehicle's chassis. In contrast, the other end of the cylinder is attached to one arm of the lever of a complex shape. The described system is shown in Figure 3, which occupies a position during transport.

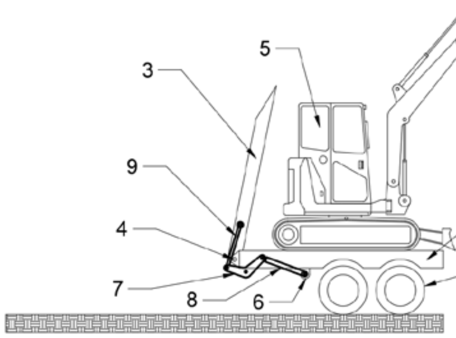

Figure 3: Illustration of the solution with a system of levers and a hydro-cylinder

The components of the system shown in Figure 3 are the carrying platform (1), pneumatics (2), loading ramp (3), loading ramp support (4), the vehicle being transported (5), hydro-cylinder support (6), a lever of a complex shape (7), hydro-cylinder (8), mechanism rod (9).

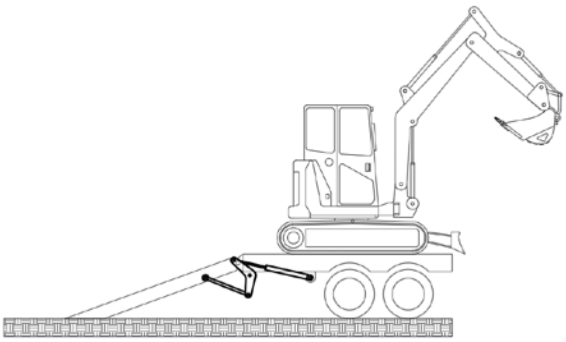

Figure 4: Illustration of the solution in the loading position

Figure 4 shows the position of the parts of the mechanism while loading the vehicle being transported.

The need to reduce manufacturing costs and maintenance of machines and equipment leads to the constant development of new and improvement of already existing solutions to engineering problems. A large number of existing optimization algorithms can be used for this purpose.

Optimization, about which more can be found in the source [3], represents obtaining the most convenient solution from a defined range according to some criterion. In the optimization process, it is necessary to define the objective function and the constraints that will shape the nature of the solution obtained from the optimization. Not all algorithms can be suitable for solving every optimization problem. Still, among many different algorithms, we could choose the one that will help solve the problem best. In this work, the Slime mould algorithm will be used for optimization. In this paper, the Slime mould algorithm, described in more detail in the paper [4], will be used to optimize the problem.

2. SLIME MOULD ALGORITHM

Many algorithms have found inspiration for their creation in nature and phenomena from it, including the slime mould algorithm (SMA) [4]. The usual way of spreading and feeding slime mould inspired the creation of a unique mathematical model that implies the existence of a positive and negative bio-oscillator response in the slime mould, depending on whether the food source is good or not. This requires the use of time-adaptive weighting factors that allow a more accurate and faster finding of a suitable result.

What is specific about the slime mould's behaviour is that even when a good food source is reached, the search for food does not stop. During the exploitation of food, the search for space for a new source does not stop. This makes it possible to find an optimal solution, avoiding reaching a local optimum.

The main stages of optimization can be defined as follows:

- Finding food;
- Approaching food;
- Wrapping food.

and can be schematically represented in Figure 5.

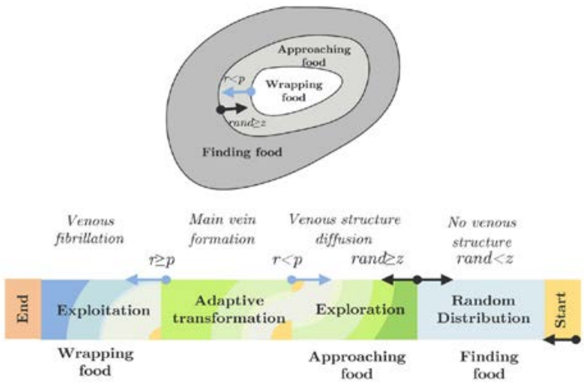

Figure 5: Stages of SMA [4]

The approach to food is achieved through the smell in the air, and for this, the contraction mode formulated as follows is the most responsible:

$$\overrightarrow{X(t+1)} = \begin{cases} \overrightarrow{X_b(t)} + \vec{vb} \cdot (\vec{W} \cdot \overrightarrow{X_A(t)} - \overrightarrow{X_B(t)}), r < p \\ \vec{vc} \cdot \overrightarrow{X(t)}, r \geq p \end{cases} \tag{1}$$

where *vb* is a parameter in bounds of [-a, a], *t* defines the current iteration, *vc* is a parameter that decreases linearly from the value 1 to zero, $X(t)$ is a vector of slime mould position, $X_A(t)$ and $X_B(t)$ are two random slime mould individuals, and $X_b(t)$ defines single location with the highest odour concentration found. The weight of the slime mould is denoted with W and can be described with equation (2).

$$\overrightarrow{X(SmellIndex(i))} = \begin{cases} 1 + r \cdot \log\left(\dfrac{bf - S(i)}{bf - wF} + 1\right), condition \\ 1 - r \cdot \log\left(\dfrac{bf - S(i)}{bf - wF} + 1\right), others \end{cases} \tag{2}$$

where *r* indicates a random value from the interval [0,1], *bF* denotes the optimal value obtained in the current iteration, *wF* denotes the worst value obtained in the iterations performed so far, and *SmellIndex* indicates an array of sorted retrieved values.

Parameter a, used as a limit for one term in equation (1), i.e. vb, is defined by equation (3).

$$a = \operatorname{arctan} h\left(-\left(\frac{t}{max\_t}\right)+1\right) \tag{3}$$

where parameter max_t indicates maximum iteration.

The slime mould's search for food is based on the contractions of the vein structures in which the cytoplasm flows. The higher the concentration of food in the new source, the greater the flow of cytoplasm and therefore, the venous structure has a greater thickness. The positive and negative response between vein thickness and food source quality is described mathematically by equation (2).

It can be said that when searching for food, the slime mould searches certain regions so that it leaves the regions where the concentration of food is weaker and goes to the regions with a higher concentration of food. The change in the location of slime mould can be mathematically described using equation (4).

$$\overrightarrow{X^*} = \begin{cases} rand \cdot (UB - LB) + LB, rand < z \\ \overrightarrow{X_b(t)} + \vec{vb} \cdot (\vec{W} \cdot \overrightarrow{X_A(t)} - \overrightarrow{X_B(t)}), r < p \\ \vec{vb} \cdot \overrightarrow{X(t)}, r \geq p \end{cases} \tag{4}$$

where the random value in a range of [0,1] is denoted with r and *rand* and *LB*, *UB* indicates lower and upper boundaries of the search range, respectively.

The source code provided with the article [4] consists of four scripts written in MathWorks Matlab programming language: main.m, initialization.m, SMA.m, Get_Fuctions_details.m.

The main.m script is the script where the number of iterations (T) and the number of search agents (N) are defined. Also, in this script, we have to define many variables for optimization and the exact name of the objective function we want to use for optimization. The objective function is called from the script Get_Fuctions_details.m and must be precisely defined. In this script, it is also necessary to define the number of variables and their limits of the search area. Starting the optimization is done by running the main.m script. At the end of the optimization, we get the best-obtained value and the convergence diagram.

3. MATHEMATICAL MODEL

The development of science and the appearance of an increasing number of real problems in all areas of human life have conditioned the application of mathematical modelling in solving various problems. Before the application of mathematical models, to obtain scientific results, it was necessary to perform a large number of experiments for scientists to confirm their theories and conclusions. Of course, this required a lot of money and precious time, which was a big problem. Therefore, it was necessary to devise a way to confirm scientific assumptions, as an experiment would do, and avoid additional costs by organizing it. This was achieved to some extent by applying mathematical modelling of the problem so that a model would mathematically describe a certain process or phenomenon. The mathematical model of a certain process or phenomenon usually consists of a set of equations, which should describe all the more important phenomena or processes that are important for the observed problem. Integral parts of the equations that represent the mathematical model are its coefficients, which describe and express some characteristics of the environment or object. Models can be simple but also complex, depending on the precision with which the real problem is described. Of course, the more complex the model, the more effort is put into its mathematical modelling, and in most cases, good models are quite complex.

The mechanism that is the subject of this paper is not very complex, so the mathematical model itself is simple. Considering that in this paper, the mechanism is constructed to determine the dimensions of its parts, the sizes of the cross-sections of the mechanism members were neglected, and all attention was paid to their lengths, as well as their characteristic positions and design details. Therefore, the mechanism was simplified and presented by a wire model, Figure 6.

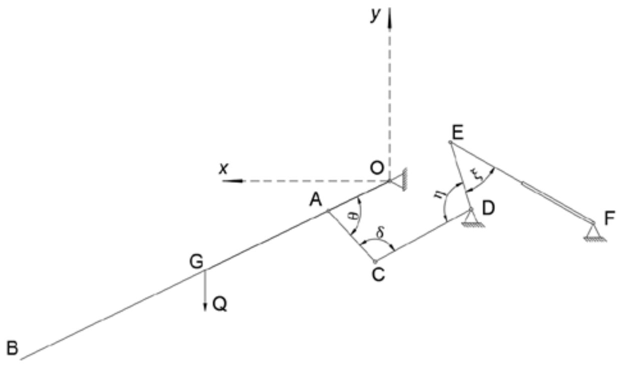

Figure 6: Mechanism wire model

The position of the supports can be seen in Figure 6; they are marked with letters O – for loading ramp support, D – for lever support and F – for hydro-cylinder support. The lengths of the mechanism members are the distances between the points marked in the picture. Considering that the lengths are used for writing the equations of motion and later for calculating the forces in the hydraulic cylinder, for the sake of transparency, new length labels are introduced, which consist of the appropriate indices up to the letter "L ". Table 1 shows the newly introduced marks.

Table 1: The connection between the corresponding marking methods

OB	L_0
OA	L_1
AC	L_2
CD	L_3
DE	L_4

Mechanism members CD and DE are rods or plates that are welded at an appropriate angle and form a single entity representing a complex shape lever. The angle between these plates is shown in Figure 6 and marked with the Greek letter η. In addition to angle η in Figure 6 can be seen angles θ, δ, and ξ as well. These angles change values over time, i.e., while the mechanism is being moved, so it can be said that they are variable.

Point G marks the centre of the ramp, and the force of weight originating from the mass Q acts in it and is directed vertically downwards.

The coordinate system is also shown in Figure 6, and its coordinate origin is at point O with the axes directed as shown.

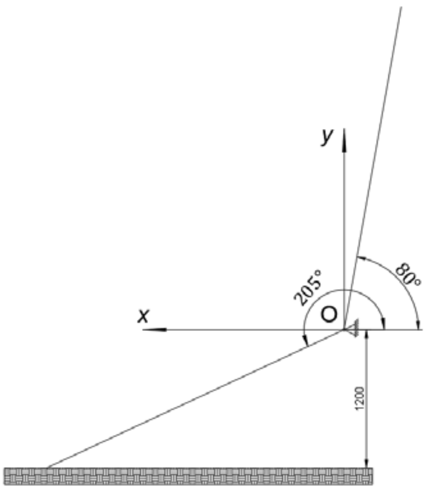

Figure 7: The position of the ramp at the beginning and end of the movement

Figure 7 shows the limit positions of the ramp, marked by the angles the ramp creates with the *x*-axis.

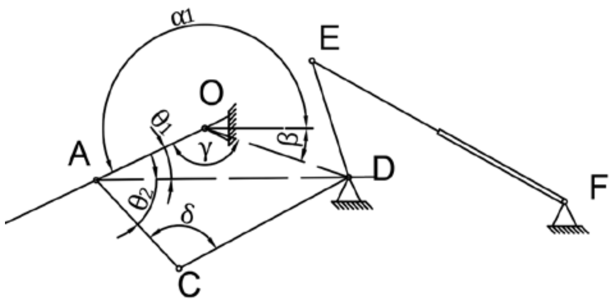

Figure 8: Auxiliary angles between members of the mechanism

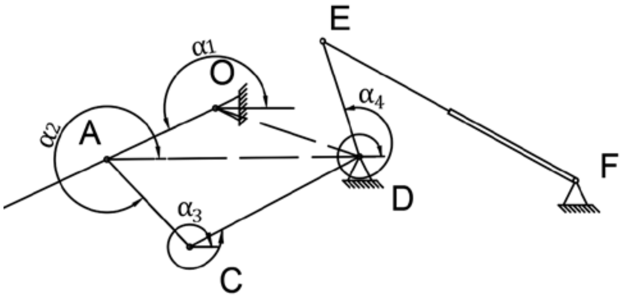

Figure 9: Angles between the mechanism members and the horizontal axis

The auxiliary angles shown in Figures 8 and 9 were defined to calculate and update the position of the mechanism members during its motion.

The positions of the lever support (D) and the hydraulic cylinder support (F) are optimization variables whose position is defined by coordinates in the direction of the coordinate axes. For the calculation, it is necessary to define the distance between the support of the lever and the support of the ramp, and it can be calculated using Equation 5.

$$L_{OD} = \sqrt{X_D^2 + Y_D^2} \tag{5}$$

Angle β can be calculated using equation (6).

$$\beta = \arctan\left(\frac{Y_D}{X_D}\right) \tag{6}$$

Due to the complexity of the mechanism and its movement, it is necessary to create a mathematical model of its movement depending on certain conditions that must be met. Due to the constant change of the angle, a counter was introduced that defines the position of the ramp in the range from 80 to 205 degrees, as shown in Figure 7. This counter is denoted by i so that for the value of $i=1$, angle α_1 has a value of 80 degrees.

The position of points A and B during movement can be defined using the following equations.

$$X_B(i) = L_0 \cdot \cos(\alpha_1(i)) \tag{7}$$

$$Y_B(i) = L_0 \cdot \sin(\alpha_1(i)) \tag{8}$$

$$X_A(i) = L_1 \cdot \cos(\alpha_1(i)) \tag{9}$$

$$Y_A(i) = L_1 \cdot \sin(\alpha_1(i)) \tag{10}$$

The calculation of angle θ depends on the value of angle α_1. If the condition defined with equation (11) is met, angle θ is calculated using equations (12-16).

$$\alpha_1(i) < 180 - \beta \tag{11}$$

$$\gamma(i) = \beta + \alpha_1 \tag{12}$$

$$AD(i) = \sqrt{L_1^2 + L_{OD}^2 - 2 \cdot L_1 \cdot L_{OD} \cdot \cos(\gamma(i))} \tag{13}$$

$$\theta_1 = \arccos\left(\left(L_2^2 + AD(i)^2 - L_3^2\right) / \left(2 \cdot L_2 \cdot AD(i)\right)\right) \tag{14}$$

$$\theta_2 = \arccos\left(\left(L_1^2 + AD(i)^2 - L_{OD}^2\right) / \left(2 \cdot L_1 \cdot AD(i)\right)\right) \tag{15}$$

$$\theta(i) = \theta_1(i) - \theta_2(i) \tag{16}$$

If the condition defined with equation (11) is not met, angle θ is calculated using equations (17-21).

$$\gamma(i) = 360° - \beta - \alpha_1 \tag{17}$$

$$AD(i) = \sqrt{L_1^2 + L_{OD}^2 - 2 \cdot L_1 \cdot L_{OD} \cdot \cos(\gamma(i))} \tag{18}$$

$$\theta_1 = \arccos\left(\left(L_1^2 + AD(i)^2 - L_{OD}^2\right) / \left(2 \cdot L_1 \cdot AD(i)\right)\right) \tag{19}$$

$$\theta_2 = \arccos\left(\left(L_2^2 + AD(i)^2 - L_3^2\right) / \left(2 \cdot L_2 \cdot AD(i)\right)\right) \tag{20}$$

$$\theta(i) = \theta_1(i) + \theta_2(i) \tag{21}$$

The angles shown in Figures 8 and 9 are obtained using equations (22-25). They are used to calculate the position of the corresponding points of the mechanism members.

$$\alpha_2(i) = \alpha_1(i) + 180 - \theta(i) \tag{22}$$

$$\delta(i) = \arccos\left(\left(L_2^2 + L_3^2 - AD(i)^2\right) / \left(2 \cdot L_2 \cdot L_3\right)\right) \tag{23}$$

$$\alpha_3(i) = \alpha_2(i) + 180 - \delta(i) \tag{24}$$

$$\alpha_4(i) = 180 - (360 - \alpha_3(i)) - \eta \tag{25}$$

The obtained angles can be used to calculate the coordinates of the remaining points needed to obtain a simulation of the movement and calculate the force at the hydraulic cylinder.

$$X_E(i) = X_D + L_4 \cdot \cos(\alpha_4(i)) \tag{26}$$

$$Y_E(i) = Y_D + L_4 \cdot \sin(\alpha_4(i)) \tag{27}$$

$$X_C(i) = X_A + L_2 \cdot \cos(\alpha_2(i)) \tag{28}$$

$$Y_C(i) = Y_A + L_2 \cdot \sin(\alpha_2(i)) \tag{29}$$

Length FE represents the length of the extended hydraulic cylinder, which changes during movement. Equation (30) describes this change in length.

$$FE = L_{FE} = \sqrt{\left(X_E(i) - X_F\right)^2 + \left(Y_E(i) - Y_F\right)^2} \quad (30)$$

The length calculated by equation (30) is needed to calculate the stroke of the hydraulic cylinder, which is a very important item when constructing a system in which the hydraulic cylinder exists. This value also represents one of the limitations in the optimization procedure because it must satisfy the appropriate condition. The stroke of the hydraulic cylinder is calculated using equation (31) as the difference of the length FE in the final and initial positions of the ramp.

$$stroke = L_{FE}(end) - L_{FE}(start) \quad (31)$$

To calculate the angle ξ, it is necessary to determine the distance between the supports D and F, which has a constant value, using equation (32).

$$L_{DF} = \sqrt{\left(X_F - X_D\right)^2 + \left(Y_F - Y_D\right)^2} \quad (32)$$

Now the angle ξ can be defined by equation (33).

$$\xi(i) = \arccos\left(\left(L_4^2 + L_{FE}^2 - L_{DF}(i)^2\right) / \left(2 \cdot L_4 \cdot L_{FE}\right)\right) \quad (33)$$

The load acting on the members of the mechanism originates from the mass of the loading arm acting at point G and, for safety, is adopted to have a higher value than it is realistic. It is assumed that the mass of the loading ramp is 500 kg. Equation (34) is used to calculate which force of own weight acts at point G.

$$F_Q = Q \cdot g = 500kg \cdot 9{,}81\frac{m}{s^2} = 4905N \quad (34)$$

where g is the acceleration of the earth's gravity, and Q is the mass of the loading ramp.

The force in the hydraulic cylinder can be obtained using the two moment-equilibrium equations for points O and D. More about the influence of the position of the hydraulic cylinder can be found in the paper [5]. These equilibrium conditions are described by equations (35) and (36). Along with these equations, the pictures corresponding to the mentioned moment equations are shown in Figures 10 and 11.

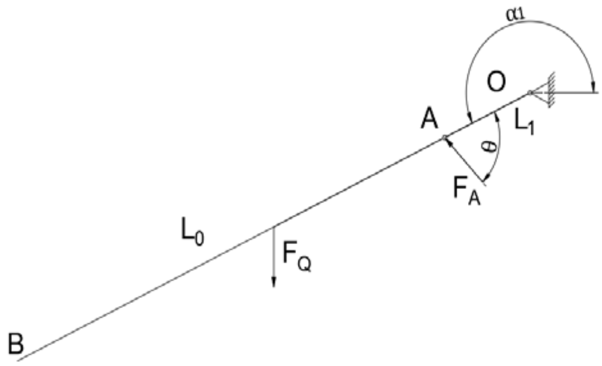

Figure 10: The wire model described by equation (35)

$$\sum M_O = Q \cdot \frac{L_0}{2} \cdot \cos(\alpha_1) - F_A \cdot L_1 \cdot \sin(\theta) \quad (35)$$

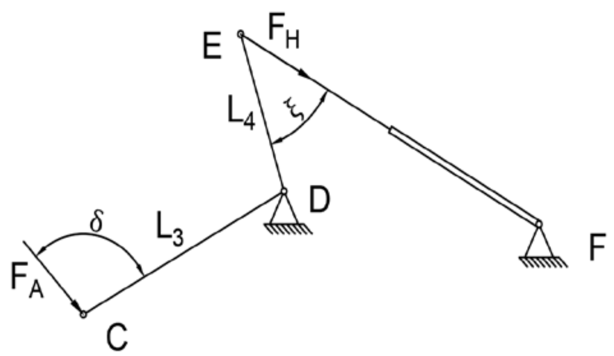

Figure 11: The wire model described by equation (36)

$$\sum M_D = F_A \cdot L_3 \cdot \sin(\delta) - F_H \cdot L_4 \cdot \sin(\xi) \quad (36)$$

Equating the equations to zero based on the equilibrium conditions, the equations for obtaining the force in the hydraulic cylinder were obtained and are shown by equations (37) and (38).

$$F_A(i) = \frac{-F_Q \cdot L_0 \cdot \cos(\alpha_1(i))}{2 \cdot L_1 \cdot \sin(\theta(i))} \quad (37)$$

$$F_H(i) = \frac{-F_A(i) \cdot L_3 \cdot \sin(\delta(i))}{L_4 \cdot \sin(\xi(i))} \quad (38)$$

The counter next to the labels shows that the obtained values are variable during movement.

4. OBJECTIVE FUNCTIONS, LIMITS OF SEARCHING AREA, AND CONSTRAINTS

4.1. Objective function

The objective functions in optimization can differ depending on what we want to achieve. The mathematical model makes it possible to calculate the force in the hydraulic cylinder, so using the final equation (38) as an objective function is possible. Therefore, the objective function equation is equation (39).

$$o = F_H \quad (39)$$

When programming the objective function, we must consider that the force value can be negative or positive, so it is necessary to take the absolute value. In addition, it is necessary to consider the penal function that enables compliance with all constraints that have been defined. Optimization aims to reduce the force in the hydraulic cylinder as much as possible.

4.2. Limits of searching

This optimization problem has nine quantities that need to be optimized: four quantities are lengths, one is angle and four are support coordinates. The lengths that need to be optimized are L_1, L_2, L_3 and L_4. Their dimensions should be between 200mm and 1200mm for constructive reasons. The angle to be optimized is the angle between the rods L_3 and L_4, denoted by η. The angle range can be between 50 and 160 degrees. The positions of the supports that need to be optimized are marked with the letters D and F. In this case, we have four optimization variables whose limits depend on the coordinate direction, and those values are shown in equations (42) and (43).

These constraints are written in vector form and are shown by equations (40) and (41).

$$LB = \left[L_{1,\min}, L_{2,\min}, L_{3,\min}, L_{4,\min}, \eta_{\min}, X_{D,\min}, Y_{D,\min}, X_{F,\min}, Y_{D,\min}\right] \quad (40)$$

$$UB = \left[L_{1,\max}, L_{2,\max}, L_{3,\max}, L_{4,\max}, \eta_{\max}, X_{D,\max}, Y_{D,\max}, X_{F,\max}, Y_{D,\max} \right] \quad (41)$$

where LB denotes lower boundaries, and UB denotes upper boundaries.

$$LB = [200, 200, 200, 200, 50, 200, -400, 1000, -400] \quad (42)$$

$$UB = [1200, 1200, 1200, 1200, 160, 1000, 0, 1600, 0] \quad (43)$$

Equations (43) and (44) show the numerical values of the limits of the optimization variables.

4.3. Constraints

Constraints play a significant role in the optimization process, shaping the solutions that will be obtained. In the concrete optimization problem, the constraints are of great importance, and there will be 19 of them. Above all, these constraints serve to avoid structurally unfeasible solutions and enable the desired trajectory of the mechanism members. Constraints, in this case, can be divided into three groups:

- constraints in the starting position;
- constraints during the movement of the ramp;
- constraints in the end position.

$$g(1) = -\theta(i) < 0 \quad (44)$$

$$g(2) = \theta(i) - 180 < 0 \quad (45)$$

$$g(3) = -\delta(i) < 0 \quad (46)$$

$$g(4) = \delta(i) - 180 < 0 \quad (47)$$

Equations (44-47) define the limit for the angles between the mechanism members, which must be in the range of [0°,180°].

$$g(5) = Y_E(1) - 200 < 0 \quad (48)$$

$$g(6) = -500 - Y_E(1) < 0 \quad (49)$$

$$g(7) = Y_E(end) - 200 < 0 \quad (50)$$

$$g(8) = -1200 - Y_E(end) < 0 \quad (51)$$

$$g(9) = -1200 - Y_E(i) < 0 \quad (52)$$

Equations (48-52) limit the positions of point E at the beginning and end of the movement and during the movement. So that at the beginning of the movement, the vertical coordinate of point E must be within limits (53), while the same limit at the end of the movement is defined by equation (54).

$$-500 < Y_E(1) < 200 \quad (53)$$

$$-1200 < Y_E(end) < 200 \quad (54)$$

The limits of the position of point C are defined by the equations (55-61).

$$g(10) = -200 - X_C(1) < 0 \quad (55)$$

$$g(11) = -500 - Y_C(1) < 0 \quad (56)$$

$$g(12) = -500 - Y_C(1) < 0 \quad (57)$$

$$g(13) = Y_C(end) - 1000 < 0 \quad (58)$$

$$g(14) = -1000 - Y_C(end) < 0 \quad (59)$$

$$g(15) = -1200 - Y_C(i) < 0 \quad (60)$$

Equation (55) defines the condition (61) for the position of point C in the horizontal direction. Equations (56-59) define the constraints of the vertical coordinate in the starting (62) and ending (63) positions.

$$X_C(1) > -200 \quad (61)$$

$$-500 < Y_C(1) < 200 \quad (62)$$

$$-1000 < Y_C(end) < 1000 \quad (63)$$

Due to the required measure for the installation of the hydraulic cylinder, it is necessary to limit its stroke as defined by equations (64) and (65).

$$stroke < L_{FE}(1) + 100 \quad (64)$$

$$stroke < 1000 \quad (65)$$

The introduced constraints are defined by equations (66) and (67).

$$g(16) = stroke - 1000 < 0 \quad (66)$$

$$g(17) = stroke - 100 - L_{FE}(1) < 0 \quad (67)$$

Limitations related to the mutual horizontal distance between supports D and F are described by equation (68) and defined by equations (69) and (70).

$$800 < X_D - X_F < 1500 \quad (68)$$

$$g(18) = X_D - X_F - 1500 < 0 \quad (69)$$

$$g(19) = 800 - X_D + X_F < 0 \quad (70)$$

5. RESULTS

After the optimization, certain results of the described variables were obtained. The parameters defined before starting the optimization were the number of iterations, the number of searching agents and the number of variables defined within the main.m script as follows:

- T=1000 – number of iterations;
- N=60 – number of searching agents;
- dimSize=9 – number of variables.

The results of the optimization process are shown in Table 2.

Table 2: Optimization results

L_1 [mm]	1200
L_2 [mm]	1200
L_3 [mm]	749.28686
L_4 [mm]	408.52464
η [°]	111.16211
X_D [mm]	497.94503
Y_D [mm]	-400
X_F [mm]	1535.3268
Y_F [mm]	-231.54711

Figure 12 shows the appearance of the mechanism with the adopted dimensions obtained in the optimization, which occupies the position with the maximum force in the hydraulic cylinder.

For the mechanism defined in this way, the objective function, i.e. the force value in the hydraulic cylinder, is shown by equation (71). Considering that the value of the force changes from a positive to a negative sign, the obtained value represents the absolute value of force that occurs in the appropriate position of the ramp.

$$o = F_H = 29817N = 29.817kN \quad (71)$$

$$stroke = 547.8mm \quad (72)$$

Equation (72) shows the stroke that needs to be achieved for the dimensions of the mechanism adopted to realize the ramp positions defined for the start and end of the movement.

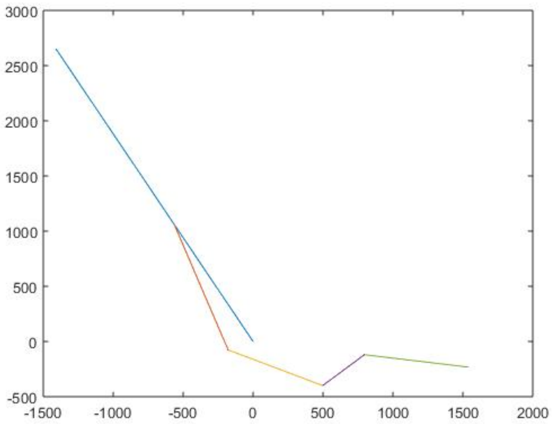

Figure 12: The most loaded position of the mechanism

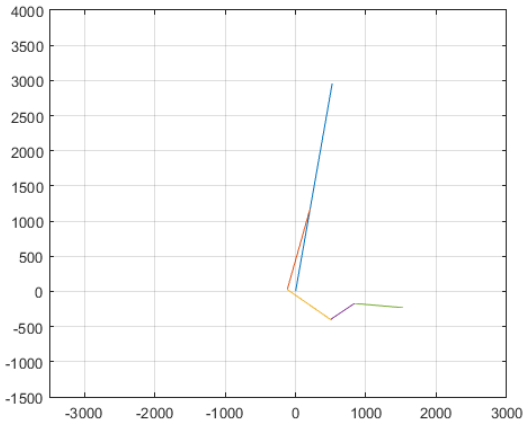

Figure 13: Starting position of the mechanism

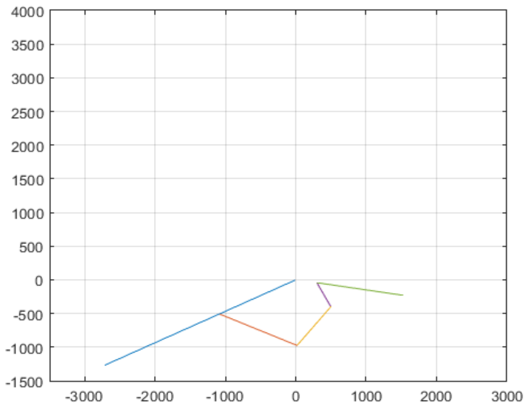

Figure 14: Ending position of the mechanism

Figures 13 and 14 show the initial and final positions of the loading mechanism members after the optimization process.

Figure 15 shows the diagram of the force change in the hydraulic cylinder depending on the change in the angle at which the ramp overlaps with the horizontal axis.

By looking at the diagram shown in Figure 15, it can be concluded which positions of mechanism members create the greatest force in the hydraulic cylinder. In addition to the perpendicular distance of the weight force from the axis of rotation, the angle of θ that the lever AC overlaps with the ramp has a significant influence.

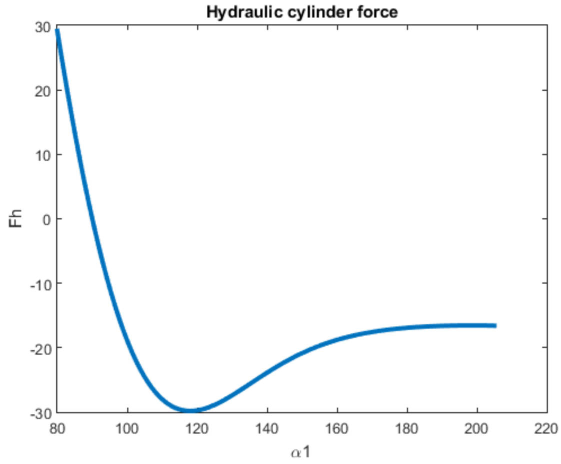

Figure 15: Hydraulic-cylinder force change

6. CONCLUSION

Optimization resulted in a solution that enables using the smallest hydraulic cylinder with the smallest force acting in it. Increasing the dimensions of the members of the mechanism makes it possible to reduce the force due to the increase in the moment arm. Limitations in the vehicle's overall dimensions make it impossible to adopt large lengths of mechanism members, resulting in a greater force in the hydraulic cylinder than expected.

ACKNOWLEDGEMENTS

This work has been supported by the Ministry of Science, Technological Development and Innovation of the Republic of Serbia through the Contracts for the scientific research financing in 2023, 451-03-47/2023-01/200102 and 451-03-47/2023-01/200108.

REFERENCES

[1] M. Gašić, M. Savković, N. Zdravković, G. Marković, "Development of Devices Used for Loading the Heavy Machines on to the Freight Trailers", Mechanics Transport Communication, Issue 3, (2011)

[2] M. Savković, G. Marković, N. Zdravković, B. Milovanović, G. Pavlović, M. Gašić, B. Sredojević, "Development and Design of the Special Vehicle for the Transportation of Heavy Weight Construction Machines", Proceedings of Seventh International Conference "Transport and Logistics", Niš (Serbia), 6th December 2019 (2019)

[3] J. R. R. A. Martins, A. Ning, "Engineering Design Optimization", Cambridge University Press (England), (2021)

[4] S. Li, H. Chen, M. Wang, A. A. Heidari, S. Mirjalili, "Slime Mould Algorithm: A New Method for Stochastic Optimization", Future Generation Computer Systems, Vol. 111, pp 300-323, (2020)

[5] N. Zdravković, M. Savković, G. Marković, G. Pavlović, "The Impact of the Position of the Hydraulic Cylinder Mounting Point on the Chassis Coad in Mobile Elevating Work Platforms", Proceedings of Sixth International Conference "Transport and Logistics", Niš (Serbia), 25-26 May 2017 (2017)

Multi-aisle automated rack warehouse simulation for average travel time

Goran Bošković[1], Marko Todorović[1*], Goran Marković[1], Zoran Čepić[2], Predrag Mladenović[1]
[1]Faculty of Mechanical and Civil Engineering in Kraljevo, University of Kragujevac (Serbia)
[2] Faculty of Technical Sciences, University of Novi Sad (Serbia)

Increased consumption of various goods in modern society requires efficient logistic systems. In order to accomplish high efficiency automated systems for internal transport of goods within a storage unit have been widely employed. Widespread use of these systems induces the need for adequate simulation models that imitate realistic warehouse workflow and can adapt to dynamic changes in operation. Travel time is one of the parameters with great impact on operational costs of the warehouse. Accurate estimation of average travel time can be used to evaluate efficiency of the logistic chain. The new three-dimensional warehouse simulation model which was proposed in this paper takes into consideration the dynamic changes in operation for obtaining average travel time estimation closer to the realistic warehouse operation

Keywords: Internal transport, Average travel time, Three-dimensional warehouse model, Warehouse simulation

1. INTRODUCTION

Nowadays, thousands of tons of goods are transported from producers through sellers to end users, i.e. customers. After the goods have been delivered by the manufacturer to the seller, they can be stored for a certain period of time in the warehouse, where they await collection. In this sense, warehouses can be divided into two types: distribution warehouses, where products from several different suppliers can be stored, and production warehouses for storing raw materials, semi-finished products, and finished products. In this regard, the storage process, as one of several logistics processes, represents an irreplaceable link in logistics systems and supply chains. The efficiency and correct function of the warehouse itself (storage capacity and speed) mostly depend on the technical parameters: the size of the warehouse, the means used for transporting and placing pallets units (forklifts, racks, rack cranes), hardware and software [1].

In order to achieve the best efficiency of the warehouse, it is important to manage it in the best possible way through the entire supply chain, from the point of receipt of goods to the warehouse, to the point of delivery of goods. Warehouse management represents an important activity in the entire process and involves managing new stock of goods, monitoring the movement of products within the warehouse and optimal arrangement of stored goods, which aims to minimize total costs and improve the satisfaction of end users. Many companies from the distribution and storage sector use developed software solutions for warehouse management (WMS - Warehouse Management System) that enable monitoring of input parameters, movement within the warehouse, output parameters of materials, semi-finished products and finished products within the warehouse in real time.

With the progress and development of economic systems, storage and distribution systems have been developed in parallel in terms of process automation in order to meet the demands of the market and production. One of the main characteristics of the automated warehouse process is reflected in very little or almost no human involvement and direct contact with goods or materials, which in some cases is one of the requirements in order to preserve product quality.

The main advantages of using automatic storage systems (AS/RS) are reflected in the increased flow of storage units, efficient use of space inside the warehouse, high reliability in operation, more precise control of stocks in the warehouse, improved conditions for storing goods inside the warehouse in terms of safety, reduction of complaints regarding damage to goods. The very concept of the operation of these systems meets the requirements of "green" logistics and reduction of CO2 emissions and ergonomics. There are several types of automatic storage systems (AS/RS) [2]:

- automatic warehouses served by cranes that transport pallets (unit-load AS/RS),
- automatic warehouses served by cranes that transport small loads - containers (mini-load AS/RS),
- automatic warehouses served by autonomous vehicles that transport pallets (AVS/RS).

Modeling of automatic storage systems represents an extensive and responsible procedure, depending on the complexity of the system itself and the goals that the system must meet in terms of end user requirements. When modeling automatic storage systems, it is necessary to take into account all relevant parameters related to the facility, transport devices, as well as the type and size of the units that are placed in the warehouse. The level of complexity of the warehouse model depends on what is expected from the simulation results. Based on the level of complexity of the storage system and the parameters incorporated, the simulation results can vary significantly regarding the performance and efficiency of the entire storage system [3].

In the paper presented by Manzini et. all [4], a warehouse model was presented using alternative design and operational configurations, which identified the most critical factors and combinations of factors that affect the efficiency of the warehouse system and presented the most significant results of the analysis.

*Corresponding author: Dositejeva 19, 36000 Kraljevo, Serbia, todorovic.m@mfkv.kg.ac.rs

Since automated storage and retrieval systems (AS/RS) represent a significant investment and significant

This reality creates a need for robust and efficient system evaluation models that can be found in [5]. This paper complements previous research on AS/RS by focusing on a specific research question related to dynamic models based on intra-warehouse travel time modeling.

In the paper [6] new analytical models are presented in order to evaluate the performance of AS/RS warehouses related to racks with deep pallet spaces. These models extend the state of the art by (1) taking into account actual criteria related to item storage and retrieval, (2) taking into account the ability of transport devices to perform different tasks simultaneously, and (3) estimating the standard deviation of the cycle time, in addition to its average values. The presented models are validated through simulations performed on different warehouse layouts, in different implementation scenarios. The ultimate goal of such models is to support storage equipment designers in evaluating the performance of their systems, taking into account a variety of realistic scenarios.

Automated storage and retrieval systems (AS/RS) and autonomous vehicle storage and retrieval systems (AVS/RS) are two competing technologies for handling, storing, and retrieving unit loads in the spare part of the automated warehouse presented in [7]. In this paper, variants of the two systems are modeled as open queuing networks (OCNs) and we use an existing OCN analysis tool, called the production system performance analyzer (MPA), to analyze the performance of AS/RS and AVS/RS. Experimental results are provided to show that MPA is a better choice than simulation for rapidly evaluating alternative configurations of two systems. We use MPA to answer a series of design questions to conceptualize AS/RS and AVS/RS designs [8].

2. 3D WAREHOUSE MODEL

In the previously mentioned works, different approaches were presented in the formation of analytical models of warehouses and storage systems in order to implement various procedures related to the calculations of the average duration of the pallet cycle within the warehouse. In the text that follows, the authors of the paper proposed a new concept in the three-dimensional representation of the warehouse with the aim of greater flexibility in terms of the configuration of storage places and corridors within the building (Fig. 1).

In the first step, a 3D model of the warehouse is formed based on overall dimensions, which can be adjusted at any time by entering new parameters. In the next step, the structure of the racks (storage places) is defined based on the width, length and height parameters of the racks as shown in the picture above. Within the same step, the warehouse is filled with pallets, which are displayed with the corresponding coordinate system in step 3. In this way, a complete three-dimensional view of the warehouse is formed, in which a number of parameters are implemented that can be exported to a table (step 4) and used in further calculations and simulations related to logistics. The entire procedure from the initial step to the final step is performed with the help of an application made in Matlab software.

In this way, the advantages of using alternative solutions for simple configuration of the design of the warehouse and storage space are demonstrated, as well as the possibility of forming different layout configurations, which contributes to the faster generation and acquisition of parameters related to the contents in the warehouse necessary for calculations of the movement of transport devices (crane, elevators or forklifts). Another of the advantages of the mentioned concept lies in the fact that there is no limit regarding the dimensions of the warehouse and the number of storage units, and the same can be applied to high-rack warehouses with a height of several tens of meters, as shown in the case studies [9].

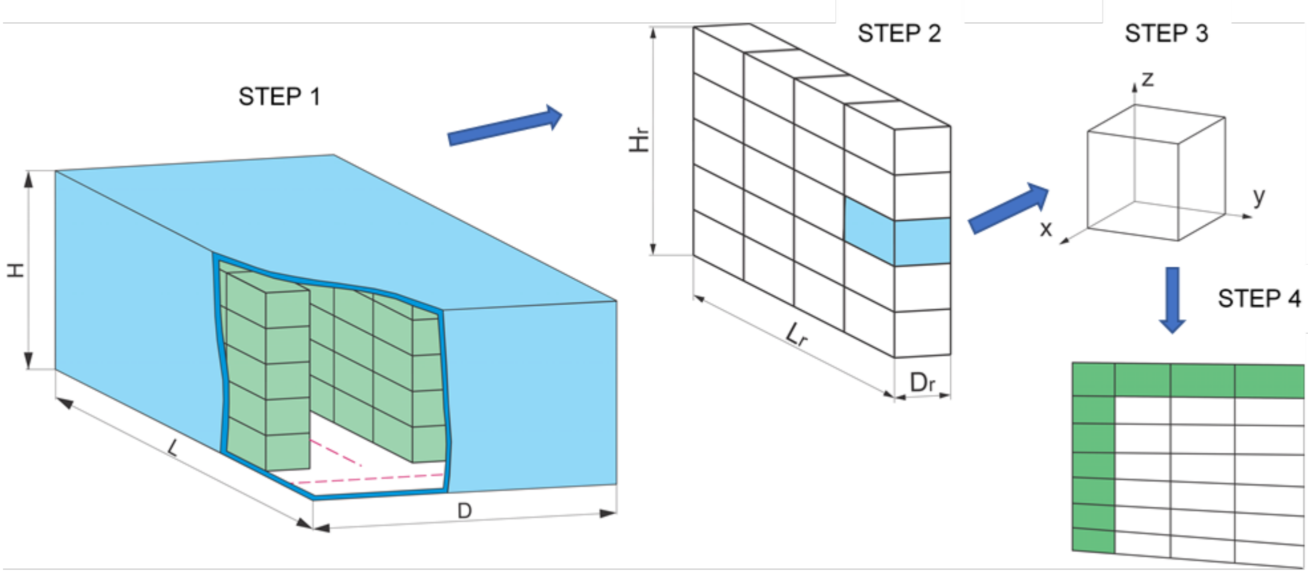

Figure 1: Schematic representation of the formation of the 3D model of the warehouse and obtaining the necessary parameters

3. MODELING OF WAREHOUSE TRANSPORTATION DEVICES

The transportation system of the described warehouse consists of a single shuttle which can travel only along a single dimension, and AS/RS devices which can transport the package along two axis. According to the illustration of the layout of the warehouse which is displayed in the figure 1, this transportation device occupies the corridor 1 and moves along the x axis. The AS/RS devices occupy corridors 2, 3 and 4, and they can move packages along y and z axis.

In this simulation, these transportation devices are idealized and constant velocity curves for all movements are assumed, meaning the acceleration times are neglected. The tasks that the transportation system of the warehouse have to perform are generated randomly, and only one task can be active at the time. These tasks cover the most common three operations that take place in a warehouse, and those are:

- a new pallet is brought to the warehouse and it needs to be transported to its storage unit where it should be stored;
- a pallet that is already stored within the warehouse needs to transported outside of the warehouse;
- a pallet that is already in the warehouse needs to be relocated to another storage unit.

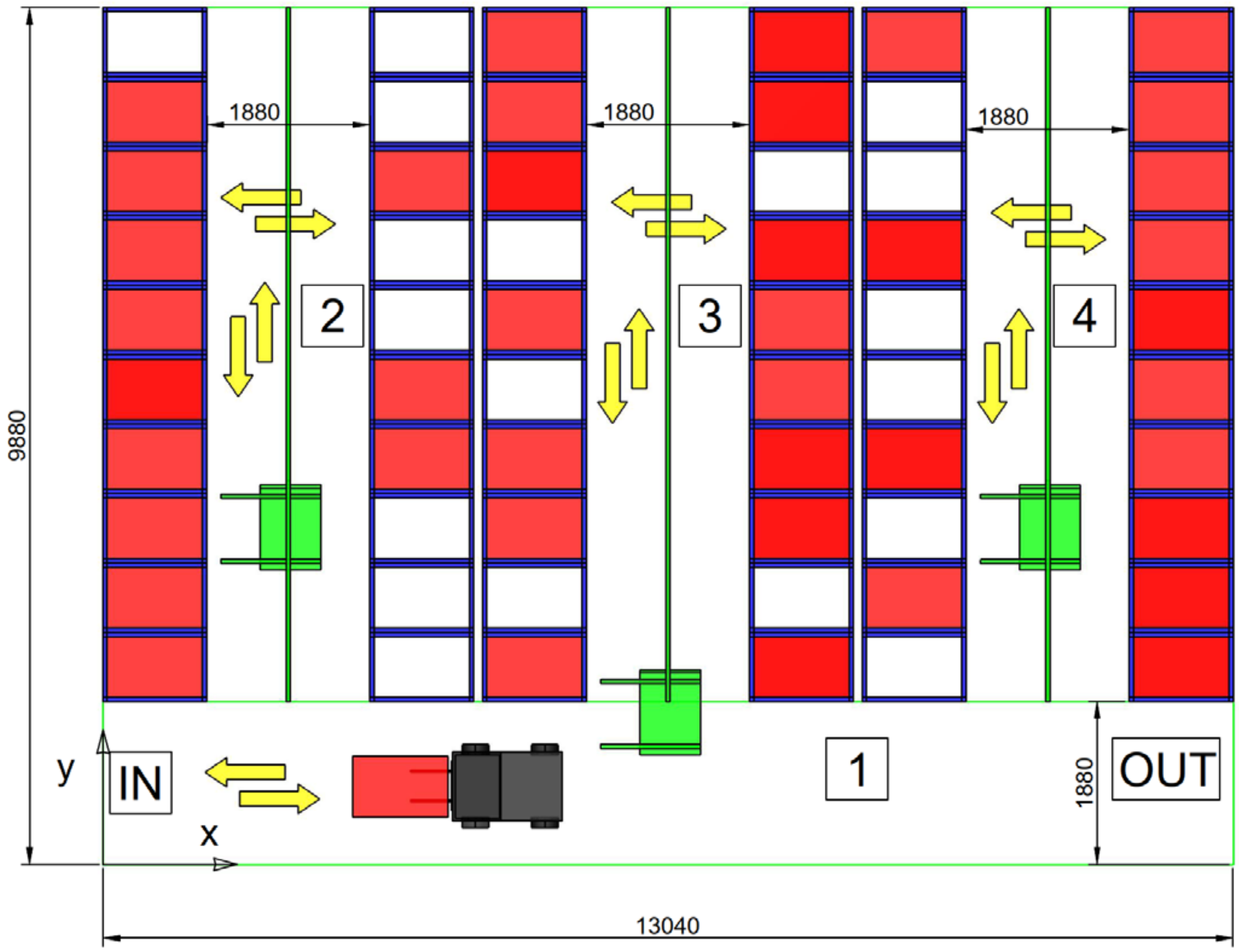

Figure 2: Illustration of the warehouse layout with marked corridors and possible directions of movement for the transportation devices in horizontal xy plane

After each task had been generated, the time needed for its completion t_i, $i=1,2,\ldots,m$ was calculated. Each operation consists of several actions. The operation of bringing a new pallet into its storage unit from the warehouse input point consists of the following actions:

- the shuttle in the corridor 1 travel from their current position x_{c1} to the warehouse input point x_{IN} with the velocity v_{x1}, the duration of this action is denoted as t_{i1}, and it can be calculated as follows:

$$t_{i1} = \frac{|x_{IN} - x_{c1}|}{V_{x1}} \tag{1}$$

- the shuttle picks the pallet up from the input point, the duration of this action is taken to be constant t_{i2}=5 s;
- the shuttle drives the pallet to the place the appropriate AS/RS device can pick it up x_r with the velocity v_{x1}, the duration t_{i3}:

$$t_{i3} = \frac{|x_{IN} - x_r|}{V_{x1}} \tag{2}$$

- the AS/RS device travels from its current position P_C (y_j, z_j), $j=2,3,4$ to the pallet P_i (y_i, z_i) where it is assumed the AS/RS device takes the shortest path s_{i4} between the two points, and the maximum velocities along the y and z axis are $v_{(y,max)}$, and $v_{(z,max)}$ respectively, so the duration of the action t_{i4} is:

$$t_{i4} = v_{y,\max}\left|\Delta y\right| + v_{z,\max}\left|\Delta z\right|; \quad \Delta y = y_i - y_j;\ \Delta y = z_i - z_j \tag{3}$$

- the AS/RS device takes the pallet by elongating its forks to the furthest end of the pallet x_{pe} and retracting them to their neutral position x_j with the velocity of v_{xj}, the duration of this action t_{i5} is:

$$t_{i5} = 2\cdot\frac{\left|x_{pe} - x_j\right|}{V_{xj}} + 5 \tag{4}$$

- the AS/RS takes the pallet to the storage unit location matching its y and z coordinate, the duration of this action t_{i6} can be calculated using the expression shown in (4), and the movement is being done under the same assumptions;

- the AS/RS deploys the pallet within the storage unit by extracting its forks, lowering them a bit, and then retracting them back to their neutral position along the x axis with velocity v_{xj}, and the duration of this action t_{i7} can be calculated using the expression (5).

With the task completed, the completion time for the task represents the sum of the mentioned durations [10]:

$$t_i = \sum_{k=1}^{n=7} t_{ik} = t_{i1} + t_{i2} + t_{i3} + t_{i4} + t_{i5} + t_{i6} + t_{i7} \tag{5}$$

The operation of taking the pallet out of the warehouse through the warehouse output point is similar to previously described operation, only the actions are being done in reversed order, so the (1)-(5) equations can be used for the task duration calculation. Moving the pallet within the warehouse has two variations: moving the pallet within the single corridor, and moving the pallet between corridors. The first variation is simpler because it employs only one AS/RS device, and the required actions are:

- the AS/RS device travels from its current position to the position of the pallet that needs to be moved, the duration of this action can be denoted as t_{i1} and it can be calculated with (3);
- the AS/RS device elongates its forks in order to pick up the pallet from the storage unit after which it retracts its forks to neutral x position, the duration of this action t_{i2} can be calculated with (4);
- the AS/RS device travels with the pallet to the new storage unit matching its y and z coordinates, the duration of the action is t_{i3} and it can be calculated as (3);
- the AS/RS device puts the pallet into its new storage unit, and retracts its forks to their neutral x position, this action takes t_{i4} time which can be calculated with (4).

The second variation employs two AS/RS devices and shuttle for moving the pallet between the corridors, so the time it takes to complete the task consists of more action durations. However, these durations can all be calculated using the expressions (1-4), and these durations are:

- t_{i1} – the time it takes for the AS/RS device to travel from its current position to the pallet that needs to be relocated;
- t_{i2} – the time it takes for the AS/RS device to take the pallet from its storage unit and put it in neutral x position;
- t_{i3} – the time it takes for the AS/RS device to travel with the pallet to the place where the shuttle can take the package;
- t_{i4} – the time it takes for the empty AS/RS device to return to its neutral position;
- t_{i5} – the time it takes for the shuttle to get to the pallet from its current position;
- t_{i6} – the time it takes for the shuttle to load the pallet;
- t_{i7} – the time it takes for the shuttle to travel with the pallet to the proper corridor;
- t_{i8} – the time it takes for the shuttle to unload the pallet;
- t_{i9} – the time it takes for the new AS/RS device to travel to the coordinate of the pallet from its current position;
- t_{i10} – the time it takes for the AS/RS device to load the pallet;
- t_{i11} – the time it takes for the AS/RS device to travel to new, empty storage unit;
- t_{i12} – the time it takes for the AS/RS device to unload the pallet to the storage unit and retract its forks to the neutral position.

In this case, the time it takes to accomplish this task, according to (5) can be calculated as:

$$t_i = \sum_{k=1}^{n=12} t_{ik} = t_{i1} + t_{i2} + \ldots + t_{i11} + t_{i12} \tag{6}$$

The average duration time for m completed operations T_{avg} can be then calculated by:

$$T_{avg} = \frac{\sum_{i=1}^{n} t_i}{m} \tag{7}$$

The second variation of pallet relocation in this simulation only happens when the racks sharing the same corridor are more than 70% full.

4. RESULTS

The parameters of the members of the transport system with the corresponding values used in the warehouse simulation according to illustration presented on Fig. 2 are shown in Table 1. The transport unit under number 1 represents a shuttle that moves only along the x axis, while with the numbers from 2 to 4 are marked stacker cranes used for transport of pallets in the indicated corridors along all three axes (x, y, z).

Table 1: Velocities of transport units in warehouse

Transport unit No.	v_x [m/s]	v_y [m/s]	v_z [m/s]
1	0.1	-	-
2	0.2	0.2	0.2
3	0.2	0.2	0.2
4	0.2	0.2	0.2

The results of the simulation are visualised using graphs in Fig. 3 with corresponding values for several important parameters such as average task duration, average input/output time and average pallet relocation time.

From the graph for average pallet relocation time, it can be concluded that the sudden change after 800 completed tasks is a consequence of that before this change, pallets were moved only through corridor 2 using stacker crane. After that, when the occupancy of racks reach 70%, relocation of pallets is done between corridors 2-4, using the relation stacker crane- shuttle-stacker crane.

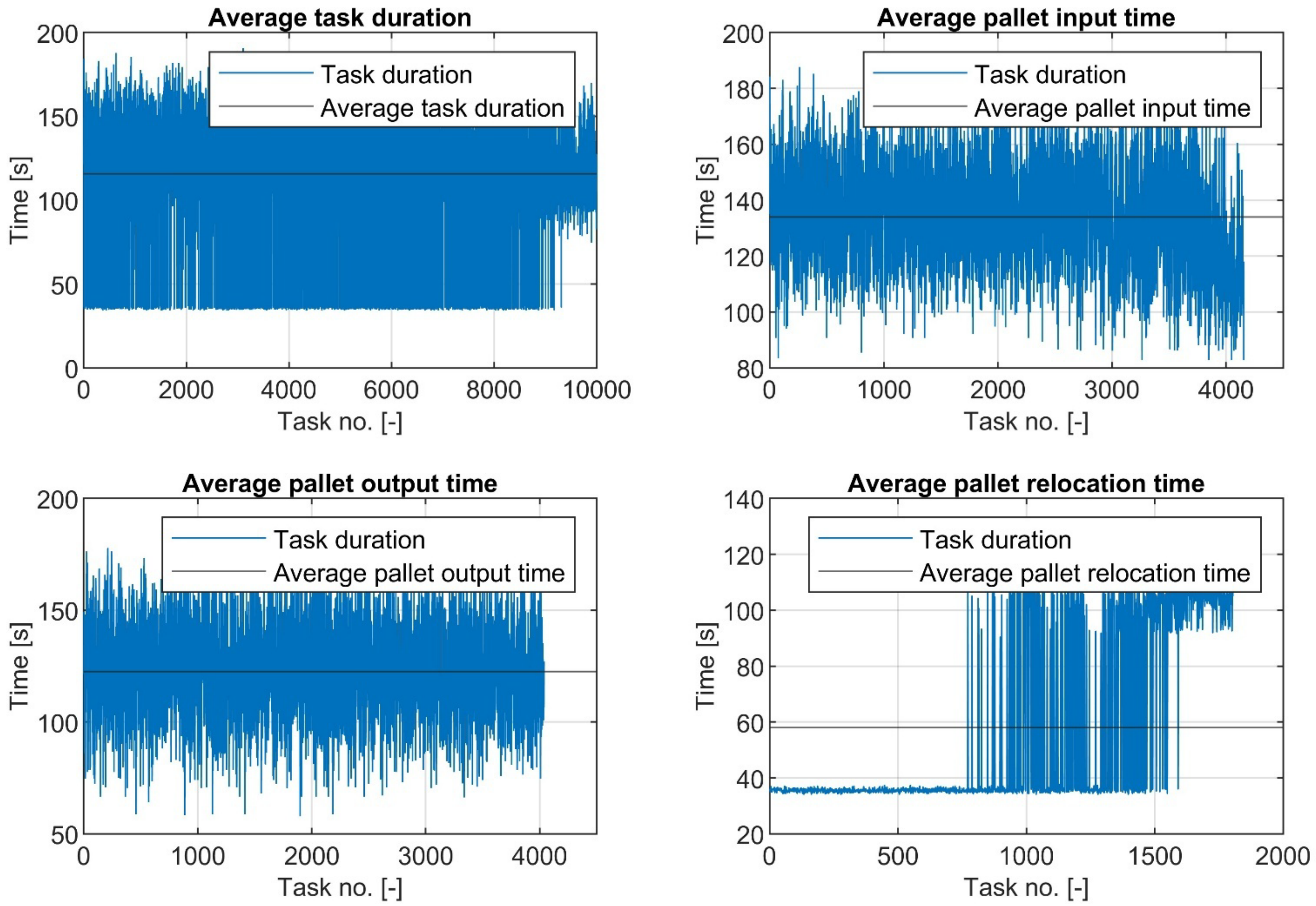

Figure 3:Graphs of simulation with corresponding values

From the graphs shown in Figure 3, the mean values of the duration time for the above-mentioned parameters can be read as well as obtained explicitly as a result of the simulation. The values of these parameters are:

Average task duration time = 115.6536 [s]
Average pallet input time = 133,9905 [s]
Average pallet output time = 122,5585 [s]
Average pallet relocation time = 57,9759 [s]

Using a random arrangement inside the warehouse, it was observed that the number of manipulative operations inside the warehouse (out of a total of 10000 in the list) is as follows:

Total number of input operations = 4157
Total number of output operations = 4038
Total number of relocation operations = 1805

5. CONCLUSION

This paper describes a tool that can be used for efficiency assessment of the automated AS/RS warehouse material handling system as a part of the internal logistic chain. The model and the simulation connect different kinds of devices with their unique characteristics, where the output from the simulation can indicate how these devices function within the observed system allowing the designers of the warehouses to see where bottlenecks are, and what and in which way should be changed in order to obtain the optimal solution either by changing the layout or picking the material handling equipment with different characteristics. Considering the way the parameters of the warehouse were modelled and the way the simulation is being done, it can also be used together with other tools such as metaheuristic biology inspired optimization algorithm.

The focus of further research in this area will be on the attempt to incorporate some of the biologically-inspired optimization methods for solving wide range of engineering problems, all with the aim of obtaining the best possible simulation results [11 ,12].

ACKNOWLEDGEMENT

This work has been supported by the Ministry of Science, Technological Development and Innovation of the Republic of Serbia, through the Contracts for the scientific research financing in 2023, 451-03-47/2023-01/200108 and 451-03-47/2023-01/200156.

REFERENCES

[1] M. Hompel , T. Schmidt, “Warehouse Management - Automation and Organisation of Warehouse and Order Picking Systems”, Springer Berlin, Heidelberg (Germany), (2006)

[2] T. Lerher,I. Potrc, M. Šraml and T. Tollazzi, “Travel time models for automated warehouses with aisle transferring storage and retrieval machine,” Eur. J. Oper. Res., Vol. 205, pp. 571–583, (2010)

[3] D.J. Muller, “AS/RS And Warehouse Modeling”, 1989 Winter Simulation Conference Proceedings”, Washington, DC, USA, 4-6 December 1989, pp. 803-810, (1989)

[4] R. Manzini, M. Gamberi and A. Regattieri, “Design and control of an AS/RS,” Int. J. Adv. Manuf. Technol., Vol. 28, pp. 766–774, (2006)

[5] J. P. Gagliardi, J. Renaud and A. Ruiz, “Models for automated storage and retrieval systems: a literature review,” Int. J. Prod. Res., Vol. 50(24), pp. 7110-7125, (2011)

[6] G. D’Antonio, M. D. Maddis, J. S. Bedolla, P. Chiabert, F. Lombardi, “Analytical models for the evaluation of deep-lane autonomous vehicle storage and retrieval system performance,” Int J Adv Manuf Technol., Vol. 94, pp. 1811–1824, (2018)

[7] S. S. Heragu, X. Cai, A. Krishnamurthy and C. J. Malmborg, “Analytical models for analysis of automated warehouse material handling systems,” Int. J. Prod. Res., Vol. 49(22), pp. 6833-6861, (2011)

[8] https://www.mecalux.com/pallet-racks/clad-rack-warehouses

[9] T. Lerher and I. Potrc, “The Design and Optimization of Automated Storage and Retrieval Systems,” Stroj. Vestn./J. Mech., Vol. 52(5), pp. 268-291, (2006)

[10] Đ. Zrnić, D. Savić, “Simulacija procesa unutrašnjeg transporta”, Mašinski fakultet, Beograd (Srbija), (1987)

[11] G. Miodragović, M. Bošković and R. Bulatović, “The application of metaheuristic algorithms in multi-objective optimization of engineering problems,” Engineering Today., Vol. 1(3), pp. 7-15, (2022)

[12] G. Pavlović, B. Jerman, M. Savković, N. Zdravković and G. Marković, “Metaheuristic Applications in Mechanical and Structural Design,” Engineering Today, Vol. 1(1), pp. 19-26, (2022)

Framework and reasonableness of applicating the concept of crane structural health monitoring in inland water harbours

Atila Zelić[1*], Ninoslav Zuber[1], Dragan Živanić[1], Mirko Katona[1], Nikola Ilanković[1]
[1]Faculty of Technical Sciences, University of Novi Sad, Serbia

This paper concisely describes the recent research carried out regarding the harbour portal slewing crane GANZ. The research was realised to develop a simple yet efficient approach to assessing the condition of old cranes in exploitation. It will also be used for the implementation of more complex and more advanced systems of monitoring the condition of not only cranes but other machines as well. The results of measurements and testing are presented with brief comments. Even though the mentioned research has been carried out with limited technical and financial possibilities, the acquired experiences and analyses collected from the preliminary results have confirmed the significance of this approach, which may also further develop in the future.

Keywords: cranes, structural health monitoring, vibration analysis, stress-strain states

1. INTRODUCTION

The process of observing certain construction or mechanical structure state and detecting the arisen damages during its usage is today known as *Structural Health Monitoring* (*SHM*). During the last two decades, intensive development of various SHM systems has been noticed, and such systems are already in extensive use for bridges, towers, airplanes, wind generators, mining, and transporting machines [1, 2, 4, 6, 7, 8]. Cranes belong to the last mentioned machine group since they are exposed to various dynamic loadings due to transporting load effects, as well as environmental influences in the course of their operation.

Integration of SHM systems into the crane structure and its facilities is of special importance for cranes operating in heavy industries (iron, steel, casting plants, etc.), nuclear plants, dangerous material plants, etc. However, the carried out research indicates the ever more increasing importance of crane condition monitoring (especially container cranes) in high seaports with intensive traffic, due to ever more growing shipment quantities in world logistic flows [3, 5, 9, 10]. Apart from that, activities in the field of inland water traffic revitalisation in the region of South-East Europe recognise the importance of the Danube harbours in the scope of European logistic chains. An enlarged quantity of goods in inland water traffic demands reliable harbour mechanisation, able to perform cargo ships loading and unloading as fast as possible. In such circumstances, even a minor failure on a crane can cause hours-long (and often even days-long) interruptions in ship attending, resulting in very high time and money losses. Aiming to eliminate these undesired consequences of crane failure in the course of its intensive operation, the implementation of a permanent monitoring system on harbour cranes (especially in harbours with intensive traffic) is of the utmost importance.

In the first part of the paper, the problem area of the crane SHM in inland water harbours is described, and a short survey of crane structure condition monitoring relevant parameters is given. The basic structure of a harbour crane monitoring system (developed within the scope of the research project TR 35036 *Application of IT in harbours of Serbia – from machines monitoring to the network system of EU environment*) in the harbour of Novi Sad is presented. The system was applied to the harbour portal slewing crane *GANZ* (max. capacity 27.5 t, Fig. 1).

Figure 1: Harbour portal slewing crane GANZ

Parameters that have to provide enough information on crane condition and operating regime, have been chosen on the basis of a study concerning relevant structure points and driving mechanism components, as well as a corresponding plan of measurements. Stress state in crane lower structure members, force in grab hoisting and closing wire ropes, as well as vibrations of bearings in grab hoisting and closing and slewing mechanisms were surveyed during operation.

In the second part of the paper, insight is given into certain results as well as the featured importance of SHM system usage on harbour cranes.

*Corresponding author: Trg Dositeja Obradovića 6, Novi Sad; zelic@uns.ac.rs

2. A BRIEF DESCRIPTION OF RESEARCH

2.1. The description of systems for identifying and testing vibrations

The basic cause of vibration testing is the insight into the nature of vibration of chosen components of crane drive mechanisms. Generally speaking, when it comes to assessing the condition of mining machines, cranes, or similar equipment for material handling, one should gravitate towards a concept of online monitoring of drive mechanisms (and steel structure), integration of used tracking technologies and collecting the required or relative parameters into one, unique information system.

The vibration is tested in two mechanisms. One is the slewing mechanism and the other is the grab hoisting mechanism in start-up periods and during stationary work. The portable vibration data collector and analyser *OneproD Falcon* were used in the research with additional software packages *OneproD* and *Vibgraph*, as well as *IEPE* accelerometers type *ASH201*.

For the sake of illustration, there is a presentation later in the paper, of vibration testing in both previously mentioned mechanisms. The absolute vibration is measured on the selected bearing housings in three mutually orthogonal directions. The simultaneous recording of vibration in all three directions is done to record the relative phase between vibrations in different directions.

The labels of measuring points on the grab hoisting mechanism are presented in Figure 2, while Figure 3 presents the measuring points on the crane rotation mechanism.

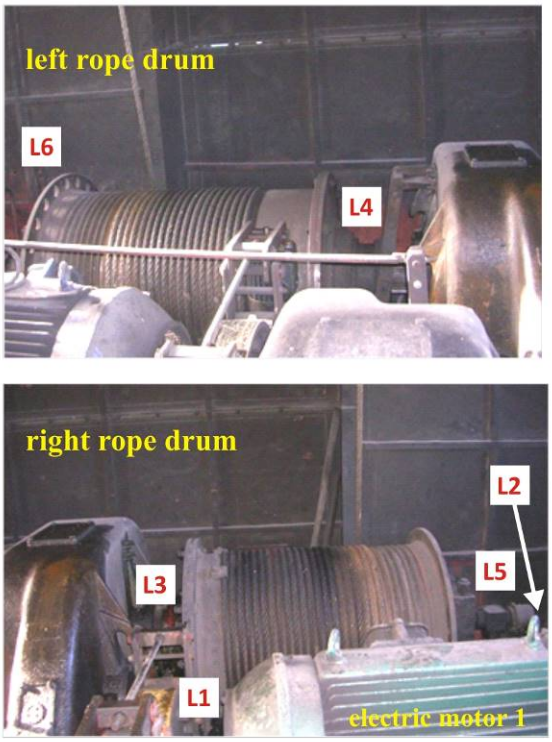

Figure 2: Overview of measuring points (grab hoisting mechanism)

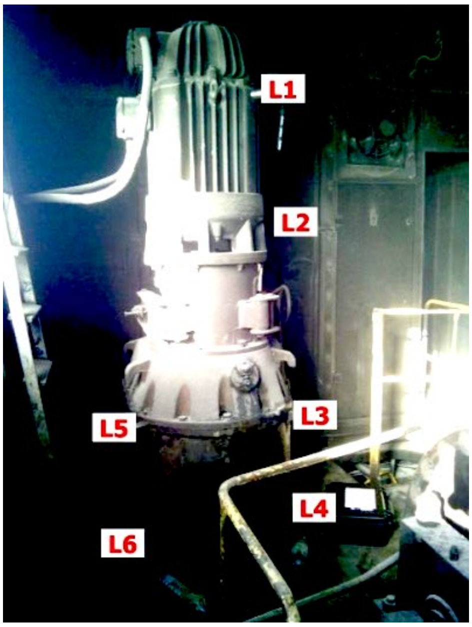

Figure 3: Overview of measuring points (slewing mechanism)

2.2. Measuring wire ropes forces and stress-strain behaviour monitoring of crane structural members

It is well-known that in order to calculate fatigue strength in the phase of crane design and assessment of residual life, (e.g. of steel wire rope or vital members of steel structure) it is necessary to know the loading spectrum. Adequate assessment of the loading spectrum which occurs when lifting the load is most important. This research measures wire rope force values (ropes for lifting and closing the grab, see Fig. 5).

For the purpose of these measurements, force transducers were designed, produced, and calibrated in the accredited laboratory (Fig. 4).

Figure 4: Force transducer calibration

Figure 5: Positions of wire ropes forces transducers

The wireless transmission of signal from force transducers to the crane computer is established using telemetry technology via transmitter units *T24-ACMi-SAf* on force transducers, receiver module *TC24A01*, *receiver unit* TC24BSu, and software T24LOG24.

The data of stress values in certain elements of crane steel structure was recorded by tensiometry measurements using strain gauges. The signal transmission from strain gauges to universal amplifiers *Spider 8* was established using cables, while the software *catmanEasy* and *nCode* were used for data recording and processing. In Figure 6, strain gauges are applied to the bottom flange plate, of the portal used for suspending the rotary column of the crane.

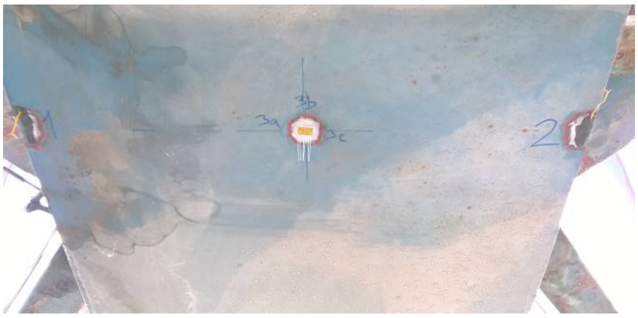

Figure 6: Strain gauges applied to the bottom flange plate

Simultaneous tracking of the stress in several points of portal structure, rotating angles of the rotating platform using incremental encoder, and the boom position angle using the inclinometer establish collecting more data as well as providing detailed analysis of the participation impact of various parameters.

3. RESULTS

Numerous results have been collected after the research. For example, the results regarding vibration examination consist of approximately 140 pages, since the data is registered to 18 measuring points in three orthogonal directions. It is clear that this paper cannot present all results, therefore it consists of the ones which were chosen specifically to illustrate the previously mentioned research.

Firstly, some results are presented in a shorter time interval, on measuring points L1 on the grab hoisting mechanism and L2 on the slewing mechanism. In each following figure (from Fig. 7 to Fig. 12) there is a time history of acceleration, overall acceleration trend, and sonogram.

Figures 7, 8, and 9 refer to the grab hoisting mechanism drive and the measuring point L1 (see Fig. 2).

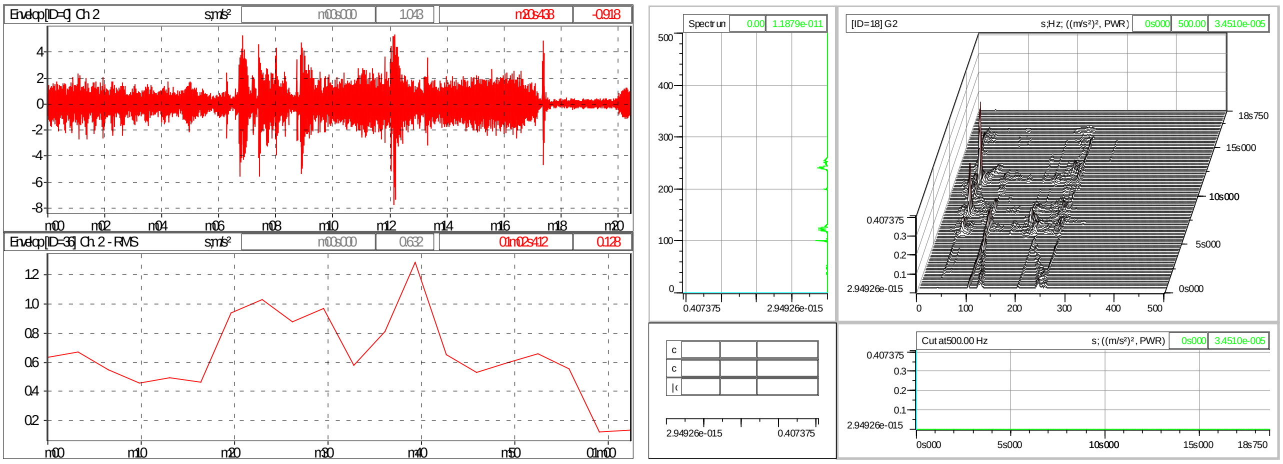

Figure 7: Time history of acceleration, overall acceleration trend, and sonogram for the direction of vibration (radial, horizontal)

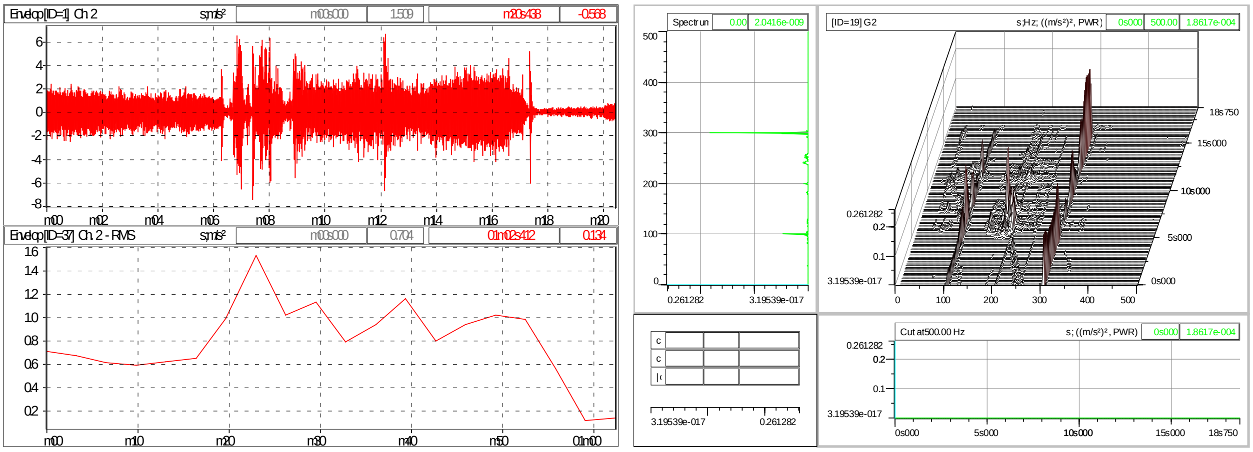

Figure 8: Time history of acceleration, overall acceleration trend, and sonogram for the direction of vibration (radial, vertical)

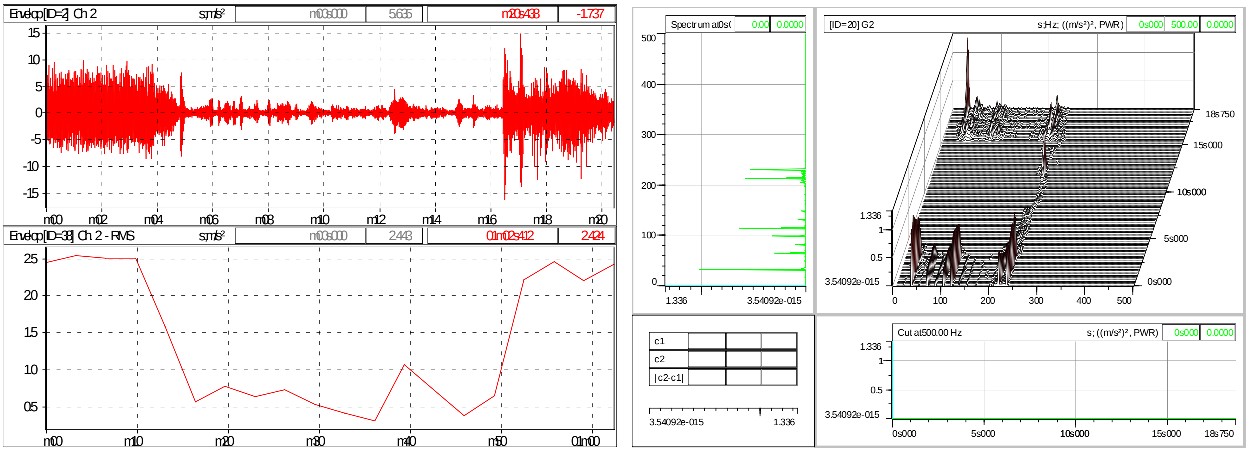

Figure 9: Time history of acceleration, overall acceleration trend, and sonogram for the direction of vibration (axial, referring to the electric motor shaft, horizontal)

The following Figures 10, 11, and 12 refer to the slewing mechanism and measuring point L2 (see Fig. 3) which is located at the place where the electric motor is coupled with the gearbox.

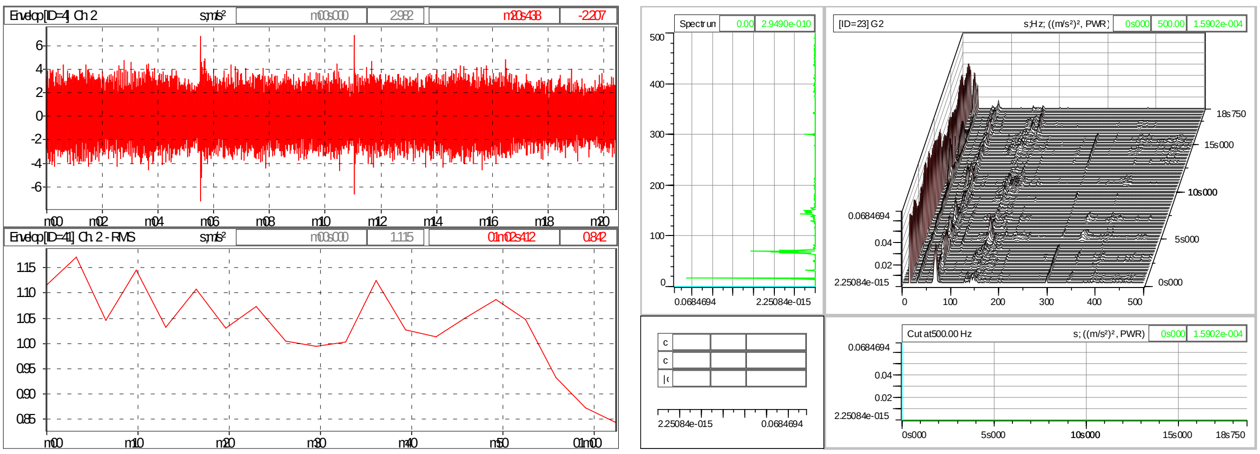

Figure 10: Time history of acceleration, overall acceleration trend, and sonogram for the direction of vibration (radial in reference to the gear ring of slewing mechanism, horizontal plane)

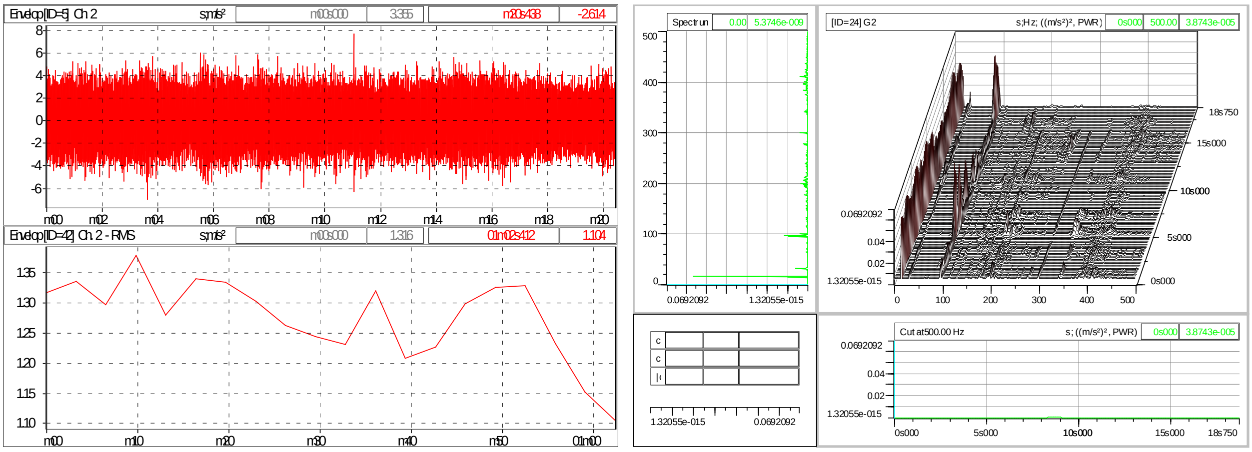

Figure 11: Time history of acceleration, overall acceleration trend, and sonogram for the direction of vibration (tangential in reference to the gear ring of slewing mechanism, horizontal plane)

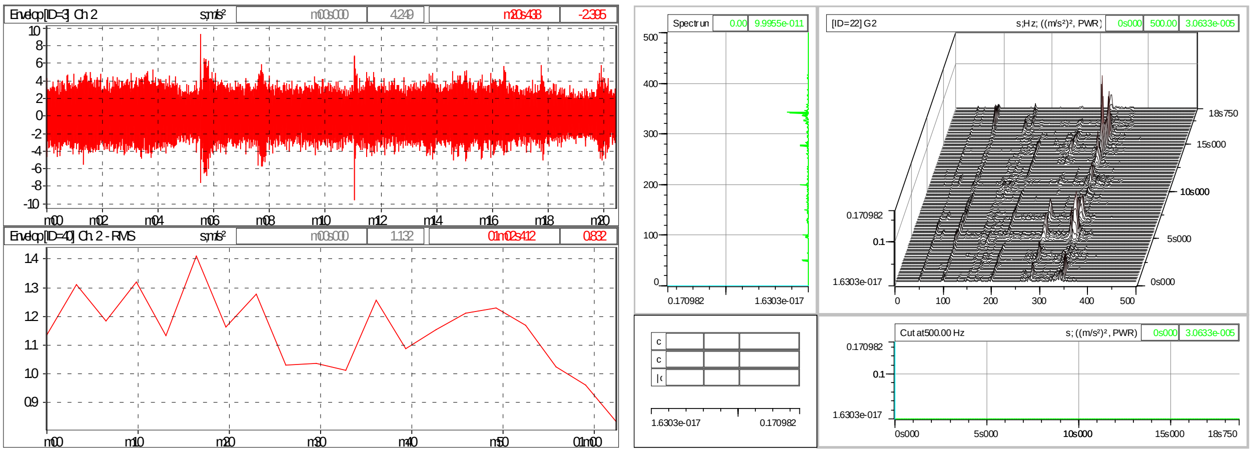

Figure 12: Time history of acceleration, overall acceleration trend, and sonogram for the direction of vibration (axial, vertical in reference to the gear ring mechanism rotation plane)

With a detailed analysis of all results of the research, it has been determined that the vibration levels are in a tolerance zone defined by the standard ISO 10816. However, the nature of signals as a consequence of the operating mode of the examined mechanisms indicates the following:

- The signals are significantly variable when it comes to the level of amplitude. Therefore, the usual procedure of tracking and recording vibration signals is not satisfactory for the examined crane.
- To assess the condition of mechanism components more adequately, along with recording the vibration signal there should also exist simultaneous and continuous following of the operating speed of the driving system. Besides tracking certain parameters, the identification of various operating modes of the examined machine, especially for its clear dynamic occurrences during the operation of harbour cranes, is of significant importance. This certainly requires more complex technically-informational monitoring systems than the solutions that were described in this paper. The justification for applying more complex systems on harbour cranes should be carefully analysed for each individual case.

The collected data about the load and stress time history was used upon examination of dynamic phenomena which follow the operation of cranes and can also serve for the analysis of fatigue of crane steel structures (only if there is continuous monitoring during longer periods of time).

Considering the condition of the examined half-a-century-old crane, its gaps between the worn-out parts, etc., and heavy working conditions, the measuring signals kept unwanted nuisances such as noises. For that reason, it was necessary to additionally process results (filtering unwanted noises and removing insignificant time history), which were renewed in the software packet *nCode Glyphworks*. In Fig. 13 there is a rainflow analysis of the stress time history in direction “b” (see Fig. 6), which is implemented to gain specific stress spectrum. However, since the two preliminary measurements were done in a slightly short period, the collected data, in this case, is not representative enough to analyse the material fatigue of the examined crane structural members. The volume of the described research has made it possible to track stress-strain states of structure in just a few measuring points. More advanced engineer analyses, to track eventual fatigue crack propagation, would demand applying increasingly more strain gauges on critical points on the crane steel structure. For example, it is interesting to mention that the stress value in measuring points of the bottom flange plate from Fig. 6 was 40÷50 MPa, confirming the crane's over-dimensioned structure.

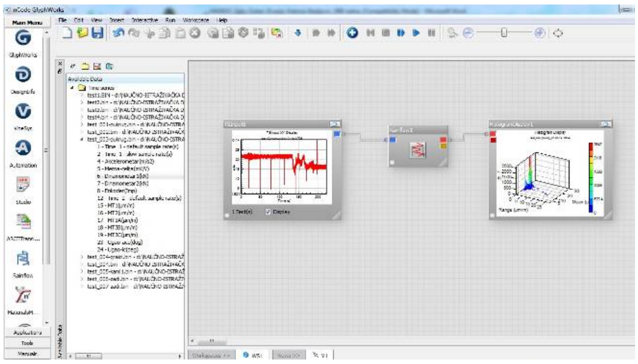

Figure 13: Rainflow analysis (software nCode Glyphworks)

It has to be accentuated that the implementation of corresponding sensors for the relevant parameters monitoring and structure condition, together with the elements for data acquisition, transfer, storage, and processing, is of utmost importance in the course of designing and manufacturing new cranes. However, the implementation of similar SHM systems also on aged cranes (the average age of cranes in inland water harbours is over 40 years!) can be very useful. In the course of the exploitation period from crane design, some operation conditions of these cranes and working tasks and demands (especially in harbours with intensive traffic) have been significantly altered. In such cases, failures are going to arise more often, structure deterioration becomes ever more intensive, and crane lifetime becomes drastically reduced.

In the end, Fig. 14 illustrates all benefits that could be offered by an adequate SHM system, integrated into the structure of the harbour crane. The recognition of the importance that this system has, as well as other more advanced solutions, has helped the experiences that were gained throughout the research to be presented in this paper.

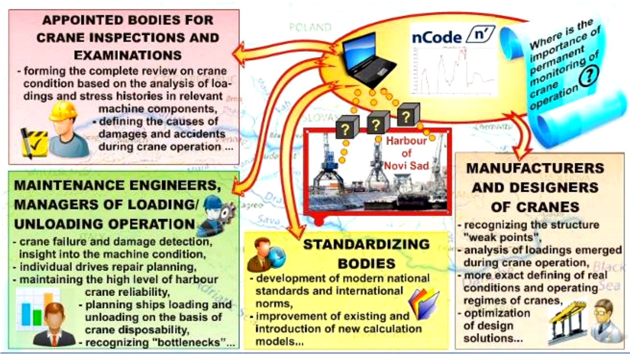

Figure 14: Importance of harbour crane SHM

4. CONCLUSION

The research described in this paper has been realised with limited technical possibilities, but still to a degree it contributes to the development of new trends in the monitoring of machine conditions. The importance of this can also be recognised in such a way where experimental research hasn't been carried out based on a laboratory or a simplified model but on a real crane in exploited conditions. Although the more complex systems of monitoring mechanisation conditions in the previously mentioned harbour to this day haven't been realised to the fullest, as far as the author's knowledge is in question, the previously described and partly executed measurements can serve as a base for further development of contemporary solutions and methods of tracking crane condition in other inland water harbours. The computer analysis of vital structural members fatigue and the remaining crane lifetime requires knowledge of the real service class, the operating mode, and assessment of representative spectrum of loads/stresses. When speaking about computer simulations, which also demand detailed knowledge of a great number of parameters, often of stochastic character, only experimental examination can provide more reliable and more legitimate results. Even though continuous monitoring conditions represent an additional expense for users of these machines, in inland water harbours, where the traffic is extreme, they are more often than not necessary for gaining a high level of reliability. The experience gained from these examinations will serve for further improvement of the basic concept of monitoring crane conditions in inland water harbours in the future, and also for finding efficient ways of networking more complex surveillance harbour systems e.g. for notifying alarming situations (interruption of work due to electric motor overload or exceeding the maximum permitted wind speed and so on).

ACKNOWLEDGEMENTS

This paper presents the results of preliminary experimental research which was realised through project TR 35036 (Application of IT in harbours of Serbia – from machines monitoring to the network system of EU environment), as well as the research results regarding project no. 451-03-47/2023-01/200156 "Innovative scientific and artistic research from the FTS (activity) domain" which was funded by the Ministry of Science, Technological Development, and Innovation.

REFERENCES

[1] W. Ostachowitz and J.A. Güemes, "New Trends in Structural Health Monitoring", Wien (Austria), (2013)

[2] C. Boller, F.-K. Chang and Y. Fujino, "Encyclopedia of Structural Health Monitoring", John Wiley & Sons, Chichester (England), (2009)

[3] W. Zhixin, H. Xiong and C. Zhaoneng, "Study of Remote Condition Monitoring and Assessing on Quayside-Container-Cranes", Proceedings of the 1st World Congress on Engineering Asset Management (WCEAM), pp. 898-903, (2006)

[4] Y. Chang, "Fatigue Life Evaluation of a Grab Ship Unloader", China Steel Technical Report, Vol. 23, pp. 36-41, (2010)

[5] B. Depale and M. Bennebach, "Residual life of steel structures and equipment: problems and application to cranes" Mechanics & Industry, Vol. 20, p. 802, (2019)

[6] X. Li, W. Liu and K. Xu, "Research of On-line System of Structure Health & Safety Monitoring and Warning for Cranes (SHSMW)", Applied Mechanics and Materials, Vol. 330, pp. 450-453, (2013)

[7] N. Li, Z. Wang and K. Ding, “Research of structural health monitoring system for the crane based on wireless strain sensors”, Applied Mechanics and Materials, Vol. 330, pp. 437-440, (2013)

[8] W. Meng and T. Hong, “Design of Stress Monitoring and Safety Assessment System for Crane Metal Structure Based on Virtual Instrument”, Applied Mechanics and Materials, Vols. 152-154, pp. 1492-1497, (2012)

[9] M. Xu, J. Ni and G. Chen, “Research on the Wireless Monitoring System for Port Crane Structure Stress”, Applied Mechanics and Materials, Vols. 278-280, pp. 920-923, (2013)

[10] H. Guojian, W. Donghui, W. Xinhua and H. Zhenyu, “Study on Crane Structural Health Monitoring and Early Warning Expert System”, Applied Mechanics and Materials, Vols. 774-776, pp. 1586-1590, (2013)

Measuring the kinematic characteristics on a reduced-size zipline model

Tanasije Jojić*, Jovan Vladić, Radomir Đokić
Faculty of Technical Sciences, University of Novi Sad, Serbia

This paper gives an overview of the procedure for creating a computational zipline model, as a basis for making an experimental model with adjusted geometric characteristics in relation to the real system. Since it is not possible to satisfy the geometric similarity between all sizes of the real zipline and the experimental zipline model, the model can be formed so that it has the same inclination angle and the same deflection ratio in the loaded and unloaded state compared to the real one. The kinematic characteristics are later measured by appropriate small-sized sensors, for example, such as those which are foreseen for Arduino. Additionally, the measured characteristics can be compared with the calculated values.

Keywords: Zipline, Kinematic Characteristics, Similitude, Measurement

1. INTRODUCTION

In this paper the development of a reduced zipline model is presented. This model can then be used for the validation of the computational model and comparison with the real zipline in accordance with the theory of similitude [1-6].

In general, it is not possible to make a model in a certain geometric scale. For example, a real zipline has a span of about 1.5 kilometres whereas rope with a diameter of 16 mm was used, [7-9]. The reduced-size zipline model could be about 5 meters long, and the smallest diameter of the rope that can be found in regular production is about 1 mm. Therefore, the modelling of the zipline was approached, which met the condition that it has a similar angle of inclination, as well as that the ratio of deflection in the loaded and unloaded state of the model is identical to the ratio of deflection on the real zipline.

After that, the measurement of kinematic characteristics was made.

2. MODEL DESCRIPTION

Fig. 1 shows the lower station of the model, on which an aluminium frame (1), a steel rope (2), a redirection pulley (3) and a tension weight (4) can be seen.

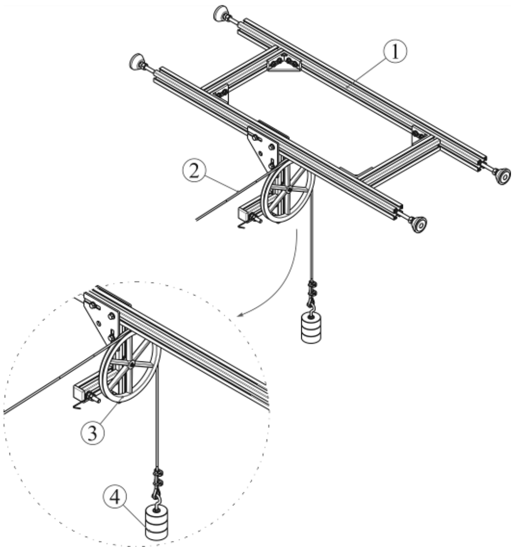

Figure 1: Model of the lower station with redirection pulley and tension weight

The field span can be varied from 4.6 to 5.1 m, while the drop can be varied from 0 m to 1.8 m. That means that the inclination angle can be adjusted from 0 to 20 degrees.

The experiments are planned to be performed on 6x7 rope construction with a fibre core with a diameter of 2 mm, 3 mm and 4 mm which are shown in Fig. 2.

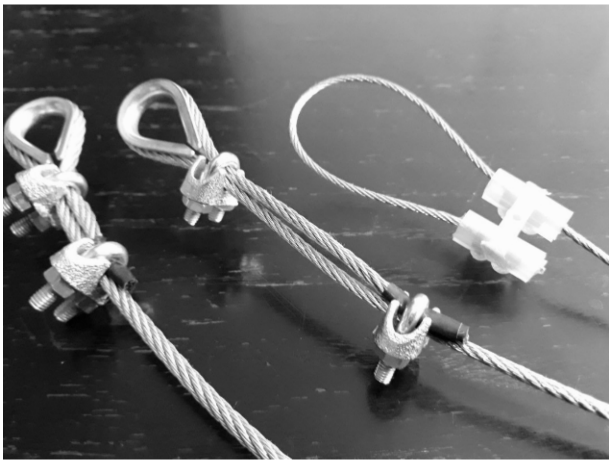

Figure 2: Wire ropes (left to right 4 mm, 3 mm and 2 mm)

The redirection pulley is made by 3D printing to have as little mass and moment of inertia as possible, and thus have minimal impact when changing the movement direction. In order to ignore the friction in the pulley bearings, the ratio of the mean bearing diameter and the nominal pulley diameter must be greater than 10. The nominal pulley diameter has been adopted as 160 mm, while the outer diameter of the W 639/3 bearing is 8 mm and the inner 3 mm. In that case the mean diameter of the bearing amounts to:

$$d_{mean} = \frac{d_{outer} + d_{inner}}{2} = \frac{8+3}{2} = 5.5 \text{ mm} \tag{1}$$

so the mentioned ratio is:

$$\frac{D_{pulley}}{d_{mean}} = \frac{160}{5.5} \approx 29 \tag{2}$$

which is enough to ignore the bearing friction. The redirection pulley model is shown in Fig. 3.

*Corresponding author: Trg Dositeja Obradovića 6, 21000 Novi Sad, Serbia, tanasijejojic@uns.ac.rs

Figure 3: Geometrical model (left) and 3D printed sample (right) of the redirection pulley

Fig. 4 shows the redirection pulley mounted to the lower station and tensioned with counter-weight.

Figure 4: Redirection pulley mounted to the lower station

Fig. 5 shows bearings for the redirection pulley and trolley wheel as well as rope fastener clamps and thimbles.

Figure 5: Bearings for redirection pulley and trolley wheel (left) and rope fastener clamp and thimble (right)

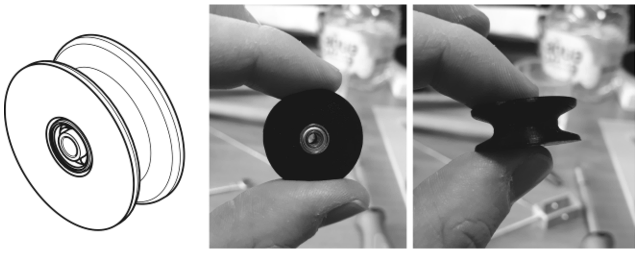

Figure 6: Geometrical model and a fabricated sample of the wheel

The geometric model and appearance of the 3D printed sample of the wheel are shown in Fig. 6, while the geometric model and appearance of the trolley can be seen in Fig. 7. The trolley wheel (Fig. 7, pos. 2), like the redirection pulley, was obtained by the 3D printing process. The wheel has an outer diameter of 26 mm and a rolling diameter of 16 mm. Since identical bearings are installed in the wheel as in the pulley, this means that the condition that the diameter of the wheel has to be 10 times greater than the mean diameter of the bearing in order to neglect bearing friction is not met. This means that existing expressions for calculating the rolling resistance coefficient can not be used. The rolling resistance coefficient must be determined for each rope and wheel individually.

The frame of the trolley (Fig. 7, pos.1) is made of a rectangular aluminium tube in which a threaded rod (Fig. 7, pos. 3) is attached from below, on which a part of the measuring equipment is attached and, if necessary, additional weight. The total weight of the empty trolley is 29 g.

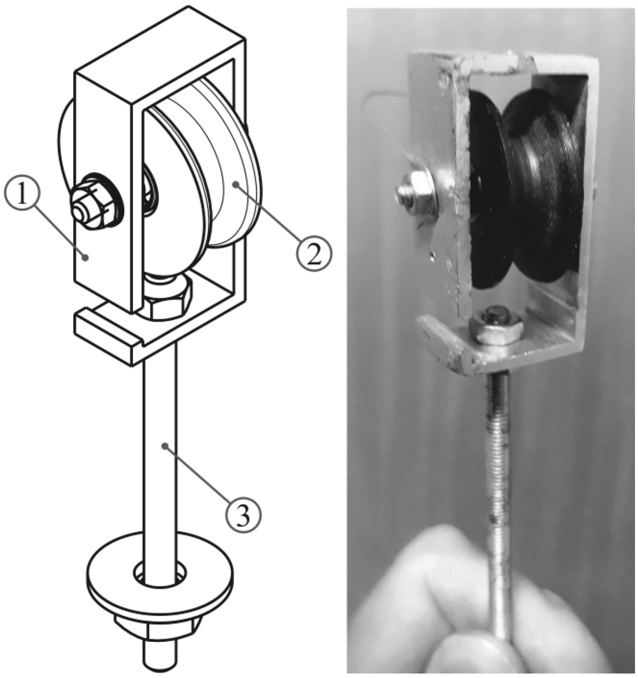

Figure 7: Geometrical model (left) and fabricated sample (right) of the trolley

3. MEASUREMENT EQUIPMENT

The measurements were performed using the LiDAR TFmini sensor, which is shown in Fig. 8 and Arduino UNO and Arduino MEGA microcontrollers, [10, 11].

LiDAR is a distance sensor which can emit near-infrared ray and measure the phase difference between the emitting ray and reflected ray to calculate the distance through TOF (Time of Flight principle).

Figure 8: LiDAR sensor

To be specific, the product transmits a modulation wave of near-infrared ray on a periodic basis, which wave will reflect after contacting the object. The product obtains the time of flight by measuring the round-trip phase difference and then calculates the relative range between the product and the detection object, as shown in Fig. 9.

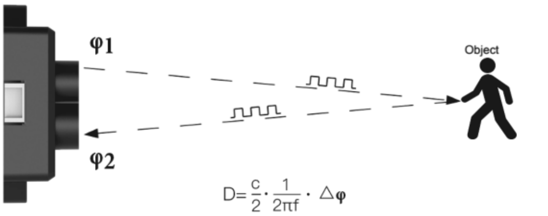

Figure 9: Schematics of TOF Principle, [12]

Fig. 10 shows a diagram of product effectiveness depending on the distance to the object.

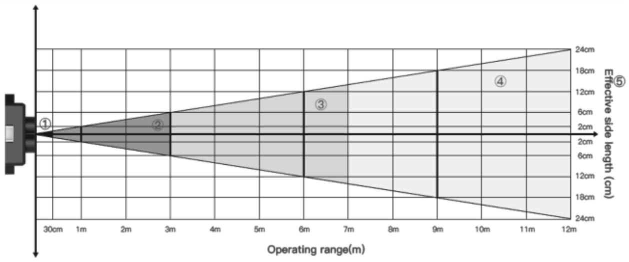

Figure 10: Effectiveness of the product as a function of range, [12]

Zone (1) represents the detection blind area within which the data is unreliable. Zone (2) represents the operating range of the sensor under extreme conditions, which refers to the outdoor glare and detection of black targets. Zone (3) represents the operating range of the sensor for a white target under normal sunshine conditions, while zone (4) represents the operating range of the sensor at the indoor environment or considerably weak ambient light.

Distances were measured from the wall to which the upper end of the rope was attached, as well as from the ceiling, as shown in Fig. 11.

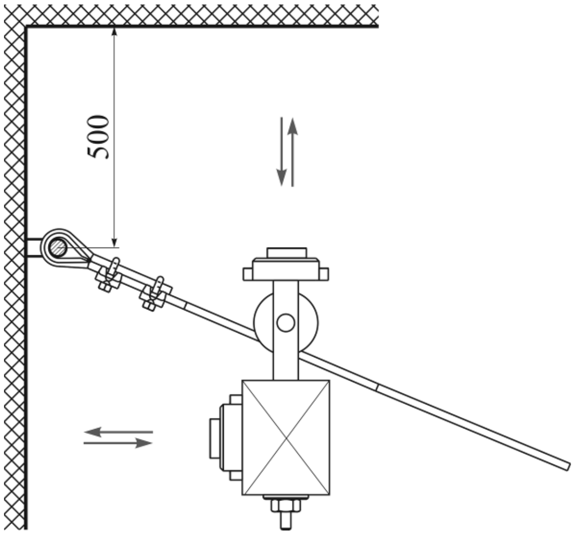

Figure 11: The starting position of the trolley with measuring equipment in the "upper station"

The initial plan was to send measured data by radio from the controller which was mounted on the trolley to the controller which was connected to the computer. Due to the low data transfer rate, this idea was abandoned and the measured values were instead recorded on the SD card.

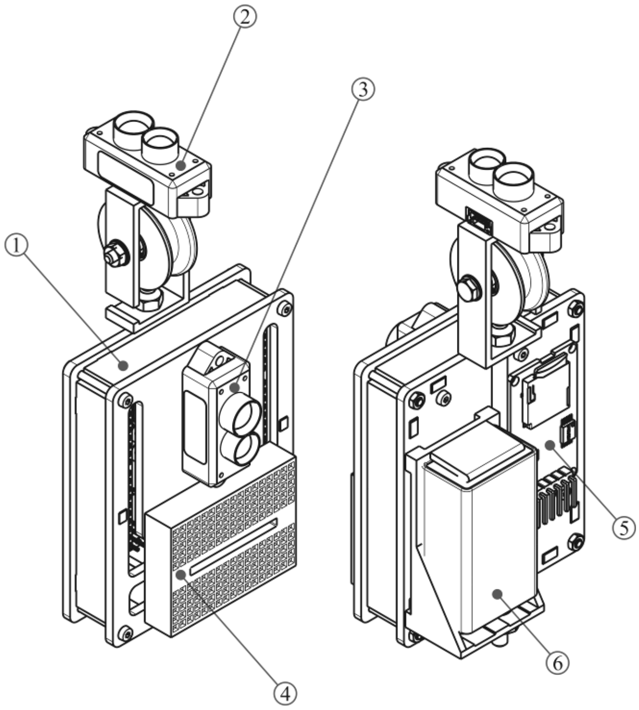

Figure 12: Trolley with measuring equipment

Figure 12 shows a trolley with measuring equipment, where (1) represents Arduino UNO microcontroller, (2) vertical distance sensor, (3) horizontal distance sensor, (4) protoboard, (5) micro SD card reader, and (6) power supply battery.

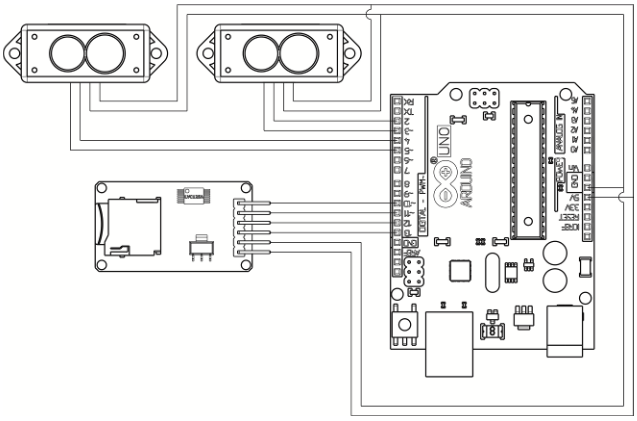

Figure 13: Wiring diagram for measuring equipment

Fig. 13 shows the wiring diagram for two LiDAR TFmini sensors to the Arduino UNO controller, which records data on an SD card.

4. DETERMINATION OF EXPERIMENT PARAMETERS

Given that there is a plan to compare the measured values from the zipline model with the measured values of the kinematic characteristics of a real zipline in the future, the inclination angle will be determined for the model identical to that found in the real zipline [3]. Therefore, it was adopted that the field span of the zipline model should be 4.7 meters and the drop 0.4 meters.

Table 1: Rope mass

Rope diameter [mm]	2	3	4
Rope weight [kg/m]	0,0143	0,0322	0,0572

Taking into account the rope’s own masses which are given in Table 1, the following tensions are predicted:

- 0,5 kg for 2 mm rope diameter
- 0,75 kg for 3 mm rope diameter
- 1,00 kg for 4 mm rope diameter

Considering the fact that it is wanted to achieve the same ratio of the deflection of the unloaded rope and the deflection when the trolley with a load is moving along the rope, it is necessary to provide a different mass of the trolley for all three cases. The mass of the trolley with measuring equipment is 185 g, so in the case of rope with a diameter of 2 mm only the trolley with the measuring equipment is lowered, while in the case of rope with a diameter of 3 mm and 4 mm, additional masses were used.

5. MEASUREMENT RESULTS

Within this point, the results of the measurement will be given. Figure 14 shows results for three different measurements for the vertical sensor and rope with a diameter of 2 mm, while figure 15 shows results for the same three measurements for the horizontal sensor. Figures 16 and 17 are showing results for three different measurements for vertical and horizontal sensors and rope with a diameter of 3 mm, while figures 18 and 19 are showing results for three different measurements for vertical and horizontal sensors and rope with a diameter of 4 mm.

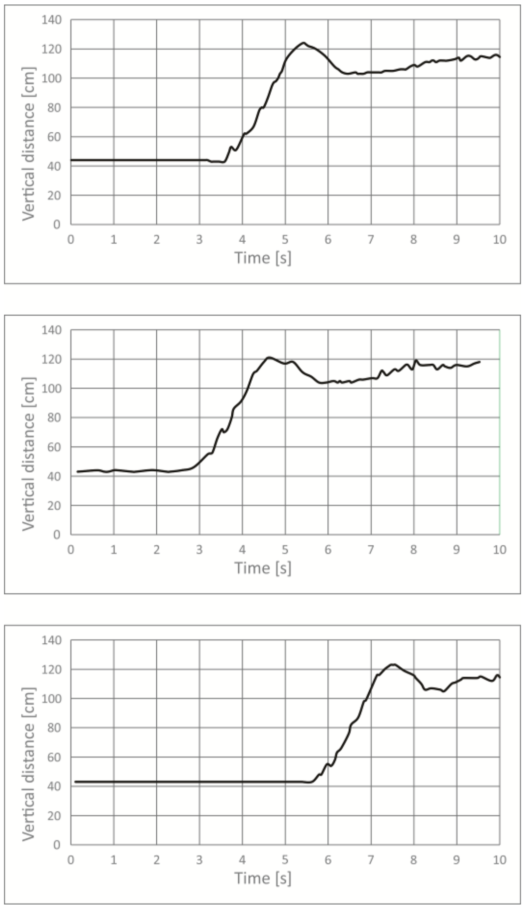

Figure 14: Vertical sensor measurements for rope with a diameter of 2 mm

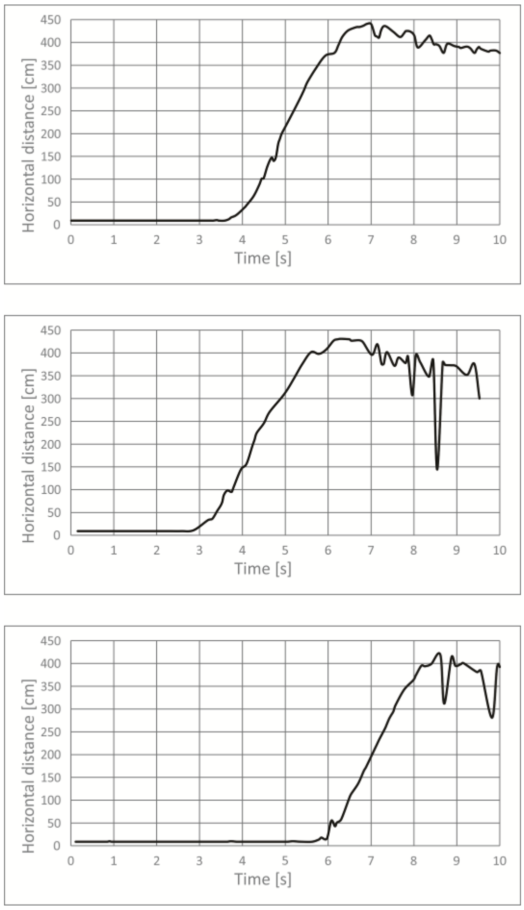

Figure 15: Horizontal sensor measurements for rope with a diameter of 2 mm

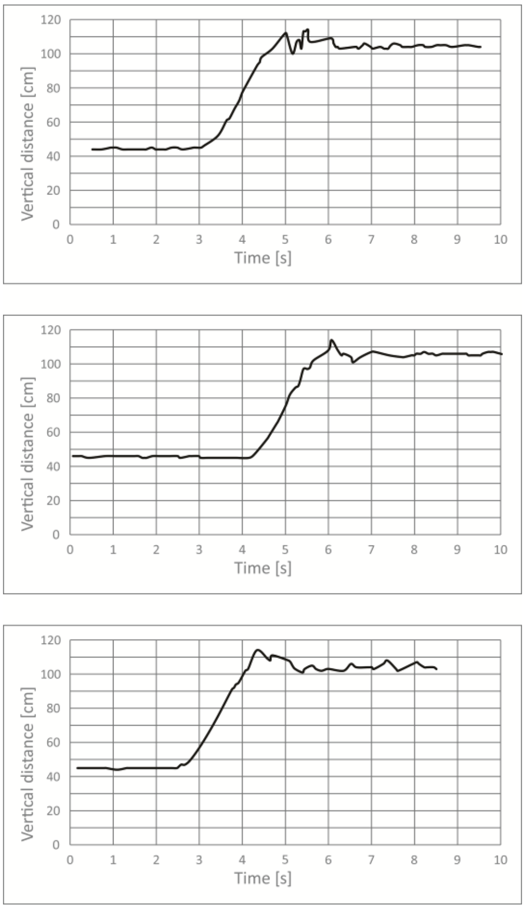

Figure 16: Vertical sensor measurements for rope with a diameter of 3 mm

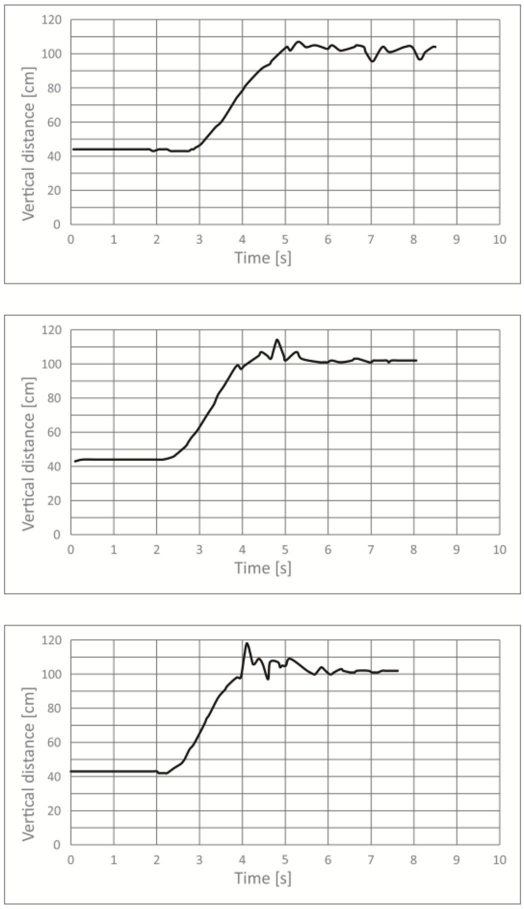

Figure 18: Vertical sensor measurements for rope with a diameter of 4 mm

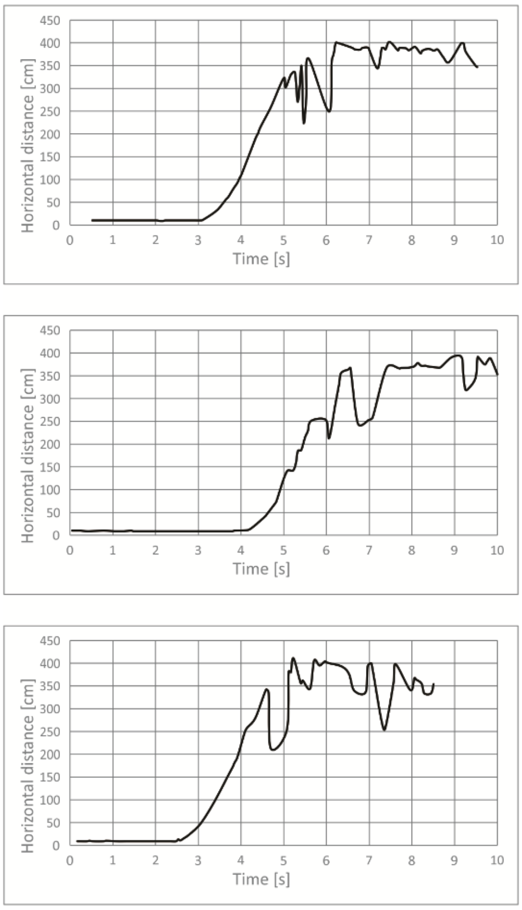

Figure 17: Horizontal sensor measurements for rope with a diameter of 3 mm

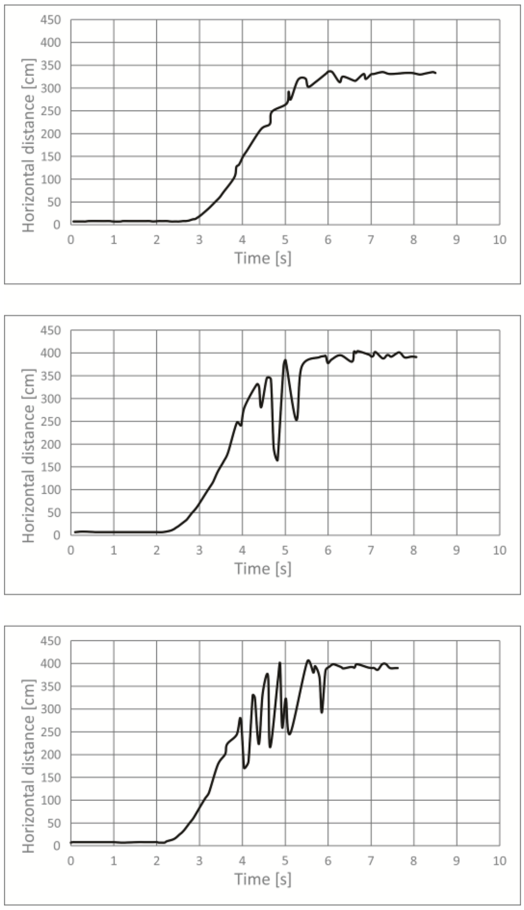

Figure 19: Horizontal sensor measurements for rope with a diameter of 4 mm

6. CONCLUSION

This paper gives an overview of making a reduced-size zipline model. The first part of the paper which describes the elements of the model, is followed by a description of the measuring equipment that can be used when measuring kinematic quantities on the reduced-size model. After that, the results are given for three characteristic measurements for each type of used rope.

Based on the measurements, it can be concluded that satisfactory diagrams are obtained. It remains to compare these values with the values measured on the real zipline in the future.

REFERENCES

[1] L. I. Sedov, “Similarity and dimensional methods in mechanics”, Russian Academy of Sciences, Moscow (Russia), (1980)

[2] J. C. Gibbings, “Dimensional Analysis”, Springer, London (United Kingdom), (2011)

[3] J. H. Williams, “Dimensional Analysis - The great principle of similitude”, IOP Publishing, Bristol (United Kingdom), (2021)

[4] S. J. Kline, “Similitude and Approximation Theory”, Springer-Verlag, New York (United States of America); (1986)

[5] E. Szűcs, “Similitude and Modelling”, elsevier scientific publishing company, Amsterdam (Netherlands), (1980)

[6] R. I. Emori and D. J. Schuring, “Scale models in Engineering”, Pergamon Press, Oxford (United Kingdom), (1977)

[7] J. Vladić, R. Đokić and T. Jojić, “Elaborat - Analysis of the zipline system in Vrdnik”, Faculty of Technical Sciences, Novi Sad (Serbia), (2017)

[8] T. Jojić, J. Vladić and R. Đokić, “Anchorage type and tension rope force impact on zipline’s kinematic characteristics”, Machine Design, Vol. 11(4), pp. 149–154, (2019)

[9] J. Vladić, R. Đokić, T. Jojić, “Theoretical analysis and determination of zipline movement parameters”, Tehnika, Vol. 68(3), pp. 405–412, (2019)

[10] J. Oxer and H. Blemings, “Practical Arduino – Cool Projects for Open Source Hardware”, Springer-Verlag, New York (United States of America), (2009)

[11] J. Bayle, “C Programming for Arduino”, Packt Publishing, Birmingham (United Kingdom), (2013)

[12] “Product Manual of TFmini”, Benewake, Beijing (People’s Republic of China)

Testing of Conveyor Belts and Formation of Verification Model Using FEM

Dragan Živanić[1*], Nikola Ilanković[1], Nebojša Zdravković[2]
[1]Faculty of Technical Sciences, University of Novi Sad, Novi Sad (Serbia)
[2]Faculty of Mechanical and Civil Engineering in Kraljevo, University of Kragujevac, Kraljevo (Serbia)

Conveyor belts, textile composites by their structure, are inhomogeneous and anisotropic. As such, they are the subject of experiments and study in order to better understand their behavior under loading, especially dynamic loading. Due to the large number of influential factors on the load bearing capacity and durability of the conveyor belt, such as the number and material of the carcass, the way of weaving of the carcass material, working conditions, etc., it is not easy to describe them with analytical and mechanical models. Therefore, a great role in understanding the exploitation characteristics of conveyor belts is played by experimental tests on conveyor belt testing devices, as well as the use of numerical methods such as FEM. At the beginning of the paper, the theoretical foundations in the field of textile composites and material fatigue are given. Then, the conveyor belt testing device UZITT MKM 5000 was presented, as well as the results of the experimental test. After, the creation of verification models using FEM using the Autodesk Inventor Nastran software package is shown. At the end, the obtained results of the experimental test and the results obtained by the MKE method were compared.

Keywords: Conveyor belt, durability, fatigue, FEM

1. INTRODUCTION

The conveyor belt is the most important element of the belt conveyor. Its role is to transport the material, to accept the impact energy at the loading place, to withstand the temperature and chemical effects that the transported material affects it, and to withstand the designed load throughout its working life. The belt can be seen as a textile composite consisting of an upper and lower rubber protective layers and a load bearing layer (carcass). The role of rubber protective layers is to protect the load bearing layer from the impact of the transported material, while the load bearing layer has a multiple role:

- it has to provide adequate tensile strength in order to withstand the load that occurs due to the material transport;
- it has to absorb the energy of the impact of the loaded material;
- it has to ensure the longitudinal and transverse rigidity of the belt in order to keep its shape during the transport of the material.

Damage to the belt occurs due to a combination of various factors - the influence of sun, rain, snow and ice, chemical reagents and mechanical effects. Therefore, it is difficult to precisely define the exact cause when belt damage occurs [1]. As the rubber protective layers protect the load bearing layer of the tape (carcass), the damage mechanisms that lead to their degradation are examined. The main cause of wear of rubber protective layers is abrasion. Abrasion occurs due to friction between the belt and the support idlers and pulleys, as well as between the belt and the material. Micro-cuts are formed and they grow larger over time and parts of the rubber layer fall off, opening a crack that leads to accelerated deterioration of the load bearing layer. As already mentioned, environmental influences can lead to premature degradation of the conveyor belt. Working environment temperatures below 0° C do not have a negative effect on the mechanical characteristics of the conveyor belt, while working environment temperatures of 80° C lead to a decrease in the tensile strength of the belt [2]. On the other hand, the influence of the temperature of the vulcanization process by which the belt is formed is significant. If the crystallization temperature of polyester and nylon fibers is reached, their tensile strength is destroyed. Warm vulcanization temperatures in the range of 140° to 160° allow the vulcanization process to be carried out safely in relation to the mechanical characteristics of the load bearing layer, while temperatures above 200° C lead to complete degradation.

The elongation of the conveyor belt at the reference load is influenced by the type of material of the load bearing layer, the number of load bearing layers and the tensile strength of the material of the load bearing layer. The tensile strength of the conveyor belt is affected by the tensile strength of the material and the number of the load bearing layers. During exploitation, the belt loses its mechanical properties. Degradation of tensile strength occurs, flexibility of the belt decreases, while resistance to delamination decreases significantly, in certain cases up to 100% [3]. The nature of the load applied to the specimen during testing significantly affects the behavior of the specimen. The specimen has a higher resistance to damage if the load is applied gradually with periods of relaxation between two load application cycles compared to single tensioning of the specimen to the nominal tensile strength. The joint of the ends of the conveyor belt is considered one of the critical zones. The strength of the belt end joint consists of two components - static tensile strength and fatigue strength. During the static tension test, the joint tears without delamination of the layers. On the other hand, during dynamic tension testing, delamination occurs first, i.e. adhesion failure between the load bearing layers. Therefore, it is important to study the fatigue resistance of adhesion between layers [4].

*Corresponding author: Trg Dositeja Obradovića 6, 21000 Novi Sad, Serbia, zivanic@uns.ac.rs

2. TEXTILE COMPOSITES

Textile composites are materials that consist of two or more different materials whose characteristics are combined to achieve better properties compared to the individual components. They can be produced using different techniques such as knitting, weaving, tailoring, etc. The main components of textile composites are the reinforcing fibers and the matrix that holds them together. Fibers are made from polyester, polyamide, aramid, glass, carbon, but also from natural fibers such as cotton, bamboo, etc. The most commonly used matrix materials are polymer materials such as epoxy resins, rubber, polyester. Ceramic and metal matrices can also be used. Textile composites have high specific strength and stiffness, low density, good vibration damping properties, corrosion resistance. There is a very wide range of areas where textile composites are applied. In the automotive industry, they are used to reduce vehicle mass and improve performance. In construction, they are used to strengthen concrete and increase resistance to earthquakes, and in the medical industry, they are used to manufacture implants and other medical devices. Textile composites are also used in the production of sports equipment such as bicycles, tennis rackets and skis. They are used in the fashion industry to produce clothing and footwear with improved performance such as water resistance and abrasion resistance [5].

2.1. Division of textile composites

One of the divisions of textile composites is according to their dimensionality, i.e. on 2D and 3D textile composites.

2.1.1. 2D textile composites

2D textile composites consist of two sets of threads - warp threads (threads in the direction of the longitudinal axis of the textile composite) and weft threads (threads in the normal direction in relation to the longitudinal axis of the textile composite). The warp and weft threads make a series of interlacings according to the type of weaving. Basic 2D textile composites, like classic conveyor belts, are produced by plain, twill and basket weaving.

In plain weaving, the warp and weft threads are interlaced one under the other, Figure 1. In this way, a high level of wrinkling is created, which negatively affects the mechanical characteristics of the material. [6].

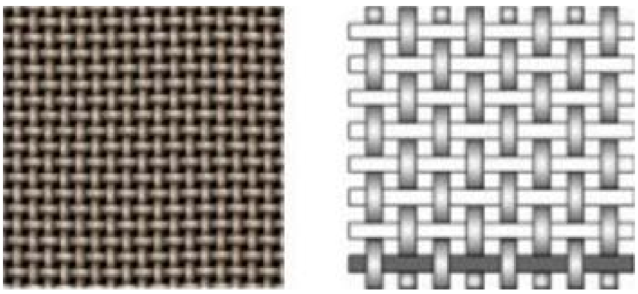

Figure 1: Plain weave

Twill and basket weaves are used to achieve better mechanical properties than plain weaves, Figure 2. In twill weaves, the warp threads interlace with two or more weft threads in a repeating pattern. It has a smoother surface than plain weaving and less wrinkling. On the other hand, it has less dimensional stability compared to plain weaving. In basket weaving, two or more warp threads are alternately interlaced with two or more weft threads. The wrinkling of the material is less compared to plain weaving, and it has a higher dimensional rigidity compared to twill weaving.

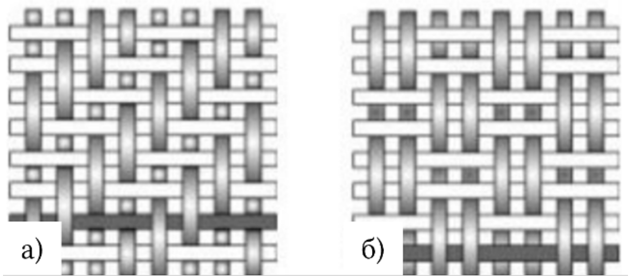

Figure 2: Twill (a) and basket (b) weave

2D textile composites have poor impact resistance as a result of material wrinkling, as well as to cyclic loading. They have poor in-plane shear characteristics due to the lack of vertical fibers in relation to the plane formed by the warp and weft threads. Another problem that arises is delamination. 2D textile composites consisting of multiple layers, such as conveyor belts, are formed by a vulcanization process. The lack of fibers that would connect the mentioned layers leads to delamination during exploitation [7].

2.1.2. 3D textile composites

3D textile composites differ from 2D textile composites in that, in addition to the warp and weft threads that form a planar structure, they also contain connecting threads that extend perpendicular to the plane. 3D textile composites can withstand out-of-plane loads, are resistant to wear and impact, while on the other hand they can form complex geometric shapes. The key advantages of 3D compared to 2D textile composites are:

- they have better structural integrity and resistance to damage due to the fact that they consist of multiple layers that are cross-connected, which allows for a more even distribution of loads and increased resistance to fractures and cracks;
- they have higher specific strength and stiffness due to better distribution of fibers and better connection between fibers and matrix;
- they have greater resistance to delamination due to the connecting threads that connect the individual plain layers.

The methods of weaving 3D textile composites are similar to those of 2D textile composites, with the addition of binding threads. Some of the types of 3D textile composites are shown in Figure 3.

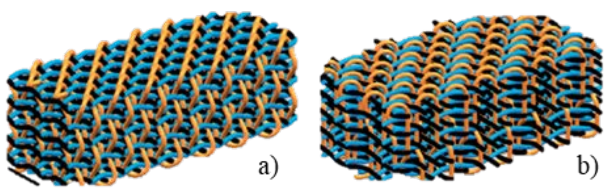

Figure 3: Plain (a) and twill (b) weave

3D textile composites are a relatively new type of material. Their development began in the late 1980s [8]. Today, research is carried out in the direction of examining the influence of the construction parameters of the material on its mechanical characteristics. In [9], various aspects related to the 3D weaving process and its application in the creation of high-performance composite materials with exceptional mechanical properties are described. Also, various production processes and the influence of parameters such as weaving density, type and amount of fibers, thread geometry, etc., on the mechanical characteristics of the material were considered. In [10], various studies were presented that dealt with the mechanical characteristics of 3D textile composites. The effects of fiber orientation, weave structure and material type on mechanical characteristics were analyzed. It has been shown that 3D textile composites behave better than 2D textile composites after the occurrence of structural damage. 2D textile composites do not have a long service life after the occurrence of significant structural damage, these damages spread rapidly along the material. On the other hand, 3D textile composites, due to their structure, can function longer after the occurrence of significant structural damage. In [11], it was pointed out that 3D textile composites, like other textile composites, are subject to negative atmospheric influences with inadequate storage conditions. It was stated that errors in the production of materials due to the complicated procedure of creating 3D shapes are not rare.

The application of 3D textile composites is not widespread in conveyor belts due to the high cost of production. One of the few examples that can be found is described in [12] where the application of a conveyor belt made as a 3D textile composite in the production of paper is mentioned, where it is necessary for the belt to be smooth on the upper side and porous on the lower side, Figure 4.

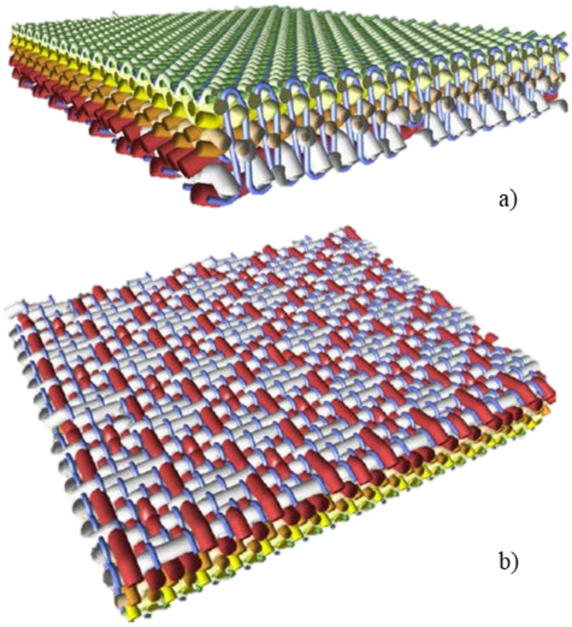

Figure 4. Smooth upper (a) and porous lower (b) surface of the conveyor belt [12]

3. FATIGUE DAMAGES OF TEXTILE COMPOSITES

3.1. Experimental methods

There are several types of testing of damage to textile composites due to fatigue because it is possible to monitor large number of parameters:

- amplitude control (voltage or deformation);
- testing frequency;
- load direction (axial, flexural, bi-axial...);
- load ratio (tension / tension, tension / pressure...).

The results obtained during the test are influenced by two categories of parameters - the parameters of the tested material and the parameters of the fatigue test method.

Regarding the parameters of the tested material, thermal conductivity has a great influence. When testing the sample at higher frequencies (5-10 Hz), the temperature of the sample increases to over 100° C. Such high temperatures can negatively affect the results obtained. During the manufacturing process of textile composites, damage may occur that will later affect earlier failure due to fatigue. Significant shear in the plane of the material can occur, which leads to the creation of folds that negatively affect the exploitation characteristics of the material. Cuts, holes or damage caused by the impact of a foreign body into the material act as stress concentrators and can significantly impair the fatigue behavior of the textile composite [13].

Regarding the parameters of the test method, it is necessary that the material specimen be large enough to include several weaving segments because the inhomogeneity of the material due to the arrangement of the fibers in it significantly affects the fatigue behavior. The choice of the specimen form is an important step in the preparation of the test. It is necessary that the specimen has a protective rubber layer on the ends so that the jaws of the testing device do not damage it. It is necessary to control the amplitude of the load or deformation because the damage that occurs during the test depends on the amplitude of the load or deformation [14].

3.2. Tension / tension experiments

Uniaxial tension / tensile testing is the most commonly used test. Either a servo-hydraulic test device or a device with servo electric motors and adequate drivers is used.

Alignment of the specimen in the jaws is of extreme importance. Bending loads must not occur. It is recommended to use hinged connections between the jaws and the force sensor in order to transmit only forces and not moments. It is desired to measure the temperature of the specimen if it is possible. It is necessary to measure the deformation of the sample, and extensiometers or encoders on the electric motor are used for this. For the test frequency, the highest possible values are chosen in order to reduce the duration of the test, but also to avoid the accumulation of high temperature in the specimen, which would lead to degradation. It is possible to monitor acoustic emission to register sound waves during composite delamination and fiber failure. By monitoring the acoustic emission during the test, the degradation process of the material could be monitored.

One of the latest techniques for monitoring the fatigue behavior of textile composites is the application of embedded sensors in the composite sample in the form of optical fibers with a Bragg grating [15]. A Bragg grating is a periodic variation of the optical refractive index that is recorded in the core of an optical fiber and is several millimeters long. When broadband light is emitted into an optical fiber, the Bragg grating acts like a selective mirror for a specific wavelength. Each grating has a certain wavelength, the Bragg wavelength λ_B, which it reflects, while letting other wavelengths through. The Bragg wavelength is directly proportional to the period of the Bragg grating. If the sensor in the form of an optical fiber is embedded in the composite sample, the deformation of the damaged sample will lead to a change in the period of the Bragg grating. This leads to the reflection of a different wavelength. The advantages of this testing technique are the absoluteness of the measurement, the passivity of the sensor in the form of optical fibers, a long service life and resistance to electromagnetic influences.

3.3. Typical damages of textile composites due to fatigue

Textile composites are made of long stiffening fibers that are bonded to a polymer matrix. Therefore, they are heterogeneous and anisotropic. The first phase of material weakening occurs due to fatigue caused by the creation of damage zones. These zones contain a large number of microscopic damages, initial delamination between fibers and matrix, as well as complete separation of fibers and matrix. The first phase of material weakening occurs very early, already after several hundred cycles. In the second phase, there is a gradual degradation of the material, which is reflected in the reduction of the stiffness of the material. Significant damage occurs in the third stage. These damages are reflected in fiber cracking and uncontrolled delamination between the fibers and the matrix, which leads to rapid deterioration of the material and ultimately to failure.

In order to notice the mentioned damages, it is necessary to apply one of the checking techniques. The simplest technique is the classic visual inspection. Depending on the difference in the refractive index of the matrix and fibers, the transparency of the composite can be high. By directing a beam of light at the sample, cracks in the matrix, voids and foreign inclusions can be detected. Furthermore, the scanning electron microscope is most often used during fractographic analyses [16]. The fracture surface is scanned with a focused beam of high energy electrons. Electrons penetrate through the surface of the sample and react with the atoms of the material in elastic and inelastic scattering processes.

4. CONVEYOR BELTS

Figure 5. shows the construction of the belt - it consists of an upper rubber protective layer, a load carrying layer (carcass) and a lower rubber protective layer.

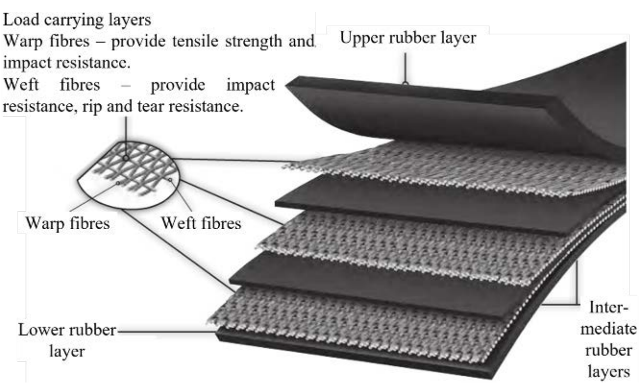

Figure 5: Conveyor belt with textile load carrying layers

4.1. Textile load carrying layers – Carcass

In belts where the carcass is made of textile materials, only one load carrying layer rarely occurs. It mainly consists of several layers. Layers are produced by weaving warp yarns that extend in the longitudinal direction of the belt and weft yarns that extend in the transverse direction. The tensile strength of warp yarns is the basic parameter for the selection of the belt because they can withstand the largest share of the load.

Textile load carrying layers can be made of cotton, cellulose, rayon, nylon, polyester, fiberglass and aramid. The best combination is polyester and nylon. In the case of belts whose load carrying layers are made of polyester-nylon material, polyester fibers deform slowly and are therefore used as warp yarns, while more elastic nylon fibers are used for weft yarns. This is a combination of the best characteristics of this type of material which provides high tensile strength with low level of deformation with excellent impact resistance, high durability and the ability to transfer large quantities of material.

4.2. Rubber protective layers

The load carrying layers require protection from abrasive influences, material impact, wear and chemical reactions in order not to lose their properties over time. This is achieved by placing a protective layer on the top and bottom of the belt. Protective layers are made of two types of materials - most often rubber and can also be made of PVC. Rubbers of different characteristics are classified into classes and the choice of class depends on the working conditions that will apply during the operation of the conveyor. In the case of the use of PVC material, the coefficient of friction between the protective layer and the drive pulley is relatively low. Also, due to the negative impact of sunlight on PVC, it is mostly used in underground applications.

The wear resistance of the conveyor belt is one of the main factors that affect the service life of the belt and thus the return on investment. The choice of type of the protective layer significantly affects the length of the service life.

5. MATERIALS AND METHODS

The aim of testing the conveyor belts was to analyze the influence of the fatigue load on the operational life of the conveyor belt. Therefore, the conveyor belt samples were tested under variable loading to determine the number of cycles the specimen could withstand before failure. This method of testing simulates the loading of the conveyor belt during operation because the force in the belt, during the movement of the conveyor belt along the conveyor route, is variable within certain limits. Samples of conveyor belts were subjected to loading in the form of a sinusoidal function where each period represents one working cycle. For example, a 2 km long conveyor transporting material at a speed of 1,68 m/s would take 2.381 s to complete one duty cycle, which is represented in the test by one specimen loading period. In this way, for the given example, the annual operation of the belt conveyor, which amounts to 13.245 cycles, is simulated with an identical number of sample load periods.

5.1. Method

Conveyor belt testing was done on a specially constructed device for this testing, UZITT MKM 5000, Figure 6.

Figure 6: UZITT MKM 5000 during experiments

The elements of the device are shown in Figure 7.

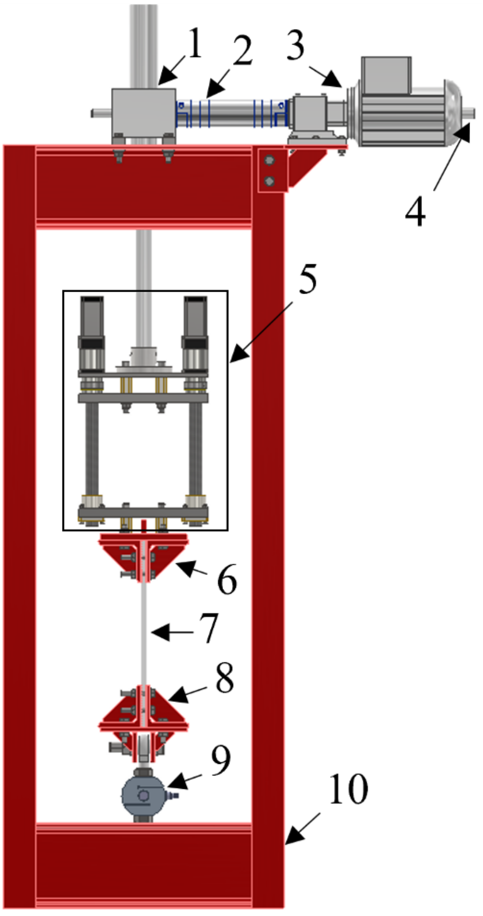

Figure 7. Elements of the testing device

The testing device is consisted of the worm gear screw jack (1), connecting shaft (2), helical geared electric motor (3), rotary encoder (4), fatigue testing module (5), upper jaw (6), belt sample (7), lower jaw (8), load cell (9) and supporting frame (10).

The device characteristics are:

- maximum load for static testing of samples: 50.000 N;
- maximum load for dynamic testing of samples: 25.000 N;
- maximum travel during static testing: 700 mm;
- maximum travel during dynamic testing: 200 mm;
- maximum speed of static tensioning: 100 mm/min;
- maximum speed of dynamic tensioning: 16 mm/s.

The fatigue testing module is shown on Figure 8. It is demountable, so it can be re-moved if static tests are carried out over 25.000 N.

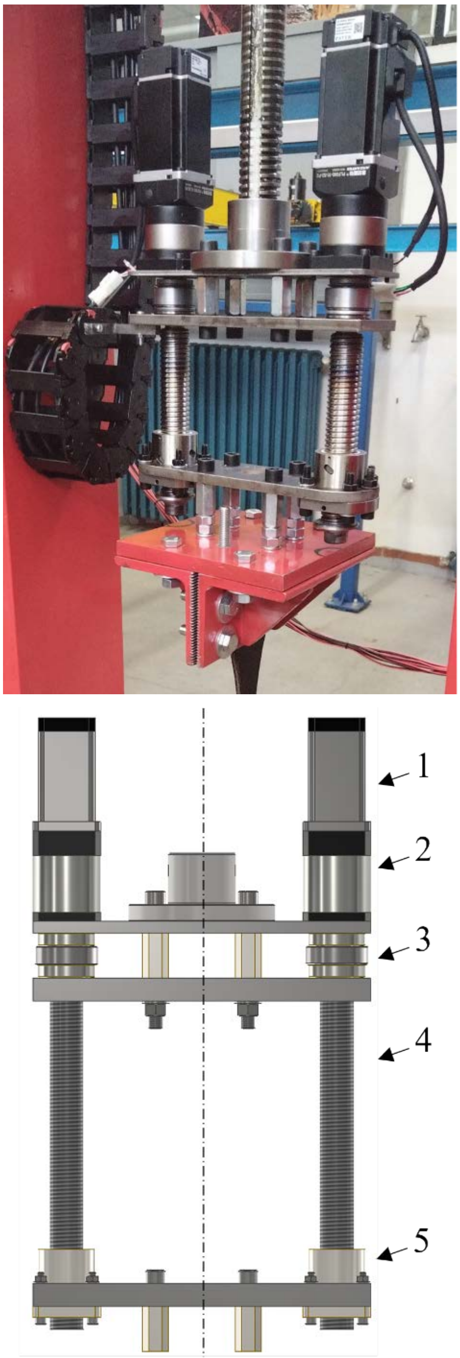

Figure 8: Fatigue testing module

It consists of two servo motors (1), two planetary gearboxes (2), two bearings (3), two threaded spindles (4), two nuts with roller balls for the threaded spindle (5) and other connecting elements.

As for the static test, the displacement of the upper jaw is measured via a rotary encoder. The tensioning speed is defined by the speed of the AC motor connected to the Hitachi NES1-007 HBE variable frequency controller.

As for the dynamic test, the displacement of the upper jaw and the tensioning speed are defined through the PLC that controls the Fatek SD3 servo drivers that regulate the operation of the servo motors.

In order for both servo motors to move identically, the PLC controls one servo driver in terms of setting the signal shape, frequency, amplitude, etc., and the second servo driver copies the movement of the first one. For this purpose, a software that has a module for static testing and a module for dynamic testing is specially designed.

5.2. Material

The conveyor belt whose load bearing layer was made by plain weaving was tested. The warp threads are made of polyester, while the weft threads are made of nylon. This type of load bearing layer is known as EP. The designation of the conveyor belt is EP 500/3 Y 526858. The characteristics of the belt are given in Table 1.

Table 1: Characteristics of the selected belt from the manufacturer's datasheet.

Characteristic	Unit	Min	Max	Value
Breaking strength longitudinally	N/mm	500	-	523
Elongation at break	%	12	-	29,5
Working elongation – 10%	%	-	1,5	1,34
Adhesion top cover / 1st ply	N/mm	3,5	-	4,4
Adhesion 1st ply / 2nd ply	N/mm	5	-	7,6
Adhesion 2nd ply / 3rd ply	N/mm	5	-	6,8
Adhesion bottom ply / bottom cover	N/mm	3,5	-	4
Tensile strength of cover	N/mm^2	20	-	20
Elongation of cover	%	400	-	522
Abrasion resistance	mm^3	-	130	122

The specimens are shown in Figure 9. The width of the specimen at the narrowest part is 25 mm, which means that the maximum force that the specimen can withstand before breaking is 13.075 N.

Figure 9: Specimens of the conveyor belt EP 500/3 Y 526858

6. RESULTS

The load ratio was chosen to be R=0.6. The test was performed at five load levels with an average value of 10 kN, 9,6 kN, 8,64 kN, 8,48 kN and 7,68 kN, where the maximum and minimum values of the load levels ranged within ±25% in relation to the average load. In this way, the maximum load values reached 95,6%, 91,7%, 82,6%, 81% and 73,4% of the maximum force that the specimen can withstand before breaking. Figure 10 shows the test.

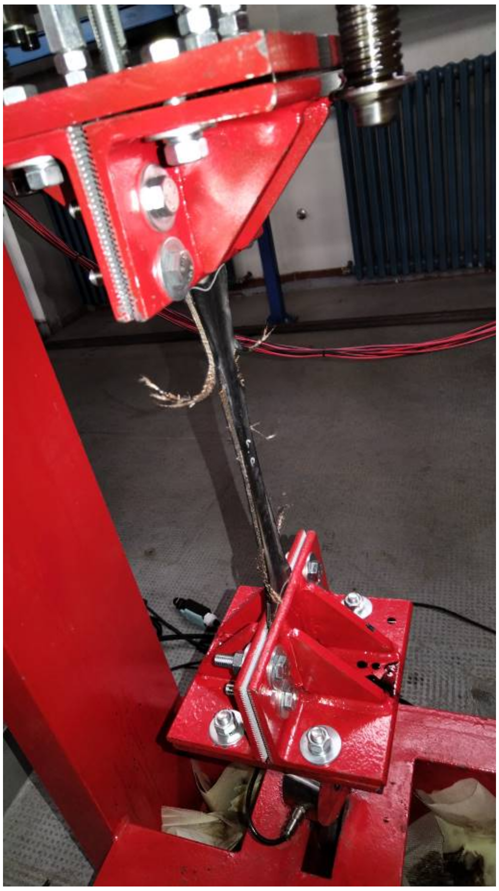

Figure 10: Specimen testing

Table 2. shows the obtained results.

Table 2: Obtained results

	Load level				
	I	II	III	IV	V
Test f. mean [kN]	10	9,6	8,64	8,48	7,68
Test f. max. [kN]	12,5	12	10,8	10,6	9,6
Percentage of breaking force [%]	95,6	91,7	82,6	81	73,4
Test f. min. [kN]	7,5	7,2	6,48	6,36	5,76
N. of specimens	10	10	10	10	10
Av. no. of cycles until fracture	823	3168	39.180	82.472	467.568
Standard dev. in number of cycles	190	384	2978	4619	28.521
Relative standard deviation [%]	22,9	12,1	7,6	5,6	6,1

By interpolating the obtained results, the following relation was obtained:

$$F_{MAX} = -451,2\ln(N) + 15.584 \quad (1)$$

where:

- F_{MAX} [N] - maximal testing force;
- N – number of cycles to fracture.

Figure 11. shows the obtained results graphically.

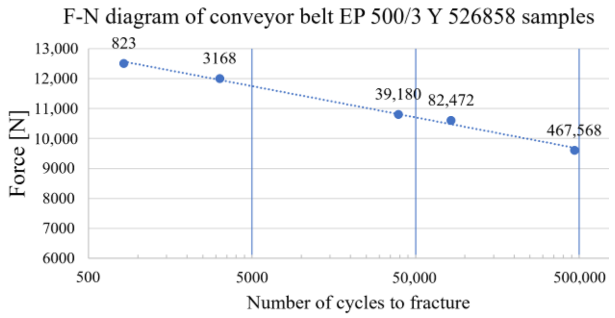

Figure 11: Graphically presented results and F-N curve.

Figure 12. shows some of the fractured specimens during testing.

Figure 12: Some of the fractured specimens

7. VERIFICATION MODEL

In order to verify the obtained experimental results, a FEM model of the belt specimen was created.

As for the FEM model, first the idealisation was done. The belt specimen was formed as a solid model and was prepared by removing the rubber protective layers that would only distort the results. The model was defined based on the material of the belt carcass. The Multi-Axial Fatigue module was activated in the Autodesk Inventor Nastran software to perform the fatigue test. Second, boundary conditions were applied. Fixed constraint was applied at the top surface of the specimen, while the loading was applied at the bottom surface of the specimen. In order to simulate the sinusoidal loading cycle, loading history table data was created. Loading scale factor in the range of 0,6÷1 was entered for 1 second in order to achieve 1 Hz test frequency. After that, mesh was applied. Local mesh control was applied on the edges of the specimen. Finally, the simulation was started.

During the first iteration of the simulation of the first specimen, analysis was done with default mesh size. After that, the simulation was done with the half of the default mesh size. It took several iterations to achieve result convergence. The final mesh size was 2 mm. The number of finite elements was 61.244.

Numerical simulations were carried out on the formed belt specimen model in an identical manner as in the physical experiment described in the previous part of the paper.

The results obtained by FEM analysis are shown in Figure 13.

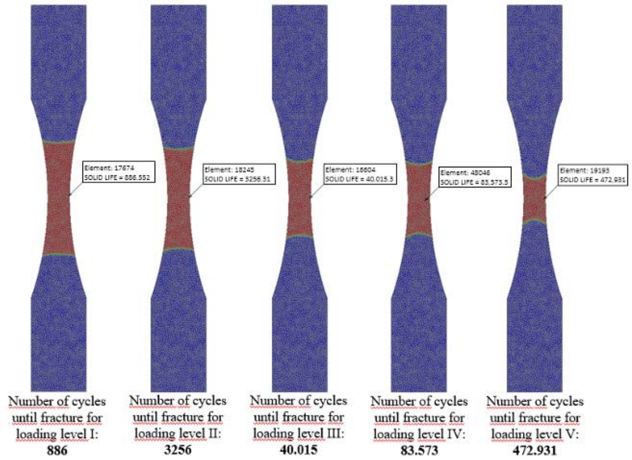

Figure 13: Results of FEM fatigue analysis

The obtained results of the FEM analysis were compared with the average values of the experimentally obtained results, which is shown in Table 3.

Table 3: Obtained results

	Loading level				
	I	II	III	IV	V
Av. no. of cycles until fracture during physical ex.	823	3168	39.180	82.472	467.568
No. of cycles until fracture according to FEM	866	3256	40.015	83.573	472.931
Percentage of result difference [%]	5	2,7	2,1	1,2	1,1

The obtained value of the average number of cycles until the belt breaks at the maximum loading of 95,6% of the nominal breaking strength, only 823 cycles, indicates that the damage occurs at the first loading cycles.

At the maximum loading of 91,7% of the nominal belt breaking strength, the number of cycles did increase (823 → 3168), but that number still does not ensure an economically profitable and acceptable lifetime of the belt.

Moving to the maximum loading level of 82,6% and 81%, there was a significant in-crease in the number of cycles to fracture. It should be noted here that higher number of cycles to failure fracture (39.180 – 82.,472) with a slight decrease in the loading level (82,6% - 81%) indicates the sensitivity of the considered influence, which requires further and more detailed analysis.

Also, a very significant increase in the number of cycles to failure fracture (467.568) is observed at a loading level of 73,4%, which may indicate a potentially very long life of the belt at lower loads loading of 70% of the nominal breaking strength.

For the example that is mentioned earlier, the tested belt would work for 4 months at maximum loads loading of about 90% of the nominal breaking strength, at 80% for about 6 years, and at 75% for about 30 years.

It must be noted that the previous calculation only considers damage to the belt sample specimen due to tension/tension fatigue, it does not consider the actual damage to the belt during exploitation, due to the bending of the belt, the impact of the material etc.

8. CONCLUSION

The paper presents basic postulates of testing textile composites such as conveyor belts on fatigue damage mechanism. The mechanisms that lead to fatigue damage are explained and are clearly differentiated from the mechanisms that lead to damage in static testing. Fatigue testing of conveyor belt specimens under tension/tension loading type is presented. Specimens were tested at a constant loading ratio *R* on a specially designed UZITT MKM 5000 device specially for this occasion.

Based on the obtained results, it was determined that the number of cycles that the belt specimen can reach before fracture significantly depends on the loading level.

For the obtained results to be practically applied, in the sense of choosing the optimal belt according to the real loading and a certain configuration of the belt conveyor, it would be necessary to verify the way of representing the working cycle of the belt as one period of the form of a sine function. Verification would be possible by testing belt material, after a known number of cycles, and comparing them with the results on specimens of new belts with the same characteristics.

As for further research directions, it is necessary to carry out experiments with variable loading ratio R to obtain a more general mathematical model. Also, it is necessary to carry out tests of conveyor belts with different numbers and materials of carcass layers to examine their influence on the fatigue life.

The difficulty in conducting the described tests is the total time required for the experiment. At the used test frequency of 1 Hz, it would take 2 years to test 10 specimens up to 6.000.000 cycles, which is, based on the life curve defined in this work, the limiting number of working cycles at 65% of the nominal breaking strength of the belt specimen. Therefore, it is necessary to determine the highest possible test frequency that does not negatively affect the mechanical characteristics of the specimen to shorten the duration of the experiment.

ACKNOWLEDGEMENTS

This research (paper) has been supported by the Department of Mechanization and Design Engineering through the project: “Testing, design and expertise in the field of mechanization in order to increase the quality of the teaching process and scientific research activities of the Department of Mechanization and Design Engineering”.

REFERENCES

[1] G. Fedorko, V. Molnar, S. Honus, M. Beluško, M. Tomaškova, „Influence of Selected Characteristics on Failures of the Conveyor Belt Cover Layer Material“, Engineering Failure Analysis, Vol. 94, pp. 145-156, (2018)

[2] A. Rudawska, R. Madlenak, L. Madlenakova, P. Drozdziel, „Investigation of the Effect of Operational Factors on Conveyor Belt Mechanical Properties“, Applied Sciences, Vol. 10(12), (2020)

[3] G. Fedorko, V. Molnar, J. Živčak, M. Dovica, N. Husakova, „Failure Analysis of Textile Rubber Conveyor Belt Damaged by Dynamic Wear“, Engineering Failure Analysis, Vol. 28, pp. 103-114, (2013)

[4] R. Blazej, M. Hardygora, „Modeling of Shear Stresses in Multiply Belt Splices“, Bulk Solids Handling, Vol. 23(4), pp. 234-241, (2003)

[5] S. Rathnayaka, R. Jayasinghe, R. Nilmini, G. Priyadarshana. „Recent Developments in Textile Reinforced Polymer Composites - A Review“, Asian Journal of Chemistry, Vol. 34, pp. 487-496, (2022)

[6] N. Amor, M. T. Noman, M. Petru, „Classification of Textile Polymer Composites: Recent Trends and Challenges“, Polymers, Vol. 13(16), (2021)

[7] Q. Hu, H. Memon, Y. Qiu, W. Liu, Y. Wei, “A Comprehensive Study on the Mechanical Properties of Different 3D Woven Carbon Fiber-Epoxy Composites”. Materials, Vol. 13(12), (2020)

[8] Y. S. Perera, R. M. H. W. Muwanwella, P. R. Fernando, “Evolution of 3D Weaving and 3D Woven Fabric Structures”, Fash Text, Vol. 8(11), (2021)

[9] M. Umair, Y. Nawab, M. Malik, K. Shaker, “Development and Characterization of Three-Dimensional Woven-shaped Preforms and their Associated Composites”, Journal of Reinforced Plastics and Composites, Vol 34(24), (2015)

[10] H. Tao, W. Yanling, W. Gang, (2018) “Review of the Mechanical Properties of a 3D Woven Composite and Its Applications”, Polymer-Plastics Technology and Engineering, Vol. 57(8), pp. 740-756, (2018)

[11] P. M. Rao, T. R. Walter, B. Sankar, G. Subhash, C. F. Yen, “Analysis of Failure Modes in Three-Dimensional Woven Composites Subjected to Quasi-Static Indentation”, Journal of Composite Materials, Vol. 48(20), pp. 2473-2491, (2014)

[12] T. Gries, I. Bettermann, C. Blaurock, “Aachen Technology Overview of 3D Textile Materials and Recent Innovation and Applications”, Appl. Compos. Mater. Vol. 29, pp. 43–64, (2022)

[13] R. Jones, J. F. Williams, T. E. Tay, “Is Fatigue Testing of Impact Damaged Laminates Necessary?”, Composite Structures, Vol. 8(1), pp. 1-12, (1987)

[14] V. M. Harik, J. R. Klinger, T. A. Bogetti, “Low Cycle Fatigue of Unidirectional Laminates: Stress Ratio Effects”, Journal of Engineering Materials and Technology, Vol. 122(4), pp. 415-419, (2000)

[15] I. De Baere, E. Voet, W. Van Paepegem, J. Vlekken, V. Cnudde, B. Masschaele, J. Degrieck, “Strain Monitoring in Thermoplastic Composites with Optical Fibre Sensors: Embedding Process, Visualisation with Micro-tomography and Fatigue Results”, Journal of Thermoplastic Composite Materials, Vol. 20(5), pp. 453-472, (2007)

[16] W. Van Paepegem, “Development and Finite Element Implementation of a Damage Model for Fatigue of Fibre-reinforced Polymers”, PhD thesis, Ghent University of Architectural and Engineering Press (Belgium), (2002)

Analysis hybrid drives of mobile machines

Vesna Jovanović*[1], Dragoslav Janošević[1], Jovan Pavlović[1]
[1]Faculty of Mechanical Engineering, University of Niš (Serbia)

In this paper, three variants of hybrid mechanic-hydrostatic transmission for moving drive of mobile machines are analysed. Kinematic and dynamic transmission ratio defined. Based on results of listed numerical example, comparative analysis transmissions conducted based on certain traction characteristic.

Keywords: mobile machine, hybrid transmissions

1. INTRODUCTION

Last twenty years have been developing and application of hybrid transmission for moving drive of mobile machines (construction, transportation, agricultural and comunal machines).

General, hybrid drive transmission contents integral connected mechanic and hydrostatic transmission which are driven by diesel engine or combined diesel and electric engine [1][2]. Depend on moving conditions of machines, engine energy transmits simultaneously via mechanical and hydrostatical part or via one of eatch transmissions part only.

Hydrostatic part of transmission enables movement regulation and energy recuperation of machines [3][4]. Movement regulation achives adapting traction characteristic to contidions and technologies of machines work, regulating paratematrs of componemts (hydraulics pumps and hydraulic motors).

In the paper, three variants hybrid transmissions *A*, *B* and *C* (Fig. 1) analysed, which differ in the connection method of the mechanical and hydrostatic parts of the transmission.

For all variants, its in common that one part of engine 1 energy via elastic coupling 2 transmits mechanical part of transmission, firstly via planetary set with central gear z_{31}, planetary gears z_{32}, toothed ring z_{33} and satellite carrier 3s, then via gearshift 5, cardan shaft 6 and drive shaft 7 till the wheels 8.

Second part of engine energy transmits hydrostatic part of transmission which consists of hydraulic pump 3 and hydraulic motor 4 with variable specific flow, linked in hydraulic closed circuit loop

Hydraulic pump receives energy via gear pair z_p/z_{34} with transmission ratio i_1, while hydraulic motor surenders energy via gear pair z_m/z_{35} with transmission ratio i_2.

In transmission *A*, the hydraulic pump receives power from the engine via the toothed ring of the planetary set, and transmission *B* via the central gear of the planetary set.

2. TRANSMISSION ANALYSIS

Analysis of segregare mechanic-hydrostatic transmissions A, B and C carried out compering next possible traction characteristics

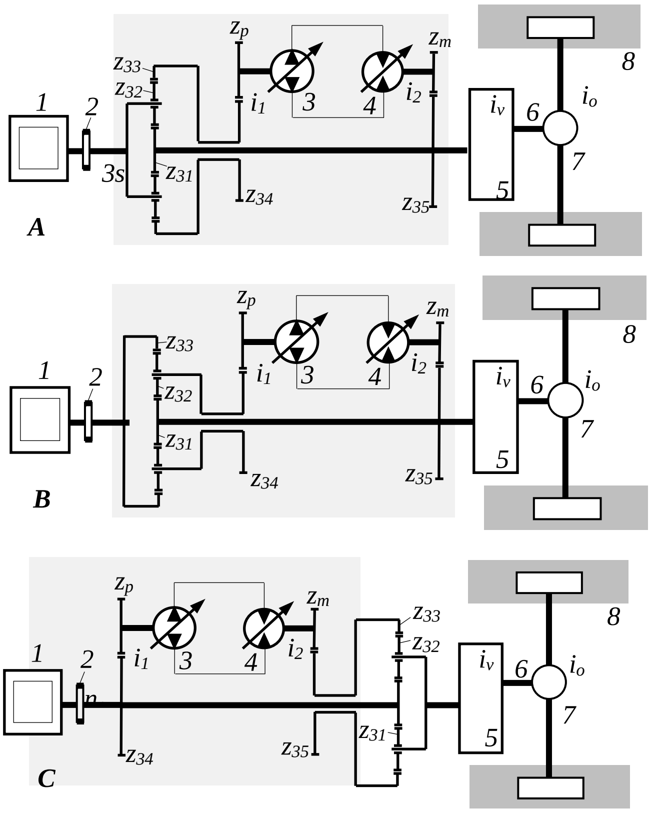

*Figure1: Conceptions of hybrid transmissions **A, B, C***

- maximum possible moving velocity, appropriate traction force and transmission level of efficiency,
- maximum possible traction force, appropriate moving velocity and transmission efficiency level.

When analysing it is taken that diesel engine has maximal power N_{en} at certain revolution number n_{en} and torque M_{en} which is overall transmission torque M_u:

$$M_{en} = M_u \tag{1}$$

Planetary set, in transmission *A* and *B* is at input part while in transmission *C* is at output part of transmission, and has a transmission ratio i_p and efficiency level η_p [5]:

$$i_p = \frac{z_{33}}{z_{31}} \tag{2}$$

*Corresponding author: A. Medvedeva 14, Niš, vesna.jovanovic@masfak.ni.ac.rs

$$\eta_p = 1 - \left[0{,}15\left(\frac{1}{z_{31}}+\frac{1}{z_{32}}\right)+0{,}2\left(\frac{1}{z_{32}}-\frac{1}{z_{33}}\right)\right] \tag{3}$$

where are: z_{31}, z_{32}, z_{33} - the number of teeth of the planetary gear set.

In general, for transmission A, B and C, traction force F_i and moving velocity v_i determined with:

$$v_i = r_d \frac{n_e \cdot \pi}{30} \frac{1}{i_{hn} \cdot i_{vi} \cdot i_o} \tag{4}$$

$$F_i = \frac{1}{r_d} M_e \cdot i_{hm} \cdot i_{vi} \cdot \eta_{vi} \cdot i_o \cdot \eta_o \tag{5}$$

where are: r_d - dynamic radius of wheel, n_e, M_e - engine revolution number and torque, i_{hn}, i_{hm} - kinematic and dynamic transmission ratio of hydrostatic part of transmission with planetary set, i_{vi}, η_{vi} - gearshift transmission ratio and efficiency level, i_o, η_o - drive shaft transmission ratio and efficiency level.

In continuous of this paper, for segregate mechanic-hydrostatic transmission *A*, *B* and *C*, kinematic i_{hn} and mechanic i_{hm} transmission ratios of hydrostatic part of transmission with planetary set are defined.

2.1. Transmission ***A***

Kinematic transmission ratio i_{hna} *of hydrostatic part of transmission* **-** In planetary set, at the input part of transmission *A* relation of revolution number is determined by equation: (Fig.2) [6] [7]:

$$n_{31} - n_{3s} = -i_p \left(n_{33} - n_{3s}\right) \tag{6}$$

where is the diesel engine number of revolutions n_{en} equal to number of revolutions n_{3s} satellite carrier i.e. input number of revolutions n_u:

$$n_{3s} = n_{en} = n_u \tag{7}$$

Central gear revolutions number n_{31} is equal to number n_i of revolutions at the output of hydrostatic part of transmission with planetary set:

$$n_{31} = n_i \tag{8}$$

From the equality of the flow rate Q_p of the hydraulic pump and the hydraulic motor Q_m:

$$Q_p = \frac{q_p \cdot n_p}{1000} \eta_{pv} = Q_m = \frac{q_m \cdot n_m}{1000} \frac{1}{\eta_{mv}} \tag{9}$$

the dependence of the number of revolutions of the hydraulic pump n_p and hydaulic motor is determined:

$$n_p = n_m \frac{q_m}{q_p} \frac{1}{\eta_{pv} \cdot \eta_{mv}} = n_i \cdot i_2 \frac{q_m}{q_p} \frac{1}{\eta_{pv} \cdot \eta_{mv}} \tag{10}$$

where are: η_{pv}, η_{mv} - volumetric efficiency level of hydraulics pump and hydraulic motor, q_p=[q_{pmax}, q_{pmin}], q_m=[q_{mmax}, q_{mmin}]- specific flow rate of hydraulic pump and hydraulic motor in interval from minimum to maximum, $i_2 = n_m/n_i$ - transmission ratio of the gear pair z_{35}/z_m through which the hydraulic motor transmits energy to the output of the transmission.

Number of revolutions n_{33} toothed ring of the planetary set:

$$n_{33} = n_p \cdot i_1 = n_i \cdot i_2 \frac{q_m}{q_p} \cdot \frac{1}{\eta_{pv} \cdot \eta_{mv}} \cdot i_1 \tag{11}$$

where: $i_1 = n_{33}/n_p$ - transmission ratio of the gear pair z_p/z_{34} through which the hydraulic pump receives energy at the input of the transmission.

Substituting equations 10 and 11 into equation 6 gives the following expression:

$$n_i - n_u = -i_p \cdot \left(n_i \cdot i_2 \frac{q_m}{q_p} \cdot \frac{1}{\eta_{pv} \cdot \eta_{mv}} \cdot i_1 - n_u \right) \tag{12}$$

from which, by further arrangement, the kinematic transmission ratio i_{hna} of the hydrostatic part of the transmission *A* is found as the ratio of the input n_u and output n_i revolutions:

$$i_{hna} = \frac{n_u}{n_i} = \frac{1 + i_p \cdot i_1 \cdot i_2 \frac{q_m}{q_p} \frac{1}{\eta_{pv} \cdot \eta_{mv}}}{1 + i_p} \tag{13}$$

Mechanical transmission ratio i_{hm} *of the hydrostatic part of the transmission.*- In planetary set at the input part of transmission *A*, the torque of diesel engine M_{en} is equal to the input torque M_u, i.e. torque of the satellit carrier M_{3s}, where there is a relationship (fig. 2) [4]:

$$M_u = M_{en} = M_{3s} = -M_{31}\left(1 + i_p \cdot \eta_p\right) \tag{14}$$

$$M_{33} = M_{31} \cdot i_p \cdot \eta_p \tag{15}$$

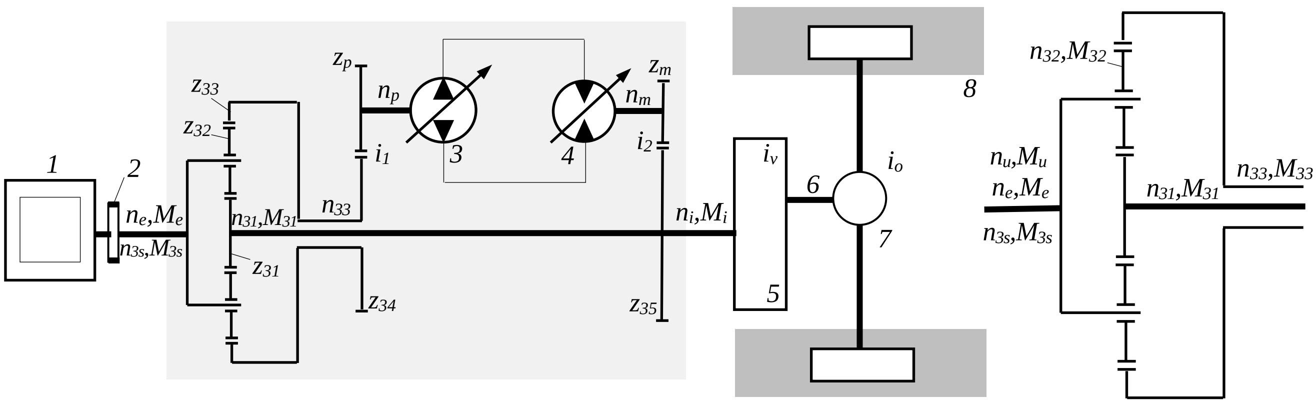

Figure. 2 Transmission A with a planetary set on the input part of the transmission where the diesel engine transmits energy to the stellite carrier and the hydraulic pump receives energy from the toothed ring of the planetary set

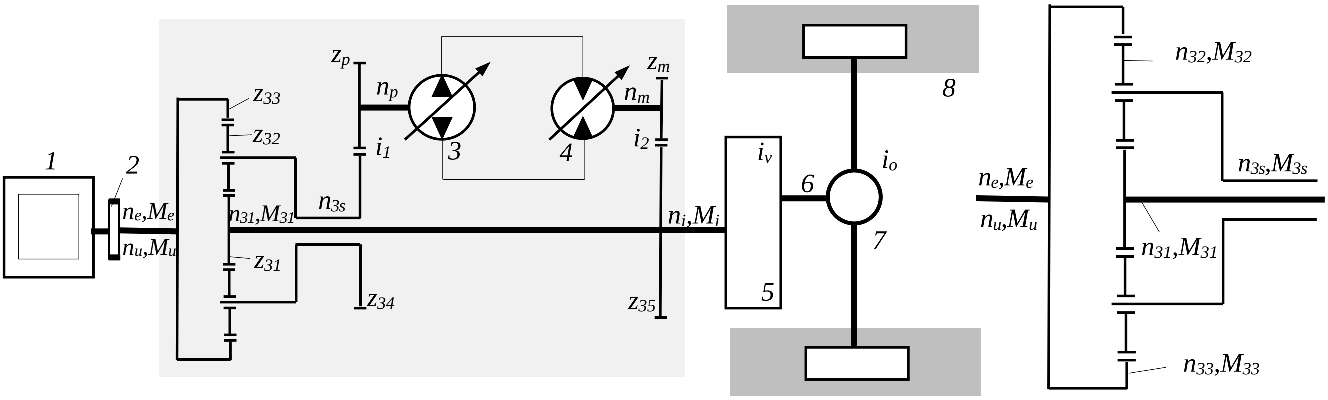

Figure. 3 Transmission B with a planetary set at the input part of the transmission where the diesel engine transmits energy to the toothed ring and the hydraulic pump receives energy from the carrier of the planetary set

so the torque of the central gear M_{31} is:

$$M_{31} = -M_u \frac{1}{1 + i_p \cdot \eta_p} \tag{16}$$

and torque of the ring gear M_{33}:

$$M_{33} = -M_u \frac{i_p \cdot \eta_p}{1 + i_p \cdot \eta_p} \tag{17}$$

Torque M_{33} of toothed ring of planetary set, via gear pair with transmission ratio i_1, transmits to hydraulic pump shaft, so that torque M_p on the hydraulic pump shaft is:

$$M_p = M_{33} \cdot i_1 \cdot \eta_1 = M_u \frac{i_p \cdot \eta_p}{1 + i_p \cdot \eta_p} i_1 \cdot \eta_1 \tag{18}$$

The torque of the hydraulic pump M_p, at a certain specific flow rate q_p of the hydraulic pump:

$$M_p = \frac{q_p \cdot p}{2\pi \cdot \eta_{pm}} \tag{19}$$

corresponds to the pressure p in the pressure line of the hydraulic pump:

$$p = \frac{2\pi \cdot M_p}{q_p} \eta_{pm} \tag{20}$$

at which, neglecting the pressure losses in the lines, the hydraulic motor has a torque M_m:

$$M_m = \frac{q_m \cdot p}{2\pi} \eta_{mm} \tag{21}$$

where are: η_{pm}, η_{mm} - mechanical efficiency level of hydraulic pump and motor

By changing equation 20 into equation 21 dependence of the torque M_m of the hydromotor and the torque M_p of the hydropump is obtained:

$$M_m = M_p \frac{q_m}{q_p} \eta_{pm} \cdot \eta_{mm} \tag{22}$$

Output torque M_i from hydrostatic part of the transmission A is equal to the sum of:

$$M_i = M_{31} + M_m \cdot i_2 \cdot \eta_2 \tag{23}$$

where are: i_2, η_2 - the transmission ratio and efficiency level of the gear pair that connects the shaft of the hydraulic motor and the shaft of the central gear of the planetary set. Substituting equations 15, 18 and 22 into equation 23 the expression obteined:

$$M_i = -M_u \frac{1}{i + i_p \cdot \eta_p} - M_u \frac{i_p \cdot \eta_p}{i + i_p \cdot \eta_p} i_1 \cdot \eta_1 \frac{q_m}{q_p} \eta_{pm} \cdot \eta_{mm} \cdot i_2 \cdot \eta_2 \tag{24}$$

from which, by further arrangement, the mechanical transmission ratio i_{hma} of the hydrostatic part of the transmission A is obtained as the ratio of output M_i and input torque M_u:

$$i_{hma} = \frac{M_i}{M_u} = -\frac{1 + i_p \cdot \eta_p \cdot i_1 \cdot \eta_1 \cdot i_2 \cdot \eta_2 \frac{q_m}{q_p} \eta_{pm} \cdot \eta_{mm}}{1 + i_p \cdot \eta_p} \tag{25}$$

2.2. Transmission ***B***

Kinematic transmission ratio i_{hnb} *of hydrostatic part of transmission* - In planetary set, at the input part of transmission B relation of revolution number is determined by equation 6 where is number of revolutions n_{33} toothed ring equal to diesel engine number of revolutions n_e i.e. input number of revolutions n_u (Fig.3):

$$n_{33} = n_{en} = n_u \tag{26}$$

central gear revolutions number n_{31} is equal to number n_i of revolutions at the output n_i:

$$n_{31} = n_i \tag{27}$$

Considering equality 10, the number of revolutions n_{3s} of the satellite carrier is:

$$n_{3s} = n_p \cdot i_1 = n_i \cdot i_1 \cdot i_2 \frac{q_m}{q_p} \cdot \frac{1}{\eta_{pv} \cdot \eta_{mv}} \tag{28}$$

Substituting equations 26, 27 and 28 into equation 6 gives the following expression:

$$n_i - n_i \cdot i_1 \cdot i_2 \frac{q_m}{q_p} \cdot \frac{1}{\eta_{pv} \cdot \eta_{mv}} = -i_p \cdot \left(n_u - n_i \cdot i_1 \cdot i_2 \frac{q_m}{q_p} \cdot \frac{1}{\eta_{pv} \cdot \eta_{mv}} \right) \tag{29}$$

from which the kinematic transmission ratio i_{hnb} of the hydrostatic part of the transmission is obtained ***B***:

$$i_{hnb} = \frac{\left(1 + i_p\right) \cdot i_1 \cdot i_2 \frac{q_m}{q_p} \frac{1}{\eta_{pv} \cdot \eta_{mv}} - 1}{i_p} \tag{30}$$

Mechanical transmission ratio i_{mb} *of the hydrostatic part of the transmission.*- For the planetary transmission set ***B***, the following torque ratios apply (Fig. 3):

$$M_u = M_{3s} = M_{en} = M_{33} = M_{31} \cdot i_p \cdot \eta_p \tag{31}$$

that is:

$$M_{31} = M_u \frac{1}{i_p \cdot \eta_p} \tag{32}$$

$$M_{3s} = -M_{31}\left(1 + i_p \cdot \eta_p\right) = -M_u \frac{1 + i_p \cdot \eta_p}{i_p \cdot \eta_p} \tag{33}$$

Torque M_p on the hydraulic pump shaft is:

$$M_p = M_{33} \cdot i_1 \cdot \eta_1 = -M_u \frac{1+i_p \cdot \eta_p}{i_p \cdot \eta_p} i_1 \cdot \eta_1 \quad (34)$$

and according to equation 22, the torque M_m of the hydraulic motor:

$$M_m = -M_u \frac{1+i_p \cdot \eta_p}{i_p \cdot \eta_p} i_1 \cdot \eta_1 \frac{q_m}{q_p} \eta_{pm} \cdot \eta_{mm} \quad (35)$$

number n_{33} of revolution toothed ring of the planetary set is obtained:

$$n_{33} = \frac{n_m}{i_2} = \frac{1}{i_2} n_p \frac{q_p}{q_m} \eta_{pv} \cdot \eta_{mv} = n_u \frac{1}{i_1 \cdot i_2} \frac{q_p}{q_m} \eta_{pv} \cdot \eta_{mv} \quad (43)$$

Substituting equations 39, 40 and 43 into equation 6 gives the following expression:

$$n_u - n_i = -i_p \left(n_u \frac{1}{i_1 \cdot i_2} \frac{q_p}{q_m} \eta_{pv} \cdot \eta_{mv} - n_i \right) \quad (44)$$

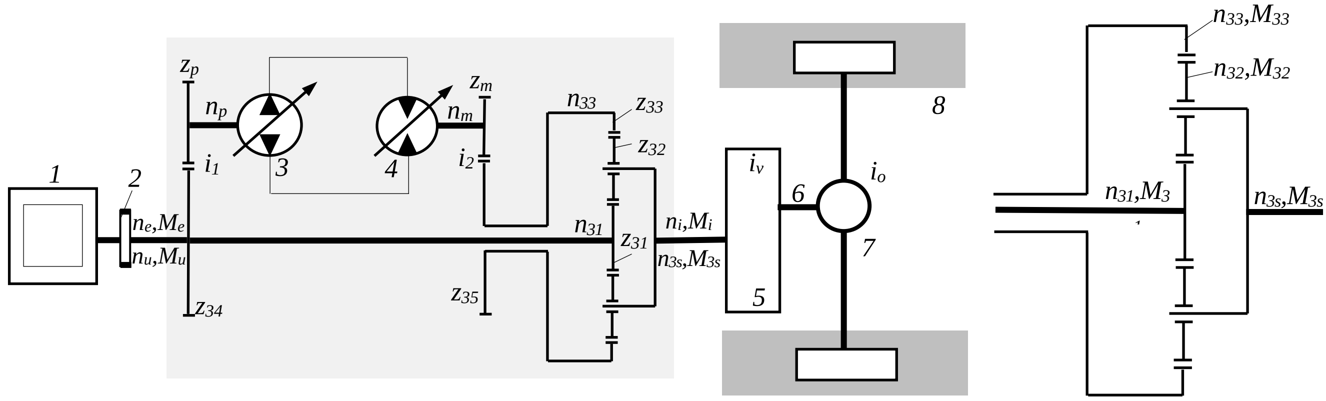

Figure 4. Transmission C with a planetary set on the output part of the transmission, where the diesel engine transmits one part of the energy to the hydropump and the other part to the central gear of the planetary set

Output torque M_i from hydrostatic part of the transmission *B* is equal to the sum of:

$$M_i = M_{31} + M_m \cdot i_2 \cdot \eta_2 \quad (36)$$

Substituting equations 33, 35 into equation 36 gives the following expression:

$$M_i = -M_u \frac{i+i_p \cdot \eta_p}{i_p \cdot \eta_p} - M_u \frac{i+i_p \cdot \eta_p}{i_p \cdot \eta_p} i_1 \cdot \eta_1 \frac{q_m}{q_p} \eta_{pm} \cdot \eta_{mm}. \quad (37)$$

from which the mechanic transmission ratio i_{hmb} of the hydrostatic part of the transmission *B* is obtained:

$$i_{hmb} = \frac{M_i}{M_u} = -\frac{\left(1+i_p \cdot \eta_p\right) \cdot i_1 \cdot \eta_1 \cdot i_2 \cdot \eta_2 \frac{q_m}{q_p} \eta_{pm} \cdot \eta_{mm} - 1}{i_p \cdot \eta_p} \quad (38)$$

2.3. Transmission ***C***

Kinematic transmission ratio i_{hnc} of hydrostatic part of transmission - In planetary set, at the output part of transmission *C* relation of revolution number is determined by equation 6 where is number of revolutions of diesel engine n_{en} as a input number of revolutions n_u equal to number n_{31} of revolutions cetral gear of planeraty set (Fig.4):

$$n_{31} = n_{en} = n_u \quad (39)$$

and number n_{3s} of revolution of satellite carrier is equal to number n_i of revolution of at the output part of transmission:

$$n_{3s} = n_i \quad (40)$$

Number n_p of revolution on the hydraulic pump shaft:

$$n_p = \frac{n_u}{i_1} \quad (41)$$

and number n_m of revolution of the hydraulic motor is:

$$n_m = i_2 \cdot n_{33} \quad (42)$$

Based on 41, 42 and 10 equations which connect number n_p of revolution hydraulic pump and hydraulic motor n_m, from which kinematic transmmision ratio of hydrostatic part of transmission C obtain like a relation of input n_u and output n_i numeber of revolution:

$$i_{hnc} = \frac{n_u}{n_i} = \frac{1+i_p}{1+\frac{i_p}{i_1 \cdot i_2} \frac{q_p}{q_m} \eta_{pv} \cdot \eta_{mv}} \quad (45)$$

Mechanical transmission ratio i_{hmc} of the hydrostatic part of the transmission. - For the planetary set at the output part of the transmission *C*, the torque M_{en} of the diesel engine, as the input torque M_u is equal to the sum of the torques M_p of the hydraulic pump reduced on the shaft of the central gear and the torque of the central gear M_{31} (Fig.4):

$$M_u = M_{en} = \frac{M_p}{i_1 \cdot \eta_1} + M_{31} \quad (46)$$

torque M_i of the hydrostatic part of transmission is equal to the torque of satellite carrier M_{3s} and determined by equation:

$$M_i = M_{3s} = -M_{31}\left(1+i_p \cdot \eta_p\right) \quad (47)$$

from which it follows that the torque M_{31} of the central gear of the planetary set is:

$$M_{31} = -M_i \frac{1}{1+i_p \cdot \eta_p} \quad (48)$$

The torque M_{33} of toothed ring of planetary set is:

$$M_{33} = M_{31} \cdot i_p \cdot \eta_p = M_m \cdot i_2 \cdot \eta_2 \quad (49)$$

from which it follows that the torque M_m of the hydraulic motor is:

$$M_m = M_{31} \frac{i_p \cdot \eta_p}{i_2 \cdot \eta_2} = -M_i \frac{1}{1+i_p \cdot \eta_p} \frac{i_p \cdot \eta_p}{i_2 \cdot \eta_2} \quad (50)$$

According equation 22, the torque on the shaft of hydraulic pump is:

$$M_p = M_m \frac{q_p}{q_m} \frac{1}{\eta_{pm} \cdot \eta_{pm}} = -M_i \frac{1}{1+i_p \cdot \eta_p} \frac{i_p \cdot \eta_p}{i_2 \cdot \eta_2} \frac{q_p}{q_m} \frac{1}{\eta_{pm} \cdot \eta_{mm}} \quad (51)$$

Substituting 48 and 51 equations into equation 46 gives the expression:

$$M_u = -M_i \frac{1}{i + i_p \cdot \eta_p} \frac{i_p \cdot \eta_p}{i_2 \cdot \eta_2} \frac{q_p}{q_m} \frac{1}{\eta_{pm} \cdot \eta_{mm}} \frac{1}{i_1 \cdot \eta_1} - M_i \frac{1}{1 + i_p \cdot \eta_p} \quad (52)$$

из којег се даљим сређивањем, добија механички преносни однос i_{hmc} хидростатичког дела трансмисије ***C*** као однос излазног M_i и улазног момента M_u: from which, by further arrangement, obtains mechanical transmission ratio i_{hmc} of hydrostatic part of transmission C like a relation output M_i and input torque M_u:

$$i_{hmc} = \frac{M_i}{M_u} = -\frac{1 + i_p \cdot \eta_p}{1 + \frac{i_p \cdot \eta_p}{i_1 \cdot \eta_1 \cdot i_2 \cdot \eta_2} \frac{q_p}{q_m} \frac{1}{\eta_{pm} \cdot \eta_{mm}}} \quad (53)$$

Previous defining expressions for kinematic and mechanic transmission ratio $i_{hma,b,c}$ of hydrostatic part of transmission *A*, *B* and *C* show that their values depend on transmission ratio i_p of planetary sets, transmissions ratio i_1, i_2 of gears pair, by which is hydrostatic part linked for mechanical part of transmission, and also depend on specific flow rate q_p, q_m of hydraulic pump and hydraulic motor.

For defined transmission parameters, regulation of traction characteristics is achieved by regulating of change in specific flows rate of hydraulic pump q_p=[q_{pmax}, q_{pmin}] and hydraulic motor q_m=[q_{mmax}, q_{mmin}] in the interval from the minimum to the maximum value.

3. EXAMPLE OF ANALYSIS

As an example, the traction characteristics of mechanical-hydrostatic transmissions A, B and C were analyzed with components of the same parameters (Table 1) defined and selected according to the catalogs of available models of specialized manufacturers (Cummins, Bosch Rexroth, ZF, Michelin) [7].

Based on previously defined expressions for determining traction characteristics, the following transmission indicators were calculated at maximum power and number of revolutions at maximum power of the diesel engine (Table 2):

- maximal velocity and corresponding traction force, also efficiency level of transmission
- maximal traction force and velocity corresponding , also efficiency level of transmission.

For the sake of comparison, the same traction characteristics were determined for the mechanical transmission variant *D* (Table 2) which in concept corresponds to hybrid transmissions A, B and C without the hydrostatic part of the transmission.

. The obtained results show that the traction characteristics of the transmissions differ. Among the mechanical-hydrostatic transmissions A, B and C, transmission B stands out in particular, which has a significantly higher maximum speed of movement and maximum traction force, and the lowest efficiency level of the transmission.

Traction characteristics of transmission V differ because, compared to transmission *A*, most of the diesel engine's energy is separated via the planetary set and transmitted through the hydrostatic part of the transmission, which, through regulation, enables greater traction characteristics with a lower efficiency level compared to the mechanical part of the transmission.

In transmission *B*, most of the drive motor's energy is transmitted through the hydrostatic part of the transmission, because the hydraulic pump receives energy from the engine via the central gear of the planetary set, unlike transmission *A*, where the hydraulic pump receives energy from the engine via the toothed ring of the planetary set.

It is characteristic that the possible maximum traction forces of mechanical transmission *D* are significantly less than the possible maximum traction forces of mechanical-hydrostatic transmissions *A*, *B* and *C*. At the same time, the speed of movement at the maximum traction force and the efficiency level are slightly higher with the mechanical transmission *D*.

Higher traction forces and their wider range in the case of mechanical-hydrostatic transmissions *A*, *B* and *C* are made possible by the regulation of the hydrostatic part of the transmission by the combined regulation of the change in the specific flows of the hydraulic pump and the hydraulic motor.

*Table 1: Transmission parameters **A, B, C, D***

Transmission parameters	Label	Value
Maximum power of the diesel engine	N_{en}	*45 kW*
Number of revolutions of the diesel engine at maximum power	n_{en}	*2200 min^{-1}*
Number of gear teeth of the planetary transmission set	$z_{31}/ z_{32}/ z_{33}$	*29/24/77*
Transmission ratio/efficiency level of the gear pair of the hydraulic pump	i_1/η_1	*0,58/0,98*
Maximal/minimal specific flow rate of the hydraulic pump	.q_{pmax}/q_{pmin}	*58,3/25 cm^3*
The volumetric/mechanical efficiency level of the hydraulic pump	η_{pv}/η_{pm}	*0,97/0,96*
Maximal/minimal specific flow of the hydraulic motor	q_{mmax}/q_{mmin}	*80/30 cm^3*
The volumetric/mechanical efficiency level of the hydraulic motor	η_{mv}/η_{mm}	*0,96/0,95*
Transmission ratio/efficiency level of the gear pair of the hydraulic motor	i_2/η_2	*2,43/0,98*
Transmission ratio/ efficiency level of the 1st gear box	i_{v1}/η_{v1}	*5,3/0,96*
Transmission ratio/ efficiency level of the 2st gear box	i_{v2}/η_{v2}	*1,39/0,97*
Transmission ratio/ efficiency level of the drive shaft	i_o/η_o	*15,28/0,95*
Dynamic radius of wheel	r_d	*0,681*

*Table 2: Traction characteristics of transmission **A, B, C, D***

The name of the traction characteristic	Label	Unit	Transmission			
			A	***B***	***C***	***D***
Maximum movement speed	v_{max}	*km/h*	*24,761*	*29,875*	*25,046*	*26,592*
Traction force at maximum speed	F	*kN*	*5,391*	*3,626*	*5,179*	*5,672*
Level of efficiency	η_t	-	*0,825*	*0,668*	*0,800*	*0,931*
Брзина кретања при максималној сили вуче	v	*km/h*	*1,406*	*0,857*	*2,285*	*6,974*
Speed of movement at maximum traction force	F_{max}	*kN*	*87,418*	*141,772*	*60,632*	*21,181*
Level of efficiency	η_t	-	*0,824*	*0,749*	*0,855*	*0,912*

4. CONCLUSION

The obtained research results given in the paper show that the traction characteristics of hybrid mechanical-hydrostatic transmissions depend on the way of connecting the hydrostatic part of the transmission to the mechanical part of the transmission. In addition, compared to mechanical transmissions, hybrid mechanical-hydrostatic transmissions enable optimal regulation and a wider range of changes in traction characteristics.

Due to the mentioned advantages, mechanical-hydrostatic transmissions are used in mobile machines that perform their primary functions by moving the moving mechanism.

Further research is related to the comparative analysis of traction characteristics of variant solutions of mechanical-hydrostatic transmissions at the maximum torque of the diesel engine and variable efficiency level of the hydraulic pump and hydraulic motor depending on the load of the transmission, that is, the pressure and flow of the hydrostatic part of the transmission.

ACKNOWLEDGEMENTS

This research was financially supported by the Ministry of Education, Science and Technological Development of the Republic of Serbia (Contract No. 451-03-9/2021-14/200109).

REFERENCES

[1] M. Šušnjar,,Z. Pandur, M. Bačić, K. Lepoglavec, H.Nevečerel, H. Kopseak, “Possibilities for the Development of an Electric Hybrid Skidder Based on Energy Consumption Measurement in Real Terrain Conditions,” Forests 14(1), (2023).

[2] Q. Zhang, F. Wang, B. Xu, “Energy efficiency improvement of battery powered wheel loader with an electric-hydrostatic hybrid powertrain“ Proceedings of the Institution of Mechanical Engineers, Part D: Journal of Automobile Engineering,” 237(1), (2022)

[3] Z. Tong, Y. Jiang, S. Tong, Q. Zhang, J. Wu, “Hybrid drivetrain with dual energy regeneration and collaborative control of driving and lifting for construction machinery,“ Automation in Construction, vol.150, (2023)

[4] A. Buchroithner, “Supersystem of Mobile Flywheel Energy Storage,“ Flywheel Energy Storage, First Online, pp.49-65, (2023)

[5] V. Jovanović, “A contribution to the synthesis of the slewing platform drive mechanism of hydraulic excavators,“ PhD dissertation, (in Serbian), University of Niš, Faculty of Mechanical Engineering (2018).

[6] D. Janošević, “Designing mobile machines“,(in Serbian), University of Niš, Faculty of Mechanical Engineering, Niš, (2006)

[7] D. Janošević, V. Jovanović, P.Milić, J. Pavlović, “Mobile machines and vehicles,“ (in Serbian), (2020)

Determination of resistance forces in the wheel loader using discrete element method

Jovan Pavlović[1*], Dragoslav Janošević[1], Vesna Jovanović[1], Nikola Petrović[1]
[1]Faculty of Mechanical Engineering/Department for Material Handling Equipment and Logistics, University of Niš, Niš (Serbia)

Determining the resistance force is an important task in the synthesis of drive mechanisms of mobile machines that interact with soil or granular material. The paper presents the three most commonly used material loading techniques used by operators in wheel loaders. Reaction forces that occur during the interaction of bucket-granular material are determined using the software based on the discrete element method which considers each particle of granular material as separate (discrete) element. Granular material in simulation is genereted with different size of particles. The research shows that the resistance forces depends on the type of material and on the loading techniques. As an example, resistance forces for a loader with a mass of 15.000 kg and a bucket volume of 2.3 m^3 are given.

Keywords: Wheel loader, resistance forces, discrete element method

1. INTRODUCTION

A wheel loaders are part of mobile machinery mainly used to load and unload bulk materials and for light excavation work. The basic function of loaders of all sizes is the cyclic transport of material which consists of the following operations (Fig.1a): loading (digging), transport and unloading of material, and returning to the new loading position. The loading operation can be performed in different ways adapted to the type and configuration of the material being handled, where the bucket, as the basic tool of the loader mechanisms, needs to overcome certain digging resistances with an appropriate digging force.

The basic function of the loaders is realized by the general configuration of the kinematic chain consisting of: the rear L_1 (Fig. 1b) and the front L_2 support movement member and the manipulator with arm L_3 and the bucket L_4.

One of the challenging tasks in the loaders simulation, as well as other mobile machines, is to determine the digging resistance forces that occurs when the material is loading. Digging resistance forces occurs in the form of a forces that can depend on the properties of the material such as porosity, humidity, density, looseness, etc. Besides the properties of the material, digging resistance forces are affected by the geometry of the bucket (the shape of the cutting edge of the bucket, the bucket volume, the shape of the teeth and the teeth detrition) and the digging trajectories of loader that can be different and adapted to the material type.

Previous research [1][2] show that it is possible to achieve reasonable estimates of the interaction forces between the bucket and soil. Authors utilize the empirical and analytical studies in soil mechanics that have assumptions and describes the bucket–soil interaction as consisting of five force components: the weight of the loaded material; the resistance force created if the bucket motion causes it to compress the dirt pile; the net friction force between soil and bucket; the digging resistance acting at the bucket cutting edge; the inertial force required to accelerate the accumulated mass.

Further research use discrete element method that has proven itself to be particularly suitable for calculating the behaviour of granular material wich. Especially when optimising the design or operation of an mobile machine, a deep understanding of the ongoing processes is essential. Computer simulations based on the Discrete Element Method (DEM) offer a possibility to comprehend the granular material behaviour. In contrast to other DEM simulations, the granular material has a strong influence on the machine dynamics during the loading (digging) operation. In paper [3] simulations in combination with optimal control to find the optimal bucket filling strategy is given. In paper [4] author propose combination of descrete elemelent method with a simulation of the whole machine, including multi body systems and hydraulics that gives realistic loads from the working process. In paper [5] a bucket design optimization is given based on simulation in discrete element method software Factors such as particle flow, particle compression and loading setup adds complexity and uncertainty to the task.

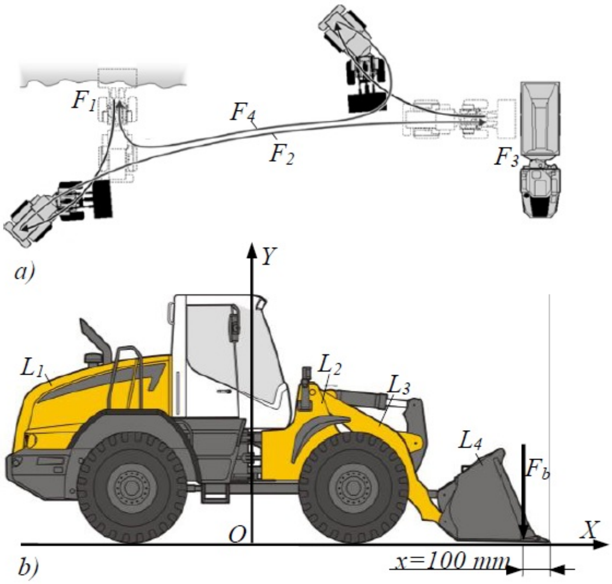

Fig. 1 Wheel loaders: a) functions of loader,b) physical model of loader

*Corresponding author: Aleksandra Medvedeva 14, Niš, jovan.pavlovic@masfak.ni.ac.rs

2. ANALYTICAL DETERMINATION OF RESISTANCE FORCES

In mathematical models of the loader resistance forces, it is consider that drive mechnisms of the loader are planar mechanism and that the resistance forces are acting in middle of bucket cutting edge.

Material loading operations are most often done by first penetrating the bucket into a pile of material and then loading the bucket by rotating the bucket around the top of the arm. In the horizontal penetration of the bucket at the speed of the loader v (Fig. 2), the following components of the digging resistance forces occur: W_{x1} - resistances along the horizontal cutting edge, W_{x2} - resistances along vertical cutting edges, W_{x3} - friction resistances of the loaded material on bottom of bucket, W_{x4} - friction resistance on the inner and outer latarel side of the bucket, W_{x5} - friction resistances on the outer surface of the bucket bottom, W_{x6} - friction resistances on the folded part of the bucket.

The sum of horizontal resistance force W_{xr} of bucket loading:

$$W_{xr} = W_{x1} + 2W_{x2} + W_{x3} + 4W_{x4} + W_{x5} + W_{x6} \quad (1)$$

At the end of the penetrating, by rotating the bucket around the top of the arm, at angular velocity ω (Fig.2), the bucket fills up, with the following vertical resistances: W_{y1} - slip resistance of the loaded material prism on the ground plane of the material pile, W_{y2} - the slip resistance of the loaded material prism on the vertical lateral plane of the material pile, W_{y3} - the resistance of penetration of the bucket lateral edges, W_{y4} - the material friction resistance on the inner and outer bucket lateral sides, W_{y5} - the vertical load of material at the bottom of the bucket [7] [8].

The sum of vertical resistance force W_{yr} of bucket loading:

$$W_{yr} = W_{y1} + 2W_{y2} + 2W_{y3} + 4W_{y4} + W_{y5} \quad (2)$$

The resistance forces components made up of a spatial system of forces that is difficult to analytically determine for the simplest forms of material digging tools.

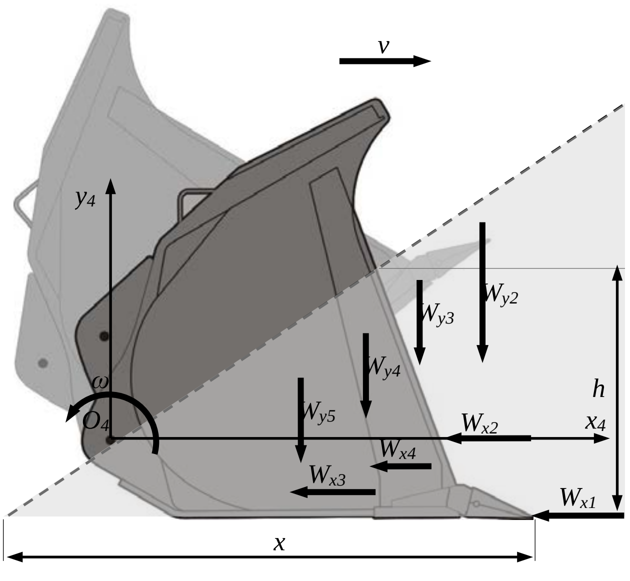

Fig. 2 Model for analytical determination of the resistance force components

3. DISCRETE ELEMENT METHOD

Because of the complexity and too many influencing factors in the analytical determination of the loaders resistance forces and other mobile machines, a discrete element method (DEM) is used, which simulates the actual loading process of the loader bucket in material that can be classifed into cohesionless, cohesive, and cemented materials.

DEM is a numerical method used to predict the motion and collision of spherical particles during transport The calculation is performed in discrete time steps. Between each time step the particles move along the straight line based on the calculated speeds and acceleration at that time step. These trajectories are used to calculate the positions (spatial coordinates) of the particles in the next time step.

Particle overlaps (contacts) are used to calculate the forces acting on each particle, which determines their speeds and acceleration for each particle in the next discrete time step.

The force and moment acting on a particle represent the sum of all forces and moments that act on a particle which involves gravitational force and the compresive force of the material Eq. (3) and Eq (4).

$$m_i \frac{dv_i}{dt} = F_{ij}^n + F_{ij}^t + m_i g \quad (3)$$

$$I_i \frac{d\omega_i}{dt} = R_i \times F_{ij}^t - \tau_{ij}^r \quad (4)$$

where: m_i - the mass of the particle, I_i - the particle moment of inertia, ν_i - the translation velocity of the particle, ω_i - rotation velocity of the particle, F_{ij}^n, F_{ij}^t - normal and tangential forces that occur due to the contact between the particle i and particle j at the current time step (Fig. 3), R_i - vector that begin form the centar of the particle and is directed in the direction of the acting force F_{ij}^t.

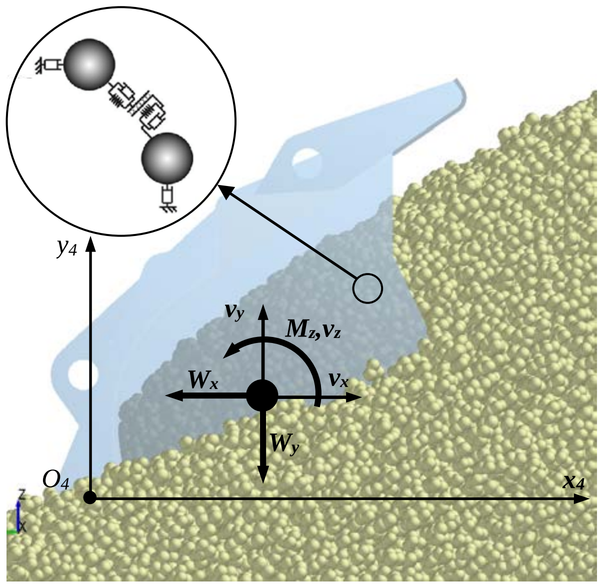

Fig. 3 Model for determination of resistance force components by discrete elements method

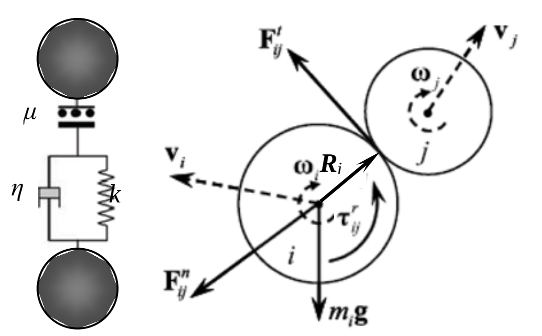

Fig. 4 Mathematical model of DEM

Based on the contact model (Fig. 4), the normal and tangential force are:

$$F_{ij}^n = \left(-k_n \delta_{ij}^n - \eta_n v_{ij}^n\right) \quad (5)$$

$$F_{ij}^t = \left(-k_t \delta_{ij}^t - \eta_t v_{ij}^s\right) \quad (6)$$

where: k_n, k_t - the elasticity coefficients in the normal and the tangential direction, η_n, η_t - the damping coefficient, μ - the friction coefficient defined in the simulation, $\delta_{ij}^n, \delta_{ij}^t$ - the displacement of the particle in the normal and tangential direction due to the action of the normal and tangential force, v_{ij}^n - relative velocity in normal direction, v_{ij}^s - slip velocity on the contact surface [6].

4. SIMULATION OF WHEEL LOADER RESISTANCE FORCES

Research related to the efficiency of loader work shows that the basic sub-operation (loading) of the manipulation task are performed in different ways. According to the results of the conducted research, the method of carrying out the loading sub-operation depends, among other things, on the type of material, working conditions (whether the material is in an unlimited or limited space) and the machine operator skills.

Examples of numerical loader simulation are given for three manipulation tasks with different loading methods: linear, stepped and parabolic.

4.1. Linear loading method

This kind of digging trajectory (Fig.5a) is used by mobile machine operators who want to take advantages of the accelerated movement of the loader, that is the inertial force that allows the bucket to penetrate into the material, whereupon the loading of the material is achieved by rotation of the bucket. This type of bucket movement reduces the working cycle, but it is only possible to use in light materials.

4.2. Stepped loading method

This digging trajectory (Fig.5b) consists of predefined number of steps. At each step, the loader is stationary while the arm is lifting and and bucket is rotating. The new step begin when loader is moved forward. This type of digging trajectory is used by less experienced operators or experienced operators who work with heavy materials, gradually filling the bucket by repeatedly advancing in a pile of materials

4.3. Parabolic loading method

This type of motion consists of the simultaneous movement of the loader and the rotation of the bucket, thus forming the movement of the bucket cutting edge in the form of a parabola, by which this type of bucket movement has been named. The operators who trying to achieve a type this of loading trajectory, due to realization difficulty, will most often carry out a parabolic movement.

Researches have shown that loader operators most often use the first method of material loading with a straight path of bucket penetration due to the easy way to control the machine because the machine movement commands and the bucket rotation commands are separated and their activation is not simultaneous. Disadvantages of this method of loading are increased movement resistance and material spillage when filling the bucket [9] [10].

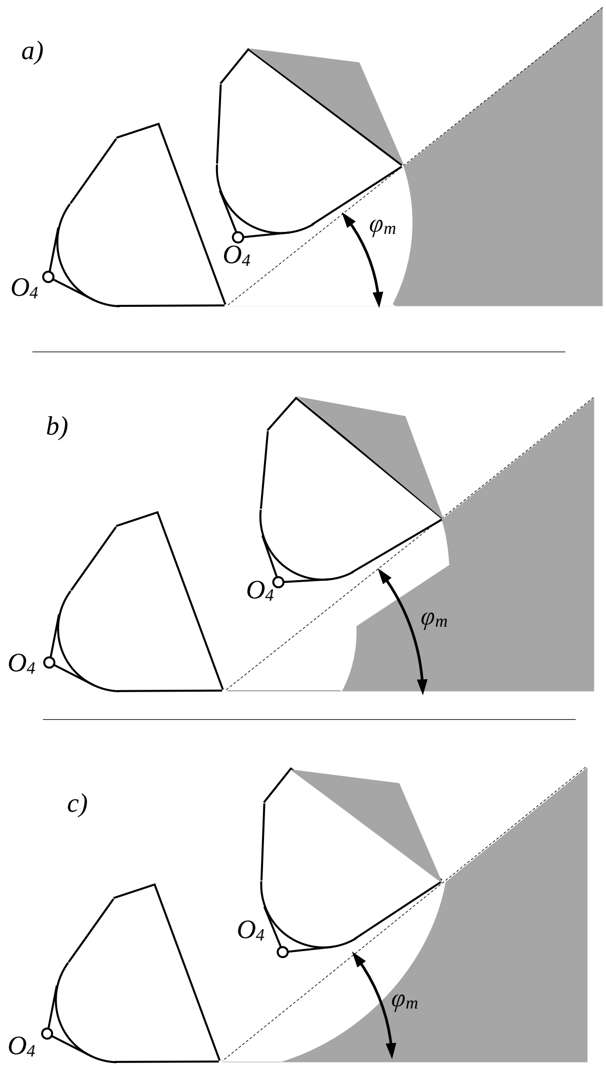

Fig. 5 Loading methods: a) linear, b) stepped and c) parabolic

5. RESULATS OF SIMULATION

The parameters of the simulation conditions were determined on the basis of the analysis of the manipulation tasks of the loader which have in mass *15000 kg*, during the cyclic transport of granular material in operational conditions. The analysis includes tasks involving the loading material in an unlimited area and transfer along a *V* path on a flat horizontal surface with unloading point.
For simulation of the loading operation there are used software *EDEM* which is based on discrete element method. Models of loading operation are with different loading trajectories of the same material. From the menu of the *EDEM* software, a mass of granular material was selected, which size was generated by a normal distribution with the highest percentage of size particle was *61,5 mm*, ranging from *51,5* to *71,5 mm*, which makes a mass of material with a volume of about *300* m^3 on a horizontal surface with a angle of inclination $\varphi_m=50^o$.

Also, from the menu of the *EDEM* software, material characteristics and coefficients of interaction with the bucket made of steel sheets were adopted (Table 1) which reflect the most common work technologies, but also the mass and volume of the bucket, i.e. the stability conditions of the simulated loader model.

5.1. Resistance forces

Resistances are determined by vectors of the resistance force W_i (Fig. 6a and Fig. 6b) and the moment of resistance M_{wi} (Fig. 7a and Fig. 7b) in the coordinate system with the coordinate origin at the bucket center of mass and the coordinate axes parallel to the axes of the absolute coordinate system of the set mathematical model of the loader. The obtained results show that the components W_{xi}, W_{yi}, W_{zi} of the resistance force vector W_i are very different in intensity and character of change during the manipulation tasks.

The highest intensity has the components W_{xi}, W_{yi} of the loading resistance forces that act during different *OZ* axis have insignificant values. The changes in components W_{xi} and W_{yi} depends on the method of the material loading.

Table 2. Characteristics of the genereted material and coefficients of interaction with the steel bucket

Input parameters	Genereted material	Steel
Density ρ *[kg/m^3]*	*1934*	*7850*
Shear modulus *G [Pa]*	$1\cdot10^7$	$7{,}93\cdot10^{10}$
Poisson's ratio ν	*0,25*	*0,25*
Interaction	**Particle-Particle**	**Particle-Steel**
Coefficient of restitution	*0,75*	*0,75*
Static coefficient of friction	*0,32*	*0,25*
Coefficient of rolling friction	*0,2*	*0,05*

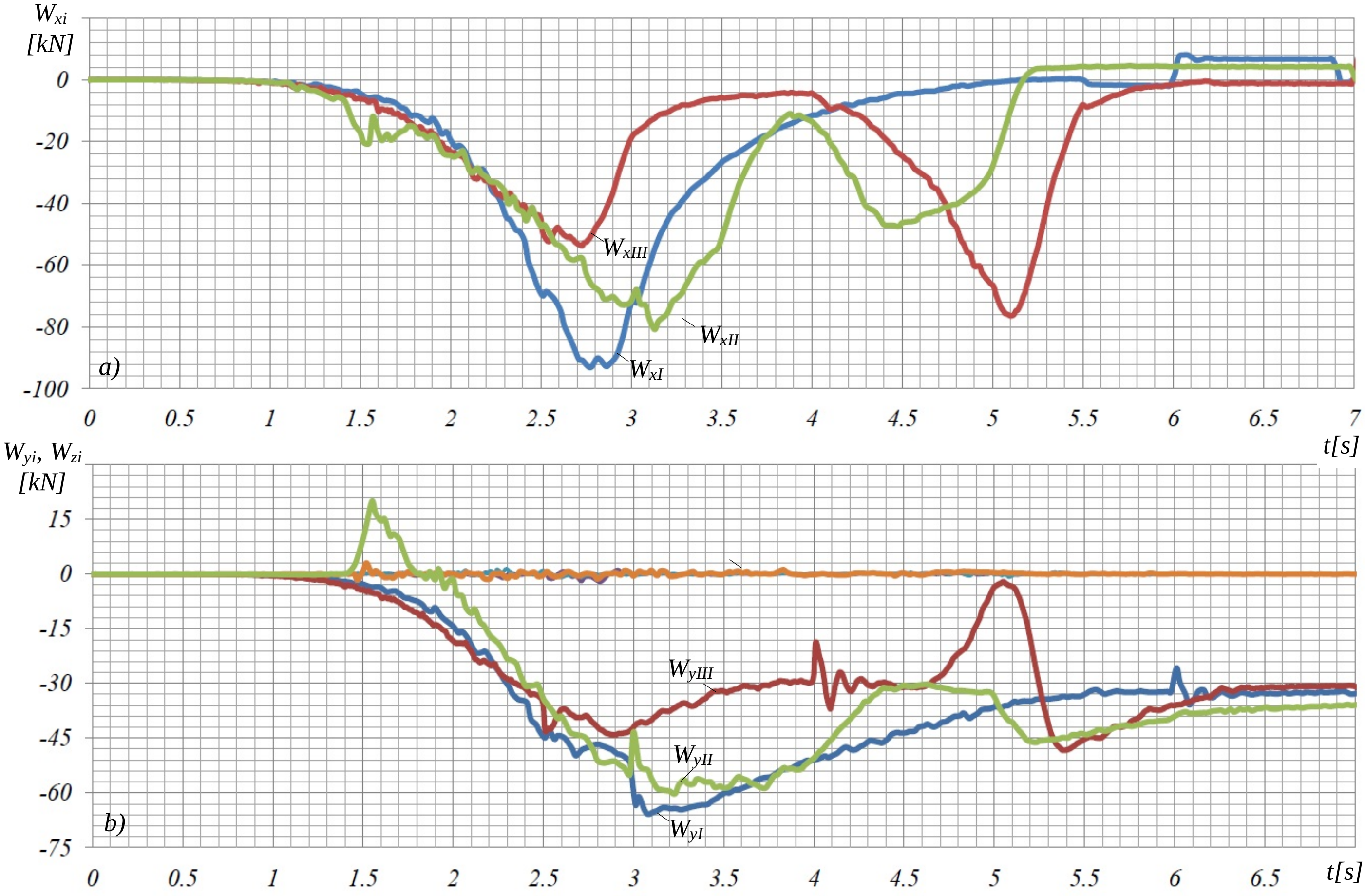

Fig. 6 Components: a) W_{xi} and b) W_{yi}, W_{zi} of the resistance force vector of linear (I), stepped (II) and parabolic (III) loading method

In the first (I) loading method, in the phase of accelerated movement of the machine, i.e. accelerated horizontal penetration of the bucket into the mass of material, the components W_{xI} and W_{yI} of the resistance forces gradually increase, and in the stopping phase of the movement of the machine they gradually decrease without significant sudden changes.

In the second (II) loading method, the W_{xII} and W_{yII} components have very suddenly changes due to the intermittent and stepwise penetration of the bucket into the mass of material. A characteristic change occurred when ($t=5s$) the W_{yII} component suddenly decreased and the W_{xII} component suddenly increased. Such a change occurred due to the horizontal penetration of the bucket at maximum speed without its closing rotation at the beginning of the second level of material capture.

In the third (III) method of material loading, the W_{xIII} and W_{yIII} components have sharp changes. The first such change appeared at the beginning of the manipulation task ($t=1.5$-2 s) when the bucket at the maximum penetration speed exerted pressure on the material so that, apart from component W_{xIII}, which acts in the negative direction of the *OX* axis, the component W_{yIII}, which acts in the positive direction of the *OY* axis, appeared as a reaction of the pressed material outside the bucket. The second characteristic change occurred ($t=3s$) when the W_{xIII} and W_{yIII} components reached their highest intensities, which were caused by the maximum horizontal speed of the bucket penetration while simultaneously raising the boom and closing the bucket .

During material transport operations the components of the force that act on bucket from loaded material, have insignificantly small values. The obtained results show (Fig. 7a and Fig. 7b) that the components of moments M_{wi} of resistance have very different intensities and character of change during operation tasks. The components M_{wzi} of the resistance moment acting around the *OZ* axis during loading operations ($t=0$-7 s) have the greatest intensity, with the character of changes, depending on the method of the material loading, similar to changes in the components W_{xi} and W_{yi} of the loading resistance forces.

The frequency of changes of low intensity of the components M_{wxi} and M_{wyi} of the resistance moments occurs during the loading operations ($t=2$-4 s) due to the action of the components W_{zi} (*Fig. 7 a*) of the forces that occur due to the interaction of the granules of the captured material when the bucket is loading.

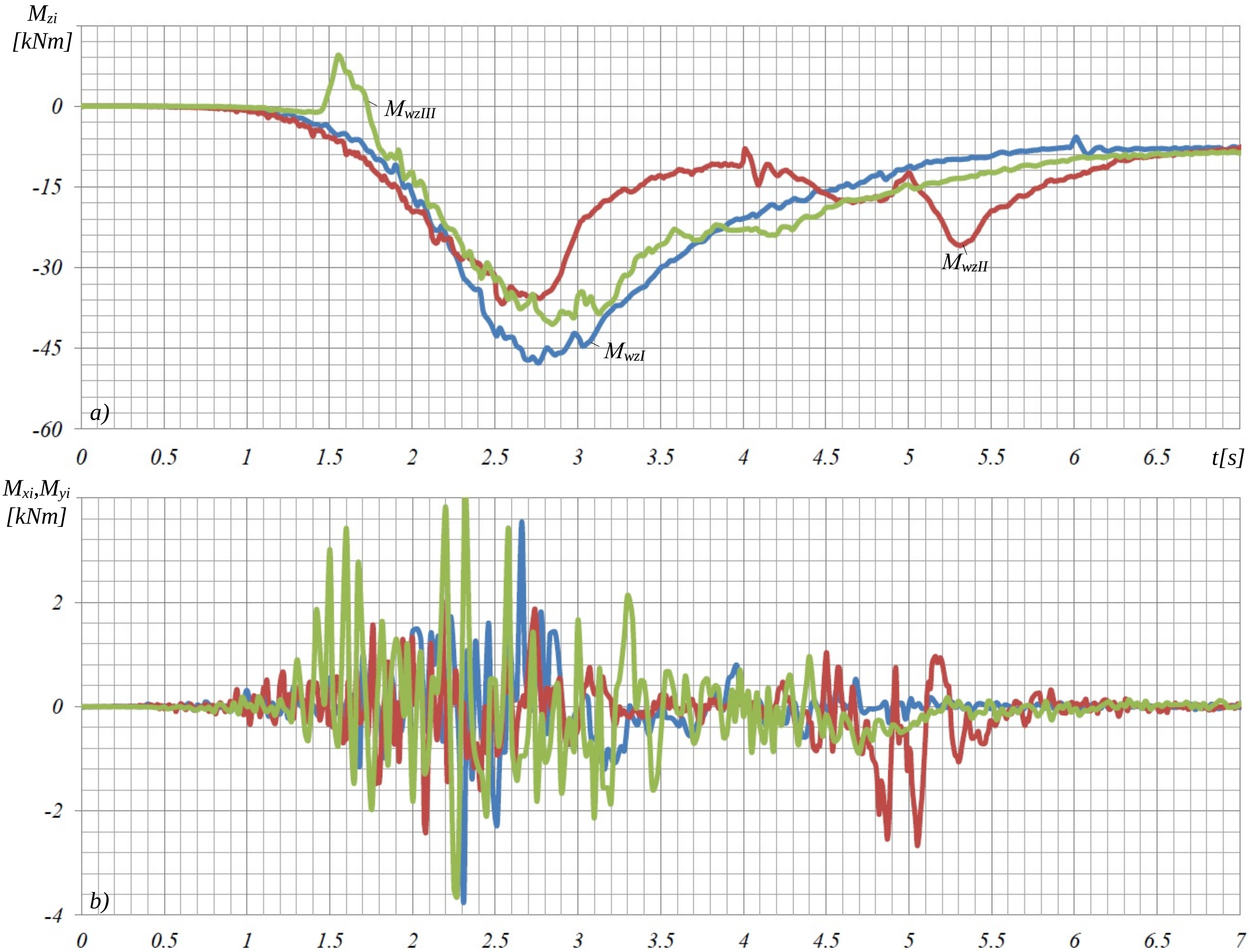

Fig. 7 Components: a) M_{zi} and b) M_{xi}, W_{yi} of the moments of resistance force of linear (I), stepped (II) and parabolic (III) loading method

CONCLUSION

Using the developed procedure of loader simulation, research was carried out with the aim of determining the type, intensity and character of the load change of the manipulator's drive mechanisms during the operation task of the loader, the impact of the load from the resistance of the loaded material on the load on the mechanisms, importance and size of kinematic, dynamic and energy parameters of individual operations of the manipulation task of the loader required for the synthesis of the drive mechanisms of the manipulator.

ACKNOWLEDGEMENTS

This research was financially supported by the Ministry of Education, Science and Technological Development of the Republic of Serbia (Contract No. 451-03-9/2021-14/200109).

REFERENCES

[1] L. Wu, “A Study on Automatic Control of Wheel Loaders in Rock/Soil Loading”, (Doctoral dissertation) University of Arizona, Faculty of the Mining and Geological Engineering, 2003.

[2] S. Sarata, N. Koyachi, T. Tsubouchi, H. Osumi, M. Kurisu, K. Sugawara, “Development of Autonomous System for Loading Operation by Wheel Loader”, In the proceedings of the 23rd International Symposium on Automation and Robotics in Construction (ISARC 2006), Tokyo, Japan, October 3-5, pages 466–471, 2006.

[3] R. Filla, B. Frank, “Towards Finding the Optimal Bucket Filling Strategy through Simulation”, Proceedings in the 15th Scandinavian International Conference on Fluid Power, SICFP’17, June 7-9, Linköping, Sweden, pp. 402-417, 2017.

[4] D. M. Lindmark, M. Servin, “Computational Exploration of Robotic Rock Loading”, Robotics and Autonomous Systems, Vol. 106, pp. 117–129, 2018. doi: 10.1016/j.robot.2018.04.010

[5] H. Takahashi, T. Yoshiaki, E. Nakano, “Analysis of Resistive Forces Acting on the Bucket of LHD in the Scooping Task”, In proceedings of the 16th ISARC, Madrid, Spain, pp. 517-522, 1999.

[6] R. Filla, “Evaluating the Efficiency of Wheel Loader Bucket Designs and Bucket Filling Strategies with Non-coupled DEM Simulations and Simple Performance indicators”, in proceedings of Fachtagung Baumaschinentechnik, Dresden, Germany, pp.1-20, 2015. doi: 10.13140/RG.2.1.1507.1201

[7] F. Henriksson, J. Minta,: “Bucket-soil Interaction for Wheel Loaders : An application of the Discrete Element Method”, (Dissertation). Linnaeus University, Faculty of Technology, Kalmar, 2016.

[8] J. Helgesson, “Optimization of Bucket Design for Underground Loaders”, (Dissertation) Chalmers University of Technology, Göteborg, 2010.

[9] A. Hemami, F. H. Ferri, “Simulation of the Resistance Forces of Bulk Media to Bucket in a Loading Process”, In proceedings of 24th International Symposium on Automation and Robotics in Construction, pp. 163-168, 2007. doi: 10.22260/ISARC2007/003

[10] O. Kanai, S. Sarata, M. Kurisu, “Autonomous Scooping of a Rock Pile By a Wheel Loader Using Disturbance Observer”, In the proceedings of the 23rd Internati-onal Symposium on Automation and Robotics in Construction (ISARC 2006), Tokyo, Japan, October 3-5, pp. 472-475, 2006.

A hybrid MCDM model for waste oil transfer station location selection

Jelena Mihajlović[1*], Goran Petrović[1], Danijel Marković[1], Dragan Marinković[2], Žarko Ćojbašić[1], Dušan Ćirić[1]
[1]Faculty of Mechanical Engineering in Niš, University of Niš, Niš (Serbia)
[2]Department of Structural Analysis, University TU Berlin, Berlin (Germany)

The facility location selection became a major interest for the organizations to establish their planned businesses for a long period of time. The choice of the best location among a set of available locations is a complex process. Although the multiple criteria decision-making (MCDM) methods are applicable for location selection problems, different solutions can be obtained using different MCDM methods. In this paper, the application of hybrid MCDM approaches, for the selection of the best location of the waste oil transfer station in the regional canter of southern and eastern Serbia - the city of Niš, is considered. Specifically, the criteria weights have been determined by the fuzzy PIPRECIA (Pivot Pairwise Relative Criteria Importance Assessment) method in combination with Geometric Mean (GM). Chosen methods, the fuzzy TOPSIS (Technique for the Order Preference by Similarity to Ideal Solution), the fuzzy WASPAS (Weighted Aggregated Sum Product Assessment), and the fuzzy ARAS (Additive Ratio Assessment) have been used for ranking alternative locations.

Keywords: Hybrid MCDM model, fuzzy, waste oil, transfer station, location selection

1. INTRODUCTION

One of the logistic systems' most observed and studied problems is the location selection problem. It primarily consists of a variety of criteria while in most cases the researchers are focused on the criteria of the minimal transportation costs. The location selection deals with the multiple available choices based on the specifically defined criteria set to provide the decision maker with the most suitable location for its object or facility. The various types of location selection problems have been observed in the open literature, specifically for this paper’s purposes the location selection for the waste oil transfer station. Since there are many possible outcomes and numerous directions or criteria types that could be taken into consideration the multiple criteria decision-making (MCDM) methods could be the best tool to solve such a problem.

The widely spread MCDM methodology was in use for the location selection problems. Some classical methods have been applied, but nowadays, more enhanced approaches emerge in the way of fuzzy and hybrid MCDM variants. Researchers in Turkey used classical MCDM methods (AHP, ANP, Electre, and Promethee) to solve the location selection problem for recycling used electrical and electronic equipment [1]. New approaches, such as fuzzy and hybrid MCDM methods, were also used for solving the location selection problems. Thus, the Fuzzy AHP method has been applied to a solid waste landfill site in the Asir region in Saudi Arabia [2]. Also, fuzzy TOPSIS was used for sustainable collection canter locations for electronic waste [3]. One of the researches described the application of the hybrid decision-making approach which has combined three MCDM methods BWM (Best-Worst Method), MULTIMOORA (Full Multiplicative Multi-Objective Optimization on the basic of Ratio Analysis), and GIS (Geographic Information System) for the sustainable landfill location selection [4]. The BWM method was applied for waste disposal technology selection [5], and the BWM-grey MARCOS model based on GIS was used for landfill location selection for healthcare waste in urban areas [6]. Also, the site assessment of a household waste processing plant was also obtained by MCDM methodology, and the Pythagorean fuzzy environment was applied [7]. Some researchers applied the interval type-2 Fuzzy ARAS method for recycling facility location problems [8].

Numerous studies have shown that no single MCDM method is the best solution for given decision-making problem, and that a hybrid combination of different theoretical approaches of MCDM methods can provide a more robust and comprehensive decision rule. Specifically, this paper aims at solving the location selection problem for the used motor oil transfer station in the regional canter of Southern and Eastern Serbia – the city of Niš. Such a facility would be adequate for collection, storage, and treatment to final disposal of the used motor oils.

The paper’s outline is as follows: hazardous waste management where hazardous waste is described with emphasizing the waste oil in correlation with environment protection involving the waste oil transfer stations 2; the structure of the hybrid approach to the decision-making process is presented in section 3; while the obtained results and their discussion are given in section 4; finally, section 5 provides concluding remarks as well as potential future research directions.

2. HAZARDOUZ WASTE MANAGEMENT

Urban growth and rural shrinkage are ongoing worldwide trends that do not seem to have an end. The urban growth is accompanied by the population migration from the villages to the cities [4]. In parallel, the rapid technology development and industrialization make the problem of increased consumption of natural resources even more pronounced and complex [9]. Therefore, the generation of different types of waste is inevitable and, to a certain level, the damage to the environment and public health is irreparable [9].

Environmental protection represents a practice of protecting the environment. This practice includes individuals, organizations, companies, and governments. The main goal is the preservation of the existing natural environment as well as the damage repair on the affected

*Corresponding author: sl.Oraovica 16220 Grdelica, Leskovac, Serbia, jelena.mihajlovic@masfak.ni.ac.rs

part of the environment. The most important postulate is sustainability and sustainable development. Sustainable development provides the more efficient use of the resources and the reduction of the total amount of produced waste. Also, if the waste is already generated the sustainable development will contribute to the general goals of environment protection.

Consequently, the top priority policies of the European Union regarding the preservation of the environment are the waste management policies. The main problem in waste generation, by the population or industry, is uneven development of the city's expansion and the development of the proper strategies and construction of the proper facilities for proper waste management. According to EPA (US Environment Protection Agency), wastes are classified as either hazardous or non-hazardous. Non-hazardous waste does not have the ability to affect the environment and public health. However, hazardous waste could have dramatic damage to the ecosystem and public health. The damage is not reversible. According to EPA, hazardous waste is waste that has at least one of the characteristics, such as ignitability, reactivity, corrosively, and toxicity.

This research was conducted by observing the first hazardous waste characteristic which is ignitability. Waste oils or used motor oils inadequately disposed of might show spontaneously combustibility, which could, under certain circumstances, potentially lead to occurrence of fires [10]. The used motor oils/lubricants, according to the Europalub statistics estimate that 49% is used in the automotive sector, 37% is used by industry, and the rest 14% is represented as base oils [11].

Developed, EU countries, were the first to encounter the used motor oil management system by creating rules and principles that, in the form of legally defined standards, regulate the functioning of management systems [11]. However, in developing countries, such as the Republic of Serbia, the disposal of used motor oils was obtained in an uncontrolled manner. The situation is improving by implementing the EU's frameworks and norms in order to indulge the world trends in environmental protection. But, it is still necessary to make a significant effort in order to raise the awareness of the importance of used motor oils proper disposal in the widest circle of the population [11].

Manufacturers or owners of used motor oils are compelled to collect, temporarily store, and furthermore provide authorized collectors (collection canter or waste management plant) with the used motor oils. This process is monitored by the state Environment Protection Agency that encourages end users to act upon the active strategy. Waste oil collectors or authorized collectors are not allowed to perform oil treatment processes inside the storage used strictly for the collection of used motor oils.

To support the process of collection of used motor oils, authorized transfer stations must be formed. The lack of a proper infrastructure threatens the possibility of proper used motor oils disposal and storage even the EU laws and standards are applied. Transfer stations are a temporary facility for waste oil collection and storage. They are used for selection and transhipment of waste oil before its transport to another facility for storage, treatment, recycle or disposal.

Generally, as the development of living standard and urbanization have been increasing, the need for the waste transfer stations has also increased. Thus, the vast number of studies dealing with such a problem is present. Some of the researches dealt with waste transfer stations impact on the environment and healthcare regarding the risks from waste manipulation and energy utilization [12].

The quality of traffic service and the total costs of the transport system depend significantly on the location of the specific facilities on the transport network. The location selection problem, in general, is a complex problem of many confronting criteria (political, economic, infrastructural, environmental criterion, as well as a development strategy, logistic costs, services, etc.) and competitive alternative solutions. Thus, this problem could be observed as multi-criteria decision-making (MCDM) problem.

MCDM methods have been extensively used to assess, evaluate, or prioritize a set of alternatives concerning a finite set of criteria or attributes in many fields. This problem must include all preferences and constraints of the decision maker and satisfy the type of desired facility site as well as the laws, regulations, and legislations that are in the act in the selected region of interest.

The location selection problem has many diverse forms such as distribution centres [13] different types of warehouses and storages, cargo and passengers' terminals, parking lots, and many others. There were also researchers which have been dealing with the location selection problems regarding the environment protection centres, waste, and hazardous waste centres. Therefore, the location selection problem becomes more complex and important as the used motor oils may have hazardous characteristics and consequently negative consequences in the case of their inadequate disposal. Furthermore, the entire environment and public health are at greater risk.

3. DECISION MAKING PROCESS

Multi-criteria decision-making deals with direct decision-making problems where a solution is chosen from a final, predefined set of potential solutions based on several diverse and often conflicting criteria, which, as a rule, have a different level of importance. Various implementations of the MCDM model through different tools can be used individually or combined into a hybrid decision network. Most of MCDM methods requires a technique for assigning the weights of criteria as each criterion must have its importance compared to other criteria. The assigned weights can be calculated through subjective or objective methods.

As shown in Figure 1, a group of experts participated in this study. They compared each criterion with the subjective Fuzzy Pivot Pairwise Relative Criteria Importance Assessment (F-PIPRECIA) method. The obtained weights coefficients based on the F-PIPRECIA method were used for further assessment, specifically with the Geometric Mean (GM) aggregation operator. Three of the fuzzy MCDM methods were applied in combination with the obtained criteria weights: the Fuzzy Technique for Order Performance by Similarity to Ideal Solution (F-TOPSIS), the fuzzy Weighted Aggregated Sum Product Assessment (F-WASPAS), and the fuzzy Additive Ratio ASsessment (F-ARAS). Finally, the results of the complete ranking of alternatives were compared.

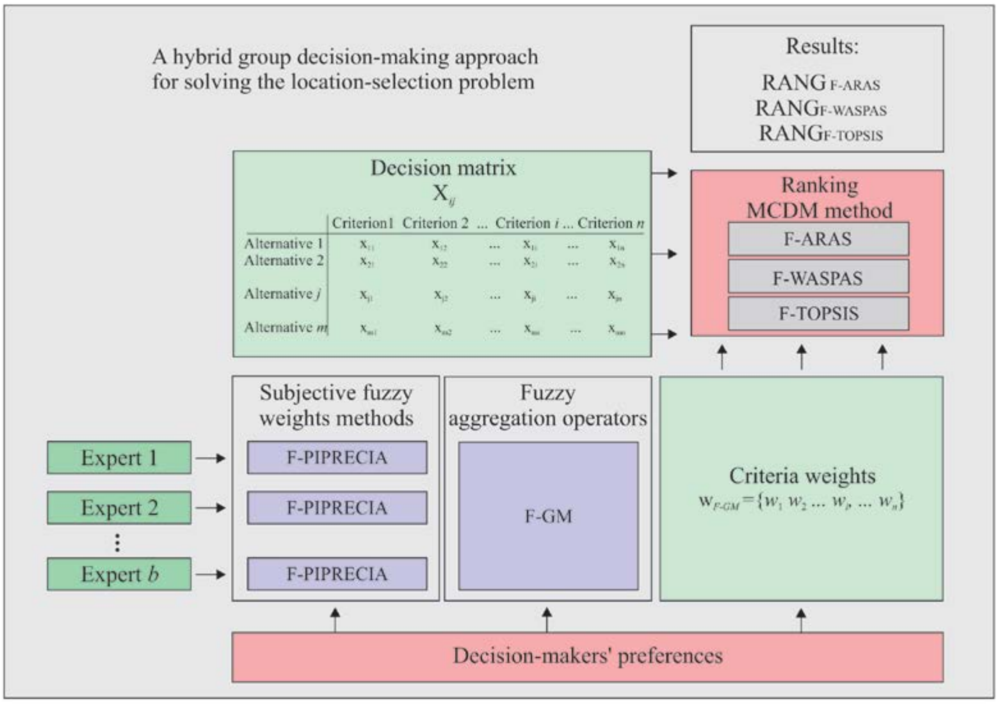

Figure 1: Schematic representation of the fuzzy matrix of the hybrid decision-making approach .

3.1. Fuzzy PIPRECIA

The Pivot Pairwise Relative Criteria Importance Assessment (PIPRECIA) method was proposed by Stankujkic et al. 2017. When the PIPRECIA method the starting point for the establishment of this method was the SWARA method, The PIPRECIA method does not require prior sorting of the evaluation criteria, like the yacht's SWARA method, so this method is more suitable for group decision-making. A more detailed framework of the proposed method could be found in referential literature [14].

3.2. Geometric Mean (GM)

The geometric mean multiplies and finds the root of values. Thus, the geometric mean is represented as the multiplicative mean. The geometric mean entails finding the product of the number and then raising that value by the reciprocal of the number of data points which contributed to the product. Geometric mean is calculated using the following equation:

$$GM = \sqrt[n]{\left(\prod_{i=1}^{n} x_{ij}\right)} \qquad (1)$$

3.3. Fuzzy TOPSIS

The Technique for Order Performance by Similarity to Ideal Solution (TOPSIS) method was propose by Huang and Yoon et al. 1981. This method includes two basic concepts: a positive ideal solution and negative ideal solution. If the alternative is closest to the positive ideal solution and, at the same time, farthest from the negative ideal solution, it is the optimal option, otherwise, it is not optimal. A more detailed framework of the proposed method could be found in referential literature [15].

3.4. Fuzzy WASPAS

The Weighted Aggregated Sum Product Assessment (WASPAS) method was proposed by Zavadskas et al. 2012. The WASPAS method consists of two aggregated parts: The Weighted Sum Model (WSM) and The Weigted Product Model (WPM). WSM determines the overall score of an alternative as a weighted sum of attribute values, while WPM was developed to avoid alternatives with poor attribute values. A more detailed framework of the proposed method could be found in referential literature [15].

3.5. Fuzzy ARAS

The Additive Ratio ASsessment (ARAS)method was proposed by Zavadskas and Turskis at al. 2010. According to the ARAS procedure, a utility function value specifying the intricate relative efficiency of a conceivable alternative is instantly commensurate with the relative effect of values and weights of the momentous criteria taken into account in paper. A more detailed framework of the proposed method could be found in referential literature [15].

4. CASE STUDY

In order to make the process of choosing a location for the colection of waste oil as safe as possible, it is necessary to manage the risks. The risk management is a very complex process, consisting of several steps and elements. Certainly, one of the most significant steps within this process is the selection of the best location. The location selection is supported by the large amount of research. Approaches for solving this problem are numerous and depended on many factors, such as the methods used to determine the risks, the criteria taken into account, the ways in which these criteria are evaluated, etc. As in all multi-criteria problems, one of the key questions remains which is the question of criteria selection.

In this study criteria set consist of 8 criterions. Those criteria have been based on the factors that affect the problem of the location selection the most and 3 possible locations, i.e., three alternative solutions.

Criterion C_1 Distance from the traffic infrastructure [km] – in case of accidents, the risk of harmful effects on the population and the environment is reduced.

Criterion C_2 Construction costs [EUR] – construction costs directly depend on the terrain of the location, soil type, climatic factors, regulatory factors and others.

Criterion C_3 Possible impact on the environment in the case of accidents [%] – the greatest risk would be if the transfer station is located in the immediate vicinity of sensitive areas of the environment.

Criterion C_4 Distance from the protected areas, natural assets, and facilities [km] – the impact of an accident during the transport of dangerous wastes could have in-comprehensible proportions on the surfaces belonging to the so-called "ecological zones".

Criterion C_5 Topography and soil characteristics [%] – it is recommended to avoid karst terrains and areas, as well as rocky areas. The site should be geologically stable and have a minimal potential impact on groundwater.

Criterion C_6 Distance and impact on the aquatic ecosystems [km] – the minimum distance of landfills and transfer stations from water courses is about 500 meters, and they are also recommended to be built in locations that have not been flooded in the previous 100 years.

Criterion C_7 Distance from the waste generators [km] – in the case of the shortest possible distance between the waste generator and the transfer station, the waste oil transport via road will take a shorter time, and potential danger to other road users and the environment is also reduced.

Criterion C_8 Population density [number of inhabitants per km2] – the number of residents exposed to hazardous waste, i.e. western oil, is a key factor in the literature for determining the consequences of an incident. The number of residents potentially exposed to hazardous waste can be determined based on population density.

The position of all location is shown in Figure 2, Alernative 1 location on the road of Čamurlijski, represented with a red symbol, Alternative 2 location the land on the road leanding to Niška Banja, represented with a blue symbol and Alternative 3 location land near the Niš Penitentiary, represented with a green symbol.

The fuzzy decision matrix based on the previously presented alternatives (locations) and the defined criteria set is formed and presented in Table 1.

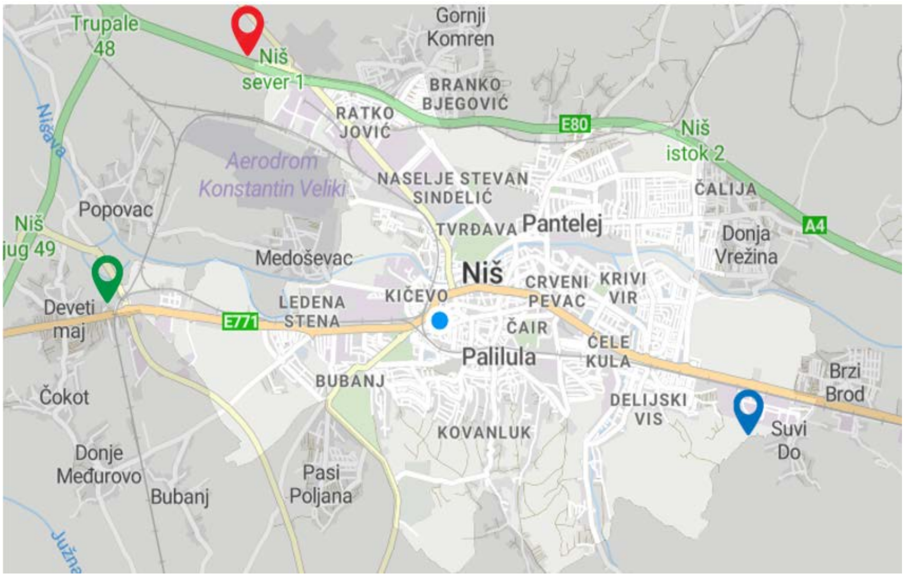

Figure 2: Proposed locations (alternative solutions) for transfer station

Table 1. Location’s performance ratings – fuzzy decision-matrix

	C_1 [km]			C_2 [EUR]			C_3 [%]			C_4 [km]		
	min			min			min			max		
A_1	5.5	5.5	5.5	16800	17000	17580	81.4	83.6	85	65.8	65.8	65.8
A_2	6.5	6.5	6.5	19000	19500	19800	74.3	75.8	76.2	52.4	52.4	52.4
A_3	6	6	6	10700	11000	11400	91.3	92.4	94.5	48.5	48.5	48.5
	C_5 [%]			C_6 [km]			C_7 [km]			C_8 [number of inhabitants per km^2]		
	max			max			min			min		
A_1	81	82.1	82.8	4	4	4	170.1	170.1	170.1	178	178	178
A_2	86.3	87.6	88	0.5	0.5	0.5	91.55	91.55	91.55	101	101	101
A_3	83.2	84.3	85.1	4.9	4.9	4.9	173.2	173.2	173.2	631	631	631

Table 2 shows the criteria comparison matrix based on the fuzzy PIPRECIA method, and it was formed on the scale that can be seen in the paper [14].

Table 2: Comparasion of criteria by 3 experts based on fuzzy PIPRECIA method

		PIPRECIA-D			PIPRECIA-I
C_1	E_1		C_8	E_1	
	E_2			E_2	
	E_3			E_3	
C_2	E_1	(0.286,0.333,0.400)	C_7	E_1	(0.250,0.286,0.333)
	E_2	(0.250,0.286,0.333)		E_2	(0.286,0.333,0.400)
	E_3	(0.333,0.400,0.500)		E_3	(0.286,0.333,0.400)
C_3	E_1	(1.400,1.600,1.650)	C_6	E_1	(1.200,1.300,1.350)
	E_2	(1.300,1.450,1.500)		E_2	(1.200,1.300,1.350)
	E_3	(1.500,1.750,1.800)		E_3	(1.300,1.450,1.500)
C_4	E_1	(0.500,0.667,1.000)	C_5	E_1	(0.250,0.250,0.333)
	E_2	(0.400,0.500,0.667)		E_2	(0.222,0.333,0.286)
	E_3	(0.500,0.667,1.000)		E_3	(0.250,0.286,0.333)
C_5	E_1	(0.400,0.500,0.667)	C_6	E_1	(1.100,1.150,1.200)
	E_2	(0.333,0.400,0.500)		E_2	(1.100,1.150,1.200)
	E_3	(0.400,0.500,0.667)		E_3	(1.200,1.300,1.350)
C_6	E_1	(1.000,1.000,1.050)	C_3	E_1	(1.200,1.300,1.350)
	E_2	(1.200,1.300,1.350)		E_2	(1.200,1.300,1.350)
	E_3	(1.100,1.150,1.200)		E_3	(1.100,1.150,1.200)
C_7	E_1	(0.250,0.286,0.333)	C_2	E_1	(0.222,0.250,0.286)
	E_2	(0.333,0.400,0.500)		E_2	(0.250,0.286,0.333)
	E_3	(0.286,0.333,0.400)		E_3	(0.222,0.250,0.286)
C_8	E_1	(1.100,1.150,1.200)	C_1	E_1	(1.000,1.000,1.050)
	E_2	(1.100,1.150,1.200)		E_2	(1.000,1.000,1.050)
	E_3	(1.000,1.000,1.050)		E_3	(1.100,1.150,1.200)

The criteria weights obtained by F-PIPRECIA MCDM method in relation to the F-GM aggregation operator are presented in Table 3.

Table 3: Aggregated criteria weights obtained by F-PIPRECIA and F-GM

	C_1	C_2	C_3	C_4	C_5	C_6	C_7	C_8
l	0.075	0.054	0.091	0.068	0.051	0.077	0.055	0.087
m	0.120	0.088	0.189	0.139	0.099	0.143	0.090	0.129
u	0.196	0.145	0.342	0.283	0.208	0.291	0.181	0.242

Based on aggregation operator and the comparison of the F-PIPRECIA+FTOPSI, F-PIPRECIA+FWASPAS and F-PIPRECIA+FARAS methods, one can see and conclude that the first alternative location on the road of Čamurlijski, is the best alternative solution, the secand alternative location the land on the road leanding to Niška Banja and the third location land near the Niš Penitentiary, (Alternative 1 > Alternative 2 > Alternative 3) for all FMCDM methods. The complete rankings are given in Table 4, according to calculated utility functions for each fuzzy approach.

Table 4: Complete ranking of the location selection for the collection of waste oil

	A_1	A_2	A_3
F-TOPSIS	0.421 **(1)**	0.396 **(2)**	0.384 **(3)**
F-WASPAS	0.841 **(1)**	0.739 **(2)**	0.738 **(3)**
F-ARAS	0.798 **(1)**	0.766 **(2)**	0.737 **(3)**

5. CONCLUSIONS

This research has shown the applicability of some hybrid fuzzy MCDM approaches (F-PIPRECIA+F-TOPSIS, F-PIPRECIA+F-WASPAS, F-PIPRECIA+F-ARAS) in the location selection for the construction of a waste oil transfer station in the territory of the city of Niš. According to the results, the best location for the construction of a waste oil transfer station is Alternative 1 (location on the road of Čamurlijski), Alternative 2 (the land on the road leanding to Niška Banja) and Alternative 3 (land near the Niš Penitentiary). This study showed that the hybrid approach did not affect the final ranking, each of the approaches gave the same results.

Future directions of research could be using a larger set of alternatives and criteria, taking into account a larger number of methods both in ranking and in weight coefficient determination, as well as the software development.

ACKNOWLEDGEMENTS

This research was financially supported by the Ministry of Science, Technological Development and Innovation of the Republic of Serbia (Contract No. 451-03-47/2023-01/ 200109) and by the Science Fund of the Republic of Serbia (Serbian Science and Diaspora Collaboration Program, Grant No. 6497585).

REFERENCES

[1] B. Müfide, T. Gülsah, Ö. Aysun, "Plant site selection for recycling plants of waste electrical and electronic equipment in Turkey by using criteria decision making methods, Environmental Engineering and Management Journal, Vol.13, pp. 163-172, (2014).

[2] J. Mallick, "Municipal Solid Wase Landfill Site Selection Based on Fuzzy-AHP and Geoformation Techniques in Asir Region Saudi Arabia", Sustainability, Vol. 13, pp. 1538, (2021).

[3] M. Sagnak, Y. Berberoglu, I. Memis, O. Yazgan, "Sustainable collection center location selection in emerging economy for electronic waste with fuzzy Best-Worst and fuzzy TOPSIS", Waste Management, Vol. 127, pp. 37-47, (2021).

[4] S. Rahimi, A. Hafezalkotob, S.M. Monavari, A. Hafezalkotob, R. Rahimi, "Sustainable landfill site selection for municipal solid waste based on a hybrid decision-making approach: Fuzzy group BMW-MULTIMOORA-GIS", Journal of Cleaner Production, Vol. 248, pp. 119186, (2019).

[5] A.E. Torkayseh, B. Malmir, M.R. Asadabadi, "Sustainable waste disposal technology selection: The stratified best-worst multi-criteria decision-making method", Waste Management, Vol. 122, pp. 100-112, (2021).

[6] A.E. Torkayesh, S.H. Zolfani, M. Kahvand, P. Khazaelpour, "Landfill location selection for healthcare waste of urban areas using hybrid BWM-grey MARCOS model based on GIS", Sustainable Cities and Society, Vol. 67, pp. 102712, (2021).

[7] C. Zhang, Q. Hu, S. Zeng, W. Su, "IOWLAD-based MCDM model for the site assessment of a household

waste processing plant under a Pythagorean fuzzy environment”, Environmental Impact Assessment Review, Vol. 89, pp. 106579, (2021).

[8] S. Karagoz, M. Deveci, V. Simic, N. Aydin, “Interval type-2 Fuzzy ARAS method for recycling facility location problems”, Applied Soft Computing, Vol. 102, pp. 107107, (2021).

[9] M. Rabbani, S.A. Sadati, H. Farrokhi-Asl, “Incorporating location routing model and decision making techniques in industrial waste management: Application in the automotive industry”, Computers & Industrial Engineering, Vol.148, pp. 106691, (2020).

[10] F. Samanlioglu, “A multi-objective mathematical model for the industrial hazardous waste location-routing problem”, European Journal of Operational Research, Vol. 226, pp. 332-340, (2013).

[11] J. Mihajlović, N. Marković, G. Petrović, D. Marković, Ž. Cojbasić, “Standards, Regulations, and Legislations of Used Motor Oil Management and Disposal – A Review”, International Conference “Heavy Machinery HM 2021”, Vrnjačka Banja (Serbia), 23 July-25 July, (2021).

[12] Q. Cheng, Z. Li, D. Song, W. Gao, H. Wu, H. Xie, Y. Chen, L. Gu, Y. Liu, “Study on weak link of energy utilization in oil transfer station system: Insight from energy level analysis method”, Energy Reports, Vol. 6, pp. 1097-1105, (2020).

[13] W.J. Gutjahr, N. Dzubur, “Bi – objective bi-level optimization of distribution center locations considering user equilibria”, Transportation Research Part E, Vol. 85, pp. 1-22, (2015),

[14] Q. Muhammad, A. Saleem, K. Neelam, N. Muhammad, K. Faisal, L. Yi, “Case study for hospital-based Post-Acute Care Cerebrovascular Disease using Sine Hyperbolic q-rung orthopair fuzzy Dombi aggregation operators” Expert System with Application, Vol. 215, pp. 119224, (2023).

[15] G. Petrović, J. Mihajlović, Ž. Ćojbašić, M. Madić, D. Marinković, “Comparasion of three fuzzy methods for solving the supplier ´ selection problem”, Facta Univerisitatis Series Mechanical Engineering, Vol. 17, pp. 455–469, (2019).

SESSION B

RAILWAY ENGINEERING

Proof tests of geometric-kinematic calculations of railway vehicles

Dragan Milković[1*], Goran Simić[1], Vojkan Lučanin[1], Saša Radulović[1], Aleksandra Kostić Miličić[1]
[1]Faculty of Mechanical Engineering /Rail Vehicles Department, University of Belgrade (Serbia)

Geometric-kinematic calculations and experimental proof tests of the mutual position of assemblies and sub-assemblies of wagons that are in relative displacement are significant in developing new types of railway vehicles and especially in the application of non-standard solutions. In the case of standard types of wagons and standard solutions, compliance with the recommended geometric dimensions and parameters of the vehicle should guarantee that even in extreme positions there will be no irregular contact between moving parts of the rail vehicle. This is especially important if it is necessary to place some elements or parts of the wagon's equipment in the zone of wheelsets and in the zone of the connection between the bogies and the car body. This check can be carried out using graphic-analytical methods, according to the methodology given in the relevant EN standards, ORE reports, and AVV publications, and the limit values of the angular and translational coordinates of the moving parts. Verification of these calculations and verification of the derived state can be done by simulating these movements on the vehicle prototype itself or using a mock-up. This paper presents limit values and proof tests, for checking the mutual position of the running gear and the vehicle car body of a tank wagon car type Zacns. The test was performed using a transfer table for simulating the rotation of bogies relative to the car body in the horizontal plane and by using pads placed under wheels for simulating rotation in the vertical plane. The check was performed by visual inspection and by distance measurements.

Keywords: Geometric-kinematic calculations, Proof tests, Mutual position of the running gear and the railway vehicle car body

1. INTRODUCTION

Geometric-kinematic calculations serve for checking the limitations of the adopted dimensions of the wagons, which are a consequence of possible movements of the wagons in relation to the track, relative movements of two wagons in the composition, and relative displacements of unsprung, primarily suspended, and secondary suspended parts of the structure. These calculations include:

- verification of the profile (dimensions) of the vehicle,
- checking the mutual position of the running gear and the car body (wheel vs.car body, car body and bogie frame),
- determination of the required dimensions of buffers plates and checking the possibility of passing through the curves,
- checking the mutual position of the draw-buff gears and the car body (hook or automatic coupler head space in sharp curves and vertical track curves),
- checking the mutual position of the two wagons and their gangways in the curve (for wagons with gangway systems).

For the unhindered movement of rail vehicles and avoiding contact with stable structures (tunnels, cuts, poles, etc.), space around the track should be provided. This space can be completely defined by some boundary contour - the reference profile (or dimensions) in the transverse plane in relation to the track and the rules, by which, starting from the reference profile, the permitted profile of the rolling stock is determined on the one hand, and on the other hand the free profile of the stable structure.

In the world, there are many different profiles in different countries and even multiple profiles on different railways in the same country. For the European standard track gauge, the EN [1] has defined a reference profile, as well as a procedure by which the vehicle profile is calculated from. This profile was obtained by analyzing the railways involved in international traffic and is an internal envelope of all profiles on these lines. Thus, the unhindered exchange of railway vehicles between all member states of the UIC was ensured.

Figure 1 shows how starting from the reference profile, by introducing the required movements of the wagon in the vertical plane for the values of Δh and narrowing E, which are the result of the movement of the wagon in the track and passing through the curve (Figure 2), the permissible profile of the vehicle is reached.

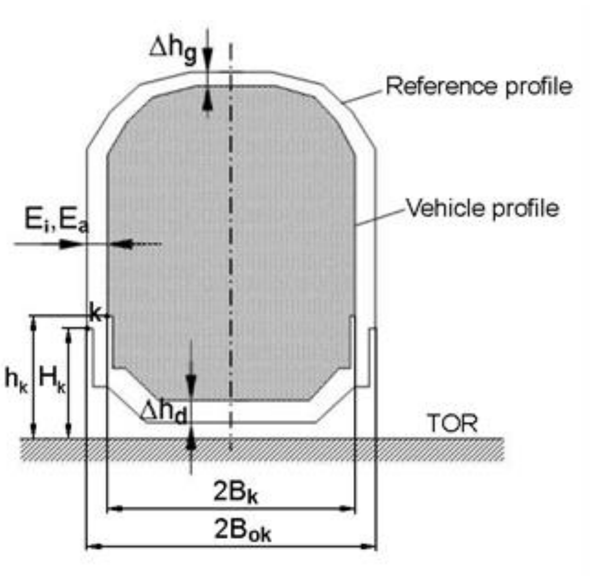

Figure 1: Reference profile and vehicle profile [1, 2]

*Corresponding author: Kraljice Marije 16, 11120 Belgrade 35, Serbia, dmilkovic@mas.bg.ac.rs

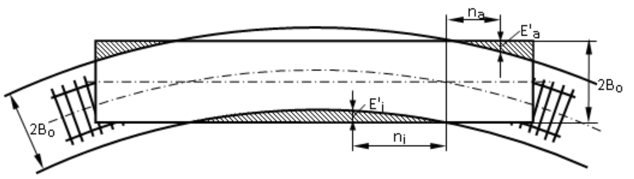

Figure 2: Geometric deviation of the vehicle and the track axes during passing through a curve [1, 2]

Calculations related to checking the undisturbed movement of draw-buff gear elements and gangways of the vehicles during vehicle movement are not in the scope of this paper.

Significant displacements of wagon sub-assemblies occur when crossing the marshalling humps, passing through sharp horizontal curves in combination with possible railway twisting, and when loading onto the ferry boats, i.e., when crossing the loading ramp. This paper presents an analytic procedure for calculating possible movements of the running assembly in relation to the car body, as well as a presentation of an experimental check with a tank wagon Zacns for the transportation of petroleum products at the most unfavourable combination of maximum deflections with rotation of the bogies in relation to the car body in both, horizontal and vertical, plane. Verification of these calculations and verification of the derived state can be done by simulating these movements on the vehicle prototype itself or using a mock-up.

2. CHECKING THE MUTUAL POSITION OF THE RUNNING GEAR AND THE CAR BODY

2.1. Criteria for an estimation of wagon capability to use on a ferry boat

The angles of rotation of the bogies in the vertical and horizontal plane, which are decisive for the use of wagons on the ferries, are given in Table 1 and calculated for the tank wagon, using its dimensions and designed gaps and plays. These angles serve for checking the possibility that some moving elements get into the irregular contact.

For calculation and testing, it is necessary first to determine the maximum values of possible displacements that can occur during exploitation, which are defined in the relevant EN standards [1], ORE B12/DT 135 [3], and General Contract for Use of wagons (AVV), Appendix 14 [4]. These values are defined for all ferry lines involved in the Trans-European Transport Rail network.

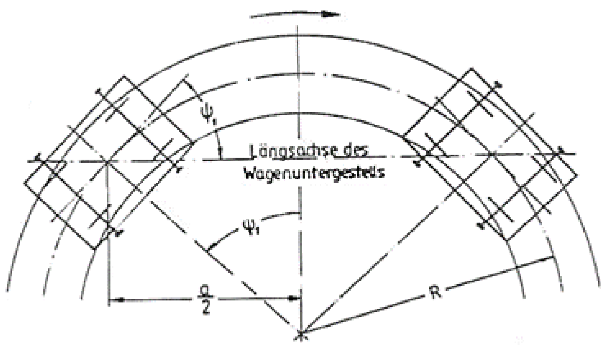

Figure 3: Rotation of the bogie vs. car body in the horizontal plane during passing through the curve [3, 5]

Figure 3 shows the curve negotiation of the 4-axle wagon with bogies and the resulting bogie vs. car body rotation.

Figure 4 presents the rotation of the bogies relative to the car body in a vertical plane during entering the ferry boat in the two critical positions. First, when entering the ramp slope, and the second position, when the first bogie enters the horizontal boat floor, with the second bogie still on the ramp.

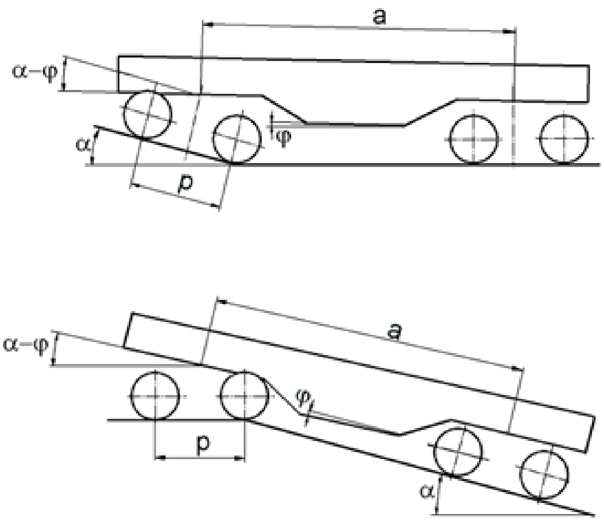

Figure 4: Rotation of the bogie vs. car body in the vertical plane during entering the ferry boat [3, 5]

Figure 5 presents the possible rotation of the bogie frame as a result of the existing wheel set vs. track play.

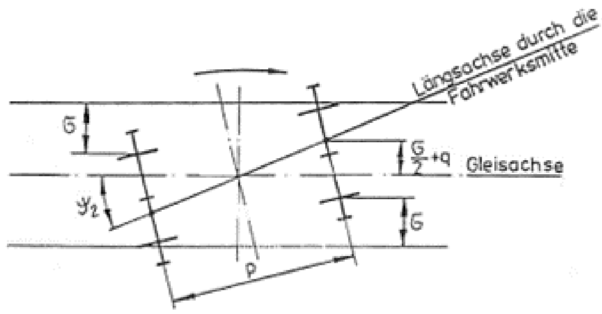

Figure 5: Rotation of the bogie due to the wheelset vs. track play [3, 5]

In the event of irregular contact, parts may be damaged, as well as functionality may be disrupted, and traffic safety may be compromised.

Because of all this, some Notifying Bodies require that, in addition to the calculation, an experimental check of the mutual position is also carried out.

The angle of the ferry boat ramp may vary from 2.5 to 3.0° depending on the boat type.

The tank wagon is equipped with a standard Y25Lsd bogie with known dimensions and clearances of the running gear parts.

Table 1: Required limit values depending on the wagon dimensions [3]

Parameter	Abbreviation	Equation	Value
The angle of the ferry boat ramp	α		2.5°
Tangent of the vertical kink angle of the ferry boat ramp	tg α		0.0437
Distance of the pivots	a		11.36 m
Bogie base	p		1.8 m
Vertical bogie inclination	φ	$\sin\varphi = \frac{p \cdot \sin\alpha}{2a}$	0.0035 rad=0.20°
Bogie deflection vertical	α- φ		2.3°
Track width (according to EN 15273-4)	$2b_o$		1.465 m
The track dimension of the wheel sets 10 mm under the running rolling radii	2b		1.41 m
Wheelset vs. track play	$2b_o - 2b$		0.055 m
Lateral play of the wheel sets vs. bogie frame	q		0.011 m
Curve radius	R		120 m
The horizontal turning angle of the bogies in the curve	ψ_1	$\sin\psi_1 = \frac{a}{2R}$	2.71°
Horizontal turning angle by adjusting the wheel sets in the track and possible lateral displacement of the wheel sets in relation to the wheel set guides and stops	ψ_2	$\sin\psi_2 = \frac{2(\frac{\sigma}{2}+q)}{p}$	2.45°
Yaw angle of the bogie relative to the wagon underframe in the curved track R	ψ_3	$\psi_1 + \psi_2$	5.16°

2.2. Testing on the transfer table

These conditions were achieved using a transfer table for simulating the rotation of bogies relative to the car body in the horizontal plane and by using appropriate pads placed under wheels for simulating rotation in the vertical plane. Table 2 presents calculated values of pads height and transfer table lateral displacement, that correspond to possible bogie and car body relative movement, according to [1, 2 and 3]. The bogie suspension springs were removed, and the bogie frames supported at the spring stops, to simulate the maximum possible vertical spring travel.

Figure 6: Rotation in the vertical plane bogie vs. car body for an angle α-φ= +2.3° [5]

The vehicle was placed on the transfer table with the first bogie.

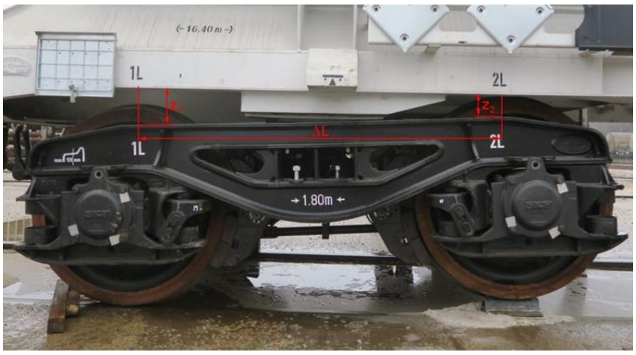

Figure 7: Rotation in the vertical plane bogie vs. car body for an angle α-φ= -2.3°[5]

Underneath the wheels of the first and the third wheel sets, the pads of height h = 72 mm were placed, as presented in Table 2, to achieve the angle α-φ= 2.3° between the bogies and the wagon underframe (Figures 6 and 7). In addition, the influence of the deviation of the wheel-rail contact points from a plane was checked by measuring the height differences between two points on the plane surface of each bogie frame longitudinal beam and the longitudinal beam of the car body (z_1 and z_2), as shown in

Figure 7. If necessary, the correct α-φ angle was achieved with additional shims of 1 mm thick sheets.

After that, the transfer table was carefully moved by distance s=1150 mm, slightly more than shown in Table 2, until an angle slightly larger than +ψ_3 is reached, Figure 8.

Table 2: Height of the pads and transfer table displacement, chosen to simulate possible displacements [5]

Case	Parameter	Abbreviation	Equation	Value
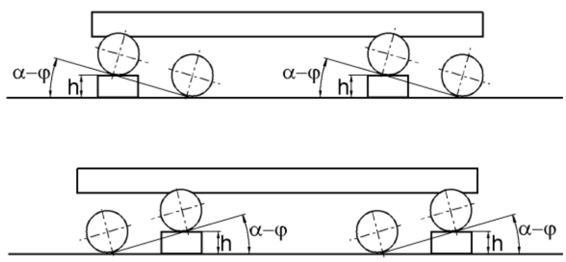	Height of the pads for vertical displacement	h	$h = p \cdot \sin(\alpha - \varphi)$	72 mm
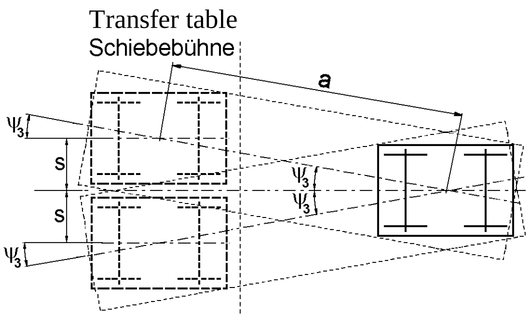	Transfer table lateral displacement	s	$s = a \cdot \sin \psi_3$	1022 mm

After that, the transfer table was carefully moved by distance s=1150 mm, slightly more than shown in Table 2, until an angle slightly larger than +ψ_3 is reached, Figure 8. The process was repeated by moving the transfer table in a different direction until the angle -ψ_3 was slightly exceeded, Figure 9.

Figure 8: Transfer table displacement to simulate rotation angle ψ>5.16° [5]

The pads are then placed under the wheels of the second and fourth wheel sets to achieve the angle -(α-φ) between the bogies and the wagon underframe.

The process was repeated by moving the transfer table in both directions.

Figure 9: Transfer table displacement to simulate rotation angle ψ<-5.16°[5]

2.3. Test results

It has been observed that there is no contact between the bogie frame and wheels on the one hand and the underframe of the car body on the other.

During the tests, no clearance of less than 20 mm was found between the bogie frame and the superstructure.

The distance between any wheel and wagon superstructure was at least 30 mm.

Figures 10 to 14 show some examples of the clearance between bogie parts and the wagon superstructure in different critical positions. The closest to the wheel is the brake pipe.

Figure 10: Running gear vs car body relative position 1

Figure 11: Running gear vs car body relative position 2

Figure 12: Running gear vs car body relative position 3

Figure 13: Running gear vs car body relative position 4

Figure 14: Running gear vs car body relative position 5

3. CONCLUSIONS

The tests carried out, with the aim to prove the relative position of the wagon moving parts, have shown that, under prescribed conditions, there is no contact between the wheels, parts of the bogie, and the car body superstructure. The distance between any wheel and superstructure was at least 30 mm. The tested tank wagon meets the requirements for use on the ferries according to ORE B12/DT135 [3]. This check using calculations and experiments is significant in the design phase of a new type of railway vehicle and especially in the application of non-standard solutions of the running gear and car body superstructure.

ACKNOWLEDGEMENTS

Authors express gratitude to the Ministry of Science, Technological Development and Innovations of the Republic of Serbia, Project Contract 451-03-9/2023-14/200105.

REFERENCES

[1] SRPS EN 15273-2:2014, Railway applications - Gauges - Part 2: Rolling stock gauge

[2] G. Simić et al, Gauge calculation of Eams wagon, University of Belgrade - Faculty of Mechanical Engineering, No: 13.04-132, Rev.1, Belgrade 2017.

[3] ERRI B 12/DT 135 - Güterwagen: Allgemein verwendbare Berechnungsmethoden für die Entwicklung neuer Güterwagenbauarten oder neuer Güterwagendrehgestelle, ERRI, 1995.

[4] General Contract of Use (GCU) for wagons Appendix 14, Additional conditions for the use of wagons on ferries and in exchange with railway operating on standard or broad gauge lines, 1-Jan-2022

[5] D. Milković et al., Prüfung der befahrbarkeit von fähren des 98 m3 Zacns Kesselwagens, Modell Sml 98, Universität Belgrad - Fakultät für Maschinenbau, Nr.: LSV I-11/22, Belgrad 2023.

Network Model and Vibration Simulation of a Railway Track

Mustafa Berkant Selek[1], Erol Uyar[2], Mücahid Candan[3*]
[*1,3]Higher Vocational School of Ege, Ege University, İzmir (Türkiye)
[3]Electric-Electronics Engineering Dept., Ege University, İzmir (Türkiye)

The stresses caused by the components used in railway systems (such as rails, rail joint laying and supports, broken rails) cause vibrations in rail vehicles and thus significantly affect the safety and comfort of trains.

The design of the suspension system, which minimizes the effects of these vibration loads transmitted to the wagon through the rail-wheel (bogie) and bogie-wagon relationship, is an important point in terms of ensuring safe and optimal running conditions, especially in high-speed trains.

The vibration behaviour in the medium and high frequency range (40–1500 Hz) of the train, which is influenced by the rail structure, can be used as an indicator of the sound propagation, the vibration sensitivity and the coupling of the rail work to the rail system.

In this study, mathematical modelling and simulation of a railway vehicle is performed to study different vibrations. The natural frequencies of a metro wagon are examined under different self-excited conditions. The dynamic behaviour of a specially designed suspension system like double-jointed bogie construction, consisting of mass dampers and springs, is selected and calculated as a model with two degrees of freedom.

In particular the resonance conditions are studied for vertical movements as a function of various parameters. The double-jointed bogie construction, consisting of mass dampers and springs, is selected and calculated as a model with two degrees of freedom. The results of Vibration Simulations of the track model are then demonstrated with graphics.

Keywords: Rail corrugation, Wear friction, Self-excited vibration, Vibration mode, Resonance, Natural frequency

1. INTRODUCTION

In terms of both passenger comfort, safety and environmental effects vibrations in rail transport, is one of the most important problem to be considered. Both in-vehicle and rail system vibrations is an important problem that needs to be brought under control at its source.

The design of the suspension system, which minimizes the effects of vibration loads transmitted to the wagon through the rail-wheel (bogie) and bogie-wagon relationship, is an important point in terms of ensuring safe and optimal running conditions, especially in high-speed trains.

The components used in the rail track structure (e.g. Rails, fixing systems and supports) and rail failures significantly affect vibration behaviour and hence the safety and comfort of trains.

The vibration behaviour of the train in the medium and high frequency range (40-1500 Hz), which is influenced by the rail structure, can be viewed as an indicator with regard to sound radiation, vibration sensitivity and the interaction of rail-track forces.

The impact on the vibration behaviour caused by wheel-rail interaction and suspension system design is therefore an especially important task to achieve travel safety and optimal travel conditions in high speed trains [1-2].

Different railway car-bogie designs and bogie constructions as seen in Figure 1 are commonly used in applications [3].

In the projecting phase, the constructor develops an appropriate design that meets the requirements, and the research engineer then creates a relevant and appropriate mathematical model to calculate the desired values and to test theoretically evaluated results.

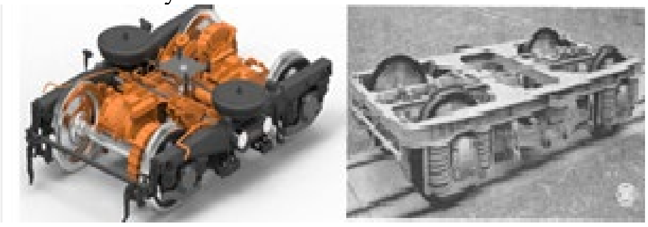

Figure 1: Different Type of Car Bogie Designs

In the projecting phase, the constructor develops an appropriate design that meets the requirements, and the research engineer then creates a relevant and appropriate mathematical model to calculate the desired values and to test theoretically evaluated results.

The designer consciously tries to set the natural vibration frequencies (natural frequencies) in such a way that no disruptive resonance phenomena occur under normal operating conditions [4-5]. In this study, a mathematical model based on the bogie-chassis construction as shown in Figure 2 is selected and the natural frequencies of the system with relevant vibration modes are calculated. The self-excited vibration tendency of the model is analysed using the complex eigenvalue method [6].

2. BASIC SUSPENSION MODEL

Taking the vertical movements into account, the basic suspension of the track can be modelled as a second degree of freedom system consisting of mass-damper-spring as shown in Figure 2.

*Corresponding author: Ege University, Higher Vocational School of Ege, Mechatronics Dept. mucahid.candan@ege.edu.tr

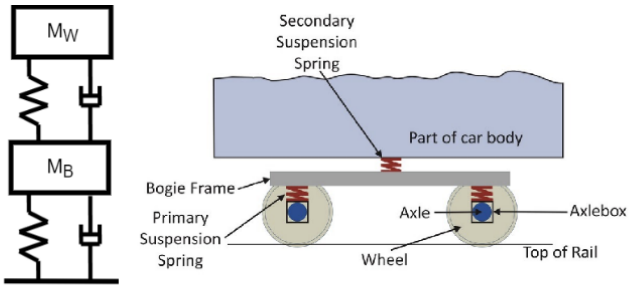

Figure 2: Mathematical model of bogie-chasse construction

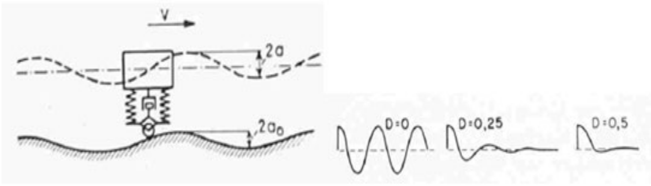

Figure 3: One dimensional model and free motions with different damping effects.

The vertical motion depending on different kind of excitations from railway can be described by following differential equation with M as mass, C damping coefficient, K as spring stiffness and F as ground forces [3].

$$M\ddot{x} + C\dot{x} + Kx = F \qquad (1)$$

The natural frequency ω_n damping constant D and resonance frequency ω_r can be calculated as follows:

$$\omega_n = \sqrt{K/M} \qquad (2)$$

$$D = \frac{c}{2M\omega_n} \qquad (3)$$

$$\omega_r = \omega_n\sqrt{1 - 2D^2} \qquad (4)$$

There are different kind of excitations which cause to vibrations on railway tracks; these can occur depending on wheel-rail interactions because of disturbances through rail failures, unbalanced mass effects and assembly-maintenance failures etc. [2-8]. Especially periodical excitations in form of frequency-spectrum influence the system parts with different Eigen-frequencies and amplitudes producing pulse train effect.

Assuming a harmonic disturbance with constant amplitude a0 free vibration tests of track with different damping ratios can be applied and frequency response can be investigated by using the following differential equation (with a=x and a_0=x_0):

$$M\ddot{x} + D\dot{x} + Kx = D\dot{x}_0 + Kx_0$$

In frequency domain with:

$$\frac{X(s)}{X_0(s)} = \frac{Ds + K}{Ms^2 + Ds + K}$$

Speed which is ϑ_k corresponds to natural frequency of track is taken as critical speed; Ratio of measured value a to input amplitude a0 for various travel speed ratios ϑ/ϑ_k and damping rates can be calculated with:

$$\frac{a}{a_0} = \sqrt{\frac{1+\left(2D\frac{\vartheta}{\vartheta_k}\right)^2}{\left(1-\left(\frac{\vartheta}{\vartheta_k}\right)^2\right)^2+\left(2D\frac{\vartheta}{\vartheta_k}\right)^2}} \qquad (5)$$

The simulation result for different vehicle speed ratios ϑ/ϑ_k and damping rates is illustrated in Figure 4. In the same figure the change of the vibrating force with the driving speed ratio and for different damping rates is also given. It is evident from Figure 4 that resonance occurs for $\vartheta=\vartheta_k$. In order to avoid critical driving conditions, these graphics provide highlighted information [3-8].

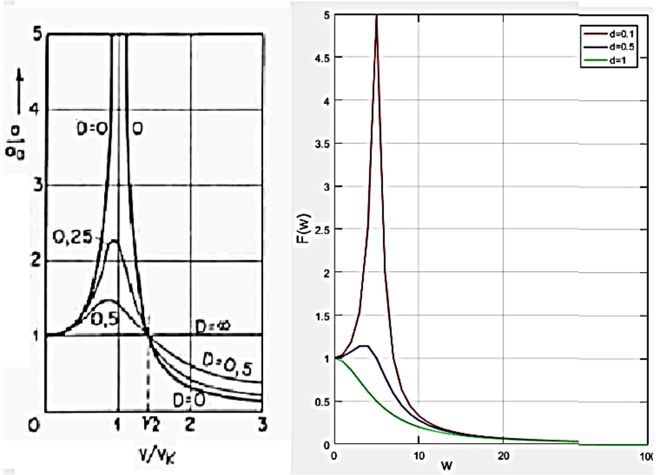

Figure 4: Change of Amplitude with speed depending on various damping coefficients

3. NETWORK MODEL

When analysing a mechanical system composed of mass, spring, and dampers, it is important to model the configuration of these elements that make up the system.

This combination can be described with a Linear Mechanical Network Operator (LMNO) model [5]. As an example, a network model of a second-order system in complex variable form is shown in Figure 5.

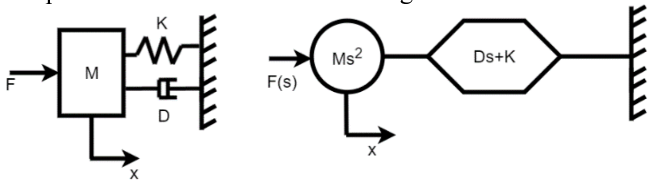

Figure 5: Representation network model of a second order system

By the transfer function:

$$X(s) = \frac{F(s)}{Ms^2+Ds+K} \qquad (6)$$

Similarly, network model can be used and applied to solve vibration equations and to calculate natural frequencies with different motion modes of more complicated systems with several degrees of freedom.

The following example of the calculations and solutions for a reduced track system with three degrees of freedom is shown in Figure 6.

By considering the orbital perturbations Y_a, Y_b, Y_c, and Y_d as system inputs, vertical motions in the z-direction with lateral and longitudinal rotational motions about the x (θ) and y (ϕ) axes as outputs, the network model of this system can be modelled with dynamical equations as given in (7) below.

The mass spring damper connections in the network model are described by network operators Z.

Further analysis of the system as determination of the free vibrations and natural frequencies etc. can then be found by solving these equations.

Network models of more complicated systems with several degrees of freedom can be described also with Network models as shown in Figure 7.

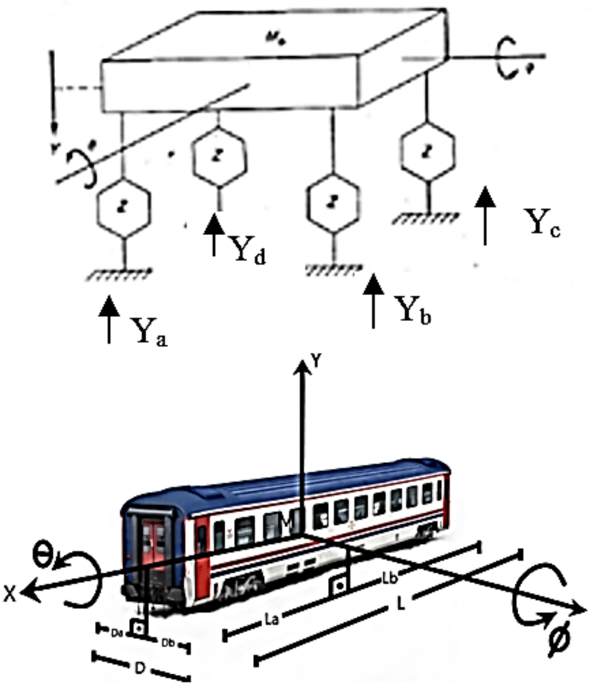

Figure 6: 3-Dof network suspension model

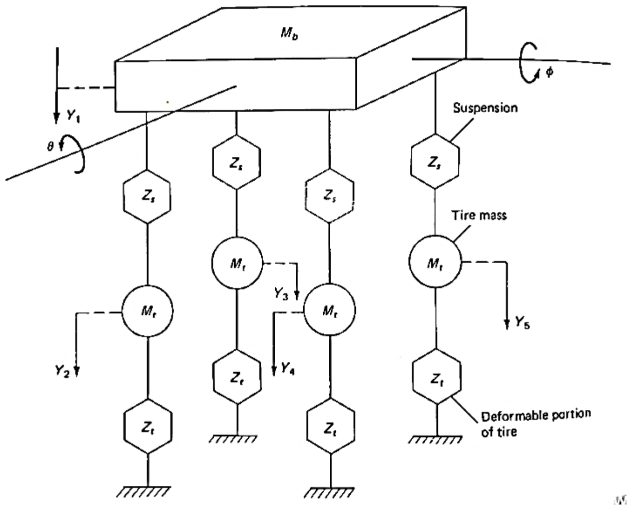

Figure 7: 7-Dof track suspension network model

Assuming a three degree of freedom system with x_1, x_2 and x_3 as variables and L, M, N as inputs, system dynamic equations of motion and solutions can be described and obtained in following form:

$$\begin{aligned} Ax_1 + Dx_2 + Gx_3 &= L \\ Bx_1 + Ex_2 + Hx_3 &= M \\ Cx_1 + Fx_2 + Ix_3 &= N \end{aligned} \tag{7}$$

Q as characteristic determinant:

$$Q = \begin{vmatrix} A & D & G \\ B & E & H \\ C & F & I \end{vmatrix} \tag{8}$$

Solution of equations (8) can be evaluated as:

$$x_1 = \begin{vmatrix} L & D & G \\ M & E & H \\ N & F & I \end{vmatrix} + Q \qquad X_2 = \begin{vmatrix} A & L & G \\ B & M & H \\ C & N & I \end{vmatrix} + Q$$

$$X_3 = \begin{vmatrix} A & D & L \\ B & E & M \\ C & F & N \end{vmatrix} + Q$$

4. EQUATIONS OF REDUCED MODEL MOTIONS

This model can be further described with a reduced system at the centre of mass and with free body model shown in Fig.7. The suspensions of each of the four Wheels consisting of spring and dampers can be expressed with network operators Z_i and inputs Y_i which present disturbances from road conditions.

The motions (z, θ, ϕ) of the car body with mass M and inertias J_ϕ, J_θ with reduced spring and dampers at real and front sides can be described with network operators.

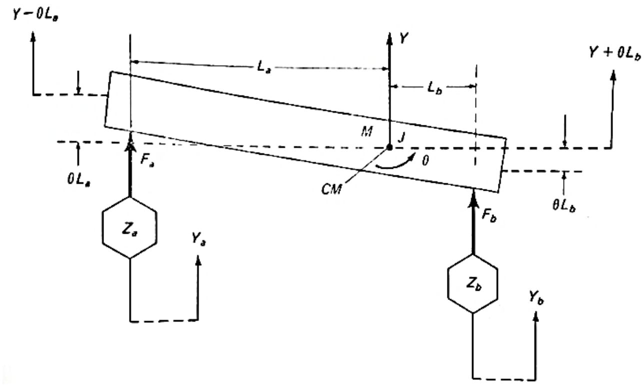

Figure 8: Reduced free body model

In order to investigate the natural frequencies and neglecting damping effects, the suspension system can be thought consisting of only reduced springs on the front and back side.

The Network operators can be written then as $Z_i=K_i$ and $F_i=K_iY_i$. Including translation and rotation the acting forces F_a and F_b at the front and back side can be expressed as following ($K_a=Z_a$; $K_b=Z_b$):

$$F_a = Z_a\big(Y_a - (Y - \theta L_a)\big)$$
$$F_b = Z_b\big(Y_b - (Y - \theta L_b)\big)$$

According to Newton Law with zero initial conditions; it can be written as:

$$\begin{aligned} &\sum F = M\ddot{y} \rightarrow F_a + F_b = Ms^2Y(s) \\ &(Ms^2 + Z_a + Z_b)Y - (Z_aL_a - Z_bL_b)\vartheta \\ &\qquad = Z_aY_a + Z_bY_b \end{aligned} \tag{9}$$

Similarly sum of the Torques about centre of mass with θ and zero initial conditions:

$$\begin{aligned} &\sum T = J\theta + K_\theta\theta(t) \rightarrow F_bL_b - F_aL_a \\ &\qquad = Js^2\theta(s) + K_\theta\theta(s) \\ &(Js^2 + Z_bL_b + Z_aL_a + K_\theta)\theta(s) \\ &\qquad - (Z_aL_a - Z_bL_b)Y \\ &\qquad = Z_bL_bY_b - Z_aL_aY_a \end{aligned} \tag{10}$$

Finally sum of the Torques about centre of mass with ϕ and zero initial conditions:

$$\begin{aligned} &\sum T = J\ddot{\varphi} + K_\phi\Phi(t) \rightarrow F_cL_c - F_dL_d \\ &\qquad = Js^2\varphi(s) + K_\phi\Phi(s) \\ &(Js^2 + Z_cL_c + Z_dL_d + K_\phi)\phi(s) \\ &\qquad - (Z_dL_d - Z_cL_c)Y \\ &\qquad = Z_cL_cY_c - Z_dL_dY_d \end{aligned} \tag{11}$$

5. NETWORK-MODEL OF THE TRACK SUSPENSION SYSTEM

According to the Chasse-Bogie design like type a given in Figure 1, a simplified but more precise mathematical model of one of the four suspensions can be described with a two degrees of freedom second order system as shown in Figure 9.

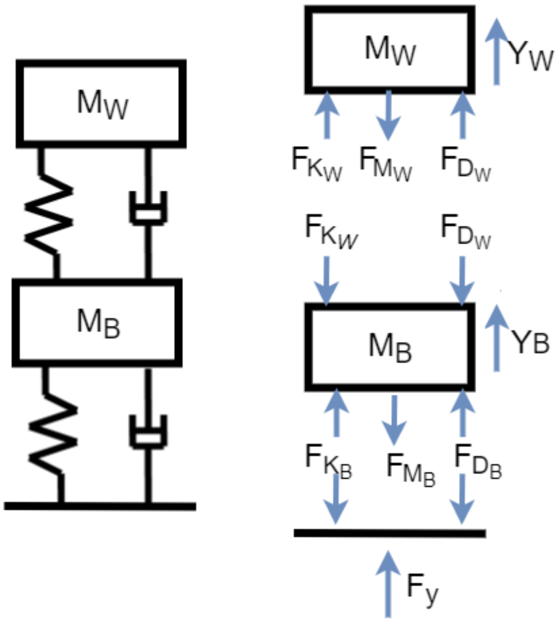

Figure 9: Bogie-car model with free-body diagram

Describing the carriage and bogie masses as M_w and M_b; coordinates with Y_w and Y_b, the spring constants with K_w and K_b, and the damping coefficients with D_w and Db following expressions can be written as:

$$F_{K_B} = K_B(Y - Y_B) \qquad F_{D_B} = D_B(\dot{Y} - \dot{Y}_b)$$

$$F_{K_W} = K_W(Y_B - Y_W) \qquad F_{D_W} = D_B(\dot{Y}_B - \dot{Y}_W)$$

$$F_{M_W} = M_W \ddot{Y}_W \qquad F_{M_B} = M_B(\dot{Y} - \dot{Y}_B)$$

According to above expressions, road disturbance is Y as input and Y_W, Y_B are outputs and the equations of motion and Network Table of the system can be written as:

$$F = F_Y = F_{K_B} + F_{D_B} \tag{12}$$

$$M_W \ddot{Y}_W = F_{K_W} + F_{D_W} \tag{13}$$

$$M_B \dot{Y}_B = F_{K_B} + F_{D_B} - F_{K_W} - F_{D_W} \tag{14}$$

$$(M_W s^2 + D_W s + K) Y_W(s) - (K_W + D_W s) Y_b = 0 \tag{15}$$

$$-(K_W + D_W s) Y_W(s) + \left(M_B s^2 + (D_B + D_W)s + (K_B + K_W)\right) Y_B(s) = (K_B + D_B s) Y(s) \tag{16}$$

The resonance frequencies and damped motions of the two degrees of freedom system can be obtained from following table and equations:

Yw	YB	Y
$Mw.s2 + Dw.s + Kw$	$-(Kw + Dw.s)$	0
$-(Kw + Dw.s)$	$Mb.s2 + (Db + Dw)s + (Kb + Kw)$	$(Kb + Db.s)$

6. SIMULATIONS AND SOLUTIONS OF THE SYSTEM

The vertical motions of car body and bogie of the two degrees of freedom system with the given model and parameters is simulated in MATLAB-Simulink as shown in Figure 10. [9-11]. Given Parameters are M_W=40 t, M_B=10 t, K_W=1500 kN/m, K_B=2500 kN/m, D_W=50 kNs/m, D_B=10 kNs/m.

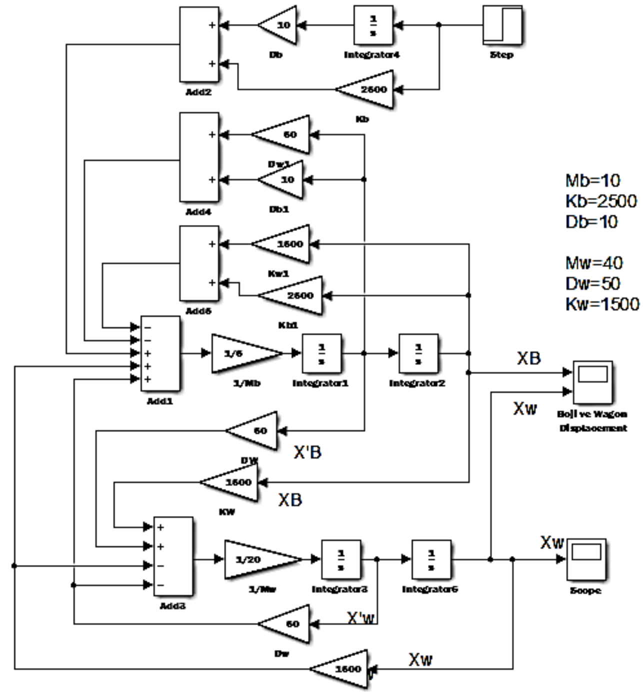

Figure 10: Simulink simulation of vertical suspension motion

Simulation results respect to time responses and natural frequencies of Bogie and car body as time and Bode Plots with above parameters are given in Figure 11 and 12 (vibration modes).

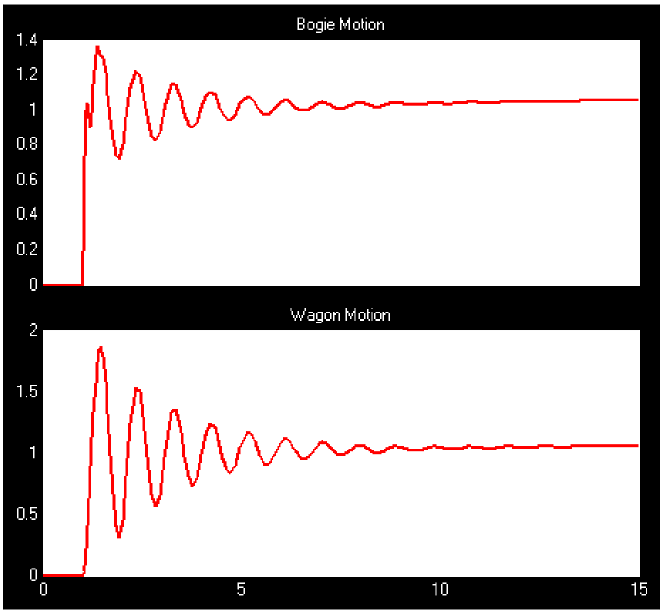

Figure 11: Time response of bogie-wagon

The natural frequencies can be calculated from above equations and following table by neglecting the damping effects.

Y_W	Y_B	Y
$M_W s^2 + K_W$	$-(K_W)$	0
$-(K_W)$	$M_B s^2 + (K_B + K_W)$	0

The roots of characteristic equation as natural frequencies can be found as ω_{n1}=4.66 rad/s and ω_{n2}=20.43 rad/s. These values can also be identified from simulated Bode Plot in Figure 12.

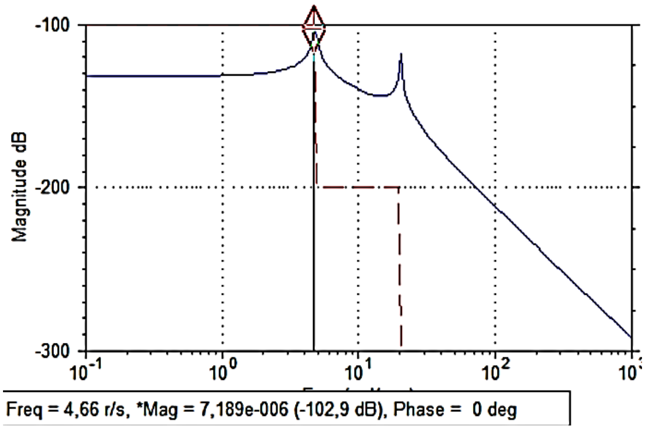

Figure 12: Bode plot and natural frequencies of vertical medium

As mentioned in introduction free motions of suspension system according to various speed and damping coefficients can be investigated and described with above simulations. The calculation of natural frequencies has great importance to estimate resonance conditions and critical speeds for ride safety and comfort.

7. INVESTIGATION OF LATERAL AND LONGITUDINAL NATURAL FREQUNCIES

Under consideration the reduced model shown in Figure 8 and the relevant equations given in table and with (9, 10, and 11) the system natural frequencies for lateral and longitudinal motions can be obtained from:

$$\omega_{n_l} = \sqrt{K_l/J_\theta} \; and \; \omega_{n_{lg}} = \sqrt{K_{lg}/J_\phi}$$

Values in formula above; K_l as reduced lateral spring constant, K_{lg} as reduced longitudinal spring constant, J_θ as reduced lateral inertia of moment, J_ϕ as reduced longitudinal inertia of moment.

Both inertias can be calculated from the specified railway and wagon data, since the lateral and longitudinal vibrations are less important than the displacements in the z direction, the details of the movements in these directions have not been further investigated.

8. CONCLUSIONS

According to the calculated natural frequencies the relevant critical speeds for the case of disturbances caused by rail connections (with const. length of 20m) can be obtained by using following expressions:

$$V = \frac{L}{T} = \frac{L}{2\pi/\omega_n} = \frac{L\omega_n}{2\pi} \qquad (17)$$

For the first natural frequency. ω_n = 4.66 rad/s seen in Figure 12 the corresponding critical speed will be calculated with (17) as V = 14.84 m/s or as V = 53.5 Km/h.

Assuming that the nominal speed of the car is around 120 km/h which corresponds to V = 33.33 m/s, the vibration frequency at this speed is ω = Vπ/20 = 10 rad/s which is quite far from the resonance state.

The car vibrations reach the highest amplitude value around ω = 4.66 rad/s, as can be seen from the curves of figure 13 obtained against harmonic inputs with different frequencies based on the simulation model given in Figure 10.

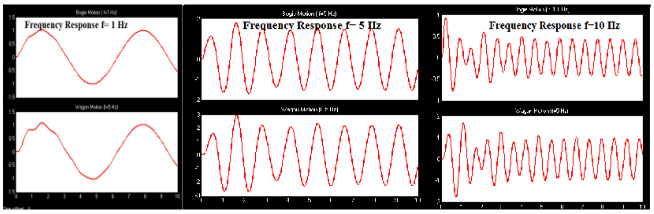

Figure 13: Frequency responses of car for w=1.6 and 10 rad/s

To obtain best results for safe and comfortable travel conditions the above mentioned modelling methods with equations and simulations can provide practical and reasonable preliminary design properties for the constructor.

REFERENCES

[1] Esveld, C., & De Man, A. (2003, January). Use of railway track vibration behaviour for design and maintenance. In IABSE Symposium Report (Vol. 87, No. 5, pp. 39-45). International Association for Bridge and Structural Engineering.

[2] Connolly, D. P., Kouroussis, G., Laghrouche, O., Ho, C. L., & Forde, M. C. (2015). Benchmarking railway vibrations–Track, vehicle, ground and building effects. Construction and Building Materials, 92, 64-81.

[3] Zweifel O. (1956) Berechnung des elastischen Verhaltens und der Eigenschwingungen von Eisenbahnfahrzeugen: ergänzte Fassung der Antrittsvorlesung in Schweizerische Bauzeitung Band: 74

[4] Eason, G., Noble, B., & Sneddon, I. N. (1955). On certain integrals of Lipschitz-Hankel type involving products of Bessel functions. Philosophical Transactions of the Royal Society of London. Series A, Mathematical and Physical Sciences, 247(935), 529-551.

[5] Hempelmann, K., Influence of operational track and vehicle parameters on corrugation growth, TU Berlin, June 1995.

[6] Man, A. P. D. (2004). Dynatrack: A survey of dynamic railway track properties and their quality.

[7] Markine, Man, A.D., Jovanović, S., & Esveld, C. (2000). MODELLING AND OPTIMISATION OF AN EMBEDDED RAIL STRUCTURE.

[8] Cochin, I. (1980). Analysis and design of dynamic systems. HarperCollins Publishers.

[9] Hung, H., Yang, Y., (2001). A review of researches on ground-borne vibrations with emphasis on those induced by trains. In: Proc. Nat. Sci. Council Part A: Phys. Sci. & Eng. p. 1-16.

[10] Avillez, J., Frost, M., Cawser, S., Skinner, C., El-Hamalawi, A., & Shields, P. (2012, August). Procedures for estimating environmental impact from railway induced vibration: a review. In ASME Proc. Noise Control And Acoustic Division Conference at InterNoise (pp. 381-392).

[11] Barke, D. W., & Chiu, W. K. (2005). A review of the effects of out-of-round wheels on track and vehicle

components. Proceedings of the Institution of Mechanical Engineers, Part F: Journal of Rail and Rapid Transit, 219(3), 151-175.

[12] Popp, K., Kruse, H., & Kaiser, I. (1999). Vehicle-track dynamics in the mid-frequency range. Vehicle System Dynamics, 31(5-6), 423-464.

Vibration measurement with wireless heterogeneous integrated displacement sensor and determination of dynamic deflection of sleepers and stiffness of railway tracks

Branislav Gavrilovic[1*], Vladimir Aleksandrovich Baboshin[2], Zoran Pavlovic[3]
[1,3]Academy of Tehnical and Art Applied Studies Belgrade, Department: Railway College,. (Serbia)
[2] Military institute (Railway troops and military communications), Department of Reconstruction of Automation, Telemechanics and Communication Devices on Railways, Sankt. Peterburg, Russia

The paper proposes a system for wireless measurement of vibrations with a heterogeneous integrated displacement sensor, which was perfected at the Technical Faculty in Novi Sad within the current project no. TR-32016 at the Ministry of Education, Science and Technological Development of the Republic of Serbia. The application of these sensors can completely simplify and eliminate the measurement imperfections that can be found with the use of wireless accelerometers due to the need for single and double integration in time in order to determine the displacement, ie dynamic deflection of railway sleepers and the stiffness of railway tracks.

Keywords: Wireless sensor networks, Railway, Vibrations of sleepers.

1. INTRODUCTION

Wireless sensor networks recently. are increasingly used in measurements in railway construction infrastructure. The most common goal of using wireless sensor devices is monitoring the condition of buildings, or Structural Health Monitoring (SHM). For this purpose, oscillation modes are usually recorded and analyzed during the regular exploitation of construction objects or in response to artificial excitation, or the correlation of oscillations at critical points for given elements is observed [1,2].

With aging tracks spanning a large area, there is a growing need for the use of wireless technologies on railways. Condition assessment and monitoring is required for rails, thresholds, fastening systems, rail pads, curtains, etc. Specific problems in the railway area are the huge number of elements that should be served and the distribution in a large area [1,3].

Permanent damage to thresholds and other elements occurs as a result of a number of causes. Natural phenomena such as landslides or natural disasters can contribute to the accelerated aging of railways. In the course of regular exploitation, damages are mostly the result of excessive loads, more often dynamic than static. Static loads mean vehicles that are too heavy. Dynamic implies short impact loads. These most often occur as a result of defective wheels [1]. Improperly sized wheels cause permanent and potentially serious damage, especially to the rails. Repeated short impact loads, which the unevenness produces, promote the formation and accelerate the growth of cracks in the metal [1], which shortens the useful life of the tracks and increases the chances of catastrophic accidents.

Other significant causes of rail damage during exploitation are the poor quality of vehicle axles and brakes and excessive lateral oscillations of compositions [1].

Measuring the displacement of sleepers under load can provide relevant information to railway engineers in the calculations of curtain stiffness and modulus of elasticity of the rail bed, as well as for checking the effectiveness of track maintenance procedures (such as cleaning and cushioning of curtains). The stiffness of the curtain has a significant effect on its rate of settlement, load distribution, dynamic loads, and stresses of certain components. Thresholds also affect the creation of communal noise, the reduction of which is sought [2,3,4,5,6,7].

Practical measurements of threshold shifts are in reality associated with numerous difficulties. The biggest difficulty is to provide a good reference system, because all parts of the railway structure are subject to vibrations. Vibrations are also transmitted to the surrounding ground on which parts of the measuring system are possibly placed. Some commonly used displacement sensors are not so effective when measuring the displacement (deflection) of thresholds or other elements. This class includes inductive and capacitive converters, systems with springs, etc. [8]. In order to be effective, these systems usually have to be installed deep into the ground under the railway, which is a challenge. If displacements are measured during high-frequency excitation, the situation becomes even more complicated due to the limitation of the dynamic characteristics of economic sensors, which determines the need for more expensive measuring systems. Also, laser-based optoelectronic systems are often used to measure displacements [8]. And in their case, the problem of the reference point arises. If the laser is closer to the measurement point, the vibrations are stronger, and if it is further away, the measurement precision decreases. An example of such a system is shown in Fig.1.

If accelerometers are used, the need for an external reference ceases because they measure the inertial acceleration to which they are exposed. The speed and position of the threshold can be determined by the method of single or double integration of acceleration over time. The disadvantage of this approach is that noise accumulates and there is a random deviation that grows

*Zdravka Celara 14, 11000 Belgrade, Serbia,e-mail: gavrilovicbranislav5@gmail.com

with time, and software correction methods are needed [9]. Software level corrections are performed periodically, i.e. they use the information that sleepers (or any other oscillating structures) return to their initial position after the expiration of a period, that is, the passage of a wagon or composition in this case.

Figure 1. Laser system for measuring the static deflection of railway sleepers

The sensor device developed at the Faculty of Civil Engineering in Belgrade [1,10] uses a digital three-axis MEMS accelerometer LIS3LV02DL [1,11] as the main sensor. The sensor system made it possible to measure the acceleration and speed of thresholds when moving full and empty trains on the track not far from the Nikola Tesla thermal power plant in Obrenovac. In doing so, a laser system with three sensor devices was used, which were glued with adhesive tape to the railroad sleepers, on the outside of the rails, at a distance of 3 m from each other. Such measurements indicated different forms of the vertical acceleration signal from threshold to threshold, and from whether a full or empty train was passing. For full trains, the vertical oscillations are smaller in amplitude, although the static deflections are larger in that case. At the same time, it was established that the exact peak values of vertical acceleration are difficult to accurately measure because the bandwidth of the accelerometers was not sufficient to ensure reliable recording of short-term impulses of great force. Accelerations in other directions were typically an order of magnitude smaller than vertical ones [1].

The double integration of the signal to obtain the shifting of the sleeper in the case of using the described wireless system does not give completely satisfactory results. It turns out that a higher sampling frequency is needed to record the spikes with sufficient resolution for digital integration. Also, there is a suspicion that a better attachment of the accelerometers to the surface is needed, because some impacts have short accelerations above g, which means that the accelerometers may lag during downward accelerations of the sleeper. Nevertheless, an approximate estimate of the displacement amplitude of the part of the sleeper on which the sensor is placed (accelerations and displacements cannot be identical along the entire surface of the sleeper) can also be given by analyzing existing recordings. Due to measurement imperfections, which include hysteresis, non-linearity, and various other errors, single and double integration in time over one period does not yield exactly zero, although the velocity and sleeper displacement should return to initial values. Of course, there are also physical reasons for deviations, such as slower harmonics of the oscillation of the composition and the differences between the wagons.

In order to eliminate the aforementioned imperfections of the accelerometric sensor device, it is proposed to use a wireless heterogeneous integrated sensor and a wireless network with these sensors, which will be described below

2. WIRELESS HETEROGENEOUS INTEGRATED DISPLACEMENT SENSOR

At the Technical Faculty in Novi Sad, a prototype of a wireless heterogeneous integrated displacement sensor was developed within the project no. TR-32016 at the Ministry of Education, Science and Technological Development of the Republic of Serbia [12].

The proposed sensor measures the distance that changes in the cavity inside the sensor and, therefore, can measure the displacement of the moving object acting on the sensor. The displacement, x, of the Manual Translation Stage (MTS), shown in Fig. 2, acting on the sensor causes the membrane to bend by the same value, x, at its center.

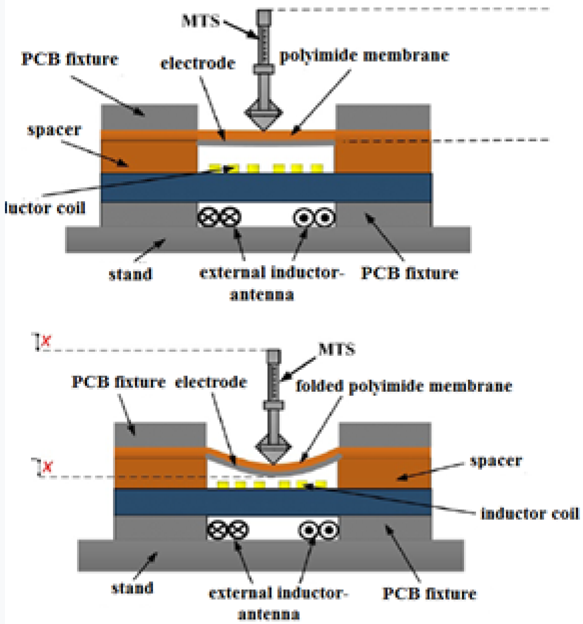

Figure 2: Measurement setup for wireless sensor measurement with sensor cross-section and positioner

The inductor is the basic part of the sensor that is used for magnetic coupling with the antenna and enables wireless measurement of the sensor. The inductor is designed in the form of a circular spiral. PCB technology of printed circuit boards with one metal layer was used for the manufacture of the inductor (Fig. 3).

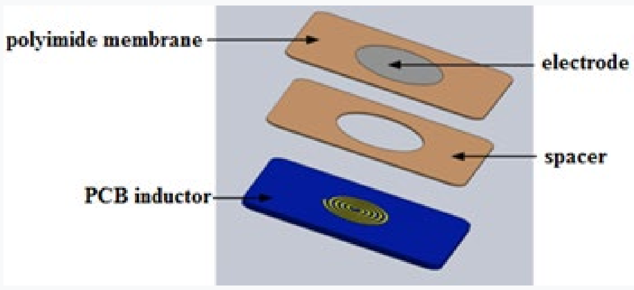

Figure 3: Split 3D view of the proposed sensor (with the polyimide membrane rotated by 180°).

A planar spiral inductor is placed parallel to the electrode and forms an LC circuit. A change in the distance between the upper electrode of the capacitor and the coil of the inductor (lower electrode) causes a change in capacitance. The resonant frequency of the LC circuit depends on the value of inductance and capacitance, that is, a change in the value of capacitance will change the resonant frequency

Numerous tests of this sensor using the HP4194A impedance analyzer. show that the dependence of the capacitance on the frequency and displacement of the object is given in Figures 4 and 5, respectively.

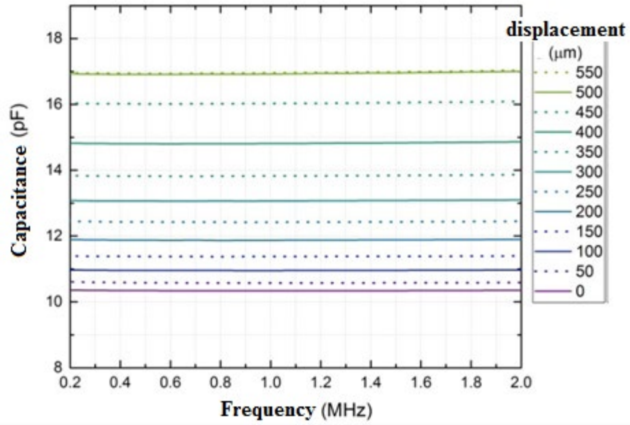

Figure 4: Dependence of capacitance on frequency for different displacement values

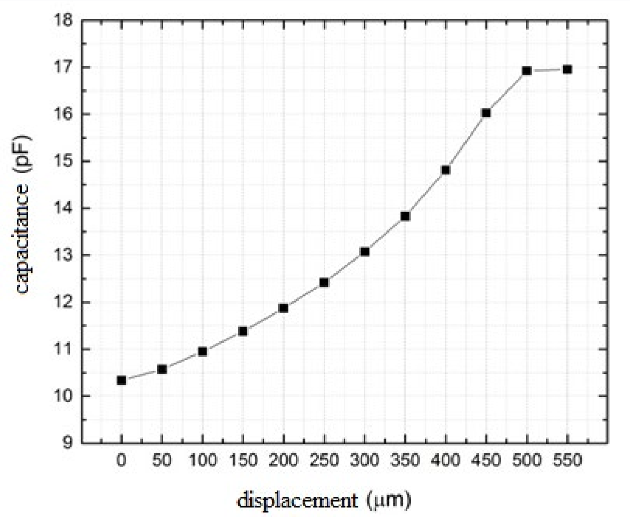

Figure 5: Dependence of capacitance on displacement

The measured impedance phases of the antenna-sensor system for displacements up to 500 μm in steps of 50 μm are shown in Fig. 6. Increasing the displacement acting on the sensor leads to greater bending of the electrode on the membrane, greater capacitance between the inductor and the electrode, and therefore less resonance sensor frequencies. The resonant frequency of the antenna is 100 MHz, while the resonant frequency of the antenna-sensor system for the first measurement point without moving the membrane is 46 MHz. The resonant frequency of the system is sufficiently lower compared to the resonant frequency of the antenna, which enables the application of the minimum phase impedance measurement method. By increasing the displacement of the sensor membrane, the minimum value of the phase moves towards lower frequencies (Fig. 6). The characteristic of the dependence of the resonance frequency in relation to the displacement obtained by experimental measurement and linear approximation is shown in Fig. 7.

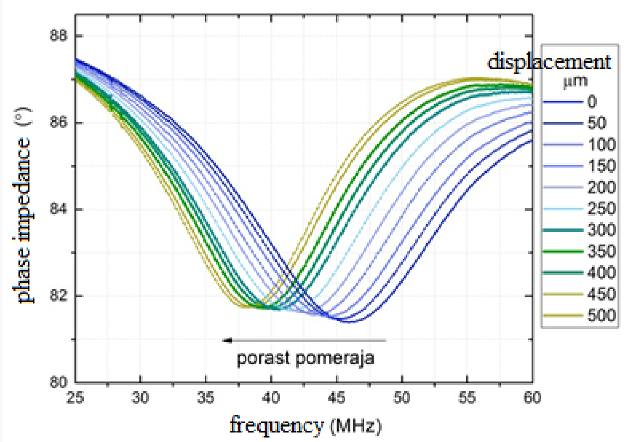

Figure 6: Wirelessly measured phase impedance of the antenna-sensor system for different displacement values

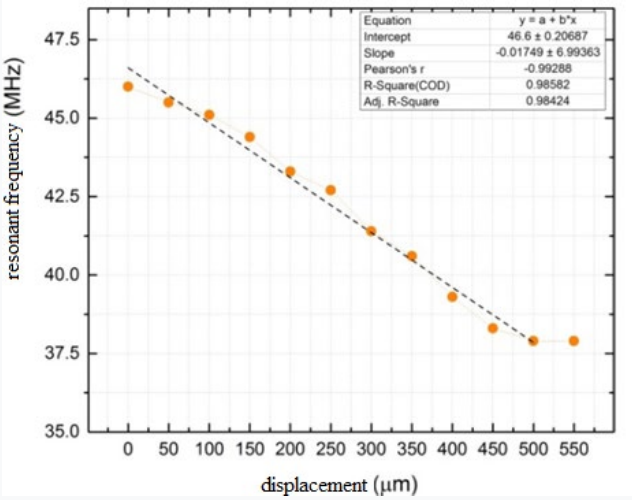

Figure 7: Measured characteristic of the resonant frequency of the displacement system together with its linear approximation.

As can be seen in Fig. 7, increasing the displacement acting on the sensor decreases the resonant frequency of the system. The resulting characteristic has good linearity in the entire measurement range and a sensitivity of 16.2 kHz/μm was achieved, which is significantly higher than the sensitivities of the sensor 1.14 kHz/μm, 8.75 kHz/μm, 1.50 kHz/μm, 12.70 kHz/μm or 1.09 kHz/μm. Additionally, the structure of the resonant sensor is simpler compared to other resonant circuits. The sensor does not require complete insulation between electrodes, connecting components with screws, smooth and precise contacts that can deform the structure and contribute to the creation of parasitic elements.

3. WIRELESS SENSOR NETWORK WITH HETEROGENEOUS INTEGRATED DISPLACEMENT SENSOR

The wireless sensor network with a heterogeneous integrated displacement sensor is in principle not significantly different from the one developed at the

Faculty of Civil Engineering in Belgrade with a digital three-axis MEMS accelerometer type LIS3LV02DL. This is due to the fact that the digital three-axis MEMS accelerometer type LIS3LV02DL can be replaced with the impedance analyzer HP4194A and thus switch to a more reliable sensor network when measuring railway sleeper vibrations (Fig. 8).

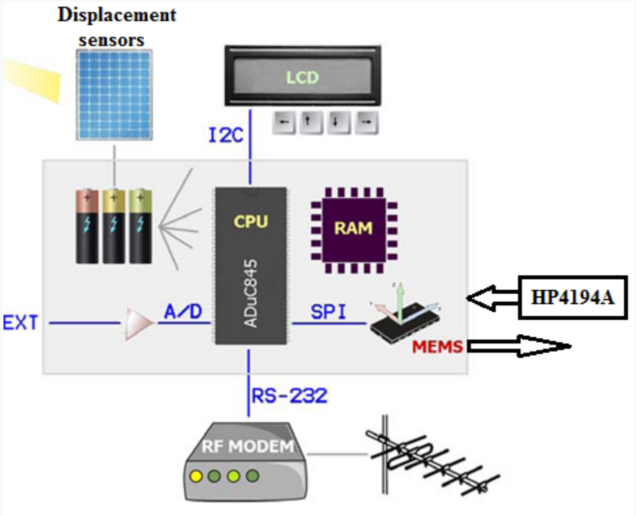

Figure 8: Wireless sensor device with heterogeneous integrated displacement sensor

The movement sensor device communicates with the central station (hub) via a radio (RF) modem of domestic production Decode PRM-4 [13]. The modem works at 863-867 MHz, which is a relatively low frequency, which does not allow a high speed of data flow, but it helps to achieve communication in closed spaces and in the presence of obstacles, due to better diffraction, which is a consequence of a higher wavelength. If a longer range is needed, Yagi-Uda antennas are used, and at the central station an omnidirectional antenna, while in the case of smaller distances, small stick antennas can be used. The range of devices with large antennas is up to 1500 m open, and it is highly variable depending on whether it is used in an urban environment with strong interference or not.

A PC, usually a portable laptop, is used as the central station of the system. For this purpose, a special program was developed for the MS Windows operating system. The energy reserves of the central station are practically unlimited, as well as the memory and processing power. In order to perform modal vibration analysis of building structures, which is the main purpose of this wireless system, it is necessary to collect raw signals from multiple wireless devices and compare them. The algorithm of the system is such that the sensor devices spend most of the time in the mode of reduced consumption. When waking up, they listen for a few seconds for a paging signal from the central station. If the same is detected, they remain in the so-called in stand-by mode for a while, waiting for a command to start measuring, data transfer, or setting some parameters. During the measurement, 3200 data are collected with a variable selection frequency, which goes from 40 to 2560 Hz, so the measurement windows are from a few seconds to over a minute. The data is then locally compressed without loss using the Huffman algorithm, since sending data by radio requires the highest energy consumption (the modem consumes about 30 mA when sending, while the consumption of other electronics is 5-10 mA in operating mode), so the goal is to minimize it and transmit as much as possible lower number of bits. Data collection and signal reconstruction are performed at the central station. Multiple methods including Reference Broadcast Synchronization or Reference Broadcast Signal (RBS) synchronization [14], back synchronization [15], and occasional tests of crystal frequencies as well as the ratio of frequencies (which is more important than absolute values) were applied to ensure good data synchronicity, which is of the order of magnitude 0.01 ms to 0.1 ms and exceeds the capabilities of mechanical sensors with sampling periods of the order of milliseconds.

4. MEASUREMENTS OF DEFLECTION AND STIFFNESS OF RAILWAY SLEEPERS WITH DISPLACEMENT SENSORS

In the current practice on the tracks of the Serbian Railways, the vibration measurement of railway sleepers was performed with a digital three-axis MEMS accelerometer LIS3LV02DL, but not with the displacement sensors from point 2 of this paper [1]. However, Fig. 9 shows similar sensors that were used in measurements of railway sleeper vibrations and track stiffness on Swedish railways [16]. During these measurements, as was expected when moving trains in zones with partially supported or unsupported sleepers, there was a change in the vertical movement of the railway sleepers, and thus (a decrease in) the total stiffness of the tracks. On the other hand, sudden changes in track stiffness could indicate changes in the regularity of railway sleepers, which was the goal of these measurements. On the other hand, sudden changes in track stiffness could indicate changes in the regularity of railway sleepers, which was the goal of these measurements.

Figure 9: Wireless sensor for measuring vibrations [16]

Figure 10 shows a diagram of the measured stiffness along a section of a railway in Sweden. Local maxima, which appear on the diagram at a regular distance, represent track stiffnesses in sections above the sleepers.

The diagram shows a sudden drop in track stiffness (sudden increase in deflection) at three thresholds near the station at km 149+807. Therefore, it can be expected that these three thresholds do not regularly rest with their lower surface on the tucan [16].

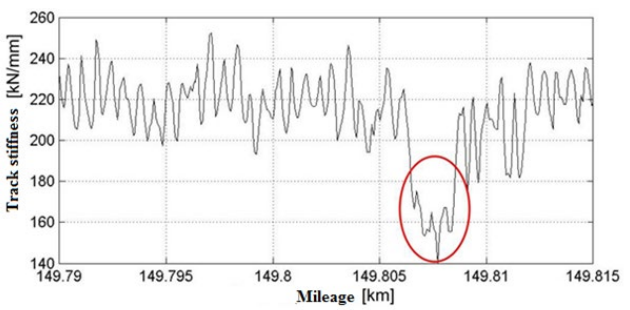

Figure 10: Changes in track stiffness along a section of a railway in Sweden [16]

5. CONCLUSION

With aging tracks spanning a large area, there is a growing need for the use of wireless technologies on railways. Condition assessment and monitoring is required for rails, thresholds, fastening systems, rail pads, curtains, etc. Specific problems in the railway sector are the huge number of elements that should be served and the distribution in a large area. For this purpose, oscillation modes are usually recorded and analyzed during the regular exploitation of railway sleepers. By using wireless heterogeneous integrated displacement sensors, which have been perfected at the Technical Faculty in Novi Sad, the imperfection of measuring dynamic deflection and track stiffness, which can be obtained by using wireless accelerometers, can be simplified and eliminated. Measurements with similar displacement sensors on Swedish railways indicate sufficient reliability of measuring the dynamic deflection of railway sleepers and the stiffness of railway tracks as criteria for determining their condition.

REFERENCES

[1] M. Malović, Lj. Brajović, V. Radić, L. Lazarević, Z. Popović: „Measurement of sleepers vibrations and determination of their dynamic deflection and train velocity", INFOTEH-JAHORINA Vol. 13, (2014).

[2] B. A. Sundaram, K. Ravisankar, R. Senthil and S. Parivallal, "Wireless sensors for structural health monitoring and damage detection techniques," Current Science, 104(11), pp 1496-1505, (2013).

[3] S. Kaewunruen and A. M. Remennikov, "Trends in vibration-based structural health monitoring of railway sleepers," in R. C. Sapri (ed), Mechanical Vibration: Measurement, Effect, and Control, pp 3-4, (2009)

[4] J. C. O. Nielsen and A. Igeland, "Vertical dynamic interaction between train and track - influence of wheel and track imperfections," Journal of Sound and Vibration, 187(5), pp 825-839, (1995).

[5] Z. Cheng, D. Chen and F. Nogata, "Fatigue behaviour of a rail steel under low and high loading rates," Fatigue and Fracture of Engineering Materials and Structures, 17(1), pp 113-118, (1994).

[6] D. Barke and W. K. Chiu, "Structural health monitoring in the railway industry: a review," Structural Health Monitoring, 4(1), pp 81-93, (2005).

[7] D. Thompson, Railway noise and vibration: mechanisms, modelling and means of control. Elsevier, Oxford | Amsterdam, (2009).

[8] B. Pan, K. Qian, H. Xie and A. Asundi, "Two-dimensional digital image correlation for in-plane displacement and strain measurement: a review," Measurement Science and Technology, 20(6), article ID 062001 (17 pages), (2009).

[9] S. J. Cox, "Deflection of sleeper in ballast," Vehicle system dynamics supplement, vol. 24, pp. 146-153, (1995).

[10] M. Malović, Lj. Brajović, Z. Mišković and G. Todorović, "Merenje vibracija mrežom bežičnih senzora," Tehnika - Naše Građevinarstvo, 66(6), pp 883-889, (2012).

[11] ST Microelectronics, LIS3LV02DL accelerometer datasheet, from http://www.st.com/st-web-ui/static/active/en/resource/technical/ document/datasheet/CD00091417.pdf

[12] M. G. Kisić, N. V. Blaž, L. D. Živanov, M. S. Damnjanović: "Projekat tehnološkog razvoja TR-32016, Ministarstvo prosvete, nauke i tehnološkog razvoja Republike Srbije", Fakultet tehničkih nauka, Univerzitet u Novom Sadu, Novi Sad, Srbija, (2017).

[13] Decode, PRM-4 radio modem datasheet, from http://www.decode.rs/documentation/PRM_4-datasheet.pdf

[14] J. Elson, L. Girod and D. Estrin, "Fine-grained network time synchronization using reference broadcasts," ACM SIGOPS Operating Systems Review - OSDI '02: Proc. of the 5th symposium on Operating systems design and implementation, 36(SI), pp 147-163, (2002)

[15] S. Rahamatkar, A. Agarwal and N. Kumar, "Analysis and comparative study of clock synchronization schemes in wireless sensor networks," International Journal on Computer Science and Engineering, 2(3), pp 536-541, (2010).

[16] E. Berggren: *Dynamic track stiffness measurement - A new tool for condition monitoring of track substructure*. Licentiate Thesis, KTH Royal Institute of Technology, p. p. 101, (2005).

[17] N. Krakover, B. R. Ilic, S. Krylov, "Displacement sensing based on resonant frequency monitoring of electrostatically actuated curved micro beams," *J. Micromech. Microeng*., vol. 26, 115006, pp. 1-11, (2016).

[18] B. Ozbey, E. Unal, H. Ertugrul, O. Kurc, C. M. Puttlitz, V. B. Erturk, A. Altintas, H. V. Demir, "Wireless displacement sensing enabled by metamaterial probes for remote structural health monitoring," *Sensors*, vol. 14, pp. 1691-1704, (2014).

[19] N. Blaž, G. Mišković, A. Marić, M. Damnjanović, G. Radosavljević, Ljiljana Živanov, "Modeling and characterization of LC displacement sensor in PCB technology," *35th Inter. Spring Sem. on Electronics Techn.*, Bad Aussee, 2012, pp. 394-398, (2012).

[20] M. Kisić , N. Blaž, K. Babković, A. Marić, G. Radosavljević, Lj. Živanov, M. Damnjanović, "Performance analysis of a flexible polyimide based device for displacement sensing," *Facta universitatis series: Electronics and Energetics*, vol. 28, no 2, pp. 287 – 296, (2015).

[21] GTS Flexible Materials Ltd, available at: http://www.gtsflexible.co.uk.

Study of the contact between design profiles of rails and rims used in the tram track of the city of Sofia

Vladimir Zhekov
National Railway Infrastructure Company, Sofia (Bulgaria)

The report examines the interaction between the design profiles of rail 49E1, grooved rails 60 R1, 60 R2, block rail B60 and rim profiles T81 and RPSf 2018, which are used in the tram track of the city of Sofia. The report aims to compare the contact interaction of T81 and RPSf 2018 rim profiles with rail profiles, showing the profile contact point graphs, the rolling radii difference and calculating the design equivalent conicity values.

Based on the analysis, conclusions were drawn about the interaction between the currently used RPSf 2018 profile and the previously used T81 profile.

Keywords: Railway track, contact point, Rail, Rim, Tram

1. INTRODUCTION

The subject of the study is the interaction of a rim profile with the conditional name RPSf 2018 [1] and profile T81[2] with rail profiles - 49E1[3], grooved rails 60 R1[4], 60 R2[4] and block rail B60[5]. Track profile RPSf 2018 [1] has been used since 2018 on the tram track of the city of Sofia, and profile T81 was mainly used before that. In the present study, the two profiles are examined in their contact with the mainly used rails in the city of Sofia and their interaction is analyzed. The contact points between the respective rim profile and the rails, the rolling radii difference and the equivalent conicity were investigated..

2. RESEARCH METHODOLOGY

In order to carry out the research, a geometrical comparison of RPSf 2018 and T81 rim profiles was initially performed, and the differences in the areas related to the contact with the rails were established.

After that, a comparative analysis of the obtained data was made from the following characteristics[6] [7] [9]:

- Contact points between rim and rail;
- Rolling radii difference;
- Equivalent conicity.

The methodology of standard EN 15302:2022[10] was used to determine the specified characteristics, and the results were validated.

The main objective of this report is to compare the results for RPSf 2018 and T81 profile in contact with rail profiles for analysis and optimization recommendations.

The graphic part of the report shows interaction with profiles 60R2 and 49E1, which are widely used. Profiles 60R1 and B60 are also included in the analysis, considering that profile 60R1 is rarely used in small curves, and profile B60 is no longer applied for tram track in city of Sofia.

3. RIM PROFILES

3.1. Rim profiles RPSf 2018 and T81

The geometric characteristics of the RPSf 2018 rim profile are shown in fig.1[1], and those of the T81 profile in fig.2.

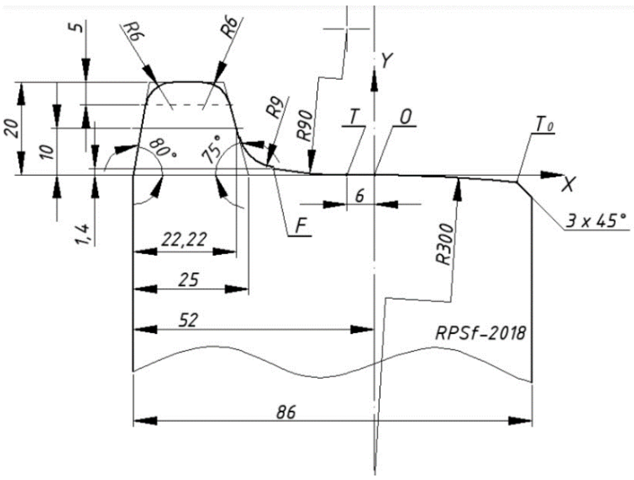

Figure 1: Rim profile RPSf 2018[1]

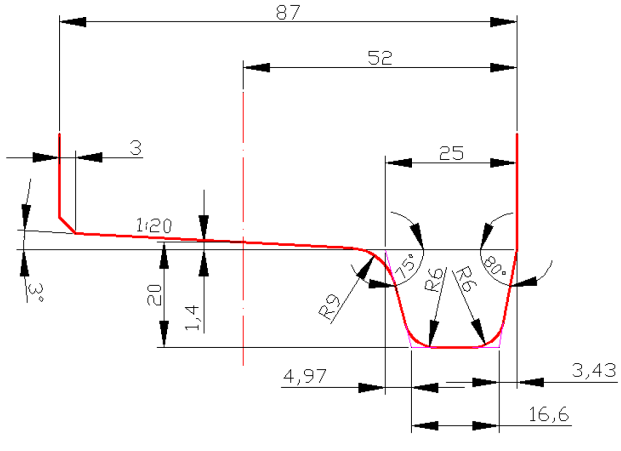

Figure 2: Rim profile T81[2]

3.2. Geometric comparison of RPSf 2018 and T81

To determine the main differences in the geometry of the two profiles, they are compared to the axis of the profiles, the distance between which is 1486 mm with a gauge of 1435 mm, and 1062 mm with a gauge of 1009 mm. The comparison is shown in Fig.3.

*Corresponding author: 122a ”Mariya Luiza” Blvd, Sofia, Bulgaria, vladijekov@gmail.com

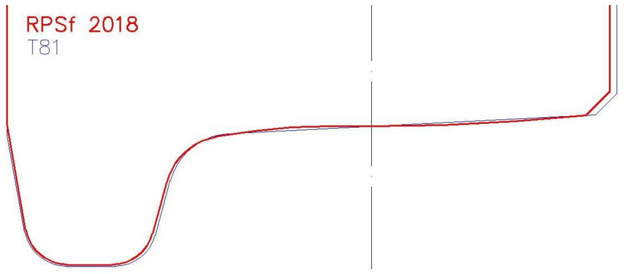

Figure 3: Comparison between rim profiles RPSf 2018 and T81

It can be seen from the graph that the T81 is a standard conical profile with a slope of 1:20, while two reverse curves with radii of 300 and 90 m are designed at the base of the RPSf 2018. Small differences in the dimensions of the flange are also found, and the same give differences in terms of the parameter SR, representing the distance between the contact surfaces of the flange. The table below summarizes the differences:

Table 1: Стойности на SR

	RPSf 2018	T81
1009 mm	1 002,52 mm	1 003,40 mm
1435 mm	1 426,52 mm	1 427,40 mm

A difference of 0.886 mm in terms of the SR parameter is found for the RPSf 2018 rim profile compared to the T81.

4. INVESTIGATION OF THE CONTACT BETWEEN RPSF 2018 AND T81 RIM PROFILES WITH RAIL PROFILES AT 1009 GAUGE

4.1. Contact interaction research

The contact interaction of RPSf 2018 and T81 profiles with rail profiles 60R2 and 49E1 is shown in fig.4 and fig.5.

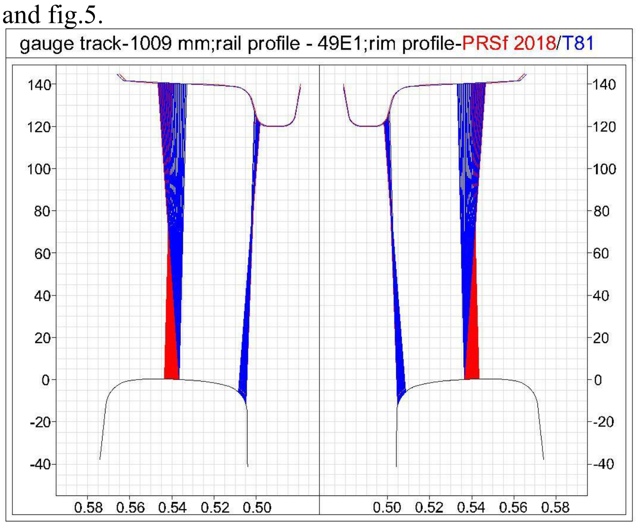

Figure 4: Comparison between rim profiles RPSf 2018 and T81 with 49E1 – gauge 1009 mm

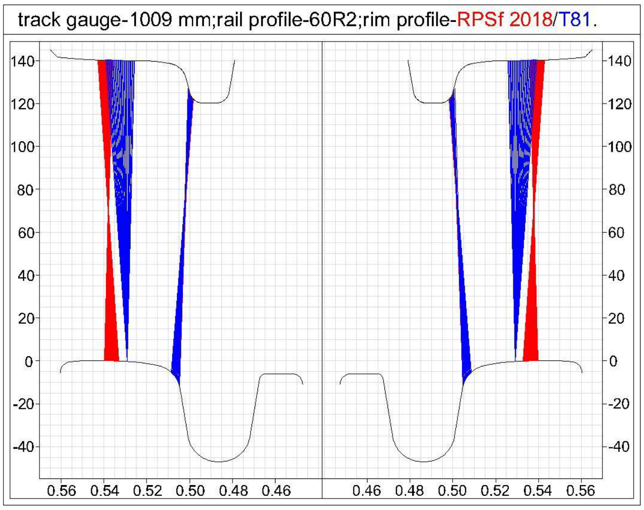

Figure 5: Comparison between rim profiles RPSf 2018 and T81 with 60R2 – gauge 1009 mm

An analysis of the graphs shows that with the RPSf 2018 profile, the contact takes place in the convex part with a radius of 300. Thus, a convex part is formed, where the contact stresses and, accordingly, the degree of wear will be higher. With profile T81, which is a standard conical profile, the contact is mainly in the central part of the rim, which is optimal.

In 60R2, 60R1 and 49E1 rail profiles, there is standard two-point contact, while in B60 block rail, contact is established with the flange, which can be considered unfavourable.

4.2. Rolling radii difference

For profiles RPSF 2018 and T81, the rolling radii difference in their interaction with rail profiles was calculated and plotted, as shown in Figure 6 with profiles 60R2 and 49E1.

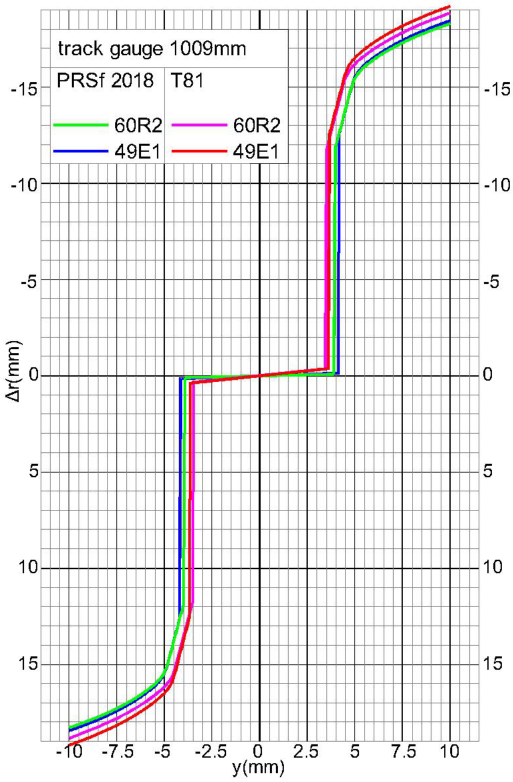

Figure 6: RRD at rim profiles RPSf 2018 and T81 with 49E1 – gauge 1009 mm

From the calculations and the graph, it is clear that for the RPSF 2018 profile the wheel rise occurs at about ~4mm, while for the T81 profile it is at ~3.5mm. It is also noticeable that the slope line formed by the RPSF 2018 profile has a very small slope, while with the T81, as a conical profile the slope formed is close to 1:20.

For the 60R1 profile, the data is identical – a rise of ~4mm for the RPSf 2018 profile and 3.59 mm for the T81.

With a block rail B60, rail rise is contacted at a very small value of lateral displacement of the track axle, as well as a too inclined straight line, which is unfavorable. Fig. 7 shows the rise graph.

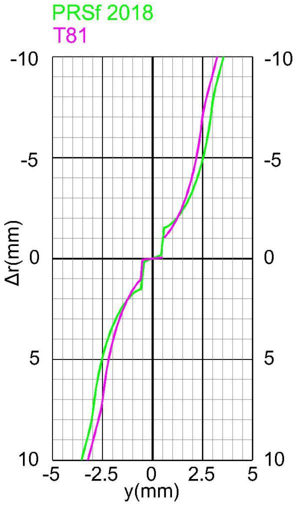

Figure 7: RRD at rim profiles RPSf 2018 and T81 with B60 – gauge 1009 mm

4.3. Equivalent conicity

Calculations have been made for the equivalent conicity for profile RPSF 2018 and T81 when interacting with rail profiles. The graph of the equivalent conicity for profiles 60R2 and 49E1 is shown in Fig. 8, and all calculated values in Table 2.

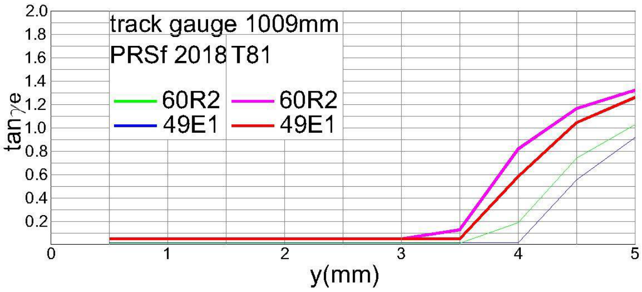

Figure 8: Equivalent conicity at rim profiles RPSf 2018 and T81 with 60R2 and 49E1 – gauge 1009 mm

Table 2: Equivalent conicity at rim profiles RPSf 2018 and T81 for rail profiles, gauge 1009 mm

Rail profile	RPSf 2018		T81	
	y mm	tanγe	y mm	tanγe
60 R2	2.7	0.011	2.3	0.052
60 R1	2.7	0.011	2.3	0.052
49E1	2.7	0.018	2.3	0.052
B60	2.7	0.967	2.3	1.065

, where y- transverse displacement amplitude;
tanγe - equivalent conicity.

From the values it is found that for a standard T81 rim profile when interacting with 60R2, 60R1 and 49E1 rail profiles, the values are about 0.052 or a slope of 1:19.2. With a B60 profile, there are high conicity values and a rapid rise of the wheel, which is unfavorable.

With profile RPSf 2018, we establish with rail profiles 60R2, 60R1 and 49E1 low values of the equivalent conicity 0.011/0.018 or a slope of `1:90.9/1:55.6. This indicates that the wheel has a low conicity, therefore the effect of directing the spoke to the center is low. Again the results with B60 are high, which as we said is unfavorable.

5. INVESTIGATION OF THE CONTACT BETWEEN RPSF 2018 AND T81 RAIL PROFILES AT 1435 MM GAUGE

5.1. Contact interaction research

The contact interaction of RPSf 2018 and T81 profiles with 60R2 and 49E1 rail profiles at a gauge of 1435 mm. is shown in fig.9 and fig.10.

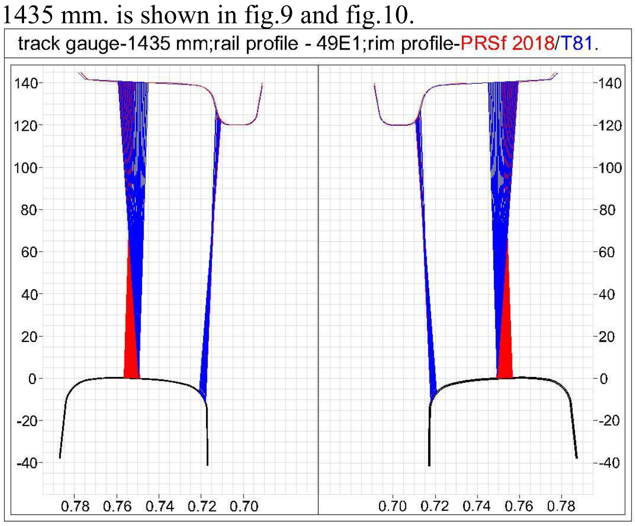

Figure 9: Comparison between rim profiles RPSf 2018 and T81 with 49E1 – gauge 1435 mm

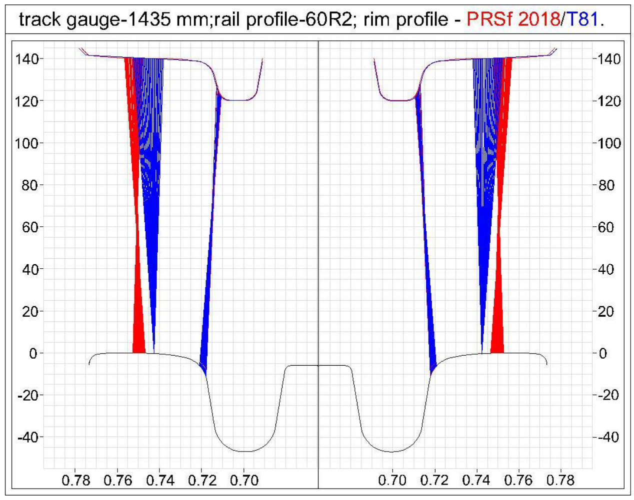

Figure 10: Comparison between rim profiles RPSf 2018 and T81 with 60R2 – gauge 1435 mm

In this case, the results are identical to what was described in item 4.1 of this report. The most important thing is that with the RPSF 2018 profile, the contact is made with the convex part of the rounding with a radius of 300 mm, which leads to higher contact stresses in this area and high wear, which will quickly cause a change in the geometry of the profile. It can be considered that the contact at T81 is more optimal.

Again with block rail B60 contact is established with the flange.

5.2. Rolling radii difference

The graphs of the difference in rolling radii in the interaction of profiles RPSF 2018 and T81 with rail profiles 60R2 and 49E1 are shown in fig. 11.

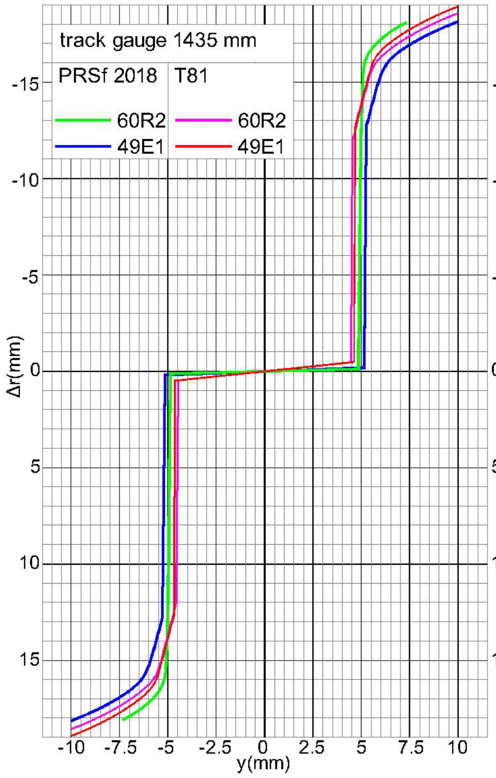

Figure 11: RRD at rim profiles RPSf 2018 and T81 with 49E1 – gauge 1435 mm

It is found that with profile RPSf 2018, the rise of the wheel occurs at y=~5 mm, while with T81 – at ~4.5 mm. Again, at profile B60, a sharp rise is identified as described in item 4.2 of this report..

5.3. Equivalent conicity

The graph of the equivalent conicity for profiles 60R2 and 49E1 is shown in Fig. 12, and all calculated values in Table 3.

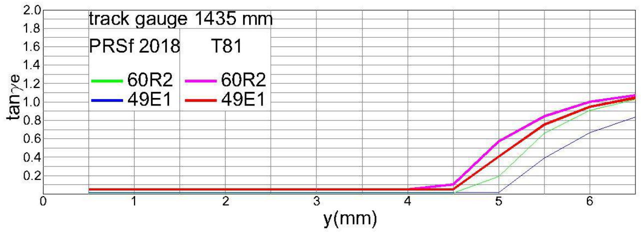

Figure 12: Equivalent conicity at rim profiles RPSf 2018 and T81 with 60R2 and 49E1 – gauge 1009 mm

Table 3: Equivalent conicity at rim profiles RPSf 2018 and T81 for rail profiles, gauge 1435 mm

Rail profile	RPSf 2018		T81	
	y mm	tanγe	y mm	tanγe
60 R2	3	0.013	3	0.054
60 R1	3	0.176	3	0.052
49E1	3	0.018	3	0.055
B60	3	0.520	3	0.531

, where y- transverse displacement amplitude;
tanγe - equivalent conicity.

The results are close to the established for track gauge 1009 mm, namely:

At RPSf 2018 there is low conicity except for contact with 60R1 which value is normal and B60 where the value is high.

6. CONCLUSION

In summary the following conclusions can be made:

- In the RPSf 2018 profile, at the contact with the main profiles 60R2, 60R1 and 49E1, there is a contact of the convex part with a radius of rounding of 300 mm. This leads to higher contact stresses in this area and wear. Contact with profile T81 is more optimal.

- With profile RPSf 2018, low values of the equivalent conicity are found with profiles 60R2, 60R1 and 49E1, and the profile has a low taper and cannot ensure the normal direction of the wheel axle to the center. With profile T81, there are optimal values corresponding to a slope of 1:20.

- B60 block rail interaction is not good, due to the discontinued application and the modernization of the panel sections, this problem will go away.

REFERENCES

[1] Михайлов Е.,Атанасов М., Евлогиева З. Взаимодействие на трамвайни колела с бандажен профил RPSf-2018 с трамвайните коловози. Научно списание „Механика Транспорт Комуникации", том 20, брой 3/3, 2022 г., статия №2235, ISSN 1312-3823 (print), ISSN 2367-6620 (online)

[2] Жеков, В., Анализ на възможностите за подобряване дълготрайността на конструкцията на градския релсов път, Дисертационен труд. Защитен на 20.04.2018г., ВТУ "Тодор Каблешков", София

[3] CEN European Committee for Standardization, EN 13674-1:2011. Railway applications – Track – Rail, Part 1: Vignole railway rails 46 kg/m and above, 2011

[4] CEN European Committee for Standardization, EN 14811:2006+A1:2010. Railway applications - Track - Special purpose rail - Grooved and associated constructio , 2011

[5] „Столична компания за градски транспорт - Холдинг" ЕАД, Правилник с технически изисквания и норми за трамваен релсов път., София. 2000 г.

[6] Allen P., Bevan A., Determination of Tramway Wheel and Rail Profiles to Minimise Derailment. ORR, 2008

[7] Emil Mihaylov, Dobrinka Atmadzhova, „Study on wheel profile of tram in operation", The first international

symposium for student swith papers from mechanical engineering SRMA 2011, Кралево, Сърбия, 2011 г. HEAVY MACHINERY - HM 2011, с. 49-54, ISBN 978-86-82631-58-3

[8] Emil M. Mihaylov, Dobrinka Atmadzhova, „Comparative analysis of accelerations of type T6A2 tram bogie frames with different types of elastic wheels”, VI International symposium for students, Кралево, Сърбия, 2014 г.

[9] Emil M. Mihaylov, Dobrinka Atmadzhova, Emil Iontchev, „Investigation of the interaction between tram wheels and the road when passing through a crossing at a right angle”, XVIII Scientific - Expert Conference RAILCON’18, Ниш, Сърбия, 2018 г., ISBN 978-86-6055-105-6, стр. 33 – 36

[10] CEN European Committee for Standardization, EN 15302:2022. Railway applications. Wheel-rail contact geometry parameters. Definitions and methods for evaluation

Investigation of the behaviour of a freight wagon braking system on a brake systems bench

Vasko Nikolov[1*], Georgi Nikolov
[1]Department of Transport Equipment, Todor Kableshkov Transport University, Sofia, Bulgaria

Abstract: *The article examines the behavior of a braking system for class S freight wagons mounted on a brake bench. A review of the regulations that determine the technical characteristics of the braking systems of railway vehicles was made. A comparison between the theoretically set technical parameters and those obtained during the bench tests was made. The behavior of the pneumatic and mechanical parts of the stand was analyzed. Conclusions from the observations and analyses are drawn.*

Keywords: brake system, safety, freight wagon, brake system bench, rolling stock

1. INTRODUCTION

Braking systems in railway transport are an important part of the active safety of railway vehicles and are essential for the safety and reliability of the transport process. For this reason, the requirements for brake systems and the main units that make them up are strictly regulated in the regulatory documents of the International Union of Railways (UIC). To ensure sufficiently high reliability during their operation, they are subjected to a number of tests. These tests are carried out on specialized test benches and also in real operating conditions.

2. AN EXPERIMENTAL PERFORMANCE

In order to demonstrate the processes taking place in the braking systems, a bench was built at the "Todor Kableshkov" Transport University to test the braking systems for freight cars used in the Republic of Bulgaria. The bench is equipped with modern registering and recording equipment, with which both laboratory exercises and specific practical problems can be solved. With its help, not only can the processes taking place in the brake apparatus during braking be simulated, but it can also be used for student training and research work.

The pneumatic part of the bench for testing brake systems of freight wagons consists of (*Fig. 1*):

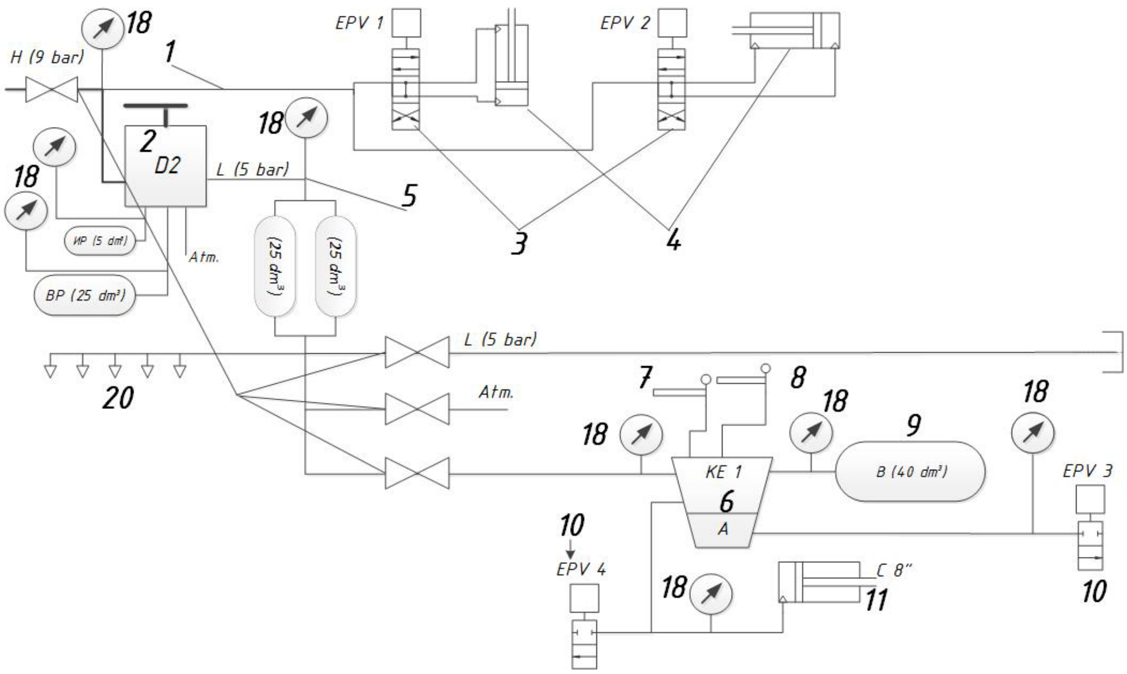

Fig. 1. Scheme of the pneumatic part of the bench for testing brake systems of freight wagons.

*Corresponding author: va_r_nikolov@abv.bg

1. Line for high pressure (9 bar);
2. Driver’s brake valve Knorr D2 with its fitting;
3. Electropneumatic valves for controlling the pneumatic cylinders;
4. Pneumatic cylinders for changing the thickness of the brake pads;
5. Main pipe (5 bar);
6. Brake valve KE 1;
7. On/off tap for brake valve KE 1;
8. Tap for switching the mode of the brake valve KE 1 (G-P);
9. Auxiliary reservoir 40 dm^3;
10. Electropneumatic valves for gap control;
11. Brake cylinder 8”;
12. Brake taps;
13. Manometers;

To measure the values of pneumatic quantities IPS-G-405 type pneumatic transmitters were used (*Fig. 2*).

Fig. 2. Pressure transmitter type IPS-G-405

The inbuilt analog-to-digital converter (ADC) of the ESP 32 microprocessor [4] is utilized to convert the analog signals into digital. The ESP32 integrates two 12-bit SAR (Successive Approximation Register) ADCs, supporting a total of 18 measurement channels (analog enabled pins) [3]. For these measurements only one ADC is used. Five measurement channels are connected to general purpose input output (GPIO) pins (32-36) to a multiplexer (*Fig. 3*) which multiplexes the data to the ADC. This allows for a sample rate of roughly 1 kHz per channel, which is more than enough to capture the dynamics of the pressure signal, which changes in the order of seconds. The ADC of the ESP 32 is set to have input range from 0 to 3.6V. Given that the ADC can sample the signal with 12 Bit, this gives a resolution of $3.6V/2^{12}$ [5] or 0.8mV.

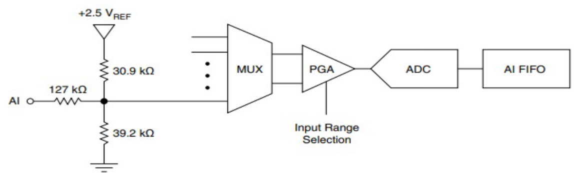

Fig. 3

The data from the ADC is then transmitted by the ESP 32 to the Raspberry Pi 4 module via universal asynchronous receiver-transmitter (UART) with baud rate of 115200. The module contains the appropriate Python software which captures the UART data. And then registers, remembers, and illustrates the obtained results. These results can be included in protocols, reports, and other documents to prove the condition of the inspected devices. To achieve high accuracy, sensitivity of the not allow interference with the results a post processing steps to compensate for the imperfections of the ADC are taken in Python as well.

First, every channel is sampled 500 times per second, and the average of those 500 samples is taken to reduce the quantization noise [4]. Second, the non-literariness of the ADC is compensated through the following function which is also part of the post processing Python script:

Bar_value_corrected=Bar_value_uncorrected-0.3*Bar_value,

The function is obtained through empirical evaluation by comparing the digital values with analog measurements. The uncorrected Bar_value itself is obtained through the following formula:

Bar_value_uncorrected =10bar*V_{sn}/(3V-0.1V),

Where 10bar is the measurement range of the pressure, V_{sn} is the measured voltage of the sensor *n* by the ADC, and 3V-0.1V is the voltage range of the signal coming from the pressure sensor (*Fig. 4*).

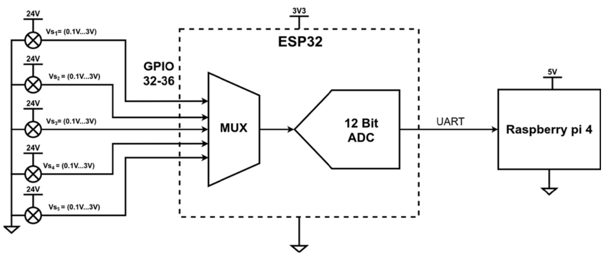

Fig. 4

In the places where the mechanical force of the brake leverage is realized, strain gauges are placed, which measure the pressure force (*Fig. 5*).

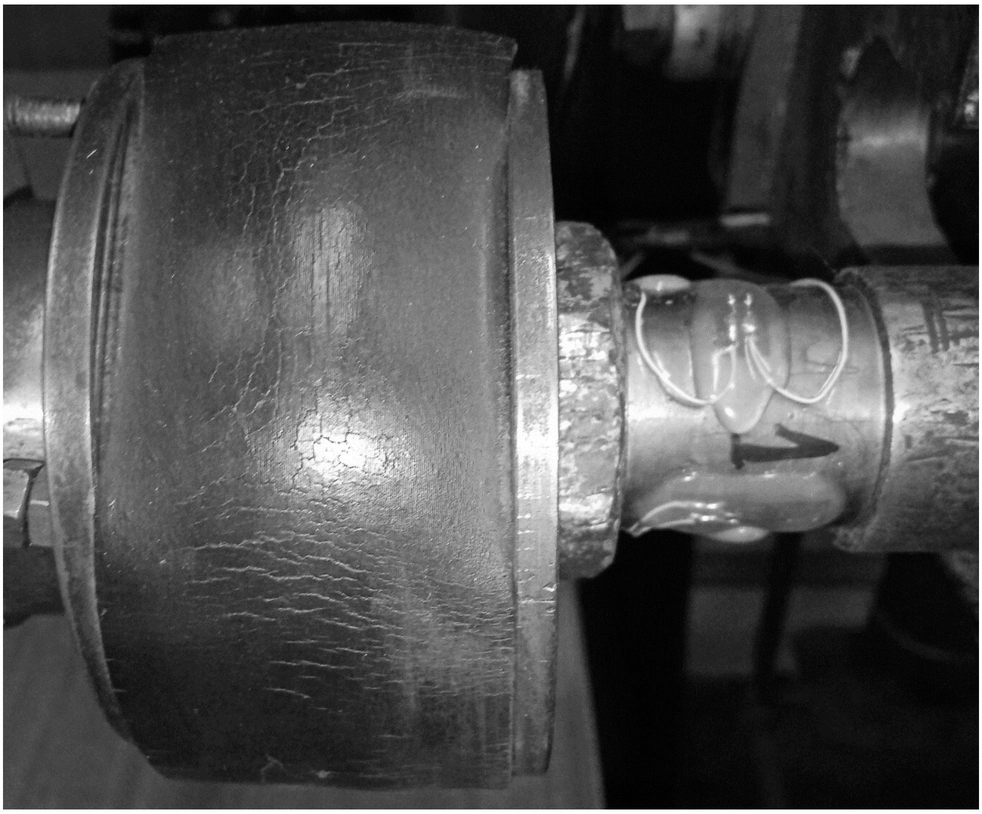

Fig. 5. The strain gauge No. 1.

The listed elements feed the signals to an analog-to-digital converter (ADC), which converts the signals and feeds them to a computing unit. Together with the above-mentioned elements, the electropneumatic valves are connected to the ADC, the purpose of which is to open nozzles of a certain diameter and thus simulate air gaps from the pneumatic devices with different intensity. Two of the electropneumatic valves actuate metal plates, thereby simulating brake pad wear. Their actuation is also registered and converted by the ADC.

All data digitized by the ADC are fed to the computing module, which processes them with suitable software, displays them in the form of graphs and records them. The obtained data can be applied in various documents. In *Fig. 6* is shown a functional scheme for managing, registering, viewing, recording, and printing the results of the conducted studies.

1p – 6p – sensors for measuring the air pressure in various chambers and devices: in the main pipe, in the auxiliary reservoir, in the command camera, in the brake cylinder;

1t – 2t – sensors for measuring the pressure in the leverage when the braking force is applied;

1. Analog-to-digital converter;
2. Computing unit for collecting data from individual sensors, processing, recording, and displaying them;
3. Printer for printing out ready protocols of the conducted tests.

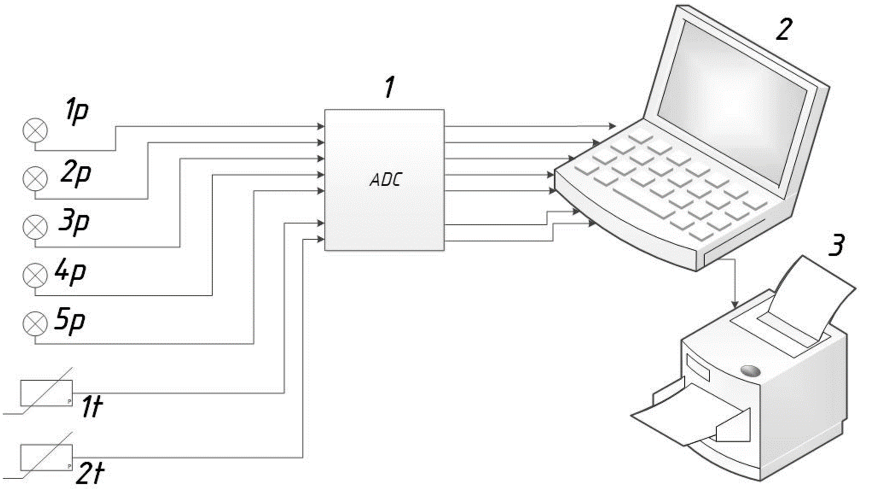

Fig. 6. Block diagram of the registering and recording part of the bench.

Fig. 7. General look of the bench.

3. REQUIREMENTS OF REGULATORY DOCUMENTS

The requirements for automatic pneumatic braking systems for freight wagons are given in UIC leaflet 540. The more important of these are:

- Brakes must be automatic.
- For the normal operation of the automatic brakes, it must be sufficient to use compressed air that passes through a main pipe with an internal diameter of the pipes of 25 or 32 mm.
- The normal working pressure of the brakes should be 5 bar.
- The application of the working pressure must lead to the readiness for work and to the releasing of the brake.
- The activating of the brake must be carried out by reducing the pressure in the main pipe, and the releasing – by increasing it.
- The brake must not return to the ready position if the pressure in the brake cylinder is higher than 0.3 bar.
- The brake is considered fully released when the pressure in the main pipe reaches 0.15 bar lower than the normal working pressure.
- To achieve full braking, it is necessary to reduce the pressure in the main line by $1.5^{\pm 0.1}$ bar.
- The maximum pressure obtained in the brake cylinder must be $3.8^{\pm 0.1}$ bar, without being related to the stroke of the cylinder piston.
- The brake must be such that the pressure in the brake cylinder is always maintained depending on the changes in the main pipe.
- A pressure change of 0.1 bar in the main pipe should force the brake valve to cause the same change in the brake cylinder after the brake starts to work.
- For the same main pipe pressure, the brake cylinder pressure must not change by more than 0.1 bar during brake or release.
- The time to fill the brake cylinder, measured between the time when air starts to enter the cylinder and when the pressure reaches 95% of its maximum, should be between 18 and 30 seconds.
- The time to empty the brake cylinder, measured between when the air starts to escape from the brake cylinder and when the pressure reaches 0.4 bar after the driver brake valve is placed in the "running" position, should be:
  - Between 45 and 60 seconds in position G.
  - Between 15 and 20 seconds in position P.

4. EXPERIMENTAL RESULTS

The experiments were carried out on the freight car brake bench described above. The function valve with which the experiments were carried out was type KE 1 (*Fig. 8*).

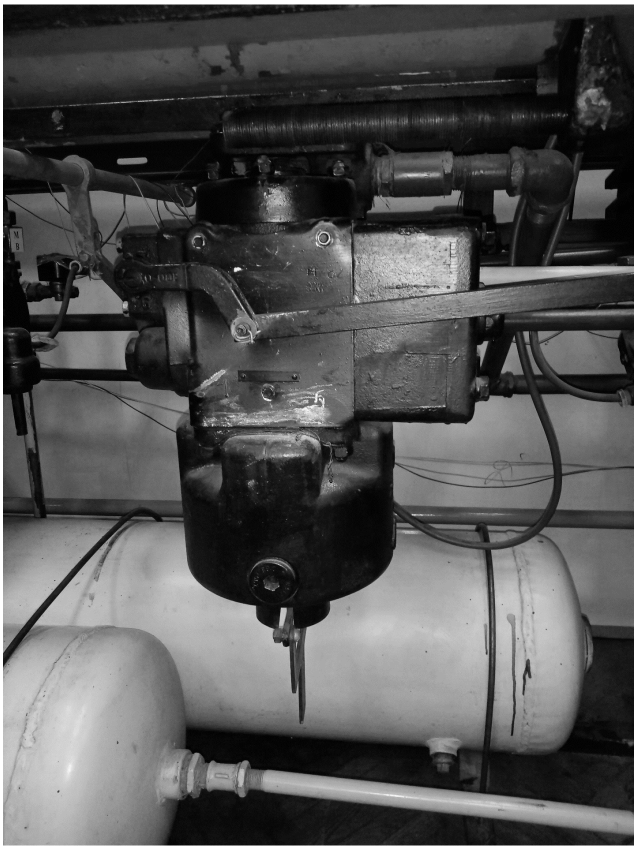

Fig. 8. Brake valve KE 1.

4.1. CHARGING OF THE BRAKE SYSTEM

A characteristic feature of automatic pneumatic brake systems (APBS) is that in order to work normally, they must first be charged with compressed air at working pressure. The working pressure is regulated by international documents (as described) and its value is 0.5 MPa (5.00 bar) [8]. The charging of the individual volumes takes place at a different speed, on the one hand, due to their different volume, and on the other hand, due to the different diameter of the pipelines and nozzles through which the compressed air passes. In the experiments carried out (*Fig. 9*) this can be clearly established. It is obvious that the time to charge the command camera is much longer than that to charge the auxiliary reservoir. Even if it is assumed that the auxiliary reservoir of the wagons in operation is of a larger volume (75 dm^3 vs. 40 dm^3 on the bench) this is a rather large difference. This must be taken into account when initially charging the brakes, as well as when releasing them using the manual brake releaser. This process is not regulated in international documents. In the regulatory documents for railway transport in the Republic of Bulgaria, this moment is reflected, and attention is drawn to this fact of the operating personnel when servicing the brakes.

Thus, during the conducted experiments, it was found that the command camera is charged in 192 seconds, and the auxiliary reservoir – in 86 seconds.

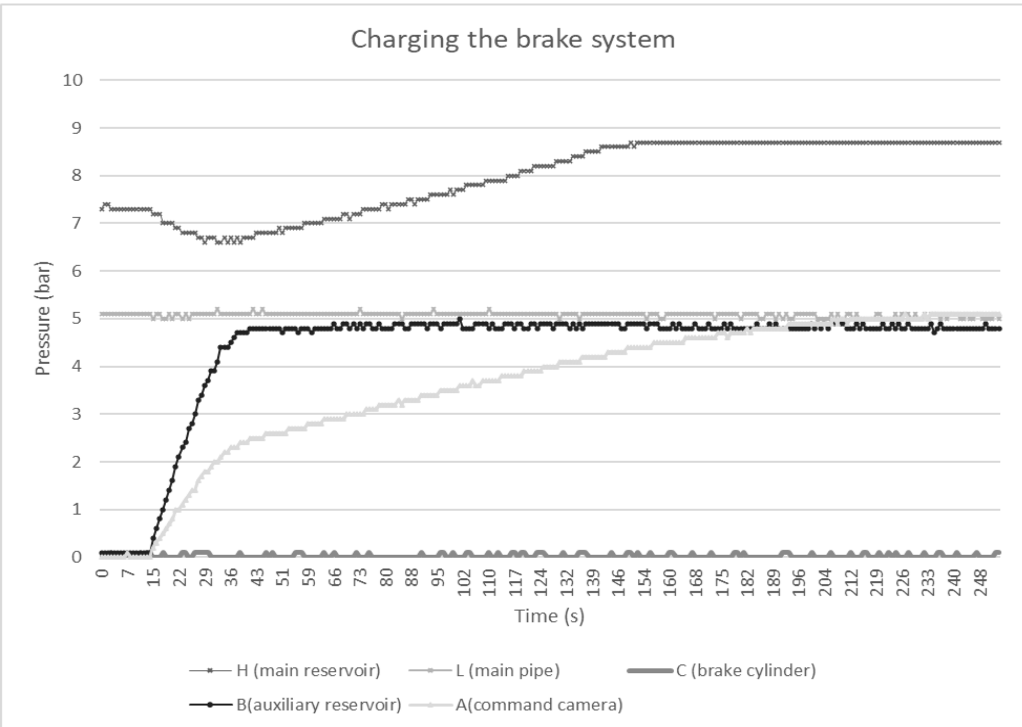

Fig. 9. Diagram of the charging process of the elements of the braking system

The obtained results show that the limiting time for successfully charging the brake system with working pressure is precisely the charging of the command camera, and this time exceeds 3 minutes. This must always be taken into account in an operational situation, especially in cases of manipulation of the manual release and other similar actions with the braking system of the wagons.

4.2. BEHAVIOR OF THE INDIVIDUAL ELEMENTS IN RELATION TO THE PRESSURE CORRESPONDENCE OF THE MAIN AIR LINE AND THE BRAKE CYLINDER

Using the brake control unit (driver’s brake valve Knorr D2), the pressure in the main pipe is reduced in stages (the first by 0.4 bar, every next by 0.15 bar). In accordance with the reduced pressure, a corresponding increase in brake cylinder pressure is observed, which corresponds to the requirements of [8]. At a pressure of 3.4 bar in the main pipe, the pressure realized in the brake cylinder is 3.5 bar. According to the regulations of [8], the maximum pressure in the brake cylinder must not exceed 3.8 bar. The pressure obtained during the experiments is lower than prescribed but does not exceed the maximum permissible value. In the braking process, compressed air from the auxiliary reservoir passes to the brake cylinder to perform the braking process, as a result of which it also decreases. The degree of reduction of this pressure is in accordance with the degree of reduction of pressure in the main pipe, and although it is inversely proportional to the pressure in the brake cylinder, it is not entirely dependent on it because of the functions of this reservoir which, in addition to its main function, must they also provide for supplementing any gaps in the brake cylinder that occurred during the braking process.

The command camera (invented by Eng. Dobrivoje Bozic) is an element that is a part of the construction of all brake valves. It is the unit that greatly expands the capabilities of the APBS by providing the brake valve with the possibility of gradually releasing the brake. According to the operating principle of this type of brake valves, the pressure in the command camera remains constant during all processes. From the experiments conducted, it was found that in reality the pressure in the command camera is not constant and depends on the pressure in the main pipe. When the braking process is carried out, the pressure in the main pipe decreases, whereby the piston in the control unit of the brake valve moves up, which causes the volume of the command camera to expand, as a result of which the pressure in it also decreases, although not to such a large extent. Thus, from *Fig. 10* it can be found that the pressure in the control camera can drop to 4.5 bar when a full brake is achieved where the pressure in the main pipe drops to 3.4 bar.

The possibility of realizing a graduated releasing can be observed in the same *Figure 9*, where again the degrees of pressure increase in the main pipe and, accordingly, the degrees of pressure reduction in the brake cylinder can be clearly noted. In accordance with an increase in pressure in the main pipe, an increase in pressure is observed in the auxiliary reservoir and in the control camera.

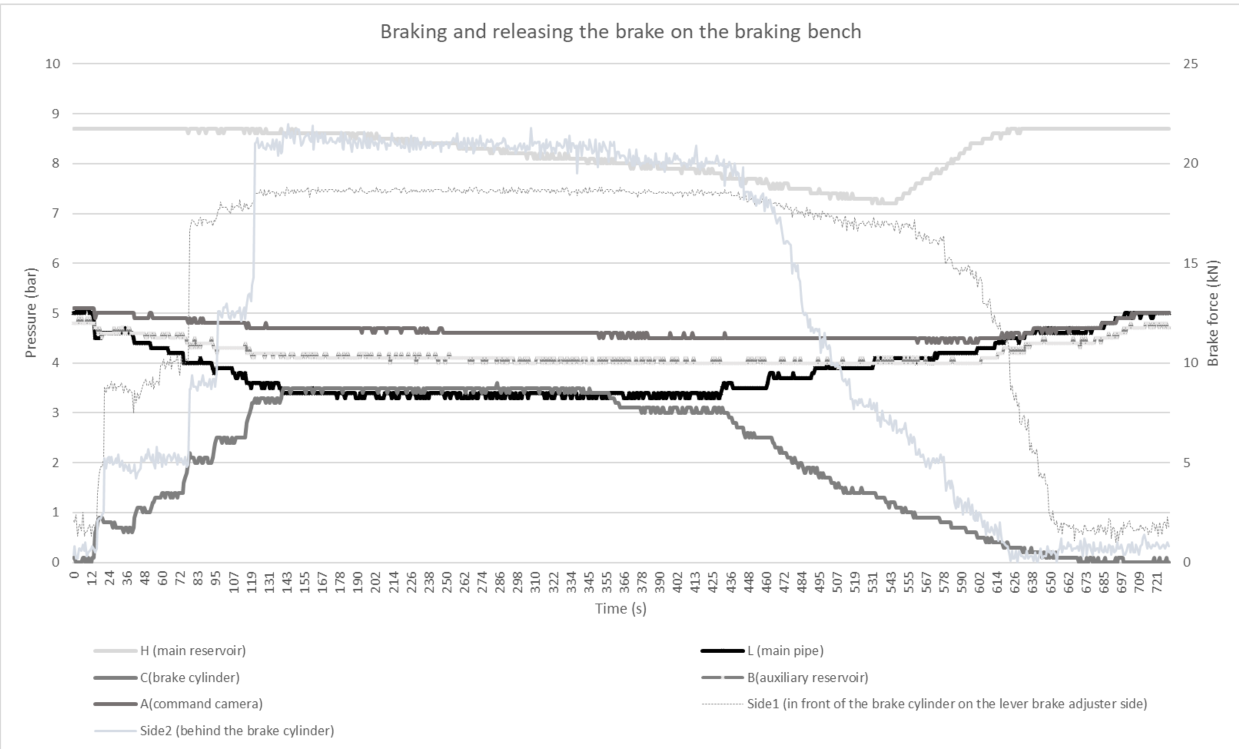

Fig. 10.

Unlike most test benches for brake systems, the bench installed in the "Train Brakes" laboratory at "Todor Kableshkov" Transport University has the ability to register and record the mechanical effort that is created by the brake cylinder and transmitted to the lever brake system. As mentioned above, this is accomplished by tensor resistors (*Fig. 3*) mounted on the longitudinal tie rods of the leverage and allows the actual mechanical action of the braking system to be determined and accounted for.

In *Fig. 10* is observed, in addition to the other parameters, the variation of the force acting in the two longitudinal rods of the lever brake system can also be observed. It can be seen that the forces in the lever brake system change in proportion to the change in pressure in the brake cylinder.

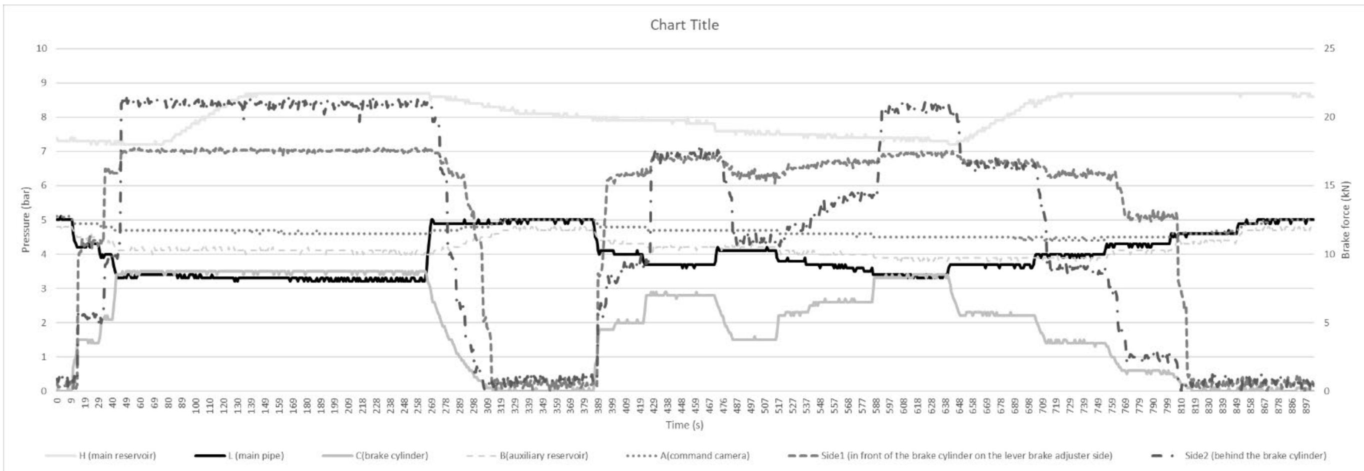

Fig. 11.

In *Fig. 11*, the change of the individual parameters of the brake system can again be observed, and the behavior of the lever brake system can also be clearly observed here. At the beginning of the braking process, the mechanical impact occurs on both sides simultaneously and the increase in forces is synchronous. When a value of 5.6 kN is reached, the force on side 2 settles to a relatively constant value, while the force on side 1 continues to increase until it reaches a value of 10.8 kN. This occurs at a pressure in the brake cylinder of 1.5 bar, in the main pipe of 4.3 bar, in the auxiliary reservoir of 4.6 bar and in the command camera of 4.9 bar. When the pressure in the main pipe is further reduced to 4.0 bar, the pressure in the brake cylinder reaches 2.1 bar, in the auxiliary reservoir 4.3 bar and in the command camera 4.8 bar. The mechanical force currently on side 1 increases to 15.9 kN and on side 2 to 9.9 kN. This is followed by a reduction of the pressure in the main pipe to 3.4 bar, during which the pressure in the brake cylinder increases to 3.5 bar, in the auxiliary reservoir it decreases to 4.1 and in the command camera to 4.7 bar. At this point, the force acting on side 1 increases to 17.5 kN, while on side 2 this increases to 21.6 kN.

This leads to the conclusion that up to a point when the pressure in the brake cylinder is lower than 3.4-3.5 bar the effort on side 1 is greater and the ratio changes from 1.9 at the lower values to 1.6 for the higher ones. After the pressure in the brake cylinder reaches and exceeds values of 3.4-3.5 bar, the force on side 1 changes only from 16.2 to 17.5 kN – 1.08 times, while the force on side 2 changes from 9 .9 to 21.5, i.e., as much as 2.17 times. This change can be explained by changing the position of the horizontal balancers of the lever brake system and the increased stroke of the piston of the brake cylinder.

With the help of the control unit (driver’s brake valve Knorr D2), the air pressure in the main pipe rises to 5.0 bar, at which point the pressure in the brake cylinder drops to 0 bar and the brake is fully released. Due to the increased pressure in the main pipe, the pressure in the auxiliary reservoir and in the command camera increases, i.e., the brake is released and fitted. The pressure exerted by the brake lever system also begins to decrease, first from side 2 and at a faster rate, and from a moment on also from side 1. The pressure reduction gradient from side 2 is greater until the end of release and only when the pressure in the brake cylinder is around 0 bar does the pressure on side 2 catch up with the pressure on side 1.

In subsequent applications with the automatic brake, applications were realized with pressure values in the main pipe initially of 4.0 bar, and shortly afterwards 3.7 bar. The pressure in the brake cylinder in the first case is 2.0 bar, and in the second – 2.8 bar. In these situations, the force on side 1 in the first case is 15.7 kN, on side 2 – 9.1 kN. Of interest are the forces from the second case, where there is an equalization of the force values on both sides – 17.1 kN.

On subsequent partial release again the pressure values on side 2 decrease significantly more than those on side 1 – 11 kN for side 2 and 15.6 kN for side 1. Another degree of partial restraint follows and again partial release, this time equalizing the pressure on the levers on both sides occurs at a pressure in the brake cylinder of 2.2 bar and 3.7 bar in the main pipe. This variation is explained by the friction in the hinges of the lever brake system. After depressurizing the brake cylinder, side 2 force again decreases faster than side 1 force.

5. CONCLUSIONS

The conducted experiments show that the bench for braking systems of freight cars can be successfully used for testing brake apparatus and for simulating braking processes and meets the most important requirements set by international and national standards for braking systems in railway transport. The experiments successfully demonstrate and visualize processes that are not described in the literature and can be used for student training and for further scientific research and development.

ACKNOWLEDGEMENTS

The authors express their immense gratitude to the management of "Todor Kableshkov" Transport University for the opportunity provided to build the system for registering and recording the work of the bench for braking systems of freight cars, as well as personally to Prof. Dts. Eng.-Math. Nencho Nenov for the invaluable assistance and help in the implementation of the project.

REFERENCES

[1] Directive (EU) 2016/798 of the European parliament and of the Council of 11 May 2016 on railway safety

[2] http://www.sensormaticltd.com/

[3] https://docs.espressif.com/projects/esp-idf/en/latest/esp32/api-reference/peripherals/adc.html

[4] https://www.espressif.com/sites/default/files/documentation/esp32_datasheet_en.pdf

[5] https://www.ni.com/National Instruments, Specifications USB-6009.

[6] KNORR-BREMSE Handbook, 1995.

[7] Nikolov, V., Nenov, N., Yosifova, D., Electronic Sensor System for Research and Diagnostics of the Train Braking System, 44th International Spring Seminar on Electronic Technology ISSE 2021.

[8] UIC code 540.

[9] Тонев, С., Основи на теорията, изчисленията и експлоатацията на подвижния железопътен състав, С., ВВТУ „Тодор Каблешков“, 1993.

Technical condition of railway vehicles as a safety factor in traffic

Marija Vukšić Popović[1*], Jovan Tanasković[2], Ivan Krišan[3]

[1] Department School of Railroad Transport, Academy of Technical and Art Applied Studies Belgrade, Belgrade (Serbia)
[2] Department of Rail Vehicles, Faculty of Mechanical Engineering, University of Belgrade, Belgrade (Serbia)
[3] Joint Stock Company for Freight Railway Transport “Serbia Cargo” Belgrade, Belgrade (Serbia)

Abstract. The railway vehicles in operation must have all subsystems functional and effective, especially brake, running gear, buffing and draw gear, suspension, etc. Any irregularities in the railway system (vehicles, tracks, signals, management, etc.) can affect transport safety. In this paper, only the influence of the vehicle's condition on railway transport safety was considered. Irregularities of railway vehicles can be observed at function failure, noticed in operation, or viewed in inspection performed by railway staff. In cases of accident or incident, the failure of the vehicle is stated in the investigation report. In operation or inspections, the failure of vehicles is stated by railway staff on labels and in workshops on measuring lists. Analysis of accidents and incidents caused by the technical condition of railway vehicles was done according to data from railway undertaker "Serbia Cargo". Analysis of irregularities was done according to data from inspections of freight railway vehicles. Analysis shows that irregularities in railway vehicles affect only some types of accidents and incidents.

Keywords: Railway vehicles, Traffic safety, Technical condition

1. INTRODUCTION

There are number of significant elements that influence safety of railway transport, so the indicators are defined that characterize traffic safety. One of these indicators are numbers of accidents and incidents. The number and type of accidents and incidents expressed by number or relatively to running kilometres and tonne of goods or number of passengers can be use as indicators of railway transport safety.

It is possible to determine traffic safety and the risk of accidents and incidents in railway traffic based on the safety indicators. By determining the main causes of train accidents and incidents, appropriate preventive measures can be proposed, and railway traffic safety can be increased. One of the causes of accidents and incidents in railway traffic is the technical condition of railway vehicles, and in this paper, only this influence on railway traffic safety was considered.

An accident is an unwanted or unplanned sudden event or a specific series of such events with harmful consequences, while an incident negatively affects traffic safety [1]. Incidents in railway traffic are avoided collisions of a train with rail vehicles or with obstacles within the clearance gauge, passing through the signals, broken rail, wheel or axle, track deformation, train brakes apart and others, and they must be investigated as well as accidents [1].

2. SAFETY INDICATORS IN RAILWAY TRAFFIC

Railway safety includes the conditions met by the railway system and railway workers, as well as other conditions relevant to the achievement of safe and undisturbed railway traffic [2]. The rulebook on common safety indicators in railway traffic [3] defines special indicators - Common Safety Indicators (CSI) for the assessment of safety levels in railway traffic. CSI relating to accidents are different types of accidents such as collisions of a train with rail vehicles or with obstacles within the clearance gauge, derailment of the train, level crossing accidents, accidents to persons involving rolling stock in motion, fires in rolling stock and others [3]. CSI can also be presented as the number of persons seriously injured and killed by a type of accident.

Common Safety Indicators (CSI) are expressed in total or relative numbers [3], where the relative CSI is the total number per train-kilometres. To compare the safety of different railway undertakers, only a comparison of the same indicators by total or relative number can be made. To establish a framework for railway safety in European Union Directive 2004/49/EC on railway safety was first adopted. In addition to the harmonisation of the content of safety rules, the safety certification and the investigation of accidents the bodies and procedures that ensure safety in the member states are harmonized through the definition of responsibilities, the principle of certification of all elements of safety and the establishment of a national safety body, as well as the accident investigation body. Directive 2016/798 [4] developing common safety targets (CST) and common safety methods (CSM) to gradually remove the need for national rules. In the Republic of Serbia, the national body for railway traffic safety is the Directorate for Railways. The accident investigation authority is the Traffic Accident Investigation Center (CINS) established by the Law on accident investigations for aviation, railways, and waterborne transport [5].

Common Safety Indicators (CSI) for accidents are the total and relative number of significant accidents, as well as the total and relative number of seriously injured and fatally injured persons by type of accident [3]. The safety of railway traffic in the last 15 years is different due to changes in safety indicators, conditions in operation and regulations. With the restructuration of national railway undertaker "Serbian Railways" in 2015, three new companies were established:

- "Infrastructure of the Serbian Railways", the company for railway infrastructure management.
- "Serbia Cargo", the company for railway transport of goods and

*Corresponding author: Marija Vukšić Popović, Zdravka Čelara 14, Belgrade, Serbia, marija.vuksic.popovic@vzs.edu.rs

- "Serbia Train", the company for railway transport of passengers.

The average number of accidents and incidents at national undertaker "Serbian Railways" from 2007 to 2011 [6] that includes cases for passenger and freight trains was 558.2 per year (Table 1), while the average number for freight railway transport of "Serbia Cargo" from 2018 to 2021 was almost half (248.8). The reasons for the difference in transport safety was that "Serbian Railways" performed both passenger and freight traffic and recorded all accidents and incidents on the Serbian public railway network. The total number of accidents and incidents on the entire public railway network of Serbia is higher than shown for "Serbia Cargo" because it includes other operators. In addition, the freight traffic of "Serbian Railways" from 2007 to 2011 was more than 30% higher than the traffic of "Serbia Cargo" in the last few years.

Table 1: Transport safety on the railway in Serbia

Year	Total number of accidents and incidents	Total number of accidents	Transport (milion tonne-kilometre)	Relative number of accidents (per milion tonne-kilometre)
"Serbian Railways"				
2007	653	158	8372	0.019
2008	541	105	8197	0.013
2009	528	112	5802	0.019
2010	574	161	6753	0.024
2011	495	130	6781	0.019
Average	**558.2**	**133.2**	**7181**	**0.019**
"Serbia Cargo"				
2016	213	119	4993	0.024
2017	392	170	5622	0.030
2018	285	161	5202	0.031
2019	244	149	4753	0.031
2020	177	109	4639	0.023
2021	182	119	4652	0.026
Average	**248.8**	**137.8**	**4977**	**0.028**

Today, more than 15 undertakers transport goods on Serbian railways. There was a decrease in the share of transportation since 2018 of the railway undertaker in the state ownership "Serbia Cargo" in favour of private undertakers. Namely, the share of private undertakers on the market of total transported goods on Serbian railways increased from 5.9% in 2018 to 24.48% in 2021, compared in tonne-kilometre [7].

The total number of accidents however did not change in more than 15 years with an average of approximately 135 cases of accidents per year. Although the total (248.8) and relative number (0,053) of accidents and incidents at "Serbia Cargo" in the last few years were significantly lower (55% for the total and 32% for the relative number), the number of the accident has not decrease. The relative number of accidents increase from 0.019 to 0.028 (Fig. 1). In fact, the share of accidents in total number of accidents and incidents increased by 58%, since it was 24% until 2011 and in the last few years was an average 57%.

3. IMPACT OF TECHNICAL CONDITION ON ACCIDENTS AND INCIDENTS

The railway vehicles in operation must have all subsystems and systems effective, especially brakes. wheelset, running gear, etc, that can affect traffic safety. The vehicle's condition can be observed through regular inspections. The irregularity of vehicle subsystems was noted in regular inspections, at failures and in workshops by railway workers. Analysis of the technical condition of railway vehicles on railway transport safety was made based on the Statistical reports on accidents and incidents at "Serbia Cargo" for 2017 [8], 2018 [9], 2019 [10], 2020 [11], and 2021 [12]. Reports show that cases of technical condition of railway vehicles leading to accidents and incidents vary from 9 to 18 cases per year for locomotives, and 19 to 43 for wagons (Fig. 3). The technical condition of locomotives on average leads to 13.8 cases of accidents or incidents per year, while the technical condition of wagons leads to almost double number of accidents or incidents (28.2).

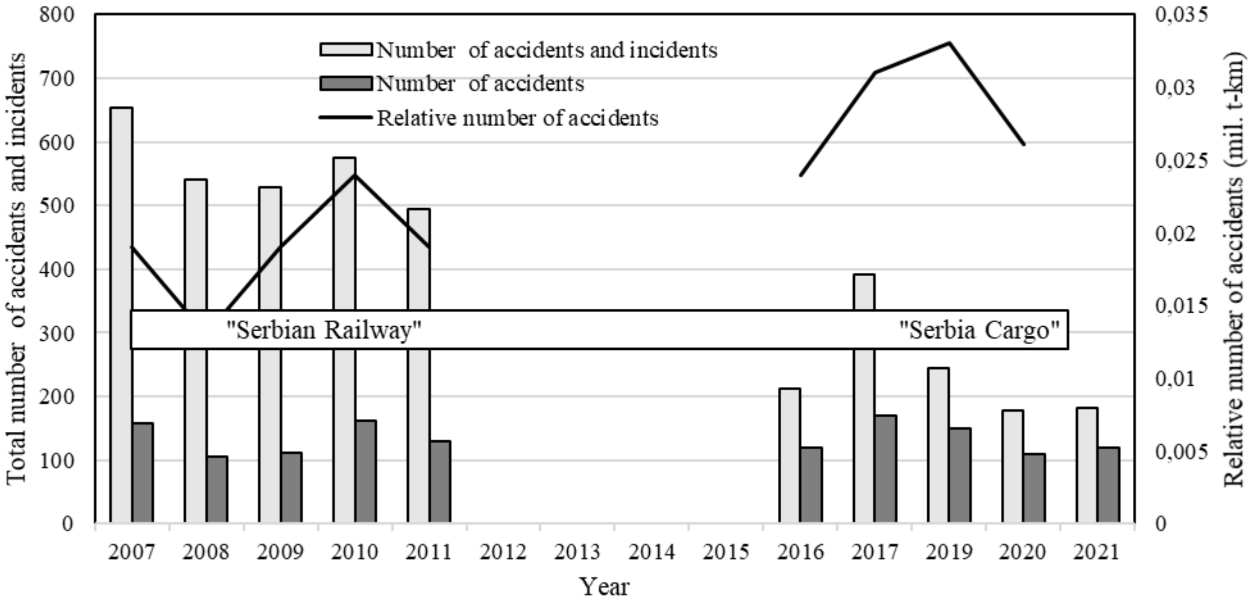

Figure 1: Total and relative railway transport safety

Besides technical conditions of railway vehicles, the origin of accidents or incidents can be technical conditions of tracks, telecommunication, control and signalling devices and power supply systems. Negligence of workers, passengers and other persons can also cause accidents or incidents, as well as unforeseeable circumstances, such as extreme weather, an earthquake etc. Origin of accidents and incidents at "Serbia Cargo" from 2017 to 2021 where irregularities of locomotives and wagons in 17% cases, irregularities of tracks, telecommunication, control and signalling devices and power supply systems in 24% cases (Fig. 4).

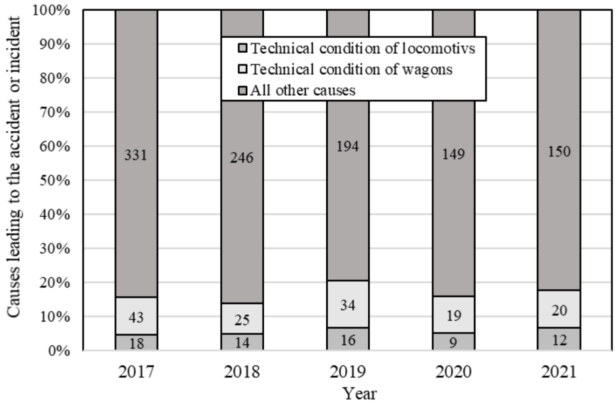

Figure 3: Technical condition of railway vehicles leading to the accident or incident

In 59% of cases, the origin was the negligence of workers, passengers and other persons and unforeseeable circumstances. Irregularities of locomotives and wagons at "Serbia Cargo" are the origin of accidents and incidents in 40.4% of all accidents and incidents caused by technical irregularities.

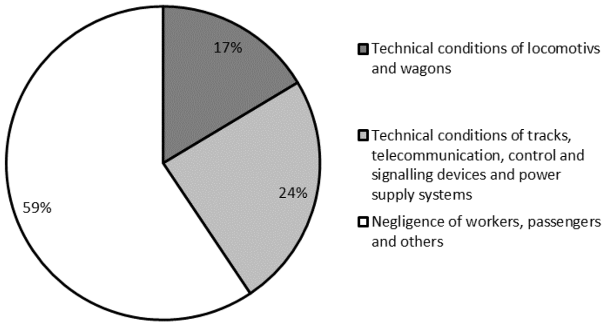

Figure 4: Average causes of accidents and incidents at "Serbia Cargo" from 2017 to 2021

The most frequent type of accident caused by the technical condition of railway vehicles at "Serbia Cargo" in the last few years were derailments of trains and fire, with an average of 15% of all accidents and incidents (Fig. 5, 6). The most frequent type of incident was train breaks apart, with an average of 56% of all accidents and incidents (Fig. 5, 6).

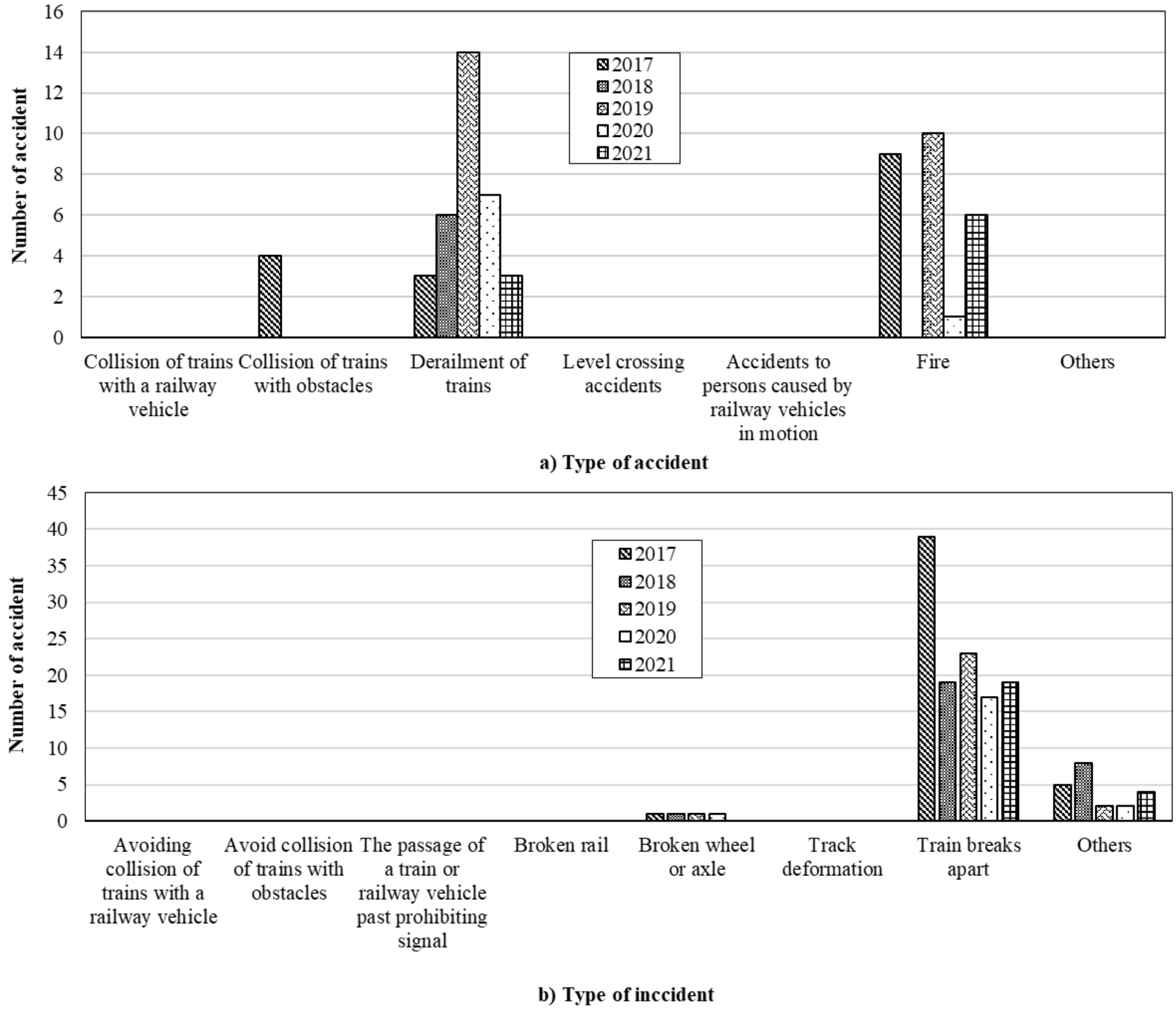

Figure 5: Accidents and incidents caused by the technical condition of the railway vehicles at "Serbia Cargo"

From 2017 to 2021 technical irregularities were the origin of accidents in 32% of cases and incidents in 68%. On average, in the analysed 5-year period, it has been 4 cases of collision of trains with obstacles, 33 cases of derailment, 31 cases of fire - a total of 68 cases of accidents caused by irregularity on railway vehicles. In the same period, incidents caused by irregularity on railway vehicles were 4 cases of broken wheels or axles, 117 cases of train breaks apart and 21 cases of other incidents - a total of 142 cases of incidents. The most frequent are train breaks apart with more than 23 breaks per year.

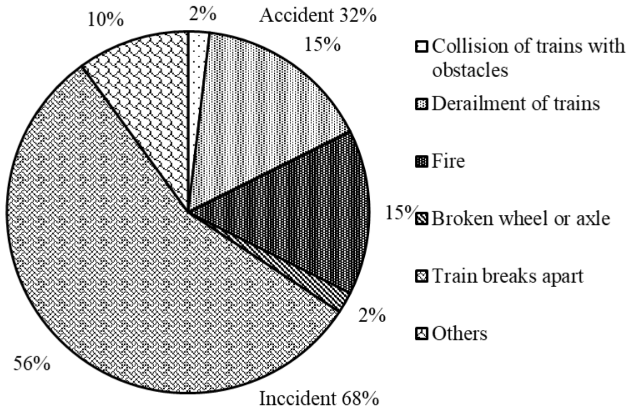

Figure 6: Accidents and incidents caused by the technical condition of the railway vehicles at "Serbia Cargo" from 2017 to 2021

In the reports on accidents and incidents at "Serbia Cargo", in the case of a derailment of railway vehicles technical irregularities of vehicles were stated as an origin, but it was usually the poor condition of the public railway network. The technical condition of the railway vehicles has not once caused accidents such as a collision of a train with a railway vehicle or level crossing accidents or accidents to persons caused by rolling stock in motion (Fig. 5a). In addition, the technical condition of the railway vehicles has not caused accidents such as an avoided collision of trains with a railway vehicle or with obstacles, the passage of a train or railway vehicle past a signal prohibiting further driving (Fig. 5b).

The frequency of accidents and incidents caused by the technical condition of the railway vehicles has stochastic distribution from 2017 to 2021, due to changes in operational conditions (Fig. 5). Although certain types of accidents and incidents may vary through the years, there is no continuous increase that indicates serious problems.

The percentage of accidents and incidents caused by the technical condition (malfunctions) of railway vehicles is only 17%. This shows that the influence of the technical condition of railway vehicles on the occurrence of accidents and incidents is small and that other conditions leading to a large number of accidents and incidents in railway transport are crucial.

4. TECHNICAL CONDITION OF RAILWAY VEHICLES

Irregularities of freight wagons are classified by functional subsystems (Fig. 7) according to their construction and function:

- Running gear (wheelset and axel box),
- Suspension,
- Brake (including hand brake),
- Bogie frame (without running gear, suspension and brake),
- Car body and underframe,
- Buffers and draw gear (including screw coupling).

Irregularities concerning loads and intermodal loading units are not discussed in this analysis.

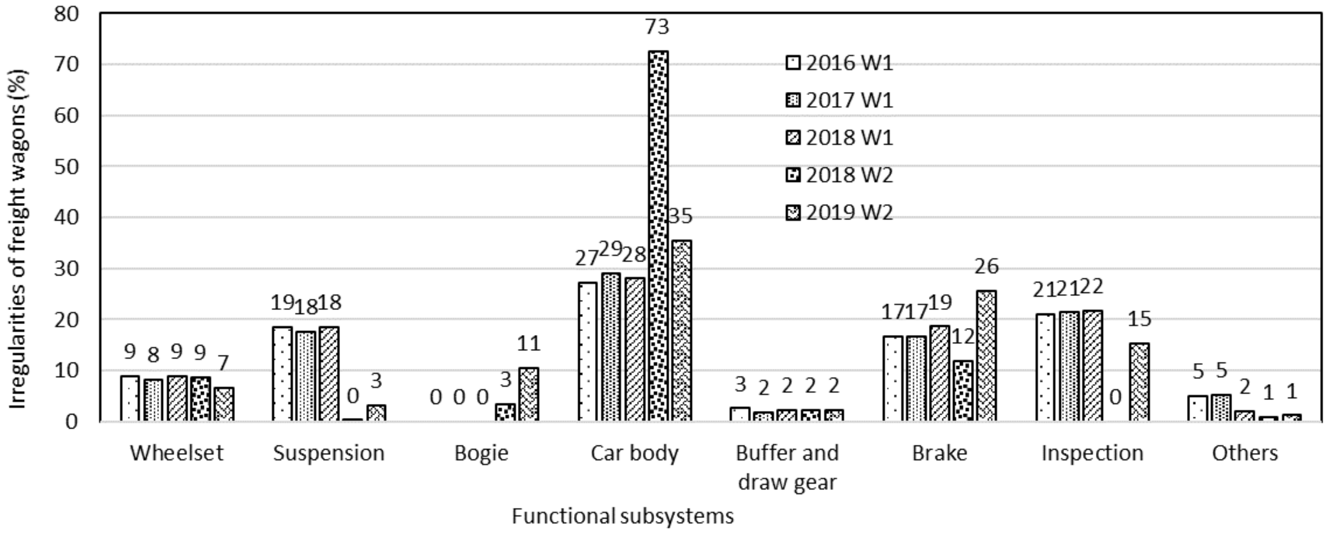

Figure 7: The frequency of irregularities in freight wagons from 2016 to 2019

Data on irregularities of freight wagons at the workshop in Niš show that 2261 wagons were taken out of operation due to malfunctions, defects and failure from 2016 to 2018. Wagons were sent for maintenance at the workshop in Niš for large-scale emergency maintenance, while 306 wagons had minor repairs (without excluding from train). The distribution of malfunctions by functional subsystems of freight wagons is presented in Fig. 7 and 8. Data from two workshops for railway vehicles were processed [13]: one in Niš from 2016 to 2018 (mark W1 on Fig. 7) and another in Belgrade from 2018 to 2019 (mark W2).

From 2016 to 2019, it was no significant deviations in number of wagon irregularities, except for the car body in 2018 in workshop 2, when malfunctions doubled. This can be a consequence of major accidents or incidents, or other repairs carried out on wagons.

Regardless of the relatively small impact of technical irregularity of railway vehicles on transport safety, it is necessary to:

- Monitor and inspect railway vehicles for indicators of failure,
- Carry out detailed analyses of the reasons for the irregularity of railway vehicles and propose measures for their reduction,
- Implement procedures and measures for reduction.

Serious accidents are the result of the superposition of several unfavourable factors or failures. For example, if trains brake apart, automatic braking is applied. If there are vehicles with malfunctioning or disconnected brakes, the parts of the uncoupled train may come to a slower stop and pass through a closed signal or road crossing. This can result in human casualties or greater expenses. Therefore, the relatively low severity of accidents and incident consequences in everyday practice should not be a reason not to take all measures to improve the technical condition of railway vehicles.

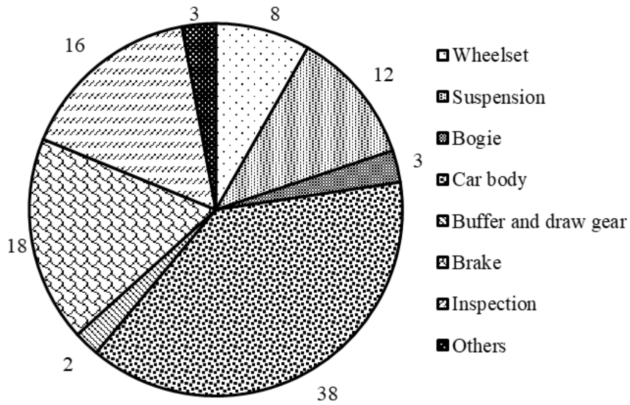

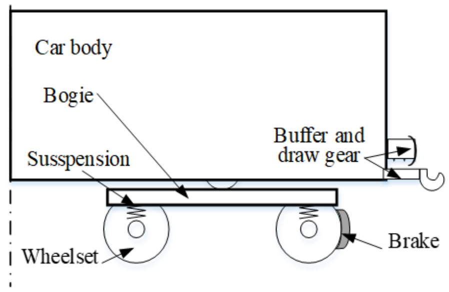

Figure 8: Average irregularities on freight wagons from 2016 to 2019

5. CONCLUSIONS

The total number of accidents on the public railway network in 2021 is approx. 15% higher than in the previous calendar year. Causes that have a great influence on this situation were unforeseeable circumstances as well as the poor condition of the public railway network, which is a consequence of long-term insufficient and inadequate investment maintenance resources and carelessness or negligence of drivers of road vehicles. Increased influence of the vehicle's condition on railway transport safety were only frequent fires in railway vehicles due to the age of the rolling stock, wear and tear of certain components, material fatigue and inadequate maintenance [14].

Regarding the precursors of accidents, in 2021 it increased by more than 300% compared to the previous calendar year, especially the number of passing trains past a signal prohibiting further driving and crossing junctions. Personal failures of railway drivers and executive staff were determined as the main reasons, which raises issues of adequacy knowledge of regulations and concentration during work. It is also noted an increase in cases of rail fracture or track deformation, which is a consequence of the general condition and deterioration of the network of public railways, as well as inadequate maintenance [14].

ACKNOWLEDGEMENTS

The publishing of this paper was supported by management of the railway operator "Serbia Cargo" and Ministry of Science, Technological Development and Innovation of Republic of Serbia. Project Contract 451-03-47/2023-01/200105.

REFERENCES

[1] Rulebook on research. recording. statistical monitoring and publication of data on accidents and incidents. „Official Gazette of the RS". No 4/2016. (2016)

[2] Law on Safety in Railway Traffic. "Official Gazette of the RS". No 41/18. (2018)

[3] Rulebook on common safety indicators in railway traffic. „Official Gazette of the RS". No 25/2019. (2019)

[4] Directive (EU) 2016/798 of the European Parliament and of the Council of 11 May 2016 on railway safety. Official Journal of the European Union. L 138/102. https://eur-lex.europa.eu/legal-content/EN/TXT/?uri=CELEX:02016L0798-20201023

[5] Law on accident investigations for aviation, railways and waterborne transport, "Official Gazette of the RS". No 66/15. (2015)

[6] Traffic and safety reports of rail transport on Serbian Railways in 2012, „Serbian Railways". Belgrade. (2013)

[7] The report on the regulation of the market of railway services for 2021. Directorates for railways. (2021). https://www.raildir.gov.rs/doc/izvestaji/Izvestaj%20_o_regulisanju_trzista_zeleznickih_usluga_za_2021.pdf

[8] Statistical report on accidents and incidents at „Serbia Cargo" for 2017. https://srbcargo.rs/wp-content/uploads/2020/02/STATISTI%C4%8CKI-IZVE%C5%A0TAJ-DEO-A-2017-GODINA.pdf

[9] Statistical report on accidents and incidents at „Serbia Cargo" for 2018. https://srbcargo.rs/wp-content/uploads/2020/02/STATISTI%C4%8CKI-IZVE%C5%A0TAJ-DEO-A-2018-GODINA.pdf

[10] Statistical report on accidents and incidents at „Serbia Cargo" for 2019. https://srbcargo.rs/wp-

content/uploads/2020/02/STATISTI%C4%8CKI-IZVE%C5%A0TAJ-DEO-A-2019-GODINA.pdf

[11] Statistical report on accidents and incidents at „Serbia Cargo“ for 2020. https://www.srbcargo.rs/wp-content/uploads/2021/11/Statisticki-izvestaj-deo-A-2020.godina.pdf

[12] Statistical report on accidents and incidents at „Serbia Cargo“ for 2021. https://www.srbcargo.rs/wp-content/uploads/2022/05/Statisticki-izvestaj-deo-A-2021.godina.pdf

[13] M. Vukšić Popović. "Failure analysis of draw gear and screw coupling of railway vehicles as a factor of safety and trains break risk". Ph.D. Thesis. University of Belgrade Faculty of Mechanical Engineering. (Serbia). (2021)

https://nardus.mpn.gov.rs/handle/123456789/18628

[14] The report directorates for railways on the security state in rail traffic for 2021. Directorates for railways. (2022) https://www.raildir.gov.rs/doc/izvestaji/Godisnji_izvestaj_o_bezbednosti_za_2021_godinu.pdf

Requirements of UIC standards for brake triangles of railway vehicles

Milan Bižić*, Dragan Petrović
Faculty of Mechanical and Civil Engineering in Kraljevo, University of Kragujevac, Serbia

The brake triangles are among the most important parts in the braking system of railway vehicles. Given that their quality and reliability directly affect the safety of rail traffic, the requirements for their suppliers are very rigorous. In this sense, the production of brake triangles can only be entrusted to those suppliers who are able to provide appropriate proofs of the quality. The aim of this paper is to analyse the requirements of the International Union of Railways (UIC) for the brake triangles of railway vehicles. Special attention is paid to the requirements for inspection of brake triangles, which includes specific static and dynamic tests. The results of conducted research are basis for analysing the possibility of conquest of production of brake triangles for international market.

Keywords: Railway vehicles, Braking, Brake triangle, Testing, UIC 833

1. INTRODUCTION

The role of braking is to ensure safely stopping and regulation the speed of the train during the running on the track. The quality and reliability of braking directly affects the safety and security of the railway transportation. Accordingly, all elements of the braking system must be designed and manufactured to successfully withstand all loads and conditions during operation, without failures.

The basic way for realization of the braking is by friction between the braking elements and the rotating elements of the railway vehicles. In case of the most freight wagons, the brake elements are brake shoes that act on the running surface of the wheel [1, 2]. The brake shoes are usually made of gray iron, and more recently of composite materials. The activation of the train braking causes the brake shoes to press against the running surfaces of the wheels where the friction occurs, which reduces the kinetic energy and slows the train down (Figure 1) [3, 4].

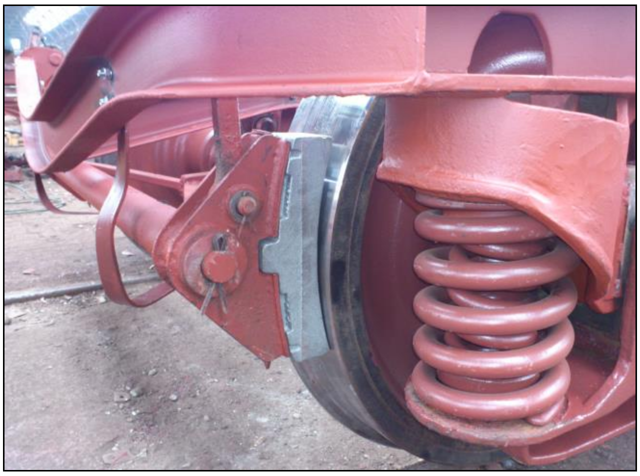

Figure 1: Brake triangle, brake shoe and wheel

The elements that provide transmission of braking force, i.e., friction between the brake shoes and running surfaces of the wheels are brake triangles (Figure 2). Given this role, brake triangles directly affect the quality of braking and therefore safety and security on the railway [5, 6]. That is why the requirements regarding their characteristics are very rigorous and they are defined in standards of International Union of Railways (UIC). These requirements must be met by every manufacturer of brake triangles for the international market.

Figure 2: Brake triangles

In accordance with the presented introductory notes, the aim of this paper is to analyze the requirements of the standard UIC 833 for the brake triangles of railway vehicles.

2. CHARACTERISTICS OF BRAKE TRIANGLES

According to the standard UIC 833, brake triangles are classified into two groups – brake triangles for nominal load F_n=60 kN and brake triangles for nominal load F_n=120 kN.

Brake triangles should be manufactured of carbon steels whose physical, geometric, chemical and mechanical characteristics must meet all the necessary requirements of ISO standards or European norms. The required Brinell hardness in relation to the tensile strength of the steel of which brake triangles are made is given in the Table 1.

The roughness of machined surfaces of brake triangles, measured as the arithmetical average variation Ra shall be within the limits as given in the Table 2.

*Corresponding author: Dositejeva 19, 36000 Kraljevo, Serbia, bizic.m@mfkv.kg.ac.rs

Table 1: Required Brinell hardness of steel for brake triangles [7]

Tensile strength [N/mm^2]	Brinell hardness [HB]
360÷440	100÷130
410÷490	115÷140
490÷590	140÷165
510÷610	145÷175

Brake triangles shall be correct throughout, including any welded areas, which must not contain any lack of fusion or reveal any defect such as lack of penetration, blowholes or inclusions. The welding operations must not have altered the characteristics of the base metal.

Table 2: Required roughness of machined surfaces of brake triangles [7]

Nature of the parts	Average variation Ra
Trunnions	3,2 μm
Parts fitted with a bush (bores or trunnions)	0,8 μm
Bores without bushes	3,2 μm

The relative positions of the functional parts of brake triangles such as trunnions, traction head and holes for the traction pin, must meet requirements given in the Fig. 3 and Table 3.

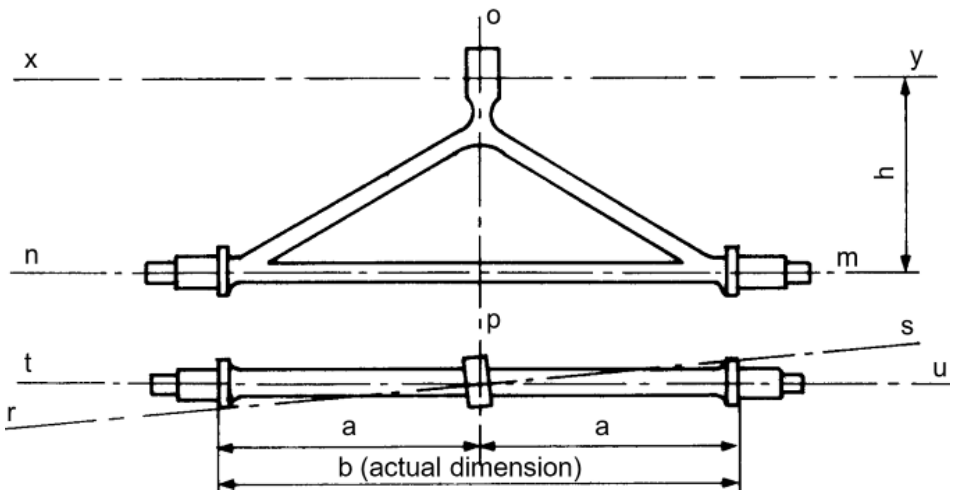

Figure 3: Relative positions of functional parts of brake triangles [7]

Table 3: Requirements for relative positions of functional parts of brake triangles [7]

Relative positions of functional parts	Variation
Parallelism of the actual centre lines of the trunnions and of the bore of the traction head (xy and mn)	≤ 5 ‰
Parallelism of the actual centre line of the hole in the traction head and of the median plane containing the actual centre line of the trunnions (tu and rs)	≤ 10 ‰
Perpendicularity of the longitudinal centre line of the traction head in relation to the actual centre line of the bore (op and xy)	≤ 3 ‰
Symmetry of the surfaces of the shoulders of the trunnions in relation to the plane containing the longitudinal centre line of the traction head, measurements *a*	$b/2 – a \leq 2$ mm

The values of loads for brake triangles testing are given in Table 4. During the action of the nominal load F_n applied in accordance with the diagram shown in Fig. 4, the height *h* of the brake triangle must not have an elastic deflection greater than 2 mm.

Table 4: Values of loads for brake triangles testing

Type	"Zero" load	Nominal load F_n	Test load F_{ep}	Load variations during fatigue test
Triangle 60 kN	5 kN	60 kN	90 kN	10 kN to 60 kN
Triangle 120 kN	10 kN	120 kN	180 kN	20 kN to 120 kN

After termination of force action, the height h must not have a permanent deflection greater than 0.1 mm. Also, there must not be any other permanent deformations that can affect the other parts of the brake triangle.

During the action of test load F_{ep} (equal to 9/6 of the nominal load F_n), applied in accordance with the diagram shown in Fig. 4, the height *h* of the brake triangle must not have an elastic deflection greater than 3 mm. After termination of force action, the same height must not have a permanent deflection greater than 0.5 mm. After testing, no defects must be present.

Furthermore, the brake triangles must withstand 10^6 cycles of tensile loads applied at a frequency between 2 Hz and 16 Hz, without any apparent defects. These loads must vary cyclically within the limits specified in Table 4.

The trunnions must have a surface hardness in the treated areas of at least 55 HRc and for a depth of at least 1 mm. The surface hardness, obtained at any point of the bushes or the bores, must be between 58 and 62 HRc. The depth of the hardened part must be constant and between 1 mm and 1,5 mm.

Each brake triangle should have embossed marks such as: manufacturer's mark, the last two figures of the year of manufacture, the mark of ownership of the purchasing Railway, etc.

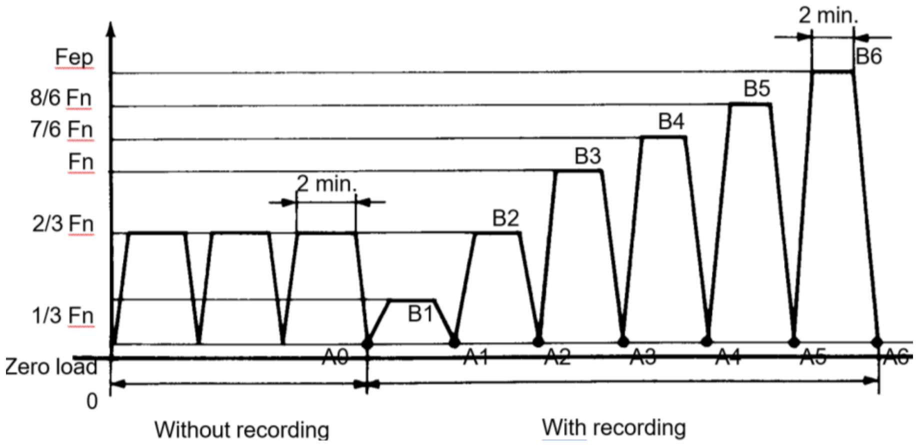

Figure 4: Load-time diagram for brake triangles testing

3. MANUFACTURE OF BRAKE TRIANGLES

The manufacture of brake triangles can only be entrusted to suppliers who have the appropriate approvals of the purchasing Railways. Each brake triangle prototype and conditions of its manufacture, must be approved by the purchasing Railway. In case of any changes in the design and characteristics of the brake triangles, as well as in their production process, the aforementioned approval procedure must be repeated.

Table 5: Checks and tests of brake triangles [7]

Nature of the tests and checks	**Type of inspection**	**Proportion of the checks and tests**					
		≤ 50	**51/150**	**151/500**	**501/1200**	**1201/3200**	**> 3200**
Appearance and dimensions of the component parts and finished items	Approval and Acceptance	As decided by the representative of the Railway					
Hardness tests on forged parts[a] and on finished parts[b]	Approval and Acceptance	2	4	6	8	10	12
Deflection tests on forged parts	Acceptance	As decided by the representative of the Railway, with a maximum of 2 per batch of 10 t					
Inspection of welds	Approval and Acceptance	As decided by the representative of the Railway. However, the approval must be renewed at least every twelve (12) months					
Static deflection test[c]	Approval	8 parts					
	Acceptance	1	2	3	4	5	6
Endurance test under pulsating tensile loads[c]	Approval	2 parts					

a. Before submission for acceptance, the supplier shall have checked, under his own responsibility, the Brinell hardness on at least 10% of the forged parts.
b. Before submission for acceptance, the supplier shall have checked, under his own responsibility, the Rockwell hardness on at least 5% of the trunnions.
c. The parts intended for these tests shall not have been submitted to a tensile force greater than 2/3 of the nominal load F_n.

The forging operations in manufacturing of brake triangles shall be carried out at temperatures which ensure that no change in the characteristics can result.

The welding process in the production of brake triangles is left to the choice of the manufacturer. However, automatic welding processes must be approved by the purchasing Railway and cannot be changed without its approval. Manual welding procedures can only be performed by welders whose ability has been previously confirmed. In both cases, the issued authorizations are valid for a maximum of 12 months.

The heat treatment operations should be performed in such a way as to guarantee uniformity of treatment at all points on the same part and for all parts of the same furnace load. The furnace or quench bath temperatures should be checked with properly calibrated recording pyrometers.

Retouching and repair are strictly prohibited without the prior consent of the purchasing Railway. Removal of surface defects by grinding, chiselling, filing or any other approved process may be permitted, provided dimensional tolerances are met.

4. INSPECTION OF BRAKE TRIANGLES

The authorized representative of the purchasing Railway performs an appropriate inspection of the manufacture of brake triangles. He can carry out any checks he deems necessary to prove that all production conditions have been met. Additionally, he can be present at welding operations and at the individual tensile tests carried out by the manufacturer, and be provided with the charts of the recording pyrometers. Also, he must be informed of any change in the manufacturing process of brake triangles.

As for the acceptance inspection of authorized representative of purchasing Railway, a batch of parts intended for the acceptance procedure must be formed. It consists of at least 10 brake triangles (type to be accepted), manufactured by the normal production methods. These brake triangles intended for the acceptance procedure must not be exposed to a load greater than 2/3 of the nominal load F_n (Table 4, Fig. 4).

The brake triangles must be subjected to checks and tests as given in the Table 5. They are performed either at the time of acceptance during submission or during manufacture.

The brake triangles intended for the endurance test under pulsating tension load must not be selected from those already subjected to the static deformation test. The tests prescribed by the acceptance program must be carried out by a laboratory approved by the purchasing Railway.

The brake triangles must be submitted for acceptance in the delivery condition, before any protective treatment. Previously, they must be subjected to static deflection tests in accordance to the details specified in Chapter 2. These tests are carried out on the number of samples which is defined in the Table 5.

4.1. Static tests of brake triangles under tension load

Static testing of brake triangles is performed on the test stand with horizontal or vertical movement, which must provide maintaining a constant load for at least 2 minutes and measuring this load with error less than 1%. The deflections must be measured by dial gauges with graduation of 0.01 mm. They must be rigidly fixed and their probes must make contact at right angles with smooth surfaces on the triangle to be tested.

The brake triangles can be tested individually or in pairs of two. The connections between the elements to be tested and the test stand must be in accordance with one of the arrangements shown in Figs. 5-8.

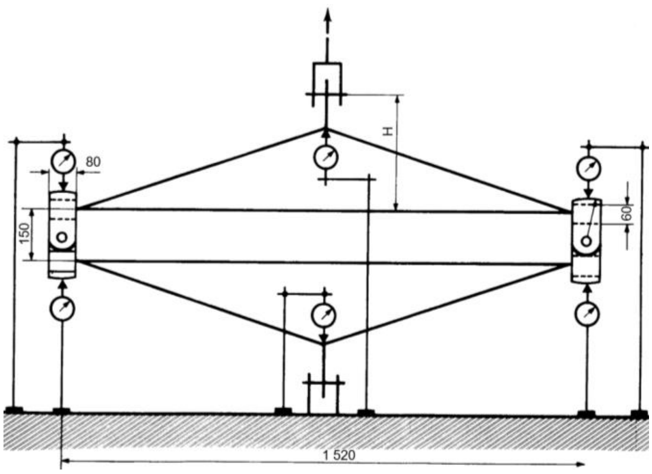

Figure 5: Connections between brake triangles to be tested and test stand for static tests – variant 1 [7]

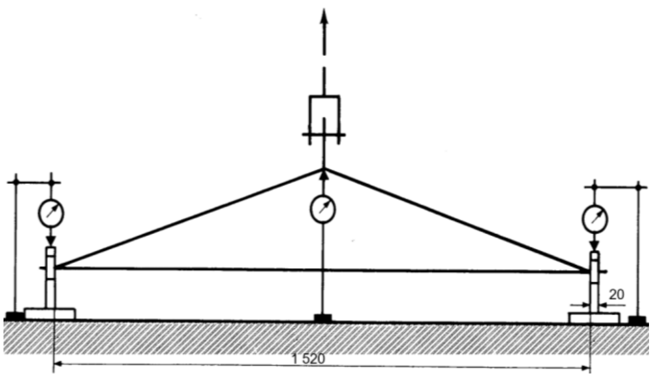

Figure 6: Connections between brake triangles to be tested and test stand for static tests – variant 2 [7]

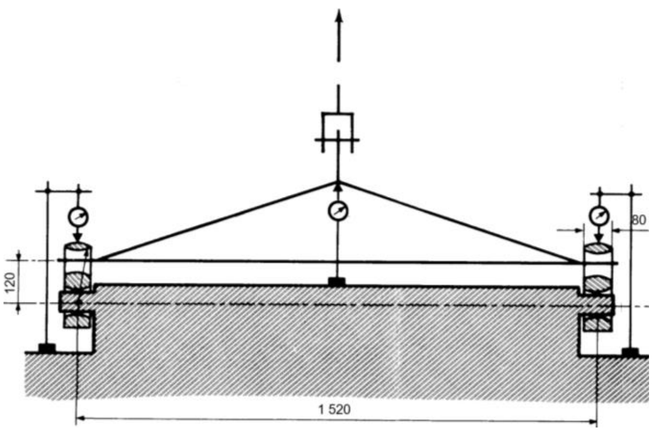

Figure 7: Connections between brake triangles to be tested and test stand for static tests – variant 3 [7]

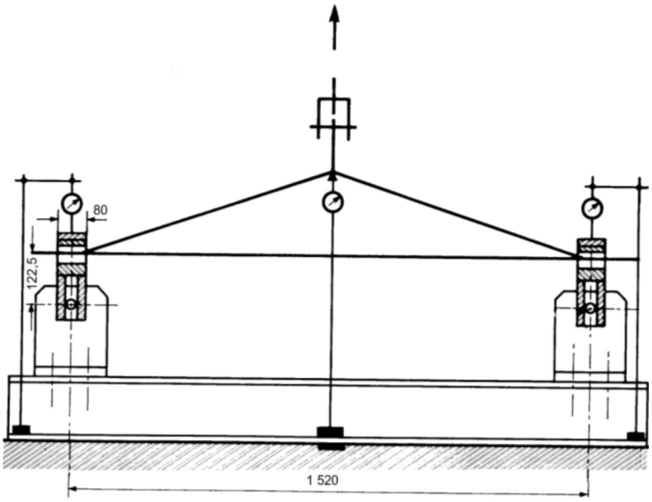

Figure 8: Connections between brake triangles to be tested and test stand for static tests – variant 4 [7]

Before conducting the static tests, three consecutive preliminary loads of 2 min duration and equivalent to 2/3 of the normal load F_n specified in Table 4 must be applied. After that, the force returns to the "zero" load which is also listed in Table 4. These procedures are performed without recording deflection values.

After that, loads equal to 1/3 F_n, 2/3 F_n, F_n, 7/6 F_n, 8/6 F_n and 9/6 F_n are then applied, in turn, for two minutes each. The application of each new load is preceded by a return to the load that must not be less than the mentioned "zero" load specified in Table 4. The deflection values reading from dial gauges is performed for each of the "zero" loads and under each of the above mentioned loads, i.e. in the points A0, B1, A1, B2, A2, B3, A3, B4, A4, B5, A5, B6 and A6 (Fig. 4).

During the described test, the following deflections should be measured:

- Elastic deflection under the nominal load F_n (equal to the difference in measurement results in points B3 and A3);
- Permanent deflection under the nominal load F_n (equal to the difference in measurement results in points A3 and A0);
- Elastic deflection under the test load F_{ep} (equal to the difference in measurement results in points B6 and A6);
- Permanent deflection under the test load F_{ep} (equal to the difference in measurement results in points A6 and A0);
- Any permanent deflection, other than that obtained in the direction in which tension was applied (determined by comparing the measurements performed to the nearest 0.1 mm by reference to a surface-plate, before and after the tensile test).

4.2. Fatigue tests under pulsating tension load

The fatigue test under pulsating tension must be carried out on a tensile test stand with vertical movement, capable of applying loads varying within the limits specified in Table 4, at a frequency in range of 2 and 16 Hz. The test stand must be equipped with devices able of counting the number of cycles and registering the values of the loads applied.

The brake triangles to be tested must be mounted in the test stand by one of the assemblies shown in Figs. 7 and 8.

4.3. Approval inspection of brake triangles

Approval is refused if any of the results of static and fatigue tests are not in accordance with the prescribed conditions.

4.4. Acceptance inspection of brake triangles

Any defect in appearance or any difference in dimensions affecting their satisfactory use will cause the brake triangles to be rejected. In addition, any result inconsistent with one of the other tests will result in the rejection of the corresponding batch of brake triangles.

5. DELIVERY AND WARRANTY FOR BRAKE TRIANGLES

5.1. Delivery of brake triangles

After the acceptance inspection, the brake triangles must be protected against corrosion in accordance with the prescribed procedure agreed with purchasing Railway. After degreasing and brushing, the rough surfaces of the brake triangles must be protected with a layer of primer paint, the composition of which has been approved by the purchasing Railway. In addition, machined surfaces must be coated with an anti-rust agent.

5.2. Warranty for brake triangles

The warranty for the brake triangles is two years regard to any defect that can be imputable to manufacture. This period starts from the end of the year which last two figures of which are shown on the triangles.

If the brake triangles are intended for installation on a new railway vehicle, the date of delivery of the vehicle on which they are installed will be considered as the beginning of the warranty.

Brake triangles that during the warranty period reveal defects that make them unfit for use or are likely to reduce their service life will be rejected. Before being finally rejected, defective brake triangles may, however, be subjected to a verification test by the ordering Railway and the supplier. When the verification test confirms that the defects are definitely attributable to manufacturing or inadequate corrosion protection, the defective brake triangles are finally rejected.

When more than 5% of brake triangles from the same delivery show defects leading to rejection, the purchasing Railway may reject the entire delivery.

6. CONCLUSION

The braking system has a very important function in railway traffic. Its efficiency and reliability directly affect the safety and security on the railway. One of the most important parts of the braking system of railway vehicles are brake triangles. Their role is ensuring the transfer of braking force to the brake shoes that act on the surface of the wheel and brake the vehicle.

Given that their quality and reliability directly affect the safety of rail traffic, the requirements for suppliers of brake triangles are very rigorous. That is why the production of brake triangles can only be entrusted to suppliers who are able to provide appropriate proofs of the quality.

In this paper, the requirements of the International Union of Railways (UIC) regarding the brake triangles of railway vehicles are analysed. The standard UIC 833 named "Technical specification for the supply of brake triangles" has been studied in detail. The requirements for characteristics, manufacturing, inspection, delivery and warranty of brake triangles are analysed. A special attention is devoted to the requirements for inspection of brake triangles, which includes specific static and dynamic tests.

The results of the paper can be convenient basis for further research directed toward designing a test stand and equipment for testing static and dynamic characteristics of brake triangles. Consequently, they can be suitable for analysing the possibility of conquest of production of brake triangles for international market.

The idea for further research is oriented towards the development of methods for optimizing of structural design of brake triangles [9, 10].

ACKNOWLEDGEMENTS

The authors are grateful to the Ministry of Science, Technological Development and Innovation of the Republic of Serbia for support (contract no. 451-03-47/2023-01/200108).

REFERENCES

[1] D.Petrović, V.Aleksandrov, Železnička vozila – Osnove, Fakultet za mašinstvo i građevinarstvo u Kraljevu Univerziteta u Kragujevcu, Kraljevo, (2013), (in Serbian)

[2] G. Simić, Vagoni – Konstrukcija i proračun, Mašinski fakulteta Univerziteta u Beogradu, Beograd, (2013), (in Serbian)

[3] D. Petrović, M. Bižić, Doprinos Dobrivoja S. Božića razvoju kočnica železničkih vozila, Tematski zbornik nacionalnog značaja "Dobrivoje S. Božić – izumitelj savremenog sistema kočenja voza", Fakultet za mašinstvo i građevinarstvo u Kraljevu, Kraljevo, str. 19-42, (2016), (in Serbian)

[4] M. Bižić, D. Petrović, Problemi kretanja železničkih vozila sa osvrtom na kočenje i značaj Dobrivoja Božića, Tematski zbornik nacionalnog značaja "Dobrivoje S. Božić – izumitelj savremenog sistema kočenja voza", Fakultet za mašinstvo i građevinarstvo u Kraljevu, Kraljevo, str. 159-186, (2016), (in Serbian)

[5] M. Günay, M. Erdi Korkmaz, R. Özmen, An investigation on braking systems used in railway vehicles, Engineering Science and Technology, an International Journal, Volume 23, Issue 2, pp. 421–431, (2020)

[6] V. Ravlyuk1, M. Ravliuk, V. Hrebeniuk, V. Bondarenko, Research of the calculation scheme for the brake lever transmission and construction of the load model for the brake pads of freight cars, IOP Conference Series: Materials Science and Engineering, 708, 012026, (2019)

[7] UIC 833, Technical specification for the supply of brake triangles, International Union of Railways, (2004)

[8] EN ISO 4287, Geometrical product specifications (GPS) - Surface texture: Profile method - Terms, definitions and surface texture parameters, (2014)

[9] Goran Miodragović, Marina Bošković, Radovan Bulatović, The application of metaheuristic algorithms in multi-objective optimization of engineering problems, Engineering Today, Vol. 1, No. 3, pp. 7-15, (2022)

[10] Goran Pavlović, Boris Jerman, Mile Savković, Nebojša Zdravković, Goran Marković, Metaheuristic Applications in Mechanical and Structural Design, Engineering Today, Vol. 1, No. 1, pp. 7-15, (2022)

Application of metal-rubber elements in the spring suspension of rolling stock

Emil Kostadinov, Nencho Nenov
Todor Kableshkov University of Transport, Sofia, Bulgaria

The present work is dedicated to the study of the spring suspension of rolling stock, performed with metal-rubber elements (MRE).

In order to reduce the amplitude of oscillation of the moving railway vehicle and to avoid the risk of resonance, special vibration damping devices are applied in the spring suspension of vehicles. The spring suspension reduces the dynamic load, which reduces the stress in the axles, axle boxes, bogies, car body, track, etc.

As is well known, MREs applied in the spring suspension of railway bogies absorb part of the kinetic energy and improve the quality of the dynamic behavior and safety of railway vehicles, i.e. in addition to having elastic features, they exercise a resistance (damping) force. Since rubber, as a structural component of MRE, changes negatively its features in the process of operating the elements, they change their operational characteristics. On the other hand, the magnitude of the resistance force differs significantly depending on which branch of the characteristics the MRE operates on (loading branch or unloading branch).

The study presents both an overview of the different types of MRE and their field of application, as well as box spring suspension structures of railway vehicles with MRE.

The above substantiates the relevance of research in the field of:

- *Determining the deformation of the MRE;*
- *Design of a axle box assembly with MRE for bogie type Y25;*
- *Strength calculations of metal-rubber elements from spring suspension;*
- *Determination and analysis of model parameters and values of selected materials.*

Keywords: Rolling stock, Spring suspension, Metal-rubber elements

1. MOTIVATION

1.1. Rubber as an engineering material

Compared to other engineering materials, rubber is very ductile. In some cases, the elongation can be higher than 100% and most of this deformation is elastic. On the other hand, metals have very small deformations below the elastic limit. Compared to metals, the tensile strength of rubber is low. The maximum level that can be achieved with rubber is 25-30 MPa. However, due to the heavy load, rubber has a very large capacity to take up work compared to the best quality of steel.

If the material is subjected to a load below the elastic limit, according to Hooke's law the deformation will be proportional to the load. This does not apply to rubber, which does not have a constant modulus of elasticity under tension or compression. Towards the end of the tensile test, metal is usually softer, while rubber is often the opposite. Rubber has no yield strength and the modulus increases until sudden failure occurs.

1.2. Application of MRE in a railway bogie

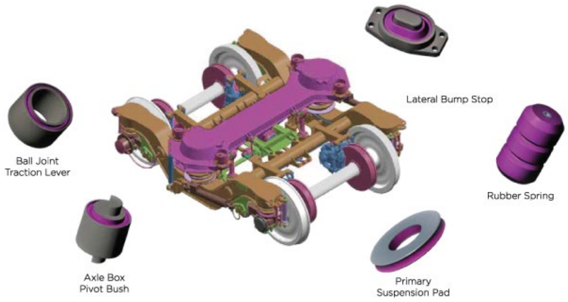

Figure 1: Application of metal-rubber elements in a passenger bogie

Metal-rubber elements are widely used in the spring system of railway bogies. Figure 1 demonstrates the application of metal-rubber elements in a passenger bogie.

MREs are used not only in the spring suspension of cargo and passenger bogies, but also in the absorbing devices of devices for connection between the wagons, such as buffers, traction devices and auto-couplings [2-15].

1.3. Overview of different types of MRE and their application field.

Table 1: Types of MRE and application field

	**Conical springs** Conical springs allow a large variation in adjustable vertical and horizontal stiffness in a limited space. They often eliminate the need for any additional shock absorber.
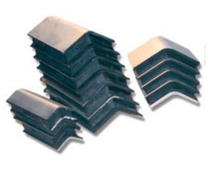	**Chevrons** Primary chevrons are reliable spring elements in primary and secondary suspensions applied worldwide for decades in a variety of railway vehicles. Basic chevrons are maintenance-free, compact in design, and available in a variety of spring designs [7-9].
	**Flat (layer) springs** Primary layer springs provide maintenance-free bearing to the primary and secondary suspension systems.
	**Rubber bearings (silen blocks)** MRE manufactures a range of rubber bearings such as ball bearings that work as mechanical joints in a variety of applications. These include road and rail vehicle suspensions, control arms,

*Corresponding author: <Todor Kableshkov University of Transport, Sofia, Bulgaria> and <*em_kostadinov@abv.bg* >

	engine and gearbox mounts and steering linkages. Rubber bearings can come in a variety of designs and with various mounting options. Typical applications of Spherilastik bearings include traction and torque reaction rods for railway and automotive machinery, hydraulic dampers and others.
	**Clock springs** Patented design suitable for suspension of heavy vehicles. These springs provide large horizontal deflections for bogie rotation and side displacement. They have almost constantly an increasing rate of stiffness along the vertical axis.
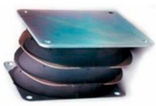	**Compensating springs** This type of spring can be used for primary or secondary suspensions of rail vehicles. These springs are usually used in pairs mounted at an angle to the vertical axis.

Rubber or metal-rubber springs have a wide industrial application as shock and vibration shock absorbing elements and load distribution between supports. MRE consist of metal plates connected to each other by natural or synthetic rubber through a process of vulcanization or injection molding. The mentioned construction makes it possible to use the advantages of the two components of the assembly: high deformation and energy absorption capacity of the rubber and large surface loads borne by metal parts. Their main advantages over metal springs are lower cost, easier installation, lower weight (six times less for the same vibration reduction capability), reduced possibility of corrosion, reduced risk of breakage and elimination of the need for lubrication. The main disadvantages of metal-rubber springs are insufficient reliability during the life of the element caused by the aging process of rubber, deterioration of mechanical properties at elevated and low temperatures, as well as the appearance of permanent deformation. MRE are used in all industrial branches. The table above gives an overview of the different types of metal-rubber supports and their area of application.

1.4. Constructions of box spring suspension with MRE

Constructions of box spring suspension with MRE are shown in Figures 1 - 9.

- Conical rubber elements in Figure 2;
- Cylindrical MRE - Figure 3;
- Rubber mounts (hourglass)- Figure 4;
- Rectangular MRE- Figure 5;

Figure 2: Conical rubber elements

- Fitted (narrowed) MRE- Figure 6;
- Identical frequency elements - Figure 7;
- Rubber-spring bogie DRRS of RWE power, axle load 35 t, maximum speed 65 km/h - Figure 8;
- Gigabox hydraulically damped rubber spring (ContiTech and SKF)- Figure 9.

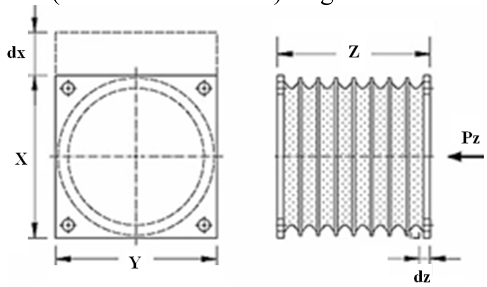

Figure 3: Cylindrical MRE

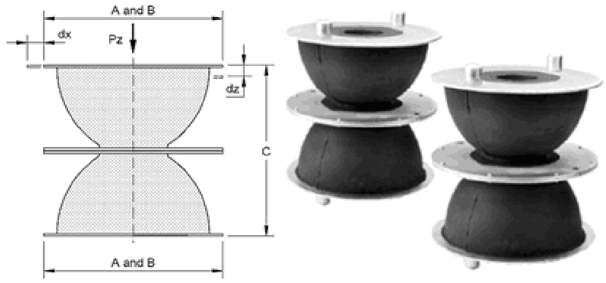

Figure 4: Rubber mounts (hourglass)

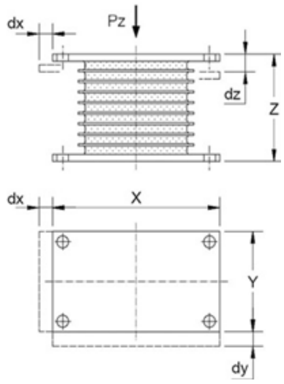

Figure 5: Rectangular MRE

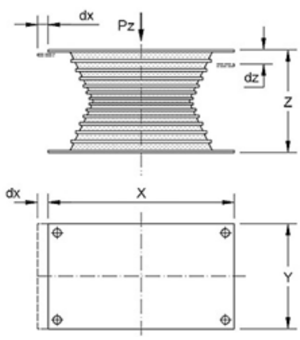

Figure 6: Fitted (narrowed) MRE

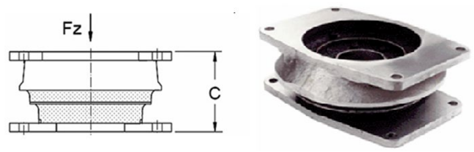

Figure 7: Identical frequency elements

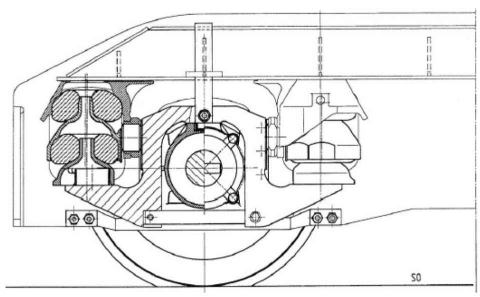

Figure 8: Rubber-spring bogie DRRS of RWE power, axle load 35 t, maximum speed 65 km/h

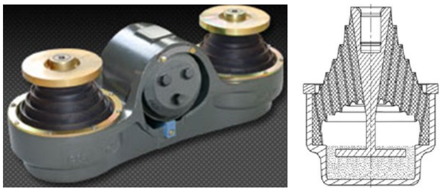

Figure 9: Gigabox hydraulically damped rubber spring (ContiTech and SKF)

The DRRS rubber spring bogie with RWE power, axle load 35 t, maximum speed 65 km/h is double rubber ring spring (DRRS). The newer design of the Gigabox axle boxes by ContiTech and SKF is an axle box bearing located in the body of the axle box together with a rubber elastic element equipped with a system of hydraulic vibration dampers [20].

The undercarriage of the Rolling Stock is used to perceive the loads from the basket and is directed towards the wheels of the rolling stock unit. At the same time, it takes on the function of springing and damping oscillations, and also perceives the load from the bearing assemblies of the axles. To date, separate, independent nodes have been used to perform each of these functions. Combining functions into a structurally unified node creates significant potential for optimization. The Gigabox concept is based on the integration of the rubber spring with a hydraulic vibration damper in the box bearing body. The given innovation concept has a synergy effect, based on the combination of the latest developments of the two companies occupying leading positions in the market.

The Gigabox system, integrated in the new ASB bogie (Figure 10 and Figure 11), reveals new possibilities, such as reducing the level of emitted noise, saving energy and increasing reliability.

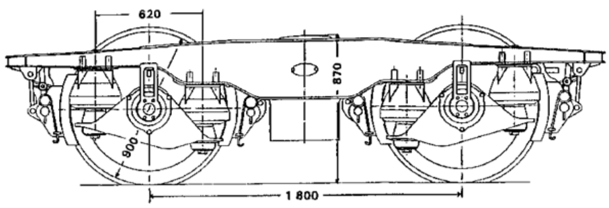

Figure 10: Bogie DRRS 35LD

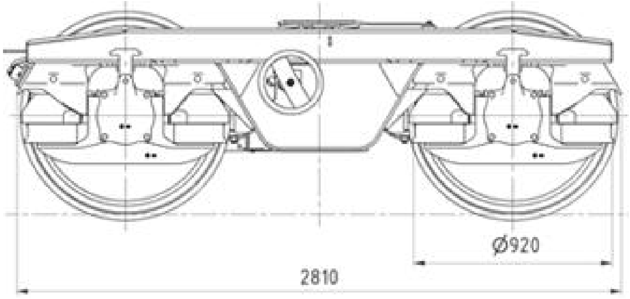

Figure 11: Bogie DRRS 25LD

In addition, the integrated rubber spring optimizes the process of guiding the bogie in the gauge, thanks to which its running qualities are significantly improved. This, in turn, reduces ongoing maintenance costs and, consequently, lowers LCC. Thanks to the improved running qualities, the new freight wagons are expected to reduce wearing and tearing of the entire system, i.e. wheels, rails, sleepers, ballast prism. Freight wagons with bogies type Y25 were taken as the basis of the joint project. The Gigabox system used in the bogie ASB is distinguished by an increased service interval of up to 1 million km. The maximum maintenance interval for a Gigabox is 10 years, which is 2 times longer than a regular box node.

2. DETERMINING THE SAGGING (DEFORMATION) OF THE MRE

The deformation of the rubber has is quite specific, determined by its characteristic features. The relative prolongations and angles of rotation amount to approximately 1, and the relationship between the stress and strain components is not explained by Hooke's law. The displacements are a non-linear function of the forces acting on the rubber element.

In the area of small deformations, the relationship between the force P acting on the MGE and its sagging Δ is linear [21] - i.e.:

$$P = D.(\chi\theta h)^{-1}.\Delta \qquad (1)$$

where: D - damping coefficient determined by the mechanical parameters of the tire in MRE; χ, θ- coefficients determined by the geometry of the MGE and the method of its loading; h – thickness of the rubber layer in MGE; Δ - sagging (deformation).

The sagging is defined by the formula:

$$\Delta = P.\chi\theta h / D. \qquad (2)$$

The coefficients χ and θ are determined based on the minimum potential energy theorem.

The relative energy W of the deformation of the MRE for small deformations, together with the feature of rubber material not to change its volume during deformation, is a function of the second invariant of the deformed state J_2, i.e.:

$$W = D.J_2 \text{ and } J_2 = -\varepsilon_x\varepsilon_y - \varepsilon_y\varepsilon_z - \varepsilon_z\varepsilon_x + \\ +(1/4).(\gamma_{xy}^2 + \gamma_{yz}^2 + \gamma_{zx}^2) \qquad (3)$$

2.1. Determination of the coefficients χ and θ and the sagging Δ for an annular MRE subjected to pressure.

An annular MRE under pressure is shown in Figure 12.

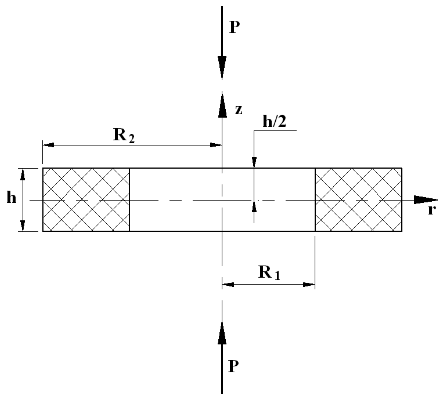

Figure 12

The geometric parameters of the ring are: R_1 – inner radius, R_2 – outer radius, h – thickness of the rubber layer, r_0 – radius defining the layer at which the radial deformation ρ is equal to zero - $\rho = 0$.

It is appropriate to place the element in a cylindrical coordinate system - z, r, Ψ. The components of the displacements can be expressed as follows: w(z) – along the z axis; $\rho = \rho(r, z)$ – along the r axis; rΨ - angle Ψ.

For the coefficients θ and χ determined by the geometry of the MRE and the method of its loading for the derived formula [21]:

$$\theta = 2.\left[\pi.\left(3+\frac{r_0^4}{R_2^2 R_1^2}\right).\left(R_2^2 - R_1^2\right)\right]^{-1} \text{ and}$$

$$\chi = 1 - \frac{th\,\psi h/2}{\psi h/2} \tag{4}$$

where R_1, R_2 and h are geometric parameters of the MRE according to Figure 12, and the value of the parameter r_0 corresponds to the maximum value of the deformation Δ.

The total sagging Δ of the MRE is determined by the calculation:

$$\Delta = \varphi.h\left(1 - \frac{th\,\psi h/2}{\psi h/2}\right) \tag{5}$$

2.2. Determination of coefficients χ and θ and sag Δ for MRE subjected to compression and sliding in translational relative displacement of reinforcing plates

The MRE subjected to compression and sliding under translational relative displacement of the reinforcing plates is shown in Figure 13.

A right-oriented coordinate system x, y, z is adopted. The dimensions of the MRE are: h - along the x axis; b – along the y axis (Figure 10 and Figure 11). The components of the displacement are expressed as follows: u = f(x) - along the x axis; - along axis y; w - along the z axis.

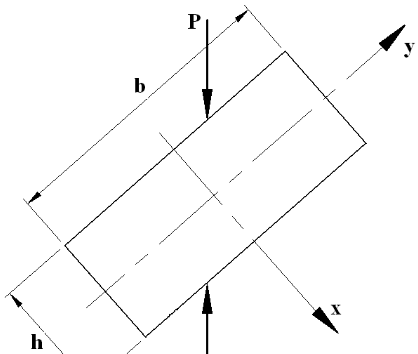

Figure 13

The following interactions are observed for the coefficients θ and χ:

$$\theta = \frac{k^2+1}{2\left[\rho^2 - \rho + 1 + k^2/4\right]}ab \text{ and } \chi = 1 - \frac{th\,\psi h/2}{\psi h/2} \tag{6}$$

The value of the parameter ρ is determined by the maximum value of the sagging Δ.

The sagging Δ of the GM is equal to:

$$\Delta = \varphi.h.\sqrt{k^2+1}.\left(1 - \frac{th\,\psi h/2}{\psi h/2}\right) \tag{7}$$

2.3. Determination of the relative displacement of metal-rubber axle boxes (MRAB) under the action of forces.

For cylindrical joints (Figure 14), r_1, r_2 – radii of the metal axle boxes of cylindrical joints

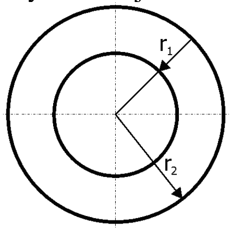

Figure 14

The determination of the relative displacement of the MRAB under the action of forces is given by the following calculations [21]:

-hinge loaded with coaxial torque M:

$$\varphi = \frac{M}{4\pi GL}\frac{r_2^2 - r_1^2}{r_2^2 r_1^2} \tag{8}$$

where G – modulus of angular deformation; L – hinge length;

-hinge loaded with axial force P_0:

$$\Delta = \frac{P_0}{2\pi GL}\ln\frac{r_2}{r_1} \tag{9}$$

-hinge loaded with radial force P_p:

$$\Delta = \frac{2P_p}{3\pi GL}\frac{L^2 + 3(r_2+r_1)^2(r_2-r_1)^3}{L^2 + 6(r_2-r_1)^2(r_2+r_1)^3} \tag{10}$$

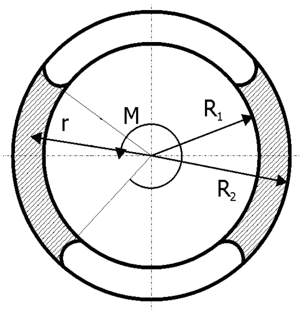

Figure 15

For Spherical joints (Figure 15) loaded with torque - M (coaxial moment), R_1, R_2 radii of the metal bushings of spherical joints; M – twisting moment:

$$\varphi = \frac{M}{12\alpha\pi G}\frac{R_2^3 - R_1^3}{R_2^3 R_1^3} \tag{11}$$

where α is part of the spherical surface occupied by rubber.

3. DESIGN OF A BUSH KNOT WITH METAL-RUBBER ELEMENTS FOR BOGIE TYPE Y25 WITH APPLICATION FOR FREIGHT WAGONS WITH LOADING – 250 kN/ax

3.1. Selection of MRE for embedding in axle box (primary suspensions) of bogie type Y25 with load - 250 kN/ax

From the literature review and study of the application of metal-rubber elements in a axle box assembly for a Y25 bogie in freight cars with a load of 250 kN/ax, let's focus on the application of MGE in the primary suspensions shown in Figure 16 [19].

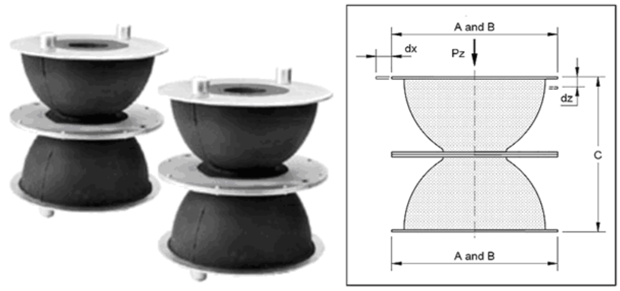

Figure 16

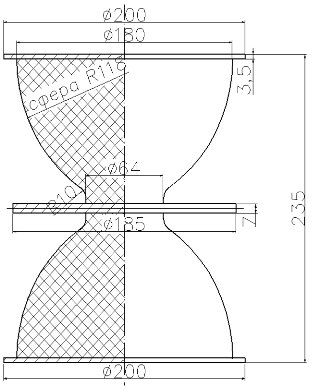

Figure 17

Table 2: Metal-rubber package (MRP)(watch type) with a deformation of 100-120 mm [19]

Parameters	Dimen-sion	Type		
		17 - 1550	17 - 1653	17 - 1869
Vertical load Pz (1 set/4 sets)	kN	63	63	90
	t	6,35/25,4	6,35/25,4	9/36
Vertical deformation dz	mm	105	105	118
Horizontal deformation dx	mm	95	95	100
Size A	mm	200	432	362
Size B	mm	185	370	340
Size C	mm	235	384	332
Mass	kg	18	46	22

According to the dimensions for installation in the box node of the Y25 bogie, I choose the MGP type Clock 17 - 1550, with dimensions shown in Figure 17.

3.2. Strength calculation of metal-rubber package (MRP) using SolidWorks 2010 software

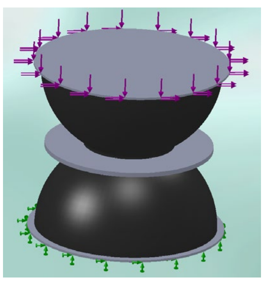

Figure 18: Loading and tightening of the MRP

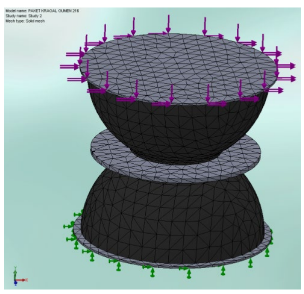

Figure 19: Mesh of the selected MRP

We load the selected MRP at the upper end with a vertical force Pz = 98.757 kN and a transverse force Py = 4.0975 kN. We fasten the lower support. The load is shown in Figure 18. Figure 19 shows the mesh with the SolidWorks 2010 software product.

The following tables give the parameters of the model and the values of the selected materials.

Table 3: Model Information

Document Name	**Configuration**	**Document Path**
RABBAR ELEMENT 216_3	Default	F:\RE 216_3.SLDASM
MEDIUM DISC -1	Default	F:\MD.sldprt
DISK EXTERNAL -1	Default	F:\DE1.sldprt
DISK EXTERNAL -2	Default	F:\DE2.sldprt
RABBER-1	Default	F:\R1.sldprt
RABBAR-2	Default	F:\R2.sldprt

Table 4: Study Properties

Study name	Study 2
Analysis type	Static
Mesh Type:	Solid Mesh
Solver type	FFEPlus
Inplane Effect:	Off
Soft Spring:	Off
Inertial Relief:	Off
Thermal Effect:	Input Temperature
Zero strain temperature	298.000000
Units	Kelvin
Include fluid pressure effects from SolidWorks Flow Simulation	Off
Friction:	Off
Ignore clearance for surface contact	Off
Use Adaptive Method:	Off

Table 5: Units

Unit system:	SI
Length/Displacement	mm
Temperature	Kelvin
Angular velocity	rad/s
Stress/Pressure	N/mm^2 (MPa)

Table 6: Material Properties

No	**Body Name**	**Material**	**Mass, kg**	**Volume, m^3**
1	SolidBody 1(Imported1)	[SW]AISI 304	8.60168	0.00107521
2	SolidBody 1(Imported1)	[SW]AISI 304	5.86297	0.000732871
3	SolidBody 1(Imported1)	[SW]AISI 304	5.86297	0.000732871
4	SolidBody 1(Imported1)	[SW]Silicon Rubber	20.6973	0.0166043
5	SolidBody 1(Imported1)	[SW]Silicon Rubber	20.6973	0.0166043

Table 7:

Material name:	**[SW]AISI 304**		
Description:			
Material Source:			
Material Model Type:	Linear Elastic Isotropic		
Default Failure Criterion:	Unknown		
Application Data:			
Property Name	**Value**	**Units**	**Value Type**
Elastic modulus	1.9e+011	N/m^2	Constant
Poisson's ratio	0.29	NA	Constant
Shear modulus	7.5e+010	N/m^2	Constant
Mass density	8000	kg/m^3	Constant
Tensile strength	5.1702e+008	N/m^2	Constant

Yield strength	2.0681e+008	N/m^2	Constant
Thermal expansion coefficient	1.8e-005	/Kelvin	Constant
Thermal conductivity	16	W/(m.K)	Constant
Specific heat	500	J/(kg.K)	Constant

Material name:	**[SW]Silicon Rubber**
Description:	
Material Source:	
Material Model Type:	Linear Elastic Isotropic
Default Failure Criterion:	Unknown
Application Data:	

Property Name	**Value**	**Units**	**Value Type**
Mass density	1246.5	kg/m^3	Constant
Tensile strength	6e+006	N/m^2	Constant

Loads and Restraints

Table 8:

Fixture

Restraint name	**Selection set**
Fixed-1 < DISK EXTERNAL -2>	on 1 Edge(s), 1 Face(s) fixed.

Load

Load name	**Selection set**	**Loading type**
Force-1 < DISK EXTERNAL -1>	on 1 Face(s) apply normal force 98757 N using uniform distribution	Sequential Loading
Force-2 < DISK EXTERNAL -1>	on 1 Face(s) apply force 4097.5 N along plane Dir 1 with respect to selected reference Face < 1 > using uniform distribution	Sequential Loading

Mesh Information

Mesh Type:	Solid Mesh
Mesher Used:	Standard mesh
Automatic Transition:	Off
Smooth Surface:	On
Jacobian Check:	4 Points
Element Size:	23.474 mm
Tolerance:	1.1737 mm
Quality:	High
Number of elements:	22175
Number of nodes:	33647
Time to complete mesh(hh;mm;ss):	00:00:06
Computer name:	NEWONE

Reaction Forces

Selection set	**Units**	**Sum X**	**Sum Y**	**Sum Z**	**Resultant**
Entire Body	N	-4098	98731	-0.3904	98816

Study Results

Default Results

Name	**Type**	**Min**	**Location, mm**	**Max**	**Location**
Stress 1	VON: von Mises Stress	0.002965 N/mm^2 (MPa) Node: 1701	(-81.35, 4.9, -153)	9.434 N/mm^2 (MPa) Node: 19659	(88.4 mm, 10.1 mm, -46.6 mm)
Displacement1	URES: Resultant	0 mm Node: 6483	(145.41, -187, -159.7)	0.0140249 mm Node: 2885	(160.5 mm, 191.9 mm, 144.5 mm)
Strain 1	ESTRN: Equivalent Strain	1.3826e-008 Element: 625	(-178.8, 2.498, -17.245)	5.02272e-005 Element: 6501	(84.4 mm, 8.88 mm, -46.9 mm)

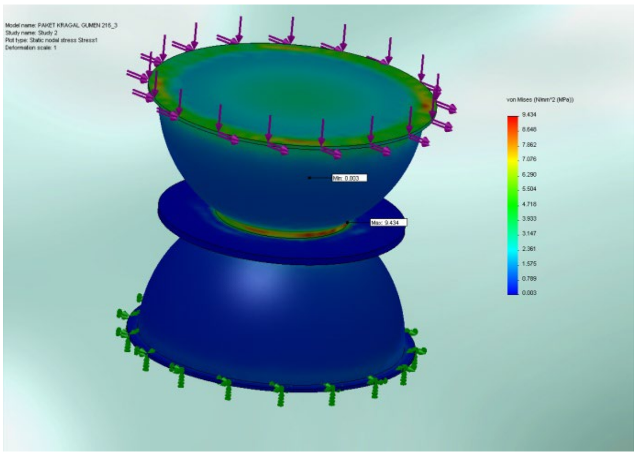

Figure 20: Tense state of MRP 216_3-Stress-Stress1

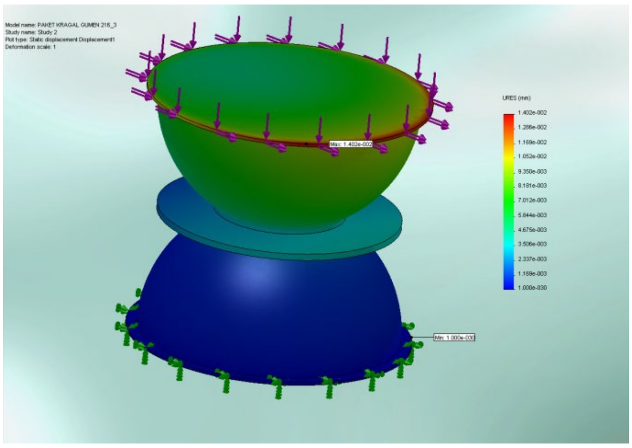

Figure 21: Deformation of MRP 216_3-Displacement-Displacement1

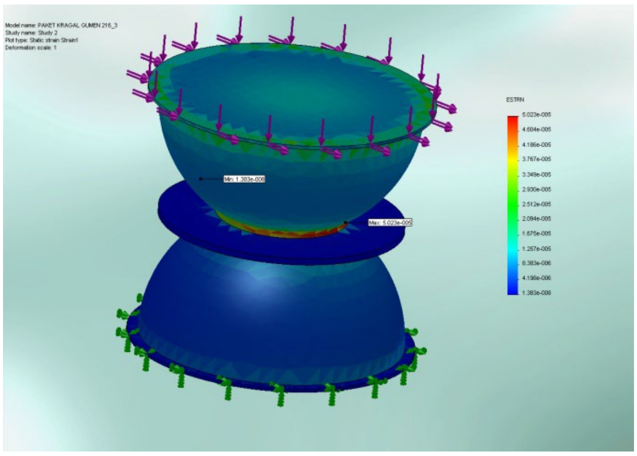

Figure 22: Strain of MRP 216_3- Strain-Strain1

We decide to implement the selected MRP in the primary suspensions of the Y25 bogie with the selected parameters (see Figure 23).

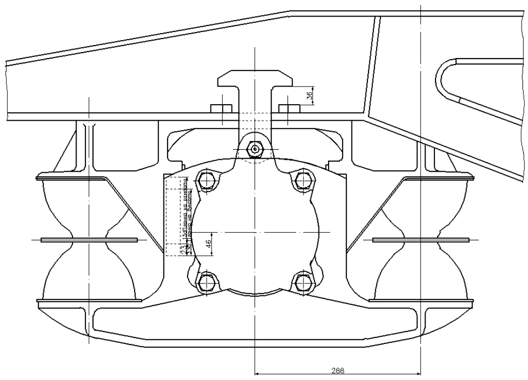

Figure 23: Installation of the selected MRP in the primary suspensions of the Y25 bogie

3.3. Strength calculations of metal-rubber elements from spring suspension

Strength calculations were made using the finite element method with the SolidWorks 2010 software product.

Metal-rubber elements shown in Figure 25 and *Figure 26* are the most frequently applied elements in the spring suspension of transport equipment. They are also applied in the construction of various technical products. The elastic element (rubber, silicone or other elastic material) has different configurations and sizes.

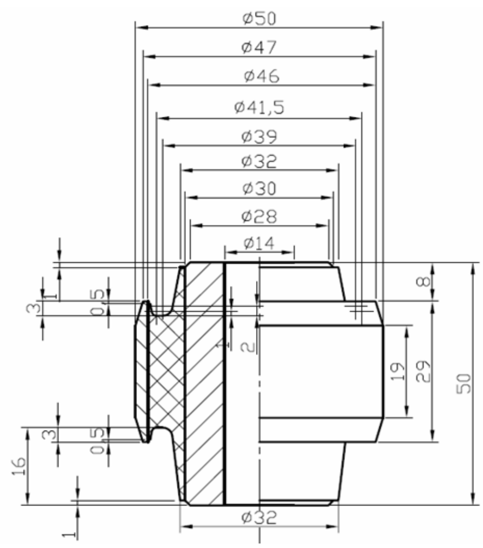

Figure 24: Metal-rubber element – dimensions

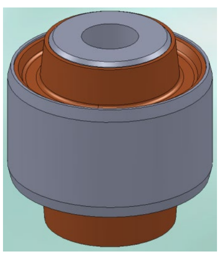

Figure 25: Metal-rubber element model

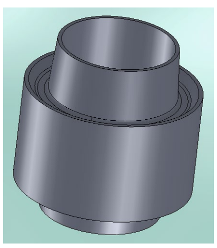

Figure 26: Rubber element

The load on the metal-rubber element applied in the spring suspension is a torsional load and a force load transverse to the longitudinal axis of the hinge. According to the requirements of the manufacturing plants, the load for such hinges has been determined experimentally and for the selected configuration is a transverse force of magnitude 500N and a twisting torque of 500 rad/s. The support is a thrust on the outer cylindrical surface of the rubber element (due to the vulcanization of the rubber and the metal outer sleeve).

The results of the calculations are as follows:

Table 9:

Material Properties

No.	Body Name	Material	Mass	Volume
1	SolidBody 1 (Imported1)	[SW]Silicon	0.0673761 kg	2.89168e-005 m^3

Material name:	[SW]Silicon
Description:	
Material Source:	
Material Model Type:	Linear Elastic Isotropic
Default Failure Criterion:	Unknown
Application Data:	

Property Name	Value	Units	Value Type
Elastic modulus	1.124e+011	N/m^2	Constant
Poisson's ratio	0.28	NA	Constant
Shear modulus	4.9e+010	N/m^2	Constant
Mass density	2330	kg/m^3	Constant
Yield strength	1.2e+008	N/m^2	Constant
Thermal conductivity	124	W/(m.K)	Constant

Loads and Restraints

Fixture

Restraint name	Selection set	Description
Fixed-1 <gk 6 3-1>	on 1 Face(s) fixed.	

Load

Load name	Selection set	Loading type
Force-1 <gk 6 3-1>	on 1 Face(s) apply force 500 N along plane Dir 1 with respect to selected reference Face< 1 > using uniform distribution	Sequential Loading
Centrifugal-1	CentriFugal with respect to Face< 1 > with angular velocity 500 rad/s and angular acceleration 0 rad/s^2	Sequential Loading

Contact

Contact state: Touching faces - Free

Mesh Information

Mesh Type:	Solid Mesh
Mesher Used:	Standard mesh
Automatic Transition:	Off
Smooth Surface:	On
Jacobian Check:	4 Points
Element Size:	3.0705 mm
Tolerance:	0.15352 mm
Quality:	High
Number of elements:	8934
Number of nodes:	15411
Time to complete mesh(hh;mm;ss):	00:00:05
Computer name:	NEWONE

Reaction Forces

Selection set	Units	Sum X	Sum Y	Sum Z	Resultant
Entire Body	N	-490.71	-0.205	96.001	500

Free-Body Forces

Selection set	Units	Sum X	Sum Y	Sum Z	Resultant
Entire Body	N	-0.00029	-3.33 e-006	-6.18 e-005	0.0003

Free-body Moments

Selection set	Units	Sum X	Sum Y	Sum Z	Resultant
Entire Body	N-m	0	0	0	1e-033

Study Results

Default Results

Name	Type	Min	Location	Max	Location
Stress1	VON: von Mises Stress	0.0029446 N/mm^2 (MPa) Node: 9914	(-22.13 mm, 28.5 mm, 5.9461 mm)	2.785 N/mm^2 (MPa) Node: 10828	(17.2 mm, 2.7 mm, 1.5 mm)
Displace-ment1	URES: Resultant Displac.	0 mm Node: 860	(-7.6 mm, 28.3 mm, 22.3 mm)	0.00066 mm Node: 1577	(14.5 mm, -11.9 mm, -3.7 mm)
Strain1	ESTRN: Equivalent Strain	4.55184e-008 Element: 4190	(-22.3 mm, 28.02 mm, 2.24 mm)	1.694e-005 Element: 8767	(-1.6 mm, -0.8 mm, -15.1 mm)

The maximum stresses obtained are 2.785 MPa in the transition region from the thin inner cylindrical part to the middle cylindrical part, shown in Figure 27, Figure 28 and Figure 29. The maximum deformations (0.00066 mm) are in the upper surface of the thin inner cylindrical part (Figure 30), and the coefficient of relative deformation (Figure 21) is $1.69.10^{-5}$.

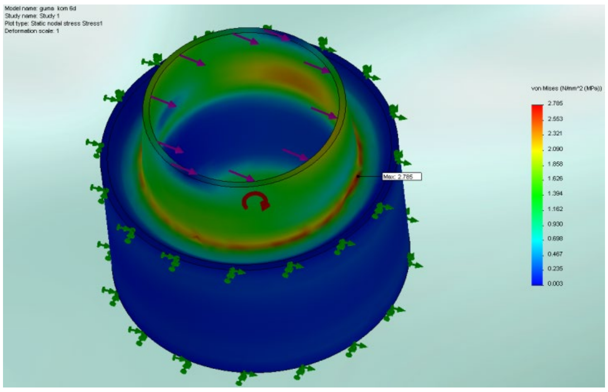

Figure 27: Stress of the elastic element of the MRAB

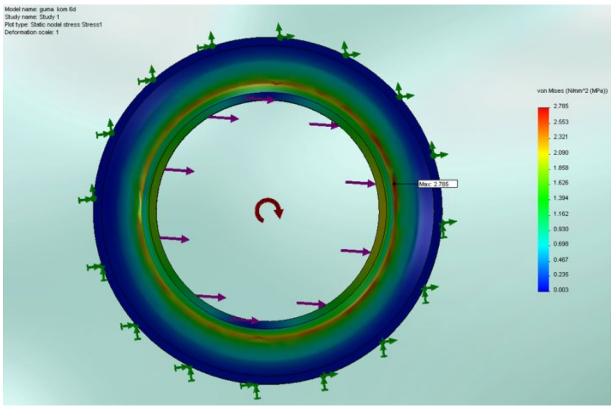

Figure 28: Stress of the elastic element of the MRAB

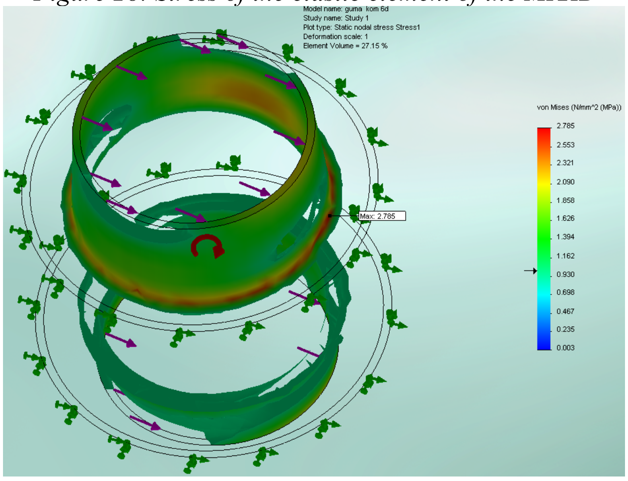

Figure 29: Distribution of stress over 1 MPa in the construction of the elastic element from the MRAB

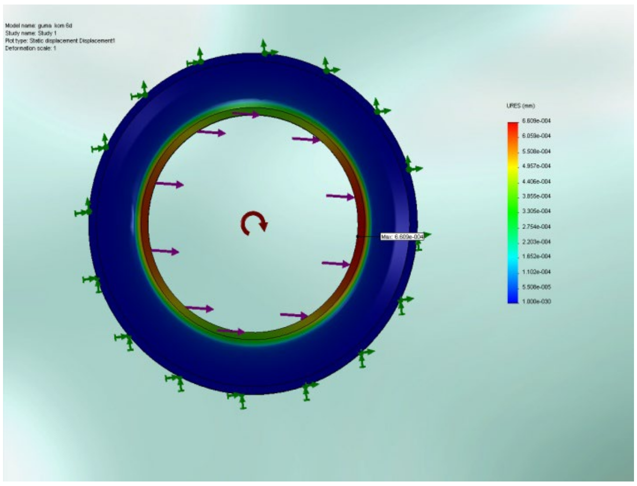

Figure 30: Deformation of elastic element

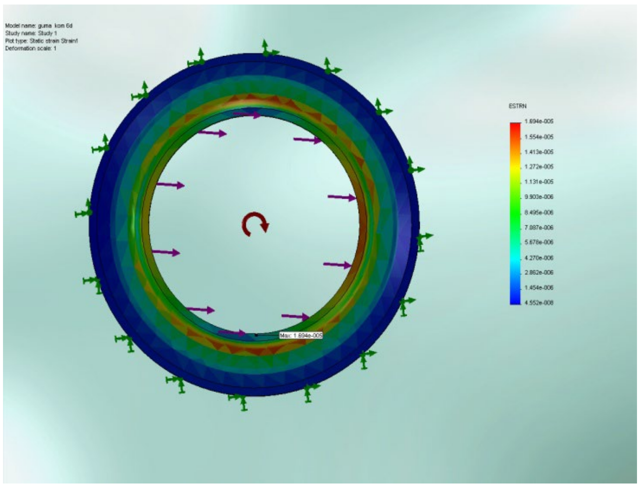

Figure 31: Coefficient of relative deformation (Strain).

CONCLUSION

Typical MREs are presented and, based on an analysis of their advantages and disadvantages, their field of application is outlined.

Based on the constructions of basic MREs, models have been developed and they have been studied.

The Gigabox Concept, based on the integration of the rubber spring with a hydraulic vibration damper in the box bearing housing, was considered.

A methodology has been developed for determining the main parameters of the MRE.

An axle unit with MRE for bogie type Y25 was designed for use in freight wagons with a load of 250 kN/ax.

Strength and deformation calculations of metal-rubber hinges from spring suspension were carried out.

The parameters of MRE models and the selected construction materials in the process of their production have been determined and analyzed.

REFERENCES

[1] Industrial Products Catalogue. Trelleborg IAVS; 2010.

[2] M.Milošević, D.Stamenković, S.Jovanović, I.Puletić, L.Mladenović, „Examination of Buffing and Draw Gear With Rubber-Metal Springs", XII Scietific-Expert Conference on Railway, Niš, 2006

[3] M.Milošević, D.Stamenković, A.Milošević, „Research of absorbed energy of rail vehicle buffers filled with rubber-metal springs", 18th International Conference „CURRENT PROBLEMS IN RAIL VEHICLES – PRORAIL 2007", Žilina, Slovakia, 2007.

[4] Stamenković, D., Radenković, S., Milić, M., Mladenović, S.: Gumeno-metalni elementi kod elektrolokomotiva, ŽELEZNICE, 2, pp. 151-159, 1995.

[5] Stamenković, D., Milošević, M., Petrov, I., Banić, M., „Development and validation of elecrolocomotives primary suspension rubber metal elements", XIV Naučno-stručna konferencija o železnici ŽELKON 10, Niš, pp. 79-82, 2010.

[6] M. Banić, et al.: „Prediction of Heat Generation in Rubber or Rubber-Metal Springs", Thermal Science, 16 (Suppl. 2), pp. 593-606, 2012.

[7] Ruzhekov T., Pentchev Ts., Dimitrov E., „Theory and design of railway equipment", ISBN: 978-954-12-0194-7, VTU, 2011, pp. 396

[8] Atmadzhova, D., Nenov, N., „Study on fatigue of rubber metal springs of primary spring suspension of electric locomotives", XV Scientific – Expert Conference on Railways Railcon 12, Nis, Serbia, pp. 41-44, 2012.

[9] Atmadzhova, D., Nenov, N., „Study of the Rubber Metal Springs Fatigue of Primary Spring Suspension of Electric Locomotives", Journal Facta Universitatis Series Mechanical Engineering, Vol. 10, No. 1, pp. 63-70, 2012.

[10] Atmadzhova, D., „A method to evaluate the service life of rubber springs in rolling-stock", Academic journal Mechanics Transport Communications, iss. 2, pp. 2.9–2.14, 2008.

[11] Atmadzhova D., Mihaylov E., „Elastic rubber elements as component parts of resilient wheels for light-rail transportation", XV Conference RAILCON'12 Niš, Serbia, at the Faculty of Mechanical Engineering Oct., 2012

[12] Petrovic, D., Bizic, M., „Improvement of suspension system of Fbd wagons for coal transportation", Engineering Failure Analysis, 25, pp. 89–96, 2012.

[13] Nenov N., Ruzhekov T., Dimitrov E., Mihov G., „Elektronic test equipment for determining parameters of railway rolling stock spring elements". XI International Scientific Conference „Sciece, education and society". Vol. III, pp.55-58, 15-17 september, Zilina, Slowak Republic, 2003

[14] Petrović D., Atmadzhova D., Bižić M., „Advantages of rubber-metal elements in suspension of railway vehicles", IIIrd International Conference on Road and Rail Infrastructure CETRA 2014, 28-30 IV, Croatia, 2014

[15] Dragan Petrović, Milan Bižić, Dobrinka Atmadzhova, „Application of Rubber Elastic Elements in Suspension of Railway Vehicles", Mechanics Transport Communications, volume 15, issue 3, 2017, pp VI-44 VI-51

[16] https://www.sujanindustries.com/our-products/railway-parts-in-india/

[17] www.koni-enidine-rail.com

[18] https://www.gmtrubber.com/products/rubber-bearings/

[19] https://www.trelleborg.com/en/anti-vibration-solutions/products-and-solutions/anti-vibration-products/spherilastik-bearings

[20] M. Hecht, „Wear and energy-saving freight bogie designs with rubber primary springs: principles and experiences", Proc. IMechE Vol. 223 Part F: J. Rail and Rapid Transit, JRRT227 © IMechE 2009

[21] Ружеков Т., Цв. Пенчев, Е. Димитров, „Теория и конструиране на железопътна техника", Изд. ВТУ „Т. Каблешков", София, 2011

Development of Laboratory for Testing of Railway Vehicles and Structures

Dragan Petrović*, Milan Bižić
Faculty of Mechanical and Civil Engineering in Kraljevo, University of Kragujevac, Serbia

The aim of this paper is to elucidate the need for the establishment and continuous development of a laboratory for testing of railway vehicles and mechanical structures at the Faculty of Mechanical and Civil Engineering in Kraljevo. The development strategy of the Centre for Railway Vehicles and Structures Testing at the Faculty of Mechanical Engineering and Civil Engineering in Kraljevo is oriented in three directions. The first direction of development refers to high-quality and efficient teaching and education of students in the field of railway engineering and structures testing, at all levels of study. The second direction of development refers to the creation of conditions for the scientific and professional advancement of the members of the Centre and Laboratory, as well as their continuous improvement in accordance with the leading world trends. The third direction refers to the scientific work of the Centre and Laboratory, which includes the verification of theoretical solutions, designed and manufactured elements, sub-assemblies and assemblies of various types of constructions. In this way, it is possible to produce high-quality graduation, master's and doctoral theses, participation in domestic and international scientific research projects and cooperation with universities, institutes and the economy. The procurement and development of modern measuring equipment and software, as well as the equipping of a suitable space for work, were necessary as a prerequisite for the highest quality performance of the aforementioned tasks.

Keywords: Railway vehicles, Wagon, Laboratory, Kraljevo, Testing, Structures

1. INTRODUCTION

The history of designing, calculating and testing of mechanical structures in Kraljevo is directly related to the Wagon Factory Kraljevo. The Wagon Factory is also the initiator of higher education in Kraljevo and, together with the Faculty of Mechanical Engineering of the University of Belgrade, the founder of the Faculty of Mechanical Engineering Kraljevo. Within the Wagon Factory Kraljevo, a unit for experimental testing of construction was organized, whose founder and first head was prof. dr Ranko Rakanović (Fig. 1). Professor Rakanović was one of the founders and the first dean of the Faculty of Mechanical Engineering Kraljevo.

Figure 1: Prof. dr Ranko Rakanović, one of the founders and the first dean of the Faculty of Mechanical Engineering Kraljevo

During the multi-decade period, more than 200 railway vehicles and other structures were tested in the Test Center of the Wagon Factory Kraljevo (Fig. 2). All these tests were carried out in accordance with the valid domestic and international standards, on which appropriate reports and studies were prepared (Fig. 3), by which these constructions obtained permission for production and use.

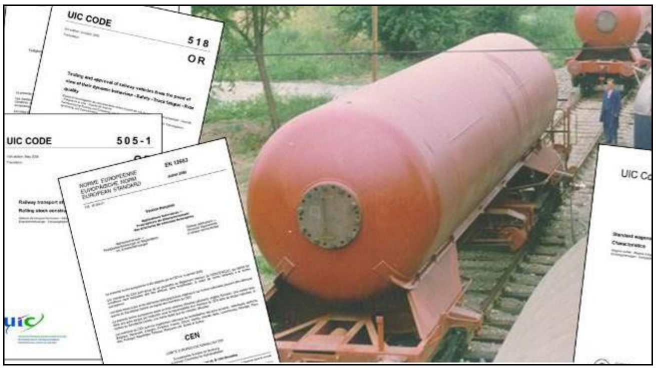

Figure 2: Impact testing of wagons according to international standards

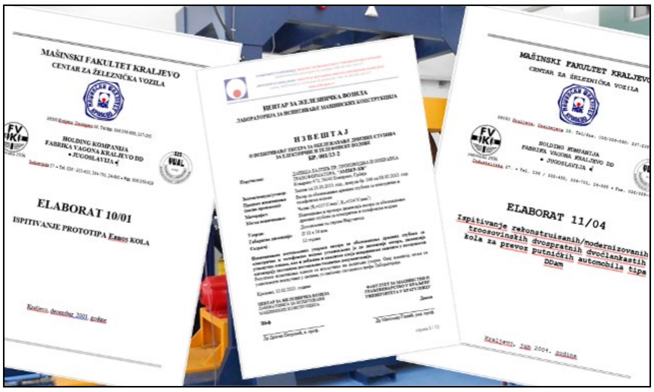

Figure 3: Reports and studies on the performed tests

In this way, the Test Center became one of the main pillars for evaluating and improving the quality of designed railway vehicles. In addition, during the design phase of new constructions, the Test Center became a very

*Corresponding author: Dositejeva 19, 36000 Kraljevo, Serbia, petrovic.d@mfkv.kg.ac.rs

significant database on the behavior of similar, previously tested constructions.

2. PROCUREMENT AND DEVELOPMENT OF MEASURING EQUIPMENT

2.1. Establishment of Laboratory at Faculty of Mechanical Engineering Kraljevo

After many transformations in the 2000s and an unsuccessful sale to the Ukrainian company Azov-impex, the Wagon Factory Kraljevo was forced to go into bankruptcy, after which it was shut down. There was a real risk that half a century of knowledge, experience and developed equipment would be irretrievably lost. With this, the Faculty of Mechanical Engineering Kraljevo would lose space and equipment for scientific research and professional work and development in the field of railway engineering and structures testing. Seeing the danger of such a development, it was decided to establish a Laboratory for railway vehicles and structures testing at the Faculty of Mechanical Engineering Kraljevo (the latter Faculty of Mechanical and Civil Engineering in Kraljevo). Based on the experience gained, cooperation with the industry, as well as international and domestic projects, the aforementioned laboratory (Fig. 4).

Figure 4: Laboratory for railway vehicles and structures testing at Faculty of Mechanical and Civil Engineering in Kraljevo

One of the main directions of the future development of railway is based on the constant tendency to increase the safety and speed of railway vehicles running. In accordance with these trends, among the most important issues is solving the problems of safety and security of the most responsible parts of railway vehicles. It is well known that failure of vehicle parts such as wheels, axles or axle-bearings leads to failure not only a given wagon, but in most cases also the entire train. The consequences are unfathomable, with great material damage, and in many cases with human victims. That is why it is best to analyze, identify and eliminate the causes that lead to failures even at the stage of designing and manufacturing the railway vehicles.

2.2. Achieved results

2.2.1. System for measuring forces in wheel-rail contact

This measuring system is intended for continuous measurement of the lateral force Y and vertical force Q occurring in contact between the wheel and the rail and is characterized by wireless signal transmission. The system is based on the measurement of wheel strains using strain gauges placed in specially selected points, digitization of the measurement signal, radio transmission to the static electronic module in the box of the wagon, as well as on the appropriate processing of the received signals. The basic components of the system are: two instrumented wheelsets of the freight wagon equipped with strain gauges, an electronic computer unit for receiving and storing signals during measurement, and a computer module for processing and displaying measurement results.

Strain gauges are placed on monobloc wheels and their purpose is to measure strains caused by the effect of vertical and lateral force (Fig. 5). The position of placing the strain gauges was determined based on the calculation of wheel deformations using the finite element method (FEM).

Figure 5: Instrumented wheelset

The measuring points are arranged in 8 equally distant positions along the circumference of the wheel, with an angular distance of 45° (Fig. 6). Two groups of 8 strain gauges on one diameter are located on the outside, and two groups on the inside of the wheel.

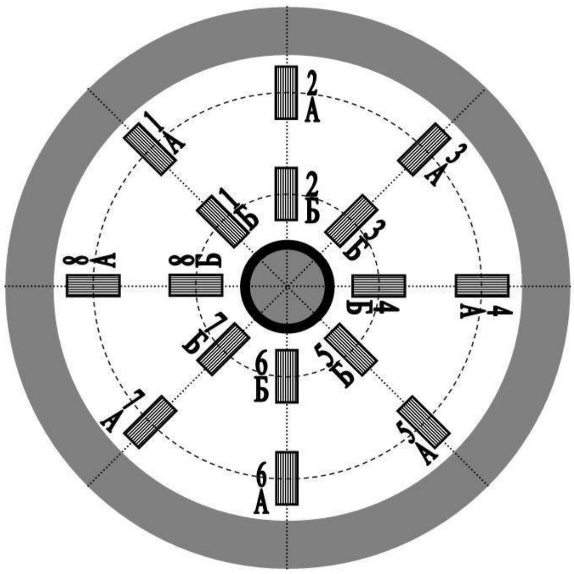

Figure 6: Arrangement of strain gauges on wheel

The transmission of measurement data from the rotating axle to the box in the measuring wagon is accomplished by radio communication using a special electronic module.

2.2.2. Test stand for calibration of instrumented wheelsets

The test stand provides the possibility of working with instrumented wheelsets in laboratory conditions with minimal testing costs. The basic function of the test stand is to simulate the contact between the wheel and the rail, i.e., the simulation of the forces *Y* and *Q* that arise in that contact.

The basic parts of the test stand are (Fig. 7): 1 – lower wheelset; 2 – horizontal movable support of the lower wheelset; 3 – upper wheelset (instrumented wheelset to be calibrated); 4 – vertical movable support of the upper wheelset; 5 – supporting structure; 6 – hydraulic systems for setting forces *Y* and *Q*; 7 – systems for registering the values of given forces *Y* and *Q*; 8 – motion drive; 9 – security systems; and 10 – control console.

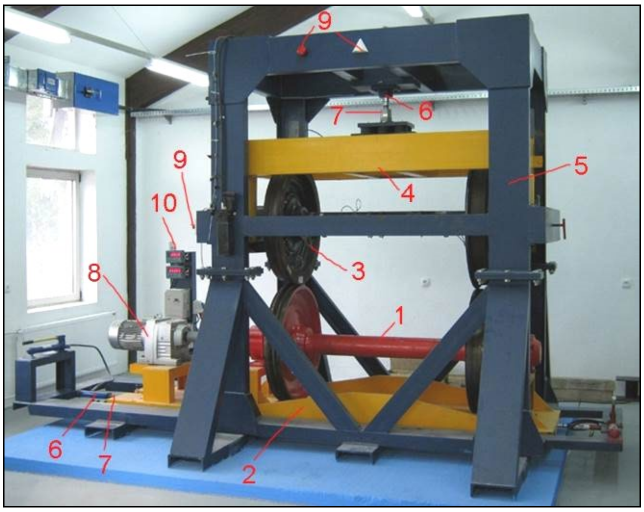

Figure 7: Test stand for calibration of instrumented railway wheelsets

The rail is simulated using the lower wheelset, while the function of the wheel is performed by the upper instrumented wheelset which is calibrated. The lower wheelset is machined so that the radii of rounding of the wheels profile correspond to the radii of rounding of the rail head profile (Fig. 8).

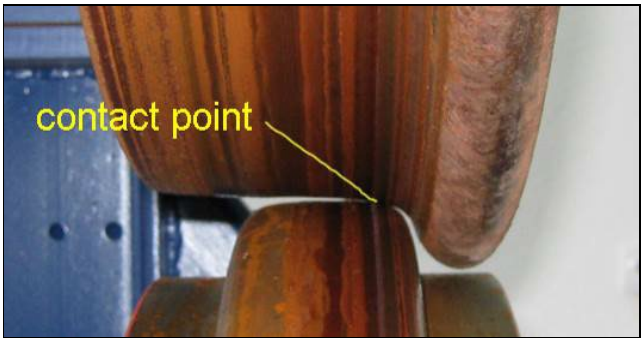

Figure 8: Imitation of rail head and simulation of wheel-rail contact on test stand

The test stand is equipped with hydraulic systems for loads setting in the vertical and lateral directions, up to 100 kN and 225 kN per wheel, respectively (Fig. 9).

The force is measured by the force converters (Fig. 10), installed in vertical and lateral directions in relation to the direction of action of the hydraulic cylinders.

During the calibration of the instrumented wheelset, the force values are read on the alpha numeric display (Fig. 11).

The motion drive is achieved by electric motor with a gearbox whose connection with the lower wheelset is realized through a cardan coupling (Fig. 12).

a)

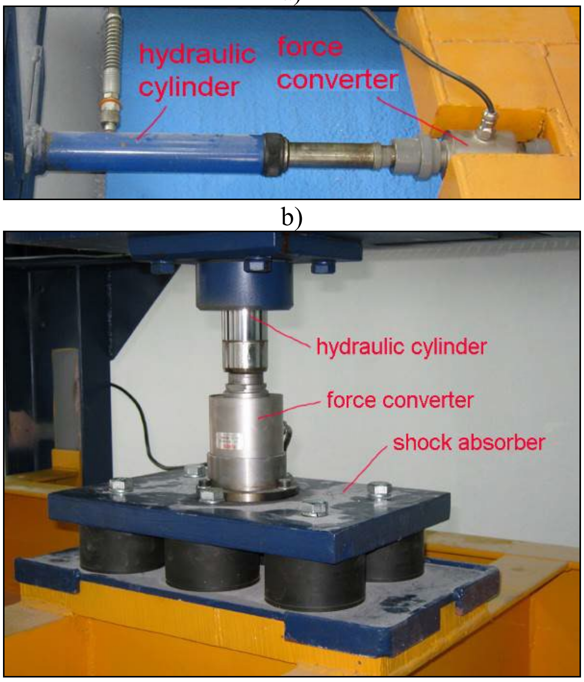

Figure 9: Hydraulic cylinders for loads setting in horizontal direction (a) and vertical direction (b)

Figure 10: Force converter

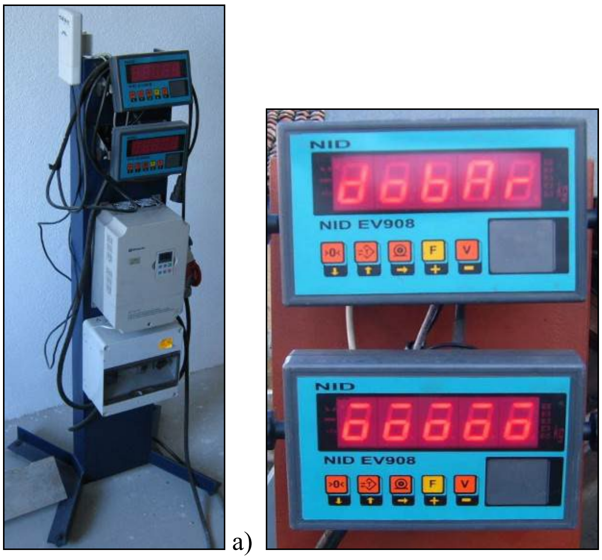

a) b)

Figure 11: Module with the main switch, frequency regulator (a) and alpha numeric displays (b) for reading the values of forces Y and Q

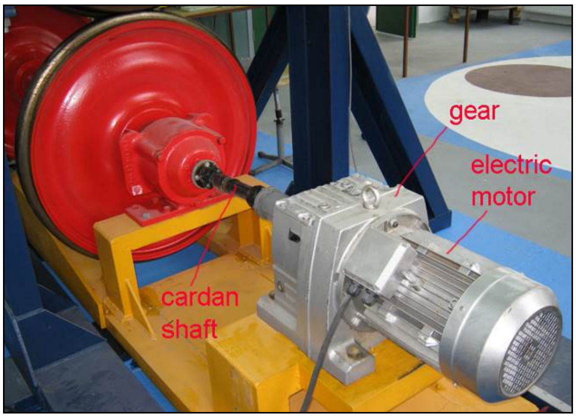

Figure 12: Motion drive with electric motor, gearbox and cardan coupling

Characteristic movements are horizontal movement of the lower wheeset that simulates the rail, and vertical movement of the upper tested (calibrated) wheeset. By the action of the hydraulic cylinder on the horizontal movable carrier, the entire system together with the lower wheelset is set in motion and creates a horizontal force in contact between the wheel and the rail – force *Y*. By the action of the hydraulic cylinder on the vertical movable carrier, this system together with the upper – tested (calibrated) wheeset moves downward and creates a vertical force in contact between the wheel and the simulated rail – force *Q*.

In this way, a laboratory simulation of the forces in contact between the wheel and the rail that occur during the movement of the railway vehicle on the track is carried out. The forces can be applied independently of each other, and the system allows changing the position of the contact point on the tread surface of the wheel. The test stand allows applying forces in the vertical direction up to 225 kN, and in the horizontal direction up to 100 kN.

The entire system is designed for the calibration of instrumented wheelsets for a normal track gauge of 1435 mm, and for working with wheelsets with an axle-load of up to 22.5 t. Assignment of forces *Y* and *Q* in the horizontal and vertical directions are provided with hydraulic cylinders driven by hand pumps. The detection of the values of the applied forces *Y* and *Q* is performed by using FLINTEC force converters, which are placed between the pistons of the hydraulic cylinders and the structures of the movable carriers of the wheelsets.

The rotational movement of the tested wheelset is realized indirectly via the lower wheelset that simulates a rail. The lower wheelset receives rotational movement via the cardan shaft, which is driven by an electric motor with a reduction gear. The power of the electric motor is 7.5 kW, and the regulation of the number of revolutions is achieved by means of a frequency regulator. The main switch, frequency regulator and alpha numerical displays for reading the values of forces *Y* and *Q* are placed on a special support that can be moved in the immediate area around the test stand.

The measurement signals obtained during the calibration of the instrumented wheelset are shown in Fig. 13.

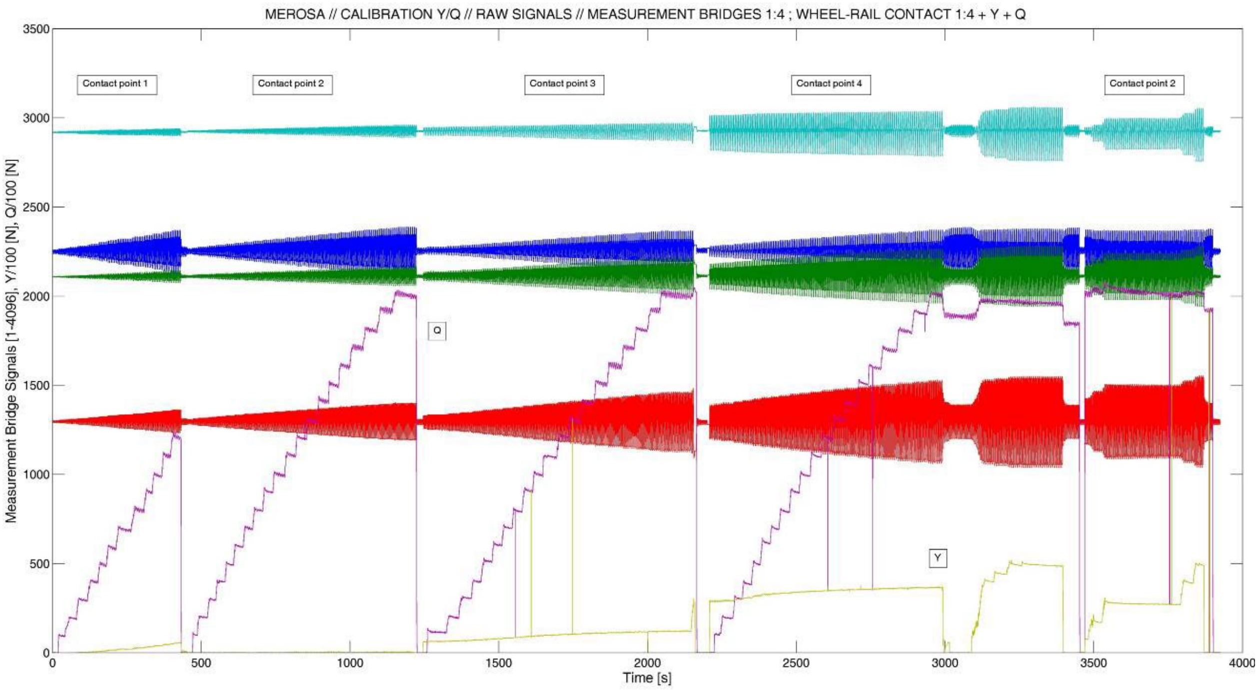

Figure 13: The measurement signals obtained during the calibration of the instrumented wheelset

The software package (Fig. 14) for adjustment of signal acquisition parameters serves for adjustment of parameters connected with acquisition of signals from strain gauges, such as resolution and speed of conversion, offset and signal intensification, temperature compensation, etc.

The procured measuring equipment classifies Centre and Laboratory for Railway Vehicles and Structures Testing at the Faculty of Mechanical Engineering and Civil Engineering in Kraljevo among very rare research centres equipped for the measurement of forces in wheel-rail contact by means of the telemetric transmission of signals. As for the education of students at the faculty, this equipment allows further development and improvement of practical teaching methods in the field of railway engineering. The equipment also enables further development and strengthening of research potentials of staff employed at Centre and Laboratory in accordance with the leading world trends. The most important scientific contribution is in the possibility of using the equipment for scientific-research purposes, primarily for development of new methods in treating the problems of measurement and identification of behaviour of freight wagons from the aspect of forces in the wheel-rail contact *Y* and *Q*, as well as their ratio *Y*/*Q*.

Figure 14: Interface of software package

2.2.3. Converter for measuring of lateral force and lateral acceleration

The converter for measuring of lateral force and lateral acceleration operates on the principle of converting the force into strain of the sensor elements installed on it. A special accelerometer with the measurement range of 5 g is also installed on it and it is used for measuring lateral acceleration (Fig. 15).

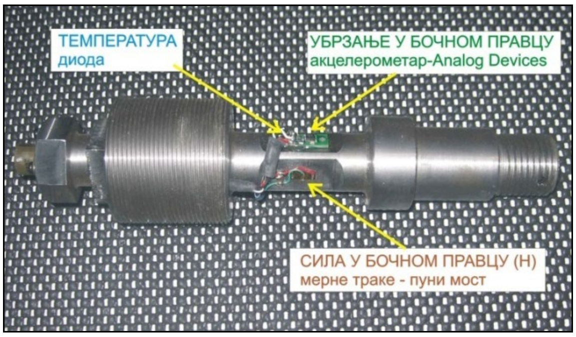

Figure 15: Converter for measuring of lateral force and lateral acceleration

2.2.4. System for measuring of height of wheel lifting

The mechanical assembly for measurement of the height of wheel lifting converts the height of lifting into the angular displacement of the legs which keep the sliders on the rail, on the front and bottom sides of the wheel. During the wheel lifting, the converter body lifts and the angles of both legs of the rail slider get reduced in relation to the normal (Fig. 16).

There are two angle converters in the converter, one for each leg, which measure the change of angle (Fig. 17). The angle converters are, the range of 20 degrees, and they produce analogue stress output in the function of angular position (Fig. 18).

Figure 16: Converter for measurement of the height of wheel lifting

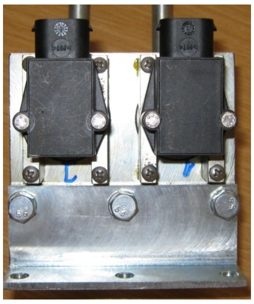

Figure 17: Angle converters used for measuring the change of angle of legs which hold the sliders

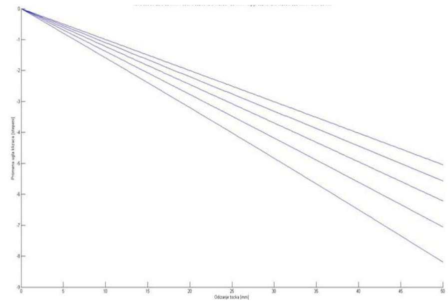

Figure 18: Change of angle of slider arm in function of wheel lifting height

2.2.5. System for measuring of compressing forces at the automatic coupling

The measuring system is intended for measurement of compression forces at the automatic coupling. A specially instrumentalized set of couplings type SA-3, which are installed on the wagons in front and behind the tested wagon in the measuring trains, was procured (Fig. 19).

Figure 19: Sets of measuring automatic couplings SA-3 with strain gauges installed

Two pairs of strain gauges are installed in the full measuring bridge at one of the couplings. Two strain gauges are installed in the direction of elongation at tension, and the other two are normal to the direction of elongation and they are used for compensation.

2.2.6. System for measuring lateral movements between test and barrier wagons

Measurement of lateral movements between test and barrier wagons is based on an optoelectronic vision system and image processing. Two CCD cameras are mounted on the test wagon and pointed towards the front end the rear barrier wagons whose buffers mutual position are to be measured, as seen in Fig. 20.

Figure 20: Measurement of lateral movements

An image of the target is acquired by a camera mounted on the front and rear sides of the test wagon. Field of view (FOV) of the camera points towards the target mounted on the barrier wagon whose buffer misalignment is to be measured. This wagon is marked with a cooperative target mounted across the gap and pointing towards camera. Target moves in direction lateral to the track following the motion of the wagon buffers and its image is acquired by the camera, using USB interface and processed by the onboard computer. The position of the target inside the field of view (FOV) of the camera follows relative position of the buffers, and is used to calculate the misalignment. Illumination is provided by a LED array and covers entire field of view (FOV) with monochromatic red light. Monochromatic light is used since it is possible to extract the red colour plane in camera and this limits total noise from external and background illumination to single colour. Illumination also provides for low level daylight or night operation.

3. CONCLUSION

Special attention in the European framework is paid to the development of the railway as a mass, safe, economical transport with the least harmful effects on the human environment. In the coming period, an even more significant investment in the development of railway transport is foreseen in order to increase safety, comfort, external and internal aesthetic characteristics, etc.

One of the most significant ways to increase safety is related to the development and introduction of a system for constant monitoring of the condition of the most important constituent elements of railway vehicles. This particularly applies to on-line monitoring of the state of the wheelsets (Fig. 21), on-line monitoring of the forces in wheel-rail contact and their ratio *Y*/*Q*, on-line monitoring of the temperature in axle-box bearings, as well as on-line monitoring of tracks condition.

In this way, it is possible to detect a malfunction immediately after its occurrence and to prevent an accident by reacting reacting in time. The research of these and similar scientific tasks has been facilitated by the development of laboratories such as Laboratory for railway vehicles and structures testing at Faculty of Mechanical and Civil Engineering in Kraljevo.

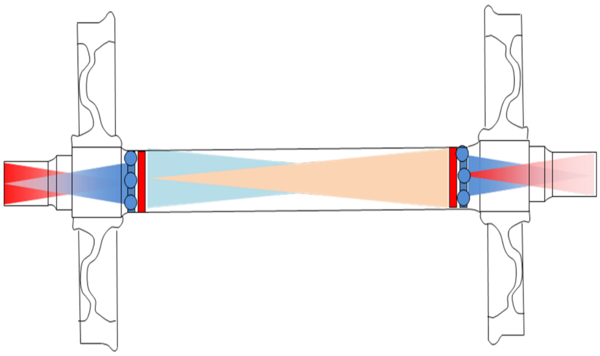

Figure 21: On-line monitoring of wheelset

Further development of this and similar laboratories will contribute to the achievement of the stated goals. The importance of the development of the laboratory is also reflected in the improvement of cooperation between the Center for railway vehicles and structures testing at Faculty of Mechanical and Civil Engineering in Kraljevo with renowned international and domestic institutions and scientists from this field.

ACKNOWLEDGEMENTS

The authors are grateful to the Ministry of Science, Technological Development and Innovation of the Republic of Serbia for support (contract no. 451-03-47/2023-01/200108).

REFERENCES

[1] http://www.mfkv.kg.ac.rs/service/pages/tenders.php, in Serbian

[2] FP-7 Project SeRViCe, Grant agreement no.: 206929, Info day 2, 29/03/2010, Hotel ''Vila Aleksandar'' Vrnjacka Banja, Serbia, in Serbian

[3] D. Petrovic, A. Babic, M. Bizic, M. Djelosevic, Measuring equipment for dynamic and quasistatic testing of railway vehicles, Proceedings of the Scientific-Expert Conference on Railways – RAILCON 10, 07-08 October 2010, Nis, Serbia, pp. 177-180, ISBN 978-86-6055-007-3

[4] R. Rakanović, D. Petrović, Z. Šoškić, T. Simović, Ispitivanje mašinskih konstrukcija, Faculty of Mechanical Engineering in Kraljevo, 2006., ISBN: 86-82631-30-X, in Serbian

[5] International standard UIC 518, Testing and approval of railway vehicles from the point of view of their dynamic behavior - safety - track fatigue - ride quality, 4th Edition, 2009.

[6] International standard UIC 530-2, Wagons - running safety, 7th Edition, 2011.

Challenges for technical specifications for interoperability (TSI) in the European Union (EU)

Miltcho Lepoev
Faculty of Transportation Engineering, Railway Construction,University of Architecture, Civil Engineering and Geodesy, 1 Hristo Smirnenski Blvd., 1146, Sofia (Bulgaria)

All countries in the EU when designing in different phases - conceptual, technical and working design, as well as during the construction and control of the linear projects of the railway infrastructure of the Republic of Bulgaria, need to comply with the recommended nature of the TSI for the various subsystems. The publication analyses the problems related to the application of TSI with a view to convergence with the national experience of the Republic of Bulgaria, and the author offers options for solving open questions and specific discussion questions related to TSI, as well as issues related to the constituent elements of interoperability and communication technologies.

Keywords: TSI, interoperability, national experience, convergence

1. INTRODUCTION

The acceptance of the Republic of Bulgaria into the European Union requires ensuring the compatibility of the Bulgarian transport system with the other systems of the member states, introducing and confirming the European standards for modern, ecological and safe transport, as well as actions to harmonize the Bulgarian legislation with the European one. Directive 2008/57/EC of the European Parliament and the Council of 17 June 2008 [1] on the interoperability of the railway system within the Community defines the conditions that must be met to achieve interoperability within the railway system of the community. These conditions address various aspects of the railway system and facilities, contact network, signaling and telecommunications, rolling stock, operation and traffic management, telematics applications. Rules have been created that relate to the design, construction, commissioning, expansion, renovation, operation and maintenance of parts of the systems, the conditions for safety and health protection of personnel.

Directive 2008/57/EC[1] adopted technical specifications for interoperability (TSIs) to which each subsystem or part of a subsystem must comply in order to satisfy the essential requirements and ensure interoperability.

2. CHALLENGES IN IMPLEMENTATION OF TSI IN BULGARIA

The application of TSIs in the Republic of Bulgaria is applicable to all projects from the main and wide-ranging network of the European Union on the territory of the country. A number of commissioning permits have already been issued under Ordinance 57[2], which transposes the rules of Directive 2008/57/EC in Bulgaria. However, there are a number of issues to be resolved such as the integration of the Bulgarian norms with the TSIs [3],[5], improvement of the interface between the individual structural subsystems and other issues [4], [6] and also some special themes connected with design strengthening and evaluation of transport facilities [12], [13], [14], [15].

3. CHALLENGES IN THE CONVERGENCE OF TECHNICAL SOLUTIONS

The legal framework and operating principles related to railways in the European Union are partly European. Until the end of 2014, technical specifications for interoperability (TSIs) were dedicated only to the Trans-European Transport Network (TEN-T), which in the case of the Republic of Bulgaria is a minor part of the railway network. Most investment projects started after Bulgaria's accession to the European Union and will be completed and will be completed according to the previous rules thanks to the transitional provisions. Therefore, the European rules for the rail system are not applicable to the entire network. They are fully applicable in the case of railway modernization projects started after 1 January 2015 and in cases where rolling stock is purchased after that date. Under operating conditions, it is necessary to note that trains cannot be divided into those that run only on the trans-European transport network and those that run only outside this network. Interoperable trains must be compatible with existing infrastructure. Therefore, infrastructure modernization projects must take into account technical compatibility with existing railway vehicles. A change in technical reality requires investment, and rail investment requires relatively long periods of time. Railway lines are not closed when reconstruction takes place. However, the lines are limited in capacity and have to make more intensive use of other railways to serve the demand and therefore cannot be rehabilitated or modernized at the same time. Safety must be ensured during the transition from interoperability to interoperability in all operating conditions, including reduced operating mode. Maintaining technical compatibility during the transition is also a must.

4. OPEN ISSUES AND SPECIFIC CASES IN TSI

Not everything considered necessary for interoperability has already been agreed. The technical specifications for interoperability indicate some open questions. Not everything that has already been agreed can be implemented at this stage, due to a number of objective reasons. Technical specifications for interoperability concern some specific cases. Open questions are summarized in the specific annexes of the relevant technical specifications for interoperability. The number of open questions is decreasing, but they still remain. If an issue is open in European law, then national rules apply. Some technical solutions are impossible to change for technical or economic reasons for specific Member States. For this purpose, specific classified solutions are described in the relevant technical specifications for interoperability. Some are permanent while others are temporary. For interims, timeframes are given in the Interoperability Technical Specifications.

5. CROSS ACCEPTANCE OF TRAINS

The railway infrastructure, consisting of intermediate stations and stations, dates back to 1866. With the construction of the Ruse-Varna railway. Of course, maintenance works must be carried out, but they do not change the technical characteristics of the infrastructure. Railway trains consist of rolling stock that is designed for a life of about 50 years, but is used for longer.

Getting an answer to the question of the compatibility of existing trains in one country with the infrastructure existing in another neighboring country is now urgent, as trains must move more and more across borders, especially within the European Union. Today, as in the past, many wagons meet international requirements and are suitable for international traffic, very few wagons meet the national requirements of more than one country, and an insignificant number of locomotives and multi-component units are technically compatible with the infrastructure of more than one country. Trains must be compatible with the infrastructure of each railway line on which they are intended to run. When a train is not fully compatible with the infrastructure, its operation may be restricted or even not allowed. Consistency with the adjacent infrastructure of many existing wagons, locomotives and multi-units must therefore be checked. For this purpose, rules for cross-acceptance of rolling stock have been defined. National technical requirements are collected and analyzed to assess their equivalence.

An infrastructure register is formulated and populated with data to ensure easily accessible and complete information about the restrictions imposed by the infrastructure on specific lines and stations [10] A rolling stock register is formulated and populated to check the correspondence between vehicles and infrastructure with data.

6. CROSS-ACCEPTANCE OF COMPETENCES

Cross-acceptance of trains composed of cross-accepted vehicles is not sufficient, as safety also depends on the competence of the staff. Drivers are required to meet health and competency requirements. For this reason, the Technical Specifications for Interoperability describing the technical limitations for infrastructure, traction power, control, management and signaling are supplemented by Technical Specifications for Interoperability describing the operational limitations.

Signaling and operating regulations vary from country to country.

Drivers must pass comprehensive examinations for each country proving their knowledge of signaling and operating rules. They should get route knowledge on each railway line. And last but not least - documents must be obtained proving their competences for each type of vehicle they have to drive. Of course, proof of their health status and language competences are also subject to cross-acceptance.

7. DIFFERENTIATION IN SIGNALING AND TELECOMMUNICATIONS TECHNOLOGIES

All solutions related to signaling, especially interlocks ensuring the safety of trains when crossing stations, interlocking systems ensuring safety when trains move one after the other on railway lines and systems ensuring safety when crossing two levels with other transport elements are directly related to operational rules that are national. The differentiation of signal aspects is only an emanation of deep differences. Changing the signaling rules would be extremely expensive and create an unacceptable safety risk. Moreover, in many cases it is not possible to change the rules of operation without changing the signaling equipment.

There are also Class B and Class A communication systems A European Class A system has already been defined, which is called the Global System for Mobile Communication for Railways GSM-R. Class B systems are primarily intended for voice communication between dispatchers and drivers. GSM-R is intended and used not only for voice communication but also for data transmission to the European Train Control System ETCS [11].

8. DIFFERENTIATION IN CONTROL AND MANAGEMENT TECHNOLOGIES

In addition to signaling, railways use control and management systems. Currently used systems use electronic motion mechanisms. It is not possible to say exactly how many national control and management systems are in use, as some systems have more than one national version and some have many technical variants, e.g. due to the long time they have been developing. National control and command systems are considered Class B, but a Class A system called the European Train Control System ETCS[6] has already been defined. Signaling and operating rules are and will remain differentiated. Alignment takes place at the level of control and management. Using multiple systems during the transition period is not the best way forward in terms of safety and economy.

9. COMPONENT ELEMENTS OF INTEROPERABILITY

Many elements used for infrastructure, traction power supply, control and management, as well as for making rolling stock are treated as products in the common European market and are called interoperability constituents, for example rails, fastening systems, etc. In addition, many products are treated as products in national markets. For example, arrows, interlocks, signals, are national interoperability components (and may be marked as nICs). Once accepted in any EU Member State, the Interoperability Constituents must be accepted unconditionally in all EU Member States. The constituent elements of interoperability are defined functionally. Their interfaces are technically defined. The requirements are included in EU legislation. National interoperability components are functionally defined in national legislation. Certificates and declarations of compliance with interoperability and interoperability are required.

10. CONCLUSION

There is no doubt that the railway lines, part of the transport corridors in the Republic of Bulgaria will be interoperable after modernization within the framework of the projects under operational programs. In rolling stock, new vehicles are usually interoperable. Any delay in the purchase would mean the economic marginalization of railways as a means of transport. That is why rapid changes are needed. Compliance of the existing infrastructure with the technical specifications for interoperability is required based on the data collected for the infrastructure registers. The registers should cover the entire railway infrastructure and all the necessary information. The easy way is to indicate the certificates proving compliance with the technical specifications for interoperability. In practice, different types of constraints must be considered and different types of inconsistencies must be specified. Without infrastructure registers, competition between different rail service providers is not possible. Without a culture of competition within rail transport, we cannot focus on competing with other modes of transport. The registers should cover not only the main railway lines but also the additional tracks and the industrial and logistics centers. Furthermore, the so-called "safety culture" is perceived as an obstacle on the way to an interoperable rail network defined by the Rail Interoperability Directive. Risk and safety measures are defined in a separate rail safety directive. According to this directive six Common Safety Methods (CSMs) are defined.

The common safety methods define the safety certification requirements of railway operators and railway infrastructure managers. General safety methods define safety supervision rules. Last but not least, a separate rule sets out the criteria for risk analysis and assessment and the acceptance criteria. This rule is directly applicable to all safety challenges that arise in the transition from intra-operational national rail systems to a single European interoperable rail system.

Everything said so far will ensure that the transport system of the Republic of Bulgaria occupies a worthy place in a united Europe as a transport corridor connecting Asia and Europe.

ACKNOWLEDGEMENTS

The author expresses his gratitude to the Research, Consultancy and Design Centre (RCDC) in UACEG, Sofia for the financial support under the contract BN-282-23.

REFERENCES

[1] DIRECTIVE 2008/57/EC OF THE EUROPEAN PARLIAMENT AND OF THE COUNCIL of 17 June 2008 on the interoperability of the rail system within the Community

[2] НАРЕДБА 57 от 9.06.2004 г. за постигане на оперативна съвместимост на националната железопътна система с железопътната система в рамките на Европейския съюз (Загл. изм. - ДВ, бр.88 от 2007 г., бр. 84 от 2010 г., бр. 5 от 2012 г.)

[3] Лепоев М., Жеков, В. Хармонизация на националните нормативни документи за проектиране на железен път с изискванията на Регламент 1299/2014.// Механика, Транспорт, Комуникации.- София, 2019, том 17, брой 3, статия № 1848, ISSN 1312-3823 (print), ISSN 2367-6620 (online)

[4] Жеков, В., Атанасов М., Оптимизация на поддържането на железния път чрез използване на изчислителни модели за предвиждане влошаването при експлоатация.// Механика, Транспорт, Комуникации.- София, 2015, том 13, брой 3/3, с.72, ISSN 1312-3823 (print), ISSN 2367-6620 (online)

[5] Жеков, В. Определяне на стойностите на проектната еквивалентна коничност за характерни профили на релсите, използвани в българската железница.// Механика, Транспорт, Комуникации.- София, 2018, том 16, брой 1, статия № 1559, ISSN 1312-3823 (print), ISSN 2367-6620 (online)

[6] Georgiev L., Zhekov V., Determination of a Construction Gauge Allowing The Movement of a Railway Vehicle for Kinematic Gauge GC, Based on National Construction Gauge 1-CM2. AIP Conference Proceedings 2439, 020009 (2021); https://doi.org/10.1063/5.0071089

[7] DIRECTIVE 2004/49/EC OF THE EUROPEAN PARLIAMENT AND OF THE COUNCIL of 29 April 2004 on safety on the Community's railways and amending Council Directive 95/18/EC on the licensing of railway undertakings and Directive 2001 /14/EC on the allocation of railway infrastructure capacity and the levying of charges for the use of railway infrastructure and safety certification

[8] 2010/713/EU: Commission Decision of 9 November 2010 on modules for the procedures for assessment of conformity, suitability for use and EC verification to be used in the technical specifications for interoperability adopted under Directive 2008/57/EC of the European Parliament and of the Council

[9] 2014/897/EU: Commission Recommendation of 5 December 2014 on matters related to the placing in service and use of structural subsystems and vehicles under Directives 2008/57/EC and 2004/49/EC of the European Parliament and of the Council Text with EEA relevance

[10] 2014/881/EU: Commission Recommendation of 18 November 2014 on the procedure for demonstrating the level of compliance of existing railway lines with the basic parameters of the technical specifications for interoperability

[11] Обща· публикация, редактор М. Павлик: „Оперативна съвместимост на железопътната система в ЕС, инфраструктура, сигнализация, подвижен състав" („lnteroperacyjnosc Systemu Kolei Unii Europejskiej, lnfrastruktura, Sterowanie, Energia, Tabor"), Варшава 2015 г., ISBN 978-83-943085-0-6

[12] Nikolova, M., Georgiev, L., "Problems and innovative solutions considering "open type" bridge deck structures in old steel riveted railway bridges", 2018 IOP Conference Series: Materials Science and Engineering; 9th INTERNATIONAL SYMPOSIUM ON STEEL BRIDGES, 10-11 September 2018, Prague; 2018 IOP

Conf. Ser.: Mater. Sci. Eng. 419 012001, https://doi.org/10.1088/1757-899X/419/1/012001

[13] Georgiev L., Ivanov St., “Longitudinal Stability Of Continuous Composite Steel-Concrete Superstructures For Railway Viaducts”, X Jubilee International Scientific Conference „Civil Engineering Design and Construction“ (Science and Practice), Sept. 20-22, 2018, Varna, Bulgaria, ISSN: 2603-4255, ISSN 2683-071X (online), pp.404-411 in BG

[14] Georgiev L., “ANALYSIS OF THE DYNAMIC BEHAVIOR OF HIGH SPEED RAILWAY BRIDGES”, International Conference on CIVIL ENGINEERING DESIGN AND CONSTRUCTION (Science and Practice), 15-17 September 2016, Varna, Bulgaria, ISBN: 978-954-92866-7-0, pp.356-366, 2016 in BG

[15] Jiponov A., Georgiev L., “Reinforced structures type "filler Beam" - Advantages in reconstruction of bridge superstructures”, 2018 IOP Conference Series: Materials Science and Engineering; 9th INTERNATIONAL SYMPOSIUM ON STEEL BRIDGES, 10-11 September 2018, Prague; 2018 IOP Conf. Ser.: Mater. Sci. Eng. 419 012002, https://doi.org/10.1088/1757-899X/419/1/012002, DOI:10.1088/1757-899X/419/1/012002

Determining The Parameters For Performing Public Passenger Rail Transport By The Carriers

Mirena Todorova[1*], Kostadin Trifonov[2]
[1]Transport management,"Todor Kableschkov" University of Transport, Sofia(Bulgaria)
[2]Transport management,"Todor Kableschkov" University of Transport, Sofia(Bulgaria)

Recently there has been a lack of rolling stock in railway transport – locomotives, wagons and railcars, which directly affects the quality and the comfort of passenger service. The delay of trains due to damage of rolling stock leads to a decrease in the number of passengers using railway transport. One of the ways to improve the condition of passenger railway transportation is liberalization of the market through implementation of a procedure under the Public Procurement Act for selection of a carrier. The subject of this study is the conditions for inclusion of new licensed transport companies for public transport. A model has been developed for determining packages of sections on which to carry out transport activity by a certain transport company based on the assessment of transport efficiency on the sections of railway network. The model is applied to the suburban transport of the capital city Sofia and the serviced sections. The obtained results can be used in developing the conditions for the forthcoming tenders for assigning assigning) a contract for provision of public transport services in the field of railway transport in the Republic of Bulgaria.

Keywords: Passenger rail transport, Liberalization, Passenger service

1. INTRODUCTION

The level of liberalization of passenger railway transport market in Europe can be divided into three groups: de jure liberalization, de facto liberalization and a non-liberalized market. De jure liberalization means that the legal system allows open market operations to provide passenger transport services but in fact there is only one traditional local carrier as it is currently in the Republic of Bulgaria.

The passenger railway services provided in Bulgaria are divided into two main segments depending on whether they are subject or not to public service obligations (PSOs). Additional criteria to define these two segments are the communication, routes and categories of trains that serve the routes. According to these criteria, transport is divided into:transport under the PSO Contract (PSOC), which is performed with high-speed trains (interregional) and passenger trains (suburban and regional) [7];

- commercial services – services performed by international trains and high-speed trains with mandatory reservation (Intercity) as well as attraction trains.
- to liberalize the market, it is necessary to carry out a new procedure under the Public Procurement Act for selection of carriers and to work in two directions: inclusion of new transport companies licensed as carriers and meeting the necessary requirements, and timely announced public procurement tenders providing opportunities for servicing certain directions and/or categories of trains.

In this regard, de facto liberalization may be hampered by the following issues that need to be addressed before the tender announcement [1,2]:

- one of the problems that needs to be solved appears from the fact that now all rolling stock, which transport is performed with under the PSO Contract, is owned and operated by the local traditional carrier. This creates difficulties to provide transport under public service contracts because there is no possibility to rent carriages or railcars;
- a year until the term of expiring it has to make clear what conditions the public procurement competition will be held under – by categories, by lines or by packages.

2. OVERVIEW OF REFERENCES

The main problem discussed in references is how to make passenger railway transportation attractive for private carriers applying the policy of open access to the railway market. An example based on the practice in Czech republic is presented in [3]. It was in 2011-2014 when the operation of the rail link between Prague and Ostrava was changed from the performance of only one incumbent operator to assigning services also to two private operators – Regio Jet in September 2011 and LEO Express in January 2013. Competition from open access led to an intense price war with 2nd class fare where the reductions reached 46% and the new operators managed to gain 55% of market share from the traditional operator. All operators are unprofitable on the route, leading to financial stress and accusations of predatory pricing by the incumbent, but service quality on the route was improved significantly with new on board services and higher frequency.

The authors of [4,5] describe the experience of the three most liberalized railways in providing railway passenger services in Europe – Sweden, Germany and Great Britain. They show evidences that competitive tendering has helped to increase demand and reduce subsidies for the rail passenger sector. However, there are also many decisions to be made about how to implement the policy of open access in passenger railway transport. For regional services with small revenues it is good for the contracting authority to lead planning and marketing while

*Corresponding author:M.Todorova, Bulgaria, Sofia, str.Geo Milev 158, mtodorova@vtu.bg

for services where ticket revenue recovers a larger proportion of costs the so called "more commercial services" it is better to advertise auctions. An alternative is to leave management to the incumbent carrier but with open access for competitors to enter the market.

The analysis of the new legal requirements facing public service contracts in rail transport is given in [6]. The book also shows the impact of the fourth rail package on the liberalization process and the EU passenger rail market. The Member States must incorporate the provisions in their national law public service contracts with effect from 2023. Competitive tendering procedures for public procurement of services must be open to all operators, must be fair and respect the principles of transparency and non-discrimination.

As for Bulgaria, it is expected that in 2024 there will be tenders for public service contracts in passenger railway transport. That is why the topic discussed in the paper is about the terms and conditions of the public procurement tender for assigning contracts for passenger transport services [7].

3. FORMATING PAGES DETERMINING THE PARAMETERS FOR PERFORMING PUBLIC PASSENGER TRANSPORT

The steady decline of passenger rail transport for the past few years has been due to the following reasons:

- the lack of sufficient rolling stock of the traditional carrier, which has led to constant delays of trains due to failures before and during the movement and violation of train binding;
- the rolling stock itself is obsolete and cannot provide comfort and hygiene, and does not allow to increase the speed of movement and reduce the travel time of trains.

All this can be solved by involving carriers with modern rolling stock, which will also attract passengers to rail transport. The public procurement competition can be carried out in the following ways:

- by train categories. This way to organize a competition enables any operator to freely perform commercial transport services keeping the following requirements: to possess a License to perform railway transport services and have rolling stock and personnel available to provide transportation. For the rest categories of trains, it is more appropriate to use another way of conducting the competition.
- by lines. The implementation of such a way is not rational, because there are many trains that run on two or more lines, as well as there are deviations where there are a few trains and passengers and it will be difficult to achieve efficiency of passenger transport.
- by packages. Grouping of transportations is performed for several lines, which is especially necessary with suburban transportations of big cities.

To carry out the creation of packages or independent examination of pairs of trains, the following three-step model given in Figure 1 is proposed.

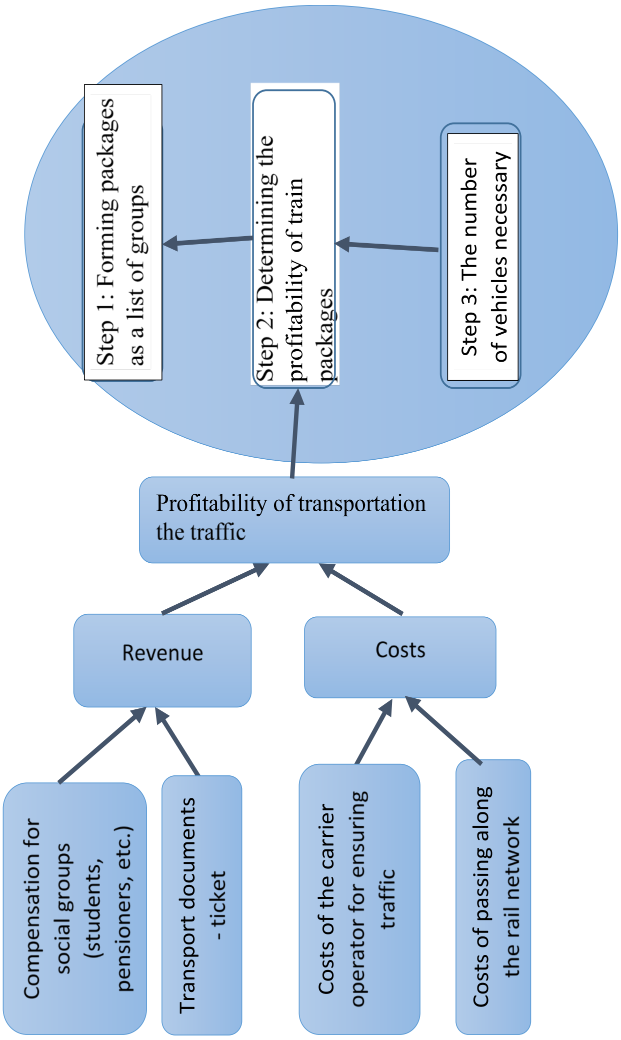

Figure 1: Model

3.1 Step 1: Defining train packages

The grouping of trains must ensure their connection, and a package can include all trains on a given deviation, all suburban trains for a given section/sections or trains of different categories but with a common initial station. For each package, it is necessary to determine the costs of ensuring the train traffic and revenues of transportation in order to determine their profitability. This is necessary because the trains on some of diversions are lightly loaded and fulfil the function of ensuring the mobility of the population in the region and the revenue from the tickets sold cannot cover the costs of ensuring train traffic. Therefore, it is necessary to make combinations of different categories of trains or trains in different time ranges, so that to combine them in a way in order to cover the costs incurred.

3.2 Step 2: Determining the profitability of train packages

For each group it is necessary to determine the costs of ensuring traffic and revenues of transport implementation.

- Costs of ensuring train traffic

Costs of passing along the rail network:

To travel on the rail network, carriers pay infrastructure charges and costs for using electricity supply and traction current delivery equipment. Infrastructure charges are determined depending on the implemented train kilometers and gross ton kilometers, i.e. they depend on the type of rolling stock, the weight of which is constantly decreasing [10].

$$PR_{kj} = \sum_k \sum_j L_{kj}.N_{kj}(r_{thkm} + r_{btkm}.Q_{kj}) \quad (1)$$

where: N_{kj} – the number of trains in the k-th group passing the j-th section

L_{ij} – the length in kilometers of the j-th section along the route of the i-th train;

Q_{ij} – the gross weight in tons of the i-th train for the j-th section;

r_{btkm} – the infrastructure charge per gross tonne kilometre;

r_{btkm} – the infrastructure charge per train kilometre.For each group it is necessary to determine the costs of ensuring traffic and revenues of transport implementation.

- Costs of the carrier for ensuring traffic [11]:

$$C_{car} = (C_{staff} + C_{rol} + C_{energ}).k_{over} \quad (2)$$

where: Cstaff -costs include the provision of transport staff;

C_{rol} – cost by maintenance of rolling stock;

C_{enerkj} – the costs of providing energy;

k_{over} – coefficient of overhead costs.

The transport costs are formed by the labour costs for the engine driver, train master and ticket collector and are calculated by the formula:

$$C_{staffkj} = \sum_k \sum_j (t_{kj}.N_{kj}(r_{ct} + r_{con}.M_{conkj}) + (t_{kj} + t_{prepkj}).N_{kj}.r_{mt}) \quad (3)$$

where: N_{kj} – number of trains running in the k-th group on the j-th section;

r_{ct}– rate (per hour) for the trainmaster, [BGN/h];

r_{con} – rate (per hour) for a ticket collector, [BGN/h];

M_{conkj} – number of ticket collectors in the given train;

t_{prepkj}– additional time for servicing the train by the engine driver;

r_{mt} –rate (per hour) for the engine driver

- The costs for the carriage fleet C_{rol} depend on their technical maintenance, cleaning and the cost of using rolling stock:

$$C_{rollkj} = \sum_k \sum_j (t_{tmkj}.N_{kj}.M_{tmkj} + t_{prepkj}.N_{kj}.M_{mt}) \quad (4)$$

where: t_{tmkj} – time of train servicing by a technician-mechanic wagon inspector (TMWI), [BGN/h];

N_{kj} – number of trains that run in the k-th group on the j-th section;

C_{ct} – rate (hourly) for (TMWI), [BGN/h];

t_{tmkj} – time for cleaning the trains, [BGN/h];

N_{kj} – number of trains running in the k-th group on the j-th section;

C_{ct} – rate (per hour) of cleaner, [BGN/h].

The cost of using rolling stock is calculated based on the contract between the operator and the owner of locomotive fleet. The charge is determined for 1000 gross tonne-kilometers of work performed during the traffic of a given passenger train and the traction rolling stock provided for this purpose: the number of trains in the k-th group passing on the j-th section; the length of the j-th section along the route of the i-th train (in kilometers); gross weight of the i-th train for the j-th section (in tonnes) and rate „r_{rskm}" for 1000 gross ton-kilometers for using rolling stock. These costs are included in the cost of providing energy.

- The costs of providing energy for the train traffic depend on the mileage and the type of traction used:

$$C_{enerkj} = \sum_k \sum_j L_{kj}.N_{kj}.Q_{rolkj}(r_{rskm} + r_{die} + r_{elek}) \quad (5)$$

where: r_{die}– cost rate for diesel traction;

r_{elek}– cost rate for electric traction.

- Revenues from train traffic

The revenues of the carrier are formed from the sale of transport documents and the compensations under the Contract for performance of public transport services. Railway transport provides preferences in the form of discounts for certain social groups: students, senior citizens, mothers with many children, disabled people, war veterans or other persons determined by an act of the Council of Ministers and these preferences are compensated to the carrier by the relevant ministry. The compensation provided in respect of the Contract for the provision of public transport services is different depending on the train category and differs for high-speed and passenger trains, and the rate for the travelled passenger- kilometers is defined every year. The payment of the accepted and approved compensations is made in parts according to the contract and the documents submitted to prove the provided public services. The amounts due to adjustments in compensations shall be paid immediately after specifying their amounts.

$$R = Rtick + Rsoc\ gr \quad (6)$$

where: Rtick – revenue from the sale of vehicle documents;

Rsoc gr – income from compensations for transportation of social groups;

Rnubl – income from compensations for providing public transport services.

Profitability of transportation

In order to ensure interest in performing transportation, it needs to be efficient and only then the package of trains formed in this way will rise interest in private carriers. Therefore, the condition for accepting a given package of trains for liberalization should be:

$$P = R- (PRkj+ Ccar) \quad (7)$$

3.3 Step 3: The number of vehicles necessary to ensure the traffic

From the theory of queuing, it is known that in order for a system to work without failures [11,12], the necessary condition is:

$$N \geq \lambda.\ Tоб \quad (8)$$

Where N is the number of vehicles, and $T_{об}$ is the turnover, which depending on the activity specificity can be determined from the traffic schedule, statistically or calculated in advance.

The minimum number of vehicles N_{min} can be determined from the above expression.

$$Nmin= \lambda . Tоб \tag{9}$$

Where:

$$\lambda = \frac{F_{max} \cdot k_{hi}}{24 . m_p . k_{cu}} \tag{10}$$

F_{max} - passenger flow in the busiest section of the line, in number of passengers per unit of time;

k_{hn} - coefficient of hourly irregularity

m_p - is the estimated passenger capacity in number of passengers per transport means;

k_{uc} - coefficient of using calculated unevenness.

Transports are characterized by their great unevenness. In cases where their volume exceeds the average values, the difference will not be transported and unrealized revenue losses will be incurred. For that reason the fleet in working condition must be larger than the minimum. To determine the reserve coefficient is a complex scientific and practical task. In general, it is calculated by comparing the losses from cargo /passengers/ not carried with the costs of acquiring a unit of rolling stock.

At the last stage it is necessary to take into account the well-known fact that some transport means are in an inoperable condition due to: accidents and incidents; basic and medium repairs and technical inspections. For this reason the actual amount of vehicles that the company must have, called the inventory fleet Ninv, is determined by the formula (11):

$$N_{inv} = \frac{N_{min} \cdot k_p}{k_{re}} \tag{11}$$

where: k_p - reserve coefficient;

k_{re} - readiness coefficient.

$$k_{re} = Tr/T \tag{12}$$

Tr is the time in working condition and T is the total time.

4. CASE STUDY

Let examine 3 sections with suburban traffic around the capital city of Sofia, which are characterized by different sizes of passenger flows and the corresponding service by suburban trains [15]. These sections are Sofia - Pernik, Sofia - Dragoman and Sofia – Bankya, which are shown in Fig.2.

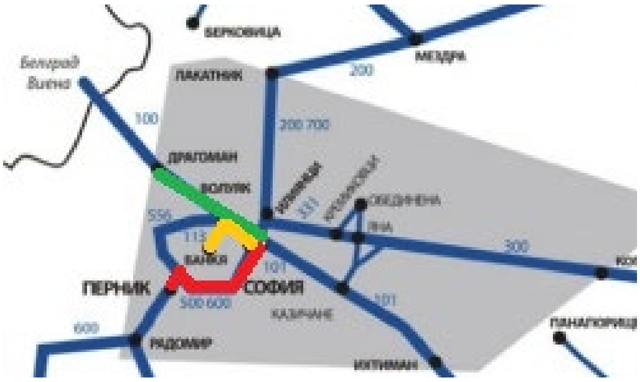

Fig.2 Scheme of the railway network of Sofia junction

Sofia – Pernik section is served by 9 suburban passenger trains running with an average travel time of 49 minutes with a route length of 33 km, and 3 passing conventional passenger trains, i.e. this section is served by 13 passenger trains. The service rolling stock for the section in even and odd directions is implemented with electric railway vehicles and carriages.

The distance from Sofia to Dragoman and back, which is 42 km long, is served by seven pairs of suburban passenger trains with an average travel time of 63 minutes. The rolling stock in even and odd direction is carried out by EMU, DMU and carriages.

Sofia – Bankya section is 19 km long and is served by four trains in both directions. The average travel time is 36.6 minutes and the ticket price is BGN 1.60, the same as the ticket price for using public transport. Commuting rolling stock in even and odd directions is carried out with EMU series 30 and DMU series 10. Since Bankya is a suburb of Sofia, some people who live in this area use railway transport as a city one. In addition to suburban passenger trains, the area is also served with buses operated by the Center of Urban Mobility.

An important factor to determine the costs of transportation is the type of rolling stock [16]. For suburban passenger services, the following are used: EMU series 30.00 and 31.00; DMU series 10.00; carriage composition of B carriages. The rolling stock structure is given in Fig.3.

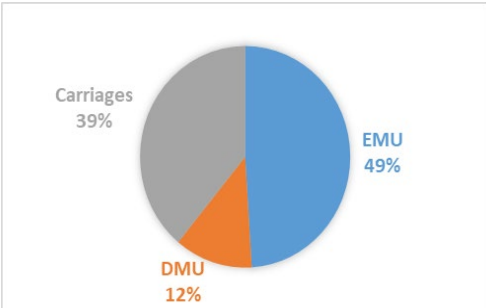

Fig.3 Rolling stock structure of suburban passenger trains in Sofia region

The costs for providing traffic on the sections are also determined using data of the weight of rolling stock, data of the number and mileage of trains, data of various rates of the carrier and infrastructure charges.

A survey on the size of passenger flows and the type of transport documents has been made for six months and it has been found that the issued transport documents are at the regular rate, zone tickets used to attract passengers with a small discount from the regular rate, transport of social groups traveling with a discount of 50 % and subscription cards (Figure 4) [16].

As it can be seen in figure 4 R_{socgr} – income from compensations for transport of social groups – is formed for 37% of commuters using suburban transport.

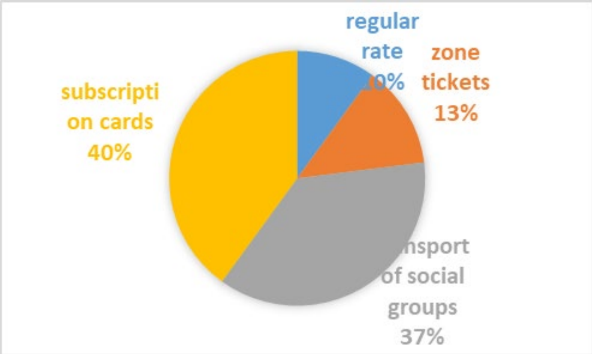

Fig.4 Issued transport documents

We will consider only the traffic of suburban trains and certain parameters according to the proposed model are given in Table 1 where R_{nubl} – income of compensations for providing public transport services – is not included.

Table 1: Rezult of model

Section	Train pairs	Profitability	Number of vehicles N_{min}	Inventory fleet N_{inv}
Sofia – Pernik	12	1 561 677	3	4
Sofia – Dragoman	7	- 699 259	2	3
Sofia – Bankya	4	-455 410	1	2
Package		407 008	6	7

Thus defined groups suburban trains served by a given carrier will bring a profit of BGN 407 008, provided that 10% administrative costs to ensure transport are accepted.

Examining the obtained results, it can be determined that the package of suburban trains with direction Sofia – Pernik – Sofia is profitable and can be included both independently and in a package with other trains (together with suburban trains in the other two sections) in a tender for liberalization of transport. In cases where there are more than one direction or service of trains bound at one starting station, a smaller reserve of carriages or trains will be required to provide traffic. Suburban trains in the other two directions are unprofitable, and if they do not participate in a package with profitable trains, it is better to keep traffic provision under state management and subsidies of government, which has to pay for the public transport services. Thus, by excluding profitable trains (or packages with them), the governmental costs of rail transport provision will be reduced and only transport needed to provide mobility of population in regions with diminishing functions will be operated with public funds.

5. CONCLUSION

The advantage of the considered model is the exact determination of financial profitability of transports for the selected option. Depending on the result, it can be decided:

- to offer participation in a tender for transport liberalization;
- to be included in a package with other transports, thus reducing the size of necessary spare fleet of rolling stock;
- if they do not participate in a package with profitable trains, then ensuring the movement of unprofitable trains should remain in the hands of the State and it should pay as before for the performance of public transport services.

The application of this approach provides a reduction of the governmental costs for providing railway transport excluding the profitable trains (or packages with them) and leaving only those that actually provide mobility of population in the regions with diminishing functions.

The disadvantages of model are: the large preliminary survey on the size of passenger flows and the type of transport documents used as well as the related revenue valuation for a given direction. In this case, it is more difficult to determine passengers using a specific train, especially if season tickets are used.

The new transport companies that will become passenger carriers may be state-owned, state-and-municipal, public-private partnership or private. Regardless of their type, they have to meet the following requirements:

- to possess a License of providing railway transport services;
- to have a Safety Certificate issued by the Executive Director of “Railway Administration” Executive Agency";
- to propose a Technical Offer including availability or concluded contract for provision of the necessary rolling stock and staff to implement [7] the transportation, which it is applied to perform;
- to propose a commercial offer.
- In this regard "de facto" liberalization might be hindered by a number of problems, which must be overcome before the call for tender:
- after the offer announcement, in a three-month period for submitting the application, it is necessary to provide all documents to prove that the applicant meets the special requirements but it is difficult to implement;
- the documents of staff have to refer only to the applicant’s structure and jobs needed but not to the actually existing appointed people. If there are no transports, why is appointed staff necessary for? The decision is to define a longer term from the announcement of competition results to the start of transport implementation in order to be able to appoint the personnel needed;
- another problem that must be solved comes from the fact that now all rolling stock used to implement transportation under the Agreement under the Law of Public Services is owned and operated by the state-owned company for passenger transport. This creates difficulties for providing transport under the public service contract because the applying companies have to provide the necessary rolling stock;

- a year before the term expires it must be cleared what conditions will be applied for the competition of procurement – by categories, lines, packages or generally by categories.

The preliminary calculations made according to the described model can help to determine the way of providing transportation for individual trains, groups or packages of trains.

ACKNOWLEDGEMENTS

This research was supported by the “Todor Kableschkov” University of Transport, Department of Transportation Technology, Organization and Management.

REFERENCES

[1] K.Trifonov, European railway passenger transport and the level of liberalization, Mechanics Transport Communications, Academic journal, 2019, vol.2, art. ID:1787

[2] M.Тодорова, Monitoring on rail transport condition in eastern European countries, Mechanics Transport Communications, Academic journal, ISSN:1312- 3823, No 3/2015,статия ID 1154, Sofia, 2015 г. , https://mtcaj.com/library/1154.pdf

[3] Z. Tomeš et al. Open access passenger rail competition in the Czech Republic, Volume 47, April 2016, Pages 203-211, https://doi.org/10.1016/j.tranpol.2016.02.003

[4] K.Nash, A. Smith orcid.org/0000-0003-3668-5593, Crozet, Y et al. (2 more authors) (2019) How to liberalise rail passenger services? Lessons from European experience. Transport Policy, 79. pp. 11-20. ISSN 0967-070X , https://doi.org/10.1016/j.tranpol.2019.03.011

[5] C.Nash, European Rail Reform-The Next Steps, University of Leeds, 2014

[6] J. Guillen, The liberalisation of the European Union passenger rail market: New challenges for future public service contracts, Competition and Regulation in Network Industries 2022, Vol. 23(1) 60–76, https://doi.org/10.1177/17835917221087167

[7] „ ORDINANCE on the assignment and implementation of obligations for performance of public transport services in railway transport", https://www.lex.bg/laws/ldoc/- 548927998

[8] St. Spahiev, Arguments for and against liberalization, Mechanics Transport Communications, Academic journal, 2022, vol.1, art. ID:2210

[9] REGULATION (EC) No 1370/2007 OF THE EUROPEAN PARLIAMENT AND OF THE COUNCIL of 23 October 2007 on public passenger transport services by rail and by road and repealing Council Regulations (EEC) No 1191/69 and No 1107/, https://eur-lex.europa.eu/legal-content/bg/TXT/?uri=CELEX%3A32007R1370

[10] M.Todorova, Infrastructure charges in new EU member states, 23nd International Symposium EURO - Zel 2015 "Recent Challenges for European Railways", 2rd – 3h June 2015, Žilina (Slovak Republic), ISBN 978-80-263-0936-9.

[11] T. Razmov, T. Kirchev, Determination of normative duration of accidental movement interruption based on costs optimization, Mechanics Transport Communications, Academic journal, 2018, vol.3, art. ID:1599

[12] JDC Little, A proof for the queuing formula, Case Institute of Technology, Cleveland, Ohio*, 1960

[13] M El-Taha, M Stidham, S Stidham Jr, Sample-path analysis of queueing systems, book, 1999

[14] Market Monitoring, Independent Regulators’ Group – Rail, https://www.irg-rail.eu/irg/about-irg-rail/general-information/1,About-the-IRG-Rail.html

[15] www.nkgi.bg

[16] www.bdz.bg

Possibility of replacing low-carbon structural steel with high-strength steels, for producing welded structures in industry of heavy machines

Djordje Ivković[1,*], Dušan Arsić[1], Radun Vulović[2], Vukić Lazić[1], Aleksandar Sedmak[3], Srbislav Aleksandrović[1], Milan Đorđević[4]

[1]Faculty of Engineering, Univesity of Kragujevac, Serbia.

[2]Institute for Information Technologies Kragujevac, Serbia

[3]Faculty of Mechanical Engineering, University of Belgrade, Serbia

[4]Faculty of Technical Sciences, Kosovska Mitrovica, Serbia

Modern trends of research and development of new products are focused on saving materials through mass reduction of various parts, so the high-strength steels (HSS) are used more often than conventional low-carbon structural steels. It is well known that high strength of HSS is providing a possibility for parts to be produced with smaller dimensions and cross-sections. This often results in decreasing in weight of parts and whole structures. In this paper possibility for replacing commonly used, low-carbon, structural steels which have good weldability, with HSS, in industry of heavy machines is analysed. Main goal of this replacement is weight reduction as well as to keep adequate load capacity and reliability of parts and structures. Properties of three structural steels were analysed: Č0562 (S355J0), ČRO460 (P460NL1) and STRENX 700 (S690QL). Furthermore, both advantages and disadvantages of HSS application, complexity of choosing the correct welding method, correct filler materials and favourable welding technology are indicated. After the trial welding on samples, experimental investigation of important mechanical and microstructural properties such as strength, plasticity, impact toughness, hardness and microstructure evaluation were conducted. Based on the obtained experimental results the specific conclusions were given.

Keywords: Welding, Structural steel, High Strength Steel, Mechanical Properties, Microstructure

1. INTRODUCTION

As the trends in modern industry are focused on material saving, lowering energy (fuel) consumption, emissions of CO_2 and etc. to achieve this, several separate or one single solution could be applied. That single solution is downgauging through application of high-strength steel (HSS), instead of commonly used low-carbon structural steel. HSS have great strength values and allow parts and structures cross-sections to be smaller, which results in lower weight of part or structure. Thus, achieved lower weight of parts and structures reduces fuel and energy consumption and in some cases due to application of stronger material structures can withstand greater loads.

When changing materials due to complex production procedure of HSS, great attention needs to be paid especially when selecting most appropriate welding technology. Consequently, to achieve full benefits of HSS application, this problem needs specific approach, as to one complex technical and technological problem.

In this paper possibility for replacing low carbon structural steel with high-strength steels Č0562/S355JR, ČRO460/S460N and S690QL, their advantages and disadvantages were analysed, as well as favourable welding technologies for the mentioned steels were selected.

2. BASE MATERIALS

2.1. Chemical composition and mechanical properties of steel Č0562/S355JR

Steel Č0562/S355JR belongs to the group of C-Mn structural steels. Because yield stress values are greater than 360 MPa, it belongs to HSS. Due to low carbon content it has good weldability and formability and it is often used in production of welded structures. Chemical composition and mechanical properties of this steel are shown in table 1 and table 2 [1].

2.2. Chemical composition and mechanical properties of steel ČRO460/S460N

Steel ČRO460/S460N belongs to group of fine-grain HSS. Its main purpose is production responsible structures. In table 3 and table 4 chemical composition and mechanical properties are displayed [1].

2.3. Chemical composition and mechanical properties of steel STRENX 700/S690QL

Production of S690QL steel is achieved with strict chemical content and complex production procedures. Consequently its strength is greater than strength of many usually applied steels. Two separate grades of this steel could be identified, one for welded structures production and the other intended for manufacturing pressurised vessels. In the table 5 and table 6 chemical composition and mechanical properties are shown [2, 3].

Table 1 [1]: Chemical composition of steel Č0562/S355JR

Steel	Chemical composition, %										
	C	Mn	Si	P_{max}	S_{max}	Cr_{max}	Ni	Al	Cu_{max}	Ti_{max}	Nb_{max}
Č0562/S355JR	0.11	1.2	0.118	0.016	0.008	0.02	0.02	0.052	0.02	0.013	0.04

*Corresponding author: Sestre Janjić br. 6, 34000 Kragujevac, Serbia, djordje.ivkovic@fink.rs

Table 2 [1]: Mechanical properties of steel Č0562/S355JR

Steel	R_m, MPa	R_{eh}, MPa	A_5,%	$KCV_{0°C}$, J
Č0562/S355JR	512	439	25	168

Table 3 [1]: Chemical composition of steel Č0562/S355JR

Steel	Chemical composition, %								
ČRO460/S460N	C	Mn	Si	P_{max}	S_{max}	Cr_{max}	Ni	Mo_{max}	Al
	0.20	1.52	0.41	0.008	0.001	0.13	0.47	0.02	0.02
	Cu_{max}	Sn_{max}	V	Ti_{max}	Nb_{max}	As_{max}	Sb_{max}	Co_{max}	Pb_{max}
	0.18	0.014	0.111	0.0029	0.002	0.009	0.001	0.001	0.001

Table 4 [1]: Mechanical properties of steel ČRO460/S460N

Steel	R_m, MPa	R_{eH}, MPa	A_5,%	Z, %	$KCV_{-40°C}$, J	$KCV_{-30°C}$, J	HV
ČRO460/S460N	725	473	19.2	38.0	32-35	42-45	207-210

Table 5[2,3]: Chemical composition of steel STRENGTH 700/S690QL

Steel	Chemical composition, %													
S690QL	C	Mn	Si	P	S	Cr	Mo	Ni	V	Al	B	Cu	Ti	N	Nb
	0.2	1.5	0.6	0.02	0.01	0.7	0.7	2.0	0.09	0.015	0.005	0.3	0.04	0.01	0.04

Table 6 [2,3]: Mechanical properties of steel STRENGTH 700/S690QL

Steel	R_m, MPa	R_{eH}, MPa	A_5,%	Tvrdoća HBW	$KCV_{-40°C}$, J
S690QL	770-940	700	14	260-310	30

3. WELDABILITY ASSESSMENT OF HIGH STRENGTH STEELS

Selection of the favourable welding technology requires a special approach as well as gathering as much information about the base materials (BM) as possible. Having great amounts of data allows greater perspective to be seen, such as material behaviour in various conditions. Except chemical composition and mechanical properties, in this particular case ability of BM to form welded joints (weldability) needs to be known. Weldability of steels can be estimated in many different ways, but in this paper analytic/computational methods have been applied. Following criterions were used: CE, CET, CEV, P_{hp} (Czech authors) and P_C (Japanese authors) [4].

Weldability assessment by CE (Carbon Equivalent) criterion is conducted using special equations according to type of steel which weldability needs to be assessed. For weldability assessment of steel Č0562/S355JR equation 1 is applied. If the calculated value of CE exceeds 0.45, analysed steel is prone to cold cracking and it can be welded only by applying additional steps and measures [5].

$$CE=C+\frac{Mn}{6}+\frac{Cr+Mo+V}{5}+\frac{Ni+Cu}{15} \quad (1)$$

For weldability assessment of steel ČRO460/S460N equation 2 is applied. For this steel critical value of CE is 0.35. If the calculated value is exceeded, additional steps and measures need to be taken during welding procedues [4].

$$CE=C+\frac{Mn}{10}+\frac{V}{3}+3\cdot N \quad (2)$$

For weldability assessment of steel STRENX 700/S690QL by CE, usually applied equations for CE calculation couldn't be applied, instead CEV (equation 3) and CET (equation 4) equations were used [2].

$$CEV=C+\frac{Mn}{6}+\frac{Cr+Mo+V}{5}+\frac{Ni+Cu}{15},\% \quad (3)$$

$$CET=C+\frac{Mn+Mo}{10}+\frac{Cr+Cu}{20}+\frac{Ni}{40},\% \quad (4)$$

For determining cold crack proneness, equations of Czech and Japanese authors were used. This equations beside chemical composition take into consideration the influence of thickness of welded parts as well as amount of diffused hydrogen, that could be brought in welded joints from filler materials (FM). Equations of Czech authors have the following form [5]:

$$P_{hp}=P_{CM}+\frac{K}{40000}+0.015\cdot log\frac{H}{2.77}, \quad za \quad K\leq 1300 \text{ and} \quad (5)$$

$$P_{hp}=P_{CM}+\frac{K}{40000}+0.075\cdot log\frac{H}{2.77}, \quad za \quad K>1300\,, \quad (6)$$

where:

$$P_{CM}=C+\frac{Si}{30}+\frac{Mn+Cu+Cr}{20}+\frac{Ni}{60}+\frac{Mo+V}{15}+5\cdot B, \quad (7)$$

s – parts thickness *mm*,
H – ammount of diffused hydorgen, *ml*/100 *g* welded joint,
K = 69·s – Stiffness, *N*/*mm*

Japanese authors formula for assessing cold crack pronenes have the following form:

$$P_C=P_{cM}+\frac{s}{600}+\frac{H}{60}, \quad (9)$$

$$P_W=P_{cM}+\frac{K}{40\cdot 10^4}+\frac{H}{60}, \quad (10)$$

where:

$$P_{CM}=C+\frac{Si}{30}+\frac{Mn+Cu+Cr}{20}+\frac{Ni}{60}+\frac{Mo}{15}+\frac{V}{10}+5\cdot B,\ \%, \quad (11)$$

s – parts thickness *mm*,
H – ammount of diffused hydorgen, *ml*/100 *g* welded joint,
K = 69·s – Stiffness, *N*/*mm*

3.1. Weldability assessment results

As results of replacing numbers in previous formulas, weldability was graded (Table 7).

Analysing displayed results it can be concluded that two out of three analysed steels need additional steps and measures to be taken during their welding procedure, due to their proneness to cold cracks.

.

Table 7 [1, 2]: Computational wledability assessment grades for analysed steels

Criterion	Designation	Calculated value for steel			Condition for welding without preheating	Preheating required		
		Č0562	ĆRO460	S690QL		Č0562	ČRO0460	S690QL
CE	CE	0.315	-	-	CE< 0.35	No	-	-
		-	0.392	-	CE< 0.45	-	Yes	-
CET	CET	-	-	0.32	-	-	-	-
CEV	CEV	-	-	0.48	-	-	-	-
Czech authors	P_{hp}	0.202	0.357	0.484	P_{hp} <0.24	No	Yes	Yes
Japanese authors	P_C	0.251	0.405	0.529	P_C<0.30	No	Yes	Yes

Based on weldability assessment results it can be concluded that for welding steels ČRO460/S460N and STRENX 700/S690QL preheating of welded parts is needed.

Preheating as well as other additional steps and measures taken during welding procedures represent additional costs, therefore an in depth economic viability analysis needs to be conducted to determine if those additional steps and measures are economically justified when compared to achieved properties [1].

For welding steel ČRO460/S460N preheating temperature was calculated using equation 12. Based on results preheating temperature of 265°C was adopted [1]:

$$T_p=1600\cdot P_{hp}-308,\ °C. \qquad (12)$$

Preheating temperature for steel STRENX 700/S690QL is adopted from recommended temperature interval 150-200°C so that no alteration of mechanical properties could occur due to high preheating temperature [2].

If welding for this two steels is done without preheating, there is great probability of cold crack formation. Their appearance isn't allowed in any structure type, specially in the responsible ones [4].

4. SELECTION OF MOST APPROPRIATE WELDING TECHNOLOGY

For reviewed HSS steels favourable welding technology needs to be selected. As the first step in the procedure, FM and methods were selected. As mentioned before, because steels ČRO460/S460N and STRENX700/S690QL are prone to cold cracking, preheating needs to be done. Based on selected FM welding parameters were selected and welding tests on steel plates were performed.

4.1. Selection of most favourable welding technology for Č0562/S355JR

For steel Č0562/S355JR GMAW procedure was selected. As a FM, VAC 60 (EN ISO 636-A:W 42 5 W3Si1) electrode wire with diameter 1.2 mm was selected, due to similar mechanical properties with base material. Chemical composition and mechanical properties of VAC 60 are given in tables 8 and 9. When welding Č0562/S355JR preheating is not required, because this steel is not prone to cold cracking. Trial welding was performed on 10 mm thick plates using parameters given in table 10. [1].

Table 8 [1,5]: Chemical composition of electrode wire VAC 60

FM		Chemical composition, %		
Commercial	EN ISO	C	Si	Mn
VAC 60	W 42 5 W3Si1	0.1	0.9	1.5

Table 9 [1,5]: Mechanical properties of electrode wire VAC 60

FM		R_m, MPa	R_{eH}, MPa	A_5, %	KV, J
Commercial	EN ISO				
VAC 60	W 42 5 W3Si1	510-590	410-490	22-30	80-125

Table 10 [1]: Welding parameters for electrode wire VAC 60

Base material thickness, mm	FM	Preheating temperature, °C	Electrode wire diameter, mm	Current, A	Voltage, V	Welding speed, cm/s	Drive energy, J/cm	Shielding gas	Shielding gas flow, l/min
10	VAC60 (MMAW)	0	1.2	170-200	25.9-26.3	0.281-0.456	8207-15911	CO_2	18-20

4.2. Selection of most favourable welding technology for ČRO460/S460N

Welding trials for ČRO460/S460N were performed using metal manual arc welding (MMAW) with prior preheating to 265°C of the parts to avoid formation of cold cracks. As FM electrode GALEB 70 (EN ISO 2560-A: E 50 2 Mn1Ni B 42 H5) was used, and thickness of base material was 20 mm. In the tables 11 and 12 chemical composition, mechanical properties, as well as welding parameters are shown [1].

Table 11 [1,5]: Chemical composition of filler material GALEB 70

FM		Chemical composition, %				
Commercial	EN ISO	C	Si	Mn	Ni	Mo
GALEB 70	E 50 2 Mn1Ni B 42 H5	0.1	0.9	1.5	0.7	0.2

Table 12 [1,5]: Mechanical properties of GALEB 70

FM		R_m, MPa	R_{eH}, MPa	A_5, %	KV, J
Commercial	EN ISO				
GALEB 70	E 50 2 Mn1Ni B 42 H5	640-710	520-600	22-26	125-155

Table 13 [1]: Welding parameters for GALEB 70

Base material thickness, mm	FM	Prehaeating temperature, °C	Electrode core diameter, mm	Current, A	Voltage, V	Welding speed, cm/s	Drive energy, J/cm
20	GALEB 70 (MMAW)	265	2.5-3.25	90-130	23-25	0.146-0.38	6958-17808

4.3. Selection of most favourable welding technology for S690QL

Due to proneness of steel STRENX 700/S690QL to form cold cracks, when welding this steel, parts need to be preheated, heated during the welding procedure and tempered (150-200°C) after welding procedure is finished. This additional heat treatment steps are performed to reduce probability of cold cracks to form [2-4].

Except additional heat treatment, when welding STRENX 700/S690QL grade of steel, special filler materials need to be applied. For root welding procedure of thicker parts made from this steel, special austenitic filler material needs to be used. Main reason for that is the ability of this FM type to reduce amount of residual stress caused by heat inputted welding procedure and to improve plasticity and impact toughness of the welded joint [6]. In this particular case, for root welding, MMAW procedure was performed using filler material INOX B 18/8/6 (EN ISO 3581-A: E 18 8 Mn B 22). The rest of welded joint was filled using GMAW procedure and filler material MIG 75 (EN 12 534: Mn3Ni1CrMo). This FM application is intended for welding fine-grain HSS [6]. Test welding was done using mentioned FM on 15 mm thick steel plates. Chemical composition, mechanical properties and welding parameters of test welding are displayed in table 14, table 15 and table 16.

Table 14 [2,6]: Chemical composition of INOX B 18/8/6 and MIG 75

FM		Chemical composition, %					
Commercial	EN ISO	C	Si	Mn	Cr	Ni	Mo
INOX B 18/8/6	E 18 8 Mn B 22	0.12	0.8	7	19	9	-
MIG 75	Mn3Ni1CrMo	0.6	0.6	1.7	0.25	1.5	0.5

Table 15 [2,6]: Mechanical properties of INOX B 18/8/6 and MIG 75

FM		R_m, MPa	R_{eH}, MPa	A_5, %	KV, J
Commercial	EN ISO				
INOX B 18/8/6	E 18 8 Mn B 22	590-690	>350	>40	>80 (+20°C)
MIG 75	Mn3Ni1CrMo	770-940	>690	>17	>47 (-40°C)

Table 16 [2]:Welding parameters for INOX B 18/8/6 and MIG 75

Base material thickness, mm	FM	Diameter, mm	Preheating temperature, °C	Current, A	Voltage, V	Welding speed cm/s	Drive energy, J/cm	Shielding gas	Shielding gas flow, l/min
15	INOX B 18/8/6 (MMAW)	3.25	140-150	120	24.5	0.2	12000	-	-
	MIG 75 (GMAW)	1.2		240-250	25	0.35	14885	82% Ar+ 18% CO_2	14

5. WELDING OF EXPERIMENTAL SAMPLES AND TESTS

Test welding of steel plates was performed according to previously described technologies. Welding of steel Č0562/S355JR was concluded withouth any additional heat treatment step (preheating, tempering) [1].

Due to cold crack pronneness steel plates from ČRO460/S460N according to weldabillity assessment need to be preheated to 265°C [1].

Additional heat treatment steps need to be applied when welding S690QL, as well. In this case except preheating (140-150°C), an interpass temperature of 200°C was defined [2]. After test welding, steel plates were inserted in furnace to slowly cool down [5].

From test welded steel plates, samples for following tests were prepared: tensile testing, measuring of impact toughness, hardness measurements and metallographic tests of specific areas of the welded joints.

For tensile test, prismatic samples with parallel sides were prepared from Č0562/S355JR and ČRO460/S460N and for steel STRENX 700/S690QL cylindrical samples were prepared.

For impact toughness measurements samples with V-cut were prepared, according to standard EN 10045-1**.** Two types of samples were prepared, one from base material, and the other from the welded joints, with the cut positioned in the middle of the welded bead.

5.1. Experimental tests of Č0562/S355JR

Total of 6 samples were prepared for tensile tests, three out of base material and three out of welded samples. Dimensions of the samples is displayed on Figure 1, and prepared samples on Figure 2. On Figure 3 tensile test results are displayed. According to SRPS C.T3. 051 strength of welded joints was reduced by 7.4% [2].

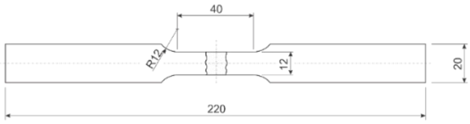

Figure 1[1]: Display of tensile test sample dimensions


a) b)

Figure 2 [1] Prepared samples for tensile test BM a) and welded joint b)

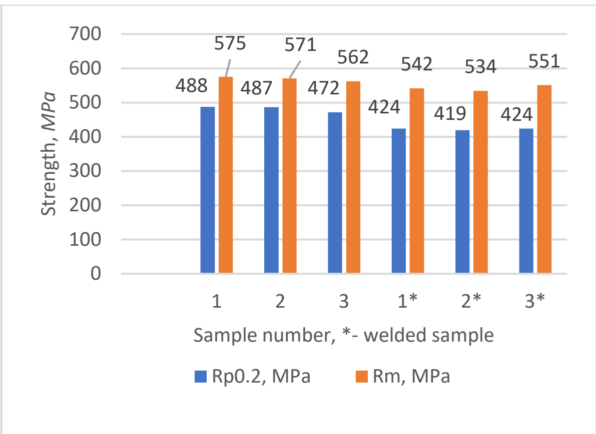

Figure 3 [1]: Results obtained by tensile test

Analysis of tensile test results shows that strength of welded joints is slightly lower than strength of BM, thus conclusion can be made that implemented welding technology according to tensile test result is favourable.

Impact toughness test was performed on six V-cut joint samples, three made out of base material and three out of welded. Samples made from welded steel plates were machined so that V-cut is positioned in the middle of the welded joint. Dimensions of prepared samples are displayed on Figure 4, real samples are shown on Figure 5 and results of impact toughness are shown in table 17 [1].

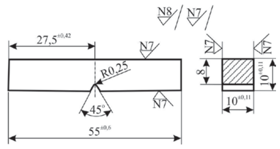

Figure 4 [2]: Appearance of toughness sample dimensions


a) b)

Figure 5 [1]: Display of prepared samples BM a) welded steel plate b) [1]

Table 17 [1]: Impact toughness test results [1]

Cut	BM			Middle of welded bead		
Sketch	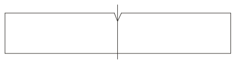			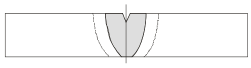		
No.	1	2	3	1	2	3
KV_2, J/cm^2	202	197	216	134	172	191

According to obtained results, welded samples have lower toughness values, but results imply that no formation of brittle structures occured, so the followed welding procedure is favourable.

Hardness measurement was performed as well, in two directions. Both directions were paralel to top and bottom surfaces. First direction was located slightly bellow the top, and the second was located slightly above the bottom sruface (across the root weld). Measured values (Figure 6) are far lower than 350HV so it can be concluded that no brittlement had occured due to heat input during the welding procedure.

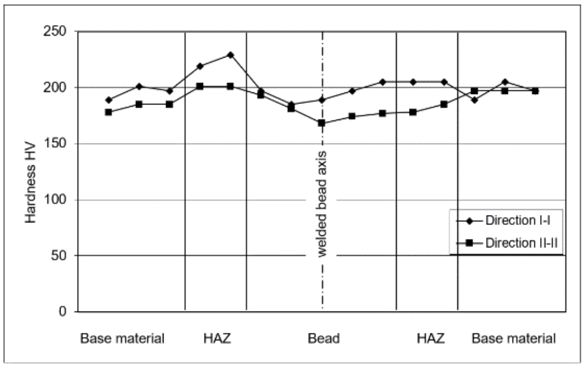

Figure 6 [1]: Hardness measurments in welded joint

On appropriate selection of welding technology, and non-existence of brittle phases/structures imply the metallographic examination of welded samples (Figure 7). Observed microstructures in BM and HAZ show fine-grain ferrite-pearlitic, and in welded bead zone Widmanstätten's microstructures is achived.

a) b) c)

Figure 7 [1]: Observed microstructures in BM a) HAZ b) welded bead c) of steel Č0562/S355JR at zoom 200x

5.2. Experimental tests of ČRO460/S460N

In this case six samples were prepared as well, three from BM and three from welded steel plates. Geometry of prepared samples is shown on Figure 8, and prepared samples on Figure 9. Results obtained during the tensile test are displayed on Figure 10.

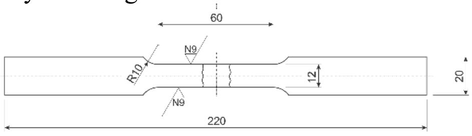

Figure 8 [1]: Display of tensile test dimensions

a) b)

Figure 9 [1]: Display of prepared samples

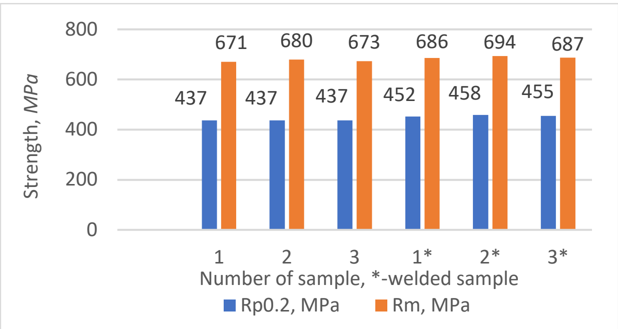

Figure 10 [1]: Results obtained by tensile test

Obtained results show that welding technology is appropriately selected due to strength values of welded samples is higher than strength of BM.

As in previous case six samples for impact toughness measurements were prepared. Results in table 18 show that welded samples have greater toughness than samples from BM implying that selected technology is suitable for welding.

Table 18 [1]: Impact toughnes test results [1]

Cut	BM			Middle of welded bead		
Sketch	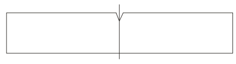			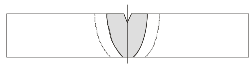		
No.	1	2	3	1	2	3
KV_2, *J/cm²*	129	94	120	228	195	246

Hardness measurements values (Figure 11) are higher compared to the values of the previous steel but, still are bellow 350HV which means that heat inputted during the welding procedure didn't cause martensitic transformation.

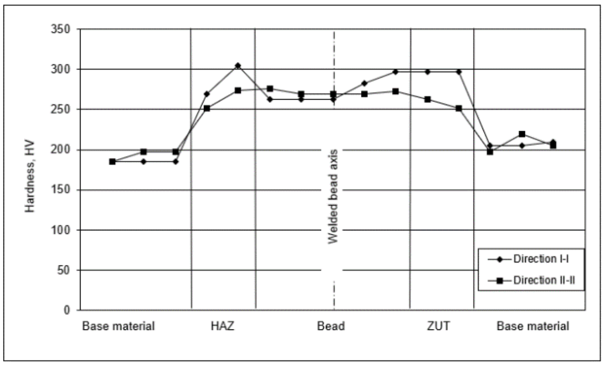

Figure 11 [1]: Hardness measurements in specific areas of welded joint

Metallographic tests were conducted to observe achieved microstructures in important areas of welded joint. In BM and HAZ ferrite-pearlitic microstructure is achieved, and in welded bead Widmanstätten's microstructure was found (Figure 12).

a) b) c)

Figure 12 [1]: Observed microstructures in BM a) HAZ b) welded bead c) of steel ČRO460/S460N at zoom 200x

5.3. Experimental tests of STRENX 700/S690QL

For the tensile test of S690QL total of six cylindrical samples were prepared. Three out of base material, three out of welded samples. Dimensions of used samples are shown on Figure 13 and obtained results are displayed on Figure 14.

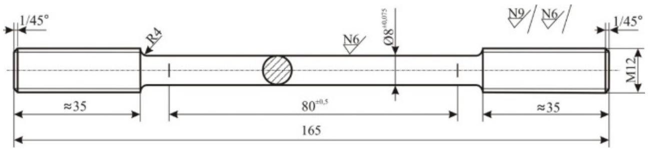

Figure 13 [2]: Display of sample dimensions

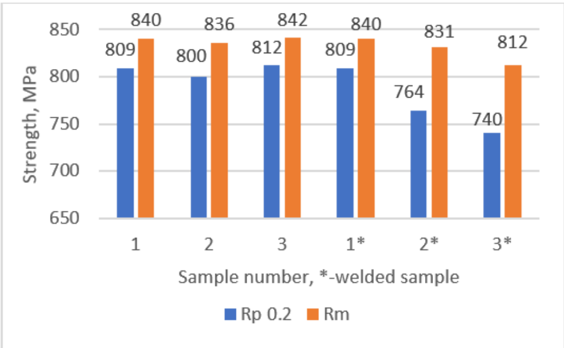

Figure 14 [2]: Results obtained by tensile test

Observing the results of tensile test, it can be notices that R_m values are almost equal, but R_{eH} values of welded samples are lower that values of BM. Even tough there is a slight difference in R_{eH} values it can be concluded that applied technology is favourable.

As in previous cases six samples were prepared, and results of impact toughness measurements, displayed in table 19, are showing great difference between BM and welded samples. This implies on possibility of brittle phases formation.

Table 19 [2]: Impact toughnes test results

Cut	BM			Middle of welded bead		
Sketch	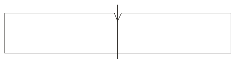			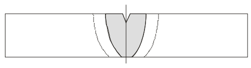		
No.	1	2	3	1	2	3
KV_2, J/cm^2	294	278	293	56	65	59

Hardness measurements results (Figure 15), in certain spots showed values above 350HV which is a sure sign that embrittlement has resulted from inputted heat during test welding. Finally performed metallographic observations in the specific areas of welded joint, show occurrence of tempered martensite and small amount of bainite in BM (Figure 16a). In the HAZ (Figure 16b) fine needle-like martensite with small amount of residual austenite could be observed and in the welded bead (Figure 16c) a tempered martensitic structure with small amount of bainite and pearlite can be observed.

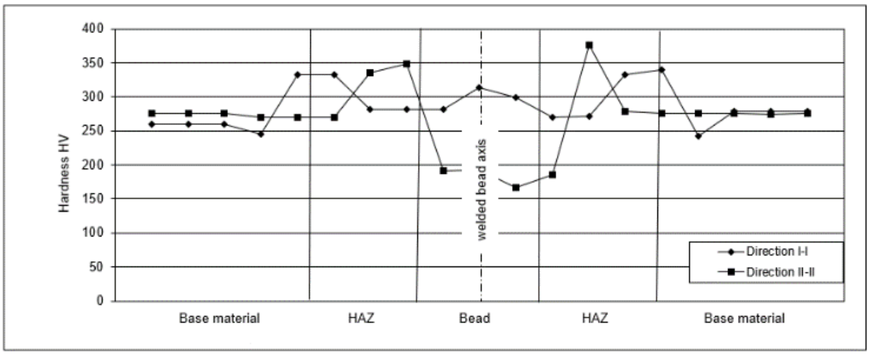

Figure 15 [2]: Hardness measurements in specific areas of welded joint

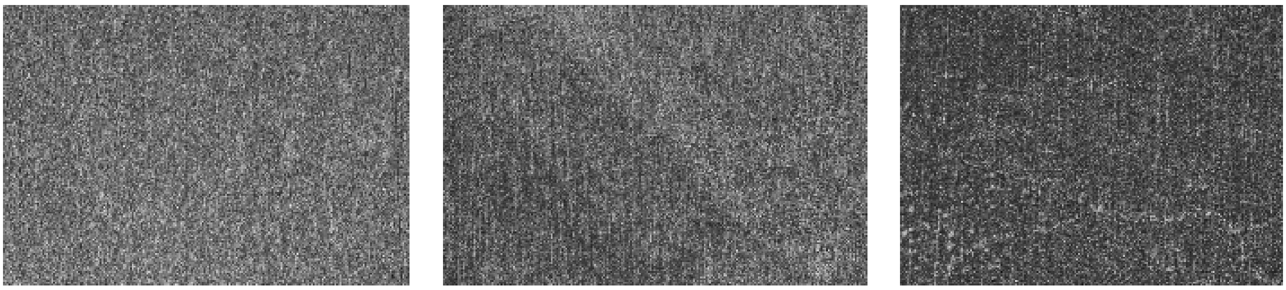

a) b) c)

Figure 16 [2]: Observed microstructures in BM a) HAZ b) welded bead c) of steel S690QL at zoom 200x

6. EFFECT OF REPLACING LOW CARBON STRUCTURAL STEEL WITH HSS

In most equations for determination parts dimensions (cross-sections), materials yield stress value is the most influential criterion. A relation between yield stress value and cross-sections dimensions of parts can be established. For the same load values, higher values of yield stress will result in smaller cross-sections and vice versa, lower yield stress requires cross-sections of parts to be greater so that same load could be withstood. Considering that all steels have same or slightly different density values, for the same length, but different size cross-section, parts will have different weight.

On a theoretical example, weight reduction potential through implementation of HSS instead of regular low-carbon structural S235JR steel will be demonstrated.

In mechanical engineering, steel S235JR is often used for producing wide variety of parts and structures.

Main reason for that is its good weldability, due to low carbon content, and adequate strength values R_m= 360-500 MPa, $R_{p0.2}$=235 MPa. This steel also has significantly lower price in comparison to other structural steels.

Complex structure of railway carriage chassis is made out of steel S235JR which yield strength is 235MPa and it has a certain weight. Implementation of steel with higher strength will result in smaller thickness of parts thus, the chassis will have less weight. As for demonstration purposes of weight saving potential evaluation, yield stress ratios of HSS and used S235JR steel could be observed. This ratio directly shows how many times the structure could be lighter if the HSS were implemented in production of chassis parts. In the table 20

Table 20: Yield stress ratios between HSS and S235JR

Steel	$R_{p0.2}$	$R_{p0.2}^{HSS}/R_{p0.2}^{S235JR}$
S235JR	235	1
S355JR	439	1.86
S460N	473	2.01
S690QL	700	2.97

Observing data from the previous table it could be concluded that implementation of HSS allows substantial weight save to be achieved. For the given theoretical example, using steel Č0562/S355JR instead of S235JR structures can be 1.86 times or 46.23% lighter, using ČRO460/S460N structures can be 2.01 times or 50.25% lighter, and using steel STRENX 700/S690QL structures can be lighter up to 2.97 times or 66.33% in comparison to to S235JR steel. Clearly, the steel STRENX 700/S690QL allows the greatest weight reduction to be made out of all analyzed steels. This is due to its yield stress values being higher than values of other steels.

It needs to be emphasized that given results are theoretical. Some parts even though they have greater strength, need to be made at certain dimensions and cross-sections so that adequate stiffness of structure could be maintained, but in general weight saving potential with application of HSS is demonstrated. Lower weight of structures allows energy/fuel consumption to be lower and energy efficiency to increase as well as payload mass.

7. CONCLUSION

The global trend in automotive and transportation industry tends to reduce structure weight so that lower energy/fuel consumption, lower CO_2 emissions and higher payload weight could be achieved. One of many other ways to achieve this goal is to replace low-carbon structural steels with HSS. These steels have great strength which is achieved by complex production process (heat treatment, rolling, cooling etc.), so when choosing appropriate welding technology great attention needs to be paid, due to possibility of achieved mechanical properties to be compromised by the heat released during welding.

In this paper application of three HSS is considered Č0562/S355JR, ČRO460/S460N and STRENX 700/S690QL.For two out of three steels, results of computational weldability assessment shows proneness of steels to form cold cracks. Additional steps and measures such as pre heating, tempering need to be taken to prevent cold crack formation. Because those additional steps are categorised as additional manufacturing costs an in depth economic analysis needs to be conducted, whether those costs are justified compared to potential benefits of HSS implementation. Additional costs and complex welding technology combined with heat treatment steps are definitely the greatest disadvantage of HSS application.

For the analysed HSS, FM, welding parameters as well as additional heat treatment steps for cold crack prone steels, were proposed. Following the proposed welding technology test welding on steel plates was performed and samples for tensile test, impact toughness, hardness measurements and metallography were prepared. Results of conducted tests imply that appropriate welding technology is selected, and that can be transferred on real-life structure parts.

In the end weight saving potential of HSS was evaluated through one theoretical example. Obtained results show theoretical potential for weight reduction. In real-life experience some parts need to be produced with certain dimensions and corss-sections so that adequate stiffness could be maintained.

ACKNOWLEDGEMENTS

Research presented in this paper was financed by the Ministry of, Science, Technological Development and Inovations of Republic of Serbia through Grant TR35024.

REFERENCES

[1] R. Vulović, “Theoreticaly-experimental evaluation of the high-strength steel weldability”, Master thesis, Universiti in Kragujevac (Serbia), (2006).

[2] D. Arsić, “Weldability assessment and selection of most appropriate welding technology for steel S690QL”, Master thesis, Universiti in Kragujevac, (Serbia), (2013).

[3] D. Arsić, V. Lazić, R. R. Nikolić, S. Aleksandrović, P. Marinković, M. Đorđević, “Application of high strength steel of the S690QL class for application to welded structures”, Proccedings of 18th International PhD. students' seminar SEMDOK 2013, Žilina-Terchová, (Slovakia), 30 January - 1 Februar 2013, pp. 5-9 (2013)

[4] D. Arsić, V. Lazić, R. Nikolić, N. Sczygiol, B. Krstić, Dj. Ivković, B. Hadzima, F. Pastorek, R. Ulewicz, Weldability assessment of various steels by hard-facing, Materials, Vol.15, No.9, pp. -, ISSN 1996-1944, Doi https://doi.org/10.3390/ma15093082, 2022

[5] M. Jovanović, V. Lazić, “Casting and welding technology”, Faculty of Engineering, University of Kragujevac, Kragujevac, (Serbia), (2015) (in Serbian).

[6] Filler materials Jesenice,“Filler materials for Welding“, SI Jesenice, (Slovenia), (2020), (in Serbian)

Investigation of the occurrence of failures in the axle box and primary spring suspension of passenger bogies

Vanio Ralev
Todor Kableshkov University of transport (VTU), Sofia, Bulgaria

The assessment of the strength and durability of the structural elements is one of the main tasks that arise when developing new machines and mechanisms. The main factor determining the durability of most machine parts is both the mechanical load and the intensity of occurrence of failures. The axle boxes are designed to take the load from the bogie frame and transmit it to the axle necks, to ensure the rotation of the wheelsets with minimal resistance, to limit the longitudinal and transverse displacement of the wheelsets. The primary spring suspension is elastic and damping system, providing transmission between the load of the bogie frame and the axle box, ensuring the necessary smoothness of the movement and damping of the vibrations that occur. The reliability of the axle box and the primary spring suspension of railway bogies, as technical systems, mainly depend on the design calculation, operating load, monitoring system, as well as their maintenance and repair. The presented article analyzes the causes of the damage to the axle box and the primary spring suspension of railway bogies in operation of the Bulgarian State Railways.

Keywords: Railway vehicles, passenger bogies, axle box, primary spring suspension, failures.

1. INTRODUCTION

Safety in rail transport is ensured by applying a systematic approach to fulfill the requirements of the relevant European and national legislation, national safety rules and generally applicable requirements to the participants in rail transport, including through the rules adopted by the manager of the railway infrastructure [1].

All rail operators, certified carriers, maintenance organizations and rail service providers must have a program to prevent rail accidents and ensure rail safety. To ensure the implementation of this program, a reliably functioning safety management system built in accordance with [1-5] is required.

Safety management is based on the collection and analysis of data to detect the sources of danger. The main sources of such data are the reports with the results of the investigation of railway accidents and incidents that have occurred in railway transport. The main objective of investigating any accident is to determine the causes that led to it and to take the necessary corrective actions in the future. The availability of statistical information on the degree of importance of the various causes leading to railway accidents will allow measures to be taken for: timely detection and control of the most dangerous factors affecting a railway system; reducing their potential consequences; developing strategies to eliminate these factors.

In the event of equipment failure due to the destruction of a detail or node, according to the matrix for the use of tools for strength analysis of parts (see Figure 1), in the event of their destruction, a strength analysis of the part in question is carried out. If, as a result, insufficient structural reliability of the part is found, then in the case of technical possibility, strengthening of the structure is carried out, as well as replacement of the existing material of the part with a material with higher strength characteristics [6-8]. If, as a result of the strength analysis, the hypothesis of insufficient structural reliability is not confirmed, then other systemic causes, such as improper operation and maintenance, are considered. After determining the root cause, appropriate conclusions are drawn; measures are developed to prevent the recurrence of such cases.

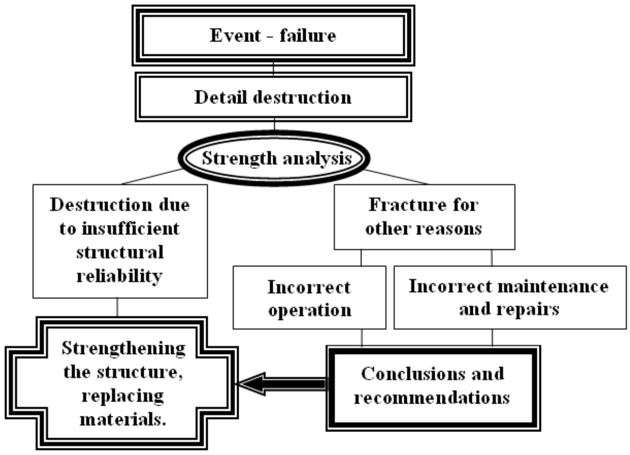

Figure 1 Scheme for the study of failure of equipment due to destruction of a part or assembly.

In 2006, in the Republic of Bulgaria, with an amendment to the Organizational Regulations of the Ministry of Transport, Information Technologies and Communications (MTITC), an investigative body was established under the direct authority of the Minister of Transport for the investigation of railway accidents and incidents – "Specialized Unit for the Investigation of Accidents and Incidents in Railway Transport" (SUIAIRT). Since 2009, the Directorate "Unit for Investigation of Accidents in Air, Water and Railway Transport" (SUIAIRT) was established, and by Decree of the Council of Ministers of the Republic of Bulgaria as of January 6, 2020, the "National Board for the Investigation of Accidents in Air, Water and Railway Transport" (NBIAAWRT) was established under the Council of Ministers directly subordinated to the Prime Minister of the State and adopted Regulations for the activity, structure and organization of National Air, Water and Rail

*Corresponding author: <VTU Todor Kableshkov, Sofia, 158 Geo Milev Str. BULGARIA> and <ralev.vanio05@gmail.com>

Accident Investigation Board. The investigative body investigates accidents and incidents in accordance with the requirements of Directive 2016/798/EP [9] and the Council of 11 May 2016 on railway safety, which has been transposed into the Railway Transport Act (RTA) [1] and Ordinance No. 59/05.12.2006 [10] on safety management in railway transport and Ordinance N-32 19.09.2007 [11] on the coordination of actions and the exchange of information in the investigation of railway accidents and incidents. Each investigated accident and incident ends with a final report prepared by the deputy chairman of the management board with competence to investigate railway accidents, which is sent to the interested parties and published on the website of the NBIAAWRT [12]. During the investigations, as well as in the final reports, recommendations are made to improve safety.

264 accidents, 54 incidents and 309 near-accident situations were registered in 2022. Figure 2 shows the registered accidents, events and near-accident situations for the period 2014-2020. Figure 3 shows the registered events for the period 2014-2020 related to the derailment and destruction of wheelsets.

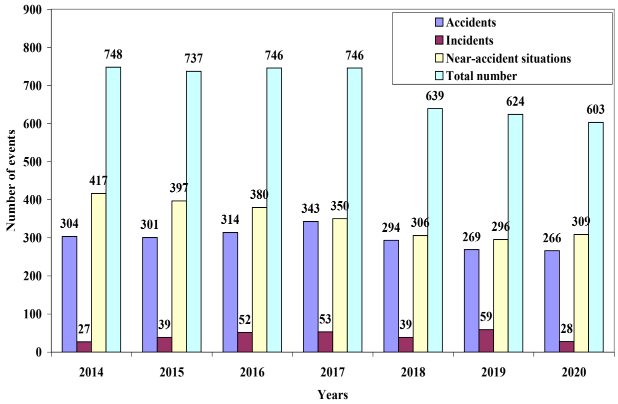

Figure 2 Registered accidents, events and situations close to accidents for the period 2014-2020.

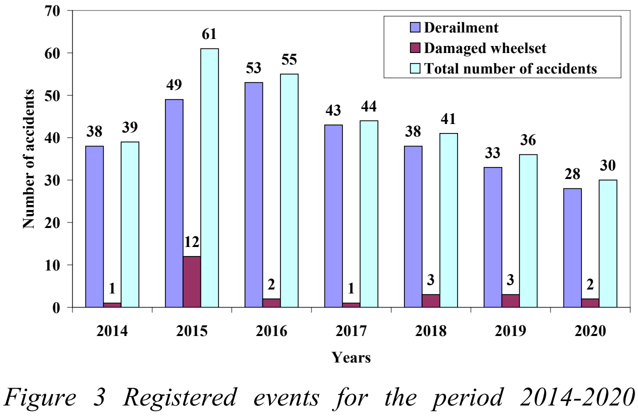

Figure 3 Registered events for the period 2014-2020 related to the derailment and destruction of wheelsets.

According to a report of the D-RAIL project [13], between 2005–2010 derailment accidents caused by Rolling stock failures (RSFs) accounted [14] for the highest proportion of accidents (38%) followed by infrastructure failures (34%), in 14 European countries (Austria, France, Germany, the UK, Sweden, Switzerland, Belgium, Bulgaria, Czech Republic, Hungary, Italy, the Netherlands, Poland, Slovenia). In fact, RSFs directly affect the infrastructure and may accelerate track deterioration, thereby increasing the probability of infrastructure failures.

Among RSFs, Rolling gear failure (RGF) usually has the greatest impact on track deterioration due to more severe Wheel-rail (WR) interactions. In work [15], an statistical analysis has been made a on the RSFs of three European railway companies. The data provided by the three companies indicated that there were approximately 95 500 damaged vehicles with a total of approximately 244 500 RSFs in a year, including Car body failures (CBFs) and RGFs. In a separate analysis on the RGFs, and the results showed that the four leading failures were wheel flat, axlebox failure, material deposition, and thermal overload, with wheel flat failure accounting for the highest proportion (19%) followed by axlebox failure (18%). In another project 2019 [16] based on the data provided by Havelländische Eisenbahn AG (HVLE), Germany, researchers used the failure mode and effect analysis (FMEA) method to analyze the likelihood of seven RSFs including axle crack, wheel out-of-round, wheel crack, wheel build-up material, wheel thermomechanical crack, wheel flat, and wrong tread profile. The results showed that among these seven failures, the occurrence probabilities of the wheel out-of-round and the wheel flat are the highest, both are approximately 0.06.

Due to limited data and a limited range of vehicle types, these statistics may not reflect the state of the entire rail industry. However, they show that the flat wheel and axle box assemblies are some of the most critical RSFs. The high impact force caused by a break in the wheel-rail contact area will also accelerate the deterioration of infrastructure elements such as rails, sleepers, fasteners and other components [17-19].

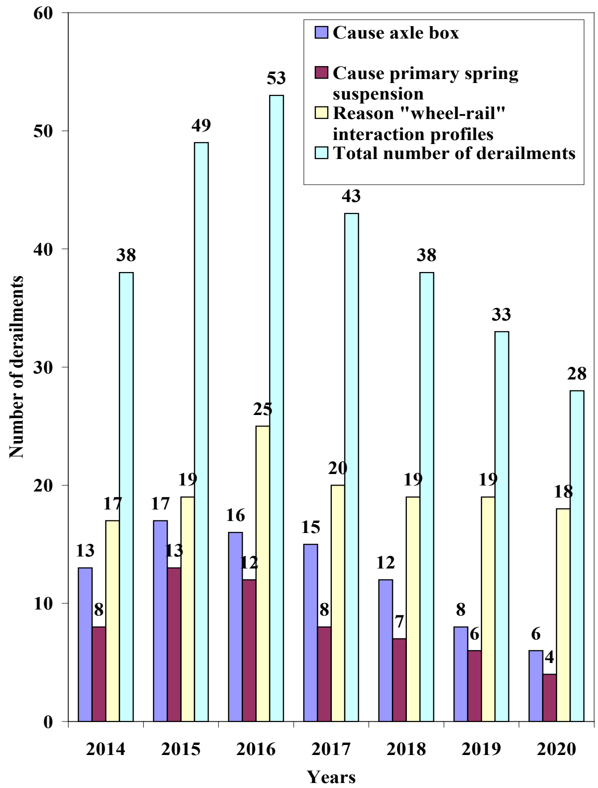

Figure 4 Registered derailments for the period 2014-2020 depending on axle box node damage, primary spring suspension and "wheel-rail" interaction profile.

Figure 4 shows the values of the registered derailments of railway rolling stock in operation in the Republic of Bulgaria for the period 2014-2020, depending on damage to the axle assembly, axle spring suspension and "wheel-rail" interaction profile, and in figure 5 shows the results regarding the causes of derailment and their percentages (a) and the most frequently detected defects in the railway vehicle - track interaction (b).

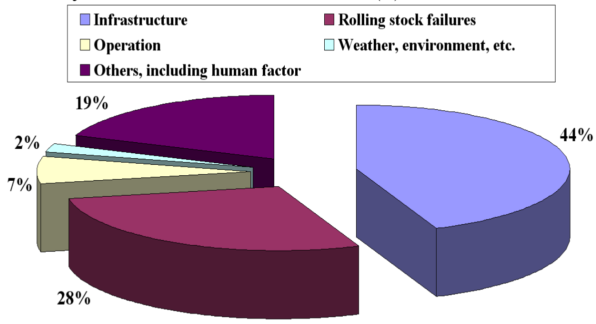

(a)

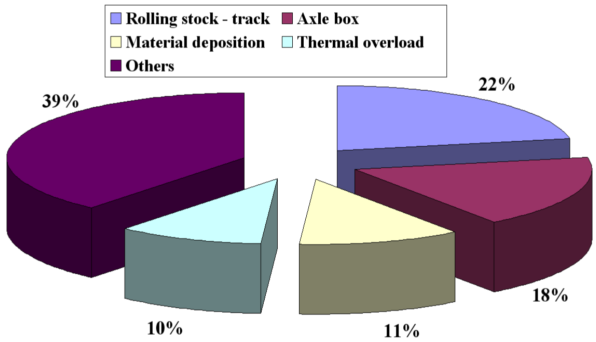

(b)

Figure 5 Derailment causes and their percentages (a) and most frequently discovered defects in the rolling stock – track (b).

2. TOOLS FOR QUALITY

Effective use of 7 quality assurance tools helps maintain quality and service standards. This helps in identifying the problem in the manufacturing process, controls and provides a solution to mitigate future defects. This helps in identifying the problem in the manufacturing process, controls and provides a solution to mitigate future defects. These quality tools are used to map quality and provide them with continuous improvement of the manufacturing process [20].

All 7 quality tools are thoroughly researched and studied within Lean Six Sigma Master study, where he teaches about manufacturing quality. Scrum is agile product quality development and incremental practices.

The 7 types of tools [21-23] are: Cause-effect diagram; Sheet Check; Control schemes; Histogram; Pareto diagram; Scatter diagram; Stratification.

Cause-effect diagram

This is also called a fishbone diagram or Ishikawa diagram. This is used to identify the cause and effect of the problem, rearrange and implement ideas in a strategic way.

Sheet Check

This is a sheet prepared in a structured manner. This is used to collect and analyze information.

Control diagrams

Charts are used to study how the process changes over time in a graphical view. Comparing current data with historical limits leads to conclusions as to whether the process is in control or out of control. Variations of external factors may apply.

Histogram

This graph is most commonly used to evaluate frequency distributions and how each value differentiates in a different data set.

Pareto diagram

This is a bar chart that shows the factors in an imprecise way.

A scatter plot

Plotting graphs with numerical data is called a scatter plot; it is used to find the relationship of the variables on each axis.

Stratification

The strategy used to separate data that is collected from different sources. Models are developed using stratification for an execution diagram or flowchart. Stratification is the first step in the 7 Quality Tools.

As tools of the quality of railway vehicles, assemblies and details, the following are most often applied: Cause and effect diagram (Ishikawa diagram) and Histogram.

3. QUANTITATIVE SAFETY ASSESSMENT METHODS

Quantitative safety assessment methods are divided into two classes: direct and indirect. As direct methods are based on the results of statistical processing of operational data and indirect methods are based on the evaluation of indicators of the structural reliability of systems and the reliability of their elements [24].

Methods for assessing the structural reliability of systems are divided into *analytical methods* and *statistical modeling methods* (Monte-Carlo method) [25, 26, 27].

To assess structural reliability, *logical-probability methods* are more often used. They describe structural schemes of objects consisting of elements that can be in only two states: operational ($x = 0$) or non-operational ($x = 1$).

Logical-probabilistic methods are based on the concept of a *minimum section* - the minimum group of elements of the structural scheme of the object, the failure of which leads to the failure of the object, and the restoration of at least one element leads to the restoration of the object as a whole regarding the specified failure. The term *critical group of elements* is also used in the same sense.

The structural reliability analysis method makes it possible to obtain the reliability characteristics as a function of time, which is not possible using other methods. The essence of the method is expressed in modeling the process of transition of the object from one state to another.

Depending on the way of analyzing the logical structure of the system, logical-probabilistic methods are divided into *inductive* and *deductive*. Characteristic of inductive methods is that the reliability analysis starts with the acceptance of failure of some element or group of elements. Failures are analyzed inductively to assess their consequences. In deductive methods, failure of the entire system is assumed, and the event is broken down to specific failures of individual elements.

Depending on the form of expression and presentation of logical connections, the following methods are distinguished:

- *Decision table.* This method expresses the relationship between the change of states occurring in complex systems, reduced to dependencies between input and output events and conditions;
- *Event Tree method*. The method serves to systematically identify the potential outcomes of a known output event;
- *Fault tree method*. The method depicts the logical dependencies between the event and the conditions and state of the system that may lead to its failure;
- *Cause-and-effect diagrams method.* The method shows the possible reasons for the occurrence of a failure or an emergency condition in the system and the possible consequences of this condition;
- *"Reliability block diagram" method.* In this method, the system is represented by blocks representing individual elements that are connected in such a way as to guarantee its reliable operation. This method applies to systems with dependent failures and component recovery. It is used in the analysis of the reliability of communication systems and control and management systems;
- *Method of networks.* In this method, functional relationships between elements are represented by a directed graph. The method is suitable for reliability analysis of communication systems, power system and computing equipment.

Structural methods are based on the presentation of the studied object in the form of logical structural-functional schemes, describing the dependence of the states and transitions from one state to another of the object on the states and transitions of its constituent elements, taking into account their interactions and the functions performed. The structural scheme constructed in this way is described by suitable mathematical models. The object's reliability is assessed based on previously known reliability indicators of its constituent elements. Reliability block diagrams represent the impact of failures in elements and blocks of a given system on its overall reliability [28].

4. PECULIARITIES OF AXLE BOX ASSEMBLY AND PRIMARY SPRING SUSPENSION IN PASSENGER BOGIES IN OPERATION OF THE BDZ

The axle boxes are designed to take the load from the bogie frame and transmit it to the axle necks, to ensure the rotation of the wheelsets with minimal resistance, to limit the longitudinal and transverse displacement of the wheelsets. They must be strong, dense, provide good lubrication of the rubbing parts, light, convenient for inspection and repair.

The primary springs connect the axlebox to the bogie frame. The springs can be designed as steel leaf or coil springs, as rubber springs, or as air springs. The aim of bogie springs is to reduce the forces and vibrations, to avoid derailment, and to uncouple vibration and noise between the wheelsets and the vehicle body.

In addition to the self-damping effect of some of the spring designs, additional dampers are used. These dampers are mainly designed as hydraulic dampers acting on the Axlebox in different directions.

The axle boxes and primary spring suspension of passenger wagons in operation of the Bulgarian State Railways EAD are mainly structures with double-row cylindrical bearings with short rollers and winged axle boxes bodies with spindle guidance (bogies type YT72, T73-AD and Görlitz V) or leading with connecting leaf springs (ferbins) (bogies type GP200 and Görlitz VI). The Y32 bogie has a cassette bearing and one-sided axle box guidance with whit longitudinal rod and silent block.

The primary spring suspension on YT72, T73-AD, Görlitz V, Görlitz VI and GP200 bogies are cylindrical coil springs on the wings of the axle box body, and on the Y32 bogie they are centrally located on the axle box body.

5. IDENTIFY CAUSES WHICH DETERMINES AXLE BOX BEARINGS DEFECTS FROM WHEELSETS

5.1. Application of an Ishikawa diagram to determine the causes of defects in wheelset and carriage bearings

Quality Management provides organizations with tools that help them find new solutions to ensure the continuation of the quality improvement process. Quality management tools are of two categories: some use definite data (numeric data), and others solve quality problems when there are no numeric data. In many cases solving some problems of quality management cannot be done in an analytical way and in these cases techniques for non-numeric data are used. For example, in the literature several tools are presented for analysing and identifying the causes that generate a problem: fishbone diagram (or Ishikawa diagram), relationship diagram, matrix diagram, affinity diagram, etc.

Several papers have been published in the literature that deal with the use of the fishbone diagram to find solutions to eliminate or reduce quality defects [29-34].

The defects of the welds are also analysed using a quality management tool and a study is given in the paper [34]. Specialty literature shows that this diagram is very much used in the industrial field.

For example, paper [35] presents a new Ishikawa diagram designed to identify the causes that generate errors in evaluating the precision of execution of parts specific to machine building.

An important application of quality management is given in the paper [35]. The papers [37, 38] present the use of modern tools of quality management in the study of the elimination of defects from some machine organs, in the field of industrial engineering.

In this paper it is used the fishbone diagram, which is based on non-numeric data, to show the causes that solve the problems proposed in the study, respectively the causes (factors) that determine the axle box bearing defects from wheelsets.

For the diagram, the problem to be solved (also known as the general objective) is established: the axle box bearing defects from wheelsets. The steps of the diagram are proposed, according to the indications given in the paper [39]: define the effect; a list of all possible causes is drawn up, using the Brainstorming method; group the identified causes and define the main categories of possible causes; the diagram is started by writing the effect into a box on the right side; the main cause categories are positioned as power channels for the effect box; the diagram is developed by writing in the boxes all the secondary causes identified for each of the main causes.

The problem of bearings defects is detailed in the book [40] and the book [41] shows, among others, the bearings theme and their reliability problems.

This article synthesize a classification of factors that determine the axle box bearing defects from wheelsets, based on the theory of the fishbone diagram (Ishikawa diagram). In order to achieve the fishbone diagram, the causes (factors) were identified and grouped in 4 main categories: Human (H), Production of bearings (P), Repair – Bearing Replacement (R), Exploitation of the wagon (E).

Figure 6 shows the fishbone diagram with a formula: H + P + R + E. The head of the fish is the studied problem: the bearing defects from axle boxes. Fish skeleton has four main ramifications according to the four main categories of causes (factors). For each of the main causes, specific secondary causes (factors) are highlighted. When determining the secondary causes, several aspects influencing the bearing defects from car wheels were considered.

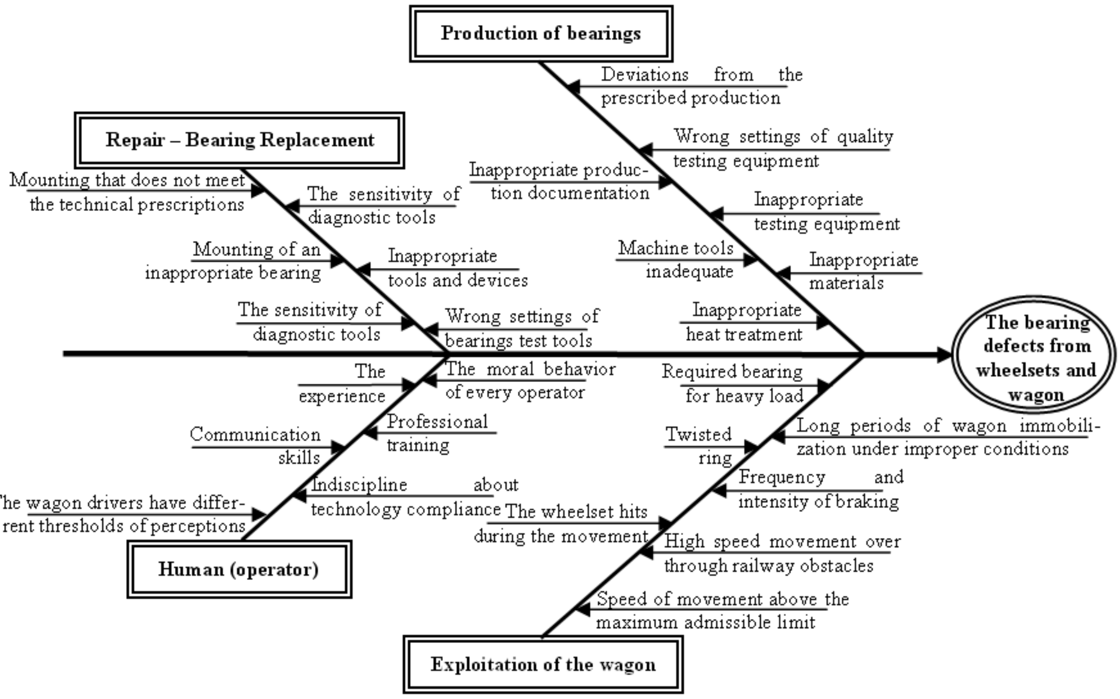

Figure 6. The bearing defects from wheelsets and wagon.

The diagram provides visual support that highlights and hierarchies the actual or potential factors that generate the problem of non-quality studied. The diagram also provides a good graphic illustration of the link between an unwanted result and the factors that determine this result

5.2. Application of a histogram for the analysis of bogie failures due to axle boxes failure for the period 2021 - 2022 years

The graphically presented analysis in figure 7 allows visual determination of the reasons for which the maximum number of marriages occurred due to a malfunction of an axle box node. One of the conditions for the reliable operation of the axle box is the prevention of lubrication defects, such as hydration and the presence of foreign impurities. Foreign impurities get into the axle box assembly from a loose axle box seal.

Based on the above, experts propose to establish the temperature level of axle box heating at which the wheelset can work after any kind of revision within a month.

In figure 7, under the numbers of the corresponding blocks are the following malfunctions: 1-malfunctions of the bearing rings; 2-malfunctions of the rollers; 3-weakening of the front attachment; 4–hydration of the lubricant; 5-incorrect selection of bearings (mismatch between radial and axial clearances); 6-malfunctions of the labyrinth seal; 7-the different sizes of the rollers in diameter and length higher than the permissible ones; 8-cracks, fractures of support rings; 9-malfunctions of the axle box body; 10-separator malfunctions; 11-contamination of the lubricant; 12-bogie malfunctions; 13-destruction of the end fastening; 14-Insufficient (excess) lubricant; 15-full destruction of bearings; 16 - Presence of more than the permissible defects on the rolling surface of the wheels.

Particular attention should be paid to the operation of the means for automatic control of the condition of the rolling stock. Based on the removal of wagons from the train composition due to heating of axle box during operation in the inter-repair period affects the quality setting of the means of automatic control of the condition of the rolling stock [42-45].

The second direction to increase the reliability of axle boxes node is the use of adapter (cassette) bearings. Structurally, cartridge bearings absorb both radial and 14% of the axial loads acting on the bearings.

The use of bearings of this type allows reducing labor-intensive work on their repair. There is no need to purchase the necessary amount of lubricant for the implementation of the production program to release the wagons from repair, storage, laboratory checks.

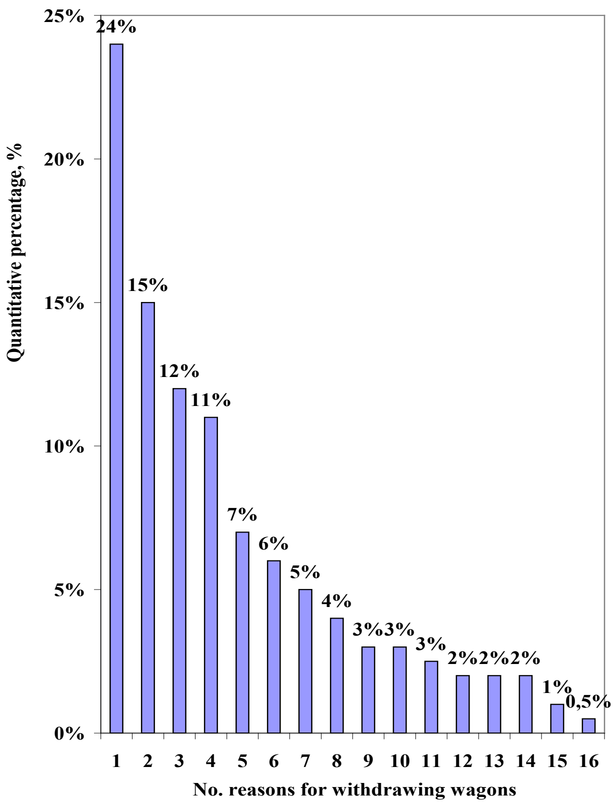

Figure 7. Histogram for the analysis of the causes of marriage due to damage to axle boxes nodes in 2021 and 2022.

In addition, the problems with the disposal of the grease that has been in operation are solved.

Upon entering a repair facility, these bearings are subject to incoming inspection. The following are checked: availability of accompanying documents; integrity of the package; completeness and appearance of the bearing.

5.3. Application of "Failure Tree" for failure analysis of axle box node of a passenger bogie.

In order to study the actual state of reliability of a passenger bogie axle box assembly, the use of the "fault tree" method is proposed. Its toolkit allows a detailed analysis of the factors that can influence the occurrence of damage and failures of individual elements.

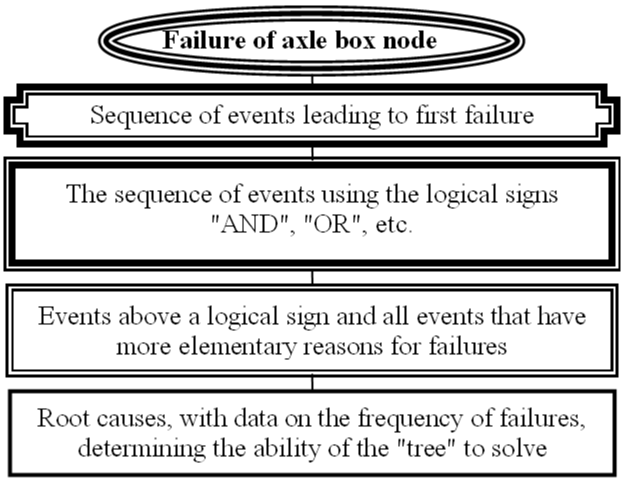

Figure 8. Basic structure of "Failure Tree"

The "Failure Tree" is the basis for the development of logic-probabilistic models of the causal relationships of the failures of complex systems with the failures of their elements and other events. Analysis of failure occurrence consists of sequences and combinations of different events and subsequent system failures (Figure 8).

Thus, the "tree" is a multi-level graph logical structure of cause-and-effect relationships, obtained as a result of observing dangerous situations in reverse order to find the possible causes of their occurrence [44].

Failure of axle box at work can occur for various reasons and develop over time according to various scenarios. In order to reduce the number of failures in a working node, it is necessary to detect all existing types of failures and make their mathematical description [43]. The first step in performing a quantitative analysis of the developed model is the construction of an equivalent "tree branch" (Figure 9), where elementary events are associated with independent variables from a numerical series ordered by elementary failures $p_1, p_2, p_3 \ldots p_n$. Here $p = (p_1, p_2, \ldots, p_n)$ is the state vector of the first event and the binary auxiliary parameter H_i is the structure function for the final event. In this case, $H_i = 1$ when the first event occurs and $H_i = 0$ when the first event does not occur.

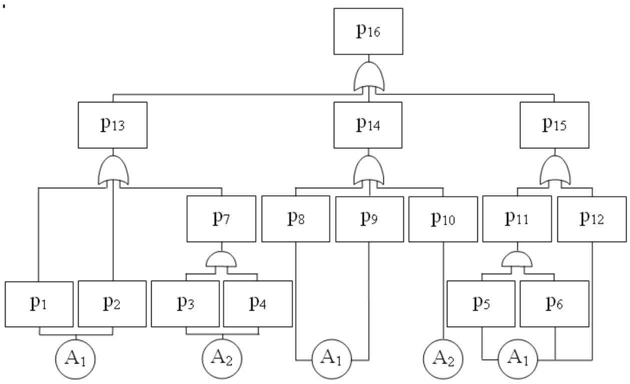

Figure 9. Example of a "Failure Tree" model for the event "Breach of hermetic of axle box"

The structure function for an “AND” event in mathematical form is:

$$H_i = \prod_{i=1}^{n} p_i = p_1.p_2.p_3...p_n . \qquad (1)$$

The structure function for an “OR” event is:

$$H_i = 1 - \prod_{i=1}^{n} [1 - p_i] = 1 - (1 - p_1).(1 - p_2)...x .$$

$$x...(1 - p_n) \qquad (2)$$

The detection of malfunctions and the restoration of a workable axle box unit is carried out during technical maintenance (TM) and repair of the wagons.

At the TM, upon detection of visible malfunctions during the heating of axle box (leakage of lubricant on the wheel disc, presence of sparks, characteristic sound) during the dismantling of unit axle box during repairs at depots or wagon repair plants, the presence of internal defects is established or violation of the lubrication regime [45]. The main problem of axle box nodes is that most of the elements are inside the case; therefore they have no possibility of testing during TM and are available for diagnostics only in a depot. The damage to the bearings leads to rapid rolling or breaking of the axle necks and derailment of the wagon.

In a simplified assessment of the reliability of axle box, it is considered as a system consisting of series-parallel connected elements: body of axle box, labyrinth ring, rear and front bearings, mounting cover, bolts, washers, inspection window (if present in the structure) , rubber seal, securing nut, securing plate.

Such a representation is valid only for systems with a disjoint structure, while wagon structures, including axle box nodes, belong to systems with a combined structure, that is, they include subsystems with a connected structure.

As a peak event T (Figure 10), we take the moment of transition of the movement of the rollers from the rolling friction mode to the sliding friction mode, accompanied by heating, displacement of axle box, a characteristic sound and smell of burnt lubricant, the formation of traces of heating (sticking, fatigue and corrosion shells), sparking, grease on the wheel disc, etc.).

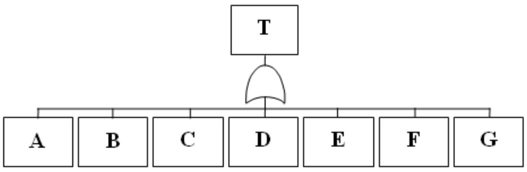

Figure 10. Top event T dissolution

Designations: event A – rollers jamming; event B – roller skew; event C – lubricants incompliance with requirements of technical documentation; event D – weakening of the mechanical fastening; event E – the formation of defects on the surface of wheel roll (uneven rolling, slide, fat, vertical flange worn sharp); event F – failure of cart; event G – axle box load increase.

The event T is controlled directly by the operator "OR", the scheme corresponds to operation∪. At the next arrangement of events A and B – operator "AND", the scheme is included with operation ∩ [46]. Analogously considering each of the events A-G, we obtain the schemes shown in Figure 11.

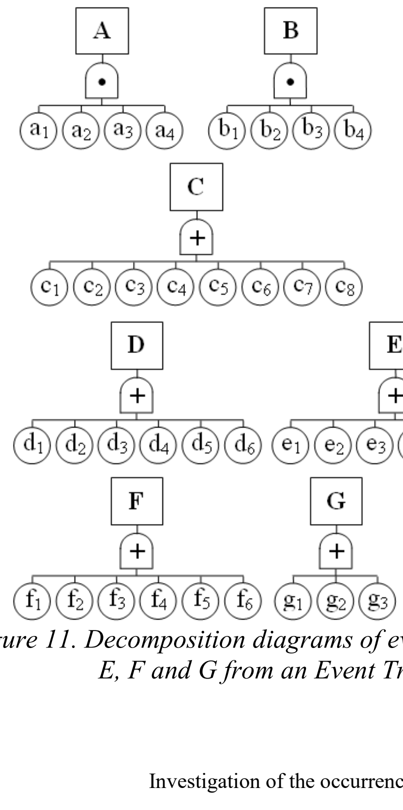

Figure 11. Decomposition diagrams of events A, B C, D, E, F and G from an Event Tree.

The designations in Figure 11 are as follows: a_1 - the value of the radial clearance exceeds the established standard; a_2 – the axial clearance is smaller than technical requirements [49]; a_3 – the length of bearing rollers exceeds technical requirements; a_4 – the diameter of the bearing rollers exceeds technical requirements; b_1 – the radial clearance is smaller than technical requirements; b_2 – the axial clearance is more than technical requirements; b_3 – the length of the bearing rollers is smaller than technical requirements; b_4 -the rollers diameter in the bearing is smaller than technical requirements; c_1 – watering of lubricants; c_2 – lack of lubricants; c_3 – excess of lubricants; c_4 – lubricants pollution; c_5 – heterogeneity of lubricants; c_6 – breaking of sealing; c_7 – breaking of the seal ring; c_8 – main cover defect formation (deformation, cracks, etc.); d_1 – wear of M12 screw in contact "bolt – neck"; d_2 – wear of M20 screw in contact "bolt – neck"; d_3 – wear of M90x4 screw in contact "castle nut – neck"; d_4 – crack in washers; d_5 – crack in nuts; d_6 – crack in the locking plate; e_1 – air distributor fault; e_2 – breaking service fault; e3 – automatic performance fault; e_4 – automatic regulator fault; e_5 – adjustment of brake rigging does not meet the technical documentation requirements; f_1 – lozenging of side frames; f_2 – overestatement of the friction wedge; f_3 – understatement of the friction wedge; f_4 – wrong selection of springs; f_5 – the depth of the axle bearing does not meet technical documentation requirements; f_6 – the gap between the slideways of axle box body and horn plate of side frame does not meet the technical documentation requirements; g_1 – wear of bearing surface of axle box body; g_2 – increase in wagon load; g_3 – uneven wagon load.

For systems with a rigidly connected structure, even slight variations in the properties of individual elements significantly affect their output parameters. Small changes within the normative parameters of the elements can give such a combination that adversely affects the operation of the system as a whole.

To perform a more in-depth analysis of the structure of a real technical system, the event tree method is used.

The list of indecomposable (elementary) events has a matrix structure. The peak and intermediate events are controlled by the "OR" operator; and we present them in the matrix in the form of pillars, we present the intermediate events governed by the operator "AND" in the form of rows, numbering the elementary events according to dependencies (1) and (2).

A matrix with 36 rows is obtained, each of which has a minimum section. Then the tree is presented as a sequential structure (Figure 12):

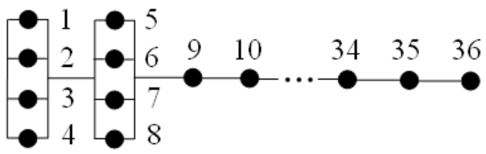

Figure 12. Sequential structural scheme of axle equipment

Based on the path and sections method, an expression is obtained for determining the failure-free operation of axle box node at a randomly taken moment in time [41]:

$$H(p) = [1 + (1 - p_1)(1 - p_2)(1 - p_3)(1 - p_4)]x$$
$$[1 - (1 - p_5)(1 - p_6)(1 - p_7)(1 - p_8)]x \quad (3)$$
$$x p_9 p_{10} p_{11} ... p_{34} p_{35} p_{36}$$

This method applies the deductive method (cause-effect), which gives it the most serious opportunities in searching for the root causes of events for static systems, as it provides a clear and detailed scheme of interconnection between the elements of the structure and the events affecting their reliability.

The considered algorithm for quantifying the reliability of a bus node is an accessible tool for studying the quantitative and qualitative analysis of the system. The obtained coefficient for determining the failure-free operation of axle box allows connecting the factors of its influence on the qualitative indicators of the operation of the wagon. Ongoing research is aimed at optimizing the intervals between repairs within the limits of a certain cycle, taking into account the safety criteria, which depend in particular on the value of the interval between the regulated diagnostics in the normative documents of the wagon repair enterprises.

As a result of calculations for the scientific project "Research of the horizontal connections in the undercarriage of railway rolling stock" under Contract No. 2076/30.06.2006 [50] with the head of the work team: Assoc. Prof. Atmadzhova, Department of "Transport equipment" of VTU "T. Kableshkov" Sofia, 2006-26-11 the probabilities of failures of the main elements of axle box node are determined: case of axle box - 0.25; bearing assembly - 0.85 and front securing - 0.2. These results are also confirmed by the development of a dissertation work on the topic "Investigation of the operational parameters of axle box roller bearings of rolling stock", dissertation of Ludmil Paskalev, VTU "T. Kableshkov", Sofia, 2021 [51].

6. IDENTIFICATION OF THE DAMAGE TO THE PRIMARY SPRING SUSPENSION OF A PASSENGER BOGIE IN OPERATION OF THE BDZ

The main elements making up the primary spring suspension of the passenger bogies are cylindrical screw springs with spindle guidance and/or with elastic guides - ferbins or a lever system with a cylinder block.

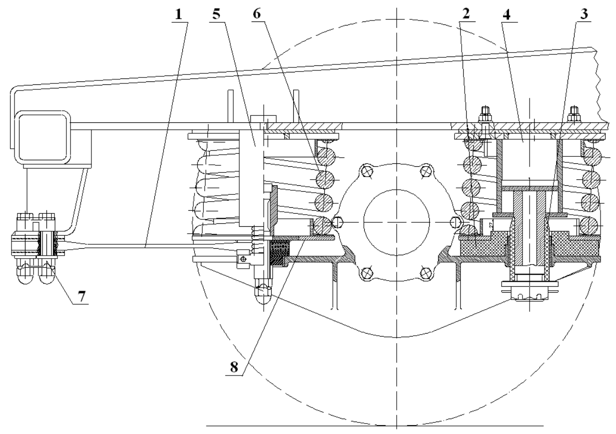

Figure 13. The primary spring suspension of bogie type Görlitz VI.
1-frame; 2- support; 3- driver - ferbina; 4 – damper; 5 – spindle.

Other elements are different constructions of dampers – hydraulic or frictional; rubber elements such as supports and various bushings and screw joints.

Figure 13 shows the construction of the primary spring suspension of the Görlitz VI type bogie.

For the period 2021 - 2022, malfunctions of the primary spring suspension elements of Görlitz VI bogies were observed at the Nadezhda Wagon Repair Depot, Sofia. In figure 14 graphically presents the percentage ratio of damage to the elements of the primary spring suspension of Görlitz VI type bogies, which are as follows: malfunctions of axle box driver (ferbins) – 20%; malfunctions of rubber elements - 7%; damage to spindle bushings (mainly wear and deformation) – 16%; malfunctions on spindles (mainly distortions and appearance of cracks in welds) – 12%; malfunctions of dampers (mainly failures of elastic or frictional elements in the structure of the dampers) – 11%; spring malfunctions (mainly change in characteristics or presence of residual deformation) – 10%; malfunctions of screw joints (breaking of threads or missing elements) – 9%; malfunctions of supports (wear, deformation or unevenness) – 5%.

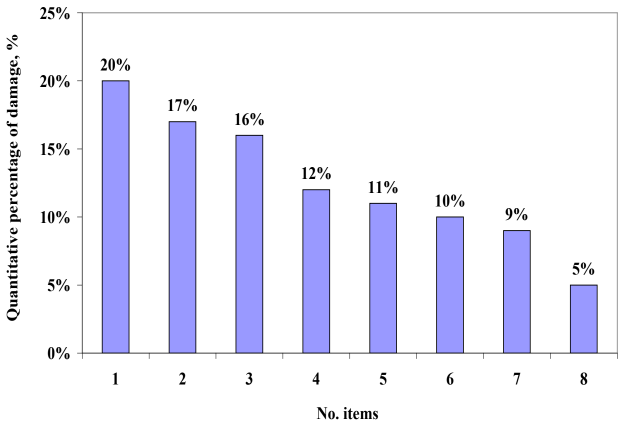

Figure 14. Histogram of damage to the primary spring suspension of a Görlitz VI bogie.

1 - faults on box guides (ferbins); 2 - malfunctions of rubber elements; 3 – damage to spindle bushings; 4 – faults on spindles; 5 – damper malfunctions; 6 - spring malfunctions; 7 – malfunctions of screw joints; 8 - faults on supports.

The observations lead to the conclusion of the need for structural changes to the primary spring suspension, including the removal of the elastic connection - ferbina and switching to a spindle guide of axle box. Leading specialists from the Department of Transport Technology at the Todor Kableshkov University of Transport - Sofia, together with BDZ EAD [50, 52] designed and reconstructed the primary spring stage of Görlitz VI and GP200 type passenger bogies, characterized by ferbin guidance of axle boxes. At the present moment, operational observations of the passenger cars with reconstructed bogies are being carried out.

CONCLUSION

Safety management is based on the collection and analysis of data to detect the sources of danger. The main source of such data is the protocols with the results of investigations of railway accidents and incidents in railway transport, and operational errors in wagon-building or repair enterprises.

The report presents registered accidents, events and near-accident situations and such related derailments and failures on wheelsets, for the period 2014-2020.

7 tools for assessing quality and maintaining quality and service standards effectively used in mechanical engineering are listed.

The causes that determine the defects of railway axle box bearings are identified, and an Ishikawa diagram is applied to determine the causes of railway wheelsets bearing defects. A Histogram has been developed for the analysis of bogie failures due to reasons of failure of axle box for the period 2021 - 2022 years.

In order to study the actual state of reliability of a passenger bogie axle box assembly, the use of the "fault tree" method is proposed. The failure probabilities of the main elements of axle box assembly are determined: the axle box body, the bearing assembly and the end attachment. The reliability of the bearing assembly has a significant impact on the reliability of the axle box as a whole. In order to increase the level of reliability, the need for the development and implementation of new designs of axle box node is indicated.

The damage to the primary spring suspension of a passenger bogie type Görlitz VI in operation of the BDZ has been identified. The need for structural changes to the primary spring suspension is indicated, with the removal of the elastic connection - ferbina and switching to a spindle guide of the bushing.

REFERENCES

[1] ЗАКОН за железопътния транспорт, Обн., ДВ, бр. 97 от 28.11.2000 г., в сила от 1.01.2002 г., изм. и доп., бр. 11 от 9.02.2021

[2] БДС 31000: БДС ISO 31000:2011 – Управление на риска. Принципи и указания.

[3] БДС 31010: БДС EN ISO 31010:2010 – Управление на риска. Методи за оценяване на риска (IEC/ISO 31010:2009)

[4] ISO 31000:2018 – Risk management – Guidelines.

[5] БДС 73: СД Ръководство 73 на ISO:2011 – Управление на риска. Речник (ISO Guide 73:2009)

[6] Райков. Р., Георгиев, Н., Стоянов, И., Стойков, Д. "Техническа експлоатация и безопасност в транспорта", ВТУ "Т. Каблешков", 2002

[7] Georgiev N., Velyova V., ESSENCE, ACTUAL PROBLEMS AND GUIDELINES FOR THE DEVELOPMENT OF TRANSPORT SECURITY)., Международна научна конференция "ТРАНСПОРТ 2021”, Научно списание том 19, брой 3, 2021 г. ISSN 1312-3823 (print), ISSN 2367-6620 (online).

[8] Николов, В. Фактори, влияещи върху безопасността в железопътния транспорт., "Машини, технологии, материали - международно виртуално списание", бр. 8-9, 2010

[9] Directive (EU) 2016/798 of the European Parliament and of the Council of 11 May 2016 on railway safety (recast) (Text with EEA relevance), 2016

[10] Наредба 59 от 05.12.2006 г. за управление на безопасността в железопътния транспорт Обн., ДВ, бр. 102 от 19.12.2006 г., бр. 12 от 11.02.2020 г., в сила от 1.02.2020 г., бр. 80 от 11.09.2020

[11] НАРЕДБА № Н-32 от 19.09.2007 г. за съгласуването на действията и обмяната на информация при разследване на железопътни произшествия и инциденти.

[12] https://www.mtc.government.bg/bg/category/180/nbrpvvzht-v-oblastta-na-razsledvane-na-proizshestviya-i-incidenti-v-zhelezoptniya-transport

[13] European project D-RAIL, https://www.d-rail.com

[14] Andreas S, Allan Z, Joseph P, et al., 2012. Development of the Future Rail Freight System to Reduce the Occurrences and Impact of Derailment. D-RAIL Project Report, European Commission.

[15] Hecht M, Leiste M, Jobstfinke D, et al., 2018. Roadmap zur Digitalisierung der Wagentechnischen Untersuchung. Technical Report, Technische Universität Berlin, Germany (in German).

[16] Regazzi D, Alfi S, Bruni S, et al., 2019. Cost-driven and eliability-driven analysis of wagon condition data (INNOWAG Project). European Commission. https://cordis.europa.eu/project/rcn/206229/factsheet/en

[17] Appel P, Hecht M, 2017. Möglichkeiten zur Lärmminderung des Schienengüterverkehrs in Deutschland. *Lärmbekämpfung*, 12(2):47-56 (in German).

[18] Mitusch K, Hecht M, 2017. Lärm des Schienengüterverkehrswie weiter nach Einführung der Verbundbremssohle. *ZEVrail*, 141(8):294-300 (in German).

[19] Bosso N, Gugliotta A, Zampieri N, 2018. Wheel flat detection algorithm for onboard diagnostic. *Measurement*, 123: 193-202. https://doi.org/10.1016/j.

[20] Гюров, Румен. Описателни техники за анализ и оценка на риска. София: Studia Analytica, 03.08.2019

[21] БДС EN 61025:2007 Анализ чрез дървото на отказите (FTA) (IEC 61025:2006) Fault tree analysis (FTA) Дата на публикуване: 28.06.2007

[22] Иванов Е., Атанасов П., ДЪРВОТО НА ОТКАЗИТЕ КАТО СИСТЕМЕН МОДЕЛ НА БЕЗОПАСНОСТТА НА РИСКОВИТЕ СИСТЕМИ, Механика Транспорт Комуникации том 14, брой 3/2, 2016 г статия № 1397, ISSN 1312-3823 (print) ISSN 2367-6620 (online)

[23] Ivanov E., Atanasov P., THE FAULT TREE AS A SYSTEM MODEL FOR SAFETY OF RISK SYSTEMS, Todor Kableshkov University of Transport, 158 Geo Milev Street, Sofia, BULGARIA MTC, 14, No 3/2, 2016, No 1397, ISSN 1312-3823 (print) ISSN 2367-6620 (online)

[24] М.Младенова, ВЕРОЯТНОСТЕН АНАЛИЗ НА БЕЗОПАСНОСТТА ТУ-София, 2015

[25] Kirova Milena, Application of a simulation method for risk evaluation of technological renovation in an industrial enterprise, Conference Paper - July 2016, “Angel Kanchev” University of Ruse, BULGARIA, 2016

[26] Kirova, M. Graphical Presentation of Risk Assessment in Management Decision Making Process, in The 7-th International Scientific Conference Business and Management `2012 – Selected Papers, 2012, No 1, pp. 386-391. 2012

[27] Kirova, M., Velikova, P. Monte Carlo simulation for risk assessment of photovoltaic installations, ICTIC - Proceedings in Conference of Informatics and Management Sciences, Slovak Republic, EDIS - Publishing Institution of the University of Zilina, pp. 82-87. 2014

[28] Митрев, Росен Пешев, Приложение на вероятностно-статистическите методи за анализ и синтез на строителни, минни и подемно-транспортни машини и системи: монография, Издателство и производство - София: Пропелер, 2021 COBISS.BG-ID – 50544136, ISBN - 978-954-392-669-5

[29] L Luca, T O Luca; Ishikawa diagram applied to identify causes which determines bearings defects from car wheels. IManEE 2019 IOP Conf. Series: Materials Science and Engineering 564 (2019) 012093; IOP Publishing doi:10.1088/1757-899X/564/1/012093

[30] Al-Bashir A 2016 Int. J. Oper. Prod. Manag 4 87-98

[31] Cirtina L M, Cirtina D, Luca L 2014 Rev. App. Mech. and Mat. 657 891-895

[32] Luca L, Stancioiu A 2012 Proc. Int. Conf. The 3-rd Int. Conf. on Aut. and Transp. Syst. (Montreux, Switzerland) 192-195

[33] Luca L 2015 App. Mech. and Mat. 809-810 1257-1262

[34] Luca L, Cirtina L, Stancioiu A 2014 App. Mech. and Mat. 657 256-260

[35] Luca L 2016 Proc. Int. Conf. IMANEE 161-165

[36] Radulescu C, Cirtina L M, Ghimisi S S 2015 Proc. Int. Conf. International Multidisciplinary SGEM GeoConferences (Bulgaria)

[37] Ghimisi S, Nicula D 2018 Actions to increase the reliability of chain transmissions, Proc. Int. Conf. The 22th edition of IManEE (Chisinau)

[38] Ghimisi S 2018 Sc. Bull. of Nav. Acad. 21 103-108

[39] Kifor C V, Oprean C 2002 Ingineria calităii (Sibiu: Editura Universitatii Lucian Blaga)

[40] Wheel loss due to faulty bearings 2017 (Quebec:Manual of Societe de l’assurance automobile du Quebec)

[41] Ghimisi S 2005 Proiectarea Transmisilor Mecanice (Bucuresti: Ed. Didactica si Pedagogica)

[42] D. Pejčić, N. Radojičić, Mladenović S.: Measurement and data acquisition system for analyzing dynamic characteristics of railway vehicles, Proceedings of RAILCON’10, Niš, pp 29-33.

[43] Atmadzhova D., Dimitrov E., Nenov N., Control System for Trains in Movement, IInt International Conference on Road and Rail Infrastructure CETRA 2012, 7- 9 May, Dubrovnik, Croatia, 2012, pp. 1059-1065, 2012

[44] Stamenković D., Banic M., Milošević M., CONDITION MONITORING TECHNOLOGIES IN RAILWAY MAINTENANCE, Proceedings of RAILCON’18, Niš, pp 129-132.

[45] Nenov N., B. Skrobanski, Modeling of system for monitoring and control of rolling stock in motion on the rail network in the republic of Bulgaria, BulTrans-2016, 14 - 16 September 2016, Sozopol, pp. 185-190, BulTrans-2016, TU Sofia, 2016

[46] Petrović D., Bižić M., DEVELOPMENT OF WIRELESS SYSTEM FOR TEMPERATURE MEASURING IN AXLE-BEARINGS OF RAILWAY VEHICLES, Международна научна конференция "ТРАНСПОРТ - 2023" Научно списание http://www.mtc-aj.com Механика Транспорт Комуникации, том 20, брой 3, 2023, ISSN1312-3823(print); ISSN 2367-6620 (online), 2023

[47] Хенли, Э. Дж. Надежность технических систем и оценка риска / Э. Дж. Хенли, Х. Кумамото ; под общ. ред. д-ра техн. наук В. С. Сыромятникова. – М.: Машиностроение, 1984. – 528 с.

[48] Райншке, К. Оценка надежности систем с использованием графов / К. Райншке, И. А. Ушаков ; под ред. проф. И. А. Ушакова. – М.: Радио и связь, 1988. – 208 с.

[49] ГОСТ 15467-79 Группа Т00 МЕЖГОСУДАРСТВЕННЫЙ СТАНДАРТ Управление качеством продукции ОСНОВНЫЕ ПОНЯТИЯ ТЕРМИНЫ И ОПРЕДЕЛЕНИЯ Product-quality control. Basic concepts. Terms and definitions.

[50] “Изследвания на хоризонталните връзки в ходовата част на железопътен подвижен състав” по Договор № 2076/30.06.2006 г. Ръководител на работния колектив: Доц.д-р инж. Добринка Борисова Атмаджова, катедра “Транспортна техника” на ВТУ „Т. Каблешков” София, 2006

[51] Паскалев Л. „ИЗСЛЕДВАНЕ НА ЕКСПЛОАТАЦИОННИТЕ ПАРАМЕТРИ НА БУКСОВИ РОЛКОВИ ЛАГЕРИ НА ПОДВИЖЕН ЖЕЛЕЗОПЪТЕН СЪСТАВ”, дисертация, ВТУ „Т. Каблешков”, София, 2021

[52] Ненов Н. Стоянов В. "Изследване и проектиране на хоризонтални връзки на пътническа талига тип GP 200", BulTrans-2010 Proceedings 24-26 September Sozopol, 2010

Application of Agile Project management Methodology in Railway Transport

Irena Petrova*, Dimitar Dimitrov
Faculty of Transport Management/Department of Technology, Organization and Management of Transport, Todor Kableshkov University of Transport, Sofia (Bulgaria)

High fuel prices and global trends towards the use of greener transport have made rail transport as such of the future through the development of high-speed railways and intermodal transport. The growing importance of rail transport worldwide requires an infrastructure that meets the demand in terms of safety, speed and capacity. Years of neglected problems in rail transport now require urgent solutions. Modernizing the railway sector to meet the demands of competitive and sustainable transport is of great social and political importance. A flexible project management approach is a modern way to solve transportation needs.

The article presents a generalized flexible model for planning and managing railway projects, ensuring the construction and maintenance of the transport infrastructure.

Keywords: Rail transport, Agile project management, Project management, Strategic planning and development, Transport infrastructure, Agile method

1. INTRODUCTION

The introduction of innovations, repair, reconstruction, construction, new technologies, decommissioning in the field of transport are activities carried out through different scale projects. Successful projects create real conditions for the advancement of the company, the region and the state, while the failure of a project leads to financial losses. The implementation of each project is accompanied by a certain amount of risk, which requires proper management of time, budget and scope. The implementation of the right transport projects for the moment, provides benefits for society, such as reducing travel time; improving the economic situation of the region; improving logistics, etc. The goal of any commercial enterprise is profit and high market share, which requires a more flexible response to customer needs and constant market changes.

Sustainable economic development requires adequate infrastructure, ensuring safe and rapid mobility of people, goods and services. Projects in the field of transport are known as investment projects and are a carrier of great benefits for society, reducing travel time, providing more comfortable travel, etc. The implementation of these projects has an impact on the economic development of the region and the countries as a whole.

In the last 5 years, the world has seen a rehabilitation in the use of rail transport, the main reasons being the high fuel prices and the pollution caused by other modes of transport. The development of rail transport is also a priority for the European Union, by building the TEN-T core network and the extended network at a later stage. These trends require rapid measures in terms of repair, construction, reconstruction, upgrading of railway infrastructure to meet increased consumer demand. The long service life of the railway transport infrastructure is also the cause of the many problems in the area. The construction of new infrastructure requires the use of serious financial resources. To reduce costs, improvements are usually made to existing infrastructure.

Prioritizing investment projects, which project happens when, is usually done through multicriteria analysis methods.

2. MODELS FOR MANAGING RAILWAY PROJECTS

2.1. Gantt chart

Gantt chart is a widely used tool as it is easy to create, read and analyze data. It is used in planning, as well as in the process of control and monitoring of the project.

The Gantt chart binds the two classification structures Work Breakdown Structure – WBS (structure of individual works) and Organisation Breakdown Structure – OBS (the organizational structure). The WBS works structure includes the list of project tasks and allows an assessment of cost, time and risk. If WBS is combined with the Gantt chart, project planning and implementation processes are much better managed thus avoiding missed deadlines, cost overruns, and more. The organizational structure OBS is a list of organizational units (people), giving information about who will be responsible for a particular job by the WBS and what is the communication between the participants. The organisational structure can verify who is responsible for a particular risk. In the columns of the organizational structure OBS are described the groups of employees, and in the rows - organizational and administrative issues. This allows a quick overview of the information who is performing the task and who is responsible for it. By bringing together the WBS and the Gantt chart, the scope of the entire infrastructure project is visualized with the aim of its effective management.

This way of data visualization makes it possible to monitor what is the process of performing each work, the critical path and see which work follows which, what the dependence between activities. The data needed to create a Gantt chart are: date of start of the project, duration and title of the works, etc.

*Corresponding author: Bulgaria, 1574 Sofia, 158 Geo Milev Str., ipetrova@vtu.bg

2.2. Critical path method (CPM)

This method determines the longest path in the sequence of project work to be critical. There may be more than one critical path in a project. All works located on the critical path are called critical works and the delay of one of them leads to a delay of the entire project. Works that do not lie on the critical path and thus do not matter for the total duration of the project are called non-critical.

The critical path method is an easy tool to reduce the lead time of any project. If for some of the critical works the number of workers is increased or special equipment is used, a reduction in project lead time can be achieved, but this will increase costs. Through few calculations it can be understood whether such an influence on critical path is cost-effective.

Many researchers work in the field of transport project management. This article does not aim to provide an overview of the topic of application of project management methods for rail transport. Some applied research, mainly published in the last 5 years will be mentioned.

Many types of project management methodologies have been described in the scientific literature. The reason for the existence and creation of a large amount of methodologies lies in the definition of a project, namely − a unique activity. There is no way in practice to find two exactly the same projects, and this requires the application of transformed methodologies for project management working for the specific case. In practice, new hybrid approaches are often developed and used, which are a combination of known methods. The Project Management is a set of procedures, practices, frameworks, standards, techniques and rules that determine how to work when managing a project.

The launch of an infrastructure project is accompanied by various procedures aimed at determining its capabilities and feasibility [3].

In study [1] the most common problems in the management of transport projects are systematized, namely: meeting difficulties in planning and realization: complete failure; delay; do not provide the expected results; implementation of the wrong projects; lack of software; funding problems; risk management problems; change in scope; problems with staff. In Bulgaria, too often projects fail to start because they are appealed in court, and this is a long and cumbersome procedure that has been going on in the bad case for more than 1 year.

Traditional project management models apply in the same way to each model, regardless of its size and the area in which it is set. The main thing with it is the thorough planning and preparation of the project documentation.

Using the traditional project management method is recommended for clear project objectives and requirements and when formal documentation is needed for all phases. [4]. In this type of projects, the requirements are very rarely changed and the opinion of the users of the final product is not sought.

2.3. Program Evaluation and Review Technique /PERT/

The PERT method is a project management method that allows analysis of all the work within the project and the time required to perform them. The use of the PERT method allows to determine the duration of the whole project using the three estimates – optimistic, pessimistic and realistic. Use the formula [58]:

$$\mathrm{E} = \frac{(\mathrm{O}+4\mathrm{M}+\mathrm{P})}{6}, \qquad (1)$$

where:

O – optimistic assessment;

M – most likely;

P — pessimistic assessment.

The use of these evaluations for the project works leads to the development of three scenarios for the development of the project, which can also be visualized through the Gantt diagram, namely: pessimistic, realistic and optimistic.

2.4. Waterfal Project Management Model

Choosing the right method for project management is a major challenge, crucial for its successful finalization within the predetermined deadlines, scope and budget. Wide popularity acquires the use of hybrid models, a combination of two or more classic project management models. The project can be planned by a Waterfal model (figure 1), and the individual subprojects are managed with the Agile method [8].

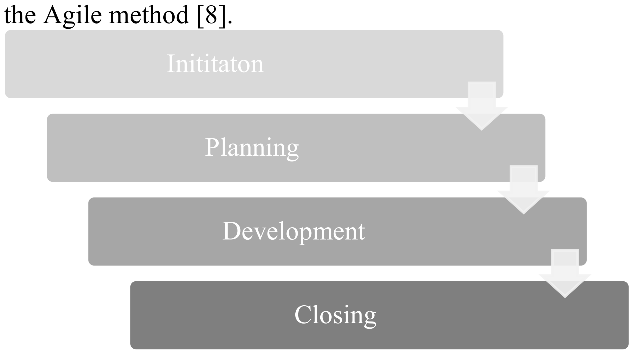

Figure 1. Classic Waterfall Model

Waterfall model follows successively the five fixed phases: project definition, scheduling, design, testing and maintenance. The next stage is passed only if the previous stage is completely over, as omission or return to the previous stage is absolutely prohibited. At each phase, a reassessment of the project is made and a decision is made whether to continue or stop. The client is not involved in the project. The project team follows the tasks and solves them as described in the plan.

Waterfall model is suitable for use in small and large projects with clear requirements. For large projects, it is very suitable because formalization leads to a reduction in the risks that accompany each project.

3. AGILE METHOD AND APPLICATION IN RAILWAY PROJECT MANAGEMENT

Agile Project Management is the modern concept of a successful project that responds to market needs. Agile project management teams are autonomous, have power over their workflow, and collaborate with customers. Communication between members takes place face-to-face in order to respond more quickly to the problems that arise. No detailed plan is required for the decisions taken. The principle of operation is to prioritize high-value work.

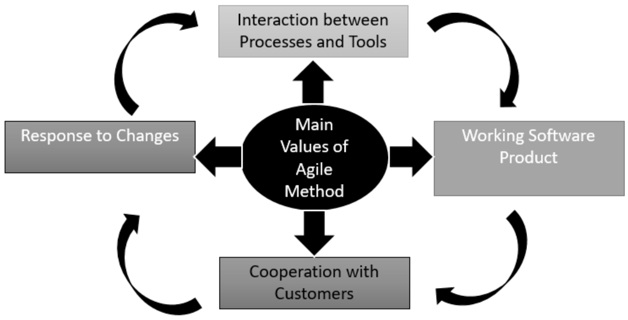

Figure 2: Basic principles of the Agile Method

Agile method is an iterative approach using short intervals called *sprints* in the process of preparing and implementing transport projects in order to make the project easier to manage. Figure 2 presents the main principles of the Agile method. Each sprint is characterized by its own requirements, project development, final result, testing. During each iteration the scope of the project can be varied by 30% [4]. An important feature of the flexible method is that on each sprint there must be a completed mini stage with a product available. The final result ordered by the customer is realized after several iterations. At the beginning of the project, the number of small pieces / sprints / and their length are determined. The operation of sprints allows better allocation of resources and easier to determine the price. On each sprint, a working product is created that is subject to future correction or improvement. After a few sprints, the final version is reached. Flexible planning is a continuous process carried out on a short-term basis, providing transparency and constant communication with the client.

In Agile Method, workflow visualization with Task Board is used. In order to improve the work, you need to constantly see what is happening. The Task Board contains the following mandatory elements:

- Things to do − **To-Do**;
- Things to work on – **Doing**;
- Things that are already finished as a job − **Done**;
- The descriptions, functionalities that will be developed − **User Stories**.

The arrangement of functionalities in the Task Board follows the principle of first (i.e. at the top) to put the important thing for the client, and many tasks can be added to it. Priority functionality means that the client derives the most value from it, not that it needs to be worked on the most.

Agile's ability to enable better quality control, provide transparency and continuous feedback make it the preferred method for managers.

In [1] the authors propose the use of a flexible priority risk management model accompanying each project. Risk management is a core activity in any project, with the typical actions – risk identification, risk assessment, source removal, or impact reduction. In a flexible project management model, risk is managed at each iteration.

Flexible project management is recommended [4] for creative, research, innovative projects that have a high level of uncertainty and unclear goals and changes over the course of the project.

4. COMPARISON BETWEEN CLASSICAL AND AGILE METHOD

Project management theory addresses five elements of a project: budget, time, scope, quality, and risk. The quality of the project depends on the vertices of the triangle – time, budget and scope formula (1). Quality refers to the specific project.

$$Q = f(T, B, S), \tag{2}$$

where:

Q – Quality
T – Time
B – Budget
S – Scope

With the concept "Project Triangle" a comparison between the traditional method and the flexible one is presented visually (*Figure 3*). There should always be at least one fixed angle of the triangle. Changing one of the parameters affects the others. In the classic project management method and two of the Scope, end Budget of the triangle are fixed. In this way, the project is deprived of opportunities for innovation. Agile Method only fixes Time and Budget, thus ensuring the start and end of the project, as well as all its funding. The possibilities for change are in the third indicator – the scope of the project.

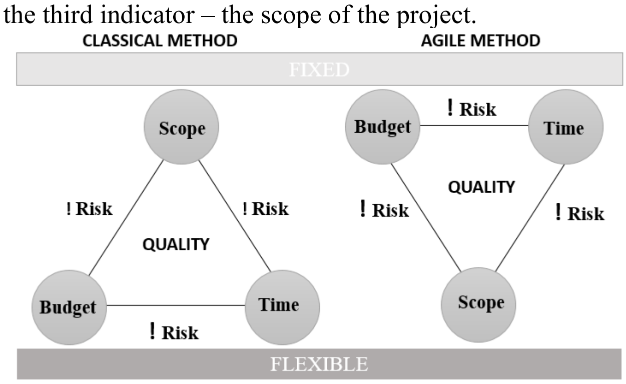

Figure 3: Classical and Agile Methods

The advantages of the classical method are many: scheduled activities, clear roles, fixed responsibilities, documentation, measurability of the project. The advantages of the flexible method include rapid detection of changes and flexible response to the scope of the project due to the change of requirements by the client [8].

In the traditional project management approach, any deviation from the fixed time and budget leads to a change in the entire project, to a complete change of the initial plan.

5. APPLICATION OF THE AGILE METHODOLOGY FOR RAILWAY PROJECT MANAGEMENT

5.1 Identification of transport projects

Infrastructure projects are related to quantitative and qualitative changes in infrastructure. When these projects are related to transport, we are talking about transport infrastructure projects.

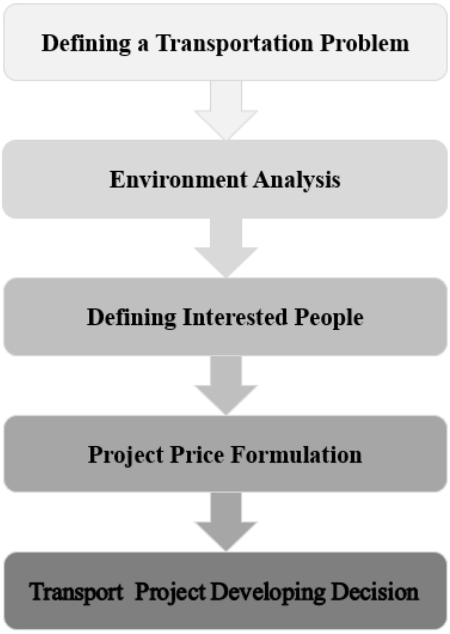

Figure 4: Stages for the identification of transport infrastructure projects

In this example, the principle of identification of currently priority railway projects is used, which are discussed below in the example.

5.2 Flexible methodology

The flexible methodology is detailed in sources [6, 7], examining an example of prioritising projects for different transport modes. The main thing in it is the determination of budget expenditures related to a specific period of time.

A mathematical formulation of the basic dependence in the Agile method, applied in an engineering field, can be represented by the interaction function of the form:

$$IFR_t \rightarrow (FxT_t, FxB_t) \rightarrow \text{most important IFR}, \quad (3)$$

Where:

t – real moment of time;

IFRt – flexible infrastructure requirements;

FxTt – flexible time;

FxBt – flexible budget.

The budgetary costs for a certain period of time can be calculated according to formula (2).

$$R_{IFRs}(t\ \in [start2end]) = \sum_{n=1}^{N}\sum_{m=1}^{M} ifr_{n,m}.c_{n,m}, \quad (4)$$

Where:

$\boldsymbol{ifr_{n,m}}$ – flexible infrastructure requirement for n mode of transport and m infrastructure site;

$\boldsymbol{c_{n,m}}$ – the budget value for the design and realization of the site;

RIFRs – budget price;

start2end – period from the beginning to the end of the project management period under review;

n – type of transport;

m – type of infrastructure.

The sum semantic dimension of the general differences for a given period is the set of:

$$\nabla IFRs\ (t\ \in [start2end]) = \sum_{n=1}^{N}\sum_{m=1}^{M} \Delta ifr_{n,m} \quad (5)$$

Where it is part of many documents relating to a specific transport project. In this regard, it can be said that there is a multiple-quantitative dimension, which is measured by the amount of documents (files) containing the semantic descriptions of differences in the Infrastructure Flexible Requirement Differences (IFRD).$\boldsymbol{\nabla IFRs \nabla IFRs}$

$$\nabla IFRs \in IFRD \quad (6)$$

Total Flexible Scope Alternatives for ***n*** modes of transport and ***m*** infrastructure can be represented by the following Linear Additive Model:

$$FA(n,m)_j = \sum_i w_i . fa(n,m)_{i,j};\ \ w_i > 0; fa(n,m)_{i,j}\ [fa(n,m)_{i,min}, fa(n,m)_{i,max}], \quad (7)$$

Where:

$\boldsymbol{FA(n,m)_j}$ is the total flexible scope for alternative *j*;

wi **–** is the weight of criterion *i*;

$\boldsymbol{fa(n,m)_{i,j}}$ –scope of criterion i for alternative *j*;

$\boldsymbol{fa(n,m)_{i,min}}$ и $\boldsymbol{fa(n,m)_{i,max}}$ – define the range of flexible scopes that can be awarded for the performance under criterion *i*.

5.3. Application of the flexible methodology

The presented flexible methodology is applied to a sample of railway projects set out in the Integrated Transport Strategy in the period up to 2030.

Step 1

Definition of a flexible requirements matrix for railway infrastructure ITFPs, in which the flexible time FxT and the flexible budget FxB for upcoming infrastructure projects are presented.

Table 1: Flexible Requirements Matrix

ID №	Infrastructure, m	FxT, cost	FxB, time
1	Modernization of railway section "Vidin - Medkovets"	882 730 910	5
2	Modernization of the railway line Sofia - Pernik	400 000 000	3
3	Modernization of the railway line Pernik - Radomir	303 271 257	2
4	Modernization of the railway line Radomir - Gyueshevo	933 320 005	5
5	Modernization of railway sections Medkovets - Ruska Byala - Stolnik	3 644 938 638	12
6	Modernization of railway line Ruse - Gorna Oryahovitsa - Dimitrovgrad	1 985 049 330	5
7	Modernization of the railway line Radomir - Kulata	1 691 154 792	5

Step 2

Prioritization of projects by levels – low, high and medium, after calculating ΔFxR by formula:

$$\Delta FxR = FxR\ max - FxR\ min \quad (8)$$

Table 2: FxR

FxR max	FxR min	ΔFxR
971004001	794457819	176546182
440000000	360000000	80000000
333598382.7	272944131.3	60654251.4
1026652006	839988004.5	186664001
4009432502	3280444774	728987727.6
2183554263	1786544397	397009866
1860270271	1522039313	338230958.4

Step 3

1. Definition of significance w_i and flexible range fa(n, m) of criterion i and alternative j.
2. Definition of the range of flexible ranges $fa(n.m)_{i,min}$ and $fa(n.m)_{i,max}$ that can be awarded for the fulfilment of criterion i.
3. Solving $FA(n.m)_j$.

Step 4

Creating an Action Plan. In accordance with the results obtained in the previous steps, a plan for the phased development of railway projects is drawn up. In this step, the possibility of improving the functionality of the railway infrastructure is taken into account.

Table 3: Range of FxR and Priority

	Project	Priority
Project 1	Modernization of railway section "Vidin - Medkovets"	**High**
Project 2	Modernization of the railway line Sofia – Pernik	Medium
Project 3	Modernization of the railway line Pernik – Radomir	Medium
Project 4	Modernization of the railway line Radomir – Gyueshevo	Low
Project 5	Modernization of railway sections Medkovets - Ruska Byala – Stolnik	**High**
Project 6	Modernization of railway line Ruse - Gorna Oryahovitsa – Dimitrovgrad	**High**
Project 7	Modernization of the railway line Radomir – Kulata	**High**

Step 5

Scope (Initial, Final and Difference) evaluation. This step involves an analysis of the extent to which the results obtained cover the needs of rail transport. It can then move on to a further iteration of the same projects in order to improve rail transport needs.

The interactive map graphically presents the results of the planned railway projects in terms of their priority for implementation. This map changes with each application of the *Agile Methodology Flexible Model* and *Agile Flexible Algorithm*.

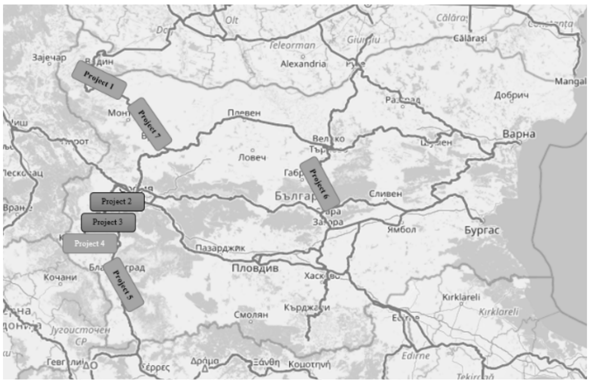

Figure 5: Project Priority Map

The results of applying the Agile Flexible Algorithm presented on the interactive map show a high priority for railway projects numbered 1, 5, 6 and 7. Projects numbered 2 and 3 are of medium priority and project 4 is of low priority.

6. CONCLUSION

To meet the increased needs of consumers and businesses for better infrastructure, shorter travel and delivery times, to improve the user experience when using transport infrastructure and transport services, adaptive pricing and to find competitive terms with other modes of transport flexible management of the projects that will provide conveniences to rail transport is required.

The application of the Agile methodology is a dynamic task that aims to respond faster to changes within the deadline, which allows stages in the implementation of projects. The implementation of the Agile Methodology Flexible Model (AMFM) leads to flexibility in project management in rail transport. Project managers must undergo training to be able to apply the flexible methodology in the management of transport projects.

Infrastructure projects in railway infrastructure are associated with very lengthy planning procedures (contractor selection, land expropriation, appeals, etc.). This has an impact on the implementation of projects, and in extreme cases even cancels the implementation of projects.

Applying the Agile methodology to railway project management will allow a quick response to market or political change by providing cost-effective solutions.

This article gives the general approach and example of using the flexible methodology for managing railway infrastructure projects. The example shows that an innovative and flexible approach must be taken, which gives freedom in the conditions of limited scope, time and budget to build and manage projects in the field of the railway sector.

REFERENCES

[1] J. Simickova, K. Buganova, E. Moskova, “Specifics of the Agile Approach and Methods in Project Management and its Use in Transport,” Transportion Research Procedia, Vol. 55, 2021, Pages 1436-1443, ISSN 2352-1465, https://doi.org/10.1016/j.trpro.2021.07.130.

[2] L. Molinari, E. Haezendonck, V. Mabillard, “Cost overruns of Belgian transport infrastructure projects: Analyzing variations over three land transport model and

two project phases”, Transport Policy, Vol.134, 2023, Pages 167-179, ISSN 0967-070X.

[3] https://doi.org/10.1016/j.tranpol.2023.02.017.

[4] A. Lalevee, N. Troussier, E. Blanco, M. Berlioz, “The interest of an evolution of value management methodology in complex technical projects management”, Volume 90, 2020, Pages 411-415, ISSN 2212-8271, https://doi.org/10.1016/j.procir.2020.01.108.

[5] M. Spundak, “Traditional Project Management Methodology – Reality or Illusion?”, Procedia-Social and Behavioral Sciences, Volume 119, 2019, Pages 939-948, ISSN 1877-0428, https://doi.org/10.1016/j.sbspro.2014.03.105.

[6] I. Petrova, “Models for straged development of transport infrastructure”, 2022, dissertation.

[7] D. Dimitrov, I. Petrova, “Strategic planning and development of transport infrastructures based on agile methodology”, 2019, IOP Conference Series Materials Science and Engineering 664:012033, DOI: 10.1088/1757-899X/664/1/012033.

[8] T. Thesing, C. Feldmann, M. Burchardt, “Agile versus Waterfall Project Management: Decision Model for Selecting the Appropriate Approach to a Project”, Volime 181, 2021, Pages 746-756, ISSN 1877-0509, https://doi.org/10.1016/j.procs.2021.01.227.

Comparative analysis of the effect of lateral swinging of the tram body on different types of electrical current collectors

Emil M. Mihaylov[1*], Emil Iontchev[2], Rosen Miletiev[3], Metodi Atanasov[4], Rashko Vladimirov[2]

[1]Department of Lifting-transport and construction machines and systems, University of Transport, Sofia, Bulgaria
[2]Department of Telecommunications and Safety Equipment and Systems, University of Transport, Sofia, Bulgaria
[3]Faculty of Telecommunication, Technical University of Sofia, Bulgaria
[4]National Railway Infrastructure Company, Sofia, Bulgaria

The article assesses the impact of side swinging of trams, with different types of suspension of the undercarriage, on their electrical current collectors. A comparative analysis has been made between the different designs of electrical current collectors based on the estimates obtained from the number of failures and emergency breaks. The rail track on which the research took place is made of grooved rails on top of panels which have frequent asymmetrical collapses of the two rails with different frequency and depth. To determine the lateral deflection angle of the body, the linear accelerations, angular velocities, and magnetic field values along the three axes of each of the trams were measured. The sensors have been mounted on the roof of the carriage just under the electrical current collector. It has been established that the lateral swinging of the body of the tram with different bogie design in combination with their respective design of the electrical current collectors influences the damage and failures to a different extent.

Keywords: Electrical current collector, Railroad, accelerometer, Gyroscope, Magnetometer, Kalman filter

1. INTRODUCTION

The current collectors are designed to be resistant to longitudinal and vertical forces during movement, ie. loads when starting and stopping, as well as the pressure on the contact wire. This gives stability to their construction at significantly lower loads in the transverse direction [1].

In the presence of damage on the rail track, which causes tilting and rocking of the body, the current collectors can withstand loads in the transverse direction.

2. STATUS OF THE PROBLEM

In the last few years there has been an increase in the number of damages on the current collectors of trams in the city of Sofia. The most common damages are: appearance and development of cracks on the elements of the pantograph, damages on the hinges, deformations of the thinner elements in the upper part, as well as damages on the connecting elements and the mechanisms of the sliders. The listed damages are typical for the railcars moving primarily on routes, which in their separate parts have sections with rail track in poor condition.

The tram trains in the city of Sofia are equipped with different types and models of current collectors. The symmetrical ones are: Пф-80, KE28. The asymmetric ones are: Fb500.54, Fb700.87 and ESgs 17-3100. Depending on their construction they have different damages.

3. MEASUREMENTS

The measurements were made along the route [2, 3, 4] from the node "Triangle" to the turning ear "Iliyantsi". This route is built with stemless grooved rails on panels. Due to the long-term operation, there are frequent asymmetrical failures of the two rails with different frequency and depth.

The sensors were placed in tram trains type T8M 700 M with inventory № 923 and type T6A2-BG with inventory № 3014. The measurements were made in operational mode. The whole route is shown in Figure 1. a., and in Figure 1.b. is shown the area for which large values of the measured parameters have been obtained.

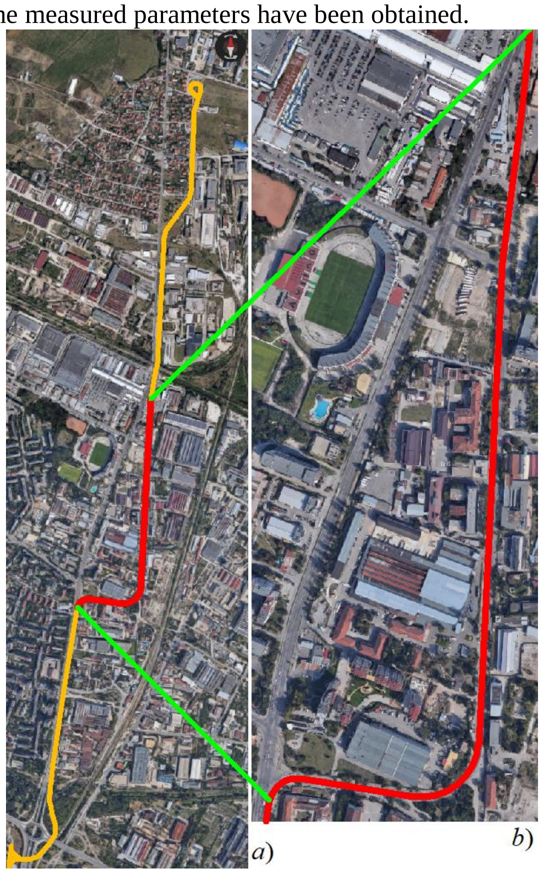

Figure 1. Measurement route.

4. PROCESSING OF THE RESULTS

An inertial measuring system was used to measure the parameters during the movement, relative to the local coordinate system - north-east-down. It includes triaxials:

*Corresponding author: University of Transport, 158 Geo Milev Street, Sofia 1574, Bulgaria, emm_1968@abv.bg

accelerometer, gyroscope and magnetometer. They are mounted on a single base, ensuring alignment between their axes. The system is fixed to the ceiling of the tram in the area where the pantograph is located, Figure 2.

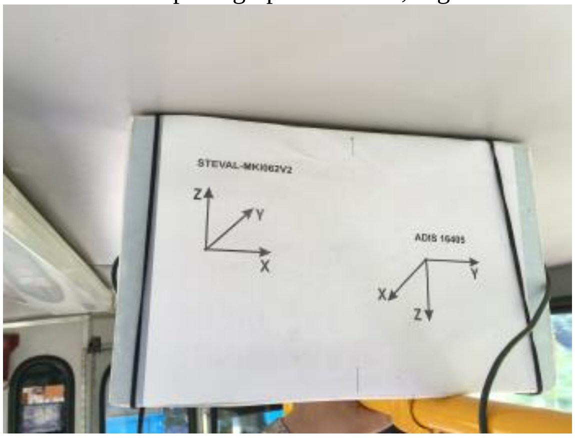

Figure 2. Inertial measuring system

The orientation of the axes of the sensors and the angles that describe the spatial position of the tram are shown in Figure 3.

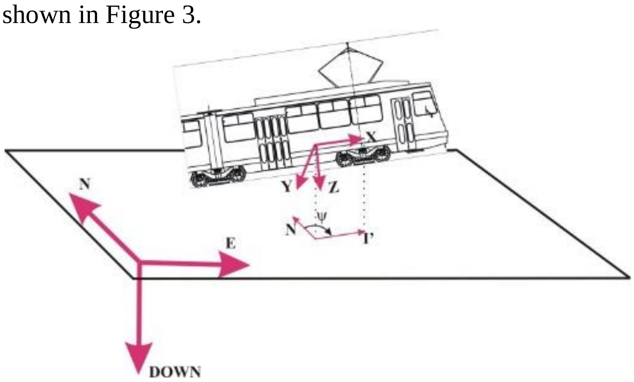

Figure 3. orientation of the tram axes and the local coordinate system

The relationship between the coordinates of the sensors in the two systems is given by the expression (1)[5]:

$$V^{local} = \left(R_{local}^{body}\right)^{T} .V^{body} \qquad (1)$$

To calculate the matrix R_{local}^{body}, it is necessary to determine the Euler angles ϕ, Θ, ψ. The sequence of rotation around the axes, when converting coordinates, from the coordinate system of the tram to the local coordinate system, is shown in Figure 4.

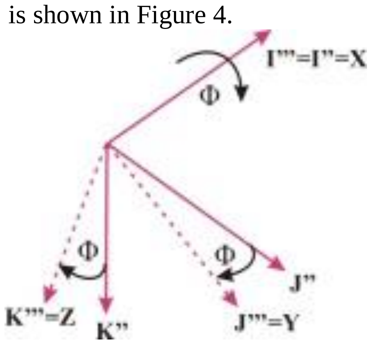

Figure 4. Sequence of rotation of the axes

An algorithm was used to process the data from the various sensors, in which a Kalman filter was used to obtain the required angles [6]. The way the data from the different sensors are combined is shown in Figure 5.

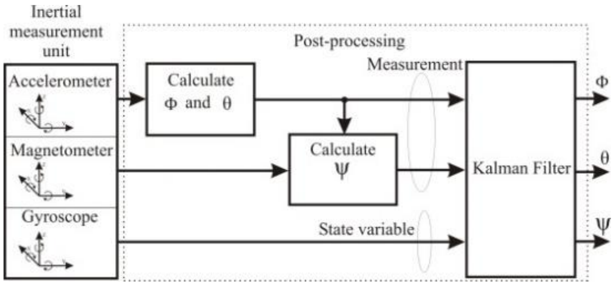

Figure 5. calculation of angles

5. RESULTS

To determine the effect of the rocking of the body on the pantograph, the parameters are taken into account: the accelerations along the transverse axis a_y, the angular speed of rotation relative to the longitudinal axis ω_x and the angle of inclination of the body in the transverse plane φ_x.

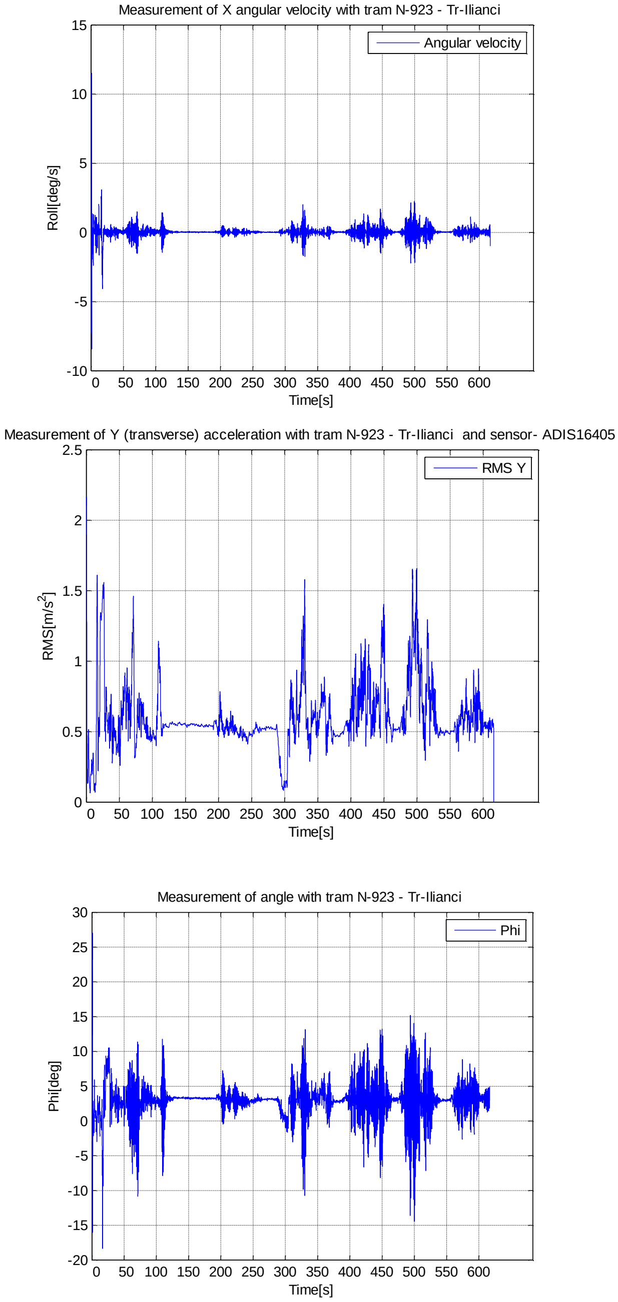

Figure 6. Results of the measurement with tram with inventory № 923.

The results obtained in the section shown in Figure 1.b. are shown in the diagrams for tram with inventory № 923 in Figure 6 and for tram with inventory № 3014 in Figure 7.

For tram with inv. № 923 the measured maximum values of the parameters are:

$$\vec{a}_{y\max,923} = 1.7\ m.s^{-2};$$

$$\omega_{x\max,923} = 3.5\ \deg.\sec^{-1},$$

$$\prec \varphi_{x\max,923} = 15\ \deg.$$

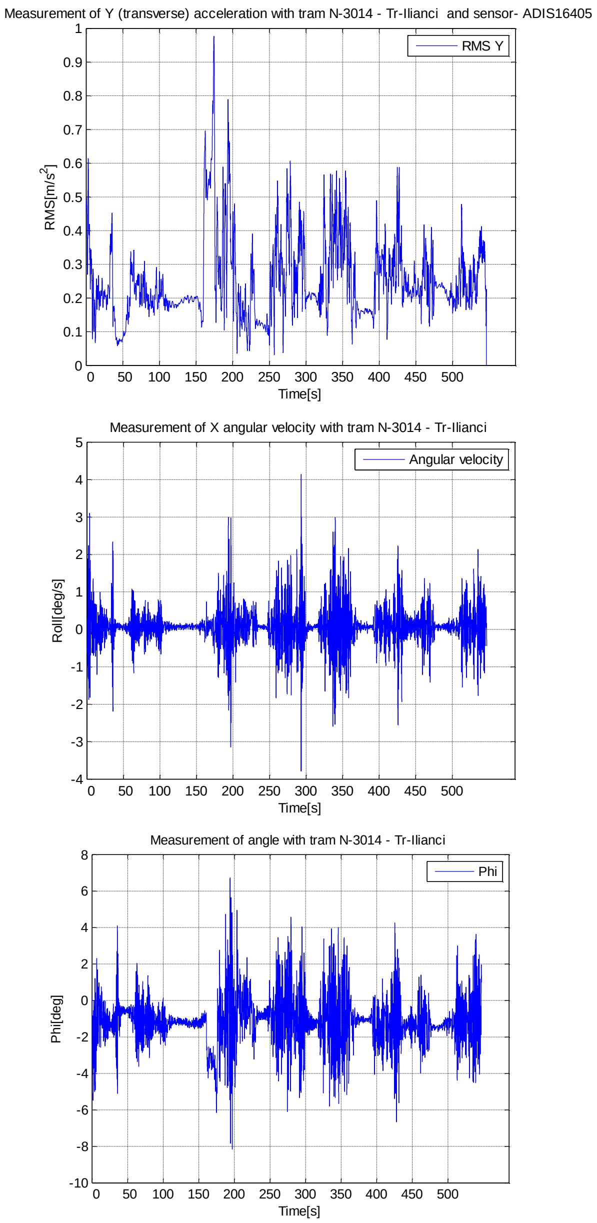

Figure 7. Results of the measurement with tram with inventory № 3014.

For tram with inv. № 3014 the measured maximum values of the parameters are:

$$\vec{a}_{y\max,3014} = 0.95\ m.s^{-2};$$

$$\omega_{x\max,3014} = 3.0\ \deg.\sec^{-1},$$

$$\prec \varphi_{x\max,3014} = 7\ \deg.$$

The values for tram with inventory number 923 are higher. This is due to differences in the type of bogie suspension. The T8M 700 M trams have a two-stage spring suspension of sets of cylindrical coil springs. While T6A2-BG trams have rigid axle guide and cylindrical coil springs in the central spring stage.

6. INFLUENCE ON THE CURRENT COLLECTORS

The construction of the current collectors (Figure 8.a) is a mechanism designed to work in one plane [7]. This is a plane defined by the X and Z axes. While in the transverse plane it can be considered as a body (Figure 8.b).

When shaking the body, the entire current collector has the same deviation. This leads to a load in the articulated hinges of the structure. The loads are different according to the type of construction, at what height they are and what masses are above them.

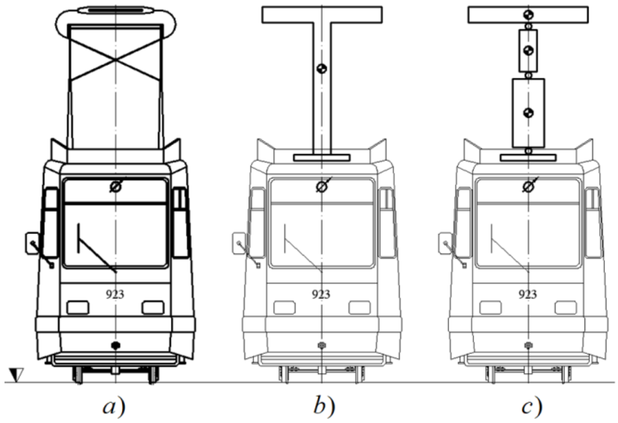

Figure 8. Schemes of the current collector as one body and as a composite body.

The pantograph can be divided into four levels:

- base - firmly attached to the roof of the body by insulating elements;
- lower level - the elements below the middle hinges;
- upper level - elements above the middle hinges;
- head - stand for the sliders with sliders.

The hinged connections, due to their immobility in the transverse direction, are considered to be thinner places in the structure (Figure 8.c).

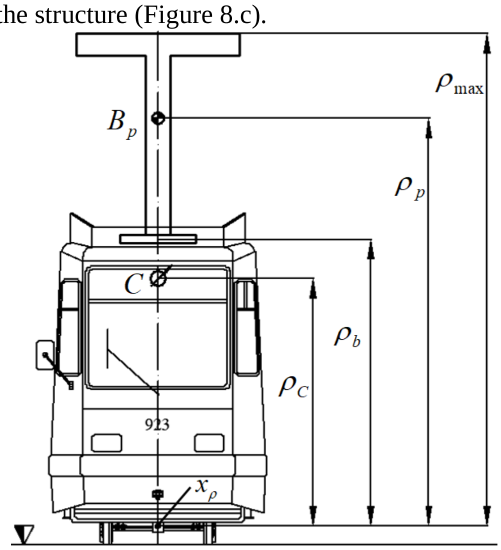

Figure 9. Location of the characteristic points in case the current collector is considered as one body.

For each of the degrees, regardless of how many elements it consists of, we assume that its mass m_i is concentrated in the center of gravity. The same applies to the hinges - regardless of their number, they are assumed to be one. These points of the structure are chosen as characteristic and the calculations for the loads are made according to them. The points of the center of gravity of each of the bodies of the pantograph are marked with B_{bi}, the centers of the hinges – with S_i. The point where the sensor is located is marked with C.

Figure 9 shows the pantograph as a single body.

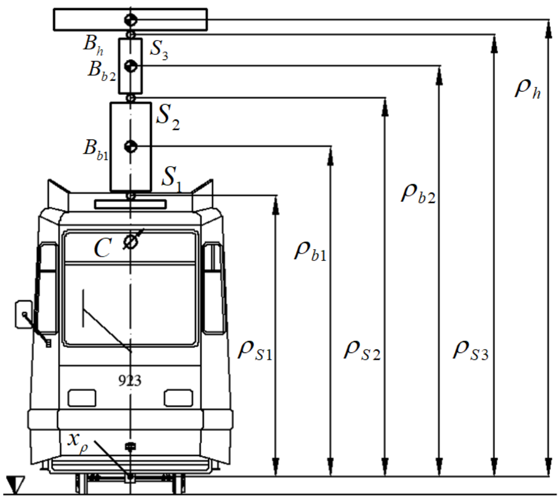

Figure 10. Location of the characteristic points in case the current collector is considered as a composite body.

Figure 10 shows the pantograph as a component body. Its degrees are separated into separate bodies.

It is assumed that the rocking of the basket is a partial rotation around an axis x_ρ parallel to the longitudinal axis of the basket - X, at a height around the axes of the wheelsets, depending on the design of the spring suspension. Values were obtained for the angular velocity ω_x when rotating around the axis x_ρ, the angle of rotation - φ_x and the accelerations along the Y axis - a_y. The distance from the axis x_ρ to each of the characteristic points is ρ_i, and to the sensor is ρ_C.

The angular velocity ω_x and acceleration ε_x, resulting from the angle of inclination of the body φ, are the same for all points of the pantograph. The measured effective values of the acceleration due to the small angle of deviation can be considered as values of the tangential acceleration.

In [1] of Figures 9. and 10. the following dependences for calculating the bending moment in the hinges are derived:

$$M_b = m_p.\varepsilon_x.\rho_p.\left(\rho_p - \rho_b\right) \quad (2)$$

$$M_{S3} = m_h.\varepsilon_x.\rho_h.\left(\rho_h - \rho_{S3}\right) \quad (3)$$

$$M_{S2} = \left(m_h + m_{b2}\right).\varepsilon_x.\rho_{(h+b2)}.\left(\rho_{(h+b2)} - \rho_{S2}\right) \quad (4)$$

$$M_{S1} = \left(m_h + m_{b2} + m_{b1}\right).\varepsilon_x.\rho_{(h+b2+b1)}.\left(\rho_{(h+b2+b1)} - \rho_{S1}\right) \quad (5)$$

The following dependencies are used to calculate the loads at the characteristic points of the pantograph [8]:

- for angular acceleration: $\varepsilon_x = \dfrac{\vec{a}_y}{\rho_C}$;
- for the tangential acceleration at the characteristic points: $\vec{a}_\tau = \varepsilon_x.\rho_i$;
- for the force at the center of gravity of each of the levels: $F_i = m_i.\vec{a}_\tau$;
- for the bending moment in the hinges: $M_i = F_i.\rho_i$;
- for the linear velocity at the characteristic points: $v_i = \omega_x.\rho_i$.

In the considered section the height of the contact wire is 5.4 m. The level at which the pantograph of the basket is mounted is 3.1 m. At this operating height of the pantograph:

- the center of gravity of the head of the pantograph $B_h \equiv G_4$ is at a height $\rho_{G4} = 5.075\,m$ from the axis of rotation x_ρ, and the distance to the hinges of the head S_3 is $d_4 = 0.075\,m$;
- the common center of gravity G_3 of the head and the upper level $\left(m_h + m_{b2}\right)$ is at a height $\rho_{G3} = 4.905\,m$ from the axis of rotation x_ρ, and its distance to the middle hinges is $d_3 = 1.032\,m$;
- the common center of gravity G_2 of the head and the upper and lower levels $\left(m_h + m_{b2} + m_{b1}\right)$ is at a height $\rho_{G2} = 4.339\,m$ from the axis of rotation x_ρ, and its distance to the main hinges is $d_2 = 1.405\,m$;
- the common center of gravity G_1 of all elements of the pantograph m_p is at a height $\rho_{G1} = 4{,}105\,m$ from the axis of rotation x_ρ, and its distance to the connection of the base with the body is $d_1 = 1{,}255\,m$;

The total mass of the symmetrical pantographs with which the measurements were made is 150 kg, distributed by elements:

- base – $m_{b,sim} = 20\,kg$;
- lower level – $m_{b1,sim} = 65\,kg$;
- upper level – $m_{b2,sim} = 45\,kg$;
- head – $m_{h,sim} = 20\,kg$.

The masses of the elements above the respective hinges are summed:

- above S_3 is $m_{h,sim} = 20\,kg$;
- above S_2 is $\left(m_{h,sim} + m_{b2,sim}\right) = 65\,kg$;
- above S_1 is $\left(m_{h,sim} + m_{b2,sim} + m_{b1,sim}\right) = 130\,kg$;
- above the attachment to the basket is $\left(m_{h,sim} + m_{b2,sim} + m_{b1,sim} + m_{b,sim}\right) = 150\,kg$;

Figure 11. shows the positions of the centers of gravity of the combined masses and their distances to the hinges against which the calculations are made.

The dependences derived in [1] are transformed and take the following form:

For the bending moment in the insulators connecting the base of the pantograph to the body is obtained:

$$M_b = m_p.\varepsilon_x.\rho_{G1}.d_1 \quad (6)$$

For the hinges connecting the pantograph head to the upper level:

$$M_{S3} = m_h.\varepsilon_x.\rho_{G4}.d_4 \quad (7)$$

For the middle hinges:

$$M_{S2} = (m_h + m_{b2}).\varepsilon_x.\rho_{G3}.d_3 \quad (8)$$

For the hinges at the base:

$$M_{S1} = (m_h + m_{b2} + m_{b1}).\varepsilon_x.\rho_{G2}.d_2 \quad (9)$$

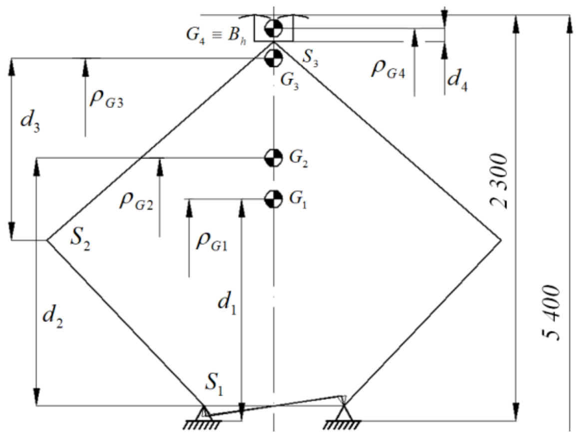

Figure 11. Location of the characteristic points of the current collector.

7. INFLUENCE ON SYMMETRICAL CURRENT COLLECTORS

The measurements were made with a tram with symmetrical pantographs types Пф-80 and KE28. The above dependences in accordance with the design of the current collectors have the following form:

The bending moment in the insulators connecting the base of the pantograph to the body is obtained:

$$M_b = \frac{m_p.\varepsilon_x.\rho_{G1}.d_1}{4} \quad (10)$$

For the hinges connecting the pantograph head to the upper level:

$$M_{S3} = \frac{m_h.\varepsilon_x.\rho_{G4}.d_4}{2} \quad (11)$$

For the middle hinges:

$$M_{S2} = \frac{(m_h + m_{b2}).\varepsilon_x.\rho_{G3}.d_3}{4} \quad (12)$$

For the hinges at the base:

$$M_{S1} = \frac{(m_h + m_{b2} + m_{b1}).\varepsilon_x.\rho_{G2}.d_2}{4} \quad (13)$$

The results of the calculation are shown in Table 1.

The high values for the hinges at the base and the hinges of the head in Пф-80 explain the more frequent damage in them.

8. INFLUENCE ON ASYMMETRIC CURRENT COLLECTORS

As no measurements were made on trams with asymmetric current collectors, it is assumed that the values of accelerations should be closer to the values measured with T6A2-BG trams. Because the type of axle suspension has similar characteristics to these trams.

Table 1.

	Пф-80	KE 28	asymmetric
ε_x, $m.s^{-2}$	1.70	0.95	1.05
M_b, Nm	328.43	183.53	175.80
M_{S3}, Nm	6.47	3.62	4.00
M_{S2}, Nm	139.84	78.14	318.90
M_{S1}, Nm	336.82	188.22	704.12

The masses of the elements above the respective hinges are summed:

- above S_3 is $m_{h,asim} = 20\ kg$;
- above S_2 is $(m_{h,asim} + m_{b2,asim}) = 60\ kg$;
- above S_1 is
  $(m_{h,asim} + m_{b2,asim} + m_{b1,asim}) = 110\ kg$;
- above the attachment to the body
  $(m_{h,asim} + m_{b2,asim} + m_{b1,asim} + m_{b,asim}) = 130\ kg$;

The dependencies in accordance with the design of the asymmetric current collectors have the following form.

The bending moment in the insulators connecting the base of the pantograph to the body is obtained:

$$M_b = \frac{m_p.\varepsilon_x.\rho_{G1}.d_1}{4} \quad (14)$$

For the hinges connecting the pantograph head to the upper level:

$$M_{S3} = \frac{m_h.\varepsilon_x.\rho_{G4}.d_4}{2} \quad (15)$$

For the middle hinges:

$$M_{S2} = (m_h + m_{b2}).\varepsilon_x.\rho_{G3}.d_3 \quad (16)$$

For the hinges at the base:

$$M_{S1} = (m_h + m_{b2} + m_{b1}).\varepsilon_x.\rho_{G2}.d_2 \quad (17)$$

The results of the calculation are shown in Table 1. The values obtained for the hinges at the base and the middle hinges are high. This explains the more frequent damage to these hinges or to the lower level body near them.

9. INFLUENCE OF ALTERNATING AND ASYMMETRIC LOADS ON THE CURRENT COLLECTORS

The parts and assemblies of railway vehicles are mostly endangered by tired destruction, which occurs years after the production and commissioning of large batches and series, usually of a mass nature, and is associated with huge material damage [9, 10, 11].

Fatigue is affected by two groups of loads - resistances and loads. The current collectors are subjected to loads of constant and random nature. The constant loads are from the static load and have relatively low values. The dynamic loads from the road have significantly higher values and reach the zone of plastic deformations of the material [11].

From the described experiment can be derived information about the behavior of the pantograph and the accelerations of its elements when passing through the collapse of one rail.

From the diagrams of Figures 6 and 7 it can be seen that the dynamic load is random and depends on the condition of the track. When driving on a route with poor road condition, at some points the stresses are in the area of the tow or above it. Periods of low and high loads alternate. That is, it is difficult to determine whether there is low-cycle or multi-cycle fatigue.

10. CONCLUSION

The assumption that the cause of damage and emergency failures is influenced by the track is confirmed. The current collectors are subjected to a large number of alternating cycles of a random nature, which leads to a strong decrease in the fatigue strength of the material.

ACKNOWLEDGMENT

The paper is published with the support of the project BG051PO001-3.3.06-0043 "Increasing, Improving and Extending the Scientific Potential of the University in Transport by Support to Development of PhD Students, Postdocs, Trainees and Young Researchers in the Field of Transport, Power Engineering and ICT in Transport" within the Human Resources Development Operational Programme co-funded by the European Social Fund of the European Union.

REFERENCES

[1] Жеков В., Иванова М., „Анализ на състоянието и проблемите на трамвайния релсов път в град София.", XXI МНК „Транспорт 2013", ВТУ „Т. Каблешков", Варна, 2013

[2] Жеков В., „Норми за проектиране на градски релсов път.", МНФ „Техника и строителни технологии в транспорта – 2014", ВТУ „Т. Каблешков", Велинград, 2014 г.

[3] Mihaylov E. M., Iontchev E., Miletiev R., Petkov B., Assessing the impact of the lateral swinging of the tram to its electrical current collector, XIX Scientific - Expert Conference RAILCON'20, Nis, Serbia, 2020 г.

[4] Ivanova, M., Zhekov V., Identifying the need of cant in the tramways curves//The fourth international symposium for students SRMA2014.- Kraljevo, Serbia 2014, ISBN 978-86-82631-76-7

[5] Farrell Jay A., Aided navigation GPS with High Rate Sensors, The McGraw-Hill Companies, 2008, ISBN 0-07-164266-8, DOI: 10.1036/0071493298

[6] Iontchev E., Miletiev R., Kapanakov P. and Hristov L., Sensor data fusion for determine object position, 54th International Scientific Conference on Information, Communication and Energy Systems and Technologies ICEST 2019, Ohrid, North Macedonia, 27-29 June 2019, pp 364-368, ISSN: 2603-3259

[7] Pablos Alfaro, Carmen de, „Analysis of a high-speed pantograph design", ICAI-Universidad Pontificia de Comillas, Madrid, 2014.

[8] Кисьов И., „Наръчник на инженера", част II, Техника, София, 1979 г.

[9] Атмаджова Д., Михалев М., Автоматизирано пресмятане на дълготрайност на елементи от подвижен железопътен състав, XX НК с международно участие на ВТУ "Т. Каблешков", 2011 г.

[10] Atmadzhova D., Some data for calculation of fatigue in probabilistic aspect of railway vehicles., XIV Conference RAILCON"10 takes place in Nis, Serbia, at the Faculty of Mechanical Engineering on October, 2010

[11] Пенчев Ц., Атмаджова Д., „Якост и дълготрайност на автомобилна и железопътна техника", ВТУ, София, 2007 г.

A Sensor Network-Based Model for Increasing Safety on High-Speed Railways

Zoran G. Pavlović*, Veljko Radičević, Branislav Gavrilović, Marko Bursać, Miloš Milanović
Belgrade Academy of Technical and Art Applied Studies, College of Railway Engineering, Republic of Serbia

Abstract: Today, railway traffic, by increasing the speed, facilitates the transportation of users and personal luggage. User mobility is currently current on the Belgrade - Novi Sad line. The user covers the distance on the specified route in 35 minutes. The terrain on which the railway is located is flat and it can be said that the possible influence of external factors (collapse of hills and mountains) related to safety is excluded. Traffic operation is regulated by the European train control system ETCS (European Train Control System). In the near future, the modernization of the railway infrastructure on the route Belgrade - Niš will begin. Considering that the central part of Serbia is hilly, the configuration of the terrain represents the emergence of critical places, there is a possibility of disrupting and endangering the safe functioning of railway traffic as well as the safety of users. For this reason, this paper proposes a model for improving the safety of the entire railway traffic system, which is based on sensors. Sensors react to changes, register and forward to take security procedures.

.

Keywords: Security, Sensors, Sensor network, Railway traffic

1. INTRODUCTION

This paper presents a model for increasing safety on the Belgrade-Nis railway. The European train control system ETCS refers to the organization of traffic, the performance of traffic services and the handling of remote control devices on the part of the Belgrade Centar - Novi Sad railway.

In the current conditions, when works are being carried out on the reconstruction, construction and modernization of the infrastructural capacities of the Novi Sad - Subotica railway section, the first remote control center was built in the Beograd Centar station, from where train traffic on the Beograd Centar - Novi Sad railway section is remotely regulated.

After the completion of the works on the Novi Sad - Subotica section, the second remote control center will be built in the Novi Sad station, from where train traffic on the Novi Sad - Subotica section will be remotely regulated.

Due to the introduction of new technologies in operation in relation to the current way of handling signaling and safety devices on the part of the Belgrade Centar - Novi Sad railway, an instruction was prepared, the application of which will ensure the traffic function, that is, ensure the conditions for orderly and safe train traffic and the movement of shunting formations on the specified part of the railway.

Trains on this part of the railway run at the highest speed allowed, namely:

– from Beograd Centar station to Novi Beograd station at the maximum permitted speed of 100 km/h;

– from the Novi Beograd station to the Batajnica station at the maximum permitted speed of 120 km/h;

– from the Batajnica station to the Nova Pazova station at the maximum permitted speed of 200 km/h on the Novi Sad tracks, and 120 km/h on the Šid tracks;

– on the Nova Pazova - Stara Pazova section, the maximum speed allowed is 200 km/h on the Novi Sad tracks, and 160 km/h on the Šid tracks;

– on the Stara Pazova section - the Karlovački Vinogradi junction, with the maximum permitted speed of 200 km/h;

– on the section of the Karlovački Vinogradi interchange - entrance to the Petrovaradin station, with the maximum permitted speed of 160 km/h;

– through the Petrovaradin station, and the inter-station distance Petrovaradin - Novi Sad, at the maximum permitted speed of 120 km/h;

– on the part of the interstation distance Petrovaradin - Novi Sad at the maximum permitted speed of 100 km/h.

At these speeds, it is necessary to ensure the safety of human lives as well as the railway infrastructure. The available computer technology is applied in the electronic business of the railway and has the possibility to improve the overall security.

The mentioned parameters and characteristics of the system indicate the regulation of traffic in the plain area, where landslides that can threaten the safe functioning of traffic are excluded [1], [2], [3].

In contrast to the above, the railway intended for high speeds on the route Belgrade - Niš passes by hills and mountains, where there is a possibility of a landslide, which implies the fall of stones and earth on the railway. At a speed of 200 km/h, the train driver as well as the dispatcher in the remote command center cannot react to the accident at that moment.

A proposal for a solution to a potential problem can be the installation of a sensor in a protective fence. This paper presents a model that includes the application of advanced internet technologies, sensors, interconnection as well as sending possible deviations registered by the sensors to the dispatcher on the remote control and to the

*Zoran G. Pavlović: < Belgrade Academy of Technical and Art Applied Studies, College of Railway Engineering, Republic of Serbia, zoran.pavlovic@vzs.edu.rs

train staff on the track.. The procedure, the research methodology in this paper includes: a review of the available professional and scientific literature in which sensors are applied for various detection of changes in the complex railway system in the segment of application for increasing safety, determining critical places where it is necessary to install sensors and create a sensor network, and finally modeling of an innovative model based on a sensor network as well as the possibility of integration into ETCS currently represented on the railways.

2. RELATED RESEARCH

Authors in work [4] inspired by conventional railway systems, such as in signalling communication where sensor logic forms the basis of the system, the capability of sensors or "Internet of Things (IoT)" has been used to improve train reliability, customer service, system maintenance and even in management railway property. Deploying sensor technology "on track" through award-winning rail applications such as tracking train speed and position via GPS and RFID, using sensor intelligence to monitor fleet axle counter temperatures, rail integrity and even equipment rooms, shaping the system of future management of railway assets. These implementations provide all convenient yet highly effective probes for excellence in managing railway engineering systems and assets that require foresight and vision. The railway transportation system is influenced by the ability to centrally consolidate the state of railway assets from the track, overhead lines, rolling stock, etc. in real time. For a rail system that has been in operation for decades, this universal platform/model for systematic sensor data collection impacts the sustainability of engineering knowledge by accurately capturing critical information that facilitates data analytics to validate maintenance or asset management....

In the paper, the authors [5] describe the problem of the operation of sensors installed on freight trains with diesel traction. Given the constant demand for heavier, longer, faster and more efficient railway freight vehicles, on-board fault detection systems are emerging as a good approach for improved exploitation of railway assets. Real-time condition monitoring reduces ineffective preventive and reactive maintenance actions, reduces waste from replacing parts that still have useful life, and improves availability and safety with real-time vehicle diagnostics. There have been significant advances in road tracking applications, but they cannot achieve continuous real-time tracking. With the trends of decreasing prices and miniaturization of electronic devices, the cost of deploying wireless sensor networks in freight trains continues to become more feasible and affordable. On the other hand, the lack of available electricity on freight cars appears as the main limitation for the application of these technologies.

The goal of this research in the author's work [6] is to use field monitoring to identify problems in transition zones, also known as critical zones, which are located between the open track and the immediate surroundings. Data were collected using onboard instrumentation, including inertial sensors mounted on bogies. The purpose of the research is to simultaneously measure the vertical displacement of successive thresholds using sensors placed on the thresholds and connected via a bus that enables data transmission between multiple nodes. The paper summarizes the initial work done with the sensor prototype. The sensors were tested in the laboratory using various electronic components and fine-tuned with a range of central frequencies using a programmable oscillator. In future work, a sensor network will be used, which can cover up to 16 thresholds in the known critical zone for obtaining data during the passage of a train.

Slope instability is a major problem in maintaining safe and operational railway structures. Conventional measurement techniques do not allow real-time monitoring of slope movements and/or are time/resource consuming. New fibber optic technology could be used to continuously monitor variations in slope movement along embankments next to railroad tracks, so that early detection and warnings can be issued to avoid catastrophic events as well as improve maintenance operations. For this purpose, a grating-based optical sensor network embedded in a steel rod was used to evaluate its feasibility for installation in a railway embankment to monitor grade movements. The initial laboratory results are highlighted, followed by a discussion on the practical application of the sensor system [7].

Sensor technology has attracted significant academic and industrial interest over the past decade. One transportation system that could greatly benefit from this technology is rail, where it is of the utmost importance to understand the structural and operational conditions of rails, as well as freight and passenger cars, to ensure safe and reliable operation. The sensors offer many important features, such as robustness, multiplexing capability and very long range probing, over conventional electrical sensors for typical railway operating conditions. The sensors are unique from other types of optical sensors because the measured information is wavelength encoded, which provides self-referencing and makes their signals less susceptible to intensity fluctuations. In addition, reflective sensors that can be interrogated from either end, providing redundancy to sensor networks. These two unique features are especially important for the rail industry where safe and reliable operations are a major concern. FBG is the most promising, cost-effective and distributed sensing technology that provides an ideal platform for monitoring the condition and condition of track construction, wagons and under frame equipment in railway systems. In the past few years, a large number of field trial railway projects using sensors for axle counting, track and train vibration measurement, undercarriage condition monitoring, train body structural condition monitoring and the interaction between overhead contact lines and current collectors (pantograph) have been successfully carried out by several research institution [8].

The automation of railway management and the application of advanced information and communication technologies are of vital importance for the further development of railway traffic and the railway system as a whole. In the author's work [9], it is shown how WSN was implemented in order to monitor the condition of infrastructure and resources on railways, but the proposal related to the possibility of using fire sensors and motion sensors on railways in Serbia.

The authors' paper [10] proposes a hybrid optical sensor system, based on Fibber Bragg Gratings (FBG) and Raman Distributed Temperature Sensing (RDTS), for monitoring key locations within large railway infrastructures such as bridges, viaducts and slopes that are potentially subject to landslides. The condition of the geometric rail track is monitored in real time using optical sensors, providing an early warning if predefined thresholds in terms of longitudinal, horizontal and transverse defects are exceeded. The sensor reading units can be located far from the observed zones, without the need for active elements on the rails and ensuring high resistance to electromagnetic interference. The proposed technology was first validated in railway laboratories and then in field tests confirming its ability to detect faults above predetermined thresholds and the absence of false alarms with regular train circulation.

Wireless sensor networks (WSNs) can be widely applied to environmental monitoring and control systems in the railway industry. In the author's paper [11], an analytical framework is proposed for studying the transmission performance of one-dimensional VSNs in a complex railway environment. In particular, VSNs along railways consist of two types of sensor nodes: ordinary sensors and powerful ones, both of which distributions follow a Poisson point process. Analytical results are obtained for the probability of successful reception and single-hop communication and end-to-end transmission under the composite channel model. An expression for the probability of successful reception in closed form under free space expansion conditions with path loss exponent $\alpha = 2$ is also derived. A simulation platform is established to evaluate the impact of various factors on transmission performance, and the analysis results are validated to be consistent with the simulations. The results in the paper can be applied to evaluate the transmission performance of VSN and provide useful guidelines for network design under railway scenarios.

Track-side intrusion detection is still a challenging problem in railway safety monitoring based on phase-sensitive time-domain optical reflect meter because the access range expands between operation and outdoor environment, and there are many unknown interfering vibration sources at different fiber locations, which are unpredictable and they change from time to time. In order to reduce the rate of unpleasant system alarms, a new data-based identification method is proposed in the article. Real implementation from sensor to final output including data acquisition, signal processing (framing, denoising), feature extraction, model design and evaluation is completed, which is a successful case of distributed optical fibber sensing in the railway sector. The results show that the average recognition accuracy of this article is as high as 98.5% in cases of frequent external intrusion [12].

The author's paper [13] proposes a passenger tracking system with ubiquitous detection sensors for railway platform safety. The objectives of the system are to detect a dangerous situation on the platform, such as a fallen passenger on the track, and to notify the central control room and the local station employee and train driver about the situation. The proposed system consists of a series of sensors, such as infrared sensors, video and thermal cameras. The information gathering unit detects and perceives hazardous factors, such as a fallen passenger, catastrophic fire, and so on, in the monitoring area using multiple vision and location sensors. The central data fusion unit provides more intelligent and meaningful information using the input tracking results from each individual camera sensor and infrared sensor for situational analysis. The multicasting information service unit provides various clients, such as local station staff, dispatch center staff and train driver with the appropriate alarm message, including standard operating procedure with video information about the accident situation to quickly deal with emergencies.

With the advancement of technology and business management capabilities, especially data management needs, railway stakeholders have higher expectations and demands for the level of informatization of the railway infrastructure. In order to support the development of railway infrastructure information, the monitoring platform will provide services for all proposed projects, projects under construction, operation and maintenance projects of China Railway, which promotes informed and standardized infrastructure management throughout the life cycle of railway construction, operation and maintenance. The monitoring platform adopts digital twin technology, integrates BIM+GIS model management, accesses the sensor data of the Internet of Things in real time, establishes railway construction, operation and maintenance of integrated monitoring of a large data center, realizes real-time monitoring of high-speed railway infrastructure. Through the mapping of virtual and reality and the interactive integration of all elements, all data, all models and all spaces, which achieved a major transformation of the management and operation of high-speed rail from phenomenon-driven to data-driven, breaking through the key technologies of intelligent prediction and early warning of high-speed rail infrastructure, in order to improve the level of service and the efficiency of high-speed rail management [14].

Railway accidents and safety are a key aspect in the railway sector all over the world. In fact, accidents often occur due to broken tracks. The need is to identify track breakage in real time before a train actually approaches the broken track and undergoes an accident. It is a complex and massive railway problem for life safety and timely service management. In the proposed system, a vibration sensor was used to detect cracks on railway tracks and obstacles. In the tunnel, the light will turn on and off when the train enters and exits the tunnel, respectively, with the help of a load cell and a circuit for energy consumption in the tunnel and using an IR sensor, the energy is consumed in the bogie [15].

The author's work [16] describes research in the field of improving the principles of management in railway traffic. Possibilities of using optical sensors in the system of providing train traffic instead of traditional railway cars operating on the basis of electric current are being considered. The method of installing and attaching the sensors to the rails is described, as well as the principle of connecting them to the system. A block diagram of the system for recording the parameters of moving units based on optical sensors is given. The results of experimental research of sensors at the shunting station are described. It has been shown that optical sensors can be used for positioning transport units, but it is proposed that the functions of the sensors be extended from discrete control to a means of measuring a number of key parameters of transport units.

Rail transport is essential in this modern world. Today, rail networks have become busier carrying more passengers and goods. This results in increased requirements for inspection and maintenance of railway assets and improper tracking or detection of people, animals or any other vehicle within the railway line. So there are many chances of accidents and loss of life and resources. But these unexpected accidents can be avoided and prevented by using this train accident prevention technology using ultrasonic sensors. This technology detects an obstacle inside the railway track using ultrasonic sensors and warns us with an alarm. By using this system we can also automatically stop the train when the obstacle remains inside the track even after the alarm sounds. The train can be stopped by providing air brakes [17].

The author's paper [18] presents the results of the development of a system for railway track diagnostics. The system was developed based on the integration of heterogeneous sensors (inertial sensors, satellite navigation system receiver, odometer and linear displacement sensors). The key element of this system is a set of inertial measurement modules, based on micromechanical gyroscopes and accelerometers, which are mounted directly on the axle boxes (bearing covers) of the wheel pairs. This architecture of the system made it possible to carry out scientific research on the results of the measurement of geometric deformations, provided by the dynamic interaction of the train and the track, as well as the measurement of parameters such as defects of the rolling surface of the rail.

In the entire transport system, railway traffic has a very important role. However, the current inspection method is mainly manual inspection, labor intensive, high risk. In recent years, with the rapid development of technology, wireless network sensors have been widely used. Sensors play an important role in bringing together big data. Sensors are getting smaller and smarter. The application of a wireless network sensor provides a new idea for railway traffic safety monitoring. Considering the current backwardness of railway transportation detection methods and the high cost of manual maintenance, this study builds a sensor-based multimode wireless sensor platform for railway monitoring. The platform mainly consists of power system, monitoring system and wireless sensor network. As the core of system power, the power system makes full use of solar energy resources, reduces system costs. And the platform achieves the goal of long-term railway monitoring without external DC power supply. The railway generates acceleration information when the train passes. Wireless network sensors monitor railway status by collecting acceleration information. The monitoring platform realizes the transmission of monitoring information in real time without external power supply. And intelligent monitoring and maintenance of the railway transport system is realized. The experimental results show that the platform can reduce the cost of manual monitoring and maintenance, and has important practical significance for railway maintenance [19].

3. CRITICAL PLACES ON THE BELGRADE-NIS RAILWAY

Knowing the characteristics of the high-speed railway profile is one of the basic prerequisites for transportation on the future Belgrade-Nis railway. Bridges, tunnels, as well as part of the environment that is hilly and mountainous, can create major technical problems for safe railway traffic (figure 1)..

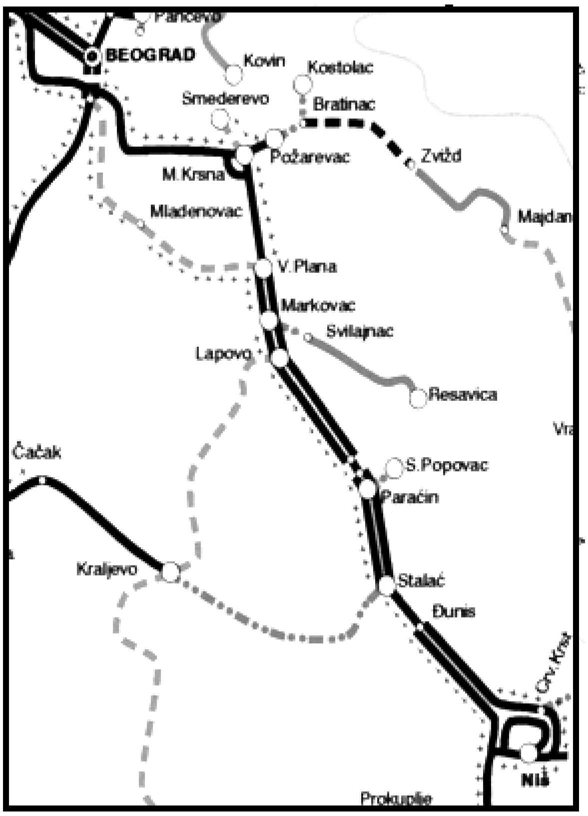

Figure 1: Belgrade-Nis railway

The construction of the high-speed railway includes the reconstruction of the existing one with deviations related to the configuration of the terrain as well as the designed, pre-planned avoidance of potential critical places. Critical places such as tunnels, bridges as well as part of the open railway can be threatened by the influence of external elements that can be found on the railway. As already mentioned, ETCS is a system for managing traffic regulation, but not a system that can register and take appropriate measures in the event of an actual landslide on the railway. the track where the train or electric train passes. Due to the impossibility of excluding all critical places, this paper proposes a model that should ensure the functioning of railway traffic.

4. AN INNOVATIVE MODEL FOR INCREASING SAFETY ON HIGH-SPEED RAILWAYS

4.1. Components of an innovative model

The development of the components of the innovative electronic business model is based on advanced Internet technologies and Internet of Intelligent Devices (IoT) technologies in railway traffic to increase safety. The model should include infrastructure consisting of hardware and software that has the role of connecting computers, connecting devices and sensors in a sensor network, and communication channels for data transmission via the Internet.

The basic components can be represented as follows (figure 2).

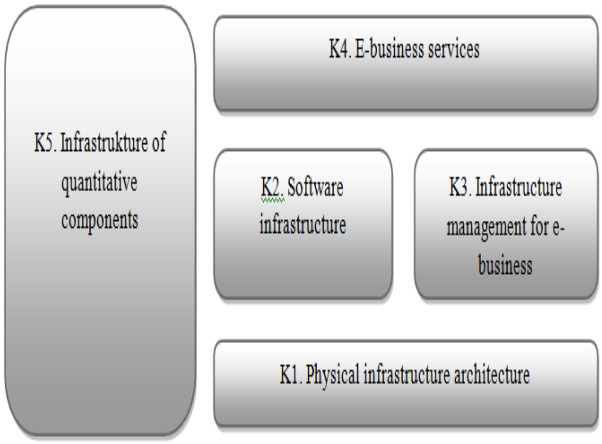

Figure 2: Basic components

The proposed innovative model for the implementation of the process of increasing safety based on advanced Internet technologies and IoT in railway traffic includes the following components [20] [21][22]:

K1. Physical infrastructure architecture
– Passive equipment;
– Servers
– Routers

K2. Software infrastructure:
– Sensors
–Wireless transmission technologies
– Wireless transmission standards

K3. E-business infrastructure management:
– Analysis of technical performance
– Monitoring of the infrastructure
– User interface

K4. E-business services:
– Content creation
– Process management
– Data analytics

K5. Infrastructure of quantitative components
– Security
– Availability
– Efficiency

Basically, the infrastructure of the innovative model should enable, on the basis of the technology (applied for the development of the model), the environment (space for the implementation of the process), organizational processes (pre-determined rules) and security systems (in the railway company responsible for safety, security and service availability) to it continuously collects changes with the help of sensors on the high-speed train, transmits information about the changes and takes appropriate measures to prevent accidents.

4.2. Multi-level infrastructure model

The infrastructure of information and communication systems for innovative business models is characterized by the interconnection of hardware and software components of the railway company with built-in sensors at critical points on the high-speed line. The infrastructure of the innovative model and electronic business system based on advanced Internet technologies includes the following layers:

– Sensors;
– Platform;
– Service layer;
– Application layer.

At the core of the multi-layered infrastructure model are sensors that can monitor and register changes at critical points, which connect via wireless internet (Wi-Fi, 3G, 4G) to the web servers of the railway company that are connected to the dispatcher in ETCS and the CDU remote control center where the electric voltage in the contact network on that part of the track is automatically switched off (figure 3).

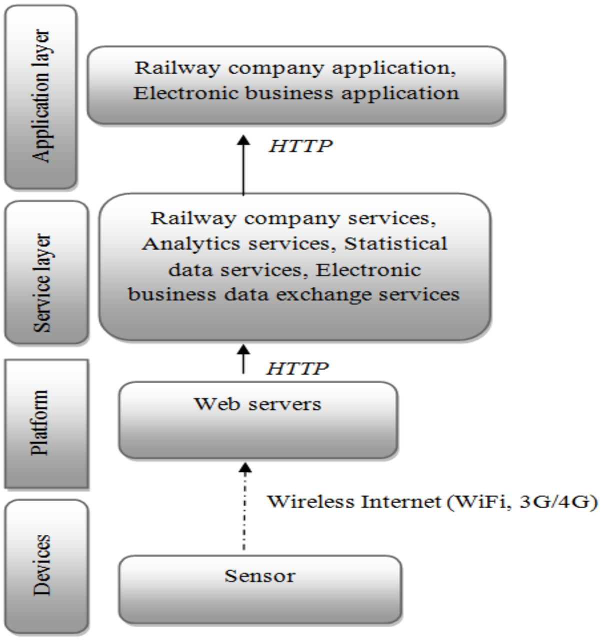

Figure 3: Multi-level infrastructure

4.3. The role of sensors in an innovative model to increase security

The rapid development of Internet technologies, IPv6 protocol and fifth generation telecommunication systems (5G) enable the connection and networking of a large number of devices over short distances that are equipped with sensors and actuators. The above implies that the infrastructure consists of three basic components: intelligent devices, network infrastructure for connecting them and systems that use data that intelligent devices detect, process and forward. In this work, sensors embedded in the protective fence are used to detect changes in the coverage area.

Smart devices can be applied in this model to increase security and are instruments with computer properties, have the ability to communicate with other devices in the environment and undertake intelligent procedures. IoT devices can be considered:

– Sensors used for detection and notification of changes in the environment;

– Actuators that serve to undertake appropriate procedures based on received detected changes;

– Modules that enable receiving commands in a specific environment;

– Microcontrollers that have built-in memory, a clock, hardware for connecting to external devices that can be sensors, actuators and transceivers for wireless data transmission;

– Microcomputers that have a microprocessor on one chip, store and input-output devices.

For complex systems in this innovative model where several smart devices are connected (ETCS, CDU dispatch center), M2M (Machine to Machine) communication is applied due to the automation and increased efficiency of business processes in electronic business. The most significant feature of M2M application is reflected in the automatic communication of several different devices and communication with the global network without the participation of people. M2M communication enables the following processes:

– Data collection - in this innovative model, data collection from various sensors that are placed on the protective fence that additionally secures critical places on the Belgrade-Niš high-speed railway;

– Data transmission through the communication network - an example of detecting changes that may occur on the railway due to landslides using sensors and data transmission through a wireless network for fast and immediate processing;

– Data processing - on the basis of the detected and received data, immediate processing is performed so that all devices responsible for safety are automatically activated to prevent accidents;

– Response to appropriate information - the response in this innovative model refers to the momentary disconnection of the electric power supply, which also means stopping all trains located on that part of the high-speed track.

4.4. Necessary steps to implement an innovative model to increase safety

The architecture of the innovative model includes applied technology, organizational processes, physical and virtual space where activities are connected in one continuous process (figure 4).

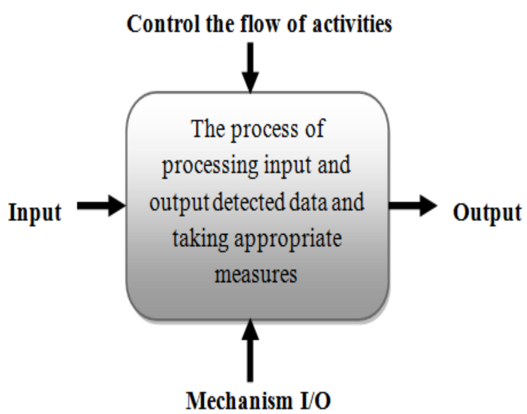

Figure 4: Structural components

This work has so far presented advanced internet technologies, devices as well as media for mutual communication and message exchange. In addition to the application of ETCS to regulate train traffic on high-speed lines, the railway company uses hardware, software components and the Internet in its daily business activities. Such a system, which is based on electronic business, can be upgraded with other innovative technologies to improve traffic safety on high-speed railways, specifically on the Belgrade-Niš railway, where, based on the identified critical points, human life as well as the infrastructural capacities of companies can be endangered.

A model for increasing safety on high-speed railways, specifically Belgrade-Nis, based on advanced internet technologies, sensor network and available hardware and software equipment. The innovative model for increasing security includes the following flow of steps:

1. Installation of a protective fence on the entire route of train traffic (Belgrade - Niš);

2. Analysis and identification of potential critical places that can negatively affect the safe functioning of traffic;

3. Install sensors in critical places with the basic purpose of detecting changes that may occur in the track belt as well as in the part of the track that may be disabled for safe traffic;

4. Installation of a larger number of sensors depending on the length of the critical part of the track belt as well as on the specification of the sensors related to the coverage range;

5. Transmission of detected changes to the responsible employee of the railway company, the nearest police station

6. Connection of sensors with actuators that have the ability to take appropriate steps where ETCS and CDU are automatically notified to turn off the electricity in the contact network and stop all trains or electric motor sets on that part of the track;

7. Daily archiving of detected changes in order to monitor the correctness of infrastructure capacities, statistical processing, analysis of the condition of critical places...

5. CONCLUSION AND PROPOSAL FOR FUTURE RESEARCH

In this paper, the challenges in the scientific and modern approach to the subject of modeling an innovative model for increasing safety on the high-speed railways on the Belgrade-Niš route were analyzed, with the aim of increasing the quality of transport services in railway traffic.

As part of this work, an analysis of the problem and proposed solution for the development of an innovative railway safety model, based on advanced Internet technologies, was performed. The paper presents existing models that are already in use and are based on sensors, applications and expected improvements. Critical places can be potential areas next to the track belt and parts of the tracks where safety can be compromised. In order to prevent potential accidents at work, a realistic solution based on technologies already applied by the railway company is presented.

This paper presents the basic guidelines for the development and application of an innovative model based on advanced Internet technologies, system components that can be used to improve the safety of infrastructural capacities as well as rolling stock.

REFERENCES

[1] Z. G. Pavlović, V. Radičević: *Application Of Intelligent Agents On High Speed Lines In Railway Traffic*, XX International Scientific-expert Conference on Railway RAILCON'22, October 13-14.2022, Niš, Serbia, pp 101-104, ISBN 978-86-6055-160-5 https://railcon.rs/Proceedings/Railcon_22_Conference_Proceedings.pdf

[2] Z. G. Pavlović, "Innovative Model Of E-Business Increasing Safety On High-Speed Railways," *2023 22nd International Symposium INFOTEH-JAHORINA (INFOTEH)*, East Sarajevo, Bosnia and Herzegovina, 2023, pp. 1-6, doi:10.1109/INFOTEH57020.2023.10094094. https://ieeexplore.ieee.org/document/10094094

[3] З. Г .Павлович , В Радичевич., З Беленцан . (2022) *Компьютерные агенты для повышения безопасности железнодорожных транспортных средств на основе искусственного интеллекта*, V Международная научно-практическая конференция «Инновационная железная дорога. Новейшие и перспективные системы обеспечения движения поездов. Проблемы и решения» , 356-366, 17 мая 2022, г. Санкт-Петербург, Петергоф, Российской Федерации, УДК 625-14,625-173,51-7, https://mail.google.com/mail/u/0/#search/gavrilovicbranislav5%40gmail.com/FMfcgzGpGTKdxMLNnsGCMtpFXMpFNpdD?projector=1&messagePartId=0.1

[4] T. Lee and M. Tso, "A universal sensor data platform modelled for realtime asset condition surveillance and big data analytics for railway systems: Developing a "Smart Railway" mastermind for the betterment of reliability, availability, maintainbility and safety of railway systems and passenger service," *2016 IEEE SENSORS*, Orlando, FL, USA, 2016, pp. 1-3, doi: 10.1109/ICSENS.2016.7808734

[5] E. Bernal, M. Spiryagin and C. Cole, "Onboard Condition Monitoring Sensors, Systems and Techniques for Freight Railway Vehicles: A Review," in *IEEE Sensors Journal*, vol. 19, no. 1, pp. 4-24, 1 Jan.1, 2019, doi: 10.1109/JSEN.2018.2875160.

[6] H. Kim, P. Weston, C. Roberts and J. A. Priest, "Trackside measurement at railway critical zones using sensors and vehicle-borne instrumentation," *5th IET Conference on Railway Condition Monitoring and Non-Destructive Testing (RCM 2011)*, Derby, 2011, pp. 1-5, doi: 10.1049/cp.2011.0595.

[7] D. Hook, W. Laing, A. Kerrouche, D. Barreto and L. S. M. Alwis, "Optical Fiber Sensor Design for Ground Slope Movement Monitoring for Railway Safety Operations," *2018 IEEE SENSORS*, New Delhi, India, 2018, pp. 1-4, doi: 10.1109/ICSENS.2018.8589835

[8] H. -y. Tam, "Fibre-optics sensor networks for condition and structural health monitoring of railway systems," *16th Opto-Electronics and Communications Conference*, Kaohsiung, Taiwan, 2011, pp. 518-518.

[9] P. Vuletić, "Application of WSN in railway intelligent transportation sysem (RITS)," *2015 23rd Telecommunications Forum Telfor (TELFOR)*, Belgrade, Serbia, 2015, pp. 103-105, doi: 10.1109/TELFOR.2015.7377424

[10] P. Velha *et al*., "Monitoring Large Railways Infrastructures Using Hybrid Optical Fibers Sensor Systems," in *IEEE Transactions on Intelligent Transportation Systems*, vol. 21, no. 12, pp. 5177-5188, Dec. 2020, doi: 10.1109/TITS.2019.2949752

[11] R. Chen, T. Shi and X. Lv, "Transmission performance analysis of wireless sensor networks under complex railway environment," *2017 29th Chinese Control And Decision Conference (CCDC)*, Chongqing, China, 2017, pp. 2970-2947, doi: 10.1109/CCDC.2017.7979018

[12] H. Meng, S. Wang, C. Gao and F. Liu, "Research on Recognition Method of Railway Perimeter Intrusions Based on Φ-OTDR Optical Fiber Sensing Technology," in *IEEE Sensors Journal*, vol. 21, no. 8, pp. 9852-9859, 15 April15, 2021, doi: 10.1109/JSEN.2020.3043193.

[13] S. Oh, G. Kim and Hanmin Lee, "A monitoring system with ubiquitous sensors for passenger safety in railway platform," *2007 7th Internatonal Conference on Power Electronics*, Daegu, Korea (South), 2007, pp. 289-294, doi: 10.1109/ICPE.2007.4692395.

[14] R. Jiang, W. Wang, Y. Xie and X. Yin, "Research and Design of Infrastructure Monitoring Platform of Intelligent High Speed Railway," *2022 IEEE 6th Information Technology and Mechatronics Engineering Conference (ITOEC)*, Chongqing, China, 2022, pp. 2096-2099, doi: 10.1109/ITOEC53115.2022.9734553.

[15] A. S. Potdar, S. Shinde, P. H. Nikam and M. Kurumkar, "Wireless sensor network for real time monitoring and controlling of railway accidents," *2017 International Conference on Trends in Electronics and Informatics (ICEI)*, Tirunelveli, India, 2017, pp. 190-197, doi: 10.1109/ICOEI.2017.8300914.

[16] D. V. Efanov, G. V. Osadchy and V. V. Khóroshev, "Testing of Optical Sensors in Measuring Systems on Railway Marshalling Yard," *2018 IEEE East-West Design & Test Symposium (EWDTS)*, Kazan, Russia, 2018, pp. 1-6, doi: 10.1109/EWDTS.2018.8524798.

[17] M. SureshKumar, G. P. P. Malar, N. Harinisha and P. Shanmugapriya, "Railway Accident Prevention Using Ultrasonic Sensors," *2022 International Conference on Power, Energy, Control and Transmission Systems (ICPECTS)*, Chennai, India, 2022, pp. 1-5, doi: 10.1109/ICPECTS56089.2022.10047195.

[18] A. M. Boronahin, Y. V. Filatov, D. Y. Larionov, L. N. Podgornaya and R. V. Shalymov, "Fusion of heterogeneous sensor information for railway track diagnostics," *2014 Sensor Data Fusion: Trends, Solutions, Applications (SDF)*, Bonn, Germany, 2014, pp. 1-6, doi: 10.1109/SDF.2014.6954716.

[19] M. Zhang, S. Qi, X. Zhang, Y. Zhao, X. Sha and L. Liu, "Multi-modal Wireless Sensor Platform for Railway Monitoring," *2019 IEEE 9th Annual International Conference on CYBER Technology in Automation, Control, and Intelligent Systems (CYBER)*, Suzhou, China, 2019, pp. 1658-1662, doi: 10.1109/CYBER46603.2019.9066728.

[20] Z. G. Pavlović, "Development Of Models Of Smart Intersections In Urban Areas Based On IoT Technologies," *2022 21st International Symposium INFOTEH-JAHORINA (INFOTEH)*, 2022, pp. 1-4, doi: 10.1109/INFOTEH53737.2022.9751263. https://ieeexplore.ieee.org/document/9751263

[21] Z. G. Pavlović, Z. Bundalo, M. Bursać and G. Tričković, "Use of information technologies in railway transport," *2021 20th International Symposium INFOTEH-JAHORINA (INFOTEH)*, East Sarajevo, Bosnia and Herzegovina, 2021, pp. 1-4, doi: 10.1109/INFOTEH51037.2021.9400521, .,https://ieeexplore.ieee.org/document/9400521

[22] Z.G.Pavlović, : *Implementation of new model for registration customer-based technologies internet intelligent device*, XVII International Scientific-expert Conference on Railway RAILCON'16, 2016, Niš, Serbia, pp 229-232, http://www.railcon.rs/zbornik/Railcon%202016%20Proceedings.pdf

Methodology for calculating the process of emergency collision in railway vehicles

Venelin Pavlov
Todor Kableshkov University of transport (VTU), Sofia, BULGARIA

Ensuring passive safety in the event of an emergency collision of railway rolling stock with obstacles requires, as does the design, manufacture and certification of a system of energy-absorbing elements (EAE). The companies producing EAE carry out bench tests of the developed structures. However, before performing bench tests, the developed structures of EAE must be subjected to a number of theoretical studies and analysis of the processes in an emergency collision. The article proposes a methodology in accordance with the requirements of Russian regulations (GOST 32410-2013, etc.) and supplemented in accordance with the requirements of the European standard EN15227-2020 for theoretical calculation of processes as a result of emergency collisions of rolling stock with obstacles. Dependencies for determining the absorbed energy in an emergency collision depending on the impact speed and various obstacles are given

Keywords: Railway vehicles, passenger trains, emergency collision

1. INTRODUCTION

Uniform goals and uniform methods for the development of European transport systems are impossible without the sustainable functioning of railway transport. And its safe use should be provided by tools to assess the level of safety and performance by operators at the general levels.

For the modern transport needs of the population, all passenger cars must have devices ensuring the safety of train movement and the most comfortable conditions for the carriage of passengers and service personnel. The passenger rolling stock in operation meets the basic safety requirements for rail transport. Modern operating conditions associated with an increase in the turnover of passengers and the speeds of passenger trains lead to increased risks for the life and health of passengers in the event of an emergency. One of the main tasks facing the rolling stock of the Bulgarian State Railways is increasing operational reliability. The aim is to ensure the safety of train movement, improve operational performance, increase axle load and speed.

When designing railway vehicles and their certification, it is necessary to conduct static, dynamic and shock tests [1, 2, 3, 4]. At the present time, in the creation of passive safety means, the test for an emergency collision of rolling stock with obstacles is practically not used. Railway companies manufacturing energy absorbing devices (EAD) conduct bench tests. When designing a passive safety system, a calculation of the energy absorption value of the developed EAD structure and the duration of its deformation must be carried out.

To pre-calculate the parameters of energy absorbing devices, the following assumptions are made [5]:

- the train and the obstacle are non-deformable (absolutely solid bodies);
- the ideal collision case is considered;
- there are no motion resistance forces acting on the train or the obstacle;
- the impact is absolutely inelastic;
- before the collision, the train has a mass M1 and the speed of the obstacle V_1, M_2 and V_2 respectively, after the collision the train and the obstacle have a speed Vc;
- the deformation diagram of the energy absorbing device is assumed to be an ideal hard-plastic characteristic.

The absorbed energy E is determined by the formula:

$$E = F.L \tag{1}$$

where F – the force perceived by the car body upon impact, and L – deformation of the EAD.

2. METHODOLOGY FOR CALCULATING THE EMERGENCY COLLISION PROCESS

The methodology for calculating the emergency collision process is based on research [4], according to the requirements of the Russian standard GOST 32410 - 2013 [6], and an added supplement according to the requirements of the European standard EN15227 - 2020 [7].

Quantities to be determined:

1. Total speed of the train and the obstacle after an emergency collision – Vc, m/s:

$$Vc = (M_1.V_1+M_2.V_2)/(M_1+M_2) \tag{2}$$

2. Increase in the speed of the composition at the time of impact Δν, m/s:

$$\Delta\nu = Vc - V_1 \tag{3}$$

3. Collision time at the moment of impact Δt, s:

$$\Delta t = \Delta\nu/a_1 \tag{4}$$

where a_1 is the acceleration of the train upon impact.

4. Force of an impact affecting the car body - F, N:

$$F = M_1. |a_1| \tag{5}$$

5. Minimum deformation length La (taking into account the acceleration limitations – a_1), m:

$$La = |a_1|^{-1}.[M_2/(M_1+M_2)].[(V_1-V_2)^2]/2 \tag{6}$$

6. Minimum length of deformation L_F (taking into account the impact force restrictions – F), m:

$$L_F = |F|^{-1}.[M_1.M_2/(M_1+M_2)].[(V_1-V_2)^2]/2 \tag{7}$$

From the two obtained values of lengths La and L_F determined by formulas (6) and (7), the larger value is selected, which at the design stage is taken as a preliminary value of the minimum necessary contraction

*Corresponding author: <VTU Todor Kableshkov, Sofia, 158 Geo Milev Str. BULGARIA> and <vpavlov1718@gmail.com>

of the EAD in the process of its operation in an emergency collision of the composition with obstacles.

7. Value of the absorbed energy E, which must be absorbed by the EAD:

$$E = F.L_F \tag{8}$$

Limits on impact force are considered; longitudinal acceleration on impact and the maximum depth of deformations.

Table 1. Minimum required length of the UPE depending on the restrictive conditions.

V, km/h	Mass of obstacles M_2, t											
	1		2		15		30		80		550	
	L_F, m	La, m	L_F, m	La, m	L_F, m	La, m	L_F, m	La, m	L_F, m	La, m	L_F, m	La, m
10	0.002	1e-6	0.004	3e-4	0.0292	0.0000	0.0569	0.0000	0.1397	0.0001	0.55	0.0001
20	0.008	2e-6	0.016	11e-4	0.1168	0.0000	0.2276	0.0001	0.5587	0.0001	2.20	0.0005
30	0.018	4e-6	0.036	24e-4	0.2628	0.0001	0.5121	0.0001	1.2571	0.0003	4.95	0.0012
40	0.032	8e-6	0.064	43e-4	0.4673	0.0001	0.9103	0.0002	2.2349	0.0005	8.80	0.0021
50	0.050	12e-6	0.099	66e-4	0.7301	0.0002	1.4224	0.0003	3.4921	0.0008	13.75	0.0033
60	0.072	17e-6	0.144	96e-4	1.0513	0.0003	2.0483	0.0005	5.0286	0.0012	19.80	0.0048
70	0.098	24e-6	0.195	130e-4	1.4310	0.0003	2.7879	0.0007	6.8444	0.0017	26.95	0.0065
80	0.128	31e-6	0.255	170e-4	1.8690	0.0005	3.6414	0.0009	8.9397	0.0022	35.20	0.0085
90	0,162	39e-6	0.323	215e-4	2.3655	0.0006	4.6086	0.0011	11.314	0.0027	44.55	0.0108
100	0.199	48e-6	0.398	266e-4	2.9204	0.0007	5.6897	0.0014	13.968	0.0034	55.00	0.0133
110	0.241	59e-6	0.482	0.0321	3.5336	0.0009	6.8845	0.0017	16.902	0.0041	66.55	0.0161
120	0.287	70e-6	0.574	0.0383	4.2053	0.0010	8.1931	0.0020	20.114	0.0049	79.20	0.0192
130	0.337	82e-6	0.674	0.0449	4.9354	0.0012	9.6155	0.0023	23.606	0.0057	92.95	0.0225
140	0.391	95e-6	0.781	0.0521	5.7239	0.0014	11.152	0.0027	27.378	0.0066	107.80	0.0261
150	0.449	109e-6	0.897	0.0598	6.5708	0.0016	12.802	0.0031	31.429	0.0076	123.75	0.0300
160	0.511	124e-6	1.020	0.0680	7.4761	0.0018	14.566	0.0035	35.759	0.0087	140.80	0.0341
170	0.577	140e-6	1.152	0.0768	8.4398	0.0020	16.443	0.0040	40.368	0.0098	158.95	0.0385
180	0.647	157e-6	1.291	0.0861	9.4619	0.0023	18.435	0.0045	45.257	0.0110	178.20	0.0432
190	0.721	175e-6	1.439	0.0959	10.5425	0.0026	20.540	0.0050	50.425	0.0122	198.55	0.0481
200	0.798	194e-6	1.594	0.1063	11.6814	0.0028	22.759	0.0055	55.873	0.0135	220.00	0.0533
Conditions: Mass of composition M_1 = 550 t, acceleration limit, a = 7.5g m/s^2; and by force F = 2.5 MN.												

Table 2. Basic collision scenarios for locomotive-hauled passenger wagons.

V, km/h	Mass of obstacles M_2, t											
	1		2		15		30		80		550	
	E, MJ	L_F, m	E, MJ	L_F, m	E, MJ	L_F, m	E, MJ	L_F, m	E, MJ	L_F, m	E, MJ	L_F, m
10	0.005	0.002	0.010	0.004	0.073	0.029	0.142	0.057	0.349	0.140	**1.375**	**0.550**
20	0.020	0.008	0.040	0.016	0.292	0.117	0.569	0.228	1.397	0.559	5.500	2.200
30	0.045	0.018	0.090	0.036	0.657	0.263	1.280	0.512	**3.143**	**1.257**	12.375	4.950
40	0.080	0.032	0.159	0.064	1.168	0.467	2.276	0.910	5.587	2.235	22.000	8.800
50	0.125	0.050	0.249	0.100	1.825	0.730	**3.556**	**1.422**	8.730	3.492	34.375	13.750
60	0.180	0.072	0.359	0.143	2.628	1.051	5.121	2.048	12.57	5.029	49.500	19.800
70	0.245	0.098	0.488	0.195	3.577	1.431	6.970	2.788	17.11	6.844	67.375	26.950
80	0.319	0.128	0.638	0.255	**4.673**	**1.869**	9.103	3.641	22.35	8.940	88.000	35.200
90	0.404	0.162	0.807	0.323	5.914	2.365	11.522	4.609	28.29	11.314	111.37	44.550
100	0.499	0.200	0.996	0.399	7.301	2.920	14.224	5.690	34.92	13.968	137.50	55.000
110	0.604	0.242	1.206	0.482	8.834	3.534	17.211	6.884	42.25	16.902	166.37	66.550
120	0.719	0.287	1.435	0.574	10.513	4.205	20.483	8.193	50.28	20.114	198.00	79.200
130	0.843	0.337	1.684	0.674	12.338	4.935	24.039	9.616	59.02	23.606	232.37	92.950
140	0.978	0.391	1.953	0.781	14.310	5.724	27.879	11.152	68.44	27.378	269.50	107.80
150	1.123	0.449	2.242	0.897	16.427	6.571	32.004	12.802	78.57	31.429	309.37	123.75
160	1.278	0.511	2.551	1.020	18.690	7.476	36.414	14.566	89.40	35.759	352.00	140.80
170	1.442	0.577	2.880	1.152	21.100	8.440	41.108	16.443	100.9	40.368	397.37	158.95
180	1.617	0.647	3.228	1.291	23.655	9.462	46.086	18.434	113.1	45.257	445.50	178.20
190	1.802	0.721	3.597	1.439	26.356	10.542	51.349	20.540	126.1	50.425	496.37	198.55
200	**1.996**	**0.798**	**3.986**	**1.594**	29.204	11.681	56.897	22.759	139.7	55.873	550.00	220.00
Conditions: Mass of the composition M_1 = 550 t, force limitation F = 2.5 MN.												

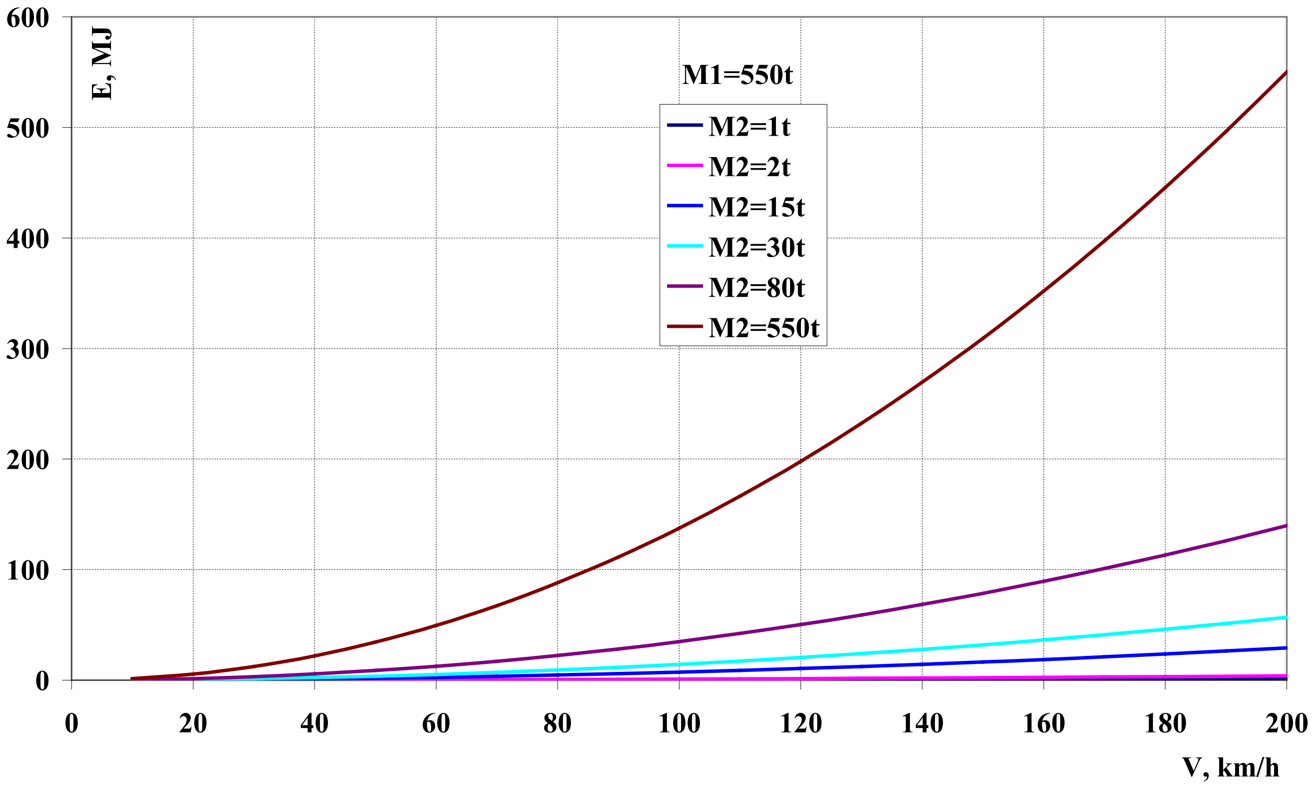

Figure 1. Absorbed energy E in collisions depending on the impact speed.

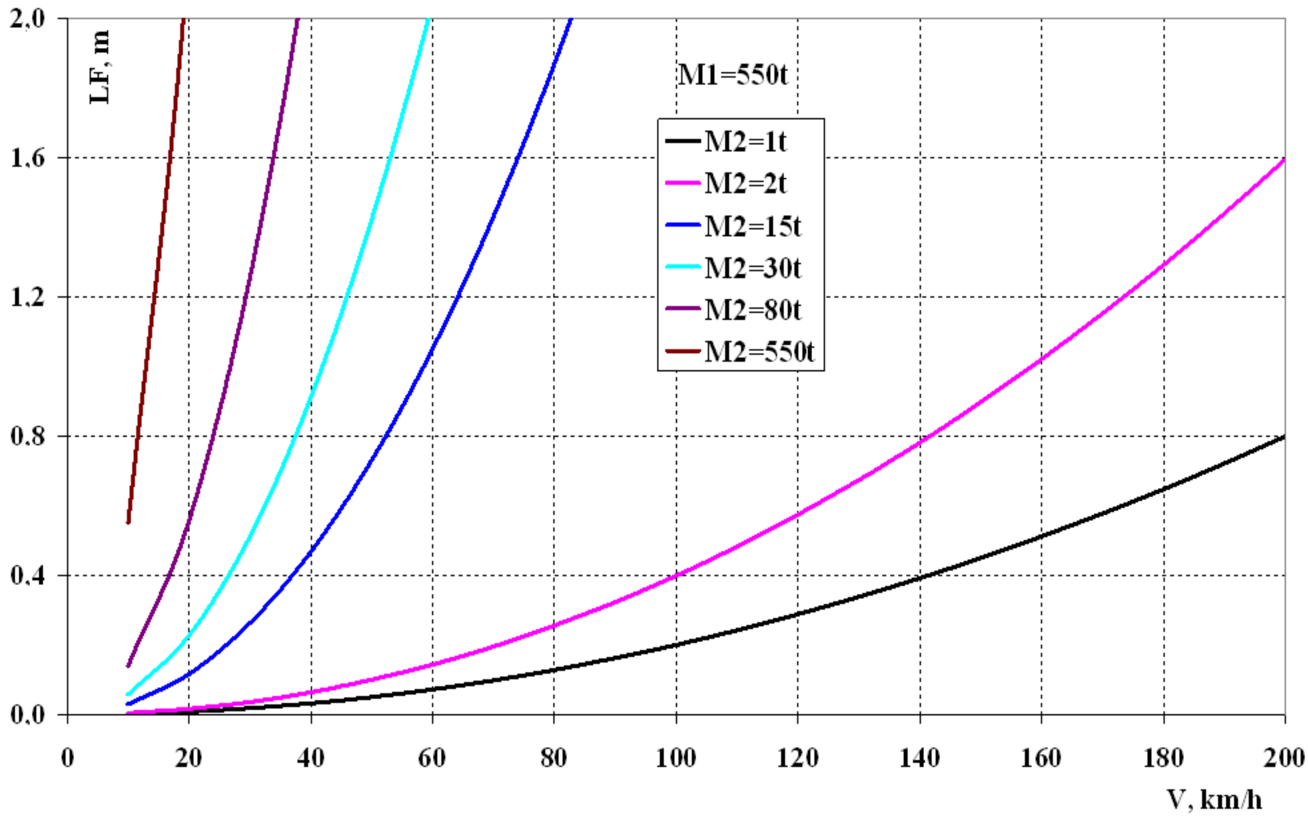

Figure 2. Length of EAD to absorb all impact energy.

Table 3. EAD parameters and conditions of collisions with various obstacles.

Mass of obstacle M_2, t	Energy E, MJ	Length L, m	Speed V_1, km/h
1	1.996	0.798	200
2	3.986	1.594	200
15	4.673	1.869	80
30	3.556	1.422	50
80	3.143	1.257	30
550	1.375	0.550	10
Conditions: Mass of the composition M_1 = 550 t, force limitation F = 2.5 MN.			

2.1. Determination of the total length and energy absorption of the EAD

For the protection of cargo and passengers, it is recommended that the acceleration value of 7.5g (75 m/s^2) [7] be accepted as the permissible limit for initial deceleration during a collision.

In the European standard EN15227 [7], in addition to modeling the obstacle, a deformable truck model with a high center of gravity is used as an absolutely rigid wall.

The following are considered as initial conditions:

- acceleration limit a = 7.5 g [7];
- limitation of the maximum force perceived by the basket - F = 2.5 MN [8];

- number of wagons in the train - N = 10 units with mass per wagon - m = 55 t;

- obstacles: No. 1 - large animal with mass M_{21} = 1 t; No. 2 - passenger car with mass M_{22} = 2 t; No. 3 - truck with mass M_{23} = 15 t; No. 4 - heavy-duty vehicle with mass M_{24} = 30 t; No. 5 - freight car with mass M_{25} = 80 t and No. 6 - stationary train with mass M_{26} - 550 t;

- the speed of the train V at the moment of impact – from 0 to 200 km/h.

The results are shown in table. 1, 2 and fig. 1 and 2.

Based on the calculations obtained considering the train as an absolutely rigid and unreformed body, the calculation of the length L of the EAD is not recommended due to the large impact force F. In the case of M_1 = 550 t and a = 7.5 g m/s^2, it turns out that at the moment of impact, a force F = M_1. $|a_1|$ = 40.47 MN acts on the car body. This force is overwhelming, according to [9]. Therefore, in the final calculations of the length L of the EAD, the limitations of force F = 2.5 MN and acceleration a = 7.5 g m/s^2 are assumed.

According to the results of the calculations, it follows that the maximum amount of absorbed energy, which is possible for implementation, is no more than 4.5 MJ, with a length L of the EAD no more than 2 m.

Provided that all wagons are equipped with the same EAD, the collision rates with different obstacles are not too high, as can be seen in Table 3.

2.2. Determination of the parameters of the EAD devices, taking into account the limitation of acceleration and changes in the mass of the composition.

In order to obtain more accurate calculation results, according to [10] it is necessary to use the assumption: the mass of the train is M_1 = 110 t.

Table 4. Basic collision scenarios for locomotive-hauled passenger coaches.

Speed V,km/h	Mass of obstacles M_2, t											
	1		2		15		30		80		550	
	E,MJ	L_F,m	E,MJ	L_F,m	E, MJ	L_F, m	E, MJ	L_F, m	E, MJ	L_F, m	E, MJ	L_F, m
10	0.005	0.002	0.010	0.004	0.066	0.026	0.118	0.047	0.232	0.093	0.458	0.183
20	0.020	0.008	0.039	0.016	0.264	0.106	0.471	0.189	0.926	0.371	1.833	0.733
30	0.045	0.018	0.088	0.035	0.594	0.238	1.061	0.424	2.084	0.834	**4.125**	**1.650**
40	0.079	0.032	0.157	0.063	1.056	0.422	1.886	0.754	**3.705**	**1.482**	7.333	2.933
50	0.124	0.050	0.246	0.098	1.650	0.660	2.946	1.179	5.789	2.316	11.458	4.583
60	0.178	0.071	0.354	0.141	2.376	0.950	**4.243**	**1.697**	8.337	3.335	16.500	6.600
70	0.243	0.097	0.481	0.193	3.234	1.294	5.775	2.310	11.347	4.539	22.458	8.983
80	0.317	0.127	0.629	0.251	**4.224**	**1.690**	7.543	3.017	14.821	5.928	29.333	11.733
90	0.401	0.161	0.796	0.318	5.346	2.138	9.546	3.819	18.758	7.503	37.125	14.850
100	0.495	0.198	0.982	0.393	6.600	2.640	11.786	4.714	23.158	9.263	45.833	18.333
110	0.600	0.240	1.188	0.475	7.986	3.194	14.261	5.704	28.021	11.208	55.458	22.183
120	0.714	0.285	1.414	0.566	9.504	3.802	16.971	6.789	33.347	13.339	66.000	26.400
130	0.837	0.335	1.660	0.664	11.154	4.462	19.918	7.967	39.137	15.655	77.458	30.983
140	0.971	0.388	1.925	0.770	12.936	5.174	23.100	9.240	45.389	18.156	89.833	35.933
150	1.115	0.446	2.210	0.884	14.850	5.940	26.518	10.607	52.105	20.842	103.125	41.250
160	1.268	0.507	2.514	1.006	16.896	6.758	30.171	12.069	59.284	23.714	117.333	46.933
170	1.432	0.573	2.838	1.135	19.074	7.630	34.061	13.624	66.926	26.771	132.458	52.983
180	1.605	0.642	3.182	1.273	21.384	8.554	38.186	15.274	75.032	30.013	148.500	59.400
190	1.789	0.715	3.546	1.418	23.826	9.530	42.546	17.019	83.600	33.440	165.458	66.183
200	**1.982**	**0.793**	**3.929**	**1.571**	26.400	10.560	47.143	18.857	92.632	37.053	183.333	73.333
Conditions: Mass of the composition M_1 = 110 t, force limitation F = 2.5 MN.												

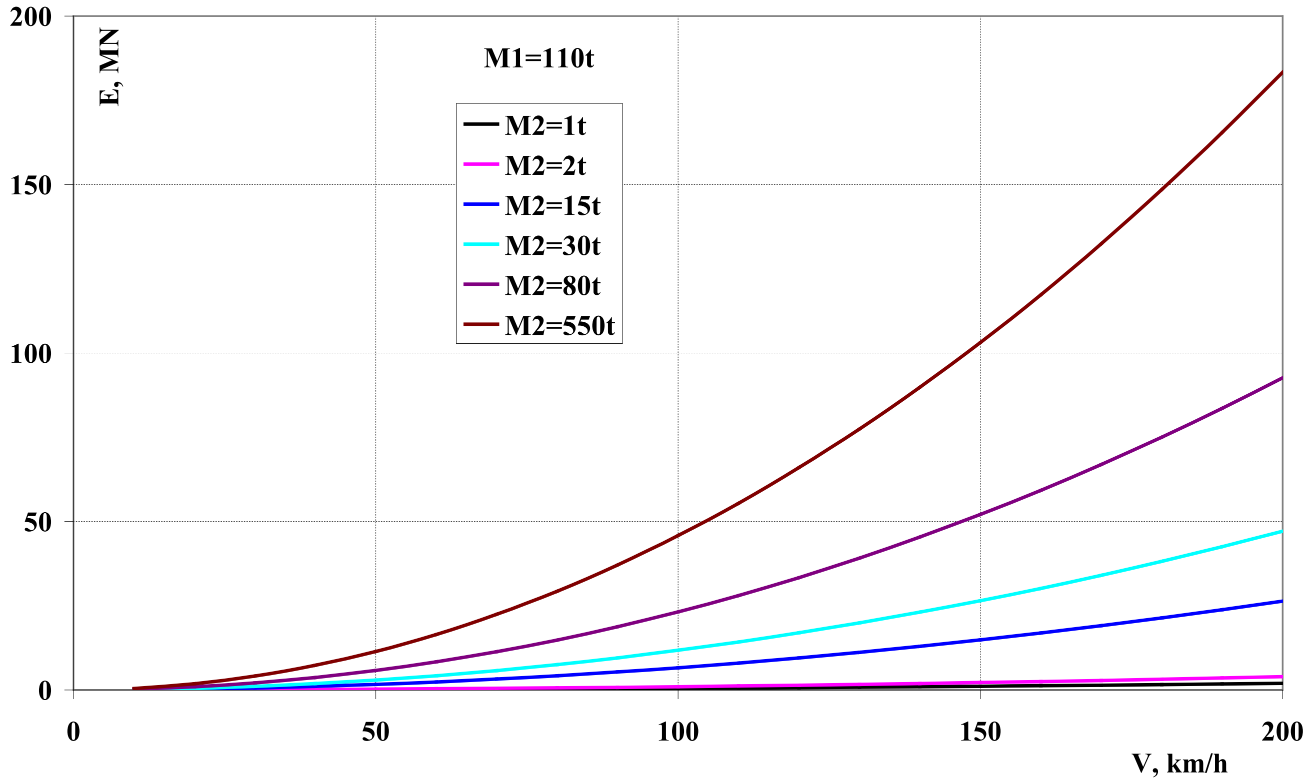

Figure 3. Absorbed energy E in collisions depending on impact speed.

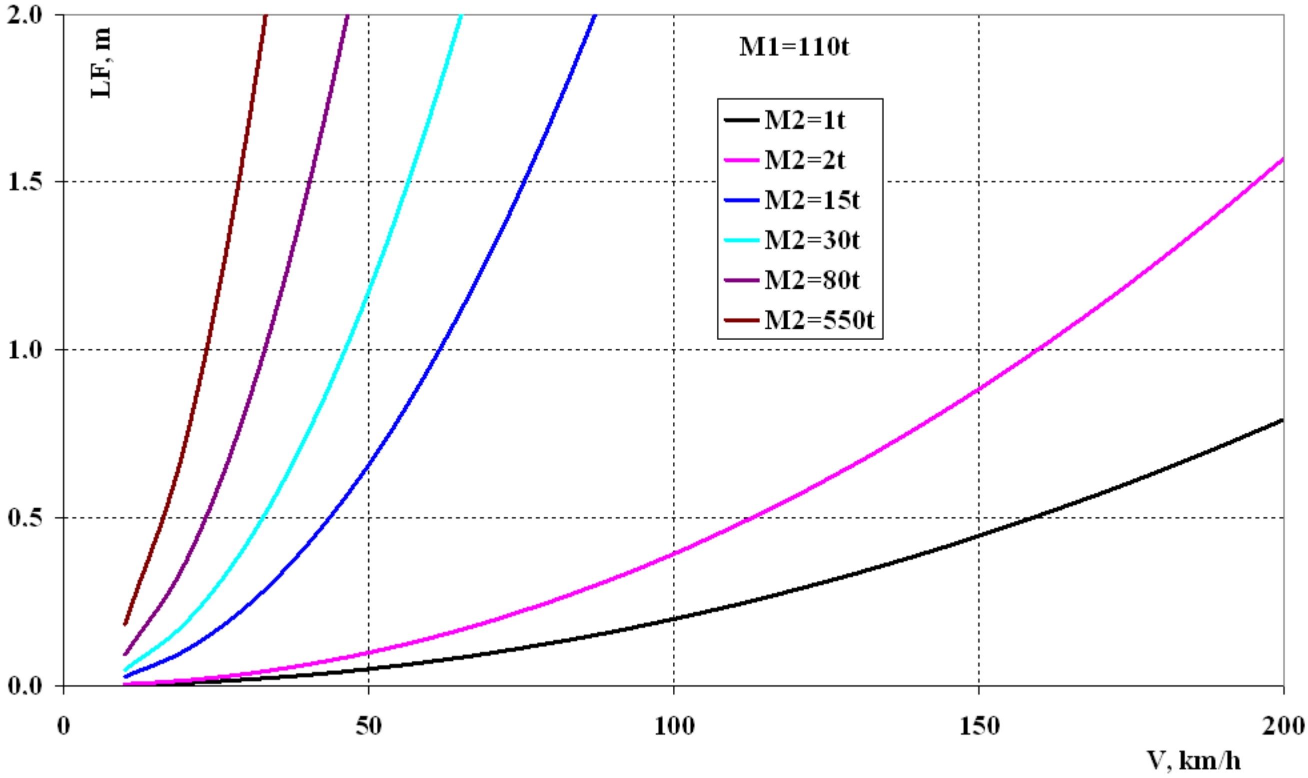

Figure 4. Length of EAD to absorb all impact energy.

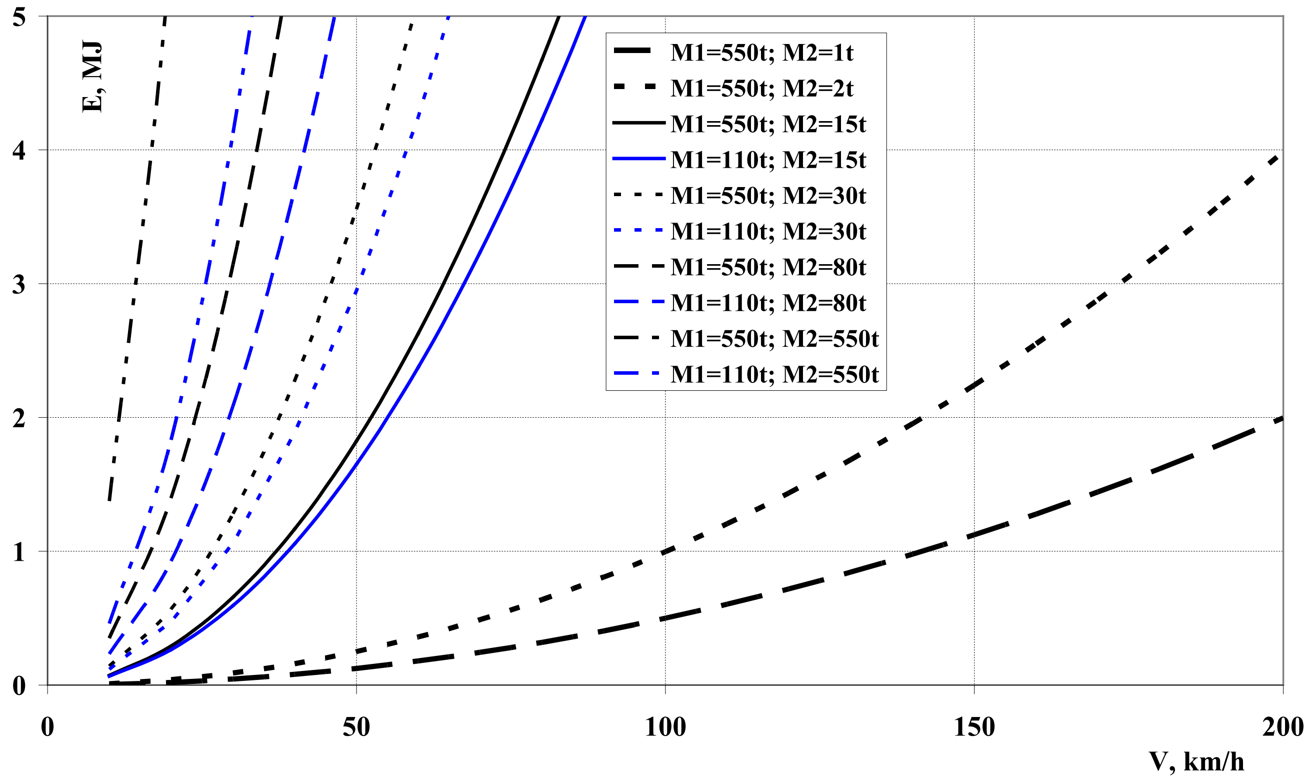

Figure 5. Comparative results of the energy E depending on the mass of the composition M_1.

Table 5. EAD parameters and collision conditions for different obstacles

Mass of obstacle M_2, t	Energy E, MJ	Length L, m	Speed V_1, km/h
1	1.996	0.799	200
2	3.986	1.594	200
15	4.673	1.869	80
30	3.556	1.422	50
80	3.143	1.257	30
550	1.375	0.550	10
Conditions: Mass of the composition M_1 = 550 t, force limitation F = 2.5 MN.			
Маса на препятствие M_2, t	Енергия E, MJ	Дължина на УПЕ - L, m	Скорост V_1, km/h
1	1.982	0.793	200
2	3.929	1.571	200
15	4.224	1.690	80
30	4.243	1.697	60
80	3.705	1.482	40
550	4.125	1.650	30
Conditions: Mass of composition M_1 = 110 t, acceleration limit, a = 2.32g m/s^2; and by force F = 2.5 MN.			

As a result of the calculations, taking into account the force limitation F = 2.5 MN, an acceleration $a = F/(M_1.0.00981) = 2.317.g \approx 2.32.g$ m/s^2 is realized (a value close to the real one).

The calculation results are presented in Table 4 and Figures 3 and 4.

When the mass of the train M_1 = 110 t, and a collision with an obstacle over 15 t, an increase in the maximum speed at the moment of impact is observed.

The summarized results of the two calculations are presented in Table 5 and Figures 5 and 6.

The results of the calculations for the mass of the compositions of 110 t and 550 t depending on the impact speed are given in Figure 7.

Calculations show that as the mass of the train decreases, in a situation closer to reality, the speed of a safe collision increases significantly.

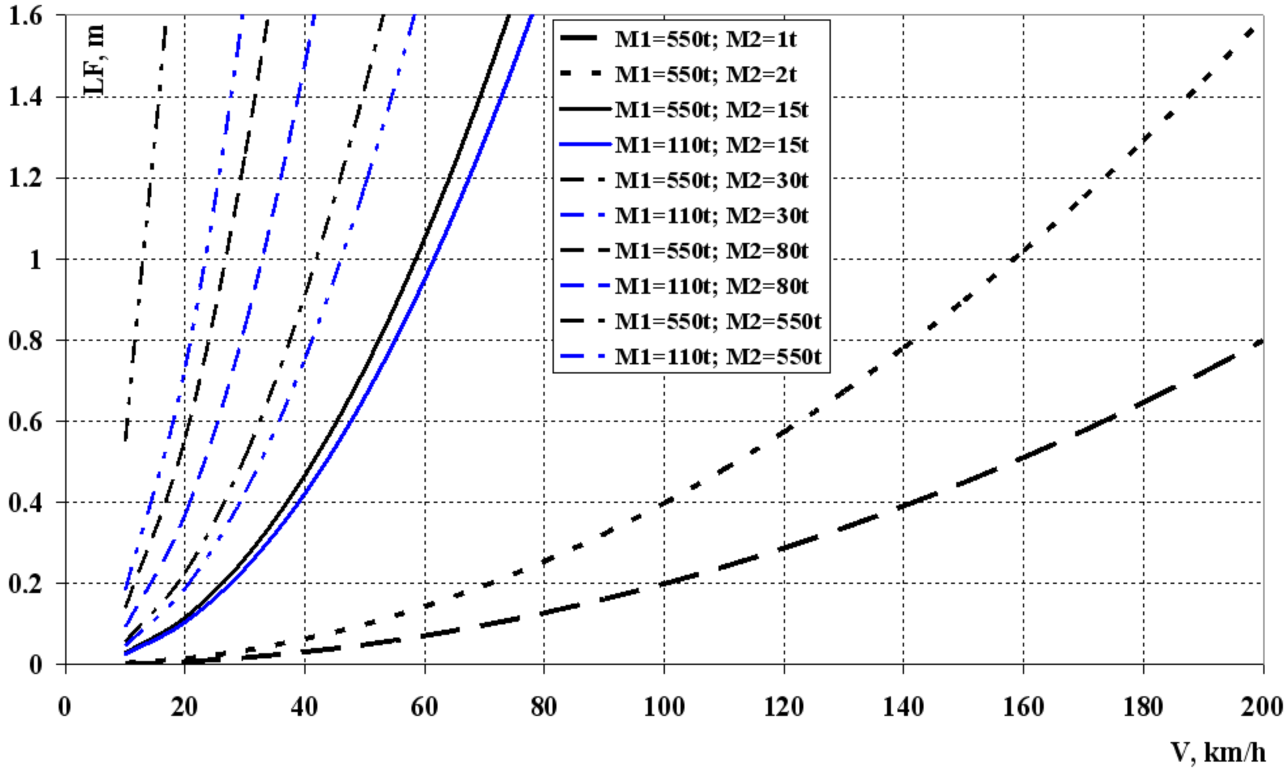

Figure 6. Comparative results of the length L of the EAD depending on the mass of the composition M_1

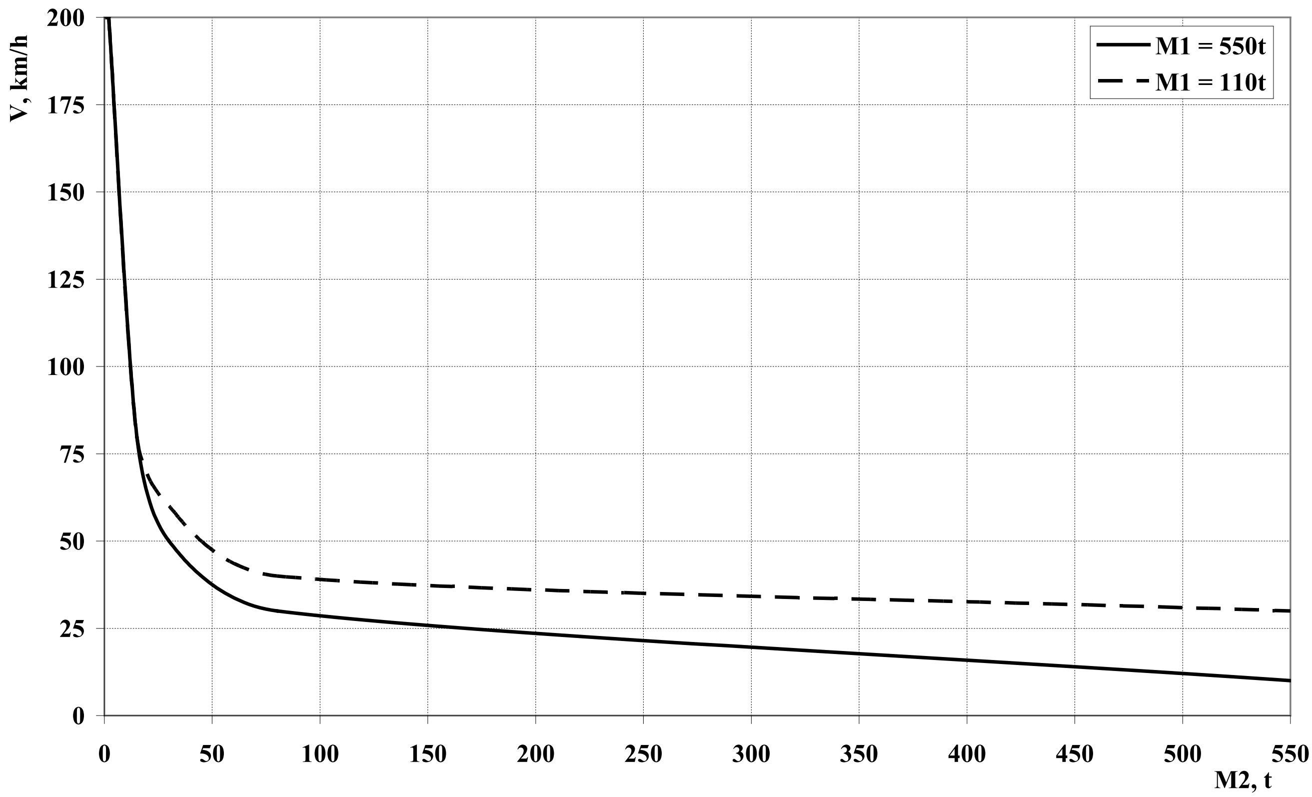

Figure 7. Dependence of the mass of the obstacles M_2 on the impact speed V at different mass of the composition M_1.

Under such conditions, the indicators of the maximum possible speeds at which safety will be ensured should be increased, but in order to test this theory, it is necessary to conduct more detailed studies in specialized programs for the study of longitudinal train dynamics, in modeling of each unit of rolling stock with EAD.

In connection with the new trends in railway transport and in order to guarantee traffic safety, in 1991. The UIC makes appropriate corrections in the UIC 526 [11-14]. The most important change is aimed at increasing the energy absorption of weaning facilities.

There is a need to use a new type of energy-absorbing element, guaranteeing sufficient energy absorption - 25% greater than the existing one realized in the constructions of towing and weaning equipment (TWE). It deserves special attention that many specialists are working on the creation of TWE structures with energy-absorbing devices, ensuring durability commensurate with the service life of the wagons and not requiring maintenance during operation [15-20].

Trends in railcar construction are the application of category "C" buffers with "crash" energy absorbing devices. The buffer with "crash" technology acts by absorbing a large part of the energy of the impact in an irreversible process.

For the Bulgarian State Railways, it is necessary to construct a buffer with "crash" elements, which will be destroyed in the event of an impact between the wagons with an impact speed of over 12 km/h and a force > 1.5 MN.

CONCLUSION

In the paper, a methodology for calculating the emergency collision process is proposed, based on research [5], in accordance with the requirements of Russian regulatory documents [6, 8], and an addendum is introduced in accordance with the requirements of the European standard EN15227-2020 [7]. The absorbed energy in an emergency collision was determined depending on the speed of the impact and with different obstacles. The masses of the composition and the obstacles were reported. The parameters of the EAD devices were determined, and the limits of force and acceleration were reported. The need for the construction and implementation in operation of a buffer with "crash" elements, which is destroyed in the event of an impact between the wagons with an impact speed of over 12 km/h and a force > 1.5 MN, is indicated.

REFERENCES

[1] D. Petrovic, “Stability of waggon carrying structure at impact”, Ph. D. thesis, Faculty of Mechanical Engineering Kraljevo, Kraljevo, (2000)

[2] D. Petrovic, “Dynamic of impact of waggons”, Zaduzbina Andrejevic, Belgrade, (2001)

[3] Рязанов Э. М., Совершенствование расчетных методов оценки работоспособности аварийных крэш-систем електропоездов, Екатеринбург (2016).

[4] Atmadzhova D., The Bulgarian State Railways experience in determining fatigue strength of rolling stock structures, XVI Conference RAILCON‘14 Niš, Serbia, pp.69-72 , (2014)

[5] Барышников, А.В. Разработка системы пассивной безопасности пассажирского вагона от аварийных столкновений но основе применения буферов с жертвенными элементами, Дисс.// Москва (2019).

[6] ГОСТ 32410–2013 Крэш-системы аварийные железнодорожного подвижного состава для пассажирских перевозок. Технические требования и методы контроля. М.: Стандартинформ, (2014).

[7] EN 15227-2020 Railway applications - Crashworthiness requirements for rail vehicles (2020)

[8] Нормы для расчета и проектирования новых и модернизированных вагонов железных дорог МПС колеи 1520 мм (несамоходных) // ВНИИВ- ВНИИЖТ. pp. 260 (1983).

[9] Вершинский, С. В. Расчет вагонов на прочность. М.: Машиностроение, pp. 432 (1971).

[10] Барышников, А. В. Выбор конструкционного решения энергопоглощающего устройства и обоснование его эффективности// Наука и техника транспорта. Vol.2 pp. 52-58 (2019).

[11] UIC 526-1 Wagons – Buffers with a stroke of 105 mm, July (2008)

[12] UIC 526-2 Wagons – Buffers with a stroke of 75 and 105 mm, October (2021)

[13] UIC 526-3 Wagons – Buffers with a stroke of 130 and 150 mm, October (2008)

[14] UIC 528 Buffer gear for coaches’, September (2007)

[15] M. Milošević, D. Stamenković, S. Jovanović, I. Puletić, L. Mladenović ’’Testing of buffers and draw gear with rubber-metal springs’’, XII Scientificexpert Conference on Railway "RAILCON '06", Niš, (in Serbian) (2006).

[16] D. Stamenković, N. Tojagić, P. Peković, Buffing Gear of Serbian Railway's Freight Cars, XII Scietific-Expert Conference on Railway, Niš, (2006).

[17] M. Milošević, D. Stamenković, S. Jovanović, I. Puletić, L. Mladenović, Examination of Buffing and Draw Gear With Rubber-Metal Springs, XII Scietific-Expert Conference on Railway, Niš, (2006)

[18] M. Milošević, D. Stamenković, A. Milošević “Research of absorbed energy of rail vehicle buffers filled with rubber-metal springs”, 18th International Conference „CURRENT PROBLEMS IN RAIL VEHICLES – PRORAIL 2007", Žilina, Slovakia, (2007).

[19] Dušan Stamenković, Miloš Milošević, FRICTION AT RUBBER-METAL SPRINGS, 11th International Conference on Tribology - SERBIATRIB ‘09, Belgrade, Serbia, 13 - 15 May (2009)

[20] Milan Banić, Dušan Stamenković, Miloš Milošević, Aleksandar Miltenović, TRIBOLOGY ASPECT OF RUBBER SHOCK ABSORBERS DEVELOPMENT, 13th International Conference on Tribology – Serbiatrib’13, Kragujevac, Serbia, 15 – 17 May (2013).

SESSION C

PRODUCTION TECHNOLOGIES

Additive manufacturing - a view through the prism of standardization

Pavle Ljubojević[1*], Tatjana Lazović[1], Snežana Ćirić-Kostić[2]
[1]Faculty of Mechanical Engineering, University of Belgrade, Belgrade (Serbia)
[2]Faculty of Mechanical and Civil Engineering in Kraljevo, University of Kragujevac, Kraljevo (Serbia)

This paper explores the significance of standardization in the field of additive manufacturing (AM). The rapid growth of AM in modern industries has highlighted the need for standardization to ensure compatibility, quality control, and market opportunities for AM products. The paper emphasizes the flexibility of AM technologies in meeting industrial and ecological requirements, revolutionizing business models, and satisfying customer needs. It provides an overview of the International Organization for Standardization (ISO) and ASTM International (American Society for Testing and Materials), two major organizations involved in developing and publishing international standards for AM. The paper discusses the technical committees, working groups, and collaborations established by ISO and ASTM to address various aspects of AM standardization. Additionally, it highlights the ongoing efforts in Serbian national standardization and proposes future research on analyzing the scopes and contents of AM standards for improved usability. Overall, the paper emphasizes the crucial role of standardization in supporting the continued advancement of additive manufacturing.

Keywords: additive manufacturing, additive technologies, standardization, standards, ISO, ASTM International

1. INTRODUCTION

The application of additive manufacturing (AM) is imperative in modern, digital industries and is rapidly growing day by day. The reason for this is the complete flexibility of technologies and procedures of AM to present concepts of industrial development, but also to the rigorous ecological, energy and environmental requirements of modern society development. AM is changing the way companies work and the way they communicate with consumers, opening up new horizons for increased profits and more sustainable business models. AM also has a powerful role in fulfilling the complicated and unique needs of customers by applying different technologies and materials. The contribution of the development of AM to competitiveness and profitability through the optimization of production processes, as well as wide opportunities for the implementation of innovative solutions that vary from the reduction of waste and the consumption of material resources and energy, to shorter supply chains and to a longer product life [1], is also significant. In recent years, new additive technologies and materials have been intensively developed. Products obtained by applying AM are increasingly used in almost all areas of modern consumer society. These products must meet many specific requirements, such as mechanical, physical, chemical, ergonomic, aesthetic, ecological and other properties, as well as safety and security properties, economy, energy efficiency and many other conditions of modern society. That's why there is a need for organization and regulation of the entire system of AM in present-day and future industries and product exploitation, and this can only be achieved through standards and standardization!

2. ADDITIVE MANUFACTURING

Additive manufacturing is a common term for technologies, which are based on the principle of making objects by adding materials [2]. The material is added in the places where it is needed and in the quantities that are needed. In doing so, material is added layer by layer, without using tools to shape or remove material. The process is based on the direct translation of a three-dimensional digital CAD model into a real physical object. Thanks to additive technologies, it is possible to make parts with reduced mass, with bionic design, make assemblies contained in one component, adjustment of the object's geometry and function to the user, integration of two or more functions in one component, make moulding tools with cooling channels, make of medical aids completely topologically adapted to the user etc [2]. Over the years, the need for standards in the field of AM has been widely recognized as a necessity in academia, research organizations, and industry. Priorities in the development and publication of standards include materials, production processes and test methods, as well as increasing market opportunities for the placement of products obtained by AM [3].

3. STANDARDS AND STANDARDIZATION

A standard is an official document that provides characteristics, specifications, guidelines or requirements used to ensure that materials, processes, products and services are fit for purpose [4]. International standards establish the desirable or mandatory performance of products and services, as well as the level, methods and means of their quality control. In this way, optimal conditions and procedures are ensured, to achieve compatibility of products and services in space and time. Engineering standards prescribe rules and provide recommendations for the construction and equipment, the performance of structures, durability, service life, quality, safety, codes of practice, test methods, analysis, evaluation, verification, measurement, production, design, drawing, use, the machines safety and production conditions, symbols and terminology, abbreviations, symbols, units, etc.

ISO is the International Organization for Standardization. It is founded to develop and publish international standards, as it said in [4]: to answer the

*Corresponding author: Kraljice Marije 16, 11120 Belgrade 35, Serbia, pljubojevic@mas.bg.ac.rs

question "What is the best way to do this?". This organization was founded in 1946 when 67 Technical Committees were constituted. At the time of writing this paper, ISO has 816 committees and subcommittees dealing with standards development, and the number is increasing every year. The organization has members from national standardization organizations of 168 countries around the world. So far, 24780 standards have been published, covering practically all features of production, technology and management [4].

The American Society for Testing and Materials - ASTM was formed in 1898. In 2001, they changed the name to ASTM International. This organization deals with the development and publication of international standards. Today, over 12,000 ASTM standards are used worldwide to improve product quality, improve health and safety, strengthen market access and trade, and build consumer confidence [5]. ASTM International employs more than 30,000 professionals from 140 countries, who create classifications, specifications, test methods, guides and practices that support industries and governments around the world. Within ASTM there are more than 140 committees for writing technical standards from a wide range of industries [6]: metals, construction, petroleum, consumer products, and many others. When emerging industries – such as additive manufacturing, nanotechnology, industrial biotechnology etc. want to advance the growth of technologies through standardization, they come to ASTM International [5].

3.1. ISO

Technical Committee TC 261 - Additive manufacturing [7,8], created in 2011, operates within the ISO organization. This committee's working groups (36 in total so far) deal with standardization in the area of AM: terms and definitions, hardware and software for the Technical Committee TC 261 - Additive manufacturing [7,8], created in 2011, and operates within the ISO organization. The working groups (36 in total so far) of this committee deal with standardization in the field of AM: terms and definitions, hardware and software for the accomplishment of different AM technologies, testing, quality of facilities and processes, procurement contracts, etc. Two working groups are ad hoc ones and the third one is the Chair's Advisory Group. The primary ISO/TC 261 working groups are WG1 – Terminology, WG 2 – Processes, systems and materials, WG 3 – Test methods and quality specifications, WG 4 – Data and Design and WG 6 – Environment, Health and Safety. Two joint working groups were formed within the cooperation of TC 261 and other committees: with committee ISO/TC 44 (Welding and allied processes) working group JWG 10 - Additive manufacturing in aerospace applications and with committee ISO/TC 61 (Plastics) working group JWG 11 - Additive manufacturing for plastics. Other working groups are joint groups - JG, formed within the ISO cooperation with ASTM International.

Active members of the ISO/TC 261 committee are representatives of national standardization organizations from 27 countries: Australia - SA, Austria - ASI, Belgium - NBN, Brazil - ABNT, Canada - SCC, China - SAC, Denmark - DS, Finland - SFS, France – AFNOR, Germany – DIN, Ireland – NSAI, Israel – SII, Italy – UNI, Japan – JISC, Republic of Korea – KATS, Netherlands – NEN, Norway – SN, Philippines – BPS, Poland – PKN, Portugal – IPQ, Russian Federation - GOST R, Singapore - SSC, Spain - UNE, Sweden - SIS, Switzerland - SNV, United Kingdom - BSI, United States - ANSI. Observer members are from 8 countries: Czech Republic - UNMZ, Iran - INSO, Jordan - JSMO, Luxembourg - ILNAS, New Zealand - NZSO, Romania - ASRO, Rwanda - RSB, South Africa - SABS and Türkiye - TSE. He is currently the secretary of this committee under the authority of the German Organization for Standardization (Deutsches Institut für Normung e.V. - DIN).

The titles of the standards issued by TC 261, which have only ISO in the designation, are given in Table 1. It is a group of three standards that refer to general principles in the field of AM: part positioning, coordinates, orientation, process categories, feedstock, main characteristics and corresponding test methods.

In addition to the standards listed in Table 1, another ISO standard is under preparation and is currently in the draft category - ISO/DIS 27548: Additive manufacturing of plastics — Environment, health, and safety — "Test method for determination of particle and chemical emission rates from desktop material extrusion 3D printer".

Table 1: Published ISO standards

ISO 17295: 2023	Additive manufacturing — General principles — Part positioning, coordinates and orientation
ISO 17296-2: 2015	Additive manufacturing — General principles — Part 2: Overview of process categories and feedstock
ISO 17296-3: 2014	Additive manufacturing — General principles — Part 3: Main characteristics and corresponding test methods

3.2. ASTM International

ASTM Technical Committee F42 on Additive Manufacturing Technologies was formed in 2009. Currently, this committee has more than 725 members, working on the development of AM standards [9]. Within the F42 committee, there are technical subcommittees that deal with specific segments within the general subject area - additive manufacturing [10].

An overview of the subcommittees of Committee F42 is given in Table 2. A list of the 28 standards published by Committee F42 that carry only the ASTM "F" designation is given in Table 3.

Table 2: Subcommittees of F42 Technical Committee

F42.01	Test Methods
F42.04	Design
F42.05	Materials and Processes (Metals, Polymers, Ceramics)
F42.06	Environment, Health, and Safety
F42.07	Applications (Aviation, Spaceflight, Medical/Biological, Transportation/Heavy, Machinery, Maritime, Electronics, Construction, Oil/Gas, Consumer, Energy)
F42.08	Data
F42.90	Executive (Terminology, US Technical Advisory Group to ISO TC 261)

Table 3: Published ASTM standards

F42.01 – Test Methods	
F2971-13 (2021)	Standard Practice for Reporting Data for Test Specimens Prepared by Additive Manufacturing
F3122-14 (2022)	Standard Guide for Evaluating Mechanical Properties of Metal Materials Made via Additive Manufacturing Processes
F3522-22	Standard Guide for Additive Manufacturing of Metals — Feedstock Materials — Assessment of Powder Spreadability
F3571-22	Standard Guide for Additive Manufacturing – Feedstock – Particle Shape Image Analysis by Optical Photography to Identify and Quantify the Agglomerates/Satellites in Metal Powder Feedstock
F3606-22	Standard Guide for Additive Manufacturing — Feedstock Materials — Testing Moisture Content in Powder Feedstock
F3624-23	Standard Guide for Additive Manufacturing of Metals – Powder Bed Fusion – Measurement and Characterization of Surface Texture
F3626-23	Standard Guide for Additive Manufacturing — Test Artifacts — Accelerated Build Quality Assurance for Laser Beam Powder Bed Fusion (PBF-LB)
F42.04 – Design	
F3413-19e1	Guide for Additive Manufacturing — Design — Directed Energy Deposition
F3529-21	Guide for Additive Manufacturing — Design — Material Extrusion of Polymers
F3530-22	Standard Guide for Additive Manufacturing — Design — Post-Processing for Metal PBF-LB
F42.05 – Materials and Processes	
F2924-14 (2021)	Standard Specification for Additive Manufacturing Titanium-6 Aluminum-4 Vanadium with Powder Bed Fusion
F3001-14 (2021)	Standard Specification for Additive Manufacturing Titanium-6 Aluminum-4 Vanadium ELI (Extra Low Interstitial) with Powder Bed Fusion
F3049-14 (2021)	Standard Guide for Characterizing Properties of Metal Powders Used for Additive Manufacturing Processes
F3055-14a(2021)	Standard Specification for Additive Manufacturing Nickel Alloy (UNS N07718) with Powder Bed Fusion
F3056-14 (2021)	Standard Specification for Additive Manufacturing Nickel Alloy (UNS N06625) with Powder Bed Fusion
F3091/F3091M-14(2021)	Standard Specification for Powder Bed Fusion of Plastic Materials
F3184-16	Standard Specification for Additive Manufacturing Stainless Steel Alloy (UNS S31603) with Powder Bed Fusion
F3187-16	Standard Guide for Directed Energy Deposition of Metals
F3213-17	Standard for Additive Manufacturing – Finished Part Properties – Standard Specification for Cobalt-28 Chromium-6 Molybdenum via Powder Bed Fusion
F3301-18a	Standard for Additive Manufacturing – Post Processing Methods – Standard Specification for Thermal Post-Processing Metal Parts Made Via Powder Bed Fusion
F3302-18	Standard for Additive Manufacturing – Finished Part Properties – Standard Specification for Titanium Alloys via Powder Bed Fusion
F3318-18	Standard for Additive Manufacturing – Finished Part Properties – Specification for AlSi10Mg with Powder Bed Fusion – Laser Beam
F42.07 – Applications	
F3456-22	Standard Guide for Powder Reuse Schema in Powder Bed Fusion Processes for Medical Applications for Additive Manufacturing Feedstock Materials
F3554-22	Standard Specification for Additive Manufacturing – Finished Part Properties – Grade 4340 (UNS G43400) via Laser Beam Powder Bed Fusion for Transportation Applications
F3572-22	Standard Practice for Additive Manufacturing – General Principles – Part Classifications for Additive Manufactured Parts Used in Aviation
F42.08 – Data	
F3490-21	Standard Practice for Additive Manufacturing — General Principles — Overview of Data Pedigree
F3560-22	Standard Specification for Additive Manufacturing – Data – Common Exchange Format for Particle Size Analysis by Light Scattering
F3605-23	Standard Guide for Additive Manufacturing of Metals — Data — File Structure for In-Process Monitoring of Powder Bed Fusion (PBF)

The percentage distribution of published standards by subcommittees (specific areas of AM to which they refer) is shown in Figure 1.

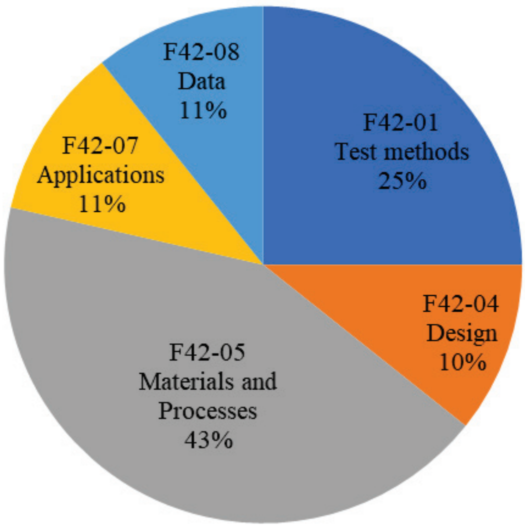

Figure 1: Distribution of published ASTM standards by subcommittees

Currently, most ASTM standards on AM are published in the field of Materials and Processes (43%), followed by Test Methods (25%). In the areas of Design, Application and Data there is an almost equal number of standards (about 11%). In the domain of Materials and Processes, one standard refers to Plastics, and all others to metals and alloys, as well as related processes. In the area of Design, there are three standards, one of which refers to metals, the second one to polymers, and the third one to directed energy deposition. Dedicated standards have been developed for medical applications, transport applications and for use in aviation.

In addition to the standards listed in Table 3, there is also a large group of standards that have been developed and published jointly by ISO and ASTM International.

3.3. ISO/ASTM

ISO and ASTM signed a cooperation agreement in 2011, with the aim of joint development and adoption of international standards that serve the global market in the field of AM. The purpose of this agreement is to eliminate duplication of effort while optimally allocating resources in the AM industry.

The working groups formed for cooperation between ISO and ASTM International on the development and publication of joint standards in the area of AM are listed in Table 4. A large number of working groups tells us about the great and growing importance of AM in all spheres of human activity.

Table 4: Joint ISO/TC 261-ASTM F 42 working groups

JG	Working group name
51	Terminology
52	Standard test artifacts
54	Fundamentals of Design
56	Standard Practice for Metal Powder Bed Fusion to Meet Rigid Quality Requirements
57	Process-specific design guidelines and standards
58	Qualification, quality assurance and post processing of powder bed fusion metallic parts
59	NDT for AM parts
61	Mechanical properties characterization of additively manufactured metallic materials
62	Guide for conducting round robin studies for additive manufacturing
63	Test methods for characterization of powder flow properties for AM applications
64	Additive Manufacturing File Format (AMF)
68	EH&S for 3D printers
69	EH&S for use of metallic and polymer materials
71	Powder quality assurance
72	Machine - Production process qualification
73	Digital product definition and data management
74	Personnel qualifications
75	Industrial conformity assessment at additive manufacturing centres
76	Revision of ISO 17296-3 & ASTM F3122-14
77	Test method of sand mold for metalcasting
78	Safety regarding AM-machines (relating to harmonized European Standards, Type C-Standard)
79	Qualification for AM processes in automotive applications
80	Quality requirements for additive manufacturing in building & construction (structural and infrastructure elements)
81	Metallic materials for additive manufacturing
82	Characterization of ceramic feedstock materials

The common ISO/ASTM standards are listed in Table 5. These are the standards, whose description and offer to users are available on the websites of both organizations. Those standards were either created or were last updated in the period from 2020-2023. Some standards have the common designation ISO/ASTM but are available on the website of only one of these two organizations. The titles of these standards are given in Tables 6 and 7.

Table 5: Published ISO/ASTM standards available on both ISO and ASTM websites [4-10]

ISO/ASTM 52900:2021	Additive manufacturing — General principles — Fundamentals and vocabulary
ISO/ASTM 52903-1: 2020	Additive manufacturing — Material extrusion-based additive manufacturing of plastic materials — Part 1: Feedstock materials
ISO/ASTM 52903-2: 2020	Additive manufacturing — Material extrusion-based additive manufacturing of plastic materials — Part 2: Process equipment
ISO/ASTM 52909: 2022	Additive manufacturing of metals — Finished part properties — Orientation and location dependence of mechanical properties for metal powder bed fusion
ISO/ASTM 52911-1: 2019	Additive manufacturing — Design — Part 1: Laser-based powder bed fusion of metals
ISO/ASTM 52911-2: 2019	Additive manufacturing — Design — Part 2: Laser-based powder bed fusion of polymers
ISO/ASTM 52911-3: 2023	Additive manufacturing — Design — Part 3: PBF-EB of metallic materials
ISO/ASTM 52915: 2020	Specification for additive manufacturing file format (AMF) Version 1.2
ISO/ASTM 52925: 2022	Additive manufacturing of polymers — Feedstock materials — Qualification of materials for laser-based powder bed fusion of parts
ISO/ASTM TS 52930: 2021	Additive manufacturing — Qualification principles — Installation, operation and performance (IQ/OQ/PQ) of PBF-LB equipment
ISO/ASTM 52931: 2023	Additive manufacturing of metals — Environment, health and safety — General principles for use of metallic materials
ISO/ASTM 52936-1: 2023	Additive manufacturing of polymers — Qualification principles — Part 1: General principles and preparation of test specimens for PBF-LB
ISO/ASTM 52942: 2020	Additive manufacturing — Qualification principles — Qualifying machine operators of laser metal powder bed fusion machines and equipment used in aerospace applications
ISO/ASTM 52950: 2021	Additive manufacturing — General principles — Overview of data processing

Table 6: Published ISO/ASTM standards available only on ISO website [4,7,8]

ISO/ASTM 52901:2017	Additive manufacturing — General principles — Requirements for purchased AM parts
ISO/ASTM 52904:2019	Additive manufacturing — Process characteristics and performance — Practice for metal powder bed fusion process to meet critical applications
ISO/ASTM TR 52906:2022	Additive manufacturing — Non-destructive testing — Intentionally seeding flaws in metallic parts

ISO/ASTM 52907:2019	Additive manufacturing — Feedstock materials — Methods to characterize metal powders
ISO/ASTM TR 52912:2020	Additive manufacturing — Design — Functionally graded additive manufacturing
ISO/ASTM TR 52916:2022	Additive manufacturing for medical — Data — Optimized medical image data
ISO/ASTM TR 52917:2022	Additive manufacturing — Round robin testing — General guidelines

Table 7: Published ISO/ASTM standards available only on ASTM website [5,9,10]

ISO/ASTM52921-13(2019)	Standard Terminology for Additive Manufacturing—Coordinate Systems and Test Methodologies
ISO/ASTM52901-16	Standard Guide for Additive Manufacturing – General Principles – Requirements for Purchased AM Parts

3.4. Standards under development

AM standards currently under development in co-production between ISO and ASTM International are listed in Table 8.

Table 8: ISO/ASTM standards under development [5,9,10]

ISO/ASTM FDIS 52902	Additive manufacturing — Test artifacts — Geometric capability assessment of additive manufacturing systems
ISO/ASTM TR 52905	Additive manufacturing of metals — Non-destructive testing and evaluation — Defect detection in parts
ISO/ASTM DIS 52908	Additive manufacturing of metals — Finished Part properties — Post-processing, inspection and testing of parts produced by powder bed fusion
ISO/ASTM DIS 52910	Additive manufacturing — Design — Requirements, guidelines and recommendations
ISO/ASTM DTR 52913-1	Additive manufacturing — Feedstock materials — Part 1: Parameters for characterization of powder flow properties
ISO/ASTM CD TR 52918	Additive manufacturing — Data formats — File format support, ecosystem and evolutions
ISO/ASTM CD 52919	Additive manufacturing — Qualification principles — Test method of sand moulds for metal casting
ISO/ASTM FDIS 52920	Additive manufacturing — Qualification principles — Requirements for industrial additive manufacturing processes and production sites
ISO/ASTM FDIS 52924	Additive manufacturing of polymers — Qualification principles — Classification of part properties
ISO/ASTM DIS 52926-1	Additive Manufacturing of metals — Qualification principles — Part 1: General qualification of operators
ISO/ASTM DIS 52926-2	Additive Manufacturing of metals — Qualification principles — Part 2: Qualification of operators for PBF-LB
ISO/ASTM DIS 52926-3	Additive Manufacturing of metals — Qualification principles — Part 3: Qualification of operators for PBF-EB
ISO/ASTM DIS 52926-4	Additive Manufacturing of metals — Qualification principles — Part 4: Qualification of operators for DED-LB
ISO/ASTM DIS 52926-5	Additive Manufacturing of metals — Qualification principles — Part 5: Qualification of operators for DED-Arc
ISO/ASTM DIS 52927	Additive manufacturing — General principles — Main characteristics and corresponding test methods
ISO/ASTM DIS 52928	Additive manufacturing of metals— Feedstock materials — Powder life cycle management
ISO/ASTM CD 52929	Additive manufacturing of metals — Powder bed fusion — Presentation of material properties in material data sheets
ISO/ASTM DIS 52933	Additive manufacturing — Environment, health and safety — Test method for the hazardous substances emitted from material extrusion type 3D printers in the non-industrial places
ISO/ASTM DIS 52935	Additive manufacturing of metals – Qualification principles – Qualification of AM coordination personnel
ISO/ASTM DIS 52938-1	Additive manufacturing of metals — Environment, health and safety — Part 1: Safety requirements for PBF-LB machines
ISO/ASTM DIS 52939	Additive Manufacturing for construction — Qualification principles — Structural and infrastructure elements
ISO/ASTM CD 52940	Additive manufacturing of ceramics — Feedstock materials — Characterization of ceramic slurry in vat photopolymerization
ISO/ASTM CD 52941	Additive manufacturing — System performance and reliability — Acceptance tests for laser metal powder-bed fusion machines for metallic materials for aerospace application
ISO/ASTM DIS 52943-2	Additive manufacturing for aerospace — Process characteristics and performance — Part 2: Directed energy deposition using wire and arc
ISO/ASTM DIS 52945	Additive manufacturing for automotive — Qualification principles — Generic machine evaluation and specification of key performance indicators for PBF-LB/M processes
ISO/ASTM AWI 52948	Additive manufacturing for metals — Non-destructive testing and evaluation — Imperfections classification in PBF parts
ISO/ASTM DTR 52952	Additive manufacturing of metals — Feedstock materials — Correlating of rotating drum measurement with powder spreadability in PBF-LB machines
ISO/ASTM DIS 52953	Additive manufacturing for metals — General principles — Registration of geometric data acquired from process-monitoring and for quality control
ISO/ASTM CD 52957	Additive Manufacturing — Design — Parts using ceramic materials
ISO/ASTM CD 52958	Additive Manufacturing of Metals — Powder Bed Fusion (PBF) — Best Practice for In-Situ Flaw Detection and Analysis for Laser-based PBF
ISO/ASTM CD 52959	Additive Manufacturing — Test Artifacts — Compression Validation Coupons for Lattice Designs

3.5. Serbian national standardization in the field of AM

The Institute for Standardization of Serbia (ISS) is the national standardization body of the Republic of Serbia [11]. Work on the adoption of Serbian standards takes place in national technical committees. Technical committees are formed according to corresponding complementary international technical committees. Committee M010 "Technical drawings, tolerances, gears, bearings and threaded fasteners", with 1189 available standards and 94 new projects works within this organization. Among others, this committee collaborates with the ISO/TC 261 - Additive manufacturing committee (since September 2017). However, due to the permanently growing number of standards, there was a need to form a new national standardization technical committee within the ISS that will deal exclusively with standards on AM. The constitutive session of this committee, which will have the designation KS M261 (as well as the corresponding ISO committee), was held in March 2023. All relevant information about the ISS KS M261 committee will be available on the ISS website [8] soon. The authors of this paper are members of this committee.

4. CONCLUSION

Based on the carried out analysis, it can be concluded:

- standardization in the field of AM is lasting almost 15 years;
- standardization for AM is developing very quickly and the number of standards is increasing from year to year, following the increase in AM popularity in the industry and customers' everyday life;
- ISO and ASTM International have published 76 standards in the area of AM, and currently, 33 standards are under development;
- in the future, there will be a need for new standards, according to the further progressively growing development of additive manufacturing and products obtained using additive technologies.

Future work could be a detailed analysis of the scopes and contents of the standards mentioned in this paper and their classification into certain categories to make using the standards easier.

ACKNOWLEDGEMENTS

This work was supported by the Ministry of Science, Technological Development and Innovations of the Republic of Serbia (Contract No. 451-03-47/2023-01/200105, dated 03.02.2023).

REFERENCES

[1] B. Elhazmiri, N. Naveed, M. Naveed Anwar and M. I. Ul Haq, “The role of additive manufacturing in industry 4.0: An exploration of different business models”, Sustainable Operations and Computers, Vol. 3, pp. 317-329, (2022)

[2] S. Ćirić-Kostić and N. Bogojević, “Principles and application of additive manufacturing” (in Serbian), University in Kragujevac, Faculty of Mechanical and Civil Engineering in Kraljevo, Kraljevo (Serbia), (2020)

[3] R. Kawalkar, H. K. Dubey and S. P. Lokhande, “A review for advancements in standardization for additive manufacturing”, Materials Today: Proceedings, Vol. 50, pp. 1983-1990, (2022)

[4] www.iso.org

[5] www.astm.org

[6] https://www.astm.org/get-involved/technical-committees/committee-all

[7] https://www.iso.org/committee/629086.html

[8] https://committee.iso.org/home/tc261

[9] https://www.astm.org/get-involved/technical-committees/committee-f42

[10] https://www.astm.org/get-involved/technical-committees/committee-f42/subcommittee-f42

[11] www.iss.rs

Analysis of specific cutting energy in longitudinal turning of unalloyed steels

Milan Trifunović[1*], Miloš Madić[1]
[1]Faculty of Mechanical Engineering in Niš, University of Niš, Niš (Serbia)

More than 90% of machining processes environmental impact is due to electrical energy consumption. Reduction in electrical energy consumption of machining processes can be achieved by optimizing existing machining processes. Specific cutting energy, unlike the cutting power, incorporates the material removed, and hence is an appropriate variable for expressing the environmental impact of a machining process. It depends upon cutting conditions, and therefore, can be easily controlled by the machine tool end user through careful selection of cutting parameters and cutting tool geometry. This article proposes an approach for identification of the most important main and interaction effects of cutting parameters and cutting tool geometry parameters regarding the specific cutting energy in dry longitudinal single-pass turning of unalloyed steels. Five parameters (depth of cut, feed rate, cutting speed, rake angle and cutting edge angle) were varied at two levels by applying fractional factorial design 2^{5-1}. Specific cutting energy was estimated for sixteen cutting regimes based on the cutting tool manufacturer's machining calculator and well-known analytical relationships. The analysis of obtained results involved the identification of main and interaction effects, determination of statistically significant effects and development of specific cutting energy prediction model.

Keywords: Turning, Fractional factorial design, Specific cutting energy, Unalloyed steels

1. INTRODUCTION

In turning, a single-point cutting tool removes material from the external or internal surface of a rotating workpiece. The primary motion is carried out by the workpiece, whereas the cutting tool performs the auxiliary motion (feed motion). The cutting speed, characterizing the velocity of the primary motion, the feed rate, characterizing the magnitude of the feed motion, and the depth of cut, which is the thickness of the material removed from the workpiece surface, constitute a set of technological cutting parameters. To successfully perform any turning operation, one needs to select the appropriate cutting tool (geometry and grade) and cutting parameters.

Cutting parameters and cutting tool geometry and grade, together with the workpiece material, cutting fluid type and supply strategy, represent the main controllable input parameters, which, as with all other machining processes, significantly influence the outputs (performances) of the turning process. The most researched performances of the turning process recently are quality of the machined surface [1, 2], machining mechanics (cutting forces) [3, 4], tool wear [5, 6], chip formation [7, 8], machining economics (machining cost and machining time) [9, 10], and surface integrity [11, 12].

Environmental performance is one of six factors that should be taken into account for the evolution of currently used manufacturing systems to next-generation manufacturing systems [13]. Recent studies in this area are related to energy consumption [9, 14, 15], power consumption [1, 4, 9], and cutting fluid consumption [15]. More than 90% of machining processes environmental impact is due to electricity demands of machine tools [16], which are dominant in terms of energy consumption in the manufacturing industry [17]. Although the cutting energy consumption accounts for only 14.8% of the machining energy consumption [18], it is crucial to investigate it since it governs new surface generation and, as a result, determines surface integrity of a machined component [19]. Specific cutting energy, unlike the cutting power, incorporates the material removed, and hence is an appropriate variable for expressing the environmental impact of a machining process [20]. It can be easily controlled by the machine tool end user through careful selection of cutting parameters and cutting tool geometry.

Given that with proper selection of cutting tool geometry, and optimization of cutting parameters one can achieve energy savings [21], the present study deals with the analysis of the effect of cutting parameters and cutting tool geometry parameters regarding the specific cutting energy in dry longitudinal single-pass turning of unalloyed steels. Walter was selected as cutting tool manufacturer. Walter machining group P2 (unalloyed steels, carbon content $0.25\% < C \leq 0.55\%$, annealed, hardness 190 HB, tensile strength R_m = 639 N/mm^2) was considered in the present study. Five parameters, three of which are the cutting parameters (depth of cut, feed rate, and cutting speed) and two are cutting tool geometry parameters (rake angle and cutting edge angle), were varied at two levels by applying fractional factorial design 2^{5-1}. Data for the analysis were obtained using a machining calculator of the cutting tool manufacturer [22]. The analysis of obtained results involved the identification of main and interaction effects regarding the specific cutting energy, determination of statistically significant effects and development of specific cutting energy prediction model.

2. EXPERIMENTAL DATA

Turning diameter was set to 80 mm, length of cut to 60 mm, and machine tool efficiency to 0.9 (CNC lathe with direct drive). The cutting tools were toolholders DDJNR2525M15 (cutting edge angle of $\kappa = 93°$, rake angle of $\gamma_{oh} = -6°$) and DDNNN2525M15 ($\kappa = 62.5°$, $\gamma_{oh} = -6°$), with DNMG150612-MP3 WPP10G (coated carbide) ($\gamma_{oi} = 22.5°$) and DNMG150612-MP5 WPP10G ($\gamma_{oi} = 15°$) inserts for medium machining. Cutting parameter ranges and levels

*Corresponding author: Aleksandra Medvedeva 14, 18104 Niš, Serbia, milan.trifunovic@masfak.ni.ac.rs

were selected considering availability and capabilities of machining calculator and recommended cutting conditions for the inserts. Factors with their names, units, labels, and values on low level (-1) and high level (+1) are shown in Table 1.

Table 1: Factors that were varied for the calculation of specific cutting energy

Factor	Unit	Label	Low level (-1)	High level (+1)
Depth of cut, a_p	mm	A	1.2	3.5
Feed rate, f	mm/rev	B	0.20	0.40
Cutting speed, v	m/min	C	301	376
Rake angle, γ_o	°	D	9.0	16.5
Cutting edge angle, κ	°	E	62.5	93.0

In order to assess the main and interaction effects of the considered factors on the resulting specific cutting energy, fractional factorial design 2^{5-1} was applied. Highest order interaction (ABCDE) was chosen as the generator of the fractional factorial design. This design has resolution of 5, that is the estimations of the main effects are not confounded with any other main effects, 2 or 3-way factor interactions. Likewise, 2-way factor interactions are confounded with 3-way factor interactions. Given that the main effects are only confounded with 4-way interactions or higher, this design provides good information about the system or process, assumed to be dominated by main effects and low-order interactions.

Based on the fractional factorial design 2^{5-1}, 16 different combinations of factor levels were tried in the "virtual" experiment and specific cutting energy (E_{cs}) values were obtained (Table 2).

Table 2: Estimated specific cutting energy values for different cutting regimes

Trial	A	B	C	D	E	E_{cs} (kJ/cm^3)
1	-1	-1	-1	-1	1	2.315
2	1	-1	-1	-1	-1	2.380
3	-1	1	-1	-1	-1	2.004
4	1	1	-1	-1	1	1.946
5	-1	-1	1	-1	-1	2.381
6	1	-1	1	-1	1	2.313
7	-1	1	1	-1	1	1.944
8	1	1	1	-1	-1	2.002
9	-1	-1	-1	1	-1	2.170
10	1	-1	-1	1	1	2.109
11	-1	1	-1	1	1	1.776
12	1	1	-1	1	-1	1.827
13	-1	-1	1	1	1	2.108
14	1	-1	1	1	-1	2.171
15	-1	1	1	1	-1	1.826
16	1	1	1	1	1	1.774

The cutting data for all experimental trials (Table 2) were calculated using machining calculator of the cutting tool manufacturer [22]. Material removal rate (MRR (cm^3/min)) and power requirement (P_{mot} (kW)) values were used for subsequent calculation of the specific cutting energy. If cutting power (P_c (kW)) is divided by MRR one can obtain the specific cutting energy, i.e., the cutting energy consumed in removing a unit volume of the workpiece material [23]:

$$E_{cs} = \frac{60 \cdot P_c}{MRR} = \frac{60 \cdot P_{mot} \cdot \eta}{MRR} \tag{1}$$

where E_{cs} (kJ/cm^3) is the specific cutting energy, P_c (kW) is the cutting power, MRR (cm^3/min) is the material removal rate, P_{mot} (kW) is the power requirement, and η is the machine tool efficiency (η = 0.9).

3. RESULTS AND DISCUSSION

When applying fractional factorial designs, the estimation of the main and interaction effects can be done as in the case of classical factorial experimental designs of 2^k type. While doing so, one should take into account the number of occurrences of the level of each factor in the experiment, as well as the number of experimental trial replicates [24]. To find the estimate of any model effect, the difference in means of the response between the high (+) and low (−) levels is used [25]. The necessary calculations needed to determine the main effects of considered factors on the specific cutting energy are shown in Figure 1.

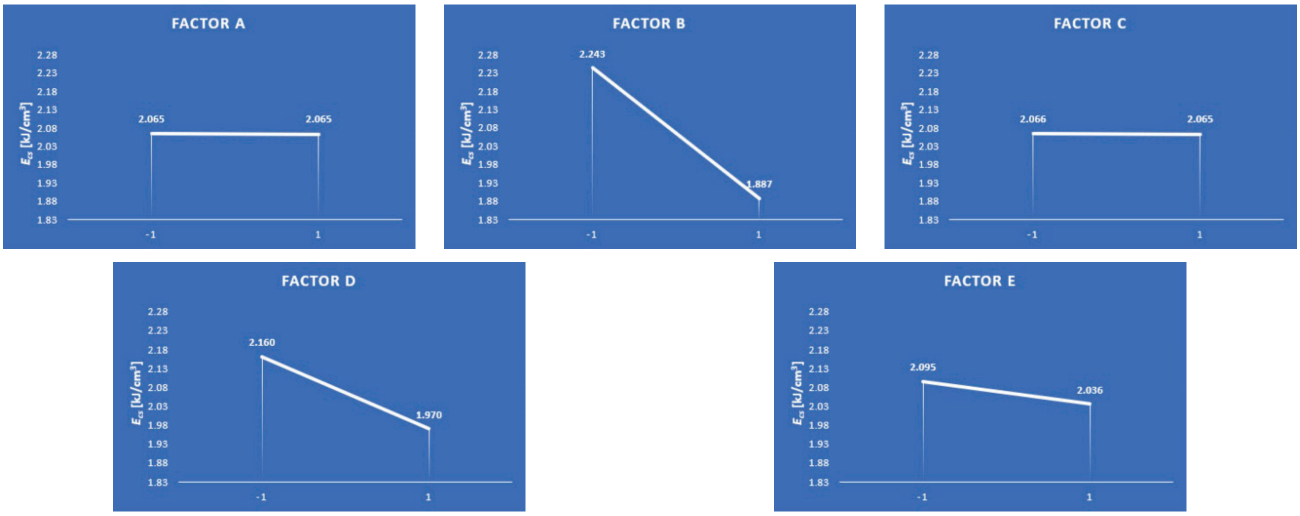

Figure 1: Main effects plots of considered factors on specific cutting energy

From Figure 1 it can be concluded that factors B (feed rate), D (rake angle), and E (cutting edge angle) have a negative correlation with specific cutting energy, i.e., with an increase in their values one obtains lower specific cutting energy. The increase in MRR due to increase in feed rate is significant and not proportional to the corresponding increase in cutting power [26], since feed rate influences the main cutting force both directly and indirectly through specific cutting force (increasing the feed rate results in decreasing the specific cutting force) [13]. This results in overall decrease in specific cutting energy. Increasing rake angle increases shear angle and results in chip thickness decrease, as well as in reduction of main cutting force and thus reduction of cutting power [27, 28]. Parle et al. [29] explained the observed trend of decreasing specific cutting energy with increasing rake angle by decreasing cutting forces due to reduced ploughing at larger rake angles. By decreasing the cutting edge angle, the uncut chip thickness decreases, leading to increase in main cutting force, and consequently to increase in cutting power. The obtained results indicate negligible effects of the depth of cut and cutting speed on the resulting specific cutting energy. With an increase in depth of cut, the main cutting force (and consequently the cutting power) rises, but simultaneously MRR rises, which in the end is not reflected in estimated specific cutting energy. With an increase in cutting speed, the cutting power rises, but simultaneously MRR rises, which in the end is not reflected in estimated specific cutting energy. Slight decrease of the specific cutting energy with an increase in the cutting speed is due to a decrease in cutting forces at higher cutting speeds [29].

Considering the absolute values of the main effects, it can be concluded that the factor B (feed rate), has the greatest effect on the specific cutting energy, followed by factor D (rake angle) and factor E (cutting edge angle).

The applied 2^{5-1} design can estimate all five main effects, as well as all ten 2-way interactions. However, this unreplicated design has no degrees of freedom left for the estimation of error. In such situations Lenth's method [30] and normal probability plots may be applied to draw a reference line for statistical significance of analysed terms. Effects that are further from 0 on the normal probability plot of the effects are statistically significant. For determining critical distance for statistical significance of model terms Lenth's pseudo standard error (PSE) was used (Figure 2).

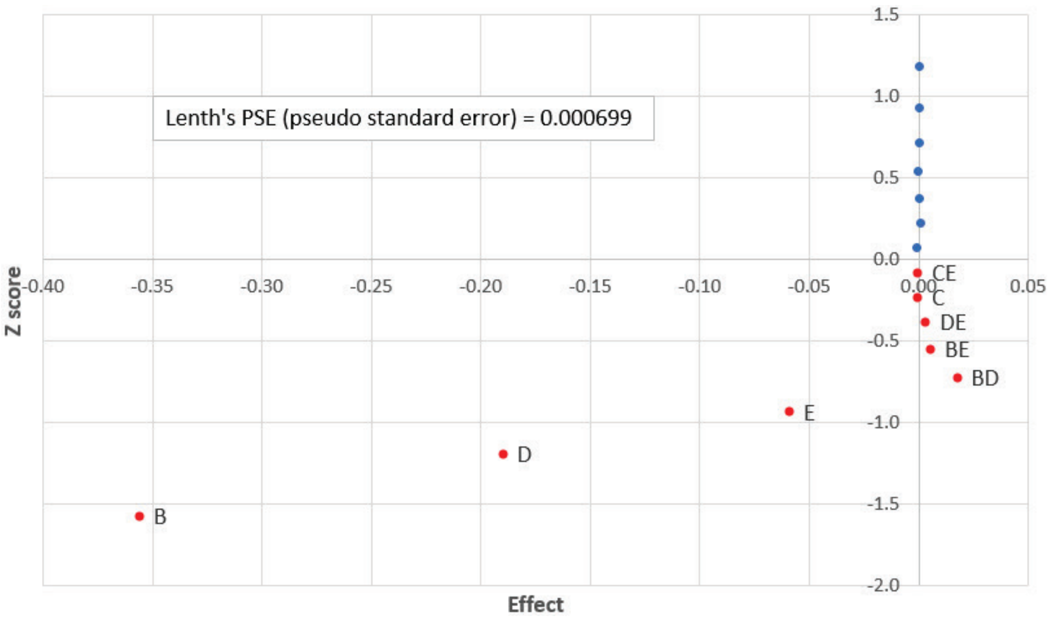

Figure 2: Normal probability plot of the effects with calculated Lenth's PSE

It is evident from Figure 2 that out of 15 terms, four main effects (factors B, C, D and E) are statistically significant, along with four 2-way interaction effects. Given that the feed rate (factor B) and rake angle (factor D) are the most influential terms, only three 2-way interaction effects (BD, BE and DE) will be considered for the analysis (Figure 3).

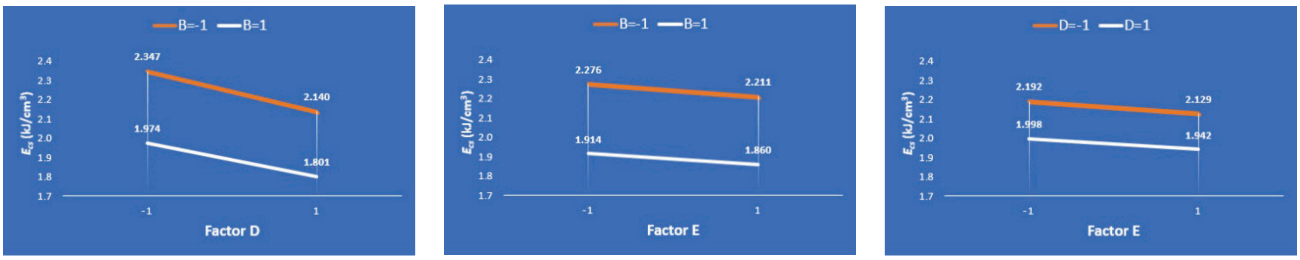

a) b) c)

Figure 3: The most important factor interaction effects on specific cutting energy

From Figure 3 one can observe that there are no significant interaction effects in terms of changing qualitative effect of the feed rate on the resulting specific cutting energy when rake angle and cutting edge angle change levels or qualitative effect of the rake angle on the resulting specific cutting energy when cutting edge angle changes levels. However, from Figure 3 a) one can observe that when feed rate is at low level (f = 0.2 mm/rev), increase in rake angle results in more decrease of specific cutting energy. The same is valid for the interaction of the feed rate and cutting edge angle (Figure 3 b)) and interaction of the rake angle and cutting edge angle (Figure 3 c)).

Based on a conducted analysis of the main effects of factors, as well as the main interaction effects on the resulting specific cutting energy, a suitable combination of factor levels that can be recommended for minimization of specific cutting energy is as follows:

A (-1 or +1) – because depth of cut has negligible effect on the resulting specific cutting energy. The recommendation for the level will depend on the specific case study (single-pass or multi-pass turning).

B (+1) – because feed rate has the biggest influence on specific cutting energy.

C (+1) – because an increase in cutting speed decreases the cutting time, increases material removal rate, and slightly decreases specific cutting energy.

D (+1) – because the rake angle has the second biggest influence, and analysis of Figure 3 a) reveals that this combination yields minimal specific cutting energy.

E (+1) – because the cutting edge angle has the third biggest influence, and analysis of Figure 3 b) reveals that this combination yields minimal specific cutting energy.

This combination of factor levels is not included in the initial experimental design. However, by using the following mathematical model, one can predict the resulting specific cutting energy for this cutting regime.

Based on determined main and interaction effects, average value of specific cutting energy for the experimental design, as well as considering the statistical significance of these terms, one can model the specific cutting energy for longitudinal single-pass turning of unalloyed steels using the following prediction model:

$$E_{cs} = 2.065 - 0.1781 \cdot f - 0.0004 \cdot v - 0.0952 \cdot \gamma_o - 0.0297 \cdot \kappa + 0.0086 \cdot f \cdot \gamma_o + 0.0026 \cdot f \cdot \kappa + 0.0015 \cdot \gamma_o \cdot \kappa - 0.0004 \cdot v \cdot \kappa \quad (2)$$

Estimated models’ coefficients correspond to the coded values of cutting parameters.

4. CONCLUSIONS

The present study focused on the analysis of main and 2-factorial interaction effects on the resulting specific cutting energy in dry longitudinal single-pass turning of unalloyed steels. By considering the cutting tool geometry and main cutting parameters, 2^{5-1} fractional factorial design was developed, and by using machining calculator and well-known analytical formulas, specific cutting energy for different cutting regimes and cutting tool geometries was estimated. Based on conducted analyses, the following conclusions may be drawn:

- The most important factor regarding specific cutting energy is the feed rate, followed by rake angle. The main effects of the cutting speed, and particularly depth of cut, are negligible.
- The depth of cut is found be statistically insignificant regarding specific cutting energy, which may be explained by previous analysis.
- There are some statistically significant 2-way interactions, particularly related to the feed rate. However, none of them show qualitative change in factor effects. In other words, in all 2-way interactions, none of considered factors fundamentally change its effect.
- Under some cutting conditions having the same MRRs one can obtain different specific cutting energy values and vice versa.
- If process engineers consider equal various regimes, which are being arbitrarily chosen within covered parameter hyper-space, there may exists difference in resulting specific cutting energy of approximately 34.3%.
- The conducted analysis is restricted to single-pass turning. For a given case study more comprehensive consideration is needed to examine the required quality characteristics, process variation, chip control and breaking, cutting time and number of passes, as well as tool life. The applied approach represents adequate preparation for practical experimental investigation and process planning and offers cost effective way to gain knowledge and perform engineering analysis.

In order to verify the observed effects and constancy of influence, for both main and interaction effects, performing of a high-resolution experiment will be in focus for the future research. Also, the analysis of multiple performance characteristics will be considered.

ACKNOWLEDGEMENTS

This research was financially supported by the Ministry of Science, Technological Development and Innovation of the Republic of Serbia (Contract No. 451-03-47/2023-01/ 200109).

REFERENCES

[1] C. Agrawal, J. Wadhwa, A. Pitroda, C.I. Pruncu, M. Sarikaya and N. Khanna, “Comprehensive analysis of tool wear, tool life, surface roughness, costing and carbon emissions in turning Ti-6Al-4V titanium alloy: Cryogenic versus wet machining”, Tribol. Int., Vol. 153, Article number: 106597, (2021)

[2] E. Abdelnasser, A. Barakat, S. Elsanabary, A. Nassef and A. Elkaseer, “Precision Hard Turning of Ti6Al4V Using Polycrystalline Diamond Inserts: Surface Quality, Cutting Temperature and Productivity in Conventional and High-Speed Machining”, Mater., Vol. 13(24), Article number: 5677, (2020)

[3] A. Suarez, F. Veiga, L.N. Lopez de Lacalle, R. Polvorosa and A. Wretland, “An investigation of cutting forces and tool wear in turning of Haynes 282”, J. Manuf. Process., Vol. 37, pp. 529-540, (2019)

[4] M. Rafighi, “The cutting sound effect on the power consumption, surface roughness, and machining force in dry turning of Ti-6Al-4V titanium alloy”, Proc. Inst. Mech. Eng. C J. Mech. Eng. Sci., Vol. 236(6), pp. 3041-3057, (2022)

[5] R. Mallick, R. Kumar, A. Panda and A.K. Sahoo, “Hard turning performance evaluation using CVD and PVD coated carbide tools: A comparative study”, Surf. Rev. Lett., Vol. 29(2), Article number: 2250020, (2022)

[6] D.M. Kim, H.I. Kim and H.W. Park, “Tool wear, economic costs, and CO_2 emissions analysis in cryogenic assisted hard-turning process of AISI 52100 steel”, Sustain. Mater. Technol., Vol. 30, Article number: e00349, (2021)

[7] A. Das, M.K. Gupta, S.R. Das, A. Panda, S.K. Patel and S. Padhan, “Hard turning of AISI D6 steel with recently developed HSN^2-TiAlxN and conventional TiCN coated carbide tools: comparative machinability investigation and sustainability assessment”, J. Braz. Soc. Mech. Sci. Eng., Vol. 44(4), Article number: 138, (2022)

[8] M. Mia, M.K. Gupta, G. Singh, G. Krolczyk and D.Y. Pimenov, “An approach to cleaner production for machining hardened steel using different cooling-lubrication conditions”, J. Clean. Prod., Vol. 187, pp. 1069-1081, (2018)

[9] A.M. Khan, S. Anwar, M. Jamil, M.M. Nasr, M.K. Gupta, M. Saleh, S. Ahmad and M. Mia, “Energy, Environmental, Economic, and Technological Analysis of Al-GnP Nanofluid- and Cryogenic LN_2-Assisted Sustainable Machining of Ti-6Al-4V Alloy”, Metals, Vol. 11(1), Article number: 88, (2021)

[10] A. Armillotta, “On the role of complexity in machining time estimation”, J. Intell. Manuf., Vol. 32(8), pp. 2281-2299, (2021)

[11] L.C. Magalhaes, G.C. Carlesso, L.N. Lopez de Lacalle, M.T. Souza, F. de Oliveira Palheta and C. Binder, “Tool Wear Effect on Surface Integrity in AISI 1045 Steel Dry Turning”, Mater., Vol. 15(6), Article number: 2031, (2022)

[12] L. Tan, C. Yao, X. Li, Y. Fan and M. Cui, “Effects of Machining Parameters on Surface Integrity when Turning Inconel 718”, J. Mater. Eng. Perform., Vol. 31(5), pp. 4176-4186, (2022)

[13] W. Grzesik, “Advanced Machining Processes of Metallic Materials: Theory, Modelling, and Applications, Second Edition”, Elsevier, Amsterdam (Netherlands), (2017)

[14] N. Khanna, P. Shah, M. Sarikaya and F. Pusavec, “Energy consumption and ecological analysis of sustainable and conventional cutting fluid strategies in machining 15–5 PHSS”, Sustain. Mater. Technol., Vol. 32, Article number: e00416, (2022)

[15] R. Fernando, J. Gamage and H. Karunathilake, “Sustainable machining: environmental performance analysis of turning”, Int. J. Sustain. Eng., Vol. 15(1), pp. 15-34, (2022)

[16] D.A. Guerra-Zubiaga, A.A. Mamun and G. Gonzalez-Badillo, “An energy consumption approach in a manufacturing process using design of experiments”, Int. J. Comput. Integr. Manuf., Vol. 31(11), pp. 1067-1077, (2018)

[17] N. Sihag and K.S. Sangwan, “A systematic literature review on machine tool energy consumption”, J. Clean. Prod., Vol. 275, Article number: 123125, (2020)

[18] T. Gutowski, J. Dahmus and A. Thiriez, “Electrical Energy Requirements for Manufacturing Processes”, Proceedings of the 13th CIRP International Conference on Life Cycle Engineering, LCE2006, Leuven (Belgium), 31 May - 2 June 2006, pp. 623-628, (2006)

[19] M.P. Sealy, Z.Y. Liu, D. Zhang, Y.B. Guo and Z.Q. Liu, “Energy consumption and modeling in precision hard milling”, J. Clean. Prod., Vol. 135, pp. 1591-1601, (2016)

[20] C. Camposeco-Negrete, “Optimization of cutting parameters for minimizing energy consumption in turning of AISI 6061 T6 using Taguchi methodology and ANOVA”, J. Clean. Prod., Vol. 53, pp. 195-203, (2013)

[21] Y. Su, G. Zhao, Y. Zhao, J. Meng and C. Li, “Multi-Objective Optimization of Cutting Parameters in Turning AISI 304 Austenitic Stainless Steel”, Metals, Vol. 10(2), Article number: 217, (2020)

[22] Walter Machining Calculator, https://mac.walter-tools.com/

[23] M. Younas, S.H.I. Jaffery, M. Khan, R. Ahmad, L. Ali, Z. Khan and A. Khan, “Tool Wear Progression and its Effect on Energy Consumption in Turning of Titanium Alloy (Ti-6Al-4V)”, Mech. Sci., Vol. 10(2), pp. 373-382, (2019)

[24] M. Radovanović and M. Madić, “Design and Analysis of Experiments”, University of Niš, Faculty of Mechanical Engineering in Niš, Niš (Serbia), (2019)

[25] D.C. Montgomery, “Design and Analysis of Experiments, Ninth Edition”, John Wiley & Sons, New York (USA), (2017)

[26] S.S. Warsi, S.H.I. Jaffery, R. Ahmad, M. Khan, L. Ali, M.H. Agha and S. Akram, “Development of energy consumption map for orthogonal machining of Al 6061-T6 alloy”, Proc. Inst. Mech. Eng. Part B J. Eng. Manuf., Vol. 232(14), pp. 2510-2522, (2018)

[27] K.N. Vedashree and S. Rao, “A Study on the Effect of Rake Angle and depth of cut on Cutting Forces during Orthogonal Cutting”, Int. J. Innov. Res. Sci. Eng. Technol., Vol. 9(5), pp. 3175-3179, (2020)

[28] S. Kalpakjian and S.R. Schmid, “Manufacturing Engineering and Technology, Fifth Edition”, Pearson Education, Upper Saddle River (USA), (2006)

[29] D. Parle, R.K. Singh and S.S. Joshi, “Modeling of Specific Cutting Energy in Micro-Cutting using SPH Simulation”, Proceedings of the 9th International Workshop on Microfactories, IWMF2014, Honolulu (USA), 5 October - 8 October 2014, pp. 121-126, (2014)

[30] R.V. Lenth, “Quick and Easy Analysis of Unreplicated Factorials”, Technometrics, Vol. 31(4), pp. 469-473, (1989)

State of the art in the field of cold forging tools

Ilija Varničić[1*], Miloš Pjević[1], Mihajlo Popović[1]
[1] Department of Production Engineering, Faculty of Mechanical Engineering, University of Belgrade (Serbia)

This paper chronologically presents the development of the geometry of cold forging tools, as well as the factors that influence the tool lifespan. Tools for plastic deformation processing are of strategic importance for large-scale and mass production. Their lifespan and properties have a great impact on process productivity and product quality. Cold forging represents an efficient metal processing technique through plastic deformation with significant material savings. One of the main challenges of this processing technique is managing high contact normal stresses in the tool, which can lead to serious tool damage. In order to better understand tribological phenomena in the cold forging process, which involve tool wear, fatigue, and failure, this paper will present a practical example of how to improve tool lifespan from the perspective of tool design and construction. The example taken is a forging tool for manufacturing a screw in four operations. The distribution of contact pressure in the contact zone between the working tool and the workpiece was examined using the finite element method for each of the geometries tested. This allowed for a comparison of the service life of the matrix for each of the tested matrix geometries.

Keywords: Cold forging, Tool geometry, Wear, Finite element method

1. INTRODUCING

Metalworking tools for cold forging are very important both for production costs and for the quality of the final product. In fact, the service life of the tool is a fundamental factor that needs to be considered in the process of designing and optimizing the forging process. Cold forging is one of the most significant forging processes and is widely used for the production of small parts where high precision and good surface quality are required. The products resulting from the cold forging process are often used directly in operation after their production, without the need for further processing. In this process, the material is introduced and deformed inside the mold cavity under the force of the press. Depending on the complexity of the process and the main processing factors, cold forging can be performed in multiple operations.

2. THE INFLUENCE OF THE MATERIAL REDUCTION DESIGN ON THE SERVICE LIFE OF COLD FORGING TOOLS

When designing a cold forging tool, it is necessary to consider that the design solution is efficient and applicable, taking into account that depending on the complexity of the product, the cost of the tool amounts to approximately 5-15% of the total production cost. The initial damage to the tool is based on plastic deformation, wear, and fatigue of the working surfaces of the tool. The necessary information for analysing tool fatigue is:

- identification of the most stressed zones;
- material fatigue properties;
- micro-structural properties, grain size and presence of micro-cavities

The mentioned critical phenomena that occur during tool operation are caused by high loads, which in some cases amount to up to 2000 MPa, inadequate lubrication, material deposition due to adhesive friction, and high stress rates. Due to these critical phenomena, the materials used to make the dies and punches must have high tensile strength and wear resistance. Wear is the loss of material from both the tool and the processed material due to high normal stresses.

Dynamic cyclic loading of the tool during material forging causes the formation of cracks and early failure of the die, which is classified as fatigue failure. This is precisely why finite element simulation models are used for tool construction to make necessary design modifications and mold efficiency. With the development of software packages, methods for simulating metal forming, such as Deform, CFTC Form, QForm, have been improved. With the help of these software tools, it is possible to determine the stress distribution on tools and make certain modifications to the tool's construction. The application of these simulation models significantly speeds up the design process and results in significant savings on experimental testing of the constructed tools [1].

By using the finite element method to investigate the distribution of normal stresses through the application of Von-Mises theorem, it has been concluded that the stress in the mold was reduced from 1535 MPa to 1050 MPa by reducing the value of the radius in the forging matrix. An example of correcting the transition radius is presented in the case of a matrix made of an insert that is made of hardened metal or a steel carrier [2].

In the works [2], the effects of the surface finishing of tools on the tribological properties of the hard metal G55 were investigated. After EDM treatment, diamond paste polishing with a grain size of 15 μm was found to reduce the friction factor by up to 0.03, while polishing with a grain size of 1 μm reduced the effect of friction to a negligible level. However, it is necessary to emphasize that reducing surface roughness also reduces micro-dents where oil can accumulate, which can lead to a counter-effect and increase wear.

*Corresponding author: Kraljice Marije 16, 11120 Belgrade, Serbia, ilijavarnica@gmail.com

By testing the process of forging with multi-stage tools, which is performed by transferring the part formed at the first station to the next work station using movable grippers and further forming it inside the tool in the next cycle, it has been found that besides the rounding radius, the material reduction angle also affects the service life of the die.

In Figure 1, the sequence of material deformation from the blank to the final shape is shown, which is carried out in five stages.

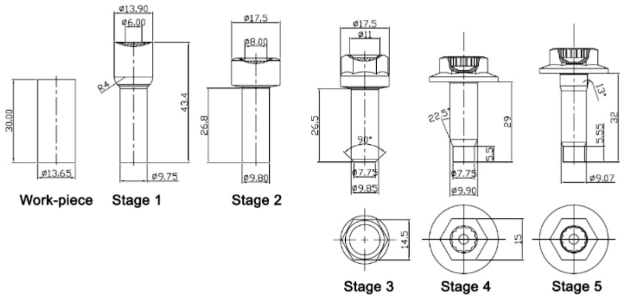

Figure 1: Sequence of material deformation in five stages

In this case of forging a screw with complex geometry and reliefs in a practical example, a critical tool failure occurred in the fourth stage of forging.

For better understanding and analysis of this problem, Figure 2a. shows a set of tools for the fourth forging phase, consisting of a movable part that forms the head of the screw and an immovable part where the shaft of the screw is formed, and where defects often occur. Figure 2b. shows a faulty tool with a broken detail at the transition radius, which further extends in a radial direction along the entire inside of the tool. This defect on the tool is a result of excessive load, therefore it is necessary to perform an analysis and optimization of the tool geometry.

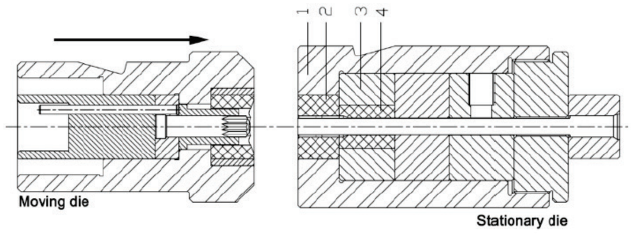

(a)

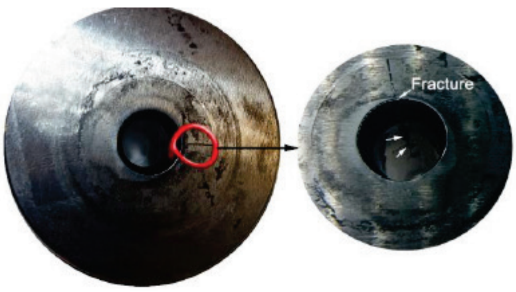

b)

Figure 2. Example one stage tools [2]

The optimization and reduction of normal stresses in the tool is carried out by [1] numerical modeling of the tool assembly using the Simufact finite element software package. Thermal disturbances in the working zone due to increased tool friction, which affect the change in the flow stress of the material, have also been taken into account.

In figure 3a, a simulation model of the tool assembly is shown, as well as the distribution of normal stresses in figure 3b, at critical points of the working tool prior to structural changes. Figure 4 depicts the optimized tool model that was achieved by dividing the tool into two parts that together form the finished part during the forging process, identical to the initial tool design. The modified design increases the tool's lifespan, eightfold in terms of cycles, from 35,000 cycles per tool to 135,000 cycles per tool.

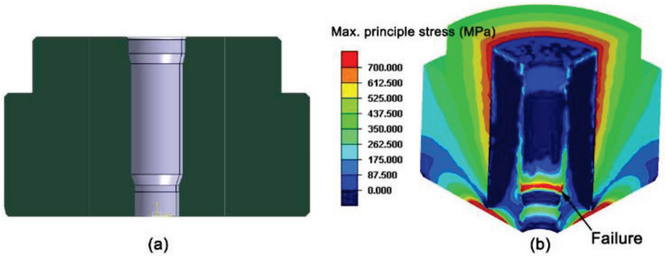

Figure 3. Example of tool before modification [2]

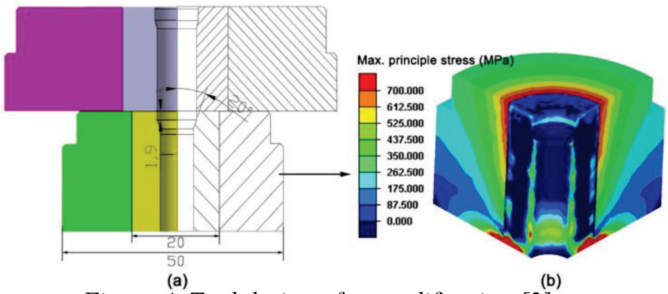

Figure 4. Tool design after modification [2]

For a better understanding of the stress state in the reduction zone, a brief analysis of the stress distribution in different reduction stages is presented.

The forging process originally constitutes a very delicate fracture mechanics problem, due to the cyclic multi-axial loading conditions and the complex mixed-mode loading. For simplification, it is assumed that the velocities of the process are relatively low, so that the problem can be changed to rather straightforward static FE analysis.

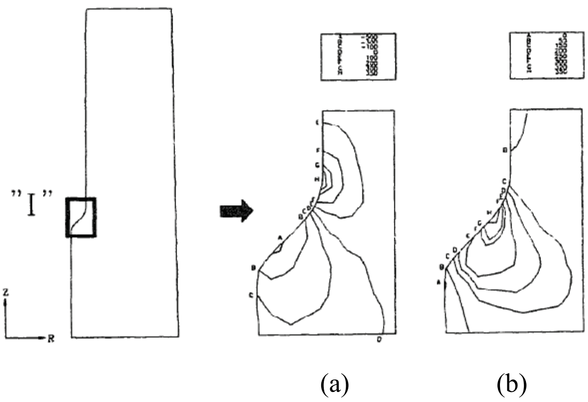

Figure 5. Stress distribution: (a) axial stress, (b) shear stress

The position of fatigue crack initiation is assumed to be in the region where the maximum stress occurs in the die during the extrusion process, as suggested in several studies [7, 8]. Whilst the crack initiation can be calculated in a single analysis from a pre-existing surface crack, the simulation of fatigue crack propagation should be described with an incremental procedure. A considerable amount of work has been done with the application of the FEM in fatigue crack propagation analyses. The main goal of these researches has focused on the determination of the stress intensity factor. If a special element is introduced in order to consider the singularity of the stress-strain in the vicinity of the crack tip, as employed in some notable studies, a more accurate solution can be obtained. For this reason, the so-called quarter point technique is used in this study. Applying isoperimetric standard elements with mid-side nodes at the crack tip according to this method, the singularity found there can be modeled easily by moving the mid-side nodes of the element towards a quarter point position in front of the crack tip. This is the way that an accurate stress intensity factor value can be obtained with a rather coarse mesh. Although the method of stress intensity factor evaluation may be carried out in various ways, it has been found in previous studies that the direct method of calculating the stress intensity factor from the displacement field at the vicinity of the crack tip leads to good results [6, 7]. The stress intensity factor, therefore, is calculated in a similar way in this study.

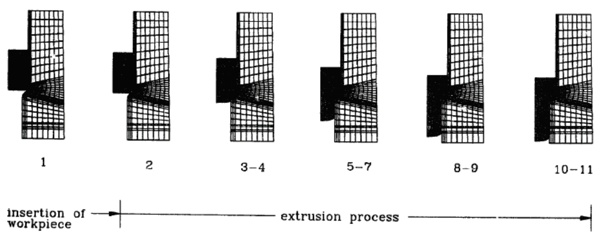

Figure 6. The stages of forming of most interest in calculating the stress intensity factor

It is very important to note that, since the correct crack tip behavior is only modeled on the special elements on the crack tip, the length of these elements is significant [9, 10]. Therefore, an L/n ratio is selected to be between the scale from one to ten [4], where a and L are crack length and the element length at the crack tip respectively and n was number of finit element. Figure 7. shows the typical mesh system of the die containing a certain crack, which was used in the analysis. It is shown that a fine mesh is used around the region containing the crack for accurate analysis. For illustration purposes, the left side of the axi-symmetric model was added. For the case of 0.1 mm crack length, the stress distribution from the vicinity of the crack tip to the horizontally straight points in the radial direction is plotted in Fig. 7. As shown in this diagram the stress value around the crack tip is very much higher than at other points.

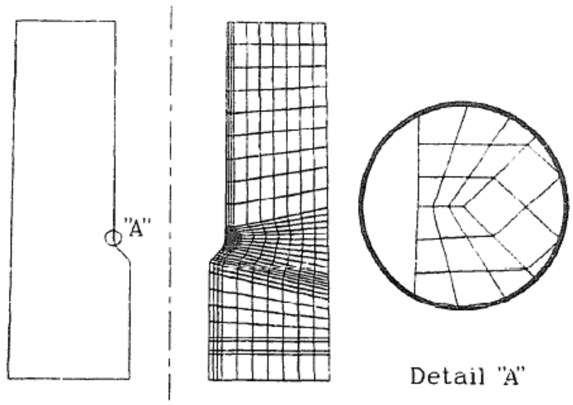

Figure 7. Mesh system for the fracture analysis by the FEM. [10]

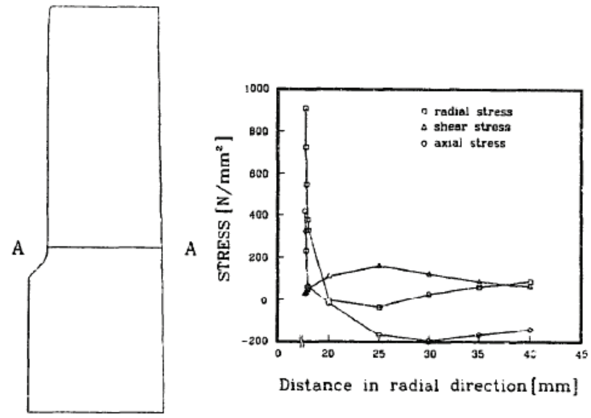

Figure 8. Stress distributions in the vicinity of the crack tip and other places for a 0.1 mm crack. [11]

The diagram of figure 9. shows examples of the stress intensity factor evaluation at the crack tip with increasing crack length. The graphs are obtained from the interpolation of all process stager instigated and show a function of process time for single loading cycle. It can be seen that the influence of mode I decreases as the crack propagates [11].

The effective stress intensity factor, which can be obtained by applying some results of figure 9. is calculated in advance to evaluate the fatigue life. Figure 10. shows the computed effective stress intensity factor exceeds the value of fracture toughness in the early stages but then drops below it with increasing crack length. From this date the crack growth rate, as well as the crack propagation direction, can be determined, suggesting the propagation of the crack for the following crack growth increment, which gives the new crack tip coordinates. For the next analysis run, remeshing of the FE model will be conducted.

The fatigue life obtained using the stress intensity factor and the effective stress intensity factor for a single crack length indicates part of the total fatigue life in the forging die. The desired fatigue life, therefore, is obtained by the summation of each result.

The surface failures of dies observed in the actual manufacturing process are about 0.01÷0.1 mm in depth. the first crack increment being taken as AN = 0.1 mm in consideration of this Fact. The fatigue life of the investigated extrusion die was evaluated. This result is shown in Fig. 10, from which it can be seen that l000-12000 cycles are required for the crack length to reach approximately 3.2 mm.

Although the difficult assumption of the initial crack increment and the ignored wedge effect of the penetrated workpiece and of lubricants flowing into the crack may affect the accuracy of result, the simulated result in this study is in good agreement will the results of experiment [11, 12] for fatigue crack propagation behavior in extrusion dies.

Process simulation by FEM is a suitable instrument to evaluate stresses and strains of forming tools. For the deformation analysis of the workpiece and the die, rigid-plastic FE analysis and elasto-plastic FE analysis were performed. For more precise results of tool loading, an internal pressure distribution derived from FE simulation of the forming process was applied. Using these results, the fatigue crack behavior and the fatigue life of the extrusion die were investigated by the introduction of some criteria for LEFM.

Experimental research, according to the study [11], found that the highest stresses in the cold forging process occur at the beginning of the conical profile in the area of the transition radius, Figure 9.

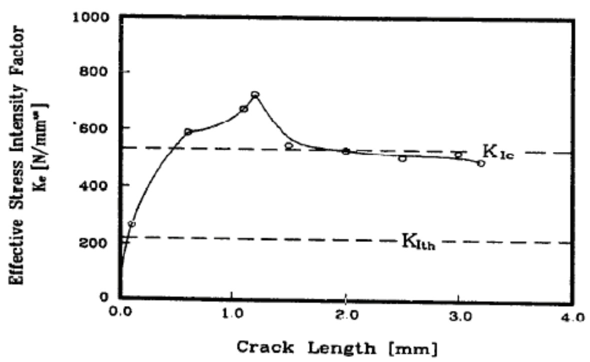

Figure 9. Effective stress intensity factor for increasing crack length [11]

As a consequence of the multiple repetition of the forging process in one tool, the stress that accumulates at the transition radius is distributed. Figure 10. shows the behavior of the crack at the transition radius of the reduction profile depending on the number of forging cycles

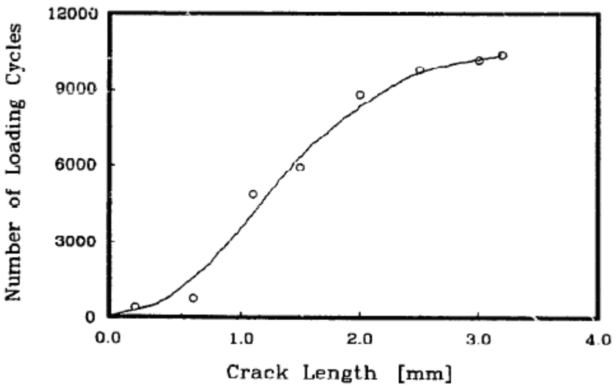

Figure 10. Computed fatigue life of the extrusion die [11]

In addition to modifications in the form of dividing the tool into segmental matrices based on research [11], the reduction of the impact of maximum normal stresses on the transition radius and reducing cones is achieved through the application of sigmoid or conical profile in the zone of intensive material deformation.

An example of the crack propagation path obtained from the above results is shown in figure 11. This diagram points out that the angle between the radial axis and the direction of crack propagation is about 30-40” and that the fatigue crack propagates in a zig-zag path along the radial direction [11].

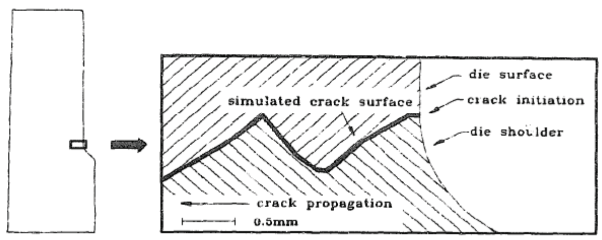

Figure 11. The zone of occurrence and propagation of the crack

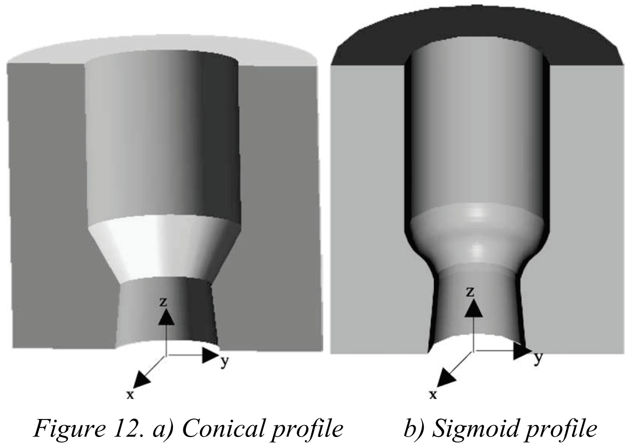

Figure 12. a) Conical profile b) Sigmoid profile

On Figures 12a and 13 is shown the reduction profile that has a conical chamfered reduction zone with an angle of 30°. The modified profile shown in figures 12b and 14 has a sigmoid profile instead of a conical reduction zone. The sigmoid profile is similar to the conical one in terms of the length of the profile and the degree of material reduction, but it is also less favorable compared to the conical profile in terms of complexity and production costs. The advantages of a sigmoid profile over a conical one lie in avoiding sharp variations in material flow and reducing the maximum value of contact stress at the beginning of the conical zone [10].

In the direct extrusion process four steps can be identified: workpiece insertion, start of the extrusion, stationary extrusion condition, workpiece expulsion. The stationary phase is the most onerous for the die resistance. This phase was simulated in axial-symmetric conditions, the matrix and the workpiece were meshed by 1000 and 800 elements, respectively. The simulation results provided the contact pressure distribution along the profile for both dies. In the case of conical matrix, the most stressed zone was at the beginning of the reduction zone where the maximum pressure value was equal to p_{max} ¼ 450 Mpa. In the case of sigmoid profile, the peak values were located at the flex point where there was the maximum value (p_{max} ¼ 417 MPa) and at the end of the tapered zone (p ¼ 409 MPa), Figures 15 and 16.

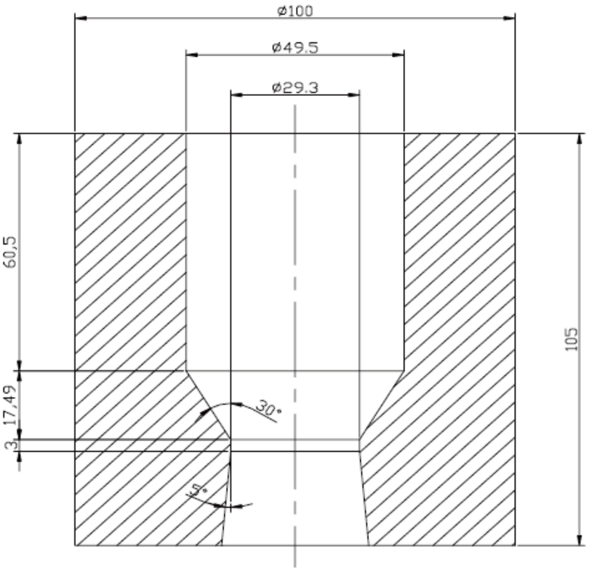

Figure 13. Truncated-conical geometry

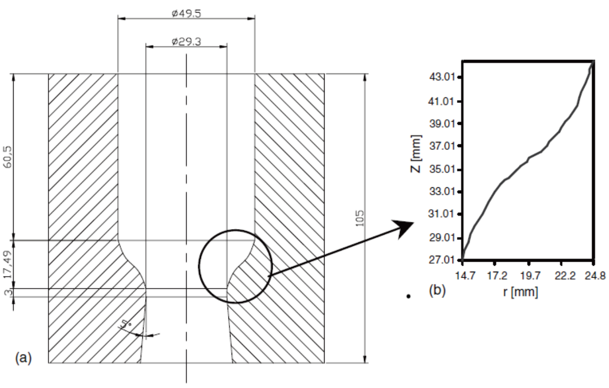

Fig. 14. Sigmoidal die (a); profile detail (b).

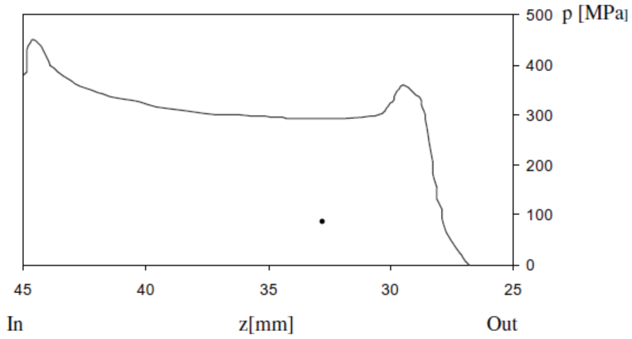

Fig. 15. Contact pressure distribution of the conical matrix.

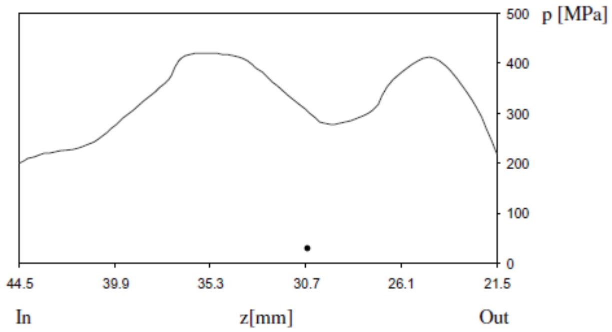

Fig. 16. Contact pressure distribution of the sigmoid matrix

3. CONCLUSION

In this paper, the influence of the material reduction design in cold forging on the die service life was presented. It was found that the reduction profile affects the material flow. As a result of the modification of the forging reduction zone profile, the maximum normal stresses are reduced, which directly affects the intensity of the die wear and, consequently, its service life. Another important factor justifying the modification of the die reduction profile is the improvement of the reduction process. It can be concluded that in the process of designing cold forging tools, the most important aspect is the design of the reduction pressure due to the concentration of stresses in the material reduction zone.

ACKNOWLEDGEMENTS

This work was supported by the Ministry of Education, Science and Technological Development (by contract No.: 451-03-47/2023-01/200105, from the 3th of February 2023.)

REFERENCES

[1] T.-W. Ku and B.-S. Kang, "Tool design for inner race cold forging with skew-type cross ball grooves", Journal of Materials Processing Technology, Vol. 214(8), pp. 1482-1502, (2014)

[2] K. Wagner, A. Putz, and U. Engel, "Improvement of tool life in cold forging by locally optimized surfaces",

Journal of Materials Processing Technology, Vol. 177(1-3), pp. 206-209, (2006)

[3] B. He, "Failure and Protective Measures on Punch & Die for Cold Extrusion", The 2nd International Conference on Computer Application and System Modelling, (2012)

[4] K. Andreas and M. Merklein, "Influence of Surface Integrity on the Tribological Performance of Cold Forging Tools", Procedia CIRP, Vol. 13, pp. 61-66, (2014)

[5] T.W. Ku and B.-S. Kang, "Tool design and experimental verification for multi-stage cold forging process of the outer race", International Journal of Precision Engineering and Manufacturing, Vol. 15(9), pp. 1995-2004, (2014)

[6] S. Yurtdaş, U. İnce, C. Kılıçaslan, and H. Yıldız, "A Case Study for Improving Tool Life in Cold Forging: Carbon Fiber Composite Reinforced Dies", Res. Eng. Struct. Mat., Vol. 3(1), pp. 65-75, (2017)

[7] K. Lange, W. Reiss, H. Arndt, A Study of Tool Fracture in Cold Extrusion, Proc. 17th NAMRC, Columbus, Ohio. (USA), (1989)

[8] K. Lange, A. Hettig, and M. Knoerr, “Increasing tool life in cold forging through advanced design and tool manufacturing technique”, J. Mater. Process. Technol, Vol. 35, pp. 495-513, (1992)

[9] D.R.J. Owen and A.J. Fawkes, “Engineering Fracture Mechanics: Numerical Methods and Applications”, Pineridge Press, Swansea (UK), (1953)

[10] C. Cosenza, L. Fratini, A. Pasta and F. Micari, “Damage and fracture study of cold extrusion dies”, Engineering Fracture Mechanics, Vol. 71(7-8), pp. 1021-1033, (2004)

[11] R.S. Barsoum, “On the use of isoparametric finite finite elements in linear fracture mechanics”, Int. J. Numer. Meth. Eng. Vol. 10, pp. 25-37, (1976)

Application of the Poka-Yoke method in small wood processing companies

Jovana Perić[1*], Milovan Lazarević[2], Mitar Jocanović[2], Vladan Grković[1], Mišo Bjelić[1]
[1]The Faculty of Mechanical and Civil Engineering in Kraljevo, University in Kragujevac, Kraljevo (Serbia)
[2]Faculty of Technical Sciences, University of Novi Sad, Novi Sad (Serbia)

In the modern business environment, achieving a high level of product quality is a key factor for the success of every manufacturing company. However, producing error-free products is always a challenge, especially in low-volume production where mistakes can have a significant impact. Therefore, the focus of this research is on a case study that addresses the issue of non-conformity between delivered products and documentation within the low-volume production system of interior doors. Specifically, this study aims to analyze the factors that contribute to errors in the packaging process of interior doors and propose solutions to prevent errors by implementing the Poka-Yoke method.

Keywords: Lean, Poka-Yoka, Errors, Small enterprise

1. INTRODUCTION

As market competitiveness increases, the need for producing high-quality products with efficient manufacturing processes becomes even more crucial [1]. In this context, the implementation of an innovative error prevention method, known as Poka-Yoke, plays a key role in achieving these objectives. Poka-Yoke, also referred to as "mistake-proofing method," aims to identify or eliminate errors in real time to ensure error-free production and reduce costs [2].

Small enterprises, such as the one presented in this research, face numerous challenges, including limited financial resources and a higher risk of financial losses due to errors in the production process. This fact emphasizes the significance of implementing a Poka-Yoke system as an effective tool for improving quality and efficiency [3]. Therefore, the focus of this research is on the application of a Poka-Yoke system in a small enterprise, with a particular emphasis on the packaging process of interior doors. In addition to error elimination, the implementation of the Poka-Yoke method leads to cost reduction by eliminating the need for rework and additional product control, directly impacting increased profits and maintaining financial stability for the small enterprise [4].

This research will provide a detailed description of the Poka-Yoke method concept and its significance in small enterprises. The methodology employed will include a description of the technological process of manufacturing interior doors, the packaging process, and the identification of problems that arise during packaging. Special attention will be given to presenting a solution based on the use of QR codes to eliminate errors and facilitate the packaging process. Within the discussion, the importance of the packaging process for interior doors in the context of implementing the Poka-Yoke system will be analyzed. In addition to error elimination, the discussion will encompass other benefits such as reducing effort and stress for operators, improving product quality, and increasing customer satisfaction.

2. POKA-YOKE

"Poka-Yoke" is a Japanese slang term often translated as "error-proofing" or "mistake-proofing." The term "Poka" refers to unintentional errors, while "Yoke" signifies avoidance [5]. This Lean tool originated as part of the Toyota Production System (TPS) in the 1960s, developed by the renowned kaizen guru, Shigeo Shingo, with the purpose of preventing human errors in the production process that could adversely impact product quality [2]. More precisely, the origin of Poka-Yoke is associated with Shingo's redesign of a process in which factory workers, while assembling a small switch, would frequently forget to insert a necessary spring under one of the switch buttons. In the redesigned process, the worker would perform the task in two steps, first preparing the two required springs and placing them in a holder, and then inserting the springs from the holder into the switch. When a spring remained in the holder, workers knew they had forgotten to insert it and could rectify the error effortlessly [6].

Since the occurrence of errors or defects is always a critical concern for every manufacturing industry, as the success of any organization directly depends on the quality of its products, especially their correctness [7]. For this reason, there is a need to implement techniques that prevent the occurrence of errors or defects, which are often caused by human factors [8]. During the actual production of any product, there are numerous simple and repetitive steps and operations performed by operators [9]. These repetitive operations lead to mental fatigue and disinterest, eventually resulting in operator errors [10]. In order to solve this problem, the Poka-Yoke method has been developed, allowing operators to avoid the occurrence of errors or defects by using mechanisms that prevent errors from happening or immediately identify errors that do occur. This ensures that the production process remains within specified tolerances, as any deviation could potentially lead to the occurrence of defects [2].

The implementation of this method is generally cost-effective and quickly applicable, making it very practical and efficient [9]. This simple yet effective approach allows operators to ensure that the produced

*Corresponding author: Dositejeva 19, 36000 Kraljevo, peric.j@mfkv.kg.sc.rs

product is defect-free, ultimately leading to better product quality and satisfied customers [2].

2.1. Poka-Yoke in small enterprises

In small enterprises, errors in the production process have a greater impact on overall business compared to larger enterprises. Specifically, the financial situation, reputation, and customer loyalty directly depend on the quality of products or services offered. Therefore, it is crucial for small enterprises to implement appropriate methods to reduce the risk of errors and improve the quality of their products [11].

The Poka-Yoke method stands out as an effective and cost-efficient way to address these issues [12]. Given that small enterprises often face limited financial resources and a lack of specialized personnel for quality control, the implementation of Poka-Yoke methods has proven to be a successful solution. This method focuses on improving existing processes and operational procedures, without requiring significant investments in equipment and technology [13]. In addition to eliminating production errors, the Poka-Yoke method leads to cost reduction by eliminating the need for rework and additional product inspections. This directly contributes to increased profits and the financial stability of small enterprises. The application of the Poka-Yoke method can also help improve production processes and increase efficiency. By eliminating errors, the time required for production is reduced, leading to increased productivity, which positively impacts overall business operations [14].

3. METHODOLOGY

3.1. Product description - interior doors

The depicted interior doors in Figure 1 are made of medium-density fiberboard (MDF) that is coated with PVC foil in various patterns. MDF is an engineered wood composite material produced from finely ground wood fibers, such as beech, spruce, fir, etc. PVC foil, on the other hand, is a plastic product that is highly resistant to water and wear.

Figure 1. Cross-sectional view of the room door

The interior doors consist of three main elements:

Door frame it includes two vertical frames (left and right) depicted in Figure 2, as well as the upper frame depicted in Figure 3. The door frame is made of 30mm thick medium-density fiberboard (MDF) that extends across the full width of the wall. It is profiled towards the door leaf and decorated with adjustable trim moldings.

The technological process of manufacturing the vertical frames and upper frame of the door involves the following operations:

• Cutting the MDF from the panel to the desired width of the frame and applying a sticker with dimensions.

• Creating grooves for decorative trim moldings, weatherstripping, and the door leaf.

• Applying a PVC foil coating to the pre-profiled frame.

• Cutting angles, trimming to length, and drilling guide holes for assembly.

• Packaging together with decorative trim moldings.

Figure 2. Door frame verticals

Figure 3. The upper part of the frame

The decorative moldings consist of four vertical moldings (two on the right and two on the left) depicted in Figure 4, as well as two upper moldings depicted in Figure 5. These moldings are made of medium-density fiberboard (MDF). They consist of a tongue with a width of 42mm and a thickness of 4mm, and a body of the molding with a thickness of 16mm and a width of 70-100mm.

The technological process of manufacturing the vertical and upper decorative moldings involves the following operations:

• Cutting the tongue from MDF panels.

• Cutting the body of the molding from MDF panels and applying a sticker with dimensions. This operation runs parallel to the cutting of the tongue.

• Joining the tongue with the body of the molding and performing necessary processing (radius and rebate).

• Applying a foil coating to the pre-profiled molding.

• Cutting angles and trimming to length.

• Packaging together with the door frame.

Figure 4. Vertical decorative moldings

Figure 5. Upper decorative moldings

The door leaf depicted in Figure 6 is made of medium-density fiberboard (MDF), consisting of a frame composed of profiled MDF bars with dimensions of 32 x 40 mm arranged in two rows. The interior of the frame is filled, depending on the sound insulation requirements, with cardboard honeycomb, tubular fillings such as extruded chipboard, etc. The filled frame is then covered with a 4mm thick MDF panel coated with PVC foil.

Figure 6. Door leaf

The technological process of manufacturing the door leaf involves the following operations:

- Cutting the bars from MDF panels.
- Cutting the panels for the covering from MDF panels.
- Manual assembly of the double frame using the pre-cut bars and inserting the filling inside the frame.
- Applying PVC foil to the pre-cut covering.
- Joining the previously assembled and filled frame with the covering.
- Cutting to size and applying a sticker with dimensions.
- Applying protective tape on the side edges.
- Drilling.
- Packaging.

3.2. Description of the product packaging process

The previous defined interior doors are delivered to the customer in two parts:

Door frame with decorative moldings, consisting of two vertical frame components (left and right), one upper frame component, four vertical decorative moldings, and two upper decorative moldings. These components are packaged in five steps:

1. The appropriate left and right vertical frames are taken from the pallet containing all the vertical frames by following the packing order (Figure 7). A label is affixed to the vertical frames indicating the dimensions of the respective component (Figure 8). Then, the vertical frames are stacked on top of each other, with their faces turned towards the front side of the door frames (Figure 9).

PERIĆ 032 D. O. O

32 223 Zablace bb – Čačak

Packing work order no. 0705/2023

Date of issue of the order: 07.05.2023. **Date of product delivery:** 07.05.2023. **Customer of the product:** MARINKO D.O.O

Door type: Foil **Design:** Bleached oak

GROUND FLOOR

Apartment 1	Apartment 2	Apartment 3	Apartment 4	Apartment 5
88x202x14	78x202x16	89x203x15	88x202x15	89x202x14
87x202x15	88x202x15	88x203x15	78x202x15	87x202x15
78x202x15	68x202x15	77x203x16	72x202x16	78x202x15
66x202x15	87x202x14	68x203x14	68x202x14	77x202x14

Note:

Issued by: ________________________

Received by: ________________________

Figure 7. Packing order

Customer:	MARINKO D.O.O
Floor:	Ground floor
Apartment:	1
Dimension of interior doors:	88x202x14
Dimension of vertical frame:	202x14

Figure 8. Label

Figure 9. Appearance of the first step

2. The appropriate vertical decorative moldings (two left and two right) are taken from the pallet containing all the vertical decorative moldings by following the packing order. A label is affixed to the vertical decorative moldings indicating the dimensions of the respective component (Figure 10). Then, one left and one right decorative molding are positioned below the door frame, with the body of the decorative molding resting on the door frame. The other two decorative moldings are placed on the top side of the door frame, with the body of the decorative moldings resting on the door frame (Figure 11).

Customer:	MARINKO D.O.O
Floor:	Ground floor
Apartment:	1
Dimension of interior doors:	88x202x14
Dimension of vertical decorative moldings:	202

Figure 10. Label

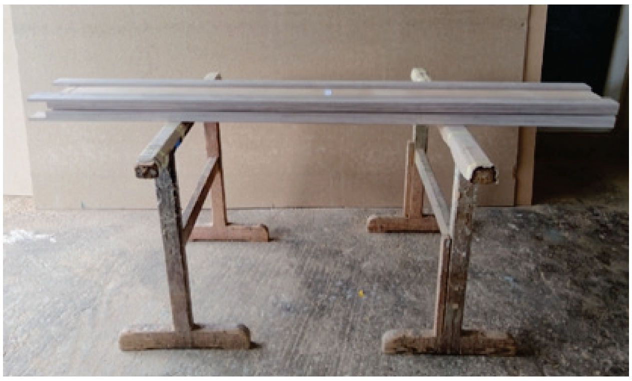

Figure 11. Appearance of the second step

3. Two appropriate upper decorative moldings are taken from the pallet containing all the upper decorative moldings by following the packing order. A label is affixed to the upper decorative moldings indicating the dimensions of the respective component (Figure 12). Then, the corresponding upper decorative moldings are positioned on the top side of the lower part of the installed vertical decorative moldings (Figure 13).

Customer:	MARINKO D.O.O
Floor:	Ground floor
Apartment:	1
Dimension of interior doors:	88x202x14
Dimension of upper decorative moldings:	88

Figure 12. Label

Figure 13. Appearance of the third step

4. The appropriate upper frame component is taken from the pallet containing all the upper frame components by following the packing order. A label is affixed to the upper part of the frame indicating the dimensions of the respective component (Figure 14). Then, the corresponding upper frame component is positioned on the top side of the upper part of the installed vertical decorative moldings (Figure 15).

Customer:	MARINKO D.O.O
Floor:	Ground floor
Apartment:	1
Dimension of interior doors:	88x202x14
Dimension of upper frame:	88x14

Figure 14. Label

Figure 15. Appearance of the fourth step

5. Then, a cardboard box is placed on the top and bottom edges, and it is wrapped with cling film (Figure 16.).

The door leaf is the second part of the interior doors that is packaged separately in two steps:

1. The appropriate door leaf is taken from the pallet where all the door leaves are located (Figure 17.), following the packaging instructions and the adhesive label on the door leaf indicating its dimensions (Figure 18.).

Figure 16. Appearance of the fifth step

Figure 17. Appearance of the first step

Customer:	MARINKO D.O.O
Floor:	Ground floor
Apartment:	1
Dimension of interior doors:	88x202x14
Dimension of door leaf:	83,6x199

Figure 18. Label

2. Then, a cardboard box is placed on the sides of the corresponding door leaf, and it is wrapped with cling film (Figure 19.).

Figure 19. Appearance of the second step

3.3. Defining problems in the packaging process

During the observation of the door packaging process, a problem was identified that occurs when the operator accidentally selects the wrong component while selecting the components for packaging, specifically the door frame with decorative moldings. This error arises due to insufficiently careful monitoring of the packaging instructions and the dimension labels on the components. As a result, the complete door frame is improperly packed and delivered to the customer. Only when the product reaches the customer is the mistake noticed because the door frame does not match the expected configuration. This leads to customer dissatisfaction, increased costs, and time loss in resolving the issue. To avoid these drawbacks, it is necessary to establish effective measures to minimize the possibility of errors in selecting the appropriate components.

3.4. Proposed solution

Considering the previously defined causes of errors and aiming to eliminate them, the Poka-Yoke mindset has been applied, combined with the advantages of using QR technology in the form of QR codes instead of stickers, as well as more efficient picking of all types of components according to the work order.

According to the proposed solution, during the first operation of the production process, an appropriate QR code is attached instead of a sticker. This QR code is unique for all components of a complete door frame with decorative moldings. The packaging process takes place at workstation marked as C, where all the components of the door frame with decorative moldings that need to be packaged are located. These components are picked according to the work order. The packaging process begins by the operator taking the corresponding component and scanning it in area A or B, depending on whether the QR code is attached to the top or bottom side of the component. Area A and B contain a wireless scanner placed at a specific height, which sends the information via Wi-Fi signal to the screens as a visual signal confirming if the correct component has been selected. A speaker next to the screens provides an audio signal confirming if the selected component is correct for the given set of door frames. For each subsequent component, the operator repeats the same sequence of activities, as shown in Figure 20.

Scanner HENCODES BQ-119 (Figure 21.) used in the process has characteristics that are ideal for the described process. It can transmit signals up to a distance of 100 meters, providing flexibility in the working environment. Additionally, the scanner is compatible with Windows, Android, and PC systems. It is easy to scan and use, without requiring additional software or drivers, which reduces complexity and implementation costs. Moreover, the scanner is cost-effective, making it an attractive choice for this type of application.

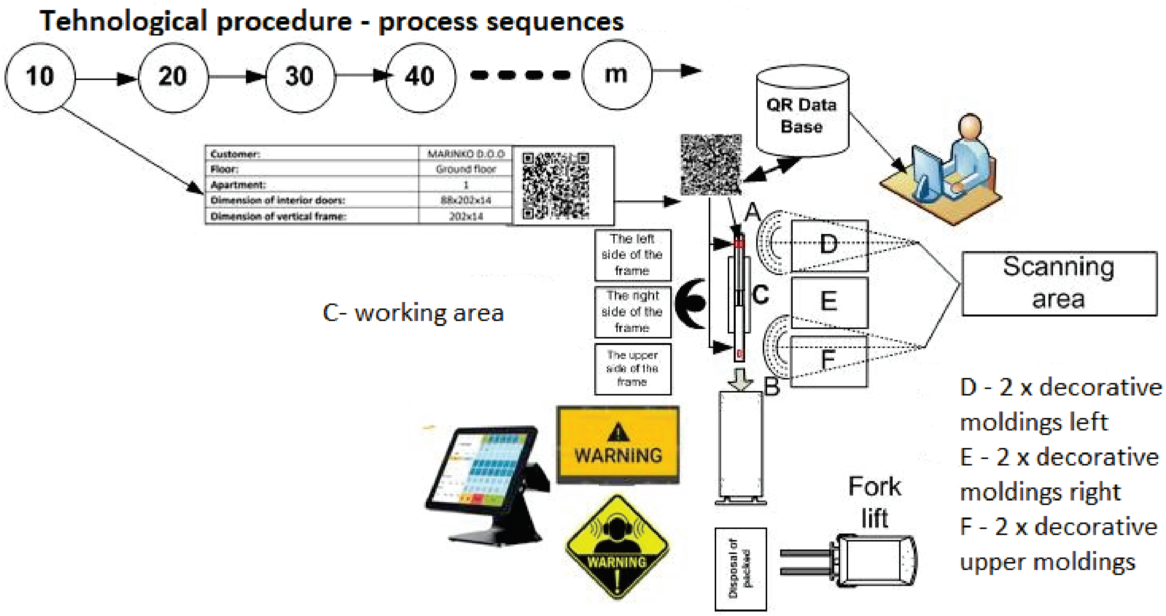

Figure 20. Packaging process

Figure 21. Scanner

4. DISCUSSION

Packaging interior doors represents a critical step in the described production process, as properly packaged and delivered interior doors are crucial for meeting customer requirements and maintaining the company's reputation. However, errors that occur during the packaging process lead to customer dissatisfaction, increased costs, and time loss in problem resolution. Furthermore, the conditions and nature of work in the door packaging process require continuous mental and physical readiness. Operators must remain consistently focused to accurately follow packaging orders and dimension labels on each component. However, this repetitive routine can lead to a decline in operator concentration, resulting in incorrectly packaged components.

In order to address this problem and alleviate the pressure on workers, the use of QR codes is proposed as an effective solution. QR codes, applied to each component, enable automatic verification of components during the packaging process. Operators simply need to scan the QR code on each component, receiving instant confirmation whether the correct component has been selected for packaging. This implementation ensures greater accuracy and reduces the likelihood of errors, providing a streamlined and efficient packaging process.

This proposed solution brings numerous advantages. Firstly, the accuracy of packaging is significantly improved, reducing the possibility of errors in component selection. Secondly, operators are relieved of pressure and tension, as they have a reliable way to verify the correctness of each step in the packaging process. Additionally, the efficiency of the packaging process is increased, as QR codes enable quick recognition and confirmation of component accuracy.

5. CONCLUSION

The implementation of the Poka-Yoke system in the aforementioned small enterprise brings significant benefits. In addition to reducing the possibility of errors in the production process, specifically in the process of packaging door frames with decorative moldings, it results in a reduction of financial burden associated with errors and protects the company's reputation. The implementation of the Poka-Yoke system also facilitates the work of operators by relieving them of the mental burden they previously had, relying solely on their concentration and the manual tracking of work orders and labels on the components

ACKNOWLEDGEMENTS

This work is co-financed by the Ministry of Education, Science and Technological Development of the Republic of Serbia on the base of the contract whose record number is 451-03-47/2023-01/200108. The authors thank the Ministry of Education, Science and Technological Development of the Republic of Serbia for supporting this research.

REFERENCES

[1] R. Kumar, R. Dwived and A. Verma, “Poka-Yoke Technique, Methodology & Design”, Indian Journal of Engineering, pp. 362-370, (2016)

[2] A. J. Kurhade, “Review on Poka-Yoke: Technique to Prevent Defects”, International Journal of Engineering Sciences & Research Technology, pp. 652-659, (2015)

[3] A. Simeonova, “Poka-Yoke - Ender's Game or Mistake-Proofing Toolbox”, Contemporary Management Practices X “Connectivity and Regions At: Burgas, (Bulgaria)”, 10 June 2019, pp. 86-90, (2019)

[4] E. A. Attiaa, K. Khader and O. Nadab, “Mistake Proofing Cam Mechanism Through Six-sigma Process: Case Study on Clothes Printing Machines”, International Journal of Engineering, Vol. 32, pp. 438-444, (2019)

[5] P. S. Patil, S. P. Parit, and Y. N. Burali, “Review Paper on Poka Yoke: The Revolutionary Idea in Total Productive Management”, International Journal of Engineering and Science, Vol. 2, pp.19-24, (2018)

[6] M. Vinod, S. R. Devadasan, D. T. Sunil and V. M. Thilak, “Six Sigma through Poka-Yoke: A Navigation through Literaturearena”, The International Journal of Advanced Manufacturing Technology, Vol. 81, pp. 315–327, (2015)

[7] A. Simeonova, “Poka Yoke: Poking into Mistakes for Total Quality!”, OmniScience: A Multi-disciplinary Journal, Vol. 6, pp. 1-8, (2016)

[8] S. Živković and M. Todorović, “Uloga ljudskih faktora u sistemu bezbednosti i zaštite”, Visoka škola Logos centar, Mostar, Bosna i Hercegovina, (2018)

[9] P. Soni and T. Yadav, “Review Paper on Productivity Improvement by Using Poka-Yoke”, International Research Journal of Engineering and Technology, Vol. 5, pp.761-763, (2018)

[10] P. Malega, “Poka–Yoke – Solution to Human Errors in the Production Process”, The International Journal of Business Management and Technology, Vol. 2, pp. 207-2013, (2018)

[11] P. Pötters, R. Schmitt and B. Leyendecker, “Effectivity of Quality Methods Used on the Shopfloor of a Serial Production – how important is Poka Yoka I Journal Total Quality Management, Vol. 29, pp. 1478-3371, (2018)

[12] S. Kumar, S. Luthra, A. Haleem and D. Garg, “Qualitative Analysis of Drivers of Poka-yoke in Small and Medium Enterprises of Indian Automobile Sector”, International Journal of Process Management and Benchmarking, Vol. 9, Pp. 232-249, (2019)

[13] B. Sreenivasa, “Poka-Yoke: A Simple way to Mistake Proofing”, International Engineering Research Journal, Vol. 2, pp. 4030-4037, (2017)

[14] A. P. Paper, H. H. Purba and S. C. Jaqin, “Novel POKA-YOKE Approaching Toward Industry-4.0: A Literature Review”, Operational Research in Engineering Sciences: Theory and Application, Vol. 3, pp. 65-83, (2020)

Development a system for designing optimal technological processing parameters at machining centers

Zvonko Petrović[1*], Milan Kolarević[2], Radovan Nikolić[1], Milica Tufegdžić[1], Nikola Beloica[3]
[1]Academy of Vocational Studies Šumadija/Department Trstenik, Trstenik (Serbia)
[2]Faculty of Mechanical and Civil Engineering in Kraljevo, University of Kragujevac, Kraljevo (Serbia)
[3]Faculty of engineering, University of Kragujevac, Kragujevac (Serbia)

Changes in the circulation of goods and services at the world level motivate manufacturers to fulfill the requirements of each individual customer in order to achieve a good position in the market. This phenomenon imposes increasingly strict requirements that the technological system must fulfill, so today flexible technological systems tend to become intelligent technological systems. The paper presents the development of a system for designing optimal technological processing parameters at machining centers based on biologically inspired Particle Swarm Optimization (PSO) algorithms.

Keywords: Flexible technological systems, Processing parameters, PSO algorithm

1. INTRODUCTION

The optimization of processing mode parameters is a method of knowledge implementation in the design of processing processes with the aim of their analysis, improvement and reaching higher techno-economic analysis. The basic assumption is that the costs of the processing process will be optimal if the costs of the processing process are optimal in all stages. The mathematical model of the objective function was formed by Stanić [1], and that function model was applied by Mečanin [2] on the optimization of the costs of the machining process by turning the spindle. The mathematical model of the function can be applied for all elementary operations with appropriate restrictions that are different for different operations. The objective function and constraints should contain enough influencing factors in order to have an objective impact on the machining process model.

2. MATHEMATICAL DESCRIPTION OF THE COSTS OF THE MILLING OPERATION DEPENDING ON THE PROCESSING MODE

The cost function, which, depending on the input to the processing system and the state of the processing system, mathematically describes the immediate costs of the operation, is represented in the OSVT-z trihedral surface located in the first octant and always concave because the parameters of the processing mode must have values greater than zero. Its form is:

$$T_Z = A_{1i} + A_{2i} \cdot V_i^{-1} \cdot S_i^{-1} + A_{3i} \cdot V_i^{\frac{1}{q_1}-1} \cdot S_i^{\frac{q_2}{q_1}-1} \qquad (1)$$

where $i = 1, 2, \ldots, n$ is the number of operations to be optimized. The geometric location of the points of conditional maxima on the surface of the cost function forms, in the OSV coordinate plane, a hyperbola, the arms of which, depending on the state of the input to the system, approach the coordinate axes faster or slower asymptotically. Otherwise, the set of conditional minimum points identifies the line of optimal costs along which the processing process should be managed in order to achieve the maximum effects of the system in terms of processing costs.

Optimal cost levels are located in the area $\{S_{\max}, V_{\min}\}$ ie. the highest processing effects are achieved at maximum step values and minimum cutting speed values. Conversely, $\{S_{\min}, V_{\max}\}$ the area is characterized by a relatively high level of processing costs. Exceptional cases deviate from this rule $q_2 = 1$ and $q_2 > 1$. For $q_2 = 1$ the same level of costs is achieved for the entire regime area, while in $q_2 > 1$ the case of the maximum processing effects located in the area $\{S_{\min}, V_{\max}\}$, and the minimum in the mode points $\{S_{\max}, V_{\min}\}$.

Processing outside the curve of optimal costs, unjustifiably frequent in production practice, causes relatively large losses of economy, especially in regime areas $\{S_{\max}, V_{\min}\}$ and $\{S_{\min}, V_{\max}\}$, because then high reproduction costs occur in the processing process [1].

The member A_{1i} is always constant because it represents the basic costs in the company that do not depend on the processing parameters but affect the total cost of production of the product. Members A_{2i} and A_{3i} depend on the processing mode, influence the total production costs and thus define the position of the minimum, which cannot be lower than the value

3. ALGORITAM PSO

Particle swarm optimization PSO (Figure 1) represents metaheuristic method of optimization based on agents (particles) population, which was accidentally discovered by James Kennedy and Russell Eberhart in 1995, while studying the simulation of social behavior of bird flocking [3]. Just as it is the case with all algorithms based on population, initial particle population is generated first. Position of the particle represents vector of parameters which are optimized.

$$\mathbf{x} = (x_1, x_2, \ldots, x_n) \qquad (2)$$

or potential solution. Random position in space which is explored, as well as initial velocities, is given to each particle. After that, the value of goal function of each particle is determined, and that value is added to it as the best value for the particle in question, and the initial position be-

*Corresponding author: Živadina Apostolovića 19, 37240 Trstenik, Serbia, zpetrovic@asss.edu.rs

comes the best position of the particle **p**

$\mathbf{p}_{\mathbf{best}}$. When all the best values of particles are determined, the particle with the minimum value is searched, and its position becomes the best position for the entire swarm p_{gbest}. Afterwards, it needs to be checked whether the criteria of optimization are satisfied, and if they are, the obtained results are shown. If the criteria are not satisfied, new velocities and positions need to be calculated.

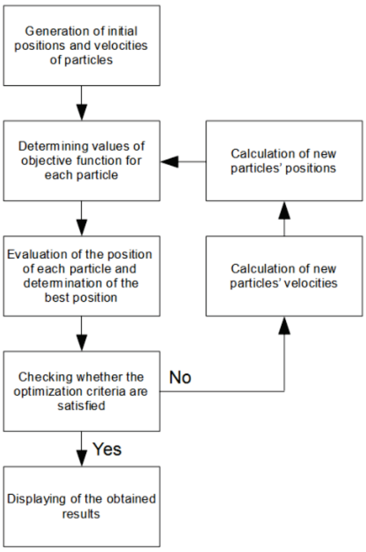

Figure1: Algorithm of the method of particle swarm optimization.

Figure 2 graphically shows how to determine new velocities and positions in two-dimensional space of search.

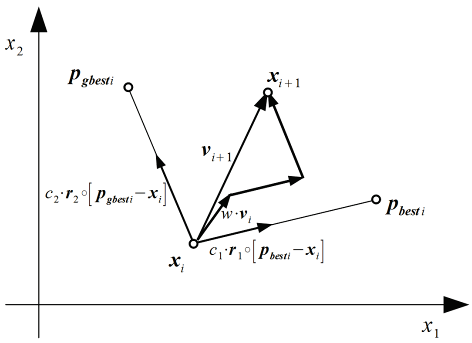

Figure 2: Updating of velocity and position of the i-th particle.

New velocity of each particle consists of three components:

1. the component which depends on instantaneous particle velocity,
2. the component which is proportional to the distance of instantaneous position of the particle and its best value,
3. the component which is proportional to the distance of instantaneous position of the particle and its best position for the entire swarm.

$$\mathbf{v}_{i+1} = w \cdot \mathbf{v}_i + c_1 \cdot \mathbf{r}_1 \circ \left(\mathbf{p}_{\mathbf{best}i} - \mathbf{x}_i\right) + c_2 \cdot \mathbf{r}_2 \circ \left(\mathbf{p}_{\mathbf{gbest}i} - \mathbf{x}_i\right) \quad (3)$$

where w represents inertia weight, c_1, c_2 are acceleration coefficients or correction factors, $\mathbf{r}_1, \mathbf{r}_2$ represent two random vectors of the length n within the limits $[0,1]$. The symbol ° represents Hadamard product:

$$\left(A \circ B\right)_{i,j} = \left(A\right)_{i,j} \cdot \left(B\right)_{i,j} \quad (4)$$

Inertia weight w impacts the first component, and for the values in the range of 0,9 – 1,2 [4] it gives the best results, that is, the algorithm has greater chances of finding the global minimum for a reasonable number of iterations. For coefficient values which are smaller than 0,8, if algorithm finds global minimum it will find it fast. Particles in this case move quickly and it can happen that they “fly over” some area, so it can happen that they do not find global minimum. On the other side, if inertia weight has bigger value, then particles search the solution space more thoroughly and the chances of finding global minimum are greater.

Acceleration coefficients c_1 and c_2, when multiplied by random vectors $\mathbf{r}_1$ and $\mathbf{r}_2$, stochastically manage the impact of the two other velocity components. Usually, their assumed value is approximately 2, in order for the middle value of the product of acceleration coefficient and random vector to be approximately 1. New position of the particle is determined by simple adding of the current position $\mathbf{x}_i$ and new particle velocity $\mathbf{v}_{i+1}$.

$$\mathbf{x}_{i+1} = \mathbf{x}_i + \mathbf{v}_{i+1} \quad (5)$$

The values of the goal function for new positions of the particle are determined again, and for each particle new and old values of the goal function are compared. If the new value is smaller, then it becomes new best value and the current position becomes the best position of that particle. The position of the particle with the smaller value becomes new best position for the entire swarm. Again, it needs to be checked whether the optimization criteria are satisfied; if they are, the results are shown, and if not, the entire procedure will be repeated until the criteria are satisfied.

This is the simplest version of the algorithm of particle swarm optimization. Other versions do not have constant values for the parameters w, c_1 and c_2, but they alter by specific rules during the implementation of the algorithm. In addition, other PSO algorithms also include different swarm topologies, that is, the way in which particles in the swarm communicate.

4. THEORY OF BELIEF FUNCTIONS

4.1. The basic concepts of Belief functions

Model of the belief function consists of variables, their values and the evidence, which supports the value of variables. Variables represent specific questions regarding the aspect of the problem under consideration. Given questions are answered using data originating from various sources, i.e., from context of published papers, from measurement data, from expert opinions, etc. Fully integrated support to the sought answer is called evidence.

Evidence can be represented by belief functions, which are defined as follows:

Definition1 [5, 6]. Let Θ be a finite nonempty set called the frame of discernment, or simply the frame. Mapping *Bel*: $2^{\Theta} \rightarrow [0,1]$ is called the (unnormalized) belief function if and only if a basic belief assignment (bba) *m*: $2^{\Theta} \rightarrow [0,1]$ exists, such that:

$$\sum_{A\subset\Theta} m(A)=1 \tag{2}$$

$$Bel(A)=\sum_{B\subset A, B\neq\varnothing} m(B) \tag{3}$$

$$Bel(\varnothing)=0 \tag{4}$$

Expression $m(A)$ can be viewed as the measure of belief which corresponds to subset A and takes values from this set.

Condition (2) means that one's entire belief, supported by evidence, can take the maximum value 1, and condition (4) refers to the fact that one's belief, corresponding to an empty set, must be equal to 0.

Value $Bel(A)$ represents the overall belief corresponding to the set A and all of its subsets.

Each subset A such that $m(A)>0$ is called a focal element.

The empty belief function is the function which satisfies $m(\Theta)=1$, and $m(A)=0$ for all subsets of $A\neq\Theta$. This function represents total ignorance about the problem under consideration.

4.2. Dempster rule of combining belief functions

Let the several independent belief function be given on the same recognition frame but with different bodies of evidence. The Dempster's combination rule (Figure 2) (5, 6) produces new belief function which represents effect resulting from the connection of the different bodies of evidence.

Let us assume that the belief functions Bel_1 and Bel_2 are created on Θ frame. Let $A_1,\ldots,A_k$, $k<2^{|\Theta|}$ be the focal elements of function Bel_1 with corresponding m – values $m_1(A_i)$ for $i=1,\ldots,k$; and let $B_1,\ldots,B_j$, $j<2^{|\Theta|}$ be focal elements of function Bel_2 with corresponding m-values $m_2(B_i)$ for $i=1,\ldots,j$ [5]

Combination of these two functions is denoted as $Bel_1\oplus Bel_2$ and its focal elements are $C_1,\ldots,C_m$ with corresponding m-values $m_3(C_k)$ for $k=1,\ldots,m$, created in the following way:

$$m_3(C_k)=K\left[\sum_{\substack{i,j\\ A_i\cap B_j=C_k}} m_1(A_i)m_2(B_j)\right] \tag{5}$$

where K represents a normalization factor

$$K=\left[1-\sum_{\substack{i,j\\ A_i\cap B_j=\varnothing}} m_1(A_i)m_2(B_j)\right]^{-1} \tag{6}$$

The normalization factor K is greater than 1 whenever Bel_1 and Bel_2 contain a part of mass of some belief that correspond to the subjective probability for the decoupled (contradictory) subsets of Θ. In fact, K represents the conflict measure of the two belief functions. Whenever two or more functions are combined, the combination rule is associative and commutative. In general, $Bel\oplus Bel=Bel$. Combination of a certain number of belief functions $Bel_1\oplus\cdots\oplus Bel_n$ is denoted as $\oplus\oplus\{Bel_1,\cdots,Bel_n\}$.

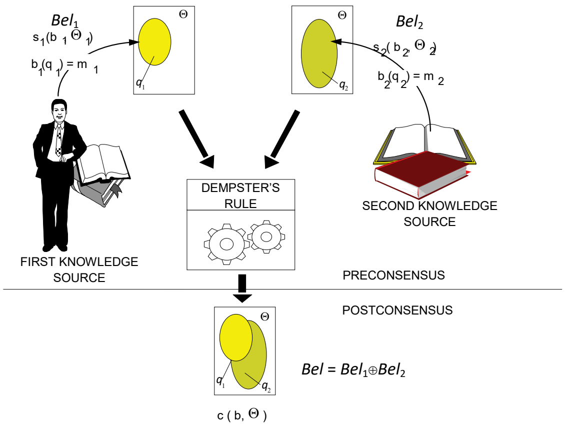

Figure 3: Graphics illustration using Dempsters rule of belief function combining [6]

4.3. What are the Evidential systems

Valuation Based Systems - VBS is an abstract framework proposed by Shenoy for representing and reasoning on the basis of uncertainty. It allows representation of uncertain knowledge in various domains, including Bayes' probability theory, Dempster-Shafer's theory of evidence which is based on belief functions and Zadeh-Dubais-Prad theory of possibility. Graphically presented VBS is called valuation network [6].

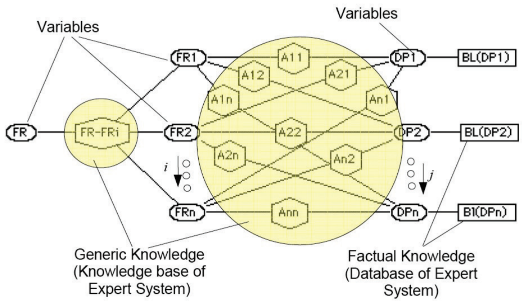

Figure 4: The concept of evidential networks

VBS consists of set of variables and set of valuations that are defined on the subsets of these variables. Set of all variables is denoted by U and represents a space covered with problem which is under consideration. Each variable represents a relevant aspect of a problem. For each variable X_i will be used ΘX_i to denote the set of possible values of variables called the frame of X_i. For a subset A (|A|>1) of U, set of valuations that are defined over ΘA represents the relationship between variables in A. Frame ΘA is a direct (Cartesian) product of all ΘX_i for X_i in A. The elements ΘA are called configurations of A.

Knowledge presented in this type of valuations is called generic or general knowledge (figure 3), which can be represented as a knowledge base in expert systems.

The VBS also defines valuations on individual variables, which represents so-called factual knowledge, and it constitutes database in expert systems (figure 3). For a problem, general-generic knowledge defines an expert. During reasoning process that knowledge won't be modified. Factual knowledge will vary in accordance with condition of a problem currently being under consideration. The VBS treats on the same way these two kinds of knowledge.

The VBS systems suited for processing uncertain knowledge described by functions of belief function theory are called Evidential Reasoning Systems or Evidential Systems, and valuation networks are now called evidential networks (EN) (figure 4).

The objective of reasoning based on the evidence is an assessment of a hypothesis, in case when the actual evidence are given (the facts). This can be accomplished by evaluating valuation networks in two steps:

- Combining all belief functions in evidential network, resulting in a so-called global belief function
- Marginalization of global belief functions in the framework of each individual variable or subsets of variables produces marginalized values for each variable or subset of variables.

Easily way of understanding the reasoning process and its graphical interpretation is the condition on which depends whether and how fast these systems will be applied in solving everyday problems. As a software support to the VBS systems application, several software tools have been developed. For evidential systems the very known are: McEvidence, Pulcinella and DELIEF.

5. GOAL AND LIMITATION FUNCTION

In this paper, 17 milling operations are optimized and in them, machining mode parameters are step $S[\mathrm{mm/o}]$ and technological cutting speed:

$$V = \frac{\pi \cdot D \cdot n}{1000}\,[\mathrm{m/min}] \tag{6}$$

in which the number of rotations n[o/min] is. They are directly related to the main processing time, so for optimum values of these parameters we have optimum time of duration of each operation, and therefore, the optimum processing time of machine part. Machine mode parameters that give minimum costs of machining process must be found within given limitations because there is a limitation by characteristics of tools and machine. Figure 3 shows 3D model of valve casing and section where the greatest number of different openings are located.

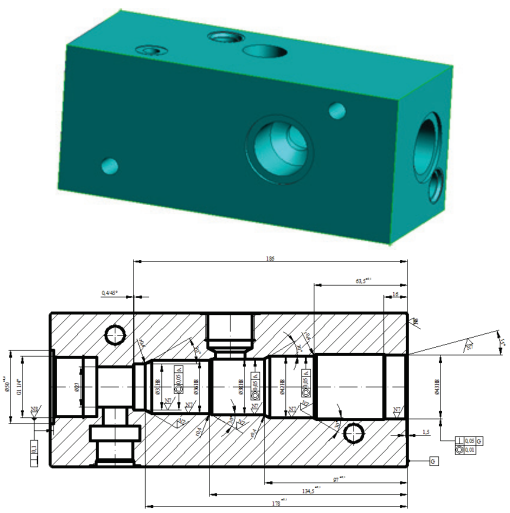

Figure5: Valve casing – a machine part whose milling operations are optimized.

Goal function which is optimized has the following form:

$$f(S_i,V_i) = \sum_{i=1}^{25} T_i = \sum_{i=1}^{25} A_{1i} + A_{2i}\cdot V_i^{-1}\cdot S_i^{-1} + A_{3i}\cdot V_i^{\frac{1}{q_1}-1}\cdot S_i^{\frac{q_2}{q_1}-1} \tag{7}$$

Values of coefficients A_1, A_2, A_3, for each of 17 goal functions, are given in Table 1 :

Table 1: Coefficient values A_1, A_2, A_3, a_i.

i	A_{1i} [min]	A_{2i} $\left[\frac{\mathrm{din}}{\mathrm{min}}\cdot \mathrm{m}^2\right]$	A_{3i} $\left[\frac{\mathrm{din}\cdot\mathrm{min}}{\mathrm{m}^2}\right]$	a_i [mm]
1	1707,801	828,8	0,748	0,2
2	1707,801	118,1	0,133	0,2
3	1707,801	14,76	0,019	0,2
4	1707,801	7,721	0,036	0,2
5	1707,801	1,505	0,007	0,2
6	1707,801	35,18	0,389	0,2
7	1707,801	1,535	0,010	0,05
8	1707,801	7,226	0,073	0,05
9	1707,801	46,33	0,486	0,05
10	1707,801	2,007	0,014	0,05
11	1707,801	81,46	0,713	0,05
12	1707,801	1,505	0,017	0,2
13	1707,801	19,48	0,671	0,05
14	1707,801	1,299	0,021	0,2
15	1707,801	137,0	1,157	0,05
16	1707,801	14,76	0,102	0,2
17	1707,801	1,612	0,252	0,05

6. OPTIMIZATION RESULTS

34 parameters are obtained as the results of this optimization process which represent optimum values of technological cutting speed and steps for 17 milling operations , and so the costs of these procedures have minimum value.

Optimum values of the steps ,velocity and cost price of all operations individually and collectively are given in Table 2:

Table 2: Optimum values of the steps, velocity and cost price of all operations individually

i	S_i [mm/o]	V_i [m/min]	T_i [din]
1	0,026	450,6	1708,29
2	0,238	625,3	1708,66
3	0,136	751,2	1708,57
4	0,012	325,3	1708,43
5	0,114	420,5	1708,21
6	0,023	240,5	1708,32
7	0,123	425,6	1710,47
8	0,030	350,4	1710,85
9	0,063	367,6	1709,96
10	0,026	560,8	1708,33
11	0,369	480,6	1708,87
12	0,119	375,4	1707,95
13	0,336	180,9	1707,88
14	0,887	350,6	1707,96
15	0,710	650,9	1707,97
16	0,600	850,6	1708,84
17	0,325	65,9	1708,94
		$\sum_{i=1}^{25} T_i$	29048,5

7. CONCLUSION

In this paper, the optimization of the costs of technological process of a part of a complex structure is performed by using the method pso. For instance, in optimization of the flexible technology when real processing time is less than given, optimization of machining parameters is implemented in order to decrease costs of production. In this case, we can choose cheaper tools of lower level of cutting characteristics, and by using the method pso, in a very short time, we can obtain results on which procedure allows decreasing of the machine mode and which does not, all of which can be presented in the space as in figure, for the purpose of checking of the obtained results.

ACKNOWLEDGEMENTS

This work is co-financed by the Ministry of Education, Science and Technological Development of the Republic of Serbia on the base of the contract whose record number is 451-03-47/2023-01/200108. The authors thank the Ministry of Education, Science and Technological Development of the Republic of Serbia for supporting this research.

REFERENCES

[1] J. Stanić, "Uvod u teoriju tehnoekonomske optimizacije procesa", Mašinski fakultet Beograd, Beograd (Serbia), (1983)

[2] V. Mečanin, "Optimizacija obradnih procesa u masinogradnji", Mašinski fakultet Kraljevo, Kraljevo (Serbia), (1996)

[3] J. Kenedy and R. Eberhart, "Particle swarm optimization", Proceedings of ICNN'95 - International Conference on Neural Networks, Vol.4, pp. 1942-1948, (1995)

[4] Y. Shi and R. Eberhart, "A modified particle swarm optimizer", Proceedings of the IEEE Conference on Evolutionary Computation, ICEC., pp. 69-73, (1998)

[5] M. Djapić, "Evidential Systems in Product and Process Development", Intelligent Manufacturing Series of Monographs No. 9, LOLA Institute, Belgrade, (2005) (In Serbian)

[6] G. Shafer, "A Mathematical Theory of Evidence", Princton University Press, Princeton (USA), (1976)

Application of the ANFIS method to support decision-making in the prediction of the factors that most influence the product price

Marija Mojsilović[1*], Radoje Cvejić[2], Goran Miodragović[1], Snežana Gavrilović[1], Selver Pepić[1]

[1]Academy of Professional Studies Sumadija, College in Trstenik, Trstenik (Serbia)
[2]Faculty of Information Technology and Engineering, University "UNION Nikola Tesla, Belgrade (Serbia)

This paper presents the application of the Anfis method in predicting the most influential factors on the formation of the optimal selling price of a product. From a large set of factors that can influence the formation of the sales price, the following costs are singled out: raw materials, labor, tools and machines, as well as the manufacturing technology, i.e. the time of manufacturing the product. The idea is to carry out an individual assessment of the impact of each of the mentioned factors on the price of the product, that is, the combined impact of two or three factors. The obtained results can serve as an input parameter in decision support systems, which would allow managers to accurately predict all factors and have a better insight into how these factors influence the formation of the sales price.

Keywords: DSS; Neural Networks; Anfis; Prediction

1. INTRODUCTION

Lately, the decision-making process is taking on an increasingly important role, not only in scientific circles, but also in practical application in an increasing number of organizations. The business of the organization in modern conditions and their economies is characterized by extremely strong competition from other organizations, constant variability of market conditions, a relatively short life span of products and services, as well as an increasingly better education of customers and users, and thus their increased discernment and demandingness [1].

Decision-making is related to the active relationship of the living world to the environment. Even the simplest forms of life, such as viruses and single-celled plants and animals, make decisions about choosing one of the possibilities or ways to solve a problem, which allows them to survive as individuals and as species in changing environmental conditions.

Of particular interest to human society are decisions made by humans, who use rational thinking and logical reasoning. Since not all the facts and consequences of many decisions are always known, a person relies on intuition and experience to make them, so that decisions do not only depend on the circumstances, but also on who makes the decisions [2][3].

A Decision Support System (DSS) is a computer-based system that assists in the decision-making process. It provides a set of tools and techniques that help users analyze and solve complex problems [4].

The use of artificial neural network models to enrich the analytical and predictive capabilities of decision support systems in manufacturing has increased. Increasing complexity and uncertainty in the manufacturing sector require improved decision-making to ensure low operating costs, high productivity and sustainable use of resources. Artificial neural networks have the inherent ability to analyze the most uncertain and complex patterns in unstructured decision-making problems.

2. ANFIS METHODOLOGY

Adaptive neuro-fuzzy inference system (ANFIS) is one of the most popular representatives of hybrid neuro-fuzzy systems. The following considerations are based on a review of references [5][6][7].

The structure of the adaptive neural network ANFIS is composed of five layers:

- Input layer
- Membership function layer
- Fuzzy rule layer
- The decision-making phase layer
- Output layer

The rule base of the ANFIS structure consists of phased IF-THEN rules. A system with two inputs and one output is used to describe these rules:

Rule 1: IF ((x is A1) and (y is B1)) THEN (z is f1)
Rule 2: IF ((x is A2) and (y is B2)) THEN (z is f2)

Where are those variables:

- x , y – input sizes,
- z – output size
- Ai , Bi (i=1,2) – fuzzy sets (linguistic variables)
- f i (i=1,2) – exits the inference system.

To form a fuzzy inference system model, neural networks are used to calculate membership function parameters based on available input-output data, taking into account knowledge of the process being studied. In the ANFIS network algorithm, the signals are fed forward through four layers, using the least squares method to determine the consequent parameters. Through the backward pass, errors are propagated backwards and the premise parameters are updated using gradient descent. Training and testing of the ANFIS network was performed in the Matlab software package. Based on the collected input-output data pairs from the experimental tests, the ANFIS network is used to identify the most influential parameters for a given output parameter, while estimating the prediction error. In this research, the prediction

*Corresponding author: Radoja Krstića 19, Trstenik, mmojsilovic@asss.edu.rs

accuracy is evaluated through the least squares error, which can be represented by the equation.

$$RMSE = \sqrt{\frac{\sum_{i=1}^{n}(P_i - Q_i)^2}{n}}$$

Where P_i and Q_i are the experimental and calculated data.

3. METHODOLOGY AND DATA

In this paper, the part of the decision-making system related to the analysis of the factors that influence the price of the product and the identification of the factors that influence the price the most will be specifically looked at.

In order to see the best optimal solution, which is the goal of this paper, which is the selling price of the product, it is necessary to know the influencing factors, which will be the input sizes.

There are many factors that affect the cost of the manufacturing process. Some of the factors that affect the price are as follows:

- Raw material costs: Raw material costs for production may include the cost of sealing materials, such as rubber, plastic or textiles, as well as the costs of other raw materials required for production, such as additives or auxiliary chemicals.
- Labor costs: Labor costs include wages and other costs related to workers, such as benefits and taxes.
- Equipment costs: The equipment required to produce a seal can affect the price, especially if expensive equipment is used or if new production equipment needs to be purchased.
- Transportation costs: Transportation costs refer to the costs of transporting raw materials, semi-finished products and finished products to and from the place of production.
- Taxes and duties: Taxes on products and duties on the import of raw materials can affect the price of products.
- Market competitiveness: The amount of competition in the gasket market can also affect price. If competition is strong, producers may be forced to lower prices to attract buyers.
- Margin: Margin is the difference between the price of the product and its costs, and represents the profit that the manufacturer makes. Manufacturers may decide to increase the margin by increasing the price of the product.

3.1. Problem Description

The goal of this research is to evaluate the factor that most affects the selling price of the product. This indicator represents a reliable value that depends on many different independent variables, some of which are presented in this research. The input factors are, table 1.:

- Raw material - The price of the raw material can influence the price of the seal, if more expensive raw materials are used, the price of the seal will be higher. Also, if the availability of raw materials is limited or the price of raw materials is on the rise, this may affect the price of the gasket. As the price is a variable category, and in the context of data collection from the work organization, which is engaged in the production of seals, the influence of the prices of raw materials on the price of the product was weighted. By looking at the statistical data available to the company and interviewing experts in the fields of economics, technology and production, it was concluded that the range of influence is from 1.75 to 5.00. where a lower weighting means a higher income than the formed price of the product.
- Labor - If labor costs are high, for example due to high wages or benefits for workers, this will be reflected in the cost of the gasket. The impact of labor participation by workers is given in percentages, where a lower percentage represents a lower coefficient for calculating wages. With a higher coefficient, it is the other way around. And these data were obtained on the basis of research and interviewing experts from the work organization.
- Tool - The tool in the production of seals has a direct influence on the formation of the price of the product. precision-made tools give better quality and a more precisely made product, but they are also more expensive. Furthermore, if tool maintenance and repair costs are high, this will affect the price of the seal, also if tool acquisition costs are high, the product price will increase. The weights for this influence range from 0.27 to 0.99, where a lower weight represents already used tools, and a higher weight represents newer or completely new tools.
- Machinery – Machinery has an impact through acquisition, maintenance and repair costs, in cases where machinery is used to produce different types of products, this will reduce costs and increase productivity.
- Technology factor - The impact of the technology factor on the price of the product is reflected if the costs of making and developing new technology are high, or if the new technology enables better product quality. And this weighting is given in percentages.
- Production time - The production time of the product affects the following way, if the production technology requires more hours, the workers are forced to make additional hours or if the production time is short, it can affect the quality of the product, which will affect the price of the seal. , as well as the number of pieces that can be produced.

Table 1: Input and output parameters

Inputs and outputs	**Parameter description**		
	The name of the input parameters	***min***	***max***
Entrance 1	raw material	1,75	5
Entrance 2	worker	32	88
Entrance 3	tool	0,27	0,99
Entrance 4	the machine	0,73	0,86
Entrance 5	technology factor	40	91
Entrance 6	production time	1,64	5
Exit	the price of the product	0,895	1,165

4. RESULTS AND DISCUSSION

MatLab is often used for data analysis and modeling, algorithm development and testing, simulations and process automation, as well as for developing interactive applications for working with data.

After generating the parameters, Figure 5 shows the loading of the data representing the input parameters, the goal is to show one input that has the greatest impact on the output size.

Table 2 presents the mean error value, mean deviation, mean square error and root mean square error for training data, test data and all data combined, as well as the reliability coefficient of the obtained model for the input that has the greatest impact on the output size.

Table 2: The influence of one input on the output - price formation

Entrance	**The input with the least error**
	Entrance no. 3
One entrance	Entrance no. 3 TRAINING – ERROR SV = 0.000000 SD = 0.009429 MSE= 0.000088 RMSE= 0.009404 TEST – ERROR SV = -0.001507 SD = 0.011016 MSE= 0.000120 RMSE= 0.010952 ALL DATA SV = -0.00022299 SD = 0.009668 MSE= 9.3101e-05 RMSE= 0.0096489

Input 3 has the smallest RMSE, which means that by observing one factor, the results show that the displayed factor, i.e. the tool, has the greatest influence on price formation. The quality of the tool used to seal can affect the cost of the seal in a number of ways. If the tool has better performance, higher sealing accuracy and less material damage can be achieved, which can reduce costs and increase productivity. Also, if the tool lasts longer, it means less maintenance and replacement costs. However, if the tool is more expensive, this will be reflected in the price of the seal. This is understandable because when making seals, the higher the quality of the tool, the higher the cost of the tool, and therefore the impact on the final formation of the price is more significant.

In Figures 1, 2 and 3, you can see all the data on errors in the training process, the test and the unified display, which were obtained in the Matlab software package, using the ANFIS methodology. Figure 4 shows the regression analysis and reliability of the model, while Figure 5 shows the graphical implementation of the training data with one input.

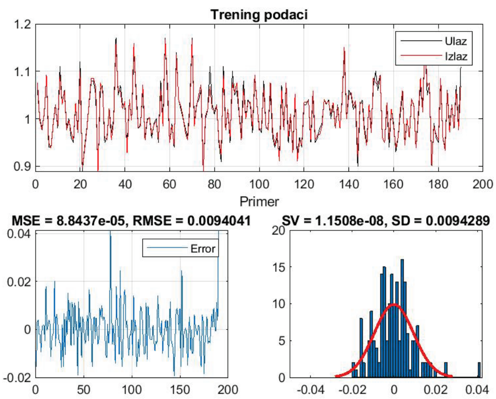

Figure 1. ANFIS network training – one input

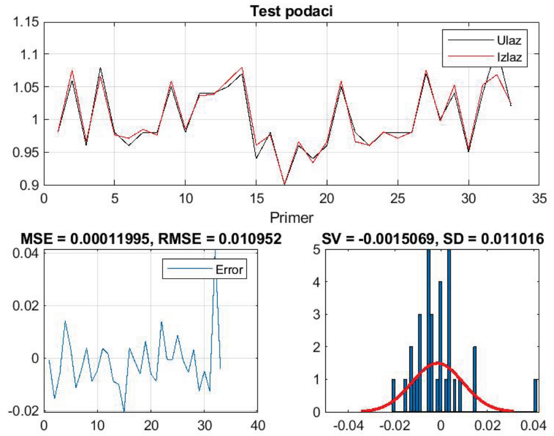

Figure 2. ANFIS network test – one input

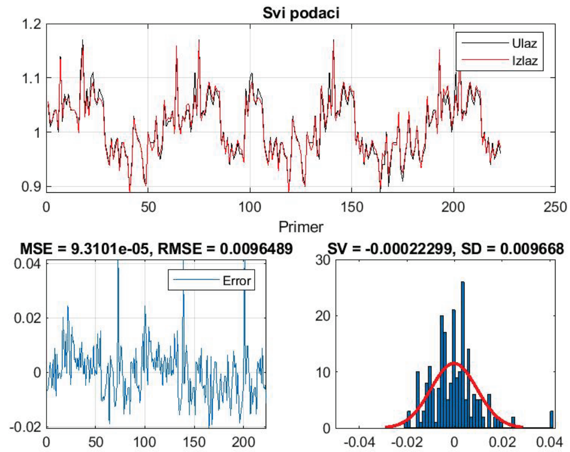

Figure 3. All ANFIS network data - one input

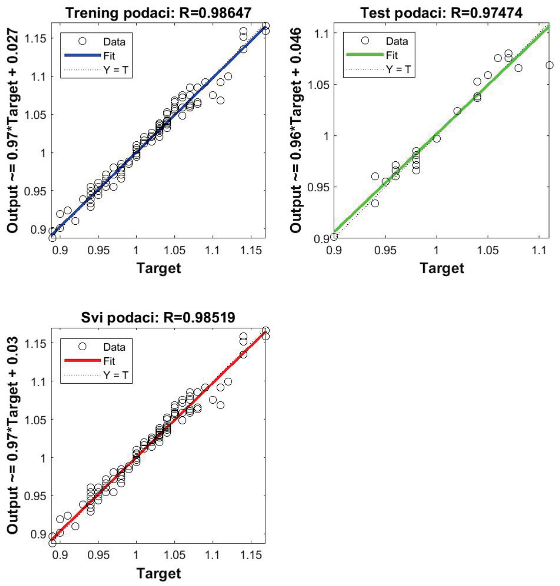

Figure 4. Regression of training, test and all data - one input

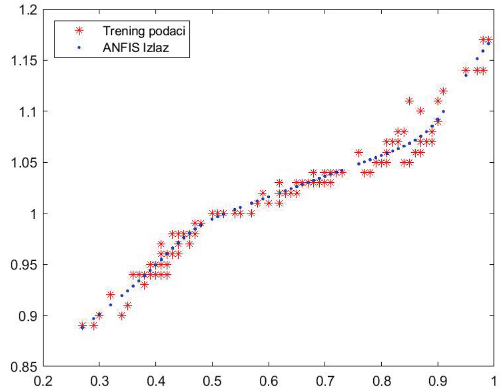

Figure 5. Regression of training, test and all data - one input

In addition to the obtained one, the greatest influence of input on output, an assessment of the impact of two factors that have the greatest impact on output was also carried out. It was found that input 1 and input 3 combined have the smallest RMSE, that is, the largest impact on the output size, which means that the raw material and the tool together have the largest impact on the price. The quality and cost of raw materials can directly affect the cost of the gasket. If the raw material is more expensive, the price of the seal will be higher. The amount of raw material required to produce the seal can also affect the price. If the raw material is obtained from a remote location or if it has to be transported far, the transportation costs will be reflected in the price of the seal. Tool quality can affect sealing accuracy, which can reduce costs and increase productivity. If the tool is more expensive, this will be reflected in the price of the seal. Tool maintenance can also affect the cost of the seal. If the tool is prone to breakdowns or requires frequent servicing, this will increase costs and affect the price of the seal.

The values of all errors of training, test and combined data for the two most influential inputs together, input 1 and input 3, on the output size, as well as the reliability coefficient of the obtained model are presented in Table 3:

Table 3: The impact of two inputs on the output - price formation

<table>
<tr><th rowspan="2">Entrance</th><th>The input with the least error</th></tr>
<tr><th>Entrance no. 1 - 3</th></tr>
<tr><td>Two entrances</td><td>Entrance no. 1 - 3
TRAINING – ERROR
SV = 0.000000 SD = 0.007634 MSE= 0.000058
RMSE= 0.007614

TEST – ERROR
SV = 0.000622 SD=0.011406 MSE=0.000127
RMSE= 0.011249

ALL DATA
SV= 9.2088e-05 SD=0.0082716 MSE=6.8122e-05
RMSE= 0.0082536</td></tr>
</table>

Figures 6, 7 and 8 represent the data obtained in the Matlab program and refer to errors during training, test and processing of all data together. Figure 9 refers to the reliability of the model given through the regression analysis of the training, test and combined data, and Figure 10 to the approximation of the training input data by the ANFIS output function.

In doing so, the effects of two combined inputs on the output were considered, and only the data for the combination of those inputs that have the greatest impact on the output variable, i.e., inputs 1 and 3, are shown.

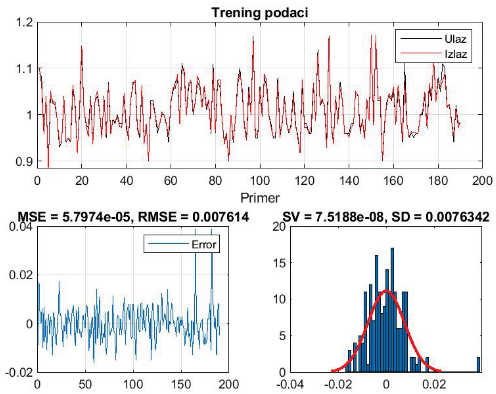

Figure 6. ANFIS network training – two inputs

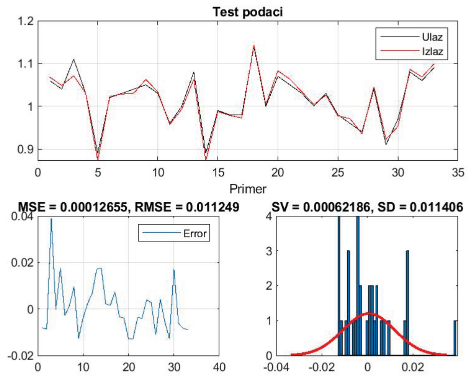

Figure 7. ANFIS network test - two inputs

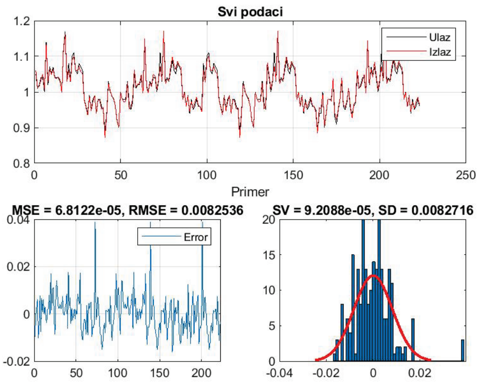

Figure 8. All ANFIS network data - two inputs

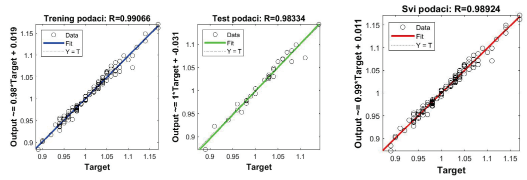

Figure 9. Regression of training, test and all data - two inputs

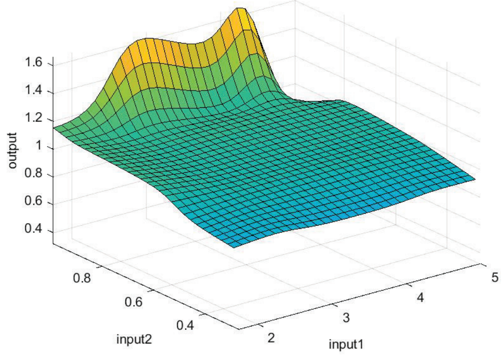

Figure 10. Graphical interpretation of training data – Matlab - two inputs

At the end, the influence of three combined factors of input variables on the output size is shown. Inputs 1, 2 and 6 have the smallest RMSE, so their joint impact on the output is the greatest, i.e., when forming the price, the greatest impact on whether it will be with a loss or with a profit is the raw material, the qualification of the worker - the cost of the worker and the time of making the parts.

The time of making parts depends on the quality of the tool and the condition of the machine, so these two factors are indirectly taken through the time of making. Input 6 that is, if the production time is shorter, it can increase productivity and reduce costs, which will be reflected in a lower price of the seal. When the production time is longer, it can reduce productivity and increase costs, which will be reflected in a higher price of the seal. In the event of urgent gasket production requirements, this may result in an increase in price due to the additional costs required to meet the delivery deadline. If the gasket is made in small batches or on demand, this can lead to an increase in price due to higher production costs per unit.

The errors of training, test and all data together when processing the three most influential input variables on the output, as well as the reliability coefficient of the obtained model are presented in Table 4:

Table 4: The impact of three inputs on output - price formation

Entrance	**The input with the least error**
	Entrance no. 1 - 2 - 6
Three entrances	Entrance no. 1 - 2 – 6 TRAINING – ERROR SV = 0.000000 SD = 0.002910 MSE= 0.000008 RMSE= 0.002902 TEST – ERROR SV = 0.000598 SD = 0.005691 MSE= 0.000032 RMSE= 0.005636 ALL DATA SV = 8.873e-05 SD = 0.0034529 MSE=1.1877e-05 RMSE= 0.0034463

Figures 11, 12 and 13 show all error data. Figures 14 and 15 show the graphical interpretation of the regression and approximation of the training, test and combined data of the three most influential inputs to the ANFIS output.

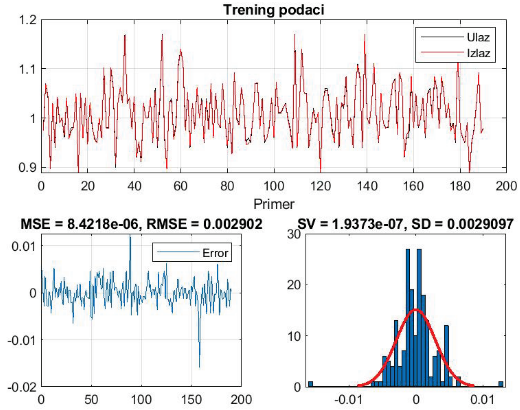

Figure 11. ANFIS network training – three inputs

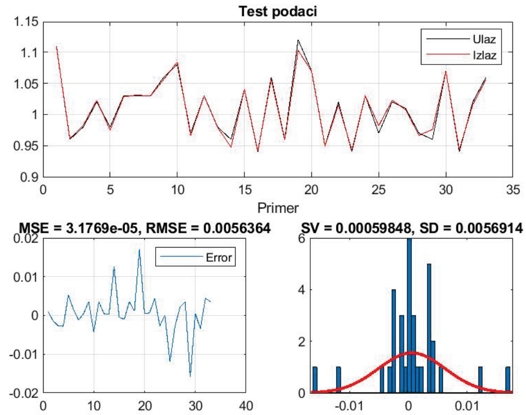

Figure 12. ANFIS network test – three inputs

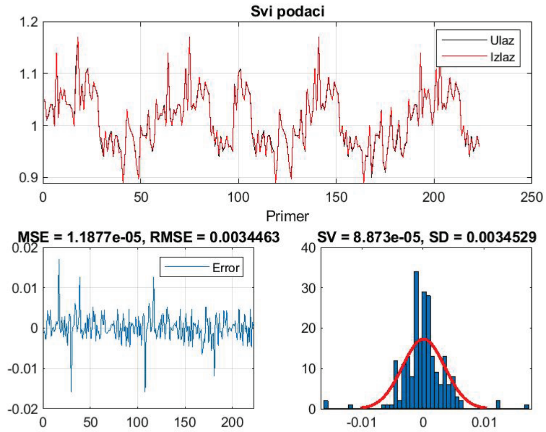

Figure 13. All ANFIS network data - three inputs

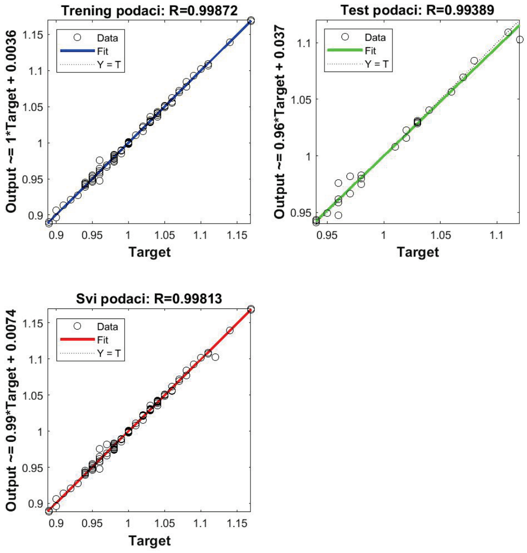

Figure 14. Regression of training, test and all data – three inputs

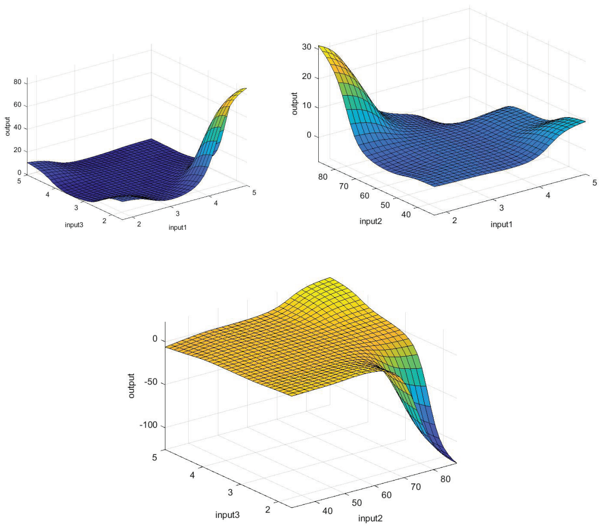

Figure 15. Graphical interpretation of training data – Matlab - three inputs

5. CONCLUSION

In this paper, a part of the decision-making system related to the production of seals in a production plant is reviewed. The best optimal solution that has the greatest impact on the selling price was considered, the factors that were considered as input sizes are: raw material, worker, tool, machine, technological factor and the time of making the part, while the output size is the selling price of the product.

Analyzing the factors that affect the price of a product is crucial for managers in making decisions about the formation of product prices, and this method provides a better insight into the factors that most affect the price.

The results of the research showed that tool costs have the greatest influence on the selling price of a product when examining one input factor. By observing the two input factors that have the greatest impact on the price, input 1 and input 3 in combination have the smallest RMSE, that is, the greatest impact on the output size, which means that the raw material and the tool together have the greatest impact on the price. At the end, the influence of three combined factors of input variables on the output size is shown, on whether the business will be at a loss or with a profit. The biggest influence on the price is the raw material, the qualification of the workers - the cost of the workers and the time of making the parts.

The Anfis method allows managers to accurately predict these factors and to have a better insight into how these factors could be used in making product price decisions.

Further improvement of this research could include the application of other artificial intelligence methods, as well as the comparison of the obtained results with the aim of finding the most optimal solution for forming the selling price of the product. In addition, it is possible to consider the inclusion of other factors that may affect the price of the product, such as the quality of the product. This could lead to even more accurate and reliable price forecasts and provide better guidance to managers in making product pricing decisions.

REFERENCES

[1] M. Milić, M, “Odlučivanje i poslovna inteigencija, Univerzitet za poslovn inženjering i menadžment”, Banja Luka, (2014)

[2] E. Turban, J.E. Aronson, T. Liang and R. Sharda, “Decision Support and Business Intelligence Systems”, 9th Ed, Pearson Education, London (UK), (2010)

[3] V.L. Sauter, “Decision Support Systems for Business Intelligence”, John Wiley and Sons, New Jersey (USA), (2010)

[4] V. Mišković, “Sistemi za podršku odlučivanju”, Univerzitet Singidunum, Beograd (Serbia), (2013)

[5] S. Gavrilović, N. Denić, D. Petković, N. V. Živić and S. Vujičić, “Statistical evaluation of mathematics lecture performances by soft computing approach”, Computer Applications in Engineering Education, Vol. 26(4), pp. 902-905, (2018)

[6] B. Anđelković, “Istraživanje i razvoj novih metoda za proračun steznih sklopova primenom neuronskih mreža i fazi logike”, doktorska disertacije, Mašinski fakultet Niš, Serbia, (2006)

[7] M. Sugeno and G.T. Kang, “Structure identification of fuzzy model”, Fuzzy Sets Syst., Vol. 28, pp. 15–33, (1988)

[8] Z. Liao, B. Wang, X. Xia, and P. M. Hannam, “Environmental emergency decision support system based on Artificial Neural Network”, Safety Science, Vol. 50(1), pp. 150–163, (2012)

[9] F. Mumali, “Artificial neural network-based decision support systems in manufacturing processes: A systematic literature review”, Computers & Industrial Engineering, Vol.165, (2022)

[10] R. Arora and H. Garg, “A robust correlation coefficient measure of dual hesitant fuzzy soft sets and their application in decision making”, Eng. Appl. Artif. Intell., Vol. 72, pp. 80–92, (2018)

Supplementary elements of traffic noise barriers

Vladan Grković[1*], Violeta Đorđević[2], Milan Kolarević[1], Branko Radičević[1], Tanja Miodragović[1]
[1]The Faculty of Mechanical and Civil Engineering in Kraljevo, University in Kragujevac, Kraljevo (Serbia)
[2]Academy of Applied Study Šumadija, Department Trstenik, Trstenik (Serbia)

Depending on the acoustic, aesthetic, and other needs, additional objects are often incorporated into traffic noise barriers, such as caps to cover the top of the barrier, emergency openings, drainage openings, wall-mounted attachments, barrier protection from traffic, vertical supports for climbing plants, sound absorbers, protective caps for posts, and similar. The most common are the caps that are installed to improve the acoustic performance of the barrier, such as:

- *noise resonators,*
- *tubular absorbers,*
- *diffraction edge,*
- *devices for passive phase interference,*
- *devices for active noise control, etc.*

Keywords: Sound resonators, Tubular absorbers, Diffraction caps

1. INTRODUCTION

Daily traffic causes a significant amount of noise that can have a negative impact on the quality of life of people in surrounding communities, creating problems with sleep, concentration, learning, and overall well-being. To reduce the impact of traffic noise on the environment, various noise control technologies have been developed, including traffic noise barriers.

Traffic noise barriers are constructions that are placed next to roads or highways, and their main function is to reduce the amount of noise that is transmitted across the road and into surrounding neighborhoods. Traditionally, noise barriers have been constructed as flat surfaces that reflect or absorb sound to reduce its propagation. However, as new needs arise in acoustics, aesthetics, and other factors, additional objects are increasingly being used in traffic sound barriers to improve their acoustic performance and aesthetic appeal. [1]

These additional objects may include caps to increase acoustic performance, emergency openings, drainage openings, wall-mounted attachments, protection against traffic damage, vertical supports for climbing plants, sound absorbers, protective caps for pillars, and more. In this paper, special attention will be paid to caps used to improve the acoustic performance of sound barriers, such as noise resonators, tubular absorbers, diffraction caps, passive phase interference devices, active noise control devices, etc.

The aim of this review is to present the division of additional objects used in traffic noise barriers, which are significant for improving their acoustic performance and aesthetic appeal. In addition, this paper will show various caps used to improve the acoustic performance of sound barriers, as well as their advantages and disadvantages. In this way, this paper will help experts in the field of acoustics, designers, and urban planners to better understand the use of traffic sound barriers and how to improve their effectiveness.

2. CLASSIFICATION OF SUPPLEMENTARY ELEMENTS OF TRAFFIC NOISE BARRIERS

The classification of the basic types of supplementary elements that are embedded in noise barriers or mounted on them is shown in Figure 1.

2.1. Cover caps (top edge of the barrier)

Caps are special elements of the barrier system that are placed on the top of noise barriers. They can be mounted on panels or on poles, and can be mounted on both panels and poles. They are named after their "cap-like appearance" and are installed for two reasons: acoustic and aesthetic.

Caps can make the profile of the barrier look smoother by removing jagged edges and gaps. Cover caps are placed on top of barriers and provide additional protection from rain, snow, and other elements It is necessary to match the size of the cap with the dimensions of the noise barrier. If the cap is too large, it can disrupt the aesthetic appearance of the barrier and negatively affect the natural cleaning of the barrier during rainfall. Also, attention should be paid to fastening and anchoring at the points where panels and pillars are connected [1][2].

Although caps provide a nicer look to the barriers, there can often be issues with their maintenance. Therefore, the design of caps and pillar must be in line with barrier maintenance plans. Permanent caps can be provided, but removable caps can also be used periodically. In both cases, drainage methods should be considered to prevent water accumulation, corrosion, bending, or other material changes.

*Corresponding author: Dositejeva 19, 36000 Kraljevo, grkovic.v@mfkv.kg.sc.rs

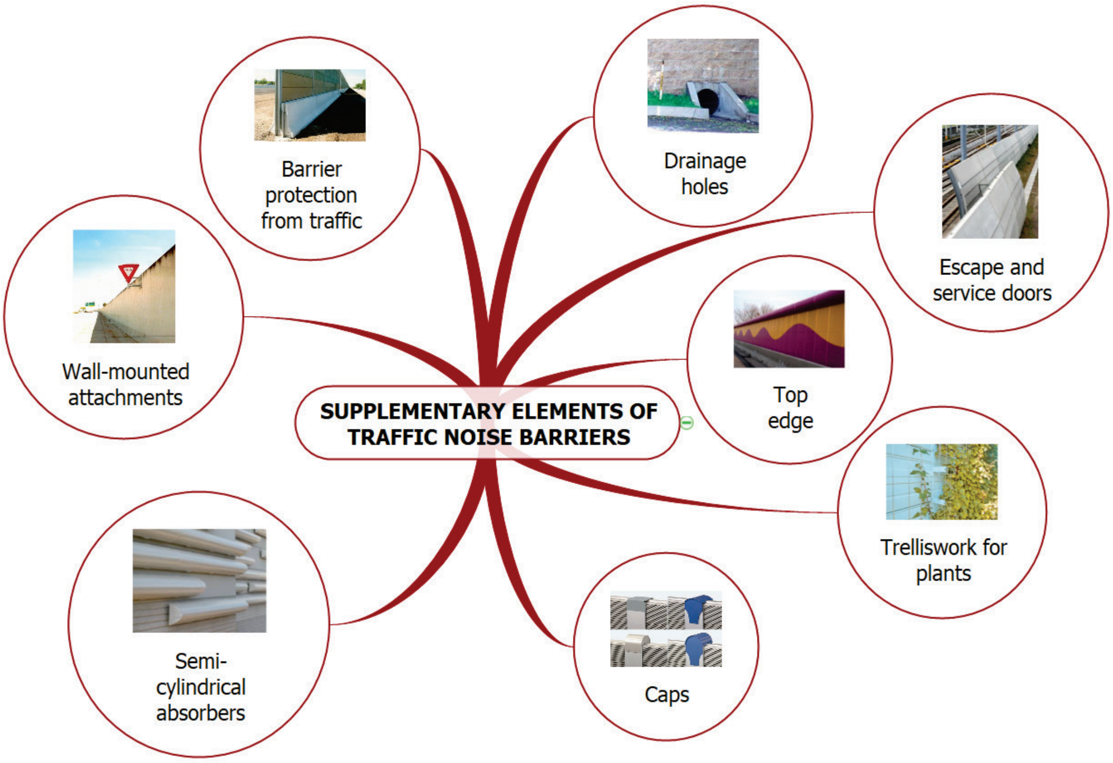

Figure 1. Types of supplementary elements that are embedded in noise barriers.

Figure 2. Decorative caps on the noise barrier [2]

In areas with high humidity, caps with ventilation openings are installed to prevent moisture condensation inside the barrier.

The caps that are installed for acoustic reasons to improve the performance of the barrier can be [1][2][3][4]:

- noise resonators
- tubular absorbers,
- diffraction caps,
- passive phase interference devices,
- active noise control devices, etc.

2.1.1. Noise resonators

Resonators for noise reduction are rarely installed inside barrier walls but are typically implemented as acoustically efficient caps that are mounted on top of the barrier (Figure 3). They are mounted on top of the barrier to improve its acoustic properties. They are often used on noise barriers installed around factories or other industrial barriers that create a lot of noise [5].

Figure 3. An example of an acoustic resonator installed on top of a barrier [5]

2.1.2. Tubular absorbers

Tubular absorbers, in a technical sense, improve the performance of the noise barrier and are usually made from the same materials as the absorbing panels they are attached to [1]. During the 1990s in Japan, a cylindrical type of cap was made, which was later modified into a mushroom type. An experimental version of the mushroom type cap was made with plants inside, like a planter or a flowerpot [6]. However, studies have shown that mushroom-type caps with plants have the same ability to reduce noise as those without plants [7].

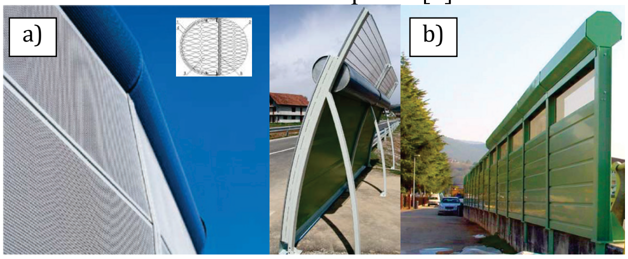

Figure 4. Noise absorbers: a) cylindrical [8] b) polygonal [9]

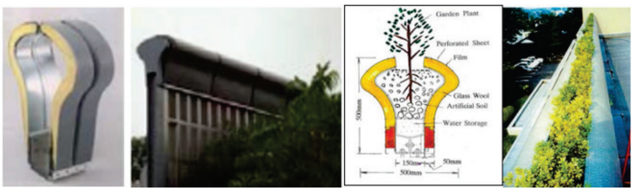

Figure 5. Mushroom-shaped caps, with and without plants. [6]

2.1.3. Diffraction caps

Diffraction caps are designed to redirect sound waves that bend and break around the barrier, reducing their ability to transmit over the barrier and thus contributing to reducing the noise level behind the barrier. The first experiments were conducted with diffraction caps in the shape of the letter T (Figure 6). Although effects similar to those of console barriers were expected, it turned out that the results were significantly greater, with a noise reduction of 1 to 3dB [1].

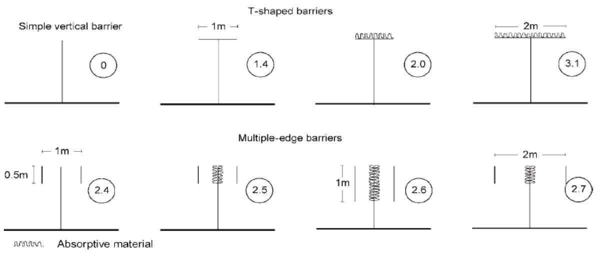

Figure 6 T-shaped diffraction caps [1]

Research continued with different shapes (rectangular, Y-shaped, arrow-shaped, etc.) as well as with diffraction shapes with multiple edges such as: modified cylinder, modified T-shape, and modified Y-shape [10][11][12][13][14][15] (Figure 7). Results from testing the models showed effects ranging around 2.5-3 dB [6].

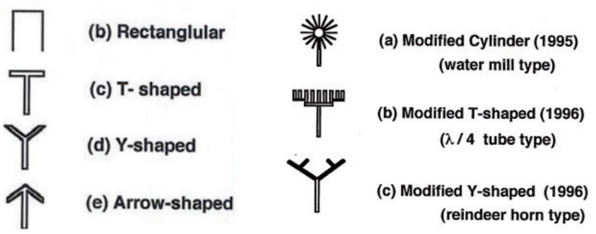

Figure 7. Different shapes of diffraction caps [6]

2.1.4. Commercial forms on the market

Commercial products that appeared after the 2000s in Japan resulted in new models of absorbers, multiple-edge diffractors, asymmetric diffraction caps, resonator types, etc. (Figure 8).

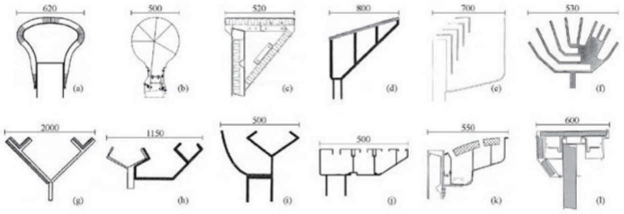

Figure 8. Commercial forms of caps that appeared on the market after 2000 [6]

2.1.5. Devices for passive phase interference

Devices for passive phase interference are used to reduce noise transmitted from one environment to another. They usually consist of plates of certain dimensions and shapes that are placed at a certain distance from the noise source. The plates are designed to redirect sound waves and create interference that reduces the overall noise in the target area [1][16].

2.1.6. Devices for active noise control

Devices for active noise control are electronic systems used to reduce or eliminate noise in a certain space. They are used in situations where other methods, such as noise barriers, are not effective enough. These devices work by detecting sound and then using an inverted signal (phase-shifted) to neutralize the original sound [1][16].

2.2. Emergency openings

When it comes to various emergency situations such as accidents, fires, floods, and the like, access is required to mitigate the consequences [1][2][17]. Therefore, it is necessary to provide emergency openings and mark them on both sides of the barrier. The markings can be placed on the barrier itself or along the path where the noise barrier is located.

Emergency openings can be created in two ways:

- by overlapping barriers, or
- by providing access doors.

When emergency openings are created by overlapping barriers (figure 9), the distance between walls depends on the equipment that needs to pass through the opening when emergency intervention is required. The length of the overlapping walls depends on acoustics and must be sufficient to minimize noise leakage. Overlapping parts of the barrier require proper design and additional safety measures such as additional lighting or modified design of the overlap for better visibility.

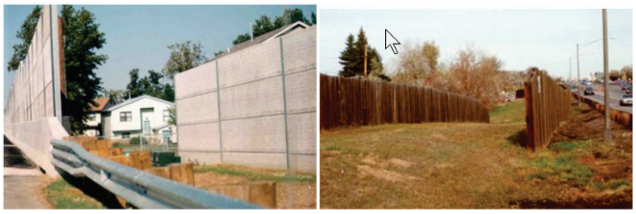

Figure 9. Emergency access openings: barrier overlap [2]

The second way to provide access for emergency cases is through access doors, which are installed at specific distances within the barrier. When not in use, these doors are locked to prevent unauthorized access. Additionally, when closed, there is no sound leakage through the barrier. These doors are usually made of metal or wood, and the material used is typically the same as the material used to construct the noise barrier.

Figure 10. Emergency access openings: access doors [18]

Sometimes it is necessary to design parts of the noise barrier wall so that they can be temporarily removed. This allows access and necessary passage for all required equipment.

2.3. Drainage openings

Noise barriers often interfere with normal water drainage from roads. This is particularly important in areas with high humidity or heavy precipitation to prevent water accumulation and damage to the barrier itself. This problem is solved by designing drainage openings [1][2][3]. Drainage openings are openings in barriers that can be of different sizes and shapes and serve to allow water to flow through the barrier instead of being retained on one side of the barrier. It is only necessary to ensure that the size and position of the drainage openings do not negatively affect the acoustic performance of the noise barrier. Also, grilles should be placed in these openings to prevent the entry of small animals. The effect of a continuous gap of drainage openings at a distance of up to 20 cm at the bottom of the noise barrier is usually within 1 dB(A) [19].

Figure 11. Drainage openings in the barrier [2]

The second method is to drain water beside or below the barrier. In these cases, drainage canal systems that run parallel to the barrier (Figure 12) or water drainage systems through pipes that pass beneath the barrier (Figure 13) are most commonly used.

Figure 12. Water Drainage System Next to the Barrier [2]

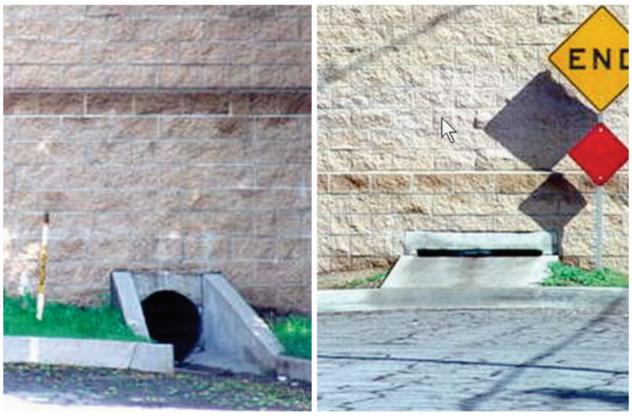

Figure 13. Drainage Openings for Water Drainage Below the Barrier [2]

When water is drained underneath a barrier, a porous stone channel is provided beneath the foundation of the barrier through which water can flow. In this case, a porous stone is placed on both sides of the barrier to close the gap while allowing water to pass through. These porous stone systems require maintenance to prevent clogging over time.

In flood-prone areas where water would actually flow over the highway and the noise barrier would restrict the flow of water and worsen flooding, barriers are constructed in a special way. The bottom plates of the concrete panels are made in such a way that floodwater can move them outward and allow the floodwaters to drain. When the water recedes, the panels return to a vertical position.

Figure 14. Movable segments of the water drainage barrier [2]

2.4. Additional elements attached to noise barriers

In some situations, a noise barrier is the only possible place for installing certain elements related to traffic, such as sign holders, lighting, poles, telephone boxes, and others. These elements are installed integrally with the noise barrier, rather than as additional elements.

Figure 15. Lighting built into the barrier [2]

In some cases, the walls can be moved or inserts can be made to install communal elements such as transformers and poles. Sign holders, telephone boxes, and similar elements are mounted directly onto the walls of the noise barrier (Figure 16). When installing these elements, attention should be paid to providing appropriate distances, both horizontally and vertically.

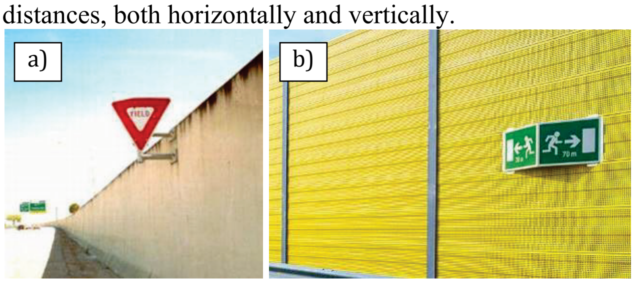

Figure 16. Elements attached to the barrier: a) [2], b) [18]

2.5. Barrier protection from traffic

Noise barriers should be protected from damage due to traffic (vehicle impacts, etc.) when they are built in a clean zone otherwise intended for vehicles. Such protection includes metal or wooden protective rails (fences) or protective barriers made of concrete. Metal and wooden protective fences are placed in front of the noise barrier at a distance that must be equal to or greater than the maximum deflection of the protective fence (Figure 17).

Figure 17. Protective fence against traffic [2]

Concrete barriers can be placed immediately in front of the noise barrier or at a certain distance, and the area between the barrier and the noise barrier is sometimes filled with stones or soil. This provides better protection against traffic. There is also the possibility of planting vegetation in that area. Concrete barriers can be made in the lower part of the noise barrier and as an integral part of the barrier. If there is a possibility of vehicle impact on both sides of the noise barrier, the barrier needs to be protected on both sides and appropriate barriers should be installed.

Figure 18. Concrete barriers for protecting the barrier from traffic [2]

2.6. Vertical supports (trelliswork) for climbing plants

Vertical mesh supports can be installed on a barrier wall to allow plants to grow along them. This helps to mask the barrier and brings nature to the walls, i.e. integrates them into the natural environment. This is particularly important in parts of the city where private surfaces need protection or existing greenery needs to be preserved. In addition, plants can help absorb pollution from the air by improving air quality near the road.

Figure19. Vertical supports for climbing plants [18]

2.7. Acoustic sound absorbers

Acoustic sound absorbers are usually installed on the inside of the reflective barrier wall to reduce the impact of sound reflection on the traffic side of the road. The density of installation depends on the need for noise reduction. Like noise absorbers in the form of caps, the outer shell of these absorbers is made of perforated metal and the interior is filled with absorption material.

2.8. Protective caps for columns

In order to protect against weathering and corrosion, steel support columns are usually covered with a cap. The various shapes and colors of these caps also serve as decorative elements for the barrier.

Figure 20. Semi-cylindrical acoustic absorbers with metal perforated cladding [20]

Figure 21. Protective caps for steel columns [18]

3. CONCLUSION

Traffic noise barriers are vital for reducing the noise from traffic and its impact on the environment. By installing additional objects in the noise barriers, such as caps to increase acoustic performance, emergency openings, drainage openings, protective straps, and others, significant improvements can be achieved in their functionality and aesthetic appearance. In this study, we focused on different types of caps used in traffic noise barriers, such as noise resonators, sound absorbers, diffraction caps, devices for passive phase disturbance, devices for active noise control, etc. Understanding and applying these additional objects can contribute to more efficient noise control and the creation of a more pleasant living environment for the community. Further research and development in this area could provide even more advanced solutions for noise reduction.

ACKNOWLEDGEMENTS

This work is co-financed by the Ministry of Education, Science and Technological Development of the Republic of Serbia on the base of the contract whose record number is 451-03-47/2023-01/200108. The authors thank the Ministry of Education, Science and Technological Development of the Republic of Serbia for supporting this research.

REFERENCES

[1] B. Kotzen, ”Environmental Noise Barriers, A guide to their acoustic and visual design”, Second edition, Taylor & Francis e-Library, London (England), (2009)

[2] G.G. Fleming, H.S. Knauer, C.S.Y. Lee and S. Pedersen, “FHWA Highway Noise Barrier Design Handbook”, NZ Transport Agency, (2004)

[3] NZ Transport Agency, “NZTA State Highway Noise Barrier Design Guide”, version 1.0, (2010) ISBN 978-0-478-36479-8 (Online)

[4] Environmental Protection Department, “Guidelines on Design of Noise Barriers”, Second Issue, Government of the Hong Kong SAR, (2003)

[5] https://forster.at/en/noise-control/rail/sound-resonator

[6] K. Yamamoto, “Japanese experience to reduce road traffic noise by barriers with noise reducing devices”, Proceedings of 10th European Congress and Exposition on Noise Control Engineering – EuroNoise 2015, Maastricht (Netherlands), 31 May-3 June 2015, pp. 33-38, (2015)

[7] Y. Shono, Y. Yoshida and K. Yamamoto, “Development of noise abatement devices applied at the top of highway noise barriers”, Journal of JSCE, No. 504/VI-25, pp. 81-89, (1994)

[8] www.trimo.si

[9] https://www.cir-ambiente.it/

[10] I. Ekici and H. Bougdah, “A Review of Research on Environmental Noise Barriers”, Building Acoustics, Vol. 10(4), pp. 289-323, (2003)

[11] G.R. Watts and P.A. Morgan, “Evaluating the Effectiveness of Novel Noise Barrier Designs”, Euronoise 2003, Naples, pp.1-6, (2003)

[12] J.J. Aznarez, D. Greiner, O. Maeso and G.A. Winter, “A Methodology for Optimum Design Of Y-Shape Noise Barriers”, Proceedings of 19th International Congress on Acoustics, Madrid (Spain), 2-7 September 2007, pp.554-559, (2007)

[13] M. Buret, K.M. Li, K.K. Lu and M. Law, “Screening by edge-modified barriers of road traffic noise in high-rise buildings”, 38th International Congress and Exposition on Noise Control Engineering “Inter-noise 2009”, Ottawa (Canada), 23-26 August 2009, pp. 2594-2600, (2009)

[14] F. Asdrubali, “Experimental evaluation of the diffracting performances of multipurpose noise barrier profiles”, Proceedings of International Conference Forum Acusticum, Budapest (Hungary), 29 August – 2 September 2005, pp. 1255-1260, (2005)

[15] R. Toledo, J.J. Aznarez, O. Maeso, D.A Greiner, “Procedure for the Top Geometry Optimization of Thin Acoustic Barriers”, 11th World Congress on Computational Mechanics (WCCM XI) - 5th European Conference on Computational Mechanics (ECCM V) - 6th European Conference on Computational Fluid Dynamics (ECFD VI), Barcelona (Spain), July 2014, pp. 1-11, (2014)

Identification of noise source based on sound intensity in vertical CNC milling machine

Tanja Miodragović[1*], Branko Radičević[1], Stefan Pajović[1], Nenad Kolarević[2], Vladan Grković[1]
[1]Faculty of Mechanical and Civil Engineering in Kraljevo, University of Kragujevac, Kraljevo (Serbia)
[2]Faculty of Mechanical Engineering, University of Belgrade, Belgrade (Serbia)

The paper presents a procedure for identifying the sound sources of a vertical CNC milling machine based on sound intensity measurements using the "two-microphone" method. Dominant noise sources for different operating modes in the machining process are determined based on contour maps of sound intensity levels measured on five sides of an imaginary parallelepiped that encompasses the machine. The research results can be used for designing noise protection systems for the dominant sound sources of the machine. The obtained results provide valuable guidance for designing machines that generate lower noise levels, which is crucial in machine certification processes.

Keywords: Identification of noise sources, sound intensity, CNC milling machine

1. INTRODUCTION

During the cutting process, the tool comes into contact with the material, resulting in the removal of a certain amount of material which leads to the occurrence of vibrations. Monitoring changes in sound intensity is crucial for determining the optimal parameters of the cutting process and achieving maximum productivity, as it enables us to predict potential machine component failures and identify errors in the production process. Furthermore, monitoring technology contributes to increased safety in manufacturing. Various studies have examined different monitoring techniques for the cutting process, dividing them into direct and indirect approaches [1,2,3].

Direct approach focuses on measuring the actual values of cutting process parameters. Although this method is highly accurate, it often requires interrupting the machining process and has strict environmental requirements. Therefore, it is primarily used in laboratory conditions and is not efficient for detecting real-time phenomena occurring during processing.

Using indirect methods, it is possible to determine cutting process parameters through the use of empirical correlations and analysis of measured signals. Despite having lower precision than the direct approach, it has the advantage of detecting errors early. Consequently, methods such as the analysis of load forces, electrical energy consumption, temperature, vibrations, and noise are frequently employed to predict the parameters associated with cutting processes. [1]

By using this method, it is possible to identify and monitor noise sources during machining, which is of great importance for effective noise management. Identifying noise sources holds significant importance in noise control processes. Currently, there are several methods for testing noise, including measuring sound pressure and sound intensity. Scalar measurements of sound pressure is highly susceptible to environmental factors. Additionally, using these methods it is difficult to determine the exact direction and location of the source of the sound. In order to measure sound pressure and determine sound power, specialized anechoic or reverberation chambers are often required, which can be expensive. [4]

It is possible to overcome these challenges using the method of sound intensity measurement. As sound intensity is measured as a vector, environmental influences are eliminated from measurement results. This method provides information about the level of sound intensity in the direction of sound propagation. Additionally, it allows for precise identification of the main source of noise and visualization of the distribution of sound intensity. Noise source identification is greatly enhanced by the use of sound intensity measurements, and the management of noise is more effective as a result. [5]

Identification of noise sources in the educational machine, the CNC 3-axis vertical milling machine UNI-FRAES3, manufactured by UNIMAT [6], holds significance from multiple aspects. In this study, we explore the process of noise source identification on the machine and emphasize its practical importance. The identification of noise sources accurately enables the proper maintenance of machines, the diagnosis of problems, the improvement of worker safety, and the optimization of designs Furthermore, noise source identification permits us to comply with standards regulating workplace noise. In the experimental part of the research, sound intensity measurements were conducted based on the ISO 9614-1 standard [7] during the milling process. The workpiece material was wood, and the tool used was a end mill with a diameter of d=1.6 mm, while the cutting parameters were a cutting depth of a=1 mm and a milling width of b=2 mm

2. THEORETICAL BACKGROUND

2.1. Sound Intensity

Sound intensity refers to the measurement of acoustic energy flow per unit area. Sound intensity is a vector quantity and its unit is W/m^2. Sound intensity is often converted to sound intensity level in decibels (dB), by dividing it by the reference intensity 1 pW/m^2 ($1x10^{-12}$). The active part of sound intensity, also known as the real part, represents the propagating component of the sound field. It refers to the actual energy being transmitted through the medium. On the other hand, the reactive part of sound intensity, or the imaginary part, represents the

*Corresponding author: Dositejeva 19, 36000 Kraljevo, miodragovic.t@mfkv.kg.ac.rs

non-propagating component of the sound field. It refers to the energy that is stored or released by the sound field without being transmitted. [8]

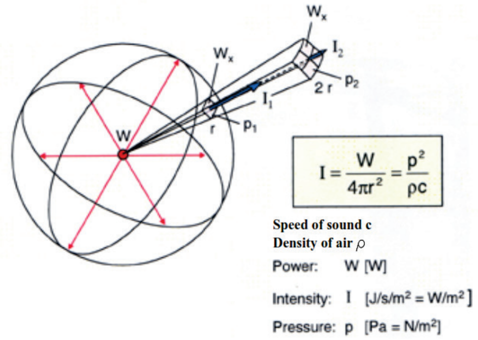

Figure 1: Definition of Sound Intensity [10]

It can be seen in figure 1 that the relationship between the three basic parameters of sound under free field conditions is illustrated by an omnidirectional sound source emitting a certain amount of power W. A surface intensity I on the surface at the distance r is the radiated sound power W divided by the surface area $4\pi r^2$. Alternatively, the intensity I at a distance r is equal to the sound pressure p squared divided by the impedance ρc of the air.

Sound fields are typically described using sound pressure, which is the quantity we perceive as the loudness of sound. However, sound fields are also fields of energy, where kinetic and potential energy are generated, transmitted, and dissipated. Sound intensity is a measure that defines the time-averaged rate of energy flow per unit area. A mathematically precise definition is that the sound intensity vector is equal to the time-averaged product of the instantaneous pressure and the corresponding particle velocity at the same position. [9]

$$\vec{I} = \overline{p(t) \cdot \vec{u}(t)} \tag{1}$$

Where p(t) is the instantaneous pressure, u(t) bis the particle velocity and the timeaveraging is indicated with a bar.

A sound intensity measurement based on Eq.1 is challenging. Currently, there are no appropriate transducers to directly measure particle vibration velocity. Consequently, indirect methods are used. In other words, it is a dual-microphone system, which is referred to as the p-p method.

2.2. "Two Microphones" Method for Noise Source Identification

Sound intensity is most commonly measured using an intensity probe. This method involves placing two microphones close together.

The advantage of using sound intensity measurement over sound pressure measurement to calculate the sound power of a source is that intensity is determined only for the direction formed by the two microphones of the intensity probe. This allows for spatial selection of the sound sources being analyzed and eliminates the influence of other sources that could potentially interfere with the analysis [5]. Measurements can be taken at several points or continuously to form a specific curve in space using the probe [8]. Measurements at discrete points are more commonly used in practice as they allow for a more convenient measurement procedure, with pauses possible between individual points. If measurements are taken at discrete points, a grid of points is formed where measurements are taken, typically a few centimeters away from the sound source.

A sound intensity probe consists of two microphones, and based on the measurements of the sound field at two closely spaced positions in space, the sound intensity can be estimated. Estimating sound intensity essentially involves estimating the phase of the sound field.

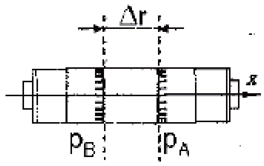

Figure 2: Face to face dual-microphone structure [4]

It's shown in Figure1 that A and B are two microphones, and Δr is the distance between them. here is a sound pressure grade between the dual microphones when the sound wave is transmitted. The particle velocity can be represented by Eq.2

$$u(t) = -\frac{1}{\rho_0}\int \frac{\partial p(t)}{\partial x}\,dt \tag{2}$$

When Δr is far smaller then wavelenght λ, $\frac{\partial p(t)}{\partial x}$ can be rewrite as $\frac{p_A(t) - p_B(t)}{\Delta r}$. The midpiont sound pressure of the dual-microphone can be seen as $p(t) = \frac{p_A(t) + p_B(t)}{2}$.

Accordingly, Eq.3 shows the sound intensity instantaneously in x direction. [4]

$$I(t) = p(t)\cdot u(t) = \frac{1}{2\rho_0 \Delta r}\left[p_A(t) + p_B(t)\right]\int\left[p_A(t) - p_B(t)\right]dt \tag{3}$$

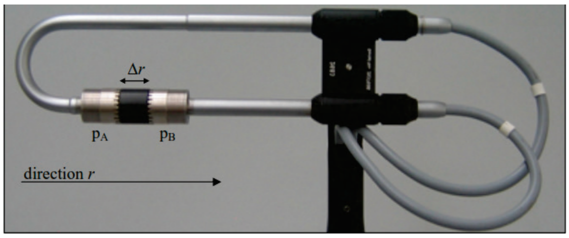

Figure 3: Sound intensity in one direction r is estimated with two closely spaced microphones

Using two microphones to estimate sound intensity has the advantages of being a common transducer in acoustics, being adaptable and being easily calibrated. Furthermore, the particle velocity and the sound pressure are calculated simultaneously at the same location.

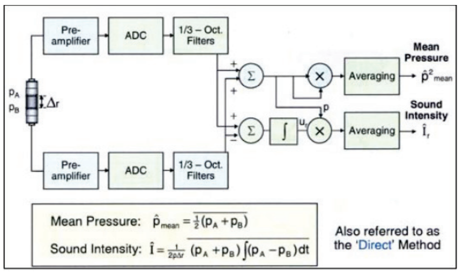

Figure 4: Estimation of Sound Intensity using Constant Percentage Bandwidth [10]

In order to estimate sound intensity, the microphone signals from the preamplifiers are converted from analogue to digital signals using a constant percentage bandwidth analyzer (see figure 4). A mean pressure is obtained by adding the outputs from the third-octave filters, squared, and averaging them.
Taking the sum and difference of the third-octave filters, we can calculate sound intensity. The difference is then integrated over time The difference is a quantity which is proportional to the particle velocity and the sum is a quantity, which is proportional to the pressure midway between the two microphones. Then the difference and the sum are multiplied and averaged.
Finally the scaling factor of $1/(2\rho\Delta r)$ generates the result, where ρ is the density of the air and Δr is the separation between the two microphones. This is called the direct method, because both intensity and mean pressure can be calculated directly according to the formulas. [10]

3. EXPERIMENT OF MILLING MACHINE NOISE SOURCE IDENTIFICATION

3.1. Classification of Milling Machine Noise

Among all the noise sources during the cutting process on vertical CNC milling machine, nearly all electrical and mechanical components of the machine can generate noise (power supply, electric or stepper motors, main and auxiliary motion systems, etc.) even during idle and rest periods. On the other hand, the tool and workpiece can generate noise only when the cutting process is underway. Static components, such as the supporting structure, can also generate noise due to mechanical excitation during the machining process. The main sources of noise on the milling machine are:

1. The drive motor of the milling machine is one of the main sources of noise. The operation of the motor can generate high-frequency sounds that are perceived as noise. The quality and efficiency of the motor can impact the level of noise it produces.

2. During the machining process, the tool (milling cutter) comes into contact with the workpiece material, resulting in vibrations that generate noise. The quality and sharpness of the cutting tool, as well as the type of material being machined, can impact the noise level.

3. The vertical CNC milling machine consists of moving parts such as the worktable, lead screws and roller bearings. These parts can produce noise during their movement, especially if they are improperly lubricated or damaged.

4. Vibrations transmitted through the machine structure can produce structural noise. If the machine is not properly installed and secured, and lacks vibration damping systems, these vibrations can be amplified and result in increased noise due to resonance effects.

3.2. Test Model Description

The size of the milling machine, as shown in the figure 5, is L×W×H (355mm × 330mm × 390mm). During the experiment, the spindle speed was kept constant at 4000 rpm.

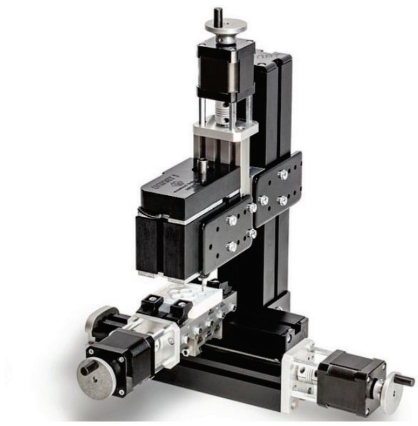

Figure 5: CNC 3-axis vertical milling machine UNI-FRAES3 [6]

3.3. Experiment Facility

The sound intensity testing system mainly consists of hardware and software components. The hardware system includes the B&K Type 2270, a two-channel sound level meter and analyzer, and components for the dual-microphone probe B&K 3654. The components for the dual-microphone probe consist of two B&K 4197 microphones with a diameter of 1/2 inch, a face-to-face probe configuration, and a spacing of 12 mm between the centers. The measurement signals are collected and processed using the B&K Type 2270 measurement analyzer. Post-processing of the measurement results can be done on a PC using the BK Connect measurement platform and Pulse Labshop software. This allows the creation of a contour plot of sound intensity level of the sound source. The main components of the measurement chain and equipment used in the experiment are shown in Figure 6 and Figure 7.

Figure 6 shows the B&K dual-microphone probe system. Figure 7 shows the B&K Type 2270 analysis system.

Figure 6. B&K dual-microphone probe system

Figure 7. B&K Type 2270 analysis system

3.4. Test Environment

Due to the limitations of the experimental conditions, the testing was conducted in a quiet and spacious room with all windows and doors open to reduce sound reflection and background noise. The temperature in the room was 20 degrees Celsius.

3.5. Measurement Points Disposition and Experiment Process

According to sound intensity measurement standards, the measurement surfaces should surround the machine tool as much as possible. [7] Figure 8 illustrates the orientation and data acquisition sequence of the measurement points. There are a total of 4x5 test fields on the front and back sides, 4x3 on the left and right sides, and 3x5 on the top side, resulting in a total of 79 experimental points covering all surfaces. Figure 7 shows the complete measurement grid of the machine and the arrangement of the grid on each measured surface. We use A-weighting during measurements as it best reflects the frequency response of the ear to sound intensity. During the experiment, the sound intensity measurement probe should be positioned perpendicular to the grid on the surface and be located at a distance of 0.5 meters from the emitting surface [7]. The sound intensity measurement probe is sequentially placed in a rectangular space to capture the central signal.

4. ANALYSIS OF EXPERIMENT RESULT

Figure 9 and Figure 10 show the measurement results of the sound intensity of a vertical three-axis CNC milling machine used for educational purposes. The presented results are obtained for a frequency range of 3 octaves. The frequency range consists of octaves: 1000 Hz, 2000 Hz, and 4000 Hz. This frequency range is chosen because it falls within the range of the intensity probe with the selected spacer and because it is the operational frequency range of the machine.

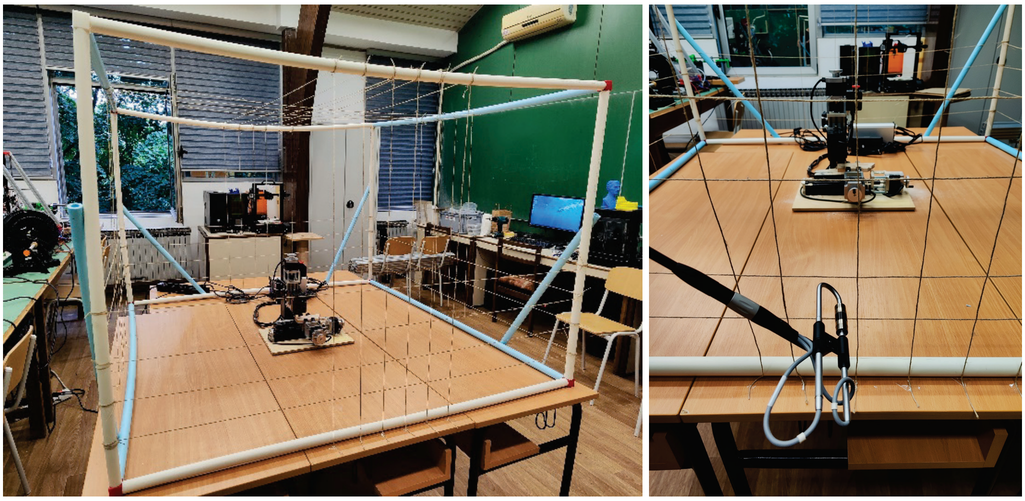

Figure 8: The measurement grid

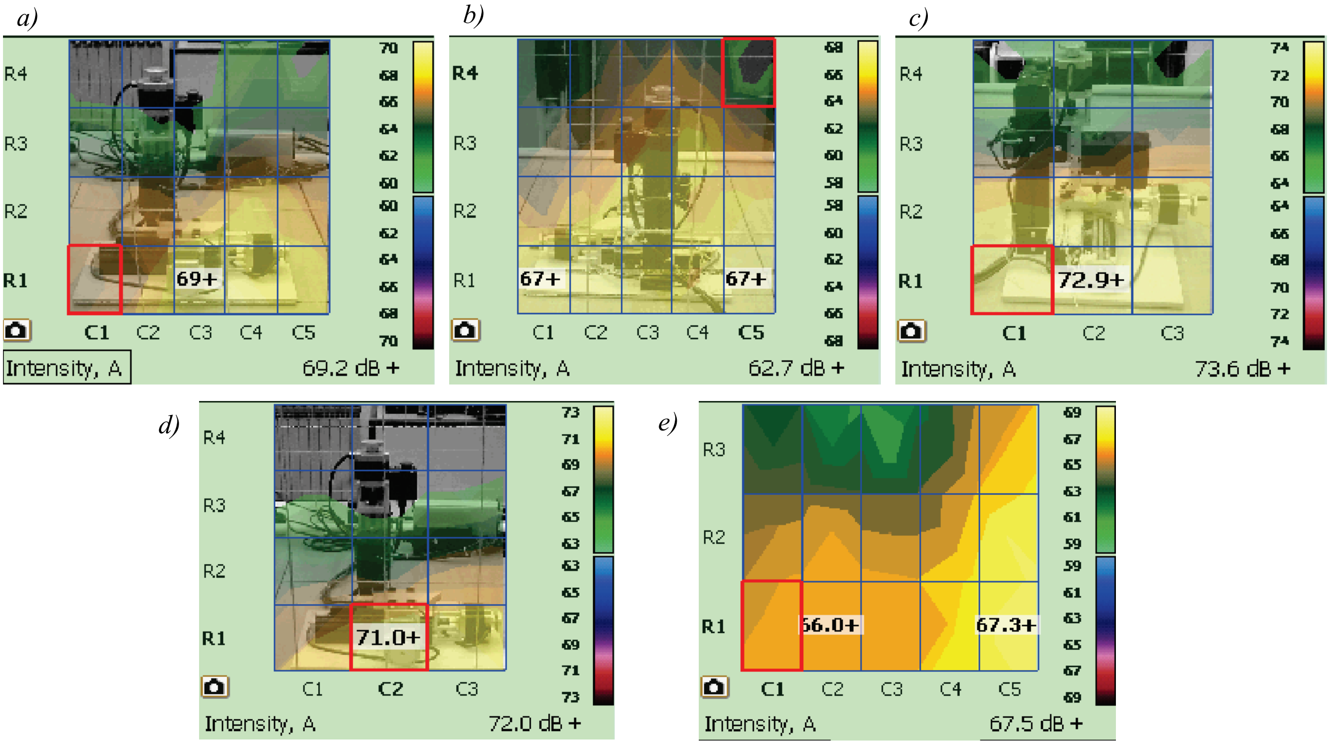

Figure 9: Sound intensity contour map on the: a) front, b) back, c) left, d) right and e) top surface

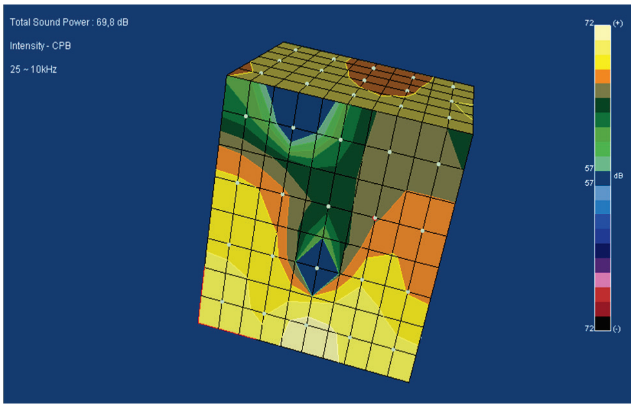

Figure 10: Equivalent sound intensity map

As can be seen from Figures 9 and 10 it seems that the milling machine's left and right sides have the highest sound intensity levels. It has been estimated that the maximum sound intensity on the right side is 71 dB(A) and on the left side it is 72.9 dB(A).

From the analysis of the entire equivalent sound intensity map, we can determine that the main noise source is the machine motor. Figure 12 shows that the sound intensity is highest on the left and right sides of the machine, with slightly higher values on the left side due to the motor bracket on the right side, which covers the entire surface of the motor.

Figure 11: The sound intensity value of every point on the a) front, b) back, c) left, d) right, and e) top surface

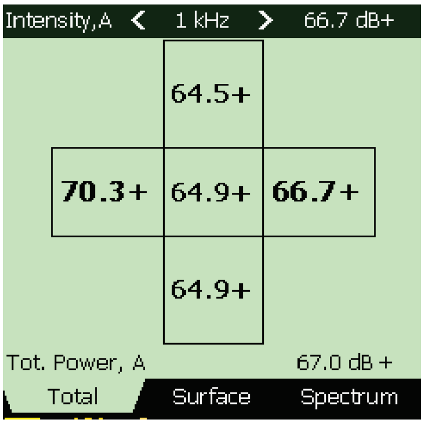

Figure 12: Total sound intensity on the measuring surfaces

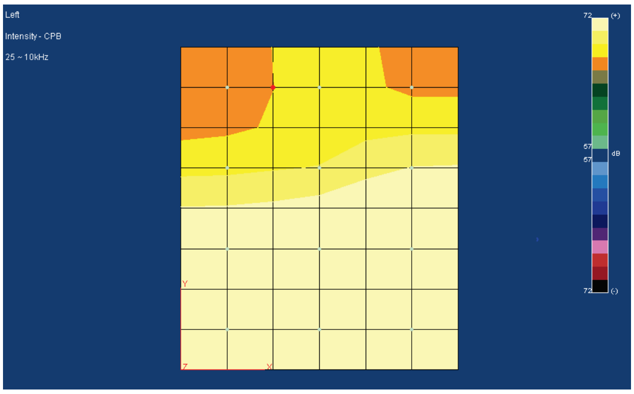

Figure 13: Sound intensity contour map on the left surface

5. CONCLUSION

In this study, the classification of noise from the CNC 3-axis vertical milling machine UNI-FRAES3 was performed, followed by the identification of noise sources on the machine surface based on sound intensity measurement method. Based on the noise map, it can be concluded that the main source of noise is the machine motor, particularly on the left surface.

The sound intensity method has a good ability to resist background noise. It has low requirements for test conditions and can be conveniently applied for noise testing and analysis of equipment. This enables us to effectively reduce the noise of experimental equipment by implementing appropriate measures. Additionally, sound intensity analysis technology can also be used to determine the sound power of sources. Sound power is more accurately determined through sound intensity rather than sound pressure, as it allows for a more precise calculation of the scalar product of the sound intensity vector and the corresponding vector of the elemental surface, with less demanding equipment and fewer restrictions in test conditions

ACKNOWLEDGEMENTS

This work is co-financed by the Ministry of Education, Science and Technological Development of the Republic of Serbia on the base of the contract whose record number is 451-03-47/2023-01/200108. The authors thank the Ministry of Education, Science and Technological Development of the Republic of Serbia for supporting this research.

REFERENCES

[1] W. Wei, Y. Shang, Y. Peng and R. Cong, “Research Progress of Noise in High-Speed Cutting Machining” Sensors, Vol. 22(10), p. 3851, (2022)

[2] C.H. Lauro, L.C. Brandao, D. Baldo, R.A. Reis and J.P. Davim, “Monitoring and Processing Signal Applied in Machining Processes—A Review,” Measurement, Vol. 58, pp. 73–86, (2014)

[3] R. Teti, K. Jemielniak, G. O’Donnell and D. Dornfeld, “Advanced Monitoring of Machining Operations,” CIRP Ann.-Manuf. Technol., Vol. 59, pp. 717–739, (2010)

[4] H. Li, Y. Li, Z. Geng and L. Wang, “Identification of Rotor System Noise Source Based on Sound Intensity Measurement”, Advanced Materials Research, Vols. 479-481, pp. 1169-1173, (2012)

[5] M. Bjelić, N. Knežević and K. Jovanović, “Automatizovano merenje intenziteta zvuka pomoću robota i intenzitetske sonde”, Proceedings of 17th International Symposium INFOTEH, Jahorina, 21-23 March 2018, pp. 17-22, (2018)

[6] https://thecooltool.com/produkte/unimat-cnc

[7] ISO 9614-1:1993(en) Acoustics — Determination of sound power levels of noise sources using sound intensity — Part 1: Measurement at discrete points

[8] S. Gade, "Sound Intensity (Part 2 Instrumentation and Applications)." Brüel & Kjær Technical Review 4, pp. 3-32 (1982)

[9] M.J. Crocker and J.P. Arenas, “Fundamentals of the Direct Measurement of Sound Intensity and Practical Applications”, Acoust. Phys., Vol. 49, pp. 163–175, (2003)

[10] Brüel & Kjær. Lecture notes. Retrieved from the course material presented by Svend Gade at the training course in Advanced Acoustics. Brüel & Kjær University, Nærum Denmark. 17-18 November 2008, (2008)

Surface treatments for traffic noise barriers

Violeta Đorđević [1], Jovana Perić [2*], Tanja Miodragović[2], Stefan Pajović[2], Mladen Rasinac[2]
[1]Academy of Applied Study Šumadija, Department Trstenik, Trstenik (Serbia)
[2]The Faculty of Mechanical and Civil Engineering in Kraljevo, University in Kragujevac, Kraljevo (Serbia)

A large number of various materials are used to make traffic noise barriers. The choice of a particular texture for the surface treatment of the barrier depends on many factors, such as the aesthetic appearance of both sides of the barrier, structural characteristics, maintenance requirements, type of material used to construct the barrier, etc. Therefore, surface treatments for barriers must also be considered. Surface treatments include textures, colors, graffiti, and coatings. The paper provides a classification of surface treatments for traffic noise barriers and guidelines for their use.

Keywords: Traffic sound barriers, Texture, Colours, Coatings, Graffiti

1. INTRODUCTION

Traffic noise barriers are an effective solution for reducing noise pollution caused by high traffic areas. These barriers are constructed using a wide range of materials, each with different textures and finishes. The choice of surface treatment for a sound barrier depends on several factors, such as aesthetic appearance, construction characteristics, maintenance requirements, and the type of material used.

In addition to selecting the appropriate material for noise barriers, it is equally important to consider surface treatments. Surface treatments include textures, colors, coatings, and graffiti, which can enhance the effectiveness of a noise barrier and improve its overall appearance. Proper surface treatments can help to minimize sound reflection and absorption, reduce corrosion and damage, and improve the visibility of barriers for motorists and pedestrians. [1]

This paper provides a classification of surface treatments for traffic noise barriers, along with guidelines for their use. The classification is based on the different types of surface treatments that are available, including the benefits and drawbacks of each type.

Overall, this paper aims to provide a comprehensive overview of surface treatments for traffic noise barriers, with the goal of helping designers and engineers to select the most appropriate surface treatments to improve the effectiveness and appearance of sound barriers in different environments.

2. SURFACE TREATMENTS

The choice of a specific texture of the surface treatment depends on many factors, such as the aesthetic appearance of both sides of the barrier, construction characteristics, maintenance requirements, type of material used to construct the barrier, and more. Therefore, surface treatments of the barrier must also be considered. Surface treatments include textures, colors, graphics, and coatings [2]. The classification of surface treatments for sound barriers is shown in Figure 1.

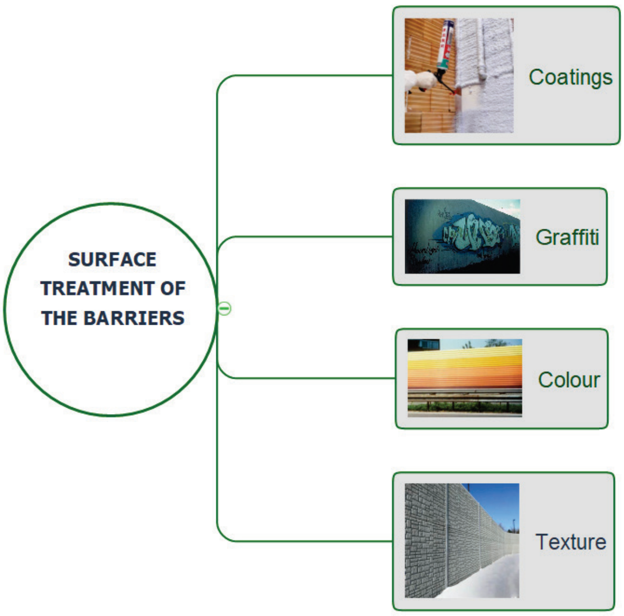

Figure 1. Classification of surface treatments for sound barriers

2.1. Texture

There are a large number of surface textures available for use in the construction of sound barriers (Figure 2). These various textures can be applied to panels as well as poles, caps, etc. Different surface textures are obtained by using different combinations of surface treatments. Depending on the type of material used to construct sound barriers, different textures can be obtained.

When the material for constructing a sound barrier is concrete, textures of smooth surface and surface of stone aggregate can be obtained, as well as textures obtained by drawing lines, manually applied techniques using rakes and brooms, pressing, application of inserts, veneer, and Stucco finishing layer.

*Corresponding author: Dositejeva 19, 36000 Kraljevo, peric.j@mfkv.kg.sc.rs

Figure 2. Surface treatment textures of barriers [1]

A smooth surface is obtained by using classical concrete finishing techniques. In the case of vertically formed panels on one or both sides, after the concrete has hardened, a finishing treatment is necessary, which includes filling voids and "grinding" the concrete with a thin cement mixture (Figure 3).

Figure 3. Concrete barrier with a smooth surface [1]

The texture in the form of the surface of a stone aggregate is achieved by using a selected type, color, and gradation of the aggregate in the concrete mix of the barrier (Figure 4). The aggregate is chosen based on its aesthetic appearance, but it must also meet all the requirements regarding strength, size, shape, etc. This exposed surface of the aggregate is easiest to achieve at the bottom, i.e., on the lower side of the prefabricated panel. On the upper side of the panel, it is harder to achieve this process, and worker experience and quality control monitoring are necessary.

To achieve different looks of relief surface texture, different types of molds are used. Molds are made of thin materials that can be made of rubber, wood, metal, or other materials and have one flat side, while the other side has a "mold" with the desired surface appearance. These molds can be used multiple times and are most often applied to the lower side of the panels of cast prefabricated materials. Newer methods enable finishing texture processing on both sides of the panel.

Figure 4. Concrete barrier with a surface in the form of a stone aggregate [1]

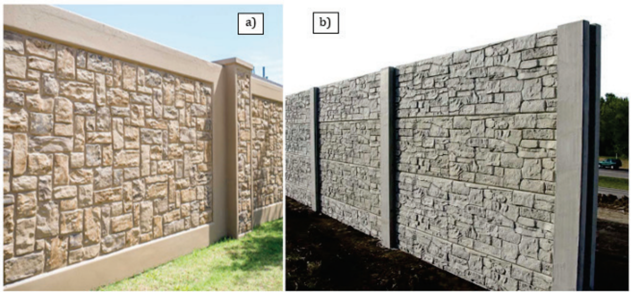

Figure 5. Texture of a concrete barrier obtained in a mold: a) [3] (b) [4]

Hand-applied finishing techniques using rakes and brooms (raking, sweeping) are applied to the upper side of prefabricated panels (Figure 6), and they can produce different manually created patterns.

Figure 6. Final processing of the concrete barrier by raking [1]

Finishing by imprinting represents the imprinting of a pattern onto the upper surface of a horizontally poured panel, using specialized techniques. The appearance of a brick-like surface texture can also be achieved (Figure 7). Such treatment is somewhat more difficult to perform than other treatments. During the stamping process, the aggregate in the panel must have sufficient thickness to allow for stamping.

Figure 7. Texture in the form of a brick obtained by embossing [1]

The use of panel inserts can provide a unique aesthetic appearance of surface texture (Figure 8). These inserts are produced separately and then placed in a recess of equal size and shape inside the prefabricated panel or embedded in the panel during the pouring process. Adequate attachment between the insert and panel must be ensured to protect against noise. Mechanical fastening or chemical bonding techniques are most commonly used.

Figure 8. Panel inserts attached to a concrete barrier [1]

Veneers are a specially produced material that is applied to the surface of the concrete barrier. Some veneers may contribute to sound absorption, but their use is mostly for aesthetic reasons. Examples of veneers include thin brick, ceramic tiles, and porous composite materials. As in the previous case, adequate attachment must be provided.

Stucco, a final layer of cement material, is directly bonded to the concrete barrier without any additives and can provide different types of texture to the concrete surface. However, the appropriate cleanliness and roughness of the surface of the concrete barrier must be achieved to ensure an adequate surface for sticking this final layer.

When the material used for making a sound barrier is built from blocks, the texture of the surface can resemble that of a stone aggregate, which is achieved through line extraction, veneer, broken edges, and Stucco methods. In terms of texture for stone blocks used in building, there are considerably fewer textures that can be obtained compared to the various textures of stone aggregates that can be obtained in a concrete panel, as there is a smaller range of aggregates used in the production of concrete blocks.

Figure 9. Sound barrier made of masonry blocks with broken stone edges [5]

Line extraction molds can also be applied to concrete blocks, but to a significantly lesser extent than in concrete. Veneers can be applied to concrete blocks in a similar way as to concrete panels. Broken stone edges are often used to achieve a rough textured surface in concrete blocks (Figure 9).

Stucco texture can be applied to masonry blocks in a similar manner as with concrete panels (Figure 10).

Figure 10. Sound barrier made of masonry blocks with Stucco texture [1]

When using bricks as a material for constructing a sound barrier, the type of brick, mortar, and bond pattern must be considered. The type of brick includes all classic types of standard brick, of which there are hundreds of varieties that can be used in the construction of sound barriers (Figure 11). Bricks can be stacked in multiple layers with mortar or in combination with walls made of concrete or concrete blocks. When it comes to the type of mortar, there are many different colors and types available for gluing bricks together. Various bond patterns are used in the construction of brick barriers. The variety of brick dimensions, colors, styles, mortar, and bond patterns provides the opportunity to create unique and interesting patterns.

Figure 11. Surface texture - brick barriers [1]

When the material for making a sound barrier is metal, surface texture can be obtained with mechanically shaped forms and embossed surfaces. Surface treatments are generally similar on both sides of the panel, but there is a possibility to achieve different shapes on each side of the barrier. Embossed surfaces imply less relief prints on metal panels.

When the material for making a sound barrier is wood, surface texture is provided by: orientation of boards, slats, grain, lamination, and type and orientation of posts. Different visual appearances can be obtained with different orientation of wooden boards used in the construction of sound barriers. There is a possibility of using a horizontal, vertical, diagonal, and combined configuration. Also, boards of different dimensions can create an interesting appearance.

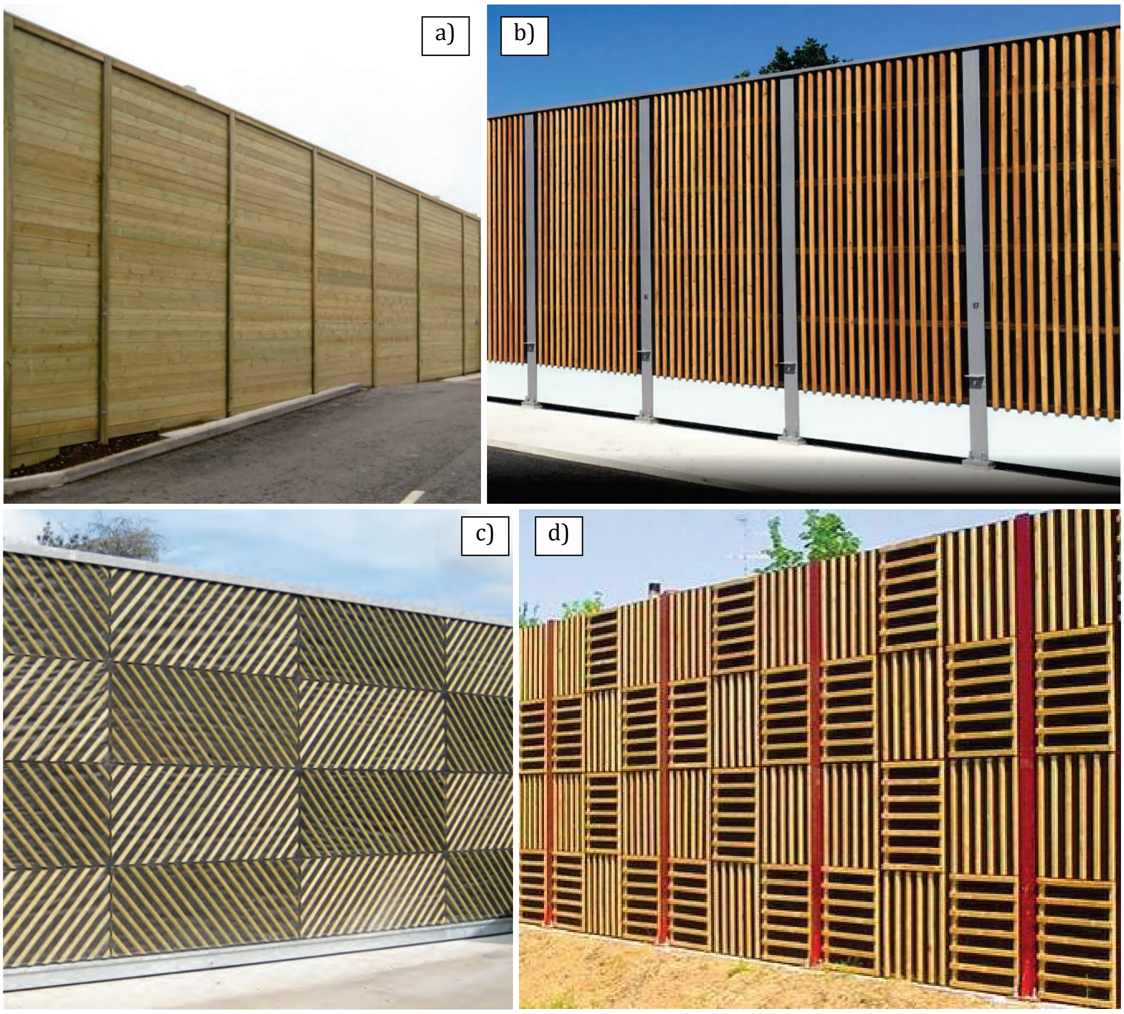

Figure 12. Texture of wooden barriers obtained by different orientation of board placement: a) horizontal [6], b) vertical [7] c) diagonal [6] d) combined [8]

Graininess involves selecting the grain and roughness of the wood, which can create an appropriate surface texture. Lamination refers to different design codes of laminated panels by ensuring the appropriate orientation of the laminated component elements (Figure 13). This creates a similar surface on both sides of the barrier.

Figure 13. Lamination - wooden barrier [1]

When the material for making a sound barrier is a transparent panel, the surface texture is limited to aesthetic design types (patterns, designs) that can be applied to such barriers [9].

Figure 14. Surface texture - transparent barriers [9]

Surface textures of plastic panels are limited to shapes and textures that can be achieved through the shaping process of panel components, and in composite materials, surface textures depend on the availability and limitations of certain components used to form the exterior surface of the barrier.

Figure 15. Surface texture – composite material barriers [1]

2.2. Color

Many barrier systems comprise acoustic panels which can be produced in a range of colours. It is of general consensus that the appearance of a barrier can be toned down to help it merge with its surroundings, or made to stand out as a striking and highly visible addition to the environment by the use of colour [10].

The color of sound barriers is included in surface treatment techniques. The desired color of the barrier can be achieved using two general techniques or their combination:

- natural color of the material used for building the sound barrier (with the possibility of adding a transparent coating) and
- applying paint, stain, pigment coating, or integral pigment that is added to the material used for building the barrier

For concrete and masonry blocks, there are various options for coloring. The color of natural concrete ingredients can be changed by adding pigments. Additionally, surface-applied stains affect the color. Pigmented panels with a surface color of the appropriate shade can also be used. When it comes to bricks, the color is limited to the color of the material used for building the barrier.

Metal barriers are generally protected with corrosion-resistant coatings and then painted. With aluminum and stainless steel, there is a possibility of retaining the natural color of the metal. Steel barrier elements can also retain a galvanized finish as a color. When wood is used as a material for building the sound barrier, there is a great choice of natural colors. Each type of wood has a certain color, and most woods can also be painted to achieve the desired color [10][11].

The color of plastic barriers is usually obtained by pigmentation of the emulsifiers used in the shaping process of barrier elements. A scratch-resistant coating can also be added for protective purposes. The desired color of a sound barrier made of recycled rubber is typically achieved by using polyurethane coatings because recycled rubber material cannot be pigmented. With composite materials, colors depend on the possibilities of the components used to form the outer surface of the barrier.

An interesting and challenging problem with colour in temperate zones is the changes of season. This is particularly an issue in rural locations where a colour chosen to blend into its surroundings in summer may be overly conspicuous during the winter months. Colour, like any other design criterion, should be chosen for a particular reason and not be chosen arbitrarily, or simply because it is available [9].

2.3. Graffiti

Sound barriers in the environment often provide an irresistibly empty canvas for graffiti. The only effective way to deter graffiti is to use plantings. Where it is not possible or appropriate to plant vegetation along barriers, alternative solutions must be found. Various methods have been developed to reduce damage to barriers and facilitate cleaning. The two basic types, which relate to the type of surface they protect, are [8]:

- anti-graffiti coatings and
- anti-graffiti film

Anti-graffiti coatings can be applied to most surfaces in the form of a sprayed or painted layer, making it easier to remove the color, typically by spraying with hot water under high pressure. Anti-graffiti films are applied to glass and acrylic transparent barriers. The film is transparent, protects the surface from scratches and paint, and is easily removed and replaced with a new one.

One possible way to deter graffiti is with an anti-graffiti design on the barriers (Figure 16). There is also a problem with the integration of anti-graffiti into the local environment. There is also the possibility of advertisements on barriers, which could lead to the potential use of barriers for advertising.

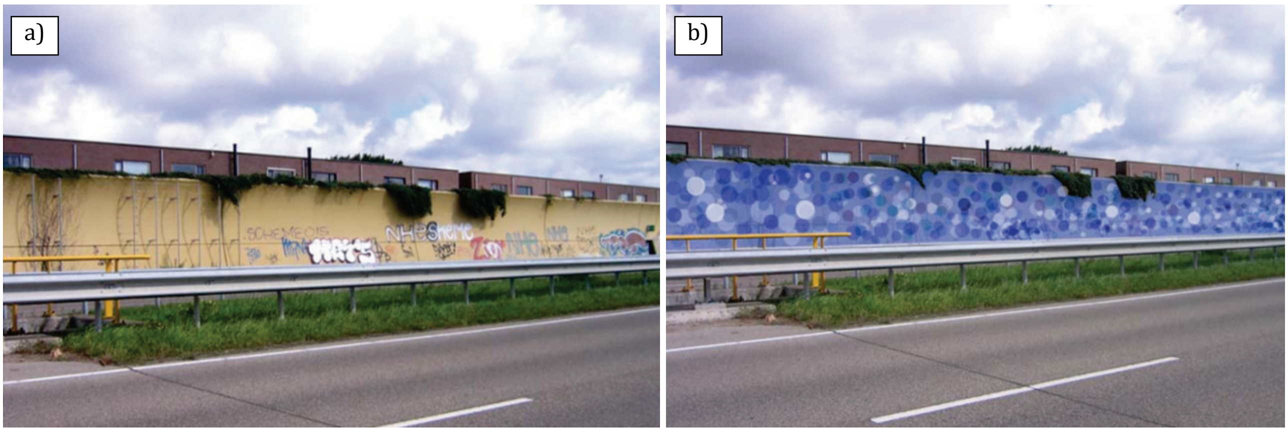

Figure 16. Examples of graffiti and anti-graffiti on sound barriers [9]

Another way to deter graffiti is through special barrier constructions, such as those that have an internal core containing panels, and rows of steel profiled mesh that protect the core and prevent graffiti, or their visibility.

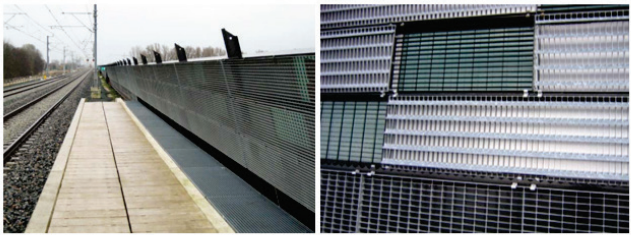

Figure 17. Examples of anti-graffiti barriers [9]

2.4. Protective Coatings

Coatings are primarily applied to concrete barriers or barriers made of masonry blocks for protective and/or aesthetic reasons. Protective reasons are the most common reasons for applying such coatings. They provide protection against wind, rain, ultraviolet light, and potential vandalism, various damages, and graffiti drawings. When it comes to aesthetic reasons, they relate to improving the appearance of the barrier. In some cases, adding a transparent protective coating can enhance the color and give shine to the surface [9].

These coatings can be transparent or pigmented. Transparent coatings are usually applied to surfaces where the color of the barrier is made of natural material, such as stone aggregate or brick. Pigmented coatings are usually applied to natural concrete surfaces. The application of coatings is mainly done by spraying, although roller or brush application can also be used.

Anti-graffiti coatings can be permanent, allowing multiple removals of graffiti by high-pressure water without replacing the coating. The other type of coating is partially or completely removed together with the graffiti and must be reapplied.

Coatings in the form of paint, in addition to providing the desired color of the barrier, can also provide a certain degree of protection. They can be water or oil-based. They can be applied in the factory of prefabricated materials before their installation or on-site during the installation of panels.

3. CONCLUSION

Noise barriers represent an effective solution for reducing traffic noise levels. A wide range of materials are used to construct noise barriers, each with its own characteristics and advantages. However, in addition to selecting materials, it is equally important to consider surface treatments for noise barriers. Surface treatments can take the form of textures, colors, coatings, and grafitti, each of which can improve the effectiveness and appearance of the barriers. Proper surface treatments can help minimize sound reflection and absorption, reduce corrosion and damage, and improve the visibility of barriers for motorists and pedestrians. Moreover, it must be emphasized that to achieve a visual and acoustic effect, combinations of materials, textures, colors and protective coatings are most often used.

ACKNOWLEDGEMENTS

This work is co-financed by the Ministry of Education, Science and Technological Development of the Republic of Serbia on the base of the contract whose record number is 451-03-47/2023-01/200108. The authors thank the Ministry of Education, Science and Technological Development of the Republic of Serbia for supporting this research.

REFERENCES

[1] NZ Transport Agency, "FHWA Highway Noise Barrier Design Handbook", (Online), (2010)

[2] Environmental Protection Department, "Guidelines on Design of Noise Barriers", Second Issue, January 2003., Hong Kong SAR

[3] https://blog.echobarrier.com/blog/sound-barrier-materials-which-are-most-effective

[4] https://wieserconcrete.com/product/noise-abatement-walls-posts-highway/

[5] http://cmd.ncma.org/concrete-masonry-provides-solution-for-sound-wall/

[6] www.jacksons-fencing.co.uk

[7] https://www.kohlhauer.com/en/ligna-2/

[8] https://www.cir-ambiente.it/cir-habitat/pannelli-fonoassorbenti-legno/

[9] B. Kotzen and C. English, "Environmental Noise Barriers, A guide to their acoustic and visual design", Second edition, Taylor & Francis e-Library, London and New York, (2009)

[10] NZ Transport Agency, "NZTA State Highway Noise Barrier Design Guide", Welington (New Zealand), (2010)

[11] G.G. Fleming, H.S. Knauer, C.S.Y. Lee, S. Pedersen, "FHWA Highway Noise Barrier Design Handbook", U.S. Department of Transportation, Cambridge (USA), (2004)

Comparison of mechanical behaviour of TIG and MIG welded joint dissimilar aluminum alloys 2024 T351 and 6082 T6

Dragan Milčić[1*], Miodrag Milčić[1], Tomaž Vuherer[2], Aleksija Đurić[3], Nataša Zdravković[1], Andreja Radovanović[4]
[1]Faculty of Mechanical Engineering, University of Niš, Niš (Serbia)
[2]Faculty of Mechanical Engineering, University of Maribor, Maribor (Slovenia)
[3]Faculty of Mechanical Engineering, University of East Sarajevo, East Sarajevo (Bosnia and Herzegovina)
[4]IMW Institut, Kragujevac (Serbia)

Different aluminum alloys are used for the production of light constructions of transport vehicles (rail vehicles, ships, airplanes) due to the low density of the material, good mechanical properties, good corrosion resistance, etc. The aim of this work is to study the mechanical properties of dissimilar assemblies of 2024 T351 and 6082 T6 aluminum alloy welded by the TIG and MIG process. Aluminum alloy 6082 T6 is well weldable by classical fusion welding processes (MIG and TIG), while aluminum alloy 2024-T351 is almost non-weldable with MIG and TIG process. Optimum technology for MIG and TIG welding process is very important for the mechanical properties of welded joints of dissimilar aluminum alloys 2024 T351 and 6082 T6. For experimental investigations of mechanical properties of welded joints of aluminum alloys 2024 T351 and 6082 T6 were sheets with a thickness of 8 mm. AlSi5 aluminum alloy wire was used as a filler wire in both TIG and MIG welding processes. TIG welding of aluminum alloys 2024 and 6082 was in argon as shielding gas, and the MIG process in a mixture of argon and helium as shielding gas. The assessment of the mechanical properties of the welded joint of dissimilar Al alloys was performed by Vickers hardness testing, tensile and bending tests of the welded samples.

Keywords: AA2024 T351, AA6082 T6, TIG welding, MIG welding, Mechanical properties

1. INTRODUCTION

Aluminum structures are often used in transport technology, in the automotive industry, in the industry of rail vehicles, in shipbuilding, in the aviation industry and even in space technologies, because aluminum alloys have a good mechanical properties and low densities [1].

Welded constructions of cars, trains, ships, airplanes, spacecraft, which are made of different aluminum alloys, are most often joined by classic metal inert gas (MIG) [2,3] and tungsten inert gas (TIG) [4] welding, friction stir (AA5754-AA7075 [5], AA2024-AA7075 [6], AA2219-AA5083 [7] and AA7075-AA6061 [8])., laser and electron beam welding [9].

Fusion welding processes easily join materials that have good weldability. The material is well weldable if it is possible to make a welded joint without defects. The weldability of aluminum alloys is affected by a number of factors such as: oxygen affinity, high thermal expansion and thermal conductivity, high shrinkage during solidification, high solubility of hydrogen in the liquid phase, which decreases drastically during solidification. By welding aluminum alloys, mechanical properties and corrosion resistance in HAZ are reduced, porosity, solidification and liquation cracks appear. Aluminum alloys are welded with additional material with increased content of Si or Mg.

If the technology of the welding procedure is not suitable, defects may appear in the area of the weld metal, which reduces the reliability of the welded structure. Weld defects such as porosity, cracks, lack of penetration or lack of fusion may appear [10].

Age-hardenable 2024 aluminum alloy belongs to the 2XXX alloy series where the main alloying element is copper. The mechanical properties of these alloys reach values similar to those of carbon steels. Such a high strength of the alloys is due to the precipitation of CuAl2 particles during natural or artificial aging. As these alloys do not have good corrosion resistance, they are often coated (plated) with pure aluminum for corrosion protection. They are used for manufacturing parts in the aviation industry due to their high strength, good fatigue properties. With the addition of elements such as Mg and Li, it is possible to reduce the specific density and improve the performance of Al alloys for applications in the manufacture of parts in the aerospace industry [11]. Alloys of the 2XXX series, as a rule, have poor weldability with fusion welding (MIG, TIG), due to high crack sensitivity. Friction stir welding is mainly used for welding these alloys [12, 13].

In this paper a comparison has been proposed on the mechanical and microstructural behaviour of welded dissimilar assemblies of 2024 T351 and 6082 T6 aluminum alloy, by two different welding techniques: MIG and TIG. The results arecompared in terms of microstructural examinations of tensile properties and hardness variations across the weld joint.

2. MATERIALS AND METHODS

In this experiment, a Fronius Transpuls Synergic 4000 direct current electrode positive (DCEP) MIG welding machine and a Fronius Magic Wave 4000 Job G/F direct current electrode negative (DCEN) TIG welding machine were used in producing the welds. Chemical compositions and the mechanical properties of AA2024-T351 and AA6082-T6 are given in Tables 1 and 2. The chemical properties of the filler material used during welding are given in Table 3.

*Corresponding author: Aleksandra Medvedeva 14, 18000 Niš, dragan.milcic@masfak.ni.ac.rs

Table 1: Chemical composition of aluminum alloy 2024 T351 and 6082 T6 [6]

	Mn %	Fe %	Mg %	Si %	Cu %	Zn %	Ti %	Cr %	Al %
6082 T6	0.4-1.0	0- 0.5	0.6-1.2	0.7-1.3	0-0.1	0-0.2	0-0.1	0-0.25	Balance
2024 T351	0.65	0.17	1.56	0.046	4.7	0.11	0.032	-	Balance

Table 2: Mechanical properties of aluminum alloy 2024 T351 and 6082 T6 [6]

	Yield strength min R_{eh} (Mpa)	Ultimate tensile strength min R_m (Mpa)	Elongation at Break min A(%)	Hardness HV
2024 T351	310	425	10	137
6082 T6	260	310	10	95

Table 3: Chemical composition of the filler material of wire EN ISO 18273 S Al 4043A (AlSi5), mas. %

Mn %	Fe	Mg	Si	Cu	Zn	Ti	Be	Al
<0,15	<0,6	<0,2	4,5-5,5	<0,3	<0,1	<0,15	<0,0003	Balance

The TIG arc was shielded with the argon gas (ISO 14175-I1-Ar 5.0), while the MIG arc was shielded with a gas mixture of Argon + He (ISO 14175-I3-ArHe-30).
The dimensions of the plates used for welding were 300 mm long, 125 mm wide and 8 mm thick.

The optimum welding parameters obtained for each welding process after optimization and used in this study are presented in Table 4 and 5.

Table 4: Welding parameters for the MIG butt weld welding process

Pass No.	Welding current I (A)	Welding voltage U (V)	Wire Feed Speed (m/min)	Gas flow rate (L/min)
1	155	21.7	6.3	18
2	180	23.2	7.5	
3	170	22.7	7.3	

Table 5: Welding parameters for the TIG butt weld welding process

Pass No.	Welding current *I* (A)	Welding voltage *U* (V)	Gas flow rate (L/min)
1	225	13.3	12
2	235	13.1	
3	195	13.3	
4	195	13.3	

Figure 1 and 2 shows face side of a MIG and TIG welded joint.

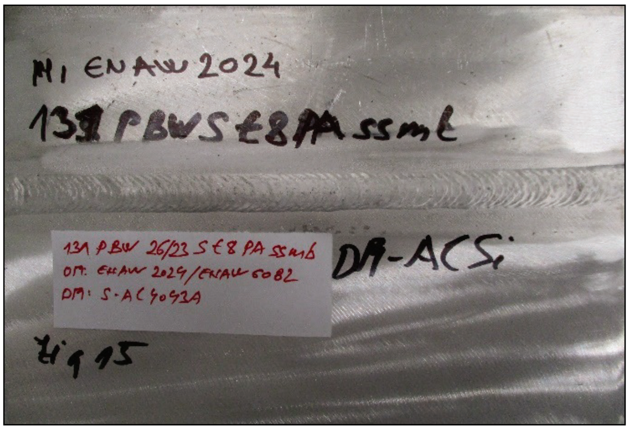

Figure 1: Face side of the MIG welded joint

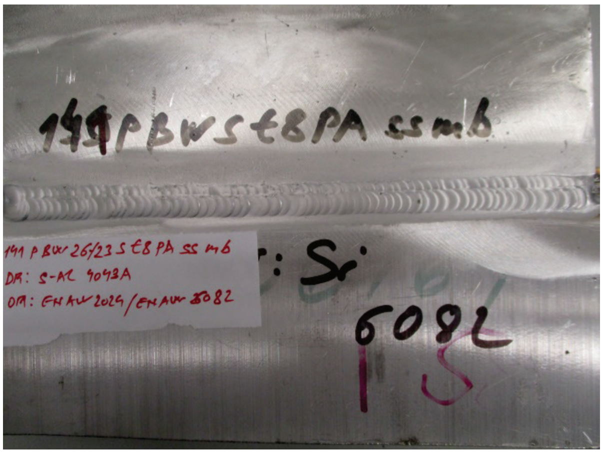

Figure 2: Face side of the TIG welded joint

Test specimens were cut using an abrasive water jet cutting machine. Test specimens were prepared for testing the macro- and microstructure, for testing hardness, for Charpy impact test, for bend and tensile testing of welded joints.

Vickers hardness was measured on a Willson VH1150 hardness tester. Tensile properties were determined at room temperature using a Shimadzu AG-X 300 kN tensile tester. Test specimens defined by the ASTM E8M standard obtained from welded samples perpendicular to the welded joint were used [7].

The bending tests were carried out on four specimens—in two the tensiled side was the face of the weld and in two the tensiled side was the root of the weld. The test was performed at room temperature using the three-point bending method.

A Leica Q500MC optical microscope (LM) was used to analyze the microstructure of the welded joint. The microstructure was examined on the cross-section of the samples after the usual metallographic preparation and etching in Keller's reagent. The tests were also carried out using the scanning electron microscope JOEL JSM-6610LV (SEM).

3. RESULTS

3.1. Static Tensile Test

The tensile properties of the welds produced by the TIG and MIG welding processes were evaluated. Two replicate specimens were tested for each weld type, and the average values were obtained. All the welded joints failed at the parent material region, indicating that the weld joints were stronger than the parent material, which is industrially accepted. Fig. 2 shows the fractured specimens for the three weld types.Figure 3 shows the specimen after breaking.

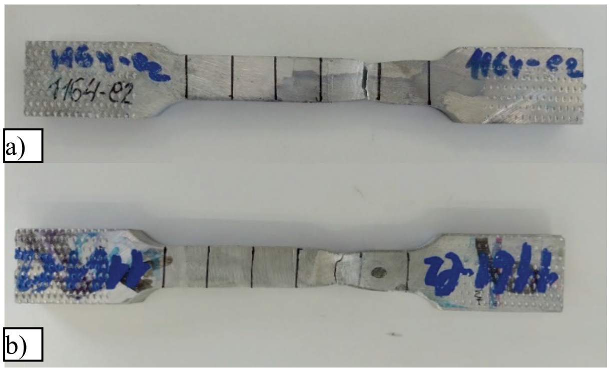

Figure 3: Fractured specimens (a) MIG joint (b) TIG joint

Stress-strain curves is shown in Figure 4, and results are summarized in Table 5. The fracture of specimen was brittle fracture in heat affected zone HAZ2 (WM / BM2-6082).

***Table 5.** Tensile test results of welded joints*

Welding type	Yield strength $R_{p0,2}$ (MPa)	Ultimate tensile strength R_m (MPa)	Elongation at break A (%)	Place of fracture
MIG	113	198	7.3	HAZ2
TIG	86	166	10.7	HAZ2

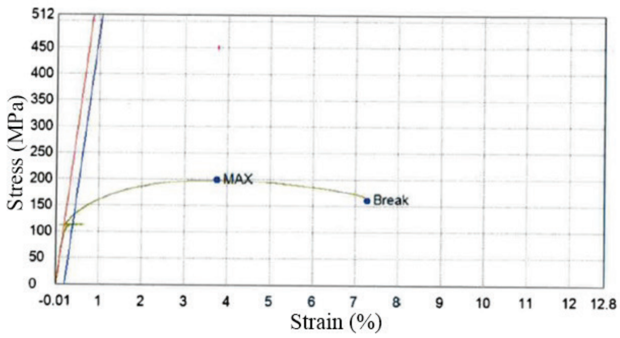

Figure 4: Stress-strain curve for MIG welding process

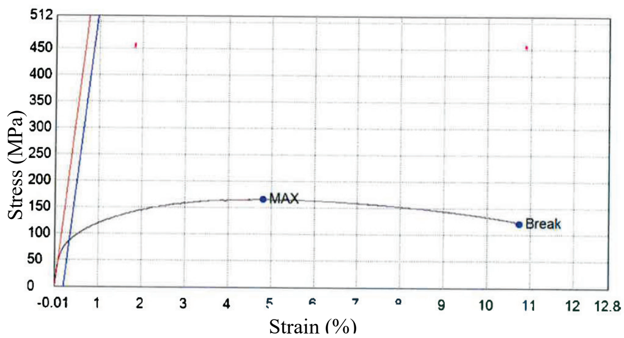

Figure 5: Stress-strain curve for TIG welding process

3.2. Hardness distribution

The hardness measurement was made in two lines, i.e., near the face and the root of the weld, three hardness measurements for each of the test zones (weld metal - WM, HAZ and base materials), figure 6. The results of the hardness measurement of the welded joint are presented in figure 7 and 8.

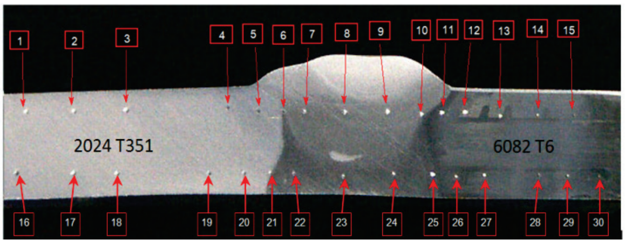

Figure 6: Hardness measure points of the welded joint

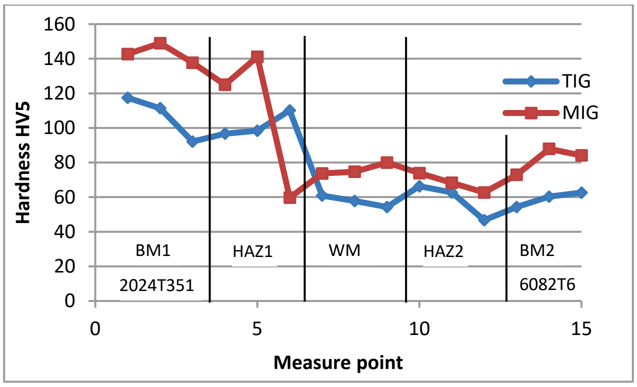

Figure 7. Hardness distribution of the joint near the face of the weld

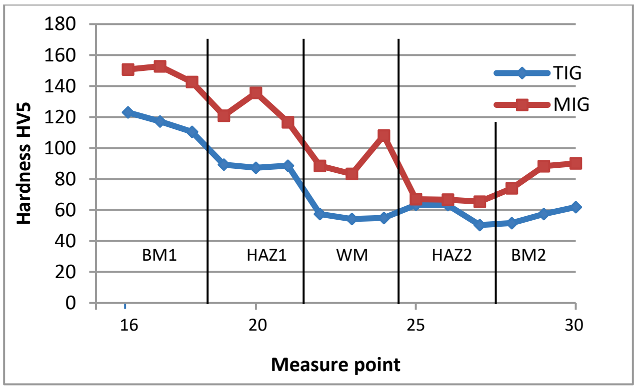

Figure 8: Hardness distribution of the joint near the root of the weld

3.3. Macro- and Microscopic Examinations

Figure 9 and 10 presents the macrostructure of the MIG and TIG welded joint observed on the cross-section of the weld axis. The joint has a regular symmetrical shape without apparent defects such as cracking, undercutting, and porosity.

The microstructure of samples was examined by optical microscopy. Optical microscopy was performed by a Leica Q500MC microscope. Typical metallographic procedure implies using the Keller's and Barker's reagent to expose morphology. Figure 11 and 12 shows the microstructures of the welded joint in heat affected zone HAZ1 (BM1-2024 / WM), in the weld metal and in heat affected zone HAZ2 (WM / BM2-6082) for MIG and TIG welding process, respectively.

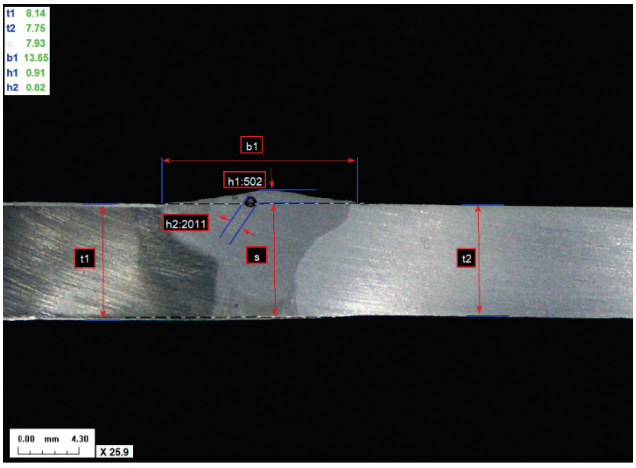

Figure 9: Macrostructure of a MIG welded joint

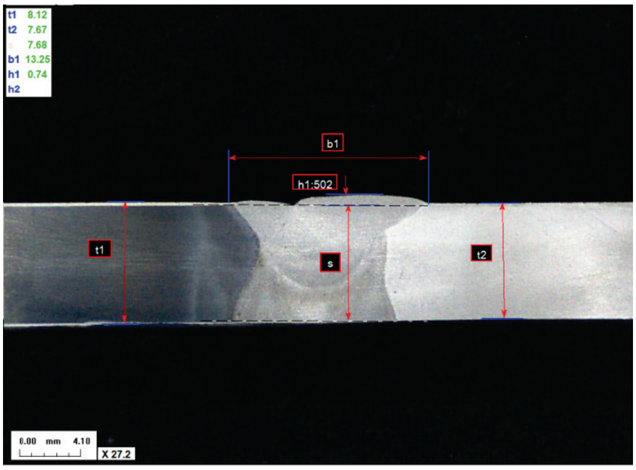

Figure 10: Macrostructure of a TIG welded joint

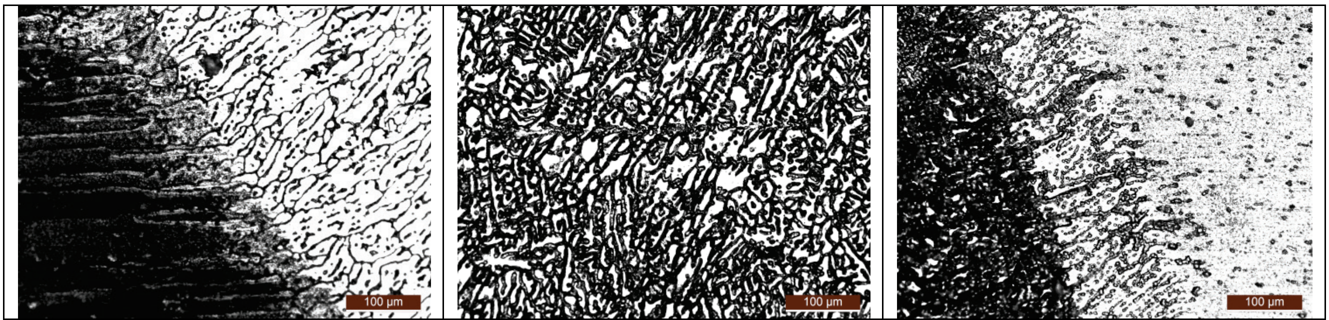

a) 3 – HAZ 1 BM1-2024/WM	b) 4 - WM	c) 5 – HAZ 2 WM/BM2-6082

Figure 11: Microstructures for the MIG welding process

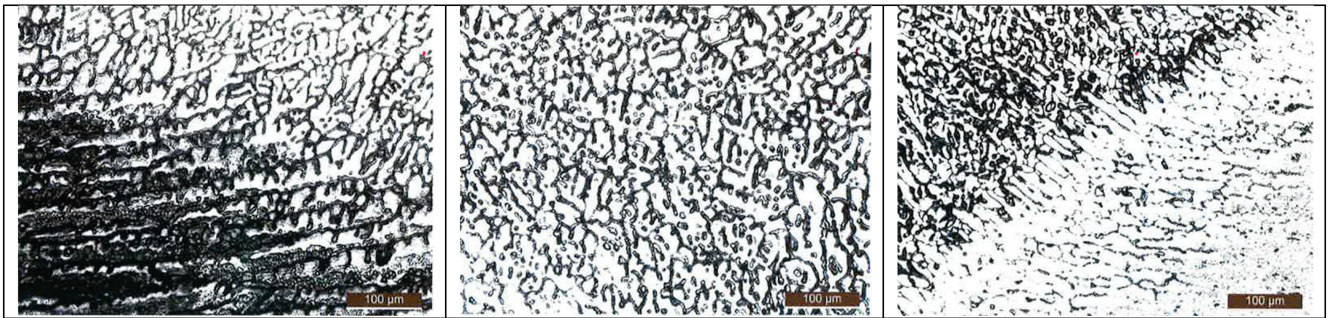

a) HAZ 1 BM1-2024/WM	b) WM	c) HAZ 2 WM/BM2-6082

Figure 12: Microstructures for the TIG welding process

4. DISCUSSION

The microstructure of the weld metal obtained by the MIG and TIG welding process is significantly different from the microstructure of the base metals, and accordingly, the mechanical properties of the welded joint are lower than the mechanical properties of the base metals. A lower ductility was also observed during the tensile test. For welding these two alloys, the technology is prescribed, and the filler material Alumig Si 5 (EN ISO 18273 S Al 4043A) for MIG welding process that is Alutig Si 5 (EN ISO 18273 S Al 4043A) for TIG welding process is chosen. Selected filler material with high silicon concentration (5%) leads to low melting temperature range, hence, giving high resistance to solidification cracking and undercut [14].

Figure 13 and 14 shows the microstructure of base materials: 2024 T351 aluminum alloy and 6082 T6 aluminum alloy. Elongated grains in the rolling direction were observed on the sample of 2024-T351 alloy. SEM/EDS analysis identified coarse intermetallic particles Al-Cu-Fe-Mn-Si (>10 µm), finer Al-Cu-Mg, Al-Cu-Mn, Al-Cu-Mg-Si and Al-Si-Cu-Mg (Figure 15). The fine particles can be precipitates of alloys elements, Al-Cu and Al-Cu-Mg based.

Microstructure of base metal – aluminum alloy 6082-T6, also consists of a wide range of intermetallic phases (IMP) formed during processing. Larger particles in the direction of rolling Al-Fe-Mn-Mg-Si-Cr, Al-Mg-Si-Mn, Al-Mg-Si (Figure 16), and fine precipitate particles Mg-Si, formed during the artificial aging process were observed.

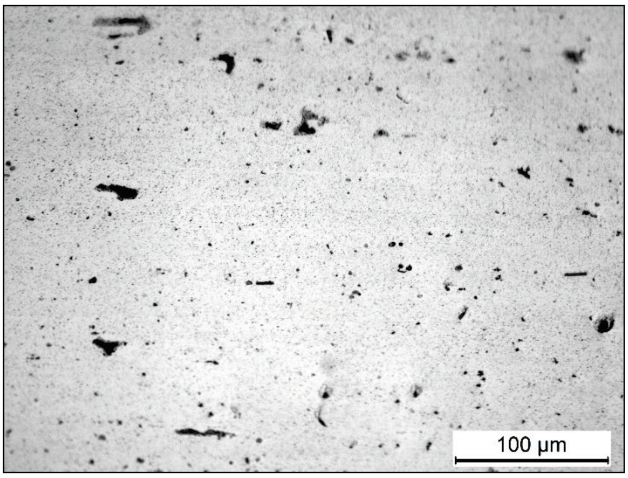

Figure 13: Distribution of second phase particles in 2024 T351 aluminum alloy (LM).

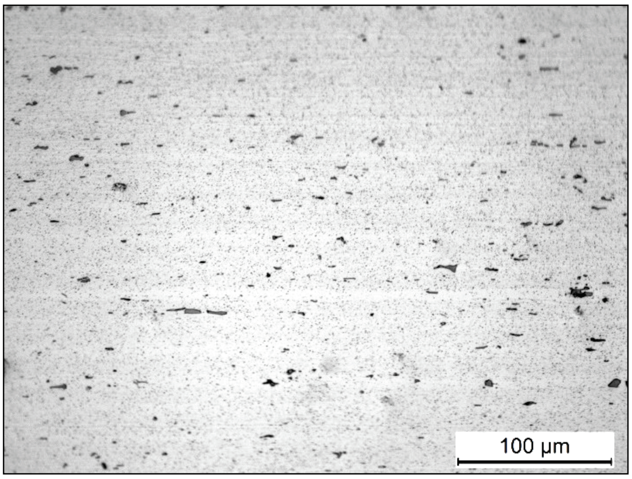

Figure 14: Distribution of second phase particles in 6082 T6 aluminum alloy (LM).

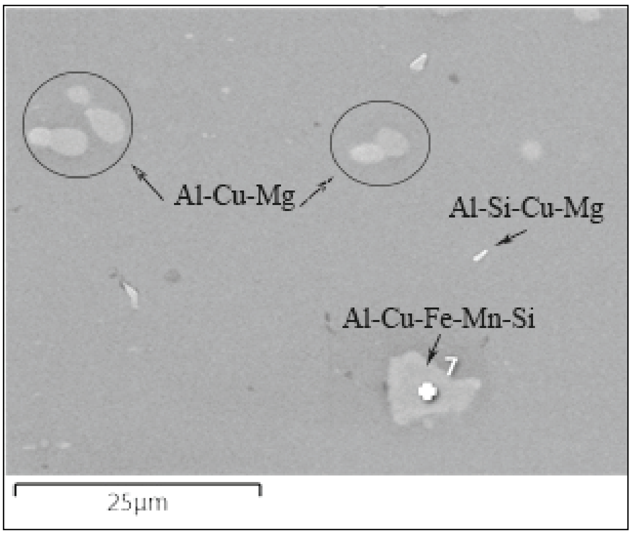

Figure 15: Second phase particles in 2024-T351 alloy (SEM).

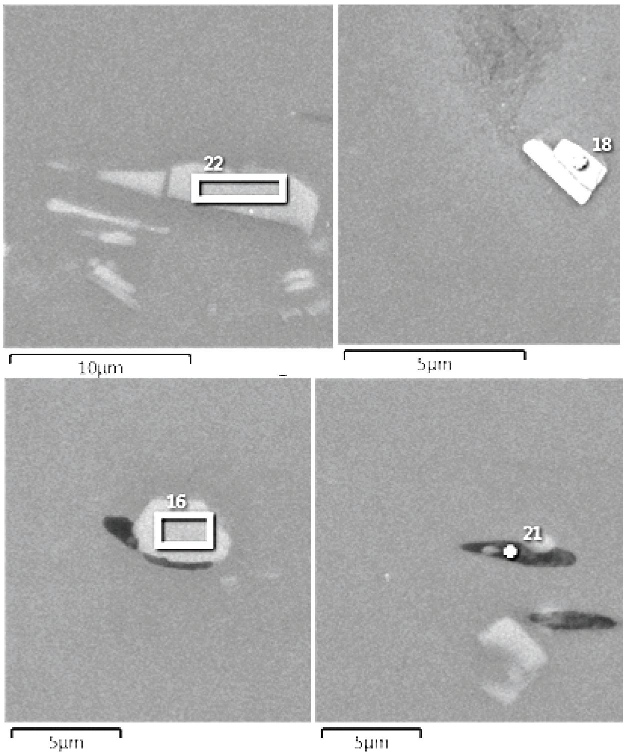

Figure 16: Second phase particles in 6082-T6 alloy. Al-Fe-Mn-Mg-Si-Cr, Al-Si-Mg, Al-Mg-Si-Mn, Al-Mg-Si (SEM).

Figure 12b shows the microstructure of weld metal (WM) in TIG weld joints for dissimilar aluminum alloys (2024-T351 and 6082-T6). In WM are observed IMP precipitated on grain boundary and inside the grain. Depending of the place in WM coarse and fine grains can be found with dendritic orientation. Beside HAZ columnar orientation of the grain can be found.

Figure 12a shows the microstructure of the HAZ 1 between the weld metal (WM) and the base metal BM 1 - 2024 T351. In WM beside HAZ 2 are observed IMP precipitated on grain boundary with columnar orientation. In HAZ, are IMP precipitated on grain boundary and inside the grain. Grain orientation is in direction of rolling.

Figure 12c shows the microstructure of the HAZ 2 between the weld metal (WM) and the base metal BM2 - 6082 T6. In HAZ 2 are observed IMP precipitated on grain boundary with orientation in direction of rilling.

In case of MIG the microstructure (figure 11) is very fine and equiaxed, having uniformly distributed grains with strengthening precipitates as compared to TIG welding processes in which dendritic grain structures is found. Because of fine grain structure the MIG joint possesses good tensile and mechanical properties than that of the TIG welding processes. The fracture location of specimen for tensile testing is in HAZ 2 (WM/BM2-6082).

It is found that hardness in weld metal region is less than that of the BM. The maximum hardness is foundin MIG and the minimum hardness is found in TIG welded joint [15].

5. CONCLUSION

The use of multi-materials structures is nowadays one of the most sought solutions to decrease weight and reduce both emission of greenhouse gases and fuel consumption in the automotive industry. In this paper, a study of comparison of mechanical behaviour of TIG and MIG welded joint dissimilar aluminum alloys 2024 T351 and 6082 T6 is given.

Aluminum alloy 6082 T6 is well weldable by classic fusion welding processes, such as MIG and TIG processes. Unlike this aluminum alloy, alloy 2024 T351, which belongs to the group of aviation alloys, is considered almost non-weldable by classical welding procedures.

The hardness and MIG and TIG welded joints is lower in the molten zone (WM) because the hardening precipitates are dissolved during melting and no structural hardening reaction takes place at this temperature.

In the tensile test we have observed the fracture surface section of the tensile specimen is in the HAZ zone on the BM side - 6082-T6. The hardness of HAZ and WM at bottom surface of weldment of butt weld is higher than the upper surface.

The maximum tensile strength of the MIG welded joint is 20% higher (198 MPa) to compared TIG welded joint (166 MPa).

ACKNOWLEDGEMENTS

This research was financially supported by the Ministry of Science, Technological Development and Innovation of the Republic of Serbia (Contract No. 451-03-47/2023-01/ 200109).

REFERENCES

[1] P.K. Mallick, "Materials, Design and Manufacturing for Lightweight Vehicles", Woodhead Publishing, Boca Raton, Fla. (USA), (2010).

[2] P.P. Lean, L.Gil and A. Ureña, "Dissimilar welds between unreinforced AA6082 and AA6092/SiC/25p composite by pulsed-MIG arc welding using unreinforced filler alloys (Al–5Mg and Al–5Si)", Journal of Materials Processing Technology, Vol. 143–144, pp. 846-850, (2003)

[3] J.N. Nawres, "Mechanical Properties of MIG Joints for Dissimilar Aluminum Alloys (2024-T351 and 6061-T651)", Al-Khwarizmi Engineering Journal, Vol. 12(3), pp. 121- 128, (2016)

[4] K. Liamine, E.D. Mohammed, O. Seddik and K. Sami, "Dissimilar welding of aluminum alloys 2024 T3 and 7075 T6 by TIG process with double tungsten electrodes", The International Journal of Advanced Manufacturing Technology, Vol. 118, pp. 937–948, (2022)

[5] Ş. Kasman and Z. Yenier, "Analyzing dissimilar friction stir welding of AA5754/AA7075", The International Journal of Advanced Manufacturing Technology, Vol. 70(1-4), pp. 145-156, (2014)

[6] S. Youbao, Y. Xinqi, C. Lei, H. Xiaopeng, Z. Shen and Y. Xu, "Defect features and mechanical properties of friction stir lap welded dissimilar AA2024–AA7075 aluminum alloy sheets", Materials & Design, Vol. 55, pp. 9-18, (2014)

[7] P. Mastanaiah, A. Sharma and G. M. Reddy, "Dissimilar friction stir welds in AA2219-AA5083 aluminium alloys: effect of process parameters on material inter-mixing, defect formation, and mechanical properties", Transactions of the Indian Institute of Metals, Vol. 69(7), pp. 1397-1415, (2016)

[8] M. M. Hasan, M. Ishak and M.R.M. Rejab, "Influence of machine variables and tool profile on the tensile strength of dissimilar AA7075-AA6061 friction stir welds", The International Journal of Advanced Manufacturing Technology, Vol. 90(9-12), pp. 2605-2615, (2017)

[9] L. Himanshu and M. Paranjayee, "Cold forming of Al-5251 and Al-6082 tailored welded blanks manufactured by laser and electron beam welding", Journal of Manufacturing Processes, Vol. 68(Part A), pp. 1615-1636, (2021)

[10] P.A. Molian and T.S. Srivatsan, "Weldability of aluminium-lithium alloy 2090 using laser welding", Journal of Materials Science, Vol. 25, pp. 3347–3358, (1990)

[11] A. Heinz, A. Haszler, C. Keidel, S. Moldenhauer, R. Benedictus and W. Miller, "Recent development in aluminium alloys for aerospace applications", Materials Science and Engineering A, Vol. 280(1), pp.102–107, (2000)

[12] M. Milčić, D. Milčić, T. Vuherer, Lj. Radović, I. Radisavljević and A. Đurić, "Influence of Welding Speed on Fracture Toughness of Friction Stir Welded AA2024-T351 Joints", Materials, Vol. 14(6), p. 1561, (2021)

[13] M. Milčić, T. Vuherer, I. Radisavljević, D. Milčić and J. Kramberger, "The influence of process parameters on the mechanical properties of friction stir welded joints of 2024 T351 aluminum alloys", Materials and technology, Vol. 53(6), pp. 771–776, (2019)

[14] AMS 4190K Alloy 4043, https://weldingwarehouseinc.com

[15] Y. Gupta, Dr. A. Tanwar and R. Gupta, "Investigation of Microstructure and Mechanical Properties ofTIG and MIG Welding Using Aluminium Alloy", OSR Journal of Mechanical and Civil Engineering (IOSR-JMCE), Vol. 13(5), pp. 121-126, (2016).

Taguchi-based determination of double-ellipsoidal heat source parameters for numerical simulations of GMAW process

Mišo Bjelić[1*], Mladen Rasinac[1], Aleksandra Petrović[1], Marina Ivanović[1], Jovana Perić[1]
[1]Faculty of Mechanical and Civil Engineering in Kraljevo, University of Kragujevac, Kraljevo (Serbia)

The results of the application of welding simulation models are highly dependent on the input parameters, particularly on the parameters of the heat source model. In this study, a method for determining the heat source parameters for a three-dimensional quasi-stationary heat transfer model for gas metal arc welding is presented. The commonly used double-ellipsoidal heat source has five input parameters, the values of which are mainly chosen based on the researcher's experience. This approach is a common source of error; to estimate these values, we applied a calibration procedure using the Taguchi method with combined objective function based on weld geometry. The simulation results show that the Taguchi method can be successfully used to determine the heat source parameters.

Keywords: Numerical simulation, Taguchi method, Heat source model, GMAW

1. INTRODUCTION

Welding thermal cycle caused by localized heat source has dominant influence on mechanical properties, deformations and residual stresses of weld and nearby metal. Modeling of heat transfer during welding is of great importance in order to understand these influences. Today's models describe not only conduction but also convection, fluid flow, free surface deformation and arc physics. Key to successful simulation of heat transfer during welding is an adequate heat source model. There is a whole variety of heat source models used today, from simple ones, such as Rosenthal's and Rykalin's [1,2]to the complex models that describe convection in the weld pool, fluid flow, free surface deformation and arc physics. One of the most frequently used models is Goldak's double-ellipsoidal model [3] with the volumetric power density distribution, Fig. 1. Five input parameters that define this model are arc efficiency, and four semi-axes of the front and rear ellipsoid. The power of the heat source is distributed, Eqs. (1-3), between the front and rear ellipsoids in a ratio that corresponds to values of parameters $f_f=2a_f/(a_f+a_r)$ and $f_r=2a_r/(a_f+a_r)$ [4].

Values of these input parameters vary significantly, as in the case of arc efficiency. Depending on the type of welding process and shielding gas, arc efficiency can vary between 0.8 and 0.88, as found by DuPont and Marder [5] in case of GMAW process with Ar shielding. Haelsig and Mayr [6] found that arc efficiency has a value, between 0.69 in case of spray arc to the 0.85 in case of short arc shielding. With pulsed transfer, arc efficiency ranges from 0.68 to 0.72 as found by Joseph et al [7]. For the other four heat source parameters, Goldak et al suggested that the values of b_h and c_h should be taken from an experimental cross-section of the weld while the values of a_f and a_r should be equal to b_h and $2b_h$, respectively. In absence of experimental cross section, values of these four parameters should be calculated using Christensen formulae [8]. As for the values of the parameters a_f and a_r, they can vary from $a_r/a_f=1.22$ [9] and up to $a_r/a_f=4$ [10]. Value of parameter a_f is often taken to be equal to c_h [10] or b_h [11]. Guided by Goldak's recommendation, Nasiri and Enzinger used the parameters of a double-ellipsoidal heat source that was approximately 10% smaller than the actual weld geometry [12].

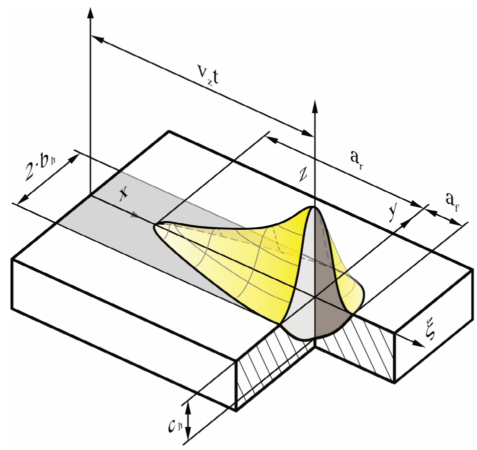

Figure 1: Goldak's double-ellipsoidal heat source

$$q_f(x,y,z)=\frac{6\sqrt{3}f_fQ}{a_fb_hc_h\pi\sqrt{\pi}}e^{-3\frac{x^2}{a_f^2}}e^{-3\frac{y^2}{b_h^2}}e^{-3\frac{z^2}{c_h^2}} \tag{1}$$

$$q_r(x,y,z)=\frac{6\sqrt{3}f_rQ}{a_rb_hc_h\pi\sqrt{\pi}}e^{-3\frac{x^2}{a_r^2}}e^{-3\frac{y^2}{b_h^2}}e^{-3\frac{z^2}{c_h^2}} \tag{2}$$

$$Q=\eta UI \tag{3}$$

The determination of the values of these five parameters is essential for obtaining accurate results from the welding heat transfer model. This goal can be achieved using inverse modeling, that is, minimizing the error between simulated and experimental values of the weld cross-section geometry [11,12]. For this purpose, the simulation model is often combined with an optimization method or the simulation model is replaced with a metamodel to reduce the required computational time [15]. This approach implies that the model being calibrated is supplied with input data until the simulation results match the experimental ones. However, random assignment of values to input parameters usually implies a large number of necesary simulations, which results in a very long time required for model calibration.

*Corresponding author: Dositejeva 19, 36000 Kraljevo, Serbia, bjelic.m@mfkv.kg.ac.rs

To avoid this, we used the Taguchi method to systematize and reduce the number of combinations of input data. These values were used as input parameters for a double-ellipoidal heat source. Thus, we were able to determine the optimal values of the heat source parameters that minimized the error between the simulated and experimental values of the weld penetration depth and weld bead width.

2. MODEL OF HEAT TRANSFER

Nonstationary partial differential equation (4) [11] can be used to describe heat transfer during welding, where ρ, cp, and λ are the density, specific heat capacity, and thermal conductivity, respectively, and L and q_l are the latent heat of melting/solidification and volumetric heat source, respectively. There are difficulties associated with an analytical solution to this type of equation due to nonlinearities in the material's physical properties. The complexity of the boundary conditions and the model of the heat source contributes to these difficulties.

$$\rho c_p \frac{\partial T}{\partial t} = \lambda\left(\frac{\partial^2 T}{\partial x^2}+\frac{\partial^2 T}{\partial y^2}+\frac{\partial^2 T}{\partial z^2}\right) - \rho L \frac{\partial f_{liq}}{\partial t} + q_l \qquad (4)$$

The latent heat of melting/solidification was calculated using the liquid phase fraction in the mushy zone between the solidus temperature T_{sol} and liquidus temperature T_{liq}, as shown in (5).

$$f_{liq} = \begin{cases} 0 & for \quad T \le T_{sol} \\ \dfrac{T - T_{sol}}{T_{liq} - T_{sol}} & for \quad T_{sol} < T < T_{liq} \\ 1 & for \quad T \ge T_{liq} \end{cases} \qquad (5)$$

It is possible to transform (4) for a constant welding speed v_w into a quasi-steady state (7). This type of transformation requires the application of a moving coordinate system ξyz, as shown in Fig. 1. The relationship between these two coordinate systems is defined by (6).

$$\xi = x - v_w t \qquad (6)$$

Now, the heat transfer equation in the moving coordinate system can be written as:

$$-v_w\left(1+\frac{L}{c_p}\frac{\partial f_{liq}}{\partial T}\right)\frac{\partial T}{\partial \xi} = \frac{\lambda}{\rho c_p}\left(\frac{\partial^2 T}{\partial \xi^2}+\frac{\partial^2 T}{\partial y^2}+\frac{\partial^2 T}{\partial z^2}\right) + q_l \qquad (7)$$

Equation (7) is solved in MATLAB iteratively using the multigrid and SOR finite difference methods.

3. EXPERIMENTAL PROCEDURE

An experimental specimen of 300x150x5.3 mm was used for calibration purposes. The base material for the specimen was P355GH steel, with the chemical composition listed in Table 1.

OK Autrod 12.50 uncoated wire with a diameter of 1.2 mm and chemical composition listed in Table 2 was used as filler material. A two-component mixture of 82% Ar and 18% CO2 was utilized as a shielding gas.

Table 1: Chemical composition of base material

C	Si	Mn	Nb	P	S
0.20	0.19	1.45	0.014	0.016	0.062

Welding was performed on one specimen using an ARC Mate 100iC welding robot and Migatronic Sigma Galaxy 400 power supply.

Table 2: Chemical composition of filler material

C	Si	Mn	P	S
0.08	0.58	1.06	0.009	0.01

Using the welding parameters listed in Table 3, a single-pass bead-on-plate weld was made along the specimen's centerline.

Table 3: Welding parameters

Voltage [V]	Current [A]	Welding speed [mm/s]	Wire feed rate [m/min]	Wire diameter [mm]	Gas flow [l/min]
21.2	208	8	5.2	1.2	12

In order to determine the dimensions of the weld geometry, a macrograph section of the weld bead was prepared after welding (Fig. 2).

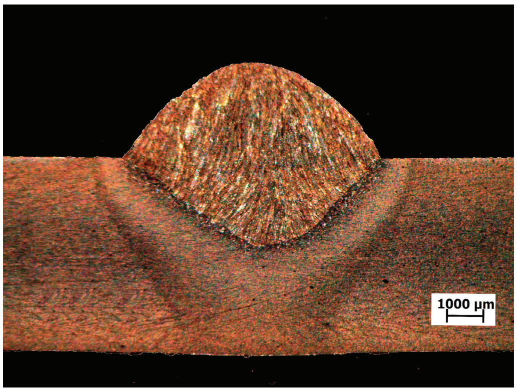

Figure 2: Macrograph of weld bead

The width and penetration depth of the weld bead were measured, as shown in Fig. 3. The measurements were conducted using an STEMI DV-4 stereo microscope equipped with an AxioCam Erc 5S camera.

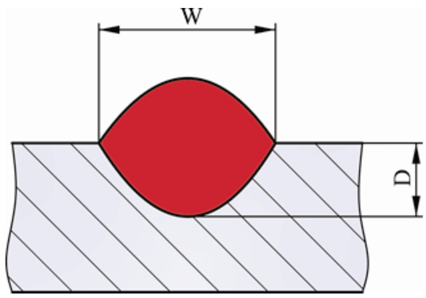

Figure 3: Measured weld geometry

The values of the measured dimensions are listed in Table 4.

Table 4: Measured weld dimensions

W [mm]	D [mm]
7.2	2.4

4. TAGUCHI METHOD

Developed by Genichi Taguchi, the Taguchi method is a statistical approach for optimizing the quality of products and processes. The method is widely used in engineering and manufacturing to enhance robustness and reliability while minimizing the effects of variability. Essentially, the Taguchi method involves identifying and controlling the factors that contribute to system variability. A set of factors can be categorized in three categories: control factors, that is, design parameters or controllable variables, noise factors, and signal factors, that is, response variables.

Taguchi method uses the signal-to-noise ratio (S/N) to evaluate a product or process' performance characteristics. The signal-to-noise ratio implies three categories of performance characteristics: lower-the-better, higher-the-better, and nominal-the-better. A lower-the-better characteristic is used when it is necessary to minimize the response. It can be expressed as (8):

$$S/N = -10\log\left(\frac{1}{n}\sum_{i=1}^{n} Y_i^2\right) \tag{8}$$

When the response must be maximized, the larger-the-better characteristic is used (9),

$$S/N = -10\log\left(\frac{1}{n}\sum_{i=1}^{n} \frac{1}{Y_i^2}\right) \tag{9}$$

When considering the nominal-the-best characteristic, there is a target or desired value for the response variable. The S/N ratio is calculated as (10):

$$S/N = -10\log\left(\frac{1}{n}\sum_{i=1}^{n} \left(\mu - Y_i\right)^2\right) \tag{10}$$

where n is the number of observed values, in this case, the number of objective functions, Yi is the value of the observed characteristic, that is, the value of the objective function, and μ is the target value or the nominal value. For all three performance characteristics, a higher S/N ratio corresponded to better performance characteristics.

Calculating the S/N ratio for each experiment or test allows a comparison between different parameter settings and identification of the combination providing the highest S/N ratio.

The observed characteristic is defined by (11)

$$Y = \left(1 - W_j^{sim}/W^{\exp}\right)^2 + \left(1 - D_j^{sim}/D^{\exp}\right)^2 \tag{11}$$

where W_j^{sim} and D_j^{sim} are the values of the simulated weld bead width and penetration depth, respectively; W_{exp} and D_{exp} are the measured values of the specimen weld bead width and penetration depth, respectively; j is the number of simulation runs. The chosen performance characteristic defined by the S/N ratio is, in this case, lower-the-better.

The minimal degrees of freedom required to choose the right experimental plan (dof_{exp}) depends on the number of factors (i) and degrees of freedom for each factor (dof^{fact}), as well as the factor interactions (dof^{int}), and is defined by (12):

$$dof_{\exp} = \sum_{i=1}^{n} dof_i^{fact} + \sum_{j=1}^{m} dof_j^{\text{int}} \tag{12}$$

In this case, each of the five factors was considered at five levels, as shown in Table 5.

Table 5: Heat source parameters and their levels

Parameter	Level					dof_{fact}
	1	2	3	4	5	
η	0.55	0.65	0.75	0.85	0.95	4
a_f/a_{fexp}	0.8	0.9	1	1.1	1.2	4
a_r/a_{rexp}	0.8	0.9	1	1.1	1.2	4
b_h/b_{hexp}	0.8	0.9	1	1.1	1.2	4
c_h/c_{hexp}	0.8	0.9	1	1.1	1.2	4

Bearing in mind that the interactions between factors were not considered, minimal dof_{exp}=20. Based on this, we chose the Taguchi's $L_{25}(5^6)$ orthogonal array, as shown in Table 6.

Table 6: $L_{25}(5^6)$ OA and parameters values

Run	η	a_f/a_{fexp}	a_r/a_{rexp}	b_h/b_{hexp}	c_h/c_{hexp}
1.	0.65	1.2	0.8	0.9	1
2.	0.65	1	1.1	1.2	0.8
3.	0.55	1.1	1.1	1.1	1.1
4.	0.75	0.8	1	1.2	0.9
5.	0.55	1	1	1	1
6.	0.55	1.2	1.2	1.2	1.2
7.	0.95	1	0.9	0.8	1.2
8.	0.75	0.9	1.1	0.8	1
9.	0.65	0.9	1	1.1	1.2
10.	0.75	1.1	0.8	1	1.2
11.	0.75	1.2	0.9	1.1	0.8
12.	0.95	1.1	1	0.9	0.8
13.	0.95	0.8	1.2	1.1	1
14.	0.65	1.1	1.2	0.8	0.9
15.	0.55	0.8	0.8	0.8	0.8
16.	0.85	1.1	0.9	1.2	1
17.	0.85	1	0.8	1.1	0.9
18.	0.85	1.2	1	0.8	1.1
19.	0.85	0.9	1.2	1	0.8
20.	0.75	1	1.2	0.9	1.1
21.	0.55	0.9	0.9	0.9	0.9
22.	0.85	0.8	1.1	0.9	1.2
23.	0.65	0.8	0.9	1	1.1
24.	0.95	0.9	0.8	1.2	1.1
25.	0.95	1.2	1.1	1	0.9

For each of the 25 combinations of double-ellipsoidal heat source parameters shown in Table 5, we performed a simulation run and obtained the simulated weld bead width and penetration depth for each combination. Table 7 lists the values of observed characteristic Y and its S/N ratio.

Table 7: Values of observed characteristics and S/N ratio

Run	W_s [mm]	D_s [mm]	W_{exp} [mm]	D_{exp} [mm]	Y	SN
1.	5.4	2.3	7.2	2.4	0.064236	23.84442
2.	6.1	1.9			0.066744	23.51178
3.	4.2	1.7			0.258681	11.74472
4.	6.4	2.3			0.014082	37.02684
5.	4.7	1.8			0.183063	14.74798

Run	W_s [mm]	D_s [mm]	W_{exp} [mm]	D_{exp} [mm]	Y	SN
6.	3.7	1.5	7.2	2.4	0.376929	8.474809
7.	6.1	3.2			0.134452	17.42864
8.	5.2	2.4			0.07716	22.2521
9.	5.2	2			0.104938	19.58132
10.	5.9	2.6			0.039545	28.05822
11.	6.7	2.4			0.004823	46.3345
12.	6.6	2.5			0.008681	41.22905
13.	6.7	2.7			0.020448	33.78718
14.	4.7	1.9			0.163966	15.70492
15.	4.7	1.9			0.163966	15.70492
16.	6.8	2.5			0.004823	46.3345
17.	6.9	2.6			0.008681	41.22905
18.	5.7	2.7			0.059028	24.57887
19.	6.4	2.3			0.014082	37.02684
20.	5.3	2.3			0.071373	22.92927
21.	4.7	1.8			0.183063	14.74798
22.	5.7	2.8			0.071181	22.95277
23.	5.3	2.2			0.076582	22.31749
24.	7.1	2.7			0.015818	36.01702
25.	6.5	2.5			0.011188	39.02474

The mean S/N ratios of the observed characteristic Y were calculated for each level of the heat source parameters and are listed in Table 8.

Table 8: Response table for S/N ratios of Y

Level	η	a_f	a_r	b_h	c_h
1	13.08	26.36	28.97	19.13	32.76
2	20.99	25.93	29.43	25.14	29.55
3	31.32	23.97	27.43	28.24	28.19
4	34.42	28.61	23.9	30.54	23.52
5	33.5	28.45	23.58	30.27	19.3
Delta	21.34	4.64	5.85	11.4	13.46
Rank	**1**	**5**	**4**	**3**	**2**

Based on the delta values in Table 8, it can be concluded that the heat-source parameters can be ranked based on their effect on the observed characteristic Y in the following descending order: $\eta > c_h > b_h > ar > af$.

Figure 4 shows the effects of the heat source parameters on the mean S/N ratio of the observed characteristic Y. As previously mentioned, a higher S/N value corresponds to better performance of the observed characteristic. The combination of heat source parameters with the highest S/N ratio is considered optimal. In this case that values are η=0,85; a_f/a_{fexp} =1.1; a_r/a_{rexp} =0.9; b_h/b_{hexp} =1.1; c_h/c_{hexp} =0.8.

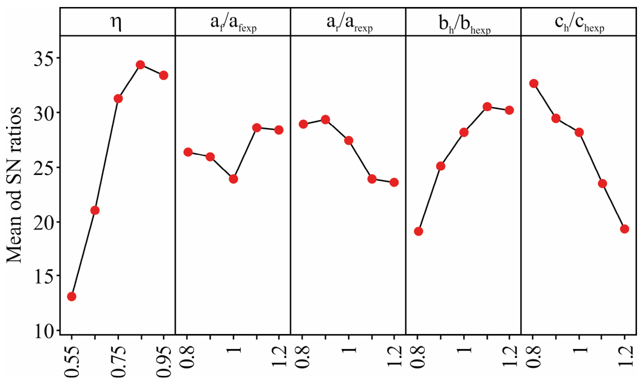

Figure 4: Main effects of heat source parameters

Because there was no experimental run with this set of heat source parameters, we performed an additional simulation run to confirm the results of the optimization. The results of the comparison between the simulated and experimental values of the weld geometry are shown in Table 9.

Table 9: Absolute and relative errors

Values	Parameter	
	W [mm]	D [mm]
Simulation	7	2.5
Experiment	7.2	2.4
Absolute error	0.2	0.1
Relative error	0.0278	0.0417

Figure 5 shows the simulated weld geometry compared with the experimental geometry.

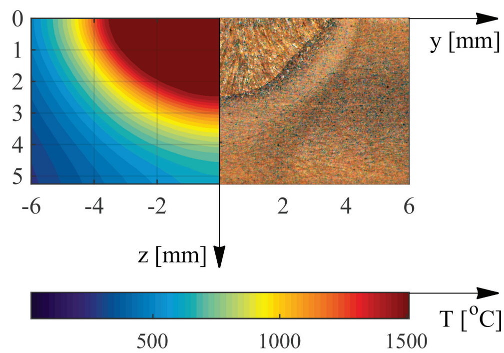

Figure 5: Comparison between simulated and experimental weld bead geometry

To investigate the effects of the heat source parameters on the observed characteristics, analysis of variance (ANOVA) was performed, and the results are listed in Table 10.

Table 10: Results of ANOVA for S/N ratios

Source	DF	SS	MS	F	p
Model	20	2961.36	148.07	12.90	0.0117
η	4	1725.92	431.48	37.6	0.002
a_f/a_{fexp}	4	74.5	18.62	1.62	0.325
a_r/a_{rexp}	4	153.58	38.39	3.35	0.134
b_h/b_{hexp}	4	447.52	111.88	9.75	0.024
c_h/c_{hexp}	4	559.84	139.96	12.2	0.016
Res. Err.	4	45.9	11.47		
Total	24	3007.25			

From Table 10, it can be seen that a model F-value of 12.90 implies the significance of the model. There is only a 1.17% chance that an F-value this large could occur due to noise. P-values less than 0.0500 indicate that the model terms are significant. In this case η, b_h, c_h are significant model terms which is consistent with results of previous analysis.

Analysis of variance allows us to evaluate the contribution of each parameter of the heat source to the mean S/N ratio of the observed characteristic Y. Those contributions are shown on Figure 6.

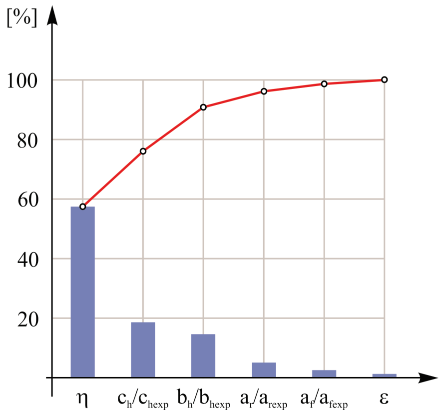

Figure 6: Pareto chart of heat source parameters contribution

The value of the parameter η was 0.85, which is consistent with the findings of DuPont et al. [3]. Parameter ch is 20% smaller, whereas parameter bh is 10% larger than the actual geometry. The relative error for the weld bead width was 2.8 while for the penetration depth was 4.2%.

5. SUMMARY AND CONCLUSIONS

As a means of improving the accuracy of our numerical model of three-dimensional heat transfer, we developed a calibration procedure for determining the input parameters of the double-ellipsoid heat source. The procedure was based on Taguchi's $L_{25}(5^6)$ OA design. As a result, this approach was found to be effective and reliable for accelerating the calibration process. Simulations based on the heat source parameters calculated using the calibration model demonstrate good agreement between simulated and actual weld geometry. The Taguchi-based calibration procedure is therefore demonstrated to be a reliable method for increasing the accuracy of simulation model output results.

ACKNOWLEDGEMENT

The authors wish to express their gratitude to the Ministry of Science, Technological Development and Innovation of the Republic of Serbia for support through contract No. 451-03-47/2023-01/200108.

LITERATURE

[1] D. Rosenthal, "The theory of moving sources of heat and its application to metal treatments", Transactions ASME, Vol. 43, pp. 849–866, (1946)

[2] N.N. Rykalin, "Calculations of thermal processes in welding", Mašgiz, Moscow (USSR), (1951)

[3] J. Goldak, A. Chakravarti and M. Bibby, "A new finite element model for welding heat sources", Metallurgical Transactions B, Vol. 15, pp. 299–305, (1984)

[4] C.S. Wu, "Welding thermal processes and weld pool behaviors", Taylor & Francis, Boca Raton-Florida (USA), 2011

[5] J.N. DuPont and A.R. Marder, "Thermal Efficiency of Arc Welding Processes", Welding Journal, Vol. 74, (1995).

[6] A. Haelsig and P. Mayr, "Energy balance study of gas-shielded arc welding processes", Welding in the World, Vol. 57, pp. 727–734, (2013)

[7] A. Joseph, D. Harwig, D.F. Farson and R. Richardson, "Measurement and calculation of arc power and heat transfer efficiency in pulsed gas metal arc welding", Vol. 8, pp. 400–406, (2013)

[8] N. Christensen, V. de L. Davies and K. Gjermundsen, "Distribution of temperatures in arc welding", British Welding Journal, Vol. 12, pp. 54–75, (1965)

[9] N. Moslemi, S. Gohari, B. Abdi, I. Sudin, H. Ghandvar, N. Redzuan, S. Hassan, A. Ayob and S. Rhee "A novel systematic numerical approach on determination of heat source parameters in welding process", Journal of Materials Research and Technology, Vol. 18, pp. 4427–4444, (2022)

[10] J.H. Chujutalli, M.I. Lourenço and S.F. Estefen, "Experimental-based methodology for the double ellipsoidal heat source parameters in welding simulations", Marine Systems and Ocean Technology, Vol. 15, pp. 110–123, (2020)

[11] G. Fu, J. Gu, M.I. Lourenco, M. Duan and S.F. Estefen, "Parameter determination of double-ellipsoidal heat source model and its application in the multi-pass welding process", Ships and Offshore Structures, Vol. 10, pp. 204–217, (2015)

[12] M.B. Nasiri and N. Enzinger, "Powerful analytical solution to heat flow problem in welding", International Journal of Thermal Sciences. Vol. 135, pp. 601–612, (2019)

[13] A. Kumar and T. DebRoy, "Guaranteed fillet weld geometry from heat transfer model and multivariable optimization", International Journal of Heat and Mass Transfer, Vol. 47, pp. 5793–5806, (2004)

[14] Y. Gu, Y.D. Li, Y. Yong, F.L. Xu and L.F. Su, "Determination of parameters of double-ellipsoidal heat source model based on optimization method", Welding in the World, Vol. 63, pp. 365–376, (2019)

[15] M.B. Bjelić, B.S. Radičević, K. Kovanda, L. Kolarik and A. V. Petrović, "Multi-objective calibration of the double-ellipsoid heat source model for GMAW process simulation", Thermal Science, Vol. 26, pp. 2081–2092, (2022)

Optimization of GMA welding parameters using the grasshopper optimization algorithm

Mladen Rasinac[1]*, Mišo Bjelić[1], Aleksandra Petrović[1], Marina Ivanović[1], Stefan Pajović[1]
[1]Faculty of Mechanical and Civil Engineering in Kraljevo, University of Kragujevac, Kraljevo (Serbia)

This paper presents the method for choosing optimal parameters for GMA welding of P355GH low-carbon steel plates. The welding parameters such as seam overhang coefficient, degree of mixing, number of passes and welding current were obtained using the grasshopper optimization algorithm (GOA). Optimal parameters were obtained to yield minimum welding costs while considering technological constraints such as maximum permissible cooling rate and maximum permissible hardness of the heat affected zone (HAZ).

Keywords: Optimization, GMA welding, Grasshopper optimization algorithm

1. INTRODUCTION

In the welding process, the costs, cycle time and quality of the welded joint are highly dependent on the welding parameters such as seam overhang coefficient, seam shape coefficient, degree of mixing, number of passes, welding speed, welding current and voltage. Determination of optimal welding parameters, with regard to different technological constraints, is important task in the process of designing the welding technology.

The main objective of this study is to optimize the butt joint welding costs, which consists of the two partial costs discussed here. Those costs are material costs made up of filler material costs and consumable material (protective atmosphere) costs, and energy costs (electric energy). The optimum parameters: seam overhang coefficient, degree of mixing, number of passes and welding current are found by grasshopper optimization algorithm (GOA) which is a recently developed metaheuristic algorithm. An illustrative example is used to demonstrate the effectiveness of the GOA in process of choosing the optimal welding parameters.

2. GMA WELDING COSTS

2.1. Structure of the GMA welding costs

In [1] are given general structure of the welding costs for different types of welding processes. Based on that structure, it is possible to derive a cost structure suitable for a specific welding process. On the Figure 1 are given costs structure for GMA welding process. In this paper are considered only material costs, T_M and energy costs, T_E, specifically, filler material costs, T_{DM}, protective atmosphere costs, T_{ZA}, and electric energy costs, T_{ES}. Other costs are not taken into account because they are generally less independent of the welding parameters.

2.2. Mathematical formulation of the GMA welding costs

In the following section are given mathematical formulations of costs.

2.2.1. Filler material costs, T_{DM} RSD

These costs can be calculated using the following

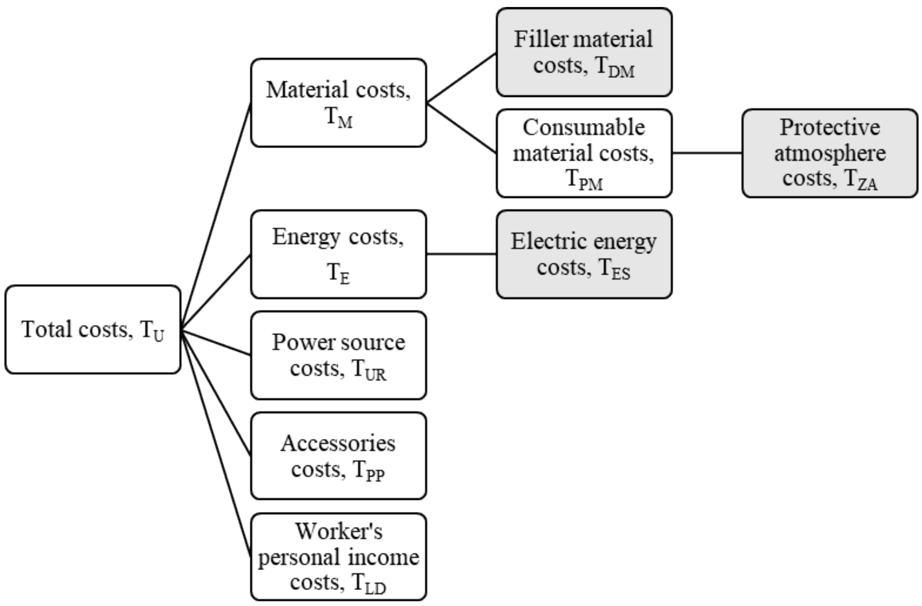

Figure 1: GMA welding costs structure [1]

*Corresponding author: Dositejeva 19, 36000 Kraljevo, rasinac.m@mfkv.kg.ac.rs

equation:

$$T_{DM} = S \cdot V_z \cdot t_z \cdot \rho_e \cdot \eta_e \cdot C_{DM} \tag{1}$$

where:

S m^2, V_z m/min, t_z min, ρ_e kg/m^3, η_e, C_{DM} RSD/kg are cross-sectional area of the groove (Figure 2), welding speed, welding time of one pass, density of filler material, specific productivity of filler material and price of the filler material, respectively. [1]

Equations for variable parameters are listed below.

$$S = c \cdot \delta + (\delta - h)^2 \cdot \mathrm{tg}\frac{\varphi}{2} \tag{2}$$

$$V_z = \frac{6 \cdot 10^{-2} \cdot m_D}{\frac{S_š}{i} \cdot \rho_e} \tag{3}$$

$$t_z = \frac{6 \cdot 10^4 \cdot \frac{S_š}{i} \cdot \rho_e \cdot l_š}{I_z \cdot K_t} \tag{4}$$

It is important to note that an equal cross-sectional area of the weld in each pass is adopted here. [1,2]

Next parameters must be calculated, using following equations:

$$m_D = 2.5 \cdot \sqrt{\frac{2 \cdot S_š}{i} \cdot \rho_e} \tag{5}$$

$$S_š = \frac{S + 0.75 \cdot \frac{e_1}{\zeta} \cdot e_1 + 0.75 \cdot \frac{e_2}{\zeta} \cdot e_2}{1 - \gamma} \tag{6}$$

$$K_t = 0.0001 \cdot I_z^2 - 0.0279 \cdot I_z + 15.5643 \tag{7}$$

Here, m_D g/s, $S_š$ m^2, K_t g/(A·h), are deposit mass, cross-sectional area of the seam and melting constant, respectively. [1] It is worth noting that the equation for melting constant was obtained by interpolating the data given in [2].

Parameters e_1 m, e_2 m are the width of the seam on the face side and on reverse side of the face, respectively.

$$e_1 = 2 \cdot (\delta - h) \cdot \mathrm{tg}\frac{\varphi}{2} + c + d_1 \tag{8}$$

$$e_2 = c + d_2 \tag{9}$$

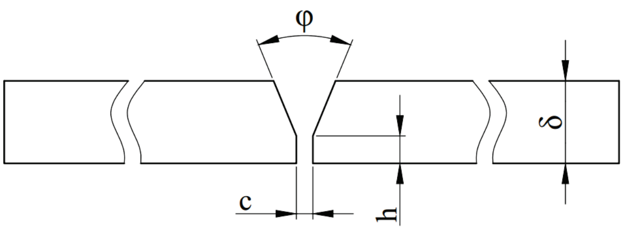

Figure 2: Dimensions of the Y groove

2.2.2. Protective atmosphere costs, T_{ZA} RSD

These costs can be calculated using following equation:

$$T_{ZA} = Q_a \cdot C_a \cdot (t_z \cdot i + t_{pz}) \cdot \frac{1}{\eta_e \cdot \varepsilon} \tag{10}$$

Where t_{pz} min and ε are preparatory-final time and intermittency. They can be calculated using following equations: [1]

$$t_{pz} = k_{pz} \cdot (t_z \cdot i + t_p) \tag{11}$$

$$\varepsilon = \frac{t_z \cdot i}{t_z \cdot i + t_{pz}} \tag{12}$$

2.2.3. Electric energy costs, T_{ES} RSD

These costs can be calculated using following equation:

$$T_{ES} = S_š \cdot V_z \cdot t_z \cdot \rho_e \cdot C_s \cdot \left[\frac{U_z \cdot I_z}{1000 \cdot \eta_s} \cdot \varepsilon + P_0 \cdot (1 - \varepsilon)\right] \cdot \frac{1}{60 \cdot PR_D \cdot \varepsilon} \tag{13}$$

Where PR_D kg/min is productivity by amount of deposited material, and is calculated by following equation: [1]

$$PR_D = S_š \cdot V_z \cdot \rho_e \tag{14}$$

2.2.4. Total costs, T_U RSD

Total costs represent the sum of partial costs and they are also the objective function. [1]

$$T_U = T_{DM} + T_{ZA} + T_{ES} \tag{15}$$

3. CONSTRAINTS

Welding is a complex process where the welded joint has to meet various requirements in terms of quality and mechanical properties.

Here, P355GH low-carbon steel is chosen for the material of the welded joint parts.

The objective function (15) is subjected to four technological constraints, which are explained in the following section.

3.1. Constraint regarding the maximum permissible cooling rate

Based on the continuous cooling transformation diagram (CCT) for steel, it is possible to determine which is critical or the maximum cooling rate, at which undesirable structures in the heat affected zone (HAZ) of the steel, especially martensite, will not form. From the CCT diagram for P355GH steel given in [3], we can see that the maximum permissible cooling rate is $50\ ^\circ$C/s.

It is possible to make relationship between the cooling rate v_h °C/s and the cooling time in the temperature interval from $800 \div 500\ ^\circ$C, $t_{8/5}$ s, from where it is possible to determine the critical or minimum allowed cooling time in that interval, i.e.:

$$t_{8/5} \geq \frac{800 - 500}{v_h} \geq \frac{300}{50} \geq 6 \text{ s} \tag{16}$$

From the cooling time equation [3]:

$$t_{8/5} = \frac{k \cdot q_l^n}{\beta \cdot (T_{sr} - T_0)^2 \cdot \left[1 + \frac{2}{\pi} \cdot \mathrm{arctg}\left(\frac{s - s_0}{\alpha}\right)\right]} \tag{17}$$

it is now possible to get the line energy q_l J/cm :

$$q_l \ge \sqrt[n]{\frac{t_{8/5}\cdot\beta\cdot\left(T_{sr}-T_0\right)^2\cdot\left[1+\frac{2}{\pi}\cdot\operatorname{arctg}\left(\frac{s-s_0}{\alpha}\right)\right]}{k}} \ge \sqrt[n]{\frac{6\cdot\beta\cdot\left(T_{sr}-T_0\right)^2\cdot\left[1+\frac{2}{\pi}\cdot\operatorname{arctg}\left(\frac{s-s_0}{\alpha}\right)\right]}{k}} \quad (18)$$

After substituting above inequality into the line energy equation [3]:

$$q_l = 60\cdot\frac{U_z\cdot I_z}{v_z} \quad (19)$$

we get the following inequality:

$$U_z\cdot I_z \ge \frac{v_z\cdot\sqrt[n]{\frac{6\cdot\beta\cdot\left(T_{sr}-T_0\right)^2\cdot\left[1+\frac{2}{\pi}\cdot\operatorname{arctg}\left(\frac{s-s_0}{\alpha}\right)\right]}{k}}}{6\cdot10^{-1}} \quad (20)$$

First constraint is:

$$U_z\cdot I_z-\frac{v_z\cdot K_1}{6\cdot10^{-1}}\ge 0 \quad (21)$$

Where:

$$K_1=\sqrt[n]{\frac{6\cdot\beta\cdot\left(T_{sr}-T_0\right)^2\cdot\left[1+\frac{2}{\pi}\cdot\operatorname{arctg}\left(\frac{s-s_0}{\alpha}\right)\right]}{k}} \quad (22)$$

After expressing the voltage over the welding current [3], the constraint finally becomes:

$$\left(14+0.05\cdot I_z\right)\cdot I_z-\frac{v_z\cdot K_1}{6\cdot10^{-1}}\ge 0 \quad (23)$$

3.2. Constraint regarding the maximum permissible hardness in the HAZ

The hardness value in the HAZ is used as one of the parameters of the weldability of steel. Maximum permissible hardness is related to the amount of diffused hydrogen.

Based on the recommended hydrogen scale for the GMA welding (D), it is possible to determine the content of diffused hydrogen per 100 g of weld metal ($1\div 5$) and maximum permissible hardness in the HAZ ($\mathrm{HV_{max}} = 450$ HV), as explained in [3].

Equation for the maximum hardness is as follows:

$$\mathrm{HV_{max}}=\frac{\mathrm{H_M}+\mathrm{H_B}}{2}-\frac{\mathrm{H_M}-\mathrm{H_B}}{2.2}\cdot\operatorname{arctg}\left(\mathrm{X}\right) \quad (24)$$

Where, $\mathrm{H_M}$ HV, $\mathrm{H_B}$ HV are hardness of martensite phase and bainite phase, respectively. X is parameter which can be calculated using following equation:

$$\mathrm{X}=4\cdot\frac{\log\left(t_{8/5}/t_M\right)}{\log\left(t_B/t_M\right)}-2 \quad (25)$$

Here, t_M s, t_B s are indices of ease of formation of martensitic, and bainite phases, respectively. The equations for these indices are given below.

$$t_M=\exp(10.6\cdot\mathrm{CE_I}-4.8) \quad (26)$$

$$t_B=\exp(6.2\cdot\mathrm{CE_{III}}+0.74) \quad (27)$$

Where parameters $\mathrm{CE_I}$ %, $\mathrm{CE_{III}}$ % represents the carbon equivalent. [3]

The hardness $\mathrm{H_M}$ and $\mathrm{H_B}$ can be calculated as follows:

$$\mathrm{H_M}=884\cdot\mathrm{C}\cdot\left(1-0.3\cdot\mathrm{C}^2\right)+297 \quad (28)$$

$$\mathrm{H_B}=145+130\cdot\operatorname{tgh}\left(2.65\cdot\mathrm{CE_{II}}-0.69\right) \quad (29)$$

Where $\mathrm{CE_{II}}$ % is carbon equivalent.

The equations for the carbon equivalent are given below. [3]

$$\mathrm{CE_I}=\mathrm{C_p}+\frac{\mathrm{Si}}{24}+\frac{\mathrm{Mn}}{6}+\frac{\mathrm{Cu}}{15}+\frac{\mathrm{Ni}}{12}+\frac{\mathrm{C_r}\cdot\left(1-0.16\cdot\sqrt{\mathrm{Cr}}\right)}{8}+\frac{\mathrm{Mo}}{4}+\Delta\mathrm{H} \quad (30)$$

$$\mathrm{CE_{II}}=\mathrm{C_p}+\frac{\mathrm{Si}}{24}+\frac{\mathrm{Mn}}{5}+\frac{\mathrm{Cu}}{10}+\frac{\mathrm{Ni}}{18}+\frac{\mathrm{C_r}}{5}+\frac{\mathrm{Mo}}{2.5}+\frac{\mathrm{V}}{5}+\frac{\mathrm{Nb}}{3} \quad (31)$$

$$\mathrm{CE_{III}}=\mathrm{C_p}+\frac{\mathrm{Mn}}{3.6}+\frac{\mathrm{Cu}}{20}+\frac{\mathrm{Ni}}{9}+\frac{\mathrm{C_r}}{5}+\frac{\mathrm{Mo}}{4} \quad (32)$$

Based on the constraint $\mathrm{HV_{max}}\le 450$ HV and (24) we have the following:

$$\mathrm{X}\ge\operatorname{tg}\left(\frac{1.1\cdot\left(\mathrm{H_M}+\mathrm{H_B}-900\right)}{\mathrm{H_M}-\mathrm{H_B}}\right) \quad (33)$$

After substituting the inequality given above in (25) we have:

$$t_{8/5}\ge t_M\cdot10\wedge\left(\frac{\log\left(t_B/t_M\right)\cdot\left(T+2\right)}{4}\right) \quad (34)$$

Where:

$$T=\operatorname{tg}\left(\frac{1.1\cdot\left(\mathrm{H_M}+\mathrm{H_B}-900\right)}{\mathrm{H_M}-\mathrm{H_B}}\right) \quad (35)$$

Using (17) it is now possible to get the line energy:

$$q_l \ge \sqrt[n]{\frac{t_{8/5}\cdot\beta\cdot\left(T_{sr}-T_0\right)^2\cdot\left[1+\frac{2}{\pi}\cdot\operatorname{arctg}\left(\frac{s-s_0}{\alpha}\right)\right]}{k}} \ge \sqrt[n]{\frac{E\cdot\beta\cdot\left(T_{sr}-T_0\right)^2\cdot\left[1+\frac{2}{\pi}\cdot\operatorname{arctg}\left(\frac{s-s_0}{\alpha}\right)\right]}{k}} \quad (36)$$

Where:

$$E=t_M\cdot10\wedge\left(\frac{\log\left(t_B/t_M\right)\cdot\left(T+2\right)}{4}\right) \quad (37)$$

After substituting q_l into (19), we get the following inequality:

$$U_z\cdot I_z \ge \frac{v_z\cdot\sqrt[n]{\frac{E\cdot\beta\cdot\left(T_{sr}-T_0\right)^2\cdot\left[1+\frac{2}{\pi}\cdot\operatorname{arctg}\left(\frac{s-s_0}{\alpha}\right)\right]}{k}}}{6\cdot10^{-1}} \quad (38)$$

Second constraint is:

$$U_z\cdot I_z-\frac{v_z\cdot K_2}{6\cdot10^{-1}}\ge 0 \quad (39)$$

Where:

$$K_2 = \sqrt[n]{\frac{E \cdot \beta \cdot \left(T_{sr} - T_0\right)^2 \cdot \left[1 + \frac{2}{\pi} \cdot \mathrm{arctg}\left(\frac{s - s_0}{\alpha}\right)\right]}{k}} \quad (40)$$

After expressing the voltage over the welding current as in (23), the constraint finally becomes:

$$\left(14 + 0.05 \cdot I_z\right) \cdot I_z - \frac{v_z \cdot K_2}{6 \cdot 10^{-1}} \geq 0 \quad (41)$$

3.3. Constraints regarding the recommended welding voltage values

Taking into account the recommended welding voltage values ($U_z = 22 \div 35$ V) given in [1], and the above-mentioned dependence between welding voltage and current, we have the following:

$$U_z = 14 + 0.05 \cdot I_z \geq 22 \text{ V} \quad (42)$$

$$U_z = 14 + 0.05 \cdot I_z \leq 35 \text{ V} \quad (43)$$

The third and fourth constraints are:

$$8 - 0.05 \cdot I_z \leq 0 \quad (44)$$

$$0.05 \cdot I_z - 21 \leq 0 \quad (45)$$

Furthermore, constraints are associated with the domain of optimization variables [1,2], as follows:

$$\begin{aligned} 7 \leq \zeta \leq 10 \\ 0.1 \leq \gamma \leq 0.6 \\ 3 \leq i \leq 5 \\ 150 \leq I_z \leq 450 \end{aligned} \quad (46)$$

4. MATHEMATICAL FORMULATION OF THE OPTIMIZATION PROBLEM

According to the mathematical modelling described above, the problem of GMA welding costs minimization is as follows:

Minimise $T_U(\mathbf{x}) = T_{DM}(\mathbf{x}) + T_{ZA}(\mathbf{x}) + T_{ES}(\mathbf{x})$

subject to

$$\begin{aligned} g_1(\mathbf{x}) &= \frac{v_z(\mathbf{x}) \cdot K_1(\mathbf{x})}{6 \cdot 10^{-1}} - \left(14 + 0.05 \cdot x(4)\right) \cdot x(4) \leq 0 \\ g_2(\mathbf{x}) &= \frac{v_z(\mathbf{x}) \cdot K_2(\mathbf{x})}{6 \cdot 10^{-1}} - \left(14 + 0.05 \cdot x(4)\right) \cdot x(4) \leq 0 \\ g_3(\mathbf{x}) &= 8 - 0.05 \cdot x(4) \leq 0 \\ g_4(\mathbf{x}) &= 0.05 \cdot x(4) - 21 \leq 0 \\ \zeta_{\min} &\leq \zeta \leq \zeta_{\max} \quad \left(\zeta = x(1)\right) \\ \gamma_{\min} &\leq \gamma \leq \gamma_{\max} \quad \left(\gamma = x(2)\right) \\ i_{\min} &\leq i \leq i_{\max} \quad \left(i = x(3)\right) \\ I_{z\min} &\leq I_z \leq I_{z\max} \quad \left(I_z = x(4)\right) \end{aligned} \quad (47)$$

5. GRASSHOPPER OPTIMIZATION ALGORITHM

The grasshopper optimization algorithm (GOA), which is a metaheuristic optimization algorithm, has been recently developed by Saremi et al. (2017). This algorithm mathematically models and mimics the behaviour of grasshopper swarms in nature for solving the optimization problems. [4,5] It has been successfully applied to various benchmark and real-world problems [6-8].

The steps in the procedure of GOA are shown below. They are as follows: [4]

Step 1: Initialize the problem and algorithm parameters
Step 2: Initialize the swarm
Step 3: Calculate the fitness (objective function) of each search agent (grasshopper)
Step 4: For each search agent: normalize the distances between search agents, update the position of the current search agent, bring the current search agent back if it goes outside the boundaries
Step 5: Update the best search agent (update the best fitness value)
Step 6: Return best fitness value

The mathematical model which is employed to simulate the behaviour of the grasshopper swarms is given below:

$$X_i = S_i + G_i + A_i \quad (48)$$

Where X_i defines the position of the i-th grasshopper, S_i represents the social interaction, G_i is the gravity force and A_i shows the wind advection. [4]

To determine the term S_i it is necessary to know the function $s(r)$ given below, which defines the social forces.

$$s(r) = f \cdot \exp\left(-\frac{r}{l}\right) - \exp(-r) \quad (49)$$

Where r is the distance, f indicates the intensity of attraction and l is the attractive length scale. This function impacts on the social interaction (attraction and repulsion) of grasshoppers. Repulsion occurs when the distance between grasshoppers is in the interval $[0\ 2.079]$. When the grasshopper is 2.079 units away from another grasshopper, there is neither attraction nor repulsion. This zone is called the comfort zone. Attraction increases from 2.079 units of distance, Figure 3. [4]

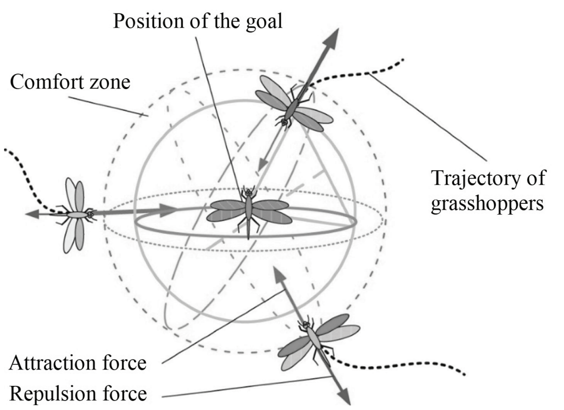

Figure 3: Corrective patterns between individuals in a swarm of grasshoppers [9]

This mathematical model cannot be used directly for optimization problems and a modified version of this equation is used to solve optimization problems in d-th dimension: [4]

$$X_i^d = c \cdot \left(\sum_{\substack{j=1 \\ j \neq i}}^{N} c \cdot \frac{ub_d - lb_d}{2} \cdot s\left(\left|x_j^d - x_i^d\right|\right) \cdot \frac{x_j - x_i}{d_{ij}} \right) + \hat{T}_d \quad (50)$$

Where c is a decreasing coefficient to shrink the comfort zone, repulsion zone and attraction zone, N is the number of grasshoppers, ub_d is the upper bound in the d-th dimension, lb_d is the lower bound in the d-th dimension, x_i^d is the position of the i-th grasshopper in the d-th dimension, x_j^d is the position of the j-th grasshopper in the d-th dimension, d_{ij} is the distance between the i-th and the j-th grasshopper and $\hat{T}_d$ is the value in the target of the d-th dimension, i.e. the best solution found so far. [4]

6. NUMERICAL EXAMPLE

To test the developed model of GMA welding parameters optimization, the data used in the example are presented in Table 1.

The goal was to find the optimal values of the welding parameters that will lead to the lowest total costs of welding the butt joint of P355GH steel plates (Figure 2).

In this algorithm, the Penalty method was used for dealing with constraints. [11]

In the proposed grasshopper optimization algorithm, a population of $N = 100$ search agents were considered. The optimized values presented here were obtained after 250 iterations and 337.4 s. The values of the parameters f and l were 0.5 and 1.5, respectively. The maximum and minimum value of the coefficient c was: $c_{\max} = 1$ and $c_{\min} = 0.00004$. Table 2 shows the optimized values of the welding parameters obtained with GOA and the value of the total costs as well as all three partial costs.

7. CONCLUSIONS AND FUTURE RESEARCH

In this study, application of grasshopper optimization algorithm for optimization of GMA welding parameters has been investigated. The optimum values of welding parameters including seam overhang coefficient, degree of mixing, number of passes and welding current are obtained to yield minimum total welding costs. Based on the optimized values of the welding parameters, it can be seen that three of them are at their limit allowed values. This is consequence of the shape of the objective function itself, which is relatively simple. The GOA which is a recently developed optimization algorithm has been used as an effective tool. The ability of the algorithm is demonstrated on an illustrative example, where it showed a high speed of finding the optimum.

In future research, it is possible to include all GMA welding costs (power source, accessories and worker’s personal income costs), as well additional technological and other constraints. Also, the costs can be determined for a more complex welded joint with several different types of seams (grooves).

Table 1: Numerical data of the GMA welding costs problem [1-3,10]

Parameter	Value	Unit
Plate thickness, δ	0.015	m
Root spacing, c	0.003	m
Root blunting, h	0.005	m
Groove opening angle, φ	45	°
Constant, d_1	0.005	m
Constant, d_2	0.0015	m
Seam length, $l_š$	0.25	m
Density of filler material, ρ_e	7800	kg/m^3
Specific productivity of filler material, η_e	1.02	–
Filler material price, C_{DM}	187	RSD/kg
Shielding gas flow (CO_2), Q_a	9.17	l/min
Shielding gas price (CO_2), C_a	144	RSD/l
Preparatory-final time coefficient, k_{pz}	0.065	–
Auxiliary time, t_p	1.2	min
Electric energy price, C_s	12.06	RSD/$(\mathrm{kW \cdot h})$
Coefficient of utilization of power source, η_s	0.8	–
Power source intermittency, ε	0.6	–
Idle power of source, P_0	1	kW
Constant, k	$1/2.9$	–
Constant, n	1.7	–
Constant, s_0	13	mm
Constant, α	3.5	–
Constant, T_{sr}	600	°C
Constant, β	1	–
Constant, T_0	20	°C
Carbon content, C	0.2	%
Silicon content, Si	0.19	%
Manganese content, Mn	1.45	%
Niobium content, Nb	0.014	%
Cu, Ni, Cr, Mo, V	0	%
Carbon content, $C_p = C$	0.2	%
Parameter, ΔH	0	%

Table 2: The GOA results

Optimized values of parameters			
ζ	γ	i	I_z
10	0.1	5	420
Costs values RSD			
T_{DM}	T_{ZA}	T_{ES}	T_U
25.1	2964.4	1.4	2990.9

ACKNOWLEDGEMENTS

This research is co-financed by the Ministry of Science, Technological Development and Innovation of the Republic of Serbia on the base of the contract whose record number is 451-03-47/2023-01/200108.

The authors express their gratitude to the Ministry of Science, Technological Development and Innovation of the Republic of Serbia for supporting this research.

REFERENCES

[1] M. Vukićević, “Welding Technology Design”, Faculty of Mechanical and Civil Engineering, University of Kragujevac, Kraljevo (Serbia), (2013)

[2] M. Sarvan and M. Mišić, “Workbook of Welding Technology”, Priština (Serbia), (1998)

[3] M. Bjelić, “Welding Technology Design – Practicum for exercises, first part”, Faculty of Mechanical and Civil Engineering, University of Kragujevac, Kraljevo (Serbia), (2021)

[4] S. Saremi, S. Mirjalili and A. Lewis, “Grasshopper Optimisation Algorithm: Theory and Application”, Advan. in Eng. Soft., Vol. 105, pp. 30-47, (2017)

[5] S.Z. Mirjalili, S. Mirjalili, S. Saremi, H. Faris and I. Aljarah, “Grasshopper Optimization Algorithm for Multi-Objective Optimization Problems”, Appl. Intell., Vol. 48, pp. 805-820, (2017)

[6] A.G. Neve, G.M. Kakandikar and O. Kulkarni, “Application of Grasshopper Optimization Algorithm for Constrained and Unconstrained test Functions”, Int. J. Swarm Intel. Evol. Comput., Vol. 6(3), (2017)

[7] H. Singh and B. Singh, “A Comparison of Optimization Algorithms for Standard Benchmark Functions”, Int. J. Advan. Res. Comput. Sci., Vol. 8(7), (2017)

[8] A. Shareef and S. Al-Darraji, “Grasshopper Optimization Algorithm Based Path Planning for Autonomous Mobile Robot”, Bull. of Electr. Eng. Inform., Vol. 11(6), pp. 3551-3561, (2022)

[9] M. Mafarja, I. Aljarah, A.A. Heidari, A.I. Hammouri, H. Faris, A.M. Al-Zoubi and S. Mirjalili, “Evolutionary Population Dynamics and Grasshopper Optimization Approaches for Feature Selection Problems”, Knowledge-Based Syst., Vol. 145, pp. 25-45, (2017)

[10] https://www.messer.rs/

[11] X.S. Yang, “Engineering Optimization – An Introduction with Metaheuristic Applications”, John Wiley & Sons, Hoboken, New Jersey (USA), (2010)

SESSION D

AUTOMATIC CONTROL AND FLUID TECHNIQUE

Event-triggered adaptive dynamic programming based optimal control for hydraulic servo actuator

Vladimir Djordjevic[1], Vladimir Stojanovic[1*], Hongfeng Tao[2], Xiaona Song[3], Shuping He[4], Weinan Gao

[1]Faculty of Mechanical and Civil Engineering, University of Kragujevac, Kraljevo (Serbia)

[2] Key Laboratory of Advanced Process Control for Light Industry of Ministry of Education, Jiangnan University, Wuxi (China)

[3] School of Information Engineering, Henan University of Science and Technology, Luoyang (China)

[4] Key Laboratory of Intelligent Computing and Signal Processing (Ministry of Education) School of Electrical Engineering and Automation, Anhui University, Hefei (China)

[5] State Key Laboratory of Synthetical Automation for Process Industries, Northeastern University, Shenyang (China)

This paper considers adaptive optimal control for hydraulic servo actuators (HSAs) with unknown dynamics. A hydraulic servo actuator is a highly complex nonlinear system with parameters that cannot be accurately determined due to various uncertainties, an inability to measure some parameters and disturbances. An event-triggered learning control problem of the HSA with unknown dynamics based on adaptive dynamic programming (ADP) via output feedback is considered. The control law is learned online based on measured input and output data instead of unmeasurable states and unknown system parameters. An event-based feedback strategy is introduced to the closed-loop system to save computing and communication resources and reduce the number of control updates. Simulation results verify the feasibility and effectiveness of the proposed approach in solving the optimal control problem of HSA.

Keywords: Data-driven control, Adaptive dynamic programming, event-triggered control, hydraulic servo actuator

1. INTRODUCTION

A HSA has a fast and accurate response. It also has a high force/mass ratio and relatively good stiffness. A high-performance controller design of the HSA attracted increasing attention due to the expanded performance requirements of technical systems in the industry in the last twenty years [1-3].

HSAs often work with high payloads in harsh and mostly external environments. The HSA is usually subject to significant uncertainties during operation in such environments due to extreme temperatures, dust, humidity, wear, variable loads and disturbances. For this reason, it is impossible to determine most of the physical parameters of HSA components. Thus, realising high-quality control of the HSA is challenging, which can only be achieved by knowing the accurate model [4-6].

For the practical implementation, it is not feasible to directly measure the whole HSA state vector, so it is more convenient to use control algorithms which apply methods based on state reconstruction rather than to perform direct measurements of the states [7].

Using optimal control methods, we can design controllers that can minimize the system's energy consumption [8]. However, the optimal control design is an offline control technique that usually depends on perfect knowledge of the systems model. Furthermore, the change in the system's dynamics during the operation will degrade the control performance of the traditionally designed optimal controller.

Adaptive dynamic programming (ADP) ensures an effective way to achieve high performance of the optimal controller, which relies on adaptive control, optimal control and reinforcement learning. [7-12]. ADP represents a data-based control technique which can guarantee the stability of the feedback control system [8]. In circumvents of unknown system dynamics and unmeasurable states, of great interest is to use of ADP techniques based on measured input/output data from linear systems, commonly called output feedback. A primary benefit of the output feedback techniques is that knowledge of the HSA dynamics is not needed for their application.

The implementation of ADP algorithms is usually based on periodic selection [13]. In order to save limited communication and computational resources, event-strategies have recently started to be applied in control algorithms based on ADP [14-15]. This way, the number of updates of the controller is reduced compared to the periodically updated controller since it is only updated when necessary. Several event-based controllers have been proposed, primarily state-feedback controllers [16-18].

In this paper, it is considered an online learning technique, where during operation, from measured input/output data, the controller learns to compensate unknown HSA dynamics, various disturbances and modelling errors, ensuring the desired performance of the control system. The optimal control law is accomplished iteratively based on output feedback, state reconstruction and ADP. The exploration noise is added to control input to meet the requirements of the persistent excitation condition [19-20]. The sum of sinusoidal signals is used as an exploration signal to ensure that the system's output carries maximum information about the system, which shortens the learning time.

Due to the implementation of the ADP-based control techniques, it is easier to realize data acquisition for the discrete-time HSA model. ADP-based methodology for discrete-time systems is proposed in [21]. The measured input and output data are used to reconstruct the state vector

*Corresponding author: Vladimir Stojanovic, vladostojanovic@mts.rs, Dositejeva 19, 36000 Kraljevo, Serbia

of the discretized HSA model, after which the ADP-base control can be implemented.

The number of control updates is reduced using an event-based control strategy since the control is updated when certain conditions are met. In this way, energy, computing and communication resources are significantly preserved.

2. HIDRAULIC SERVO ACTUATOR

The HSA under study is shown in Figure 1, and it consists of a servo valve and a hydraulic cylinder. The model of the HSA is derived from complex nonlinear equations that depend on many parameters which cannot be accurately obtained [6].

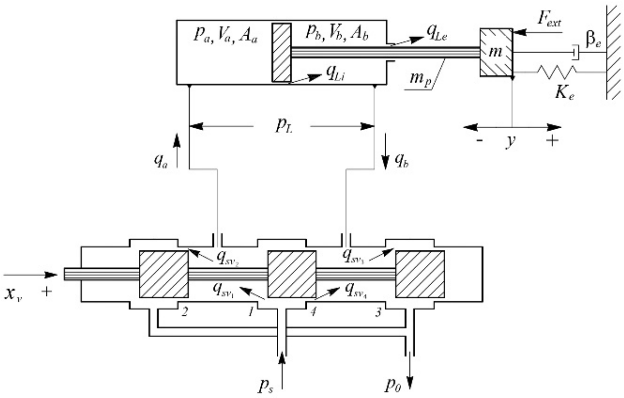

Figure 1: The HSA configuration

From Figure 1. we can see that the ratio of the piston is equal

$$\alpha = \frac{A_b}{A_a} \tag{1}$$

fluid volumes of the head and rod piston side are equal

$$\begin{aligned} V_a &= V_{a0} + yA_a \\ V_b &= V_{b0} + (L-y)\alpha A_a \end{aligned} \tag{2}$$

and internal leakage flows are equal

$$q_{Li} = c_{Li}\left(p_a - p_b\right) \tag{3}$$

where A_a and A_b are effective areas of the head and rod position side, V_{a0} and V_{b0} are initial volumes, y is piston displacement, L is piston stroke, p_a and p_b are forward and return pressure, c_{Li} and is the internal leakage flow coefficient.

Assuming that an external leakage is negligible, the model of HSA can be described by following equations

$$m_t\ddot{y} = A_a p_a - A_b p_b - F_f(\dot{y}) - K_e y - F_{ext} \tag{4}$$

$$\dot{p}_a = \frac{\beta_e}{V_a(y)}\left(q_a - A_a\dot{y} - q_{Li} - q_{Lea}\right) \tag{5}$$

$$\dot{p}_b = \frac{\beta_e}{V_b(y)}\left(q_b - \alpha A_a\dot{y} - q_{Li} - q_{Leb}\right) \tag{6}$$

$$q_a = q_{sv1} - q_{sv2} = c_{v_1}\,\mathrm{sg}(x_v)\,\mathrm{sign}(p_s - p_a)\sqrt{|p_s - p_a|} - c_{v_2}\,\mathrm{sg}(-x_v)\,\mathrm{sign}(p_a - p_0)\sqrt{|p_a - p_0|} \tag{7}$$

$$q_b = q_{sv3} - q_{sv4} = c_{v_3}\,\mathrm{sg}(-x_v)\,\mathrm{sign}(p_s - p_b)\sqrt{|p_s - p_b|} - c_{v_4}\,\mathrm{sg}(x_v)\,\mathrm{sign}(p_b - p_0)\sqrt{|p_b - p_0|} \tag{8}$$

where m_t is total mass, K_e is load spring gradient, F_f friction force, F_{ext} disturbance force, x_v is spool displacement and $\mathrm{sg}(x)$ denotes function

$$sg(x) = \begin{cases} x & x \ge 0 \\ 0 & x < 0 \end{cases} \tag{9}$$

The state and input variables according equations (4)-(8) are

$$\begin{aligned} x(t) &= \left[x_1(t) \quad x_2(t) \quad x_3(t) \quad x_4(t)\right]^T = \\ &= \left[y(t) \quad \dot{y}(t) \quad p_a(t) \quad p_b(t)\right]^T \end{aligned} \tag{10}$$

$$u(t) = x_v(t) \tag{11}$$

However, if we introduce term of the load pressure

$$p_L = p_a - \alpha p_b \tag{12}$$

we can simplify dynamic equations. The HSA can be expressed in a more compact form using new state vector

$$\begin{aligned} x(t) &= \left[x_1(t) \quad x_2(t) \quad x_3(t)\right]^T = \\ &= \left[y(t) \quad \dot{y}(t) \quad p_L(t)\right]^T. \end{aligned} \tag{13}$$

Taking an operating point $x_0 = \left[y_0 \quad \dot{y}_0 \quad p_{L0}\right]^T$ and assuming dominance of the first order term from the Taylor series expansion the linearized continuous-time description of the reduced order is stated as follows

$$\dot{x}(t) = Ax(t) + Bu(t) \tag{14}$$

$$y(t) = Cx(t) \tag{15}$$

where

$$A = \begin{bmatrix} 0 & 1 & 0 \\ 0 & -\dfrac{B_c}{m_t} & \dfrac{A_a}{m_t} \\ 0 & -K_d & K_p \end{bmatrix}, B = \begin{bmatrix} 0 \\ 0 \\ K_x \end{bmatrix}, C = \begin{bmatrix} 1 & 0 & 0 \end{bmatrix} \tag{16}$$

The sensibility constants can be found as follows

$$K_d = A_a\left(\frac{\beta_e}{V_a} + \alpha^2\frac{\beta_e}{V_b}\right)^{-1}$$

$$K_p = \frac{\beta_e\left(K_{pA} - c_{Li}\left(1+\alpha^2\right)\right)}{V_a\left(1+\alpha^2\right)} + \frac{\alpha\beta_e\left(K_{pB}\alpha^2 + c_{Li}\left(1+\alpha^2\right)\right)}{V_b\left(1+\alpha^2\right)}$$

$$K_x = \frac{\beta_e}{V_a}K_{xA} - \alpha\frac{\beta_e}{V_b}K_{xB}$$

where K_{pA} and K_{pB} are the flow sensibility constants regarding the pressure at the cylinder chambers, K_{xA} and K_{xB} are the sensibility constants regarding the spool position.

3. OPTIMAL PROBLEM FORMULATION

For practical implementation in the HSA control system, we will consider the discretized system described by:

$$x_{k+1} = A_d x_k + B_d u_k \tag{17}$$

$$y_k = C x_k \tag{18}$$

in which $A_d = e^{Ah}$ $B_d = \int_0^h \left(e^{A\tau} d\tau\right) B$ and $h > 0$ is the sampling period, assuming $\omega_h = 2\pi / h$ is non-pathological sampling frequency. In other words, one cannot find any two eigenvalues of A with equal real parts and imaginary parts that differ by an integral multiple of ω_h. The state, input, and output vector at the sampled instant kh are x_k, u_k, y_k, respectively. Then, both $\left(A_d, C\right)$ and $\left(A_d, Q^{1/2}C\right)$ are observable and $\left(A_d, B_d\right)$ is controllable.

The event-triggered design is based on a periodic sampling with a non-pathological $h > 0$. We use $\hat{u}_k$ to represent the sampled value of u_k, that is

$$u_k = u_{kj},\ k \in \left[k_j, k_{j+1}\right), \tag{19}$$

where $\left\{k_j\right\}_0^\infty$ is a monotonically increasing sequence of the sampling time instants, and the control input is only updated at the discrete-time instants: $k_0, k_1, k_2, \ldots$

For the convenience of discussion, define the sampling error of the input data as

$$\Delta_k = \hat{u}_k - u_k. \tag{20}$$

Hence, the discrete-time system described by (17)-(18) can be rewritten as

$$x_{k+1} = A_d x_k + \left(B_d u_k + \Delta_k\right), \tag{21}$$

$$y_k = C x_k. \tag{22}$$

Further, the performance index for the discretize system described by (17)-(18) is

$$J_d\left(x_0\right) = \sum_{j=0}^{\infty} \left(y_i^T Q_d y_i + u_i^T R u_i\right), \tag{23}$$

where $Q_d = Qh$ and $R_d = Rh$. The optimal control law minimizing (23) is

$$u_k = -K_d^* x_k, \tag{24}$$

where the discrete optimal feedback gain matrix is

$$K_d^* = \left(R_d + B_d^T P_d^* B_d\right)^{-1} B_d^T P_d^* A_d, \tag{25}$$

and P_d^* is the unique symmetric positive definite solution to

$$A_d^T P_d^* A_d - P_d^* + C^T Q C - A_d^T P_d^* B_d K_d^* = 0. \tag{26}$$

Up to now, this known optimal control design method is mainly applicable to low order simple linear systems. In fact, for high order large scale systems, it is usually difficult to directly solve P_d^* from (26), which is nonlinear in P_d. Nevertheless, many efficient algorithms have been developed to numerically approximate the solution of (26). One of such algorithms was developed by Hewer [22]. By iteratively solving the Lyapunov equation

$$\left(A_d - B_d K_j\right)^T P_j \left(A_d - B_d K_j\right) + C^T Q C + K_j^T R K_j = 0, \tag{27}$$

which is linear in P_j, and updating K_j by

$$K_j = \left(R_d + B_d^T P_{j-1} B_d\right)^{-1} B_d^T P_{j-1} A_d, \tag{28}$$

the solution to the nonlinear equation (26) is numerically approximated. It has been concluded that sequence $\left\{P_j\right\}_{j=0}^\infty$ and $\left\{K_j\right\}_{j=0}^\infty$ computed from this algorithm converge to P_d^* and K_d^*, respectively. Moreover, for $j = 0, 1, \ldots$, the matrix $A_d - B_d K_j$ is a Schur matrix.

It should be noted that Hewer's algorithm is model based policy iteration (PI) algorithm which cannot be implemented when the system matrices are all unknown, since it is an algorithm relying on system parameters. In order to implement it, we will develop an adaptive optimal control algorithm for the discretized system (17)-(18) via output feedback which does not rely on the knowledge of the system matrices.

4. EVENT-TRIGGERED ADP-BASED CONTROL

Motivated by [21, 23] the extended sate equation using input/output sequence on time horizon $\left[k-N, k-1\right]$ can be written as

$$\begin{aligned} x_k &= A_d^N x_{k-N} + V\left(N\right) \bar{u}_{k-1,k-N}, \\ \bar{y}_{k-1,k-N} &= U\left(N\right) x_{k-N} + T\left(N\right) \bar{u}_{k-1,k-N}, \end{aligned} \tag{29}$$

where

$$\bar{\Delta}_k = \begin{bmatrix} \Delta_{k-1}^T & \Delta_{k-2}^T & \ldots & \Delta_{k-N}^T \end{bmatrix}^T,$$

$$\bar{u}_{k-1,k-N} = \begin{bmatrix} \hat{u}_{k-1}^T & \hat{u}_{k-2}^T & \ldots & \hat{u}_{k-N}^T \end{bmatrix}^T,$$

$$\bar{y}_{k-1,k-N} = \begin{bmatrix} y_{k-1}^T & y_{k-2}^T & \ldots & y_{k-N}^T \end{bmatrix}^T,$$

$$V\left(N\right) = \begin{bmatrix} B_d & A_d B_d & \ldots & A_d^{N-1} B_d \end{bmatrix}^T,$$

$$U\left(N\right) = \begin{bmatrix} \left(C A_d^{N-1}\right)^T & \left(C A_d^{N-2}\right)^T & \ldots & C^T \end{bmatrix}^T,$$

$$T\left(N\right) = \begin{bmatrix} 0 & CB_d & CA_d B_d & \ldots & CA_d^{N-2} B_d \\ 0 & 0 & CB_d & \ldots & CA_d^{N-3} B_d \\ \vdots & \vdots & \ddots & \vdots & \vdots \\ 0 & 0 & \ldots & 0 & CB_d \\ 0 & 0 & \ldots & 0 & 0 \end{bmatrix},$$

and $N = \max\left(\rho_u, \rho_v\right)$ is the observability index, where ρ_u is the minimum integer which can make $U\left(\rho_u\right)$ full column rank, ρ_v is the minimum integer which can make $V\left(\rho_v\right)$ full row rank.

A lemma about the uniqueness of state reconstruction is shown below.

Lemma 1. Given a controllable and observable system (17)-(18), the system state is obtained uniquely in terms of measured input/output sequences by

$$x_k = \Theta z_k \tag{30}$$

where $M_u = V\left(N\right) - M_y T\left(N\right)$, $M_y = A_d^N U^+\left(N\right)$, $\Theta = \begin{bmatrix} M_u & M_y \end{bmatrix}$, $z_k = \begin{bmatrix} \bar{u}_{k-1,k-N} & \bar{y}_{k-1,k-N} \end{bmatrix}^T \in \mathbb{R}^q$, where $q = N\left[\dim\left(u\right) + \dim\left(y\right)\right]$.

Now, based on (27)-(28) online output feedback learning strategy for linear discretized system(17)-(18) can be introduced in the form $u_k^* = -\bar{K}_d z_k$, providing suboptimal property of the closed-loop system. The discrete-time model (17) can be stated as follows

$$x_{k+1} = A_j x_k + B_d \left(K_j x_k + \hat{u}_k \right), \tag{31}$$

where $A_j = A_d - B_d K_j$. Setting $\bar{K}_j = K_j \Theta$ and $\bar{P}_j = \Theta^T P_j \Theta$ from (27) and (31) it can be obtained

$$\begin{aligned} & z_{k+1}^T \bar{P}_j z_{k+1} - z_k^T \bar{P}_j z_k = \\ & \phi_k^1 \operatorname{vec}\left(\bar{H}_j^1\right) + \phi_k^2 \operatorname{vec}\left(\bar{H}_j^2\right) - \left(y_k^T Q y_k + z_k^T \bar{K}_j^T R \bar{K}_j z_k\right) \end{aligned} \tag{32}$$

where

$\bar{H}_j^1 = B_d^T \bar{P}_j B_d$,

$\bar{H}_j^2 = B_d^T \bar{P}_j A_d \Theta$,

$\phi^1 = \hat{u}_k^T \otimes \hat{u}_k^T - \left(z_k^T \otimes z_k^T\right)\left(\bar{K}_j^T \otimes \bar{K}_j^T\right)$,

$\phi^2 = 2\left[\left(z_k^T \otimes z_k^T\right)\left(I_q \otimes \bar{K}_j^T\right) + \left(z_k^T \otimes \hat{u}_k^T\right)\right]$.

Some exploration noise e_k, which satisfies the persistent excitation condition [24,25], must be added into the input signal during the online learning phase. Then, $\bar{K}_{j+1}$ can be computed as

$$\bar{K}_{j+1} = \left(R_d + \bar{H}_j^1\right)^{-1} \bar{H}_j^2. \tag{33}$$

Here, (32) is called policy evaluation, which is used to uniquely solve $\bar{P}_j$, and (33) is policy improvement, which is used to update control gain $\bar{K}_{j+1}$. Then, we present our output feedback adaptive optimal control algorithm.

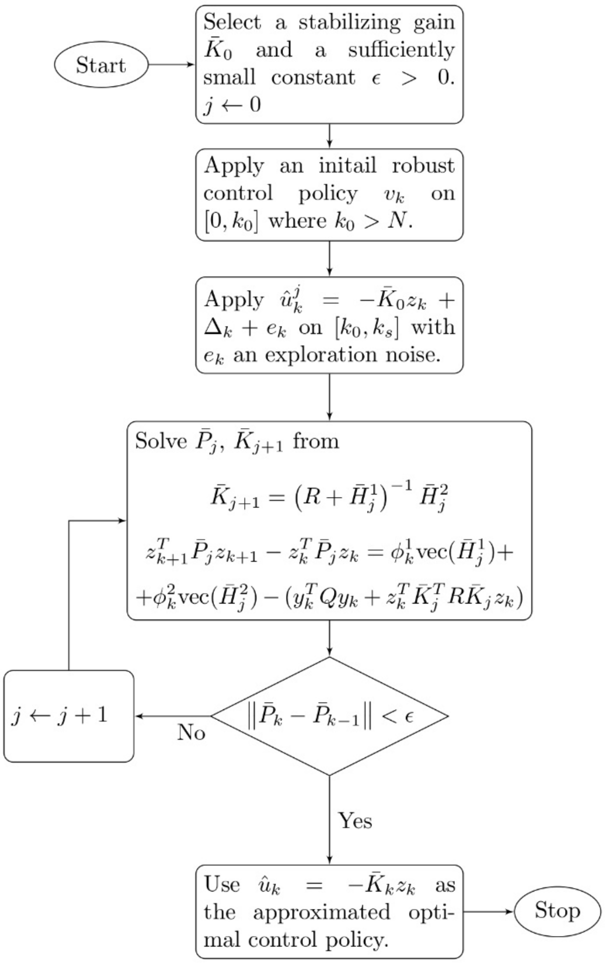

Figure 2: Flowchart of event-triggered ADP-based controller design

5. SIMULATIONS

A basic prerequisite for energy savings in processes of production, transportation, and energy consumption is a high-quality synthesis of optimal control algorithm. In this section, we conduct simulations on the valve-controlled hydraulic actuator to show the effectiveness of the output feedback event-triggered ADP control algorithm in the case with unknown system matrices and unmeasurable states.

Through iterative calculation, the approximated optimal control gain and performance index for the discrete-time system can be obtained. Furthermore, the discrete control policy is implement on the continuous plant by zero-order holder. Adapted sampling time is $h = 0.1s$.

The model parameters are: the viscous friction $B_c = 200 Ns/m$,the bulk modulus of the fluid $\beta_e = 2 \cdot 10^8 Pa$, $K_e = 0.1$ denotes the load sprint gradient, F_{ext} represents the load force disturbance on the piston, $p_s = 40 bar$ is the supply pressure, $p_0 = 1.5 bar$ is the tank pressure, $V_{a0} = V_{b0} = 9.4 \cdot 10^{-6} m^3$ represent initial chamber volumes, $L = 0.9 m$ is the piston stroke, $m = 20 kg$ is the piston mass.

The effective areas of the head and the rod side of the piston are $A_b = 2.3 \cdot 10^{-4} m^2$ and $A_a = 4.5 \cdot 10^{-4} m^2$, respectively. The internal leakage coefficient $c_{Li} = 5 \cdot 10^{-14}$ and discharge coefficients of valve orifices $c_{vi} = 1.15$.

For the purpose of demonstration the event-triggered ADP method with the HSA, the weight matrices, Q and R , are chosen to be identity matrices, the observability index is $N = 3$, initial state vector is $x_0 = \begin{bmatrix} 5 & -5 & 10 \end{bmatrix}$ and the convergence threshold ε is selected 0.1.

It should be noted that our event-driven ADP control design does not require exact knowledge of the system matrices. However, only for numerical verification via simulation, it is assumed that the system matrices are known.

Figure 3. shows the errors between $\bar{P}_j$ and $\bar{P}_d^*$, and $\bar{K}_j$ and $\bar{K}_d^*$, which indicates convergence of $\bar{P}_j$ and $\bar{K}_j$.

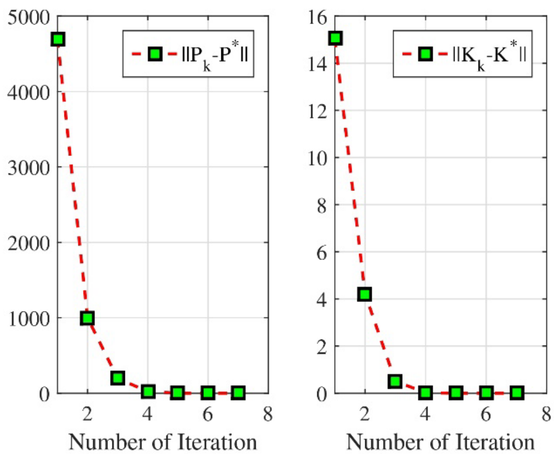

Figure 3: Convergence of $\bar{P}_j$ and $\bar{K}_j$ to their respective optimal values $\bar{P}^*$ and $\bar{K}^*$ during the learning process

The evolution of the maximum cost for HSA is shown in Figure 4, where V_1 is maximum cost by using the initial control policy, and V_7 is the maximum cost by using control policy after seven iterations. It can be seen that the approximated cost function V_7 has been remarkably reduced relative to the initial cost V_1

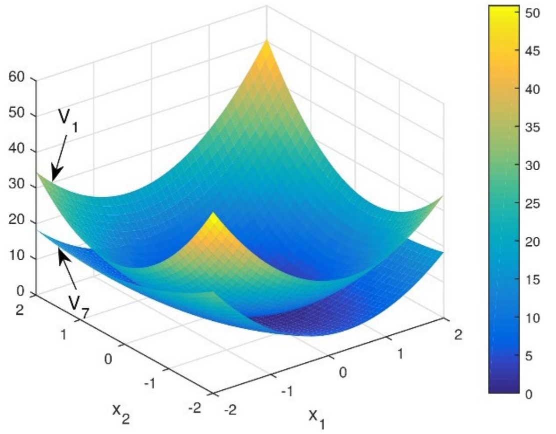

Figure 4: Comparison of the cost functions during learning

The improved control policy and initial control policy are compared in Figure 5.

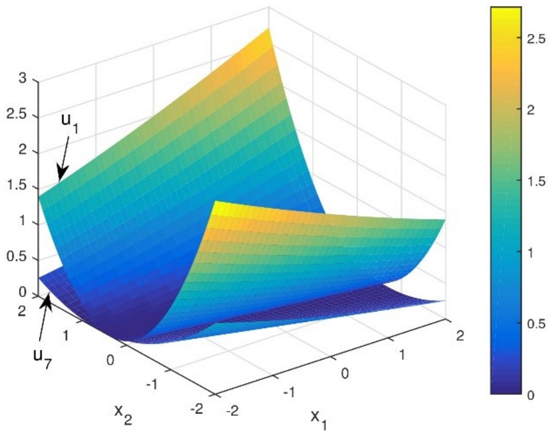

Figure 5: Comparison of the control polices during the learning process

Figure 8 shows the control input and states of HSA system described by (17)-(18) by using the ADP-based controller with periodic sampling.

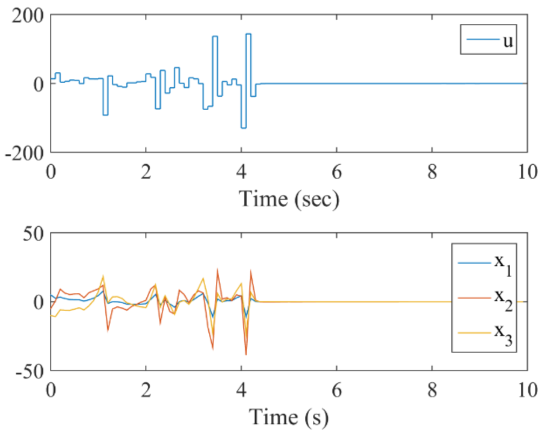

Figure 6: Control input and states of the HSA model by using the ADP-based control

To illustrate the benefits of the event-triggered ADP method, the control input and the states obtained by using the event-triggered ADP controller is shown in Figure 7.

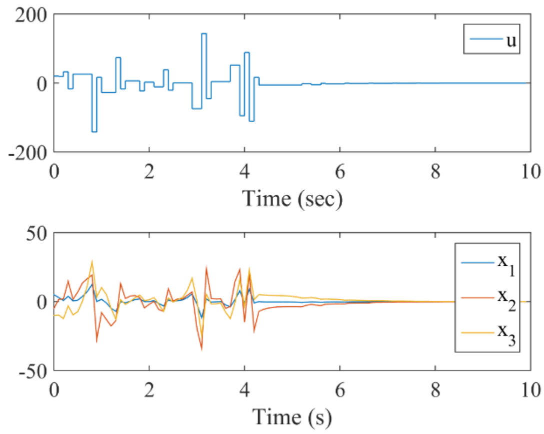

Figure 7: Control input and states of the HSA model by using the event-triggered ADP-based control

The comparison of sampling numbers by using the event-triggered ADP controller versus the ADP controller with periodic sampling is shown in Figure 8.

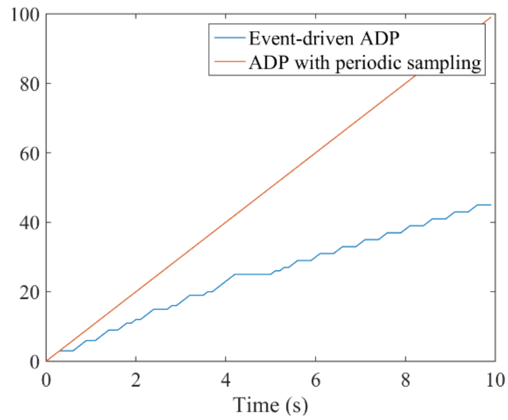

Figure 8: Comparison of the total sampling numbers

It can be observed that similar control effects have been achieved by two methods, however, for the event-triggered ADP method, the control input is updated only when squared norm of the triggered error reaches the threshold, and it is kept constant otherwise. It is also show that about 54% communication between the controller and the HSA is reduced by using the event-triggered ADP method. The sequence of steps of event-triggered samples is shown in Figure 9.

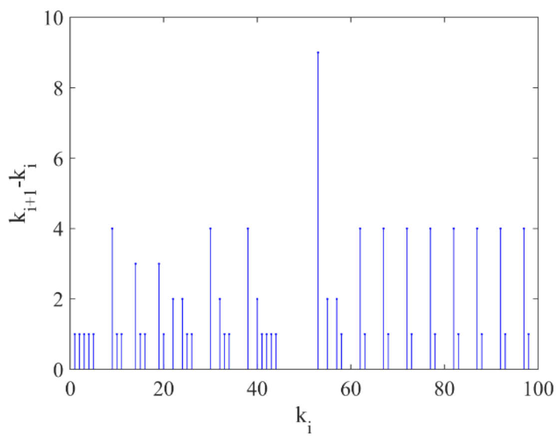

Figure 9: Sequence of steps of event-triggered sampling

6. CONCLUSIONS

The paper applies the event-triggered data-driven optimal controller based on adaptive dynamic programming to the hydraulic servo actuator with a completely unknown dynamic. Using the output feedback and state reconstruction, we avoided measuring HSA states. The controller based on adaptive dynamic programming is designed using input and output measurements. The event-triggered strategy has reduced the number of controller updates. Simulation results demonstrate the validity and effectiveness of the proposed control approach.

ACKNOWLEDGEMENTS

This research has been supported in part by the Serbian Ministry of Science, Technological Development and Innovations (451-03-47/2023-01/200108).

REFERENCES

[1] J. Vyas, B. Gopalsamy and H. Joshi, “Electro-Hydraulic Actuation Systems: Design, Testing,, Identification and Validation”, Springer, Singapore (2019)

[2] A. Vacca and G. Franzoni, “Hydraulic Fluid Power: Fundamentals, Applications, and Circuit Design”, John Wiley & Sons, New Jersey (USA), (2019)

[3] N. Nedic, V. Stojanovic and V. Djordjevic, “Optimal control of hydraulically driven parallel robot platform based on firefly algorithm”, Nonlinear Dyn., Vol. 85, pp. 1457–1473, (2015)

[4] V. Stojanvoic, N. Nedic, D. Prsic, Lj. Dubnonjic and V. Djordjevic, “Application of cuckoo search algorithm to constrained control problem of a parallel robot platform”, Int. J. Adv. Manuf. Technol., Vol. 87, pp. 2497–2507, (2016)

[5] V. Filipovic, N. Nedic and V. Stojanovic, “Robust identification of pneumatic servo actuators in the real situations”, Forsch. Ingenieurwes., Vol. 75, pp. 183–196, (2011)

[6] M. Jelali and A. Kroll, “Hydraulic Servo-Systems: Modelling, Identification and Control”, Springer, London (UK), (2003)

[7] F. L. Lewis and D. Liu, “Reinforcement Learning and Approximate Dynamic Programming for Feedback Control”, John Wiley & Sons, New Jersey (USA), (2013)

[8] F. L. Lewis, D. Vrabie and V. L. Syrmos, “Optimal Control”, John Wiley & Sons, New Jersey (USA), (2012)

[9] J. J. Murray, C. J. Cox, G. G. Lendaris and R. Saeks, “Adaptive dynamic programming”, IEEE Trans. Syst. Man Cybern. Part C Appl. Rev, Vol. 32, pp. 140–153, (2002)

[10] P.J. Werbos, “Beyond Regression: New Tools for Prediction and Analysis in the Behavioral Sciences”, PhD Thesis, Harvard University (USA), (1974)

[11] W. Gao and Z. P. Jiang, “Learning-based adaptive optimal tracking control of strict-feedback nonlinear systems”, IEEE Trans. Neural Networks Learn. Syst., Vol. 29, pp. 2614–2624, (2017)

[12] T. Bian and Z.P. Jiang, “Value iteration and adaptive dynamic programming for data-driven adaptive optimal control design”, Automatica, Vol. 71, pp. 348–360, (2016)

[13] W. Gao, Y. Jiang, Z. P. Jiang and T. Chai, “Output-feedback adaptive optimal control of interconnected systems based on robust adaptive dynamic programming”, Automatica, Vol.72, pp. 37–45, (2016)

[14] K. J. Åstrom, “Event based control” in Analysis and Design of Nonlinear Control Systems, Springer, Berlin, Heidelberg (Germany), (2007)

[15] B. Jiang, H. R. Karimi, Y. Kao and C. Gao, “Takagi-Sugeno model based event-triggered fuzzy sliding mode control of networked control systems with semi-Markovian switchings,”, IEEE Trans. Fuzzy Syst., Vol. 28, pp. 673–683, (2012)

[16] Y. S. Ma, W. W Che, C. Deng, and Z. G. Wu, “Observer-based event-triggered containment control for MASs under DoS attacks”, IEEE Trans. Cybern., Vol. 52, pp. 13156–13167, (2021)

[17] X. Wang, H. R. Karimi, M. Shen, D. Liu, L. W. Li and J. Shi, “Neural network-based event-triggered data-driven control of disturbed nonlinear systems with quantized input”, Neural Networks, Vol.156, pp. 152–159, (2022)

[18] M. Shen, Y. Gu, J. H. Park, Y. Yi and W. W. Che, “Composite control of linear systems with eventtriggered inputs and outputs”, IEEE Trans. Circuits Syst. II Express Briefs, Vol.69, pp. 1154–1158, (2021)

[19] R. Pintelon and J. Schoukens, “System Identification: A Frequency Domain Approach”, John Wiley & Sons, New Jersey (USA), (2012)

[20] C. R. Rojas, J. C. Aguero, J. S. Welsh, G. C. Goodwin and A. Feuer, “Robustness in experiment design”, IEEE Trans. Autom. Control, Vol. 57, pp. 860–874, (2011)

[21] F. L. Lewis and K. G. Vamvoudakis, “Reinforcement learning for partially observable dynamic processes: Adaptive dynamic programming using measured output data”, IEEE Trans. Syst. Man Cybern. Part B Cybern., Vol. 41, pp. 14–25, (2010)

[22] G. Hewer, “An iterative technique for the computation of the steady state gains for the discrete optimal regulator”, IEEE Trans. Autom. Control, Vol. 16, pp. 382–384, (1971)

[23] W. Gao, Y. Jiang, Z. P. Jiang and T. Chai, “Adaptive and optimal output feedback control of linear systems: An adaptive dynamic programming approach”, Proceeding of the 11th World Congress on Intelligent Control and Automation, Shenyang, (China), 29 June 4 July 2014, pp. 2085-2090, (2014)

[24] K. J. Åstrom and B. Wittenmark, “Adaptive Control”, Dover Publication, New York (USA), (2008)

[25] P. A. Ioannou and J. Sun, “Robust Adaptive Control”, Dover Publication, New York (USA), (2012)

Design and Implementation of an Aeropendulum Controller via Loop Shaping

Luka Filipović[1], Milan Ristanović[1*], Dušan Božić[1]
[1] Faculty of Mechanical Engineering, University of Belgrade, Belgrade (Serbia)

This paper presents a robust control design for an aeropendulum system using the loop shaping method. We describe the system setup, derive its mathematical model, and conduct system identification to capture its dynamics accurately. The loop shaping technique is then used to design a controller, considering system uncertainties and noise. The effectiveness of the controller is validated through experiments, demonstrating robust performance in the face of time delay and model uncertainties.

Keywords: Loop Shaping, Robust Control, Aeropendulum

1. INTRODUCTION

Control systems engineering is a discipline of immense complexity, with the design of controllers for non-linear systems presenting a significant challenge. A particular case in point is the aeropendulum, a dynamic mechanical setup that offers a robust platform for studying the principles of aerodynamics and control systems.

In the field of aeropendulum control, diverse developments have been observed. Robust control strategies, like the H_∞ control design proposed by [2], effectively manage system uncertainties. This research focused on controlling the angular position of a pendulum rod using motorized propellers and presented simulations to validate the efficiency of their applied methodology. Other work, like that of [6], applied a robust position control and disturbance compensation strategy using a soft computing paradigm. This study showed the superior time optimal control behavior of their proposed controller through real-time experiments, outperforming fixed gain controllers. The use of an aeropendulum system as a hands-on experiment for control systems engineering was also explored by [3]. Their teaching approach allowed students to design and test both classical and modern controllers, demonstrating the practicality of various control strategies. Moreover, advancements have been made in integrating fuzzy logic into control designs. A notable study by [1] designed an adaptive fuzzy controller for a twin rotor MIMO system, proving its superior performance compared to non-adaptive fuzzy and PID controllers through experimental results. Another significant work by [4] used Takagi-Sugeno fuzzy modeling for output feedback control design of an aeropendulum. Their observer-based fuzzy regulator was validated via MATLAB simulations, showcasing its effectiveness. Further, [8] proposed a novel fuzzy PID controller for the angular position control of a non-linear propeller pendulum system. The time-varying gains of their controller outperformed classical PID controller in reference tracking, particularly in the presence of system uncertainties and external disturbances.

This paper focuses on the design of an effective controller for an aeropendulum using the loop shaping method, a technique highly valued for its capability to handle system uncertainties and maintain the robustness of control systems.

The first section of this paper provides a detailed description of the laboratory equipment used in our study. This equipment, while being a relatively low-cost solution, is professionally designed and assembled, making it an ideal educational tool for control systems engineering.

Subsequently, we turn to the mathematical modeling of the aeropendulum system. We derive this model based on the law of change of kinetic moment, which is essential for understanding the complex dynamics of the aeropendulum. To enable the use of linear control design techniques, we then proceed to linearize our non-linear system.

Recognizing the crucial role of accurate system identification, we then focus on identifying the aeropendulum system and deriving its transfer function. Given that the mathematical model involves unknown coefficients, we provide a comprehensive explanation of how we identify these variables.

After successfully identifying the model, we focus on our primary aim: designing a controller for the aeropendulum using loop shaping. We deeply examine the mechanism of loop shaping, a technique that carefully tailors the system's feedback to meet the set objectives. Our final aim is to develop a controller that ensures both system stability and acceptable performance in different conditions. To substantiate the effectiveness of our proposed design, we compare simulated and experimental results in the closing section of our paper, bridging the gap between theoretical study and practical application.

2. EXPERIMENTAL SETUP

Aeropendulum, on which the experiment was done, consists of an aluminum rod, that length is $l = 0.5$m and the propeller attached at the end of the rod. The rotation of the elise is used to control the angle of the pendulum. It is connected to the brushless DC (BDC) motor whose working voltage is 7.4V and maximal current is 1.8A. Because the microcontroller was used for motor control and its supply voltage is 3.3V it is necessary to use a driver. For this purpose, the H bridge driver was constructed with integrated circuit L6203 (DMOS Full Bridge Driver) as its main component. For angle measurement Spectrol 149 potentiometer is used. Its output is connected to an instrumentation amplifier with MCP6024 'rail-to-rail in-

*Corresponding author: Kraljice Marije 16, 11120 Belgrade (Serbia) and mristanovic@mas.bg.ac.rs

put/output' operational amplifier. In this way, not only is measured output amplified, but also the calibration is simplified because two trimmer helipot potentiometers enable easy shift and gain settings. We calibrated the sensor so that a zero angle means 0V and an angle of 90° is 3V. For control algorithm implementation microcontroller LM4F232H5QD from Texas Instruments is used. In order to give the set value and to maintain readings of the angle, the controller was connected with Matlab/Simulink on a computer through a UART communication channel. Considering the noise in the measured signal, largely stemming from the PWM signal and commutator sparking on the motor, we incorporated a digital filter.

The main components of the experimental setup are shown in Figure 1, with number descriptions in Table 1.

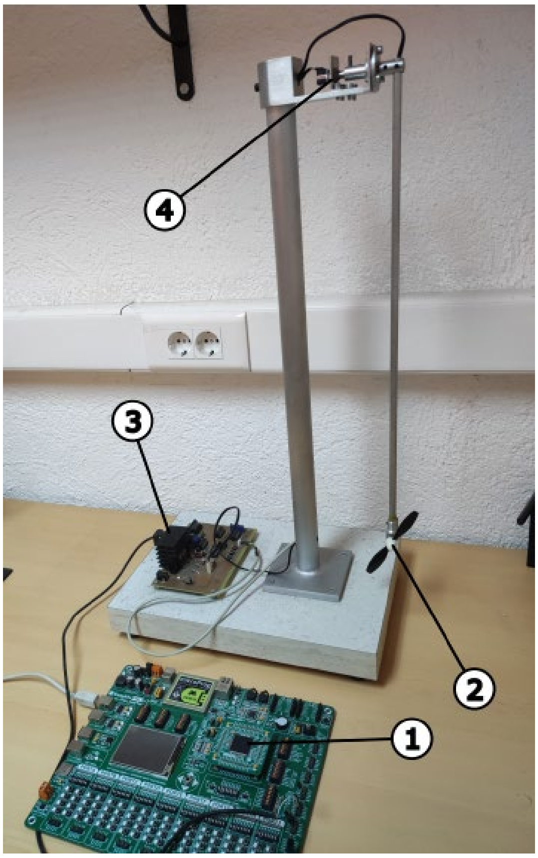

Figure 1: Experimental setup

Table 1: Main components of experimental setup

Number	Name
1	ARM Cortex M4 microcontroller
2	BDC Motor with propeller
3	PCB (H-bridge and MCP6024)
4	Potentiometer for angle measurement

3. MATHEMATICAL MODEL

In order to generate a controller and calculate its gains we need a mathematical model of a system in a transfer function form. First, we need assumptions that will simplify the physical model of the pendulum so that the differential equations would contain the important physicality of a system but the smallest order possible. We assumed that: the system has one degree of freedom - the angle between the rod and vertical line ϕ; there is no deformation, parts are rigid; angle measurements are without delay; thrust force is proportional to voltage. We derive a mathematical model from the law of change of kinetic momentum:

$$\frac{d\vec{L}_O}{dt} = \sum_{i=1}^{n} \vec{M}_O^{\vec{F}_i^e}, \tag{1}$$

where $\vec{L}_O$ is a vector of kinetic momentum of the system, $\vec{M}_O^{\vec{F}_i^e}$ is a momentum vector from pole O of an i-th external force, or in scalar form through the axis of rotation:

$$\frac{dL_{Ox}}{dt} = \sum_{i=1}^{n} M_{Ox}^{\vec{F}_i^e}. \tag{2}$$

Knowing that the kinetic momentum of a rigid body around the x-axis is the moment of inertia times angular speed $L_x = J_x \omega_x = J_x \dot{\varphi}$ and the external forces momentums (Fig. 2) differential equation is:

$$J_x \ddot{\varphi} = lF_p - mgd_1 \sin\varphi - a\dot{\varphi} - b\dot{\varphi}\left|\dot{\varphi}\right| - c\dot{\varphi}\operatorname{sgn}\left(\dot{\varphi}\right), \tag{3}$$

where $a\dot{\varphi}$ is linear viscous trust in bearings, $b\dot{\varphi}\left|\dot{\varphi}\right|$ - air trust, $c\dot{\varphi}\operatorname{sgn}\left(\dot{\varphi}\right)$ - dry trust in bearings and potentiometer, a, b, c are friction linear parameters, m is system's mass, g is gravity constant, F_p is propulsion force, $d_1 = l/2$ half the rod's length, J_x moment of inertia of the system and φ is the angle between rod and vertical line. We can further simplify by assuming that a single linear attenuation $c\dot{\varphi}$ can substitute these three trust components:

$$J_x \ddot{\varphi} = lF_p - mgd_1 \sin\varphi - c\dot{\varphi}. \tag{4}$$

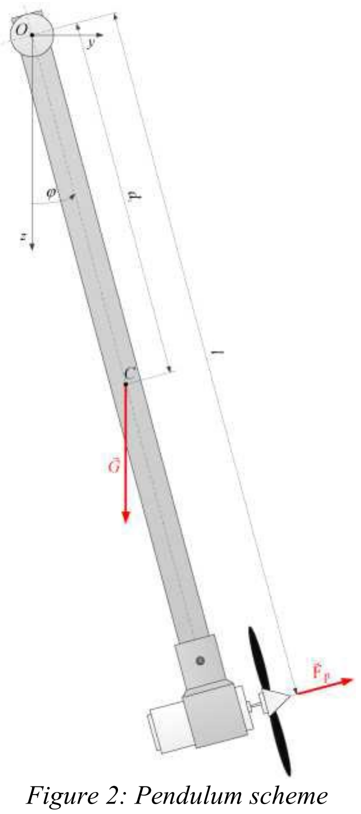

Figure 2: Pendulum scheme

As mentioned above, trust force is linearly dependent on motor drive voltage $F_p = Kv$ and for small enough angles the approximation $\sin(\varphi) \approx \varphi$ is justified (for $\varphi < 30°$ error is 2.36%) so the final differential equation is:

$$J_x\ddot{\varphi} + c\dot{\varphi} + mgd_1\varphi = lKv, \quad (5)$$

from which the transfer function can be easily inferred after the Laplace transformation:

$$G(s) = \frac{V(s)}{\Phi(s)} = \frac{lK}{J_x s^2 + cs + mgd_1}, \quad (6)$$

where $V(s)$ is the left Laplace transformation of motor voltage (input variable) and $\Phi(s)$ is the left Laplace transformation of pendulum angle (output variable). Now we know that the system is second order with no finite zero, but the coefficients must be somehow determined. For this purpose identification method was used.

4. SYSTEM IDENTIFICATION

System identification is a process of getting a mathematical model of a system based on collected data of the system's responses [5]. The idea is that if we know the inputs and corresponding outputs of a system we are able to determine a convenient model. This is a black box approach, when nothing about the system is known and gaining good results is hard. The grey box method uses a priori knowledge about the system and thus simplifies and improves the identification method. As it was shown, based on knowledge of mechanics, it is clear that our system is second order without finite zeroes. So, we know the structure but do not know the coefficients in the differential equation (transfer function). Grey box system identification is to be used.

Step input is the simplest input one can give to the system and extract important dynamical characteristics (time constant, rise time, settling time...). That is why it is used extensively as an input signal in system identification. In order to collect as much data as possible it is better to use more than one step signal (Fig. 3). In our case, the system is nonlinear in the whole range of angles. To stay in the linear zone, step angles are not too big and as a nominal angle value the $\varphi = 15°$ (middle of the range $0° < \varphi < 30°$) is chosen. Similar to identification data, the validation data is made, but with different order and size of step inputs, in order to check if the identification gave a successful overall model and not only for trained data.

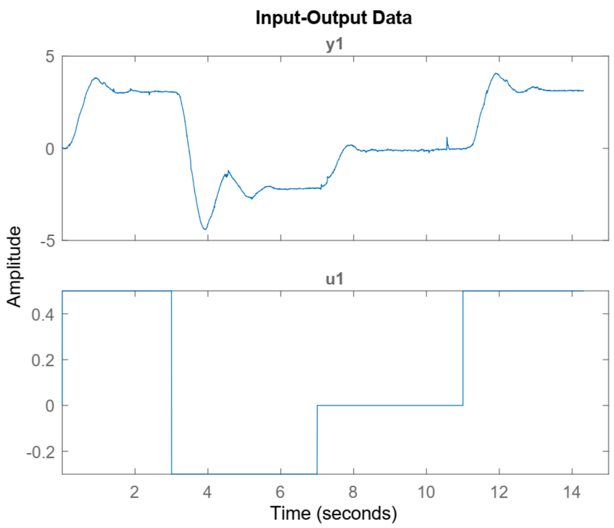

Figure 3: Input-output data for system identification

Using numerical methods for fitting the best possible second order dynamical system to recorded data (Fig.3) transfer function:

$$G(s) = e^{-0.19s}\frac{6.114}{0.04593s^2 + 0.1367s + 1} \quad (7)$$

was inferred. As shown on Fig.4 there is 87.49% fit to the validation data. Therefore, the transfer function from (7) is considered as valid mathematical model for our system.

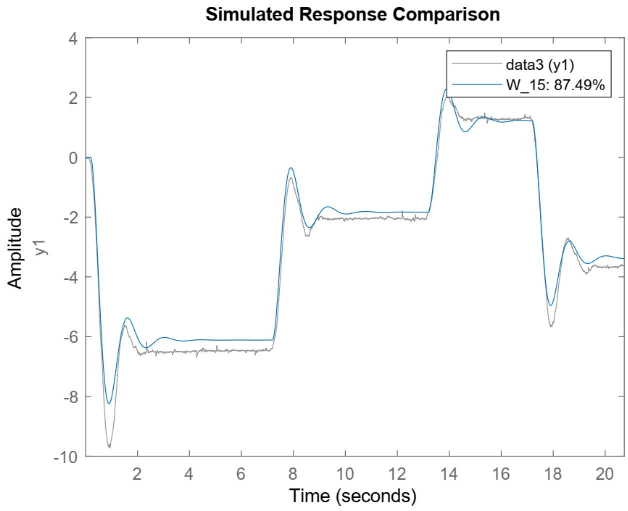

Figure 4: Fit to validation data of G transfer function

5. CONTROL ALGORITHM

In the previous section, the model of an uncontrolled object was derived (7). As we can see, it has a time delay of $\theta = 0.19s$ so the frequency domain (where this only changes phase but gain remains the same) is more natural to use.

To effectively manage the time delay, we employed the Padé approximation. This method offers a finite-dimensional approximation of time delays in linear systems, making it particularly useful for our scenario.

By employing MATLAB's built-in function for Padé approximation, we were able to derive second-order transfer function, as it produced an accurate match to the delay $e^{-0.19s}$ up to the bandwidth frequency, as follows:

$$G_{delay}(s) = \frac{s^2 - 31.58s + 332.4}{s^2 + 31.58s + 332.4}. \quad (8)$$

This approximation allowed us to seamlessly integrate the delay into our control design process.

As a reference control, an I controller was designed with a desired phase margin of $\varphi_m = 60°$ (because of the time delay, greater robustness is necessary) with cross frequency chosen between $\omega_{\pi/2}$ and $\omega_{\pi-\varphi_m}$. This way the calculated gain is $K_I = 0.1387$.

5.1. Loop shaping design

The primary objective of our loop shaping design approach involves carefully molding the open-loop frequency response, L, to meet certain desired characteristics. The block diagram of one degree-of-freedom feedback control system is presented in Figure 5.

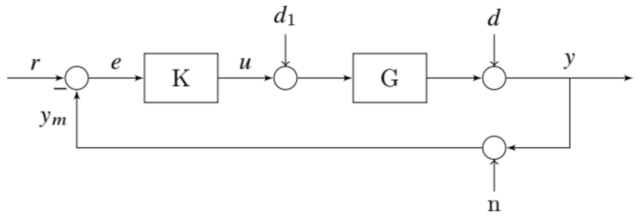

Figure 5: Block diagram of the feedback control system

From the block diagram in Figure 5. we derive the following equations:

$$y = TGKr + Sd + SGd_1 - Tn, \quad (9)$$

$$e = r - y = Sr - Sd + Tn + SGd_1, \quad (10)$$

$$u = KSr - Ksn - KSd + Sd_1 \quad (11)$$

where y is output, r is the reference input, y_m is measured output, n it the measurement noise, d is output's disturbance, d_1 it the input's disturbance. Also, sensitivity function S and complementary sensitivity function T are defined as:

$$S = (I + GK)^{-1} = (I + L)^{-1}, \quad (12)$$

$$T = (I + GK)^{-1} GK = (I + L)^{-1} L. \quad (13)$$

The relation between sensitivity S and complementary sensitivity function T is given by the formula:

$$S + T = I \quad (14)$$

The sensitivity function provides insights into the robustness of a control system with respect to modeling errors, disturbances, and noise, while the complementary sensitivity function provides information about the tracking performance of the system. A small sensitivity implies that the system is robust to uncertainties and disturbances. Conversely, a large sensitivity means that the system is sensitive to uncertainties and disturbances. A small value of T implies poor tracking performance, whereas a large T implies good tracking of reference signal. For the error e to be minimized with respect to the reference signal r and disturbances d and d_1, S must be small, as inferred from equation (10). To diminish the impact of noise n on the error e, we aim for a smaller T. However, from relation (14), it's apparent that we can't achieve minimal values for both S and T at the same frequency simultaneously. Usually, reference and disturbance signals are low frequency signals, so in that range S function has to be small, and noise is high frequency signal, and in that region, T has to be small. The fundamental trade-off in control system design can be understood from the sensitivity complementary equation 14. Improving disturbance rejection (i.e., reducing S) generally leads to a larger T, which may increase the system's sensitivity to measurement noise. Conversely, improving noise rejection (i.e., reducing T) may increase S, thereby making the system more sensitive to model uncertainties and external disturbances. Our goal is to design controller to balance certain trade-offs. By adjusting the loop transfer function in a specific frequency domain, we can achieve the required levels of stability and performance. The Loop Shaping process involves making sure the magnitudes of the sensitivity function S and complementary sensitivity function T follow certain guidelines over different frequency ranges.

The general idea of loop shaping is based on so-called Inverse-based controlled design, where the goal is to make a loop shape which has a slope of -20 dB/decade throughout the frequency range, namely:

$$L(s) = \frac{\omega_c}{s}, \quad (15)$$

where ω_c is desired gain crossover frequency. If the plant is defined as G, then corresponding controller to (15) is:

$$K(s) = \frac{\omega_c}{s} G^{-1}(s). \quad (16)$$

One of the key disadvantages of this method is that it often leads to controllers that are non-causal and improper, meaning that they can have more zeros than poles [7]. These types of controllers are physically unrealizable and can lead to unstable systems. A viable strategy to overcome these drawbacks involves approximating the inverse plant with a transfer function that is proper, i.e., it has the same or fewer zeros than poles. Although such an approximation inherently implies a trade-off between the fidelity of the representation and the complexity of the system, it can lead to controllers that are both causal and implementable. This approach ensures our controller is practical by mirroring the inverse behavior of the plant up to a chosen frequency. Following this, the controller parameters can be finely tuned to meet the desired system performance specifications.

Specifically, we seek to achieve a slope of approximately -20 dB/decade in the crossover region, increasing to -40 dB/decade or steeper beyond this frequency. This ensures adequate system responsiveness without unnecessary sensitivity to high-frequency noise. Moreover, high gain at low frequencies can be maintained to enhance the capabilities of reference tracking and disturbance rejection. Simultaneously, it is ideal to match the gain crossover frequency with the desired closed-loop bandwidth to ensure optimal system performance.

However, due to the time delay in our plant, G, which contributes an additional phase shift of $-\theta\omega$, we need to limit the crossover frequency to approximately $\omega_c < 1/\theta \approx 5\,\text{rad/s}$.

Loop shaping is inherently an iterative design process. Given the trade-off between robustness and performance, a single controller design might not fulfill all desired objectives. Consequently, we experimented with designing multiple controllers, each with a different crossover frequency within the permissible limit.

Firstly, we derived approximated transfer function of our inverted plant (17) so that they have good matching for frequencies up to about 10 rad/s. That is shown in Figure 6.

$$G_{ax.}^{-1}(s) = \frac{0.04593s^2 + 0.1367s + 1}{0.0016s^2 + 0.02s + 1} \quad (17)$$

After that, using equation (16), we obtained desired controllers for three different crossover frequencies, $\omega_{c1} = 1\,\text{rad/s}$, $\omega_{c2} = 2\,\text{rad/s}$ and $\omega_{c3} = 3\,\text{rad/s}$:

$$K_{LS1} = \frac{0.04593s^2 + 0.1367s + 1}{0.009782s^3 + 0.1223s^2 + 6.114s}, \quad (18)$$

$$K_{LS2} = \frac{0.09186s^2 + 0.2734s + 2}{0.009782s^3 + 0.1223s^2 + 6.114s}, \quad (19)$$

$$K_{LS3} = \frac{0.1378s^2 + 0.4101s + 3}{0.009782s^3 + 0.1223s^2 + 6.114s} \tag{20}$$

where K_{LS1} is controller for ω_{c1}, K_{LS2} controller for ω_{c2} and K_{LS3} controller for ω_{c3}.

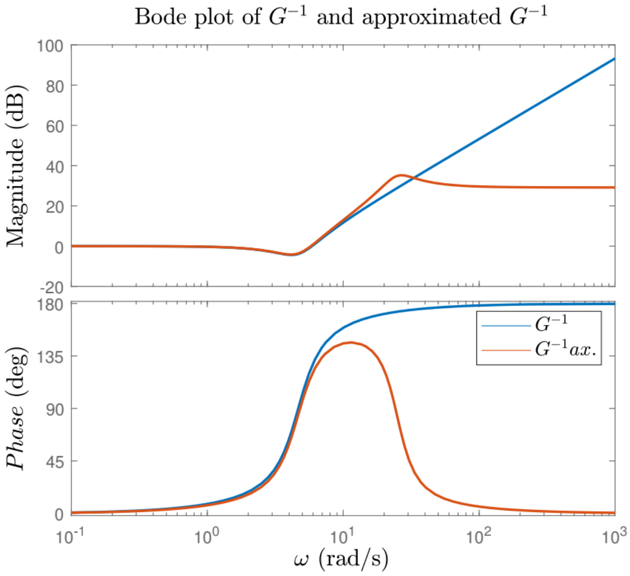

Figure 6: Bode plot of G^{-1} and approximated G^{-1}

From Figures 7, 8, 9 and 10 we obtain following parameters, shown in Table 2, for different crossover frequencies ω_c:

Table 2: System performance parameters for different crossover frequencies ω_c

	ω_{c1}	ω_{c2}	ω_{c3}	Units
G_m	16.7	10.7	7.18	dB
P_m	77.9	65.6	53.4	Degree
M_S	1.67	3.48	5.64	dB
M_T	-0.0008	-0.03	1.23	dB
t_r	1.65	0.512	0.252	seconds
t_s	3.22	1.03	1.47	seconds
PO	≈ 0	0.168	1.5	%

where G_m is the gain margin, P_m is phase margin, M_S is maximum value of sensitivity function, T_S is maximum value of complementary sensitivity function, t_r is rise time, t_s is settling time, PO is overshoot. M_S is typically required to be less than 6 dB, and T_S less than 1.25 dB [7]. Large values of M_S and M_T indicate bad performance and robustness of the system. Based on the obtained results, we selected controller K_{LS2} due to better performance compared to K_{LS1} and similar performance to K_{LS3}, but with a smaller overshoot (PO). Furthermore, K_{LS2} exhibited smaller values of M_S and T_S compared to K_{LS3}, making it a more robust choice.

Two main issues with this controller design are: first, it was designed based on an open loop of the system, without the direct insight of closed loop response and second, it has no precise algorithm as to how to choose the controller, but rather it is based on trial and error approach.

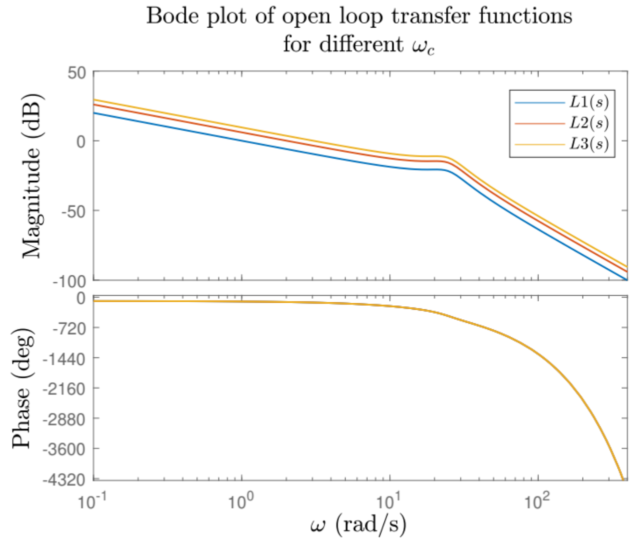

Figure 7: Bode plot of open loop transfer functions for different crossover frequencies ω_c

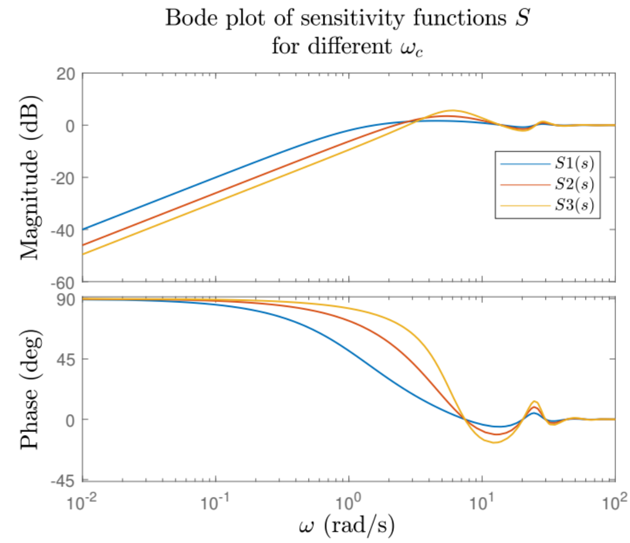

Figure 8: Bode plot of sensitivity functions S for different crossover frequencies ω_c

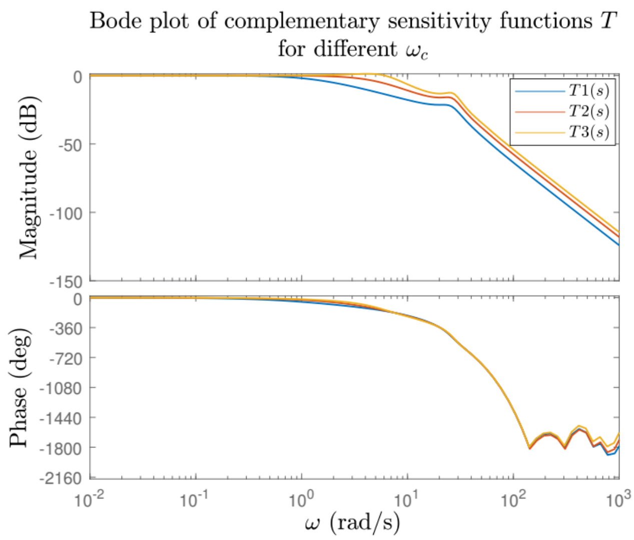

Figure 9: Bode plot of complementary sensitivity functions S for different crossover frequencies ω_c

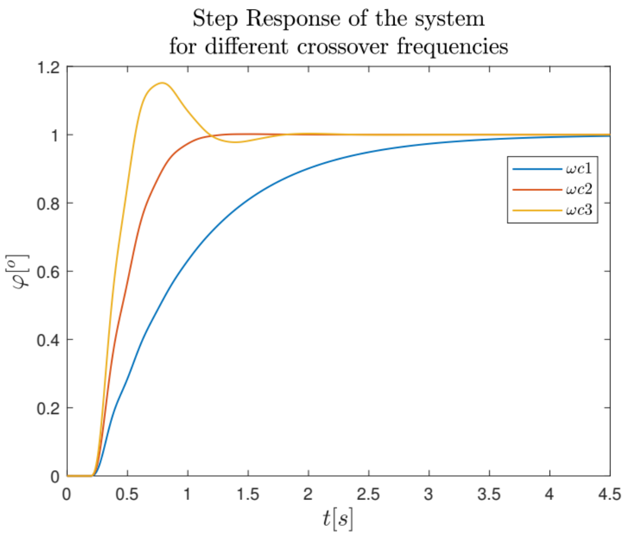

Figure 10: Step response simulation of the system for different crossover frequencies ω_c

6. EXPERIMENTAL RESULTS

For the experiments, the controllers were discretized and implemented into a microcontroller as a digital filter in direct canonical form 1, with a sample time of 0.01s.

The first experiment was a step change of the desired angle of 5 degrees from 15° to 20°. The response angle with generated control input to the system with I controller is shown in figure 11 and with Loop-shaped controller in figure 12. It is clear that I controlled system was slower, but it does not overshoot. The Loop-shaped controller has a faster response but with a cost of slight overshoot.

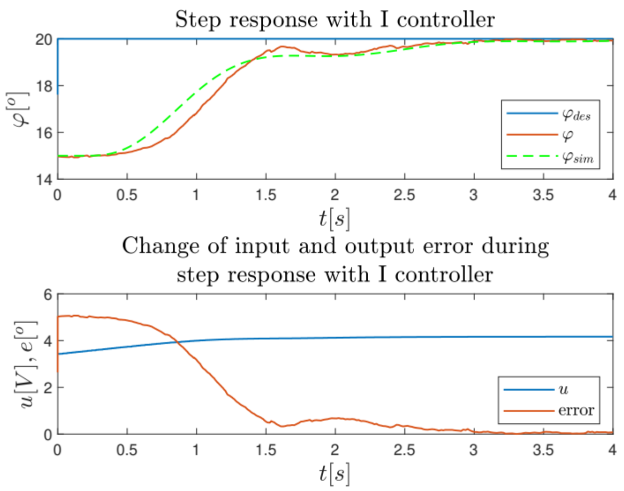

Figure 11: Step response and generated input for an angle change of 5° with I controlled system

The second experiment was disturbance response. The system was put out for approximately 3o from its nominal value. The resulting response with I controlled system is shown in figure 13 and with the Loop-shaped controller in figure 14. Again the I controller was slower to regain the desired angle compared to the Loop-shaped controller.

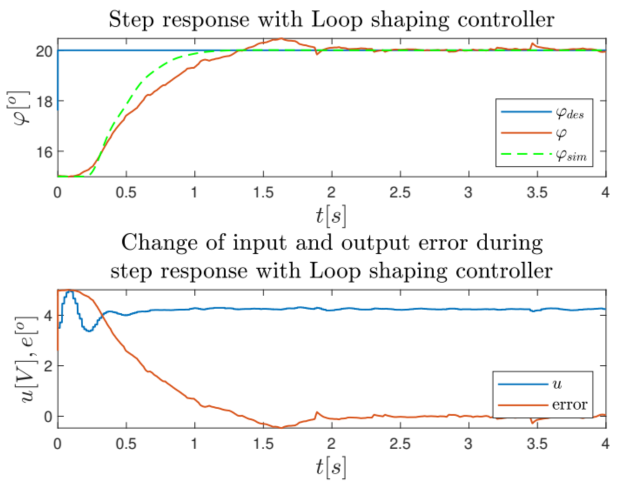

Figure 12: Step response and generated input for an angle change of 5° with Loop-shaped controller

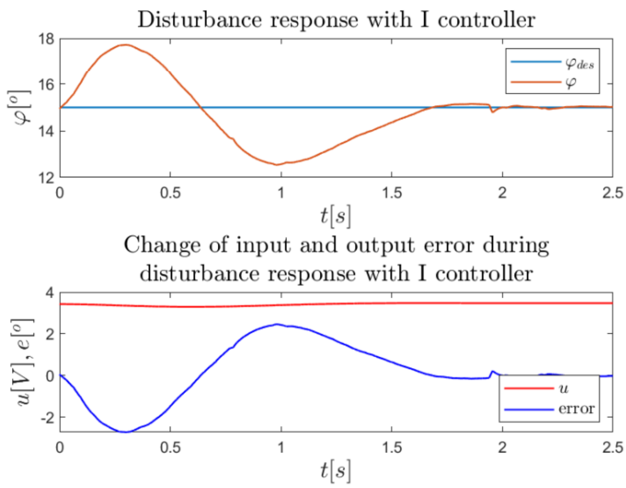

Figure 13: Disturbance response and generated input for I controlled system

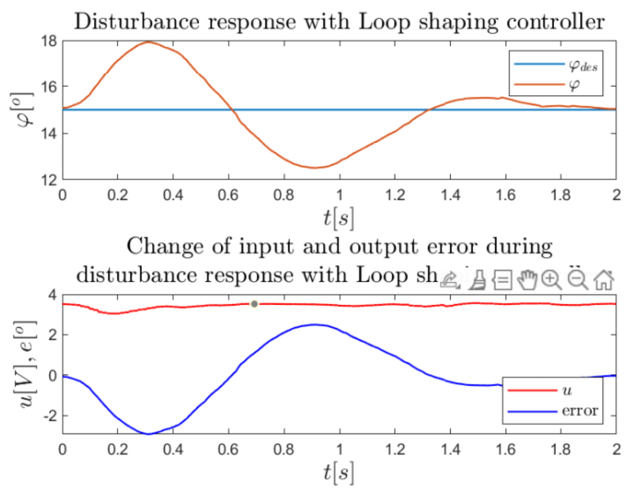

Figure 14: Disturbance response and generated input for Loop-shaped controller

From these experiments, it is evident that the I controller consistently generates the smoothest control output. The control signal produced by the Loop-shaped controller also exhibits a satisfactory level of smoothness, although not to the same extent as the I controller.

7. CONCLUSION

In our study, we've used a loop shaping controller design for an aeropendulum, starting with a clear explanation of the equipment and the math behind it. We then identified unknown parts of our model, using a method called Pade approximation to account for the delay in the system.

An initial controller was deployed with an integral action. However, seeking enhanced performance, a loop shaping controller design was developed. Three iterations of this controller, each with different crossover frequencies, were designed and evaluated. The most effective variant was chosen after meticulous consideration of their individual merits and drawbacks.

Comparative analysis with a traditional Integral controller unveiled a marginal improvement in the loop shaping controller's performance, particularly in response time and stability. The two controllers exerted similar influence over the system.

In conclusion, this research proposes the loop shaping controller design as a potential tool for improving the control systems of aeropendulum. This research might be a stepping stone to further studies on advanced control strategies for similar systems.

ACKNOWLEDGEMENTS

This research has been financed by the Ministry of Science, Technological Development and Innovation of the Republic of Serbia - Grant No. 451-03-47/2023-01/200105.

REFERENCES

[1] Ahmed Abdulelah et al. “Controlling the pitch and yaw angles of twin rotor MIMO system in simulation-based platform using fuzzy logic controller and PID controller”. In: Open J. of AI 2.1 (), pp. 1-6.

[2] Ricardo Breganon et al. “Loop-Shaping -HCM Control of an Aeropendulum Model”. In: International Journal of Applied Mechanics and Engineering 26.4 (2021), pp. 1-16.

[3] Eniko T. Enikov and Giampiero Campa. “Mechatronic Aeropendulum: Demonstration of Linear and Nonlinear Feedback Control Principles With MATLAB/Simulink Real-Time Windows Target”. In: IEEE Transactions on Education 55.4 (2012), pp. 538-545. DOI: 10.1109/TE.2012.2195496.

[4] Umar Farooq et al. “Observer based fuzzy LMI regulator for stabilization and tracking control of an aeropendulum”. In: 2015 IEEE 28th Canadian Conference on Electrical and Computer Engineering (CCECE). 2015,pp. 1508-1513. DOI: 10.1109/CCECE.2015.7129504.

[5] L. Ljung. System Identification: Theory for the User. Prentice Hall information and system sciences series. Prentice Hall PTR, 1999. isbn: 9780136566953.

[6] Omer Saleem et al. “Online adaptive PID tracking control of an aero-pendulum using PSO-scaled fuzzy gain adjustment mechanism”. In: Soft Computing 24 (2020), pp. 10629-10643.

[7] Sigurd Skogestad and Ian Postlethwaite. Multivariable feedback control: Analysis and Design. Hoboken, US-NJ: John Wiley, 2005.

[8] Yener Taskin. “Fuzzy PID controller for propeller pendulum”. In: IU-Journal of Electrical & Electronics Engineering 17.1 (2017), pp. 3201-3207.

H∞ control of Aeropendulum

Dušan Božić[1], Luka Filipović[1], Milan Ristanović[1*]
[1]Faculty of Mechanical Engineering, University of Belgrade, Belgrade (Serbia)

This paper introduces a robust control design for an aeropendulum system, utilizing the H∞ control technique. The aeropendulum setup and equipment are described, followed by the derivation of a mathematical model and system identification to accurately represent the system dynamics. The H∞. control method is then applied to create a controller, considering system uncertainties and disturbances. The efficacy of the controller is verified through experimental results, showing robust performance despite model uncertainties and time delay.

Keywords: H∞, Robust Control, Aeropendulum

1. INTRODUCTION

This paper aims to advance the field by focusing on the design of an effective controller for an aeropendulum using the H∞ control technique. This method is highly regarded for its ability to manage system uncertainties and enhance the robustness of control systems, providing significant advantages over other techniques such as classical loop shaping. In fact, our previous research has investigated the application of the loop shaping control method in aeropendulum control.

While classical loop shaping has been widely utilized, our study represents an upgrade by adopting the H∞ control technique. The H∞ control method offers superior capabilities in handling system uncertainties, improving stability, and achieving enhanced performance in control systems. By leveraging the strengths of the H∞ control technique, we aim to further advance the control design for the aeropendulum.

Prior work by [2] extended the application of the H∞ control method to an aeropendulum system that consisted of two motors with propellers. However, this work was primarily focused on simulation-based results. In contrast, our study expands upon this research by incorporating both experimental and simulation-based results. Previous studies have expanded the application of the H∞ control method to aeropendulum systems [6]. This included various developments such as robust control strategies employing particle swarm optimization and fuzzy inference systems [6], and adaptive fuzzy controllers for position stabilization and trajectory tracking [1]. In addition, the Takagi-Sugeno fuzzy modeling for output feedback control [4] and the integration of fuzzy logic into traditional PID control for superior performance in nonlinear systems [8] have been examined.

The initial part of this paper provides an in-depth description of the laboratory equipment employed in our investigation. This equipment, a relatively low-cost yet professionally designed and assembled solution, serves as an effective teaching tool for control systems engineering. Next, we delve into the mathematical modeling of the aeropendulum system, based on the law of change of kinetic moment, a crucial step in understanding the complex dynamics of the aeropendulum. To facilitate the use of linear control design techniques, we then proceed to linearize this inherently non-linear system.

Recognizing the importance of accurate system identification, we subsequently focus on determining the aeropendulum system and deriving its transfer function. Given that our mathematical model involves unknown coefficients, we provide a thorough explanation of how these variables are identified.

Finally, having a well-identified model, we focus on the principal objective: designing an H∞ controller. We delve into the principles of H∞ control, illustrating how it shapes the system's response to ensure stability and satisfactory performance under various conditions, while minimizing the impact of disturbances. Our proposed controller design is then validated through a comparative analysis of simulated and experimental results in the final section of this paper.

2. EXPERIMENTAL SETUP

Aeropendulum, on which the experiment was done, consists of an aluminum rod, that length is $l = 0.5$m and the propeller attached at the end of the rod. The rotation of the elise is used to control the angle of the pendulum. It is connected to the brushless DC (BDC) motor whose working voltage is 7.4V and maximal current is 1.8A. Because the microcontroller was used for motor control and its supply voltage is 3.3V it is necessary to use a driver. For this purpose, the H bridge driver was constructed with integrated circuit L6203 (DMOS Full Bridge Driver) as its main component. For angle measurement Spectrol 149 potentiometer is used. Its output is connected to an instrumentation amplifier with MCP6024 'rail-to-rail input/output' operational amplifier. In this way, not only is measured output amplified, but also the calibration is simplified because two trimmer helipot potentiometers enable easy shift and gain settings. We calibrated the sensor so that a zero angle means 0V and an angle of 90° is 3V. For control algorithm implementation microcontroller LM4F232H5QD from Texas Instruments is used. In order to give the set value and to maintain readings of the angle, the controller was connected with Matlab/Simulink on a computer through a UART communication channel. Considering the noise in the measured signal, largely stemming from the PWM signal and commutator sparking on the motor, we incorporated a digital filter.

The main components of the experimental setup are shown in Figure 1, with number descriptions in Table 1.

*Corresponding author: Kraljice Marije 16, 11120 Belgrade (Serbia) and mristanovic@mas.bg.ac.rs

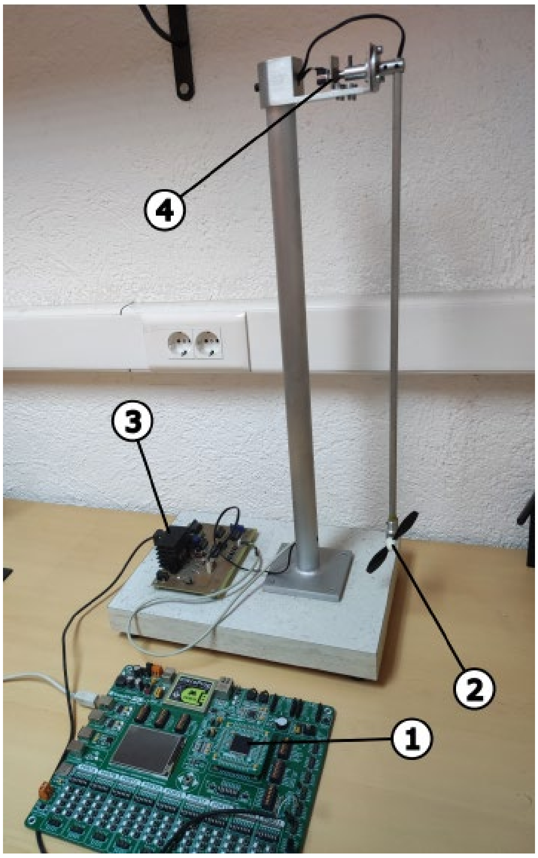

Figure 1: Experimental setup

Table 1: Main components of experimental setup

Number	Name
1	ARM Cortex M4 microcontroller
2	BDC Motor with propeller
3	PCB (H-bridge and MCP6024)
4	Potentiometer for angle measurement

3. MATHEMATICAL MODEL

In order to generate a controller and calculate its gains we need a mathematical model of a system in a transfer function form. First, we need assumptions that will simplify the physical model of the pendulum so that the differential equations would contain the important physicality of a system but the smallest order possible. We assumed that: the system has one degree of freedom - the angle between the rod and vertical line ϕ; there is no deformation, parts are rigid; angle measurements are without delay; thrust force is proportional to voltage.

We derive a mathematical model from the law of change of kinetic momentum:

$$\frac{d\vec{L}_O}{dt} = \sum_{i=1}^{n} \vec{M}_O^{\vec{F}_i^e}, \tag{1}$$

where $\vec{L}_O$ is a vector of kinetic momentum of the system, $\vec{M}_O^{\vec{F}_i^e}$ is a momentum vector from pole O of an i-th external force, or in scalar form through the axis of rotation:

$$\frac{dL_{Ox}}{dt} = \sum_{i=1}^{n} M_{Ox}^{\vec{F}_i^e}. \tag{2}$$

Knowing that the kinetic momentum of a rigid body around the x-axis is the moment of inertia times angular speed $L_x = J_x\omega_x = J_x\dot{\varphi}$ and the external forces momentums (Fig. 2) differential equation is:

$$J_x\ddot{\varphi} = lF_p - mgd_1\sin\varphi - a\dot{\varphi} - b\dot{\varphi}|\dot{\varphi}| - c\dot{\varphi}\operatorname{sgn}(\dot{\varphi}), \tag{3}$$

where $a\dot{\varphi}$ is linear viscous trust in bearings, $b\dot{\varphi}|\dot{\varphi}|$ - air trust, $c\dot{\varphi}\operatorname{sgn}(\dot{\varphi})$ - dry trust in bearings and potentiometer, a, b, c are friction linear parameters, m is system's mass, g is gravity constant, F_p is propulsion force, $d_1 = l/2$ half the rod's length, J_x moment of inertia of the system and φ is the angle between rod and vertical line. We can further simplify by assuming that a single linear attenuation $c\dot{\varphi}$ can substitute these three trust components:

$$J_x\ddot{\varphi} = lF_p - mgd_1\sin\varphi - c\dot{\varphi}. \tag{4}$$

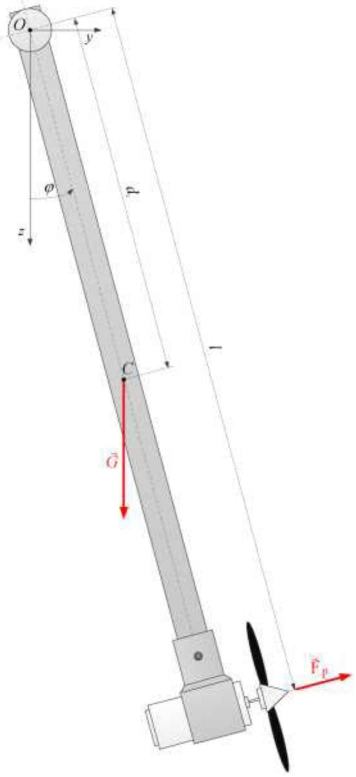

Figure 2: Pendulum scheme

As mentioned above, trust force is linearly dependent on motor drive voltage $F_p = Kv$ and for small enough angles the approximation $\sin(\varphi) \approx \varphi$ is justified (for $\varphi < 30°$ error is 2.36%) so the final differential equation is:

$$J_x\ddot{\varphi} + c\dot{\varphi} + mgd_1\varphi = lKv, \tag{5}$$

from which the transfer function can be easily inferred after the Laplace transformation:

$$G(s) = \frac{V(s)}{\Phi(s)} = \frac{lK}{J_x s^2 + cs + mgd_1}, \tag{6}$$

where $V(s)$ is the left Laplace transformation of motor voltage (input variable) and $\Phi(s)$ is the left Laplace transformation of pendulum angle (output variable). Now we know that the system is second order with no finite zero, but the coefficients must be somehow determined. For this purpose identification method was used.

4. SYSTEM IDENTIFICATION

System identification is a process of getting a mathematical model of a system based on collected data of the system's responses [5]. The idea is that if we know the inputs and corresponding outputs of a system we are able to determine a convenient model. This is a black box approach, when nothing about the system is known and gaining good results is hard. The grey box method uses a priori knowledge about the system and thus simplifies and improves the identification method. As it was shown, based on knowledge of mechanics, it is clear that our system is second order without finite zeroes. So, we know the structure but do not know the coefficients in the differential equation (transfer function). Grey box system identification is to be used.

Step input is the simplest input one can give to the system and extract important dynamical characteristics (time constant, rise time, settling time...). That is why it is used extensively as an input signal in system identification. In order to collect as much data as possible it is better to use more than one step signal (Fig. 3). In our case, the system is nonlinear in the whole range of angles. To stay in the linear zone, step angles are not too big and as a nominal angle value the $\varphi = 15°$ (middle of the range $0° < \varphi < 30°$) is chosen. Similar to identification data, the validation data is made, but with different order and size of step inputs, in order to check if the identification gave a successful overall model and not only for trained data.

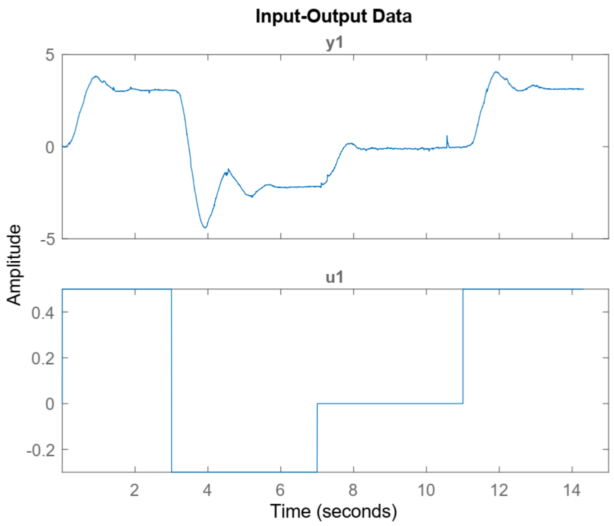

Figure 3: Input-output data for system identification

Using numerical methods for fitting the best possible second order dynamical system to recorded data (Fig.3) transfer function:

$$G(s) = e^{-0.19s} \frac{6.114}{0.04593s^2 + 0.1367s + 1} \tag{7}$$

was inferred. As shown on Fig.4 there is 87.49% fit to the validation data. Therefore, the transfer function from (7) is considered as valid mathematical model for our system.

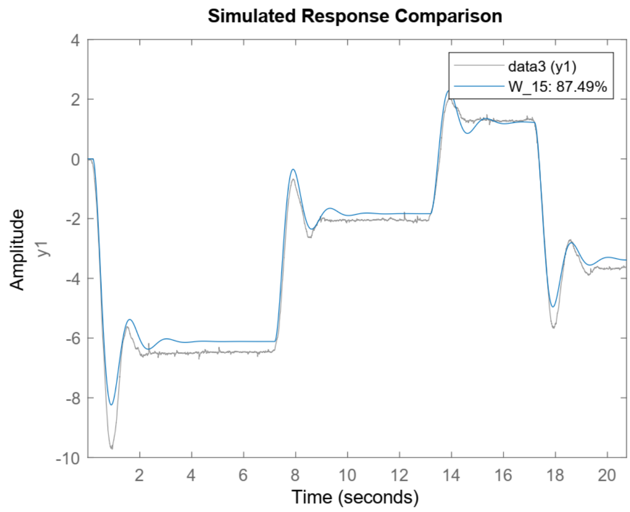

Figure 4: Fit to validation data of G transfer function

5. CONTROL ALGORITHM

In the previous section, the model of an uncontrolled object was derived (7). As we can see, it has a time delay of $\theta = 0.19s$ so the frequency domain (where this only changes phase but gain remains the same) is more natural to use.

To effectively manage the time delay, we employed the Padé approximation. This method offers a finite-dimensional approximation of time delays in linear systems, making it particularly useful for our scenario. By employing MATLAB's built-in function for Padé approximation, we were able to derive second-order transfer function, as it produced an accurate match to the delay $e^{-0.19s}$ up to the bandwidth frequency, as follows:

$$G_{delay}(s) = \frac{s^2 - 31.58s + 332.4}{s^2 + 31.58s + 332.4}. \tag{8}$$

Now that we have an appropriate approximation of the time delay, we can compute an I controller as a reference control. It was designed with a desired phase margin of $\varphi_m = 60°$ (because of the time delay, greater robustness is necessary) with cross frequency chosen between $\omega_{\pi/2}$ and $\omega_{\pi-\varphi_m}$. This way the calculated gain is $K_I = 0.1387$.

5.1. H_∞ controller

The main idea of H_∞ controller is to use infinity norm of some system response indicator and optimize it to have the smallest value possible, with respect to some free parameter. This free parameter can be one degree-of-freedom feedback control (K), which block diagram is shown on 5.

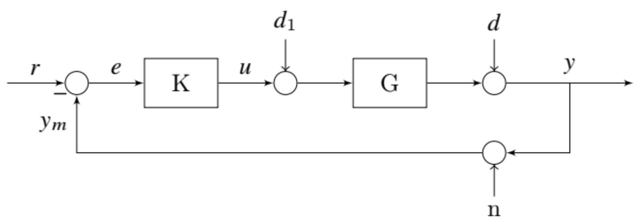

Figure 5: Block diagram of the feedback control system

From the block diagram in Figure 5. we derive the following equations:

$$y = TGKr + Sd + SGd_1 - Tn, \tag{9}$$

$$e = r - y = Sr - Sd + Tn + SGd_1, \tag{10}$$

$$u = KSr - Ksn - KSd + Sd_1 \tag{11}$$

where y is output, r is the reference input, y_m is measured output, n it the measurement noise, d is output's disturbance, d_1 it the input's disturbance. Also, sensitivity function S and complementary sensitivity function T are defined as:

$$S = \left(I + GK\right)^{-1}, \tag{12}$$

$$T = \left(I + GK\right)^{-1} GK. \tag{13}$$

$$S + T = I \tag{14}$$

The sensitivity function provides insights into the robustness of a control system with respect to modeling errors, disturbances, and noise, while the complementary sensitivity function provides information about the tracking performance of the system. A small sensitivity implies that the system is robust to uncertainties and disturbances. Conversely, a large sensitivity means that the system is sensitive to uncertainties and disturbances. A small value of T implies poor tracking performance, whereas a large T implies good tracking of reference signal. For the error e to be minimized with respect to the reference signal r and disturbances d and d_1, S must be small, as inferred from equation (10). To diminish the impact of noise n on the error e, we aim for a smaller T. However, from relation (14), it's apparent that we can't achieve minimal values for both S and T at the same frequency simultaneously.

H∞ optimal control strategy can be developed by tackling both the magnitudes of sensitivity function $S(s)$ and closed loop transfer function $T(s)$ and optimizing them with respect to infinity norm, leaving the engineer with the task of selecting reasonable weights for the desired response. But in the optimization process conflict requests might occur, leaving it to the algorithm to choose which to dismiss. This can generate unwanted results so we choose only the sensitivity function as the system's response indicator.

The reason for considering S is obvious from the above stated analysis. Additionally, the minimization of magnitude $|S|$ is sufficient, phase is irrelevant. Typical specifications in terms of S include [7]: minimum bandwidth frequency ω_B; maximum tracking error at selected frequencies; maximum steady-state tracking error A; the shape of S over selected frequency ranges; maximum peak magnitude of S, $\left\|S(j\omega)\right\|_\infty \le M$ ||. These specifications can be satisfied by an upper bound $1/\left|\omega_p(j\omega)\right|$:

$$\left|S(j\omega)\right| < \frac{1}{\left|\omega_P(j\omega)\right|}, \forall\omega \Leftrightarrow \left\|\omega_P S\right\|_\infty < 1. \tag{15}$$

Naturally, this upper bound is selected to give an asymptotic plot with the above required specifications as:

$$\omega_P(s) = \frac{s/M + \omega_B}{s + \omega_B A}. \tag{16}$$

By choosing a weight like this, desired open loop magnitude diagram is with the slope of -20 dB/dec in the frequency range below crossover. In some cases, in order to improve performance, a steeper slope below bandwidth is more desirable, thus the higher order weight must be defined. For the slope of -40 dB/dec the weight is:

$$\omega_{P2}(s) = \frac{\left(s/M^{1/2} + \omega_B\right)^2}{\left(s + \omega_B A^{1/2}\right)^2}. \tag{17}$$

In our case, option (17) proved to be worse in performance in both simulation and experiment. This can easily be seen on step simulation response of the system controlled by H∞ controller. The parameters in weighting functions are the same, but the overshoot with the weights as in (17) is obviously big, so the chosen weight is (16).

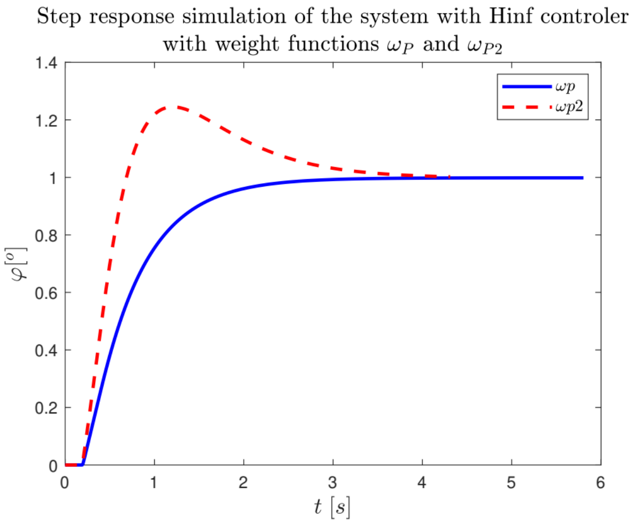

Figure 6: Step response simulation of the system with H∞ controller with different weight functions

Additionally, by defining weighting function only for sensitivity function, we take in consideration only the system response, but the cost of the input is not considered. That is why mixed sensitivity is introduced as:

$$\left\|N\right\|_\infty = \max_x \sigma\left(N(j\omega)\right) < 1; N = \begin{bmatrix} \omega_P S \\ \omega_u KS \end{bmatrix}, \tag{18}$$

where $\sigma(N) = \sqrt{\left|\omega_P S\right|^2 + \left|\omega_u KS\right|^2}$. Now we can penalize input with the weight ω_u and controller K can be gained by solving the optimization problem:

$$\min_K \left\|N(K)\right\|_\infty. \tag{19}$$

The measuring resolution of the angle of the aeropendulum is 0.025°, so there is no need to demand a much smaller steady-state statical error. We have selected the value of $A = 10^{-3}$. Because of the time delay of the system, an additional phase contribution of $-\theta\omega$ must be taken into account. The bandwidth frequency is limited by approximately $\omega_{B\max} < 1/\theta \approx 5\,\text{rad/s}$. Therefore, we choose $\omega_B = 2\,\text{rad/s}$ as desired in (16). The peak specifcation (M) prevents amplification of noise at high frequencies and also introduces a margin of robustness. For real physical systems, it is shown [6] that it must be greater than 1, so the value of $M = 1.2$ is chosen. Maximum input is 7.4V, so the input weight matrix of $\omega_u = 8I$ is selected. Using numerical methods [3] to solve minimization problem (19) gained controller is:

$$K = \frac{680.1s^2 + 2024s + 14806}{s^3 + 554.9s^2 + 7.0151s + 140.3}. \quad (20)$$

6. EXPERIMENTAL RESULTS

For the experiments, the controllers were discretized and implemented into a microcontroller as a digital filter in direct canonical form 1, with a sample time of 0.01s. We choose this sample time, because of the rule of thumb to have at least 10 samples in the system's rise time, which is approximately one second.

The first experiment was a step change of the desired angle of 5 degrees from 15° to 20°. The response angle with generated control input to the system with I controller is shown in figure 7 and with controller in figure 8. The figures also show simulation results and output error through time. We can conclude that the simulation results are similar to the experimental one, which is very important and also proves that the model is correct.

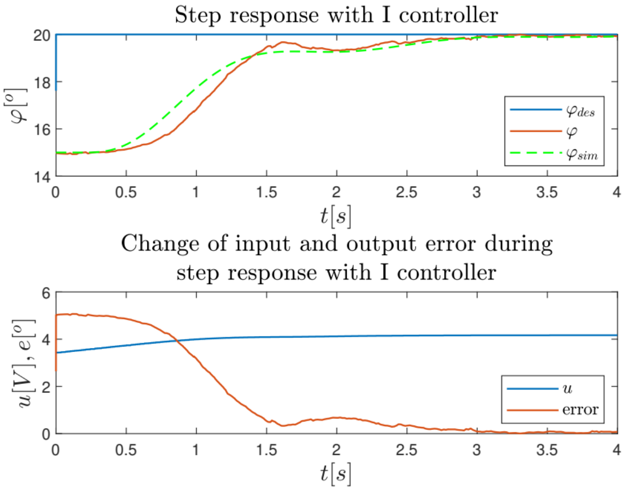

Figure 7: Step response (simulation and experiment) and generated input for an angle change of 5° with I controlled system

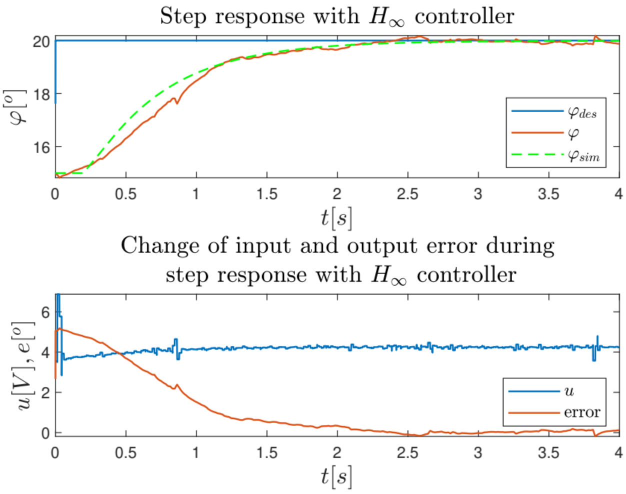

Figure 8: Step response (simulation and experiment) and generated input for an angle change of 5° with H∞ controlled system

It is clear that I controlled system is slower, with a slight decrease of output variable before reaching desired value, as if there was an overshoot. On the other side, the H∞ controller was faster and reaches the desired value of angle straightforwardly.

The second experiment was disturbance response. The system was put out for approximately 3° from its nominal value. The resulting response with I controlled system is shown in figure 9 and with H∞ controller in figure 10. Again the I controller was slower to regain the desired angle, although the difference is not as clear as in the step response case.

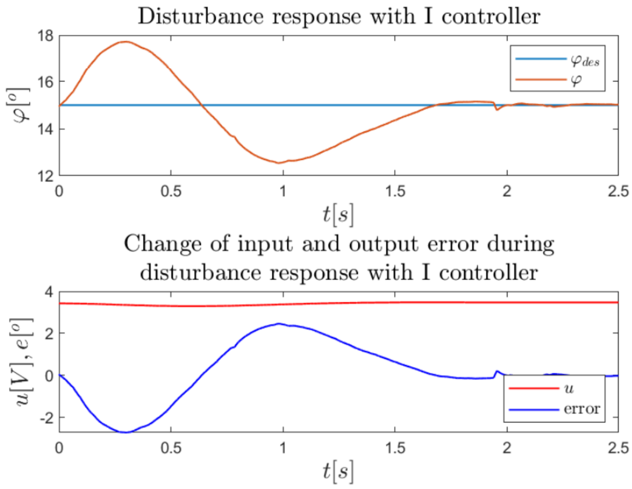

Figure 9: Disturbance response and generated input for I controlled system

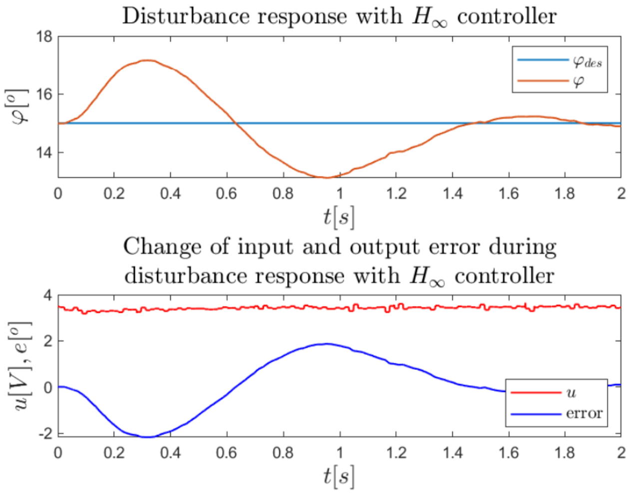

Figure 10: Disturbance response and generated input for H∞ controlled system

From both experiments, it is also clear that I controller generates a much smoother control output whereas the H∞ control output is very bouncy. This could prove to be problematic for some systems. All in all, H∞ controller provided better dynamical system response and is fairly easy to obtain numerically when the system model is known, but it has its drawback with its bouncy control output.

7. CONCLUSION

In this research, we investigated the use of H∞ controller design for an aeropendulum system. In the beginning, we studied our equipment closely and used system identification to work out the exact math behind it.

After that, we used something called Padé approximation to turn the system's time delay into a rational function, which was helpful when we started designing the controller.

We focused on the comparison between the H_∞ controller and a controller solely incorporating integral action. The H_∞ controller showcased superior system response, thus demonstrating its effectiveness in handling the aeropendulum system.

However, it's important to note that while the H_∞ controller yielded an improved system response, the smoothness of the control signal was compromised. This highlights a trade-off to be considered when prioritizing system performance.

In conclusion, the H_∞ controller design presents an intriguing improvement in system response for the aeropendulum at the expense of a rougher control signal. This suggests an avenue for future research: to develop an advanced control strategy that can balance both system performance and the smoothness of the control signal. The potential for refinement in this controller design offers a promising direction for further explorations in the field of control systems for aeropendulum.

ACKNOWLEDGEMENTS

This research has been financed by the Ministry of Science, Technological Development and Innovation of the Republic of Serbia - Grant No. 451-03-47/2023-01/200105.

REFERENCES

[1] Ahmed Abdulelah et al. “Controlling the pitch and yaw angles of twin rotor MIMO system in simulation-based platform using fuzzy logic controller and PID controller”. In: Open J. of AI 2.1 (), pp. 1-6.

[2] Ricardo Breganon et al. “Loop-Shaping H_∞ Control of an Aeropendulum Model”. In: International Journal of Applied Mechanics and Engineering 26.4 (2021), pp. 1-16.

[3] Naiwrita Dey, Ujjwal Mondal, and Debasish Mondal. “Design of a H-infinity robust controller for a DC servo motor system”. In: (2016), pp. 27-31. DOI: 10.1109/ICICPI.2016.7859667.

[4] Umar Farooq et al. “ Observer based fuzzy LMI regulator for stabilization and tracking control of an aeropendulum”. In: 2015 IEEE 28th Canadian Conference on Electrical and Computer Engineering (CCECE). 2015, pp. 1508-1513. DOI: 10.1109/ CCECE.2015.7129504.

[5] L. Ljung. System Identification: Theory for the User. Prentice Hall information and system sciences series. Prentice Hall PTR, 1999. isbn: 9780136566953.

[6] Omer Saleem et al. “Online adaptive PID tracking control of an aero-pendulum using PSO-scaled fuzzy gain adjustment mechanism”. In: Soft Computing 24 (2020), pp. 10629-10643.

[7] Sigurd Skogestad and Ian Postlethwaite. Multivariable feedback control: Analysis and Design. Hoboken, US-NJ: John Wiley, 2005.

[8] Yener Taskin. “ Fuzzy PID controller for propeller pendulum”. In: IU-Journal of Electrical & Electronics Engineering 17.1 (2017), pp. 3201-3207.

Analysis of the Current Situation in Serbia Related to the Education in the Field of Applied Artificial Intelligence

Anđela Đorđević1, Marko Milojković[1], Miodrag Spasić[1*], Dejan Rančić[2], Saša S. Nikolić[1], Miroslav Milovanović[1]
[1]Faculty of Electronic Engineering/Department of Control Systems, University of Niš, Niš, Serbia
[2]Faculty of Electronic Engineering/Department of Computer Science, University of Niš, Niš, Serbia

Abstract: The fastest growing and most exciting scientific field today is Artificial Intelligence (AI) with its real world applications. The current transformation of society and business needs for AI specialists with specific competencies and skills dictate the transformation of the Serbian educational system and its adjustment toward modern demands. This paper presents some results and analysis of conducted surveys in the scope of the Erasmus+ project "Future is in Applied Artificial Intelligence" related to the current state of AI education in Serbia, existing university AI courses, knowledge and attitude of students and teachers toward AI contents, needs of the employers and the preferred future directions of the transformation of education system toward a competency-based digital society through formulating adequate AI learning requirements.

Keywords: Applied artificial intelligence, engineering education, competency-based education

1. INTRODUCTION

The best way to explain the importance of education in the field of Artificial Intelligence (AI) is to cite European Commission [1]: „Like the steam engine or electricity in the past, AI is transforming our world, our society and our industry. Growth in computing power, availability of data and progress in algorithms have turned AI into one of the most strategic technologies of the 21st century. The stakes could not be higher. The way we approach AI will define the world we live in. Amid fierce global competition, a solid European framework is needed“. EU strives for a coordinated approach in order to make the most of the opportunities offered by AI [2] as well as to address the challenges it brings. The EU's desire is to lead the world in the development and use of AI, relies on numerous comparative advantages: the best world researchers, scientists, laboratories, start-up centres, leading world industry, especially in the field of robotics, a single digital market, and plenty of research, industrial and public sector data that can be used to feed AI algorithms.

EU defined three main goals in the future development of AI [3]: 1. Increase of technological and industrial capacities and wide adoption of AI by the business sector; 2. Preparation for socio-economic changes brought by AI; 3. Creation of an appropriate ethical and legal framework based on the values of the Union. All three goals strongly depend on the transformation of education and its ability to support the current and future market demands for AI experts. The focus is on establishing research centres and centres of excellence focused on AI as well as encouraging their cooperation and networking through an AI-on-demand platform as a central access point for unifying existing AI tools and resources. The action plan for digital education [4] implies the transition of the education system towards the preparation of the workforce for the upcoming transformation of society under the influence of AI as well as the development of skills and competences needed to work with IT (competency-based education) [5]. This kind of education can be accomplished only through the partnership with the private sector aimed at the full inclusion of the private sector in dictating research and innovation priorities to the higher education institutions as well as ensuring their co-financing [6].

The Republic of Serbia also recognized the importance of educational transformation toward AI in the Strategy for the National Development of Education by 2030 and Strategy for the Development of Artificial Intelligence in the Republic of Serbia for the period 2020-2025 [7], which both emphasize the need for the synchronization of education policies, in particular, considering sciences, technical and technological developments in modern society as well as harmonizing the national regulations in education with international documents and initiatives. Numerous national and international projects can help the Serbian education system to accomplish the goal of accelerated development of Serbia and catch up with already developed countries. Recording and analysis of the current state is always an integral part of these projects and this paper presents the obtained results of one such a study.

2. FRAMEWORK OF THE ANALYSIS

Analysis of the current state of education in the field of applied artificial intelligence was conducted as part of the starting activities of the Erasmus+ project "Future is in Applied Artificial Intelligence" (FAAI) [8]. The coordinator of the project is the University of Bielsko-Biala from Poland and other project participants are: University of Library Studies and IT, Bulgaria; The University of Niš Serbia; The University of Ss. Cyril and Methodius in Trnava, Slovakia; and University of Montenegro, Montenegro. The duration of the project is 24 months (September 2022 - August 2024).

The main goal of the project “The Future is in Applied Artificial Intelligence” is for students to get acquainted with the possibilities of AI systems for solving problems in management, industry, engineering, administration, and education; evaluations of existing AI systems and tools, emphasizing comparative studies and user experiences; and research on the economic, social, and cultural impacts of AI. The project aims to join

*Corresponding author: Aleksandra Medvedeva 14, 18000 Niš, Serbia, miodrag.spasic@elfak.ni.ac.rs

together Universities and businesses and provide innovative solutions to develop Artificial Intelligence experts. Conducted study (online questionnaires) aimed at exploring the needs and expectations of business organizations in order to propose training specialists in the field of Applied AI.

The project activates are organized through the following work packages:

- WP1-Project management
- WP2-Good practices in the use of AI and ML
- WP3-Setup the Artificial Intelligence learning requirements
- WP4-Artificial Intelligence framework for training in HE
- WP5-Piloting

The focal point of the first half of the project - WP2 (Good practices in the use of AI and ML) and WP3 (Setup the Artificial Intelligence learning requirements) was to conduct a study on the current state of education in the field of applied AI in the project participant countries as well as an analysis of obtained results, in order to offer the solutions and directions for the transformation of the education system by formulating adequate AI learning requirements.

3. METHODOLOGY OF ASSESSMENT

In the first phase of the project 2022-1-PL01-KA220-HED-000088359 "Future is in Applied Artificial Intelligence" (FAAI) under the Erasmus+ program, a study was conducted on the state of the subject area, namely Applied Artificial Intelligence in the project partner countries (Poland, Slovakia, Serbia, Bulgaria, Montenegro). The survey was performed online using AdminProject - European Project Management Software forms tools during a period from the 1st to the 28th of February 2023. The survey contained 8 online forms with both open and closed questions. The questionnaires considered different questions for job offerings, labor market in the field of Artificial Intelligence (AI), existing training programs, and good practices, and collecting IT specifications of good practices in AI. Emphasize was on specifying needed competencies in AI by IT graduates in Information Systems and Technologies and employers. To obtain a wide range of data, multiple question fields, with an additional open-field option, were offered to mitigate the effect of narrowed answer suggestions.

The following surveys were conducted (numbers in the brackets represent the total number of completed surveys in that category):

- Research 1: Existing training courses in the field of applied AI (92)
- Research 2: Study of the labour market in the field of applied AI (74)
- Research 3: Survey of scientific projects in applied AI (63)
- Research 4: Survey for academics (lecturers) (80)
- Research 5: Questionnaire for IT students, masters and alumni in Information Systems and Technologies (1043)
- Research 6: Questionnaire for employers: Specifying graduate competencies in Data Science (38)
- Research 7: Collecting IT specifications of good practices in AI (25)
- Research 8: Collecting real cases of applied AI (279)

4. SURVEY RESULTS

4.1. Existing training courses in the field of applied AI

In Serbia, the majority of currently available courses in applied artificial intelligence (AAI) are inside master academic studies (MAS) programs (more than 70%) and they contain advanced AI topics which usually require some prior knowledge. These courses cover a range of topics, including Artificial intelligence in medicine, Artificial intelligence in speech and audio technologies, Artificial intelligence applied in control systems, Natural language processing, Artificial intelligence and machine learning in communication systems, Artificial neural networks in electronic systems engineering, etc. To enrol in these courses, a basic understanding of programming in Python/R, statistics, mathematical modelling, data mining, or algorithms is usually required. Overall, the availability of courses in applied AI in Serbia provides students with a valuable opportunity to develop skills and competencies that are in high demand in the job market. The hands-on experience gained from these courses can help students stand out from the crowd and secure rewarding careers in the field of AI. Upon completion of the courses, respondents reported developing competencies such as: selecting appropriate machine learning methods for specific problems (75%), utilizing proper training and testing methodologies for deploying machine learning algorithms (62.5%), identifying appropriate performance metrics for evaluating machine learning tools for a given problem (62.5%), recognizing the breadth and utility of machine learning methods (50%), explaining techniques to mitigate over fitting and curse of dimensionality in the context of machine learning algorithms (43.75%), and comparing and contrasting various machine learning methods (37.5%). In a much less percentage, students can gain competencies related to the ethics of AI, like: being aware of the wide range of ethical considerations around AI systems, as well as mechanisms to mitigate problems (17.5%) or debating the possible effects (both positive and negative) of decisions arising from machine learning conclusions (25%).

4.2. Study of the labour market in the field of applied AI

A study conducted on the labour market for applied AI in Serbia has revealed that most required positions related to AI in Serbian IT companies are in Consulting (24.5%), Manufacture/development (20%), Customer service (15.5%), Finance (11.25%), Design (8.75%) and Research (8%). Employers mostly require a Bachelor degree (41.45%), a Master degree (30.85%) or No education level, skills only (18%).

Vacant jobs are mostly full-time positions intended for data scientists, data engineers, and data analysts. The chart below (see Fig. 1) illustrates the various positions available in this field.

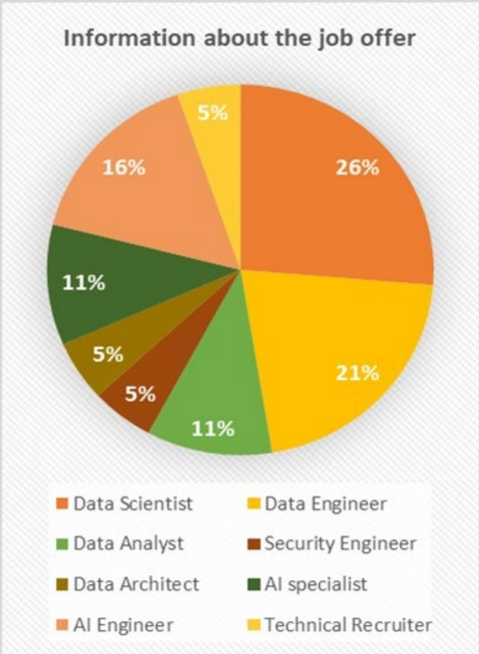

Figure 1. Offered job position.

The questionnaire conducted as part of the study indicated that the most essential competencies required for the positions mentioned above are the ability to select appropriate machine learning methods for specific problems (67%), represent information using a probabilistic formalism and apply relevant reasoning methods (60%), recognize the breadth and utility of machine learning methods (53%), and compare and contrast machine learning methods (40%). Conversely, the least essential competencies include identifying an appropriate performance metric for evaluating machine learning algorithms/tools for a given problem (27%), recognizing problems related to algorithmic and data bias, as well as privacy and integrity of data (24%), and being aware of the wide range of ethical considerations around AI systems and mechanisms to mitigate problems (13%).

Knowledge of programming languages is a crucial factor for applied AI, with Python being the language required by most companies, according to labour marketers. Other languages that are necessary for obtaining positions in this field include C++, C#, R, and Java, as shown in Fig. 2.

This survey has also revealed the popular ecosystems and libraries used for developing AI models. The survey gathered opinions from applicants on their preferred tools for developing popular AI models such as multilayer neural networks (MLP), convolution (CNN) and recurrent neural networks (RNN), or decision trees and random forest. It was also found that Apache Hadoop is the preferred ecosystem for developing AI models, with 40% of the respondents choosing it. Anaconda and Kaggle were the second and third most popular ecosystems, with 13.7% of both. R Studio was next, with 6.7% of respondents. Furthermore, it was shown that the most requested AI libraries were Scikit-learn, TensorFlow, and Keras. Scikit-learn was the most popular library, with almost 70% of respondents choosing it, while TensorFlow was the second with 27%. Keras was the third most popular library, with 20%.

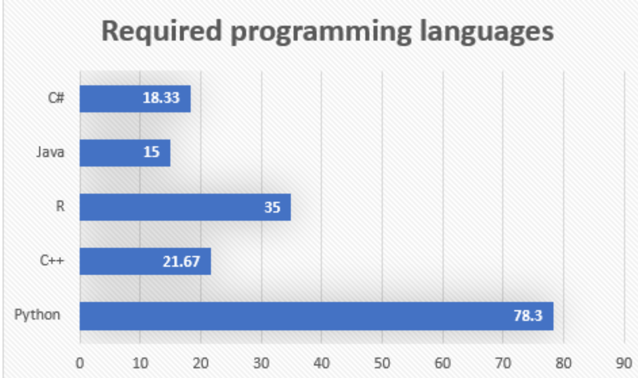

Figure 2. Required knowledge of programming languages.

The importance of soft skills in the field of AI is highlighted and the following soft skills were identified as the most necessary ones:

1. Customer Focus - actively identifying market demands and meeting client needs
2. Business Fundamentals - having a fundamental knowledge of the organization and the industry
3. Planning & Organizing - prioritizing work and completing assigned tasks promptly
4. Communication - understanding and effectively communicating ideas
5. Creativity - delivering high-quality work while focusing on the final result and intellectual risk-taking
6. Critical Thinking - solving problems and making effective decisions.
7. Working with Tools & Technology - selecting, using, and maintaining tools and technology to facilitate work activity
8. Collaboration - efficiently cooperate with others and appreciate the multicultural difference

4.3. Survey for academics (lecturers)

The development of applied AI courses requires the enhancement of teachers' potential. The key issues are need for more competent personnel, inadequate experience in implementation, and the high costs of solutions. One solution is for universities to expand their courses of applied AI and enable teachers to acquire practical experience and enhance their knowledge and skills. The participation of external experts from the IT industry is essential. Strengthening collaboration between universities and enterprises is important to attract qualified specialists to teach and engage teachers in project work. To further improve their skills, universities should allow teachers to take thematic courses of their interest. Also, participation in open-source projects is an effective way for teachers to enhance their abilities and receive support from like-minded individuals.

The main obstacles/issues that teachers in the field of applied AI recognize are limitations resulting from the study program, formal barriers in submitting a new form of classes, and inadequate or maladjusted laboratory/lecture room equipment. These limitations can negatively impact the quality of education and the students' ability to learn and develop their skills. To overcome these obstacles, universities should regularly evaluate and update their study programs, and provide teachers with the necessary training and support to improve their teaching methods. Another solution is establishing partnerships with industry and other institutions to access better resources and equipment and offer more practical and relevant courses. Universities should also create a system to collect feedback from students and teachers to identify areas that need improvement and ensure their needs are met. In addition, it is important to foster a culture of innovation and experimentation in education, where teachers and students are encouraged to explore new approaches and technologies to enhance learning and teaching.

4.4. Questionnaire for IT students, masters and alumni in Information Systems and Technologies

One of the conducted surveys was to evaluate the interest of students related to apply AI. Many students responded, indicating a clear need for applied AI content and training courses among the target population. Most of the respondents were young individuals between the ages of 21 and 24, either still in university (67%) or newly employed (see fig. 3). Only 26% of the applicants answered that they participated in classes which were based on applied AI. Despite their limited knowledge students' significant interest in applied AI adds value to the project's aim to identify the underrepresented skills, the reasoning behind talented individuals lacking traditional credentials to secure employment and the areas in applied AI that require immediate attention. Responses from students keen on participating in applied AI courses reveal that such courses must be attractive by focusing on data collection from diverse sources and analysis of such data using machine learning and data mining techniques.

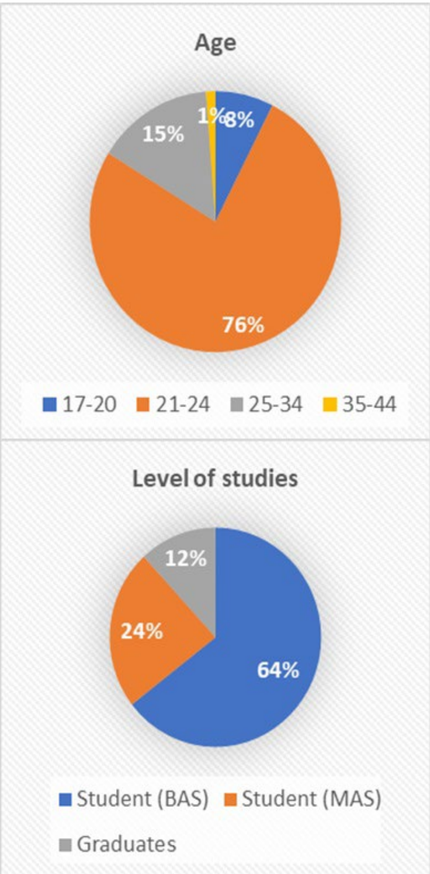

Figure 3. Structure of the respondents.

The vast majority of working respondents (78%) indicated that applied AI issues are important or somewhat important to their job and that courses on applied AI would be valuable for their future career development. This highlights the need for structured applied AI training programs. In today's job market, developing digital and soft skills is becoming increasingly important, and young people and their employers recognize this.

Any designed applied AI training program should also emphasize the development of soft skills, particularly those related to teamwork, communication, and time management. The most important soft skills that more than half of participants recognized as necessary are: the ability to communicate in a second (foreign) language, the ability to work in a team, ability to identify, propose and resolve problems, the capacity to learn and stay up-to-date with learning, ability to apply knowledge in practical situations, ability to design and manage projects, while a minority (up to 20% of responders) emphasized skills like conservation of the environment, ability to show awareness of equal opportunities and gender issues, ability to take the initiative and to foster the spirit of entrepreneurship and intellectual curiosity, ability to act with social responsibility and civic awareness, ability to undertake research at an appropriate level, and ability to act on the basis of ethical reasoning.

5. CONCLUSION

The importance of artificial intelligence and its real world applications in today's world cannot be stressed enough. There is no field of technique or real life that is not influenced by artificial intelligence in one way or another. Any country which tends to be relevant today must pay special attention toward the transformation of its educational system in the direction of building AI aware and skilled society based on adequate digital competencies.

Erasmus+ project “Future is in Applied Artificial Intelligence” (FAAI) has the main goal to identify the current state of development as well as the needs and expectations of business organizations in order to propose the direction of transformation of educational systems of project participant countries (one of them is Serbia) toward the field of Applied AI. The first step in this project was to take a snapshot of the current situation in Serbia regarding AI education in Serbia, university courses currently offered for students, the knowledge and attitude of students and teachers toward AI content, and the needs of the employers in terms of adequate competencies.

This goal was achieved through a series of conducted studies (online questionnaires) whose results were partially presented in this paper. The presented analysis, as well as the expected results in the continuation of the project, represents valuable guidelines for Serbian education institutions in the form of AI learning requirements in order to build a strong work force capable of understanding and implementing AI-based solutions for the future.

ACKNOWLEDGEMENTS

This paper is a product of work that has been supported by the Erasmus+ project: Future is in Applied Artificial Intelligence (FAAI), project no. 2022-1-PL01-KA220-HED-000088359. Views and opinions expressed are however those of the author(s) only and do not necessarily reflect those of the European Union or the National Agency (NA). Neither the European Union nor NA can be held responsible for them.

REFERENCES

[1] European Commission – Internal Communication, 2018. Artificial Intelligence for Europe. Available online: https://eur-lex.europa.eu/legal-content/EN/TXT/PDF/?uri=CELEX:52018DC0237&from=EN

[2] S. Russell and P. Norvig, "Artificial Intelligence: A Modern Approach, Pearson", 4th edition, 2020.

[3] European Commission, 2020. On Artificial Intelligence - A European approach to excellence and trust. Available online: https://commission.europa.eu/system/files/2020-02/commission-white-paper-artificial-intelligence-feb2020_en.pdf

[4] European Commission – Internal Communication, 2020, Digital Education Action Plan (2021-2027) - Resetting education and training for the digital age. Available online: https://eur-lex.europa.eu/legal-content/EN/TXT/PDF/?uri=CELEX:52020DC0624&from=EN

[5] X. Huang, "Aims for cultivating students' key competencies based on artificial intelligence education in China", Education and Information Technologies, vol. 26, pp. 5127–5147, (2021).

[6] M. Tedre, T. Toivonen, J. Kahila, H. Vartiainen, T. Valtonen, I. Jormonainen, and A. Pears, "Teaching machine lLearning in K–12 classroom: Pedagogical and technological trajectories for artificial intelligence education", IEEE Access, vol. 9, pp. 110558-110572, (2021).

[7] Strategy for the Development of Artificial Intelligence in the Republic of Serbia for the period 2020-2025,"Official Gazette of the RS", No. 30/18, Government of Republic of Serbia. Available online: https://www.media.srbija.gov.rs/medsrp/dokumenti/strategy_artificial_intelligence.pdf

[8] Future is in Applied Artificial Intelligence. Available online: https://faai.ath.edu.pl

Conceptual modeling of hysteresis in piezo crystals using neural networks

Lazar Kelić*, Dragan Pršić
Faculty of mechanical and civil engineering in Kraljevo (Srbija)
Automatic control and fluid technology, Kraljevo (Srbija)

Abstract: Piezoelectric materials are a subset of a larger class of materials known as ferroelectric materials. Ferroelectricity is the characteristic of certain materials that have a spontaneous electrical polarization that can be reversed by the application of an electric field. Like the magnetic equivalent (ferromagnetic materials), ferroelectric materials exhibit hysteresis loops based on the applied electric field and the history of that applied electric field. Hysteresis compensation is necessary wherever high precision positioning or piezo control of the mechanism is required. For forecasting purposes, of hysteresis, the Bouc-Ven model was most often used, and more recently, hysteresis modeling using neural networks has begun. The paper will show a way of conceptual predicting, and then for hysteresis, using a neural network.

Keywords: ferroelectric materials, hysteresis, neural network

1. INTRODUCTION

The Bouc-Wen model is first proposed by Bouc in 1967 [4], where a function that describes the hysteresis behaviour between the displacement and restoring force was proposed, and it was then generalized by Wen in 1976 [5]. This model consists of a first-order nonlinear state equation and an output equation where the input and state signals appear linearly. Through appropriate choices of parameters in the model, it can represent wide variety of hysteresis behaviours[1].

In the paper [2] is presented the results of the successful application of deep learning based black-box models for characterizing the dynamic behavior of micromanipulators. The excitation signal is a multisine spanning the frequency band of interest and the selected model is validated with semi static individual sinusoidal curves. Various architectures are tested to achieve a reasonable result and we try to summarize the best approach for the fine tuning required for such application. The results indicate the usefulness and predictive power for deep learning based models in the field of system identification and in particular hysteresis modeling and in micromanipulation applications [2].

Paper [3] aims to identify parameters of Bouc-Wen hysteretic model using timedomain measured data. It follows a general inverse identification procedure, that is, identifying model parameters is treated as an optimization problem with the nonlinear least squares objective function. Then, the enhanced response sensitivity approach, which has been shown convergent and proper for such kind of problems, is adopted to solve the optimization problem. Numerical tests are undertaken to verify the proposed identification approach.[3].

From the previous examples and results, it can be seen that the problem of hysteresis is quite old and has been dealt with in many ways. The Bouc-Wen model is the most widespread and is based on an inhomogeneous differential equation with the appropriate definition of parameters. Neural networks have been in use since a recent date and, unlike the Bouc-Wen model, provide greater precision, especially at higher operating frequencies. The use of a neural network described in this paper offers much higher hysteresis prediction accuracy than existing neural network models due to the larger number of input parameters. Those input parameters describe the state of the piezo material itself, from which the sensor or actuator is made. The approach conceived in this way gives us the most approximate form of hysteresis at the output of the neural network for each individual piezo element, and not for a series of piezo elements, as was the case until now.

2. PREDICTION OF HYSTERESIS

This paper describes the method of conceptual predicting hysteresis using neural networks, but with the use of several input parameters that describe the current physical state of the piezo element itself. In this way, a significantly higher accuracy is achieved, which can be seen in chapter 3 on the graphics obtained in MATLAB using the deep network designer tool. . PZT is a Bouc-Wen form of hysteresis that, for the purposes of simulation mentioned in the paper, is modeled using the software package MATLAB Simulink. model, chosen to fit the hysteresis loop is described by the following non-linear differential equation (1):

$$\frac{\mathrm{d}z}{A-|z|^{n}\left[\beta+\gamma \operatorname{sgn}\left(\xi' z\right)\right]}=\mathrm{d}\xi \tag{1}$$

where A, , , β γ n are loop parameters controlling the shape and magnitude of the hysteresis loop z(ξ) . Due to the symmetry of hysteresis curve, only the branches

*Corresponding author: Dositejeva 19, 36000 Kraljevo. Serbia, kelic.l@mfkv.kg.ac.rs

AB, BC and CD , corresponding to positive values of the imposed displacement $\xi\ \tau(\ )$, will be considered.

The model parameters are to be determined such as the steady-state solution of equation (1), under symmetric cyclic excitation, to satisfy the matching conditions considered in (2)[6].

$$z(0)=z_0 \text{ at } A,\ z(\xi_m)=z_m,\ z(\xi_0)=0,\ z(0)=-z_0 \text{ at } D \tag{2}$$

This chapter shows the block diagram of the model for training the neural network and the block diagram of the working model of the neural network for prediction and of hysteresis in piezo elements.

2.1 A working model of a neural network

The principle of hysteresis compensation using the neural network shown in Figure 1 is as follows:

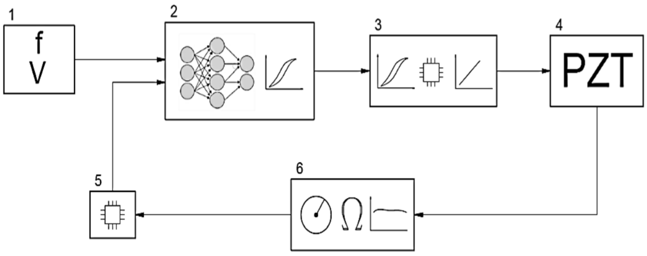

Fig 1.Working principle of predicting hysteresis using a neural network while taking into account the electro-mechanical parameters of the piezo element

the signal generator (1), together with the signal supplied from the microcontroller (5) represents the input parameters to the neural network. Based on those parameters, and after the training process carried out according to the scheme from the previous picture, the neural network (2) itself knows in advance what form of hysteresis, for a certain generated signal from the signal generator (1), is generated by the specific piezo element (4) that is used at that moment. The output from the neural network (2) describes the shape and magnitude of the hysteresis based on the signal that will drive the piezo element (4), generated by the signal generator (1) and the signal coming from the microcontroller (5).That output is then sent to the microcontroller (3), which will, if necessary, correct the control voltage of the piezo element (4), in order to achieve linearity and exact and required position of the piezo element (4) at every moment.

The improvement compared to the current state of science is reflected in the fact that the previous solutions hysteresis using neural networks described in the paper, only takes into account the behavior of a large number of pieces of piezo elements. In this way, an approximate form of hysteresis is obtained for a specific type and type of piezo element.

The assumption thus obtained does not take into account the degradation of the piezo element during exploitation and does not take into account the imperfections of the piezo element during the production itself. The principle shown in the picture also takes those parameters into account. Piezo crystal current measurement device (6) measures electrical resistance at each voltage used to drive a particular piezo element. Also, the device for measuring the current state of the piezo element (6), measures the electrical resistance of the piezo element housing itself and measures the electrical capacitance of the piezo element. The obtained parameters are then forwarded to the microcontroller (5), which adjusts the obtained values and converts them into a format suitable for input to the neural network (2).

Hysteresis usually has a smooth function, but during exploitation or due to the inhomogeneity of the material, it may cause noise or a sharp change in the hysteresis function in some area. In the described way, with all the mentioned measurements, we can predict where noise or a sudden change in the hysteresis function will occur. Such prediction is more accurate than existing solutions and therefore the piezo element itself can be used in places where even greater precision and even greater control of the piezo element itself or the mechanism driven by the piezo element is necessary.

2.2 Neural network training method

Training of the neural network for hysteresis prediction shown in Figure 2: the signal generator (1) generates a signal of the required amplitude and frequency to drive the piezo element (4), also the same signal is fed to the input of the neural network (3). The mechanical elongation of the piezo element (4) is measured by a digital comparator (6) which is connected to the microcontroller (5). The device for measuring the state of the piezo element (7) measures the electrical resistance at all voltages in the range required for the operation of the piezo element (4), measures the electrical resistance of the housing of the piezo element (4), and measures the electrical capacitance of the piezo element (4).

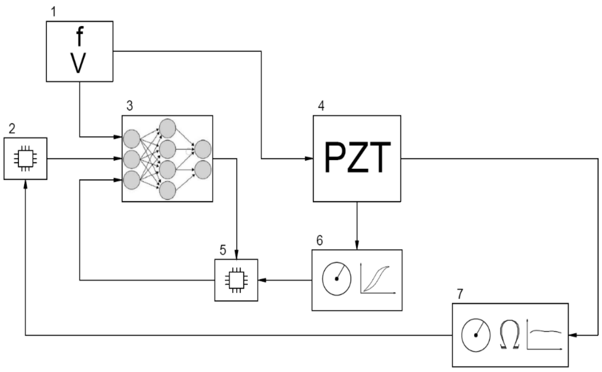

Fig 2.Method of training the neural network for prediction of hysteresis, taking into account the electromechanical state of the piezo element

The obtained measurements are forwarded to the microcontroller (2). The microcontroller (2) adjusts the signals so that they are suitable for input to the neural network (3). The microcontroller (5), based on the comparison of the generated signal of the desired position of the piezo element (4) and the actual value measured by the digital comparator (6), corrects the parameters of the neural network (3) in order to obtaining a match between the desired value and the measured value. When the values approach an acceptable level, the signal generator (1) changes the frequency and amplitude parameters.

The training continues until the desired and measured values are close to an acceptable level. The training then continues with all the desired parameters in terms of frequency and amplitude. In this way, the neural network (3) will be trained for the specific piezo element (4) that is being used at the given moment. Training should be carried out with as many different piezo elements as possible in order to obtain the highest possible accuracy of hysteresis prediction. An improvement over existing solutions is that this training model takes into account both electrical parameters that can tell us in what physical and mechanical state the piezo element is at a given moment.

During exploitation, these parameters change, and in this way we will be able to predict the hysteresis after the degradation of the piezo element, which gives us the possibility of more precise management of the piezo element. Also in this way, inhomogeneities in the piezo element itself, which arise during the production of the piezo element itself, will be shown. The inhomogeneity of the material will also be detected by the neural network (3), after training it will predict, and then the microcontroller in operation will compensate for it.

3. SIMULATION AND RESULTS

For simulation purposes, the MATLAB 2021 a software package was used. Within that package, the Deep Network Design tool was used. Within that tool, the process of creating and training a neural network is maximally simplified in order to quickly create a simulation and process the results.

The NARX Feedback Neural Network was used for the above method of hysteresis prediction. It was used because it gives the best results, both for the existing methods and for the new method described in the paper. Figure 3 shows the shape of the hysteresis in the time domain in the upper graph, and the deviation from the exact solution in the lower one. We can see that the deviation is small, and the largest in the places of sudden changes (maximum value).

Figure 4 shows the hysteresis in the time domain in the upper plot and the deviation from the exact solution in the lower plot, but unlike Figure 3, Figure 4 shows the plots of the case where more input parameters to the neural network were used. All input parameters are explained in section 2.2 and Figure 2 shows the block diagram of the neural network training model with multiple input parameters.

Figure 4 shows the hysteresis in the time domain in the upper plot and the deviation from the exact solution in the lower plot, but unlike Figure 3, Figure 4 shows the plots of the case where more input parameters to the neural network were used. All input parameters are explained in section 2.2 and Figure 2 shows the block diagram of the neural network training model with multiple input parameters.

4. CONCLUSION

In both cases, the NARX Feedback Neural Network with 100 neurons in the hidden layer was used. The algorithm used for training is Bayesian Regularization. Finally, comparing the graphics from Figure 3 and Figure 4, we can conclude that the improvement is significant with the use of more input parameters that describe the physical state of the piezo element itself and as mentioned at the very beginning of the paper, in this way we can predict the hysteresis for each piezo element individually at every moment of its working life (each percentage of degradation can be immediately predicted based on the input parameters described in this paper), while with the existing solutions, hysteresis prediction was only possible for the entire series of piezo elements based on a large number of samples from the same series.

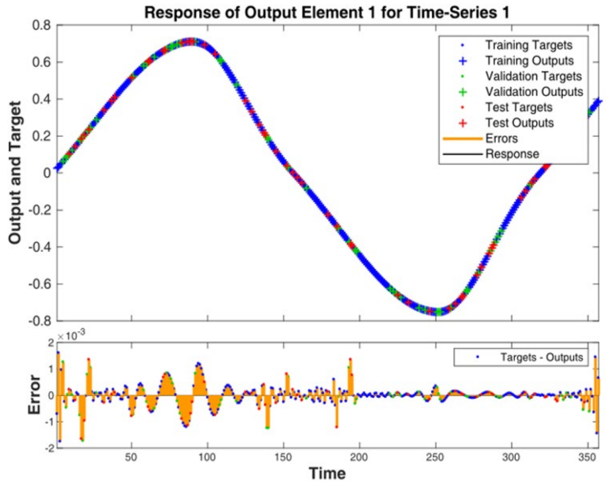

Fig 3.Hysteresis in the time domain in the upper graph and the deviation from the exact solution in the lower graph.

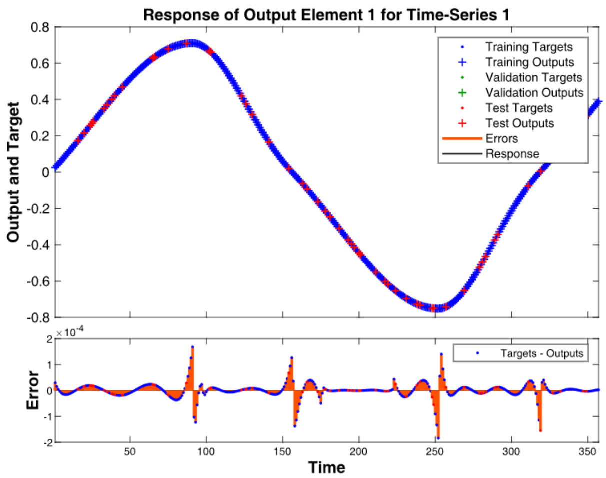

Fig 4. Hysteresis in the time domain in the upper plot and the deviation from the exact solution in the lower plot.

ACKNOWLEDGEMENTS

This research has been supported in part by the Serbian Ministry of Science, Technological Development and Innovations (451-03-47/2023-01/200108).

REFERENCES

[1] H. Qin, N. Bu, W. Chen, and Z. Yin, "An Asymmetric Hysteresis Model and Parameter Identification

Method for Piezoelectric Actuator,” Mathematical Problems in Engineering, vol. 2014, pp. 1–14, 2014, doi: 10.1155/2014/932974.

[2] M. P. Soares Barbosa, M. Rakotondrabe, and H. V. Hultmann Ayala, “Deep Learning Applied to Data-driven Dynamic Characterization of Hysteretic Piezoelectric Micromanipulators,” IFAC-PapersOnLine, vol. 53, no. 2, pp. 8559–8564, 2020, doi: 10.1016/j.ifacol.2020.12.566.

[3] L. Wang and Z.-R. Lu, “Identification of Bouc-Wen hysteretic parameters based on enhanced response sensitivity approach,” J. Phys.: Conf. Ser., vol. 842, p. 012021, May 2017, doi: 10.1088/1742-6596/842/1/012021.

[4] R. Bouc, “Forced vibration of mechanical systems with hysteresis,” in Preceedings of the 4th International Conference on Nonlinear Oscillations, Prague,Czechoslovakia,1967.

[5] Y.-K. Wen, “Method for random vibration of hysteretic systems,” Journal of the Engineering Mechanics Division,vol.102, no. 2, pp. 249–263, 1976.

[6] T. Sireteanu , O. Solomon, A.M. Mitu, M. Giuclea, „An analytical approach for approximation of experimental hysteretic loops by Bouc-Wen model,“ PROCEEDINGS OF THE ROMANIAN ACADEMY, Series A, Volume 14, Number 4/2013, pp. 335–342

Advanced electro-hydraulic systems for driving the movement of radial gates

Dragan Nauparac[1*],
PPT-Engineering, Belgrade (Serbia)

Radial gates are standardly used on spillway fields on dams for the evacuation of large periodic waters or for regulating the flow of water. The design of electrohydraulic systems for driving gate movement is considered. All elements of the design of such systems are analyzed in order to obtain the most advanced solution. This is especially important because the projected service life for such systems is 35 years until major overhaul. Special attention has been paid to transfer the dynamic behavior of the radial gate movement to an adequate load on the piston rod end of the hydraulic cylinder.

Keywords: Radial gate, Electrohydraulic system, Radial gate movement

1. INTRODUCTION

The radial gate is a standard design solution within the requirements set for controlling the flow (overflow) of water at dams. There are several constructive solutions, depending on the application. According to the place of installation, there are so-called external sradial gates and underground radial gates. There are radial gates where water flows over the upper gates edge, where water flows under down gate edge or a hybrid solution where water can flow under the gate edge and above the gate edge at same time. Basically it is a steel structure that stops the water over the arched surface of the stop sheet, Figure 1. The application of radial gates is older than the application of hydraulic actuation systems in practice, so the first drives for radial gates were electro-mechanical with a gear box and chain and in some cases with a counterweight.

Figure 1: Radial gate [1]

2. RADIAL GATE AS STRUCTURAL LOAD FOR HYDRAULIC CYLINDERS

2.1. Hydraulic drive configuration

According to its functional purpose, the radial gate needs to be lowered and raised in order to stop or generate the flow of water. The lifting and lowering can be such that there is only the gate lowered and the gate raised position, but it can also be lifting and lowered between the down and upper end positions. (regulating radial gate) One or two cylinders can be used to raise and lower the radial gate. Most often, when one cylinder is used, it is connected to the middle point of the gate, but there is also an option for particularly rigid constructions of radial gates where the cylinder is located on one side.

The force for dimensioning the electrohydraulic system for driving the movement of the radial gate can be determined based on the classic approach.

2.2. LIFTING FORCE CALCULATION

Hydrostatic pressure is the main load acting on the valve. The support hinge must be located in such a way that the line of action of the resultant hydrostatic pressure passes through its center.

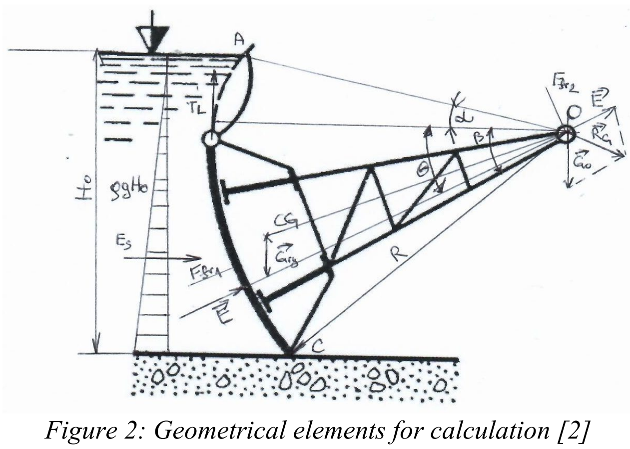

Figure 2: Geometrical elements for calculation [2]

Basic load for radial gate is hydrostatic force:

$$E = \rho g \frac{H_0^2}{2} b_{gs} \tag{1}$$

The gate weight G_{rg} can be preliminarily determined by the approximate dependence A.R. Berezinsky: [2]

$$G_{rg} = 1.5 A \sqrt[4]{A} \tag{2}$$

A-Surface covered with radial gate

Friction force in seals:

$$F_{fr1} = E b_y f_{seal} \tag{3}$$

E – hydrostatic pressure

*Dragan Nauparac, PPT-Engineering, Toplicin Venac 3, 11 000 Belgrade, SRB, dragan.nauparac@ppt-inzenjering.rs

b_y – wide of seal

f_{seal} – friction coeficinet

Friction force in support hinges:

$$F_{fr2} = R_o f_h \tag{4}$$

R_o – resultant force at hinge

f_h – hinge friction coeficient

Hydrodynamic pressure Wg. It is determined by the same formula as for a flat valve:

$$W_r = p_w b_s b_{gs} \tag{5}$$

p_w – pressure caused by rarefaction of the water flow

b_s – wide of stringer

b_{gs} – wide of radial gate ideal crosssection

The total force for lifting the radial gate is determined based on the forest of moments of all forces in relation to the pivot point:

$$\begin{aligned} &-T_L R\cos\alpha + k_1 G_{rg} R_G \cos\beta + k_2 F_{fr1} R_y + k_2 F_{fr2} r \\ &+W_r R\cos\Theta \end{aligned} \tag{6}$$

Total lifting Force is:

$$T_L = \frac{k_1 G_{rg} R_G \cos\beta + k_2 F_{fr1} R_y + k_2 F_{fr2} r + W_r R\cos\Theta}{R\cos\Theta} \tag{7}$$

Lifting power is:

$$N = \frac{T_L v_{rg}}{\eta}[\mathrm{kW}] \tag{8}$$

v_{rg} – 0.3-0.5 m/min

η – 0.6-0.8

k_1 – 1.1-coeficient of spare

k_2 – 1.2-coeficient of spare

2.3. RADIAL GATE AS STRUCTURAL LOAD

How do we define structural load? Because it is a steel structure with a difficult or complex distribution of masses and there is no possibility of defining the reduced mass. Is it a load with variable damping and variable stiffness? Basically, when moving, we have a change in the friction force, so the damping is variable while the stiffness of the structure is unchanged. But this must be taken conditionally because when we look at the steel construction of the gate together with the two hydraulic cylinders, then the overall stiffness of the system changes as a function of the position of the piston rods of the cylinders, where we have different volume of oil and it is oli spring with with a change in stiffness.

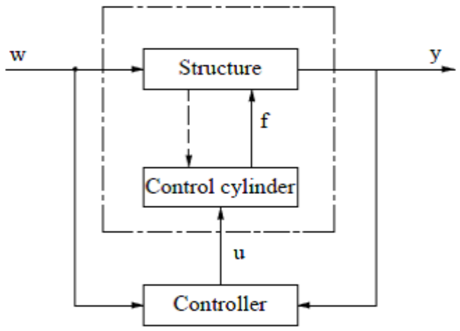

Figure 3: Block diagram of active/semi-active structural control systems [3]

Figure 3 shows a block diagram of the actuator (cylinder) and the structural load. In what is bounded by the dashed line is the interaction of the cylinders and the structure and these two parts of the system cannot be considered separately. f shows the force with which the actuator acts on the structure, y is the displacement of the structure, u is the control signal. If we modify the block diagram, Figure 4 from Figure 3, we can put the interaction of the structure and the actuator (transfer function) into a feedback loop.

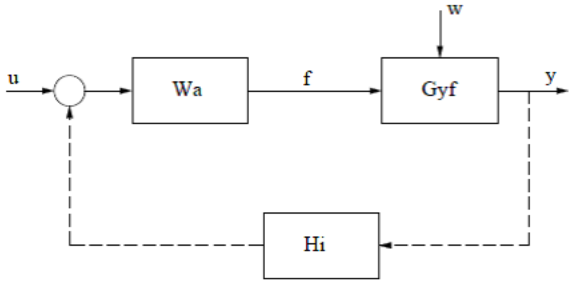

Figure 4: Model of interaction between the actuator and structure [3]

It is clear that one transfer function is related to the actuator Wa and the other refers to the action of the force on the structure and its output is the movement of the structure. If we now construct the cumulative transfer function, we get:

$$W_{yx} = \frac{W_{yf} W_a}{1 + W_{yf} W_a H_i} \tag{9}$$

We can also create a control-force transfer function that acts on the structure:

$$W_{fu} = \frac{W_a}{1 + W_{yf} W_a H_i} \tag{10}$$

From the transfer function, the control-force acting on the structure, that the dynamics from the control to the force on the structure does not depend only on the actuator, but also contains the dynamics of the structure. This is the initial step in modeling the structural load, and the final one should be in the form, which shows this interaction through second-order transfer functions.

What will be aimed at in the future work is to determine the first, second and higher harmonics of the steel structure of the radial gate using the finite element method, so that the structural load can be shown as form of block diagram, as in the Figure 5:

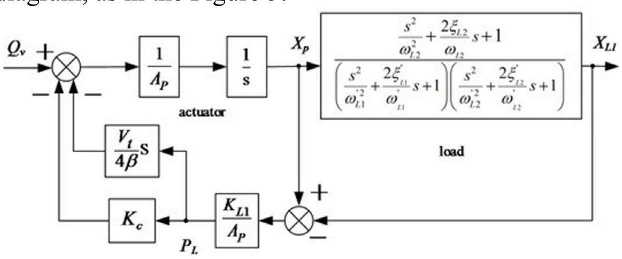

Figure 5: Block diagram for structural load [4]

In this way, it allows us to more accurately define, through simulations, the load on the hydraulic cylinder that is connected to the radial gate, which results in a much better design of the control algorithm for any configuration of the hydraulic part of the system. The load modeled in this way allows the control algorithm to be defined so that in some moments it is controlled by force and in others by stroke according to different criteria: Force is greater than permitted, controlled by force, less than permitted controlled by stroke, error between desired and of the actual force is greater than the error of the set positions and real cylindder rod positions, it is controlled by force and vice versa or according to the speed of change of force and position.

3.ELECTROHYDRAULIC SYSTEM FOR CONTROLLING THE MOVEMENT OF THE RADIAL GATE-TWO CYLINDER MOVEMENT

In practice, there are several typical solutions for controlling the movement of radial gates and several special modifications. Basically, typical solutions are shown in Table 1. (Appendix 1) The basic thing when choosing the concept of an electrohydraulic system for driving the movement of a radial gate is whether the rigidity of the gate is such that we can work with so-called passive synchronization or with active synchronization. For passive synchronization, the stiffness of the gate must be such that the pressure changes are fast, for small position changes, and that as such pressure changes can be equalized by hydraulically connecting both sides of the gate movement drive, see row 1, Table 1. With passive synchronization, we do not measure the positions of the left and the right side of the gate. Only the gate position can be measured. In case of overloading of this system, which leads to jamming of the gate, the system stops according to the high pressure signal and the correction of the cylinder positions is usually done manually, by lowering the upper side. From this we conclude that passive synchronization is expected to be highly robust in keeping the error of synchronous movement within certain limits. In any case, for the application of passive synchronization, it is necessary to make a stiffer construction, which is less rational from the point of view of the production cost. In cases where a more rational design of the gate, less stiffness, must be used, then the concept of active
synchronization must be used, which means that the feedback loops are closed according to the position of this cylinder, the error is calculated and the corresponding control signal is generated by computer. Before the mass application of computers in practice, active synchronization was solved in two basic ways: Through a mechanical differential transmission, where one cable entered on each side of the gate and when a difference in movement was generated, we had a corresponding displacement that was mechanically transmitted to the valve that should to slow down the faster cylinder. Another way was via selsin (operating and differential) and when a certain voltage proportional to the error of synchronous movement is generated through a comparator, by comparing certain values of the set and actual error voltage, it was possible to activate a certain electromagnetic valve in the relay technique. There was another solution, which was to stop the faster side until the positions were equal and then continue the movement to the next stop, row 2, Table 1 (Appendix 1) shows current project solutions of electro-hydraulic systems for driving radial gate with options where feedback signal are analog (4-20mA) or digital (SSI, ProfiBus, ProfiNet,CAN ,...).

4. ADVANCED SOLUTIONS FOR ELECTROHYDRAULIC SYSTEMS

Certain design solutions from the general progress of electrohydraulic actuation systems motion control technology can be applied in the control of radial gates. What cannot be significantly improved by control technology is if the gate has high external friction. One of the requirements for the manufacture and installation of gate is that, in relation to the weight of the gate being lifted, the lateral friction (one side) cannot exceed 20% in relation to 50% of the mass of the gate. And within that 20% of friction, one side of the fastener must not differ in friction force by more than 50%.

In addition to classic algorithmic solutions, we should not forget the option with slowing down the movement by changing the flow on the side where the pressure approaches the maximum value.

The progress is reflected above all in the application of the proportional technique, which enables great adaptability according to the current conditions of movement. Here, above all, we mean the external temperature and the quality of the sealing and guiding and sealing of the gate. There are some conditions that do not change and are visible only after assembly and the first manipulations. The electrohydraulic system should be adaptive to those conditions as well. Here, first of all, we mean the actual parallelism of the side walls of the flow tract as well as the position of the gate position in relation to them and the flatness of the threshold (horizontal surface where the gate rests). These conditions define the permissible error of the synchronous movement of the shutter as well as the stiffness of the gate, i.e. the deformation that can occur at maximum working pressure on one side of the gate. Experimentally, the operating stiffness of the gate can be determined as follows:

$$K_z = \frac{\Delta p}{z}\,[\mathrm{Pa/mm}] - \text{stiffness} \tag{11}$$

$$\Delta s = \frac{F_{\max}^{lift} - F_{\max}^{hold}}{A\dfrac{\Delta p}{z}}\,[mm] - \begin{matrix}\text{permissible gate tilt} \\ (\text{synchronization error})\end{matrix}\ [5] \tag{12}$$

The above explained calculation of stiffness should be a part of the off-line identification parameter procedure.

The basic question is when to use the proportional technique and when not to use the concept of active synchronization. One of the basic criteria is the speed of gate movement and the maximum permissible synchronous movement error. In addition, it is also important what the actual mass of the shutter is because with large masses, there is a risk of causing vibrations with a high initial speed. In that case, a proportional technique (flow regulator or proportional distributor) is necessary in order to accelerate to a stationary speed without the risk of vibrations. An alternative solution to this is a piston-axial pump with two flows, a low flow for starting movement and a higher flow for stationary movement speed. This option can also be used for volumetric discrete control of synchronous movement during lifting. Lowering of the segment shutter is most often by its own weight. Sometimes it is necessary to add pressure on the side of the piston during descent, due to friction that can significantly dampen the dynamics of error correction of the shutter's synchronous movement. In addition to this,

due to corrosion and due to the work of seals on the piston, it is good to have the working fluid on the other side at a certain pressure.
By using a PLC computer to control the movement of the radial gate, it is possible to implement different control algorithms, work diagnostics and work monitoring, as well as to quickly switch to the backup hydraulic control contour in the event of a failure.

5. IDEAL GATE MOVEMENT

In any case, the error of the synchronous movement of the gate is one of the most important parameters of the quality of the function of raising and lowering the radial gate. But in addition to the error of synchronous movement, it is especially important that the distribution of the load is such that there is a minimum difference between the left and right sides during movement. When there is a minimum pressure difference due to the load, then we have equal pressure drops on the control valves. This is especially important when feeding both cylinders from one pump. In some cases, we have a situation where each cylinder on its side has its own pump unit and then we do not have the influence of one cylinder on another based on the supply pressure. [6]

Figures 6, 7 and 8 show the pressures in the cylinder rod chamber during lifting and lowering. For all three cases of movement, the error of synchronous movement is within the permissible limits with different pressure changes.

6. THE OPTIMAL CHOICE OF THE CONTROL ALGORITHM FOR THE MOVEMENT OF RADIAL GATE

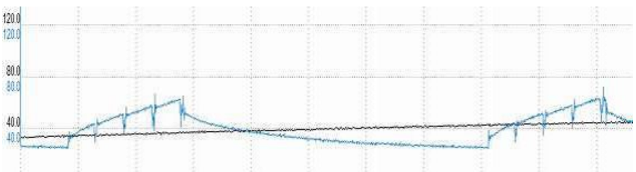

Figure 6: Stationary lowering of radial gate [7]

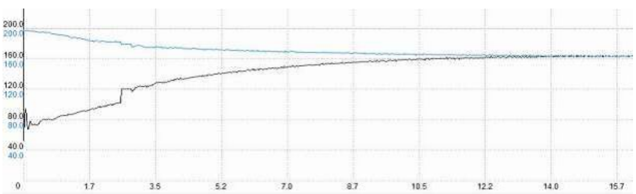

Figure 7: Start lifting of radial gate [7]

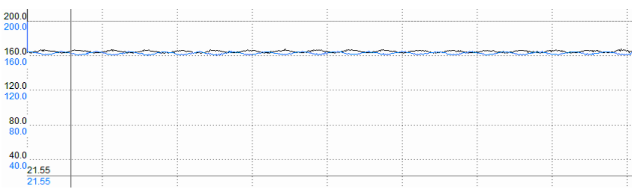

Figure 8: Stationary lifting of radial gate [7]

The configuration of the electrohydraulic system also affects the choice of control algorithm. Basically there are several approaches which can be described as follows: (see Table 1, Appendix)

-the faster cylinder slows down
-the slower cylinder accelerates
-the slower cylinder accelerates and the faster cylinder slows down at the same time

Another part of the control structure is how we generate the acceleration or deceleration signal. It can work with continuous flow change and with discrete flow change, which also depends on the configuration of the electrohydraulic system. (see Table 1, Appendix)
Thirdly, and what is particularly important, for the working executive device (control valve) for slowing down or accelerating, but there is also an additional option - the reserve executive device for slowing down and accelerating if the intensity of control reaches saturation. In this way, we solve two things: First, if there are unforeseen disturbances, the quality of the synchronous movement function will be maintained, and second, if there is a failure on the working executive device (control valve), we have a spare option that we can use to maintain the working ability of the synchronous movement of the radial gate in a slightly lower dynamic quality.
Force (pressure) feedbacks are mandatory if the synchronous motion control algorithm is to be improved.

7. CONCLUSION

From the previous analysis, the complexity of designing an electrohydraulic system for driving the movement of the radial gate can be seen. It is clear that one of the project activities represents the most precise determination of the character of the load, and the second part of the project activities includes defining such a configuration of the electrohydraulic system that the algorithmic solution for control synchronous movement can provide sufficient robustness even in the event of unforeseen disturbances that affect the movement of the radial gate while maintaining the working ability of movement gate and in the case of any component of the electrohydraulic system. It is clear that the choice of a PLC computer for the control signal provides advanced work monitoring and correctness diagnostics. With all of the above, a compromise must be made to ensure that the electrohydraulic system is also easy to maintain.
The first step in the technology of definition-modeling of structural load is presented, as well as the direction for future work towards a universal model of structural load for the case of radial gate.

ACKNOWLEDGEMENTS

This work was created as a systematization of the design experience in the engineering company, PPT-Engineering, Belgrade, which specializes in the design of this class of electrohydraulic systems. I am grateful for the opportunity to present part of our experience.

REFERENCES

[1] D.Nauparac, N.Visnic and N. Cero, "Comparison Of The Quality Of Synchronous Motion Of Radial Gates For Different Configurations of Electric-Hydraulic Drives" Fluid Power, Maribor (2019)
[2] Государственный университет морского и речного флота им, С.О. Макарова, лекция 14

[3] S.J.Dyke, B.F Spencer, P.Quast. M.K.Sain, “Role of Control-Structure Interaction in Protective System Design“, ASCE Joiurnal of Engineering, Mechanics, Vol121, No.2, Feb.1995., pp.322-338
[4] S.Zaho,K.Chen, Y.Zaho, G.Ying,C.Yin,X.Xiao, A High Order Load Model and Control Algorithm for an Aerospace Electro Hydraulic Actuator, IeCAT, 2021
[5]Vujić, D, Problematika sinhronizacije rada hidrauličkih pogona zatvarača na hidrotehničkim postrojenjima sa posebnim osvrtom na vibracionu stabilnost, magistarski rad, Mašinski fakultet u Kragujevcu, 1980. Godina
[6]Rae, S, Drive & Control Systems for Gates in Civil Engineering Application, Bosch- Rexroth, 2014,
[7] Projekti za elektrohidrauličke instalacije za pogon segmentnih zatvarača, Ustava Opovo, Ustava Pančevo projekti PPT-Inženjeringa, Beograd, SRB, 2010-2012. godina
[8] R.Ortmann, Possibilities of synchronization controls, Conferinta De Sisteme Hidropneumatice De Actionare, Timisoara 19-22 octombrie 1995, Romania

Appendix 1:

Table 1-Basic electrohydraulic configuration

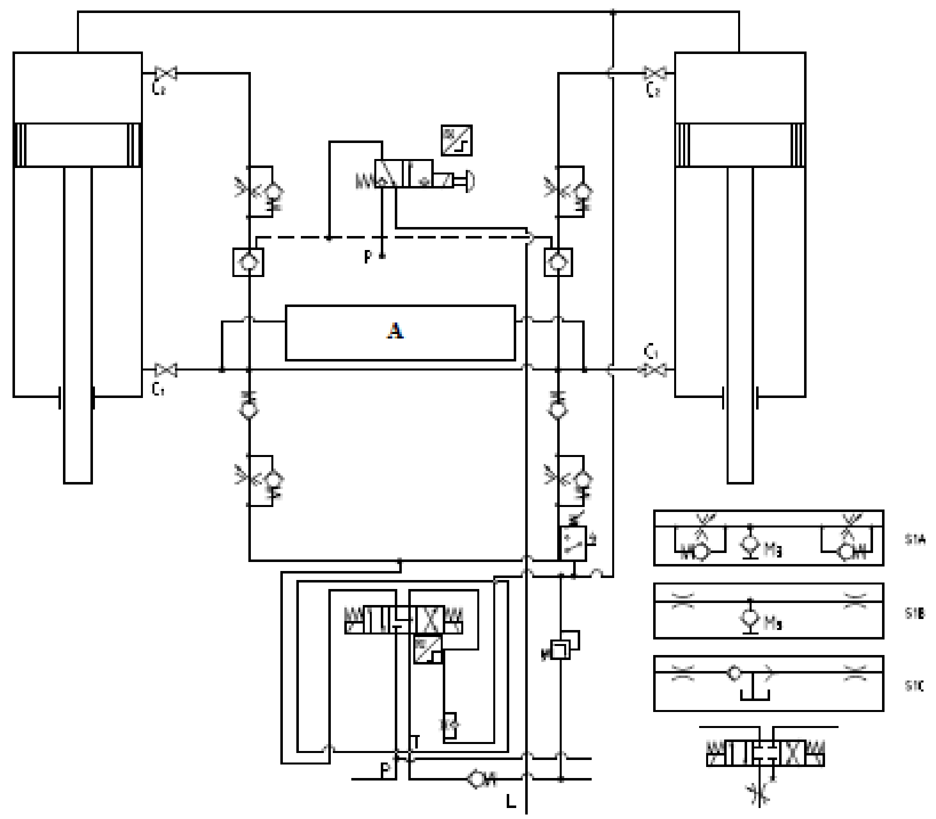	Lowering: Under the influence of own weight The basic configuration can be used passive synchronization, depending on the options for part of the hydraulic contour <A>. Option with 4/3 directional control valve is for active synchronization.
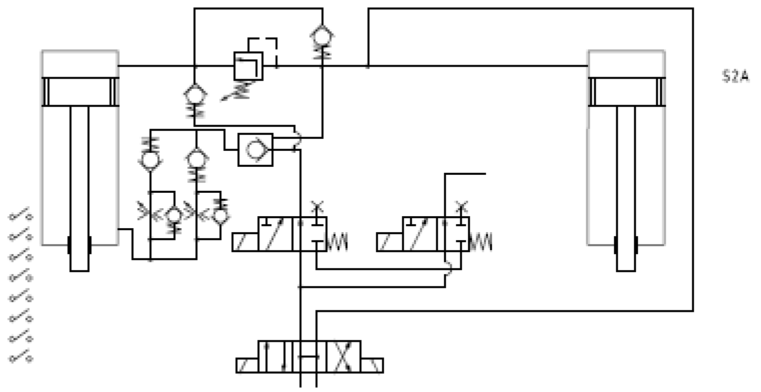	Stepwise movement, in each step the faster cylinder waits for the slower one to equalize the positions. Different lifting and lowering velocity can be set.[8]

<table>
<tr><td>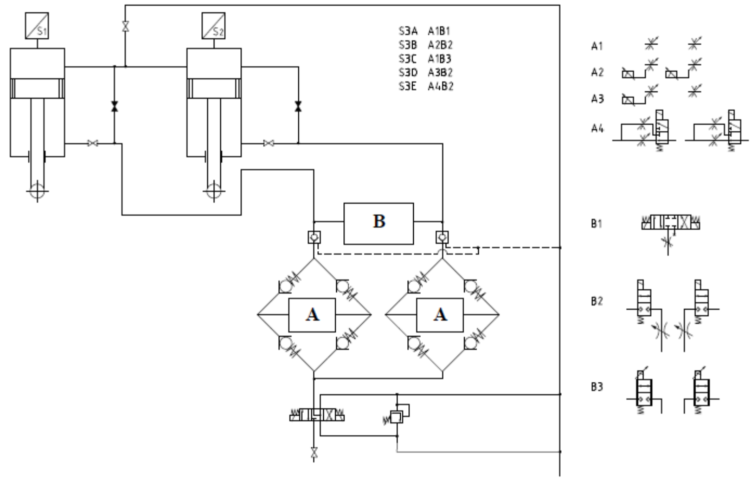
</td><td> The configuration allows several options: - deceleration of the faster cylinder during lifting and lowering -deceleration of the faster and acceleration of the slower cylinder at the same time during lifting and lowering. -reserve hydraulic contour </td></tr>
<tr><td>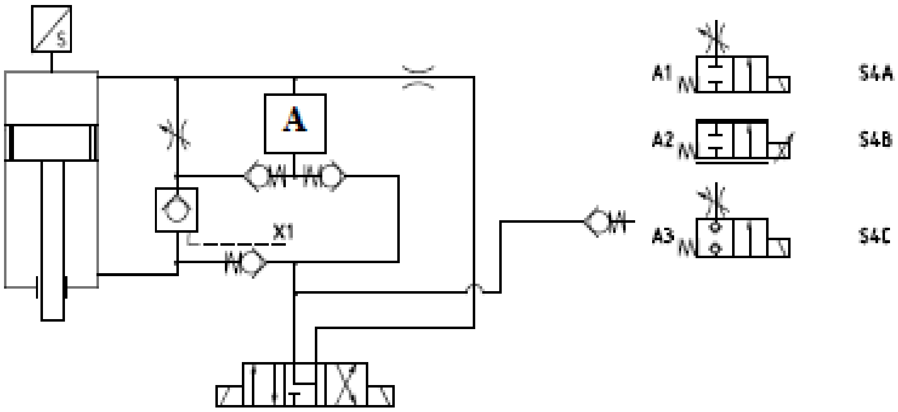
</td><td>When lifting we have deceleration when lowering we have acceleration for one cylinder rod with the same control valve in all three options for its selection.</td></tr>
<tr><td>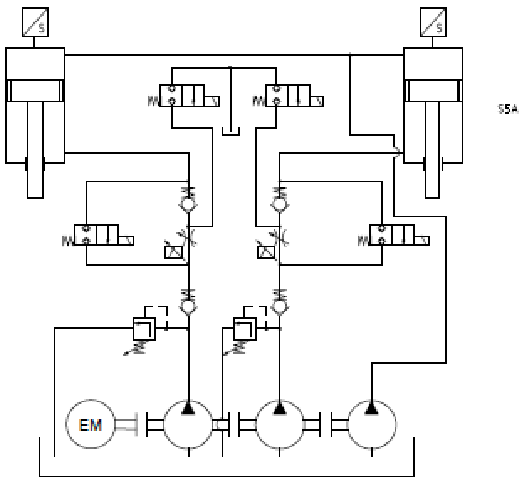
</td><td> Lowering: Under the influence of own weight At the same time, the faster cylinder can be decelerated and the slower cylinder accelerated. No additional pressure can be generated from the piston side of the cylinder. </td></tr>
</table>

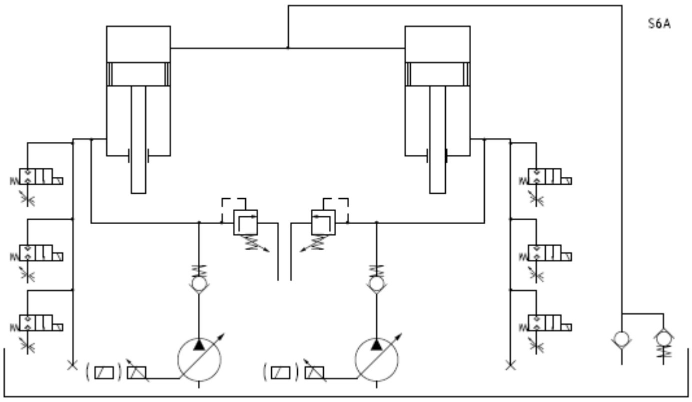

When lifting we have deceleration when lowering we have acceleration for one cylinder rod with the same control valve in all three options for its selection. More discrete values are generated for flow which is an additional control option over duration of bleed of flow control.

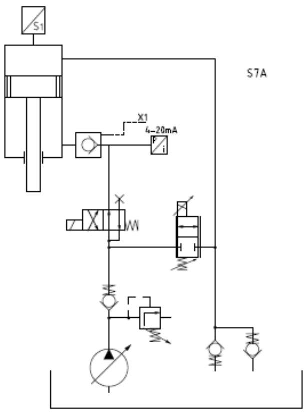

The simplest configurations for raising and lowering, one for each cylinder, proportional control, necessary pressure feedback to adjust parameters for bleed of control option.

Table 2-System configuration selection elements

System charact.	S1A	S1B	S1C	S2A	S3A	S3B	S3C	S3D	S3E	S4A	S4B	S4C	S5A	S6A	S7A
Low velocity		+		+	+		+	+	+	+		+		+	
High velocity	+		+			+							+		+
Short distance				+											
Medium distance	+	+	+		+		+	+	+					+	
Long distance		+	+			+				+	+		+		+
Synch. Accuracy Less than 80-50 mm		+	+	+											
Synch. Accuracy Less than 40 mm	+				+		+	+	+	+	+	+		+	
Synch. Accuracy Less than 10-15 mm						+							+		+
Disturb. High				+		+		+				+			
Disturb. Medium	+		+		+		+		+	+			+	+	+
Distirb. Low		+									+				

Modeling and simulation hydraulic excavator's arm

Almir Osmanović[1*], Elvedin Trakić[1], Salko Čosić[1], Mirza Bečirović[1],
[1]Faculty of mechanical engineering/Mechatronic, University of Tuzla, Tuzla (Bosnia and Herzegovina)

With the development and implementation of new techniques in hydraulics, hydraulic systems are increasingly applied as systems by which the transfer is made and power management for the systems with which the operation is performed with working organs that perform technological operations of mobile machinery and equipment. In this paper is present application of hydraulic components and systems as part of mechatronic subsystems on mobile machines. There are advanced modern hydraulic components that enable fast change of direction of the executive organs working machines with continuously changing pressure and flow rate. Also in the work is present the application of software tools that allow the simulation of hydraulic system, from which then allows flexibility in terms of finding the best solutions in the design of the above systems. It is significant to note also that the developed model with some corrections can be used for simulation, analysis and control of the hydraulic system on similar mobile machines similar with similar or same configuration, with respect to a number of different types of mobile machines that are in use.

Keywords: Hydraulics, Hydrostatic power transmission, Mechatronic systems, Control, Modeling, Simulation, Mobile machine and equipment.

1. INTRODUCTION

Hydraulics has increased the use of mechanization and automation of machinery and work processes with the growth of manufacturing, construction, affordable technology, and other industries in alongside electronics. Because of its benefits over competing technologies, hydraulics has been adopted more widely and developed into one of the most important parts of mechatronic systems in every industry. Due to the ever-increasing expectations for performance and the practicality of their use, hydraulic systems present a design challenge. These systems are also made with the intention of lowering overall dimensions while boosting reliability and resilience. These systems' failures have been brought on by a loss of power brought on by a drop in system pressure and an increase of contaminants [1]. The loss of stability in these systems results in large pressure oscillations and, with them, reduces the usability of such systems, which is the subject of this paper. The following are the fundamental features of a hydraulic system for mobile machines: Hydraulic methods are most frequently used to control drive components. Since there isn't much room for installation, more parts are incorporated into a single unit. The parts must be easily maintainable and of straightforward construction. Because of its compactness, high stiffness, relatively low weight, and capacity to transfer significant forces (moments), hydraulic systems are often used in the transfer of power. It is a simple way to change rotary action into translational movement and can hold heavy weights without overloading.

2. HYDRAULIC SYSTEM OF EXCAVATOR

Hydrostatic circuits are often operated as open or closed depending on the fluid that is unfolding the circuit in the system. Figure 1 shows the system's functional layout [2]. The most crucial factor in choosing and defining the hydrostatic system is system pressure. Low pressure can reach as low as $16 \cdot 10^5$ [Pa], medium pressure can reach as high as $25 \cdot 10^5$ [Pa], and high pressure can reach as high as $42 \cdot 10^5$ [Pa]. The pressure required for the same hydraulic power option requires less system flow and fewer parts, making the system smaller and lighter [3]. On the other hand, when pressure rises, losses and noise also do, shortening the system's lifespan.

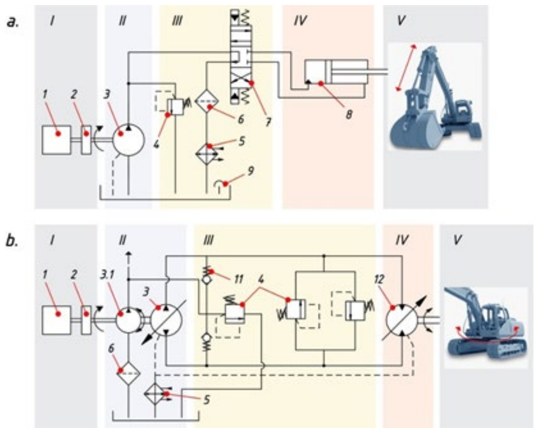

Figure 1. Model of hydraulic system: a) open, b) closed.

2.1. Hydraulic manipulator

An excavator arm, also known as a boom or manipulator, is a key component of a hydraulic excavator. The arm is typically made up of several segments or sections that are connected by hydraulic cylinders, allowing it to extend, retract, and rotate in various directions. The excavator arm is usually connected to the machine's main body or chassis via a pivot joint, which allows the arm to move up and down. The pivot joint is powered by a hydraulic cylinder, which provides the force and movement necessary to lift and lower the arm. At the end of the excavator arm, there is usually an attachment or end-effector, such as a bucket or a grapple, which is used to pick up and move materials. The attachment is connected to the arm via a quick coupler, which allows the operator to quickly and easily swap out different attachments depending on the task at hand. The excavator arm can also be equipped with various sensors and cameras to help the operator monitor the movement and

*Corresponding author: Urfeta Vejzagića 4, 75 000 Tuzla and osm.almir@gmail.com

positioning of the arm, as well as the materials being handled. In addition, the arm can be controlled by a variety of different inputs, including joysticks, pedals, and touchscreen displays. Overall, the excavator arm is a critical component of a hydraulic excavator, enabling the machine to perform a wide range of tasks in different environments and applications, such as construction, mining, and demolition.

Figure 2. Hydraulic excavator.

2.2. Kinematic structure of a hydraulic manipulator

The kinematic structure of a hydraulic manipulator refers to the arrangement and configuration of the links, joints, and actuators that make up the arm or boom of the machine. A hydraulic manipulator typically consists of several segments or links that are connected by joints, which allow the segments to move relative to each other. The most common kinematic structure for a hydraulic manipulator is a serial chain, which consists of a series of links that are connected end-to-end in a linear fashion. The links are usually powered by hydraulic cylinders, which provide the force and movement necessary to manipulate the materials being handled by the machine. The joints that connect the links can be of different types, depending on the range of motion and degree of freedom required for the manipulator. The most common types of joints include: Revolute joints: These joints allow the segments to rotate relative to each other around a single axis. Prismatic joints: These joints allow the segments to slide or extend along a single axis. Spherical joints: These joints allow the segments to rotate relative to each other around multiple axes. Planar joints: These joints allow the segments to move in a single plane or flat surface.

The kinematic structure of a hydraulic manipulator can also include various types of end-effectors or tool attachments, such as buckets, grapplers, and breakers, which can be used to perform specific tasks. Overall, the kinematic structure of a hydraulic manipulator plays a crucial role in determining its range of motion, degree of freedom, and versatility in different applications.

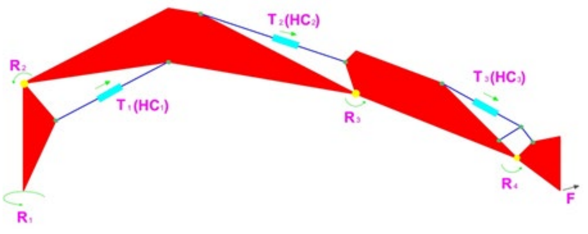

Figure 3. Simple kinematic structure of the hydralic excavator manipulator.

3. MODELLING AND SIMULATION

Analysis of complex systems requires the use of techniques consisted of modelling and simulation of that system. The process of simulation of excavator kinematic chain is consisted of defining [3]:

- the mathematical model of the excavator kinematic chain
- the mathematical model of the parameters of manipulator working movements, including trajectory of movement, partial and total time of movement, and correlation between kinematic chain and surface, as well as correlation between kinematic chain and working object.

In this work, a model of an excavator arm with hydraulic components was developed using the Matlab/ Simulink program. Using SimMechanics the model of hydraulic excavator with corresponding model of hydraulic components has been developed. Rigid bodies are presented as convex surfaces because of Simulink restriction, with boom consisting of two welded convex surfaces. Any influence of this welding is neglected in the simulation process. Figure 3 shows the mechanical structure of excavator arm.

Here in this paper is considered a simplified mechanical structure, shown in Figure 4, following the idea, where the hydraulic excavator arm modelled as a three-planar, provided that it is taken into account and the rotation of the platform. In Figure 4 is marked with $O_0X_0Y_0Z_0$ stationary coordinate system. Angle θ_1 the angle of rotation of the platform about the axis Y_0 and θ_2, θ_3, θ_4, angles of rotation of the mast, arrows and buckets, respectively around the axis perpendicular to the plane formed by the boom and bucket.

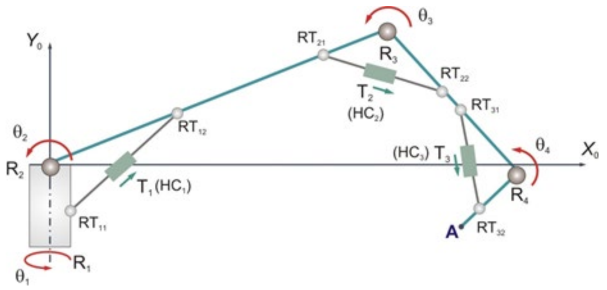

Figure. 4 Structure of the hydraulic excavator.

With R_1, R_2, R_3 and R_4 are indicated rotating joints that allow rotation of the platform, mast, boom, and bucket masts, while T_1, T_2 and T_3 shown translational joints to reinforce the hydraulic cylinders (marked with HC_1, HC_2 and HC_3 in figure 4). The material and part geometry data for hydraulic excavator arm are given in Table 1.

Tabel 1. Geometrical data for excavator arm.

		Boom	***Arm***	***Backet***
Length [m]		*6,0*	*3,5*	*1,25*
Mass moment of inertia [kgm²]	I_{xx}	*102,5*	*31,25*	*83,3*
	I_{yy}	*9040,0*	*1542,5*	*130,2*
	I_{zz}	*9062,5*	*1551,2*	*130,2*
Mass [kg]		*3000,0*	*1500,0*	*1000,0*

Simulink model hydraulic excavator is shown in Figure 5.

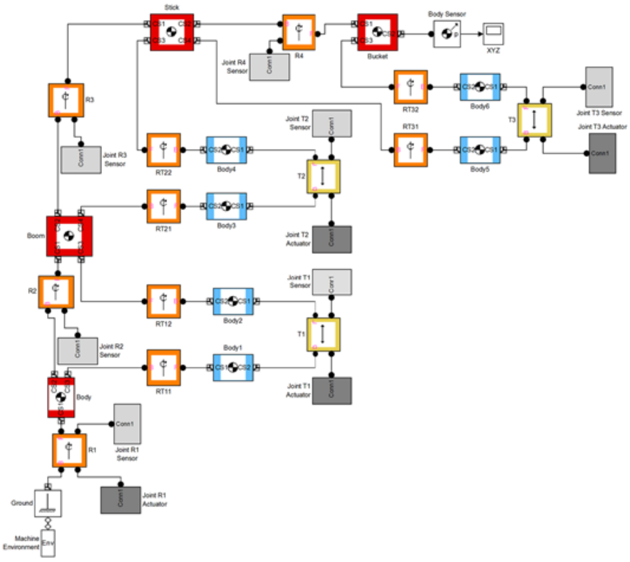

Figure 5. Simulink model of hydraulic excavator.

Articulated variables - the rotation angles and the corresponding moments for joints R_1, R_2, R_3 and R_4 are monitored by sensor system, whose structure is present in Figure 6.

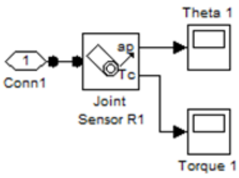

Figur 6. The sensor system for joint rotary joint R_1.

Joints R_1, T_1, T_2 and T_3 are driven, whereby the consideration of two cases:

1. Only the mechanical component defined by the trapezoidal profile velocity joint R_1, T_1, T_2, and T_3 is covered in the first.
2. Operation of prismatic joints T_1, T_2 and T_3 is accomplished via hydraulic cylinders.

The initial position of the excavato arm, with the all three hydraulic cylinder, and their geometric data is shown in Figure 7.

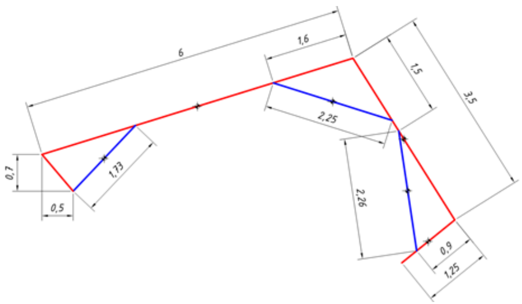

Figure 7 .The initial position of articles hydraulic excavator (Note: All units are in meters).

3.1. The simulation of joints R_1, T_1, T_2, and T_3 with a specified speed

The joints R_1, T_1, T_2, and T_3 are simulated with a specified velocity profile. The movement shown in Figure 8 forms the actuator's structure. Component Signal Builder creates the trapezoidal speed profile shown in Figure 8. The motion in all joints R_1, T_1, T_2, and T_3 is supposed to work synchronously, with the same phases of rapid movement, uniform movement at a constant speed. The unit trapezoidal signal is then strengthened, where reinforcement for the joints R_1, T_1, T_2, and T_3 amounts to KR_1=0.25; KT_1=0.12; KT_2=0.12; and KT_3=0.10, depending on the process that is to be achieved.

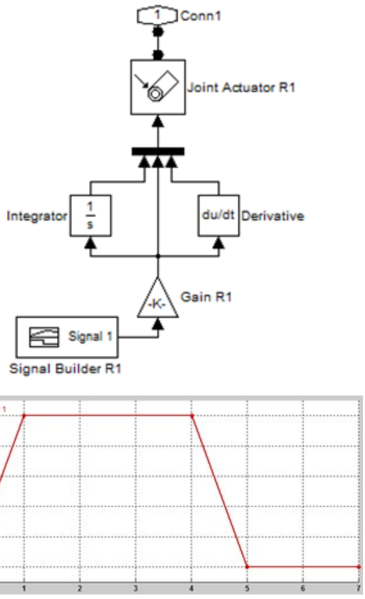

Figure 8. The structure of the actuator for rotating joint

The simulation was performed for a period of 7 seconds. Figures 9 shows the configuration of the hydraulic excavator at the beginning and end of the simulation.

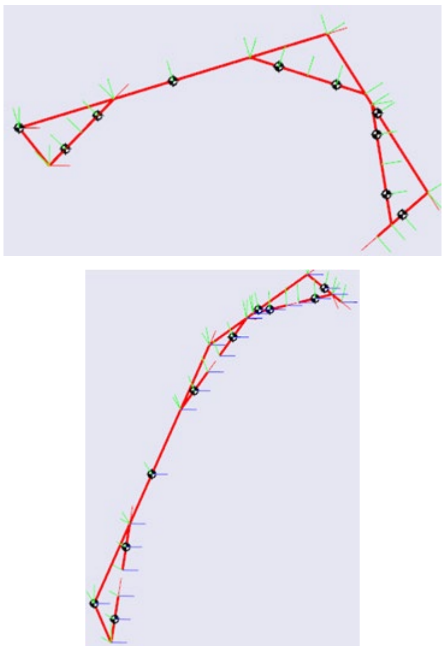

Figur 9. Hydraulic excavator arm: a) at the beginning of the movement; b) at the end of movement.

Figure 10 shows the results of the simulation, particularly the movement of individual joints as well as the forces along the joint axis, and the moment for the joint's axis of rotation, while Figure 11 shows the trajectory indicated by point A.

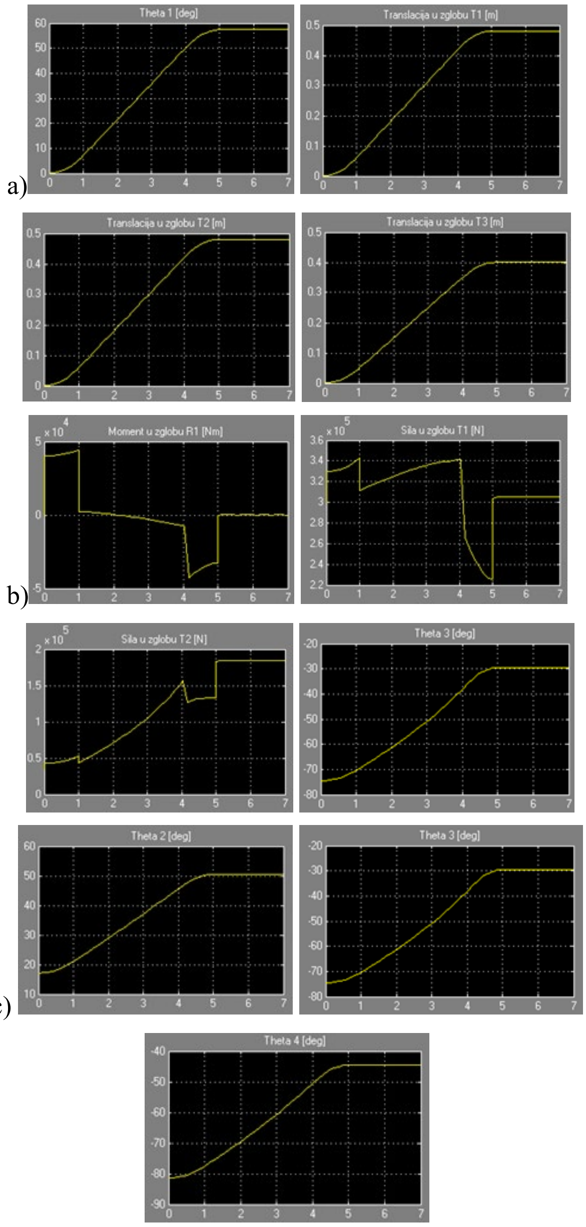

Figure 10. a) The corners and translation of driven joints R_1, T_1, T_2 and T_3, b) Forces and moments required for the execution of movement in the joints R_1, T_1, T_2 and T_3, c) rotation of joint R_2, R_3 and R_4.

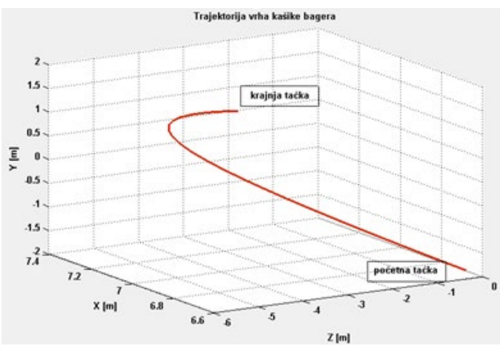

Figure 11. The trajectory described by the top bucket hydraulic excavator (point A).

The connection between the coordinates that define the hydraulic excavator's bucket tip, point A, and the angles in the joints R_1, R_2, R_3, and R_4, was made in order to validate the simulation model of the excavator that had been created. In other words, the manipulator mechanism's direct kinematic problems is solved. The equations below provide the direct kinematic model in the Denavit-Hartenberg notation.

$$X_A = \cos(\theta_1)\cdot\left[L_2\cos(\theta_2)+L_3\cos(\theta_2+\theta_3)+L_4\cos(\theta_2+\theta_3+\theta_4)\right],$$
$$Y_A = L_2\sin(\theta_2)+L_3\sin(\theta_2+\theta_3)+L_4\sin(\theta_2+\theta_3+\theta_4),$$
$$Z_A = -\sin(\theta_1)\cdot\left[L_2\cos(\theta_2)+L_3\cos(\theta_2+\theta_3)+L_4\cos(\theta_2+\theta_3+\theta_4)\right], \quad (1)$$

where L_2, L_3, and L_4 are the lengths of the hydraulic excavator's boom, arm and bucket, respectively. The values of point A's coordinates in the global, inertial system can be obtained by entering the values of the angles θ_1, θ_2, θ_3, and θ_4 into equations (1). Figure 12 displays the differences between the coordinate values acquired by simulation and the analytical solution.

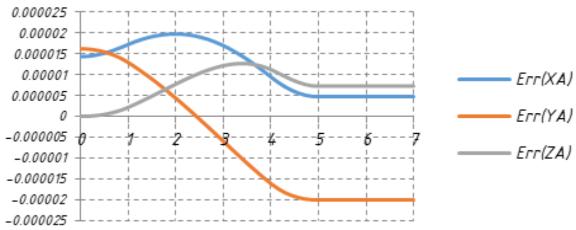

Figure 12. Deviations of the values of coordinates of point A obtained by simulation from the analytical solution

It can be concluded that the developed simulation model of the mechanical component of the hydraulic excavator is accurate because the deviations of the values of the coordinates calculated for point A in relation to the analytical solution obtained by applying the direct kinematic solution, according to equation (1), are of the order scale of 10^{-5} [m].

3.2. Simulation with hydraulically reinforced prismatic joints T_1, T_2 and T_3

In the second case, the translator joints T_1, T_2 and T_3 are reinforced with hydraulic cylinders, and the structure of the-Joint T_i Actuator components (for i=1,2,3) from Figure 5 at the next level shown in Figure 13a.

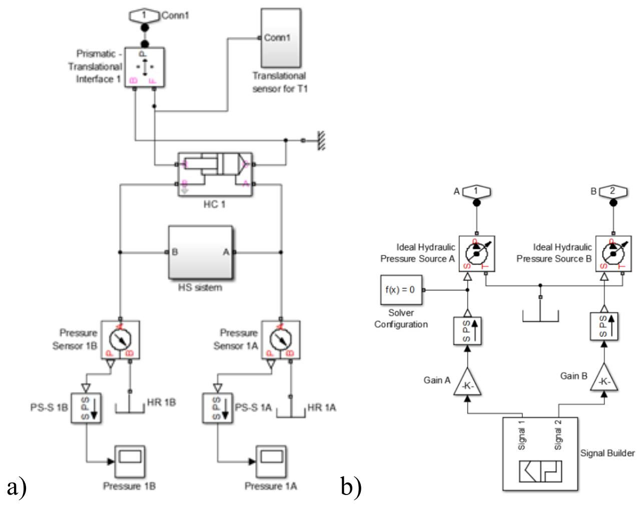

Figure 13. a) The structure of the hydraulic drive prismatic joint, b) Structure components HS System 1

a) b) c)
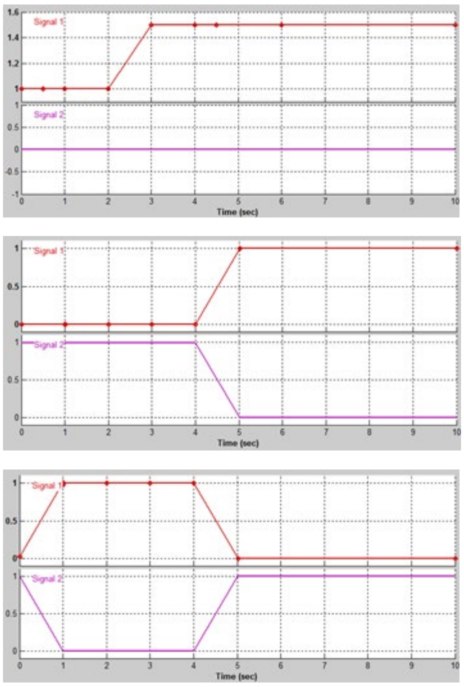

Figure 14. Signals on a) HC_1, b) HC_2, c) HC_3.

The translatory movement of the connecting rod of the hydraulic cylinder is transferred to the prismatic joint by means of the Prismatic-Translational Interface component [4]. In [4], the drive of a two-member planar arm with hydraulic cylinders is presented. In this part, the hydraulic cylinder is driven by a pump whose output pressure is proportional to the signal formed by the Signal builder component, Figure 13b. With the help of Gain A and Gain B components, the desired values of the pressures on the hydraulic cylinders are achieved. Thus, cylinder HC_1 works with a pressure of 1.5e7 to 2.25e7 Pa, cylinder HC_2 with 2e7 Pa, and cylinder HC_3 with 0.5e7 Pa, while the excavator is not loaded with a load. Time changes of the control signals for all three cylinders are shown in Figure 14. The simulation was performed for a period of 10 [s]. From figure 14. it can be seen that the boom and bucket start to rise first. After the bucket is fully extended (max. stroke of the HC3 piston rod is 0.4 [m]), it starts to lower in the fourth second, and in the fifth second, when the bucket is completely lowered, the arm of the bucet is raised. The maximum strokes of cylinders HC_1 and HC_2 are 0.4 [m] and 0.5 [m], respectively.

The results of the simulation are presented in Figures 15, namely the movements in the joints in Figures 15a and the forces that cause these movements in Figures 15b. Because the highest loads are exactly in the boom, it makes sense that the T1 joint would have an oscillatory character with the highest amplitude of oscillations. The mathematical model is acceptable and can be used for further study because the results reported are suitable and match actual cases.

a) b)
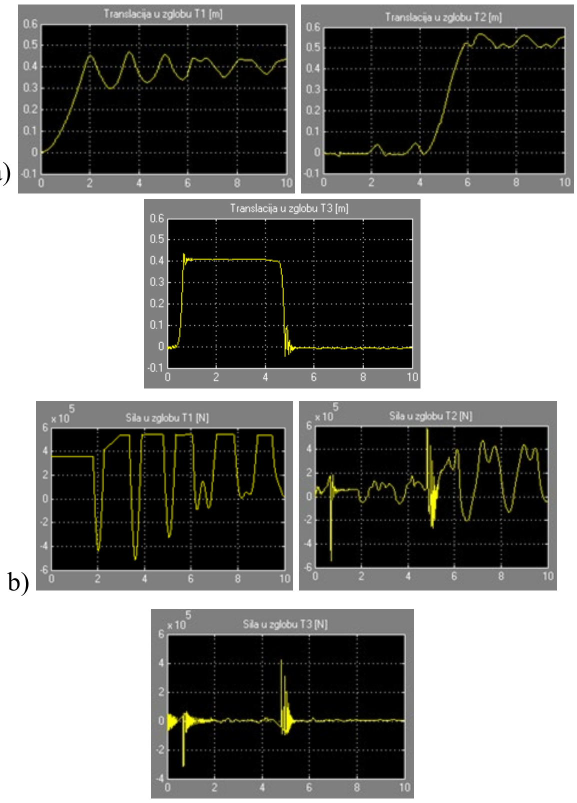

Figure 15. a) Movements in prismatic joints T_1, T_2 and T_3, b) Movement forces in the joints T_1, T_2 and T_3.

4. CONCLUSION

The subject of improving the ability to control and efficiency of the system is the primary focus of ongoing research in the field of hydraulic systems. As mechatronic subsystems, the following requirements must be met during the design and implementation of hydraulic systems at hydraulic excavator:

- because of the demands for growing functionality and performance, are complex and have a tendency to become more complex;
- hardware and software that control the operation of the entire system with perfect analog and digital integration,
- The amount of time available for development and implementation is being drastically cut back.

The paper presents a model of the hydraulic system as a subsystem of a mobile machine. The possibilities of combining new software tools with practical problems are presented with the aim of solving everyday problems that arise in the operation of mobile machines, from the aspect of improving controllability, usability, extending the working life of the mobile machine, reducing exploitation costs, and the possibility of easier and simpler maintenance of the hydraulic system.

Based on the presented simulation results for both cases, it can be concluded that the developed hydraulic excavator model can serve as a platform for future research, e.g. research into the optimal management strategy, etc., whereby the exact geometry, characteristics of hydraulic cylinders, properties of hydraulic oil would be defined for a certain type of hydraulic excavator.

5. REFERENCE

[1] G. Bauer, "Ölhydraulik". Wiesbaden: Vieweg + Teubner Verlag. (2011).

[2] A. Osmanović. "Mechatronic approach to the analysis of controlled hydraulic servosystems", PhD Thesis, University of Tuzla, Faculty of Mechanical Engineering, (2014).

[3] D. Janosevic, "Projektovanje mobilnih mašina", Masinski fakultet Niš, Serbia, (2006).

[4] S. Vechet, J. Krejsa, "Hydraulic arm modeling via Matlab SimHydraulics", Engineering Mechanics, Volumen16, No. 4, 287-296, (2009).

[5] B. Vanwalleghem, "Optimization of the efficiency of hydrostatic drives". 8th International Fluid Power Conference, Dresden – Germany, (2012).

[6] H. Yousefi, "On Modeling, System Identification and Control of Servo-Systems with a Flexible Load". PhD Thesis, Lappeenranta University of Technology, Finland. (2007).

[7] S. Çetin, A. A.Volkan, "Simulation and hybrid fuzzy-PID control for positioning of a hydraulic system". Nonlinear Dynamics, Volume 61, Issue 3 , pp 465-476, (2010).

[8] A. Osmanović, E. Trakić, "Hidraulika", Mašinski fakultet Tuzla, (2021).

[9] A. Shukla, "Stability Analysis and Design of Servo-Hydraulic Systems". PhD Thesis, University of Cincinnati. (2002).

[10] B. Bax, "Applying and analyzing robust modern control on uncertain hydraulic systems". PhD Thesis, University of Missouri – Columbia, (2006).

[11] C.L. Hwang, C.H. Lan, "The position control of electrohydraulic servomechanism via a novel variable structure control". Processing - International Journal of Mechatronics and Automation (IJMA 4)., 369-391, (1994).

[12] H. Hahn, A. Piepenbrink, K.D.Leimbach, "Input - output linearization control of an electro servo-hydraulic actuator. Control Applications, Proceedings of the Third IEEE Conference, Volume 2, 995 – 1000, (1994).

SESSION E

APPLIED MECHANICS

Influence on the support resistance of a mobile platform due to the effect of high-intensity impulsive force

Aleksandra B. Živković[1*], Slobodan R. Savić[1], Nebojša P. Hristov[2], Damir D. Jerković[2], Andjela G Mitrović[1], Marija V Milovanović[3], Lazar M Arsić[3]

[1]Faculty of Engineering, University of Kragujevac, Serbia
[2]Military Academy, University of Defence, Belgrade, Serbia
[3]Military Technical Institute, Belgrade, Serbia

In this study, a Finite Element Method (FEM) analysis was performed to evaluate the support resistance of a vehicle's chassis under the effect of a high-intensity, impulsive force of very short duration. The FEM model of the chassis was created, and material properties were defined to simulate the actual scenario. The model was subjected to the impulsive force, and the results were analysed to determine the support resistance of the vehicle's base. The findings of the analysis can help enhance the structural integrity of the vehicle's chassis under impulsive loading conditions, thus improving the safety and reliability of the vehicle. In conclusion, the study provides valuable insights into the support resistance of a vehicle's chassis under impulsive loading conditions. The results of the analysis can help improve the design and performance of the vehicle's base, ensuring the safety and reliability of the vehicle under different loading conditions.

Keywords: Simulation, FEM, Support Resistance

1. INTRODUCTION

System stability is an important aspect of vehicle design, particularly in heavy-duty vehicles and mobile platforms. The resistance offered by the support structure of the vehicle is a critical factor that affects its stability and performance under different loading conditions. In this context, the development of mathematical and mechanical models to determine the support resistance of a vehicle's base is essential for ensuring its stability and reliability.

The main objective of this study is to establish a mathematical and mechanical model to evaluate the stability of the mobile wheel platform of a vehicle. To accomplish this objective, Finite Element Method (FEM) analysis was conducted to simulate the impact of an impulsive force on the vehicle's chassis [1, 2].

Figure 1 depicts the schematic of the vehicle with the forces acting on its chassis, along with the support resistances that the vehicle experiences due to the impact force. The support structure of the vehicle is critical to ensuring its stability and reliability under varying loading conditions. The impulsive force acting on the vehicle's base causes stresses and strains that influence the performance of the vehicle. Therefore, it is vital to evaluate the support resistance offered by the vehicle's base to ensure its stability and prevent any damage or failure of the vehicle's structure.

The schematic in Figure 1 shows the different forces acting on the vehicle, including the inertial force, the reaction force, and the weight force. These forces induce stress and strain in the support structure, leading to deformations and potential damage to the vehicle. However, the support resistance of the vehicle's base provides the necessary stability to counteract the forces and maintain the vehicle's structural integrity. Therefore, it is essential to determine the support resistance of the vehicle's base under varying loading conditions, including impulsive forces, to ensure its stability and reliability.

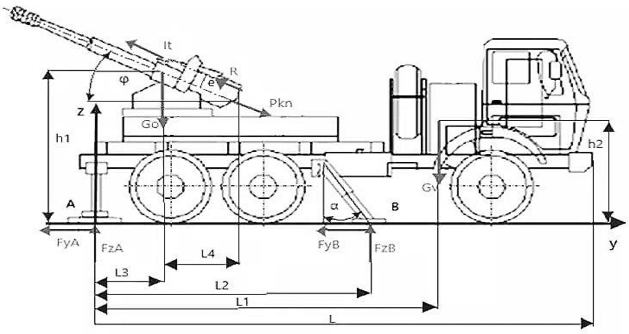

Figure 1: Vehicle with acting forces and support resistance

The forces acting on the vehicle as shown in Figure 1 are as follows: Pkn is the tractive force, It is the inertia force of the moving mass, R is the resistance force due to traction, Go is the weight force of the Pkn source, Gv is the weight force of the vehicle Nc, Nb is the longitudinal component of the reaction force of the support arms C and B, and Xc and Xb are the vertical components of the reaction force of the supports C and B.

In detail, Pkn represents the force exerted on the vehicle by the towing vehicle or the ground during acceleration, while It represents the force that resists the change in motion of the vehicle's recoiling mass. R is the force that opposes the motion of the vehicle due to the friction between the tires and the ground. Go is the force that results from the weight of the tractive force source acting on the vehicle. Gv is the weight force of the vehicle itself, which acts vertically downwards.

Furthermore, Nb and Nc are the reaction forces that occur at the contact points of the support arms B and C, respectively. Nb is the force acting in the longitudinal direction of the vehicle, while Nc acts vertically upwards. Xc and Xb are the components of the reaction force acting

*Corresponding author: Sestre Janjić 6, 34000 Kragujevac, e-mail: aleksandra.zivkovic.bm@gmail.com

vertically downwards due to the support arms C and B, respectively.

Understanding these forces and their magnitudes is essential in designing the vehicle's support structure to ensure stability and prevent failure or damage under impulsive loading conditions. The FEM analysis can help in evaluating the impact of these forces on the vehicle's base and optimize the support resistance to maintain the vehicle's structural integrity [3, 4].

In addition to the forces shown in Figure 1, geometric distances relative to the coordinate origin located at support A are also depicted. The angle φ represents the elevation angle of the forces Pkn, It, and R, while the angle ψ represents the direction angle of these forces.

2. THE MATHEMATICAL MODEL OF STABILITY

The mathematical model of stability for the FAP 2026 vehicle involves analysing the effects of forces acting on the vehicle's supports under the influence of a high-intensity, short-duration impulsive load. Due to the nature of the problem, certain limitations and assumptions need to be established before setting up the model. These include factors such as the structural properties and material behaviour of the vehicle, as well as the geometry and orientation of its components. Additionally, it is necessary to consider the dynamic effects of the impulsive load on the vehicle, including its magnitude, duration, and direction, as well as the response of the vehicle's supports to these forces [5]. By taking these limitations and assumptions into account, a more accurate and reliable mathematical model can be developed to analyse the stability of the vehicle:

1. The vehicle body is placed on a flat and horizontal surface.
2. Wheel support is excluded.
3. The point of action of the weight force Go of the source PKn is located on the axis of the source.
4. The last two wheels of the vehicle share a common axle, and the system behaves like a 4x4.
5. The system is considered as a rigid body placed on rigid supports, i.e., beams.
6. Two stability limit cases are considered: the effect of the tractive resistance force along the longitudinal axis of the vehicle and perpendicular to it.
7. The inertia and displacement of the vehicle's driving axles are neglected.
8. The platform on which the device is mounted is symmetric with respect to the longitudinal and vertical planes of symmetry of the vehicle.
9. The position of the centre of mass of supported parts does not change during the movement of the recoiling mass.

The simplified mathematical-mechanical models of the lateral and longitudinal stability of the vehicle are shown in Figure 2 and Figure 1, respectively. All forces acting on the vehicle are marked on the figures, with their respective positions of action.

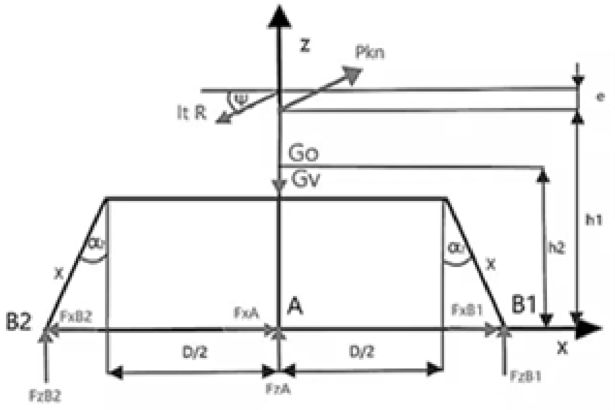

Figure 2: The model of the lateral stability of the vehicle

The equations of equilibrium for the longitudinal stability model, shown in Figure 1, are given in expressions 1, 2 and 3.

$$\sum_{yi} = R \cdot \cos\varphi - F_{yA} - F_{yB} = 0 \tag{1}$$

$$\sum_{zi} = F_{zA} + F_{zB} - R \cdot \sin\varphi - G_O - G_V = 0 \tag{2}$$

$$\sum_{MA} = P_{kn}\cdot\cos\varphi\cdot h_1 - R\cdot\cos\varphi\cdot h_1 - R\cdot\cos\varphi\cdot e + P_{kn}\cdot\sin\varphi\cdot L_3 - R\cdot\sin\varphi\cdot L_3 - P_{kn}\cdot\sin\varphi\cdot L_4 - G_O\cdot L_3 + F_{zB}\cdot L_2 - G_V\cdot L_1 = 0 \tag{3}$$

The equations of equilibrium for the lateral stability model, shown in Figure 2, are given by equations 4, 5 and 6.

$$\sum_{xi} = R \cdot \cos\psi + F_{xB1} - F_{xB2} + F_{xA} = 0 \tag{4}$$

$$\sum_{zi} = F_{zA} + F_{zB2} + F_{zB1} + R \cdot \sin\psi - G_O - G_V = 0 \tag{5}$$

$$\sum_{MA} = F_{zB1}\cdot(D/2 + x\cdot\sin\alpha_2) + P_{kn}\cdot e\cdot\cos\psi - R\cdot(h_1+e) - F_{zB2}\cdot(D/2 + x\cdot\sin\alpha_2) = 0 \tag{6}$$

Table 1 presents the values of geometric and other variables depicted in Figures 1 and 2.

Table 1: Values of geometric and variables of the system

Mass of the Pkn source (mo):	1800 kg
Vehicle mass (mv):	16200 kg
Maximum value of the recoiling force (Pknmax):	3037.8244 kN
Maximum value of the resistance force (Rmax):	173.09 kN
Acceleration due to gravity (g):	9.81 m/s^2
Total vehicle length (L):	7.720 m
X-coordinate of the vehicle's center of gravity (L1):	5 m
Distance from support A to support B (L2):	4 m
X-coordinate of the Pkn source center of gravity (L3):	2.5 m
Distance from the center of gravity Pkn source to the its end (L4):	0.400 m
Height of Pkn source in position (h1):	1.420 m + 0.580 m = 2 m
Y-coordinate of the vehicle's center	1.2 m

of gravity (h2):	
Total vehicle width (D):	7.720 m
Length of arm B (x):	1.5 m
Elevation angle (φ):	-5° +70^0
Heading angle (ψ):	-25° +25°
Angle of arm B in the longitudinal section (α1):	15°-20°
Angle of arm B in the transverse section (α2):	10^0
Dynamic arm (e):	0.0005 m

3. DETERMINATION OF SUPPORT REACTION BY FEM ANALYSIS

The goal and essence of this work is FEM analysis of the resistance in the supports for 21 combinations of the direction angle and elevation angle of the Pkn force. For the purpose of this calculation, additional restrictions and assumptions were adopted through FEM analysis:

1. The force R and the force Pkn act in the same direction, and the value of e is neglected due to its small magnitude.
2. The weight force of the cause of the force Pkn is also neglected, as its value is much smaller compared to the force Pkn, the resistance force R, and the weight force of the vehicle Gv.

In addition to the above, it is necessary to find the unit vector of forces Pkn and R. As assumption 1 states that the forces act in the same direction, the unit vector for both of them is identical.

3.1. Determining the unit vector

The determination of the unit vector of the force Pkn and the resistance force R is performed in order to obtain the cosines of the angles, which are the input data in the computer simulation. The figure shows the action of forces Pkn and R in space, with respect to the coordinate system. The line OS represents the axis of the Pkn force generator. Point S represents the point of action of the force in space, while point S' represents its projection.

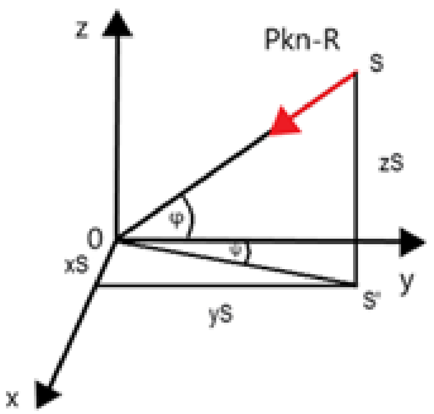

Figure 3: The spatial representation of the force action

The vector of the force is calculated based on equations 7, 8, 9, and 10.

$$\overrightarrow{OS} = \overrightarrow{r_0} - \overrightarrow{r_s} \tag{7}$$

$$OS_x = x_s - x_0 \tag{8}$$

$$OS_y = y_s - y_0 \tag{9}$$

$$OS_z = z_s - z_0 \tag{10}$$

The magnitude of vector (OS) $^{\rightarrow}$ is calculated based on equation 11.

$$|\overrightarrow{OS}| = \sqrt{OS_x{}^2 + OS_y{}^2 + OS_z{}^2} \tag{11}$$

The unit vector $\overrightarrow{OS_0}$, whose direction coincides with the direction of forces Pkn and R, is calculated based on equation 12.

$$\overrightarrow{OS_0} = \frac{\overrightarrow{OS}}{|\overrightarrow{OS}|} \tag{12}$$

The coefficients next to the vectors i $^{\rightarrow}$, j $^{\rightarrow}$, k $^{\rightarrow}$ represent the cosines of the angles that the unit vector makes with the x, y, and z axes. Table 2 shows all three components of the Pkn-R force, depending on the direction and elevation angles. The values from Table 2 represent input data in the FEM analysis model.

Table 2. Components of the Pkn-R force

Angles		***Components of the Pkn-R force***		
φ (^{0})	***ψ (^{0})***	***X (N)***	***Y (N)***	***Z (N)***
-5	-25	108428.1	812034.5	2745095
-5	0	0	812616.8	2747063
-5	25	-108428	812034.5	2745095
0	-25	379152.6	2839533	0
0	0	0	2864734	0
0	25	-379153	2839533	0
10	-25	-318964	-2388771	-1548786
10	0	0	-2403717	-1558476
10	25	318964	-2388771	-1548786
30	-25	58991.4	441795,7	-2829848
30	0	0	441889,4	-2830448
30	25	-58991.4	441795,7	-2829848
45	-25	200452.4	1501219	2431638
45	0	0	1504908	2437613
45	25	-200452	1501219	2431638
65	-25	-214544	-1606756	2361993
65	0	0	-1611281	2368645
65	25	214544.3	-1606756	2361993
70	-25	241394.2	1807839	2209106
70	0	0	1814291	2216991
70	25	-241394	1807839	2209106

3.2. FEM Analysis

The 3D model of the vehicle used for analysis consists of 10 nodes and 9 bars. To ensure that the model is statically determinate, the structure has been modified by adding a shell of 100 mm on each side of the bar. The simplified 3D model of the vehicle is shown in Figure 4. Using FEM analysis of the 3D model under the load of the force Gv and the difference of forces Pkn-R, the values of the support reaction at points A, B1 and B2 were obtained. The calculation was performed for 21 combinations of angles. The obtained results were used to optimize the design of the vehicle structure to ensure sufficient bearing resistance in the identified critical points.

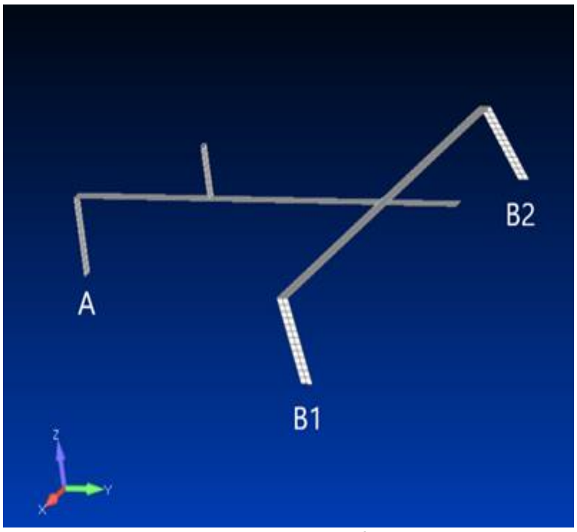

Figure 4: The 3D model of the vehicle

4. THE RESULTS

The results of the FEM analysis show the maximum support reaction force and the minimum support reaction force. These values were obtained for a specific combination of angles and elevations of the force vectors Pkn and R. Table 3 shows the magnitudes of forces in supports A, B1 and B2. The maximum force values are marked in red, while the minimum values are marked in blue.

The forces are a result of the FEM analysis of the 3D vehicle model under the influence of the Gv force and the difference between the Pkn and R forces for 21 combinations of angles. It is important to note that the model was designed as a shell structure with additional shells added to the construction of the rods on both sides of each rod, which allowed for a static determination of the model.

The analysis also revealed that the stress values in the structure are within the allowable limits, indicating that the design is structurally sound and able to withstand the applied loads. However, the analysis highlighted areas of high stress concentration, particularly in the areas where the shell was attached to the frame.

Based on the results of the FEM analysis, it can be concluded that the maximum force on support A is 1926770.638 N when φ = 30° and ψ = ±25°, while the minimum force on support A is 964914.2533 N when φ = 0° and ψ = 0°. The maximum force on support B1 is 985063.1165 N when φ = 0° and ψ = -25°, and the minimum force on support B1 is 463081.1936 N when φ = -5° and ψ = -25°. Finally, the maximum force on support B2 is 985062.4296 N when φ = 0° and ψ = +25°, while the minimum force on support B2 is 463081.093 N when φ = -5° and ψ = +25°. These results provide valuable information for further design and optimization of the vehicle model.

This means that the analyzed parts of the structure are sufficiently strong and can withstand the loads simulated in this model. However, in further development and optimization of the structure, changes may be necessary to reduce the intensity of the forces in the supports, which would increase the overall strength of the structure and reduce the risk of breakage and damage [6].

Table 3. The results

Angles		***Intensities of support reactions***		
φ (⁰)	***ψ (⁰)***	***A (N)***	***B1 (N)***	***B2 (N)***
-5	-25	1831877	463081.1936	468259.0695
-5	0	1832566	465028.1988	465028.1024
-5	25	1831877	468259.1525	463081.093
0	-25	971524.2292	985063.1165	919038.6512
0	0	964914.2533	954834.4363	954833.7319
0	25	971524.3979	919039.2477	985062.4296
10	-25	1400489.913	845926.0336	816329.9761
10	0	1401204.963	831342.0282	831341.4753
10	25	1400490.005	816330.4184	845925.4652
30	-25	1926770.638	581904.3987	570246.9936
30	0	1926587.244	575872.2749	575872.2434
30	25	1926770.638	570247.0247	581904.3899
45	-25	1695926.11	588129.0075	579788.5256
45	0	1697775.806	582702.2879	582701.9701
45	25	1695926.109	579788.6484	588128.6741
65	-25	1602871.451	682059.4282	635159.1628
65	0	1604503.958	658008.2712	658007.927
65	25	1602871.497	635159.4152	682059.1785
70	-25	1598866.831	661252.799	643742.5915
70	0	1600991.944	651351.7494	651351.3996
70	25	1598866.837	643742.9235	661252.343

5. CONCLUSION

In conclusion, the FEM analysis of a 3D vehicle model subjected to high-intensity and impulse force, namely the Pkn force, the opposing R force and the force Gv. The vehicle model consisted of 10 nodes and 9 bars, and in order to achieve static determinacy, it was added a shell of 100 mm to the construction of each bar on both sides, resulting in a shell-shaped model.

Through FEM analysis, it was obtained the values of the support reaction forces at points A, B1 and B2, which indicate the structural strength of the vehicle under the given loading conditions. The results showed that the analysed parts of the construction are strong enough to withstand the simulated loads, with the maximum reaction forces occurring at a φ angle of 30° and a ψ angle of ±25°.

However, further development and optimization of the construction may require modifications to reduce the intensity of the reaction forces in the supports, which could lead to an increase in overall structural strength and a reduction in the possibility of damage and breakage [7].

It is important to note that this model is just one of the many possible configurations of the vehicle's construction, and that additional analyses and optimizations would be necessary to determine the most efficient and safe solution [8]. The FEM analysis was performed for 21 combinations of angles, with the model subjected to the force Gv and the difference in forces Pkn-R. The results of the analysis have shown that the maximum resistance forces in the supports A, B1 and B2 occur when the angles φ and ψ are within a certain range. These forces are well below the yield strength of the material used, indicating that the analysed parts of the structure are sufficiently robust to withstand the simulated loads. However, further optimization of the design may be necessary to reduce the intensity of forces in the supports, thereby increasing the overall strength of the structure and minimizing the risk of damage and breakage [9].

REFERENCES

[1] H. Benaroya and M. Rehak, “Finite Element Method in Probabilistic Structural Analysis: A Selective Review,” Appl. Mech. Rev. Vol. 41 (5), pp. 201-213, (1988).

[2] R. Rajappan and M. Vivekanandhan, “Static and Model Analysis of Chassis by Using FEA” Proceedings of the National Conference on Emerging Trends in Mechanical Engineering 2013.

[3] N. M. Ghazaly, “Applications of Finite Element Stress Analysis of Heavy Truck Chassis: Survey and Recent Development,” Journal of Mechanical Design and Vibration, Vol. 2 (3), pp. 69-73, (2014).

[4] W. Ehlert, B. Hug and I.C. Schmid, “Field Measurements and Analytical Models as a Basis of Test Stand Simulation of the Turning Resistance of Tracked Vehicles,” Journal of Terramechanics, Vol. 29 (1), pp. 57-69, (1992).

[5] L. Kwasniewski, H. Li, J. Wekezer and J. Malachowski, “Finite Element Analysis of Vehicle–Bridge Interaction,” Finite Elements in Analysis and Design, Vol. 42 (11), pp. 950-959, (2006).

[6] A. Kengkongan Ary, A. Rio Prabowo and F. Imaduddin, “Structural Assessment of an Energy-Efficient Urban Vehicle Chassis using Finite Element Analysis – A Case Study,” Procedia Structural Integrity, Vol. 27, pp. 69-76, (2020).

[7] M. Azizi Muhammad Nora, H. Rashida, W. Mohd Faizul Wan Mahyuddinb, M. Azuan Mohd Azlanc and J. Mahmud “Stress Analysis of a Low Loader Chassis,” Procedia Engineering, Vol. 41, pp. 995-1001, (2012).

[8] T. Han Fui, R. Abd. Rahman, “Statics and Dynamics Structural Analysis of a 4.5 Ton Truck Chassis,” Jurnal Mekanikal, Vol. 24, pp. 56-67, (2007).

Methods for modeling bolted connections using FEM

Vladimir Milovanović[1], Miloš Pešić[2*], Rodoljub Vujanac[1], Marko Topalović[2], Milan Stojiljković[1]
[1]Faculty of Engineering, University of Kragujevac, Kragujevac (Serbia)
[2]Institute for Information Technologies, University of Kragujevac, Kragujevac (Serbia)

Abstract: In constructions with complex geometry, bolted connections are most often used to connect parts. Modeling a complete bolted connection which consists of bolt, nut and washers using 3D finite elements is either not always possible or requires a lot of engineering time. For this reason, it is necessary to approximate the bolted connection using other types of finite elements. This paper presents methods for modeling bolted connections using different types of finite elements. A complete bolted connection loaded in shear and bending was modeled using 3D finite elements. The bolted connection analysis results obtained using 3D finite elements were used as a reference. After that, the bolted connection was modeled using 1D beam finite element in combination with 3D, RBE2 and RBE3 finite elements. By comparing the results of the numerical analyses, an approximation of the bolt connection which best corresponds to the reference model was obtained. It can be concluded that the shown approximation of bolted connections gives satisfactory results and significantly saves engineering time.

Keywords: Finite element method, Bolted Connection, Beam finite element, RBE2, RBE3

1. INTRODUCTION

The successful design of heavy machinery largely depends on the way of joining the various parts used. Those parts can be made of different materials, and the method of joining those parts into a whole (construction) is of extreme importance. Bolt connections are often used to connect different parts of machines. For the detachable assembly of parts in machinery, bolts are crucial components and ensure the necessary axial or preload forces for the various parts of the machines or structures. To guarantee the security and dependability of machines, the axial force or preload of a bolt must be carefully regulated. Bolt connection failure frequently results from inadequate or excessive preload. Tightening stress in bolt must be taken into account when designing them in order not to break or overload the connection itself [1,2].

When creating finite element (FE) model of a complex structure, it takes a lot of engineering time to model a realistic bolted connection. Detailed modeling of a complete bolted connection requires the definition of contact pairs between all components. In addition to the engineering time wasted on model creation, this significantly increases the calculation time.

In this paper, different types of finite elements were used for the bolted connection modeling in order to determine their influence on the final results. The aim of this paper is to simplify the bolted connection model by applying different types of finite elements, reduce the model creation time and the duration of numerical calculations, while obtaining results that correspond to the results of the verification model. The verification FE model represents a complete bolted connection created by applying 3D finite elements and defining contact pairs. This FE model is loaded in shear and bending. After that, the bolted connection FE model is simplified by applying 1D, RBE2 and RBE3 finite elements. Initially, simplified models were created without washers. Then, washers were modeled and their influence on the calculation results was considered. By comparing the results obtained by using different types of finite elements with and without considering washers, the combination that gives the results closest to the verification model was determined.

2. BOLT CONNECTION

In the bolted connection, a certain axial force is created already in the state of rest, when the bolt is tightened. After settlement, the prestressing force occurs. This represents the static loading of the bolted connection, which causes static stress and associated elastic deformations in it. During the exploitation of the connected components, the bolted connection is affected by an additional load in the form of constant or variable working force. As a result, there is an additional elongation of the screw and a partial relief of the previously clamped washer. It is very important to determine the clamping force in order to maintain the structure or machine properly [3].

In addition to joining two or more components, bolted connections are also used for tensioning, regulation, measurement, and movement transmission. The basic elements of bolt connections are a bolt and a nut, where the bolt has an external thread, and the nut has a corresponding internal thread. The nut can be an independent part of the bolt connection, or it can be replaced by a part of the connected machine part, in which the internal thread should then be made. Since the bolt and nut are the most commonly used machine parts in all areas of technology, their shape, size, and material are standardized.

When it comes to modelling bolted connections using FEM, there are many publications in which FEM analyzes of bolted joints are discussed in order to analyze stress distribution and stress concentrations, contact pressure distributions, load sharing of the bolted joint components [4,5,6]. Modeling complete bolted connections requires a lot of engineering time, so it is necessary to simplify the model of the bolted connection. Many publications can be found in the literature that consider how it is possible to simplify bolted connections and significantly reduce the duration of calculations and

*Corresponding author: Jovana Cvijića bb, 34000 Kragujevac, Serbia, e-mail: milospesic@uni.kg.ac.rs

modeling time [7,8,9]. These approximations of bolted connections are most often reduced to the neglect of certain components of the bolted connection and the introduction of different types of finite elements. Within this paper, a comparative analysis of approximations of bolted connections using various types of finite elements with and without modeling washers is given. By comparing the results of the approximated models with the completely modeled bolted connection, the approximation that best corresponds to the real bolted connection was determined.

3. VERIFICATION MODELS

3D eight-node hexahedral finite elements were used for modeling the FE mesh of the verification model. The FE mesh in the contact regions is created so that the nodes of the different parts coincide ("node to node") in order to obtain the most reliable results and achieve a better convergence of numerical calculations. The numerical analysis of the bolted connection was performed in the Nastran software, while the pre and post-processing is carried out in Femap software [10].

The FE mesh of the verification model is shown in Figure 1. The assembly is formed of: upper plate, lower plate, upper washer, lower washer, bolt, and nut. The verification FE model, was modelled with 26912 3D hexahedral eight-noded finite elements and it is shown in Fig. 1.

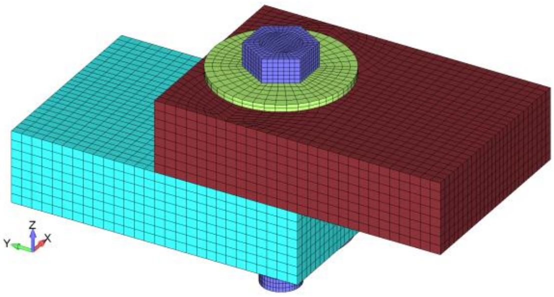

Figure 1. Verification 3D model

The characteristics of steel s355 were adopted for the material of the bolted connection assembly. Within this paper, two cases of the bolted connection loading were considered - shearing and bending (verification models 1 and 2, respectively), which is shown in Fig. 2 and Fig. 3. The boundary conditions of the model are set so that the upper plate of the assembly is fixed, while bending/shearing forces of 30 kN are applied to the lower plate. On all FE models, a bolt tightening force of 60 kN is defined.

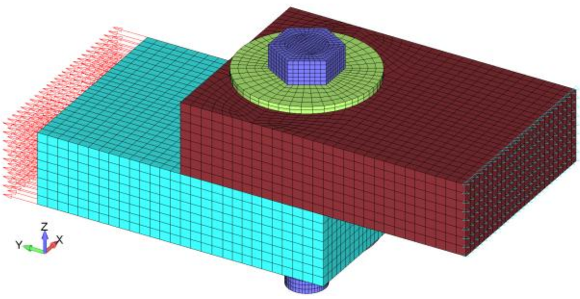

Figure 2. Boundary conditions and loading of verificatiom model 1 – shearing

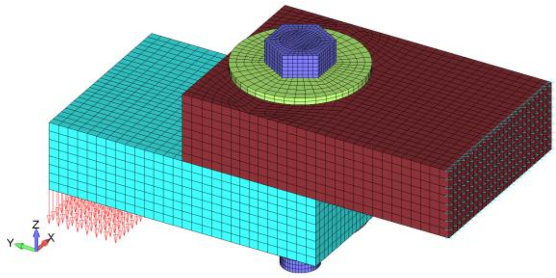

Figure 3. Boundary conditions and loading of verification model 2 – bending

Figure 4 shows the von Mises stress distribution field of the numerical analysis for the verification model 1 loaded in shearing. Results are shown in the plates which are interconnected by a bolt connection. Maximal value of von Mises stress is 147.38 MPa.

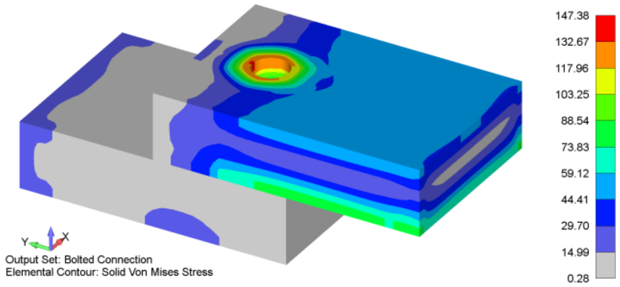

Figure 4. Von Mises stress – shearing

The total displacement field in the plates which are interconnected by a bolt connection is shown in Figure 5. Maximal value of total displacement is 0.32 mm.

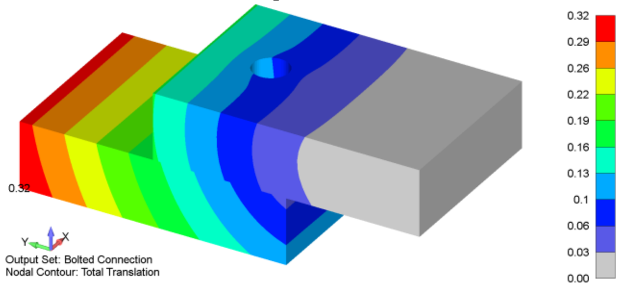

Figure 5. Total displacement – shearing

Figure 6 shows the von Mises stress distribution field of the numerical analysis for the verification model 2 loaded in bending. Maximal value of von Mises stress is 382.89 MPa.

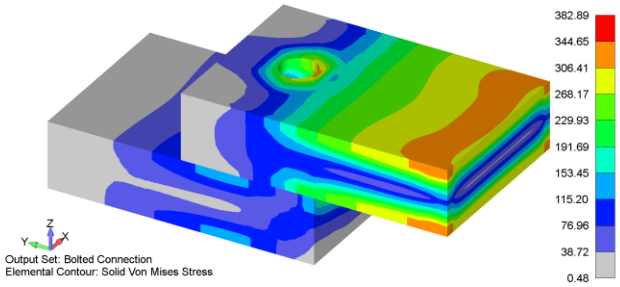

Figure 6. Von Mises stress – bending

The total displacement field in the plates is shown in Figure 7. Maximal value of total displacement is 1.80 mm.

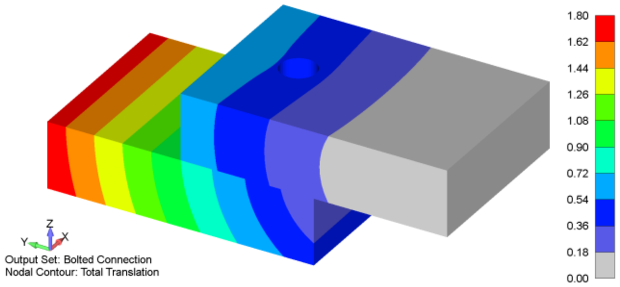

Figure 7. Total displacement – bending

4. FE MODELS WITHOUT WASHER

4.1. Approximate FE models loaded in shearing

In this chapter, the shear loading case of a bolted connection as shown in Fig. 2 is considered. In all approximate models, the bolt is modeled using a 1D beam finite element. The nut and washers were not modeled, and instead RBE2, RBE3 and 1D beam finite elements were used to connect the plates to the bolt as shown in Figure 8.

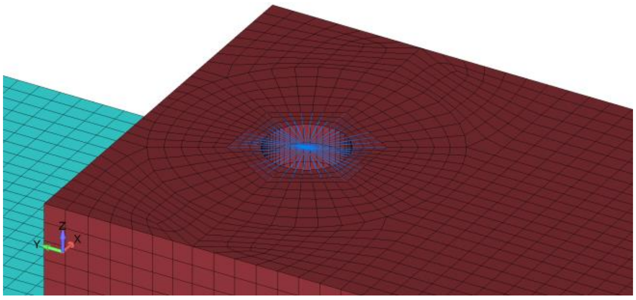

Figure 8. Aproximated FE model without washer

The FE model 1 was created using the RBE2 finite element type for the bolt to plate connection. This type of finite elements represents the so-called “rigid elements” that adds (infinite) stiffness to the structure. To create this type of finite element, the nodes at both ends of the beam element (bolt) is selected as an independent node, while the nodes on the plates at the contact with the bolt head or nut are selected as dependent nodes.

The FE model 2 was created using the RBE3 finite element type for the bolt to plate connection. This type of finite elements is created in a similar way as in FE model 1. The difference is that RBE3 finite elements represents interpolation elements that serve to "distribute forces" around the connected nodes, without adding any stiffness.

The FE model 3 was created using 1D beam elements for bolt to plate connections. A new property has been created in which new beam finite elements are defined. The cross-section of these elements is defined so that by combining these elements, the surface of the bolt head, i.e. the nut, is covered. The material of these elements is defined as completely rigid.

A comparison of these results for shearing load is given in the form of a von Mises Stress – *x* coordinate dependence diagram in the finite elements marked in Figure 9.

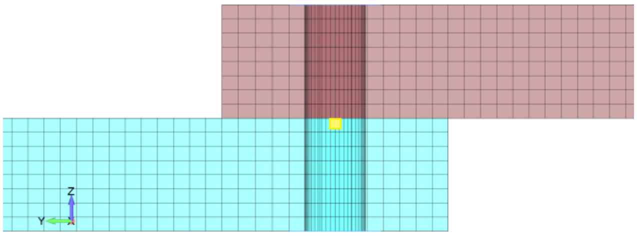

Figure 9. Finite elements for displaying results

Figure 10 shows the diagram of the dependence of the von Mises stress on the x coordinate.

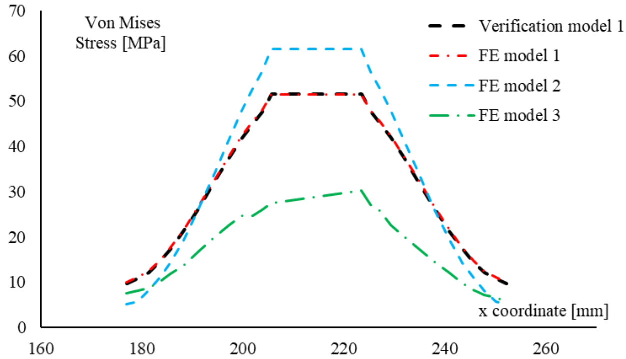

Figure 10. Von Mises Stress – x coordinate diagram

Comparison of the maximum von Mises stress values in both plates for FE models 1, 2, and 3 with verification model 1 is given in Fig 11.

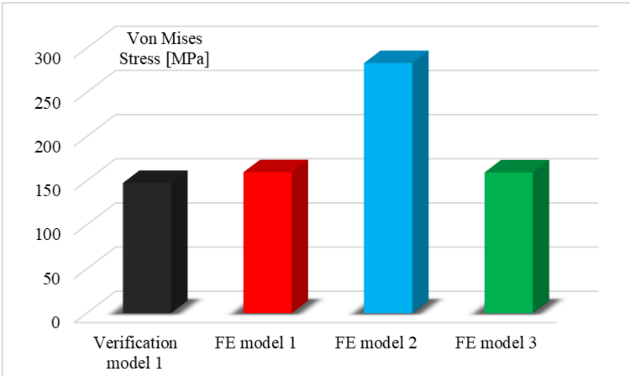

Figure 11. Maximum von Mises Stress values in plates

Table 1 shows a comparison of the maximum values of total displacement for FE models 1, 2, and 3 with verification model 1 loaded in shearing.

Table 1. Comparison of total displacement max. values

FE models	Total displacement [mm]
Verification model 1	0.32
FE model 1	0.32
FE model 2	0.33
FE model 3	0.32

As can be seen from the results above, FE model 1 (model created by combining the beam finite element and the RBE2 elements) has the best matching of the maximum von Mises stress value, stress distribution, and total displacement value compared to the verification model 1. It can be observed that FE model 2 (combination of RBE3 finite elements with a beam finite element) gives the worst matching results with the verification model 1. Also, FE model 3 (combination of beam finite elements) gives good matches of maximum von Mises stress value, while stress distribution in the model is significantly different from the verification model 1.

Fig. 12 and Fig. 13 show von Mises stress field and total displacement field for FE model 1, respectively.

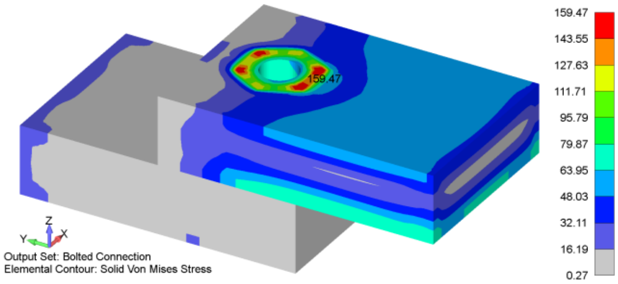

Figure 12. Von Mises stress field distribution for FE model 1

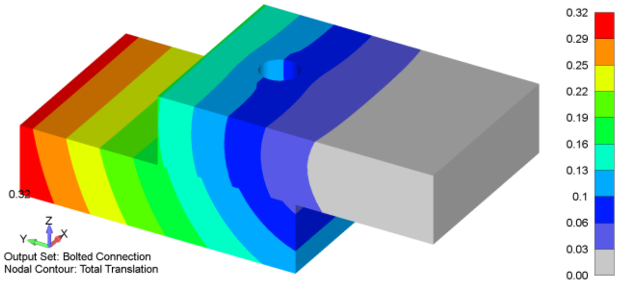

Figure 13. Total displacement field distribution for FE model 1

4.2. Approximate FE models loaded in bending

The approximate FE models used for the case of the bolted connection loaded in bending are the same as for the shear case (FE models labelled as FE models 4, 5 and 6 correspond to approximation FE models 1, 2 and 3 respectively loaded in bending.). The boundary conditions and loads are set to correspond to the bending load case of the bolted connection as shown in Figure 3.

A comparison of results is given in the form of a von Mises Stress – *x* coordinate dependence diagram in the finite elements marked in Figure 14.

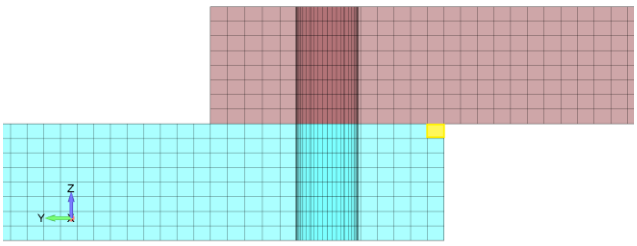

Figure 14. Finite elements for displaying results

Figure 15 shows the diagram of the dependence of the von Mises stress on the x coordinate.

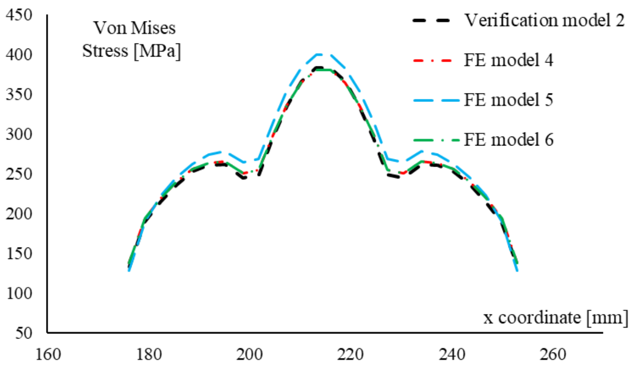

Figure 15. Von Mises Stress – x coordinate diagram

Comparison of the maximum von Mises stress values in both plates for FE models 4, 5, and 6 with verification model 2 is given in Fig 16.

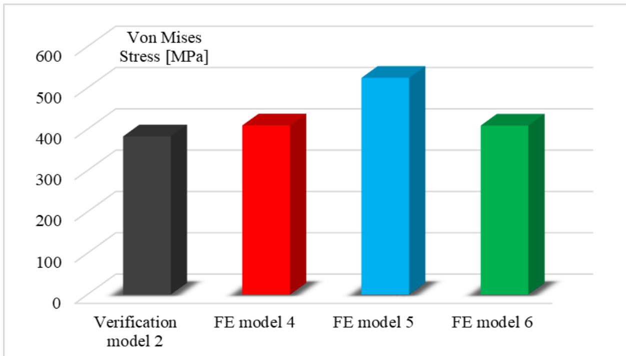

Figure 16. Maximum von Mises Stress values in plates

Table 2 shows a comparison of the maximum values of total displacement for FE models 4, 5, and 6 with verification model 2 loaded in bending.

Table 2. Comparison of total displacement max. values

FE models	Total displacement [mm]
Verification model 2	1.80
FE model 4	1.74
FE model 5	1.81
FE model 6	1.74

Based on the results above, it can be concluded that for the case of bending, best match of the results with the verification model 2 gives FE model 4 (combination of beam and RBE2 finite elements). It should be noted that, although FE models 4, 5, and 6 give good matches for the maximum stress values, the locations where the maximum values occur are not the same.

Fig. 17 and Fig. 18 show von Mises stress field and total displacement field for FE model 4, respectively.

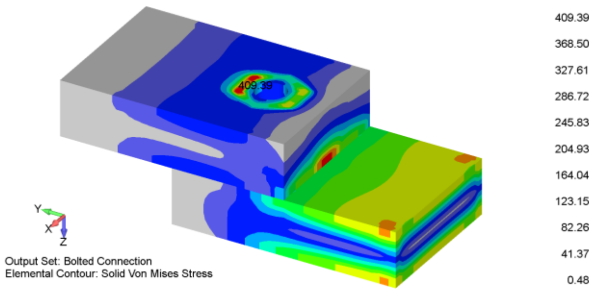

Figure 17. Von Mises stress field distribution for FE model 4

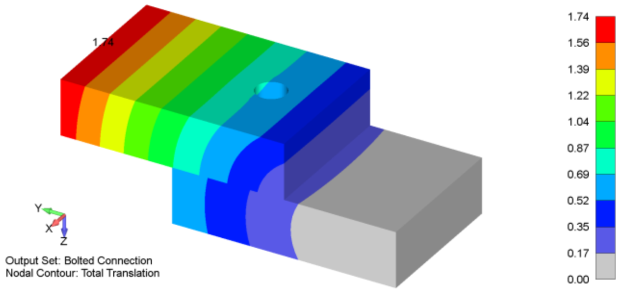

Figure 18. Total displacement field distribution for FE model 4

5. FE MODELS WITH WASHER

5.1. Approximate FE models loaded in shearing

Based on the results from the previous chapter, in models without washers, it can be observed that higher stress concentrations occur at the place of washers. This occurs as a result of connecting the plates and the beam finite element (bolt) with rigid elements. For this reason, approximate FE models with washers are considered in this chapter (Fig. 17).

As in the previous chapter, in all approximate models, the bolt is modeled using a 1D beam finite element. The nut is not modeled. RBE2, RBE3 and 1D beam finite elements were used to connect the plates to the bolt. Approximate FE models labelled as FE models 7,8 and 9 correspond to FE models 1,2 and 3 respectively with added washers.

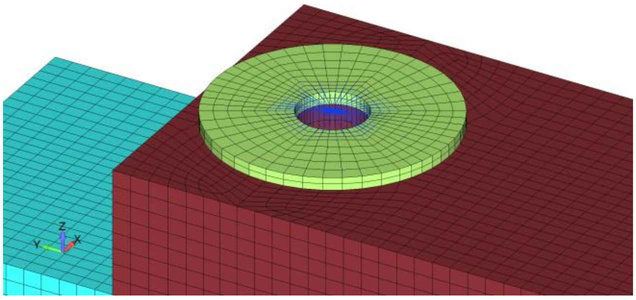

Figure 17. FE model with washer

The boundary conditions and loads are set to correspond to the shearing load case of the bolted connection as shown in Figure 2.

A comparison of results is given in the form of a von Mises Stress – x coordinate dependence diagram in the finite elements marked in Figure 9.

Figure 18 shows the diagram of the dependence of the von Mises stress on the x coordinate.

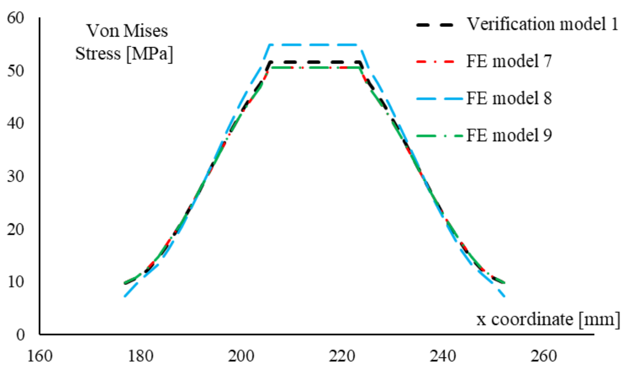

Figure 18. Von Mises Stress – x coordinate diagram

Comparison of the maximum von Mises stress values in both plates for FE models 7, 8, and 9 with verification model 1 is given in Fig 19.

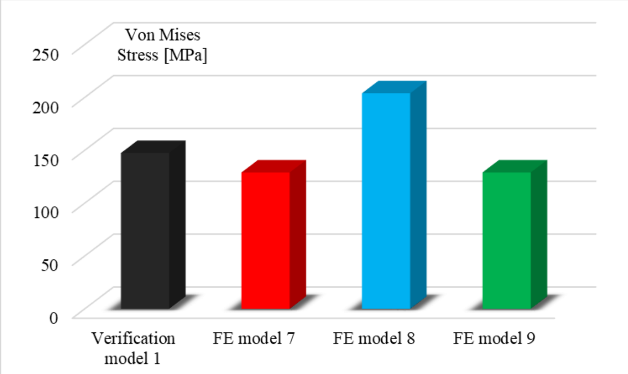

Figure 19. Maximum von Mises Stress values in plates

Table 3 shows a comparison of the maximum values of total displacement for FE models 7, 8, and 9 with verification model 1 loaded in shearing.

Table 3. Comparison of total displacement max. values

FE models	Total displacement [mm]
Verification model 1	0.32
FE model 7	0.32
FE model 8	0.32
FE model 9	0.32

Based on the results above, it can be concluded that FE model 7 (combination of the beam and the RBE2 finite elements) has the best matching of the results compared to the verification model 1. Also, as in the case of the no-washer models, FE model 8 (the combination of RBE3 finite elements with a beam finite element) gives the worst matching in results with the verification model 1.

Fig. 20 and Fig. 21 show von Mises stress field and total displacement field for FE model 7, respectively.

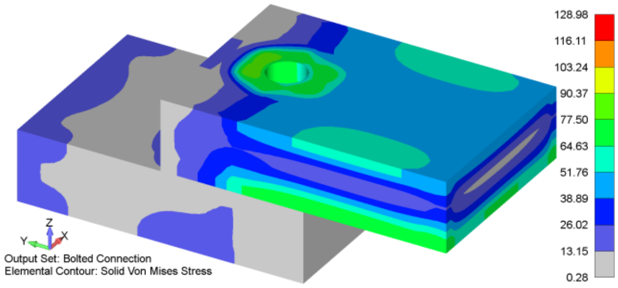

Figure 20. Von Mises stress field distribution for FE model 7

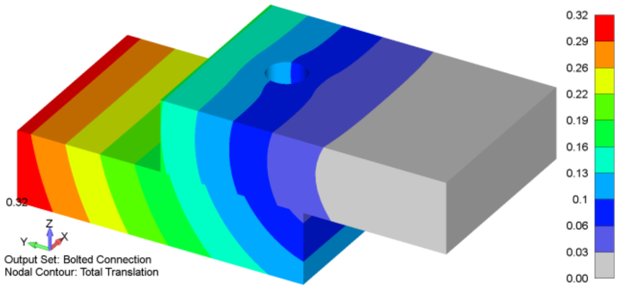

Figure 20. Total displacement field distribution for FE model 7

5.2. Approximate FE models loaded in bending

The FE models used for the case of the bolted connection loaded in bending are the same as for the shear case (approximate FE models labelled as FE models 10, 11 and 12 correspond to FE models 7, 8 and 9 respectively loaded in bending.). The boundary conditions and loads are set to correspond to the bending load case of the bolted connection as shown in Figure 3.

A comparison of results is given in the form of a von Mises Stress – *x* coordinate dependence diagram in the finite elements marked in Figure 14.

Figure 21 shows the diagram of the dependence of the von Mises stress on the x coordinate.

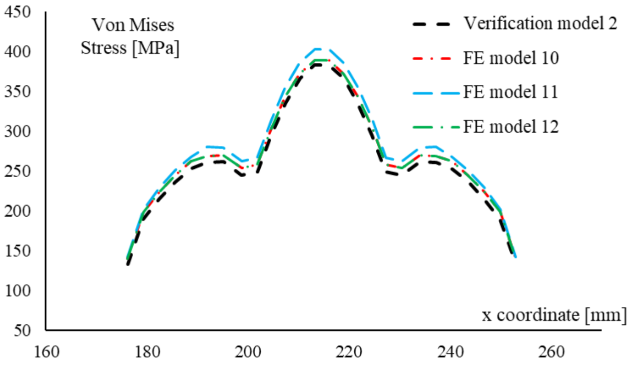

Figure 21. Von Mises Stress – x coordinate diagram

Comparison of the maximum von Mises stress values in both plates for FE models 10, 11, and 12 with verification model 2 is given in Fig 22.

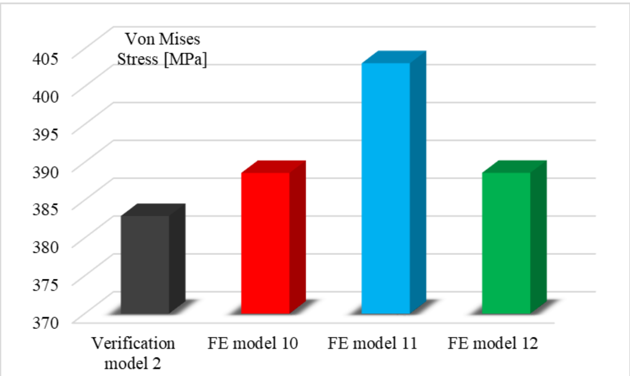

Figure 22. Maximum von Mises Stress values in plates

Table 4 shows a comparison of the maximum values of total displacement for FE models 10, 11, and 12 with verification model 2 loaded in bending.

Table 4. Comparison of total displacement max. values

FE models	Total displacement [mm]
Verification model 2	1.80
FE model 10	1.78
FE model 11	1.82
FE model 12	1.78

By analyzing the results above, it can be concluded that, for the case of bending, the best matches of the results with the verification model 2 gives FE model 10 (combination of beam with RBE2 finite elements). It should be noted that, although FE models 10, and 12 give good matches for the maximum stress values, the locations where the maximum values occur are not the same.

Fig. 23 and Fig. 24 show von Mises stress field and total displacement field for FE model 10, respectively.

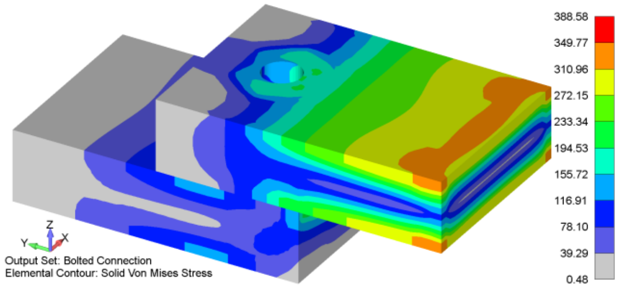

Figure 23. Von Mises stress field distribution for FE model 10

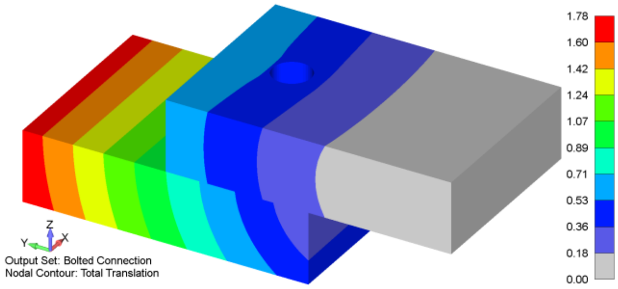

Figure 24. Total displacement field distribution for FE model 10

6. DISCUSION

In Table 5 are shown the maximum values of von Mises stress and total displacement for all FE models.

Table 5: Results of numerical analysis

FE models	Maximal stress [MPa]	Total displacement [mm]
Verification model 1	147.38	0.32
Verification model 2	382.89	1.80
FE models without washer – shearing		
FE model 1	159.47	0.32
FE model 2	283.08	0.33
FE model 3	159.28	0.32
FE models without washer – bending		
FE model 4	409.39	1.74
FE model 5	524.61	1.81
FE model 6	409.02	1.74
FE models with washer - shearing		
FE model 7	128.98	0.318
FE model 8	203.93	0.326
FE model 9	128.98	0.318
FE models with washer – bending		
FE model 10	388.58	1.78
FE model 11	403.07	1.82
FE model 12	388.60	1.78

As can be seen from the table 5, FE model 1 and 4 (the models created by combining the beam finite element and the RBE2 element) has the best match in maximum values of von Mises stress and total displacement, as well as stress distribution compared to the verification models 1 and 2, i.e. shearing and bending load cases. It is important to point out for FE models without washers that all of them show stress concentration locally at the place where washers should be inserted. Modeling both washers and specifying contact between them and the plates (FE models 7 and 10) can reduce this stress concentration in the plates, as can be seen in Fig. 20 and Fig. 23.

7. CONCLUSION

Based on everything presented in the paper, the following can be concluded:

- Modeling the bolt using beam finite element in combination with RBE2, RBE3 and beam finite elements can significantly reduce the modeling time. In addition, contact definition between all parts of the bolt connection is avoided, which significantly reduces the calculation time. On the other hand, in this way, the side contact of the bolt and the plates is not taken into account and its influence on the analysis cannot be considered.
- The best matches with the verification models for both load cases are obtained by combining the beam finite element (bolt) with RBE2 finite elements, while the worst matches are obtained by combining the beam finite element (bolt) with RBE3 finite elements.
- Approximating the bolted connection without modeling the washers results in large stress concentrations on the plates where the washers should exist. Therefore, it is recommended to model the washers to remove this stress concentration.
- In approximated FE models containing washers, the best results are also given by the combination of the beam finite element (bolt) with RBE2 finite elements.

ACKNOWLEDGEMENTS

This research is partly supported by the Ministry of Education and Science, Republic of Serbia, Grant 451-03-68/2022-14/ 200378, and Grant TR32036.

REFERENCES

[1] S. Basava and D. P. Hess, “Bolted joint clamping force variation due to axial vibration”, Journal of Sound and Vibration, Vol. 210, pp. 255–265, (1998)

[2] S. Izumi, T. Yokoyama, A. Iwasaki and S. Sakai, “Three-dimensional finite element analysis of tightening and loosening mechanism of threaded fastener”, Engineering Failure Analysis, Vol. 12, p. 604-615, (2005)

[3] K. Y. Jhang, H. H. Quan, J. Ha, and N. Y. Kim, “Estimation of clamping force in high-tension bolts through ultrasonic velocity measurements”, Ultrasonic, Vol. 34, p. 179-183, (2001)

[4] Sh. G. Yasmin, P. P. Rao, K. Bommisetty, “3-D Finite Element Analysis of Bolted Joint Using Helical Thread Model”, International journal of engineering research & technology (IJERT), Vol. 2, Iss. 12, (2013)

[5] T. Soo Kim, H. Kuwamura, “Finite element modeling of bolted connections in thin-walled stainless steel plates under static shear”, Thin-Walled Structures, Vol. 45, Iss. 4, pp. 407-421, (2007)

[6] P.M.L. Vilela, H. Carvalho, G. Queiroz, “Modelling of bolted connections by the finite element method”, Vol. 1, Iss. 2-3, pp. 405-413 (2017)

[7] Kim J., Yoon J.-C., Kang B.-S., “Finite element analysis and modeling of structure with bolted joints”, Applied Mathematical Modelling, Vol. 31, Iss. 5, pp. 895-911, (2007)

[8] V. Giannella, R. Sepe, R. Citarella, E. Armentani, “FEM Modelling Approaches of Bolt Connections for the Dynamic Analyses of an Automotive Engine”, Applied Sciences, Vol. 11, Iss. 10, Art. no. 4343, (2021)

[9] N. Tanlak, F.O. Sonmez1, E. Talay, “Detailed and simplified models of bolted joints under impact loading”, J. Strain Analysis, Vol. 46, Iss. 3, pp. 1 - 13, (2011)

[10] Femap, Finite Element Modeling and PostProcessing Application FEMAP v2021.2, Siemens, 202

Optimal dynamic balancing of planar mechanisms: An Overview

Marina Bošković[1*]
[1]Faculty of Mechanical and Civil Engineering Kraljevo, University of Kragujevac, Kraljevo (Serbia)

The problem of dynamic balancing of planar mechanisms using the optimization technique is discussed in the paper. The application of different optimization algorithms in the process of dynamic balancing of three types of planar mechanisms: planar serial manipulator, four-bar linkage, and multi-bar mechanisms was analyzed. The aim of the paper is to provide an overview of recent research in optimal dynamic balancing of planar mechanisms. The author hopes that this study can be used as an informative reference for future research in balancing of mechanisms.

Keywords: Multi-objective optimization, Dynamic balancing, Planar mechanisms, Review

1. INTRODUCTION

During the operation of the mechanisms, inertial forces and moment occur, which are transmitted to the fixed joints and create dynamic loads. These dynamic loads have a negative impact on the functionality of the mechanism, i.e they cause the appearance of vibrations and noise, lead to inaccuracy of executive members, and affect the appearance of fatigue and friction. At the beginning of the last century, with the appearance of the first steam machine and internal combustion engine, this problem became evident and researchers faced the task of creating the theoretical bases for the mechanism balancing. In modern industry, which implies mass production and the use of mechanisms with high operating speeds, the mentioned negative impacts are unacceptable and their elimination is of crucial importance. In this sense, it is necessary to balance the mechanisms, that is partial or complete elimination of dynamic loads arising as a result of inertia. In other words, balancing of the mechanism implies the determination of such redistribution of moving masses of the mechanism that will provide small dynamic loads on the frame of the mechanism. The goal of balancing is to reduce vibrations, as well as to achieve better dynamics, reliability, and accuracy of the mechanism.

In general, there are two ways of balancing the mechanism: static balancing and dynamic balancing. Static balancing means the balancing of forces that are the result of inertia (shaking forces) and that appear in the fixed joints of the mechanism. The condition for achieving static balance is that the sum of all forces during motion must be equal to zero. Hence, it is necessary to make the center of mass stationary. On the other hand, dynamic balancing implies the simultaneous balancing of shaking forces and shaking moment [1, 2]. To achieve dynamic balancing, the following two conditions must be satisfied: 1) the sum of all forces must be equal to zero, and 2) the sum of all moments must also be equal to zero. Therefore, static balancing is a broader term than dynamic balancing, i.e dynamic balancing is a subset of static balancing (Figure 1) [3].

In various engineering fields (robotic mechanisms used in space) the achievement of dynamic balancing is of key importance. Otherwise, if the above-mentioned balancing conditions are not satisfied, the capabilities of the mechanism are significantly reduced.

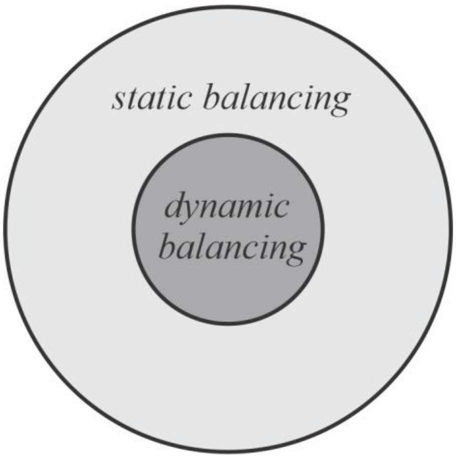

Figure 1: Static and dynamic balancing

Dynamic balancing of the mechanism can be achieved by using additional balancing components (counter-masses, counter-rotations, springs, and special four-bar linkages). The complete balancing of shaking forces and moment is a complex problem, so partial balancing techniques are most often used. Triciamo and Lowen [4,5] presented partial balancing techniques based on counterweights, which minimize the joint reaction forces, the driving torque, and the shaking moment, while the shaking forces have a maximum value. However, the application of additional balancing components in the dynamic balancing procedure increases the mass and inertia of the mechanism. These mechanisms are robust and require a higher consumption of materials and energy, and a larger space for accommodation, which is usually not acceptable from an economic aspect.

In order to avoid this, optimization techniques are increasingly applied for the purpose of dynamic balancing. In the paper below, a review of previous research, and a discussion of various optimization methods applied to achieve a dynamic balancing of different types of planar mechanisms are given.

The problem of balancing mechanisms is actual and very interesting to researchers. There are several laboratories in the world dealing with this problem and new results are published regularly. Mechanism balancing theory continues to be developed and new approaches and solutions are constantly being reported. The actuality of the balancing problem is also indicated by the fact that numerous studies have been conducted that reveal the

*Corresponding author: Dositejeva 19, 36000 Kraljevo, Serbia, e-mail: boskovic.m@mfkv.kg.ac.rs

specifics of the balancing theory. A detailed overview of the research and development of the methods in this field can be found in [6].

The rest of the paper is organized as follows: In Section 2, multi-objective optimization methods for dynamic balancing of mechanisms are presented. Section 3 provides an overview of the methods of optimal balancing of the planar serial manipulator, while Section 4 presents previous research in the dynamic balancing of four-bar linkage using optimization algorithms. The application of optimization techniques in the balancing of multi-bar planar mechanisms is presented in Section 5. Finally, in Section 6, conclusions and directions for future research are provided.

2. FORMULATION OF THE OPTIMIZATION PROBLEM AND APPLICATION OF THE MULTI-OBJECTIVE OPTIMIZATION IN THE DYNAMIC BALANCING OF PLANAR MECHANISMS

Since the goal of dynamic balancing is the minimization (elimination) of the joint reaction forces shaking forces and shaking moment, the problem can be defined as follows:

$$\min\left(F_1\left(\mathbf{X}\right),F_2\left(\mathbf{X}\right),...,F_n\left(\mathbf{X}\right)\right) \tag{1}$$

on condition:

$$g_j(\mathbf{X}) \le 0, \quad j=1,...,m \tag{2}$$

where $F_i\left(\mathbf{X}\right)\left(i=2,...,n\right)$ are objective functions, $g_j(\mathbf{X})$ are constraints of functions, and m is a number of constraints. $\mathbf{X}=\left\{x_1,x_2,...,x_D\right\}$ is a vector of design variables, and D denotes the number of design variables.

Based on the above, the dynamic balancing of planar mechanisms implies the simultaneous optimization of two or more objective functions i.e the considered problem can be solved using multi-objective optimization (MOO). In general, MOO is applied in all areas when one has to make a decision that implies a compromise between two or more conflicting objectives. Unlike single-objective optimization, in MOO there is no unique solution that simultaneously optimizes each of the defined objective functions. Therefore, in the case of MOO, the objective functions are contradictory and there are a greater number of optimal solutions.

In the literature, two methods are most often used to solve MOO problems:

1. the method of weighting factors
2. the method of *Pareto* front

The method of weighting factors implies the use of weighting coefficients (factors) in order to linearize the problem, i.e to form a unique objective function. This reduces the multi-objective optimization problem to a single-objective optimization problem. In the *Pareto* front method, linearization of the problem is achieved by using the best values for each of the objective functions. These values are equivalent to the weighting factors and enable the transformation of multi-objective into single-objective optimization.

3. OPTIMAL DYNAMIC BALANCING OF PLANAR SERIAL MANIPULATOR

Due to its simplicity and wide representation in various areas of industry, this type of manipulator is very interesting to researchers and has been often discussed in the literature.

The minimization of torques in the joints of a 2-DOF serial manipulator (Figure 2) using the method of optimal mass redistribution of the links was analyzed in [7, 8]. Each link of the planar manipulator is represented by an equivalent system of three point masses. For such an equivalent system, the equations of motion were determined, and then the problem of minimizing the torques in the joints was solved using MOO. The method of weighting factors was used in MOO procedure, and the objective function was defined as follows:

$$\text{Minimize } F(\mathbf{X})=w_1\tau_1+w_2\tau_2 \tag{3}$$

where w_1 and w_2 are weighting factors, and τ_1,τ_2 denote torques in the joints of the manipulator.

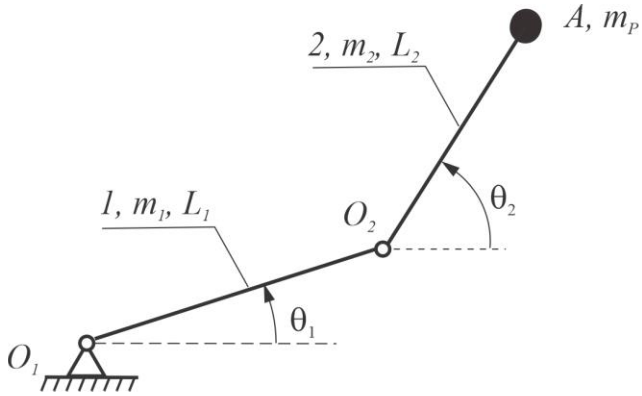

Figure 2: Serial manipulator

The same optimization problem was considered by Arakelian et al. [9] and they applied the method of adding counterweights to solve it [10, 11]. Harl, Oblak and Butinar [12] considered the problem of minimizing joint reaction forces in a serial manipulator. The problem of minimization of these quantities was solved by an adequate choice of the length of the manipulator links and the application of weighting factors in the MOO procedure. A comparison of the effectiveness of two methods used for balancing the dynamic joint reaction forces of a planar manipulator was presented by Šalinić et al. [13]. In the first method, the balancing of the joint reaction forces is achieved by applying interpolation polynomials [14], while in the second method, the same goal is achieved by adding counterweights to the manipulator links. By using the Lagrange's equations with multipliers [15], applying velocity transformation methods and representing the manipulator links with an equivalent system of point-masses, it is possible to calculate the dynamic joint reaction forces. To solve the MOO problem (minimization of two objective functions that determine the joint reaction forces), the differential evolution algorithm was applied. The objective function was defined as follows:

$$F=\frac{w_1}{\delta}\sqrt{\sum_{i=0}^{\delta} f_1^2\left(t_i\right)}+\frac{w_2}{\delta}\sqrt{\sum_{i=0}^{\delta} f_2^2\left(t_i\right)} \tag{4}$$

where w_1 and w_2 are weighting factors which values are $w_1=w_2=0.5$. The quantities under the root determine the resultant forces in the joints of the manipulator.

It should be emphasized that the application of optimization techniques in all analyzed studies of dynamic balancing of the planar serial manipulator gives satisfactory results, i.e it leads to a significant reduction in the values of the considered dynamic quantities.

4. OPTIMAL DYNAMIC BALANCING OF FOUR-BAR LINKAGE

Four-bar linkages (Figure 3) are widely used in mechanical devices (especially in rotary engines) owing to their simplicity, ease of manufacturing, and low cost. These mechanisms are usually applied for achieving a special motion duty like path generation. However, they operate at high speeds in the industry and it causes an unbalancing problem. In the text below, the problem of dynamic balancing of this type of planar mechanisms will be considered using the optimization procedure.

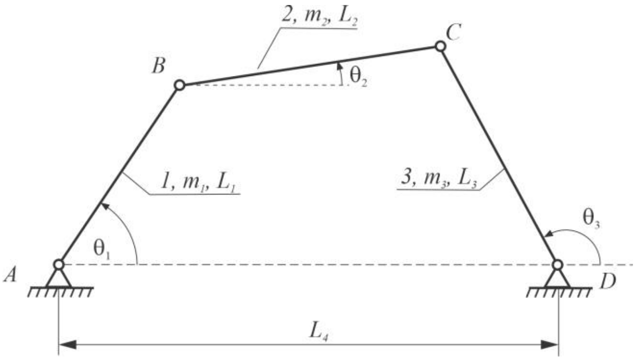

Figure 3: Four-bar linkage

K. Chaudhary and H. Chaudhary [16] presented an optimization technique that achieves dynamic balancing of the four-bar linkage based on the redistribution of the mass of the links. Namely, the minimization of shaking forces and moment was carried out using the genetic algorithm (GA). The problem of minimizing these dynamic quantities is solved as a MOO problem. In the first case, the weighting factors are used to solve the MOO problem, reducing the problem to a single-objective one. The objective function was defined as follows:

$$\text{Minimize } F(\mathbf{X}) = w_1 f_{sh} + w_2 n_{sh} \tag{5}$$

where w_1 and w_2 are weighting factors, f_{sh} denotes shaking force, and n_{sh} indicates shaking moment. In the second case, the *Pareto* front was applied to solve the MOO problem. The results obtained using both methods show a significant reduction in the value of dynamic loads.

The same problem was analyzed by Erkaya [17]. The problem of balancing of the four-bar linkage is formulated as an optimization problem and was solved by applying a Genetic Algorithm (GA). The MOO problem (minimization of shaking force and shaking moment) was solved by using weighting factors. Three cases, in which the values of these factors vary, were analyzed. It has been shown that an adequate choice of weighting factors and the structure of the objective function play a significant role in obtaining optimal values of design variables.

Bošković et al. [18] solved the problem of dynamic balancing of the four-bar linkage by applying a new algorithm called the Sub-Population Firefly Algorithm (SP-FA). The proposed algorithm is a modified (improved) version of the standard Firefly Algorithm (FA). By applying the SP-FA algorithm, the simultaneous minimization of eight objective functions was performed, which include joint reaction forces, driving torque, shaking forces, and shaking moment. By applying the proposed algorithm, the use of weighting factors was avoided and a significant reduction in the values of shaking force and moment was achieved (Figure 4). Also, the values of joint reaction forces are significantly smaller compared to the original (Figure 5). Thus, the efficiency of the proposed algorithm was proven.

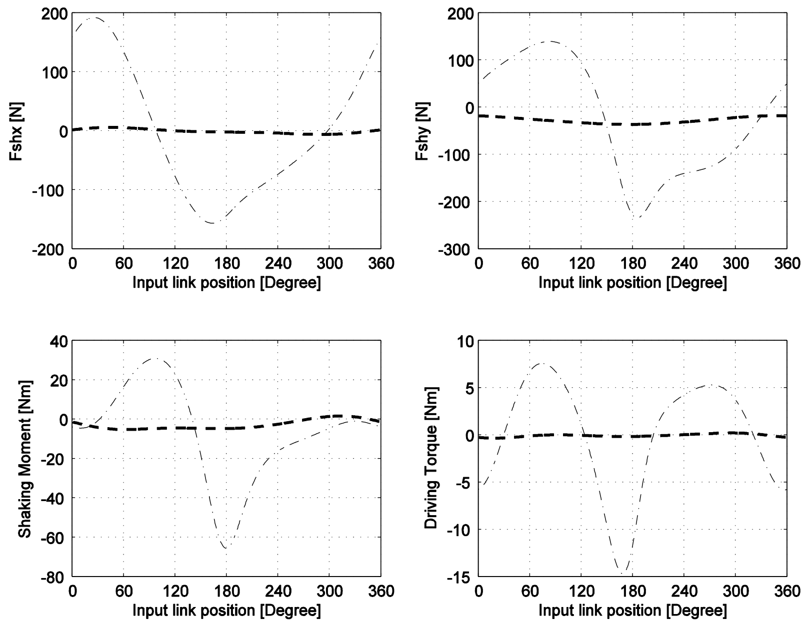

Figure 4: Original and optimized values of shaking forces, shaking moment and driving torque [18]

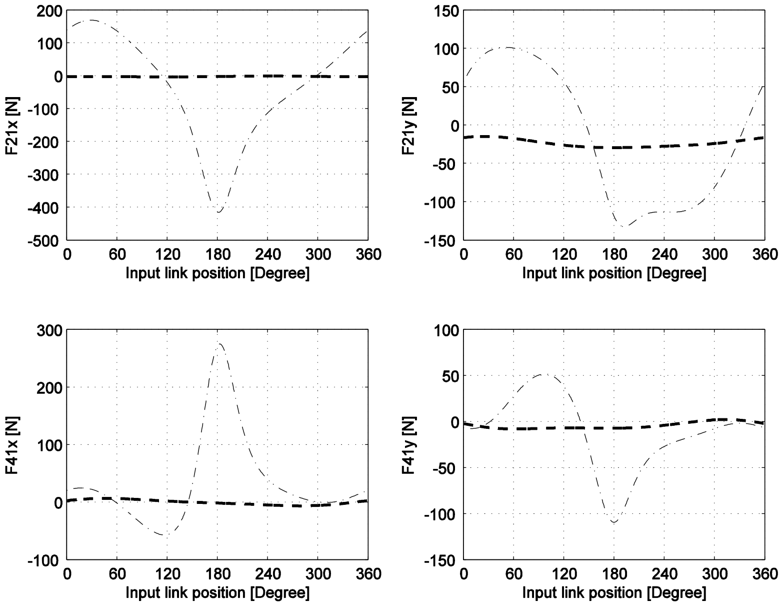

Figure 5: Original and optimized values of ground joint reaction forces [18]

Based on research and results obtained in [17, 18], Bošković et al. [19] developed a new algorithm called the Hybrid Cuckoo Search and Firefly Algorithm (H-CS-FA) and applied it to solve the problem of dynamic balancing of the four-bar linkage. Authors analyzed three cases where the simultaneous minimization of eight, nine and three objective functions is performed. The obtained results were compared with the results obtained by applying the basic algorithms (CS and FA), thus proving the effectiveness of the proposed H-CS-FA.

Percentage decrease of values of dinamic quantities obtained in [17, 18, 19] is shown in Table 1. It is obvious that the application of proposed optimization algorithms in the dynamic balancing procedure gives excellent results.

Table 1: Comparative view Percentage decrease of values of dinamic quantities

	Erkaya [17] (Case 1)	Erkaya [17] (Case 2)	Erkaya [17] (Case 3)	Bošković [19] (Case 1)	Bošković [19] (Case 2)	Bošković [19] (Case 3)	SP-FA [18]
F21x	95.52	88.04	93.50	97.83	90.293	90.92	99.26
F21y	77.18	31.66	59.10	71.33	69.22	75.65	71.88
F41x	84.69	51.48	78.28	80.63	84.64	76.03	92.91
F41y	74.95	21.59	56.58	53.90	72.67	77.69	85.12
Fshx	90.96	69.35	86.30	90.38	79.06	99.19	96.78
Fshy	77.54	37.61	61.54	71.95	69.70	77.40	75.85
Msh	76.21	25.51	58.73	51.63	69.34	76.38	83.39
M1	73.46	57.65	70.49	90.32	92.55	94.76	97.54

In the latest research, Etesami et al. [20] proved that the problem of dynamic balancing of the four-bar linkage is essential for its greater efficiency. A multi-objective Differential Evolution algorithm is used for *Pareto* optimization balancing of a four-bar linkage while considering the shaking moment and horizontal and vertical shaking forces as objective functions. The Pareto charts of five-objective optimization show a large number of non-dominated points, which provide more choices for optimal balancing design of the planar four-bar mechanism. A comparison of the results obtained from this study with those reported in the literature shows a significant decrease in shaking forces and shaking moment.

5. OPTIMAL DYNAMIC BALANCING OF MULTI-BAR MECHANISMS

In the last two decades, five-bar planar mechanisms (Figure 6) have been extensively used in various industrial fields, especially in robotic applications for mass production such as assembly, transportation, and positioning, as well as haptic and medical devices. There are a variety of five-bar planar manipulators depending on whether the actuators are rotary or linear [21].

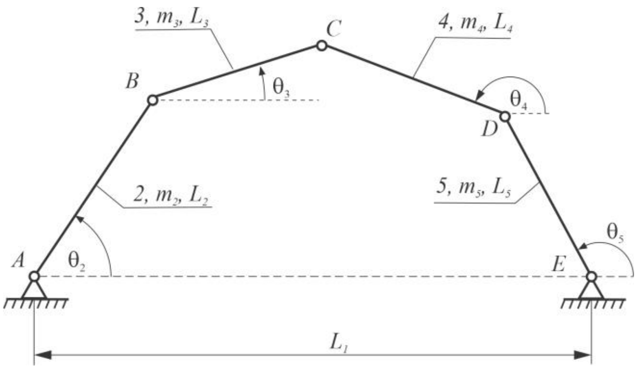

Figure 6: Five-bar mechanism

D. Kavala Sen et al. [21] analyzed the problem of dynamic balancing of five-bar planar manipulator for the largest trajectory in a usable workspace. The minimization of shaking forces and shaking moment was considered as an optimization problem which was solved by application of three different population-based optimization techniques: Particle Swarm Optimization, Genetic Algorithm, and Differential Evolution. The results show that an adequate selection of weighting factors and appropriate optimization algorithm allows achieving a significant reduction in the values of shaking force and moment.

Six bar mechanism (Figure 7) is a one degree of freedom mechanism which is constructed from six links. Klann linkage used to drive the legs of a walking machine. Six-bar mechanism is used in Watt mechanism, Stephenson mechanism, missile launcher and bellow valves etc [22].

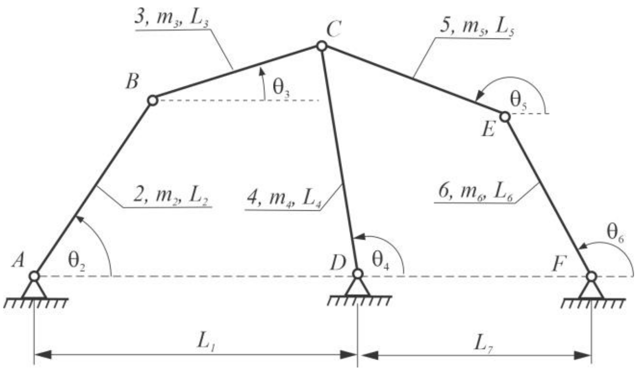

Figure 7: Six-bar mechanism

Belleri and Kerur [22] analyzed the problem of optimal dynamic balancing of the planar six-bar mechanism. The goal is to eliminate or minimize shaking force and shaking moment by applying genetic algorithm (GA). Two cases, with differently defined values of the weighting factors, were considered. It has been shown that the selection of weighting factors has a crucial role to obtain the optimum values of design parameters. The obtained values of shaking force and shaking moment are significantly reduced compared to the original values.

A further step in the investigation of the balancing problem of the six-bar mechanism was made in [23]. By adding counterweights, dynamic balancing of the considered mechanism was performed. The problem of minimization of the shaking force and the shaking moment was considered as a MOO problem and was solved using the Differential Evolution (DE) algorithm. The *Pareto* front is used to determine the best solutions according to three optimization criteria: only the shaking force, only the shaking moment, and both the shaking force and shaking moment. Numerical results show that the values of dynamic quantities are significantly reduced in relation to the original.

6. CONCLUSION

The theory of balancing mechanisms continues to develop and papers about new solutions in this area are constantly appearing. Special attention is paid to balancing methods based on the application of optimization algorithms. The continuous development and the appearance of new biologically inspired algorithms create the basis for further research in the field of optimal balancing. At the moment, it is difficult to say which is the best approach in multi-objective optimization of planar mechanisms. Depending on the chosen optimization algorithm and the user's requirements, one multi-objective optimal balancing method can be chosen over the other.

ACKNOWLEDGEMENTS

Author wishes to acknowledge the support of the Ministry of Science, Technological Development and Innovation of the Republic of Serbia, through the Contract for the scientific research financing in 2023, 451-03-47/2023-01/200108.

REFERENCES

[1] V.Wijk, "Methodology for analysis and synthesis of inherently force and moment-balanced mechanisms", PhD Thesis, Faculty of Engineering Technology, University of Twente (Netherlands), (2014)

[2] M.Bošković, "Modern approaches in kinematic and dynamic analysis of planar mechanisms", PhD Thesis, Faculty of Mechanical and Civil Engineering Kraljevo, University of Kragujevac (Serbia), (2019)

[3] B. Wei and D. Zhang, „A Review of Dynamic Balancing for Robotic Mechanisms", Robotica, Vol. 39(1), pp. 55–71, (2021)

[4] S.T. Tricamo and G.G. Lowen, „A novel method for prescribing the maximum shaking force for a four-bar linkage with flexibility in counterweight design", J. Mech., Trans., and Automation, Vol.105(3), pp. 511-519, (1983)

[5] S.T. Tricamo and G.G. Lowen, „Simultaneous optimization of dynamic reactions of a 4-bar linkage with prescribed maximum shaking force", J. Mech., Trans., and Automation, Vol. 105(3), pp. 520-525, (1983)

[6] V. Arakelian, "Shaking Force Balancing of Mechanisms: An Overview", IJMEM, Vol.15(6), pp. 263-266, (2021)

[7] H. Chaudhary and S.K. Saha, „Minimization of constraint forces in industrial manipulator", IEEE International Conference on Robotics and Automation, Rome (Italy), pp. 1954–1959, (2007)

[8] V. Gupta, H. Chaudhary and S.K. Saha, „Dynamics and actuating torque optimization of planar robots", J. Mech. Sci. Technol., Vol. 29, pp. 2699–2704, (2015)

[9] V. Arakelian, J. P. Baron and P. Mottu, „Torque minimisation of the 2-DOF serial manipulators based on minimum energy consideration and optimum mass

redistribution“, Mechatronics, Vol. 21, pp. 310–314, (2011)

[10] J. J. Uicker, G. Pennock and J. Shigley, „Theory of machines and mechanisms“, Oxford University Press, New York (USA), (2003)

[11] M. Zlokolica, M. Čavić and M. Kostić, “Mechanics of Machines” (In Serbian), Faculty of Technical Sciences, Novi Sad (Serbia), (2005)

[12] B. Harl, M. Oblak and B. Butinar, „Minimization of joint reaction forces of kinematic chains by a multi-objective approach“, Struct. Multidiscip. Optim., Vol. 27, pp. 243–249, (2004)

[13] S. Šalinić, M. Bošković and R.R. Bulatović, “Minimization of dynamic joint reaction forces of the 2-dof serial manipulators based on interpolating polynomials and counterweights”, Theoretical and Applied Mechanics, Vol. 42(4), pp. 249-260, (2015)

[14] J. Angeles, „Fundamentals of robotic mechanical system: theory, methods and algorithms“, Springer Science + Business Media, New York (USA), (2007)

[15] A. I. Lurie, „Analytical mechanics“, Springer - Verlag, Berlin Heidelberg New York, (2002)

[16] K.Chaudhary and H.Chaudhary, “Dynamic balancing of planar mechanisms using genetic algorithm”, J Mech Sci Technol, Vol.28(10), pp. 4213-4220, (2014)

[17] S.Erkaya, “Investigation of balancing problem for a planar mechanism using genetic algorithm“, J Mech Sci Technol, Vol.27, pp. 2153-2160, (2013)

[18] M. Bošković, S. Šalinić, R. Bulatović and G. Miodragović, „Multiobjective optimization for dynamic balancing of four-bar mechanism“, 6th International Congress of Serbian Society of Mechanics, Tara (Serbia), 19-21 June 2017, (2017)

[19] M. Bošković, R.R. Bulatović, S. Šalinić, G.R. Miodragović and G.M. Bogdanović, “Optimization of dynamic quantities of a four-bar mechanism using the Hybrid Cuckoo Search and Firefly Algorithm (H-CS-FA)”, Arch Appl Mech, Vol. 88, pp. 2317–2338, (2018)

[20] G. Etesami, M.E. Felezia and N. Nariman-Zadeh, “Pareto Optimal Balancing of Four-bar Mechanisms Using Multi-Objective Differential Evolution Algorithm”, JCAMECH, Vol. 51(1), pp. 55-65, (2020)

[21] D. Kavala Sen, A. Yildiz and O. Kopmaz, “Optimal Design of a Five-Bar Planar Manipulator and Its Controller by Using Different Algorithms for Minimum Shaking Forces and Moments for the Largest Trajectory in a Usable Workspace”, Machines, Vol.10(11), (2022)

[22] B.K. Belleri and S.B. Kerur, “Balancing of planar six-bar mechanism with genetic algorithm”, J JMEE, Vol.4(4), pp. 303-308, (2020)

[23] M.T. Orvañanos-Guerrero, M. Acevedo, C.N. Sánchez, D.U. Campos-Delgado, A. A. Ghavifekr, P. Visconti and R. Velázquez, “Complete Balancing of the Six-Bar Mechanism Using Fully Cartesian Coordinates and Multiobjective Differential Evolution Optimization”, Mathematics, Vol.10(11), (2022)

Modified 2D arc-star-shaped structure with negative Poisson's ratio

Vladimir Sinđelić[1*], Aleksandar Nikolić[1], Nebojša Bogojević[1], Olivera Erić Cekić[1], Snežana Ćirić Kostić[1]
[1] Faculty of Mechanical and Civil Engineering in Kraljevo, University of Kragujevac, Kraljevo (Serbia)

The metamaterials with negative Poisson's ratio have played an important role in engineering practice in the last decade. Their use in space, aviation, the automotive industry, and biomedicine increasing constantly. The basic idea of making these metamaterials is to use additive manufacturing to create a structure that has a negative Poisson's ratio, unlike conventional materials that are most often used in industry (steel, wood, rubber, etc.). The design process of these metamaterials takes place by first considering the properties of the elementary structure, and then by multiplying that structure, a metamaterial with the same Poisson's ratio as the basic structure will be obtained. The paper discusses a modified 2D arc-star-shaped structure in relation to the already existing variant in the literature. The influence of the parameters of the newly proposed structure on Poisson's ratio by using the finite element method was analyzed.

Keywords: Metamaterials, Negative Poisson's ratio, Auxetic structures, Arc-star-shaped structure

1. INTRODUCTION

Various branches of industry, such as aviation, space, or automotive, as well as biomedicine have needs for the application of ultralight materials which have the appropriate mechanical properties. Conventional materials (wood, metal, rubber, etc.) often cannot meet these two criteria simultaneously. For this reason, so-called mechanical metamaterials are increasingly used. The word "metamaterials" is a combination of the Greek word "meta" which means above and the Latin word "materia" which means material.

The most common requirement for these materials is that they have a negative Poisson's ratio (NPR in the further). Conventional materials have a positive Poisson's ratio. If this kind of material is pressed in one direction there will be an elongation in the direction perpendicular to the direction of pressure, as it is shown in Fig. (a). On the contrary, in materials with a NPR due to pressure in one direction, the shortening occurs in the perpendicular direction, as shown in Fig. 1 (b).

The basic idea of making these metamaterials is to use additive manufacturing to create a structure that has a NPR. The design process of these metamaterials takes place by first considering the properties of the elementary structure, and then by multiplying that structure, a metamaterial with the same Poisson's ratio as the basic structure will be obtained.

Decades ago, a structure in the form of a honeycomb was used as the main mechanical metamaterial, the geometry of which corresponded to a structure with a positive Poisson's coefficient. However, in recent years, studies around the world have shown the possibility of designing mechanical metamaterials with a NPR.

Metamaterials with this property are called "Auxetic structures" in the literature. The word "Auxetic" comes from the Greek language, which in literal translation would represent "pulled in" [1-3]. The first structure with a NPR was created from a structure in the form of a honeycomb, in such a way that the two vertices of the structure of the honeycomb are drawn toward the center of the structure, as shown in Fig. 2. The structure obtained in this way was named re-entrant Honeycomb.

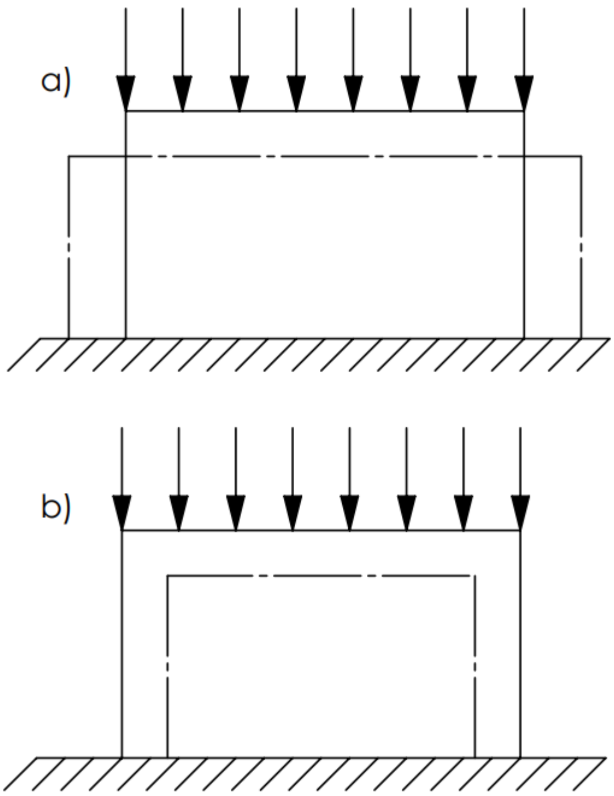

Figure 1: Deformations under pressure: (a) Conventional materials, (b) Metamaterials with negative Poisson's ratio

In the last decade, the re-entrant honeycomb structure has undergone a series of shape changes, with a tendency to retain its original behavior.

Thus, in reference [4] the new shape of the re-entrant honeycomb structure was presented, whereas an analytical and finite element method (FEM in the further) results were compared. Reference [5] provides an analytical model, the FEM model, as well as experimental verification on a model of a re-entrant honeycomb structure made by using additive manufacturing.

*Corresponding author: Dositejeva 19, 36000 Kraljevo, Serbia, e-mail: sindjelic.v@mfkv.kg.ac.rs

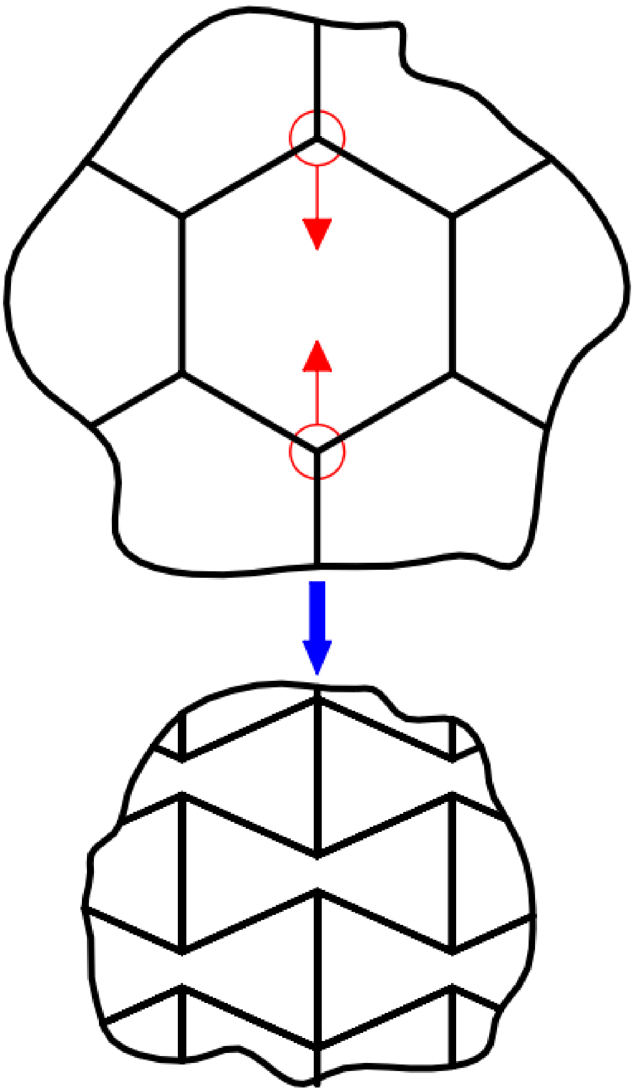

Figure 2: Honeycomb and Re-Entrant Honeycomb

The results of testing of energy absorption characteristics of the structure made by the combination of two structures with a NPR were given in [6]. In more detail, this structure was created by the fusion of the re-entrant honeycomb structure and a star-shaped structure. The star-shaped structure got its name because its geometry resembles a four-pointed star. Its shape guarantees that it will have the behavior of a structure with a NPR. Like the re-entrant honeycomb structures, it is also subject to changes in shape with the same goal of increasing the NPR and improving other mechanical properties. Changes in the shape of the star-shaped structure were experimentally examined in two papers [7-8]. The goal of these studies was to find an optimal shape that will improve the mechanical properties of the 2D star-shaped structure.

In the paper [9], a new form of 2D arc-star-shaped structure was analyzed, as well as two of its variants in 3D space. The shape of this structure is based on the classic star-shaped structure. This paper contains theoretical, numerical, and experimental analyses, to examine the influence of changes in the geometrical parameters of the structure on the NPR.

In this study, a modified 2D-AS structure is presented, based on the 2D-AS structure from the previously mentioned reference. The investigation of the modified 2D-AS structure was carried out by numerical analysis (FEM), the results of which were compared with the numerical results of the 2D-AS structure, to obtain higher values of NPR.

2. A MODIFIED 2D-AS STRUCTURE

2.1. Design of the modified 2D AS structure

Figure 3 shows the 2D-AS structure with all geometric parameters necessary for its construction: the length *L*, height *h*, thickness *t*, depth *d*, arc radius *r*, arc angle *θ*, angle coefficients *a* and *b* and total lengths L_x and L_y in the horizontal and vertical directions, respectively.

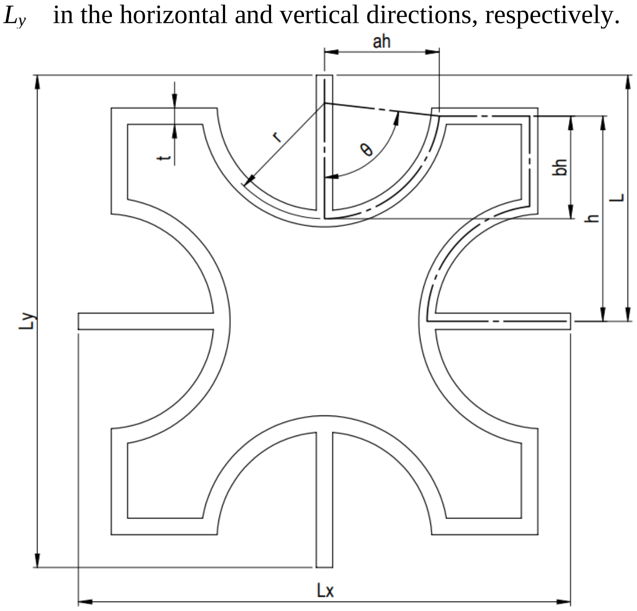

Figure 3: Geometric parameters of the 2D-AS structure [9]

The values of coefficients *a* and *b* are within the limits $0<a<1$ and $0<b<1$ [9]. Also, the parameters *a, b, θ*, and *r* are related in the following manner:

$$\theta = 2\arctan\frac{bh}{ah}, \tag{1}$$

$$r = \frac{ah}{\sin\theta}. \tag{2}$$

The modified 2D-AS structure was created by redesigning the end branches of the 2D-AS structure, i.e. by adding another circular arc of radius R, as shown in Fig. 4.

Now, the relation between parameters *a*, *h*, and *R* holds:

$$R = \sqrt{2}\cdot(h - ah)/2. \tag{3}$$

The relative density of the modified 2D-AS structure (RD) can be obtained as below:

$$RD = \frac{V_S}{V_C}, \tag{4}$$

where

$$V_S = 4dt\left(\frac{r\cdot\pi}{180}\cdot\theta + R\cdot\pi + L - h + bh\right) \tag{5}$$

represents the volume of solid model of the modified 2D-AS structure, and

$$V_C = L_x \cdot L_y \cdot d = 4dL^2 \qquad (6)$$

represents the total volume that the solid model of the modified 2D-AS structure takes up in space.

By applying equations (4), (5) and (6) we obtain an expression for calculating the relative density of the modified 2D-AS structure:

$$RD = \frac{t \cdot \left(\frac{r \cdot \pi}{180} \cdot \theta + R \cdot \pi + L - h + bh \right)}{L^2}. \qquad (7)$$

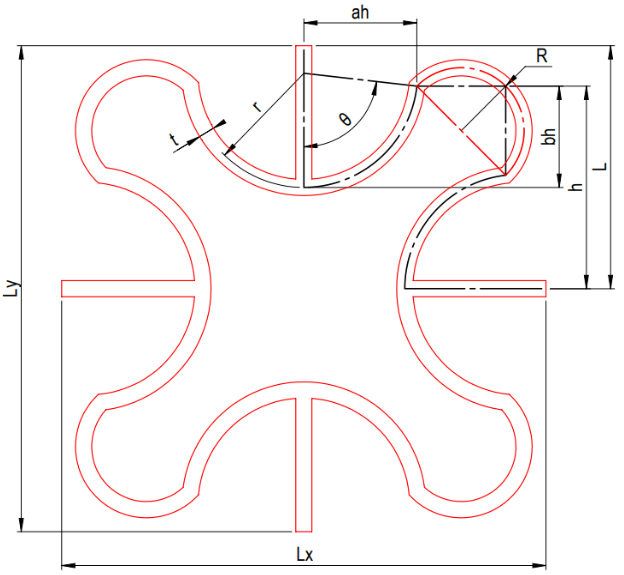

Figure 4: Geometric parameters of the modified 2D-AS structure

2.2. Deformation of the modified 2D-AS structure – numerical example

We report here the change of Poisson’s ratio value of the modified 2D-AS structure relative to the initial shape of the structure by using the finite element method in the ANSYS software package.

The Fig. 5 shows how the elementary modified 2D-AS structure was extracted from the whole in the example of the 3x3 array. As it is shown in the Fig. 6, the bottom end A of the elementary structure is clamped. The vertical displacement of Δyx=3mm was introduced at the upper end B of the structure. The examined structure had fixed dimensions: L=30 mm, h=25 mm, t=2 mm, d=3 mm, and bh=12.5 mm except the value of the ah which takes the values from 8 mm to 22 mm with a step of 2 mm. The mesh size was 1x1 mm, and the number of finite elements varied depending on the parameter ah.

Based on the given vertical displacement Δyx, the horizontal displacements $\Delta xx/2$ of points C and D were measured in Ansys, as sketched in Fig. 6.

The value of the Poisson’s ratio is determined according to the formula [10]:

$$\nu = -\frac{\varepsilon_x}{\varepsilon_y} = -\frac{\Delta_{yx}}{\Delta_{yy}} \cdot \frac{L_y}{L_x}, \qquad (8)$$

where ε_x and ε_y represents dilatation and Δyx and Δxx are displacements in horizontal and vertical directions, respectively.

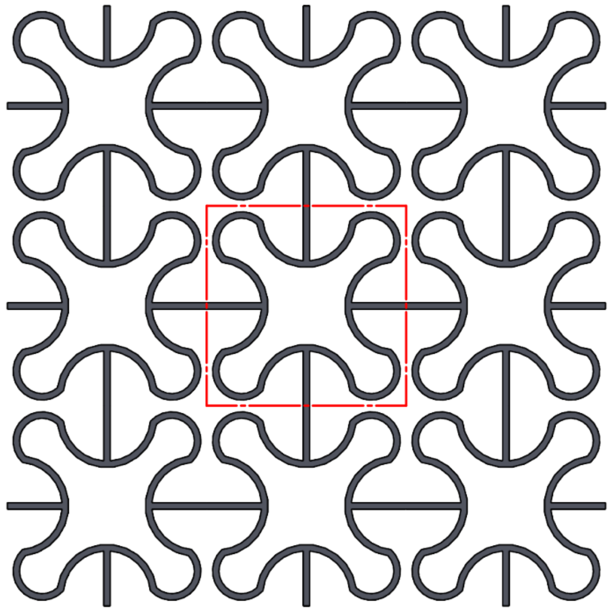

Figure 5: Schematic illustration of the modified 2D-AS structure in a 3x3 array

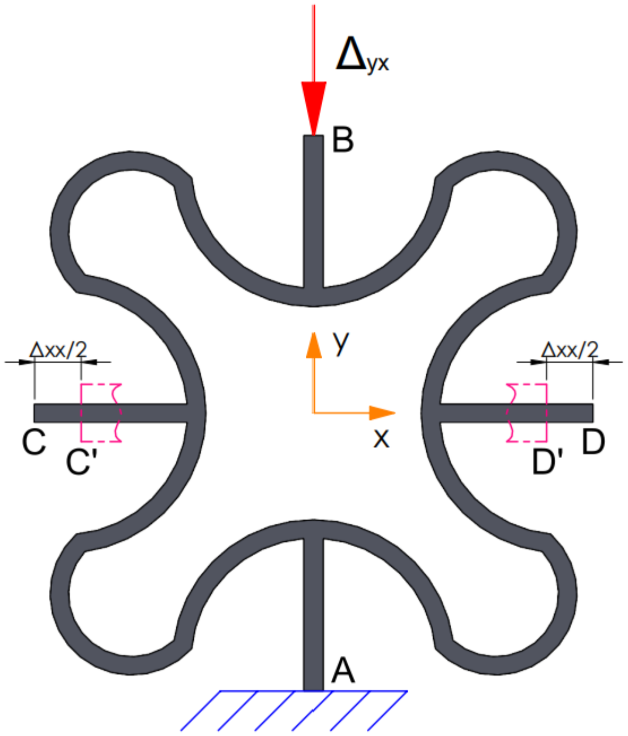

Figure 6: Deformation of the modified 2D-AS structure

The horizontal displacements Δxx for the various parameters ah of the modified 2D-AS obtained by Ansys are given at Figs. 1-14.

Now, based on the specified displacements in the vertical direction Δyx=3mm and the measured displacements in the horizontal direction Δxx, the value of Poisson's ratio can be obtained for each of the specified values of the parameter ah by using formula (8).

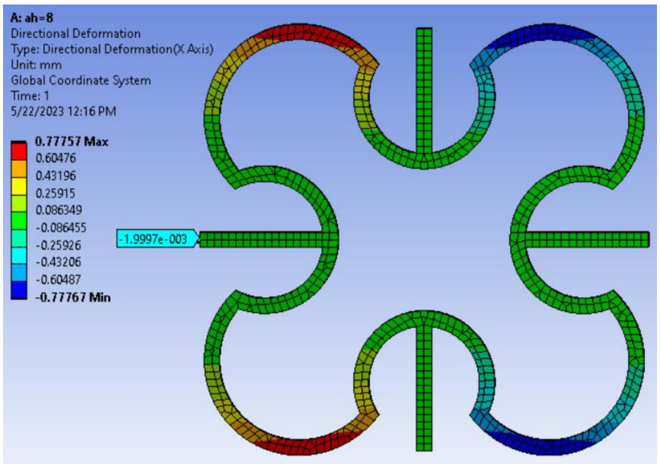

Figure 7:Horizontal displacements Δxx for *ah=8 mm*

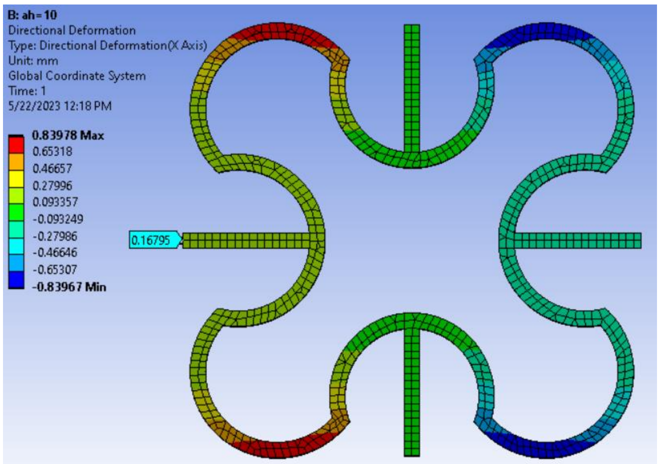

Figure 8: Horizontal displacements Δxx for *ah=10 mm*

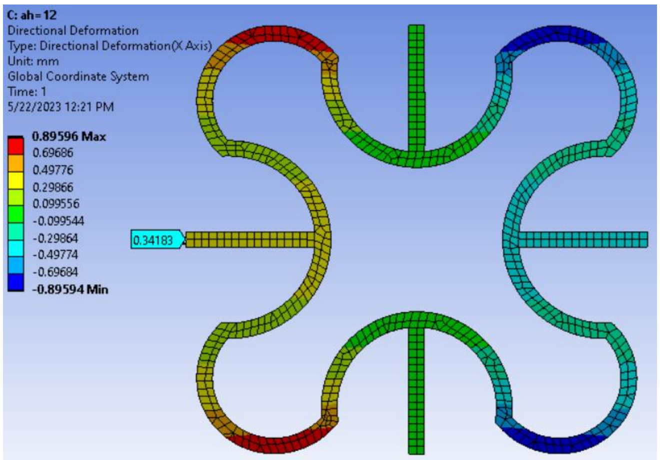

Figure 9:Horizontal displacements Δxx for *ah=12 mm*

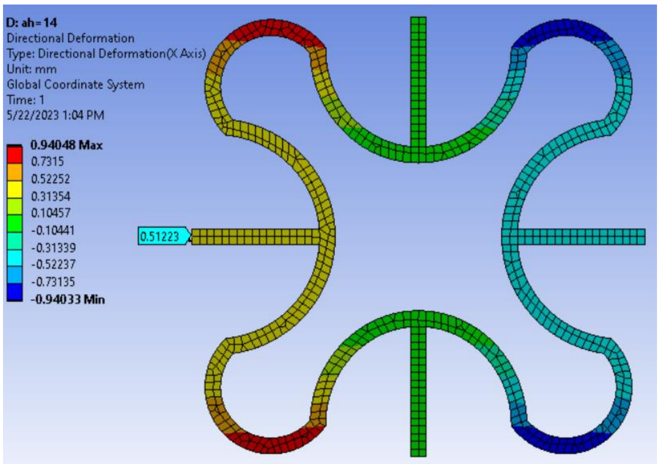

Figure 10: Horizontal displacements Δxx for ah=14 mm

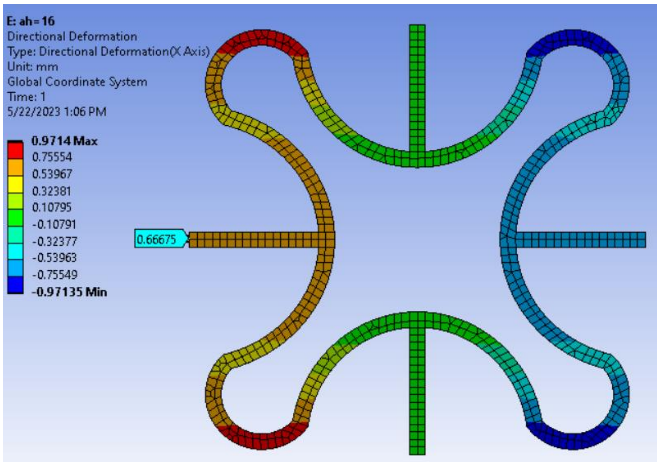

Figure 11: Horizontal displacements Δxx for *ah=16 mm*

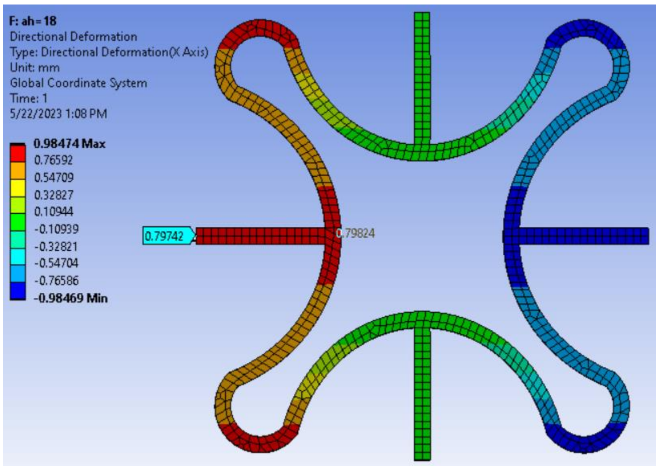

Figure 12: Horizontal displacements Δxx for *ah=18 mm*

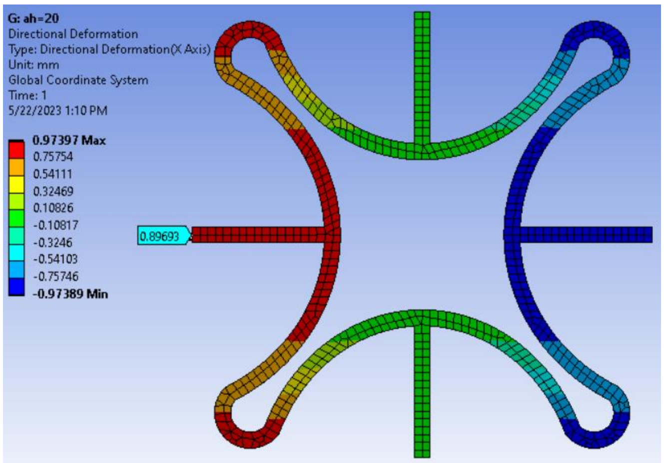

Figure 13:Horizontal displacements Δxx for ah=20 mm

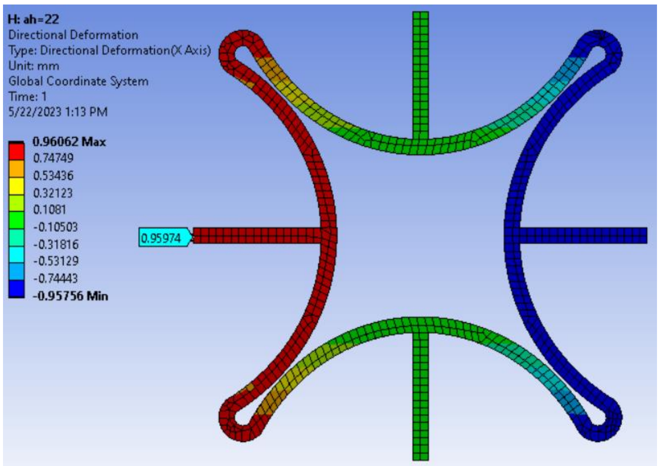

Figure 14: Horizontal displacements Δxx for ah=22 mm

The comparison of the obtained values of the Poison’s ratio of the 2D-AS structure and the modified 2D-AS structure for the various values of the parameter *ah* is shown in Table 1. For the first three values of the parameter *ah*=8,10, and 12 mm the decrease in the absolute values of the Poisson’s ratio of the modified 2D-AS relative to 2S-AS is observed. For values of the parameter *ah*>13 mm, the absolute value of the Poisson's ratio in the modified 2D-AS is larger compared to the classical 2D-AS. It is interesting to note that for *ah*=13, an equal values of Poisson's ratio are obtained for both structures, modified 2D-AS and 2D-AS, which can be seen in the diagram shown in Fig. 15. Curves which describe the change of the Poisson's ratio of 2D-AS and the modified 2D-AS structure are thin solid line and slightly thicker dashed line, respectively.

Furthermore, the numerical values of the relative density RD of both above mentioned structures for the variable values of the parameter *ah* are given in Table 2. The relative density determined for the modified 2D-AS is higher than the corresponding density for the classical 2D-AS structure. The difference is the largest at *ah*=8 mm and amounts to 6.63%, and the smallest at *ah*=22 mm and amounts to 0.83%.

We can also conclude that the modified 2D-AS structure at very small parameters *ah*, in the examined case for *ah*=8 mm, does not behave like a structure with NPR. This behavior of the structure for *ah*=8 mm can be attributed to the fact that at the extreme limits of parameter R has a very large value, where it tends to close the structure, and therefore the arch with the radius *r* does not have enough space to be able to retract the structure at a given vertical displacement.

Table 1: The Poisson’s ratio of 2D-AS and modified 2D-AS for various values of parameter ah

ah [mm]	Poison’s ratio ν		The relative difference
	2D-AS	Modified 2D-AS	
8	-0.027	0.001	-103.7%
10	-0.128	-0.112	-12.5%
12	-0.232	-0.228	-1.72%
14	-0.334	-0.341	2.1%
16	-0.427	-0.445	4.21%
18	-0.508	-0.532	4.72%
20	-0.571	-0.598	4.73%
22	-0.613	-0.640	4.40%

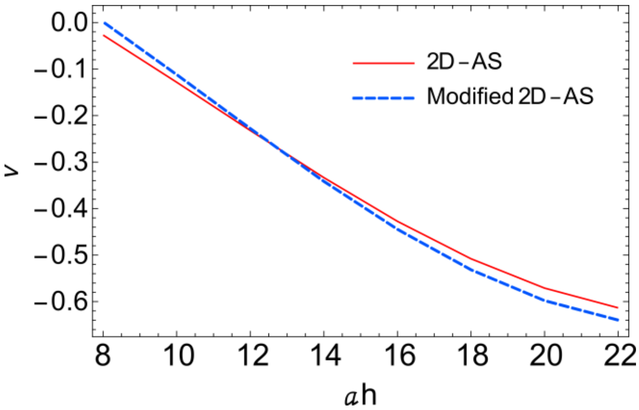

Figure 15: Graphical representation of the Poisson’s ratio of the 2D-AS and modified 2D-AS for various parameter ah

Table 2: The relative density RD of 2D-AS and modified 2D-AS for various values of parameter ah

ah [mm]	Relative density RD		The relative difference
	2D-AS	Modified 2D-AS	
8	0.116	0.123	6.63%
10	0.107	0.114	6.23%
12	0.098	0.104	5.75%
14	0.089	0.094	5.17%
16	0.081	0.084	4.44%
18	0.072	0.074	3.54%
20	0.063	0.065	2.37%
22	0.054	0.055	0.83%

3. CONCLUSION

In this paper, a modified 2D-AS structure based on the 2D-AS structure [9] was designed. Numerical simulations, based on Ansys software, showed that the modified 2D-AS structure has higher values of NPR than the 2D-AS structure, only in the case when the values of the parameter *ah* are greater than 13mm. In fact, it has been shown that changing the shape of parts of the structure can affect the NPR value.

This paper has opened the door for new research on the further modifications of 2D-AS structure with the aim of achieving the maximum possible NPR value for the same or slightly different value of relative density RD.

ACKNOWLEDGEMENTS

This research was supported under grant no. 451-03-9/2021-14/200108 by the Ministry of Education, Science and Technological Development of the Republic of Serbia. This support is gratefully acknowledged.

REFERENCES

[1] L.J. Gibson and M.F. Ashby, “Cellular solids, Structure and properties - Second edition”, Cambridge Solid State Series, (1997)

[2] T.C. Lim, “Auxetic Materials and Structures”, Springer, Engineering Materials, School of Science and Tehnology, Singapore, (2022)

[3] T.C. Lim, “Mechanics of Metamaterials with Negative Parameters”, Springer, Engineering Materials, School of Science and Tehnology, Singapore, (2022)

[4] E. Hakati, N. Daoubi, A. Bezazi and F. Scarpa, “In-plane elasticity of a multi re-entrant auxetic hooneycomb”, Compos. Struct., vol. 180, pp. 130-139, (2017)

[5] J. Shwn, K. Liu, Q. Zeng, J. Ge, Z. Dong and J. Liang, “Design and mechanical property studies of 3D re-entrant lattice auxetic structure”, Aerosp. Sci. Technol., vol 118, pp. 106998, (2021)

[6] H. Wang, Z. Lu, Z. Yang and X. Li, “A novel re-entrant auxetic honeycomb with enhanced in-plane impact resistance”, vol. 208, pp. 758-770, (2019)

[7] X. Li, L. Gao, W. Zhou, Y. Wang and Y. Lu, “Novel 2D metamaterials with negative Poisson’s ratio and negative thermal expansion”, Extreme Mech. Lett., vol. 30, pp. 100498, (2019)

[8] N. Xu, H.T. Liu, M.R. An and L. Wang, “Novel 2D star-shaped honeycombs with enhanced effective Young’s modulus and negative Poisson’s ratio”, Extreme Mech. Lett., vol. 43, pp. 101164, (2021)

[9] Z.Y. Zhang, J. Li, H.T. Liu, Y.B. Wang, “Novel 2D arc-star-shaped structure with tunable Poisson’s ratio and its 3D configurations”, Mater. Today Commun., vol 30, pp.103016, (2022)

SESSION F

THERMAL TECHNIQUE AND ENVIRONMENT PROTECTION

Carbon dioxide emissions calculation of the transport process in road freight transport

Nikola Petrović[1*], Vesna Jovanović[1], Dragan Marinković[1,2], Jovan Pavlović[1]

[1]Faculty of Mechanical Engineering/Department of Transport Engineering and Logistics, University of Niš, Niš (Serbia)
[2]Faculty of Mechanical Engineering and Transport Systems, Department of Structural Analysis, Berlin Institute of Technology, Berlin (Germany)

Transport plays an important role in the social and economic development of the country, but it negatively affects all elements of the environment (air, water, soil, fauna, and flora). The total production of greenhouse gases (GHG) in transport has increased by a quarter in the past decades in the 32 member countries of the European Environmental Protection Agency. Carbon dioxide (CO_2) is the main component of transport emissions of greenhouse gases, and road transport has the largest share of these emissions. In recent years, in addition to determining the shortest movement paths or the shortest travel time of freight vehicles, special attention has been paid to determining the amount of CO_2 emitted. In the paper, the ecological optimization procedure of the freight vehicle utilization for the calculation of the CO_2 emitted amount for the transport of a certain amount of goods is presented through a numerical task.

Keywords: Road freight transport, Carbon dioxide emissions, CEN-EN 16258 standard

1. INTRODUCTION

In relation to the environment, traffic and transport are sources of harmful emissions of polluting substances and thus exert pressure on the environment and cause health problems for people. Most traffic activities affect the air, and the combustion of hydrocarbon fuels in internal combustion engines has a major impact. Also, driving releases toxic and carcinogenic substances (CO, NOx, SO_2, heavy metals and particles) and substances that contribute to the global warming of the earth's atmosphere (CO_2, N_2O, and CH_4) [1].

Transport is one of the main sectors responsible for the disruption caused by climate change. Climate change: greenhouse gases (mainly carbon dioxide CO_2) have a lasting impact on the earth's climate, leading to the expansion of desert areas, rising sea levels, serious damage to agriculture, and other devastating environmental and health side effects [1].

Traffic accounts for 23% of CO_2 emissions related to energy consumption [2]. And unlike other sectors, it has yet to reduce its carbon intensity. In the European Union, total CO_2 emissions fell by 20% from 1990 to 2016, while transport emissions increased by 27% [1] [2]. Within the transport sector, less pressure is exerted through the measures on road freight transport than on the use of passenger cars.

The total production of basic pollutants from transport has the largest share in road traffic. Road freight transport is the backbone of the economy and is irreplaceable for the transport of goods. It burns 17 million barrels of oil per day, and consumption is still increasing [2]. Road freight transport is the fastest-growing emitter of CO_2. Transportation of goods by road consumes about 50% of the total amount of diesel produced [2]. Road freight transport activities will more than double from 2015 to 2050. This will offset any expected efficiency gains and lead to an increase in emissions by 2050, not a decrease.

Trucks are the fastest-growing source of global oil demand. They call for a 40 percent expected increase in oil demand by 2050 and a 15 percent increase in global CO_2 emissions. Trucks have overtaken passenger cars as the main consumers of oil. Heavy trucks on long journeys generate most of the CO_2 emissions of road freight transport. But economical alternatives are lacking. Road freight transport offers a level of flexibility, affordability, and overall level of service at competitive prices that limit modal shift opportunities. More efficient logistics and vehicles are part of the road map to decarbonization, but by themselves, they are not enough to achieve reductions in climate targets. So, to meet climate goals, zero-emission truck fuels should be in general use by 2050.

For heavy goods vehicles, CO_2 emissions rose by 5.5% between 2000 and 2019. The impact of this growth on emissions is reinforced by the dominant and growing share of road traffic. The most important factor that partially compensates for the effect of transport activity was the improvement of energy efficiency (reduction of energy consumption per ton-kilometer). There is no single alternative fuel for trucks. Given the current state of research and commercial applications, none of the known zero-emission truck fuels will be widely used in the short to medium term. "Electric roads" could efficiently power trucks over long distances, but they will only cover some journeys. Hydrogen, electric batteries, and advanced biofuels also have inherent limitations. However, they can be supplemented. Policies should ensure that synergies are exploited to maximize possible CO_2 reductions, even in the short and medium term. More research and pilot projects will give us the flexibility to scale up technologies that meet public policy goals. Priorities will be needed, e.g., for investments in supply infrastructure. Future breakthroughs in advanced biofuels may lead to synthetic renewable fuels or carbon storage and sequestration, but sound policy will not rely on this.

Improving the fuel efficiency of heavy goods vehicles is a key component of road freight

**Corresponding author: Aleksandra Medvedeva 14, 18000 Niš, nikola.petrovic@masfak.ni.ac.rs

decarbonization. Aerodynamic reconstruction, reduced tire rolling resistance, reduced vehicle weight, increased engine efficiency, and hybridization are already in use. Widespread adoption will be aided by ambitious standards for fuel economy and CO_2 emissions. For urban freight transport, alternative fuels are the solution. Different measures should consider pricing mechanisms, stricter emissions standards, zero emission zones, and charging infrastructure. Incentives for the adoption of alternative fuels by large fleets can be quantified.

Until 2019, the electrification of the vehicle fleet did not yet play a significant role in reducing CO_2 emissions for road freight transport. However, it is expected to become more important in the coming years.

The decarbonization of road freight transport requires carbon-free fuels. There is a need to increase the implementation of tested decarbonization measures for trucks and use more data to make evidence-based decisions. Vital indicators for decisions on the implementation of measures, e.g., vehicle capacity utilization, exist but are usually owned by private companies. Access to such information for the purpose of implementing public measures is of key importance. Ways can be found to use it without violating privacy or commercial interests. Data analysis should also be improved. New modeling tools and multidisciplinary approaches would provide more relevant insights to both policymakers and industry.

Fuel economy standards apply to more than 80% of light vehicles. However, only four countries (Canada, China, Japan, and the USA) currently have fuel economy standards for trucks, covering 51% of the world's road freight transport market [2].

Today, an ordinary recipient of goods has no insight into the amount of polluting substances being emitted until the goods are produced and their shipment practically reaches the "door". The total transport capacity for the carrier is also increasing, so it is possible to conclude that the transport of goods is an increasing problem for the quality of the environment.

The introductory part of the paper presents statistical data related to the emission of harmful gases, especially CO_2 emissions caused by road freight transport. After that, the second part presents an overview of relevant scientific and practical literature. In the third chapter, the positive and negative characteristics of road transport are shown, and in the fourth chapter, the environmental optimization of the exploitation of freight vehicles is described, i.e., the standard procedure for the allocation of carbon dioxide in the components of logistics chains. The fifth chapter shows the calculation of the required working fleet, the amount of CO_2 emitted in kg per vehicle and per pallet, as well as the total amount of CO_2 emitted in kg for the transport of a certain amount of goods. Presentation and discussion of the obtained results, as well as concluding remarks, are given in the last chapter.

2. LITERATURE REVIEW

Every change that takes place in the economy and production of a country affects all segments of the development of the country as a business entity. If an economic entity does not have the flexibility and ability to adequately respond to changes that occur and affect its development, stagnation or cessation of economic growth occurs. Such events affect the development of all transport modes, both in the world and in the Republic of Serbia. Although the Republic of Serbia has an extremely favorable geographical position as a transit country, transport plays a very important role in the constant growth of the economic development of our country. Trade internationalization increases the demand for modern freight services. Freight transport is vital in the supply chain industry due to increasing concerns about its environmental impact [3, 4]. Emissions of pollutants in the Republic of Serbia for the period from 1990 to 2018, in terms of types of pollutants, were decreasing from year to year, although this reduction was initially faster and more intense, while for the period from 2015 to 2018, one could say that the percentage of pollutant emissions was stagnant and that it was in balance, without a tendency to decline significantly [5].

As the development of our country has been noticeable in the last few years, especially in the development of road infrastructure, the challenges faced by freight transport are different. Today, freight transport users expect better service, fewer delays and congestion, less time lost at border crossings, etc. Performance measurement allows the service provider to compare the goals they set with the results they managed to achieve. According to the White Book [6], performance optimization implies greater use of more energy-efficient transport modes. 30% of road freight transport over 300 km should be directed to other modes such as rail and water transport by 2030, and more than 50% by 2050, facilitated by efficient and green freight corridors. To fulfill this goal, the development of appropriate infrastructure is also required. By 2050, it is necessary to connect all airports with a railway network, preferably at high speeds; provide sufficient connectivity of all seaports with railways for freight transport; and, where possible, with inland waterways [6].

When it comes to the literature related to the impact of transport on air pollution, it is necessary to point out that more attention is paid to the impact of certain transport modes on air pollution.

The paper [7] harmonizes the greenhouse gas declaration process for supply chains by identifying, among all the allocation units specified in the EN-16258 standard, the one that best describes the contribution to GHG emissions. For this purpose, the concepts of the theory of cooperative games were used. First, the authors developed three transportation scenarios that allow for the study of the GHG impact of a shipment: a vehicle routing problem, a network flow model, and a mixed scenario. The authors' approach extends previous research as they consider that shipment characteristics in terms of origin, destination, weight, and volume consume transport capacity to varying degrees, affect commercial vehicle routing, and thus determine GHG. Second, they present the results of a computational study based on introduced transport scenarios that compares the allocation vectors resulting from the EN-16258 allocation rule, which serves as a benchmark for the contribution to GHG emissions. Moreover, they show how often the EN-16258 allocation principles conform to a set of game-theoretic fairness criteria. The results show that the allocation unit "distance" is the closest to the benchmark of game theory and most often in accordance with the criteria of game-theoretic fairness [7].

The paper [1] proposed recommendations for a global standard for all transport modes based on EN 16258 for freight and logistics transport. First, the most relevant standards and methods are covered and explained. Based on ISO IVA 16, they are then compared and combined into one overview. A case study of the introduction of CarbonCare (an emission calculator) and its global transport customers is considered to include practical guidance for the draft. Finally, the draft is discussed with experts from all modes of transport, culminating in recommendations not only for transport but also for the harmonization of storage and handling, including simplicity, accuracy, flexibility, and feasibility [1].

In the paper [8], the authors investigated the available modeling tools for the analysis of CO_2 emissions from transport. Covering a range of techniques from transport microsimulation to global techno-economic models, this paper provides insight into the various strengths and weaknesses of these tools. It also examines the value of having a wide range of perspectives for analyzing transport emissions. The conclusions of the paper are suggestions that the wide range of models creates a rich environment for researching a range of policy issues related to transport emissions, and the potential for combining modeling approaches further improves the understanding that can be achieved [8].

Lynn H. Kaack et al. introduce five general strategies for decarbonizing freight transportation and then focus on the literature and data relevant to estimating the global decarbonization potential through modal shift [9]. The authors compare freight activity (in tons-km) by mode for every country where data are available and also describe major intraregional freight corridors, their modal structure, and their infrastructure needs. Most countries are experiencing strong growth in road freight and a shift from rail to road. Modal shift can be promoted by policies targeting infrastructure investments and internalizing the external costs of road freight, but the authors find that not many countries have such policies in place. Also, they identify research needs for decarbonizing the freight transportation sector both through improvements in the efficiency of individual modes and through new physical and institutional infrastructure that can support modal shift [9].

Considering the environmental awakenings at the global level, distribution companies must start to take measures to limit their impacts. In a paper [10], the authors create a multi-criteria decision support system taking into account economic, environmental, and social criteria in an intermodal transport system. Research shows how a judicious choice of path and transport mode in an intermodal transportation system can reduce the emissions of greenhouse gases and energy consumption; in other words, how the route and transport mode selections can help us reduce the environmental impacts.

Road freight transport is already a significant contributor to global warming, and its emissions are predicted to rise dramatically in the coming years. A carbon footprint calculation can be used to estimate CO_2 emissions and understand how an organization's activities affect global sustainability. To this end, the main task of the paper [11] is initially to assess the impact of GHG emissions resulting from road freight transport. After that, the EN 16258 standard is adopted to calculate the carbon footprint of the truck fleet of freight transport operators in Greece. Based on the obtained results, the authors evaluate the performance of the company's fleet by adopting relevant sustainability indicators. They also evaluate the use of compressed natural gas (CNG) as an alternative fuel and its impact on CO_2 emissions and operating costs. The paper ends with a list of additional measures for further reduction and compensation of CO_2 emissions.

3. ROAD FREIGHT TRANSPORT

The comparative advantages of road freight transport in relation to other transport modes have caused its rapid development in all countries, including those where a network of railways, river waterways, and pipelines has been developed. Road freight transport has numerous comparative advantages and specificities in relation to other transport modes, which, with its expansive development, make it the primary traffic factor on the transport market.

Road freight transport is the most massive form of transport for transporting cargo over short and medium distances. The main positive characteristics of road freight transport are:

- Great maneuverability,
- Pronounced mobility,
- Autonomy of transport means,
- Door-to-door delivery with high speed and
- A very wide range of applications.

While the following can be singled out as negative characteristics:

- Large investments,
- Significant energy consumption,
- Low productivity, and
- Environmental pollution.

In addition to the above, the general social justification and justification for using road freight transport are reflected in:

- Transport of goods over short distances (direct transport)
- Combined transport with rail or water transport (from-to port dock)
- Transportation of perishable and expensive goods over long distances
- Carrying out own transportation in order to continue the production process in the industry
- Carrying out transport by road that, according to the transport request, cannot be quickly transported by other means.

4. ECOLOGICAL OPTIMIZATION OF THE EXPLOITATION OF FREIGHT VEHICLES

The standard procedure for the allocation of carbon dioxide in the components of logistics chains can be described in three steps [12].

The first step involves describing the logistics chain, calculating fuel consumption, and determining carbon dioxide emissions. The transport activities of transport services from point A to point B are described here. Energy and fuel consumption are calculated for each transport activity, and carbon dioxide emissions are calculated based on these figures.

A logistics chain consists of one or more separate transport activities. In describing the logistics chain, it is important to collect and/or describe the following data:

- Actual distance traveled in kilometres,
- Mode and type of vehicle,
- Calculation unit (container, pallet),
- Accompanying transport activities, and
- The beginning and end of each transport activity

If we look at the transport activities, it can be said that there are two main forms here, namely the maximum truck load (full truck load) and less than the maximum truck load (less than truck load).

Fuel consumption per transport activity is then converted into CO_2 emissions, and the calculation is as follows: multiply the number of liters of diesel consumed by 3.17 kg [12]. Fuel consumption is determined based on the full trip, and there is a possibility of empty miles (kilometers).

As for the second step, the CO_2 emission per transport activity at shipment level is assigned to a specific unit of account (e.g., container).

The total carbon dioxide emission of the activity performed by the freight transport vehicle is calculated in the first step. Then that total must be allocated to the performance expressed in, for example, the number of goods transported for customer #1.

In the third step, the results for all transport activities are added up, and after that, the results are combined and assigned to clients. During this process, the allocation is always viewed from the perspective of the consignee. Several different freight vehicles participate in the transport of most shipments. These can be vehicles of one company, but parts of the transport can also be external. The CEN-EN 16258 standard requires that emissions caused by external transport activities are also included in the total emissions. To determine the total emission in the last step, it is very important that all allocations are made using the same calculation unit. The base unit can be a cubic meter (m^3), a liter (l), or a similar standard unit of loading. The unit mentioned on the bill of lading is a good starting point. The total carbon dioxide emissions caused by a particular shipment are then the sum of all accompanying transport activities.

The described steps refer to the allocation of carbon dioxide based on the selected calculation unit, however; when different types of cargo are transported in one vehicle, and therefore the calculation units are different, an additional step is required for carbon dioxide allocation that exceeds the CEN-EN standard 16268. It involves the identification and application of a generic unit of account; in most cases, this will be a conversion to a unit based on volume (m^3) or weight (kg).

If an entrepreneur wants to summarize the total carbon dioxide emissions of all trucks in his company for a long period of time, he will be faced with several different calculation units. To facilitate the comparison of carbon dioxide performance, the transport company must use a single unit of account, which will take into account both "heavy" and "light" goods. This comparison and summation of carbon dioxide emissions is made possible NUMERICAL EXAMPLE by the use of "Uniform Transport Performance CO_2", which combines the load factor of the truck in relation to the distance traveled and the corresponding carbon dioxide emission.

5. NUMERICAL EXAMPLE

Task: It is necessary to transport 1200 t of cement from warehouse S to construction site A in one day (Figure 1). The static coefficient of utilization of the vehicle's carrying capacity is 1. Working hours are 12 hours. The load capacity of the vehicle is 12 tons. The distance between warehouse S, construction site A, and garage G are 15 km and 10 km, respectively. The average traffic speed is 20 km/h, and the loading and unloading times are 2 min/t and 15 min/vehicle, respectively. Additional time losses amount to 15 minutes. Average diesel fuel consumption of a truck: 24.4 l/100 km. Amount of CO_2 emissions per liter: 1 liter of diesel = 3.17 kg of CO_2. When determining the amount of CO_2 emitted in kg per vehicle and per pallet, the following data are known:

- Sack packing = 50 kg; number of sacks per pallet = 40 pcs.
- Weight of package/pallet= 50 kg x 40 *pieces* = 2000 kg
- Vehicle load in number of pallets: Np=12 t /2 = 6 pallets
- Total number of pallets: 1200 t / 2 t= 600 pallets
- Consumption of diesel fuel expressed in kilometers per liter:

$$P_{diesel} = \frac{24.4(l)}{100(km)} = 4.1(km/l)$$

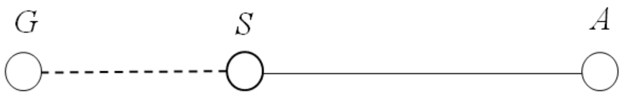

Figure 1: Transport route of vehicle movement during cargo transport

For the radial travel path, it is necessary to calculate:

a) The necessary working vehicle fleet,

b) The amount of CO_2 emitted, according to the CEN-EN 16258 standard, in kg per vehicle and per pallet,

c) The total amount of CO_2 emitted, according to the CEN-EN 16258 standard, in kg for the transport of a given quantity of goods.

Task solution:

a) When determining the working fleet, for the sake of a more transparent calculation, it is necessary to determine the duration of one turnover, the number of turnovers during the day, and the number of vehicles at work on the transport road S-A.

The duration of one turnover on the transport road S-A is

$$\begin{aligned} T_{oSA} &= t_{uS} + \frac{L_{SA}}{V_{s_{SA}}} \cdot 60 + t_{iA} + \frac{L_{SA}}{V_{s_{SA}}} \cdot 60 + t_{d_{SA}} \\ &= \tau_{uS} \cdot \gamma_{SA} \cdot q + \frac{L_{SA}}{V_{s_{SA}}} \cdot 60 + t_{iA} + \frac{L_{SA}}{V_{s_{SA}}} \cdot 60 + t_{d_{SA}} \end{aligned} \quad (1)$$

or after inserting numeric values

$$T_{oSA} = 2 \cdot 1 \cdot 12 + \frac{15}{20} \cdot 60 + 15 + \frac{15}{20} \cdot 60 + 15$$

$$T_{oSA} = 114\,(min) = 1.90\,(h)$$

The number of turnovers during the day on the transport road S-A is

$$z_{o1dSA} = \frac{H_r \cdot 60 - 2 \cdot \dfrac{L_{GS} \cdot 60}{V_{s_{GS}}}}{T_{oSA}} \qquad (2)$$

or after inserting numeric values

$$z_{o1dSA} = \frac{12 \cdot 60 - 2 \cdot \dfrac{10 \cdot 60}{40}}{114} = \frac{690}{114} = 6.05$$

is adopted $z_{01dSA} = 6$

The required number of vehicles at work on the transport road S-A is

$$A_{rSA} = \frac{z_{\lambda_{SA}}}{z_{o1dSA}} \qquad (3)$$

or

$$A_{rSA} = \frac{100}{6} = 16.67, \text{is adopted } A_{rSA} = 17 \text{ vehicles}$$

b) Emissions of CO_2 in kg per vehicle and per pallet for the transport route S-A

Since the number of turnovers during the day is $z_{oldSA}=6$ turnovers, the vehicle's distance traveled during the day is

$$K_{m1} = z_{o1dSA} \cdot L_{SA} + 2 \cdot L_{SG} \qquad (4)$$

$$K_{m1} = 6 \cdot 15 + 2 \cdot 10 = 110\,(km)$$

Diesel fuel consumption per vehicle

$$P_{SA}^{diesel} = \frac{K_{m1}}{P_{diesel}} \qquad (5)$$

$$P_{SA}^{diesel} = \frac{110\,(km)}{4.1\,(km/l)} = 26.83\,(liter)$$

Amount of CO_2 emissions per vehicle

$$E_{SA}^{CO_2} = P_{SA}^{diesel} \cdot P_{CO_2}^{1l_{diesel}} \qquad (6)$$

$$E_{SA}^{CO_2} = 26.83 \cdot 3.17 = 85.0511\,kg\,CO_2$$

Amount of CO_2 emissions per pallet

$$E_{p}^{CO_2} = \frac{E_{SA}^{CO_2}}{N_p} \qquad (7)$$

$$E_{p}^{CO_2} = \frac{85.0511}{6} = 14.175\,kg\,CO_2$$

c) The total amount of CO_2 emitted in kg for the transport of a given amount of goods

$$\sum E_{SA}^{CO_2} = A_{rSA} \cdot E_{SA}^{CO_2} \qquad (8)$$

$$\sum E_{SA}^{CO_2} = 17 \cdot 85.0511 = 1455.8687\,kg\,CO_2$$

6. CONCLUSION

Due to the negative impact on the environment and human health, on the one hand, and the necessity of sustainable development, on the other hand, the transport sector is currently facing a major test. Therefore, in many countries, great efforts are being made in the creation and implementation of traffic development strategies that will simultaneously enable greater mobility of goods and ensure the improvement of environmental conditions. Therefore, there is a growing interest in finding and applying different planning, regulatory, technological, and economic instruments that can contribute to the realization of these strategies. To improve quality, the EU's obligations are at a high level, translated into concrete targets for reducing GHG emissions for member countries, public health issues and their connection with air quality, targets for air quality in the EU, fuel security, and the necessity of switching to alternative energy sources.

The very organization of goods transportation is an important element of economic development because it enables the development of production, encourages the opening of various companies that generate cash flow, and ultimately enables consumption. The increase in traffic in the world economy has a number of disadvantages, such as congestion, increased noise and stress for road users, pollution of the environment by the release of harmful gases, etc., so there is a need for new technologies that will minimize the negative consequences of conventional freight transport.

To fight the climate crisis, we need to bring down CO_2 emissions in this field. To do so, the European Commission is proposing new targets that will raise our ambition and meet the EU's climate and zero pollution objectives while lowering demand for fossil fuels.

There is currently no globally accepted standard for the allocation of greenhouse gas (GHG) emissions to shipments in road freight transport. The only official international standard for the calculation of emissions in transport operations is the European norm EN-16258. However, even this norm still allows a choice between several alternative emission allocation schemes. A true global standard for CO_2 emissions is not yet available. Furthermore, most emission standards are developed by associations for a single transport mode or for specific regions (e.g., North America).

Transport modeling provides a useful tool for investigating the dynamics, scope, and magnitude of emissions. The paper presents a numerical example of the procedure for calculating the emitted amount of CO_2 for the transport of a certain amount of goods by freight vehicles. For the radial driving route, the required inventory and working vehicle fleet were calculated, according to the CEN-EN 16258 standard, as well as the amount of CO_2 emitted per vehicle and per pallet, as well as the total amount of CO_2 emitted in kg for the transport of a given amount of goods. The required number of vehicles at work on the transport road S-A is 17, the amount of CO_2 emission per vehicle is 85.0511 kg CO_2 and per pallet is 14.175 kg CO_2, and the total emitted amount of CO_2 in kg for the transport of 1200 t of cement from warehouse S to construction site A is about 1455 kg CO_2. In future research, hybrid-powered vehicles as well as alternative fuel vehicles can be included in order to calculate the amount of CO_2 emissions and compare the obtained results.

ACKNOWLEDGEMENTS

This research was financially supported by the Ministry of Science, Technological Development and Innovation of the Republic of Serbia (Contract No. 451-03-47/2023-01/ 200109)

REFERENCES

[1] P. Wild, “Recommendations for a future global CO2-calculation standard for transport and logistics,” Transportation Research Part D, Vol. 100, (2021)

[2] https://www.itf-oecd.org/low-carbon-road-freight

[3] N. Petrović, V. Jovanović, B. Nikolić, J. Pavlović and J. Mihajlović, “A comparative analysis of road and rail freight transport through the Republic of Serbia from the aspect of external costs,” Acta Technica Jaurinensis, Vol. 15(3), pp. 130 – 137, (2022)

[4] N. Petrović, N. Bojović, M. Petrović and V. Jovanović, “A study of the environmental Kuznets curve for transport Greenhouse gas emissions in the European Union,” Facta Universitatis Series: Mechanical Engineering, Vol. 18(3), pp. 513 – 524, (2020)

[5] Republic Bureau of Statistics, Statistical Calendar ofthe Republic of Serbia-2021, online edition, Belgrade, (2021)

[6] EU Commission, WHITE PAPER “Roadmap to a Single European Transport Area – Towards a competitive and resource efficient transport system,” COM (2011) 144 final, (2011)

[7] F. Kellner, M. Schneiderbauer, “Further insights into the allocation of greenhouse gas emissions to shipments in road freight transportation: The pollution routing game,” European Journal of Operational Research, Vol. 278, pp. 296 – 313, (2019)

[8] C. Linton, S. Grant-Muller and W. F. Gale, “Approaches and Techniques for Modelling CO_2 Emissions from Road Transport,” Transport Reviews, Vol. 35(4), pp. 533 – 553, (2015)

[9] L. H Kaack, P. Vaishnav, M. G. Morgan, I. L. Azevedo and S. Rai, “Decarbonizing intraregional freight systems with a focus on modal shift,” Environ. Res. Lett., Vol. 13(8), (2018)

[10] M. Sawadogo, D. Anciaux, “Reducing the environmental impacts of intermodal transportation: a multi-criteria analysis based on ELECTRE and AHP methods,” 3rd International Conference on Information Systems, Logistics and Supply Chain Creating value through green supply chains, Casablanca, Morocco, pp. 224, (2010)

[11] A. Gialos, V. Zeimpekis, M. Madas, K. Papageorgiou, “Calculation and Assessment of CO_{2e} Emissions in Road Freight Transportation: A Greek Case Study,” Sustainability, Vol. 14, (2022)

[12] F. Broek, A. Engel and H. Maurer, “Allocation methodology CO_2: Road Freight Transport,” Project Identification Code: 2014/0142, (2014)

Pollutants in the air

Svetlana K. Belošević[1*], Maja B. Djukić[2]
[1]Faculty of Technical Sciences, University of Priština in Kosovska Mitrovica, Kosovska Mitrovica (Serbia)
[2]University of Kragujevac, Faculty of Science, Kragujevac (Serbia)

Air pollution is a major problem all over the world in both developed and developing countries. Environmental protection has been the main topic of politicians, economists, ecologists, and the broader scientific community for more than a decade. Accelerated industrialization and the development of technology have led to great changes that man has willingly accepted without thinking about how all this affects nature and the environment. The modern and very fast way of life of recent years has left a great negative impact on the natural environment. Without caring about the consequences of achieving a simpler and seemingly more beautiful way of life, man has endangered his environment. The result of this kind of human behavior is a polluted environment that has been talked about for ten years and must be talked about to preserve it. Environmental protection covers a wide range of activities, from the protection of soil, water, natural resources, and beyond, to the protection of air, without which not a single person on our planet could breathe. The composition of air is known to everyone, but what is in the air that affects its pollution? In this paper, we will show what pollutants are in the air, focusing on the region of Raška, the city of Kraljevo, how they affect, and how to reduce them with the goal of a healthier environment.

Keywords: air, pollutants, environmental protect

1. INTRODUCTION

Today's modern lifestyle has greatly affected all aspects of life, including the environment. Environmental protection has been the main topic of politicians, economists, ecologists, and the broader scientific community for more than a decade. Accelerated industrialization and the development of technology have led to great changes that man has willingly accepted without thinking about how all this affects nature and the environment. The modern and very fast way of life of recent years has left a great negative impact on the natural environment. Without caring about the consequences of achieving a simpler and seemingly more beautiful way of life, man has endangered his environment. The result of this kind of human behavior is a polluted environment that has been talked about for ten years and must be talked about to preserve it. Environmental protection covers a wide range of activities, from the protection of soil, water, natural resources, and beyond, to the protection of air, without which not a single person on our planet could breathe.

The composition of air is known to everyone, but what is in the air that affects its pollution? In this paper, we will show what pollutants are in the air, focusing on the region of Raška, the city of Kraljevo, how they affect, and how to reduce them with the goal of a healthier environment.

2. MAJOR AIR POLLUTANTS

The U.S. Environmental Protection Agency (EPA) [1] defines air pollution as the presence of contaminants or pollutant substances in the air that interfere with human health or welfare or produce other harmful environmental effects. [2]

The definition of an air pollutant or air pollution depends on the context of time, space, and impact for a particular set of circumstances. [3]

Many discussions have been held to differentiate between unpolluted and polluted air. However, chemistry blurs all distinctions because the same chemical compounds or particles from a natural source (e.g., volcanoes) have the same harmful effects as when they come from anthropogenic sources. Unpolluted air is therefore only a guide to show the extent of air pollution. In recent decades, air pollution has been associated primarily with the harm caused by pollution, particularly harm to human health in the form of respiratory disease [4]. Air pollutants affect both human health and ecosystems.

It has been reported that in developing countries most of the air pollution (approx. 70–80%) is caused by vehicular emissions particularly from larger number of older vehicles with low vehicle maintenance, low fuel quality and improper road infrastructure [5,6].

The United Nations Environmental Programme estimates that indoor and outdoor air pollution are responsible for nearly 5% of the global disease burden, including excess cases of asthma and other allergic respiratory diseases, adverse pregnancy outcomes (e.g., stillbirth and low birth weight) [7]. People in developing countries are particularly vulnerable to air pollution. Approximately two million people in rural areas die each year from exposure to high concentrations of particulate matter (PM) suspended in the indoor air. Excess mortality due to outdoor PM and sulfur dioxide contribute to mortality of about 500,000 people annually. [8]

The effects of air pollution on living systems like plants, animals and human beings and other materials is worse. It may affect the biochemical and physiological processes of plants and ultim ately lead to yield loss.

Pollutants present in the air cause three specific types of damage: they harm human health; they destroy and degrade the environment and ecosystems; they damage property and cultural monuments. The main air pollutants are PM particles, ozone (O_3), carbon monoxide

*Corresponding author: Svetlana Belošević, Kneza Miloša 7, 38220 Kosovska Mitrovica, Serbia, svetlana.belosevic@pr.ac.rs

(CO), sulfur dioxide (SO_2), nitrogen dioxide (NO_2), and lead (Pb).

2.1. Particulate matter

PM stands for particulate matter, also called particle pollution: the term for a mixture of solid particles and liquid droplets found in the air. They are so small that they can only be detected with the aid of an electron microscope (Figure 1.).

Particle pollution includes:

- PM10: inhalable particles generally 10 micrometers or less in diameter; and
- PM2.5: fine, inhalable particles generally 2.5 micrometers in diameter and less.

Some of these particles are emitted directly from a source, such as construction sites, dirt roads, fields, smokestacks, or fires. Most particles are formed in the atmosphere by complex reactions of chemical substances such as sulfur dioxide and nitrogen oxides emitted by power plants, industry, and motor vehicles.

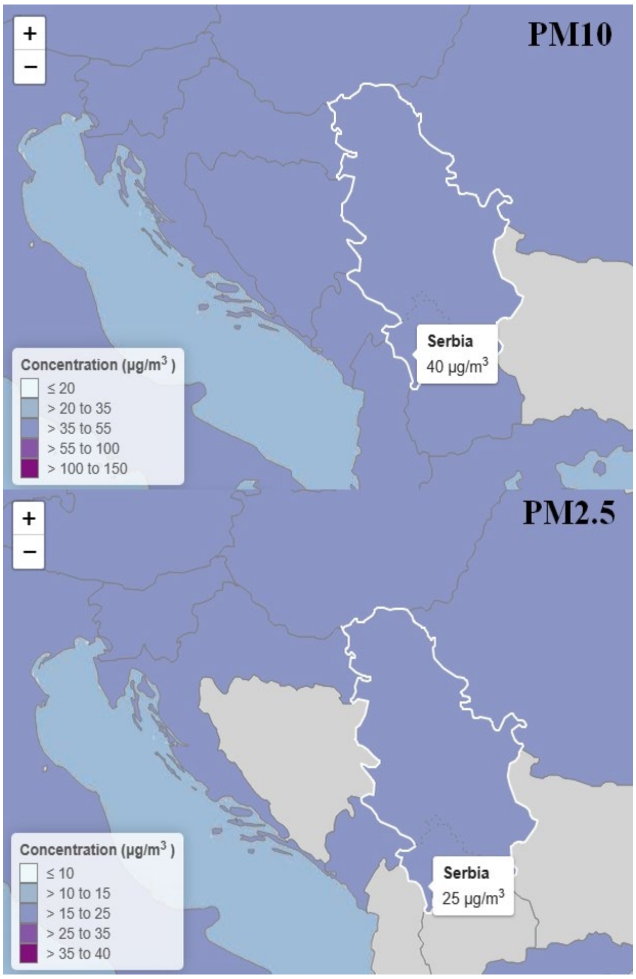

Figure 1: The concentration of pollutant particles PM10 and PM 2.5 in the air on the territory of the Republic of Serbia for a period of one year. Source: whoairquality [9]

2.2. Ozone

Ozone (O_3) is a highly reactive gas consisting of three oxygen atoms. It is both a natural and man-made product that occurs in the Earth's upper atmosphere (stratosphere) and lower atmosphere (troposphere). Depending on where it is in the atmosphere, ozone affects life on Earth in positive or negative ways.

Tropospheric or ground-level ozone - what we breathe in - is formed primarily by photochemical reactions between two major classes of air pollutants, volatile organic compounds (VOC) and nitrogen oxides (NO_x). These reactions are traditionally thought to be dependent on the presence of heat and sunlight, which leads to higher concentrations of ozone in the air during the summer months. Ozone contributes to what we typically perceive as "smog" or haze, which remains most common in the summer, but can occur year-round in some southern and mountainous regions.

Although some stratospheric ozone is transported to the troposphere and some VOC and NO_x is naturally occurring, most ground-level ozone is the result of reactions with human-generated VOC and NO_x (Figure 2.). Significant sources of VOC include chemical plants, gasoline pumps, oil-based paints, automotive paint shops, and printing plants. Nitrogen oxides are mainly produced during combustion at high temperatures. Significant sources are power plants, industrial furnaces and boilers, and motor vehicles.

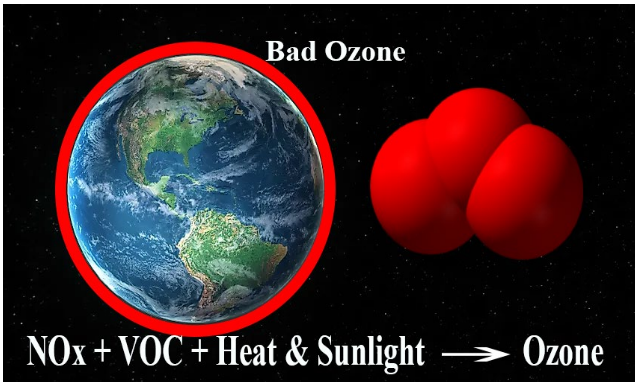

Figure 2. "Bad" Ozone is created by chemical reactions between NO_x and VOC in the presence of heat and sunlight.

Where ozone is formed, the highest concentrations usually occur in the afternoon hours when solar radiation is most intense. However, in areas located in the lee of major sources of VOC and NO_x, ozone peaks may occur in the afternoon and evening after the wind has carried ozone and its VOC and NO_x precursors many kilometres away from their sources. Therefore, high ozone concentrations can occur in remote areas and at different times of day, including early evening or nighttime. Ozone has two properties that are important for human health. First, it absorbs UV light, reducing human exposure to harmful UV radiation that causes skin cancer and cataracts. Second, when inhaled, it reacts chemically with many biological molecules in the respiratory tract, leading to several adverse health effects.

2.3. Carbon monoxide

CO is a colorless, odorless gas produced by the incomplete reaction of air with fuel. CO Pollution occurs primarily from emissions from fossil fuel-fired engines, including motor vehicles (Figure 3.). Higher levels of CO generally occur in areas with high traffic volumes. Other sources of emissions from CO include industrial processes (e.g., metal processing and chemical manufacturing), residential wood burning, and natural sources such as forest fires. Wood stoves, gas furnaces, cigarette smoke, and unvented gas and kerosene heaters are indoor sources of CO.

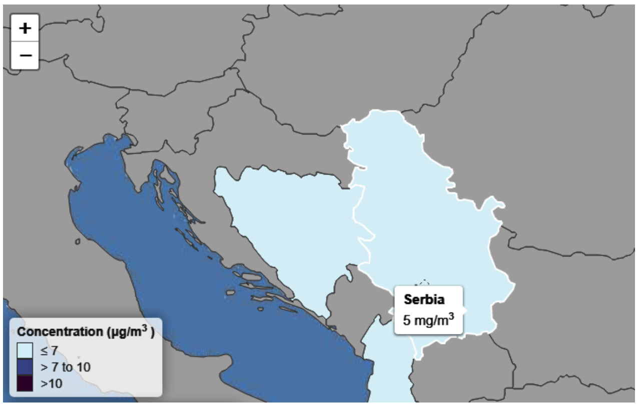

Figure 3. The concentration of CO in the air on the territory of the Republic of Serbia, averaging period 24h. Source: whoairquality [9]

CO can cause adverse health effects by reducing oxygen delivery to the body's organs and tissues. Exposure to lower concentrations of CO is particularly serious for heart patients and can cause chest pain, limit the ability to exercise, or, with repeated exposure, contribute to other cardiovascular effects. At very high concentrations, CO is toxic and can cause death.

2.4. Sulfur dioxide

Sulfur dioxide is a gas consisting of one sulfur atom and two oxygen atoms (SO_2) in each molecule. The largest source of SO_2 in the atmosphere is the combustion of sulfur-containing fossil fuels such as coal or oil in power plants and other industrial facilities. Other sources of SO_2 emissions include industrial processes such as the extraction of metals from ores, and natural sources such as volcanoes, locomotives, ships, and other vehicles and equipment that burn sulfur-containing fuels (Figure 4.).

Like nitrogen dioxide, sulfur dioxide can form secondary pollutants after it is released into the air. Secondary pollutants formed with sulfur dioxide include sulfate aerosols, particulate matter, and acid rain.

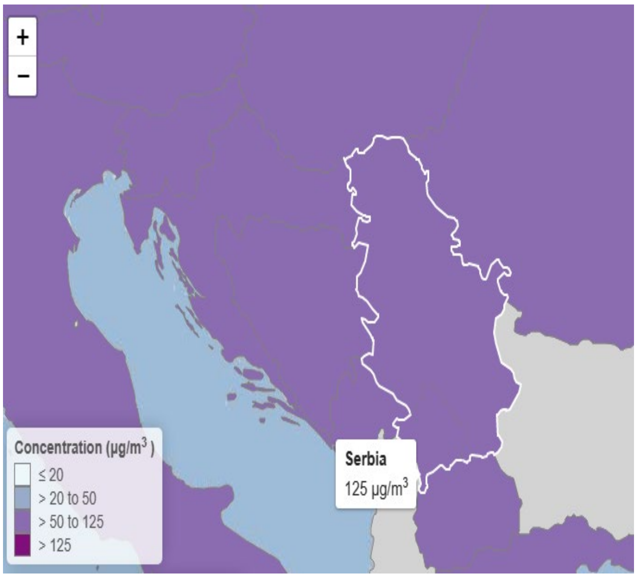

Figure 4. The concentration of SO_2 in the air on the territory of the Republic of Serbia, averaging period 24h. Source: whoairquality [9]

Short-term SO_2 exposures can damage the human respiratory system and make breathing difficult. People with asthma, especially children, are particularly sensitive to the effects of SO_2. In addition, SO_2 reacts in the atmosphere to form other sulfur oxides and then forms particulate matter, which is also harmful when inhaled.

2.5. Nitrogen dioxide

Nitrogen dioxide (NO_2) is a chemical compound that belongs to a group of highly reactive gasses called nitrogen oxides (NO_x), which are the main polluters of the Earth's atmosphere (Figure 5.). Nitrogen dioxide is easy to recognize. It can be recognized by its reddish-brown color and characteristic pungent odor. This odor is found in traffic-polluted streets. Nitrogen dioxide is a widespread pollutant released into the atmosphere from many different sources, including internal combustion engines. According to the World Health Organization (WHO) [10], NO_2 has adverse health effects: long-term exposure can impair lung function and increase the risk of respiratory disease. Outdoor anthropogenic NO_2 emissions are mainly from combustion engines (mainly diesel engines) and power plants, but also from heating or electricity generation.

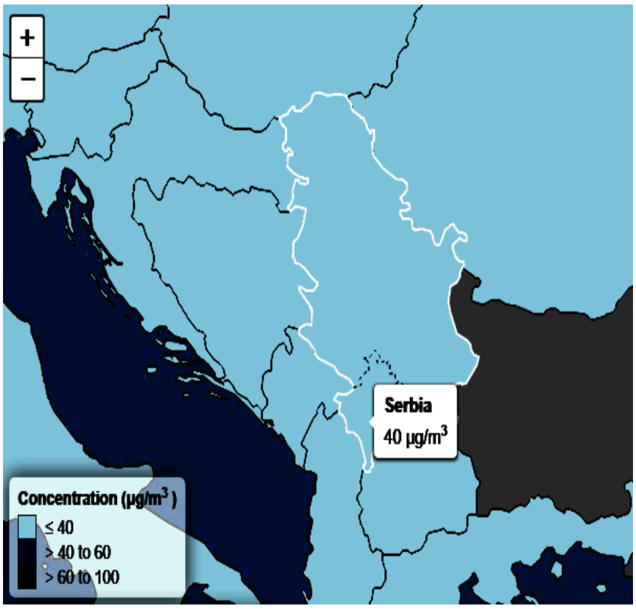

Figure 5. The concentration of NO_2 in the air on the territory of the Republic of Serbia for a period of one year. Source: whoairquality [9]

2.6. Acid rain

It can be said that pollution is like a boomerang for mankind. People try to fight off their pollutants with all the means at their disposal... only for them to come back and hit them in unexpected places and unpredictable ways. Like Nemesis. Acid rain is an example of pollution that people are trying to drive out by building more and more smokestacks that release acid gases. And it's coming back to haunt them!

Acid rain is normal rain made acidic by certain air pollutants. While normal rain cleans, rejuvenates, and enriches the environment, acid rain pollutes and damages it. The measure of the acidity of a medium is its pH. Rain is formed when water vapour condenses into clouds and falls to the ground. At the onset of precipitation, rain is neutral - neither acidic nor alkaline [11]. As it travels through the air, it dissolves suspended chemicals and expels particles that are suspended in the air. In clear air, rain picks up only naturally occurring substances such as dust, pollen, some carbon dioxide (which forms light carbonic acid), and chemicals produced by light and volcanic activity. These substances make rain slightly acidic, with a pH of about 5.7. Natural rainwater reacts with carbon dioxide (CO_2) in the atmosphere to form carbonic acid (H_2CO_3). Some of the carbonic acid in rainwater then breaks down (dissociates), producing more hydrogen and bicarbonate ions, both of which are dissolved in the rainwater.

"Acid rain" is the term for rain when the pH is below 5.6.

How is acid rain formed? When rain falls through polluted air, more acid-forming substances occur, and in higher concentrations than usual [12]. Chemicals that often occur in polluted air at higher concentrations than normal include sulfur oxides (SO_2 and SO_3, commonly referred to as SOx) and nitrogen oxides (NO_2, N_2O, and NO, commonly referred to as NOx) (Figure 6.).

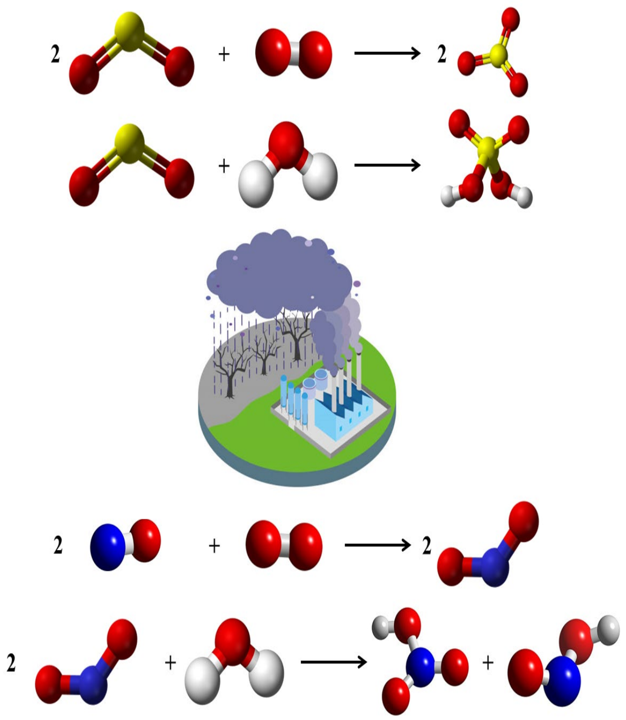

Figure 6. Acid rain reaction

In some situations, hydrochloric acid vapours and mists of other acids such as phosphoric acid may also be present. These gases dissolve in the precipitation and make it more acidic than natural rain. This results in acid rain. Acid fog occurs when chemical pollutants dissolve in very humid air.

How is acid rain formed?

Precipitation removes gases and particles from the atmosphere through two processes:

1. Rain, which is the incorporation of particles into cloud droplets that fall to the ground.

2. Washout, which is the material under a cloud being washed away by rain or snow as it falls.

Contaminants can also be deposited by direct contact or by gravity, which is called dry settling [13, 14]. Once deposited, acidic products can be neutralised by alkaline soils or transported from lakes by seepage and runoff, contributing to water acidification and affecting the aquatic ecosystem. One of the major sources of carboxylic acids is biomass burning [15]. Carboxylic acids contribute to 16% to 36% of the acidity of rain [16].

Acid-neutralising substances such as ammonia, calcium carbonate, and magnesium carbonate are also present in the atmosphere, and the "net" acidity of rain depends on the mixture of chemicals in the air through which the rain falls.

3. MEASUREMENT RESULTS

In the territory of the city of Kraljevo, the level of air pollution is monitored by measuring the above-mentioned pollutants at several measuring points in the city and its surroundings. In accordance with the specific configuration and population of the terrain, distribution of pollutants, and meteorological conditions (wind rose), monitoring was carried out at 9 measuring points places and the samples at the measuring places were taken throughout the year [17].

For the sampling of sulfur dioxide and black smoke-soot index, devices were used air sampling PROEKOS AT-801X and ASV 4G 8R with digital time reading start, elapsed time, current and total air flow during the day. For sampling sediments, sedimentators with F 20 cm probes were used. placed on pedestals in accordance with the provisions. A reflectometer was used to determine the concentration of the black smoke-soot index ASV RF1 with four monochromatic light sources λ=830 nm and a photocell in the center. For sampling suspended particles smaller than 10 microns RM10, suspended particles RM2.5 and heavy metals from the fraction of suspended particles RM10 was used sequential ambient air sampler Model SEQ 47/50 Sven Leckel (Germany). [17]

The figure 7. shows the values of the pollutants on an annual basis. Higher concentrations of pollutants, especially PM2.5 and PM10 particles, were observed in winter months during the heating season, which is due to the influence of the type and quality of fuel used for heating systems. High concentrations of pollutants are also caused by intensive traffic and unfavorable meteorological conditions.

To reduce the concentration of pollutants in the air, various measures must be taken:

- Renewal of heating systems and use of natural gas as a source of thermal energy;
- Introduction of traffic-calmed zones in the narrower urban area and expansion of pedestrian zones and bicycle paths;
- Increase in the number of filters in industrial chimneys;
- Increase in green areas and plantings;
- Education of the population to raise awareness of the reduction of air pollution.

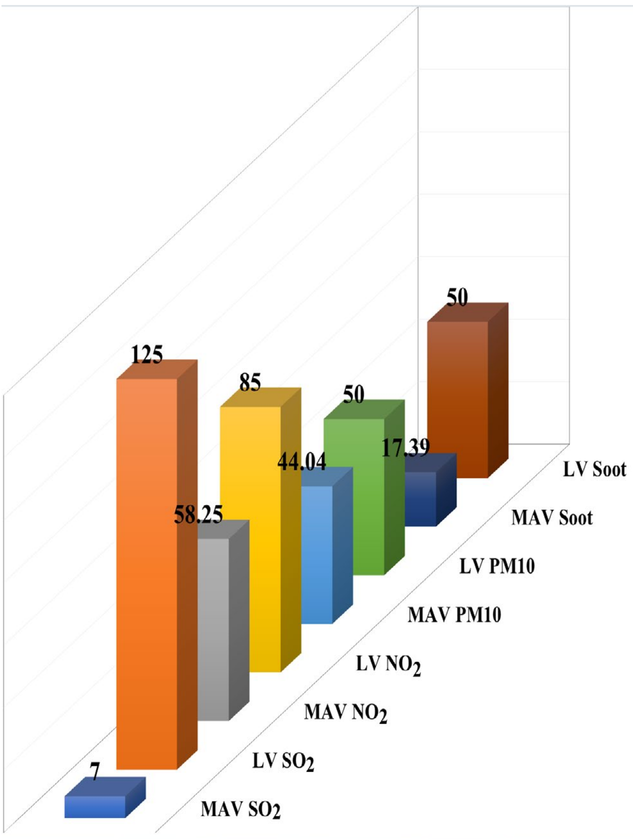

Figure 7. Graphic representation of concentrations of pollutants for a period of one year in µg/m^3 (MAV – Mean annual value, LV – Limit value). Source: Report of the Institute for Public Health Kraljevo [17]

4. CONCLUSION

In addition to many advantages, the fast life of man brought with it many disadvantages. The daily needs of a person to get to work on time, but also to return home to his family faster, have conditioned the daily use of cars, which are one of the main air pollutants. In the narrowest city circle, traffic is allowed in almost all cities of Serbia and Europe. Modern construction tends towards tall and beautiful buildings with little greenery and lots of parking spaces due to the excessive number of cars. The result of all this is an excessive concentration of exhaust gases that pollute the air in populated areas. When the red light comes on, warning of excessive concentrations of pollutants in the air, one thinks a little, but is it already too late?

One of the principles of environmental protection is the polluter pays. Air is available to man completely free of charge, so the question arises: Is it necessary for man to pay for the air, and would he then pollute the air less and care more about preserving the environment? It is our duty to preserve our environment, our surroundings, and the air we breathe, because we did not inherit this planet from our ancestors but borrowed it from our descendants.

ACKNOWLEDGEMENTS

This work was supported by the Serbian Ministry of Education, Science and Technological Development (Agreements No. 451-03-47/2023-01/200122).

REFERENCES

[1] U.S. Environmental Protection Agency | US EPA

[2] Environmental Acronyms, Abbreviations and Glossary of Terms, National Service Center for Environmental Publications, 1991, https://nepis.epa.gov/Exe/ZyPURL.cgi?Dockey=9100VQRW.txt

[3] P. Saxena, V. Naik, Air pollution: sources, impacts and controls. doi: 10.1079/9781786393890.0000

[4] Y. Sadanaga, J. Matsumoto, Y. Kajii, “Photochemical reactions in the urban air: Recent understandings of radical chemistry”, Journal of Photochemistry and Photobiology C: Photochemistry Reviews 4 p. 85–104, (2003)

[5] J. Wanga, C. Lia, E. Wanga, “Potential and flux landscapes quantify the stabilityand robustness of budding yeast cell cycle network”, PNAS, vol. 107, n. 18, p. 8195–8200, (2010)

[6] A. Bigazzi, M. A. Figliozzi, “Review of Urban Bicyclists' Intake and Uptake of Traffic-Related Air Pollution”, Transport Reviews, v. 34, p. 221-245, (2014)

[7] J. P. Holdren, K. R. Smith, “Energy, the environment, and health. In: Goldemberg J, editor. The world energy assessment: energy and the challenge of sustainability”, New York: UN Development Programme; pp. 61-110, (2000)

[8] United Nations Environmental Programme. Chapter 2. Air pollution and air quality. Global environmental outlook 3. London (UK): UNEP; (2012)

[9] https://whoairquality.shinyapps.io/AirQualityStandards

[10] World Health Organization (WHO)

[11] R. Charlson, H. Rodhe, “Factors controlling the acidity of natural rainwater”, Nature 295, 683–685 (1982).

[12] S. G. Fowler, D. Cook, M. F. Thomashow, “Low Temperature Induction of Arabidopsis CBF1, 2, and 3 Is Gated by the Circadian Clock”, Plant Physiology, vol. 137, pp. 961–968, (2005)

[13] T. I. Moiseenko, “Acidification and critical loads in surface waters: Kola, northern Russia”, AMBIO 23 p. 418–24 (1994).

[14] S. A. Abbasi, P. Krishnakumari, F. I. Khan, “Hot Topics: Everyday Environmental Concerns”, Published by Oxford University Press OUP, (2000)

[15] T. Abbasi, S.A. Abbasi, "Biomass energy and the environmental impacts associated with its production and utilization", Renewable and Sustainable Energy Reviews, Elsevier, vol. 14 (3), p. 919-937, (2010). ISBN 10: 0195645340ISBN 13: 9780195645347

[16] D. M. Bastidas, V. M. La Iglesia, “Organic acid vapours and their effect on corrosion of copper: a review”, Corrosion Engineering, Science and Technology, The International Journal of Corrosion Processes and Corrosion Control, volume 42 (3), (2007)

[17] Annual report on air quality 2022 of the city of Kraljevo https://www.kraljevo.rs/wp-

content/uploads/2023/02/2022-Godisnji-izvestaj-za-aerozagadjenje-.docx.pdf

Determinations of equation in 1D conduction: Experimental investigation for wall heating

Aleksandar Vičovac[1*]
[1]Thermal Earth Ltd, Ammanford, Carmarthenshire, Wales, United Kingdom

The paper presents the results of research to determine the optimal feed water inlet temperature. In the standard calculations of the designers, the value of the feed water is determined according to the external design temperature. In this case, the new design water temperature value that supplies the wall panels will depend on the outside temperature and the return temperature from the system.

Keywords: wall heating panels, boundary conditions, Transient and One Dimensional.

1. INTRODUCTION

Lately, wall heating occupies an increasing part in buildings as a heating body. The time that the wall panel transmits energy in the space depends on the inlet temperature Theoretical and experimental work was done in this study to optimise the feed water temperature for the wall and floor panels. The working condition of the panel system at a specific temperature delivers the maximum comfort conditions with a continual flow of fluid (softened water).

The research's primary objective is to optimise supply water temperature in panel low-temperature heating systems, such as wall and floor heating.

The idea is to control the temperature at the panel's entrance so that it is as low as it can be while still being high enough to create the proper ambient temperatures across all the rooms. As a result, it is best to reduce the feed water's temperature as much as feasible.

2. RESEARCH QUESTIONS

In a published paper [1] Faxen–Rydberg–Huber Heat conduction in the panel, in which the uniformly heated pipes are evenly spaced, can be described by Fourier's partial differential equation for steady two-dimensional heat conduction through an infinite plane wall, with the heat line sources. In the literature, Faxen–Rydberg–Huber expression is indicated as the least complicated solution to this problem. In the paper [2] Wall heating pipes attached to a thermally insulating core had the highest thermal output, were easy to control, suitable for building retrofit, and most affordable while providing limited thermal storage. The performance of the wall system was retained when locating the pipes in plasterboard separated from the core bay an air gap. The aim of this paper is to show 1-D thermal conductivity, which does not depend on the type of building material. This work eliminates the interruption of heating of the building and the complexity of automation. The final equation can be used by designers with the appropriate choice of coefficients of the polynomial equation according to the type of object.

Panel heating systems are quite common in new and contemporary buildings because of their excellent energy efficiency and minimal energy loss. Panel heating systems are different from traditional air conditioning, heating, and cooling systems since they heat surfaces rather than the air, resulting in significant energy savings while also significantly increasing comfort and pleasantness in the room. Coefficients of heat propagation, including those for heat transfer, heat conduction, and radiation, are the fundamental characteristics of panel systems. The findings of experiments conducted in an air-conditioned test room were used to compute the values of the radiation coefficients, heat transfer coefficients, and heat conduction coefficients in the study [3].

Thermostat-set air temperatures and room air temperatures are compared [2], and the results demonstrate that all panel heating systems provide good results with no appreciable variations. The inter-floor floor-ceiling and ceiling panel heating systems showed the greatest variations and the lowest values of the temperatures of the inner surfaces of the outer walls. [4]

In addition to its potential for energy savings and capacity to maintain a comfortable temperature, radiant, panel heating and cooling systems also make use of low intensity energy sources such heat pumps and solar panels. A thorough and straightforward model is required to forecast and adopt these aspects of panel systems such that the designers find it useful. Heat exchange in the panel is a component of this model. A cooling and heating-related analytical heat exchange model has been created. The examples demonstrate that this model's correctness is consistent with that of its constituent parts, allowing engineers to readily apply it to real-world situations. [5]

Panel heating systems, the most energy-efficient subsystems for supplying heating space with heat, are increasingly used because of increased demand for more energy-efficient systems for heating buildings. When compared to alternative heat supply subsystems, these 'heat exchangers' broad surfaces and coverage of the heating space enable the heating panels to reach the same comfort levels at much lower surface temperatures.

Furthermore, because of the low temperature regime, these subsystems are frequently employed in conjunction with extremely effective heat pump subsystems. As a result of the high energy efficiency of both subsystems and the use of renewable energy sources, these heating and cooling systems are 30% to 50% more desirable for new residential buildings in Europe, particularly in Germany, Austria, and Denmark.

*Corresponding author: Aleksandar Vičovac, aleksandar.vicovac@gmail.com

This study used both theoretical and experimental methods to optimise the temperature of the feed water for wall and floor panels. The functioning condition of the panel system at a specific temperature reaches the highest levels of comfort when a steady flow of fluid (softened water) is present.

The primary objective of the study is to maximise the supply water temperature in panel low-temperature heating systems, such as wall and floor heating.

To obtain the correct ambient temperatures in all the rooms, it is important to control the temperature at the panel's entrance as low as possible while yet being adequate. As a result, the feed water's temperature should be as low as feasible.

According to the 'temperature curve,' it is usual practise to regulate the supply water's temperature at the facility level based on the ambient temperature. The temperature curve is typically a straightforward broken line that traverses several empirically modified places on the diagram.

This form of regulation is essentially arbitrary, and it does not take into consideration the present status of the building, such as whether it is heated or merely being heated, if it is currently sunny or windy, what the relative humidity is, whether certain windows are open, and so on.

It would be excellent with panel heating systems if the interior air temperature in the room ($t_{in.}$) could be controlled by altering the temperature of the supply water in the panels while the flow remained constant. The wall and floor panels would always be gently heated in this manner. The advantages of this method of regulation are twofold: optimal comfort and building thermal stability.

The ability to change the ambient temperature in the space by altering the flow through the panels is an appropriate and nearly exclusively utilised solution. The flow rate is controlled via "on-off" drives on each panel's circulation circuits. As a result of this regulating approach, there is a period when the heating panel is warm and a period when it is cooled. Because heating panels have their own thermal inertia, the temperature of the panel does not change instantly when it is turned on or off. In addition to the thermal inertia of the panel, the speed of opening and closing the control valves of the "on-off" drive on the circulation circuits also has an influence.

The length of the intervals between which the circuit's valves are closed is determined by the temperature of the supply water in the panels. The greater the temperature of the supply water, the faster the necessary temperature in the room will be attained, and the thermomotor drive will close the valve at the panel's entry. If the supply water temperature is lower, the delay between opening the valve, achieving circulation in the panel, and heating the wall or floor will be longer.

As a result, the objective is to optimise the heating curve as much as possible and to continually change it based on the facility's thermal response of building.

3. WALL HEATING SYSTEMS INVESTIGATED

The building in which the experiment was performed was designed completely with wall panels that cover the thermal losses of the building. The axial distance of the pipe in the wall panels is 10 cm, the diameter of the pipe is Ø = 16x2mm. The building belongs to energy class "B". To determine the relationship of the desired water temperature for the stated conditions, it is necessary to decompose the system into two basic models. We see the model of the heat accumulator in the vertical section as a model of a rod. We can do the same analogy if we cut the wall panel in the vertical section. The longitudinal section of the wall panel contains a circular section of the pipe, thermal mortar between the pipes, lime-cement mortar, and the wall construction. The heat accumulator and the wall panel in cross section can be shown as a system for conducting heat through the rod. The main goal is to observe the physical model through a mathematical model of the rod temperature theory at the return temperature, which represents the object's response to changes. Every change on comparable rods is interconnected, respectively. The two-stick model is shown in figure 1.

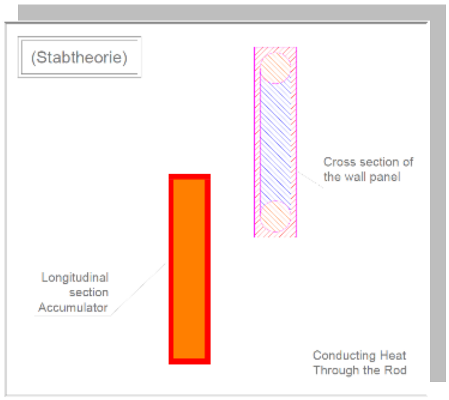

Figure 1: Two-stick model

4. EXPERIMENTAL VALUE OF POLYNOMIAL

4.1. To accomplish the outcomes indicated in the introduction, it is required to monitor and observe the process that occurs during the operation of the wall and floor heating system. The experiment measured the following quantities:

- Air temperature in the premises.
- External air temperature.
- Water temperature at the entrance to the panels (flow temperature).
- Water temperature on the return from the panel (return temperature).
- "On-off" position of the thermic-motor drives on the circulation circuits of the panel.
- Water Temperature at the Flow of the mixing valve.
- Water Temperature on Return from the panel.
- Water temperature in the Buffer.
- Water Temperature at the Flow of the water-to-water heat pump.
- Water Temperature on Return from the water-to-water heat pump.

The experiment began prior to the object's subcooling. After a period of subcooling, the system begins heating. The set value of the accumulator's temperature and the mixing circuit of the wall and floor heating follow the same linear curve at the start of the heating. The set temperature value in the accumulator and mixing circuit is raised by dT=1K at specific time intervals. During the heating process, the ambient temperature gradually approached the thermostat's pre-set value. The thermostat's on/off switching is depicted on Figure 1a and 1b i.e., the thermostatic heads diagram. The primary purpose is to determine the feed water temperature for the panel system so that the ambient temperature is equal to or close to the user-specified value. The premises exposed to measurement were utilised during working hours during the measurement period. The system was constantly turned on during the heating time. The ambient temperature graphic shows changes caused by staff activity.

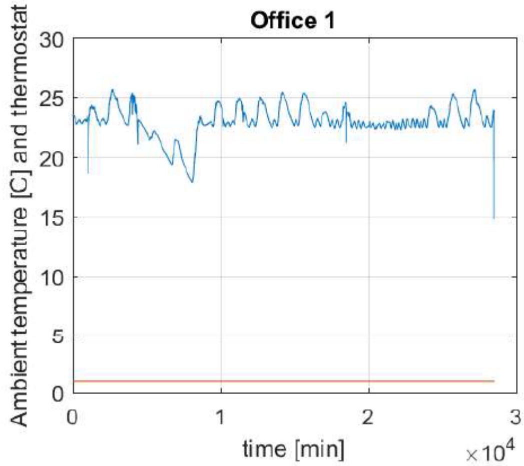

Figure 1a

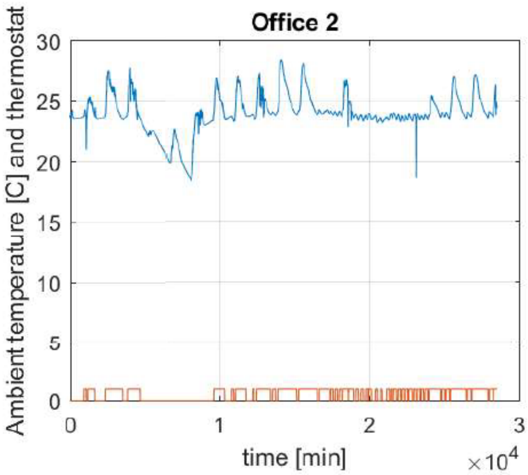

Figure 1b

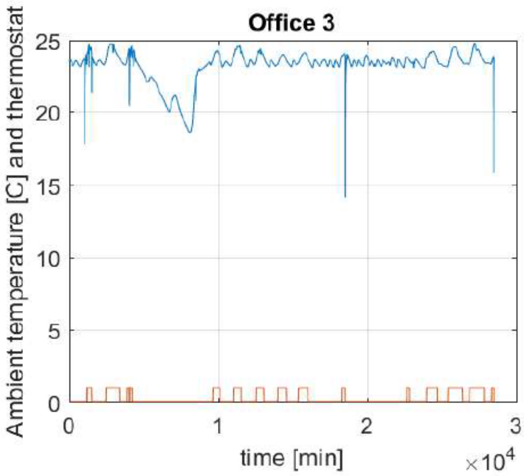

Figure 1c

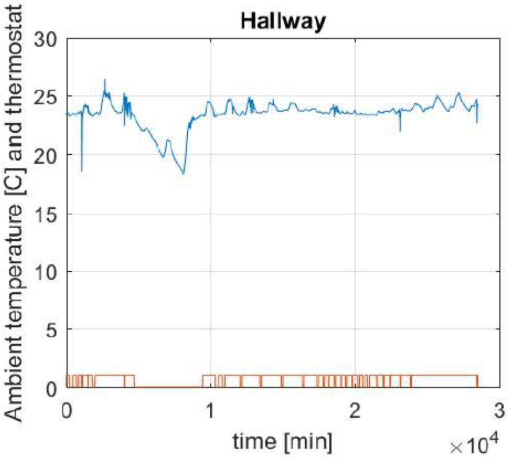

Figure 1d

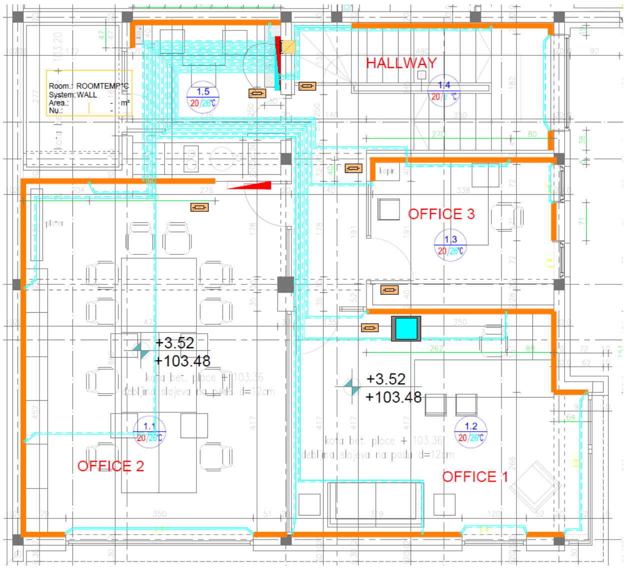

Figure 2: Wall panels - disposition

4.2. The Table 1 provides the coefficients with the terms of the polynomial equation. Its characteristic is to find the first negative coefficients next to the members of the polynomial, i.e., functional dependence of the inlet temperature of the supply water of wall heating in relation to the outside temperature. It is interesting to note that only two coefficients next to the terms of the polynomial equation are negative only for wall panels located in a space that is oriented to the north side of the world and that is not affected by solar radiation.

4.3. Experimental results

Table 1: Short test results wall heating (key wall panels)

Polynomial matrix of measurement temperature	$\theta_n = a_3 \cdot \theta_o^3 + a_2 \cdot \theta_o^2 + a_1 \cdot \theta_o + a_0$
Wall 8	$-0.0015 \cdot \theta_o^3 + 0.0204 \cdot \theta_o^2 - 0.2352 \cdot \theta_o + 25.8575$
Wall 19	$-0.0018 \cdot \theta_o^3 + 0.0198 \cdot \theta_o^2 - 0.267 \cdot \theta_o + 27.136$
Average Polynomial Coefficient Wall 1 – Wall 20	$-0.00165 \cdot \theta_o^3 + 0.0201 \cdot \theta_o^2 - 0.2511 \cdot \theta_o + 26.497$

a)

b)

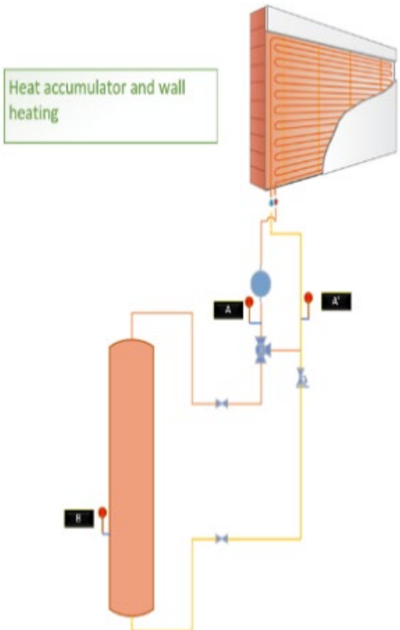

Figure 3: (a) Test hardware, (b) Experimental hydraulical scheme.

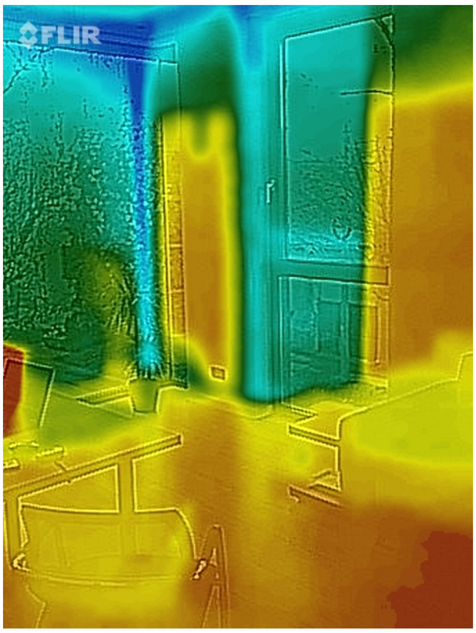

Figure 4: Wall and floor heating – thermal camera

5. METHODOLOGY

5.1. One–dimensional, steady heat transfer is, often, an idealization of the actual process we are attempting to model 3. For example, in modelling heat transfer through a plane wall it is typically assumed that the ambient temperatures, on either side of the wall, are at steady, fixed values – when these temperatures will change with the changing environmental conditions (such as night and day). We know that a 1–D, steady analysis would be appropriate for such situations providing the characteristic time for ambient temperature change is significantly larger than the characteristic diffusion time (or thermal relaxation time) of the wall. For such cases, the heat transfer in the wall could be modelled as a quasi–steady process, i.e., a succession of steady processes. This approach formed the basis of the so–called lumped capacity (or small Biot number) approximation for transient heating/cooling of an object.

5.2. When this criterion is not met – which is of interest here – it becomes necessary to model the interacting dependence of time and position on the temperature field. Analytically, this implies that the governing differential equations for the temperature field will involve partial derivatives, as opposed to ordinary derivatives.

$$\frac{\partial T}{\partial t} = \frac{\partial^2 T}{\partial^2 t}, \left(\frac{\partial T}{\partial t}\right)_0 = 0, \mathrm{T}_{(x=1,t)} = 0\,, \quad \mathrm{T}_{(x,t=0)} = 1 \qquad (1)$$

$$T = \sum_{n=1}^{\infty} A_n \cdot \cos(\lambda_n x) \cdot e^{-\lambda_n^2 \cdot t} \qquad (2)$$

$$A_n = -\int_0^1 \mathrm{x} \cdot \sin(n\pi x)\, dx \cdot \left[\int_0^1 \mathrm{x} \cdot \sin^2(n\pi x)\, dx\right]^{-1}$$

$$A_n = \frac{2\cos(n\pi)}{n\pi} = \boxed{\frac{\mathbf{2 \cdot (-1)^n}}{\boldsymbol{n\pi}}} \qquad (3)$$

And the complete solution is $\mathrm{T} = \omega + \mathrm{s}$, or

$$\mathrm{T} = \mathrm{x} + \frac{2}{\pi}\sum_{n=1}^{\infty} \frac{(-1)^n \sin(n\pi x)}{n} e^{-(n\pi)^2 \cdot t} \qquad (4)$$

The method of splitting the solution for T into two parts, i.e., $T = \omega + s$,

is sometimes known as "partial solutions". The goal in using this method is to transform a problem that cannot, directly, be solved with SOV into a problem (or problems) that can. The partial solutions technique is one example of a general method known as superposition, in which two or more solutions to a modified problem are superimposed (or, equivalently, added) to form a solution to the whole problem (DE, BCs, and IC) under consideration. The feature of the DE and BCs that allows for this method is linearity – for which a sum of independent solutions to the DE will also be a solution. Inhomogeneous DE. Consider now an example in which heat generation occurs in the wall. Say the surface at $\mathrm{x} = 0$ is adiabatic and the surface at $\mathrm{x} = 1$ is maintained $\mathrm{T} = T_1$. Initially the wall is at a uniform temperature of T_1. At time $t = 0$ uniform heat generation occurs in the wall, of strength q_0'''.

A matrix polynomial is polynomial with square matrices as variables. Given on ordinary, scalar-valued polynomial:

$$P_{(x)} = \sum_{i=0}^{n} a_i \cdot x^i = a_0 + a_1 \cdot x + a_2 \cdot x^2 + \ldots + a_n \cdot x^n, \quad (5)$$

This polynomial evaluated at a matrix A is:

$$P_{(A)} = \sum_{i=0}^{n} a_i \cdot A^i = a_0 \cdot I + a_1 \cdot A + a_2 \cdot A^2 + \ldots + a_n \cdot A^n, \quad (6)$$

Where "I" is the identity matrix (9).

Cyclic subspace. In linear algebra and functional analysis, a cyclic subspace is certain special subspace of vektro space with a vector in the vector space and a linear transformation of the vector space. The cyclic subspace associated with a vector v in a vector space V and linear transformation T of V is called the *T-cyclic subspace generated by v.* The concept of cyclic subspace is a basic component in the formulation of the cyclic decomposition theorem in algebra.

$\boxed{\text{T – cyclic subspace of V generated by v}}$;

$$\mathrm{T}^{\mathrm{k}}(\mathrm{v}) = -\mathrm{a}_{\mathrm{k}-1}\mathbf{T}^{\mathrm{k}-1}(\mathbf{v}) - \cdots - \mathrm{a}_1\mathbf{T}(\mathrm{v}) - \mathrm{a}_0\mathrm{v} \quad (7)$$

$$\mathrm{m}_{\mathrm{v}}(\mathrm{t}) = t^k + a_{k-1}t^{k-1} + \cdots + a_1 t + a_0 \quad (8)$$

$$\begin{bmatrix} \square & \square & \square & & \square & \boxed{-a_0} \\ 1 & 0 & 0 & \cdots & 0 & -a_1 \\ 0 & 1 & 0 & & 0 & -a_2 \\ & \vdots & & \ddots & & \vdots \\ 0 & 0 & 0 & \cdots & 0 & -a_{k-2} \\ 0 & 0 & 0 & & 1 & -a_{k-1} \end{bmatrix} \quad (9)$$

We observe how wonderfully the connection of the first term of the T-annulator of the invariant subspace occurs, analogous to the theory of cyclic space. The invariant subspace is represented by the unit vector matrix polynomial.

How to transition from scalar to vector space and discover a vase with a vector subspace in the matrix's cyclic shape is expected. The heat accumulator, with the beginning point of system heating at the bottom of the buffer, can also be discovered.

The theory of two rods connected now does not rely solely on one physical quantity, as was the case at the start of the presentation when the heating temperature of the wall panels was solely dependent on the outside temperature, but another connection was added through the theory of heat conduction through an infinite length rod, and it is the temperature of the system's initial state on the return branch of the wall panels. An analogue may be found with the heat accumulator, where the system heating begins at the bottom of the buffer.

Experimentally and theoretically, the system may regulate the system of the set value of the heating temperature of heating devices, in this instance the wall and floor panel system, using a function with two variables.

The subspace invariants are then related to the matrix polynomial from rod theory. Here's where we got it:

$$m = \sqrt{\frac{\alpha \cdot O}{\lambda \cdot A}}; \quad \frac{d^2\theta}{dx^2} - m^2 \cdot \theta = 0 \quad (10)$$

$$P_{(A)} = \sum_{i=0}^{n} a_i \cdot A^i = a_0 \cdot I + a_1 \cdot A + a_2 \cdot A^2 + \ldots + a_n \cdot A^n \quad (11)$$

$$\boxed{[\mathrm{I}] = \frac{[\theta]_{1\,x\,n}}{[\theta_A]_{1\,x\,n}} \cdot e^{-m \cdot x}} \quad (12)$$

$$\boxed{\theta_n = a_n \cdot \theta_o^n + a_{n-1} \cdot \theta_o^{n-1} + a_1 \cdot \theta_o + \frac{{a_o}^2}{\theta_A} \cdot} \; \boxed{e^{\frac{-2 \cdot (-1)^n}{\left(\frac{1}{2}(2n-1) \cdot \pi\right)}}} \quad (13)$$

Variables are stated as follows:

θ_n - Desired value water temperature,
θ_o - Outside temperature,
θ_A - Return water temperature of wall or floor heating.

6. ANALYSIS OF MEASUREMENT RESULTS

The rooms that were sampled were occupied during the measuring period during working hours. The system was turned on continually during the winter period. On the ambient temperature diagram, variations brought on by employee activity are apparent.

Experimental data was processed using the "MATLAB-MathWorks" software suite. "MS-Office Excel" was used to automatically record all measurable data.

The flow and return temperstures of panel systems are depicted in the figures below as changing in temperature.

The number of activations, or shutdowns of the heat pump's compressor, determines the value of the amplitude and frequency of the push and return branches solely. The amplitude's value and the heat accumulator's temperature hysteresis are closely correlated. The geothermal heat pump and the heat accumulator are hydraulically coupled.

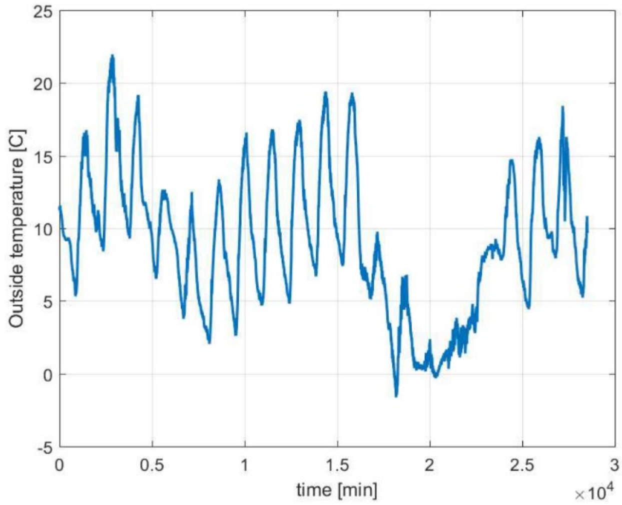

Figure5: Outside temperature

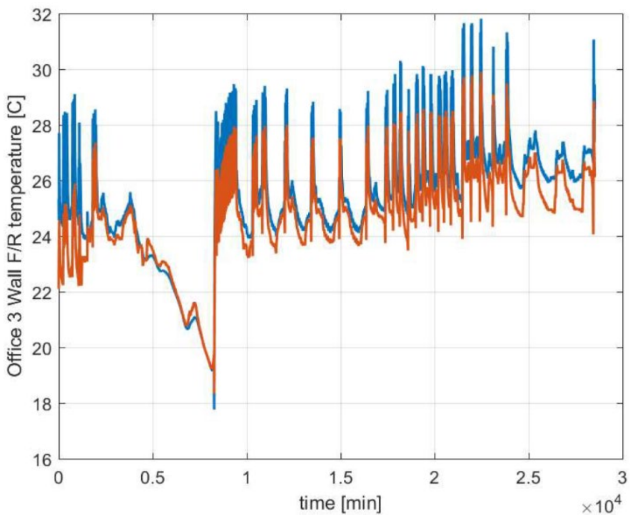

Figure 6: Inlet, outlet water temperature wall heating in the office 3.

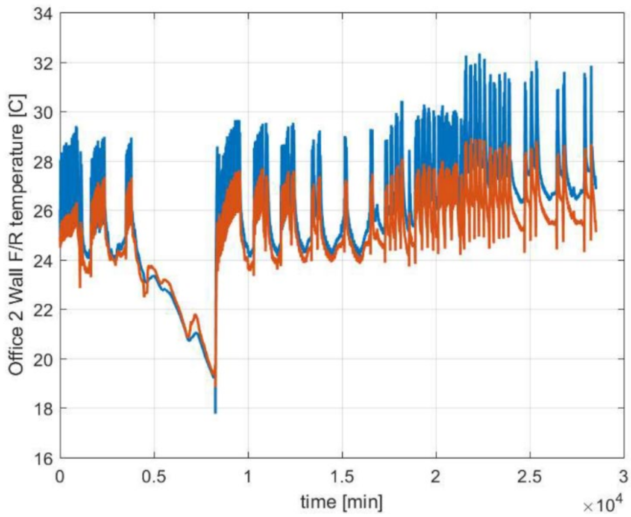

Figure 7: Inlet, outlet water temperature wall heating in office 2.

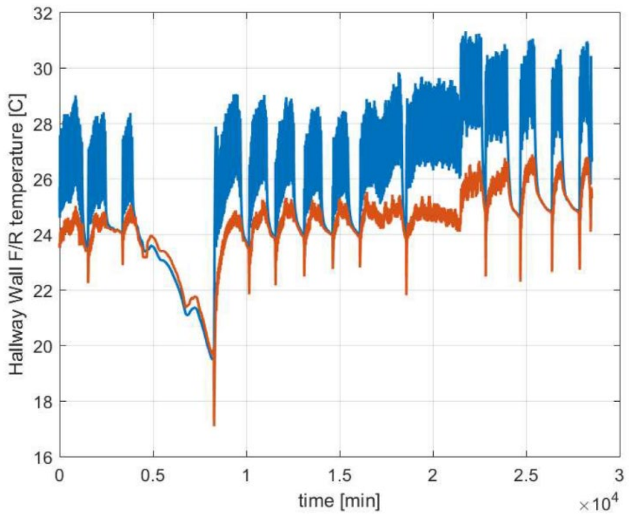

Figure 8: Inlet, outlet water temperature wall heating in Hallway

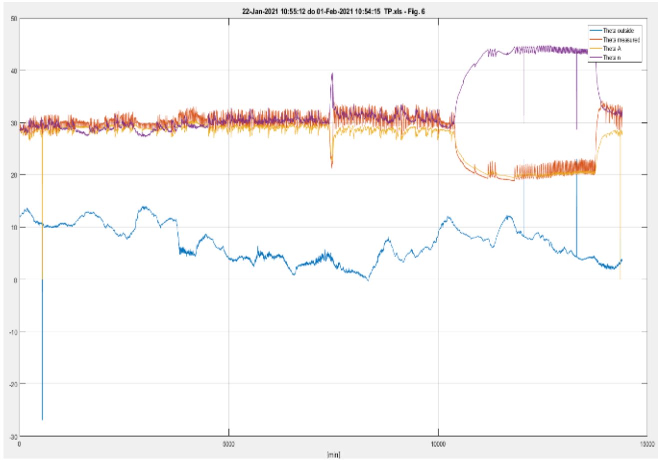

Figure 9: Test resulte of equation number (13)

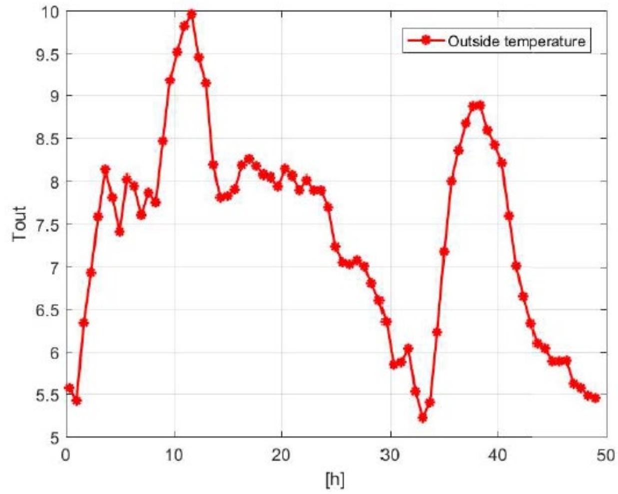

Figure 10: Outside temperature in the sampled time frame.

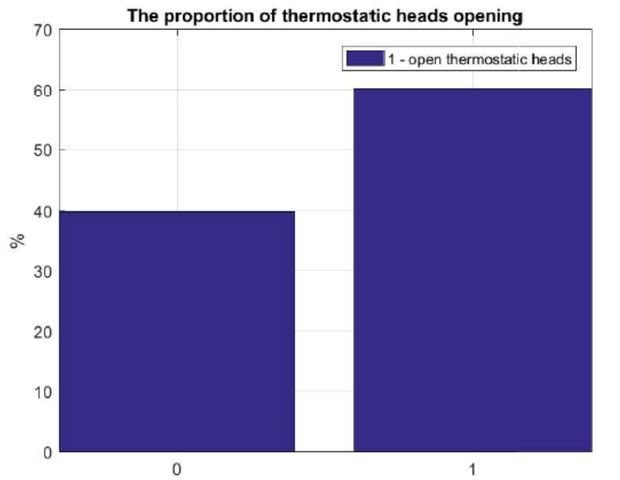

Figure 11: The typical graph shows the fluid's set value in relation to an external curve, showing how much the valve was opened to the ambient temperature condition – high flow temperature.

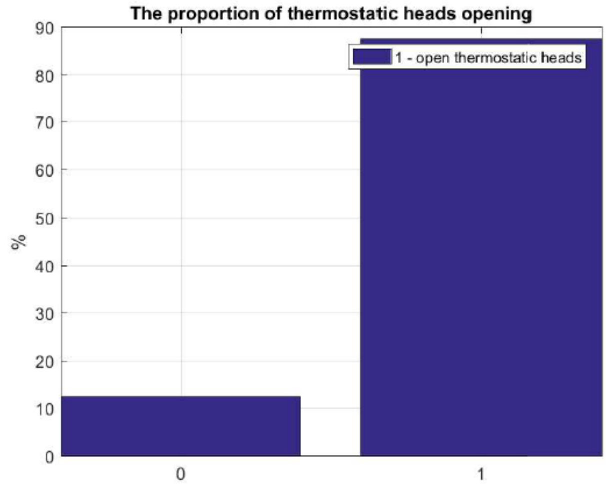

Figure 12: The new results graph shows the fluid's set value in related within equation (13) - 1D conduction heat transfers, optimized flow temperature.

7. CONCLUSION

The supply temperature of the wall panels depends on two physical quantities - on the outside air temperature and on the return temperature of the fluid. Applying the equation in practice can remove thermostatic heads on manifolds. The equation can be used by thermal-technical designers. Each object belongs to a different class. The coefficients are different depending on the class of the object. Integrating the equation in the heating system gives users a high degree of comfort and stable ambient temperatures.

Additionally, heat pump manufacturers can benefit from the equation obtained from 1D conduction heat transfers. Previously, the conventional system required a minimum of two or more points to build the operating curve for the system's fixed water temperature. It may be substituted by the specified equation and applied to any object. A machine learning system may be used on a given system to adjust the coefficients in the heated building.

There are various technical solutions in use that accurately manage the ambient temperature and are linked to the BMS system. As is well known, such systems need substantial investments. In equation 13, a sensor on the return pipe network must be added and programmed into the existing PLC systems.

ACKNOWLEDGEMENTS

This research did not receive any specific grant from funding agencies in the public, commercial, or not-for-profit sectors.

REFERENCES

[1] Ružica I. Todorović, Miloš J. Banjac, Bogosav M. Vasiljević, “Analytical and experimental determination of the temperature field on the surface of wall heating panels”, Thermal Science, (Vol. 19, No. 2, pp. 497-507), Year 2015.

[2] Jakub Oravec, Ondřej Šikula, Michal Krajčík, Müslüm Arıcı, Martin Mohapl, A comparative study on the applicability of six radiant floor, wall, and ceiling heating systems based on thermal performance analysis, Journal of Building Engineering 36 (2021) 102133.

[3] Aliihsan Koca, Zafer Gemici, Yalcin Topacoglu, Gursel Cetin, Rusen Can Acet, Burak Kanbur, “Experimental investigation of heat transfer coefficients between hydronic radiant heated wall and room”, Energy and Buildings (Volume 82, Pages 211-221), October 2014.

[4] Milorad Bojić, Dragan Cvetković, Vesna Marjanović, Mirko Blagojević, Zorica Đorđević, “Performances of low temperature radiant heating systems”, Energy and Buildings (Volume 61, Pages 233-238), June 2013.

[5] I.B. Kilkis[a], S.S.Sager[b], M.Uludag[b], “A simplified model for radiant heating and cooling panels”, [a] HEATWAY Radiant Floors and Snowmelting, 3131 W.Chesnut Expressway, Springfield, MO 65802, USA, [b] Mechanical Engineering Department, Middle East Technical University, Ankara 06531, Turkey, Simulation Practice and Theory 2 (1994) 61-76, June 1994.

The proposal of the recuperator design for the rotary kilns with a driving mechanism in the calcination zone

Nenad Stojić[1*], Nebojša Bogojević[1], Miljan Marašević[1], Dragan Cvetković[2], Aleksandar Nešović[3]

[1]Faculty of Mechanical and Civil engineering in Kraljevo, University of Kragujevac, Kraljevo, Serbia
[2]Institute for Information Technologies, University of Kragujevac, Kragujevac, Serbia
[3]Faculty of Engineering, University of Kragujevac, Kragujevac, Serbia

The rotary kilns have been used in the industry in various applications, mostly in the cement industry and for calcination of dolomite ores. The rotary kilns characterize the high-temperature processes and therefore the heat losses are very high. In the order to increase the efficiency of the kiln and reduce fuel consumption, several different designs of recuperators are developed. One of the problems in the design of the recuperator is the position of the driving mechanism or tyre of the rotary kiln. This paper has presented a solution of the two separated recuperators in order to resolve the previous mentioned problems and increase the overall efficiency of the rotary kiln. The analytical model has been used for the determination of the geometry and heat losses of the recuperator while the CAD model has been used for the calculation of the heat losses and analysis of the airflow in the recuperator. The results obtained from both models have shown a good correlation and show that with the presented two-part recuperator design is possible to increase the efficiency of the rotary kiln when the driving mechanism or tyre is placed on the kiln shell in the calcination zone.

Keywords: recuperator, design, model, flow simulation, rotary kiln, energy efficiency, heat transfer, heat exchanger

1. INTRODUCTION

Rotary kilns are widely used in many industries, with the most technologically significant role in cement production [1] and the calcination of dolomite ore in magnesium production. Rotary kilns are devices that are applied in almost all processes in which it is necessary to raise the input raw material to a high temperature in a continuous process [2].

The operation principle of rotary kilns is very simple, and it is based on heating the material to the point where chemical reactions generate degradation and change in its structure. The kiln is slanted at an appropriate angle in relation to the horizontal axis, and the rotary movement is achieved through the drive mechanism. The raw material is inserted at the upper end of the kiln and under the influence of gravitational force and rotational motion it slides towards the lower end of the kiln, where the burners for burning fuel are located. Figure 1 shows the basic parts of a rotary kiln, which consists of a kiln mantle, drive mechanism, supporting wheel, kiln head cover, kiln head seal, kiln end seal, kiln end exhaust chamber, centrifugal fan and burner.

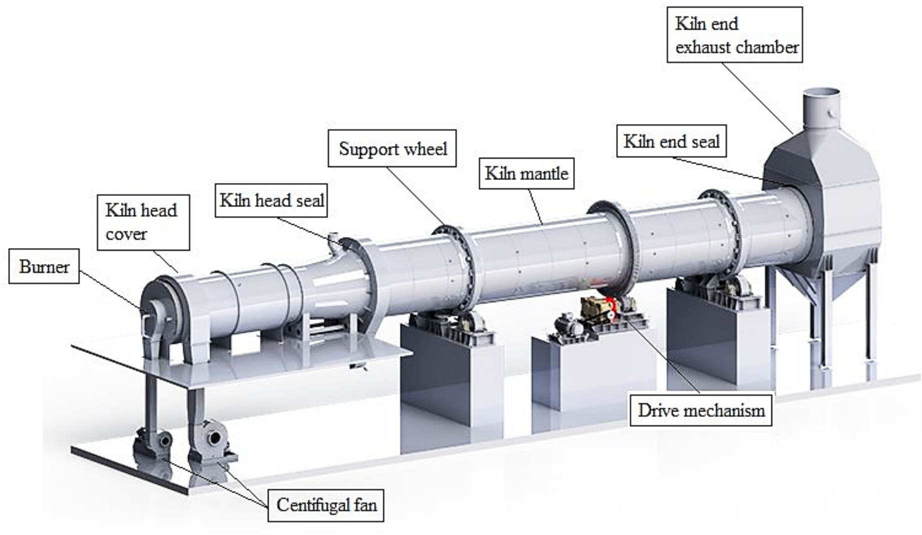

Figure 1. The basic parts of a rotary kiln

The importance of these devices is evidenced by the fact that the world production of cement and clinker increased by more than 240% in the first 20 years of the 21st century [3,4]. In the case of rotary kilns in which high-temperature processes take place, an increase in energy efficiency can be achieved by using waste heat. Nearly 40% of the total input energy is wasted, 19.15% is waste heat contained in combustion products, 5.61% is waste heat due to cooling of clinker, and 15.11% is waste heat from the mantel of the rotary kiln [5].

*Corresponding author: Dositejeva 19, 36000 Kraljevo, Serbia, stojic.n@mfkv.kg.ac.rs

Taking into account the operation principles, the amount of energy required to carry out the calcination process as well as the estimated energy losses, it is clear that one of the primary tasks is to find ways to increase the energy efficiency of these kilns. The proposed measure is also in line with the aspirations for the adoption of national strategies with the aim of increasing the energy efficiency of the industrial sector. Finding a solution to increase the energy efficiency of the rotary kiln, would affect the reduction of energy consumption, which would have a positive effect on environmental protection and the reduction of greenhouse gas.

Several types of kilns are used in industrial applications, such as vertical kilns and horizontal rotary kilns. In horizontal rotary kilns, the position of the drive mechanism depends primarily on the temperature regimes of the technological process in the kilns. This paper analysed the possibility of using the waste heat from a mantle of the rotary kiln with the drive mechanism placed on its central part, as shown in Figure 2.

2. THE USE OF WASTE HEAT FROM THE ROTARY KILN MANTLE

The heat loss from the rotary kiln mantle represents a significant loss that depends on the purpose of the kiln, whose value is in the range of 3-25% of the total input energy [5-8]. Depending on the area of application, heat loss from the mantle of the rotary kiln is, about 8-15% in the cement industry [9], in the magnesium production process 24.8% [10], in the calcination process of dolomite ore 17.7% [2] even up to 26.35 [11] of the total input energy. If the heat losses were used for preheating processes of the raw material or combustion air before entering the rotary kiln, the energy efficiency of the rotary kiln would be significantly increased.

The simplest solution would be to insulate the mantle, but at high-temperature regimes, this solution may compromise the structural stability of the rotary kiln. A solution with inspection openings for monitoring the temperature and condition of the surface of the rotary kiln mantle is shown in the references [5,7]. One of the solutions for utilizing heat losses from the kiln mantle is shown in references [12, 13]. The solution in the form of a recuperator for preheating water is shown in reference [9, 14, 15, 16].

Unlike the previously presented solutions for utilizing heat loss from the rotary kiln mantle, the authors in the reference [2] propose a recuperator that uses the total heat loss from the mantle to preheat the combustion air. The step-shaped heat recuperator is placed above the calcination zone. Due to the very small distance between the rotary kiln surface and the recuperator, the proposed solution is ineffective for rotary kilns with high eccentricities. The significance of this problem was investigated in reference [17], where it was concluded that the positioning of the recuperator in relation to the supporting wheel and the drive mechanism of the rotary kiln plays a significant role in order to utilize the total heat losses. In the reference [18], the authors proposed modified solutions for the recuperator presented in the reference [2]. The solution of the recuperator in the case when the supporting wheel is located in the zone where the heat losses are the highest was not examined in detail by the author [18], but a schematic presentation of the possible solution was given, including the solution for using preheated air.

The aim of this paper is to analyse the possible design of the recuperator for the use of the total heat loss in the case when the drive mechanism and/or the supporting wheel is located in the zone where the heat loss from the rotary kiln mantle is the highest. The proposed design uses the total heat loss from the kiln mantle for air preheating. The energy of the preheated air may be used in the combustion process and/or for preheating the input dolomite ore, which would have a positive effect on reducing fuel consumption.

3. PROPOSED DESIGN

The schematic presentation of the construction in the case, when the driving mechanism is located in the zone of the highest temperatures, is shown in Figure 2. In this case, the increase in energy efficiency would be achieved by the construction consisting of two recuperators, as shown in Fig. 2. The diameter of the rotary kiln is 2.8 m, and the length of the 80 m, but both recuperators would be placed only on the part of the kiln mantle with the highest temperatures, above the calcination zone, in total length of 15.45 m.

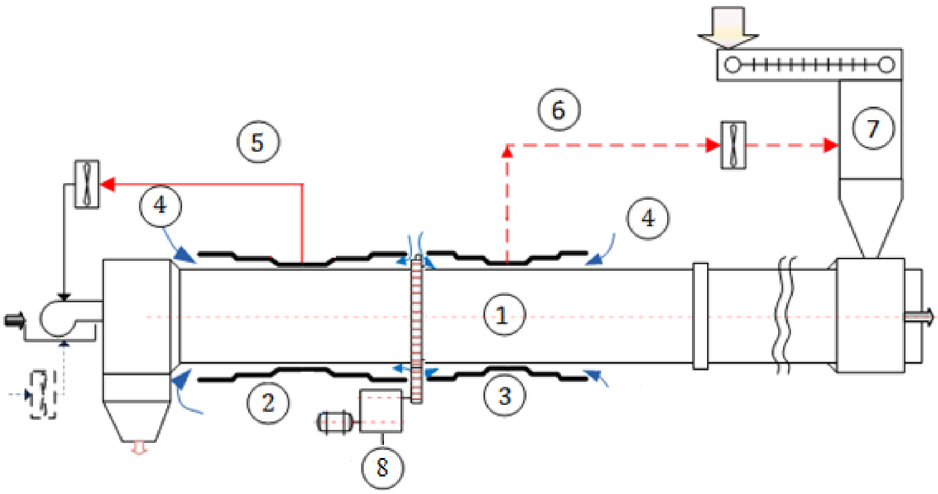

Figure 2. Schematic presentation of the proposed design; 1-rotary kiln, 2-recuperator 1, 3-recuperator 2, 4-airflow, 5-combustion air, 6-air used for preheating input material, 7-feeder

The first recuperator (position 2 in Figure 2) is used for preheating air used for fuel combustion and it is placed on the left side of the driving mechanism with a total length of 9.27 m. The preheated air from the second recuperator (position 3 in Figure 2) is used to preheat the input material and it is placed on the right side of the driving mechanism with a total length of 6.18 m.

The proposed design has not been applied in practice, but this paper analyses the possibility of implementation by applying a mathematical model as well as a thermodynamic flow analysis of the proposed design in the SOLID WORKS software package.

4. HEAT LOSS FROM THE MANTLE OF THE ROTARY KILN

The heat loss of the rotary kiln mantle was calculated based on the balance equation (1). This heat loss was calculated and verified [2] whereby the kiln mantle was divided into 24 segments with the aim of obtaining approximately equal temperatures on its surface. The total heat loss is:

$$\dot{Q} = \sum_{i=1}^{24} \dot{Q}_{conv\,s,i} + \sum_{i=1}^{24} \dot{Q}_{rad\,s,i} = \sum_{i=1}^{24} \alpha_{s,i} A_{s,i} (t_{s,i} - t_o) + \sum_{i=1}^{24} \sigma \varepsilon A_{s,i} \left(T_{s,i}^4 - T_o^4\right) \quad (1)$$

where are

$\dot{Q}_{convs,i}$ - convective heat loss from the i-th segment calculated for the case of natural convection around a horizontal cylinder [19] taken from [20],

$\dot{Q}_{rads,i}$ - radiation heat loss from the i-th segment calculated for the case of a pipe in a big room [21].

The obtained results were presented in the reference [18] and they represent the input data for defining geometry for both recuperators in this paper.

5. MODELLING METHODS

An analytical cell model for define the unknown geometry and operating parameters of both recuperators was applied. In addition to the analytical model, the rotary kiln with appropriate recuperators was modelled in the SOLID WORKS software package and the analysis of the recuperator operation was performed using the FLOW module for the same input parameters as for the analytical model.

5.1. Cell modelling

The first recuperator is designed to preheat air to the highest temperature which is needed for fuel combustion. The remaining heat loss from the rotary kiln mantle would be used for preheating of additional amount of air to the highest possible temperature which will be used for preheat the input material (dolomite). The recuperators are divided into segments of corresponding lengths, similar as the kiln itself.

The air flowing through the formed annular duct between the kiln mantle and the recuperator in i-th segment, and it is heated by convective heat loss ($\dot{Q}_{convs,i}$) from the mantle of rotary kiln and ($\dot{Q}_{convr,i}$) from the recuperator, so for i-th segment it is:

$$\dot{Q}_{conv\,s,i} + \dot{Q}_{conv\,r,i} = \frac{\dot{m}_a}{2} \cdot c_{p,a} \cdot \left(t_{a\,out,i} - t_{a\,in,i}\right) \quad (2)$$

where $t_{a\ in,i}$ and $t_{a\ out,i}$ are the inlet and outlet air temperature at the i-th segment. For the end (first) segments, the inlet temperature of the air is equal to the ambient air temperature $t_{a\,in,1} = t_{a\,in,8} = t_0$). Halves of defined mass airflows ($\dot{m}_a/2$) are introduced from one and from other side of both recuperators (see Figure 2) whereby the air flow is directed towards extraction point. The other important balance equations needed for the i-th segment are:

$$\dot{Q}_{s,i} = \dot{Q}_{conv\,s,i} + \dot{Q}_{rad\,sr,i} \quad (3)$$

$$\dot{Q}_{rad\,sr,i} = \dot{Q}_{conv\,r,i} + \dot{Q}_{r,i} \quad (4)$$

In the equation (3), $\dot{Q}_{s,i}$ represents the heat loss from the rotary kiln mantle on the i-th segment which is transferred to the air by convection $\dot{Q}_{convs,i}$ and $\dot{Q}_{radsr,i}$ represents the amount of heat which is transferred by radiation from the kiln mantle to the surface of the recuperator.

Equation (4) represents the balance equation for the recuperator surface where $\dot{Q}_{convr,i}$ represents the convective heat loss that is transferred to the air from the recuperator surface and $\dot{Q}_{r,i}$ represents the heat loss to the environment. For a known insulation thickness, the heat loss $\dot{Q}_{r,i}$ can be calculated. A detailed explanation of the equations is shown in the reference [18, 2].

The thermodynamic characteristics of the air used in the analytical model were calculated in accordance with the references [22-24].

5.2. CAD model

The CAD model which is developed in the SOLID WORKS software package is used for analysis of the recuperator work. The CAD model is formed by the results obtained from the analytical model as shown in Figure 3. The thermodynamic and flow analysis is conducted in the FLOW module of the SOLID WORKS software package. Boundary conditions for flow simulation are:

- air of the temperature of 8°C enters at the annular duct between the rotary kiln mantle and recuperators at ambient pressure from both sides (see Figure 2),
- the air mass flows for both recuperators are the same as in the analytical model,

• the temperatures on the segments of the CAD model are the measured values of the temperatures on the rotary kiln mantle used in the analytical model.

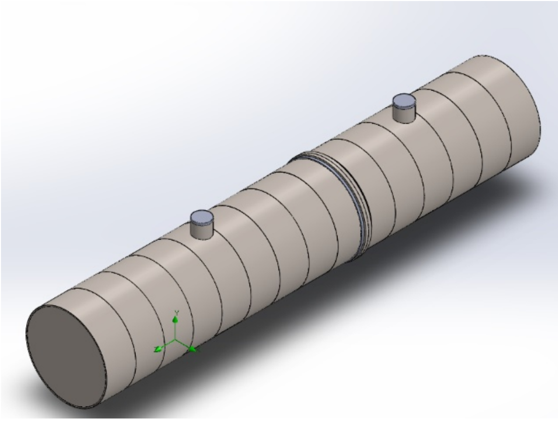

Figure 3. The CAD model formed in SOLIDWORK

6. RESULTS

Both air streams preheated in the recuperators were extracted at the position placed so that both halves utilize equal heat losses of the kiln mantle for each air streams. In the first recuperator and the second recuperator, two air streams are mixed isothermally above the kiln section with the highest surface temperature. It is advantageous from a thermodynamic standpoint since the temperature difference between the air and the kiln surface can be compared to the temperature difference along a counter-current heat exchanger.

Figure 4 shows the maximal temperatures of preheated air at both recuperators and the position where preheated air should be extracted for a defined inlet parameter. The temperatures of the kiln and recuperator surfaces are also shown in Figure 4.

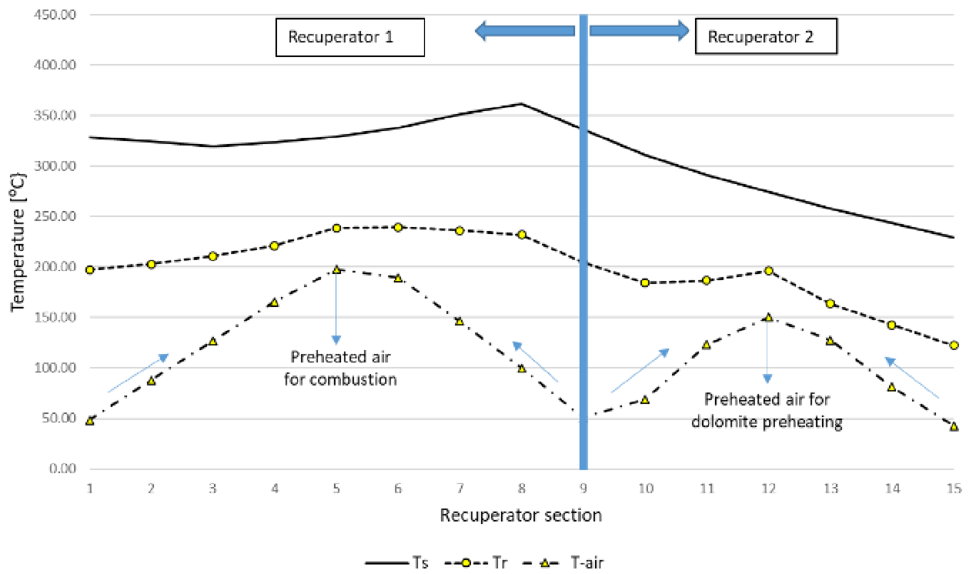

Figure 4. The preheating air and recuperators surface temperatures

The stepped shape of the recuperator and the diameters for each segment obtained by the analytical model are shown in Figure 5. For both recuperators, the dashed line in Figure 5 represents the minimum permissible segment diameter.

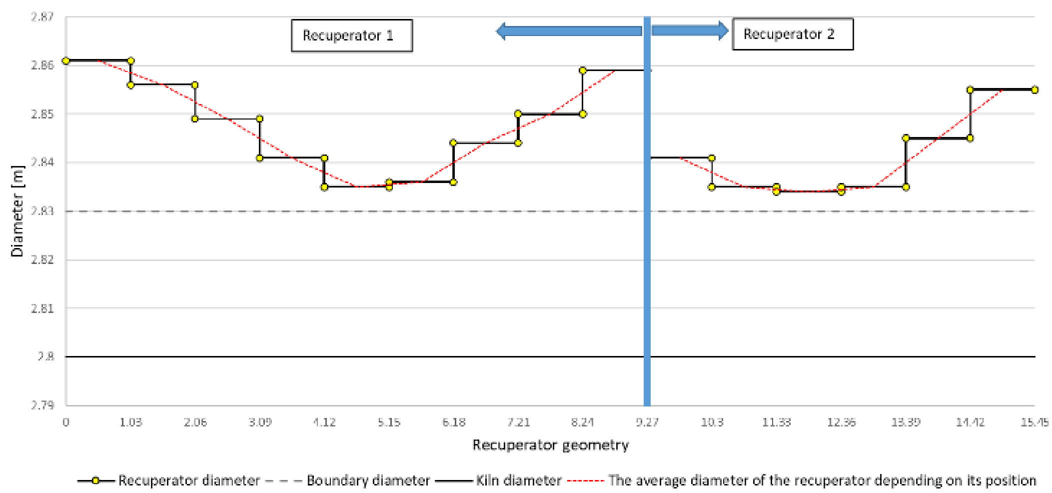

Figure 5. The diameters of recuperators along its length for each segment

In the case of the first recuperator, for a mass air flow of 3.3788 kg/s and an inlet temperature of 8°C, the maximum outlet temperature of the preheated air obtained by the analytical model is 198.68°C. This amount of preheated air is used for fuel combustion. In the second recuperator, for a mass air flow of 1.9973 kg/s and an inlet temperature of 8°C, the maximum outlet temperature of the preheated air obtained by the analytical model is 146.8°C and this air is used for preheating the input material.

The result obtained by the CAD model for the same input parameters as in analytical model are shown on the Figure 6.

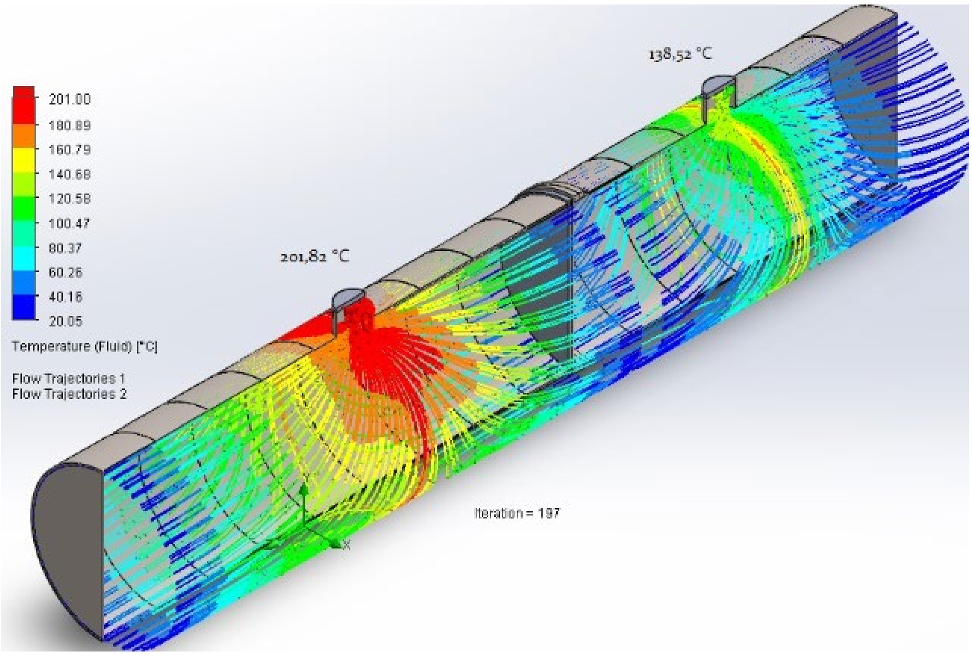

Figure 6. The result obtained by FLOW analysis

Based on the FLOW analysis, for the first recuperator and input parameters such as air temperature of 8°C and mass flow rate of 3.7888 kg/s, the maximum outlet temperature is 201.82°C, which is 1.58% higher than the value obtained by the analytical model. For the second recuperator, for a mass flow of 1.9973 kg/s and an inlet air temperature of 8°C, the maximum outlet temperature of preheated air is 138.52°C, which is 5.98% less than the value obtained by the analytical model.

Based on the material and heat balance equation shown in reference [11] the potential reduction of fuel consumption and improvement of kiln efficiency can be calculated. In this case for obtained results reduction of fuel consumption is about 2000 l/day which represent a saving of 9,9%.

7. CONCLUSION

In this paper, the possibility of using the total heat losses from the mantle of a rotary kiln in the case where the driving mechanism of the rotary kiln is placed in the central part was analysed. In order to increase the energy efficiency of the rotary kiln, a design solution consisting of two recuperators was proposed. A mathematical cell model was created to determine the total available energy as well as to determine the geometry of the recuperators and the maximal temperature of preheated air. In addition, the working analysis for the recuperators was done using CFD in the SolidWorks software package. The results obtained using the presented models shows a good correlation and show that in the proposed way it is possible to use the energy from the rotary kiln mantle by using two recuperators and achieve significant energy savings. The reduction of about 2000 l/day in fuel consumption illustrates the importance of recuperators for utilizing waste heat from rotary kiln mantles.

ACKNOWLEDGEMENTS

This study has been supported by the Republic of Serbia, Ministry of Education, Science and Technological Development through project number 451-03-47/2023-01/200108.

REFERENCES

[1] Vijayan, S.N., Sendhilkumar, S., Industrial Applications of Rotary Kiln in Various Sectors - A Review, Int. J. Eng. Innov. Res. 3 (2014) 342–345

[2] Karamarković, V., et al., Recuperator for waste heat recovery from rotary kilns, Applied Thermal Engineering, Volume 54, Issue 2, 30 May 2013, Pages 470-480

[3] Golewski, G. L., Energy Savings Associated with the Use of Fly Ash and Nanoadditives in the Cement Composition, Energies, 13 (2020), 9, 2184

[4] U.S.G. Survey, National Minerals Information Center, (n.d.) https://www.usgs.gov/centers/nmic/mineral-commodity-summaries

[5] Tahsin Engin, Vedat Ari, Energy auditing and recovery for dry type cement rotary kiln systems –A case study, Energy Conversion and Management 46 (2005), pp. 551–562

[6] A. Atmaca, R. Yumrutaş, Analysis of the parameters affecting energy consumption of a rotary kiln in cement industry,Appl. Therm. Eng., 66 (1) (2014), pp. 435-444

[7] G. Kabir, A.I. Abubakar, U.A. El-Nafaty, Energy audit and conservation opportunities for pyroprocessing unit of a typical dry process cement plant, Energy, 35 (3) (2010), pp. 1237-1243

[8] Q. Yin, W.-J. Du, L. Cheng, Optimization design of heat recovery systems on rotary kilns using genetic algorithms, Appl. Energy, 202 (2017), pp. 153-168

[9] Caputo, A.C., et al., Performance modeling of radiant heat recovery exchangers for rotary kilns, Appl. Therm. Eng. 31 (2011) 2578–2589

[10] B. K. Chakrabati, Investigations on heat loss through the kiln shell in magnesite dead burning process: a case study, Appl. Therm. Eng. 22 (2002) 1339-1345

[11] Nenad P. Stojić (2022), RECUPERATORS FOR THE USE OF WASTE HEAT FROM ROTATING CYLINDRICAL SURFACES, Doctoral dissertation, Faculty of Mechanical and Civil Engineering in Kraljvo, University of Kragujevac, April 2022

[12] Luo, Q., et al., A Thermoelectric Waste-Heat-Recovery System for Portland Cement Rotary Kilns, J. Electron. Mater. 44 (2015) 1750–1762

[13] Mirhosseini, M., et al., Power optimization and economic evaluation of thermoelectric waste heat recovery system around a rotary cement kiln, J. Clean. Prod. 232 (2019) 1321–1334

[14] W.-J. Du, Q. Yin, L. Cheng, Experiments on novel heat recovery systems on rotary kilns, Appl. Therm. Eng., 139 (2018), pp. 535-541

[15] Q. Yin, et al., Design requirements and performance optimization of waste heat recovery systems for rotary kilns, Int. J. Heat Mass Transf., 93 (2016), pp. 1-8

[16] Yin, Q., et al., Optimization design and economic analyses of heat recovery exchangers on rotary kilns, Appl. Energy. 180 (2016) 743–756

[17] Zheng, K., et al., Rotary kiln cylinder deformation measurement and feature extraction based on EMD method, Eng. Lett. 23 (2015) 283–291

[18] Stojić, Nenad P. et al., Improving design and operating parameters of the recuperator for waste heat recovery from rotary kilns, Thermal Science 2021 OnLine-First Issue 00, Pages: 239-239

[19] Churchill W, C.H., Correlating equations for laminar and turbulent free convection from a horizontal cylinder, Int. J. Heat Mass Transf. 18 (1975) 1049–1053

[20] Werner Kast, H.K., Heat Transfer by Free Convection: External Flows, in: VDI Heat Atlas, 2nd ed., Springer, Heidelberg, 2010: pp. 667–672

[21] Kabelac D, Vortmeyer S, Radiation of Surfaces, in: VDI Heat Atlas, Heidelberg, 2010: pp. 947–959

[22] Kleiber M, Joh R, Calculation Methods for Thermopysical Properties, in: VDI Heat Atlas, 2nd ed., Springer, Heidelberg, Germany, 2010: pp. 121–152

[23] Kleiber M, Joh R, Properties of Selected Importanat Pure Substances, in: VDI Heat Atlas, 2nd ed., Heidelberg, Germany, 2010: pp. 153–299

[24] Kleiber M, Joh R, Properties of Pure Fluid Substances, in: VDI Heat Atlas, 2nd ed., Heidelberg, Germany, 2010: pp. 301–417

The usage of natural gas HHV from small cogeneration systems implemented in a 3rd generation DH plant

Milan Marjanović[1*], Miloš Nikolić[2], Rade Karamarković[2], Anđela Lazarević[3], Đorđe Novčić[2]

[1]Faculty of Technical Sciencies/Department for Mechanical Engineering, University of Kragujevac, Čačak (Serbia)
[2]Faculty of Mechanical and Civil Engineering/Department for Energy and Environment Protection, University of Kragujevac, Kraljevo (Serbia)

[3]Faculty of Mechanical Engineering/Department for Management in Mechanical Engineering, University of Niš, Niš (Serbia)

Compared with households, Serbian district heating (DH) companies pay higher natural gas and electricity prices. These facts together with the lack of incentives for DH connection and relatively mild winters encourage customers to disconnect and use split systems. To reduce the heating cost and retain customers, DH companies try to reduce operating costs. A promising way is to implement small cogeneration systems that meet their electricity demand. For a case study DH system, the paper analyzes the usage of heat from passive condensation and oil cooling in natural gas-fired cogeneration systems with capacities in the range of 100 kW_e to 2 MW_e. The available heat from cogeneration systems is modeled based on the manufacturers' data. The case study is a boiler room with a total installed capacity of 37.73 MW and a nominal temperature regime 130/75 ºC. As the plant operates with approximately constant water flow and variable supply and return water temperatures, the average temperature regime is 69.4/49.5ºC for the average outdoor temperature of 5.4ºC. The average regime and mild weather enable the usage of oil cooling and flue gas condensation from the cogeneration plant. The heat recuperation for variable minimum temperature differences from parallel and in-series connections of an oil cooler (OC) and a flue gas condenser (FGC) based on meteorological data are simulated. Paradoxically, the system is the least efficient during the coldest weather, when the heat from oil cooling is wasted, and FGC operates as a dry flue gas cooler.

Keywords: District heating, Modelling, Cogeneration, Higher heating value, Heat exchanger

1. INTRODUCTION

Lund et al. [1] classified district heating systems into four generations based on the historical development, temperature, heat carriers, and characteristics of the applied technologies. Additionally, low-temperature systems of the fifth generation have emerged [2] [3]. This progression aligns with the Second Law of Thermodynamics and focuses on reducing the temperature of the medium and improving the exergetic efficiency of district heating systems.

Taking into account the water temperature, district heating systems in the Republic of Serbia operate during one heating season as second, third, and fourth-generation systems. In fact, they predominantly function as third and fourth-generation systems. There are two reasons for this: (i) the climate, characterized by significant fluctuations in outdoor temperature [4], and (ii) the control based on an approximately constant flow of water in district heating systems. Inland, in smaller towns, these systems typically operate for 180 days per year and are not used for heating domestic hot water. There are no incentives for connecting new users. Compared to households, district heating systems face higher prices for natural gas and electricity. As a result, heat utilities are losing customers. To reverse these negative trends, companies are making every effort to increase efficiency levels and implement more cost-effective technologies. Examples include the use of solar power plants to reduce pumping costs [5], the application of heat pumps and cogeneration plants. A feasibility study [6] has shown that cogeneration systems, where the electrical power covers its own consumption, are profitable for district heating company Toplana Kraljevo. Due to the relatively low number of operating hours (below 3000 h/year) and the declining efficiency of gas engines at lower power levels, the optimal electrical power range for the examined heat utility was found to be between 0.8 and 1.2 MWe. The aim of this study is to determine whether it is economically viable to directly utilize the high heat value of flue gas and the heat released by engine cooling oil in a typical district heating plant in Serbia. The case study is JEP Toplana Kraljevo but the outcome could be generalized to the majority of Serbian DH companies. Figure 1 illustrates the supply and return water temperatures in relation to the outdoor temperature. For the average outdoor temperature during the heating season of 5.4°C, the supply and return water temperatures are approximately 69.4°C and 49.5°C, respectively, with slight variations depending on wind intensity. As can be seen, the average return water temperature is suitable for utilizing waste heat from engine cooling oil and the high heat value of the flue gas. The cooling oil typically exits the gas engine at a temperature of 55°C, which is often the dew point temperature of the flue gas resulting from the combustion of natural gas. The mentioned heat can be utilized through active and passive condensation systems [7] [8]. Active systems involve the use of additional energy for utilizing the high heat value of the flue gas through heat pumps [3], while passive systems involve direct heat exchange.

*Corresponding author: Svetog Save 65 32102 Čačak, milan.marjanovic@ftn.kg.ac.rs

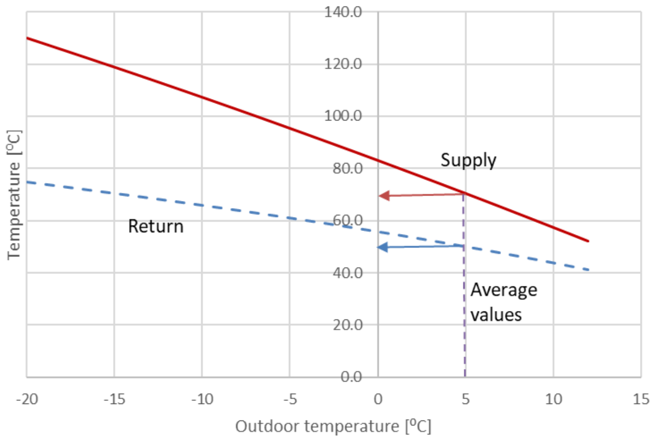

Figure 1: Supply and return temperatures in the examined DH system depending on the outdoor temperature.

2. EXAMINED SYSTEM

Figure 2 shows the examined system. In contrast to conventional systems, this study examines the utilization of an oil cooler (plate heat exchanger) and a flue gas condenser (FGC). Initially, the goal was to analyse both parallel and series connections and determine the optimal dynamics of these connections. However, this approach was abandoned due to the fact that even at the highest operating temperature of the JEP Toplana, the heat loads on the oil cooler and FGC are below 8%. In gas engines, it is customary to cool the oil using air coolers (AC), while the flue gas exits the engine at temperatures above 100°C. In the analysed case, whenever the return temperature would be below 52°C - Δt_{min}, the oil cooler would operate, while the FGC would always operate but with reduced efficiency at higher DH return temperatures compared to the dew point temperature of the flue gas.

Subsequently, the study focuses on determining the optimal design parameters of the FGC to achieve an optimal system configuration.

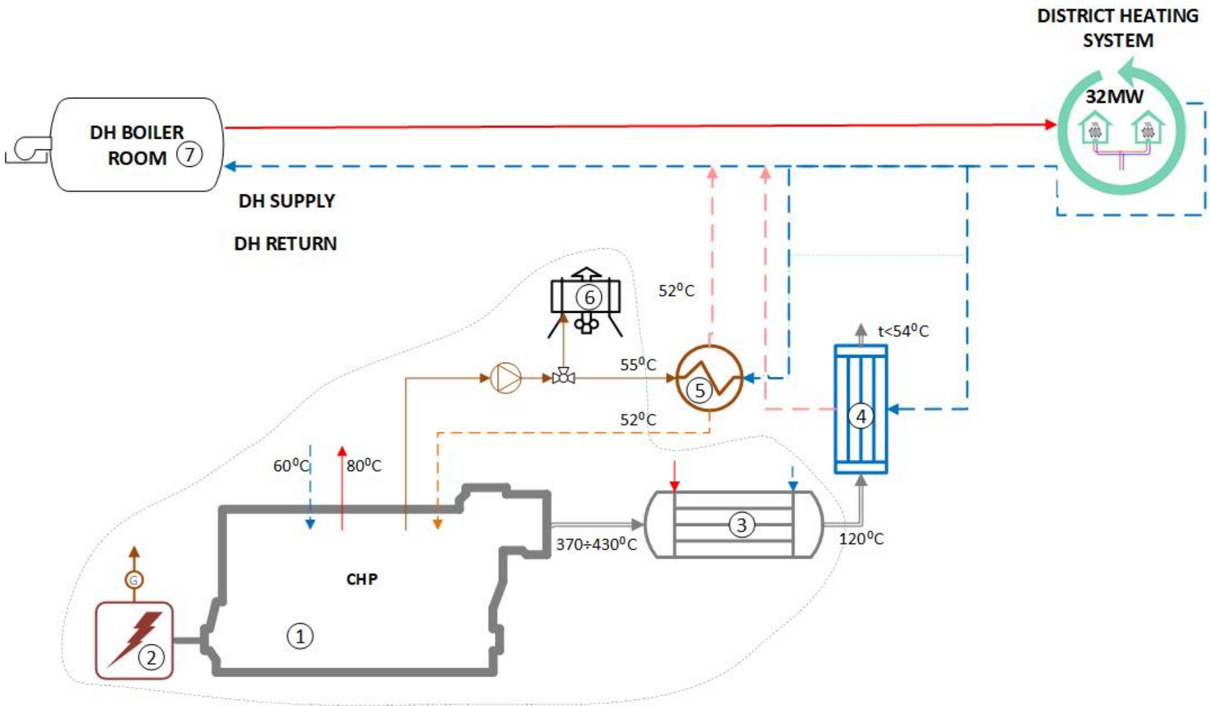

Figure 2: The examined system. 1 – gas engine, 2 – power generator, 3- flue gas dry cooler, 4 – flue gas condenser (FGC), 5 – oil cooler, 6 – air cooler (AC), 7 – boiler room

3. MODELLING

3.1. DH company JEP Toplana Kraljevo

The application of the system was analysed on a cogeneration plant that would be installed in the Central Boiler Room, which has a total installed power of 37.727 MW: 3 boilers, each with the nominal power of 12 MW, and 3 dry flue gas recuperators each with the capacity 575.76 kW. The supply and return water temperatures are shown in Figure 1, while Figure 3 illustrates the variation in heat load depending on the ambient temperature. The presented curve is obtained based on average measured values, which vary depending on the wind. The city is situated in a valley and is characterized by moderate winds. DH company operates intermittently with operating hours between 5 AM and 9 PM during the whole heating season.

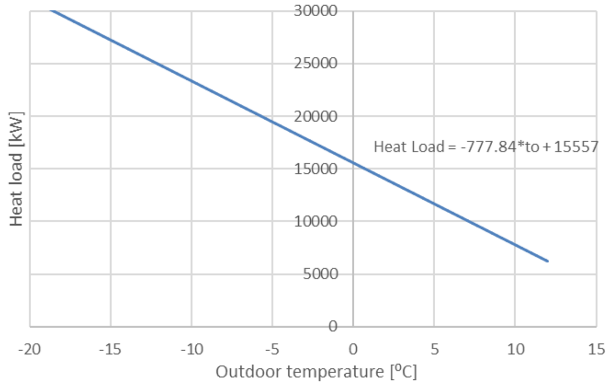

Figure 3: The average heat load depending on the environment temperature.

3.2. Weather Conditions

The heating season of 180 days long has an average outdoor air temperature of 5.4°C. The external design temperature is projected to be -14.7°C. Most of the systems connected to the district heating (DH) network were designed based on an external design temperature of -20°C, which was determined using data from the period 1961-1990. In this study, daily temperature profiles were calculated based on average monthly temperatures (minimum, maximum, and average temperatures) [9] and used in the simulations [10].

3.3. CHP

Gas engines have been modelled based on literature [11] and manufacturer data [12][13][14]. Depending on the nominal electrical power Pel, the electrical efficiency levels of gas engines for various nominal powers are provided in Table 1.

Table 1: Electrical efficiency of gas engines depending on the nominal capacity

P_{el}	η_{el} [%]
< 300 kWe	34%
300÷1000 kWe	η_{el}=0.001 P_{el}+38.784
1000÷2000 kWe	η_{el}=0.0031 P_{el}+38.784

Table 2 displays the flue gas exit temperatures at the outlet of the gas engine.

Table 2: Flue gas exit temperature depending on the nominal capacity of a gas engine

P_{el}	t_{FG}
< 600 kWe	370 ºC
600÷1200 kWe	t_{FG} =0.132 P_{el}+3289.19
>1200 kWe	430 ºC

Table 3 shows the ratio of heat contained in the flue gas and the engine’s cooling water.

Table 3: The ratio of heat contained in the cooling water and the flue gas

P_{el}	$Q_{flue\ gas}/Q_{cooling\ water}$
< 600 kWe	0.53
600÷1000 kWe	1/(0.0008 P_{el}+0.0075)
>1000 kWe	1.07

The amount of heat released to the surroundings by the engine oil varies from 4.4% to 6.2% of the nominal electrical power of the engine. In this study, the average value was considered, which is Q_{oil} = 0.0565 Pel.

Manufacturers provide all details for combustion with 5% oxygen in dry flue gas. In this case, the gas obtained from the national distributor [15] was used, with the following volumetric composition: N_2 = 0.99%, CO_2 = 0.471%, CH_4 = 96.184%, C_2H_6 = 1.624%, C_3H_8 = 0.508%, C_4H_{10} = 0.175%, C_5H_{12} = 0.049%. By combusting the given gas with an excess air coefficient of 1.28, the volumetric composition of the flue gas in wet products is obtained as follows: CO_2 = 7.673%, N_2 = 73.053%, O_2 = 4.25% (5% in dry products), H_2O = 15.024%, with a dew point temperature of 54.02 °C.

Table 4 presents the potentials in the flue gas and oil for selected nominal powers of gas engines and the previously mentioned flue gas. In the table, "40 °C" refers to the thermal energy released when the flue gas is cooled down from 120 °C to 40 °C.

Table 4: The available heat flow rate in the flue gas and oil depending on the installed capacity

P_{el} [kW]	B [m_N^3/s]	Q_{fg} 40ºC [kW]	Q_{fg} 50ºC [kW]	Q_{fg} 60ºC [kW]	Q_{fg} 70ºC [kW]	Q_{oil} [kW]
100	0.008542	31.9	18.1	9.4	7.8	5.7
500	0.037	138.1	78.6	40.6	33.8	28.3
800	0.0587	219.1	124.7	64.4	53.6	45.3
1000	0.073	272.5	155.1	80.0	66.7	56.6
1200	0.0814	303.9	172.9	89.3	74.4	67.9
1500	0.0996	371.8	211.6	109.2	91.0	84.9
2000	0.1283	478.9	272.5	140.7	117.2	113.2

3.4. Heat exchangers

A plate heat exchanger is intended for cooling the oil and heating the water of the district heating system. The overall heat transfer coefficient for these exchangers ranges from 350 to 1200 W/m^{2}K [16]. In this study, the surface area of the exchanger was calculated assuming a heat conduction coefficient of 850 W/m^{2}K and a minimum temperature difference of 3 K in the exchanger. Considering that the oil is cooled in the 55/52°C regime, this exchanger does not operate when the return water temperature of the district heating system exceeds 49°C. In such cases, air cooling is required (see position 6 in Figure 2). The price of the exchanger is calculated based on manufacturer quotes and approximated by the expression:

$$C_{HE} = 627.34 \cdot A + 131.51,$$

where C_{HE} [€] is the price and A [m^2] is the surface area of the exchanger.

The calculation of the FGC is somewhat more complex since it can also operate as a dry flue gas cooler.

Figures 4 and 5 show the modeling procedure and applied algorithms, whereas Table 5 explains the applied nomenclature. Figure 4 shows how the nominal FGC is dimensioned. Based on the nominal condition, i.e. desired performance of the FGC, its surface area is calculated. This is done by calculating the overall heat transfer coefficient by [17] for film condensation of a binary mixture with an inert gas. In the case when the FGC functions as a dry flue gas cooler, the overall heat transfer coefficient decreases and is calculated by [18]. The obtained values were checked by [16] and [19] and agree with the theory as the overall heat transfer coefficient is 1.5 to 2 times higher when the condensation of the flue gas takes place. The previous explains why there are three branches in both algorithms. One is for the FGC, the other for FGC operating as a dry cooler, and the third is for the FGC with two segments: one with and the other without the condensation.

To design the nominal FGC (see Figure 4) the following parameters are required: minimal temperature difference in the FGC Δt_{min}, water inlet t_{wNul} and outlet temperatures t_{wNizl}, and natural gas consumption in the CHP, B_{CHP}. To calculate the actual performance of the FGC (Figure 5) the model requires the following input parameters: overall heat transfer coefficients in the dry k and the condensation zone k_k, natural gas consumption in the CHP B_{CHP}, surface area for the heat exchange A, water flow rate $\dot{m}_w$, and water inlet temperature t_{wul}. Flue gas enthalpies are calculated by [20].

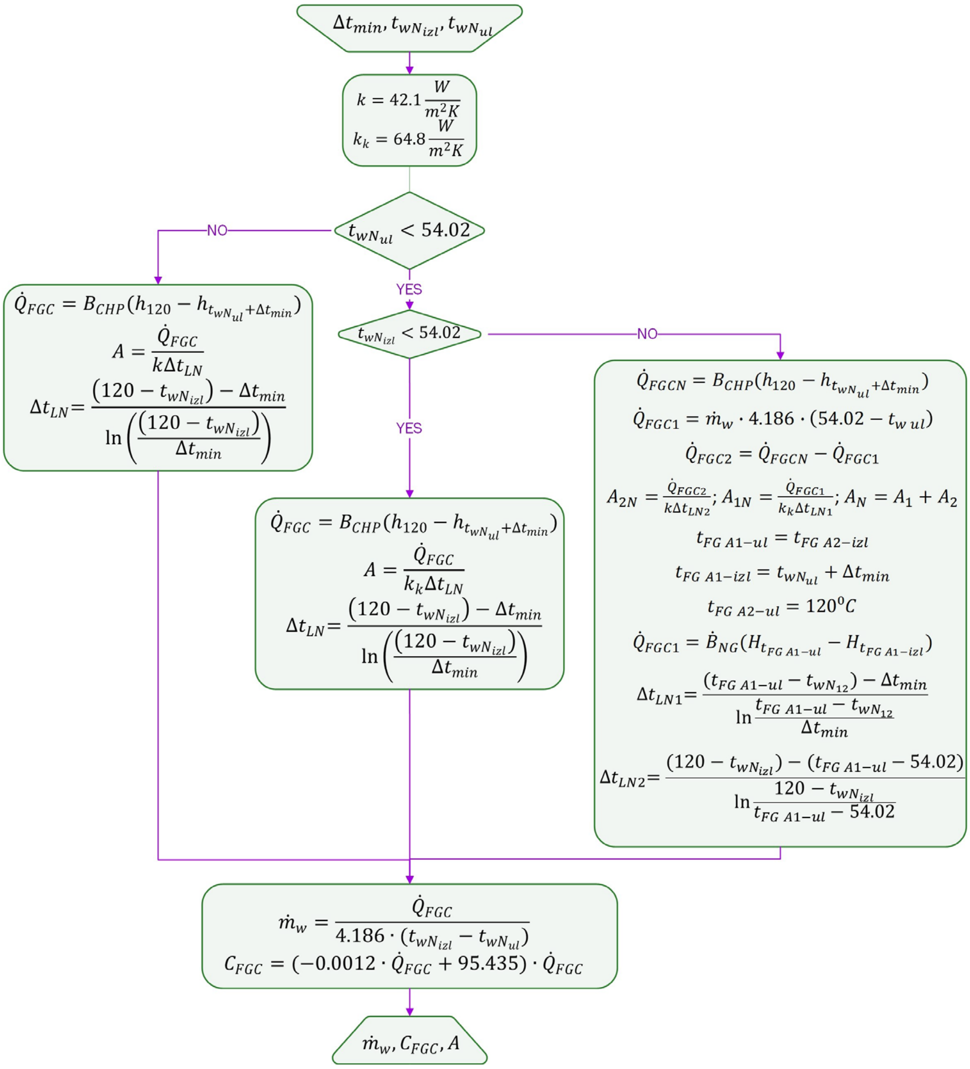

Figure 4. Algorithm for modeling of the nominal FGC

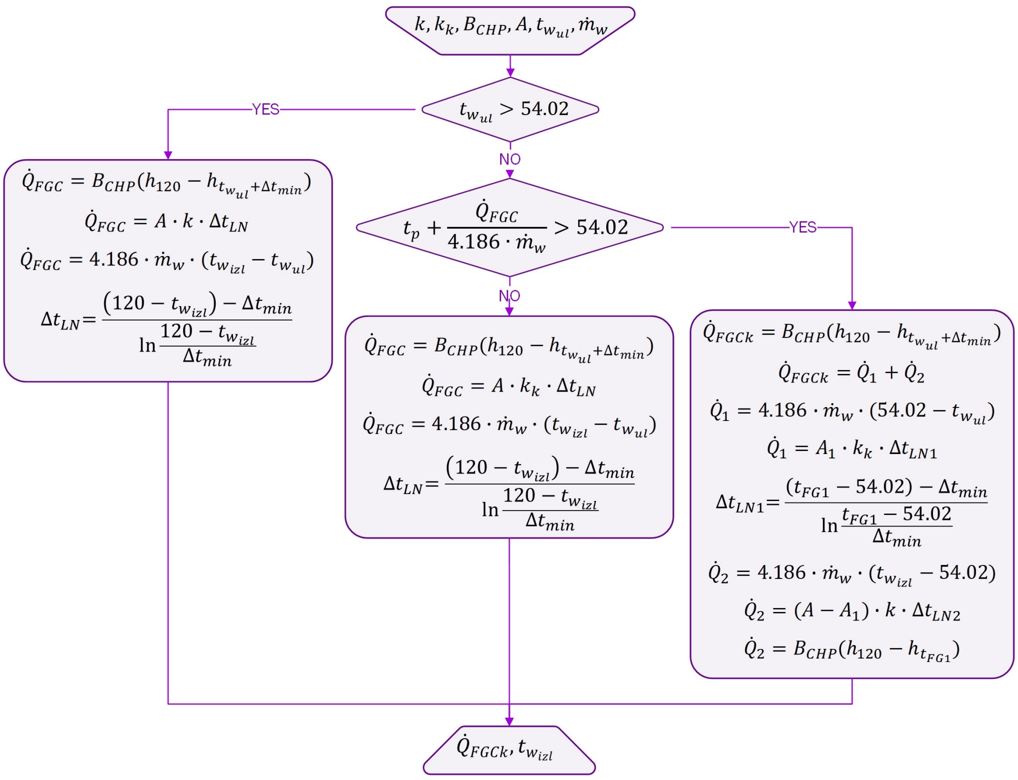

Figure 5. Algorithm for modeling actual performance of the FGC

Table 5: Nomenclature for algorithms shown in Figures 4 and 5.

Terms	Unit and quantity
Δt_{min}	[ºC] minimal temperature difference
t_{wNizl}	[ºC] nominal water temperature at the outlet of the FGC
t_{wNul}	[ºC] nominal water temperature at the inlet of the FGC (DH return)
k	[W/m^{2}K] overall heat transfer coefficient (dry cooling of the flue gas) in the FGC
k_k	[W/m^{2}K] overall heat transfer coefficient in the FGC
A	[m^2] surface area
Δt_{LN}	[ºC] logarithmic temperature difference
h_{120}	[kJ/m$_N^3$] enthalpy of the flue gas at 120ºC per mN3 of natural gas
$h_{t_{wNul}+\Delta t_{min}}$	[kJ/m$_N^3$] enthalpy of the flue gas at the outlet of FGC
B_{CHP}	[m$_N^3$/s] fuel consumption of the FGC
$\dot{m}_w$	[kg/s] water flow rate in FGC
Q_{FGC}	[kW] nominal heat flow rate in the FGC
Q_{FGC1}	[kW] heat flow rate in the part of FGC with condensation
Q_{FGC2}	[kW] heat flow rate in the part of FGC without condensation
Q_{FGCN}	[kW] designed power of the FGC
A_{1N}	[m^2] surface area of the FGC where condensation take place
A_{2N}	[m^2] surface area of the FGC where condensation does not take place
t_{FGA2ul}	[ºC] flue gas temperature between the zones with and without condensation
$t_{FGA2izl}$	[ºC] flue gas temperature at the exit of the dry zone
t_{FGA1ul}	[ºC] flue gas temperature at the entrance of the dry zone
$t_{FGA1izl}$	[ºC] flue gas temperature at the exit of the condensation zone
t_{wN12}	[ºC] nominal water temperature between the condensation and dry zones
Δt_{LN1}	[ºC] logarithmic temperature difference in the condensation part of the FGC
Δt_{LN2}	[ºC] logarithmic temperature difference in the dry part of the FGC
t_{FG1}	[ºC] flue gas temperature between the zones with and without condensation
t_{wizl}	[ºC] water temperature at the outlet of the FGC
Q_{FGCK}	[kW] thermal power of the FGC

4. RESULTS

A test was conducted on an oil cooler operating in the 49/52°C regime. In this operating mode, the cooler utilizes 47.1% of the available energy for oil cooling, which corresponds to 0.471·180·16·0.0565 P_{el} in kWh/year.

The performance of a total of 6 different nominal designs of the FGC was investigated: 40/42°C (nominal water inlet and outlet temperatures), 40/50°C, 48/50°C, 50/55°C, and 52/55°C.

Figure 6 shows the performances of the FGC 48/50ºC for average days in each month during the heating season. The climate conditions dictate that this exchanger operates mostly as an FGC rather than a Dry Flue Gas Cooler (DFGC), even in January. The steeper functions on the graph represent the operation when the water temperature at the exchanger's inlet is very close to the dew point temperature of 54.02°C, resulting in condensation occurring in one part of the exchanger while not in the other. This phenomenon becomes less pronounced as the nominal range of water inlet and outlet temperatures decreases. Interestingly, the OC (Oil Cooler) cannot be used during low outdoor temperatures, and additional energy is not required for FGC operation because the temperature difference is sufficient to overcome the chimney draft. The power of the exchanger is highest at the lowest return water temperatures, specifically temperatures lower than the nominal design conditions. The most significant influence on the thermal power absorbed by the FGC is whether the return water temperature is lower than the dew point temperature of the flue gas. Considering that the convective heat transfer coefficient is 1.5 to 2 times smaller for return water temperatures above the dew point temperature [17], the FGC power is reduced accordingly for water temperatures above the dew point temperature.

Figure 7 illustrates the surface areas of the exchanger based on the nominal temperature regime and the installed power of the gas engine. Lower nominal water temperatures result in larger exchanger surfaces. This is understandable because more energy is extracted from the flue gas. The 40/50 regime has a larger surface area compared to the 40/42 regime because it has a smaller logarithmic temperature difference.

Figure 8 displays the total heat collected by the exchangers during the heating season, depending on the conditions for which they are designed. It is evident that lower nominal temperatures and smaller temperature ranges result in better exchanger performance. The 40/42 exchanger outperforms the 40/50 exchanger because the latter operates more frequently in transitional conditions, where there is no condensation in certain parts of the exchanger (refer to Fig 4).

Exchangers designed for smaller temperature differences in the water operate more frequently in conditions involving condensation. Furthermore, exchangers designed to operate just below the dew point temperature exhibit excellent performance because they achieve even better efficiency at lower water inlet temperatures (corresponding to the peak in Figure 6).

Considering the average efficiency of heat energy production in the analysed boiler plant at 92.2%, a price of 0.287 €/kWh, and the heating value of natural gas at 9.564 kWh/m^3, the payback period of the investment depends not on the cogeneration plant's power but on the conditions for which it is designed. Table 6 shows the payback periods of the investment. Exchangers that are designed very close to the dew point temperature of the flue gas exhibit the most favourable ratio of surface area to total utilized energy for the given climatic conditions. The least favourable ratio for FGC design is in the middle of the expected temperature range for condensation.

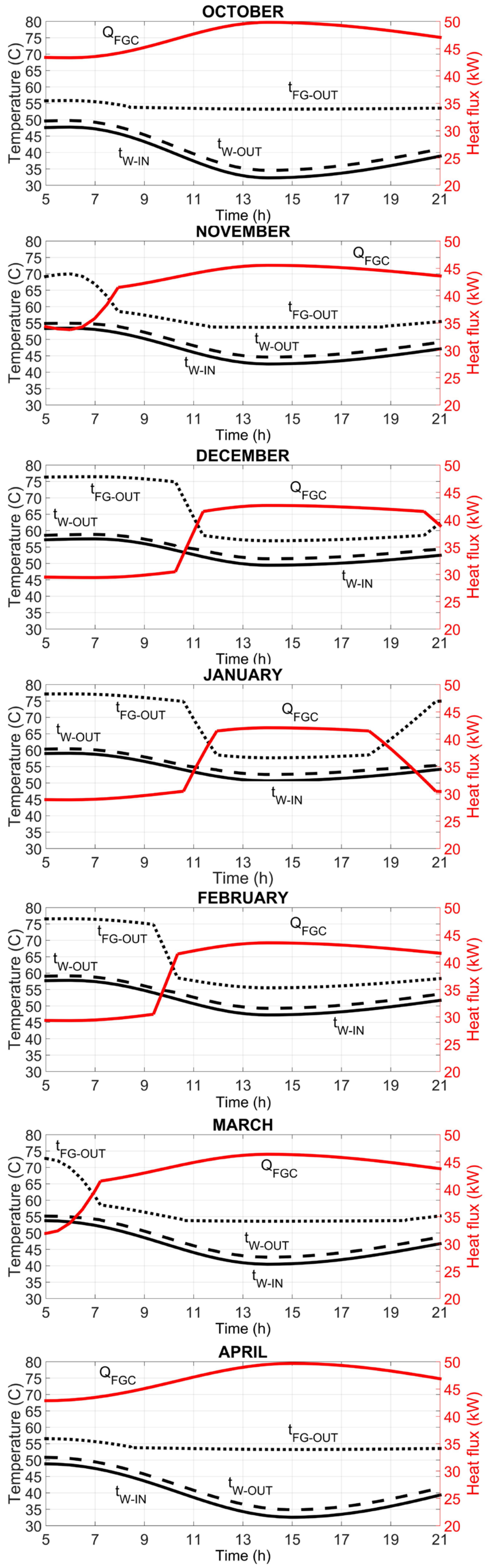

Figure 6: Performance of the FGC with nominal temp. regime 48/50ºC and Δt_{min}=8ºC throught the heating season. $t_{W\text{-}IN}$ temperature of the DH return water, $t_{W\text{-}OUT}$ water preheating temeprature, $t_{FG\text{-}OUT}$ flue gas temeprature after the FGC and Q_{FGC} thermal power of the FGC.

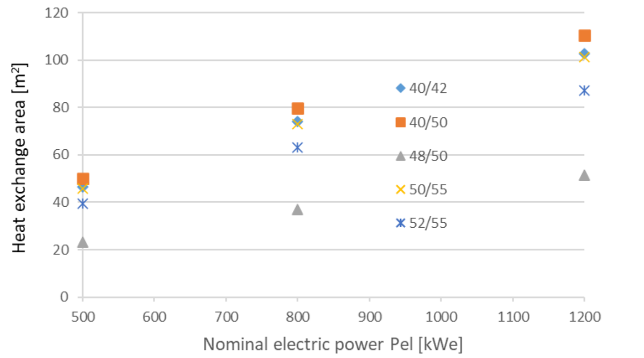

Figure 7: Required surface areas for heat exchange depending on the nominal regime and electric power of the CHP.

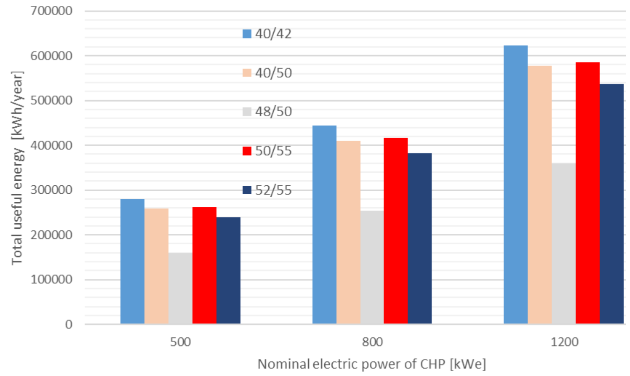

Figure 8: The total heat harvested by the FGC depending on the nominal temperature regime and electric power of the CHP.

Table 6: Simple payback periods depending on nominal temperature regimes (40/42 means water inlet and outlet temperatures are 40ºC and 42ºC, whereas the flue gas inlet and outlet temperatures are 120ºC and 48ºC)

Nominal temp. regime	40/42	40/50	48/50	50/55	52/55
Simple payback period	1.5	1.7	1.3	0.75	0.8

5. CONCLUSIONS

The main conclusions are:

- The usage of HHV from the analyzed gas engines in the case study DH system is highly profitable with a simple payback period in the range from 0.75 to 1.5 years. The real payback period would be longer because of operation and maintenance costs. Although profitable, the system technically complicates the CHP plant as it requires a new chimney and additional pumping power. In the analyzed system, the additional fan power could not be replaced by the usage of heat from the oil cooler.
- 47.1% of the heat liberated by the oil cooler can be used in the DH system.
- The nominal conditions by which the FGC is designed are the most influential factor that determines the profitability of the investment.

- The temperature rise of DH water in the FGC should be as small as possible. In that case, during shorter periods the FGC would operate as a dry flue gas cooler.
- The most profitable FGC are those that are designed to heat DH water to the dew point temperature with as smaller as possible temperature rise.
- The colder the weather the less efficient the analyzed system. At low environment temperatures, the heat from oil cooling could not be used and the FGC operates as a dry flue gas cooler with 1.5 to 2 times smaller capacity.

ACKNOWLEDGEMENTS

This research was supported by the Ministry of Education, Science and Technological Development of the Republic of Serbia (Grant No. 451-03-47/2023-01/200108).

REFERENCES

[1] H. Lund *et al.*, "4th Generation District Heating (4GDH). Integrating smart thermal grids into future sustainable energy systems.," *Energy*, vol. 68, pp. 1–11, 2014, doi: 10.1016/j.energy.2014.02.089.

[2] S. Buffa, M. Cozzini, M. D'Antoni, M. Baratieri, and R. Fedrizzi, "5th generation district heating and cooling systems: A review of existing cases in Europe," *Renew. Sustain. Energy Rev.*, vol. 104, no. February, pp. 504–522, 2019, doi: 10.1016/j.rser.2018.12.059.

[3] H. Lund *et al.*, "Perspectives on fourth and fifth generation district heating," *Energy*, vol. 227, p. 120520, 2021, doi: 10.1016/j.energy.2021.120520.

[4] "Republički hidrometerološki zavod," 2023. https://www.hidmet.gov.rs/ciril/meteorologija/klimatologija.php.

[5] "Toplana Kraljevo elektrana," 2023. https://toplanakv.rs/fotonaponska-elektrana-snage-50-kw-postavljena-na-krovu-centralne-kotlarnice/.

[6] R. Karamarković, M. Nikolić, Đ. Novčić, and D. Šimunović, "Feasibility study for the implementation of a natural-gas-fired CHP plant in JEP Toplana Kraljevo," Kraljevo, 2020.

[7] B. Hebenstreit *et al.*, "Techno-economic study of a heat pump enhanced flue gas heat recovery for biomass boilers," *Biomass and Bioenergy*, vol. 71, no. July 2011, pp. 12–22, 2020, doi: 10.1016/j.biombioe.2014.01.048.

[8] L. Feng, D. Lin, F. Lin, and Z. Xiling, "Application of absorption heat pump and direct-contact total heat exchanger to advanced-recovery flue-gas waste heat for gas boiler," *Sci. Technol. Built Environ.*, vol. 25, no. 2, pp. 149–155, 2019, doi: 10.1080/23744731.2018.1506676.

[9] "Average climate data for Kraljevo 1991-2020," 2021. https://www.hidmet.gov.rs/ciril/meteorologija/stanica_sr_kraljevo.php.

[10] T. A. Huld, M. Šúri, E. D. Dunlop, and F. Micale, "Estimating average daytime and daily temperature profiles within Europe," *Environ. Model. Softw.*, vol. 21, no. 12, pp. 1650–1661, 2006, doi: 10.1016/j.envsoft.2005.07.010.

[11] M. C. Ekwonu, S. Perry, and E. A. Oyedoh, "Modelling and simulation of gas engines using aspen HYSYS," *J. Eng. Sci. Technol. Rev.*, vol. 6, no. 3, pp. 1–4, 2013, doi: 10.25103/jestr.063.01.

[12] Siemens Energy, "SGE-S series gas engines and gen-sets biogas," *S Ser. SL Engines*, 2017, [Online]. Available: https://www.siemens-energy.com/global/en/offerings/power-generation/gas-engines/sl-engines.html.

[13] Siemens, "We power the world with innovative gas turbines," *Siemens gas turbine Portf.*, p. 60, 2017, [Online]. Available: https://assets.new.siemens.com/siemens/assets/api/uuid:ab8578bf-d86f-45d9-a26b-7ac7a274fadd/siemens-gas-turbine-portfolio.pdf.

[14] MAN, "Gas Engines for Power Generation," 2023. https://www.engines.man.eu/man/media/content_medien/doc/global_engines/power/Power_Gas_EN_181016_web.pdf.

[15] SrbijaGas, "Natural Gas Composition," 2023. https://www.srbijagas.com/?page_id=1410.

[16] W. Roetzel, "VDI Heat Atlas," in *VDI Heat Atlas*, 2010, pp. 2–5.

[17] E. Schluder, "VDI Heat Atlas," in *VDI Heat Atlas*, 2010.

[18] S. H. Exchangers, "VDI Heat Atlas," *VDI Heat Atlas*, 2010, doi: 10.1007/978-3-540-77877-6.

[19] D. Che, Y. Liu, and C. Gao, "Evaluation of retrofitting a conventional natural gas fired boiler into a condensing boiler," *Energy Convers. Manag.*, vol. 45, no. 20, pp. 3251–3266, 2004, doi: 10.1016/j.enconman.2004.01.004.

[20] M. Kleiber and R. Joh, "Properties of Pure Fluid Substances," in *VDI Heat Atlas*, 2nd ed., Heidelberg, Germany, 2010, pp. 301–417.

SESSION G

CIVIL ENGINEERING

Masonry development of building construction on the territory of Serbia

Bojan Milošević[1,2*], Vladimir Mandić[1], Dušan Turina[2], Aleksandar Kostić[2], Katarina Krstić[2]
[1] The Faculty of Mechanical Engineering and Civil Engineering in Kraljevo, the University of Kragujevac (Serbia)
[2] Academy of Technical and Art Applied Studies, Belgrade, School of Civil Engineering and Geodesy, Belgrade (Serbia)

Human evolution has led to the development of Civil Engineering and Building Construction and it has not diminished the importance of traditional masonry. The need for quality building material leads to its industrial output. There are a lot of regulations that appear in this process, by which the process of designing, building and maintenance of masonry is defined. The aim of this project is to present the development of masonry system in building construction, masonry units needed for their output, as well as legal standards which define carrying capacity of structural units of these buildings. This project also presents the survey results conducted among constructors and their knowledge of masonry regulations.

Keywords: masonry units, masonry, masonry design redulations

1. INTRODUCTION

From the beginning of the world till today, masonry represents the most common type of building structures. During the period from the 17th century till the 20th century, a lot of buildings were built as solid masonry systems, especially in Europe and a lot of them are still in function [1]. Following the European model of solid masonry, the solid system usage also began on the territory of Serbia, firstly on facilities of importance to the state administration.

At the end of the 19th century and during the first half of the 20th century, a lot of masonry structures were built for the needs of public and state services [2]. Among the first buildings built in solid system was State Office – Djumrukana (Figure 1). Building changes on state and public structures, led to changes in building residential dwellings. Therefore, these structures were built as solid constructions with brick and stone walls instead in post and petrail system. During the 20th century, the buildings in solid masonry system were usually residential dwellings, while public buildings were mostly built combining contemporary materials.

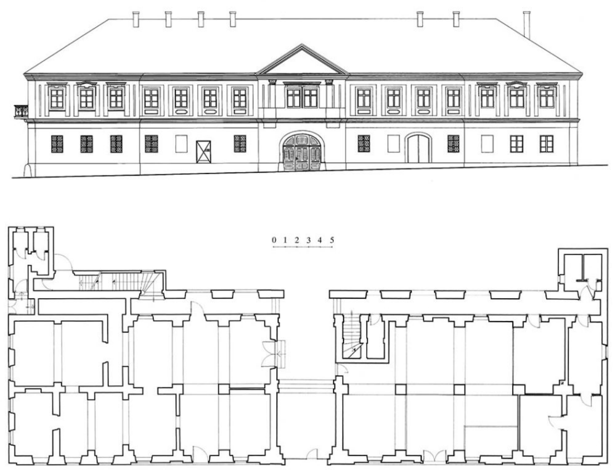

Figure 1: Building facade and base of Customs office - Djumrukana [3]

Although masonry lost its lead regarding structural units of modern buildings, the usage of masonry and masonry units is, even today, the inevitable part of building construction structures. Today, masonry is present in building individual residential dwellings, low-rise office buildings, administrative, public, industrial and agricultural structures while it is rarely applied in building bridges and tunnels [4].

In the past, the buildings were mostly carried out as solid masonry systems, applying brick, which was the basic masonry unit, while today, most of the masonry systems are built combining other materials, such as reinforced concrete. Material development in building industry led to the usage of the units not made of clay, as the basic masonry material today.

Defining dimensions of structural units moved from the empirical to the calculations based on precisely defined theoretical settings. The development of structural systems of building construction required appropriate regulations which defined analysis procedure and the production of the required building material as well as building structures.

The modernity of masonry units has been kept during the long period of construction thanks to cheap and simple output, ecological materials, simple construction and good heat features (masonry calculations) [5]. The aim of this project is to present the development of solid masonry on the territory of the Republic of Serbia, as well as applied materials, dimensions of structural elements and legal regulations which followed the building of the structures. This project also presents a survey regarding the knowledge of legal regulations and masonry types within designing and performance practice on the territory of the Republic of Serbia

2. THE DEVELOPMENT OF BUILDING INDUSTRY – MASONRY UNITS

We can say that stone and wood were the first materials used for building residential dwellings. The development of masonry materials moved towards applying lighter masonry units, so the units made of mud were used instead of stone. They were dried in the sun at

*Corresponding author: Hajduk Stankov 2, 11050 Beograd; milosevic.b@mfkv.kg.ac.rs

first, and then, by developing the output process, baked in furnaces. Because of the simpler and cheaper construction process, brick took the lead in building construction process over stone elements.

The hard process of hand modelling masonry units was industrialized in the 19th century. In 1850, in England, Joseph Gibbs patented hollow blocks using wooden molds, but made it clear that the cavities should be filled during the building construction. In America, S. Palmer patented the machine for the output of hollow blocks, which were large dimensions and not that simple to use.

Since Austria had a long tradition in the brick output, the quality of their products was known throughout Europe. At first, as a result of importing machines from Austria, masonry units in Serbia had the same dimensions as the ones used in Austria. The development of building output encouraged the rapid development of industrial output of building materials on the territory of the Republic of Serbia.

Figure 2: Brick with logo [6]

Most of the brickyards on the territory of Vojvodina began to work in the second half of the 19th century when a lot of brick and roofing tile shops were opened. In that period, roofing tile and brick from Apatin stood out representing quality and durability, and as such, they were exported to Budapest. At one point, there were about forty-five brickyards in Apatin, and one of the biggest was owned by Johan Mayer.

As there were a lot of brickyards on the territory of Vojvodina, each of the owners made bricks which size depended on the molds they had, so there were a lot of different brick sizes on the market, which was a problem for the builders. Because of the possible misuse during the trade, the brickyard owners labelled the bricks using their name-logo. (Figure 2.)

The first brickyard in Valjevo was opened in 1832 by order of Prince Milos, for the church building needs. The brick was also needed for the works on Nenadovic Tower, which was a gunpowder mill at that time. Soon, a lot of roofing tile and brick shops were opened and some of them became strong industrial facilities.

At the beginning of the 20th century, larger, closed furnaces were gradually used instead of the small ones and they were known as "svabare", which, because of the alternating ignition and attenuation, used a lot of wood. Later, Ringle's massive and round annular furnaces appeared with big chimneys. During one burning process, "svabara" could be stored with approximately thirty thousand bricks, roofing tiles or Spanish tiles. In this period, brick and roofing top work was considered seasonal and was carried out only during summer months – from May to September.

At the end of the 19th century and at the beginning of the 20th century, the industries for brick and roofing tile output known as Arapovic industry, Ignjatovic industry, Petkovic industry and Djura's brickyard worked on the territory of Valjevo. This brickyard was significant for a great period of building process in Valjevo. In 1948, the output in Djura's brickyard was transferred into state's ownership, while in 1951, it was returned to the owner to a limited use. However, in 1958, the brickyard was nationalized and worked within the GP Jablanica company. In 1970, due to the lack of raw materials and fuel, the brickyard was closed [7].

Figure 3: D. Stankovica brickyard in Paracin [8]

After First World War, four brickyards worked in Paracin because of the increased needs for building material. At the same time came the technology change of brick construction, from handmade to machine-made. Handmade brick was made at the beginning but the output was soon moved to machine-made brick. Stankovic brickyard stood out in terms of technology (Figure 3). It produced machine-made brick while the others produced handmade brick. In 1948, Stankovic brickyard was forfeited and continued to work by the name "Neimar" (a builder), until 1973 when it stopped working due to the lack of quality raw materials [8].

In 1923, Paunovic brothers from Vukovar and Baron Josif Rajacic from Sremski Karlovci opened a brickyard in 1923 in Strazilovo, which was nationalized after the Second World War. In 1955, masonry hollow units with fine sides were produced in this brickyard for the first time (Figure 4). After all the transformations that it has been through, this brickyard is still one of the leading manufacturers of masonry blocks and clay products for mezzanine floors in Serbia [9].

Figure 4: Block [9]

The process of building structures was, apart from introducing new materials, also under the influence of the means development for construction equipment and tools performances, which became more efficient and more modern. In the first period of the industrial brick output on the territory of Serbia, its dimension was different and mostly depended on the manufacturer who participated in the production. After First World War, brick dimensions were 14/29/6.5 (width/length/height), which was the result of import and production process from Austria. A smaller brick size was used in Germany, 12/25/6.5 (width/length/height) which was accepted in 1932 on the territory of the Republic of Serbia [10]. The old brick size had been used until 1933.

In the 19th century, the production of masonry units in the European Union countries was at a significant level and so, besides solid bricks, there were also keyed bricks that could fit in without using mortar. In the middle of the 19th century, hollow masonry units appear, whose output was carried out using the machines that extruded clay through the molds under pressure. Although the people were familiar with modern technologies regarding the production of brick products in Serbia in the 19th century, the only masonry unit that was used was solid brick.

Materials that used to be regarded as waste, were used for the production of masonry units. From 1900, clinker, which was treated as waste, after years of examination, became applied building material. In 1911, the base for clinker usage from blast furnaces was set for concrete output. In 1917, Francis J. Straub patented clinker blocks

Thermoblocks were made in 1924, when a Swedish scientist, Johan Axel Eriksson patented a new material for quick, easy and ecological construction. Industrial output of aerated concrete began in Sweden in 1929. It was in 1951 that it began in Germany, and has been in progress until today. In 2005, the production of masonry units made of aerated concrete began on the territory of Serbia. Masonry units made of aerated concrete can be used for building all types of walls.

Masonry units that are used today are made of the most different materials. Today, the shape and the dimensions of masonry units are defined by legal standards and divided into specific groups and categories. Besides the carrying capacity norm, these units often comply with the required thermal conditions

3. THE DEVELOPMENT OF MASONRY SYSTEMS

The changes within the building output started with the political changes on the territory of Serbia, at the beginning of the 19th century. There were also changes in structural systems of buildings with the appearance of new building materials. This period also brought the gradual change of the system, from Balkan post and petrail buildings to city houses by European model [4,10,11]. At first, embracing solid building system within the masonry did not mean completely leaving post and petrail system at building residential dwellings.

The construction of buildings with brick as a dominant material for wall production, was part of solid structural system and by 1919, reinforced concrete had been used occasionally, mostly with large public buildings which had bigger span and complex structural system. Rubble stone and chipped stone were mostly used for the construction of cellar room walls. In order to prevent displacing and separation of certain parts of the building, the walls at mezzanine floor level, were planted with clamps and turn buckles.

At first, the mezzanine floor at multi-storey buildings was built of logs arranged one next to another, as wooden construction, from brick vaults or bricks placed between steel beams (traverse ceiling). With the appearance of concrete, mezzanine floor was built as ribbed floor slab rested on the walls with horizontal confining members placed onto them.

The big innovation and change in the structural system of masonry came with the appearance of reinforced concrete which was primarily used for the production of mezzanine floors and foundations, while brick was still the only material used for wall production. The usage of reinforced concrete on the territory of Serbia was left out in the period after First World War, due to the lack of cement and reinforced bar [12].

Revolution in building construction which was the result of new material introduction, led to discontinuity in knowledge dissemination regarding the dominant masonry model. The need for the construction to slowly move from empirical rules to numerical method of defining the structural system dimensions came with the structural system development of building. This method was based on mechanical features of the materials. The first structural analysis was carried out for mezzanine floors made of reinforced concrete.

Until the middle of the 20th century, the masonry layout as solid system was carried out applying the empirical methods which were used for centuries. The carrying capacity of solid masonry was based on the big cross-sections of structural elements which caused the appearance of low voltages in them. This way of solid construction layout made a big mass which turned to be uneconomical in modern civil engineering and building construction, due to high labor costs and a large consumption of building material [13].

At first, the building foundations were made of brick or natural stone, whereby hard-burnt clinker brick was usually used for foundation construction of smaller projects. With the appearance of reinforced concrete, building of the foundations was carried out by setting up foundation bays or, rarely, foundation plates under the whole structure, or square plates under the stanchions.

According to Belgrade Building code, from 1897, the masonry technical features were defined, as well as the rules for its construction. The defined structural wall thickness was, that the walls of the highest level dig had to be, at least a brick and a half thick. In every lower level dig, the wall width was thickened by half a brick (Figure 5) and could have the same width through two level digs (Figure 6). Structural walls of ground floor facilities could be a brick thick if the span between the structural walls was not over 5 metres and the height of the walls was not over 3 metres. The defined partition wall thickness was half a brick unless they were neither higher than 4.2 metres nor longer than 6.0 metres. As the mezzanine floors between the basement and the ground floor were mostly built using steel traverse, the placing of the steel traverse onto the walls with the thickness less than a brick and a half, was prohibited.

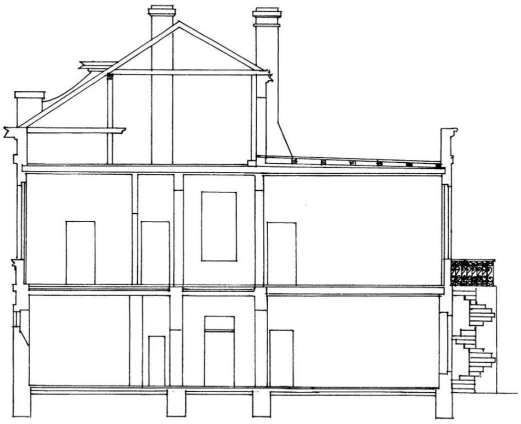

Figure 5: The house of Rista and Beta Vukanovic – cross section [14]

In the development phase, the usage of solid system wall thickness depended on the depth of the room (space between structural walls). In 1931, the new brick size was adopted and the structural wall thickness was defined. If the span between the structural walls was not over 4.0 metres, the thickness of the structural or partition wall toward the adjacent flat was 25 centimetres. For the span from 4 metres to 6.5 metres the wall thickness was 38 centimetres, for the span from 6.5 metres to 8.5 metres the thickness was 51 centimetres and for the span from 8.5 metres to 10 metres, the thickness was 64 centimetres. Paying attention to the height of the structure, the thickness of the wall was increasing from the top to the bottom of the structure per brick width. (Figure 6) In this way, the dimensioning of brick walls is approximate while in case of reinforced concrete usage, structural analysis is required. The stanchions of different cross-sections and chimneys were also built in solid masonry system.

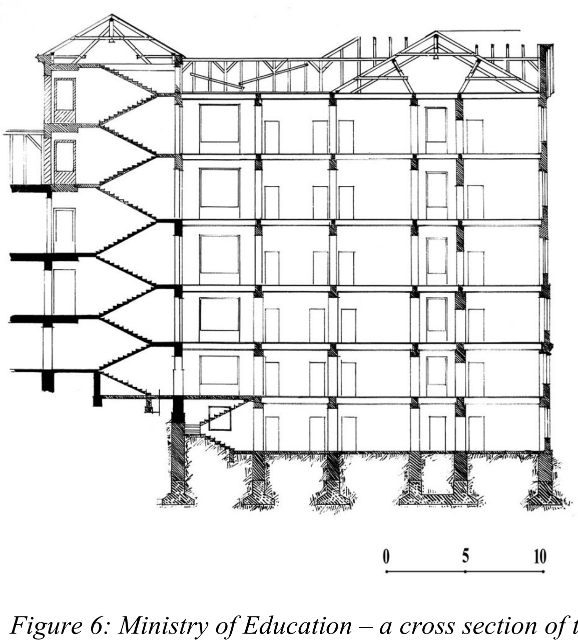

Figure 6: Ministry of Education – a cross section of the building [15]

In modern masonry, the walls are less thick than the ones built at the beginning of the 20th century. According to the current regulations on the territory of the Republic of Serbia, minimum structural wall thickness required is 10 centimetres, whereby full masonry units should be used and not the ones with holes.

The reduction of wall thickness resulted in increasing the tensile stress in the walls due to the shear force in wall level. In the middle of the 20th century, the masonry with horizontal confining members was built at first, on the territory of the Republic of Serbia. They were built without vertical confining members and rigid ceilings. The bigger usage of reinforced concrete led to building structures with horizontal confining members and rigid reinforced concrete ceilings, which depended on the floors of the building with or without vertical confining members. (Figure 6)

4. REGULATIONS DEVELOPMENT

The first laws in Civil Engineering and Building Construction came in the second half of the 19th century, regarding the fire protection problems and dwelling conditions. Following the model of European laws, Belgrade Building Act was defined in 1896, which mostly consisted of building construction regulations, while the technical references were defined by the special building code [16,17,18]. In this way, the old techniques of building projects were slowly deserted. According to the law from 1896, the brick dimension 14/29/6.5 (width/length/height) was defined for the first time and by the end of the 19th century, it had been changed depending on the manufacturer.

A thorough explanation of the regulations, defined by the law in 1896, was given in Belgrade Building code, in 1897. Following general regulations, this code defined the form of engineering documents required for the building application as well as placing the structure next to property line. The engineering specifications regarding the building structure were defined by regulations, as well as structural wall thickness, which included external walls, medium load-bearing walls and those with the chimneys.

The building and legal coordination of legal standards began after First World War on the territory of Yugoslavia. It was completed in 1920, by publishing Yugoslavian engineering terminology. In 1925, the content of the following Building act appeared and it was published in 1931. This act included the planning, organization and construction of buildings and, as such, it had been used until the end of the Second World War, when it got new regulations and additions. The Building act from 1931 introduced the possibility of concrete and reinforced concrete usage for the structural unit construction together with required structural analysis.

The beginning of the 20th century was significant, not only because of the Building act but also, the building standards by which the structural material features were defined. The features for the bricks made of clay and the ones made of lime and sand were defined by the standards and adopted in 1932. The masonry designing was included in Temporary technical regulations for brick walls, which was put into effect in 1949. Significant changes in project designing happened after a disastrous earthquake in

Skopje in 1963. That period was a crossroad for setting up detailed regulations for seismically active areas. Code on technical measures and conditions for building wall execution was adopted in 1970.

The following generation of rules and regulations was put into effect during the period from 1980 to 2020, with detailed designing regulations. In this period, Code on technical standards for building construction structures in seismic areas appeared in 1981, as well as Code on technical standards for brick walls in 1991. For structure designing of building construction, Code on building structures from 2019 was also important. These regulations had been valid until 2020, when European standards – Eurocodes were introduced on the territory of the Republic of Serbia, whereas the current technical regulations and rules were no longer efficient.

The following generation of rules and regulations was put into effect during the period from 1980 to 2020, with detailed designing regulations. In this period, Code on technical standards for building construction structures in seismic areas appeared in 1981, as well as Code on technical standards for brick walls in 1991. For structure designing of building construction, Code on building structures from 2019 was also important. These regulations had been valid until 2020, when European standards – Eurocodes were introduced on the territory of the Republic of Serbia, whereas the current technical regulations and rules were no longer efficient.

By putting European technical regulations into effect, a certain knowledge of principles and analyses are required for Civil Engineers because, they are different from previous regulations. In Eurocode 6, there are general rules for designing unreinforced and reinforced masonry where it is necessary to define national annexes, which should be components to European technical regulations. In Eurocode 6, [19] the norms for the analysis of prestressed walls built of masonry units, appeared for the first time.

For appropriate masonry designing in seismically active areas, the knowledge of Eurocode 8 is also required. In this regulation there are defined conditions regarding the masonry material and also the limits, regarding the dimensions and form of the structures as well as structural wall dimensions for different types of masonry. When it comes to designing and construction of simple structures, according to Eurocode 8, [20] a special safety structure checking due to effects of seismic forces is not required, if a Design Engineer follows the basic rules defined by this standard [21].

5. SURVEY

This project also includes a survey conducted among experts in Civil Engineering and Building Construction regarding their knowledge of criterion, important for building construction structures as well as solid masonry. The interview consists of the following questions:

1. How old are you?
2. What is the level of professional qualification that you finished?
3. Did you attend the course regarding the masonry analysis during the studies?
4. Which field do you work in?
5. Have you worked on the designing projects?
6. Have you worked on the project execution?
7. The current regulation for masonry designing in Serbia is?
8. Which masonry analysis software have you heard of?
9. Would you attend the masonry analysis course applying the appropriate software?
10. Which manufacturer of masonry units have you heard of?
11. Would you consider it significant if a manufacturer of masonry units offers you a technical support regarding the designing and the installment of the products?

The first group of questions includes basic data: age, professional qualification of the respondents, whether the respondent attended the course regarding the masonry analysis or worked on projects regarding the analysis and masonry execution. The second group of questions includes the knowledge of the respondents regarding the current situation of material market on the territory of the Republic of Serbia, current legal regulations, the possibility of using the appropriate masonry analysis software as well as the presence of masonry units by different manufacturers which can be found on the territory of the Republic of Serbia.

5.1. Analysis of survey results

The survey among people who work on masonry designing and execution in building construction has been conducted by sending a google questionnaire to their email addresses. The survey analysis has been done based on the results. This survey has been conducted among 122 respondents and the number of the respondents by their age has been shown on the graph (Figure 7). Two thirds of the respondents are 25 to 45 years old while one third are 45 to 65 yearold. When it comes to professional qualification (Table 1.), two thirds of the respondents are related to Civil Engineering and Building Construction while one third of the respondents are related to Architecture.

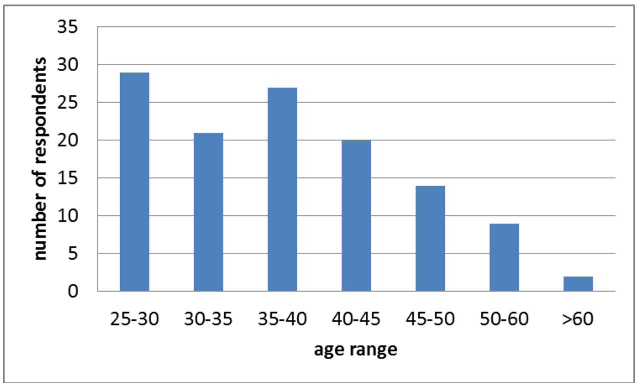

Figure 7: Age range

Table 1: Professional qualification of the respondent

Professional qualification	Number of respondenst
Bachelor with Honours in Civil Engineering	29
Bachelor with Honours in Architecture	16
Civil engineer	15
Architectural engineer	3
Bachelor in Architecture	2
Bachelor in Civil Engineering	2
Master in Architecture	9
Master in Civil Engineering	19
Professional Bachelor's degree in Architecture	4
Professional Master's degree in Civil Engineering	23

When asked whether they had attended Masonry course, 39 per cent replied negative, while 61 per cent replied they had attended the course (Figure 8). Based on professional qualification and the age of the respondent, we can see that Masonry course was not attended by older adults as well as the ones related to Architecture.

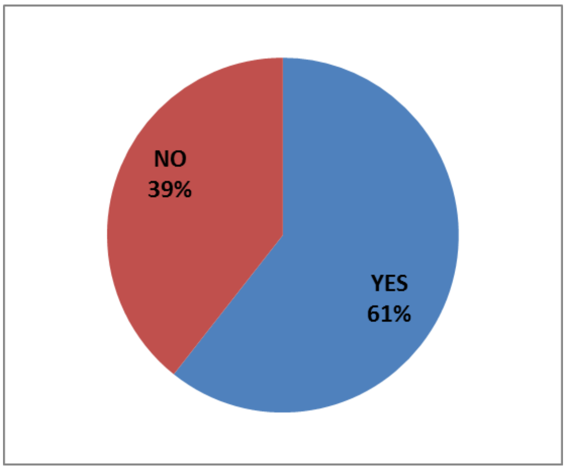

Figure 8: Percentage of the respondents who attended Masonry course during the studies

When asked which field they worked in, out of the total number, there were 149 answers. Out of 64 per cent of the respondents who worked on masonry projects, 27 per cent worked on masonry projects of execution, 37 per cent worked on masonry designing projects, 30 per cent performed other types of work while 6 per cent did not perform any work in the field of Civil Engineering and Building Construction (Figure 9).

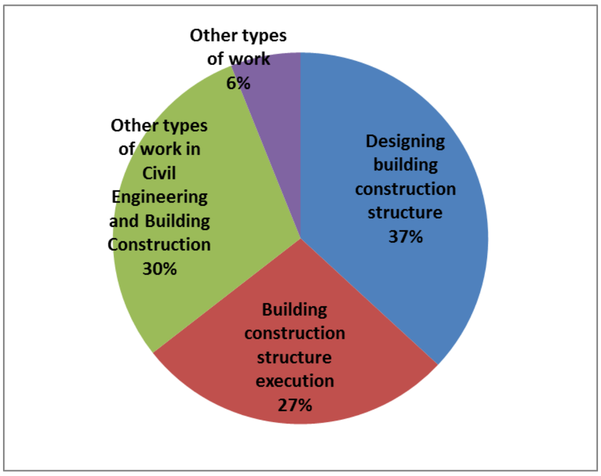

Figure 9: Percentage of the respondents based on the types of work they performed at work

When asked whether they had worked on masonry designing projects, there were 205 answers. Out of 46 per cent of the respondents who worked on projects regarding masonry designing, 14 per cent worked on projects of masonry designing and reinforced masonry, 18 per cent worked on confined masonry projects, 29 per cent worked on projects of confined reinforced masonry with solid walls, while 25 per cent did not work on masonry designing (Figure 10).

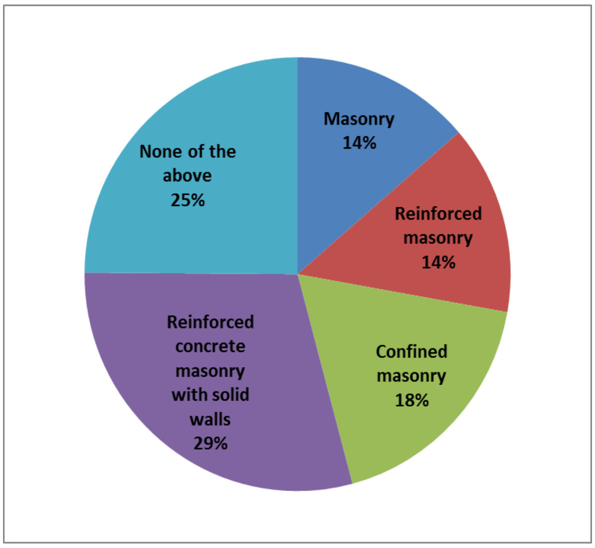

Figure 10: Percentage of the respondents who worked on the designing of specific types of masonry

When asked whether they had worked on masonry execution projects, there were 236 answers. Out of 54 per cent of the respondents who worked on projects regarding masonry execution, 19 per cent worked on masonry execution projects, 15 per cent worked on reinforced masonry projects, 20 per cent worked on confined masonry projects, 24 per cent worked on projects of confined masonry with solid walls while 22 per cent did not work on masonry execution (Figure 11).

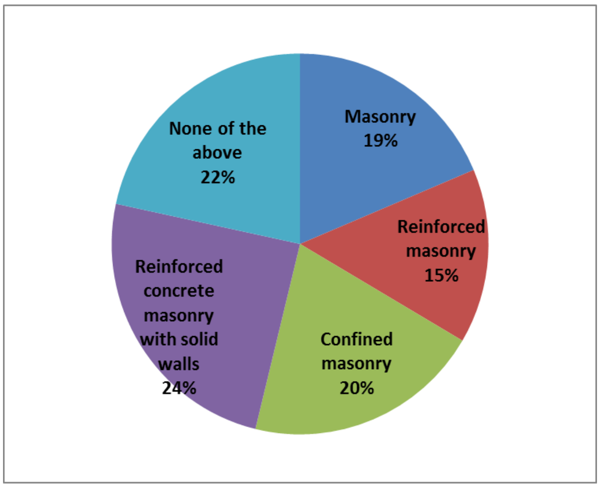

Figure 11: Percentage of the respondents who worked on projects of specific types of masonry

Out of the total number of the respondents, 65 per cent replied correctly while 35 per cent replied incorrectly, regarding the current regulation for masonry analysis in the Republic of Serbia (Figure 12). The number of the respondents who are not familiar with the current masonry regulation is a little bit bigger than one third, which can be related to respondent's age as well as the number of the respondents related to Architecture.

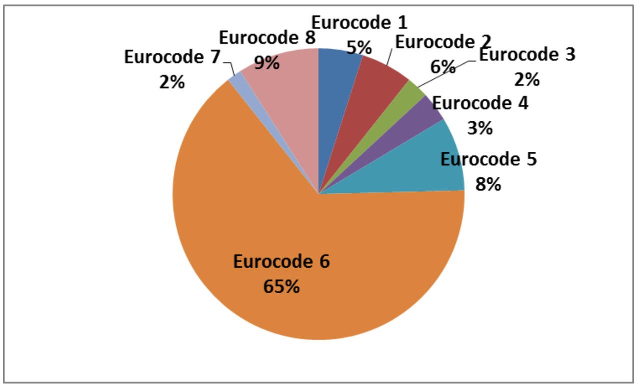

Figure 12: Percentage of the respondents regarding the knowledge of current technical regulation in the Republic of Serbia

When asked whether they knew any masonry analysis software, there were 149 answers, which showed that the most familiar was Radimpex software with 49 per cent, followed by AmQuake with 31 per cent. Other softwares were less familiar on the territory of the Republic of Serbia and all together, that is 20 per cent out of the total number of the answers (Figure 13).

When asked whether they would attend software training course regarding masonry analysis, all the respondents replied, out of which, 54 per cent replied they were interested in the course while 36 per cent replied negative (Figure 14). We can say that the number of the uninterested respondents match the number of older adults as well as the ones related to Architecture.

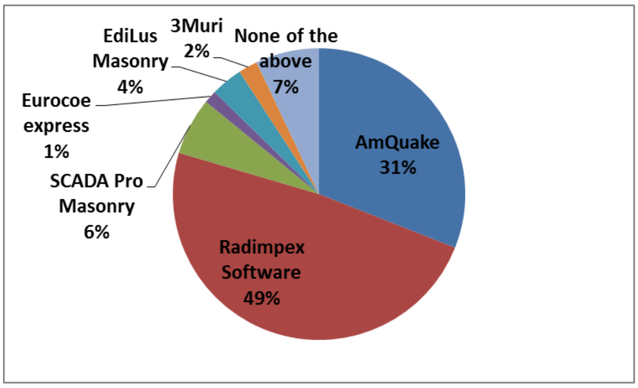

Figure 13: Percentage of the respondents regarding their knowledge of masonry analysis softwares

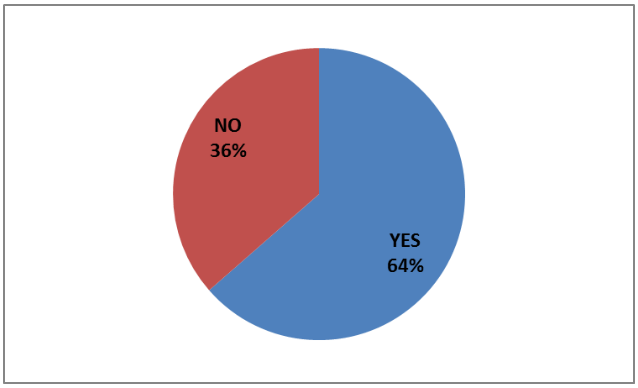

Figure 14: Percentage of the respondents interested in attending appropriate software training course regarding masonry analysis

When it comes to manufacturers of masonry units known on the territory of the Republic of Serbia, there were 396 answers. The least known are the products of Univerzum Ciglana, while the products of other manufacturers are generally known (Figure 15).

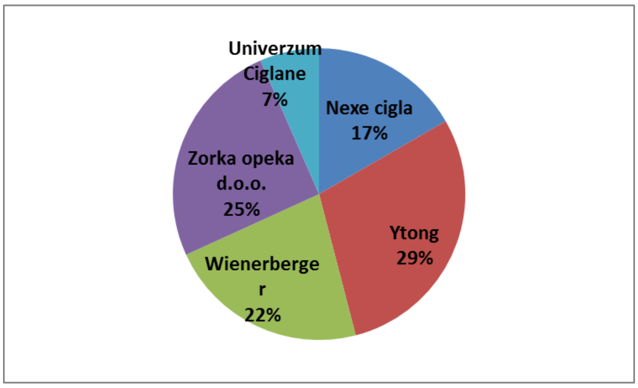

Figure 15: Percentage of the respondents regarding their knowledge of the manufacturers of masonry units in the Republic of Serbia

In case manufacturers of masonry units offer technical support regarding the designing and the process of product installment, 86 per cent replied it would be a significant support, 3 per cent replied the support would not be needed while 11 per cent have no opinion regarding the subject (Figure 16).

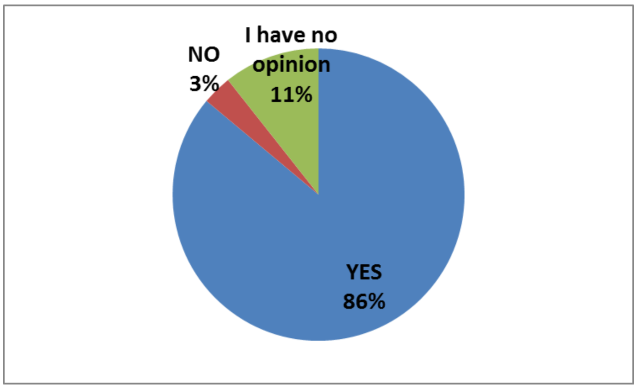

Figure 16: Percentage of the respondents interested in technical support of the manufacturers of masonry units

This survey shows that one third of the respondents are not familiar with masonry legal regulations and also, not interested in attending appropriate software course regarding masonry analysis. It is very important to know that a lot of respondents are interested in technical support which would be given by manufacturers of masonry units regarding the designing process and the installment of masonry units.

6. CONCLUSION

In the end, we can see that the situation, regarding masonry structures in building construction, is various and unadjusted. From the moment of masonry system usage till today, there have been changes in applying appropriate materials (masonry units, binding agent, concrete) for masonry, as well as structural systems, the way of defining the size of structural elements and current regulations.

Putting Eurocode 6 into effect, within one standard, all the required regulations for appropriate designing of the masonry system structures are included. This regulation includes the variety of masonry units, which can be used for building different structural systems of building constructions. Eurocode 6 enables simple and even analysis procedure, which defines clear guidelines regarding masonry and masonry resistance to fire.

ACKNOWLEDGEMENTS

The research presented in this project has been done within the Project for "Innovation of masonry articles in building construction" financed by Ministry of Education, Science and Technological Development, "The development of higher education 2021/2022".

REFERENCES

[1] A.Čaušević, N. Rustempašić, "Rekonstrukcija zidanih objekata visokogradnje", Arhitektonski fakultet, Univerzitet u Sarajevu (Bosna i Hercegovina), (2014)

[2] A. Banković, Z. Vuksanović-Macura, „Stvaranje modernog Beograda od 1815. do 1964. iz zbirke muzeja grada Beograda", Muzej grada Beograda (Srbija), (2019)

[3] 2023. https://beogradskonasledje.rs/katalog_kd/carinarnica

[4] Z. Vuksanović-Macura, "Život na Ivici, stanovanje sirotinje u Beogradu od 1919-1941", Orion, Boegrad (Srbija), (2018)

[5] R. Salatić, R. Mandić, M. Marinković, "Seizmički proračun zidanih zgrada prema Evrokodu 8", Izgradnja, Vol 67 (5-6), pp. 221-234, (2013)

[6] 2023. https://www.secenacigla.rs/

[7] D. POPOVIĆ, "ĐURINA CIGLANA", Glasnik, br.39, Arhiv Valjeva, (2005)

[8] M. Pekić, V. Vučković, D.Kaličanin, „Ciglana Dragutina Stankovića iz Paraćina", ETNO-KULTUROLOŠKI ZBORNIK, Knjiga XXIV, pp. 49-60, (2021)

[9] 2023. https://nexecigla.polet.rs/product-item/

[10] Lj. Đukanović, "Razvoj tehnika građenja u stambenoj arhitekturi Beograda tokom 19. i početkom 20. veka" Nasleđe, Vol 18, pp. 49-63, (2017)

[11] Lj. Đukanović, "Tehnike građenja i razvoj građevinske delatnosti u stambenoj arhitekturi Beograda u međuratnom periodu" Nasleđe, Vol. 20, pp. 69-87, (2019)

[12] M. Aćić and B. Stevanović, "Zidane zgrade – greške i propusti u građevinskoj praksi" Izgradnja, Vol. 65(5-6), pp. 3315–338, (2011)

[13] B. Stevanović, "Zidane konstrukcije", Materijali i konstrukcije, vol 48 (4), pp. 50-56,(2005)

[14] 2023. https://beogradskonasledje.rs/katalog_kd/kuca-bete-i-riste-vukanovic

[15] 2023. https://beogradskonasledje.rs/katalog_kd/zgrada-ministarstva-prosvete-2

[16] M. Tomažević, "Uvođenje evrokodova i proračun seizmičke otpornosti zidanih konstrukcija", Materijali i konstrukcije, Vol 51 (2), pp. 3-24, (2008)

[17] B. Stevanović, „Evrokod 6 – Zidane konstrukcije", Izgradnja, Vol. 64, (1-2), pp. 79-82, (2010)

[18] B.Milošević, "AmQuake: Statička i dinaimčka analiza zidanih konstrukcija", Akademija tehničko umetničkih strukovnih studija u Beogradu, Fakultet za mašinstvo i građevinarstvo u Kraljevu, Univezitet u Kragujevcu (Srbija), (2022)

[19] Evrokodovi za konstrukcije Evrokod 8: EN 1998-1-1:2004, Proračun seizmički otpornih konstrukcija. Deo 1-1: Opšta pravila, seizmička dejstva i pravila za zgrade, Građevinski fakultet Univerziteta u Beogradu, Beograd, 2009.

[20] Evrokodovi za konstrukcije Evrokod 6: EN 1996-1-1:2005, Proračun zidanih konstrukcija. Deo 1-1:Opšta pravila za armirane i nearmirane zidane konstrukcije, Građevinski fakultet Univerziteta u Beogradu, Beograd,

[21] S. Marinković, B. Milošević, Ž. Petrović, D. Turina, D. Penava, „Pushover analysis for upgrading of existing residential masonry building", Engineering TODAY, Vol 1, No. 3 (2022), pp. 31-40 Faculty of Mechanical and Civil Enginnering in Kraljevo, ISSN 2812-9474, E-ISSN 2812-9938 https://doi.org/10.5937/engtoday2203031M

Kriging interpolation of precipitation for Lake Ćelije catchment

Vladimir Mandić[1], Slobodan Kolaković[2*], Milan Stojković[3], Bojan Milošević[1,4], Iva Despotović[1,4]

[1] Faculty of mechanical and civil engineering in Kraljevo, University of Kragujevac, Kraljevo (Serbia)
[2] Faculty of technical sciences, University of Novi Sad, Novi Sad (Serbia)
[3] The Institute for Artificial Intelligence Research and Development of Serbia, Novi Sad (Serbia)
[4] Academy of Technical and Art Applied Studies, Belgrade, School of Civil Engineering and Geodesy, Belgrade (Serbia)

The research analyzed the necessary conditions for the successful application of the Kriging method of spatial interpolation for the purposes of average annual precipitation interpolation on a certain area. The Kriging method is widely used in the field of interpolation of spatially distributed data, which also includes rainfall data. The paper analyzes the influence of the number of rainfall gauging stations, as well as model parameter adoption, on the results of spatial interpolation of precipitation. Precipitation interpolation was performed for the experimental catchment of Lake Ćelije, which is located on the Rasina River in the Republic of Serbia. The conducted research presents conclusionson on the influence of the number of rainfall gauging stations on the interpolation results, as well as the suggestions for the practical application of the mentioned method for the needs of spatial interpolation of average annual precipitation on a cathcment.

Keywords: Kriging, Average annual precipitation, Hydrology, Spatial interpolation

1. INTRODUCTION

Precipitation data plays a crucial role in hydrology modeling. Precipitation, in the form of rain, snow, or hail, is a primary input for hydrological models as it directly impacts the water balance of a region [1], [2]. Accurate and detailed precipitation data is essential for several reasons. Firstly, it helps in understanding the spatial and temporal patterns of precipitation, allowing identification of areas with high or low rainfall. This information is vital for water resource management, flood prediction, and drought monitoring [3].

Moreover, precipitation data is instrumental in estimating water runoff and streamflow, which are crucial components of hydrological modeling [4]. Precipitation data aids in calibrating and validating hydrological models by comparing simulated and observed precipitation values [5]. This iterative process improves the accuracy and reliability of the models, enabling better water resource planning and management decisions.

By incorporating accurate precipitation data into hydrological models, scientists can make informed decisions regarding water resource management, flood control, and drought mitigation strategies [6]. Precipitation data is therefore indispensable for hydrologists and plays a crucial role in ensuring sustainable water management practices [7].

Determining the average annual precipitation over a catchment can be a challenging task due to several factors. One of the main problems is the spatial variability of precipitation within the catchment [8]. Precipitation patterns can vary significantly over relatively short distances, making it difficult to accurately represent the average precipitation for the entire catchment. Rain gauges, which are commonly used to measure precipitation, are often sparsely distributed within a catchment, leading to limited coverage and potential inaccuracies in estimating the average.

Rainfall measurements are often subject to various sources of error, such as evaporation, wind effects, and gauge undercatch, which further complicate the estimation of average annual precipitation. Additionally, the impact of climate change introduces another layer of complexity. Climate change can alter precipitation patterns, leading to shifts in the timing, intensity, and duration of rainfall events. Historical precipitation records may not adequately represent future conditions, making it challenging to predict the average annual precipitation accurately [9].

Overcoming these problems employs various techniques and technologies. This includes the use of remote sensing data from satellites and radar systems to capture a broader spatial coverage of precipitation. Statistical methods, such as spatial interpolation and data assimilation techniques, are also employed to fill gaps in the measurements and improve the representation of average precipitation [10]. Climate models and downscaling techniques can provide insights into future precipitation trends, aiding in the estimation of average annual precipitation under changing climatic conditions.

Spatial interpolation methods are used to estimate precipitation values at locations where direct measurements are not available [11], [12]. These methods help fill data gaps, create continuous spatial representations of precipitation, and improve the accuracy of hydrological modeling.

When comparing spatial interpolation methods for precipitation data, several factors should be considered. Inverse Distance Weighting (IDW) is a simple and computationally efficient method that assigns weights to nearby points based on their distance. Kriging method take into account the spatial correlation between measurements and yield optimal estimates by minimizing the prediction error variance. Splines are a flexible interpolation method

*Corresponding author: Trg Dositeja Obradovića 6, 21000 Novi Sad; kolakovic.s@uns.ac.rs

that fits smooth curves or surfaces through the measured points. They capture complex spatial patterns and can represent precipitation surfaces with high accuracy. The choice of interpolation method should be based on the specific characteristics of the data, the desired accuracy, and the trade-off between simplicity and computational complexity[13].

2. METHODS

Kriging is a widely used geostatistical interpolation method for spatially estimating values, including precipitation, based on a set of measured data points. It takes into account both the spatial correlation between points and the overall trend in the data. The fundamental concept behind Kriging is to provide optimal estimates by minimizing the prediction error variance[14].

The Kriging method was developed by the French mathematician Georges Matheron. Georges Matheron, inspired by Danie G. Kriges work in mining geology, sought to find a statistical approach to estimate ore deposits' spatial distribution. Matheron's key insight was that the spatial correlation between samples could be quantified and used to make optimal predictions at unmeasured locations. In the 1960s, Matheron developed the mathematical framework for Kriging, which he named after Danie G. Krige.

Kriging gained recognition for its ability to estimate values with minimum variance, making it an optimal interpolation technique [15]. Over the years, Kriging and geostatistics have evolved, finding applications beyond mining and ore estimation. The method has been widely adopted in various disciplines, including hydrology, environmental sciences, agriculture, and spatial analysis.

There are different types of Kriging methods, including Ordinary Kriging (OK) and Universal Kriging (UK). Ordinary Kriging assumes a constant mean and provides unbiased estimates. It is suitable when there is no systematic trend in the data [16]. Universal Kriging, on the other hand, incorporates additional predictor variables, such as elevation, to account for a spatial trend. In this research Ordinary Kriging (OK) has been used to interpolate annual precipitation over analysed catchment.

Kriging involves several equations that describe the estimation process based on the spatial correlation structure of the data. The Kriging estimate, Z^*, at an unmeasured location is calculated as a weighted sum of the measured values, Z_i, at the neighboring points, Equasion 1 and Figure 1:

$$Z^* = \sum_{i=1}^{n} \lambda_i * Z_i \tag{1}$$

where λ_i represents the weight assigned to each measured point.

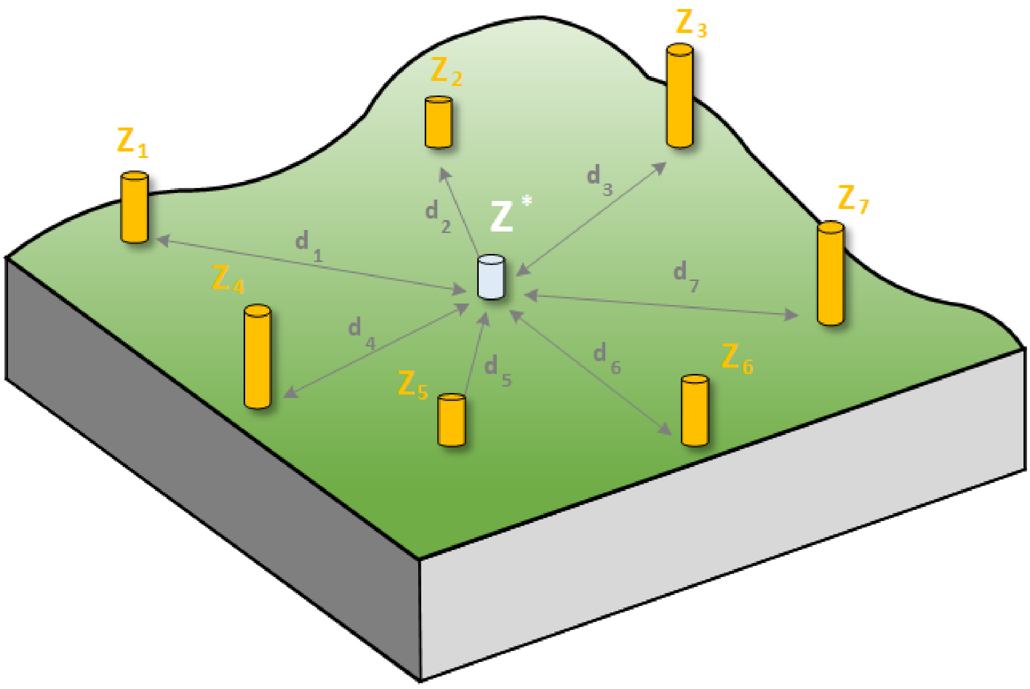

Figure 1: The Kriging method spatial interpolation basic principle

Kriging estimates the value at an unmeasured location by calculating weights for neighboring measured points. The weights, λ, are calculated using the following equation:

$$\lambda_i = \frac{1}{C^T} * \gamma_i \tag{2}$$

where C is the covariance matrix between the measured points and γ is the vector of variogram values between the measured points and the unmeasured location.

Kriging method involves constructing a variogram, which describes the spatial correlation between pairs of data points. The variogram provides information about the spatial dependence of the variable being interpolated, such as precipitation. The variogram, γ, quantifies the spatial correlation between pairs of data points as a function of their separation distance. It quantifies how the similarity between measurements decreases as the distance between them increases.

$$\gamma_i = \frac{(Z_j - Z_i)^2}{2} \tag{3}$$

where Z_i and Z_j are the values of the variable being interpolated (e.g., precipitation) at locations x and x+d, respectively. The variogram provides essential information about the spatial dependence and is used to model the spatial correlation in Kriging.

A semivariogram model is fitted to the calculated variogram to describe the relationship between the variogram and the distance. The semivariogram model allows extrapolation of the spatial correlation beyond the measured data points, Figure 2.

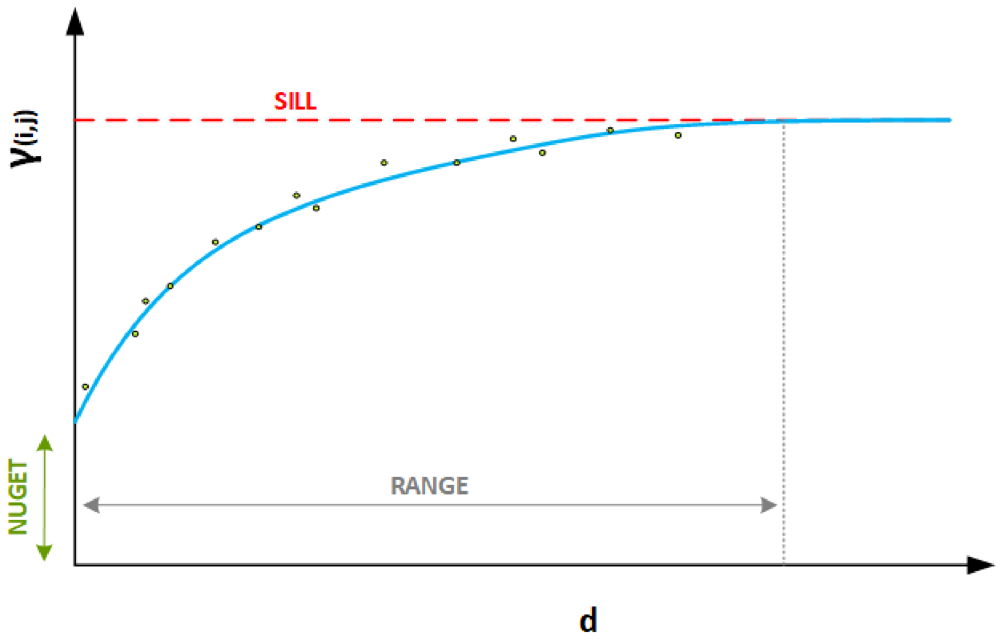

Figure 2: Semivariogram with characteristic values.

The Semivariogram characteristic values include: $RANGE\ (R)$ - the range represents the maximum distance beyond which the spatial correlation becomes negligible; $NUGGET\ (C_0)$ - the nugget represents the y-intercept of the semivariogram, or the semivariance at the origin (d = 0); $SILL\ (C)$ - the sill represents the semivariance at large distances (beyond the range) where the semivariogram levels off.

The semivariogram model parameters define the mathematical function that best fits the empirical semivariogram. These parameters may include the range, nugget, and additional parameters specific to the chosen model (e.g., slope, sill-to-nugget ratio). The model parameters help describe the shape of the semivariogram curve and are used for predicting semivariance at unmeasured distances. Commonly used models include exponential, spherical, Gaussian, and linear models. In this research linear model for prediction of semivariance has been used.

Once the variogram is determined, Kriging calculates weights for neighboring points based on their spatial relationship and the variogram model. Points that are closer to the target location receive higher weights since they are expected to have a stronger influence on the interpolation. The weights are then used to calculate a weighted average of the measured points, resulting in the estimated value at the target location.

3. MATERIALS

For the purposes of this research, the experimental catchment of the Rasina River up to the profile of the Ćelije dam was chosen. The analyzed catchment is located in the central part of the Republic of Serbia (Figure 3).

The river Rasina springs on Goč mountain, below the peak of Ržište at an altitude of about 1100m. Mount Goč is located in the north-western part of the analyzed catchment (Figure 3), northen from the mountains Željin and Kopaonik. Near the town of Brus, the Rasina River receives its large right tributary, the Graševačka River, which drains the waters from Kopaonik Mountain below Pnčićev Vrh (2017m). The river Rasina, near the town of Razbojna, receives its second large right tributary, the river Blatašnica, which collects surface water from the southern sides of the Jastrebac mountain below the peak of Karaula (849m).

In 1979, the valley of the river Rasina was dammed in its north-eastern part by the Ćelije dam, which formed the lake. The main purpose of the Ćelije lake is to collect water for the water supply of the city of Kruševac. The construction of the dam, with a building height of 55m, created a lake with a volume of 41 million m³ of water, a water surface of 2.85 km², an average and maximum depth of 14 and 41m, respectively.

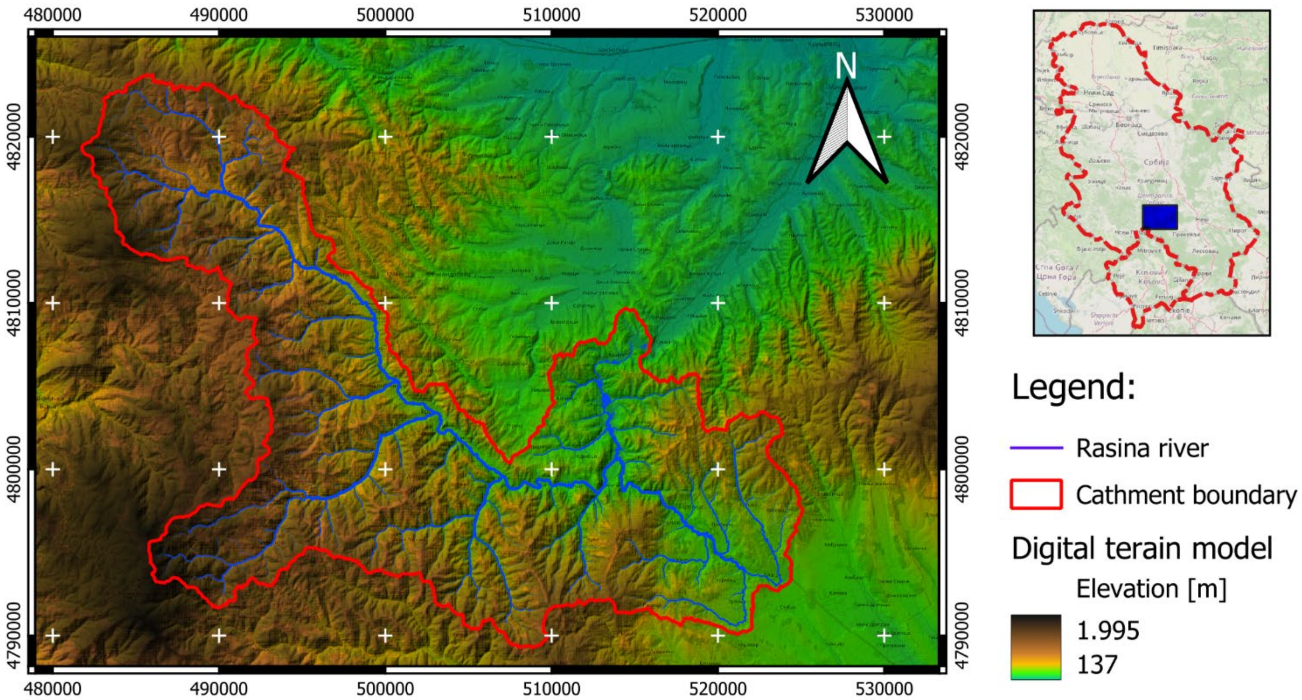

Figure 3: Rasina river cathcment

Due to the long period of exploitation of the water resource from Lake Ćelije, the reservoir area of the lake was filled with river sediment, which results in a reduction of the available volume of water in the lake for water supply. In recent years, there has been a need for the creation of a revitalization and silting project for Lake Ćelije. The first step of water management analyzes is the preparation of a hydrological study of the rainfall-runoff water balance on the analyzed catchment. One of the crucial data of the hydrological analysis is the determination of the average annual precipitation in the Rasina river basin.

In the preparation of hydrological studies, it is very common to analyze data only from measuring stations located in the considered watershed. As part of this research, a check of the previously presented approach and an analysis of the influence of the number and spatial distribution of rain gauge stations on the results of determining the average annual precipitation in the basin were carried out.

The catchment of the river Rasina up to the profile of the Ćelije dam was chosen as an experimental cathment due to the existence of a large number of rain gauge stations both in the basin itself and in its surroundings. For the purposes of analyzing the influence of the number of rain gauge stations on the calculation results of the mean annual precipitation in the analyzed catchment, the avalable rain gauge stations were grouped into four groups according to which four calculation scenarios were formed (Figure 4):

- Scenario 1: includes only rain gauge stations located in the analyzed catchment,
- Scenario 2: includes rain all rain gauge stations located on the catchment and up to 10 km from the border of the watershed,
- Scenario 3: includes rain all rain gauge stations located on the catchment and up to 20 km from the border of the watershed, and
- Scenario 4: includes rain all rain gauge stations located on the catchment and up to 30 km from the border of the watershed.

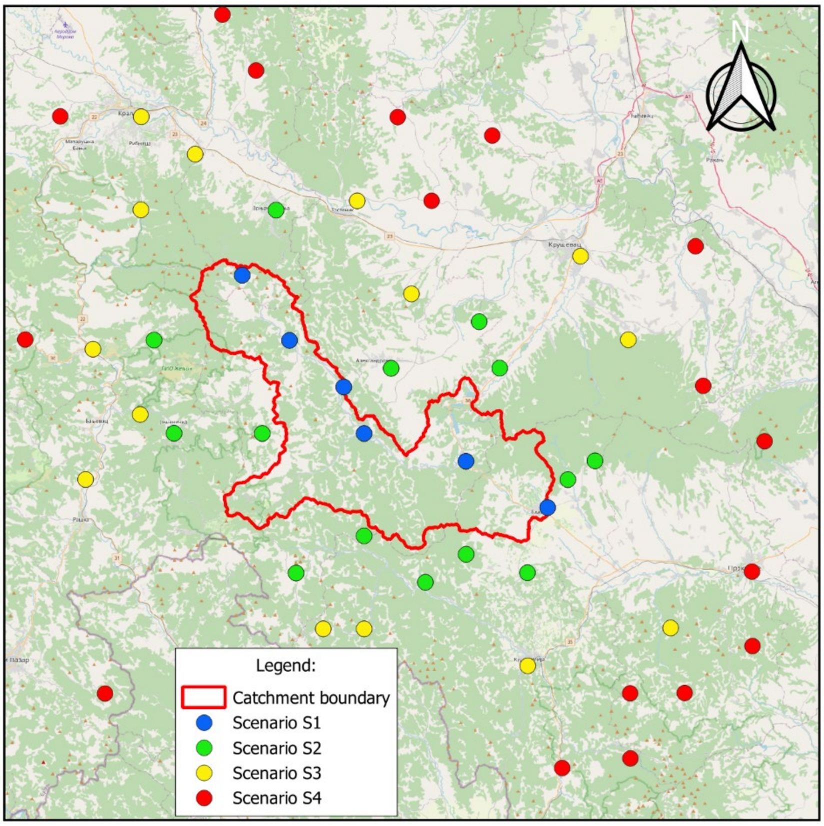

Figure 4: Rain gauge station on the Ćelije lake catchment acording to calculation scenarios

4. RESULTS AND DISCUSSION

As part of this research, spatial interpolation calculations of mean annual precipitation data were performed for four calculation scenarios that differ in the number of rain gauge stations included in the calculation. Spatial interpolation was performed using the Kriging method, more precisely Ordinary Kriging, which is widely used in the aforementioned area.

When adjusting the function to the data on the semivariogram, it was determined that the data on the mean annual precipitation from the measuring stations do not follow the Normal probability distribution. The normalization of the measured data was performed using a logarithmic transformation. For the approximation of the semivariogram, the linear approximation given by the equation was used:

$$\gamma(d) = a * d + b \tag{4}$$

where a and b are the calibration coefficients of the equation and d represents the Euclidean distance.

During the calibration of the semivariogram function, it was determined that the best agreement between the measured data and the function occurs for the maximum value of the distance of 10,000 m and the limitation of the minimum and maximum number of stations included in the calculation to 3 and 20, respectively.

By spatial interpolation of data on average annual precipitation, a 3D surface was formed in raster format, pixel size 100*100 m, where each pixel has an interpolated value of precipitation. The average value of precipitation in the analyzed basin of Ćelije Lake was determined as the average value of the sum of all pixels within the catchment boundary.

The problem of visual representation of interpolated precipitation values from the 3D surface was solved by drawing contour isolines of precipitation with an equidistance of 100 mm of annual precipitation. Plotting the isolines of precipitation allows insight into the change in the spatial distribution of precipitation for different calculation scenarios.

Figure 5 shows the results of spatial interpolation of annual precipitation for four calculation scenarios. The results of spatial interpolation for calculation scenario S1, which includes only rain gauge stations located in the analyzed watershed, are shown in Figure 5 - a. The irregular shape and sudden breaking of the precipitation isolines for the S1 scenario indicate that the chosen spatial interpolation method requires a larger number of rain gauge stations for successful application. From the results shown, it can be concluded that the method of ordinary Kriging requires more than 6 measuring stations, as used in the calculation for scenario S1.

The results of spatial interpolation of rainfall for scenarios S2, S3 and S4, shown in Figure 5 - b, c and d, show that the Ordinary Kriging method gives significantly better results when the number of measuring stations is larger. Regular shapes of precipitation isolines without sudden breaks confirm the previously stated conclusion.

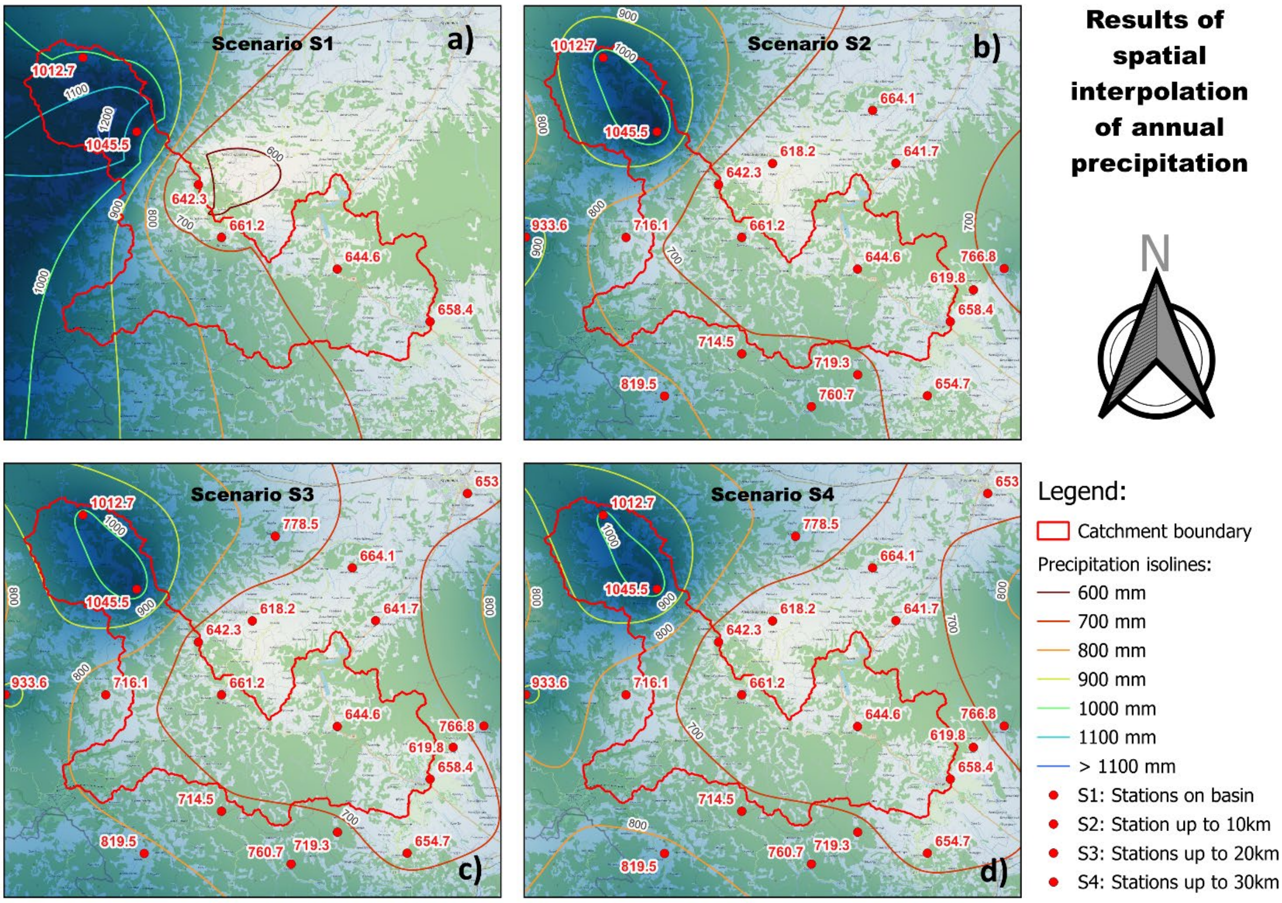

Figure 5: Results of spatial interpolation of annual precipitation for four calculation scenarios

It can be clearly concluded from Figure 5 that scenario S1 does not give good calculation results due to the small number of measuring stations, but from the shown figure it is not possible to clearly conclude how much the differences in annual precipitation interpolation values are for the remaining three calculation scenarios for the analyzed Ćelije lake catchment. The values of average annual precipitation for the analyzed catchment for all four calculation scenarios are shown in table 1.

Table 1: Annual precipitation for four calculation scenarios

Scenario:	Distance from catchment boundary: [km]	Number of stations: [/]	Average annual precipitation: [mm]
S1	0	6	799
S2	10	20	745
S3	20	34	744
S4	30	51	743

Based on the data shown in Table 1, it can be concluded that the mean annual precipitation values for the analyzed Čelije lake catchment differ slightly for calculation scenarios 2-4. It can also be concluded that the results of spatial interpolation using the Ordinary Kriging method change slightly with the increase in the number of rain gauge stations over 20.

In order to determine the reasons for such similar results, it is necessary to perform a comparative analysis of the rainfall isolines for the analyzed watershed. Figure 6 shows a comparative analysis of isolines for all four calculation scenarios.

From Figure 6, it can be clearly concluded that, except for the precipitation isolines for scenario S1, the precipitation isolines for the other three calculation scenarios are spatially quite close, even to the extent that they overlap in some cases. The matching of precipitation isolines is manifested by very similar values of average precipitation in the analyzed Lake Ćelije catchment.

At the end of the analysis, it can be concluded that the Ordinary Kriging method does not provide satisfactory results of spatial interpolation of precipitation when the number of rain gauge stations is small. With the increase in the number of rain gauge stations over 20, the spatial interpolation results converge to a constant value very quickly.

.....

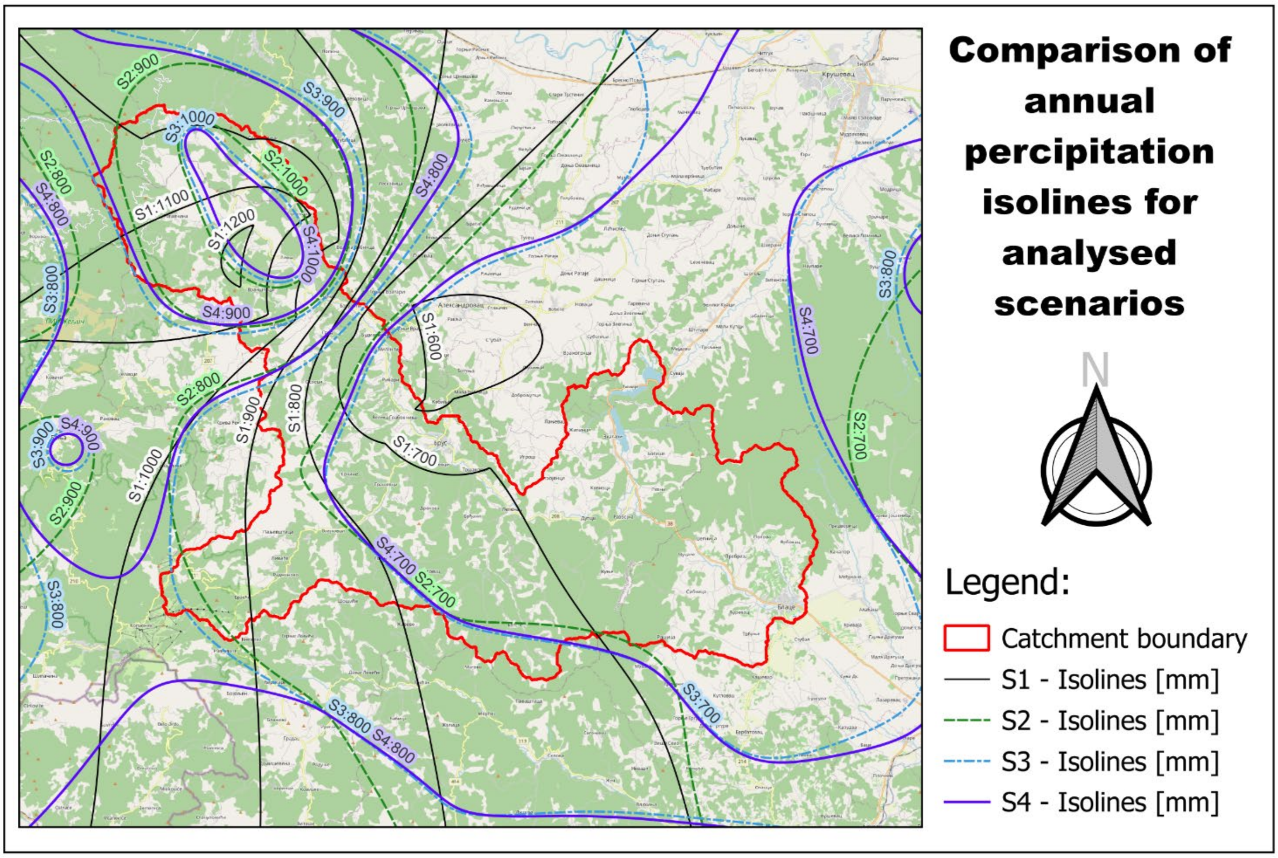

Figure 6: Comparative analysis of precipitation isolines for all four calculation scenarios

5. CONCLUSIONS

As part of this research, an analysis of the influence of the number of rain gauge stations on the results of spatial interpolation of mean annual precipitation for the surface of the experimental catchment, Lake Ćelije, was carried out, and the following conclusions were determined:

- when making hydrological studies, it is very important to include the surrounding rain gauge stations in the analysis,
- the results of hydrological analyzes based on a small number of rain gauge stations in the catchment are not reliable,
- The Ordinary Kriging method of spatial interpolation is very sensitive to a small number of rain gauge stations, as a result of which it does not give satisfactory results,
- with an increase in the number of rain gauge stations over 20, the Kriging method very quickly converges to a constant value of average annual precipitation in the analyzed basin.

ACKNOWLEDGEMENTS

This study has been supported by the Republic of Serbia, Ministry of Education, Science and Technological Development through project number 451-03-47/2023-01/200108.

REFERENCES

[1] K. J. Beven, *Rainfall-runoff modelling: the primer*. John Wiley & Sons, 2011.

[2] V. Mandić, "Хидролошко-хидраулички модел за процену ризика преливања воде преко саобраћајнице у профилима путних пропуста на бујичним сливовима," Универзитет у Новом Саду, Факултет техничких наука, 2022.

[3] A. Michelon, L. Benoit, H. Beria, N. Ceperley, and B. Schaefli, "Benefits from high-density rain gauge observations for hydrological response analysis in a small alpine catchment," *Hydrology and Earth System Sciences*, vol. 25, no. 4. pp. 2301–2325, 2021.

[4] M. Mazzoleni, L. Brandimarte, and A. Amaranto, "Evaluating precipitation datasets for large-scale distributed hydrological modelling," *J. Hydrol.*, vol. 578, p. 124076, Nov. 2019.

[5] V. Mandić, M. Šešlija, S. Kolaković, S. Kolaković, G. Jeftenić, and S. Trajković, "Mountain Road-Culvert Maintenance Algorithm," *Water*, vol. 13, no. 4, p. 471, Feb. 2021.

[6] W. Gan, X. Chen, X. Cai, J. Zhang, L. Feng, and X. Xie, "Spatial interpolation of precipitation considering geographic and topographic influences - A case study in the Poyang Lake Watershed, china," in *2010 IEEE International Geoscience and Remote Sensing Symposium*, 2010, pp. 3972–3975.

[7] H. E. Beck *et al.*, “Global-scale evaluation of 22 precipitation datasets using gauge observations and hydrological modeling,” *Hydrol. Earth Syst. Sci.*, vol. 21, no. 12, pp. 6201–6217, Dec. 2017.

[8] V. Mandić, I. Despotović, M. Šešlija, S. Mihajlović, and S. Kolaković, “Efficiency analysis of two spatial interpolation methods of precipitation on the Kolubara river basin,” in *X International Conference “Heavy Machinery-HM 2021”, Vrnjačka Banja, 23– 25 June 2021*, 2021, no. 10, p. G.43-G.50.

[9] S. Kolaković, V. Mandić, M. Stojković, G. Jeftenić, D. Stipić, and S. Kolaković, “Estimation of Large River Design Floods Using the Peaks-Over-Threshold (POT) Method,” *Sustainability*, vol. 15, no. 6, p. 5573, Mar. 2023.

[10] M. Portuguez-Maurtua, J. L. Arumi, O. Lagos, A. Stehr, and N. Montalvo Arquiñigo, “Filling Gaps in Daily Precipitation Series Using Regression and Machine Learning in Inter-Andean Watersheds,” *Water*, vol. 14, no. 11, p. 1799, Jun. 2022.

[11] G. Q. Tabios and J. D. Salas, “A COMPARATIVE ANALYSIS OF TECHNIQUES FOR SPATIAL INTERPOLATION OF PRECIPITATION,” *J. Am. Water Resour. Assoc.*, vol. 21, no. 3, pp. 365–380, Jun. 1985.

[12] G. Jeftenić, A. Rašeta, S. Kolaković, M. Panić, S. Kolaković, and V. Mandić, “A Methodology Proposal for Selecting the Optimal Location for Small Hydropower Plants,” *Teh. Vjesn. - Tech. Gaz.*, vol. 28, no. 5, pp. 1462–1470, Oct. 2021.

[13] S. A. Jewell and N. Gaussiat, “An assessment of kriging-based rain-gauge–radar merging techniques,” *Q. J. R. Meteorol. Soc.*, vol. 141, no. 691, pp. 2300–2313, Jul. 2015.

[14] J. O. Skøien, R. Merz, and G. Blöschl, “Top-kriging - geostatistics on stream networks,” *Hydrol. Earth Syst. Sci.*, vol. 10, no. 2, pp. 277–287, Apr. 2006.

[15] G. Laaha, J. O. Skøien, and G. Blöschl, “Spatial prediction on river networks: comparison of top-kriging with regional regression,” *Hydrol. Process.*, vol. 28, no. 2, pp. 315–324, Jan. 2014.

[16] F. Zhang, S. Zhong, Z. Yang, C. Sun, and Q. Huang, “Spatial Estimation of Mean Annual Precipitation (1951–2012) in Mainland China Based on Collaborative Kriging Interpolation,” 2016, pp. 663–672.

Manufacturing technologies for GFRP's with thermosetting polymeric binders

Cristina Sescu-Gal[1*], Cătălin Frâncu[1], Cornelia Dobrescu [2], Petre Bălan[3]

[1]Faculty of Mechanical Engineering and Robotics in Construction, Technical University of Civil Engineering, Bucharest, (Romania)

[2] Faculty of Engineering and Agronomy from Brăila, Department of Engineering and Management Sciences, "Dunărea de Jos" University, Galati (Romania)

[3]Chief eng. Dypety S.R.L., Moinești, (Romania)

The manufacture of GFRP's (Glass-Fibres Reinforced Polymers) with thermosetting polymer binders has seen a remarkable development, with the aim of identifying replacement materials for steel products. The development of composite materials led to the identification of GFRP products, which can be used as substitutes for traditional materials for reinforcing concrete elements. The concern of researchers in the field is directed towards obtaining some mechanical and geometrical characteristics that ensure concrete structures the characteristic resistance properties. Having very good results regarding mechanical tensile strength, the products can be used for reinforcement in concrete elements for structures such as: platforms placed on the ground, piles for indirect foundations, moulded walls, concrete tubes for sewage networks, etc. Through these processes, bars, nets, wires or tubular elements with constant or

Keywords: glass fiber reinforced polymers, reinforced concrete, bars, model

1. INTRODUCTION

The development of fibre-reinforced polymer matrix composite materials led to the identification of revolutionary solutions in construction, based on the superior properties of classic products. Initially, the fields where polymer composite materials found their applicability were the (aero) space, naval or chemical industry however, they also entered the construction field, as construction materials. Although at first they were used on a small scale, since the 1980s, new areas of use have been discovered, especially in the form of the application of composite reinforcements in concrete, where special performance requirements are imposed, such as non-magnetic properties or resistance to attacks severe chemicals. The pioneers in the field of using composite materials in construction were Japan and Canada, followed by the USA and Europe.

The range of new products used in construction includes polymer composite materials reinforced with fibres such as slats, fabrics, bars, nets, etc. The fibres used in the manufacture of composite materials are carbon fibre, glass fibre and aramid fibre. Due to their non-metallic fibrous origin, these bars differ from steel bars by possessing linear elastic behaviour until failure, low specific weights, high strength/weight ratio, high durability especially in highly corrosive environments [1]. Products such as lamellae, fabrics, carbon fibre bars are used successfully in consolidations of reinforced concrete structures, especially in marine structures, structures subject to corrosive agents, structures that require ensuring reduced electrical conductivity or electromagnetic transparency. Bar products, nets made of fiberglass, are used as reinforcement for concrete elements, having characteristics superior to steel in terms of corrosion resistance, electromagnetic and electrostatic neutrality. To increase the adhesion to the concrete, the FRP reinforcement bars are provided with special, helical ribs or by sand coating during manufacture.

2. MANUFACTURING TECHNOLOGIES OF FRP COMPOSITE MATERIALS

2.1. General

Currently, there are different processes adopted for the manufacture of fibre-reinforced polymer matrix composite materials. Bhatt, A.T e.t. in the paper [2] give an overview of the various manufacturing processes known in the FRP industry and compare them in terms of their advantages, limitations, application, fibre types, types of resin system etc.

2.2. Manufacturing processes of polymer composite materials

Although there are several manufacturing processes for composite materials, they contain some common steps, such as: creating a structure of fibre networks, which must be soaked (wet-out) and infiltrated by the resin matrix, which it must be solidified. Each process presents characteristics that define the type of product, the properties of the composite material being specific to each manufacturer. Among the many manufacturing technologies, we note the most well-known [3]:

The Hand Lay-up process is the oldest and simplest method used for the production of plastic laminates. It is still used today, being a cheap solution that does not require investment. A similar procedure is used in which the method of application of the resin is done by spraying (Spray-up).

The Resin Transfer Moulding - RTM consists of infiltrating dry semi-finished fibres with a resin with low viscosity and hardening in shape. The process is carried out in three main stages, namely, the production of the fibre semi-finished product (preformed fibres) and their

*Corresponding author: Technical University of Civil Engineering 122-124 Lacul Tei Blv., Bucharest, Romania, cristina.sescu-gal@utcb.ro

placement in a pattern or matrix (form), the infiltration of the resin under a moderate-high pressure into the fibre semi-finished product, respectively the hardening (curing) composite structure in shape.

The process Vacuum Assisted Resin Transfer Moulding - VARTM differs from the previous process by transfer of resin in vacuum. In the first stage, the manufacturing of the parts must be done in a single open matrix. In the second stage, the resin is injected in combination with vacuuming for the perfect impregnation of the fibres.

The process of forming by Compression Moulding is the most used method of forming thermosetting materials. This technique involves forming materials by pressing, using matched dies. Pressing can be done cold (at low pressure) or hot (at high pressure).

The process of Filament Winding consists in winding the continuous fibres on a rotating device or mandrel. There are two types of filament winding, namely wet winding and dry winding.

The pultrusion process is a continuous process for the manufacture of composites, carried out on automatic systems, which determines a high productivity. Pultrusion is a continuous forming process, the final composite product being a material with a constant cross-section.

2.3. Manufacturing technology of FRP reinforcing bars from glass fibres impregnated with thermosetting polymer binders.

The manufacture of FRP rebar is based on pultrusion technology, known since 1948 and patented in the USA in 1951 [4]. The process combines extrusion and reactive casting technologies. The reinforcing fibres characteristic of the product to be made is first passed through a bath in which they are impregnated with a reactive system, which represents the polymeric substance from which the matrix of the composite material will be constituted. The obtained preparation is introduced into a heated die, used for reticulation and profiling of the semi-finished product to be produced. The properties of the obtained material are determined by the technological parameters of the manufacturing process and the properties of the component materials.

The studied FRP products are bars obtained through the pultrusion process by Dypety company, with the equipment in figure 1, which has the following characteristics: total installed power of 29 kW, maximum bar manufacturing diameter 40 mm, winding speed of 200 rpm, chain transmission.

Figure 1:Pultrusion plant [4].

The manufacturing technological flow is automated and includes the following main operations:

- fibre placement;
- fibre impregnation;
- resin polymerization (fibres) in the heated matrix;
- cooling and winding/cutting bars (diameter function).

3. PROPERTIES OF FRP FIBERGLASS REBAR IMPREGNATED WITH THERMOSETTING POLYMERIC BINDERS

The analysed products are of the type of bars with diameters between Ø4 and Ø40mm, with a circular cross-section and the helical ribs, figure 2.

The raw materials used to manufacture an FRP bar are fibres produced by extruding molten glass and an unsaturated polyester resin matrix. The physical properties of the polyester resins used are shown in table 1 [5], and of glass fibres in table 2 [3].

Table 1: The physical properties of the polyester

No. crt.	Type of parameters	U.M.	Value
1.	Viscosity at 25ºC	mPa s	400 ÷ 1000
2.	Gel time at 25ºC	minute	10 ÷ 20
3.	Traction module	MPa	3780
4.	Elongation at break	%	min. 3.0

Table 2: The physical properties of the fibre glass

No. crt.	Type of parameters	U.M.	Value
1.	Diameter	μm	8 ÷ 14
2.	Density	kg/m^3	2490 ÷ 2700
3.	Modulus of elasticity	N/mm^2	(69 ÷ 85) · 10^3
4.	Tensile strength	N/mm^2	3160 ÷ 4590
5.	Elongation	%	3 ÷ 7,2

3.1. Mechanical properties of glass fibre FRP rebars

The properties of FRP reinforcing bars made of glass fibres impregnated with thermo-strengthening polymer binders were determined by laboratory tests carried out within the experimental program carried out at the Research Institute for Equipment and Technologies in Construction - ICECON S.A., Bucharest, Romania, both on FRP bars from glass fibres as well as on concrete structures reinforced with glass fibre FRP bars.

The tests showed the following values for fiberglass FRP bars, presented in Table 3 in the form of an extract.

Table 3: Test values performed on FRP bars

No. crt.	Diameter of FRP bars [mm]	Section area [mm^2]	Mechanical resistance R_m [N/mm^2]
1.	Ø 8	50.3	1186.7
2.	Ø 12	113.0	1104.0
3.	Ø 22	380.0	683.3
4.	Ø 25	491.0	791.7
5.	Ø 28	616.0	655.7
6.	Ø 32	804.0	680.7

In order to have the most appropriate picture of the results obtained, within the program tests were carried out on the concrete steel bars used in Romania for the reinforcement of concrete resistance structures for constructions, namely concrete steel type B 500C, according to the Technical Regulation "Technical Specification regarding steel products used as reinforcements: requirements and performance criteria - ST 009-2011". This type of steel is characterized by a yield strength of 500 N/mm^2. The tests showed the following values for steel reinforced bars, presented in Table 4 in the form of an extract.

Table 4: Test values performed on steel reinforced bars

No. crt.	Diameter of steel bars [mm]	Section area [mm^2]	Mechanical resistance R_m [N/mm^2]
1.	Ø 8	50.3	650
2.	Ø 12	113.0	692.1
3.	Ø 22	380.0	653
4.	Ø 25	491.0	692
5.	Ø 28	616.0	640
6.	Ø 32	804.0	670

Comparing the values obtained for glass fibre FRP bars and steel reinforcement bars, figure 2, we can see that at small diameters FRP bars have higher mechanical strengths than steel bars, and at medium and large diameters the values of mechanical strengths are roughly similar.

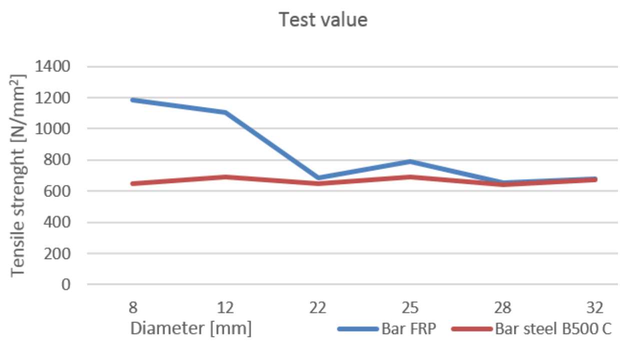

Figure 2: Values of the tests carried out for the two types of bars

3.2. Characteristics determined by comparative experimental tests carried out on model of beams

As part of the experimental program, models of concrete beams reinforced with concrete steel bars and FRP bars were made in the following configurations:

Model 1 - Concrete beam reinforced with steel-concrete bars

Model 2 - Reinforced concrete beam with FRP bars and concrete steel stirrups;

Model 3 - Reinforced concrete beam with matted FRP bars (FRP bars were braided in the mid-section of the spiral wire girders);

Model 4 - Reinforced concrete beam with FRP bars tied by wire;

Model 5 - Concrete beam reinforced with concrete steel bars tied by wire bonding;

Model 6 - Concrete beam reinforced with FRP bars.

For all the concrete sections, the same percentage of reinforcement was used, calculated according to the design standards. The geometric characteristics of the beams used in the experimental program are:

- dimensions of the cross section 0.20 x 0.20 m;
- beam length 1.50 m.

The method of making the reinforcements is presented in figure 3.

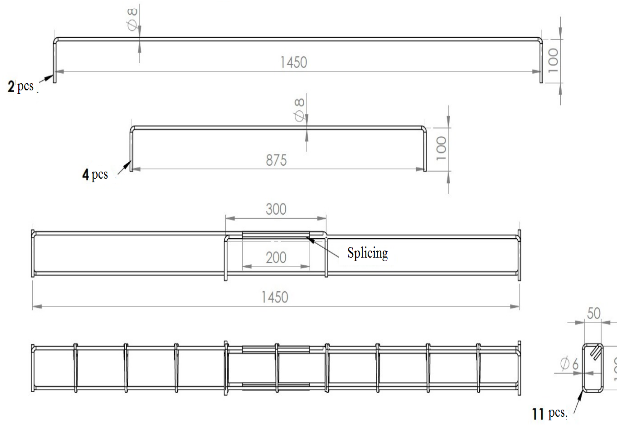

Figure 3: Bars of reinforcing the concrete beam

The beams have a square cross section, executed on a real scale, figure 4. To determine the characteristics were required to bend with a concentrated load applied to the middle of the beam openings.

Figure 4: Concrete beam with a square cross section

Following the tests performed on the 6 (six) models, the following characteristics were determined:

- deformations specific to the stress steps;
- the value of the force that determined the appearance of the cracks on the concrete element;
- the value of the force at which the concrete element was broken.

The application of force was done in 5 (five) steps.

The specific deformations of the types of models obtained from the laboratory tests are presented in table 4.

Table 4. The specific deformations of the type’s o models reinforced beams

Type of model	*Model 1*	*Model 2*	*Model 3*	*Model 4*	*Model 5*	*Model 6*

Nr. loading steps	*Force applied [N]*	*Concrete steel reinforced beam [mm]*	*Reinforced beam with FRP and concrete steel stirrups [mm]*	*Reinforced beam with FRP splicing [mm]*	*Reinforced beam with bonded FRP [mm]*	*Reinforced beam with bonded concrete steel [mm]*	*FRP reinforced beam [mm]*
1	*1 800*	*1,25*	*3,43*	*3,38*	*3,51*	*1,74*	*5,02*
2	*3 800*	*4,41*	*16,00*	*9,41*	*12,73*	*4,80*	*18,00*
3	*5 800*	*7,54*	*29,30*	*15,51*	*23,90*	*8,18*	*30,87*
4	*8 500*	*11,43*	*59,00*	*25,03*	*40,13*	*12,49*	*58,38*
5	*10 000*	*17,00*	*-*	*32,89*	*-*	*21,87*	*-*

The experimental program also included observing the behaviour of concrete beams with steel bar and FRP reinforcement. Thus, the stress force was applied until the beams broke, observing the value at which the first cracks appeared. The behaviour of the models under the action of the applied force is summarized in table no. 5.

Table 5: The value of the cracking and breaking force

No. crt.	Concrete model type	The value of the force at which the cracks appeared [N]	The force value at which the beam broke [N]
1.	Model 1	10 000	11 300
2.	Model 2	3 000	9 400
3.	Model 3	5 100	12 140
4.	Model 4	2 950	8 700
5.	Model 5	10 000	10 500
6.	Model 6	2 650	9 150

Figure 5 shows the test of a beam.

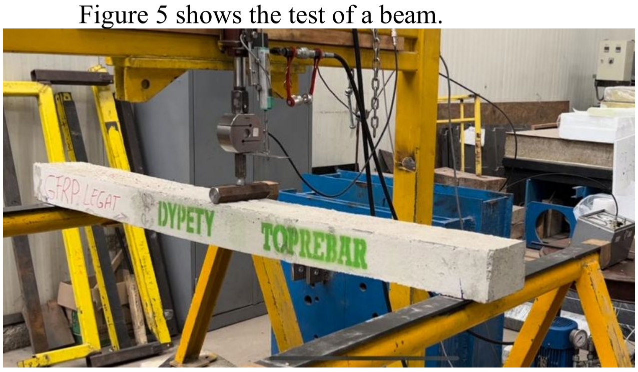

Figure 5: Performing the test

3.3. Characteristics determined by comparative experimental tests performed on beam models, with cross section " I ", required for bending with a concentrated load applied of the middle of the beam opening

Another stage of the experimental program consisted in the realization of beams with complex section, type „ I " having the following dimensions of the cross section:

- upper sole width: 0.90 m;
- lower sole width: 0.60 m;
- beam height: 0.75 m (upper sole thickness 0.10 m, lower sole thickness 0.15 m, heart height 0.50 m, heart thickness 0.45 m);
- beam length: 1.50 m.

To make the reinforcement, steel and FRP bars were used in the following configurations:

Model 1 - Reinforced concrete beam with steel-concrete bars;

Model 2 - Reinforced concrete beam with FRP bars.

The models were statically requested by forces applied in a vertical and horizontal direction.

Following the tests performed on the 2 (two) models, the following characteristics were determined:

- the value of the force that determined the appearance of the cracks on the concrete element.

The same percentage of reinforcement was used for all concrete sections, calculated according to design regulations. In figure 6 is show the model of concrete beam with cross section „I".

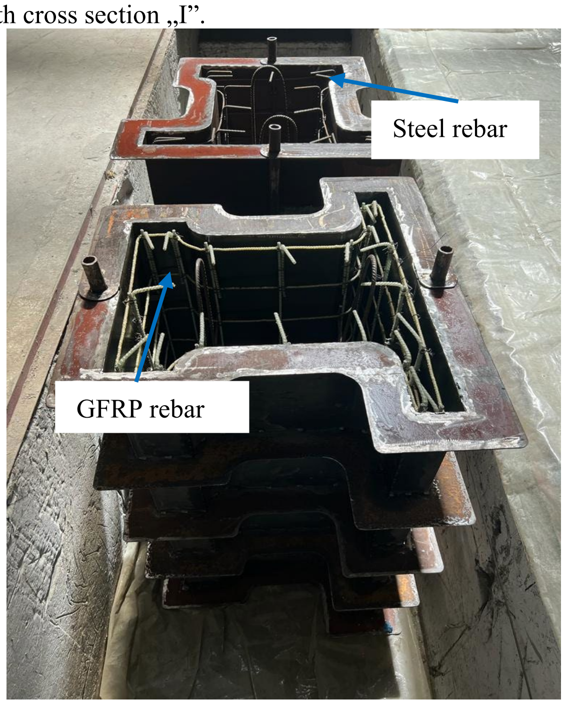

Figure 6: Model concrete beam with cross section „I"

The deformations specific to the types of models obtained from laboratory tests are presented in Tables 6.

Table 6: The values of the cracking force

No. crt.	Concrete model type	The value of the force at which the cracks appeared [N]
1.	Reinforced concrete beam with steel-concrete bars	585 600
2.	Reinforced concrete beam with FRP bars	341 600

Figure 6 shows the test of a beam.

Figure 6: Performing the test

Analysing the obtained results we can conclude the following:

- cracks appeared at lower forces in beams with reinforcement made only of FRP bars (Model 2, 4 and 6);

- the values of the forces at which the beams broke are closer compared to the values at which the cracks appeared.

These observations confirm the properties of FRP bars with respect to low values of elongation compared to steel and higher or similar values of mechanical strengths.

4. EQUIVALENCE OF CALCULATION RESISTORS OF CONCRETE STEEL BARS B500 AND FIBERGLASS BARS IMPREGNATED WITH POLYMERIC BINDERS FRPS

The evaluation of the calculation resistances of the concrete steel bars was done in accordance with the provisions of the standard SR EN 1992-1-1: 2004 /A1: 2015 „Eurocode 2. Design of concrete structures. Part 1-1: General rules and regulations for buildings".

According to this standard, the calculation strength of the steel products used for concrete reinforcement shall be calculated as the ratio between the steel flow limit and a safety coefficient having a value of 1.15.

Thus, the calculation resistance at the tensile stress, for concrete steel bars B500 is 435 [N/mm^2].

The evaluation of the calculation resistors of fiberglass bars impregnated with thermo-hardening polymeric binders – FRF type was performed based on the results obtained from the experimental program which showed that the permissible value (for calculating) the effort at the request for stretching shall be determined by dividing the breaking strength by a safety coefficient value of at least 1.80. Thus, depending on the diameter of the FRF reinforcement bar, the calculation value at the tensile request is:

- for FRF type bars with a diameter of Ø 7 mm - 611 [N/mm^2];

- for FRF type bars with a diameter between Ø 8 and Ø11mm - 555.6 [N/mm^2];

- for bars with a diameter of more than Ø 12 mm – 333.3 [N/mm^2].

In table no. 7 the values of the calculation resistance are presented, depending on the diameter of the type of reinforcement bars.

Table 7: Tensile strength for steel reinforced bars and FRP fiberglass

NNo. crt.	Diameter [mm]	Tensile strength	
		Bare steel B 500 [N]	FRP fiberglass bars [N]
1.	Ø 3.0	3 074	4 318
2.	Ø 4.5	6 917	9 716
3.	Ø 5.0	8 539	11 995
4.	Ø 5.5	10 333	14 514
5.	Ø 7.0	16 737	23 509
6.	Ø 8.0	21 861	27 922
7.	Ø 9.0	27 668	35 339
8.	Ø 10.0	34 158	43 628
9.	Ø 11.0	41 332	52 790
10.	Ø 12.0	49 188	37 688

From the analysis of the values presented in table no. 7, it can be identified that for the same reinforcement area, the tensile strength of FRF type glass fibre bars is superior to both the tensile strength values of B 500 concrete steel bars. Also, the following equivalences can be established between the diameters of the analysed products, from the point of view of the calculation resistances, presented in table 8.

Table 8: Tensile strength for steel reinforced bars and FRP fiberglass

No. crt.	FRP fiberglass bars [mm]	Bare steel B 500 [mm]
1.	Ø 4.5	Ø 5.0
2.	Ø 5.0	Ø 5.5
3.	Ø 7.0	Ø 8.0
4.	Ø 8.0	Ø 9.0
6.	Ø 9.0	Ø 10.0
8.	Ø 10.0	Ø 11.0
9.	Ø 11.0	Ø 12.0
10.	Ø 12.0	Ø 11.0

The calculations were carried out for the range of diameters between Ø 3.0 mm ÷ Ø 12 mm and correspond to the fiberglass bars impregnated with thermo-strengthening polymer binders analysed.

ACKNOWLEDGEMENTS

The authors wish to thank the ICECON Research Institute where the experimental program was carried out and the company Dypety SRL.

REFERENCES

[1] S.F.Husain, M. Sharinq and A. Masood, "GFRP bars for RC structures - A Review," International Conference on Advances in Construction Materials and Structures (ACMS-2018), https://www.researchgate.net /publication/323096663;

[2] A.T. Bhatt, P.P. Gohil and V. Chaudhary, "Primary Manufacturing Processes for Fibre Reinforced Composites: History, Development & Future Research

Trends,” IOP Conf. Series: Materials Science and Engineering 330 (2018) 012107 doi:10.1088/1757-899X/330/1/012107

[3] T. Nagy-Gyorgy, “Utilizarea materialelor compozite polimerice la consolidarea elementelor din zidărie de cărămidă şl beton armat”, PhD Thesis, Polytechnic University of Timișoara (Romania), (2004)

[4] Y.Liu, H-T Zang e.t., ” Experimental Study on Mechanical Properties of Novel FRP Bars with Hoop Winding Layer” Advances in Materials Science and Engineering Volume (2021), Article ID 9554687, https://doi.org/10.1155/2021/9554687

[5] https://en.wikipedia.org/wiki/Pultrusion

[6] Product data sheet from Polimal 122-2 TP;

[7] Experimental research program ICECON S.A and Dypety SRL, 2021-2022).

Methods for determining the characteristics of biocomposites

Jovana Bojković[1*], Vesna Bulatović[2], Branko Radičević[1], Nenad Stojić[1], Miljan Marašević[1]
[1]Faculty of Mechanical and Civil Engineering, University of Kragujevac, Kraljevo (Republic of Serbia)
[2]Faculty of Technical Science, Department for Civil Engineering, University of Novi Sad, Novi Sad (Republic of Serbia)

The use of biocomposite materials in the world is rapidly developing. The production of new biomaterials has made a big shift towards sustainable production, which also has a positive effect on ecology. Biocomposites are defined as a combination of two or more different materials, each of which has its characteristic properties. To define the use of a new biocomposite, it is necessary to examine its characteristics as a whole. The characteristics of that biocomposite are defined by the application of methods for extracting physical and mechanical properties, more precisely, porosity, bulk density, water absorption, airflow resistance, and heat flux, from which the coefficient of thermal conductivity is calculated. In this way, it is possible to determine the exact application of the material and compare it with long-used materials in the defined area of application. Therefore, new biocomposite materials can be used as an alternative to conventional materials.

Keywords: Biocomposite, Porosity, Bulk density, Thermal conductivity, Airflow resistance

1. INTRODUCTION

Reduction of CO_2 emissions, energy saving, and increasing application of biocomposite materials is becoming increasingly common area of research for many researchers around the world [1]–[4]. To improve the previously mentioned facts, the properties of biocomposite materials are tested. These tests are performed to define the area of application of the material. Pochwała et al. [5] studied the thermal conductivity of biocomposites, while Curto et al. [6] studied the thermal and acoustic characteristics of composite materials made from lime as binder and hemp as aggregate. Brzyski et al. [7] examined the physical and mechanical properties of the same biocomposites. Tests have shown that changing the ratio of the amount of binder and aggregate affects the mechanical (flexural strength) and physical properties (porosity, density, thermal conductivity...) [8], [9]. By examining the characteristics of composite materials on a biological basis, it can be established whether they can be used as an adequate substitute for already used materials with similar properties. Such materials can be used as components in the production of lightweight concrete [10]–[12] or as insulating materials from a thermal and acoustic point of view [13], [14]. How the properties of biocomposites, such as porosity, affect their application was investigated [15]. The effect of the thickness of the samples, the type of aggregate filler, and its volume fraction in the mixture, on the thermal and acoustic properties of the biocomposite was examined by Bojković et al. [16].

The results presented in the previously mentioned works define the possibility and area of application of the new biocomposite material, most often created by the maximum utilization of biomass. In this way, sustainable management of the used type of waste will be ensured, to protect the environment and give new use value to this material following the principles of sustainable development in construction. This paper aims to present methods for determining the characteristics of biocomposite to more easily define its application, durability, and the possibility of replacing the previously used but expensive construction material. On the other hand, since they are biomaterials, their application would have a positive effect on the environment.

2. MATERIALS AND METHODS

2.1. Material

The experimental part of the research, which is carried out to determine the characteristics of the material to define its application, is shown on a biocomposite made by combining wood waste (sawdust), Styrofoam whose granule size is 0.3 cm, and a mixture of lime and gypsum as a binder. The samples were formed using circular cross-section molds, 30 mm thick and 110 mm in diameter (Figure 1). The test was performed after 28 days of drying of the samples at a room temperature of 20±2°C.

Figure 1. Samples

2.2. Methods for determining airflow resistance

One of the main non-acoustic parameters that show the behavior of porous materials (biocomposites), which are used in sound insulation systems, is airflow resistance. A characteristic such as this is determined before the material enters the production process. According to the SRPS ISO 9053 [17] standard, there are two methods for measuring airflow resistance, namely the constant flow method and the variable airflow method. The constant air flow method (Figure 2) is based on the passage of a one-direction airflow through a sample of the tested material that is in the shape of a rectangular parallelepiped or a circular cylinder. The resulting pressure drop is measured between the two free

*Jovana Bojković: Dositejeva 19, 36000 Kraljevo, Republic of Serbia, bojkovic.j@mfkv.kg.ac.rs

surfaces of the sample while the airflow is created using a vacuum pump. The pressure drop is measured using a differential pressure gauge. Different from the previous method, the method with variable airflow (Figure 3) is based on a slow changing of airflow through a material sample of the same shape as in the previously mentioned method and measuring the alternating components in the volume enclosed by the sample. An alternating airflow rate is produced by a piston while the alternating pressure in the sample holder is measured by a side-mounted condenser microphone connected to a measurement amplifier.

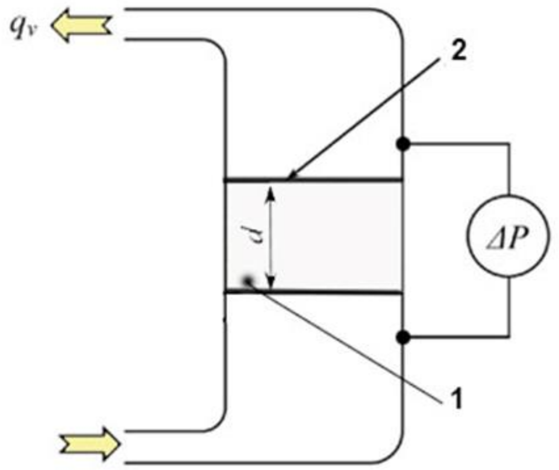

Figure 2. Constant airflow method

Description of Figure 2:
1. Porous material-sample
2. Cross-section of the sample

qv - volumetric air flow
d - thickness of the material sample
ΔP - pressure change

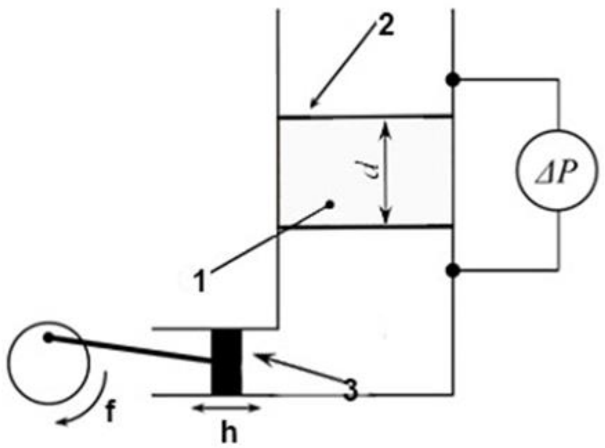

Figure 3. Variable airflow method

Description of Figure 3:
1. Porous material - sample
2. Cross-section of the sample
3. Cross-section of piston

d - sample thickness
ΔP – pressure change
f – frequency
h – the stroke of the piston

2.2.1. Apparatus for measuring flow resistance with constant airflow

In the method with constant airflow, which is more often applied in practice, the airflow is realized using a vacuum pump consisting of two air flow meters that work on the principle of a rotameter with a ball. Through the throttle valves, the airflow is adjusted for each rotameter individually. With one meter, the airflow varies in the range of 0.2-6 l/min, while air flows of 5-32 l/min are adjusted on the other meter. The vacuum pump makes it possible to reach the speed of the airflow in the "measuring cell" in which the sample of the material to be tested is placed and which is following the recommendations of the SRPS ISO 9053 standard [17]. "Measuring cell" is a plexiglass tube that is closed on one side to ensure conditions for maintaining negative pressure. The length of the tube is 300mm and the inner diameter is 100mm. By placing the sample in the cell and turning on the vacuum pump, negative pressure is created on one side while atmospheric pressure is on the other side of the sample. The difference between these two pressures is measured using a differential gauge. The measuring chain for determining the airflow resistance through the sample is shown in Figure 4.

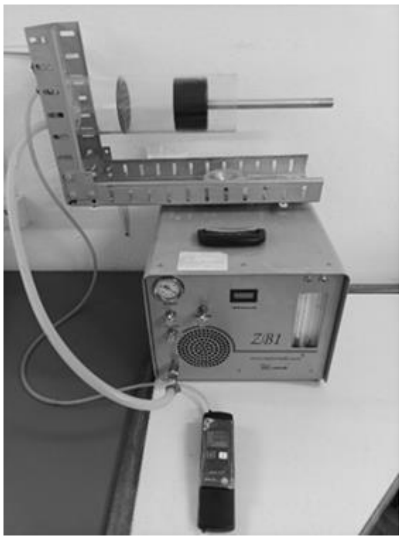

Figure 4. Measuring chain for determining airflow resistance

The pressure drop is a difference between the atmospheric pressure on one end of the sample and the sub-pressure created by the vacuum pump on the other. The ratio of the measured pressure drops (Δp) to the volumetric flow rate (q_v) that drop is the airflow resistance (R), which is calculated by the following formula:

$$R=\Delta p/q_v \tag{1}$$

The ratio of the airflow resistance to the sample cross-section area is the specific airflow resistance (R_s),

$$R_s=R/A \tag{2}$$

The specific airflow resistance (R_s) is the basis for the calculation of the longitudinal (specific) airflow resistance (r) for the corresponding sample thickness by means of the formula:

$$r = R_s/d \tag{3}$$

2.3. Methods of measuring thermal conductivity

There are two groups of methods for experimental testing of thermal conductivity, stationary and non-stationary. In stationary methods, thermal conductivity is obtained by direct measurement of heat flux and temperature on the surface of the sample when a stationary state is reached. In the second group of methods, non-stationary, the temperature distribution changes over time, and the rate of temperature change is also measured. This measurement determines the thermal diffusivity of the material. By knowing the density of the tested material, specific heat, and thermal diffusivity, its thermal conductivity can be calculated. Both groups of methods for determining thermal conductivity have numerous advantages and disadvantages [18]. In general, stationary methods are somewhat more complex than non-stationary ones, that is, the time interval for measuring thermal conductivity is quite long, the measuring equipment is complex and there are often difficulties during measurements that may arise as a result of contact thermal resistance [19]. In contrast to stationary, non-stationary methods are characterized by a shorter time interval of measurement, simpler apparatus, and smaller samples [20]. Depending on the type of material, the geometry of the sample, and the demanding measurement accuracy, the appropriate test method is selected.

The group of stationary methods for determining thermal conductivity include [16]:

- Method with flux meter,
- Method with direct electric heating,
- Method of a protected hot plate,
- Method of radial heat flow,
- Method with axial heat flow,
- Comparative method with axial heat flow (cut-bar method),

while the group of non-stationary methods includes:

- Pulse transient method,
- Laser pulse method,
- Transient flat source method,
- Line heat source method (hot wire method),
- 3ω method.

Among the listed methods, the stationary method with a fluxmeter is most often used in practice. The advantages of this method are the wide range of tested materials as well as the speed of obtaining results. The fluxmeter method is following the European standard EN12667 [21]. The measuring apparatus consists of two plates between which the sample is placed. One plate is heated, the other is cooled, and the heat flux is measured using a flux meter. A schematic representation of the method is given in Figure 5.

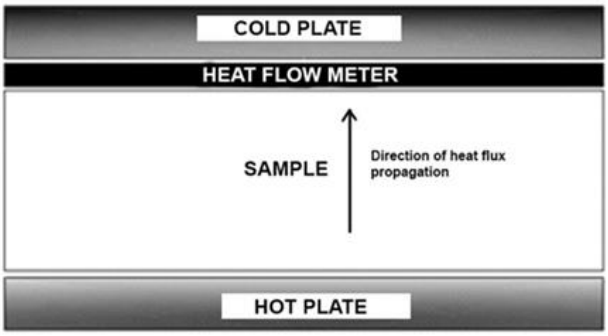

Figure 5. Schematic representation of the method

Based on the measured heat flux values, the thermal conductivity coefficients can be calculated according to the following formula:

$$q = \frac{t_1 - t_2}{\frac{\delta}{\lambda}} \tag{4}$$

$$\lambda = \frac{q \times \delta}{t_1 - t_2} \tag{5}$$

where q represents the heat flux, λ the coefficient of thermal conductivity, δ the thickness of the sample, while t_1 and t_2 are the measured temperatures on one and the other surface of the sample.

2.4. Determination of porosity and water absorption

Porosity is defined as the presence of empty spaces in the structure of a material and can be divided into two groups: pores, which are not visible to the naked eye, and cavities, which are much larger and clearly visible. Pores and cavities can be open or closed depending on their connection and are most often irregular in shape. The porosity of the material is expressed by the porosity coefficient φ. In order to determine the porosity of the biocomposite, the samples are first placed in a tank where they are vacuumed under pressure for a time interval of 3 hours. Then water is poured into the tank, which completely covers the samples of the biocomposite being tested, while the vacuuming continues for another 1 hour. After that, the pump is turned off and the vacuuming process continues for another 18±2 hours until the samples are completely saturated with water. Then the saturated weight of the samples is measured in air (m_{sat}) and hydrostatic balance (m_{hydr}). Finally, the samples are dried in an oven until their weight stabilizes, after which they are measured again (m_{dry}). This procedure for determining the porosity of a material is in accordance with the research done by Lagouin et al. [22].

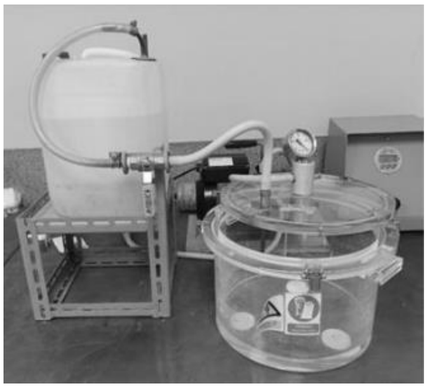

Figure 6. Vacuuming system

Figure 7. Sample holder

Material porosity and water absorption are calculated based on measured mass values according to the following formulas:

Porosity

$$\varphi = \frac{m_{sat} - m_{dry}}{m_{sat} - m_{hidr}} \cdot 100 \tag{6}$$

Water absorption

$$U_v = \frac{m_{sat} - m_{dry}}{m_{dry}} \cdot 100 \tag{7}$$

Bulk density is determined based on the volume of an irregularly shaped body (V) according to [23]:

$$\gamma = \frac{m_{dry}}{V} \tag{8}$$

3. RESULTS AND DISCUSSION

Based on the measured and calculated values shown in Table 1, it can be concluded what kind of biocomposite it is, that is, its application can be defined. The mutual dependence of all parameters starting from porosity, water absorption, heat flux, and longitudinal resistance of airflow is noticeable in the tested samples. For example, water absorption depends on porosity, that is, the higher the porosity of the samples, the higher the water absorption, and vice versa. As the porosity increases, the longitudinal resistance to airflow and the heat flux decrease. The differences occurring in the measured and calculated values for three samples of the same thickness can be subsumed under the standard deviation (SD) (Table 2).

By determining the characteristics listed in Table 1, it can be defined whether this biocomposite can be used as a sound or heat insulator. More precisely, based on the value for the longitudinal (specific) resistance of the airflow, it can be concluded what the material is in terms of sound insulation. The values of the absorption coefficient of the material can be calculated based on the longitudinal (specific) resistance of the airflow, using various theoretical models. On the other hand, heat flux and thermal conductivity coefficient define this biocomposite from the aspect of thermal insulation. Comparing it with Styrofoam, whose thermal conductivity coefficient ranges from λ = 0.035 - 0.040 W/mK, it can be concluded that this biocomposite has a three times higher thermal conductivity coefficient, that is, it is a worse thermal insulator than Styrofoam. In a similar way, this biocomposite can be defined in terms of sound insulation.

By comparing and analyzing the obtained results, linear correlations between porosity and flow resistance as well as porosity and coefficient of thermal conductivity were made. Based on the values, it can be concluded that an excellent correlation has been established between the previously mentioned values for the mean value of biocomposite P with a thickness of 3 cm, where the values of the correlation coefficients are R^2 = 0.9986 and R^2 = 0.9857 (Figures 8 and 9). However, the correlation between porosity and volumetric mass did not turn out to be good and amounts to R^2 = 0.3229 (Figure 10).

Table 1. Measurement results for biocomposite P

Mark	Sample thickness	Porosity	Bulk density	Absorbing water	Heat flux	Thermal conductivity coefficient	Longitudinal specific resistance to air flow
	d (cm)	**φ (%)**	**γ (g/cm³)**	**Uv (%)**	**q (W/m²)**	**λ (W/m·K)**	**r (kPa·s/m²)**
P1	3	57.268	0.637	91.652	40.3	0.121	480.636
P2	3	57.881	0.632	91.857	40.18	0.119	479.980
P3	3	56.913	0.620	89.897	40.51	0.122	481.221
P_{medium}	3	57.3	0.629	91.135	40.3	0.121	480.612

Table 2. The standard deviation for measured values

		STDEV
Porosity	φ	0.490
Bulk density	γ (g/cm³)	0.009
Absorbing water	Uv	1.077
Heat flux	q (W/m²)	0.167
Thermal conductivity coefficient	λ (W/mK)	0.002
Longitudinal specific resistance to air flow	r (kPa·s/m²)	0.621

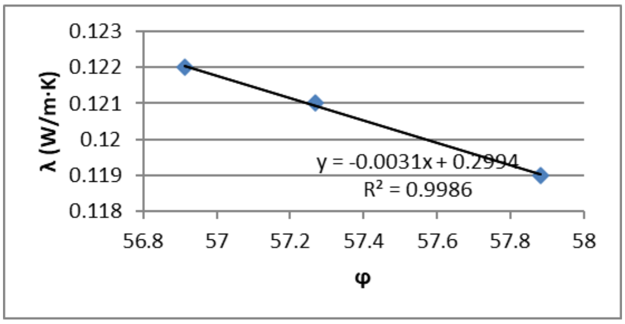

Figure 8. Linear correlation φ-λ

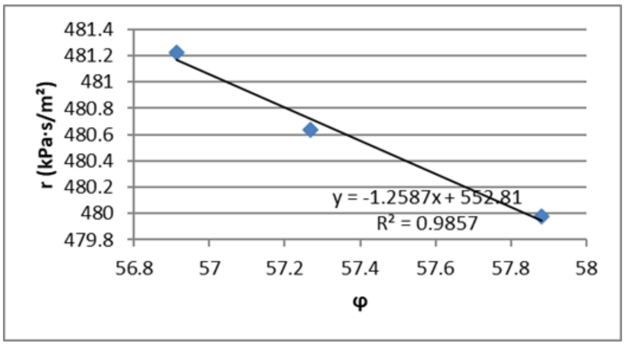

Figure 9. Linear correlation φ-r

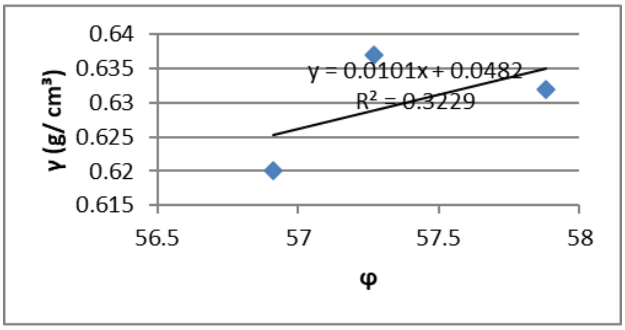

Figure 10. Linear correlation φ-γ

4. CONCLUSION

The increasingly frequent use of bio-based composites makes a big shift towards sustainable production and has a positive impact on the environment. Using waste and by-products from other industries, such as sawdust, which is generated as waste from the wood industry, enables additional use value for waste material and creates conditions for sustainable development in this segment of the economy. The tests mentioned in this paper can define the exact application of the new biocomposite. However, the same tests can also define the negative side of the tested material. More precisely, it was determined that the biocomposite made from wood industry waste material, Styrofoam granules and lime and gypsum as a binder, is a good sound and poor heat insulator. High values of air flow resistance and thermal conductivity coefficient support this key. This fact can determine the path of further research. By changing the ratio of materials in the biocomposite, different values of the tested properties will be obtained and, in this way, the optimal mixture can be defined in terms of sound or thermal insulation.

ACKNOWLEDGEMENTS

This study has been supported by the Republic of Serbia, Ministry of Education, Science and Technological Development through project number 451-03-47/2023-01/200108.

REFERENCES

[1] W. Z. Taffese and K. A. Abegaz, "Embodied Energy and CO2 Emissions of Widely Used Building Materials: The Ethiopian Context," *Buildings 2019, Vol. 9, Page 136*, vol. 9, no. 6, p. 136, May 2019, doi: 10.3390/BUILDINGS9060136.

[2] L. Lin, Y. Fan, M. Xu, and C. Sun, "A Decomposition Analysis of Embodied Energy Consumption in China's Construction Industry," *Sustainability 2017, Vol. 9, Page 1583*, vol. 9, no. 9, p. 1583, Sep. 2017, doi: 10.3390/SU9091583.

[3] I. Ryłko-Polak, W. Komala, A. B.- Materials, and undefined 2022, "The Reuse of Biomass and Industrial Waste in Biocomposite Construction Materials for Decreasing Natural Resource Use and Mitigating the Environmental Impact of," *mdpi.com*, 2022, doi: 10.3390/ma15124078.

[4] A. Reilly and O. Kinnane, "The thermal behaviour and embodied energy of hemplime construction," in *Proceedings of the International Conference for Sustainable Design of the Built Environment (SDBE), London, UK*, 2017, pp. 20–21.

[5] S. Pochwała, D. Makiola, S. Anweiler, and M. Böhm, "The Heat Conductivity Properties of Hemp–Lime Composite Material Used in Single-Family Buildings," *Materials 2020, Vol. 13, Page 1011*, vol. 13, no. 4, p. 1011, Feb. 2020, doi: 10.3390/MA13041011.

[6] D. Curto, A. Guercio, and V. Franzitta, "Investigation on a Bio-Composite Material as Acoustic Absorber and Thermal Insulation," *Energies 2020, Vol. 13, Page 3699*, vol. 13, no. 14, p. 3699, Jul. 2020, doi: 10.3390/EN13143699.

[7] P. Brzyski and G. Lagód, "Physical and mechanical properties of composites based on hemp shives and lime," *E3S Web of Conferences*, vol. 49, p. 00010, Aug. 2018, doi: 10.1051/E3SCONF/20184900010.

[8] Y. L. Wang, X. Y. Guo, P. Y. Huang, K. N. Huang, Y. Yang, and Z. B. Chen, "Finite element investigation of fatigue performance of CFRP-strengthened beams in hygrothermal

environments,” *Compos Struct*, vol. 234, p. 111676, Feb. 2020, doi: 10.1016/J.COMPSTRUCT.2019.111676.

[9] J. Liu, T. Guo, M. H. Hebdon, X. Yu, and L. Wang, “Behaviors of GFRP-steel bonded joints under cyclic loading after hygrothermal aging,” *Constr Build Mater*, vol. 242, p. 118106, May 2020, doi: 10.1016/J.CONBUILDMAT.2020.118106.

[10] M. P. Sáez-Pérez, M. Brümmer, and J. A. Durán-Suárez, “A review of the factors affecting the properties and performance of hemp aggregate concretes,” *Journal of Building Engineering*, vol. 31, p. 101323, 2020, doi: 10.1016/j.jobe.2020.101323.

[11] R. Agliata, S. Gianoglio, and L. Mollo, “International journal of Architecture Technology and Sustainability Volume 4 Is 1 Hemp-lime composite for buildings insulation: material properties and regulatory framework”, doi: 10.4995/vitruvio-ijats.2019.11771.

[12] S. Prétot, F. Collet, C. Garnier, and S. Pretot, “LIFE CYCLE ASSESSMENT OF A HEMP CONCRETE WALL: IMPACT OF THICKNESS AND COATING. LIFE CYCLE ASSESSMENT OF A HEMP CONCRETE WALL: IMPACT OF THICKNESS AND COATING,” 2013, doi: 10.1016/j.buildenv.2013.11.010ï.

[13] S. Amziane and M. Sonebi, “Overview on biobased building material made with plant aggregate,” 2016. doi: 10.21809/rilemtechlett.2016.9.

[14] M. S. Abbas, F. Mcgregor, A. Fabbri, and M. Y. Ferroukhi, “The use of pith in the formulation of lightweight bio-based composites: Impact on mechanical and hygrothermal properties,” *Constr Build Mater*, vol. 259, p. 120573, 2020, doi: 10.1016/j.conbuildmat.2020.120573.

[15] M. S. Abbas, F. Mcgregor, A. Fabbri, and Y. M. Ferroukhi, “3 rd International Conference on Bio-Based Building Materials INFLUENCE OF ORIGIN AND YEAR OF HARVEST ON THE PERFORMANCE OF PITH MORTARS”, doi: 10.26168/icbbm2019.6.

[16] J. Bojković, M. Marašević, N. Stojić, V. Bulatović, and B. Radičević, “Thermal and Sound Characterization of a New Biocomposite Material,” *Materials*, vol. 16, no. 12, p. 4209, Jun. 2023, doi: 10.3390/ma16124209.

[17] “SRPS EN ISO 9053-1:2019.” Accessed: Feb. 01, 2023. [Online]. Available: https://iss.rs/sr_Cyrl/project/show/iss:proj:62289

[18] T. Tritt, *Thermal conductivity: theory, properties, and applications*. 2005. Accessed: Feb. 01, 2023. [Online]. Available: https://books.google.com/books?hl=sr&lr=&id=whJNfKmziiIC&oi=fnd&pg=PA1&dq=T.M.+Tritt,+Thermal+Conductivity:+Theory,+Properties,+and+Applications,+Kluwer+Academic/Plenum+Publishers,+New+York,+New+York%3B+2004+&ots=rzMB0CAqYW&sig=7dS4EObpPQGboj88KioraDeLgcE

[19] B. F.-R. of S. Instruments and undefined 1997, “A steady-state high-temperature apparatus for measuring thermal conductivity of ceramics,” *aip.scitation.org*, Accessed: Feb. 01, 2023. [Online]. Available: https://aip.scitation.org/doi/abs/10.1063/1.1148202

[20] W. dos S.-J. of the E. C. Society and undefined 2008, “Advances on the hot wire technique,” *Elsevier*, doi: 10.1016/j.jeurceramsoc.2007.04.012.

[21] “EN 12667:2001 - Thermal performance of building materials and products - Determination of thermal.” Accessed: Feb. 01, 2023. [Online]. Available: https://standards.iteh.ai/catalog/standards/cen/f845e9a0-09c4-43ef-955c-6478a0497fb4/en-12667-2001

[22] M. Lagouin, C. Magniont, P. Sénéchal, P. Moonen, J. E. Aubert, and A. Laborel-préneron, “Influence of types of binder and plant aggregates on hygrothermal and mechanical properties of vegetal concretes,” *Constr Build Mater*, vol. 222, pp. 852–871, Oct. 2019, doi: 10.1016/j.conbuildmat.2019.06.004.

[23] “SRPS EN 1015-10:2008/A1:2008.” Accessed: Feb. 01, 2023. [Online]. Available: https://iss.rs/sr_Cyrl/project/show/iss:proj:19766

Static analysis of the RC multi-storey building depending on model and soil parameters

Stefan Mihajlović[1*], Miloš Šešlija[2], Vladimir Mandić[1], Iva Despotović[1], Marijana Janićijević[1]
[1]Faculty of mechanical and civil engineering, University of Kragujevac, Kraljevo (Republic of Serbia)
[2]Faculty of technical sciences, University of Novi Sad, Novi Sad (Republic of Serbia)

The following paper contains a static analysis reinforced concrete multistorey building with flooring P+5 residential and business purposes. The building is designed as a reinforced concrete frame structure consisting of beams and columns of the same cross-section on all floors. The ground floor, which will be used for business purposes, is designed with reinforced concrete walls on the brim of the structure. The base of the building has rectangular cross-section dimensions of 15x25m, with a basic span construction of 5 m. Analysis of all relevant loads which are acting on the structure was considered according to Eurocode standards.

In the paper, the bending moments of the fundamental slab are analyzed with special emphasis on the on interaction analysis of the fundamental slab and soil which is modeled as a half-space. For such a model are given the dependence of the bending moments on the dimensions of the half-space by which the soil is represented and the characteristics of the soil itself, which are given by different deformation modules. For structure analysis software Tower 8 was used..

Keywords: static analysis of structure, half-space, foundation, fundamental slab, concrete structures, multi-storey building, geomechanics

1. INTRODUCTION

The need for population migration is a phenomenon that has existed for as long as the human species. Due to the search for better living conditions in the last ten years, an increase in the number of inhabitants can be observed in areas with better economic development. This led o the concentration of a large number of people in a small space, so there was a need to build buildings in urban areas. The buildings most often built in such conditions [7] are residential and business multi-story buildings.

The analysis of static influences was done for a multi-story reinforced concrete building (RC building) with flooring *Gf+5*, where the ground floor will be used as an office space and the typical floor levels are purposed for collective housing.

The physical and mechanical properties of the soil [1] and other data necessary for the next phase of the design process are obtained based on the geomechanical investigations [3] carried out before the start of the design process. The load applied to the structure is determined according to the Eurocode (EC) recommendations. For such determined load values, a static calculation was made in the case when the fundamental slab rests on the ground modeled as a half-space. The static influences in the elements of the RC multi-story building are analyzed with special consideration to the soil model, which is shown as a half-space of different sizes and characteristics of the soil.

2. TECHNICAL CHARACTERISTICS OF THE BUILDING

The RC multi-storey building is designed as a skeleton structure with frames in two vertical directions. The basic grid of the construction is 5m, and the layout of structural elements is shown in Figure 1.

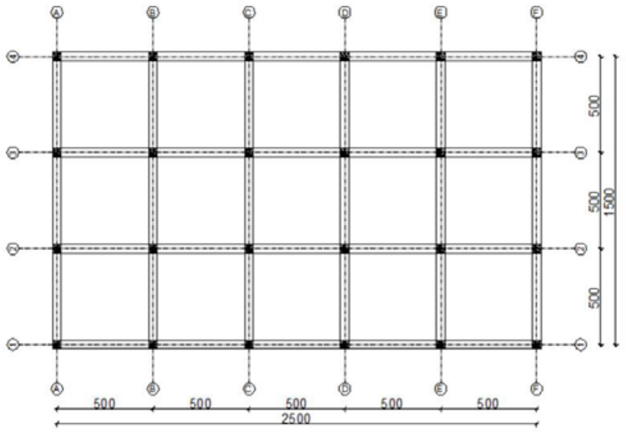

Figure 1: Disposition of structural elements of a RC building

Typical stories are rectangular bases measuring 15x25 m, the structural elements that make up the frame are columns with a square cross-section measuring 45x45 cm and beams with a rectangular cross-section measuring 30x45 cm. In addition to linear elements, the ground floor is reinforced with RC walls around the perimeter of the building. The reinforcement plan of the basic structural elements is shown in Figure 2.

The building consists of 6 floors whose floor heights are equal and amount to 2.8 m. The mezzanine structures are designed as reinforced concrete slabs with a thickness of 16 cm. The load is transferred from the roof over the floor to the soil across a foundation slab thick 45 cm, whose strength increased is with reinforced concrete beams [2]. A solution in the form of a flat impassable roof is planned for the roof construction of the building. Class C30/37 concrete and ribbed reinforcement B500B are intended to be used for the building of all RC elements of the multi-story building. The section on the long side of the structure is shown in Figure 3.

*Stefan Mihajlović: Dositejeva 19, 36000 Kraljevo, Republic of Serbia and mihajlovic.s@mfkv.kg.ac.rs

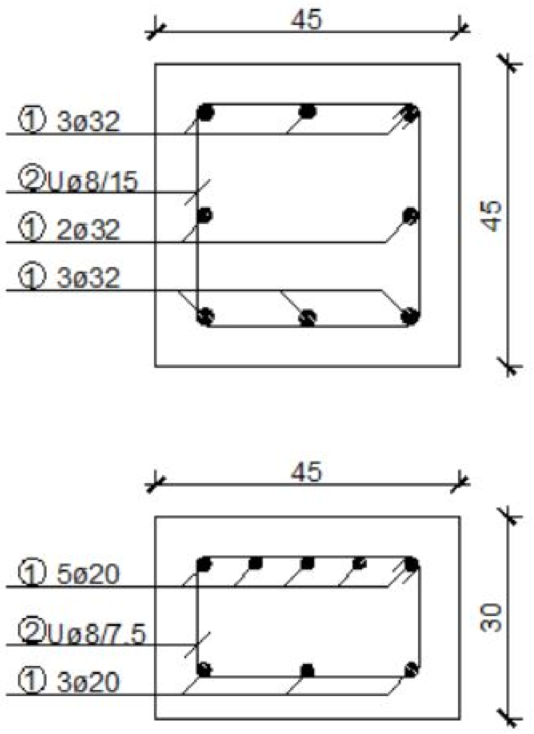

Figure 2: Beam and column reinforcement plan

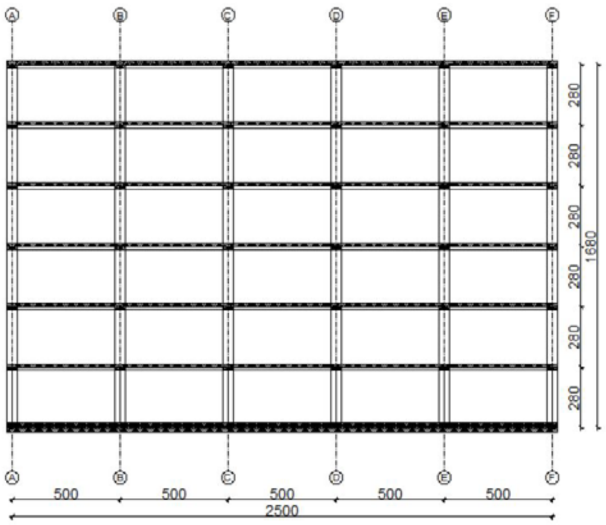

Figure 3: Vertical section of the structure

The analysis of all relevant loads that affect the construction and dimensioning of characteristic reinforced concrete elements was done according to European standards – Eurocodes.

Constructive elements of the building are dimensioned according to the effects due to permanent, snow and wind loads and seismic loads. Forms of oscillation of the structure are shown in Figure 4, Figure 5, and Figure 6.

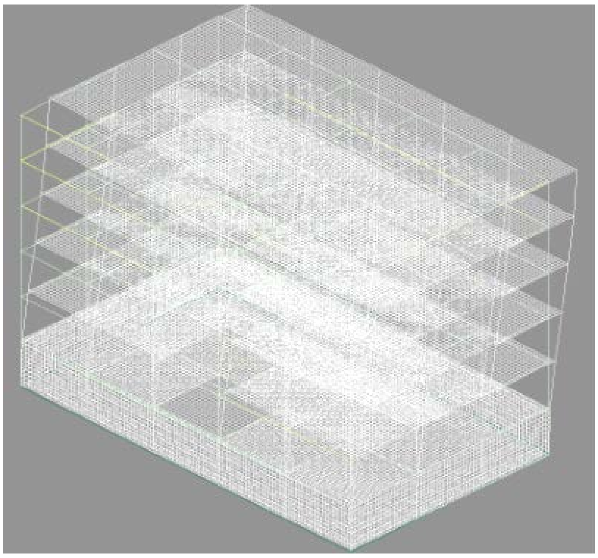

Figure 4: Form of oscillation for the first tone of the oscillation

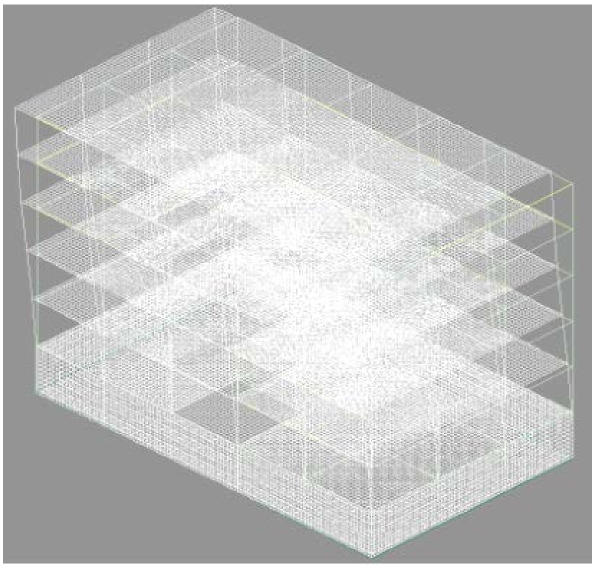

Figure 5: Form of oscillation for the second tone of the oscillation

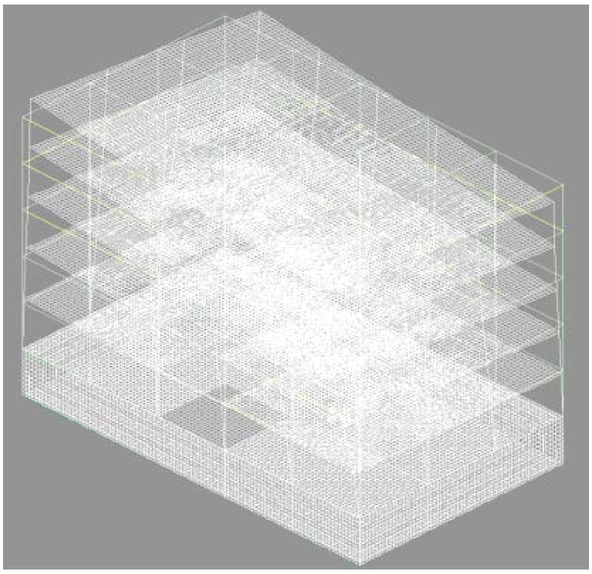

Figure 6: Form of oscillation for the third tone of the oscillation

3. MODELING OF THE CONSTRUCTION OF THE BUILDING AND THE SOIL

Modeling, calculation, and dimensioning of the structure were done in the software package "Tower 8.0", in which the calculation of static influences was done according to the linear theory of elasticity, taking into account geometric and material linearity.

3.1. Modeling of the construction of the building

For the modeling depending on the dimensions of the structural elements, linear finite elements were used (for modeling columns with dimensions 45x45 cm and beams with dimensions 45x30 cm), surface finite elements (for modeling mezzanine ceilings and external perimeter walls on the ground floor). Figure 7 shows the calculation model of the supporting elements of the structure.

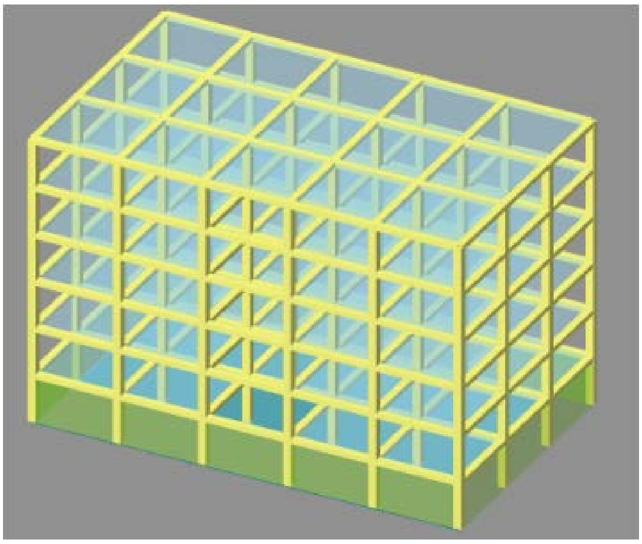

Figure 7: Model of RC construction

3.2. Modeling of the soil

The soil under the foundation slab of the RC structure is modeled as a half-space [6]. This type of soil model implies the representation of certain characteristics of the soil with volume finite elements [5], which is shown in Figure 8.

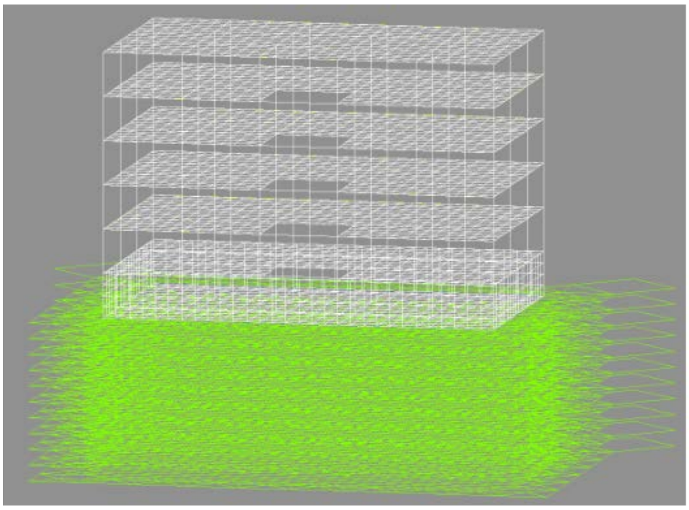

Figure 8: Model of soil under the foundation slab

The static influences were analyzed for the half-space of different dimensions - the depth of the half-space Hh in the amount of 10 m, 15 m, and 20 m and the extension beyond the dimensions of the foundation slab Hb in the amount of 3 m, 5 m, and 8 m [4].

The dimensions of the half-space need to be rationally evaluated and adopted so that the calculation model is simpler, and the obtained calculation results are sufficiently accurate.

Soil characteristics are shown by different soil deformability modules in the amount of 10 MPa, 25 MPa, and 50 MPa.

4. ANALYSIS OF THE RESULTS

In the continuation of the paper, the static influences were analyzed - bending moments M_x and M_y in the foundation slab, bending moments M_x and M_y in the section of the foundation slab, bending moments M_3 in the top of the column on the last story, stresses in the soil σ and soil settlement s for the specified cases of the soil model and soil characteristics.

The dependences of static influences are shown in relation to the size and depth of the half-space with which the soil is modeled for different values of soil deformability [8].

4.1. Static influences for the modulus of deformability *E=10 MPa*

Table 1: Maximum bending moments M_x in the foundation slab

E=10 MPa		Mx [kNm]		
	Hb [m]	3	5	8
Hh [m]	10	382.13	382.18	414.70
	15	514.41	514.32	514.42
	20	514.12	513.90	514.06

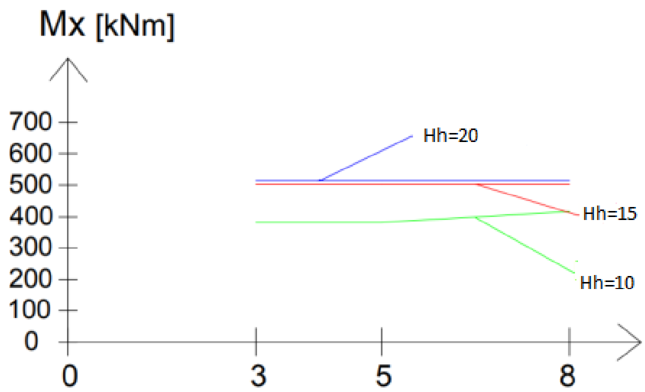

Figure 9: Maximum bending moments Mx i n the foundation slab

Table 2: Maximum bending moments M_y in the foundation slab

E=10 MPa		My [kNm]		
	Hb [m]	3	5	8
Hh [m]	10	414.69	418.75	564.31
	15	565.14	573.43	574.84
	20	567.42	576.63	578.93

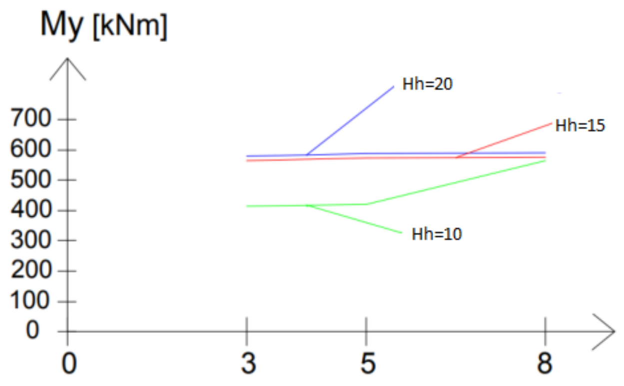

Figure 10: Maximum bending moments M_y in the foundation slab

Table 3: Maximum bending moments M_x in the section of the foundation slab

E=10 MPa		Mx [kNm]		
	Hb [m]	3	5	8
Hh [m]	10	33.86	48.04	67.47
	15	70.37	98.94	107.01
	20	78.71	110.96	121.70

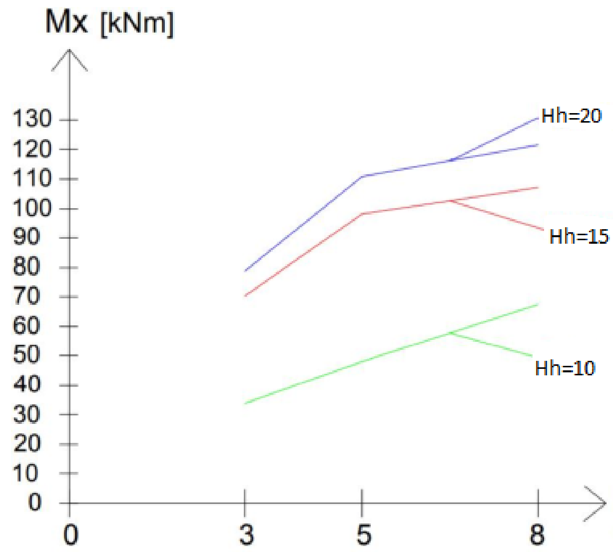

Figure 11: Maximum bending moments M_x in the section of the foundation slab

Table 4: Maximum bending moments M_y in the section of the foundation slab

E=10 MPa		My [kNm]		
	Hb [m]	3	5	8
Hh [m]	10	17.43	18.49	25.25
	15	27.60	29.53	30.62
	20	29.31	31.35	32.90

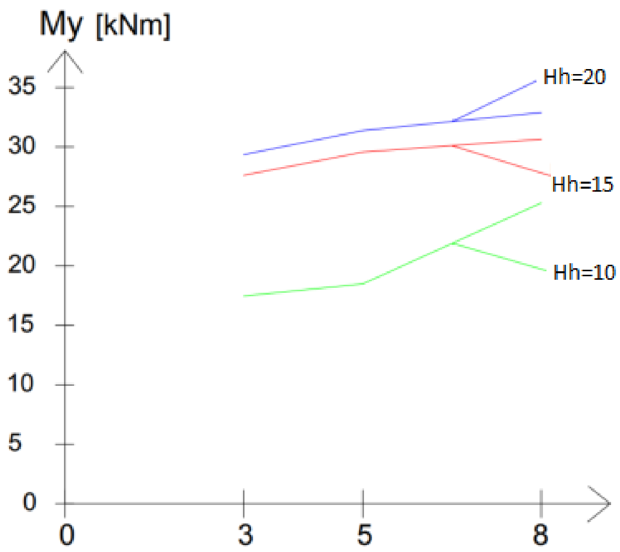

Figure 12: Maximum bending moments M_y in the section of the foundation slab

Table 5: Bending moments M_3 in the top of the column on the last story

E=10 MPa		M3 [kNm]		
	Hb [m]	3	5	8
Hh [m]	10	154.93	158.55	207.67
	15	211.55	218.89	221.47
	20	215.31	223.59	227.19

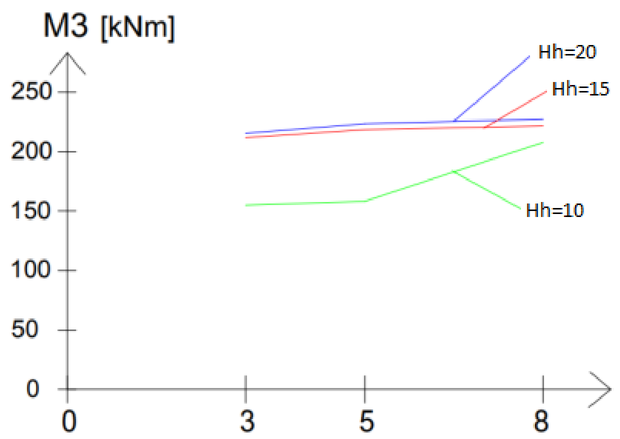

Figure 13: Bending moments M_3 in the top of the column on the last story

Table 6: Normal forces N_x in the foundation slab

E=10 MPa		Nx [kN]		
	Hb [m]	3	5	8
Hh [m]	10	4.50	4.17	5.67
	15	6.24	6.84	7.20
	20	6.38	7.54	8.07

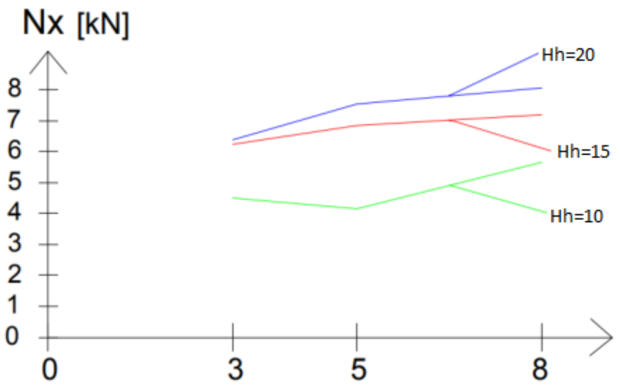

Figure 14: Normal forces N_x in the foundation slab

Table 7: Normal forces N_y in the foundation slab

E=10 MPa		Ny [kN]		
	Hb [m]	3	5	8
Hh [m]	10	4.39	4.15	5.64
	15	6.06	5.58	5.53
	20	5.99	5.56	5.55

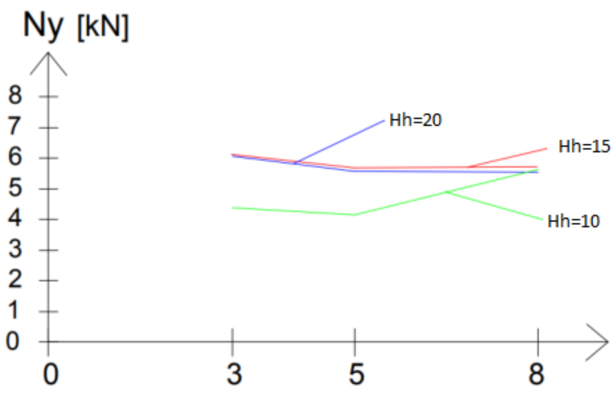

Figure 15: Normal forces N_y in the foundation slab

Table 8: Stresses in the soil σ

E=10 MPa		σ [kN/m²]		
	Hb [m]	3	5	8
Hh [m]	10	1427.48	1433.54	1933.75
	15	2141.77	2119.33	2136.42
	20	2240.35	2193.02	2217.76

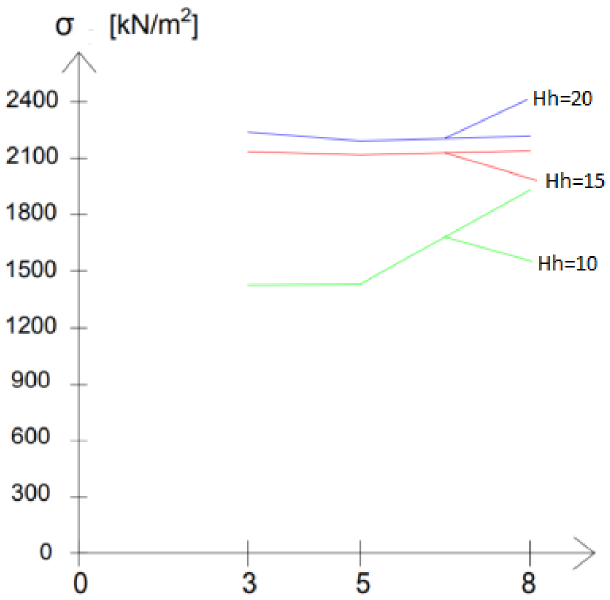

Figure 16: Stresses in the soil σ

Table 9: Soil settlement s

E=10 MPa		s [mm]		
	Hb [m]	3	5	8
Hh [m]	10	69.25	65.87	86.80
	15	123.44	110.29	102.93
	20	150.87	122.45	112.74

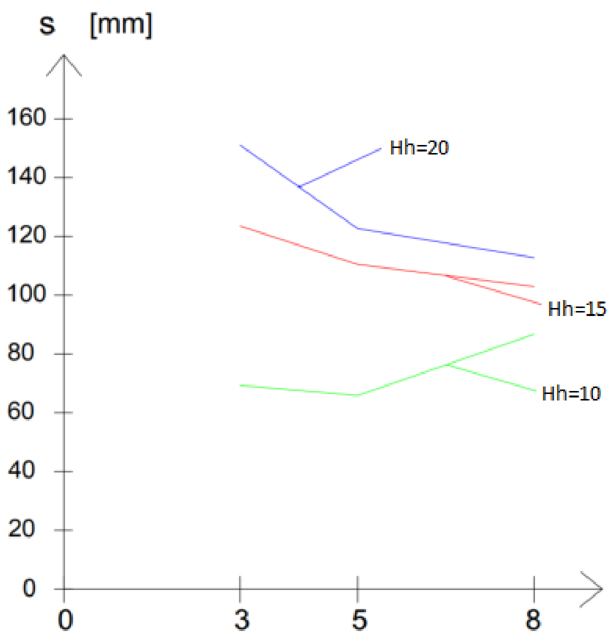

Figure 17: Soil settlement s

4.2. Static influences for the modulus of deformability *E=25 MPa*

Table 10: Maximum bending moments M_x in the foundation slab

E=25 MPa		Mx [kNm]		
	Hb [m]	3	5	8
Hh [m]	10	379.94	380.03	511.81
	15	511.78	511.81	511.95
	20	379.94	511.60	511.82

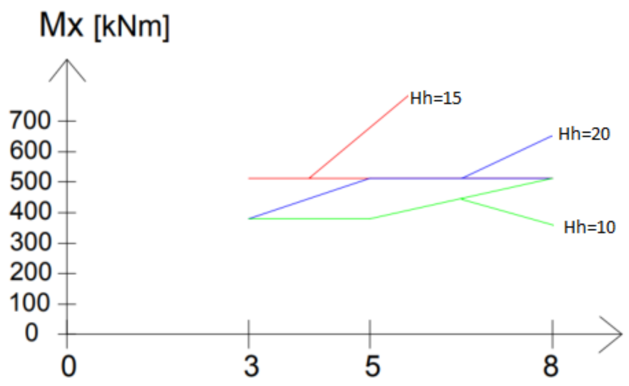

Figure 18: Maximum bending moments M_x in the foundation slab

Table 11: Maximum bending moments M_y in the foundation slab

E=25 MPa		My [kNm]		
	Hb [m]	3	5	8
Hh [m]	10	405.95	409.19	551.28
	15	552.16	559.04	560.03
	20	411.30	561.85	563.49

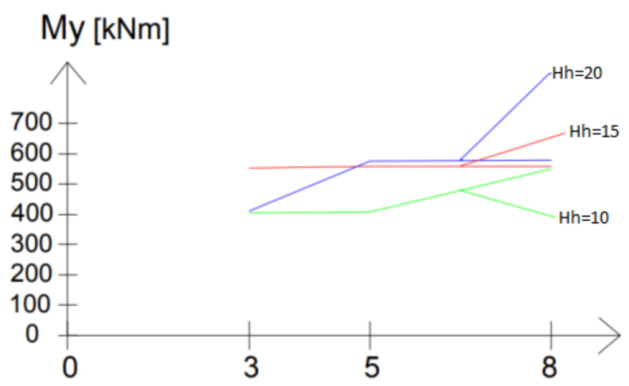

Figure 19: Maximum bending moments M_y in the foundation slab

Table 12: Maximum bending moments M_x in the section of the foundation slab

E=25 MPa		Mx [kNm]		
	Hb [m]	3	5	8
Hh [m]	10	18.42	31.67	43.11
	15	72.23	75.55	78.94
	20	41.06	84.52	92.09

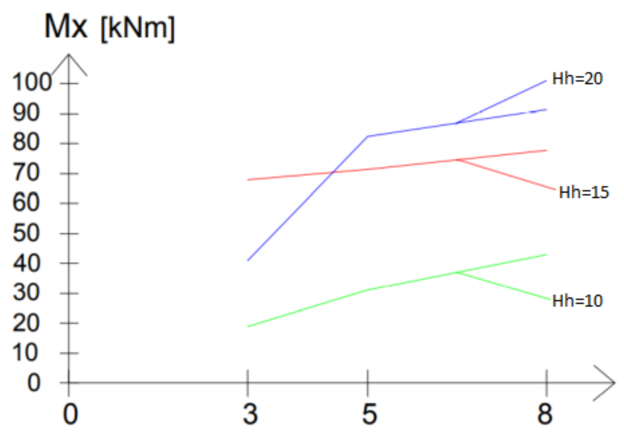

Figure 20: Maximum bending moments M_x in the section of the foundation slab

Table 13: Maximum bending moments M_y in the section of the foundation slab

E=25 MPa		My [kNm]		
	Hb [m]	3	5	8
Hh [m]	10	14.21	15.64	22.08
	15	23.40	25.07	26.95
	20	16.84	26.36	27.53

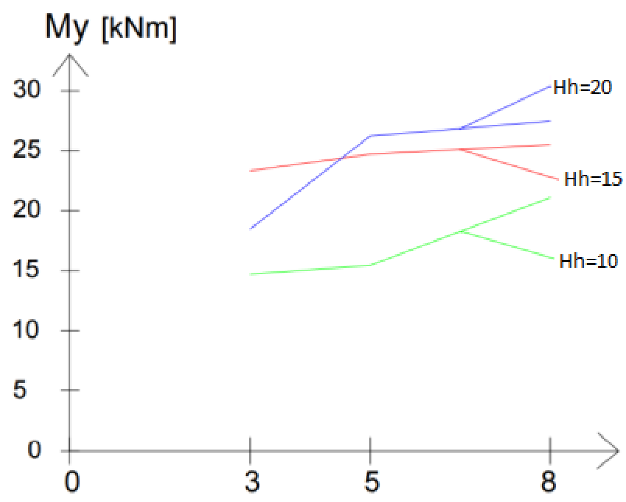

Figure 21: Maximum bending moments M_y in the section of the foundation slab

Table 14: Bending moments M_3 in the top of the column on the last story

E=25 MPa		M3 [kNm]		
	Hb [m]	3	5	8
Hh [m]	10	151.01	151.26	197.54
	15	201.60	207.26	209.16
	20	157.11	211.37	214.13

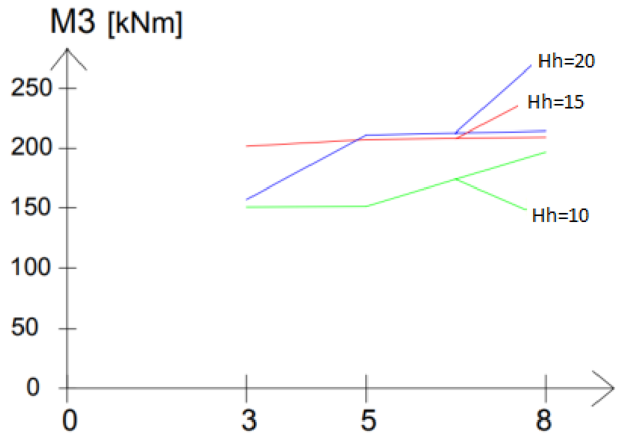

Figure 22: Bending moments M_3 in the top of the column on the last story

Table 15: Normal forces N_x in the foundation slab

E=25 MPa		Nx [kN]		
	Hb [m]	3	5	8
Hh [m]	10	4.36	4.06	5.52
	15	6.03	5.40	5.57
	20	5.52	6.07	6.23

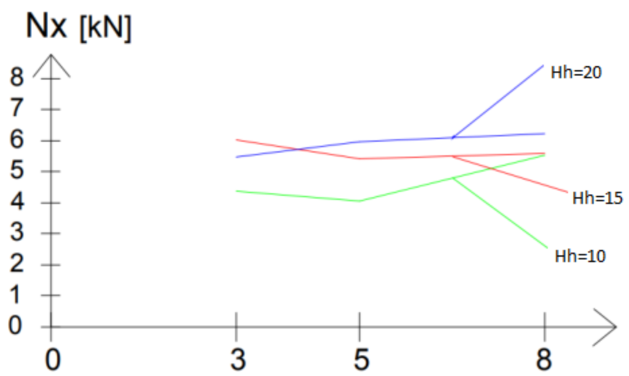

Figure 23: Normal forces N_x in the foundation slab

Table 16: Normal forces N_y in the foundation slab

E=25 MPa		Ny [kN]		
	Hb [m]	3	5	8
Hh [m]	10	4.28	4.06	5.51
	15	5.84	5.44	5.42
	20	4.38	5.42	5.40

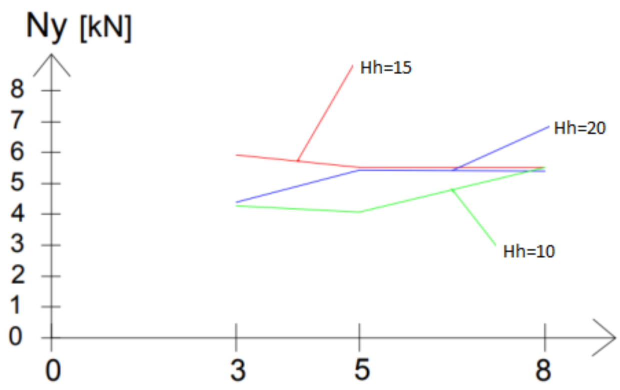

Figure 24: Normal forces N_y in the foundation slab

Table 17: Stresses in the soil σ

E=25 MPa		σ [kN/m²]		
	Hb [m]	3	5	8
Hh [m]	10	1391.85	1395.13	1878.86
	15	2092.13	2061.56	2074.80
	20	1627.62	2136.31	2156.77

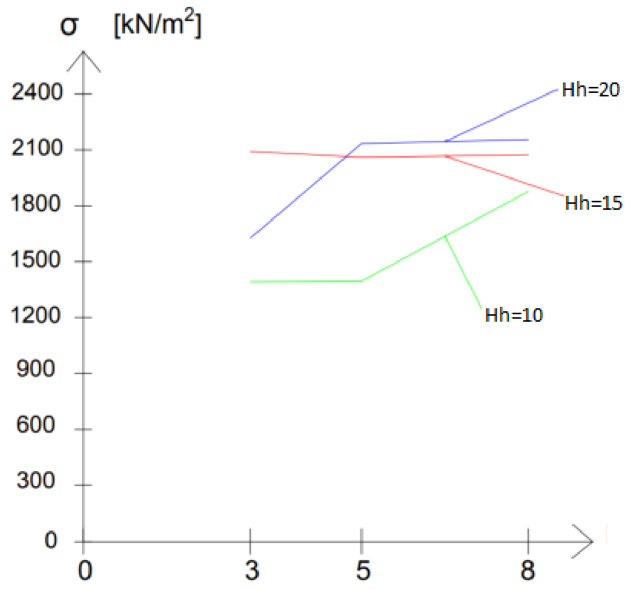

Figure 25: Stresses in the soil σ

Table 18: Soil settlement s

E=25 MPa		s [mm]		
	Hb [m]	3	5	8
Hh [m]	10	27.34	25.99	34.37
	15	48.79	43.53	40.89
	20	44.29	48.50	44.92

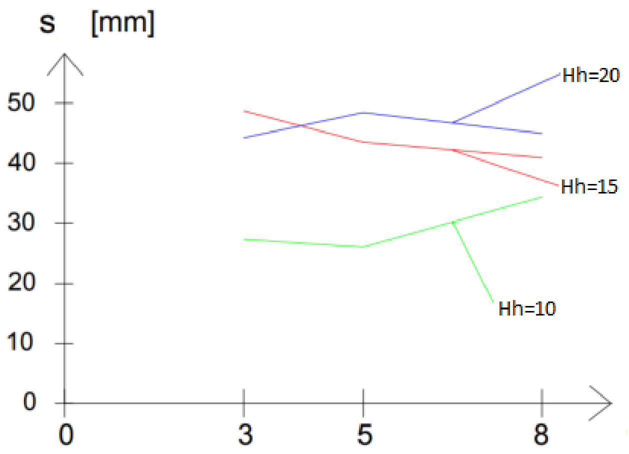

Figure 26: Soil settlement s

4.3. Static influences for the modulus of deformability *E=50 MPa*

Table 19: Maximum bending moments M_x in the foundation slab

E=50 MPa		Mx [kNm]		
	Hb [m]	3	5	8
Hh [m]	10	505.78	505.89	505.92
	15	506.18	506.22	506.38
	20	375.91	375.87	376.06

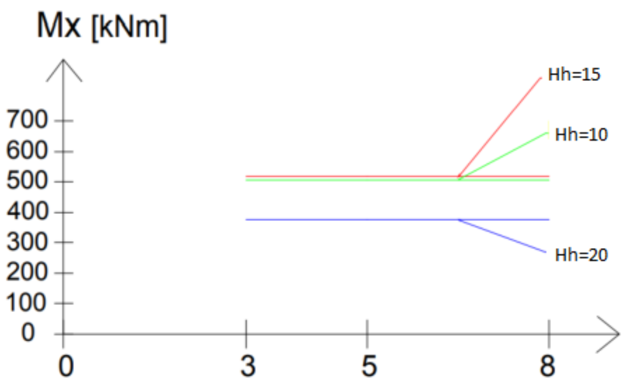

Figure 27: Maximum bending moments M_x in the foundation slab

Table 20: Maximum bending moments M_y in the foundation slab

E=50 MPa		My [kNm]		
	Hb [m]	3	5	8
Hh [m]	10	532.84	536.17	536.24
	15	536.99	542.45	543.14
	20	399.70	404.42	405.30

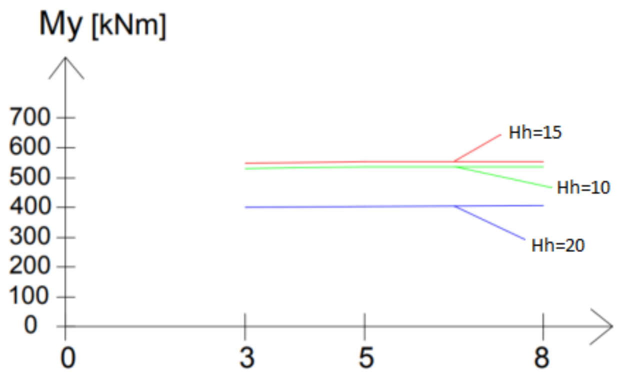

Figure 28: Maximum bending moments M_y in the foundation slab

Table 21: Maximum bending moments M_x in the section of the foundation slab

E=50 MPa		Mx [kNm]		
	Hb [m]	3	5	8
Hh [m]	10	4.21	19.73	18.69
	15	23.28	42.41	46.55
	20	21.05	38.59	42.07

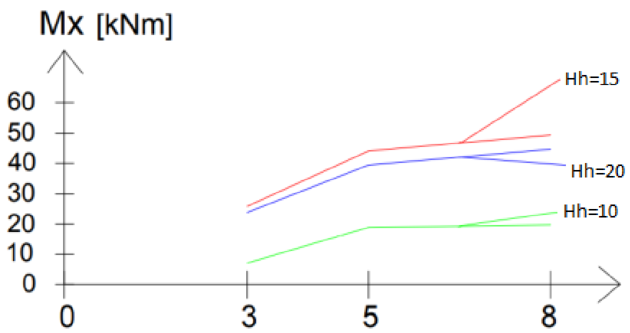

Figure 29: Maximum bending moments M_x in the section of the foundation slab

Table 22: Maximum bending moments M_y in the section of the foundation slab

E=50 MPa		My [kNm]		
	Hb [m]	3	5	8
Hh [m]	10	16.48	17.49	17.31
	15	19.24	20.29	21.93
	20	15.60	16.42	16.97

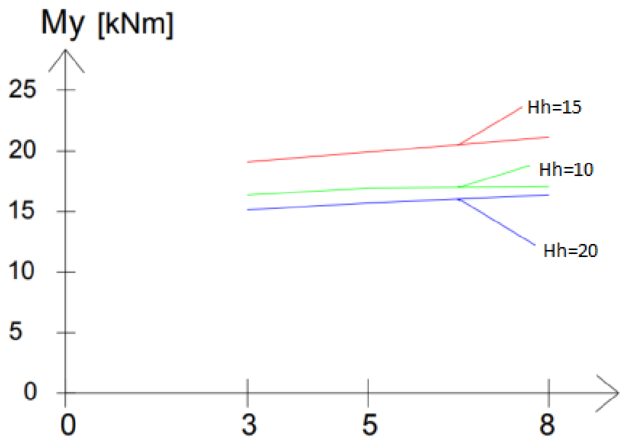

Figure 30: Maximum bending moments M_y in the section of the foundation slab

Table 23: Bending moments M_3 in the top of the column on the last story

E=50 MPa		M3 [kNm]		
	Hb [m]	3	5	8
Hh [m]	10	149.36	159.15	154.37
	15	191.68	195.78	197.14
	20	184.89	187.52	187.83

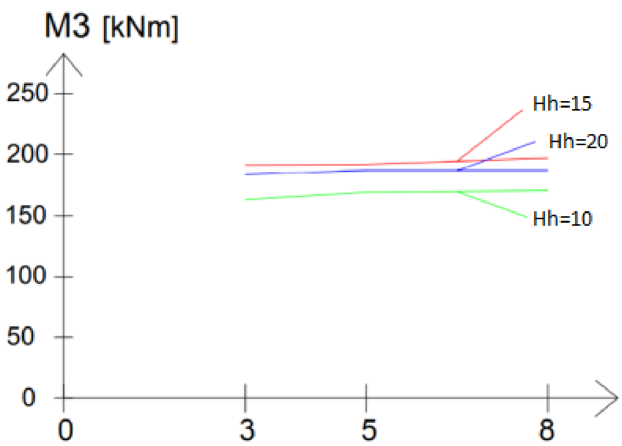

Figure 31: Bending moments M_3 in the top of the column on the last story

Table 24: Normal forces N_x in the foundation slab

E=50 MPa		Nx [kN]		
	Hb [m]	3	5	8
Hh [m]	10	5.63	5.27	5.31
	15	5.76	5.18	5.20
	20	4.37	3.85	3.85

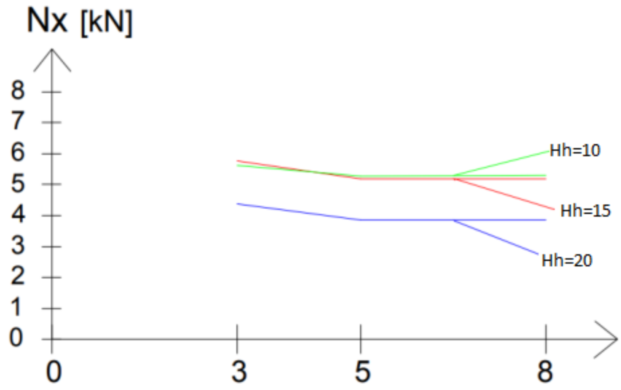

Figure 32: Normal forces N_x in the foundation slab

Table 25: Normal forces N_y in the foundation slab

E=50 MPa		Ny [kN]		
	Hb [m]	3	5	8
Hh [m]	10	5.56	5.29	5.32
	15	5.62	5.23	5.23
	20	4.22	3.89	3.86

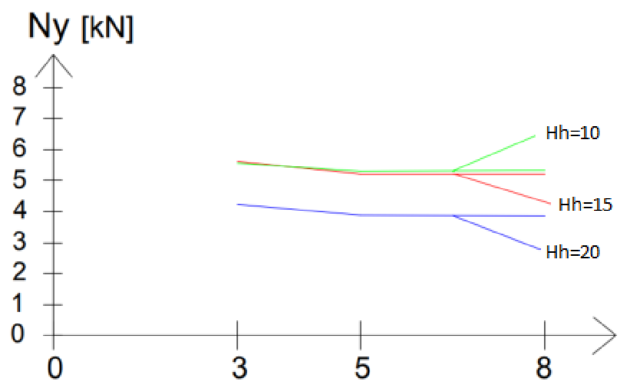

Figure 33: Normal forces N_y in the foundation slab

Table 26: Stresses in the soil σ

E=50 MPa		σ [kN/m^2]		
	Hb [m]	3	5	8
Hh [m]	10	1833.48	1834.74	1829.56
	15	2042.43	2005.85	2016.71
	20	1592.06	1541.65	1554.87

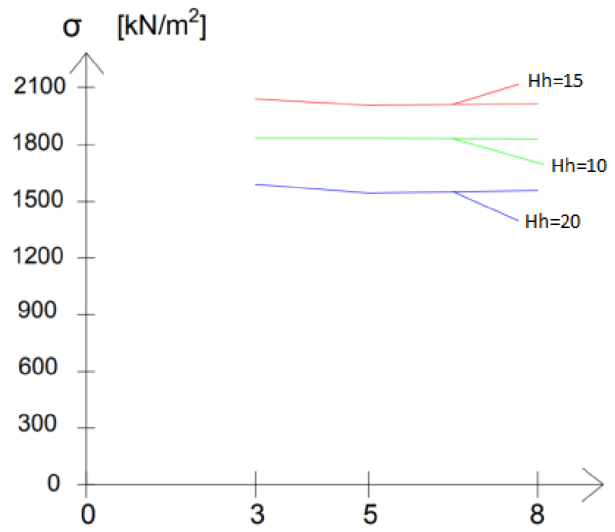

Figure 34: Stresses in the soil σ

Table 27: Soil settlement s

E=50 MPa		s [mm]		
	Hb [m]	3	5	8
Hh [m]	10	18.14	17.23	16.99
	15	24.04	21.44	20.32
	20	21.84	17.79	16.60

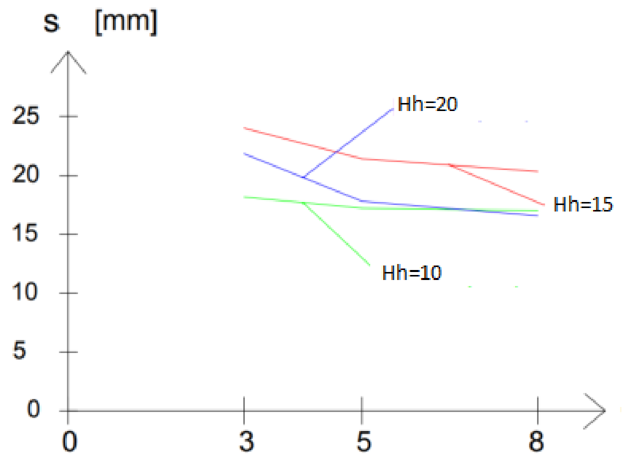

Figure 35: Soil settlement s

5. CONCLUSION

Based on the presented diagrams and tabulated values, a comparison of the static influences can be made depending on the variable parameters and the given modulus of deformability. The variable parameters are the depth of the half-space (Hh) and the dimensions of the half-space, i.e. the extension of the half-space beyond the dimensions of the fundamental slab (Hb), which is explained in the part of soil modelling [9].

5.1. Static influences for the modulus of deformability E=10 Mpa

The static influences are similar for half-space depths of 15 m and 20 m, while in the case of a half-space depth of 10 m the value static influences are lower.

5.2. Static influences for the modulus of deformability E=25 Mpa

The values of the static influences are similar for the half-space depths of 15 m and 20 m, while in the case of the half-space depth of 10 m, the values are smaller, and for *Hb* of 5m and 8m. For *Hb* of the 3m the values are significantly different, so it is not possible to assess the dependence of static influences.

5.3. Static influences for the modulus of deformability E=50 Mpa

The values of static influences (bending moments and normal forces) are similar for the half-space depths of 10m and 15m, while for the half-space depth of 20m, the values are slightly lower. With the increase in *Hb*, the values of static influences generally decrease. The values of the moments at the top of the column are similar for the half-space depths of 15m and 20m, while the values for the half-space depth of 10m are slightly lower.

Based on these values, it is necessary to estimate with which value the depth of the half-space and the extension over the dimensions of the base plate to model the soil. For the presented case, the most optimal solution would be to adopt a half-space depth of 15m and an extension length of 5m.

REFERENCES

[1] D. Milović, “Mehanika tla”, Univerzitet u Novom Sadu, Institut za industrijsku gradnju (Novi Sad), (1982)

[2] S. Stevanović, “Fundiranje I”, Naučna knjiga (Beograd), (2008)

[3] M. Vasić, “Inženjerska geologija”, Fakultet tehničkih nauka (Novi Sad), (2001)

[4] P. Pavlović, “Prilog analizi interakcije konstrukcija-tlo kod armirano-betonskih dijafragmi”, Magistarski rad, Fakultet tehničkih nauka (Novi Sad), (1996)

[5] D. Milović and M. Đogo, “Problemi interakcije tlo-temelj-konstrukcija”, Fakultet tehničkih nauka (Novi Sad), (2009)

[6] S. Mihajlović, “Projekat fundiranja višespratne zgrade i analiza interakcije temeljne ploče i tla”, Zbornik radova Fakulteta tehničkih nauka (Novi Sad), (2019)

[7] S. Mihajlović, S. Marinkovic, V. Mandić, I. Despotović and M. Janićijević, “Analysis of cost and time required for the construction of RC diaphragms depending on the method of execution”, Proceedings of X International Conference “Heavy Machinery HM 2021”, Vrnjačka Banja (Serbia), 23 June 25 June 2021, pp. 535-542, (2021)

[8] J. E. Bowles, “Foundation Analysis and Design”, McGrow-Hill Book Comp (New York), (1988)

[9] M.I. Gorbunov-Pasadov and T.A. Malikova, “Rasčet konstrukcii na uprugom osnovanii”, Strojizdat (Moskva), (1984)

Nonlinear static „pushover” analysis of multi-storey reinforced concrete building

Marijana Janićijević[1*], Bojan Milošević[1], Stefan Mihajlović[1], Jovana Bojković[1], Saša Marinković[2]
[1]Faculty of Mechanical and Civil Engineering, University of Kragujevac, Kraljevo (Republic of Serbia)
[2]Marko Barlov PR izgradnja stambenih i nestambenih objekata LMT Inženjering Kraljevo

Contemporary structural design implies the nonlinear behaviour of ductile structural elements for the design of seismic actions, which implies the application of nonlinear analysis. Pushover analysis evaluates the seismic performance of the structure and combines the behavior of bearing and non-bearing elements thus forming a description of the overall degree of damage to the construction for different levels of seismic action.

This paper presents the results of the nonlinear static "pushover" analysis of a multi-storey reinforced concrete building designed according to EN 1992-1-1 and EN 1998-1. The structure was exposed to a monotonically increasing lateral load. The analysis was performed using four different material nonlinearity models (infrmFB, infrmDB, infrmFBPH, infrmDBPH) for two orthogonal directions in the SeismoStruct program. The assessment of seismic performance of the structure was performed based on the results of the "pushover" analysis for each of the applied nonlinear material models.

Keywords: pushover analysis, material nonlinearity, target displacement, seismic action

1. INTRODUCTION

The territory of the Republic of Serbia belongs to seismically active areas, so when designing and constructing buildings, it is necessary to apply regulations and methods that ensure seismic resistance. In this sense, it is necessary to use appropriate input data (depending on local conditions) and appropriate design and building methods. The objectives of seismic design are: to limit damage to structures, protect human life, and ensure the use of facilities that are important for emergency response in the event of earthquakes.

According to the modern seismic codes for the design of structures resistant to the effects of earthquakes, the concept of the design of reinforced concrete structures, in addition to ensuring strength capacity, is based on reducing the elastic seismic inertia effects while ensuring adequate ductility of the critical zones[1]. The structure doesn't need to remain elastic under the influence of the intended seismic loading. The development of inelastic deformations of the bearing elements is allowed to preserve the integrity of the entire structure. Based on the linear design approach, it is not possible to determine the nonlinear deformations that will occur due to the given seismic action, and therefore the extent of damage to the structure remains unknown [2]. A comprehensive design approach includes the non-linear behavior of structural elements during moderate and strong earthquakes, in pre-defined critical zones, which enables the dissipation of seismic energy. The energy dissipation capacity depends on the extent of the non-linear response of the structure. The main feature of the aseismic design is the use of behaviour factors, balancing strength, and ductility introduced through different classes of ductility. For dissipative structures, the value of the behavior factor is greater than 1.5, resulting in hysteretic energy dissipation in specific areas (critical zones). According to EN 1998-1, buildings can be classified into three different ductility classes depending on the degree of energy dissipation: low ductility class (*DCL*), medium ductility class (*DCM*), and high ductility class (*DCH*). Modern seismic analysis is based on the determination of the dynamic properties of the structure, the determination of the seismic force based on the given ground displacement and the mechanical properties of the structure, and the calculation of the effects on the structure as a result of the action of the relevant seismic forces. After the aforementioned influences are determined, all elements and critical sections are dimensioned for the appropriate combination of all loads acting on the structure (including the seismic load). The bearing capacity and the required deformation capacity of the considered structure are achieved by applying appropriate structural solutions and by elaborating specific details according to the seismic design requirements.

2. NONLINEAR STATIC ANALYSIS

In aseismic design, pushover analysis can be used as an alternative to linear-elastic analysis. The pushover method is a non-linear static method of calculating new or existing objects. The method was created based on procedures for the design and rehabilitation of damaged buildings, which contain engineering concepts based on the behavior of the structure. It was realized that more attention should be paid to damage control during design. This can only be achieved by introducing non-linear calculations into the methodology of seismic calculations. One of the most suitable approaches, on which the pushover analysis is based, is to combine the nonlinear static method of gradual pushing with the spectral response methodology [3]. With this analysis, the structure is exposed, in addition to the gravity load, to the lateral forces from the earthquake.

The pushover analysis aims to define the dependence of the displacement of the last floor or roof of the structure, the so-called control point, and the shear force in the foundation that causes the first yielding in the structure. The control point should be located at the highest level of the structure. When the strength of individual load-bearing elements reaches the stress value at the limit of large elongations, yielding occurs in those elements and so-

* Marijana Janićijević: Dositejeva 19, 36000 Kraljevo, Republic of Serbia and janicijevic.m@mfkv.kg.ac.rs

called plastic hinges are formed. Incremental lateral load is applied until the target displacement is reached and a nonlinear capacity curve is formed. It is assumed that the structure can make several such cycles and behave in a hysteretic manner [4]. To obtain the capacity curve, the analysis is applied up to the displacement control value, which is 150% of the target displacement value. This curve is usually determined to represent the first mode of the structure's response based on the assumption that the response to seismic action occurs primarily in the fundamental mode of vibration of the structure. Given that the building is a system with multiple degrees of freedom, the capacity curve of such a system (MDOF system) transforms into the capacity curve of an equivalent system with one degree of freedom (SDOF system), so that the capacity of the structure can be compared with the given seismic requirements [5].

By applying this method, it is possible to select places where potential plasticization of the system would occur, thus creating the conditions for the desired fracture mechanism to form on the system. In this way, the controlled development of nonlinear deformations prevents the system from reaching a state of complete collapse.

The assessment of the seismic performance of the structure in this work was carried out using the program for structural analysis SeismoStruct. This program is based on the finite element method and can use various non-linear modeling techniques. When calculating the behavior of spatial frames during the analysis with static and dynamic effects, the program analyzes the structural elements with the help of materially and geometrically nonlinear models. In this way, the program can calculate the response of the structure and its elements [6].

3. NUMERICAL EXAMPLE

3.1. Behaviour factor q

The capacity of structural systems to resist seismic forces in the nonlinear range generally allows them to be designed to resist seismic forces that are less than those corresponding to linear-elastic response.

To avoid an explicit inelastic structural analysis during design, the dissipative capacity of the structure is taken into account by applying an elastic analysis based on the response spectrum reduced concerning the elastic, so-called design spectrum. This reduction is achieved through the predominantly ductile behaviour of the structure and its elements, by introducing the behaviour factor q.

The behaviour factor q is an approximation of the ratio of seismic forces that the structure would experience if its response were fully elastic with 5% viscous damping and seismic forces that can be used in the elastic analysis while ensuring a satisfactory response of the structure. Its value defines the level of seismic load at the boundary between the elastic and plastic behaviour of the structure. The higher its value, the smaller the values on the design spectrum. Therefore, for lower values of the seismic load, the construction will move into the elastic area of operation. The value of the behaviour factor q can be different in different horizontal directions of the structure, while the ductility class is the same in all directions.

Upper limit value of the behaviour factor q shall be derived for each design direction as follows:

$$q = q_0 \cdot k_w \geq 1{,}50 \tag{1}$$

where:

q_0 is the basic value of the behaviour factor, depending on the type of the structural system and its regularity in elevation;

k_w is the factor reflecting the prevailing mode in structural systems with walls [7].

For buildings that are regular in elevation, the basic values of q_0 for the various structural types are given in Table 1.

Table 1. Basic value of the behaviour factor, q_0

STRUCTURAL TYPE	DCM	DCH
Frame system, dual system, coupled wall system	$3{,}0\alpha_u/\alpha_1$	$4{,}5\alpha_u/\alpha_1$
Uncoupled wall system	3,0	$4{,}0\alpha_u/\alpha_1$
Torsionally flexible system	2,0	3,0
Inverted pendulum system	1,5	2,0

α_1 and α_u are defined as follows:

α_1 is the value by which the horizontal seismic design action is multiplied to first reach the flexural resistance in any member in the structure, while all other design actions remain constant;

α_u is the value by which the horizontal seismic design action is multiplied, to form plastic hinges in a number of sections sufficient for the development of overall structural instability, while all other design actions remain constant [7].

Since the construction belongs to the group of constructions of the frame system and for the adopted ductility class DCH, the basic value of the behaviour factor is calculated as:

$$q_0 = 4{,}5 \cdot \frac{\alpha_u}{\alpha_1} \tag{2}$$

The value of α_u / α_1 is 1.3 for multi-storey, multi-bay frames, or frame-equivalent dual structures and factor k_w has a value of 1.

Total behaviour factor is:

$$q = q_0 \cdot k_w = 4.5 \cdot 1.3 \cdot 1 = 5.85 \tag{3}$$

3.2. Construction modeling

A five-story reinforced concrete building was analyzed according to the recommendations in EN 1990, EN 1991, EN 1992-1, and EN 1998-1. The raster of the structure is shown in Figure 1. The length of a span in longitudinal and transverse directions is 5 m. The basic dimensions of the building are 15 x 25 m, and the height of the floors is constant at 2.8 m. The concrete material is C30/37 according to Eurocode 2, and the reinforcing steel is class B500B.

Figure 1. 3D model of the structure in SeismoStruct

During the analysis, the effects of seismic action and gravity (constant and variable) load were considered. Seismic impacts were determined by multimodal analysis with a design spectrum for the horizontal direction. To calculate the earthquake impact on the structure, an elastic response spectrum, type 1 (EN 1998) was used, for ground type C (*S*=1.15, *Tb*=0.2s, *Tc*=0.6s, and *Td*=2s), with the reference peak ground acceleration which amounts *ag*=0.2*g*. Since the building has a business-residential function, it corresponds to the class of importance II, for which the value of the important factor is γ=1. The damping value is 5% and the correlation factor due to damping is η=1.

For the analyzed construction, a high ductility class DCH was adopted.

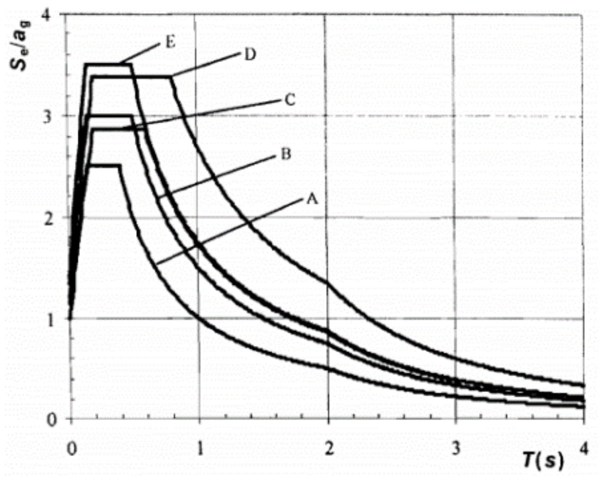

Figure 2. Recommended type 1 elastic response spectrum for soil categories A to E (5% damping)

The loads acting on the structure are as follows: permanent loads (*Gi*)- self-weight of the structural elements and an additional permanent load; the variable-live load (*Qi*) and the seismic load (*Si*). The assumed value of the permanent constant load is 6 kN/m2 on all floors. The load intensity of the variable-live load is also 2 kN/m2 on all floors. The value of the reduction factor of the variable-live loads is *Ψ2,i*=0.3 (EN1990).

In T-section beams, the effective flange width, over which uniform conditions of stress can be assumed, depends on the web and flange dimensions, the type of loading, the span, the support conditions, and the transverse reinforcement [8]. The effective width of the flange should be based on the distance l_0 between the points of zero moments, which may be obtained from Figure 3:

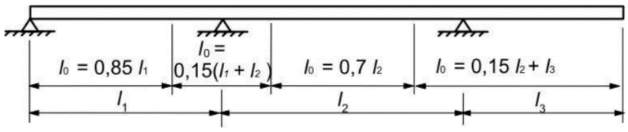

Figure 3. Definition of l_0 for calculation of effective flange width

The effective flange width b_{eff} for a T beam or L beam may be derived as [8]:

$$b_{eff} = \sum b_{eff,i} + b_w \leq b \tag{4}$$

with:

$$b_{eff,i} = 0{,}2 \cdot b_i + 0{,}1 \cdot l_0 \leq 0{,}2 \cdot l_0 \tag{5}$$

$$b_{eff,i} \leq b_i \tag{6}$$

(for the notations see Figure 3 above and Figure 4 below).

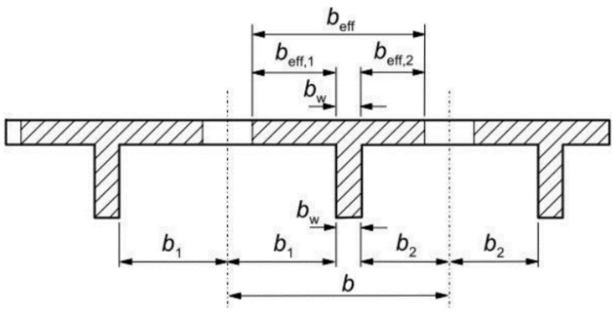

Figure 4. Effective flange width parameters

For structural analysis, where great accuracy is not required, a constant width may be assumed over the whole span. The value applicable to the span section should be adopted [8].

The dimensioning of the construction elements was carried out based on the authoritative combinations in the software package TOWER 8. The columns are square-shaped with dimensions of 0.45 x 0.45 m, and the beams are T and L cross-sections with dimensions: flange width 1.85 m, flange thickness 0.16 m, web width 0.45 m, and web height 0.19 m. The columns are reinforced with 12Ø28 and are weighted with stirrups UØ12/10cm on the length of the critical area and on the rest of the length UØ12/15cm. The beams at the support are reinforced in the upper zone with 5Ø20 and in the lower zone with 3Ø20, and the field in the lower zone with 3Ø20 and the upper zone with 2Ø20. Beam flanges are reinforced in the upper zone with Ø12/10cm and the lower zone with Ø12/20cm in both orthogonal directions. The cross-sections as well as the adopted layout of the element reinforcement are shown in Figure 5. The building meets the requirements of regularity in terms of base and height.

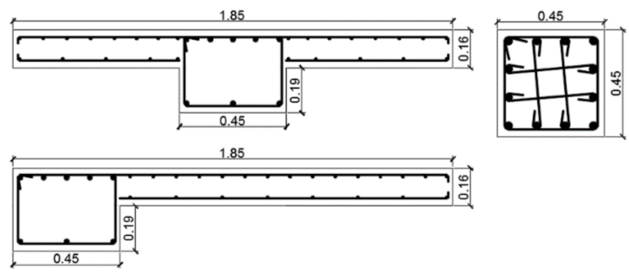

Figure 5. Cross sections of elements

The steel model used in the SeismoStruct is shown in Figure 6, and the concrete model is shown in Figure 7.

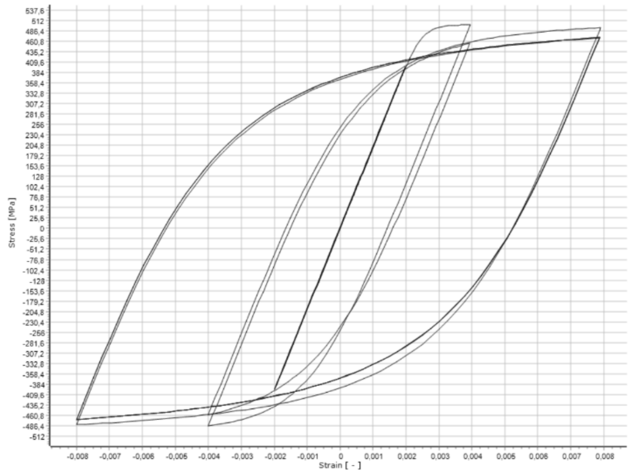

Figure 6. Uniaxial stress-strain relationship for steel reinforcement

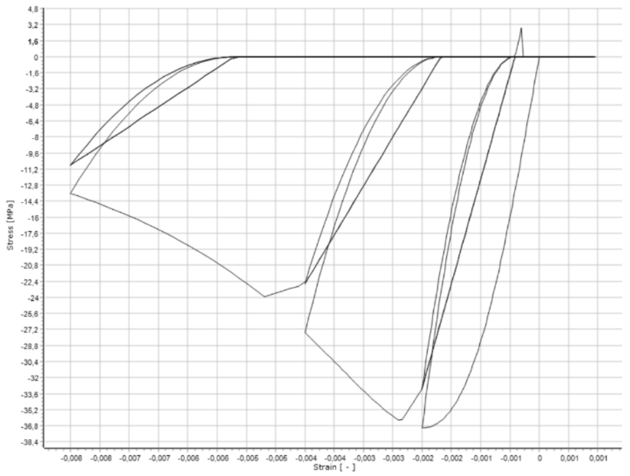

Figure 7. Uniaxial stress-strain relationship for concrete

In critical sections, in addition to the load-bearing conditions, the conditions of local ductility are also met:

For beams:

reinforcement coefficient of the tensioned zone:

ρ=0,7486 % $\leq \rho_{max}$=0,752 %

compression zone reinforcement coefficient:

ρ'=0,4489 % $\geq \rho_{tension}/2$

length of the critical zone:

l_{cr}= 1 m $\geq l_{cr,des}$ = 0,652 m

For columns:

total reinforcement coefficient:

ρ_{min}= 0,01 $\leq \rho$ = 0,0334 $\leq \rho_{max}$ = 0,04

length of the critical zone:

l_{cl}/h_c = 2,45/0,45 = 5,44 > 3 $\rightarrow l_{cr}$ = 0,675m

Fulfillment of requirements for adequate section weighting:

$$\alpha \cdot \omega_{wd} \geq 30 \cdot \mu_{\phi} \cdot \nu_d \cdot \varepsilon_{sy,d} \cdot \frac{b_c}{b_0} - 0{,}35 \rightarrow (0.333 > 0.2406)$$

After defining all the geometric and mechanical characteristics of the structure, a nonlinear static "pushover" analysis was carried out. The procedure was carried out for two orthogonal directions (X and Y) and the modal distribution of lateral forces.

Table 2. Forces in frame nodes for X and Y directions

Level	X	Y
V	183.366	122.244
IV	142.497	94.998
III	106.873	71.248
II	71.248	47.499
I	35.606	23.737

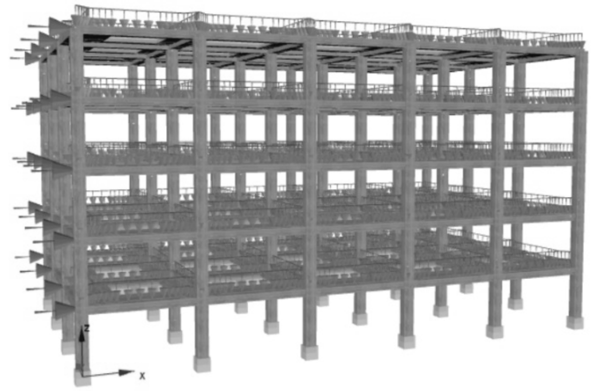

Figure 8. Applied loads in SeismoStruct for the X direction

Figure 9. Applied loads in SeismoStruct for the Y direction

Four different models were created in the program for seismic analysis to show the different effects of material nonlinearity: inelastic frame element (*infrmFB* and *infrmDB*) and inelastic plastic-hinge frame element (*infrmFBPH* and *infrmDBPH*).

InfrmFB- The force-based model in SeismoStruct is a type of finite element model used to simulate the nonlinear behavior of structures under seismic loads. It is based on the force-based beam-column element approach, which considers the internal forces and deformations of each element in the structure [9].

In this model, each element of the structure is modeled as a series of the interconnected beam and column elements, which are connected at nodes. The internal forces and deformations of each element are calculated based on the axial force, bending moment, and shear force diagrams.

One of the advantages of the Force-based model is that it can accurately simulate the behavior of structures under different types of seismic loads, including ground motion and lateral forces. It can be used to evaluate the seismic performance of structures and to design retrofitting measures to improve their seismic behaviour [10].

In recent years, force-based models have been used extensively in conjunction with modern computational tools, such as finite element analysis and computer-aided design software, to optimize the seismic design of structures and to ensure their safety and performance during earthquakes.

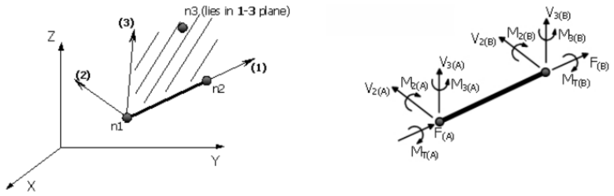

Figure 10. Local axes and output notation for elements [6]

InfrmDB- The displacement-based model in SeismoStruct is a type of finite element model used to simulate the nonlinear behavior of structures subjected to seismic loads. It is widely used in seismic analysis and design because it provides a more realistic representation of the actual behavior of structures under seismic loads. In this model, each element of the structure is divided into several smaller sub-elements, each of which is assumed to behave linearly elastically. The sub-elements are connected through nodes, and the displacement of each node is calculated based on the displacement of the neighboring nodes. The model also includes non-linear elements, such as plastic hinges, to represent the behavior of the structure beyond its elastic limit [11].

One of the advantages of the displacement-based model is that it is more accurate and reliable than the linear elastic model in predicting the response of structures under seismic loads. It can take into account the nonlinear behavior of the structure, such as the cracking and yielding of materials, and can provide more realistic estimates of the deformations and forces within the structure.

InfrmFBPH- The force-based plastic hinge model is a widely used modeling technique in the seismic analysis of structures. In this model, the plastic hinges are represented by two springs that act in parallel, one for the compression side and one for the tension side of the member [10]. The stiffness and strength of these springs are based on the yield strength and the cross-sectional properties of the member.

The model assumes that the member behaves in an elastic manner until the yield strength is reached, at which point plastic deformation occurs [12]. The plastic deformation is then accommodated entirely by the plastic hinge, while the rest of the member remains elastic. The plastic hinge is assumed to have a fixed length, which is defined by the user.

InfrmDBPH- In The Displacement-based plastic hinge model, the plastic hinges are represented by a non-linear element that is connected to the elastic members on either side of the hinge. The element has a specific displacement capacity, beyond which it undergoes plastic deformation. The element's displacement capacity is based on the yield strength and the cross-sectional properties of the member.

The displacement-based plastic hinge model assumes that the member behaves elastically until the displacement capacity of the plastic hinge is reached, at which point the plastic deformation occurs. The model accounts for the degradation of stiffness and strength of the member after reaching the displacement capacity of the plastic hinge.The infrmDBPH element consists of 3 sub-elements, two joints at the edges of the member, which model plastic rotational deformations around the second and third local axes, and an elastic element in the middle, which models the part of the element that remains elastic [12].

A total of 8 "pushover" load cases are defined. For all 8 load cases, the increment method is controlled by displacements and a maximum displacement of 150% of the target displacement for the control point (master node), shown in Figure 11.

Figure 11. Master node

4. RESULTS

4.1. Target displacement

Target displacement is an important concept in seismic analysis, which refers to the expected amount of movement or deformation that a particular structure or component will experience during an earthquake or other seismic influence.

In general, the target displacement for a structure will depend on a variety of factors, including the expected severity and frequency of seismic events in the region, the type and size of the structure, and the materials used in its construction. By carefully analyzing these factors and designing structures to withstand the expected levels of displacement, engineers can help minimize the risk of damage and ensure the safety of people and property in areas prone to earthquakes.

Target displacement is defined as the seismic demand determined from the elastic response spectrum, through the displacement of the equivalent system with a single degree of freedom (SDOF) [citiraj dinamiku konstrukicja]. The mass of the equivalent SDOF system m* is determined as:

$$m^* = \sum m_i \Phi_i = \sum \overline{F}_i \tag{7}$$

and the transformation factor is given by:

$$\Gamma = \frac{m^*}{\sum m_i \Phi_i} = \frac{\sum \overline{F}_i}{\sum\left(\frac{\overline{F}_i^{\,2}}{m_i}\right)} \tag{8}$$

Force F^* and displacement d^* of the equivalent SDOF system is calculated as:

$$F^* = \frac{F_b}{\Gamma} \tag{9}$$

$$d^* = \frac{d_n}{\Gamma} \tag{10}$$

where F_b and d_n are based-shear and displacement, respectively, of the control node of the multi-degree of freedom (MDOF) system [7].

Yield force F_y^*, which also represents the limit bearing capacity of an idealized system, is equal to the base shear when a formation of the plastic mechanism occurs. The initial stiffness of the idealized system is defined so that the area under the actual and idealized force-displacement curve is equal. Based on this assumption, the yield displacement of the idealized SDOF system is given by:

$$d_y^* = 2\left(d_m^* - \frac{E_m^*}{F_y^*}\right) \tag{11}$$

where E_m^* is the actual deformation energy up to the formation of the plastic mechanism (Figure 12)[7].

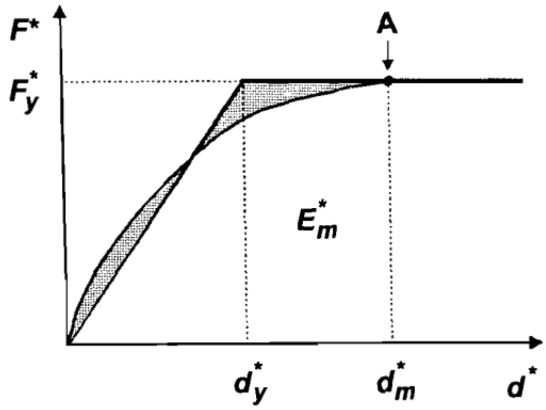

Figure 12. Idealized elastic-perfectly-plastic force displacement relation

Period T^* of the idealized equivalent SDOF system is determined by:

$$T^* = 2\pi\sqrt{\frac{m^* d_y^*}{F_y^*}} \tag{12}$$

Control displacement of the SDOF system for unlimited elastic behaviour equals:

$$d_{et}^* = S_e(T^*)\left[\frac{T^*}{2\pi}\right]^2 \tag{13}$$

where $S_e(T^*)$ is the acceleration obtained from the elastic response spectrum for the period T^*.

For $T^*<T_c$, target displacement is obtained from the following expressions:

If $F_y^*/m^* \geq S_e(T^*)$, response is elastic:

$$d_t^* = d_{et}^* \tag{14}$$

If $F_y^*/m^* < S_e(T^*)$, response is inelastic:

$$d_t^* = \frac{d_{et}^*}{q_u}\left(1 + (q_u - 1)\frac{T_C}{T^*}\right) \tag{15}$$

where q_u equals:

$$q_u = \frac{S_e(T^*)m^*}{F_y^*} \tag{16}$$

For $T^* \geq T_c$, target displacement is obtained from the expression (8), where d_t^* should not exceed the value $3d_{et}^*$.

Target displacement for the MDOF system is finally determined as:

$$d_t = \Gamma d_t^* \tag{17}$$

Based on the obtained calculation results, a very similar form of force-displacement dependence is noticeable, for both orthogonal directions. The highest value of the displacement of the master node when reaching 150% of the target displacement has the *infrmDBPH* model, and the least is the *infrmFB model.*

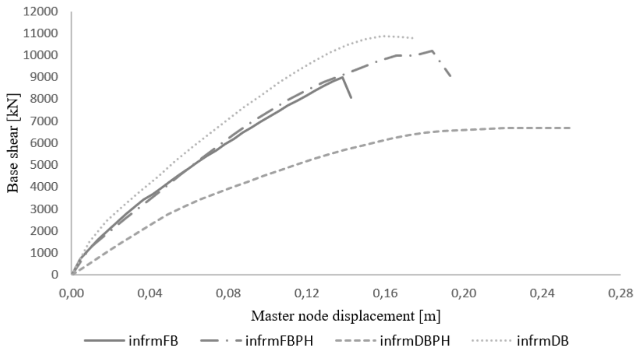

Figure 13. Pushover curves for X direction

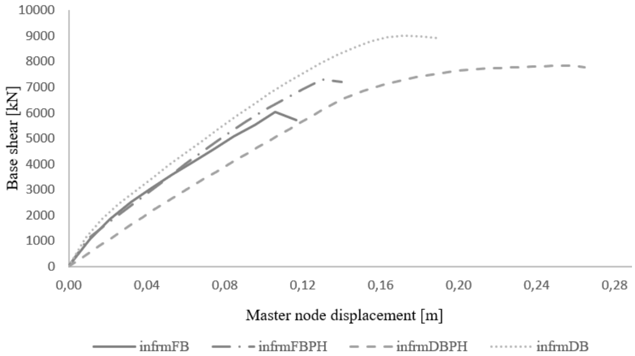

Figure 14. Pushover curves for Y direction

This is also very well visualized in Figure 15 plotting maximum base shear forces for all of the pushover load cases.

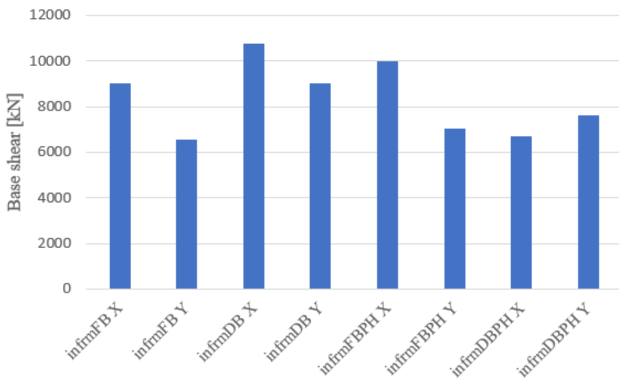

Figure 15. Maximun base shear vs. pushover load case

A manual verification of the results was performed. The calculation of the target displacement as well as the comparison with the results from the software is shown in Table 3 for the X direction and Table 4 for the Y direction.

Table 3. Calculation of target displacement for X direction

	infrmFB	infrmDB	infrmFBPH	infrmDBPH
Γ	1.063	1.063	1.063	1.063
F_y^*	9942.93	10856.61	10190.58	6693.19
d_m^*	0.23	0.153	0.1302	0.2378
E_m^*	888.81	395.66	448.66	623.58
d_y^*	0.281	0.233	0.172	0.289
T^*	0.751	0.654	0.580	0.928
$S_e(T^*)$	4.509	5.175	5.831	3.648
$d_t^*=d_{et}^*$	0.064	0.056	0.050	0.080
$d_t=\Gamma\cdot d_t^*$	0.068	0.060	0.053	0.085
SeismoStruct	0.067	0.060	0.059	0.083

Table 4. Calculation of target displacement for Y direction

	infrmFB	infrmDB	infrmFBPH	infrmDBPH
Γ	1.063	1.063	1.063	1.063
F_y^*	7652.32	9011.74	8126.6	7843.11
d_m^*	0.2338	0.172	0.13	0.2392
E_m^*	703.92	399.84	432.64	723
d_y^*	0.284	0.255	0.154	0.294
T^*	0.859	0.751	0.613	0.864
$S_e(T^*)$	3.939	4.506	5.517	3.917
$d_t^*=d_{et}^*$	0.074	0.064	0.053	0.074
$d_t=\Gamma\cdot d_t^*$	0.078	0.068	0.056	0.079
SeismoStruct	0.078	0.067	0.065	0.078

Relative floor displacement is shown in Figure 16 for the X direction and in Figure 17 for the Y direction. As shown in the Figures, model *infrmFBPH* has the lowest value of relative floor displacement.

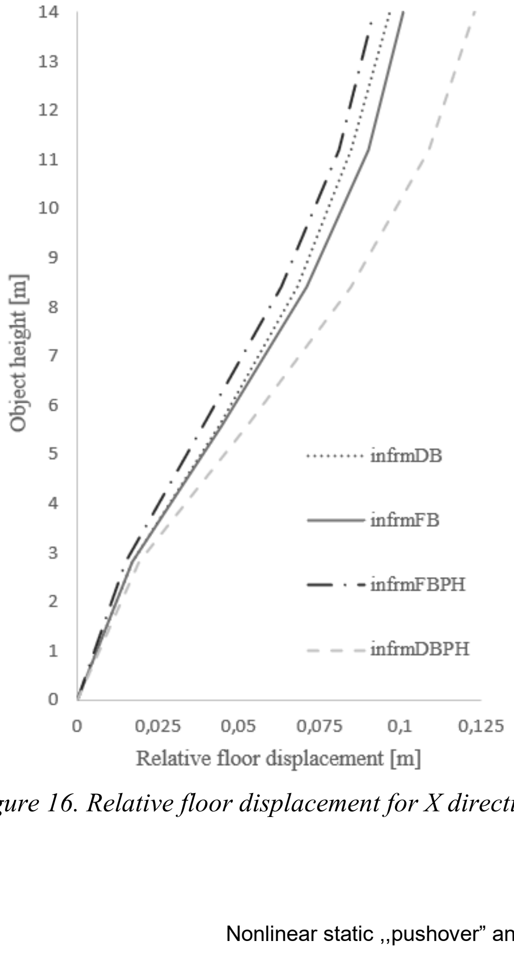

Figure 16. Relative floor displacement for X direction

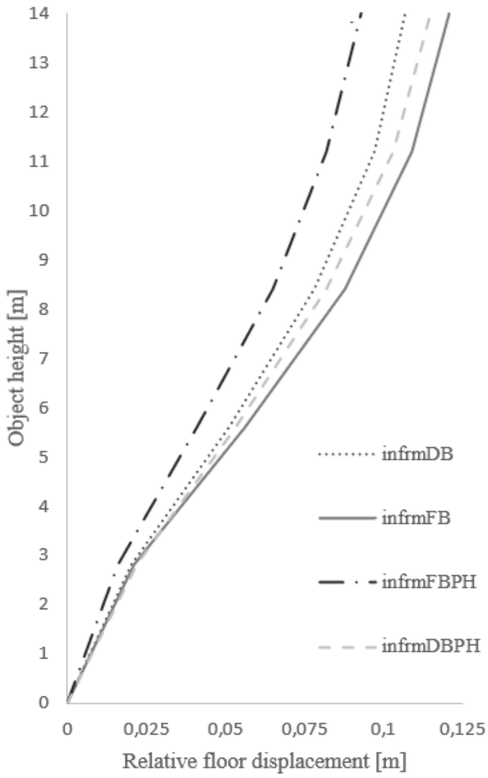

Figure 17. Relative floor displacement for Y direction

The schedule for the appearance of plastic hinges when reaching 150% of the target displacement is shown in Figure 18 and Figure 19. The considered criteria for the appearance of plastic hinges are shear capacity, yielding, concrete strain, fracture, and chord rotation. Figure 18 shows the schedule for the appearance of plastic hinges for the X direction and Figure 19 for the Y direction. As can be seen in the figures, plastic hinges occur when shear capacity and yielding conditions are exceeded.

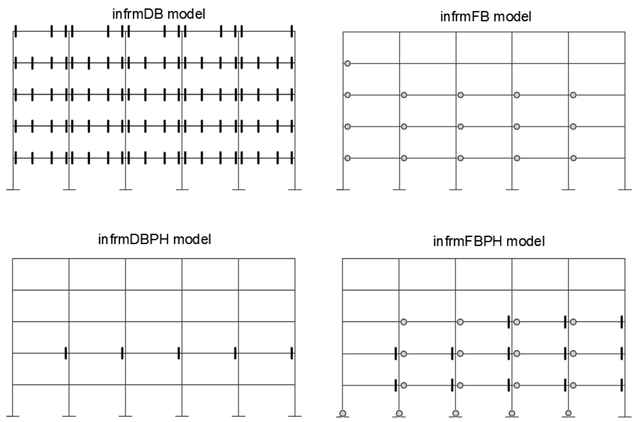

Figure 18. Schedule of appearance of plastic hinges for X direction (| -shear capacity; ●- yielding)

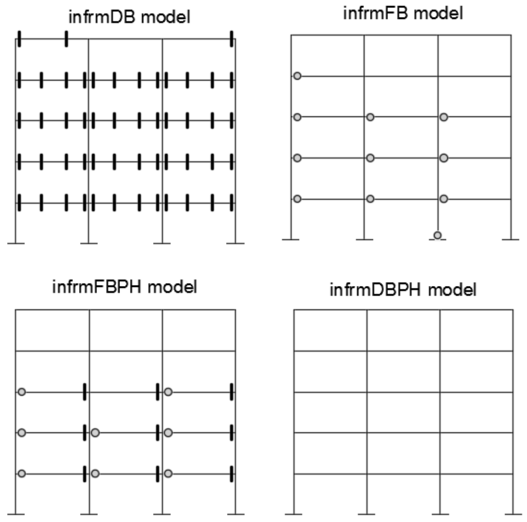

Figure 19. Schedule of appearance of plastic hinges for the Y direction (| -shear capacity; ●- yielding)

Another criterion for evaluating the seismic performance of this building is the value of total chord rotation capacity. This value is calculated according to the expression 18 given in EN 1998-3:

$$\theta_{um} = \frac{1}{\gamma_{el}} \cdot 0.016 \cdot (0.3^{\nu}) \cdot \left[\frac{\max(0.01;\omega')}{\max(0.01;\omega)} \cdot f_c\right]^{0.225} \cdot \left(\frac{L_v}{h}\right)^{0.35} \cdot 25^{\left(\alpha \cdot \rho_{sx} \cdot \frac{f_{yw}}{f_c}\right)} \cdot (1.25^{100 \cdot \rho_d}) \quad (18)$$

where:

γ_{el} is equal to 1.5 for primary seismic elements and 1.0 for secondary seismic elements,

$\nu = N/bhf_c$ (b width of compression zone, N axial force positive for compression),

ω, ω' is the mechanical reinforcement ratio of the tension and compression, respectively, longitudinal reinforcement,

$L_v = M/V$ is the ratio moment/shear at the end section,

h is the depth of cross-section,

α is the confinement effectiveness factor,

$\rho_{sx} = A_{sx}/b_w s_h$ is the ratio of transverse steel parallel to the direction *x* of loading,

f_c and f_{yw} are the concrete compressive strength (MPa) and the stirrup yield strength (MPa),

ρ_d is the steel ratio of diagonal reinforcement (if any), in each diagonal direction [7].

Table 5 shows the results of the value obtained by applying expression 18, as well as their comparison with the limit values when reaching 150% of the target displacement.

Table 5. Values of total chord rotation for X and Y direction

	X direction		Y direction	
	demand	limit	demand	limit
infrmFB	0.0061	0.0683	0.0075	0.0744
infrmDB	0.0011	0.0409	0.0013	0.0436
infrmFBPH	0.0036	0.0693	0.0038	0.0811
infrmDBPH	0.0069	0.073	0.0089	0.721

5. CONCLUSION

Nonlinear static pushover analysis of a reinforced concrete building was performed using four different material nonlinearity models for two orthogonal directions. By observing the results of the seismic performance assessment of this object, the following conclusions are reached:

- pushover curves and target displacement: *infrmDBPH* model has the highest value of displacement (0.25 m for the X and 0.26 m for the Y direction); the *infrmFB* model has the lowest value of displacement (0.15 m for the X and 0.11 m for the Y direction);
- relative floor displacement: for the X direction, model *infrmDBPH* has the highest value (0.123 m) and *the infrmFPBH* model has the lowest value (0.092 m); for the Y direction, model *infrmFB* has the highest value (0.121 m) and *infrmFBPH* model has the lowest value (0.093 m);
- plastic hinges: due to exceeding the yield criteria, the models where plastic hinges appear are *infrmFB* and *infrmFBPH*; from the aspect of shear capacity criteria, the only model in which plastic hinges do not occur is *infrmFB* model;
- total chord rotation: the highest values have *the infrmDBPH* model (0.0069 for the X, and 0.0089 for the Y direction), and the lowest values have *the infrmDB* model (0.0011 for the X and 0.0013 for the Y direction).

Analyzing the results, it is concluded that the models with the mean values of the considered criteria (shear capacity, yielding, relative floor displacement, chord rotation capacity) are *infrmFB* and *infrmFBPH* models. Models *infrmDB* and *infrmDBPH* have extreme values of chord rotation and relative floor displacement.

REFERENCES

[1] Lađinović, Đ.: Savremene metode seizmičke analize konstrukcija zgrada. Materijali i konstrukcije, 2008., vol. 51, № 1, p.p. 25-40.

[2] Svilar, M., Prokić A.: Pushover analiza armiranobetonskog okvira. *7. međunarodna konferencija-savremena građevinska dostignuća u građevinarstvu 23-24.april 2019. Subotica*, **2019.**, p.p. 363-370.

[3] Obradović N., Mitković P., Radovanović S.: Nelinearna statička metoda postupnog guranja – pushover analiza AB okvira sa zidanom ispunom. *Zbornik radova Međunarodnog simpozijuma o istraživanjima i primeni savremenih dostignuća u građevinarstvu u oblasti materijala i konstrukcija*, Vršac, 18-20. oktobar 2017, **2017.**, pp. 245-254.

[4] Petronijević M., Marjanović M., Radeka P.: Seismic Assessment of RC Buildings using N2 Method. Zbornik radova- Šesto međunarodno naučno-stručno savetovanje Zemljotresno inženjerstvo i inženjerska seizmologija, Beograd 13-15. jun 2018, **2018.**, pp. 387-395.

[5] Radujković A., Rašeta A., Lađinović Đ.: Seizmička analiza AB okvirne konstrukcije primenom nelinearne metode N2, Zbornik Radova, DGKS, Simpozijum 2008, Zlatibor 2-26. septembar 2008, **2008.** pp. 369-376.

[6] SeismoStruct-User Manual, **2021.**

[7] EN 1998-1, Design of structures for earthquake resistance - Part 1: General rules, seismic actions and rules for buildings, European Committee for Standardization. Brussels, **2004.**

[8] EN 1992-1-1, Design of Concrete Structures, Part 1-1: General rules and rules for buildings, European Committee for Standardization. Brussels, **2004.**

[9] Scott M. H., Fenves G. L.: Plastic Hinge Integration Methods for Force-Based Beam-Column Elements. Journal of structural engineering ASCE, **2006.** pp. 244-252.

[10] Salehi M., Siders P., Liel A. B.: Seismic collapse analysis of RC framed structures using the gradient inelastic force-based element formulation. 16th World Conference on Earthquake, Santiago Chile 9-13. January 2017, **2017.**, vol. 12, № 2990.

[11] Tarquini D., Almeida J. P., Beyer K.:An enhanced displacement-based element to account for tension shift effects. 16th World Conference on Earthquake, Santiago Chile 9-13. January 2017, **2017.**, vol. 12, № 3167.

[12] Rajić N., Lađinović Đ.: Nonlinear static seismic analysis of multi-story RC building, *6. međunarodna konferencija-savremena građevinska dostignuća u građevinarstvu 21.april 2017. Subotica*, **2017.**, p.p. 287-295.

SUPPORTED BY:

The Ministry of Science, Technological Development and Innovation of the Republic of Serbia

The Serbian Chamber of Engineers

TeamCAD d.o.o. Zemun-Belgrade

Banim reklame d.o.o. Kraljevo

Radijator Inženjering d.o.o. Kraljevo

Messer Tehnogas AD Belgrade

CIP - Каталогизација у публикацији Народна библиотека Србије, Београд

621(082)
621.86/.87(082)
629.3/.4(082)
622.6(082)
681.5(082)

INTERNATIONAL Triennial Conference Heavy Machinery (11 ; 2023 ; Vrnjačka Banja)
Proceedings / The Eleventh International triennial conference Heavy machinery
HM 2023, 21 – 24 June 2023, Vrnjačka Banja, Serbia ; [editor Mile Savković]. - Kraljevo : Faculty of Mechanical and Civil Engineering, 2023 (Vrnjačka Banja : SaTCIP). - 1 knj. (razl. pag.) : ilustr. ; 30 cm

Tiraž 60. - Str. 5: Preface / Mile Savković. - Bibliografija uz svaki rad.

ISBN 978-86-82434-01-6

a) Машиноградња -- Зборници b) Транспортна средства -- Зборници
v) Производно машинство -- Зборници g) Шинска возила -- Зборници
d) Аутоматско управљање -- Зборници

COBISS.SR-ID 120402697

Faculty of Mechanical
and Civil Engineering in Kraljevo
University of Kragujevac
Serbia, 36000 Kraljevo, Dositejeva 19
Phone/fax +381 36 383 269, 383 377

E-mail: office@mfkv.kg.ac.rs
www.mfkv.kg.ac.rs